Seismic Source Characterization for the Diablo Canyon Power Plant, San Luis Obispo County, California

March 2015

Seismic Source Characterization for the Diablo Canyon Power Plant, San Luis Obispo County, California

Report on the results of a SSHAC level 3 study, conducted in partial compliance with the request for information pursuant to Title 10 of the Code of Federal Regulations 50.54(f) regarding Fukushima near-term task force recommendation 2.1: Seismic

Report prepared for:

Pacific Gas and Electric Company
San Francisco, California

Report prepared by:

SSHAC Level 3 Technical Integration (TI) Team

March 2015
Rev. A

Primary Report Authors (TI Team Members) and Affiliations

William Lettis	Lettis Consultants International, Inc., Walnut Creek, California
Hans AbramsonWard	Lettis Consultants International, Inc., Walnut Creek, California
Glenn Biasi	University of Nevada, Reno, Reno, Nevada
John Caskey	San Francisco State University, San Francisco, California
Kathryn Hanson	Amec Foster Wheeler, Oakland, California
Stephen Thompson	Lettis Consultants International, Inc., Walnut Creek, California

Report Contributors and Affiliations

Norman Abrahamson	Pacific Gas and Electric Company, San Francisco, California
Serkan Bozkurt	Lettis Consultants International, Inc., Walnut Creek, California
Nick Gregor	Nick Gregor Consulting, Oakland, California
Nora Lewandowksi	Lettis Consultants International, Inc., Walnut Creek, California
Alex Remar	Lettis Consultants International, Inc., Walnut Creek, California
Nancy Sutherland	Amec Foster Wheeler, Inc., Oakland, California
Kathryn Wooddell	Pacific Gas and Electric Company, San Franciso, California

Availability Notice

This report is available for download online at http://www.pge.com/dcpp-ltsp.

How to cite this document:

Pacific Gas and Electric Company (PG&E), 2015. Seismic Source Characterization for the Diablo Canyon Power Plant, San Luis Obispo County, California; report on the results of a SSHAC level 3 study, Rev. A, March. Available online at http://www.pge.com/dcpp-ltsp.

TABLE OF CONTENTS

Page

LIST OF TABLES xiii
LIST OF FIGURES xv
LIST OF PLATES xxvii
LIST OF APPENDICES xxvii
LIST OF ABBREVIATIONS, ACRONYMS, AND SYMBOLS xxviii
ACKNOWLEDGMENTS xxxii
EXECUTIVE SUMMARY ES-1
1.0 INTRODUCTION 1-1
1.1 Objectives of the SSC Study 1-2
1.1.1 NRC Directive, Regulatory Criteria, and Guidelines 1-3
1.1.2 Site-Specific SSC Model 1-4
1.1.3 Interface with the SWUS GMC Model 1-4
1.2 Previous Seismic Hazard Studies for DCPP 1-5
1.3 Products of the Project 1-6
1.4 Changes During the Project 1-7
2.0 PROJECT ORGANIZATION 2-1
2.1 Implementation of the SSHAC Level 3 Process 2-1
2.1.1 Description of the SSHAC Methodology 2-1
2.1.2 Selection of SSHAC Study Level 2-2
2.2 Project Organization 2-3
2.2.1 Project Sponsor and Project Manager 2-4
2.2.2 Project Technical Integrator 2-4
2.2.3 Technical Integration Team 2-4
2.2.4 Participatory Peer Review Panel 2-7
2.2.5 Evaluator Experts and Integrator Experts 2-8
2.2.6 Resource Expert 2-9
2.2.7 Proponent Expert 2-9
2.2.8 Hazard Analyst 2-9
2.2.9 Database Manager 2-10
2.2.10 Outside Observers 2-10

2.3 Database Development and New Studies 2-10
2.3.1 CCCSIP Offshore and Onshore Studies 2-11
2.3.2 USGS CRADA Studies 2-11
2.3.3 Other Studies 2-11
2.3.4 Independent SSHAC Data Collection and Evaluation Studies 2-12
2.3.5 Quality Assurance 2-12
3.0 PROJECT PLAN 3-1
3.1 Diablo Canyon SSC Project Plan 3-1
3.1.1 Evaluation.....3-1
3.1.2 Integration 3-4
3.1.3 Peer Review 3-5
3.1.4 Documentation 3-5
3.2 Diablo Canyon SSC Key Tasks and Activities 3-6
3.2.1 Task 1—Preparation of Project Plan and Identification of Significant Issues.....3-6
3.2.2 Task 2—Database Development 3-6
3.2.3 Task 3—Kickoff Meeting.....3-7
3.2.4 Task 4—Initial Data Evaluation and Preparation for Workshop 1 3-8
3.2.5 Task 5—Workshop 1: Hazard-Significant Issues and Available Data.....3-8
3.2.6 Task 6—Data Evaluation and Preparation for Workshop 2 3-9
3.2.7 Task 7—Workshop 2: Alternative Models 3-10
3.2.8 Task 8—Preliminary Model Development and Preparation for Workshop 3 3-11
3.2.9 Task 9—Workshop 3: Preliminary Model and Hazard Feedback ...3-12
3.2.10 Task 10—Final Model Development and PPRP Final Briefing 3-13
3.2.11 Task 11—Development of Hazard Input Documents 3-14
3.2.12 Task 12—Development of Draft SSC Report.....3-14
3.2.13 Task 13—PPRP Review of Draft SSC Report.....3-14
3.2.14 Task 14—Development of Final SSC Report.....3-15
3.2.15 Task 15—PPRP Closure Letter 3-15
4.0 SSC DATABASE: GEOLOGY, SEISMOLOGY, AND GEOPHYSICS 4-1
4.1 Overview and Purpose.....4-1
4.2 Legacy Data.....4-2

4.2.1 Final Safety Analysis Report Data 4-2
4.2.2 1988 LTSP Report and Data....4-2
4.2.3 Shoreline Fault Zone Report and Data 4-3
4.2.4 LTSP Legacy Seismic Profiles Database....4-4
4.3 Recently Acquired Data (Post-2011) 4-4
4.3.1 Central Coastal California Seismic Imaging Project 4-5
4.3.1.1 New Offshore (LESS) Data....4-6
4.3.1.2 Onshore (ONSIP) Data and Geologic Mapping Program 4-6
4.3.2 PG&E–USGS CRADA and PG&E LTSP Studies....4-7
4.3.2.1 USGS Analyses of Offshore Data 4-7
4.3.2.2 USGS Analyses of Seismicity Data....4-8
4.3.2.3 USGS Analyses of Aeromagnetic Data....4-9
4.3.2.4 USGS Structural Cross Section Across Irish Hills 4-9
4.3.2.5 GPS and Geodetic Data 4-10
4.3.2.6 California State Mapping Program 4-11
4.3.2.7 PG&E Offshore Seismic Stratigraphy Study....4-11
4.3.2.8 LTSP Quaternary Analyses of Fluvial and Marine Terraces in the Los Osos and Edna Valleys....4-12
4.3.2.9 San Francisco State University Studies 4-13
5.0 SEISMOTECTONIC SETTING OF THE DIABLO CANYON REGION 5-1
5.1 Tectonic Setting 5-1
5.1.1 Mesozoic Subduction....5-2
5.1.2 Cenozoic Transition from Subduction to Transform Plate Margin....5-2
5.1.3 Neogene Rotation of Western Transverse Ranges, Basin Formation, and Onset of Transpression in the Diablo Canyon Region 5-4
5.1.4 Early to Mid-Pleistocene Deformation of the San Luis Range....5-7
5.1.5 Contemporary Tectonic Setting 5-7
5.1.6 Contemporary Strain Rates and Orientations Based on Geodetic and Seismicity Analysis 5-10
5.2 Site Area Faults....5-12
5.2.1 Hosgri Fault Zone 5-13
5.2.2 Los Osos Fault Zone 5-15
5.2.3 Southwestern Boundary Zone and San Luis Bay Fault....5-16

5.2.4 Shoreline Fault Zone 5-17
5.3 Regional Seismic Setting 5-18
5.4 Alternative Styles of Active Deformation in the Diablo Canyon Vicinity 5-20
6.0 SEISMIC SOURCE CHARACTERIZATION OVERVIEW 6-1
6.1 Definition and Applicability 6-1
6.2 Types of Seismic Sources 6-1
6.3 Primary and Connected Fault Sources 6-3
6.3.1 Fault Geometry Models 6-9
6.3.2 Fault Slip Rate Model 6-12
6.3.3 Rupture Models 6-12
6.3.3.1 Approach 6-12
6.3.3.2 Motivation 6-13
6.3.3.3 Rupture Source Types 6-14
6.3.4 Slip Rate Allocation Models 6-15
6.3.5 Magnitude Distribution Models 6-16
6.3.5.1 Approach 6-17
6.3.6 Time Dependency Model 6-19
6.4 Regional Fault Sources 6-20
6.5 Areal Source Zones 6-21
7.0 FAULT GEOMETRY MODELS 7-1
7.1 Definition and Applicability 7-1
7.2 Approach 7-1
7.2.1 Seismogenic Thickness and Depth of Faulting 7-2
7.2.2 Depth to Top of Rupture 7-4
7.2.3 Fault Geometry 7-5
7.2.4 Sense of Slip (Style of Faulting) 7-8
7.3 Hosgri Fault Zone Geometry Models 7-9
7.3.1 Fault Location Adjacent to the DCPP 7-10
7.3.2 Fault Dip 7-11
7.3.3 Fault Length 7-13
7.4 San Luis–Pismo Block Fault Geometry Models 7-13
7.4.1 Outward-Vergent Model 7-15
7.4.1.1 Possible Analog 7-17

7.4.2 Southwest-Vergent Model....7-18
7.4.2.1 Possible Analog....7-20
7.4.3 Northeast-Vergent Model....7-20
7.4.3.1 Possible Analogs....7-22
7.5 SLPB Logic Tree Model Weights....7-23
8.0 FAULT SLIP RATE MODEL....8-1
8.1 Definition and Applicability....8-1
8.2 Approach....8-1
8.2.1 Geologic Slip Rate CDFs....8-2
8.2.2 Quaternary Uplift Rate....8-4
8.2.2.1 San Luis Range....8-4
8.2.2.2 Cayucos Study Area....8-6
8.2.2.3 Los Osos and Edna Valleys Study Area....8-8
8.3 Hosgri Fault....8-10
8.3.1 Onshore San Simeon Slip Rate Estimate....8-11
8.3.2 Point Estero Slip Rate Estimate....8-14
8.3.3 Piedras Blancas Anticlinorium/West Hosgri Slip Rate Constraints....8-15
8.3.4 Age Constraints on Channels Buried Beneath Continental Shelf....8-17
8.3.4.1 Upper Pleistocene Sequence Stratigraphy....8-17
8.3.4.2 Shelf Progradation Following the Mid-Pleistocene Transition....8-18
8.3.4.3 Characterization of Uncertainty in Channel Ages....8-20
8.3.5 Southern Estero Bay Slip Rate Estimate....8-22
8.3.6 Point Sal Slip Rate Estimate....8-25
8.3.7 Development of a Hosgri Fault CDF....8-27
8.3.8 Equivalent Five-Point Distribution and Comparison to Other Studies....8-30
8.3.8.1 Previous PG&E Studies....8-30
8.3.8.2 UCERF2....8-31
8.3.8.3 UCERF3....8-31
8.3.8.4 DeMets Analysis of GPS Velocity Data....8-31
8.4 Shoreline Fault....8-32
8.4.1 Terrace Sequence Slip Rate Estimate....8-33

8.4.2 Channel I Slip Rate Estimate 8-36
8.4.3 Channel A Slip Rate Estimate 8-38
8.4.4 Development of Slip Rate CDF 8-43
8.4.4.1 Assessment of Slip Rate for Southern Part of Shoreline Fault 8-43
8.4.4.2 Estimate of Dextral Slip Rate Contributed from the Southwestern Boundary Zone 8-44
8.4.4.3 Shoreline Fault Slip Rate at the DCPP 8-50
8.4.5 Equivalent Five-Point Distribution and Comparison to Other Studies 8-50
8.5 Los Osos Fault 8-51
8.5.1 Information on Slip Sense and Slip Rate 8-51
8.5.2 Development of Slip Rate CDFs 8-53
8.5.3 Equivalent Five-Point Distribution and Comparison to Other Studies 8-54
8.6 San Luis Bay Fault 8-55
8.6.1 Information on Slip Sense and Slip Rate 8-55
8.6.2 Development of Slip Rate CDFs 8-56
8.6.3 Equivalent Five-Point Distribution and Comparison to Other Studies 8-56
8.7 Other Site Vicinity Faults 8-57
8.7.1 Wilmar Avenue Fault 8-57
8.7.2 Oceano Fault 8-58
9.0 RUPTURE MODELS 9-1
9.1 Applicability to the SSC Model 9-1
9.2 Diablo Canyon SSC Rupture Models 9-3
9.2.1 Methodology to Develop Rupture Sources 9-3
9.2.1.1 Types of Rupture Sources 9-3
9.2.1.2 Definition of Rupture Topology 9-5
9.2.1.3 Rupture Source Endpoints 9-5
9.2.1.4 Definition of Rupture Models 9-8
9.2.1.5 Rupture Event Analogs 9-8
9.2.2 Hosgri Fault Rupture Model 9-14
9.2.3 Outward-Vergent Rupture Model 9-17
9.2.4 Southwest-Vergent Rupture Model 9-20

9.2.5 Northeast-Vergent Rupture Model 9-23
9.3 Slip Rate Allocation Model 9-27
9.3.1 Slip Rate Allocation Methodology 9-27
9.3.2 Hosgri Slip Rate Allocation Model 9-31
9.3.2.1 Allocation of the Mean Slip Rate 9-32
9.3.2.2 Hosgri Rupture Source Slip Rates for the SSC Logic Tree 9-35
9.3.3 OV Slip Rate Allocation Model 9-35
9.3.3.1 Allocation of the Mean Slip Rate—OV Model 9-36
9.3.3.2 OV Rupture Source Slip Rates for the SSC Logic Tree....9-37
9.3.4 SW Slip Rate Allocation Model 9-38
9.3.4.1 Allocation of the Mean Slip Rate—SW Model 9-39
9.3.4.2 SW Rupture Source Slip Rates for the SSC Logic Tree ...9-41
9.3.5 NE Slip Rate Allocation Model 9-42
9.3.5.1 Allocation of the Mean Slip Rate—NE Model 9-42
9.3.5.2 NE Rupture Source Slip Rates for the SSC Logic Tree....9-44
9.4 Slip Rate of the Hosgri Fault North of the DCPP 9-45
10.0 MAGNITUDE DISTRIBUTION MODELS 10-1
10.1 Definition and Applicability 10-1
10.2 Approach.....10-1
10.2.1 Candidate Magnitude PDF Models 10-2
10.2.1.1 Truncated Exponential Model 10-3
10.2.1.2 Simplified Maximum Magnitude Model.....10-3
10.2.1.3 Characteristic Earthquake Model 10-4
10.2.1.4 WAACY Model.....10-4
10.2.2 Selection of Values for Characteristic and Maximum Magnitudes ..10-5
10.2.2.1 Segmentation Concepts.....10-6
10.2.2.2 Selection of Characteristic and Maximum Rupture Lengths 10-7
10.2.2.3 Magnitude-Area Relations 10-10
10.2.3 Application of Magnitude PDFs to Rupture Sources 10-13
10.2.4 Model Evaluation—MFDs at Points 10-15
10.2.4.1 Estimating Fault Activity at Points 10-16

10.2.4.2 Geometric Reduction Approach 10-16
10.3 Hosgri Magnitude Distribution Model 10-18
10.4 Outward-Vergent Magnitude Distribution Model 10-22
10.5 Southwest-Vergent Magnitude Distribution Model 10-26
10.6 Northeast-Vergent Magnitude Distribution Model 10-31
10.7 Magnitude-Frequency Distributions for Specific Points on the Primary Faults10-35
10.7.1 Hosgri Fault Source 10-36
10.7.2 Shoreline Fault Source 10-37
10.7.3 Los Osos Fault Source 10-38
10.7.4 San Luis Bay Fault Source 10-39
11.0 TIME DEPENDENCY MODEL 11-1
11.1 Definition and Applicability 11-1
11.2 Approach 11-2
11.2.1 DCPP Regional Data and Estimation of Equivalent Poisson Ratios 11-2
11.2.2 Conditional Probability of an Earthquake 11-4
11.2.3 Development of Equivalent Poisson Ratios 11-6
11.2.4 Evaluation of Recurrence Model Functional Forms 11-9
11.2.5 Equivalent Poisson Ratios for Primary and Connected Faults 11-10
11.2.6 Equivalent Poisson Ratios for Regional Faults 11-11
11.2.7 Other Processes Affecting Recurrence 11-13
11.3 Logic Tree 11-13
11.3.1 Poisson or Non-Poisson Earthquake Distributions 11-15
11.3.2 Equivalent Poisson Ratios for Logic Tree Application 11-15
11.4 Summary 11-16
12.0 REGIONAL FAULT SOURCES 12-1
12.1 Definition and Applicability 12-1
12.2 Approach 12-1
12.3 Methodology to Implement the UCERF3 Statewide Model for the Diablo Canyon SSC Model 12-2
12.4 San Andreas Fault Source 12-3
12.5 UCERF3 Regional Fault Sources 12-5
12.6 Non-UCERF3 Regional Fault Sources 12-6

12.6.1 Descriptions of Non-UCERF3 Regional Fault Sources 12-7
12.6.1.1 Lompoc and Purisima Structures 12-7
12.6.1.2 Queenie Structure.....12-7
12.6.1.3 Santa Lucia Bank Fault.....12-8
12.6.1.4 West Basin–Southwest Channel Fault 12-9
12.6.2 Characterization of Non-UCERF3 Regional Fault Sources 12-10
13.0 AREAL SOURCE ZONES 13-1
13.1 Definition and Applicability 13-1
13.2 Approach.....13-2
13.2.1 Baseline Model: 2008 NSHMP Gridded Seismicity 13-2
13.2.2 Adjustments to the Baseline Model.....13-3
13.3 Regional Areal Source Zone 13-5
13.4 Vicinity Areal Source Zone 13-6
13.4.1 Boundary Between the Vicinity and Local Source Zones 13-6
13.4.2 Vicinity Areal Source Zone Rate and Maximum Magnitude.....13-7
13.5 Local Areal Source Zone.....13-9
13.5.1 Local Source Zone Rate 13-10
13.5.2 Justification for the Virtual Fault Approach.....13-17
13.5.3 Virtual Fault Sense of Slip, Geometry, and Maximum Magnitude 13-19
13.5.4 Discussion of the Local Areal Source Zone 13-23
14.0 HAZARD SENSITIVITY 14-1
14.1 Hazard Sensitivity Runs 14-1
14.2 Contribution by Source, Deaggregation, and Sensitivity Analyses.....14-2
14.2.1 Fractional Contribution by Source.....14-2
14.2.2 Deaggregation.....14-4
14.2.3 Fractile Hazard Curves for the SSC Model 14-4
14.2.4 Slip Rate Sensitivity.....14-4
14.2.5 Fault Geometry Sensitivity.....14-5
14.2.6 Time Dependency Model and Complex/Splay Rupture Sensitivity 14-6
14.2.7 Magnitude Distribution Model Sensitivity.....14-7
14.2.8 Summary of Sensitivity Analyses.....14-8
15.0 REFERENCES 15-1

LISTS OF TABLES FIGURES, AND APPENDICES

Tables

Table 3-1 Working Meetings Conducted During the Diablo Canyon SSC Study

Table 6-1 Historical Earthquake Ruptures That Are Considered Analogs for Characterizing Rupture Sources in the Diablo Canyon SSC Model

Table 6-2 Primary and Connected Fault Sources

Table 6-3 Models That Comprise the Primary Fault Source Characterization

Table 6-4 Fault Geometry Models (FGMs) and Logic Tree Combinations

Table 6-5 Primary and Connected Fault Section Codes and Descriptions

Table 6-6 Rupture Source Types

Table 6-7 Rupture Source Types and Magnitude PDFs

Table 7-1 Fault Geometry Models and Logic Tree Combinations

Table 8-1 UCERF3 Modeled Slip Rates

Table 8-2 Slip Rates Calculated from the Shoreline Fault in San Luis Obispo Bay

Table 9-1 Rupture Models and Number of Rupture Sources

Table 9-2 Rupture Source Types

Table 9-3 Hosgri Fault Rupture Model

Table 9-4 Outward-Vergent (OV) Rupture Model

Table 9-5 Southwest-Vergent (SW) Rupture Model

Table 9-6 Northeast-Vergent (NE) Rupture Model

Table 9-7 Three-Point Approximation Method of Keefer and Bodily (1983)

Table 9-8 Mean Slip Rate Allocation for the Hosgri Rupture Sources

Table 9-9 Mean Slip Rate Allocation for the Hosgri Rupture Sources Opposite the DCPP

Table 9-10 Hosgri Rupture Model Slip Rates in the SSC Logic Tree

Table 9-11 Mean Slip Rate Allocation for the OV Rupture Sources

Table 9-12 OV Rupture Model Slip Rates in the SSC Logic Tree

Table 9-13 Mean Slip Rate Allocation for the SW Rupture Sources

Table 9-14 SW Rupture Model Slip Rates in the SSC Logic Tree

Table 9-15 Mean Slip Rate Allocation for the NE Rupture Sources

Table 9-16 NE Rupture Model Slip Rates in the SSC Logic Tree

Table 9-17 Hosgri Slip Rate Allocation North of the DCPP (Evaluated for Fault Sections HN and SI)

Table 10-1 Magnitude PDFs Used in the Diablo Canyon SSC Model

Table 10-2 Rupture-Source Categories and Magnitude PDFs

Table 10-3 Segment Boundaries Used in the Hosgri Magnitude Distribution Model

Table 10-4 Hosgri MDM Magnitude PDF Categories and Key Magnitude Parameters—Linked and Characteristic Rupture Sources

Table 10-5 Hosgri MDM Magnitudes and Scenario Frequencies for Complex and Splay Rupture Sources

Table 10-6 Segment Boundaries Used in the Outward-Vergent Magnitude Distribution Model

Table 10-7 Outward-Vergent MDM Magnitude PDF Categories and Key Magnitude Parameters—Linked and Characteristic Rupture Sources

Table 10-8 Outward-Vergent MDM Magnitudes and Scenario Frequencies for Complex and Splay Rupture Sources

Table 10-9 Segment Boundaries Used in the Southwest-Vergent Magnitude Distribution Model

Table 10-10 Southwest-Vergent MDM Magnitude PDF Categories and Key Magnitude Parameters—Linked and Characteristic Rupture Sources

Table 10-11 Southwest-Vergent MDM Magnitudes and Scenario Frequencies for Complex and Splay Rupture Sources

Table 10-12 Segment Boundaries Used in the Northeast-Vergent Magnitude Distribution Model

Table 10-13 Northeast-Vergent MDM Magnitude PDF Categories and Key Magnitude Parameters—Linked and Characteristic Rupture Sources

Table 10-14 Northeast-Vergent MDM Magnitudes and Scenario Frequencies for Complex and Splay Rupture Sources

Table 11-1 Hosgri Fault Equivalent Poisson Individual Estimates

Table 11-2 SLPB Fault Equivalent Poisson Individual Estimates

Table 11-3 San Andreas Fault Equivalent Poisson Individual Estimates

Table 11-4 EPR Values for Hazard Calculation

Table 12-1 Equivalent Poisson Rate Estimated for the San Andreas Fault Source

Table 12-2 UCERF3, FM 3.1 Fault Sections Whose Ruptures Were Completely Removed from the UCERF3 Solution and Equivalent Primary or Connected Fault Source Used Instead

Table 12-3 UCERF3, FM 3.1 Fault Sections Whose Ruptures Were Partially Removed from the UCERF3 Solution and Equivalent Primary or Connected Fault Source Used Instead

Table 12-4 Non-UCERF3 Regional Fault Sources in the Diablo Canyon SSC Logic Tree

Table 12-5 Parameters for the Non-UCERF3 Regional Fault Sources

Table 13-1 Regional and Vicinity Areal Source Zone Parameters

Table 13-2 Number of Predicted vs. Observed Earthquakes $M \geq 3$ in the Vicinity Source Zone

Table 13-3 Number of Predicted vs. Observed Earthquakes $M \geq 3$ in the Local Source Zone

Table 13-4 Independent Earthquakes $\mathbf{M} \geq 3$ in the PG&E Catalog, 1988 Through 2013

Table 13-5 Independent Earthquakes $M \geq 2.5$ in the Updated UCERF3 Catalog, 1988 Through 2013

Table 13-6 Independent Earthquakes $M \geq 4$ Used and Considered to Estimate Earthquake Rates in the Local Source Zone Based on the Updated UCERF3 Catalog and McLaren and Savage (2001)

Table 13-7 Alternative Gutenberg-Richter *a*- and *b*-Value Pairs and Weights for the Local Source Zone

Table 13-8 Style of Faulting and Geometry Parameters for Virtual Faults

Table 13-9 Maximum Magnitude Logic Tree Parameters for the Local Source Zone

Table 13-10 Equivalent Slip Rates of the Virtual Faults in the Local Source Zone

Table 14-1 Grouping of Rupture Sources by Fault Source for Hazard Sensitivity

Figures

Figure 2-1 Diablo Canyon SSC Project Organizational Chart

Figure 3-1 Diablo Canyon SSC Study SSHAC Level 3 Flow Chart

Figure 5-1 Simplified Geologic Map and Shaded-Relief Topographic Map of the Central California Coast Region

Figure 5-2 Schematic Cross Section of the Convergent North American–Farallon Plate Boundary During Late Mesozoic Franciscan Subduction

Figure 5-3 Post–30 Ma Development of the San Andreas Transform Boundary

Figure 5-4 Deep Crustal Cross Section Along Seismic Line PG&E-3

Figure 5-5 Generalized Stratigraphic Columns for the Project Study Area

Figure 5-6 Episodes of Rotation of the Western Transverse Ranges and Resolved Pacific–North American Plate Motion

Figure 5-7 Present-Day Configuration of Tectonic Plates Along the Western Margin of North America

Figure 5-8 Tectonic Setting of the San Gregorio–Hosgri Fault System and California Coast Ranges

Figure 5-9 Crustal Domains of South-Central Coastal California

Figure 5-10 Analysis of GPS Data Using the GPSTRN and SSPX Inversion Algorithms

Figure 5-11 Analysis of Focal Mechanism Data Using the FLTSLP and SATSI Inversion Algorithms

Figure 5-12 Fault Patterns Predicted from Principal Stress and Strain Axes in the Irish Hills

Figure 5-13 Synthesis of Fault-Parallel Rates for Stations Within a Coastal Transect Equidistant from the San Andreas Fault

Figure 5-14 Resolved GPS Strain Rates on Tectonic Block Boundaries

Figure 5-15 GPS Strain Rates from the NeoKinema Model in South-Central Coastal California

Figure 5-16 Regional Distribution of Seismicity from 1987 to 2013 and Faults in the Site Area

Figure 5-17 Seismicity Map and Cross Section A-A′ Across the East and West Traces of the HFZ with Interpreted Seismic Depth Section K-K′ and Cross Section B-B′ Across the Shoreline Fault

Figure 5-18 Comparison of Shoreline Seismicity Relocations in Map and Cross Section Views

Figure 5-19 Example of Bathymetric Interpretation of Submerged Wave-Cut Platforms

Figure 5-20 Seismicity Recorded by PG&E and the USGS, 1987 through August 2010

Figure 5-21 Regional Distribution of Seismicity, 1987 through 2008

Figure 5-22 $M \geq 5$ Pre-1987 Historical Earthquakes

Figure 5-23 Seismicity and Focal Mechanism Data from Estero Bay Area and Irish Hills

Figure 5-24 Earthquake Focal Mechanism Data

Figure 5-25 Transpressional Shear Tectonic Model

Figure 6-1 Logic Tree Structure for the Primary and Connected Fault Sources

Figure 6-2 Primary and Connected Fault Sections in the Hosgri and Outward-Vergent (OV) Fault Geometry Model, DCPP Vicinity

Figure 6-3 Primary and Connected Fault Sections in the Hosgri and Southwest-Vergent (SW) Fault Geometry Model, DCPP Vicinity

Figure 6-4 Primary and Connected Fault Sections in the Hosgri and Northeast-Vergent (NE) Fault Geometry Model, DCPP Vicinity

Figure 6-5 Primary and Connected Fault Sections in the Fault Geometry Models, Southern Region

Figure 6-6 Primary and Connected Fault Sections in the Fault Geometry Models, Northern Region

Figure 6-7 Differences Between Traditional Fault Source and Rupture Source Concepts

Figure 6-8 Schematic Diagrams of Magnitude Probability Density Functions Used in the Diablo Canyon SSC Model

Figure 6-9 Areal Source Zones Used in the Diablo Canyon SSC Model

Figure 7-1 CDF Plots Showing Seismicity Distribution with Depth, with D90 and D95 Values on CDF

Figure 7-2 Cross Section Showing Seismicity Distribution with Depth with D90 and D95 Values

Figure 7-3 Development of Fault Sources for All FGMs

Figure 7-4 Uplift Rate Contour Map of the San Luis Range Area

Figure 7-5 Comparison of Hosgri Fault Maps

Figure 7-6 Evidence of Central and Western Hosgri Fault Trace Activity

Figure 7-7 Distances of the Eastern, Central, and Western Hosgri Fault Traces from the DCPP

Figure 7-8 Hosgri Fault Dip from First-Motion Polarity

Figure 7-9 Seismicity Cross Section Oriented Perpendicular to the Hosgri Fault

Figure 7-10 Cross Sections of Hosgri Fault Geometry Models Compared to Seismicity Profiles

Figure 7-11 Hosgri Fault Geometry Models

Figure 7-12 Constraints on Fault Models and Cross Section Locations

Figure 7-13 Primary and Connected Fault Sources in the Outward-Vergent (OV) Fault Geometry Model, DCPP Vicinity

Figure 7-14 Vibroseis line 204 North

Figure 7-15 Representative Cross Sections A-A′ and B-B′ in the OV Model

Figure 7-16 Representative Cross Sections C-C′ and D-D′ in the OV Model

Figure 7-17 ONSIP Geologic Cross Section B-B″

Figure 7-18 Sandbox Model of a Transtensional Basin Deformed by Transpression

Figure 7-19 Map Showing the Gurvan Bogd Fault System, Mongolia, and Related Topography

Figure 7-20 Simplified Structural Map Showing Displacements on Faults That Ruptured During the 1957 Gobi-Altay Earthquake, Mongolia

Figure 7-21 Primary and Connected Fault Sources in the Southwest-Vergent (SW) Fault Geometry Model, DCPP Vicinity

Figure 7-22 Representative Cross Sections A-A′ and B-B′ in the SW Model

Figure 7-23 Representative Cross Sections C-C′ and D-D′ in the SW Model

Figure 7-24 Surface Deformation, Seismicity, and Postulated Fault Ruptures Associated with the 2003 **M** 6.5 San Simeon Earthquake

Figure 7-25 Primary and Connected Fault Sources in the Northeast-Vergent (NE) Fault Geometry Model, DCPP Vicinity

Figure 7-26 Representative Cross Sections A-A′ and B-B′ in the NE Model

Figure 7-27 Representative Cross Sections C-C′ and D-D′ in the NE Model

Figure 7-28 Postulated Geometry of Faults That Ruptured During the 1977 Caucete Earthquake, Sierra Pie de Palo, Argentina

Figure 7-29 Los Osos Fault Parameter Values

Figure 7-30 San Luis Bay Fault Parameter Values

Figure 8-1 Example of Simple Uncertainty PDFs, Including the Triangular, Trapezoidal, and Boxcar Distributions

Figure 8-2 Miller and Rice (1983) Discrete 3- and 5-Point Approximations to a Continuous Probability Distribution

Figure 8-3 MIS 5 Marine Terrace Sequence, San Nicolas Island, California

Figure 8-4 Comparison of Marine Terrace Uplift Rates on the Irish Hills Coastline from Alternative Paleosea-level Models

Figure 8-5 Irish Hills—Alternative Uplift Rate Models

Figure 8-6 Irish Hills Uplift Rate PDFs

Figure 8-7 MIS 5 Marine Terrace Sequences at Cayucos, Point Loma, and Punta Banda, California

Figure 8-8 Marine Terrace Observations, Cayucos Study Area

Figure 8-9 Marine Terrace Observations, Ellysly Creek

Figure 8-10 Edna Valley and Los Osos Valley Quaternary Terraces and Surfaces

Figure 8-11 Slope Map Illustrating the Relationship Between the Memorial Park Surface and Inferred Location of Ancestral Los Osos Creek Through Wind Gap

Figure 8-12 Comparison of Clay Profile Data: Memorial Park Surface (SP1) and Marine Terraces at San Simeon

Figure 8-13 Hosgri Fault Slip Rate Sites

Figure 8-14 Map of Oso Terrace Strandline and Offset Projections

Figure 8-15 Alternative Correlations and Paleosea-Level Models Used to Evaluate Ages of San Simeon Marine Terraces

Figure 8-16 Oso Terrace: Offset and Age PDFs, CDF, and Summary Statistics for San Simeon Slip Rate

Figure 8-17 Map of the Cross-Hosgri Slope

Figure 8-18 Cross-Hosgri Slope: Offset and Age PDFs, CDF, Summary Statistics, and Mean Slip Rate

Figure 8-19 Excerpt of Profile PBS-34 Showing Regional Transgressive Unconformities and Sequence Stratigraphic Interpretation

Figure 8-20 Age Model for Quaternary Unconformities

Figure 8-21 Age Model for Unconformity T05 and Age Constraints on Channels in Estero Bay and Point Sal

Figure 8-22 Excerpt of Profile PBS-T2 Showing Channels Deep in Stratigraphy West of the HFZ in Estero Bay

Figure 8-23 Excerpt of Line 1020 Showing Channel F West of the HFZ at Point Sal Study Area

Figure 8-24 Map of Channels, Faults, and Bedrock Surface on Shelf, Estero Bay Study Area

Figure 8-25 Estero Bay: Piercing Point DBw-Ee1-De Separation and Uncertainty

Figure 8-26 Fence Diagram Showing Correlation of Channels De and Ee

Figure 8-27 Interpreted Fence Diagram Showing Channel DBw West of the HFZ

Figure 8-28 Offset and Age PDFs, Slip Rate CDF, and Summary Statistics for Estero Bay Channels

Figure 8-29 Locations of Possible Paleochannels Interpreted from Point Sal 3D Data

Figure 8-30 Excerpt of Line 1368 Showing Channel F East of HFZ in the Point Sal Study Area

Figure 8-31 Point Sal Channel F Separation and Uncertainty

Figure 8-32 Offset and Age PDFs, Slip Rate CDF, and Summary Statistics for Offset Channels at Point Sal Study Area

Figure 8-33 Hosgri Slip Rate CDF Compilation and Selection of 5-Point Distribution

Figure 8-34 Overview Map of the Shoreline Fault

Figure 8-35 Shaded Relief Image of the Bedrock Surface Interpreted from 3D Seismic-Reflection Data in San Luis Obispo Bay Study Area, Showing Faults, Channels, and Figure Extents

Figure 8-36 Time Slice at 119.3 ms Showing Terrace Riser and Assessment of Offset Across Shoreline Fault

Figure 8-37 Excerpt of Line PBS-279A Showing Stratigraphic Context of Terrace Sequence

Figure 8-38 Late Quaternary Sea-Level Curves and Age Models for Terrace Sequence, Channel I, and Channel A

Figure 8-39 PDFs of Uncertainty in Offset and Age of Terrace Riser, and Slip Rate CDF

Figure 8-40 Smoothed Similarity of Bedrock Surface and Crossline 1276 Showing Channel I Intersection with Shoreline Fault

Figure 8-41 Smoothed Similarity of Bedrock Surface and Crossline 672 Showing Stratigraphic Constraints on Age of Channel I

Figure 8-42 PDFs of Uncertainty in Offset and Age of Channel I, and Slip Rate CDF

Figure 8-43 Time Slice at 72 ms and Crossline 1775 Showing Channel A Intersection with Shoreline Fault

Figure 8-44 Time Slice at 66.3 ms Showing Crosscutting Relationships Between Channels A, B, and C

Figure 8-45 Profile Showing Differences in Depth of Incision in Upper Reaches of Channels A, B, and C

Figure 8-46 PDFs of Uncertainty in Offset and Age of Channel A, and Slip Rate CDF

Figure 8-47 PDFs of Uncertainty in Vertical Rate of the SWBZ, and Slip Rate CDF

Figure 8-48 Resolution of Shoreline-Parallel Component of the Southwest Boundary Zone Slip Rate

Figure 8-49 Assessment of the Amount of SWBZ Slip Rate Contributed to the Northern Shoreline Fault

Figure 8-50 Excerpt of Seismic-Reflection Profile PBS-32 and Contours of Bedrock Surface Showing Absence of Vertical Separation Across the Point Buchon Fault

Figure 8-51 Shoreline Fault Slip Rate at the DCPP

Figure 8-52 Los Osos Fault—Footwall Uplift Rate PDFs

Figure 8-53 Cross Section and Structure Contour Map of AT2 Horizon in the Morro Bay Area

Figure 8-54 Subsurface Data from Morro Bay Used to Constrain the Rate of Footwall Deformation for the Los Osos Fault – NE Fault Model

Figure 8-55 Los Osos Fault Differential Uplift CDFs for OV, SW, and NE Fault Models
Figure 8-56 Los Osos Fault Rake PDFs for OV, SW, and NE Fault Models
Figure 8-57 Los Osos Fault Net Slip Rate CDF for OV Model
Figure 8-58 Los Osos Fault Net Slip Rate CDF for SW Model
Figure 8-59 Los Osos Fault Net Slip Rate CDF for NE Model
Figure 8-60 Comparison of Los Osos CDFs for OV, SW, and NE Models
Figure 8-61 San Luis Bay Fault—Footwall Uplift Rate PDFs
Figure 8-62 San Luis Bay Fault Net Slip Rate CDF for OV Model
Figure 8-63 San Luis Bay Fault Net Slip Rate CDF for SW Model
Figure 8-64 San Luis Bay Fault Net Slip Rate CDF for NE Model
Figure 8-65 Comparison of San Luis Bay CDFs for OV, SW, and NE Models
Figure 9-1 Rupture Source Types Used in the Diablo Canyon SSC Model
Figure 9-2 Surface Rupture Map for the 1896 Rikuu Earthquake, Japan
Figure 9-3 Surface Rupture Maps for the 1940 and 1979 Imperial Valley Earthquakes, California
Figure 9-4 Surface Rupture Map and Displacement Profile for the 1992 Landers Earthquake, California
Figure 9-5 Surface Rupture Map for the 1999 Hector Mine Earthquake, California
Figure 9-6 Tectonic Setting and Surface Rupture Map for the 2002 Denali Earthquake, Alaska
Figure 9-7 Horizontal and Vertical Slip Measurements for the 2002 Denali Earthquake, Alaska
Figure 9-8 Surface Rupture Map for the 2010 El Mayor–Cucapah Earthquake, Mexico
Figure 9-9 Slip Rate Allocation Model Concept
Figure 9-10 Slip Rate Allocation for the Hosgri Slip Rate CDF
Figure 9-11 Slip Rate Allocation for the Shoreline Slip Rate CDF (OV Model)
Figure 9-12 Slip Rate Allocation for the San Luis Bay Slip Rate CDF (OV Model)
Figure 9-13 Slip Rate Allocation for the Los Osos Slip Rate CDF (OV Model)
Figure 9-14 Slip Rate Allocation for the San Luis Bay Slip Rate CDF (SW Model)
Figure 9-15 Slip Rate Allocation for the Los Osos Slip Rate CDF (NE Model)
Figure 10-1 Schematic Diagrams of Magnitude Probability Density Functions Used in the SSC Model

Figure 10-2 Logic Trees for the Non-Fixed Parameters in the WAACY Magnitude PDF Model

Figure 10-3 Fault Trace Complexity at the Intersection of the Oceanic and San Simeon Faults

Figure 10-4 Magnitude-Scaling Relations Considered in the Diablo Canyon SSC Model

Figure 10-5 Schematic Diagrams of Category A, B, and C Rupture Sources

Figure 10-6 Geometric Reduction Rate for Magnitude-Frequency Distributions at Points along a Fault

Figure 10-7 Magnitude-Frequency Distributions for a Fault vs. a Point on a Fault

Figure 10-8 Alternative Estimates of M_{max} and M_{char} for Rupture Source H-01

Figure 10-9 Alternative Estimates of M_{max} and M_{char} for Rupture Source H-02

Figure 10-10 Alternative Estimates of M_{max} and M_{char} for Rupture Source H-03

Figure 10-11 Alternative Estimates of Primary and Secondary Rupture-Plane Magnitudes for Rupture Source H-04

Figure 10-12 Alternative Estimates of Main and Splay Rupture-Plane Magnitudes for Rupture Source H-05

Figure 10-13 Alternative Estimates of M_{max} and M_{char} for Rupture Source H-06

Figure 10-14 Alternative Estimates of M_{max} and M_{char} for Rupture Source H-07

Figure 10-15 Alternative Estimates of M_{char} for Rupture Source H-08

Figure 10-16 Alternative Estimates of M_{char} for Rupture Sources OV-01, SW-01, and NE-01

Figure 10-17 Alternative Estimates of M_{max} and M_{char} for Rupture Sources OV-02, SW-02, and NE-02

Figure 10-18 Estimates of Primary and Secondary Rupture-Plane Magnitudes for Rupture Source OV-03

Figure 10-19 Alternative Estimates of Primary and Secondary Rupture-Plane Magnitudes for Rupture Source OV-04

Figure 10-20 Alternative Estimates of M_{char} for Rupture Source OV-05

Figure 10-21 Estimates of Main and Splay Rupture-Plane Magnitudes for Rupture Source OV-06

Figure 10-22 Alternative Estimates of M_{char} for Rupture Source OV-07

Figure 10-23 Alternative Estimates of Primary and Secondary Rupture-Plane Magnitudes for Rupture Source OV-08

Figure 10-24 Alternative Estimates of M_{char} for Rupture Source OV-09

Figure 10-25 Alternative Estimates of M_{char} for Rupture Source OV-10

Figure 10-26 Alternative Estimates of Primary and Secondary Rupture-Plane Magnitudes for Rupture Source SW-03

Figure 10-27 Alternative Estimates of Primary and Secondary Rupture-Plane Magnitudes for Rupture Source SW-04

Figure 10-28 Alternative Estimates of M_{char} for Rupture Source SW-05

Figure 10-29 Estimates of Main and Splay Rupture-Plane Magnitudes for Rupture Source SW-06

Figure 10-30 Alternative Estimates of M_{max} and M_{char} for Rupture Source SW-07

Figure 10-31 Alternative Estimates of Primary and Secondary Rupture-Plane Magnitudes for Rupture Source SW-08

Figure 10-32 Alternative Estimates of M_{char} for Rupture Source SW-09

Figure 10-33 Estimates of Main and Splay Rupture-Plane Magnitudes for Rupture Source SW-10

Figure 10-34 Estimates of Primary and Secondary Rupture-Plane Magnitudes for Rupture Source NE-03

Figure 10-35 Alternative Estimates of Primary and Secondary Rupture-Plane Magnitudes for Rupture Source NE-04

Figure 10-36 Alternative Estimates of M_{char} for Rupture Source NE-05

Figure 10-37 Estimates of Main and Splay Rupture-Plane Magnitudes for Rupture Source NE-06

Figure 10-38 Alternative Estimates of Main and Splay Rupture-Plane Magnitudes for Rupture Source NE-07

Figure 10-39 Alternative Estimates of Primary and Secondary Rupture-Plane Magnitudes for Rupture Source NE-08

Figure 10-40 Alternative Estimates of M_{char} for Rupture Source NE-09

Figure 10-41 Estimates of Main and Splay Rupture-Plane Magnitudes for Rupture Source NE-10

Figure 10-42 Alternative Estimates of M_{char} for Rupture Source NE-11

Figure 10-43 Individual Logic Tree Path and Weighted-Sum “Point” MFDs, Hosgri Rupture Source H-01

Figure 10-44 Rupture-Source MFDs Contributing to the Hosgri Fault Source “Point” MFD

Figure 10-45 Hosgri Fault MFD, Summed Incremental and Cumulative Earthquake Rates at a Point Nearest the DCPP

Figure 10-46 Subsection (Point) Participation Rate for the Hosgri Fault Nearest the DCPP from the UCERF3 Inversion

Figure 10-47 Rupture-Source MFDs Contributing to the Shoreline Fault Source (OV Model) “Point” MFD

Figure 10-48 Shoreline Fault (OV Model) MFD, Summed Incremental and Cumulative Earthquake Rates at a Point Nearest the DCPP

Figure 10-49 Rupture-Source MFDs Contributing to the Los Osos Fault Source (OV Model) “Point” MFD

Figure 10-50 Los Osos Fault (OV Model) MFD, Summed Incremental and Cumulative Earthquake Rates at a Point Nearest the DCPP

Figure 10-51 Rupture-Source MFDs Contributing to the Los Osos Fault Source (NE Model) “Point” MFD

Figure 10-52 Los Osos Fault (NE Model) MFD, Summed Incremental and Cumulative Earthquake Rates at a Point Nearest the DCPP

Figure 10-53 Rupture-Source MFDs Contributing to the San Luis Bay Fault Source (OV Model) “Point” MFD

Figure 10-54 San Luis Bay Fault (OV Model) MFD, Summed Incremental and Cumulative Earthquake Rates at a Point Nearest the DCPP

Figure 10-55 Rupture-Source MFDs Contributing to the San Luis Bay Fault Source (SW Model) “Point” MFD

Figure 10-56 San Luis Bay Fault (SW Model) MFD, Summed Incremental and Cumulative Earthquake Rates at a Point Nearest the DCPP

Figure 11-1 Conditional Probability Calculation Illustrated for Exponential and Lognormal Recurrence Probability Distributions with Equal Long-Term Mean Rates

Figure 11-2 Conditional Probability Ratio of Lognormal to Exponential for Four Values of Coefficient of Variation

Figure 11-3 Displacement-per-Event Model Input for the Hosgri Fault and Calculated Long-Term Mean Rates for Three Slip Rates

Figure 11-4 Survivor Functions for a Lognormal CDF, CV = 0.6, and Three Values of Long-Term Mean

Figure 11-5 Relative Weighting of LTM and tMRE For Extracting Conditional Probability Ratios (Lognormal, CV = 0.6)

Figure 11-6 Equivalent Poisson Ratio Complimentary Cumulative Distributions for Two Minimum Values of tMRE (Lognormal, CV=0.6)

Figure 11-7 CV from 12 Well-Studied Paleoseismic Sites on Strike-Slip Faults

Figure 11-8 Mean EPR Estimates for a Range of CV Values (Solid Lines) and CV-Weighted Net EPR Estimates (Dotted) and the CV Weighting Function

Figure 11-9 EPR Values for Three Recurrence Distribution Models, a Fault Slip Rate of 1.7 mm/yr, and T_{min} = 242 yr

Figure 11-10 San Andreas Fault EPR Values for Three Displacement-per-Event Cases and the Lognormal Recurrence Model

Figure 12-1 Active Faults Within the 320 km (200 mi.) DCPP Site Region

Figure 12-2 San Andreas Fault Source and Sections Defined by UCERF3

Figure 12-3 UCERF3 Regional Fault Sources

Figure 12-4 Non-UCERF3 Regional Fault Sources

Figure 12-5 Comparison of UCERF3 Fault Models 3.1 and 3.2

Figure 12-6 UCERF3 Fault Models 3.1 and 3.2 in the Greater DCPP Vicinity

Figure 12-7 San Andreas (Cholame #8) Rupture Rate Summary Plot

Figure 13-1 Areal Source Zones Used in the Diablo Canyon SSC Model

Figure 13-2 Seismicity Oct. 1987–Dec. 2013 from Hardebeck (2014a) Within the Vicinity and Local Areal Source Zones

Figure 13-3 Seismicity Oct. 1987–Dec. 2013 from the PG&E Catalog Within the Vicinity and Local Areal Source Zones

Figure 13-4 Seismicity Oct. 1987–Dec. 2014 from the Updated UCERF3 Catalog Within the Vicinity and Local Areal Source Zones

Figure 13-5 Seismicity $M \geq 4$ in the Vicinity and Local Areal Source Zones since 1830 from the Updated UCERF3 Catalog and the Compilation of $M \geq 5$ Earthquakes from McLaren and Savage (2001)

Figure 13-6 Regional Areal Source Zone Showing 0.1° Gridded Seismicity Rates from the 2008 NSHMP

Figure 13-7 Vicinity Areal Source Zone Showing 0.1° and Finer 0.02° Gridded Seismicity Rates Based on the 2008 NSHMP

Figure 13-8 Evaluation of Hardebeck (2014a) Earthquake Catalog for Estimating the Magnitude of Completeness for the Local Source Zone

Figure 13-9 Hardebeck (2014a) Earthquake Catalog *b*-Value Estimates for the Local Source Zone

Figure 13-10 Annual Earthquake Rates from PG&E and Updated UCERF3 Catalogs and Alternative Exponential Distributions for the Local Source Zone

Figure 13-11 Earthquake Rates and Uncertainties for the Local Source Zone, Showing Constraints for $M \geq 4$

Figure 13-12 Single-Event Focal Mechanisms of Central Coastal California, Oct. 1987 to Dec. 2008, Between San Luis Obispo Bay and Ragged Point

Figure 13-13 Composite Focal Mechanisms and Interpreted Seismicity Lineaments of Central Coastal California, Oct. 1987 to Dec. 2008, Between San Luis Obispo Bay and Ragged Point

Figure 13-14 Best-Fit Planar Seismicity Alignments and Composite Focal Mechanisms from the OADC-FM Method, Estero Bay Area

Figure 13-15 Best-Fit Planar Seismicity Alignments and Composite Focal Mechanisms from the OADC-FM Method, Irish Hills Area

Figure 13-16 Geologic Map of the Irish Hills Showing Faults Interpreted from Geologic, Well-Hole, and Seismic-Reflection Data

Figure 13-17 Geologic Cross Section of the Irish Hills Showing Faults Interpreted from Geologic, Well-Hole, and Seismic-Reflection Data

Figure 13-18 Local Areal Source Zone and Virtual Faults

Figure 13-19 Logic Tree for the Local Areal Source Zone

Figure 14-1 Comparison of Mean Hazard Curves Using the Diablo Canyon SSC and 2011 Shoreline Report SSC Models

Figure 14-2 Fractional Contribution from Individual Seismic Sources to the Total Mean Hazard

Figure 14-3 Deaggregation of Rock Hazard for Hazard at 10^{-4} Annual Probability of Exceedance

Figure 14-4 Fractile Hazard Curves Based on the Diablo Canyon SSC Model and the Central Common Functional Form and CB14 GMPEs

Figure 14-5 Tornado Plots for the Slip Rate Sensitivities

Figure 14-6 Tornado Plots for the Fault Geometry Sensitivities

Figure 14-7 Tornado Plots for the Time Dependency Model and Complex/Splay Rupture Sensitivities

Figure 14-8 Tornado Plot for the Magnitude Distribution Model Sensitivities

Figure 14-9 Summary Tornado Plots for the SSC Model Sensitivity Analyses for 5 Hz Spectral Frequency

Figure 14-10 Summary Tornado Plot for the SSC Model Sensitivity Analyses for 0.5 Hz Spectral Frequency

Plates

Plate 7-1 Quaternary Fault Map of Diablo Canyon Vicinity

Plate 9-1 Hosgri Rupture Sources

Plate 9-2 San Luis–Pismo Block Rupture Sources

Appendices

Appendix A Project Participant Biographies

Appendix B PPRP Closure Letter to Project Sponsor

Appendix C Final Seismic Source Characterization Hazard Input Document

Appendix D SSHAC Workshop Summaries

Appendix E Data Summary and Geospatial Databases

Appendix F Earthquake Catalogs Used in the SSC Study

Appendix G Implementation of the WAACY Composite Magnitude Probability Density Function

Appendix H Method for Estimating Time Dependent Fault Hazard in the Absence of an Earthquake Recurrence Record

LIST OF ABBREVIATIONS, ACRONYMS, AND SYMBOLS

2D	two-dimensional
3D	three-dimensional
AEP	annual exceedance probability
AMEC	AMEC Environment & Infrastructure, Inc.
APS	Arizona Public Service
BPT	Brownian passage time
b_{tail}	*b*-value of the high-magnitude portion of the WAACY magnitude PDF
CB14	Campbell and Bozorgnia (2014) ground-motion model
CBR	center, body, and range
CCCSIP	Central Coastal California Seismic Imaging Project
CDF	cumulative distribution function
CDP	common depth point
CEC	California Energy Commission
CEUS	Central and Eastern United States
CGS	California Geological Survey
CHS	cross-Hosgri slope
CP	conditional probability
CPR	conditional probability ratio
CRADA	Cooperative Research and Development Agreement
CSUMB	California State University, Monterey Bay
CV	coefficient of variation
DCPP	Diablo Canyon Power Plant
DPE	displacement per event
ECSZ	Eastern California shear zone
EE	Evaluator Expert
ELP	early–late Pliocene unconformity
EPR	equivalent Poisson ratio
EPRI	Electric Power Research Institute
FGM	Fault Geometry Model
GMC	ground-motion characterization
GMPE	ground-motion-prediction equation

GMRS	ground motion response spectrum
GPS	global positioning system
HFZ	Hosgri fault zone
HID	hazard input document
hypoDD	software for double-difference earthquake hypocenter location
Hz	hertz
IE	Integrator Expert
InSAR	interferometric synthetic aperture radar
IOF	Inferred Offshore Fault
IPRP	Independent Peer Review Panel
ISFSI	Independent spent fuel storage installation
ka	thousand years ago (*also*, thousand years old)
km	kilometer
kyr BP	thousand years before present
LESS	low-energy seismic survey
LGM	Last Glacial Maximum
LiDAR	light detection and ranging
LOF	Los Osos fault
LTM	long-term mean
LTSP	Long Term Seismic Program
m	meter
M	moment magnitude
MBES	multibeam echosounding
M_{char}	characteristic magnitude
MDM	Magnitude Distribution Model
MFD	magnitude-frequency distribution
MIS	marine oxygen-isotope stage
MLLW	mean lower low water
M_{max}	maximum magnitude
M_{min}	minimum magnitude
MPS	Memorial Park surface
MPT	Mid-Pleistocene Transition

MRE	most recent event
M_S	surface-wave magnitude
MTJ	Mendocino Triple Junction
NCEDC	Northern California Earthquake Data Center
NE	Northeast-Vergent
NGA	Next Generation Attenuation
NGA-West2	Next Generation of Attenuation relationships for the Western United States
NRC	Nuclear Regulatory Commission
NSHMP	National Seismic Hazard Mapping Project
N_{sig}	number of standard deviations
NTN	near-top-of-Neogene
NTTF	Near-Term Task Force
OADC	optimal anisotropic dynamic clustering
ONSIP	Onshore Seismic Interpretation Project
OV	Outward-Vergent
PB	Piedras Blancas
PBO	Plate Boundary Observatory
PDF	probability density function
PE	Proponent Expert
PG&E	Pacific Gas and Electric Company
PNNL	Pacific Northwest National Laboratory
PPRP	Participatory Peer Review Panel
PSHA	probabilistic seismic hazard analysis
PTI	Project Technical Integrator
PVNGS	Palo Verde Nuclear Generating Station
PXP	Plains Exploration & Production Company
QA	quality assurance
RE	Resource Expert
RI	recurrence interval
SAF	San Andreas fault
SLBF	Santa Lucia Bank fault
SLPB	San Luis–Pismo block

SLRF	San Luis Range fault
SONGS	San Onofre Nuclear Generating Stations
SRSS	square root of the sum of the squares
SSC	seismic source characterization
SSE	safe shutdown earthquake
SSHAC	Senior Seismic Hazard Analysis Committee
SW	Southwest-Vergent
SWBZ	Southwestern Boundary zone
SWUS	Southwestern United States
TDI	technically defensible interpretations
TI	technical integration
T_{min}	minimum length of time since the most recent event
tMRE	time since the most recent event
tomoDD	double-difference tomography code
UCERF	Uniform California Earthquake Rupture Forecast
USGS	U.S. Geological Survey
V_{S30}	average shear-wave velocity over the uppermost 30 m of a geologic column
WAACY	magnitude frequency distribution model named for authors Wooddell, Abrahamson, Acevedo-Cabrera, and Youngs
WTR	Western Transverse Ranges

ACKNOWLEDGMENTS

The primary authors of this Diablo Canyon SSC report are the six members of the Technical Integration (TI) Team who, in keeping with the specifications for a SSHAC Level 3 process, assume responsibility for the seismic source characterization model and the analyses presented herein. These authors hereby acknowledge the contribution of others who made this effort possible.

Pacific Gas and Electric Company provided funding for the Diablo Canyon SSC project and is the project sponsor. Kent Ferre served as the PG&E project manager and offered support and guidance through the project. Norm Abrahamson from PG&E served as the Project Technical Integrator and provided important interface support between the SSC project team and the Southwest US (SWUS) ground motion characterization SSHAC Level 3 project.

Independent technical review was provided by the Participatory Peer Review Panel (PPRP). The PPRP consisted of Kevin Coppersmith (Chairman), Steve Day, Neal Driscoll, and Tom Rockwell. The PPRP provided continual review and feedback during the course of the project, and was invaluable in improving the SSC effort and documentation.

The authors also wish to thank other contributors to development of the SSC model and to the final report, including Nick Gregor, who served as the project seismic hazard analyst; Kathryn Wooddell, who shared ongoing research on the WAACY magnitude frequency model; Marcia McLaren, who provided information on the PG&E seismic network and updated catalog; Bill Page and Scott Steinberg, who served early roles on the TI Team; and Serkan Bozkurt, who served as the database manager for the project and assisted the TI Team in their analysis of GIS data. Nora Lewandowski provided important support throughout the project, including workshop documentation, data documentation, and assistance with report preparation. Alex Remar produced the report graphics. Nancy Sutherland provided technical editorial support for the final report.

As with all SSHAC Level 3 studies, successful completion of the project is dependent on the participation of the seismic hazard community, both as Resource Experts and as Proponent Experts. Over 100 individuals participated at one or more of the project workshops, and gave willingly of their data, interpretations and models, and ideas for evaluating seismic sources in south-central coastal California. Because of the large number of these experts, they are not listed here, but their names are provided in Chapter 2 of the report. However, we especially want to acknowledge the contributions of Jeanne Hardebeck, Samuel Johnson, Jessica Murray, Victoria Langenheim, and Janet Watt from the U.S. Geological Survey who were very generous with their time, and provided early results of their research in the south-central coastal region of California to the TI Team. Jeff Unruh, John Baldwin, and Charles DeMets also provided important technical contributions to the TI Team assessment process.

During the course of the SSC study, extensive new data were acquired, analyzed, and interpreted for the Central Coastal California Seismic Imaging Project (CCCSIP). CCCSIP was performed by PG&E under the direction of Stuart Nishenko. Dan O'Connell and Phil Hogan were instrumental in collecting and processing the seismic

reflection data. Gary Greene, Phil Hogan, and Hans AbramsonWard (a member of the TI Team) led the interpretation teams for offshore data; Jeff Unruh, Rob Givler, Jamey Turner, and Josh Goodman led the interpretation teams for onshore data. Jan Rietman participated in developing the LTSP legacy database. California Geological Survey representatives of the CCCSIP Independent Peer Review panel (IPRP) Chris Wills (panel member), Timothy Dawson (staff support), and Gordon Seitz (staff support) also provided important insights regarding interpretation and implications of the CCCSIP results.

EXECUTIVE SUMMARY

This report documents the seismic source characterization (SSC) model developed for use in the updated probabilistic seismic hazard analysis (PSHA) for the Pacific Gas and Electric Company (PG&E) Diablo Canyon Power Plant (DCPP, or "Diablo Canyon"). Diablo Canyon is located near San Luis Obispo along the coast of south-central California. The updated site-specific SSC model, herein referred to as the Diablo Canyon SSC model, was developed using the Senior Seismic Hazard Analysis Committee (SSHAC) Level 3 process and describes the potential for future earthquakes (magnitudes, locations, and rates) in the region surrounding the Diablo Canyon site.

On March 12, 2012, the U.S. Nuclear Regulatory Commission (NRC) issued a request for information pursuant to 10CFR50.54(f), requiring that all operating nuclear plants in the U.S. perform a site-specific PSHA and develop a ground motion response spectrum in accordance with Regulatory Guide 1.208 for comparison to the plant license safe shutdown earthquake ground motion. Licensees were required to re-evaluate the seismic hazard using present-day NRC regulatory criteria and guidance. For plants in the Western United States, including Diablo Canyon, the directive required that the site-specific PSHA be performed using the SSHAC Level 3 process to develop the SSC and ground motion characterization (GMC) models. This report fulfills the requirement for development of an SSC model under the SSHAC Level 3 process for use in the updated Diablo Canyon PSHA. Details of the SSHAC process are provided in NUREG/CR 6372, *Recommendations for Probabilistic Seismic Hazard Analysis: Guidance on Uncertainty and Use of Experts*, and guidance on the implementation is provided in NUREG 2117, *Practical Implementation Guidelines for SSHAC Level 3 and 4 Hazard Studies*.

The goal of following the SSHAC Level 3 process is to provide reasonable regulatory assurance that the center, body, and range of the technically defensible interpretations have been adequately captured in the model. The SSC model described herein was planned, conducted, and reviewed in compliance with the SSHAC Level 3 procedures. Accordingly, the Diablo Canyon SSC model captures the center, body, and range of technically defensible interpretations. Following the SSHAC Level 3 implementation guidelines, the updated SSC model constitutes a "replacement" of earlier SSC models developed for Diablo Canyon.

The SSHAC Level 3 process defines clear roles and responsibilities for all participants. All technical assessments, including development and documentation of the final SSC model, were performed by the Technical Integration (TI) Team. Work performed by the TI Team was conducted under the continuous observation of the Participatory Peer Review Panel (PPRP), which was charged with performing both a technical and process review of the study. The PPRP was responsible for reviewing the activities of the TI Team to ensure that the project satisfactorily considered available data, methods, and models; captured the center, body, and range of technically defensible interpretations; and adequately documented the technical bases of all decisions. PPRP concurrence that these goals have been met is the key indicator of successful compliance with the requirements of a SSHAC Level 3 process.

Development and documentation of the Diablo Canyon SSC model was performed from June 2011 to March 2015. The project included a kickoff meeting in August 2011 in San Francisco, California. Three formal SSHAC Level 3 workshops were conducted in San Luis Obispo, California and were made open to the public. Workshop 1 identified significant seismic hazard issues and data available to address those issues. Workshop 2 reviewed the databases assembled by the TI Team and discussed alternative models and methods related to the Diablo Canyon SSC model. Resource Experts (REs) and Proponent Experts (PEs) participated in Workshops 1 and 2, respectively, and the PPRP participated as observers at both workshops. At Workshop 3, the TI Team presented the preliminary SSC model and preliminary hazard sensitivity results to the PPRP. The PPRP participated actively at the Workshop and provided direct feedback on the preliminary SSC model and sensitivity results. The TI Team presented its final SSC model to the PPRP at two final briefing meetings in July and October 2014. In the course of the project, 36 working meetings were held in Walnut Creek and San Francisco, California to facilitate interaction between the TI Team members. Various members of the PPRP attended 13 of the working meetings as observers. As is typical of a SSHAC Level 3 study, the total number of contributing participants, including members of the Project Team and experts consulted, was over 100 individuals.

Seismic Source Characterization Database

As required by the SSHAC Level 3 implementation guidelines, a comprehensive database of available geologic, seismologic and geophysical data was developed for the project and made available to all the project participants. The database was evaluated by the TI Team and used to help construct the Diablo Canyon SSC model.

The database developed for the Diablo Canyon SSC model builds upon a large legacy database developed by PG&E for the 1988 Long Term Seismic Program (LTSP) PSHA and updated through 2010 for the PG&E Shoreline fault study, and incorporates both more recent data as well as new modeling methods and approaches. Significant recent contributions to the database come from two PG&E-sponsored programs:

1. Between 2010 and 2012, PG&E performed a series of three-dimensional (3D) and two-dimensional (2D) low-energy and high-energy seismic-reflection surveys, along with other geophysical investigations, to improve constraints on fault slip-rate and geometry near Diablo Canyon. PG&E documented these new data in the *Central Coastal California Seismic Imaging Project* (CCCSIP) report.
2. In addition to CCCSIP, studies funded as part of the PG&E–USGS Cooperative Research and Development Agreement (CRADA) and the ongoing LTSP provided new geologic and geophysical data to further improve the source characterization of the Hosgri, Los Osos, San Luis Bay, and Shoreline fault zones.

Tectonic and Geologic Setting

Diablo Canyon is located along the coastal margin of the San Luis Range in south-central coastal California. The site region (320-kilometer [km] radius) lies within the right-lateral transform boundary between the Pacific Plate and the Sierra Nevada/Great Valley microplate. The plate boundary consists of a zone of right-lateral strike-slip faults and transpressional deformation over 100 km wide at the latitude of Diablo Canyon, and with

the majority of relative motion being accomodated on the San Andreas fault. The contemporary transpressional transform plate boundary is dominated by north-northwest-striking dextral faults and more west-northwest-striking reverse and reverse oblique faults.

Diablo Canyon is located on the southwestern slope of the Irish Hills in the western part of the San Luis Range (Figure ES-1). The San Luis Range is a west-northwest-trending topographic and structural high that formed within a region of west-northwest-trending reverse and oblique slip faults. To the west, these faults are truncated by or merge with the more northerly trending Hosgri fault zone. The San Luis Range is interpreted to have been uplifted approximately as a rigid block during the late Quaternary by reverse or oblique-reverse slip on the Los Osos fault to the north-northeast, and reverse or oblique-reverse slip on faults comprising the Southwestern Boundary zone to the south.

Geodetic data and inversions of earthquake focal mechanisms show that the contemporary tectonic setting of the San Luis Range and surroundings is one of transpressional dextral shear with localized areas of crustal shortening and thickening, such as within the Irish Hills near Diablo Canyon. Geodetic data constrain regional crustal velocities in the vicinity of Diablo Canyon to 1–3 mm/yr of dextral shear subparallel to the San Andreas fault zone, with comparable rates of crustal shortening permissible orthogonal to the plate boundary west of the San Andreas fault zone.

Sensitivity analyses have shown that four faults contribute significantly to seismic hazard at Diablo Canyon, including the Hosgri fault zone, the Los Osos fault zone, the San Luis Bay fault within the Southwestern Boundary zone, and the Shoreline fault zone (Figure ES-1). For the SSC model, these faults were characterized along the reach of each fault that is closest to Diablo Canyon because this part of each fault most significantly affects hazard at Diablo Canyon. Both the Hosgri fault zone and Shoreline fault are characterized by distinct microseismicity, whereas diffuse microseismicity occurs throughout the Irish Hills and Estero Bay area to the north (Figure ES-1).

The Hosgri fault zone is the southern part of the larger 410 km long San Gregorio–San Simeon–Hosgri fault system. The fault lies entirely offshore and extends for approximately 110 km from an intersection with the San Simeon fault on the north to its termination near Point Pedernales on the south. The location of the Hosgri fault zone is known primarily from the interpretation of seismic-reflection data and consists of multiple traces in a zone up to 3 km wide directly offshore of Diablo Canyon. Multichannel seismic reflection data, focal mechanisms, and the distribution of microseismicity combine to show that the Hosgri fault zone is nearly pure strike-slip on a steeply (90°–75°) east-dipping fault to a depth of approximately 12 km.

The Los Osos fault zone borders the northeastern margin of the San Luis Range. The fault generally separates the uplifting San Luis Range from the more slowly uplifting Edna and Los Osos valleys and locally subsiding Morro Bay to the northeast. The fault is a 2 km wide system of discontinuous, subparallel, and en-echelon fault traces extending from an intersection with the Hosgri fault zone in Estero Bay on the northwest to an intersection with the West Huasna fault southeast of San Luis Obispo, for a distance of over 55 km. The dip of the Los Osos fault is not well constrained. Results from geomorphic lineament and drainage mapping, interpretation of reprocessed onshore seismic-reflection data, interpretation of high-resolution offshore seismic-reflection data,

analysis of seismicity data, and structural analysis suggest a southwest dip of 45°–80°, with a reverse or dextral oblique reverse fault motion that accommodates some or all of the uplift of the range. The amount of oblique movement likely varies with strike, with more northerly trending parts of the fault accommodating greater amounts of strike slip, consistent with the regional stress/stain field.

The southwestern margin of the San Luis Range is bordered by a complex zone of late Quaternary reverse, and oblique-slip faults collectively known as the Southwestern Boundary zone. The faults generally strike west-northwest and dip moderately to steeply northeast. Within the Southwestern Boundary zone, the San Luis Bay fault zone lies closest to Diablo Canyon. The general location of the San Luis Bay fault zone is well constrained onshore but is less well constrained offshore both in San Luis Obispo Bay and in its interactions farther west with the Hosgri fault zone. Offshore the fault zone is interpreted to extend either to an intersection with the Shoreline fault zone (for a total fault length of 8 km) or across the Shoreline fault zone to an intersection with the Hosgri fault zone (for a total fault length of 16 km).

The Shoreline fault zone was originally identified from a seismicity lineament trending approximately N50°W to N60°W offshore and parallel to the coast in the vicinity of Diablo Canyon. Directly offshore of Diablo Canyon to the Point San Luis area, the hypocentral distribution of seismicity forms a nearly vertical alignment that extends to a depth of approximately 8–10 km. Along the northern part of the lineament, the hypocentral distribution of seismicity is more diffuse and forms a generally vertical alignment to a depth of approximately 12–15 km. Subsequent to recognition of the seismicity lineament, studies using multibeam bathymetry identified a prominent ocean-bottom lineament in bedrock roughly parallel to the coastline and coincident with the seismicity lineament. The bathymetric lineament is also coincident with clear bedrock discontinuities (both displaced bedding and juxtaposition of different bedrock lithology) and is interpreted to be the fault that produced the seismicity lineament. Based on the distribution of mapped offshore, submerged marine terraces, there is little to no observable vertical separation across the fault.

Subsequent interpretation of high-resolution seismic-reflection data confirms that the bedrock lineament is, in fact, coincident with a subsurface fault that intersects with the Hosgri fault zone northwest of Point Buchon on the north, and extends into San Luis Obispo Bay to the southeast. The southeastern extent of the fault is not well constrained but may extend onshore to an intersection with the Casmalia fault. Within San Luis Obispo Bay, high-resolution 3D seismic data clearly show that the fault displaces sediment of late Quaternary age, providing clear geologic evidence of late Quaternary fault activity. Offset paleo-terrace risers and one or more buried channels crossing the fault within San Luis Obispo Bay show right-lateral displacement but also indicate a very low, long-term slip rate. Focal mechanisms show that the Shoreline fault zone is primarily a right-lateral fault.

Seismic Source Characterization Model

The Diablo Canyon SSC models earthquakes produced by the four identified Primary faults near Diablo Canyon described above, as well as more distant faults in the Diablo Canyon region, including the San Andreas fault. The SSC model also accounts for

seismicity occurring off of the modeled fault sources through the use of areal source zones. The model, therefore, includes two types of seismic sources, fault sources and areal sources. An important concept captured in the Diablo Canyon SSC model is the recognition that faults near Diablo Canyon are part of a larger network of interconnected faults that constitute the San Andreas transform boundary. Because of their connectivity, earthquakes from this fault system are not likely to be limited to a single named fault, but instead may occur on a variety of connected faults that link end-to-end, or branch from each other. Given this recognition, the Diablo Canyon SSC model defines several distinct terms that are used very specifically in the model to characterize faults, as follows:

- *Fault source*—A piecewise planar source of earthquakes that is a model representation of a geologic fault zone that is seismogenic. Geologic fault zones that are sufficiently active and well defined are included in the SSC model as fault sources. Potential earthquakes from less active and less well-defined geologic fault zones are captured in the SSC model as part of areal source zones.
- *Primary fault source*—One of the four fault sources that has been shown to contribute significantly to the seismic hazard at the Diablo Canyon (described above).
- *Connected fault source*—A fault source that connects to a Primary fault source (either directly or via another Connected fault source) in the SSC model.
- *Fault section*—A portion of a Primary or Connected fault source. These are the building blocks for rupture sources.
- *Rupture source*—A series of adjacent fault sections that are considered capable of hosting a maximum earthquake (i.e., rupture over the entire area of the combined fault sections) and smaller, floating earthquakes (i.e., not confined to a specific section or sections of the rupture source).
- *Regional fault sources*—Fault sources within the Diablo Canyon site region other than the Primary and Connected fault sources.

Fault sources are characterized by their location, geometry, depth extent, slip sense, slip rate, magnitude-frequency distribution shape, and probability of occurrence of an earthquake in a given time period. Four types of fault sources are included in the Diablo Canyon SSC model:

- Primary and Connected fault sources
- San Andreas fault source
- UCERF3 regional fault sources (modeled for the Uniform California Earthquake Rupture Forecast, version 3)
- Non-UCERF3 regional fault sources

Areal sources account for earthquakes that occur away from fault sources explicitly characterized for the SSC model. Areal sources are characterized with a defined location, crustal thickness, rate of earthquakes, maximum earthquake magnitude, and magnitude-frequency distribution shape. There are three areal source zones in the Diablo Canyon SSC model, named the Local, Vicinity, and Regional areal source zones, with increasing distance from Diablo Canyon.

Primary and Connected Fault Sources

Primary fault sources are the four fault sources that contribute most to seismic hazard at Diablo Canyon based on the results of past PSHA analyses and sensitivity analyses conducted for this study. Significant attention was paid to these four fault sources during the course of the study because of their contribution to total hazard and hazard uncertainty. The Primary fault sources are all within 12 km of the DCPP at closest source-to-site distance, and include the Hosgri, Los Osos, San Luis Bay, and Shoreline fault sources. Connected fault sources connect directly to the Primary fault sources in the SSC model, but hazard sensitivity analyses have shown that they contribute very little to hazard at Diablo Canyon.

In contrast to earlier PSHAs, the Primary and Connected fault sources in this SSC are modeled to rupture independently and in various combinations. Historical earthquakes have shown that fault ruptures may span multiple connected faults and various fault branching relationships. Thus, future ruptures on Primary fault sources may be more complex than was considered in previous PSHAs for Diablo Canyon. This Diablo Canyon SSC model explicitly includes sources to account for ruptures of various combinations of connected faults through the use of Rupture Models, as described below.

The SSC model for Primary and Connected fault sources is organized into a series of models for each fault parameter that, in combination, describe the logic tree input for hazard calculation (Figure ES-2). These models include the (1) Fault Geometry Model, (2) Fault Slip Rate Model, (3) Rupture Model, (4) Slip Rate Allocation Model, (5) Magnitude Distribution Model, and (6) Time Dependency Model. All but the Fault Slip Rate Model are explicit nodes on the logic tree; the Fault Slip Rate Model is used to define the budget for allocating slip rate to rupture sources in the Slip Rate Allocation Model.

The *Fault Geometry Model* (FGM) describes the location, dip, and width of Primary and Connected fault sources. Three separate FGMs were developed to characterize faults bounding and underlying the San Luis–Pismo block. These alternative FGMs are termed the Outward-Vergent (OV) Model, the Southwest-Vergent (SW) Model, and the Northeast-Vergent (NE) Model. The three alternative FGMs for the San Luis–Pismo block fault sources allow the uncertainties in fault location, dip, and connectivity to be correlated among the faults. This attribute acknowledges that in many cases the uncertainty in dip of one fault source is not independent of the dip uncertainty of a nearby fault source, especially if the fault sources likely intersect at depth. Three alternative FGMs (termed H90, H85, and H75) also were developed to characterize uncertainty in the downdip geometry of the Hosgri fault zone. Each Hosgri FGM may combine with each San Luis–Pismo block model FGM for a total of nine possible combinations to describe the Primary and Connected fault sources in the Diablo Canyon SSC model. Combined, these models encompass the epistemic uncertainty in location, geometry, depth, and sense of slip for Primary and Connected faults in the Diablo Canyon area.

The *Fault Slip Rate Model* describes the slip rate and its uncertainty for each Primary fault source and certain Connected fault sources. Fault slip rates and their uncertainties are characterized as cumulative distribution functions (CDFs) that capture the center, body, and range of technically defensible slip rates. The fault slip rate CDFs provide target slip rate budgets that must be accounted for among the various rupture sources that

are modeled to occur on the network of fault sources described in each FGM. In the Diablo Canyon SSC model, this is done by assigning fractions of the fault slip rates to each of the multiple rupture sources that occupy the section of each fault source closest to Diablo Canyon.

Each FGM has a corresponding *Rupture Model* that describes the combinations of fault sections that may rupture together. Each Rupture Model consists of a set of rupture sources. A rupture source is a series of adjacent fault sections that are considered capable of hosting a maximum earthquake and smaller, floating earthquakes. Rupture sources are "layered" onto the fault network defined by a FGM to describe variability in how connected faults rupture together. All rupture sources are considered to occur within each Rupture Model. The rupture-source framework used in the Diablo Canyon SSC model captures epistemic uncertainty and aleatory variability as follows: (1) the Rupture Models represent different logic-tree branches that (together with branches for the rupture-source slip rates and various magnitude probability density function [PDF] models) collectively sample and represent the range of epistemic uncertainty in the slip budget and the way that slip budget is distributed spatially and with respect to magnitude and style of faulting; and (2) the collection of rupture sources (and their respective magnitude PDFs) within each Rupture Model is designed to capture the corresponding aleatory variability in magnitude (and rupture dimensions) and distance to the site.

For the Diablo Canyon SSC, four types of rupture sources are defined and allowed to occur in each Rupture Model, (1) Characteristic rupture sources are those that are confined to a single named fault source of limited length and that have a uniform sense of slip, (2) Linked rupture sources are those that include fault sections of multiple named fault sources that have a uniform sense of slip, (3) Complex rupture sources are those that contain multiple named fault sources that have more than one sense of slip on adjacent fault sections, and (4) Splay rupture sources that include overlapping faults that rupture simultaneously. The complex and splay rupture sources in the Diablo Canyon area are highlighted because they require special consideration by the ground motion model regarding how to implement ground motion contributions from multiple portions of the fault rupture.

The *Slip Rate Allocation Model* describes the slip rate from each fault source that is allocated to individual rupture sources in a single Rupture Model. Accordingly, there is one Slip Rate Allocation Model for the Hosgri Rupture Model (that applies to all three Hosgri FGMs) and three Slip Rate Allocation Models for the San Luis–Pismo block Rupture Models, one each for the OV, SW, and NE Rupture Models. Because each Rupture Model contains rupture sources that link across numerous faults with different fault slip rates, the Slip Rate Allocation Model creates a slip rate for each rupture source such that when the contributions from all rupture sources that include a particular fault source are summed, the combined slip rate equals the target slip rate budget for that particular fault source, and the uncertainties in slip rate for each rupture source combine to equal the uncertainty in the slip rate of the fault source..

The *Magnitude Distribution Model* describes the minimum (M_{min}) and maximum (M_{max}) magnitudes and the relative frequency of earthquake magnitudes from M_{min} through M_{max} that may occur on a rupture source. For the Diablo Canyon SSC model, four earthquake

magnitude-frequency distribution (MFD) functional forms are defined to account for both aleatory and epistemic uncertainty, (1) a truncated exponential, or Gutenberg-Richter, distribution, (2) a simplified maximum magnitude distribution, (3) a characteristic earthquake distribution, and (4) a recently developed modified characteristic earthquake distribution (WAACY model). Different types of rupture sources are modeled with one or more of these MFD functional forms depending on their length, connectivity and complexity. The MFD functional forms and slip rates assigned to each rupture source that involves a particular point on a fault are used to develop combined MFDs at a point on the fault in order provide a way to understand the combined effect of many rupture source "layers" on a portion of a fault. The resulting MFDs for the section of each Primary fault source closest to Diablo Canyon compare favorably to participation MFDs developed by the UCERF3 model.

The *Time Dependency Model* describes the recurrence of moderate to large earthquakes occurring on the Primary and Connected fault sources in the Diablo Canyon area, and the San Andreas fault source. Earthquake recurrence in PSHA is commonly modeled as a time-independent Poisson process (i.e., earthquakes are modeled to occur randomly in time). There is growing evidence, however, that earthquake occurrence is too regular on many faults for the Poisson model to be correct. Furthermore, simple elastic rebound theory of elastic strain accumulation and release suggests there is some renewal process involved in earthquake recurrence on individual faults. Thus, a non-Poisson model for earthquake occurrence must be considered technically defensible. To account for the probability that moderate to large earthquakes on faults do not follow a Poisson process, equivalent Poisson ratios (EPRs) are applied to the Primary and Connected fault source rates as well as the San Andreas fault source. The EPRs are multipliers of the Poisson rate that capture uncertainty in the recurrence functional form, long-term mean recurrence rate of moderate to large earthquakes, coefficient of variation in the recurrence model, and the time elapsed since the most recent event (Figure ES-2).

Regional Fault Sources

Fault sources within the Diablo Canyon site region other than the Primary and Connected fault sources are known as *regional* fault sources. The largest regional fault source, the San Andreas fault source located approximately 80 km northeast of Diablo Canyon, represents a few percent of the total hazard at long periods at the hazard levels being evaluated for Diablo Canyon. Aside from the San Andreas fault source, the other regional fault sources contribute *in the aggregate* less than 1% to hazard. The regional fault sources are included in the Diablo Canyon SSC model using the characterization of earthquake rates developed for UCERF3. Some offshore faults near Diablo Canyon, such as the West Basin–Southwest Channel fault (the modeled source of the 1927 Lompoc earthquake) were not characterized in the UCERF3 model. For these faults simple conservative characterizations of location, geometry, slip rate, and magnitude distribution were used because sensitivity analyses performed early in the project showed that these faults contributed negligible amounts to the total hazard at Diablo Canyon.

Areal Source Zones

Earthquakes occurring off the recognized fault sources within the 320 km Diablo Canyon site region are modeled to occur within three areal source zones, a Local areal source zone, a Vicinity areal source zone, and a Regional areal source zone (Figure ES-2). For the Diablo Canyon SSC model, two approaches are used to model these areal source zones: those modeled with virtual faults and those modeled as point sources from a grid.

For the Local areal source zone that includes Diablo Canyon and adjacent areas of the Irish Hills and Estero Bay, earthquakes are modeled as occurring on a set of subparallel virtual faults, with defined aleatory and epistemic uncertainties in location, rake, dip, activity rate, and M_{max}. This Local areal source zone represents an area where the general characteristics of faults are known (to varying degrees of uncertainty) or may be constrained by available information, but where the fault activity and/or slip rate are unresolved. The rates of earthquakes in this areal source zone are determined based on observed seismicity rates and considerations of geologic rates of deformation.

For the Regional and Vicinity areal source zones in the Diablo Canyon SSC model, earthquakes are modeled as a set of point sources on regularly spaced grids. This approach is used at greater distances from the DCPP site where less precision is warranted. The rates of earthquakes in the gridded source zones are calculated based on observed and spatially smoothed seismicity rates and model predictions about maximum earthquake size.

Conclusions Regarding the Diablo Canyon SSC Model

The goal of the Diablo Canyon SSC study was to develop an SSC model using the SSHAC Level 3 process for use in the updated PSHA for the DCPP. The issuance of the PPRP Closure Letter confirms that the SSHAC Level 3 process has been fulfilled. Accordingly, this Diablo Canyon SSC model provides a complete update of seismic sources in the Diablo Canyon area and can be used to update the PSHA for the DCPP.

The Diablo Canyon SSC model incorporates an extensive body of new data and emerging new concepts, methods, and models to characterize epistemic uncertainty and aleatory variability in fault characteristics, including location, geometry, earthquake magnitudes and rates, and earthquake recurrence. These new data, methods, and models led to a complete replacement SSC model from earlier published SSC models for Diablo Canyon. The Diablo Canyon SSC model incorporates several significant advancements relative to the previous models, as follows:

- The SSC model uses recently acquired offshore and onshore 2D and 3D seismic reflection data, multibeam bathymetric data, geodetic data, and an updated seismicity catalog to better define the location, geometry, and slip rate of faults in the Diablo Canyon area.
- Three geometrically consistent, integrated FGMs were developed that collectively capture the epistemic uncertainty in fault location, geometry and sense of slip for each fault rather than independent characterizations of individual faults that often times lead to incompatible fault geometries and fault intersections.

- The SSC model incorporates the UCERF3 model to characterize most regional faults, and is consistent with the UCERF3 model for the local site area faults.
- The Diablo Canyon SSC model directly embraces the concept of multi-fault (or linked fault) ruptures and develops a suite of Rupture Models that collectively capture the epistemic uncertainty and aleatory variability in fault slip rate and earthquake magnitude distribution.
- Through use of the recently developed WAACY earthquake magnitude PDF, the Diablo Canyon SSC model incorporates broad aleatory variability in magnitude on rupture sources by incorporating large-magnitude, multi-fault ruptures yet remaining consistent with paleoseismic data that may preclude the simpler truncated exponential magnitude distribution.
- The Diablo Canyon SSC model also includes rupture sources to explicitly model splay cases, which involve joint rupture of multiple overlapping faults (e.g., the Hosgri and Shoreline faults), and complex cases, which involve joint rupture of faults with different sense of slip (e.g., strike-slip and reverse).
- In addition, the model incorporates the concept of time dependence for earthquake recurrence by employing equivalent Poisson ratios (EPRs) to capture uncertainty in elapsed time since the last earthquake.

Hazard sensitivity results using the Diablo Canyon SSC model and a simplified version of the new GMC model developed for nuclear sites in the southwestern United States show that the Hosgri fault is the main contributor to hazard at Diablo Canyon. The main contributors to hazard uncertainty are the slip rate of the Hosgri fault, and the EPR for the Hosgri fault (i.e., uncertainty in earthquake recurrence model). Other important contributors to hazard at Diablo Canyon are the San Luis Bay fault, the Los Osos fault, the Local areal source zone, and the Shoreline fault.

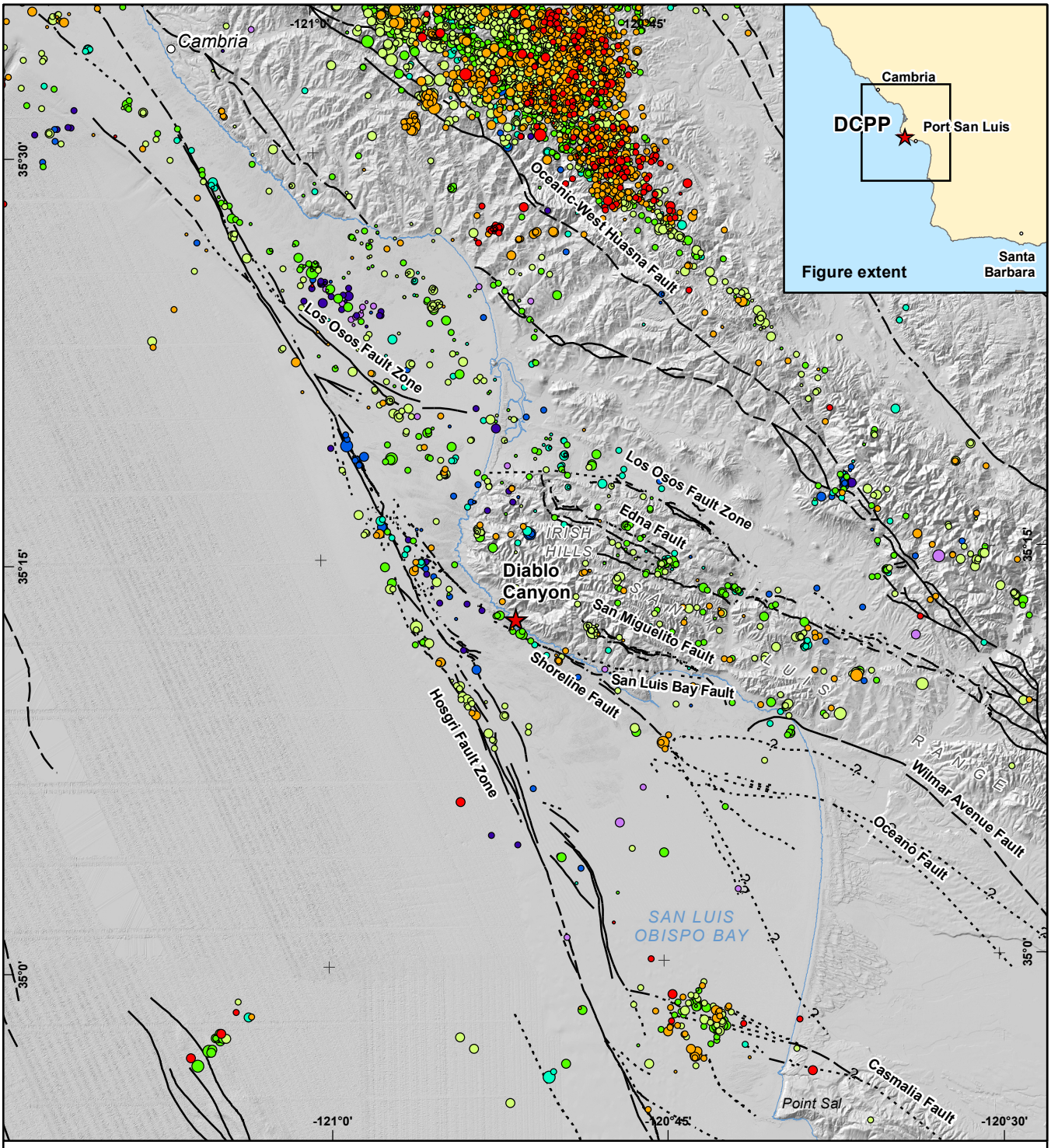

EXPLANATION

Fault, solid where well located, dashed where approximately located, dotted where inferred, queried where existence uncertain

Earthquake Data

Depth (km)

- 0.0–1.9
- 2.0–3.9
- 4.0–5.9
- 6.0–7.9
- 8.0–9.9
- 10.0–11.9
- 12.0–13.9
- 14.0 +

Magnitude

- 0.0–0.9
- 1.0–1.9
- 2.0–2.9
- 3.0–4.1

Note: Quaternary fault traces compiled from Lettis and Hall (1994), Lettis et al. (2004), AMEC (2011), PG&E (2013a; 2014, Chapter 3; 2014, Chapter 9).

Sources:
- Relocated earthquake data from Hardebeck (2014a).
- Project DEM compilation v2013.07.

N

0 4 8 mi.

0 10 20 km

Map projection and scale: WGS 84 / UTM Zone 10N, 1:400,000

Regional Distribution of Seismicity from 1987 to 2013 and Faults in the Site Area

DCPP SSC REPORT

Pacific Gas and Electric Company

Figure **ES-1**

File path: S:\1005\005\Final_Report_Figures\Figure_ES-01.mxd; Date: 03/06/2015; User: Alex Remar, LCI; Rev.1

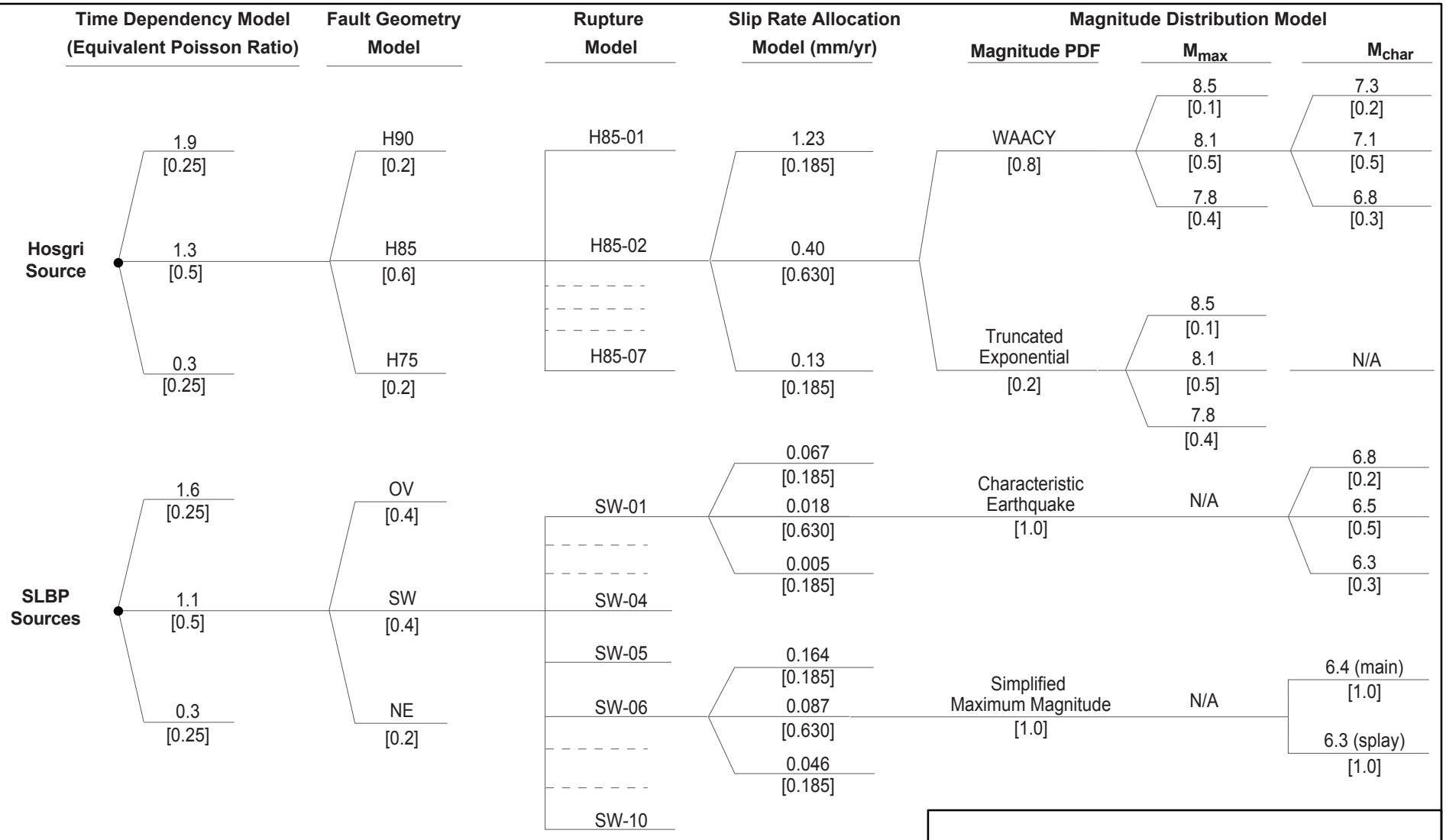

Notes: In the example tree, rupture source H85-02 is a longer *linked* rupture source, so the WAACY and truncated exponential magnitude PDF models are considered. Rupture source SW-01 is a *characteristic* rupture source, so only the Youngs and Coppersmith (1985) characteristic earthquake magnitude PDF is considered. Rupture source SW-06 is a *splay* rupture source, so only the simplified maximum magnitude earthquake magnitude PDF model is considered. See text.

Logic Tree Structure for the Primary and Connected Fault Sources

DCPP SSC REPORT

Pacific Gas and Electric Company

Figure **ES-2**

File path: S:\1005\005\Final_Report_Figures\Figure_ES-02.ai; Date: 03/10/2015; User: Serkan Bozkurt, LCI; Rev.1

1.0 INTRODUCTION

A seismic hazard update was performed for the Diablo Canyon Power Plant (DCPP, or "Diablo Canyon") using an updated seismic source characterization (SSC) model and an updated ground motion characterization (GMC) model as basic inputs to a site-specific probabilistic seismic hazard analysis (PSHA). The study was undertaken to fulfill the U.S. Nuclear Regulatory Commission (NRC) requirement that the owner of the power plant, Pacific Gas and Electric Company (PG&E), conduct a PSHA for the DCPP using Senior Seismic Hazard Analysis Committee (SSHAC) Level 3 procedures (NRC, 2012a). The SSC and GMC models were developed using processes that are appropriate for a SSHAC Level 3 study as described in NUREG/CR-6372 (Budnitz et al., 1997) and in the detailed implementation guidance provided in NUREG-2117 (NRC, 2012b). The SSC model describes the future earthquake potential (e.g., magnitudes, locations, and rates) for the region surrounding the DCPP site, and the GMC model describes the distribution of the ground motion at the site as a function of magnitude, style of faulting, source-to-site geometry, and site condition.

This report presents the SSC model developed for the Diablo Canyon site region, an area with a 320-kilometer (km), or 200-mile (mi.), radius. The model is site-specific and was developed under a SSHAC Level 3 study sponsored by PG&E. The GMC model for rock ground motions was developed as part of a broader SSHAC Level 3 study that was designed to be generally applicable for the Southwestern United States (SWUS) and specifically applicable for two project sites: the DCPP and the Palo Verde Nuclear Generating Station (PVNGS) in Arizona. The SWUS GMC study was sponsored jointly by PG&E and Arizona Public Service (APS; the owner of PVNGS) and is presented in GeoPentech (2015). The DCPP site response analysis, site-specific adjustments to the GMC model, and PSHA results are presented in PG&E (2015a).

The Diablo Canyon SSC SSHAC Level 3 study was conducted from June 2011 through March 2015. The project included a kickoff meeting on August 25, 2011, conducted at PG&E headquarters in San Francisco, California; three formal workshops conducted in San Luis Obispo, California; 36 working meetings conducted in Walnut Creek and San Francisco; and two final briefing meetings held in Walnut Creek, California. In addition, there were two field reconnaissance visits to the DCPP site area near San Luis Obispo attended by members of the TI Team and PPRP. As is typical with a SSHAC Level 3 study, the total number of participants, including members of the project team and experts consulted, was over 100 individuals. The roles and responsibilities of these individuals are described in *Chapter 2*. Key participants in the study and their professional biographies are provided in *Appendix A*.

This chapter presents an overview of the Diablo Canyon SSC study, including the objectives of the study, the regulatory requirements and guidelines that govern the study, and the scope and organization of the study.

1.1 Objectives of the SSC Study

The objective of this SSHAC Level 3 SSC study is to develop an "updated" SSC model for use as input in the updated Diablo Canyon PSHA. As described in Section 6 of the SSHAC implementation guidelines (NUREG-2117; NRC, 2012b), an "update" to an existing NRC-approved SSC model may include accepting the original model, refining the existing model, or a complete replacement of the model (i.e., "accept, refine or replace"). The level of update is dependent on the hazard significance of any new or emerging data, methods, and models, and/or the level to which any "*large changes in the input models would need to be developed and documented in a SSHAC process to engender high levels of assurance*" (NRC, 2012b, p. 116).

As described in *Section 2.2*, PG&E developed an initial SSC model in 1988 for its Long Term Seismic Program (LTSP; PG&E, 1988; 1991). PG&E refined the model first as part of the independent spent fuel storage installation (ISFSI) hazard study (PG&E, 2004) and again as part of the Shoreline fault zone study (PG&E, 2011). Each of these SSC models were reviewed by the NRC (1991, 2012c). Based on a review of new and emerging data, methods, and models since 2011, and given the complexity of tectonic faulting in the Diablo Canyon area, PG&E decided that the 2011 SSC model for the DCPP (PG&E, 2011) should be "replaced" by a new SSC model. New data developed since 2011 include the advanced seismic studies performed under PG&E's Central Coastal California Seismic Imaging Project (CCCSIP; PG&E, 2014), regional GPS data, and several geologic, marine seismic-reflection, and seismicity studies performed by the U.S. Geological Survey (USGS). These studies are described further in *Chapter 4*. New methods and models include concepts developed by the USGS for the Uniform California Earthquake Rupture Forecast, Version 3 (UCERF3) fault probability model (Field et al., 2013) and by K. Wooddell, N. Abrahamson, and others for evaluating maximum magnitude distributions for fault sources (*Appendix G*). These studies provided important new insights on representing uncertainties in fault location and geometry, deformation rates, and the potential for multifault or "linked" fault ruptures. Another new method, developed for this study, provides an approach to capture uncertainty related to time-dependent recurrence behavior of fault sources (*Appendix H*). A key objective of this study is to evaluate and integrate these new data, methods, and models, as appropriate, into a new, or "replacement," SSC model for the Diablo Canyon region.

Another objective of the updated SSC model is to satisfy NRC requirements that PG&E perform an updated PSHA using SSHAC Level 3 procedures (NRC, 2012a). The goal of following the SSHAC Level 3 process is to provide reasonable regulatory assurance that the center, body, and range (CBR) of the technically defensible interpretations (TDI) in the SSC model have been adequately captured in building the SSC model. Accordingly, the project was planned, conducted, and reviewed in compliance with the SSHAC procedures, as discussed in *Section 1.3* below.

Finally, an important objective of the project is to conduct the SSHAC Level 3 study under an open and transparent process. To meet this objective, all the formal SSHAC workshops were held in San Luis Obispo and were open to the public. Summaries of

these workshops are provided in *Appendix D*. Documents related to the Diablo Canyon SSC study are available at the PG&E web site http://www.pge.com/dcpp-ltsp.

1.1.1 NRC Directive, Regulatory Criteria, and Guidelines

On March 12, 2012, the NRC issued a 50.54(f) letter titled "Request for Information Pursuant to Title 10 of the Code of Federal Regulations 50.54(f) Regarding Recommendations 2.1, 2.3 and 9.3, of the Near-Term Task Force [NTTF] Review of Insights from the Fukushima Dai-Ichi Accident." In particular, Recommendation 2.1 requested that all operating nuclear plants in the United States perform a site-specific PSHA and develop a ground motion response spectrum (GMRS) in accordance with Regulatory Guide 1.208 for comparison to the plant license safe shutdown earthquake (SSE) ground motion (NRC, 2012a). Licensees are required to re-evaluate the seismic hazard using present-day NRC regulatory criteria and guidance. For plants in the Western United States, including Diablo Canyon, the directive requires that the site-specific PSHA be performed using the SSHAC Level 3 process to develop the SSC and GMC models.

As stated in the 10 CFR 50.54(f) letter, Attachment 1 to Seismic Enclosure 1, "Licensees of plants located in the Western United States (Columbia, Diablo Canyon, Palo Verde, and San Onofre) should develop an updated, site-specific PSHA. Any new or updated seismic hazard assessment should consider all relevant data, models, and methods in the evaluation of seismic sources and ground motion models." Consistent with Regulatory Guide 1.208, "A Performance-Based Approach to Define the Site-Specific Earthquake Ground Motion," licensees should use a SSHAC study as described in NUREG/CR-6372 "Recommendations for PSHA: Guidance on Uncertainty and Use of Experts." Consistent with current practice, as described in NUREG-2117, "Practical Implementation Guidelines for SSHAC Level 3 and 4 Hazard Studies," a SSHAC Level 3 study should be performed.

The development of the updated SSC model for use in the Diablo Canyon PSHA update was performed in accordance with the SSHAC Level 3 process described in NUREG/CR-6372 (Budnitz et al., 1997) and following the implementation guidance provided in NUREG-2117 (NRC, 2012b). Development of the SSC model follows regulatory criteria provided in 10 CFR 100.23 for the identification and characterization of seismic sources, and regulatory guidance provided in Regulatory Guide 1.208 for developing an SSC model for use in developing a performance-based GMRS. As described in *Chapter 2*, the procedures and processes provided in NUREG-2117 were followed in developing the scope of work and project plan for updating the Diablo Canyon SSC model. The final closure letter from the Participatory Peer Review Panel (PPRP; See *Chapter 2*) that notes conformance to the requirements of the SSHAC process is provided in *Appendix B*.

1.1.2 Site-Specific SSC Model

The updated SSC model developed for the Diablo Canyon PSHA update is intended to be specific to the Diablo Canyon site. The SSC model is hazard informed, meaning that sensitivity analyses were performed to identify and focus the assessment process on those seismic source issues that are most significant to hazard at the site. The updated SSC model is described in *Chapters 6 through 13* and involved characterization of seismic sources in the 320 km (200 mi.) Diablo Canyon region, with a focus on those seismic sources most significant to hazard. Sensitivity analyses performed during the course of the study were presented at the three workshops (and are provided as attachments to *Appendix D*); sensitivity analyses on the final SSC model are presented in *Chapter 14*. The model incorporates the CBR of the TDI as required by the SSHAC process, and includes the following elements, as described in *Chapter 6*:

- Identification and characterization of active faults near the site, both onshore and offshore (location, geometry). (*Chapter 5*)
- Development of alternative integrated "Fault Geometry Models" that capture the range of uncertainty in fault location and geometry. (*Chapter 7*)
- Development of a "Fault Slip Rate Model" that captures the range in uncertainty in individual fault slip rates. (*Chapter 8*)
- Development of "Fault Rupture Models" that capture the range of uncertainty in various types of fault rupture combinations involving the site area faults. (*Chapter 9*)
- Development of a "Slip Rate Allocation Model" that allocates fault slip rate to individual fault rupture sources in each Fault Rupture Model. (*Section 9.3*)
- Development of alternative "Magnitude Distribution Models" that capture uncertainty in the distribution of earthquake magnitudes for the fault rupture sources in each Fault Rupture Model, including uncertainty in characteristic and maximum earthquake magnitudes. (*Chapter 10* and *Appendix G*)
- Development of "Time Dependency Models" that incorporate uncertainty in the time-dependent behavior of earthquakes on faults. (*Chapter 11* and *Appendix H*)
- Characterization of the San Andreas fault and other fault sources within the Diablo Canyon site region. (*Chapter 12*)
- Characterization of areal source zones to capture off-fault seismicity. (*Chapter 13*)

The complete instructions for implementing the Diablo Canyon SSC model is contained in a Hazard Input Document (HID), which is provided as *Appendix C*.

1.1.3 Interface with the SWUS GMC Model

In parallel with development of the updated SSC model for the Diablo Canyon PSHA update, PG&E was also participating in the SWUS GMC study. The SWUS GMC model provides an updated GMC model for the entire SWUS, with particular applicability to the DCPP and PVNGS project sites. The SWUS GMC model is provided in GeoPentech (2015).

Important interface issues for the Diablo Canyon SSC and GMC models were identified and addressed during the study. Dr. Norm Abrahamson served as the Diablo Canyon Project Technical Integrator (PTI) for both the Diablo Canyon SSC and SWUS GMC projects and attended all of the SSHAC workshops for both projects; see *Chapter 2* for a description of the roles and responsibilities of SSHAC participants. Dr. Abrahamson provided important insights and direction to both projects on known and potentially significant interface issues. He also advised on important sensitivity analyses to identify potentially significant interface issues. At least one member of each project's Technical Integration (TI) Team attended the workshops of the other project. In this manner, both the TI teams were cognizant of interface issues relevant to development of their respective model. In addition, two individuals—Dr. Steven Day and Dr. Thomas Rockwell—served on the PPRPs for both the Diablo Canyon SSC and SWUS GMC projects and provided important peer review and oversight.

1.2 Previous Seismic Hazard Studies for DCPP

PG&E developed the LTSP in 1985 to conduct an initial PSHA for the DCPP, to continuously monitor emerging new science (i.e., methods and models) and new site-specific information, and to perform periodic updates to the PSHA as new data, methods, and models warrant. As part of this program, PG&E formally developed an SSC model for the 1988 PSHA (PG&E, 1988). The model was reviewed and approved by the NRC in 1991 (NRC, 1991). PG&E later refined the model as part of the ISFSI hazard study in 2004 (PG&E, 2004) and as part of the Shoreline fault zone study in 2011 (PG&E, 2011). The 2004 SSC refinement mainly involved revising the Hosgri fault characterization to be primarily strike slip based on new data that rejected the reverse and reverse-oblique alternatives included in the 1988 SSC model. The 2011 SSC update involved adding the Shoreline fault zone to the model, reassessing the downdip geometry of the Hosgri fault zone and Los Osos fault, and reassessing the existence and offshore continuation of the Rattlesnake and Olson traces of the San Luis Bay fault zone. The Shoreline Fault Zone Report (PG&E, 2011) was reviewed and approved by the NRC in 2011 (NRC, 2012c).

For development of the updated SSC model in this report, the Shoreline fault SSC model was used as the "base case" model to perform sensitivity analyses to identify hazard significant issues specific to the DCPP site. The intent of the sensitivity analyses was to inform the SSHAC study participants of those issues of greatest significance to the hazard results and to focus further evaluation and integration of data and information on characterizing the uncertainty in these key model parameters.

As part of the SSHAC Level 3 process, an important aspect in developing the updated SSC model was to avoid cognitive bias (e.g., anchoring) to the pre-existing SSC models and characterizations and to be open to new data, evaluations, and alternative interpretations. This was accomplished as follows:

- Including discussion of cognitive bias at the start of each workshop and working meeting by the TI Lead, and by conscious reminders by the TI Lead or other TI

team members during each workshop and working meeting if apparent cognitive bias arises.

- Developing a TI Team of which four of the six members were not affiliated with the original LTSP SSC model, and two of the members were not involved with the Shoreline SSC refinement model.
- Developing a new SSC model that "replaces" the existing Shoreline SSC model with fundamentally new methods and models for characterizing earthquake sources.

1.3 Products of the Project

The documentation of the SSHAC Level 3 process and of the technical evaluation and integration assessment to develop the Diablo Canyon SSC model are an essential part of a SSHAC Level 3 study. As part of the documentation process, the following work products have been developed; they either are provided as part of this report or are available on PG&E's website (http://www.pge.com/dcpp-ltsp):

3. The SSC Model—The Diablo Canyon SSC model is described in *Chapters 6 through 13* of this report, including the technical bases for each element, parameter, and weight of the SSC logic tree. Each chapter focuses on one or more elements of the logic tree, provides the TI Team evaluation of the available data, methods, and models, and describes how this information is integrated into the model to capture the CBR of the TDI.
4. Hazard Input Document (HID)—Both a preliminary and final HID were prepared for the project. The final HID is provided in *Appendix C*. The HID provides instructions for implementing the SSC model logic tree for input to the PSHA, but does not provide the underlying technical basis, rationale, or justification for the logic tree parameters or branch weights.
5. Project Plan—A project plan was developed to define the objective of the study and the organization, roles and responsibilities of the project participants, the scope of workshops and working meetings performed for the project, and the overall project schedule. The project plan is summarized in *Chapters 2 and 3*. *Appendix A* contains professional biographies of key project participants.
6. Workshop Summaries—As required by the SSHAC Level 3 process, three formal structured workshops were performed for the project as part of the Evaluation and Integration process. Summaries of each workshop are provided in *Appendix D*.
7. Earthquake Catalog—Several earthquake catalogs were developed for the Diablo Canyon SSC model. The catalogs are described in *Chapter 5* and *Appendix F*, and the catalogs that are not readily available to the public are provided as attachments to *Appendix F*.
8. Summary Tables—Summary tables were developed to document the evaluation of existing information (reference tables) and the contents of a comprehensive geospatial database (geodatabase tables). These tables are provided in *Appendix E*. The geospatial database developed for the project includes "legacy" data from earlier LTSP studies as well as new data developed during this project or in

parallel with this project (e.g., PG&E, 2014). Key data sets used in the analysis are described in *Chapter 4.0*.

1.4 Changes During the Project

The Diablo Canyon SSC SSHAC Level 3 update project took place over a four-year period from early 2011 to early 2015. During this time, several important changes occurred that are documented in the project plan and summarized here. At the beginning of the project in 2011, the Diablo Canyon SSHAC Level 3 update included an update to both the SSC model and the GMC model. The combined SSC/GMC SSHAC Level 3 project lasted until the end of Workshop 1, during which significant issues, available data, and data needs were identified (see *Section 3.2.5*). Shortly after Workshop 1 ended, a decision was made by licensees in the southwestern United States to combine the Diablo Canyon GMC SSHAC Level 3 study with other GMC SSHAC Level 3 studies being performed in the SWUS at Palo Verde and San Onofre. This combined study became known as the SWUS GMC SSHAC Level 3 study (GeoPentech, 2015). Workshop 1 was repeated for the SWUS GMC study. The Diablo Canyon SSC SSHAC Level 3 study continued uninterrupted, with interface with the SWUS GMC study as described in *Section 1.1.3*.

Several important changes also took place in the membership of the SSC SSHAC project team during the four-year study. The Technical Integration (TI) Team, which is described in detail in *Section 2.2.3*, originally included Dr. William Page and Mr. Scott Steinberg from PG&E. These two members were replaced by Mr. Hans AbramsonWard and Dr. Glenn Biasi after Workshops 1 and 2, respectively. When they joined the TI Team, both Mr. AbramsonWard and Dr. Biasi were brought fully up-to-date with the project. Both were also provided training in the SSHAC process.

Mr. AbramsonWard had been a member of the TI Team technical support staff (*Section 2.2.3*) and had attended Workshop 1; therefore, he was thoroughly familiar with the data acquisition process and evaluations performed to date. Dr. Biasi first participated in the project as a Proponent Expert (*Section 2.2.7*) for Workshop 2. He joined the TI Team after Workshop 2 to provide expertise on the UCERF3 model, assist with the evaluation of seismicity data, and develop the time dependency models. Dr. Biasi was fully briefed on all data and evaluations performed to date, including several working meetings to review prior proceedings of the SSHAC process.

In addition, Ms. Kathryn Hanson was added to the TI Team following Workshop 2. Ms. Hanson had participated in all phases of the SSHAC proceedings as a member of the Technical support staff (*Section 2.2.3*), including attending Workshops 1 and 2 and most of the project working meetings. She was fully involved in the data acquisition, compilation, and evaluation process. She joined the TI Team to formally participate in the integration and model building process.

2.0 PROJECT ORGANIZATION

This chapter presents an overview of the organization of the Diablo Canyon SSC study, including a description of the SSHAC Level 3 process and implementation, an overview of the project organization and project team, and the work scope and schedule for completing the project. The information presented in this chapter is largely a summary of the Diablo Canyon SSC Project Plan titled "Project Plan for Development of the Diablo Canyon Seismic Source Model Using SSHAC Level 3 Methodology." The project plan is available on the PG&E website (http://www.pge.com/dcpp-ltsp).

Successful completion of a SSHAC Level 3 study involves fulfilling the SSHAC process and completing the SSHAC technical assessment (evaluation and integration) in building the SSC model. Thus a key part of performing a successful SSHAC Level 3 study is adherence to the SSHAC requirements, guidance documents, and process (i.e., the "SSHAC process"). The Diablo Canyon SSC Project Plan was developed to ensure consistency with a SSHAC Level 3 study and to fulfill both the process and technical aspects of such a study. During development of the Diablo Canyon SSC study in 2011, the SSHAC Guidelines document NUREG/CR-6372 (Budnitz et al., 1997) existed and a draft version of NUREG-2117 (NRC, 2012b) was available to govern planning of the project. These documents were used to select the SSHAC level of study (*Section 2.1.2*) and to define the project organization (*Section 2.2*), project team (*Sections 2.3 through 2.8*), and appropriate scope of work (*Section 2.9*).

2.1 Implementation of the SSHAC Level 3 Process

This section provides a description of the SSHAC methodology (*Section 2.1.1*) and discussion of selection of the SSHAC study level (*Section 2.1.2*).

2.1.1 Description of the SSHAC Methodology

In 1997, the Senior Seismic Hazard Analysis Committee (SSHAC) published NUREG/CR-6372 (Budnitz et al., 1997), which detailed a methodology for capturing epistemic uncertainty in input parameters for PSHAs. Factors motivating the development of this methodology were derived from two observations:

1. Different PSHA studies (e.g., EPRI, 1988; Bernreuter et al., 1989) developed significantly different estimates of the mean seismic hazard for nuclear facilities.
2. The primary reason for the difference in hazard estimates was that the SSCs and GMCs did not adequately characterize the epistemic uncertainty within those characterizations.

Recognizing the importance of characterizing epistemic uncertainty, the SSHAC spent approximately four years developing a methodology for characterizing epistemic uncertainties in SSCs and GMCs. Since publication of the original SSHAC methodology, there have been additional publications that have elaborated on the guidance and how it

should be applied (e.g., Hanks et al., 2009, Coppersmith et al., 2010; Coppersmith and Bommer, 2012; NRC, 2012b).

The SSHAC process is a formal, structured process for developing SSCs and GMCs, and has been identified in NRC Regulatory Guide 1.208 (NRC, 2007) as an acceptable process for use in performing PSHA for nuclear sites. The SSHAC process provides the following guidelines for how all aspects of the SSC development should be conducted:

- Identification of significant issues and data.
- Identification and solicitation of expert judgments and alternative models.
- Evaluation of the available data, expert judgments, and alternative models.
- Integration of the information into an SSC model that incorporates the range of technically defensible interpretations.
- Documentation of the model development.
- Participatory peer review of the technical results and process.

As described in the SSHAC implementation guidelines (NRC, 2012b), the goal of following a SSHAC process is to provide reasonable regulatory assurance that the center, body and range (CBR) of the technically defensible interpretations (TDI) in the SSC models have been adequately captured, and thus provides the basis for developing seismic hazard estimates that are reproducible, defensible, transparent, and stable (i.e., if someone else were to conduct a similar study, the results would not be significantly different).

The SSHAC process involves two fundamental activities, evaluation and integration, for development of the SSC model:

- Evaluation: The compilation and consideration of available and emerging data, models, and methods developed by the larger technical community that are relevant to the SSC model
- Integration: Developing an SSC model that represents the CBR of the TDI in light of the evaluation process

These two activities are performed under the SSHAC process by a Technical Integration (TI) team composed of Evaluator and Integrator Experts, and discussions with Resource and Proponent Experts under a formal, structured workshop environment that encourages interactive discussion and debate.

2.1.2 Selection of SSHAC Study Level

The SSHAC methodology defines four different levels of study that can be conducted to achieve the goal of capturing the CBR of the TDI. Levels 1 through 4 are distinguished by an increasing level of sophistication, resources, and participation by technical experts.

A SSHAC Level 3 study was selected by PG&E in 2011 for the DCPP PSHA update based on recent and ongoing SSHAC Level 3 studies sponsored and endorsed by the NRC and on review of a then draft version of NUREG-2117, which describes the implementation of SSHAC Study Levels 3 and 4. At the time of project conception and

initiation in early 2011, major updates to the Central and Eastern United States (CEUS) ground motion model (EPRI, 2003, 2006) and seismic source model (EPRI, 2012) had been completed or were in progress. These studies were jointly sponsored by and endorsed by the NRC, U.S. Department of Energy, and Electric Power Research Institute (EPRI), and established a precedence for using a SSHAC Level 3 study to characterize complex tectonic settings such as the New Madrid seismic source zone. In addition, NUREG-2117 explicitly states, "From the regulatory perspective of the NRC, there is no essential difference between Level 3 and Level 4 studies, and throughout these guidelines they are considered as parallel and equally valid options" (NRC, 2012b). Thus, considering the CEUS seismic hazard model update studies as a precedent and having access to draft versions of NUREG-2117, PG&E determined that a Level 3 study, rather than a Level 4 study, was the appropriate SSHAC level for the hazard update for DCPP.

After PG&E decided in 2011 to perform a SSHAC Level 3 study, the NRC issued the 10 CFR 50.54(f) letter in March 2012 that explicitly requires a SSHAC Level 3 study for nuclear sites in the Western United States, including Diablo Canyon (NRC, 2012a). Thus the SSHAC Level 3 study initiated by PG&E in 2011 fully satisfies the 2012 NRC request.

2.2 Project Organization

The project organization for the Diablo Canyon SSC SSHAC Level 3 update is shown on Figure 2-1. As described by Budnitz et al. (1997), Hanks et al. (2009), and NRC (2012b), specific roles and responsibilities of individuals within a SSHAC process are clearly defined because the guided interaction between the different roles allows for the center, body, and range of the SSC to be robustly characterized. For the Diablo Canyon SSC study, the roles listed below were explicitly designated and documented as shown on Figure 2-1. Members of the project team (Technical Integration Team and Participatory Peer Review Panel) were selected based on one or more of the following criteria:

1. Prior knowledge of the Diablo Canyon SSC logic tree model (to provide site-specific experience and knowledge of site data).
2. No prior knowledge of the Diablo Canyon SSC model or the DCPP area (to provide fresh, unbiased perspectives).
3. Independent knowledge of the seismic and tectonic setting of the DCPP area.
4. Independent knowledge of data, methods, and technical approaches that may be relevant to the DCPP area.
5. Prior SSHAC Level 3 experience.

In addition, one of the goals identified by Hanks et al. (2009) is to involve younger scientists on SSHAC Level 3 studies. This capacity-building goal aims to increase the number of people with experience with the SSHAC process within the scientific community in general and within the owner organization specifically, and to provide a legacy for future SSHAC projects. The justification for the selection of the TI team and PPRP members given these criteria is provided below within the descriptions of the project roles. Biographies of key project participants are provided in *Appendix A*.

For those members of the project team with no prior experience or knowledge of the DCPP area and LTSP models, and/or with no prior SSHAC experience, a work plan (Project Plan) was provided to bring all members of the project team to a common level of understanding of the technical data, along with explicit training in the SSHAC process (described in *Section 3.1*). Specific roles of the Diablo Canyon SSC Project Team are described below.

2.2.1 Project Sponsor and Project Manager

PG&E was the Project Sponsor for the Diablo Canyon SSC study. Mr. Kent Ferre served as the Project Manager for the project on behalf of PG&E. Mr. Ferre provided overall coordination and administrative support for the study, and was responsible for adhering to budget, schedule scope, and project deliverables. Mr. Ferre also provided coordination and interface with other ongoing PG&E studies in the Diablo Canyon region, including the CCCSIP studies, PG&E–USGS Cooperative Research and Development Agreement (CRADA) studies, and other specialty contract studies (see *Section 2.3*). Mr. Ferre was the main point of contact with the Project Technical Integrator (PTI) and the SSC TI Team lead. Mr. Ferre convened regular meetings with the PTI and TI Team members to provide administrative support in terms of logistics for team meetings and workshops, access to PG&E data files, and to ensure that available resources (financial and staff) were available to support the project.

2.2.2 Project Technical Integrator

The Project Technical Integrator (PTI) is a technical expert with knowledge of the SSHAC process who coordinates the technical completion and interface of the GMC and SSC SSHAC Level 3 studies. The PTI serves as the primary point of contact with the Project Manager on administrative issues and with the TI Team Lead(s) on technical issues to assure the successful completion of the project. Dr. Norman Abrahamson, Chief Geosciences Consultant with PG&E, served as the PTI for the Diablo Canyon SSC study and as the PTI and TI Lead for the SWUS GMC study (GeoPentech, 2015).

2.2.3 Technical Integration Team

The Technical Integration Team (TI Team) is responsible for developing and documenting the SSC model for input to the PSHA. As described in *Section 2.1.1*, the SSC model was developed through the two-step SSHAC process of evaluation and integration. Thus, all members of the SSC TI Team served as both Evaluator Experts and Integrator Experts, as described in *Section 2.2.5*.

The TI evaluation process for Diablo Canyon included identifying the hazard-significant issues, available data to address those issues, and data needs that may be fulfilled by the ongoing (concurrent) CCCSIP and other studies, developing a project database (including both legacy data and recently developed data), evaluating the data relative to their quality and applicability to the assessment of seismic source parameters, and interacting with Resource and Proponent Experts to fully evaluate the strengths, weaknesses and

uncertainties in the data and/or proponent interpretations and alternative models. The TI integration process included developing an SSC model that reflected the TI Team's assessment of the CBR of the TDI.

The evaluation and integration process was performed through the completion of three formal structured workshops and 36 working meetings of the TI Team, as described in *Chapter 3*. Workshop 1 identified issues significant to hazard at DCPP, the available data to address these issues, and potential data needs. Resource Experts attended the workshop to present their data and methods (without interpretation), and were questioned by the TI Team to fully evaluate the data quality, methods of data acquisition, applicability of the data to the assessment of seismic source parameters, and uncertainty in the data. Workshop 2 identified proponent models and alternative interpretations related to seismic source issues. Proponent Experts attended the workshop to present their interpretations and models; they were questioned by the TI Team in order to fully evaluate each expert's confidence and uncertainty in the interpretation/model, as well as alternative interpretations and models. After Workshops 1 and 2, the TI Team convened working meetings to begin the integration and model building process in light of the data evaluation, with the objective of building an SSC model that fully represents the CBR of the TDI. Workshop 3 provided the opportunity for the TI Team to present the preliminary SSC model and to obtain feedback from hazard sensitivity analyses performed on the model, as well as from the PPRP. After Workshop 3, the TI Team finalized its assessments and completed the final SSC model. Documentation of the SSC model is provided in this final project report. Documentation of the proceedings of the three workshops is provided in *Appendix D*.

Because of the concurrent studies being performed in the Diablo Canyon area (*Section 2.3*), emerging new data, interpretations, and models became available at different times of the SSHAC process. Thus, for the Diablo Canyon SSC study, Resource and/or Proponent Experts were invited to all three workshops and several working meetings to inform the TI Team of new, emerging information and to update the project database. Thus the SSHAC evaluation and integration process occurred iteratively during the course of the study, and several branches of the preliminary SSC logic tree were completed or updated after Workshop 3. Because of this, a special working meeting on June 23–24, 2014, was convened to present this information to the PPRP and to obtain PPRP feedback.

Throughout the evaluation and integration process, the hazard analyst performed sensitivity analyses to continually focus the TI team on those issues and source parameters of most significance to hazard at the DCPP site. Several sensitivity analyses were suggested by the PTI and/or the Hazard Analyst because of potentially significant interface issues with the GMC model.

The TI Team also had a support staff of Evaluator Experts that are not officially part of the TI Team but assisted the team during the data compilation and evaluation part of the project. Members of the SSC technical support staff are shown on Figure 2-1. Although the TI support staff assisted with the data evaluation, it was the exclusive role of the TI

Team to perform the integration and model-building part of the study and ultimately to take intellectual responsibility for the results of the study. As such, the TI Team was solely responsible for ensuring the following:

- The various data, models, and methods proposed by the larger technical community and relevant to the hazard analysis were considered in the evaluation.
- The final SSC model represents the CBR of the TDI.

For the Diablo Canyon SSC update study, Dr. William Lettis, President of Lettis Consultants International, Inc. (LCI), was the TI Team Lead. Dr. Lettis provided expertise with the SSHAC Level 3 process, seismic source characterization, and PSHA. In addition, Dr. Lettis participated in development of the LTSP SSC model and significant updates to the Diablo Canyon LTSP model, including those for the ISFSI study and the Shoreline fault zone study, and brought significant prior knowledge of the seismic and tectonic setting of DCPP to the TI Team.

The TI Team membership changed over the course of the study (*Section 1.4*). The initial TI Team consisted of Dr. Lettis, Dr. John Caskey, Associate Professor of Geosciences at San Francisco State University, Dr. Stephen Thompson, Principal Geologist with LCI, and Dr. William Page and Mr. Scott Steinberg, Geologists with PG&E's Geosciences Department. Following Workshop 1, Dr. Page was replaced by Mr. Hans AbramsonWard, Principal Geologist with LCI; following Workshop 2, Mr. Steinberg was replaced by Dr. Glenn Biasi, Research Associate Professor with the Nevada Seismological Laboratory at the University of Nevada, Reno. Also following Workshop 2, Ms. Kathryn Hanson, Principal Geologist with Amec Foster Wheeler Environment & Infrastructure, was added to the TI Team. All three of the added TI Team Members participated as TI Team Staff Support Members before joining the TI Team and were fully informed of the data evaluation.

The TI Team remained stable throughout the data integration and model building process. Dr. Lettis served as the TI Team Lead for the project duration, and provided expertise as described above. Mr. AbramsonWard provided expertise in earthquake geology and fault characterization and expertise in the interpretation of marine geophysical data for purposes of characterizing faulting and active tectonics. Dr. Biasi provided expertise with seismology and seismic source characterization for PSHA through evaluation of earthquake recurrence data and statistical evaluation of historical surface-fault ruptures. Dr. Biasi was a contributor to the UCERF3 effort and was familiar with the process and results of that study and how they may be considered for the Diablo Canyon SSC model. Dr. Caskey provided expertise in earthquake geology and fault characterization and has conducted independent research on faults in central coastal California, including the San Gregorio fault. Drs. Biasi and Caskey have no prior experience working on seismic source characterization for Diablo Canyon, and thus provided fresh perspectives with no cognitive bias. Ms. Hanson and Dr. Thompson provided expertise in earthquake geology and seismic source characterization for PSHA and were familiar with the seismic and tectonic setting of Diablo Canyon. Ms. Hanson participated in the original LTSP SSC model development, and both Ms. Hanson and Dr. Thompson participated in the

Shoreline fault zone study and resulting SSC logic tree model update. Mr. AbramsonWard and Dr. Thompson are younger scientists whose involvement satisfies the SSHAC goal of building broader capacity for future SSHAC projects (Hanks et al., 2009).

2.2.4 Participatory Peer Review Panel

The Participatory Peer Review Panel (PPRP) is a panel of experts with experience in SSHAC methodology and/or PSHA who provide participatory peer review of both the SSHAC implementation process and technical judgments of the TI Team. For the technical review, the PPRP ensures that (1) the full range of data, methods, and models is considered and evaluated by the TI Team, and (2) the CBR of the TDI is captured and documented by the TI Team in the integration and model-building phase. For the process review, the PPRP ensures that the TI Team conforms to the requirements of a SSHAC Level 3 study.

The PPRP members attended all the formal workshops and participated in field reviews and selected working meetings of the TI Team. The PPRP consisted of the following members (Figure 2-1):

- Dr. Kevin Coppersmith (Chairman), President of Coppersmith Consulting, Inc.
- Dr. Steven Day, Professor of Seismology at San Diego State University.
- Dr. Neal Driscoll, Professor of Geology and Geophysics at Scripps Institution of Oceanography at the University of California, San Diego.
- Dr. Thomas Rockwell, Professor of Geological Sciences at San Diego State University.

Dr. Coppersmith provided expertise and experience with the SSHAC Level 3 process, familiarity with previous SSC models at Diablo Canyon, and knowledge of methods and technical approaches used in seismic source characterization. Dr. Day provided expertise in seismology and earthquake physics with relevance to seismic source characterization. Dr. Driscoll provided expertise with marine geology and geophysics data acquisition and interpretation, and had familiarity with ongoing seismic studies for the San Onofre Nuclear Generating Stations (SONGS) site until those studies were terminated in 2013. Dr. Rockwell was familiar with the seismic and tectonic setting of the Diablo Canyon area (south-central coastal California), participated in the LTSP field studies in the late 1980s, and is a technical expert in earthquake geology and fault characterization for PSHA. The composition of the PPRP thus includes individuals with prior SSHAC Level 3 experience, as well as capturing the breadth of technical requirements for the project. Both Dr. Rockwell and Dr. Day also served on the PPRP for the SWUS GMC study to help ensure coordination between the two parallel projects.

Throughout the Diablo Canyon SSC study, the PPRP provided important feedback to the Project Sponsor and TI Team. Consistent with NUREG-2117 (NRC, 2012b), the PPRP attended Workshops 1 and 2 as observers. At the end of the day during each of these workshops, the PPRP caucused and then met with the Project Sponsor and members of the TI Team to discuss their observations and to provide technical and “process”

suggestions for the TI Team to consider. For Workshop 3, the members of the PPRP were active participants, questioning the TI Team on various aspects of the preliminary SSC model, probing the documentation of various analyses by the TI Team, and making suggestions for the TI Team to consider regarding additional technical and/or process issues or additional documentation of TI Team judgments. Following each of the three workshops, the PPRP issued comments in writing to the TI Team, and the TI Team responded to the PPRP comments.

Specific responsibilities of the PPRP were as follows:

- Attend the "Kickoff" SSHAC training meeting and review of the Project Plan
- Review the workshop agendas and list of Resource and/or Proponent Experts. Provide comments/suggestions
- Attend all three workshops and provide written comments
- Review the preliminary SSC model and actively participate in Workshop 3 to provide feedback to the TI Team
- Attend working meetings as requested by the TI Team. One or more members of the PPRP attended 12 of the 36 working meetings (*Section 3.1.3*)
- Review the draft Final Report and provide written comments for consideration by the TI Team
- Upon review and acceptance of the Final Report, provide a PPRP closure letter (*Appendix B*)

As required by the SSHAC regulatory guidance, the PPRP is a fundamental means of ensuring the quality of the project activities and the associated documentation. The members of the Diablo Canyon SSC PPRP fully executed their roles and responsibilities, and provided timely and expert advice throughout the course of the project.

2.2.5 Evaluator Experts and Integrator Experts

Evaluator Experts (EEs) and Integrator Experts (IEs) are experts capable of (1) evaluating the relative credibility of multiple alternative hypotheses to explain observations, and (2) integrating this evaluation into an SSC model that represents the CBR of the TDI. All members of the TI Team were EEs and IEs, and used their professional judgment to objectively quantify epistemic uncertainty based on evaluations of the data, knowledge, and alternative models presented by the Resource and Proponent Experts. In addition, a technical support staff of selected EEs assisted the TI Team in their evaluation of certain data sets and proponent models. Members of the TI support staff had individual knowledge of data, interpretations, or proponent models, or were participating in the CCCSIP onshore and offshore geologic and geophysical studies, and, thus, were valuable contributors to the TI Team evaluation process. These support staff EEs are identified in the project organizational chart shown on Figure 2-1, and are further discussed in *Section 2.3*.

2.2.6 Resource Expert

Resource Experts (REs) have specialized knowledge of a particular data set and provided this information without a proponent bias to the TI Team. REs were invited to Workshops 1 and 2 and were also contacted outside of the workshop environment by the TI Team to present and discuss their specialized knowledge regarding the strengths and weaknesses of the data sets. Prior to the workshops, each RE was provided with specific topics and/or questions regarding their data to address in an impartial manner without presenting any interpretation of their data relative to the SSC issues. For the Diablo Canyon SSC study, 20 REs were identified and attended Workshop 1. The REs and their presentations are summarized in *Appendix D*, and links to videos of their presentations are on the PG&E web site: http://www.pge.com/dcpp-ltsp. Several of the REs returned to Workshops 2 and 3 to provide additional updates on their ongoing work, in particular related to the completion of the CCCSIP and CRADA studies. As noted in *Appendix D*, some of the REs are members of the TI Team that provided resource data presentations at Workshop 1. All workshop participants were made aware of the fact that members of the TI Team were temporarily assuming the role of RE for a specific presentation, and then returned to their role as a TI Team member.

2.2.7 Proponent Expert

In contrast to the unbiased RE, a Proponent Expert (PE) advocates a particular hypothesis, interpretation, model, or technical position. As described in NUREG-2117 (NRC, 2012b), a PE's opinion may range from mainstream to extreme (outlier) views. PEs were invited to Workshops 2 and 3 and were also contacted outside of the workshop environment by the TI Team to present and discuss their position. For the Diablo Canyon SSC study, 30 PEs were identified and attended Workshop 2, while 8 PEs attended Workshop 3. These PEs, and summaries of their presentations, are provided in *Appendix D*. Links to videos of their presentations are on the PG&E web site: http://www.pge.com/dcpp-ltsp. Some of the PEs are members of the TI Team that provided proponent model interpretations at the workshops. All workshop participants were made aware of the fact that members of the TI Team were temporarily assuming the role of PE for a specific presentation, and then returned to their role as a TI Team member.

2.2.8 Hazard Analyst

The Hazard Analyst is responsible for performing the sensitivity analyses and PSHA calculations. For the Diablo Canyon SSC update, the Hazard Analyst was involved in all phases of the study (e.g., evaluation, integration) to provide (1) insights into how to represent uncertainty for different parameters; (2) sensitivity analyses to identify hazard-significant issues; (3) sensitivity analyses for feedback on the preliminary and final SSC models; and (4) feedback on the preliminary and final Hazard Input Document (HID) models for implementation in the PSHA (*Appendix C*). For the Diablo Canyon SSC study, Dr. Nick Gregor, Independent Consultant, was the Hazard Analyst (Figure 2-1). The Hazard Analyst attended all three workshops and interacted frequently with the PTI and TI Team.

2.2.9 Database Manager

A comprehensive geospatial database of geologic, geophysical, seismological and tectonic information was established for the project. The Database Manager was responsible for developing and maintaining the geodatabase, attributing the geodatabase, properly scaling all information, and providing timely, efficient access to all project participants during the course of the study. In addition, the Database Manager attended all three Workshops to record and document the workshop proceedings, and many of the TI Team working meetings to provide interactive analysis and evaluation of the data. Mr. Serkan Bozkurt, Principal GIS Analyst with LCI, was the Database Manager for the Diablo Canyon SSC study (Figure 2-1).

2.2.10 Outside Observers

Outside observers are not explicitly defined within the SSHAC guidance (Budnitz et al., 1997), but are discussed in the NUREG-2117 implementation guidelines (NRC, 2012b). For the Diablo Canyon SSC update, observers at the Workshops included the project sponsor, NRC staff, personnel with the USGS and California Geological Survey (CGS), members of the public, and other stakeholders (*Appendix D*). These outside observers did not participate in the SSHAC process (e.g., evaluation, integration, peer review, documentation). The workshops were open to the public and any outside observer was welcome to attend. Time for both observer comment and public comment was accommodated at the end of each day and at the conclusion of each workshop.

2.3 Database Development and New Studies

Development of the project geodatabase included compilation of a large amount of existing, or “legacy,” data and the development of new data, interpretations, and models using, in some cases, new methods of investigation and analysis. Technical support staff assisted the TI Team in the compilation of the legacy data, including offshore geophysical data, onshore geologic mapping, and seismicity data. These support staff included Ms. Marcia McLaren, seismologist with PG&E; Dr. William Page and Mr. Scott Steinberg, geologists with PG&E; Dr. Stu Nishenko, geophysics with PG&E; and Ms. Nora Lewandowski, Sr. Staff Geologist with LCI (Figure 2-1). In addition, several new data acquisition studies were performed during the course of completing the Diablo Canyon SSC SSHAC Level 3 study, including the CCCSIP offshore and onshore studies, independent research by USGS investigators under the PG&E–USGS CRADA program, studies funded by PG&E to university researchers and consultants, independent research by university researchers and CGS, and new data acquisition studies by the SSC TI Team. A brief summary of these studies conducted by specialty contractors to PG&E is given below. Additional discussion of the data sets developed as part of these studies is provided in *Chapter 4*.

2.3.1 CCCSIP Offshore and Onshore Studies

California Assembly Bill (AB) 1632 required PG&E to collect new onshore and offshore geophysical data to reduce uncertainties in the characterization of seismic sources in the Diablo Canyon area using current state-of-the-practice methods and approaches. In 2011, PG&E began the CCCSIP, a program that included the collection, processing, and interpretation of new 2D and 3D seismic-reflection data in the offshore and onshore regions near Diablo Canyon (PG&E, 2014). These data were used for the following purposes:

- To better define the location and geometry of faults in the vicinity of Diablo Canyon (the Hosgri, Shoreline, San Luis Bay and Los Osos fault zones, and other potentially active faults)
- To further evaluate slip rate of the Hosgri and Shoreline fault zones.
- To further evaluate the possible intersection of various faults in the offshore and onshore areas (Hosgri-Shoreline intersection, Hosgri–San Luis Bay intersection, Hosgri–Los Osos intersection, Edna–Los Osos intersection, Shoreline–Southwestern Boundary intersection, Shoreline–Diablo Cove relationship, etc.).
- To identify and interpret the distribution of submerged marine terraces and shorelines in the offshore region of Diablo Canyon.
- To develop an improved, fully integrated onshore-offshore geologic map of the Diablo Canyon area.

2.3.2 USGS CRADA Studies

Several principal investigators from the USGS received funding under the PG&E–USGS CRADA program to perform non-site-specific research studies in south-central coastal California. Dr. Sam Johnson collected, processed, and interpreted high-resolution 2D seismic-reflection data to evaluate the lateral continuity and intersection of the Hosgri and San Simeon faults and to develop a slip rate estimate for the Hosgri fault zone. Dr. Jeanne Hardebeck analyzed the available seismicity data using current and newly developed techniques to improve earthquake hypocentral locations, identify seismicity lineaments (e.g., the Shoreline seismicity lineament and seismicity lineaments in Estero Bay), and identify potential inclined seismicity planes in the Irish Hills. Drs. Robert Jachens and Vicki Langenheim collected and evaluated potential field data (magnetic and gravity) to evaluate crustal structure in the Diablo Canyon area. Drs. Jessica Murray and Wayne Thatcher collected and analyzed geodetic data to evaluate rates of regional deformation in south-central coastal California. Finally, Drs. Janet Watt and Russ Graymer independently evaluated stratigraphic and structural relationships within the Irish Hills.

2.3.3 Other Studies

Additional studies by specialty contractors to PG&E were performed during the course of the Diablo Canyon SSC study. For example, Dr. Charles DeMets of the University of Wisconsin evaluated geodetic data to constrain deformation of the eastern margin of the

Pacific Plate. Consulting geologists mapped Quaternary stratigraphy and faulting on the continental shelf offshore the Diablo Canyon area and mapped fluvial and marine terraces in Los Osos and Edna Valleys. Results from these and other studies were compiled into the project database presented in *Appendix E*.

2.3.4 Independent SSHAC Data Collection and Evaluation Studies

During the process of data evaluation, the TI Team performed additional field review and data collection in the Diablo Canyon area. Dr. John Caskey and his student Aileen Chea at San Francisco State University performed field mapping to evaluate stratigraphic and structural relationships along the Los Osos fault zone in the Los Osos and Edna Valleys. These studies included identification and mapping of marine terraces in the Cayucos area. Members of the TI Team also performed field reconnaissance along several onshore faults to independently evaluate several geologic field exposures. The TI Team used the information gained from these field reviews to inform their judgment as to the quality of existing information and to gain further understanding of stratigraphic and structural relationships.

2.3.5 Quality Assurance

The SSHAC process was performed in accordance with NUREG-2117 (NRC, 2012b). These guidelines provide for the development of a project plan, documentation that the project plan has been completed as described, and full peer review by a Participatory Peer Review Panel. As such, the SSHAC process fulfills the intent, documentation, and technical review of a quality assurance (QA) program (e.g., NRC, 2012b). In developing the Diablo Canyon SSC study project plan, PG&E as the project sponsor decided that the SSHAC process would fulfill the needs and requirements of a formal QA program. Studies performed outside of the SSHAC process, including the CCCSIP studies, were performed under PG&E's Nuclear Quality Assurance program.

The results from other studies performed by the professional community, such as the PG&E–USGS CRADA studies, were evaluated through the SSHAC process as peer-reviewed publications or project reports, and/or as Resource or Proponent Expert presentations at Workshops 1, 2, or 3.

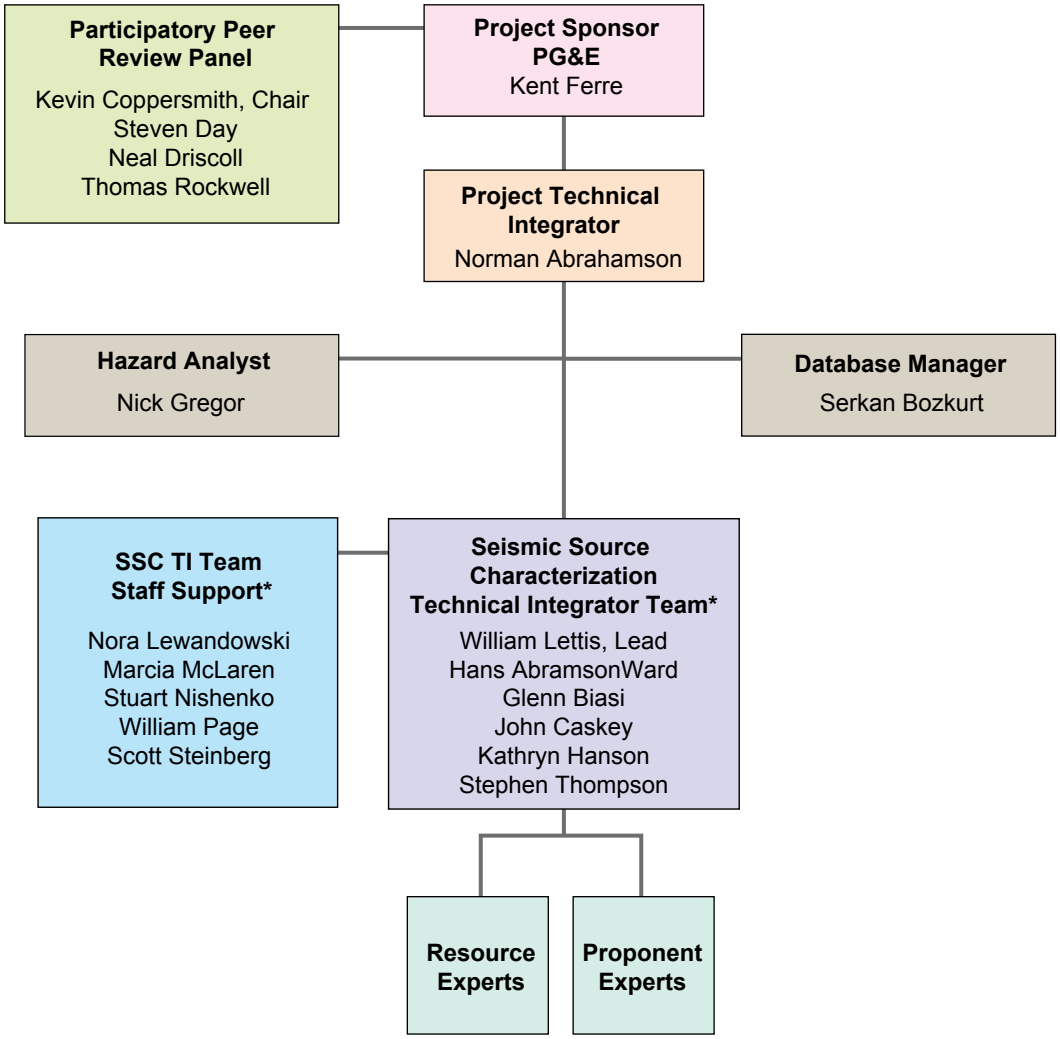

*Evaluator Experts

Diablo Canyon SSC Project Organizational Chart

DCPP SSC REPORT

Pacific Gas and Electric Company

Figure **2-1**

File path: S:\1005\005\Final_Report_Figures\Figure_2-01.ai; Date: 02/13/2015; User: Alex Remar, LCI; Rev.1

3.0 PROJECT PLAN

This chapter provides an overview of the project work plan and key activities performed to fulfill the SSHAC Level 3 process for developing the Diablo Canyon SSC model. The sequence of steps for a SSHAC Level 3 project, as specified in NUREG-2117 (NRC, 2012b) and implemented in this study, is illustrated on Figure 3-1.

3.1 Diablo Canyon SSC Project Plan

A Project Plan was developed at the initiation of the Diablo Canyon SSC SSHAC Level 3 study. Key aspects of the Project Plan are summarized in this chapter and in *Chapter 2*. Two revisions to the Project Plan were made during the course of the study; one revision to reflect changes to the project organization following separation of the SSC and GMC components of the study into two separate studies (i.e., this study and the SWUS GMC study), and a second revision to reflect changes to the project schedule of activities and composition of the project TI Team. The Project Plan is available on the PG&E Website: http://www.pge.com/dcpp-ltsp.

As shown on Figure 3-1, a SSHAC Level 3 study involves completing activities related to four components: evaluation, integration, peer review, and documentation. These components of the SSHAC process are described below and the respective activities completed were essential parts of this SSHAC Level 3 study.

3.1.1 Evaluation

The process of evaluation involves the consideration of all data, models, and methods proposed by the larger technical community that are relevant to the hazard at DCPP. For DCPP, the process of evaluation included the following:

- Identification of hazard-significant issues.
- Compilation of relevant data, models, and methods (e.g., published research papers, geologic and geophysical data).
- Collection and analysis of new data to address focused issues.
- Evaluation of the data, models, and methods with respect to their impact on the SSC model.

The overall goal of the evaluation process was to compile and evaluate all of the data that are relevant to the SSC. This process was performed during formal workshops, informal working meetings, and between working meetings. Table 3-1 lists the 36 working meetings conducted during the Diablo Canyon SSC study and the main topics of discussion.

Records of the evaluation process are kept in the form of summary tables of references (mainly published papers and unpublished reports; see *Section 3.1.4*) and the project geospatial database (geodatabase). The project geodatabase included relevant seismic, geologic, and geophysical data and was based initially on the existing Long-Term

Seismic Program (LTSP) database (current through the 2011 Shoreline Fault Zone Report; PG&E, 2011). The project geodatabase was updated progressively as new information became available from the CCCSIP studies, PGE–USGS CRADA studies, and other SSHAC-related studies and analyses as further described in *Chapter 4*. The data evaluation process was led by the TI Team, with specific input from the TI Team support staff and Resource and Proponent Experts (REs and PEs). Most of the interactions between the REs and PEs and the TI Team occurred at the formal project workshops, but various REs and PEs also were contacted by the TI Team in other settings (e.g., working meetings).

Because the Diablo Canyon SSC model developed by this study is a replacement for the existing SSC model, an important part of the evaluation process was to avoid cognitive bias (e.g., anchoring) to pre-existing characterizations. Through sensitivity analyses, those parts of the SSC model that are most significant to hazard were the focus for evaluation and update. However, those parts of the SSC model that are less significant to hazard were also reviewed and updated to reflect the current state of scientific knowledge, as appropriate. The PPRP reviewed the evaluation process through attending workshops, reviewing interim project documentation, and participating in field reviews and/or working meetings.

Table 3-1. Working Meetings Conducted During the Diablo Canyon SSC Study

Working Meeting Number	Date(s)	Topic(s)	PPRP Member(s) in Attendance
1	July 18, 2011	SSHAC introduction and initial sensitivity analyses review	
2	September 13, 2011	PG&E geophysics and geologic studies status reports, LTSP SSC model review	
3	October 11, 2011	LTSP 2011 Logic Tree review and revision	
4	November 1, 2011	Preparation for Workshop 1 and final review of SSC Model V0	
5a	December 20, 2011	Review of Workshop 1, Data Evaluation Process, data needs, and 2012 schedule	
5b	January 11, 2012	Review of Tectonic Model, WM5A meeting minutes and action items, Data Needs Table	
6	January 25, 2012	Strike-slip tectonic model logic tree development, review of data needs table, priorities, and budget	
7	February 13, 2012	Strike-slip tectonic model sensitivity analyses, presentation of draft OFR USGS offshore geologic maps, results of Pt. Buchon 2D/3D	

Working Meeting Number	Date(s)	Topic(s)	PPRP Member(s) in Attendance
		seismic survey interpretation	
8	March 12, 2012	Hosgri fault zone characterization	
9a	March 28, 2012	Characteristic earthquake review	Rockwell
9b	April 11, 2012	Logic tree and sensitivity for magnitude PDF and earthquake recurrence	Coppersmith
10	May 14, 2012	SSC work plan review, overall logic tree structure	Driscoll
11	June 19-20, 2012	Project and Workshop 2 planning, logic tree structure, sensitivity analyses, Hosgri, Los Osos, San Luis Bay, and Shoreline logic trees	Coppersmith, Day, Driscoll, Rockwell
12	July 30-31, 2012	Recurrence model, logic tree structure, sensitivity analyses, Hosgri, Los Osos, San Luis Bay, and Shoreline logic trees	
13	August 13-14, 2012	Sensitivity logic tree, proponent expert identification and Workshop 2 planning, data evaluation sheets	
14	September 13, 2012	Workshop 2 planning, sensitivity logic tree	
15	September 27, 2012	Workshop 2 planning	
16	October 17-18, 2012	USGS workshop on UCERF3	
17	October 25-26, 2012	Workshop 2 planning, logic tree sensitivity review	Coppersmith
18	December 11, 2012	Review Workshop 2's 2013 plan, data needs table	Rockwell
19	February 20, 2013	2013 Schedule and Assignments, Offshore seismic stratigraphy project PE presentation	Coppersmith
20	February 21, 2013	UCERF3.2 workshop for NSHMP	
21	May 29-30, 2013	Hosgri and Shoreline fault geometry and slip rates, UCERF, magnitude PDF models, Hosgri fault model building	
22	August 6-8, 2013	Alternative tectonic model evaluation	
23	September 20, 2013	Alternative fault model evaluation	Rockwell
24	October 11, 2013	Alternative fault model and deformation model evaluation	
25	November 5-6, 2013	Presentation of draft SSC Model V2	Coppersmith, Day, Driscoll, Rockwell

Working Meeting Number	Date(s)	Topic(s)	PPRP Member(s) in Attendance
26	December 5, 2013	Mchar, MFDs	
27	December 17, 2013	Earthquake Rate and Rupture model review, slip rate target revision	
28	February 19-20, 2014	HID Outline and Workshop 3 agenda review	
29	March 5, 2014	Rupture Models, Sam Johnson PE presentation, Recurrence model	Coppersmith, Rockwell
30	April 16, 2014	Review of OADC and ONSIP results, Fault models, rupture source modifications	
31	May 14, 2014	Schedule and report outline/table of contents review	
32	June 23-24, 2014	Modifications to Preliminary Fault and Deformation models, open items following Preliminary SSC Model	Coppersmith, Driscoll, Rockwell
33	July 24-25, 2014	DCPP SSC Model Final Briefing	Coppersmith, Day, Driscoll, Rockwell
34	September 17, 2014	Review of AB1632 studies	
35	September 19, 2014	SSHAC implementation of AB1632 results	
36	October 31, 2014	Time Dependency Model, Second Final Briefing Meeting	Coppersmith, Day, Driscoll, Rockwell

3.1.2 Integration

The process of integration involves developing an SSC model that represents the center, body, and range (CBR) of the technically defensible interpretations (TDI) in light of the evaluation process (i.e., informed by the assessment of existing data, models, and methods). Following the evaluation process, the TI Team integrated the relevant data, models, and methods to develop a replacement SSC model that captures the CBR of the TDI. For the Diablo Canyon SSC model, the process of integration included the following steps:

- Developing a preliminary version of the SSC model.
- Performing hazard sensitivity analyses to document the impact of model parameters on the seismic hazard at the frequencies of interest.
- Obtaining feedback from REs, PEs, and the PPRP on the preliminary model and hazard sensitivity.
- Developing the final version of the SSC model.

Because of ongoing parallel data acquisition and interpretation studies under the CCCSIP and the PGE–USGS CRADA program, this process was iterated until a final SSC model was developed following Workshop 3.

For the Diablo Canyon SSC model, the TI Team performed the integration process, and the Hazard Analyst performed the iterative hazard sensitivity analyses. The REs and PEs were generally less active in this process, but were called upon by the TI Teams, as needed, to provide clarification on existing data sets, to resolve new issues or discuss new interpretations or alternative methods or models, and to provide feedback on specific elements of the preliminary SSC model. The REs and PEs were not involved with development of the final SSC model. The majority of the integration process occurred following Workshops 2 and 3 during informal working meetings (Table 3-1) and internal work. The workshops were designed primarily to obtain information (Workshops 1 and 2) and to present the preliminary SSC model and sensitivity results (Workshop 3), and to obtain feedback. The PPRP was involved throughout the integration process through attending the formal workshops, reviewing interim project documentation, and attending selected working meetings.

3.1.3 Peer Review

A Participatory Peer Review Panel (PPRP) is an integral component of a SSHAC Level 3 study. The overall goal of the participatory peer review was to ensure that the SSHAC process is adequately followed and that the technical results adequately characterize the CBR of the TDI. As described in NUREG-2117 (NRC, 2012b), the review was participatory in that it was a continuous process throughout the study, and not a singular review at the end of the study. The PPRP was kept abreast of project developments through a combination of attending workshops, reviewing interim project documents, and attending selected field reviews and/or working meetings. Working meetings attended by the PPRP are listed in Table 3-1. The TI team addressed PPRP comments and made modifications during the project following each workshop and following many of the project working meetings.

3.1.4 Documentation

As described in NUREG-2117 (NRC, 2012b), documentation is an integral component of a SSHAC Level 3 study in that it provides a record of the final technical results, the process by which they were accomplished, and the SSHAC Level 3 process that was implemented. In addition, the documentation provides the basis for review by any pertinent regulatory officials, if needed. Documentation of the Diablo Canyon SSC study also will provide the basis for future PSHA updates for the DCPP. The following documentation is provided for the Diablo Canyon SSC study:

- This Final Report describing the technical judgments and rationale for the logic tree elements (i.e., nodes), parameters, and weights.
- Workshop summaries (*Appendix D*) and video recordings of the workshop presentations (links on the PG&E website: http://www.pge.com/dcpp-ltsp).

- The reference and geospatial databases, with summary tables describing their contents (*Appendix E*).
- The earthquake catalogs used for the SSC model (*Appendix F*).
- The final Hazard Input Document (HID; *Appendix C*).

3.2 Diablo Canyon SSC Key Tasks and Activities

The four components of the SSHAC Level 3 study were implemented through a Kickoff Meeting, a series of three formal workshops (SSHAC Workshops 1, 2 and 3), working meetings, and internal work. Given the extensive amount of new data and information that was developed and collected over the duration of the project, the process of evaluation followed by integration and model development was repeated iteratively during the project. This process of evaluation/integration is documented in the workshop proceedings (*Appendix D*), and is described further under the key tasks and activities below.

3.2.1 Task 1—Preparation of Project Plan and Identification of Significant Issues

The initial task for the Diablo Canyon SSC project was to prepare a Project Plan and begin preparation for the Kickoff Meeting (informally called Workshop 0 because it is not a formal workshop of the SSHAC Level 3 process as defined in NUREG 2117; NRC, 2012b). Preparation for the Kickoff Meeting included identifying and establishing contractual relationships with the TI Team and support technical staff, the PPRP, Database Manager and Hazard Analyst, initial development of the project geospatial database (see Task 2), reviewing the 2011 SSC model developed for the Shoreline fault study (PG&E, 2011), and conducting an initial sensitivity analysis to identify hazard significant issues using the 2011 SSC and GMC models as the “base case” model. Identifying which elements of the SSC model have the greatest influence on hazard and/or have the greatest level of uncertainty allowed the TI Team to focus on those elements of the model, both in terms of the data compilation and data evaluation effort as well as areas where additional analysis and/or data acquisition may be warranted given the available project resources (budget, schedule, staff).

3.2.2 Task 2—Database Development

This task included the compilation of applicable data and information into bibliographic reference and geospatial databases for use by the TI Team in their evaluation. Before the Kickoff Meeting, development of the geodatabase began with acquiring and attributing the pre-existing PG&E LTSP database of available seismic, geologic, geophysical, and geographic information compiled through 2011 as part of the Shoreline fault study (PG&E, 2011). After the Kickoff Meeting, this pre-existing geospatial database was developed further as the SSC study progressed in response to data needs identified by the TI Team and TI support staff, with additional input from the PPRP and REs and PEs during Workshops 1 and 2. In addition to the compilation of existing data, this task included compiling new data acquired during the ongoing CCCSIP studies, PG&E–

USGS CRADA studies, and other SSC studies performed under PG&E's ongoing LTSP (herein called other PG&E studies). The "legacy" data of offshore seismic-reflection profiles collected in the 1970s and 1980s and used in the PG&E 1988 LTSP study were also compiled and incorporated into the database.

Data compilation began at the time of project authorization and continued to the point at which the final SSC model was developed after Workshop 3. In particular, many of the CCCSIP studies were not finalized until after the conclusion of Workshop 3 (PG&E, 2014). The Diablo Canyon geospatial database served as the repositories for all project-related geospatial data. Elements of the database include georeferenced geologic and geomorphic maps and associated GIS files; LiDAR and other topographic survey data; aerial imagery; geographic boundary layers; earthquake catalogs; magnetic and gravity data; oil and gas, water, and geotechnical borehole data; fault trench data; and geologic sampling locations. The geospatial database also includes the substantial collection of seismic survey data, mainly in SEG-Y format. A catalog detailing the individual geospatial database components was compiled in Microsoft Excel and is provided in *Appendix E*. The catalog includes a brief description of the data set, data type, date, file path, author, and version information. The earthquake catalogs used in the SSC study are a special subset of the geospatial database and are described and presented in *Appendix F*.

The Database Manager was responsible for developing and maintaining the project geodatabase throughout the course of the project. The Database Manager attended all the workshops and many of the project working meetings. In particular, following Workshops 1 and 2, the Database Manager took an active role in compiling the data, information, methods, and models presented by the Resource Experts (Workshop 1) and Proponent Experts (Workshop 2). The Database Manager also worked closely with specialty contractors to compile the PG&E "legacy" data and data from the ongoing PG&E programs (CCCSIP, PG&E–USGS CRADA, and other PG&E studies).

In addition to the geospatial database, a comprehensive bibliography of literature (reference library) was compiled for use by the TI Team (*Appendix E*). This reference library was compiled in a Microsoft Access database and maintained by the TI Team technical staff. The library built upon the pre-existing Shoreline fault study reference list (PG&E, 2011) and other reference lists developed as part of the PG&E–USGS CRADA. The reference library included published and unpublished data and reports provided by the REs and PEs, as well as additional literature identified by the TI Team during the course of the project. A record of the reference library and how individual references were considered by the SSC TI Team was documented in the data summary tables in *Appendix E*.

3.2.3 Task 3—Kickoff Meeting

A Kickoff Meeting (informally called Workshop 0 in the Project Plan) was convened on August 25, 2011, and was attended by the PTI, the SSC TI Team and technical support staff, the PPRP, the Database Manager, and the Hazard Analysts. Because the Diablo Canyon SSHAC project included both SSC and GMC components at that time, the GMC

TI Team and staff and additional PPRP members were also present. The meeting had the following objectives:

- Present and explain the SSHAC methodology (i.e., SSHAC training).
- Present the draft Project Plan and schedule for the study.
- Present the 2011 LTSP model sensitivity analysis to identify key seismic source characteristics most significant to hazard at the site.
- Identify REs and PEs who will be used in the study to address the significant parameters and features.

The TI Team Lead provided a review of the LTSP from initial development of the 1988 SSC and GMC models (PG&E, 1988) to the 2011 SSC and GMC models developed as part of the Shoreline fault zone study (PG&E, 2011). The outcome of the Kickoff meeting included revisions to the draft Project Plan and the identification of the initial set of REs for Workshop 1. The PPRP provided a letter documenting their observations and comments on the draft Project Plan. Based on the initial sensitivity analysis, important data needs or data gaps were identified for consideration by the TI Team and for discussion at Workshop 1.

3.2.4 Task 4—Initial Data Evaluation and Preparation for Workshop 1

This task consisted of the start of the "evaluation" process and preparation for Workshop 1. The TI team evaluated all of the available data, methods, and models in the current database at that time. Following the Kickoff Meeting, additional data developed by PG&E-funded studies and the initial results of the CCCSIP study were compiled and added to the project geospatial database.

Based on the initial sensitivity analysis and identification of significant issues performed for the Kickoff Meeting, key parameters of the SSC model that were identified as significant to hazard were noted, and data availability, gaps, and needs to address those hazard-significant parameters were considered during the selection of REs to present at Workshop 1. Prior to Workshop 1, REs were identified and a list was provided to the PPRP for their review. The PPRP provided additional suggestions for additional REs for consideration and/or significant issues or topics to be covered at the workshop. The REs were contacted prior to the workshop and provided with a specific request for information, data, or discussion topics as described in Task 5.

3.2.5 Task 5—Workshop 1: Hazard-Significant Issues and Available Data

Workshop 1 lasted for three days between November 29 and December 1, 2011, and was attended by the PTI, the SSC TI Team and staff, the GMC TI Team and staff, the PPRP, the Database Manager, the Hazard Analysts, and the REs. Because the workshop was held prior to the separation of the Diablo Canyon SSC and the SWUS GMC projects (and prior to the most recent revision of this SSC Project Plan), the PPRP then consisted of six members, including the four PPRP members for the Diablo Canyon SSC study (Figure 2-1). The SSC portion of the workshop included two full days. The third day of the workshop was a joint SSC/GMC session to discuss mutually important hazard significant

issues and the relevant data to address those issues. The Workshop 1 summary, including the SSC REs who attended, is provided in *Appendix D*.

The goal of Workshop 1 was to discuss issues significant to hazard, identify available data to address the significant issues, and identify gaps in data or knowledge that can be obtained through further investigations to reduce epistemic uncertainty related to the significant issues. REs were asked to discuss specific data sets and to assist in identifying available data to address significant issues. Legacy data from the prior LTSP studies were presented, if relevant to the current Diablo Canyon SSC project. Prior to the workshop, letters were sent to participating REs identifying directed topics and issues that they should be prepared to address at the meeting. The letters helped focus the workshop discussion on key issues related to a particular data set, including quality and resolution of data, expected use of data, uncertainty, or limitations in the data or interpretations. The REs were asked to present data in oral sessions and/or to participate in interactive discussion sessions with the TI Team and other REs. The presentations and following discussion informed the TI Team of the available data and evaluations and interpretations of the data. In addition, data needs identified during the course of Workshop 1 were compiled by the TI Team and used to help define the scope of further PG&E-funded studies. Digital video files of the workshop and electronic files of presentation materials were posted on PG&E's website (http://www.pge.com/dcpp-ltsp) and have been made publically available as part of the SSHAC documentation process.

The PPRP attended Workshop 1 as observers and provided verbal comments at the end of each day and at the conclusion of the workshop. The day after the workshop ended, the PPRP caucused for a half-day meeting to review the workshop proceedings. During this meeting, the PPRP prepared written comments and feedback to the PTI and TI Teams. The PTI and TI Team Leads provided written responses to the PPRP comments.

SSC Topics addressed at Workshop 1 included the following:

- Project overview and objectives.
- Review of SSHAC procedures and workshop ground rules (SSHAC "Training").
- Presentation of sensitivity analyses on the "base case" SSC and GMC model.
- Presentations of new data and information collected from ongoing CCCSIP, PG&E–USGS CRADA, and other PG&E studies.
- Interactive discussion of the TI Team with Resource Experts (selected presentations).
- Exploration of key data, data uncertainties, and appropriate use and limitations of the data interpretations with the Resource Experts.
- Identification of additional data gaps, data needs, and/or analyses.

3.2.6 Task 6—Data Evaluation and Preparation for Workshop 2

Following Workshop 1, the decision was made to separate the Diablo Canyon SSHAC study into the Diablo Canyon SSC project and the SWUS GMC project (GeoPentech, 2015). Thus, beginning with this task and all subsequent tasks, the focus of work was on

developing the SSC model; interaction was maintained with the SWUS GMC project as described in *Section 1.1.3*.

Task 6 consisted of continuing the data evaluation process and preparing for Workshop 2. The SSC TI Team evaluated the data, information, and interpretations provided by the REs, and additional information collected from the ongoing field and research programs, through a series of working meetings of the TI Team and internal work of TI Team members between working meetings. One or more members of the PPRP attended selected working meetings. Table 3-1 provides a list of the working meetings and identifies those attended by one or more members of the PPRP. The project geospatial database and reference database were progressively updated during this task as new data became available and were used interactively during the working meetings. At many of the working meetings, the Database Manager was available to superpose various data layers, project data in various 3D renditions, and perform various data manipulations and analyses.

In preparation for Workshop 2, a primary objective of Task 6 was to identify the range of potential alternative interpretations or models resulting from the evaluation of available data, and to identify PEs to discuss and defend these alternative interpretations or models. The SSC TI Team compiled and evaluated additional relevant data identified in Workshop 1, and considered the range of alternative interpretations of these data. Under the direction of the TI Team, the Hazard Analyst performed sensitivity analyses to identify those models and/or interpretations of the data that are most significant to hazard. The sensitivity analyses were performed using the GMC base case model and an updated SSC base case model. The sensitivity analyses were used to assist the SSC TI Team in their evaluation of the data and to identify potential PEs for invitation to Workshop 2. Working meetings of the TI Team included presentations of hazard sensitivity results by the Hazard Analysts. Prior to Workshop 2, PEs were identified and their names were provided to the PPRP for their review and comment. The PEs were contacted prior to the workshop and provided with a specific request for discussion topics as described in Task 7.

3.2.7 Task 7—Workshop 2: Alternative Models

Workshop 2 occurred over three days between November 6 and 8, 2012. The workshop was attended by the PTI, the TI Team and staff, the PPRP, the Database Manager, the Hazard Analysts, and Proponent Experts (PEs). In addition, several members of the SWUS GMC TI Team attended the workshop to assure that any potential interface issues were identified and addressed. The Workshop 2 summary, including the PEs who attended, is provided in *Appendix D*.

The primary goal of Workshop 2 was to use the PEs to explore the center, body, and range of alternative proponent models and interpretations for the SSC, with a focus on those parameters of the SSC model that are most significant to hazard. In addition, several of the PEs identified other alternative models or technical issues that were not captured in the SSC base-case model, such as the concept of complex fault ruptures,

linked fault ruptures, and non-Poisson earthquake recurrence. These alternative models or technical issues were identified during the workshop for future evaluation by the TI Team and were considered for integration, as appropriate, into the preliminary SSC model in Task 8.

The workshop provided a forum to explore alternate interpretations of data and alternative hypotheses derived from the data in a series of presentations and structured dialog between the various PEs and the TI Team. The information gained from these interactions, combined with information within the project geospatial database and reference database, were used to form the basis for development of the preliminary SSC model in Task 8. Workshop 2 also was used to identify additional data gaps, data needs, and/or analyses that may be performed to further evaluate alternative models or key model parameters and uncertainties. Digital video files of the workshop and electronic files of presentation materials were posted on PG&E's website (http://www.pge.com/dcpp-ltsp) and have been made publically available as part of the SSHAC documentation process.

The PPRP attended Workshop 2 as observers, and provided verbal comments at the end of each day and at the conclusion of the workshop. Following the three-day workshop, the PPRP caucused to review the workshop proceedings. The PPRP prepared written comments and feedback to the Project Sponsor, PTI, and TI Team. The PTI and TI Team Lead provided written responses to the PPRP comments.

Topics addressed at Workshop 2 included the following:

- Project overview and objectives
- SSHAC procedures and workshop ground rules (SSHAC Training)
- New data and information collected from ongoing CCCSIP, PGE–USGS CRADA, and other PG&E studies
- Interactive discussion with Proponent Experts (selected presentations)
- Exploration of key parameters, data or model uncertainties, and alternative models
- Identification of additional data gaps, data needs, and/or analyses

3.2.8 Task 8—Preliminary Model Development and Preparation for Workshop 3

Task 8 consisted of completing the initial data evaluation process (including the new data and proponent models presented at Workshop 2), integrating the information into a preliminary SSC model in light of the data evaluation process, and preparing for Workshop 3. The evaluation and integration process was performed through a series of working meetings of the TI Team and internal work by individual members of the TI Team between working meetings. The evaluation process included the consideration of and analysis of the available data and range of alternative proponent models. During this task, new data, methods, and models progressively became available from completion (or near-completion) of various CCCSIP and PG&E–USGS CRADA studies. At several working meetings, REs and PEs were asked to provide presentations to the TI Team on

the new data, methods, and models. These presentations were superseded by subsequent presentations at Workshop 3 with the exception of a presentation by Dr. Sam Johnson. The presentation by Dr. Johnson at a working meeting is available on the PG&E web site.

In preparation for Workshop 3, the TI Team completed the initial data evaluation process and integrated the information into a preliminary SSC model. Due to the ongoing CCCSIP studies, several elements of the preliminary model were iteratively modified as new data were evaluated and integrated into the assessment process. At the conclusion of this task, and in preparation for Workshop 3, several of the preliminary model assessments were not complete.

Following development of the preliminary SSC model, the hazard analyst performed a series of sensitivity analyses to explore the model elements, weights, and issues of greatest significance to hazard. Specific seismic sources were identified in terms of hazard contribution. The sensitivity analyses were performed using the base case GMC model. The purpose of the sensitivity analysis was to provide hazard feedback to the TI Team in Workshop 3.

3.2.9 Task 9—Workshop 3: Preliminary Model and Hazard Feedback

Workshop 3 occurred over three days between March 25 and 27, 2014. The workshop was attended by the PTI, the TI Team and technical staff, the PPRP, the Database Manager, the Hazard Analysts, and selected REs and PEs. Similar to Workshop 2, several members of the SWUS GMC TI Team attended the workshop to assure that any potential interface issues were identified and addressed. The Workshop 3 summary, including the REs and PEs who attended, is provided in *Appendix D*.

The primary goal of Workshop 3 was for the TI Team to present the preliminary SSC model to the PPRP, to receive feedback from the PPRP on the model, and to receive feedback from the Hazard Analysts on the hazard sensitivity results. In addition, the first day of the workshop included presentations from selected REs and PEs on data or analyses performed following Workshop 2.

During Workshop 3, the TI Team presented the preliminary SSC model to the PPRP and selected REs and PEs. Unlike during Workshops 1 and 2, members of the PPRP were active participants in Workshop 3 to fully query the model parameters, level of documentation, uncertainty, and rationale in developing the model. Thus the workshop provided an opportunity for the PPRP to review and challenge the TI team's evaluations and the technical justifications used to develop the structure of the SSC logic trees and weights on branches of the logic trees (e.g., whether any significant interpretations are missing, how the TI Team has integrated the alternative models and data uncertainties into a single SSC). In addition, the REs and PEs were invited to provide comments following the discussion between the TI Team and PPRP. The TI Team used this feedback in developing the final version of the SSC logic trees.

At the time of Workshop 3, several analyses on specific elements of the SSC model were not complete; thus, the preliminary SSC model presented at the workshop included

several incomplete assessments. In particular, the model did not include full implementation of the "WAACY" magnitude-frequency distribution (*Appendix G*) and included only a preliminary model of time-dependence uncertainty for fault sources (*Appendix H*). These deficiencies in the model were identified to the PPRP during the workshop, and were reserved for subsequent presentations to the PPRP at working meetings following Workshop 3 during Task 10.

Following presentation of the preliminary SSC model, the Hazard Analyst presented preliminary hazard calculations and sensitivity analyses based on the preliminary SSC model to the TI Team and the PPRP. The hazard sensitivity analyses were used to focus subsequent work by the TI Team in developing the final SSC model on those elements and/or uncertainty in the model that have greatest significance to hazard at the site.

The proceedings of Workshop 3 were documented in a workshop summary report (*Appendix D*), and the PPRP submitted a letter to the Project Sponsor, PTI, and TI Team Lead documenting their observations of the workshop. The PTI and TI Team Lead provided written responses to the PPRP comments. Digital video files of the workshop and electronic files of presentation materials were posted on PG&E's website (http://www.pge.com/dcpp-ltsp) and have been made publically available as part of the SSHAC documentation process.

Topics addressed at Workshop 3 included the following:

- The preliminary SSC model
- Hazard calculations and sensitivity analysis of the preliminary SSC model to identify hazard-significant issues and parameters
- PPRP review and challenge of the TI Team preliminary SSC model
- Identification of shortcomings of the preliminary SSC model
- Identification of key models and parameters requiring further evaluation
- Identification of additional analyses to better constrain the final SSC model

3.2.10 Task 10—Final Model Development and PPRP Final Briefing

This task involved developing the final SSC model for the Diablo Canyon SSC study. After Workshop 3, the TI Team revised the preliminary SSC model in response to the PPRP comments, expert comments, and any additional information collected as part of the SSHAC process and ongoing studies. In particular, the CCCSIP studies were completed during this task. The data and interpretations from the CCCSIP studies were fully evaluated and integrated through the SSHAC process into the final SSC model.

The final SSC model was developed through a series of working meetings to discuss questions and comments that were raised by the PPRP and/or experts on the preliminary SSC model. Because the preliminary SSC model was incomplete at the time of Workshop 3, one of the initial working meetings held during this task was to complete the preliminary SSC model and present the model to the PPRP. In addition, because of the recently completed CCCSIP studies, the TI Team invited several REs and PEs from these studies to working meetings to better understand the data and interpretations of these studies.

The TI Team presented the final SSC model to the PPRP during a "final briefing," which occurred during two separate meetings as the model was completed (July 23–24 and October 31, 2014). To assist with the briefing, which was attended by the Project Sponsor, the TI Team and technical staff, the PPRP, and the Database Manager, the PPRP was provided the draft final model HID for review and comment (Task 11). Besides the presentation of the final SSC model, the final briefing included presentations of the assessments performed in preparing the final model. The goal of the final briefing was for the TI Team to present the final SSC model, including how the PPRP, PE, and RE comments from Workshop 3 were addressed. The intent of these presentations was to provide the PPRP with a clear representation of how the TI Team integrated the CBR of the TDI into the SSC model. The dialogue and interaction with the PPRP were used to help refine the final SSC model and the final project documentation of the Diablo Canyon SSC project.

After the final briefing meeting, the SSC model was finalized and a final HID was developed.

3.2.11 Task 11—Development of Hazard Input Documents

According to the definition given in NUREG-2117 (NRC, 2012b), the Hazard Input Document (HID) provides the essential elements of the SSC model that the Hazard Analyst needs for input to the PSHA calculation. The HID is owned by the TI Team and expresses all the details of the model, including logic trees, parameter weights, and derived parameters, but it does not include any discussion or description of the technical bases or judgments by the TI Team for the model elements. Two HIDs were prepared during the study, a preliminary HID that described the preliminary SSC model and a final HID that describes the final SSC model. The final HID is included as Appendix C.

3.2.12 Task 12—Development of Draft SSC Report

Following completion of the SSC model and the hazard sensitivity calculations, the TI Team prepared a draft final report that covered the following topics:

- The SSHAC process completed during the study.
- The tectonic setting of the Diablo Canyon region.
- The geospatial database developed for the study, including the seismicity catalog.
- An overview of the SSC model concepts and logic tree structure.
- A specific description of the SSC model elements and model uncertainties.
- A discussion of hazard results, including sensitivity analyses.

3.2.13 Task 13—PPRP Review of Draft SSC Report

The draft SSC report was submitted to the Project Sponsor and the PPRP for their review and comment. The PPRP review focused on the adequacy of the evaluation and integration process to capture the CBR of the TDI, and documentation of the technical bases for the final model assessments. Written comments from the PPRP were provided to the TI Team and a teleconference call was held to clarify any comments as needed.

The comments were resolved in writing, and incorporated into the final SSC report (Task 14).

3.2.14 Task 14—Development of Final SSC Report

This final SSC report was prepared after incorporating comments and feedback from the PPRP and the Project Sponsor. The final report was submitted to the project sponsor and to the PPRP, along with written responses to their comments, for final review and concurrence.

3.2.15 Task 15—PPRP Closure Letter

Following final review of the final SSC report, the PPRP issued a Closure Letter that summarized their perspective of the Diablo Canyon SSC SSHAC Level 3 study. The letter describes the PPRP review process, the adequacy of the study in fulfilling the SSHAC Level 3 process of evaluation and integration in developing the SSC model, and the adequacy of the documentation of the technical bases that the SSC model reflects the CBR of the TDI. The Closure Letter was issued from the PPRP to the Project Sponsor and is provided in *Appendix B*.

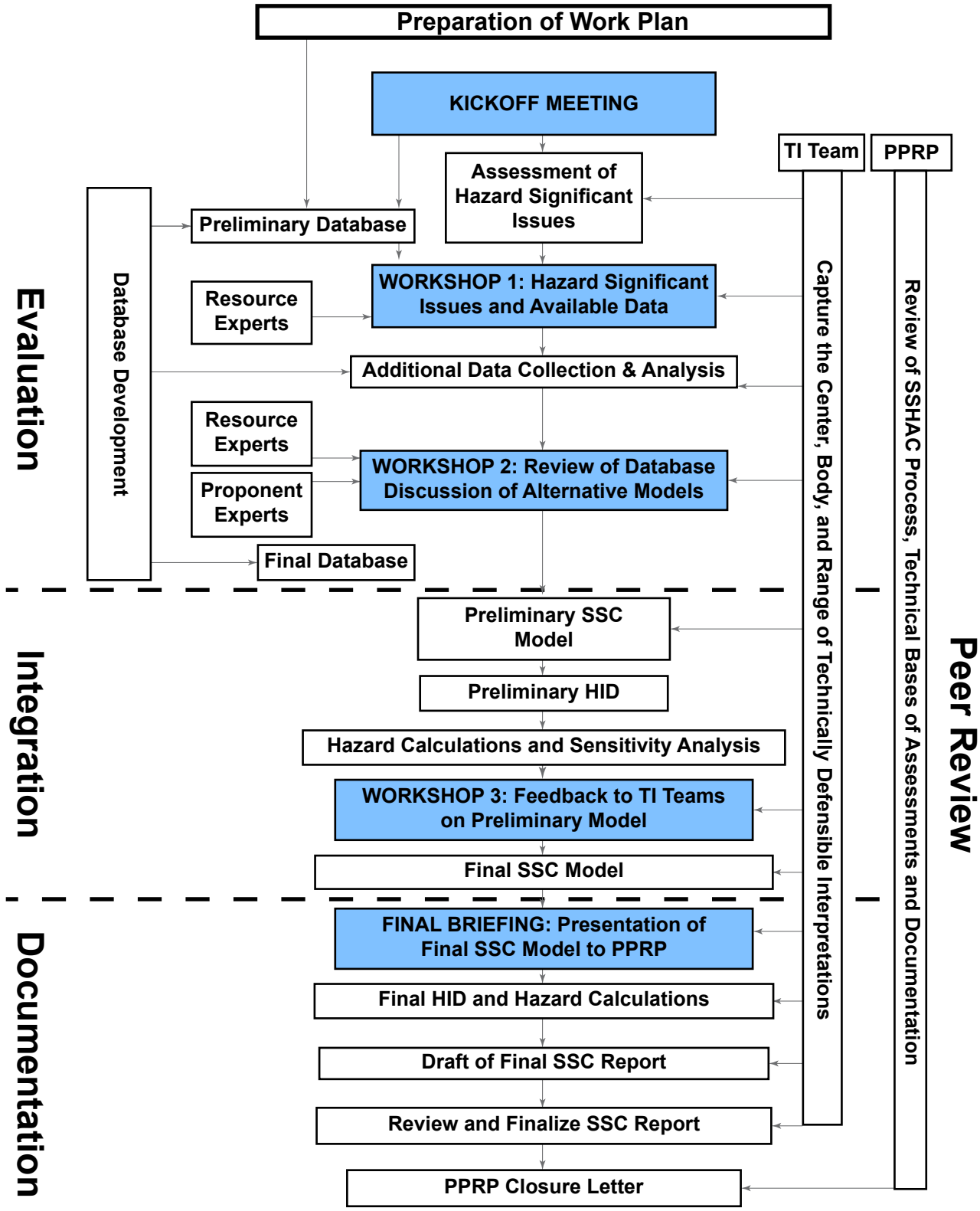

Note: Schematic overview of the activities involved in the execution of a SSHAC Level 3 SSC Study showing the four components in the process.

Source: Modified from Coppersmith and Bommer (2012).

Diablo Canyon SC Study
SSHAC Level 3 Flow Chart

DCCP SSC REPORT

Pacific Gas and Electric Company

Figure **3-1**

File path: S:\1005\005\Final_Report_Figures\Figure_3-01.ai; Date: 02/13/2015; User: Alex Remar, LCI; Rev.1

4.0 SSC DATABASE: GEOLOGY, SEISMOLOGY, AND GEOPHYSICS

This chapter summarizes the data, both legacy data sets from the earlier site characterization and original Long Term Seismic Program (LTSP), and more recent data collection and analyses conducted as part of the AB 1632 program, PG&E–USGS Cooperative Research and Development Agreement (CRADA) and PG&E LTSP studies that were available for consideration by the SSC Technical Integration (TI) Team in the development of the SSC model. This chapter describes the scope of the studies and analyses, and provides information on the project database and location of appropriate reports summarizing the information. The organization and content of the project database is described in *Appendix E*. The results of the studies and their use by the SSC TI Team in the development of the SSC model are described further in *Chapters 7, 8, 9, 10, 11, and 12* of this report.

4.1 Overview and Purpose

As outlined in NUREG-2117 (NRC, 2012b) the evaluation process starts with the identification and review of the available body of hazard-relevant data, models, and methods. This body of knowledge may be supplemented by new data gathered within the project.

The Diablo Canyon SSC Study builds on an extensive database originally developed as part of the LTSP. This program was initiated in 1985 to address four elements of the License Condition Item 2.C.(7) of the Diablo Canyon Unit 1 Facility Operating License DPR-80 issued in 1984 that required a reevaluation of the seismic design bases for the DCPP. A description of the onshore and offshore databases compiled as part of the LTSP to address Elements 1 (Geologic and Seismic Data Compilation, Collection, and Evaluation) and Element 2 (Earthquake Magnitude Reevaluation) was provided in the original LTSP Final Report and Addendum (PG&E, 1988, 1991). The database compiled as part of the initial LTSP included documents and data from the Safety Analysis Reports (PG&E, 1973, 1974, 1975).

Continued seismic monitoring and the acquisition of high-resolution potential field (magnetics and gravity), seismic reflection, bathymetric, and topographic data were conducted subsequent to submittal of the original LTSP Final Report and Addendum (PG&E, 1988, 1991). Many of the regional geophysical data sets were collected from 2008 to 2010 as part of the PG&E–USGS CRADA. These new data were combined with onshore and offshore geologic data to update earlier models for the area and were integrated with more site-specific studies of the Shoreline fault zone carried out by PG&E. The results of these analyses were summarized in the Shoreline Fault Zone Report (PG&E, 2011).

Section 4.2 provides a summary of the data collection activities and resulting database developed as part of the initial Final Safety Analysis Report (FSAR), LTSP, and 2008–2011 CRADA studies, which in total are referred to as the Legacy Data Set.

Extensive additional new seismologic, geologic, and geophysical data sets were acquired in 2012–2014 as part of the AB 1632 program, PG&E–USGS CRADA, and ongoing PG&E LTSP. Sensitivity studies conducted during the early stages of the Diablo Canyon SSC Study, as well as review and discussions of the existing databases during Workshop 1, provided perspective on the types of data and analyses that would fill data gaps relevant to important SSC issues and would provide information that could potentially reduce SSC model uncertainties. The specific issues addressed by these studies and the resulting databases that were used by the SSC TI Team in its evaluation are described in *Section 4.3*. The database that contains the results of these studies is described in *Appendix E*.

4.2 Legacy Data

Legacy data include data acquired as part of the initial FSAR, LTSP, and 2008–2011 CRADA studies. Brief summaries of the types of data collected and evaluated as part of these studies are described in the following sections.

4.2.1 Final Safety Analysis Report Data

Geologic, seismologic, and geotechnical information that was collected for licensing the operating DCPP, construction of the raw water reservoir, and construction of the 230 kV and 500 kV switchyards are documented in Sections 2.5.1 and 2.5.2 of the DCPP FSAR Update, submitted in support of the continued operation of Units 1 and 2 (PG&E, 1973, 1974, 1975). Borehole, trench, and mapping data collected in the 1960s and 1970s (e.g., Jahns, 1966, 1967a, 1967b, 1968; Jahns et al., 1973) for the power plant were subsequently compiled and reviewed to evaluate conditions beneath the power block and between the power block and the independent spent fuel storage installation (ISFSI; PG&E, 2004). These documents also were reviewed in the detailed evaluation of the potential seismic hazard posed by the Diablo Cove fault (PG&E, 2014, Chapter 12).

4.2.2 1988 LTSP Report and Data

Databases developed as part of the DCPP LTSP for use in the PG&E (1988) PSHA were documented in the LTSP Final Report and Addendum (PG&E, 1988, 1991). As part of the data collection program:

- 990 km of high-resolution and deep-penetration seismic reflection surveys were commissioned, and the data processed and analyzed.
- 9,037 km of post-1978 seismic reflection data were purchased or acquired from government agencies and analyzed.
- 5,849 km of pre-1978 seismic reflection data were reviewed.
- Marine terraces were mapped in detail and dated along 90 km of the south-central California coast.

- 66 trenches and natural exposures totaling 8,210 linear feet (2,503 linear meters) were logged and interpreted.
- 240 boreholes varying in depth from approximately 15 feet (4.6 m) to approximately 120 feet (36.6 m) were drilled and logged.
- More than 300 water-well and oil-well records were acquired.
- Rock samples were collected offshore by diver geologists.
- Drop core samples were collected.

Additionally, the installation and operation of the PG&E Central Coast Seismic Network, an 18-station high-gain network of telemetered seismographs were installed along the coastal region from Ragged Point to Point Sal. This network was designed to supplement the seismographic coverage of the region around the Diablo Canyon site by the University of California, Berkeley, the California Institute of Technology, and the USGS.

4.2.3 Shoreline Fault Zone Report and Data

Many of the regional geophysical data sets discussed in the *Report on the Analysis of the Shoreline Fault Zone, Central Coastal California* (PG&E, 2011) were collected as part of the PG&E/USGS CRADA. These new data were combined with onshore and offshore geologic data to update earlier models for the area and were integrated with more site-specific studies of the Shoreline fault zone carried out by PG&E.

The following data were collected from 2008 to 2010:

- Geologic Map Data—Onshore and offshore geologic mapping was conducted in 2009 and 2010 to prepare a “seamless” onshore/offshore geologic map of the Shoreline fault zone study area. This effort included detailed mapping of extensive rock exposures in the sea cliffs and on the wave-cut platform exposed at low tide from Lion Rock (north of Diablo Cove) to south of Rattlesnake Creek, and collection of 50 rock samples from the seafloor near the coastline by divers. Selected rock samples were analyzed to determine bulk physical properties (e.g., density and magnetic susceptibility). Coastline mapping utilized Light Detection and Ranging (LiDAR) surveys and orthophoto maps. Offshore interpretation of the geology utilized multibeam echosounder (MBES) bathymetry data magnetic field data, and seismic-reflection data in addition to the rock samples. The mapping and analysis are described in Appendix B of PG&E (2011)
- Potential Field-Magnetic Surveys—Three magnetic surveys were conducted in the DCPP area in 2008 and 2009. These included a regional fixed-wing aeromagnetic survey from San Simeon to Point Concepcion (Langenheim et al., 2009), a marine magnetic survey from Estero Bay to San Luis Obispo Bay (Sliter et al., 2010), and a helicopter magnetic survey from Point Buchon to Point San Luis (New Sense Geophysics, 2010).
- Potential Field-Gravity Surveys—The USGS compiled, edited, and reprocessed nearly 30,000 gravity measurements to produce an isostatic residual gravity map for the region, from Monterey Bay on the north to the Santa Barbara Channel on the south (Langenheim et al., 2008).

- Multibeam Echosounder Surveys—MBES bathymetry data for the Estero Bay to San Luis Obispo Bay nearshore region were acquired by the Seafloor Mapping Lab at the California State University Monterey Bay during 2007, 2009, and 2010 (CSUMB, 2012). Improvement in resolution relative to the original LTSP 1988 data reflects both the use of modern swath mapping techniques, and the fact that mapping could be done closer to shore than in previous surveys.
- LiDAR Survey—PG&E contracted TetraTech to conduct a LiDAR survey from fixed-wing aircraft during one of the lowest tides of the year (–1.5 feet relative to mean lower low water [MLLW] at 3:02 p.m. on 28 January 2010). See Appendix G of the Shoreline Fault Zone Report for more details on the extent of coverage (PG&E, 2011, Appendix G).
- High-Resolution Seismic-Reflection Profiling—High-resolution single-channel seismic-reflection data were acquired by the USGS in 2008 and 2009 between Piedras Blancas and Pismo Beach, along shore-perpendicular transects spaced 800 meters (m) apart extending from close to shore to beyond the 3-mile limit of California State waters. These data were collected, along with the marine magnetic data described above, as part of the PG&E–USGS CRADA, the California State Waters Mapping Program, the USGS Coastal and Marine Geology Program, and the USGS Earth Surface Processes Program and have been published as USGS Open File Report 2009-1100 (Sliter et al., 2010)

4.2.4 LTSP Legacy Seismic Profiles Database

In 1986, PG&E commissioned a multichannel seismic-reflection survey in California State waters from north of the Piedras Blancas anticlinorium to south of the DCPP. This 1986 survey was one of the last high-energy surveys permitted in California State waters. For the LTSP, PG&E also purchased additional exploration survey seismic-reflection profiles collected in this same general area between Point San Simeon and the DCPP. These lines were primarily from the Western Geophysical surveys undertaken in 1974, 1975, and 1982. The interpretation of these newly acquired survey data was integrated with the data purchased by PG&E and previous PG&E data from the 1970s, and presented in the LTSP documentation (PG&E, 1988, 1990a). Many of these legacy archive data were included in the study by Willingham et al. (2013).

These data have been archived for use in subsequent mapping and interpretation efforts, and for comparison to data acquired more recently (e.g., PG&E, 2014, Chapters 2 and 3). This database has been supplemented with more recently acquired seismic-reflection data, such as the high-resolution seismic-reflection data collected by the USGS in 2008 and 2009, which are described above in *Section 4.2.3*, and the low energy seismic-reflection data described below in *Section 4.3.1.1*. Legacy marine and onshore surveys that are included in the database are described in *Appendix E*.

4.3 Recently Acquired Data (Post-2011)

Assembly Bill 1632 (Blakeslee, Chapter 722, Statutes of 2006) directed the California Energy Commission (CEC) to assess the potential vulnerability of California's large-

baseload power-generation facilities (1,700 megawatts or greater) to a major disruption due to a seismic event or plant aging. The 2008 CEC report "An Assessment of California's Nuclear Power Plants: AB 1632 Report" (referred to herein as the "AB 1632 Report") contained a recommendation from the CEC that PG&E use 3D geophysical seismic-reflection mapping and other advanced techniques to explore fault zones near the DCPP. This recommendation was made to supplement PG&E's LTSP and help resolve uncertainties surrounding the seismic hazard at the DCPP (CEC, 2008). The seismic survey data collected in response to the AB 1632 report are described in *Section 4.3.1*.

In addition to the AB 1632-related activities, extensive additional new seismologic, geologic, and geophysical data sets were acquired in 2012–2014 as part of the PG&E/USGS CRADA, and the ongoing LTSP. These studies are included in the project database (*Appendix E*). Key studies from these programs are summarized in *Section 4.3.2*.

4.3.1 Central Coastal California Seismic Imaging Project

Between 2010 and 2012, PG&E performed a series of three-dimensional (3D) and two-dimensional (2D) low-energy and high-energy seismic-reflection surveys, along with other geophysical investigations, to explore fault zones near the DCPP, as recommended in the AB 1632 Report. PG&E documented its activities performed in accordance with the CEC recommendation in the *Central Coastal California Seismic Imaging Project Report* ("CCCSIP Report").

Geologic and geophysical surveys conducted by PG&E as part of the CCCSIP provided new geologic and geophysical data to further improve the source characterization of the Hosgri, Los Osos, San Luis Bay, and Shoreline fault zones. Marine and land survey activities were prioritized based on (1) identification of the key seismic source parameters that had a significant impact to hazard at the DCPP site and (2) the overall likelihood that information from the proposed survey would reduce the uncertainty associated with each parameter. The following hazard-significant parameters were considered for investigation:

1. Hosgri fault slip rate
2. Hosgri fault dip
3. Shoreline fault slip rate
4. Hosgri–San Simeon fault step-over
5. Los Osos fault dip
6. Los Osos fault sense of slip
7. Los Osos fault slip rate
8. Hosgri/ Shoreline fault zone rupture
9. Shoreline southern end
10. Shoreline segmentation

Sections 4.3.1.1 and 4.3.1.2 describe, respectively, the high-resolution 3D low-energy seismic survey (LESS) data collected offshore and the data collected for the Onshore Seismic Interpretation Project (ONSIP).

4.3.1.1 New Offshore (LESS) Data

To determine the shallow geologic conditions along the proposed north segment of the Shoreline fault, PG&E commissioned low-energy, high-resolution 3D and 2D seismic-reflection profiling surveys offshore of Point Buchon. The surveys were undertaken in late 2010 and early 2011 and were designed to cover the area where the proposed north segment of the Shoreline fault zone (PG&E, 2011) was inferred to trend into the Hosgri fault zone (HFZ). These surveys significantly filled data gaps in the previous seismic-reflection data and provided data for refining interpretations. The low-energy sound source restricted penetration to the shallow subsurface, but allowed for high-resolution acoustic imaging that facilitated structural interpretation within a small area offshore of Point Buchon.

The 3D/2D data set in the Point Buchon study area allowed for more detailed mapping than was previously possible. Specifically, the 3D seismic volume and the close spacing of the seismic-reflection profiles (12.5 m for the 3D survey and 100 m for the 2D survey) permit better correlation of faults and folds to more confidently characterize geology and more accurately determine structural trends and extents. The main structural elements mapped in the Point Buchon study area are the HFZ, the Point Buchon fault zone (part of the Shoreline fault in this SSC model), and a prominent syncline that deforms Tertiary strata in the southern two-thirds of the study area. A description of the 3D/2D data and structural interpretations are provided in PG&E (2014, Chapter 2).

An extensive LESS acquisition program was undertaken in 2011 and 2012 for PG&E to better define the Shoreline fault zone and to image buried channels that could be used to determine offsets along both the Shoreline and the Hosgri fault zones. For this investigation, detailed 3D/2D seismic-reflection profile surveys were conducted to determine whether fault offsets of “piercing points” could be imaged and defined for possible slip-rate calculations. These low-energy (~1.5 kilojoules [kJ]) 3D seismic survey areas were located along the southern extensions of the Shoreline fault zone in San Luis Obispo Bay and along parts of the HFZ in Estero Bay and the Point Sal offshore areas. A description of the data acquisition and interpretation is provided in PG&E (2014, Chapter 3).

High-resolution 3D LESS mapping of marine channels offset by the HFZ at two locations (western Estero Bay and offshore Point San Luis) was used to measure fault offsets and estimate fault slip rates as described in *Section 8.3*.

The potential slip rates associated with the Shoreline fault in the San Luis Obispo Bay study area, as estimated from interpretation of the 3D LESS data set, are described in *Section 8.4*.

4.3.1.2 Onshore (ONSIP) Data and Geologic Mapping Program

The Onshore Seismic Interpretation Project (ONSIP) 2011 Data Report and, the *2012 3D Onshore Seismic Survey Report* (PG&E, 2014, Chapters 7 and 8, respectively) present the interpretations of 3D/2D seismic-reflection profiling and tomography data collected in

the Irish Hills in 2011. Both high-resolution shallow-penetration (low-energy) and deep-penetration (high-energy) seismic data were collected to constrain the geometry of the Los Osos, San Miguelito, and San Luis Bay faults, as well as illuminate the deeper structure of the Pismo syncline and the Edna fault system within the central Irish Hills. Interpretations of these data are considered in the assessment of the geometry of individual faults (see *Section 7.4*) and the characterization of a local areal source zone encompassing the Irish Hills–Estero Bay area (*Section 13.5*).

Geologic mapping was performed in support of the onshore seismic studies (PG&E, 2014, Chapter 9). In addition to developing strip maps in corridors centered on the seismic reflection lines, the mapping program also reviewed and refined the earlier mapping of the Los Osos fault by Lettis and Hall (1994). Among the topics addressed by mapping was an assessment of whether the Los Osos fault zone may be an oblique- or strike-slip fault instead of a reverse-slip fault, as previously interpreted. LiDAR- and field-reconnaissance-based evaluation of streams crossing lineaments and faults associated with the Los Osos fault zone along the northeastern margin of the Irish Hills concluded that there was no evidence of a strike-slip component to the Los Osos fault zone (see discussion in *Section 8.5*).

4.3.2 PG&E–USGS CRADA and PG&E LTSP Studies

Data collection efforts from 2012 to 2014 involved various groups and agencies. Descriptions of these data and analyses and interpretations thereof are presented in several recent publications and reports. Key studies are described in the following sections.

4.3.2.1 USGS Analyses of Offshore Data

The PG&E–USGS CRADA supported the collection, integration and analysis of multiple offshore data sets including high-resolution seismic-reflection profiles, multibeam bathymetry, and marine magnetic data. Among other goals, these investigations were designed to evaluate geometry of the HFZ and potential kinematic interaction with branching faults, and to identify features that could be used as piercing points to estimate slip rate. The results of these investigations are presented in two publications by Johnson and Watt (2012) and Johnson et al. (2014). A brief description of the data and results is presented below.

As noted in *Section 4.2.3*, approximately 1,500 km of single-channel seismic-reflection data were collected offshore Central California between Point Sal and Piedras Blancas in 2008 and 2009 (Sliter et al., 2010). These data, which were collected primarily on N60°E-trending profiles that were perpendicular to the HFZ and spaced approximately 800 m apart (locally 400 m). The profiles, which were collected along an approximately 94 km long portion of the fault zone, cross the fault zone 121 times.

Seismic profiles were integrated with similarly dense marine magnetometer data and high-resolution bathymetric data collected within California State waters (from the

shoreline to 5.6 km offshore) for the California Seafloor Mapping Program (Sliter et al., 2010).

Marine magnetic data were collected on the same surveys and merged with onland data collected by fixed-wing aircraft (Langenheim et al., 2009) and helicopter (Langenheim, Watt, and Denton, 2012) and then gridded to 50 m (Johnson and Watt, 2012). Additional magnetic transects were run midway between seismic lines, resulting in a uniform spacing of 400 m.

High-resolution bathymetric and backscatter data was collected by the California State University of Monterey Bay (CSUMB) Seafloor Mapping Lab in 2007, 2008, and 2010. The CSMP database, along with information on data collection and processing is available at CSUMB (2012). Spatial resolution is typically 1 m in water depths <50 m, and 2 m for water depths of >50 m.

The near-surface continuity of the multiple strands of the Hosgri fault interpreted from these data and the discussion of fault-zone heterogeneity and development of shallow structures and tectonic geomorphology due to fault trend, fault bends, and fault interactions are considered in the evaluation of the geometry, rupture models, and maximum magnitude assessment for the HFZ (*Sections 7.3, 9.2.2, and 10.3*, respectively).

In 2012, the USGS extended high-resolution multibeam coverage beyond California State waters in outer Estero Bay to capture farther offshore portions of the Hosgri fault zone and the unstable shelf break to the north (Hartwell et al., 2013). During this cruise, a small area covering a linear southwest-facing bathymetric slope, referred to as the cross-Hosgri-slope (CHS) was remapped, with a survey designed to enhance data density and minimize poorly oriented data artifacts. The metadata and high-resolution bathymetric data collected in this survey are available in the electronic supplement to the Johnson et al. (2014) publication. Digital fault traces were provided electronically to PG&E as part of a draft offshore geologic map (J. Watt, pers. comm. to H. AbramsonWard, Dec. 10, 2013). Johnson et al. (2014) interpret this slope feature as the shoreface of a latest Pleistocene sand spit and, based on detailed analysis of the relict shoreface, estimate a latest Pleistocene slip rate for the eastern (main) trace of the Hosgri fault in Estero Bay (see *Section 8.3.2*).

4.3.2.2 USGS Analyses of Seismicity Data

Hardebeck (2010) first recognized the Shoreline fault zone as an approximately 25 km long vertical strike-slip fault based on seismicity relocations. More recently under the PG&E–USGS CRADA, Hardebeck (2012b) updated the San Luis Obispo-area seismic velocity model of Hardebeck (2010) based on double difference tomography and relocated the seismicity using the Optimal Anisotropic Dynamic Clustering (OADC) algorithm (Ouillon et al., 2008) to objectively identify the simplest planar fault geometry that fits all of the earthquakes to within their location uncertainty. As described in Hardebeck (2013) the relocations and earthquake focal mechanism data were used to evaluate the geometry of the Shoreline fault zone at depth, as well as the adjacent section of the offshore Hosgri fault. In addition to evaluating the geometry and possible

intersection with the HFZ, Hardebeck (2013) also provides estimates for maximum magnitude, magnitude frequency distributions, and resulting slip rate for the Shoreline fault based on analysis of these data. These results are considered in the characterization of the geometry, slip rate, and maximum magnitude for the Shoreline fault (*Sections 7.4, 8.4, and 10.4-10.6*). Hardebeck (2014a) is an update to the Hardebeck (2010) relocated earthquake catalog and is provided in *Appendix F*.

4.3.2.3 USGS Analyses of Aeromagnetic Data

As part of the post-2011 CRADA effort, the USGS created a magnetic map of the Irish Hills and surrounding areas (Langenheim, Watt, and Denton, 2012). The map is a mosaic of surveys collected by three separate means:

- Fixed-wing aircraft at a nominal height of 305 m (Langenheim et al., 2009).
- Boat, with the sensor at sea level (Sliter et al., 2010).
- Helicopter.

The helicopter survey was flown by New-Sense Geophysics in October 2009 along flight lines spaced 150 m apart and at a nominal terrain clearance of 50–100 m. Tie lines were flown 1,500 m apart. Data were adjusted for lag error and diurnal field variations. Further processing included microleveling using the tie lines and subtraction of the reference field defined by International Geomagnetic Reference Field (IGRF) 2005 extrapolated to August 1, 2008. Data were interpolated to a square grid with a grid interval of 50 m using the principle of minimum curvature (Briggs, 1974). The magnetic base levels of three surveys were then adjusted to bring them onto a common magnetic datum. Abrupt lateral changes in magnetization that may represent lithologic or structural boundaries were identified using three different approaches.

The data and map were presented to the TI Team by Dr. Langenheim at the November 2012 SSHAC Workshop 2 (Langenheim, 2012). Tectonic reconstructions based in part on analysis of this data set are used to evaluate the long-term history of the San Gregorio–San Simeon–Hosgri fault system (see *Section 5.1.2*).

4.3.2.4 USGS Structural Cross Section Across Irish Hills

An interpretation of the structure of the Irish Hills was presented by Dr. Graymer of the USGS at the November 2012 SSHAC Workshop 2 (Graymer, 2012). The underlying hypothesis of this structural interpretation is that thickening of the Tertiary section beneath the Pismo syncline axis is primarily explained by thrust repetition at depth.

The geometry of faults within the Irish Hills implied by this model, as well as other alternative models based on interpretation of the ONSIP data (e.g., PG&E, 2014, Chapter 7), are incorporated into the characterization of the Irish Hills–Estero Bay Local Source Zone (*Section 13.5*).

4.3.2.5 GPS and Geodetic Data

The acquisition of global positioning system (GPS) measurements and related geodetic data and analyses has been undertaken by various researchers as described below. The results of these studies have been considered by the TI Team in the evaluation of the overall seismotectonic setting of the study region (*Chapter 5*), and evaluation of sense and rate of slip on faults near the DCPP (*Chapter 8*).

Interseismic Velocity Field from GPS Measurements
Murray-Moraleda et al. (2011) compiled a new spatially dense secular velocity field for the Central California coast region from GPS measurements. GPS data included measurements from the EarthScope Plate Boundary Observatory (PBO) permanent GPS network, as well as existing survey-mode GPS (SGPS) archive data and additional SGPS data collection for 27 sites (measured one to three times between 2007 and 2010). The USGS also established nine semipermanent GPS sites to improve spatial coverage in the CCCR and obtain well-constrained velocities in a short amount of time. The resulting velocity field and a first order model using the approach of McCaffrey (2005) to quantify slip rates on major faults of the region was presented by Murray-Moraleda et al. (2011).

An updated analysis of the patterns and rates of deformation west of the San Andreas fault in Central California using this data set was presented by Dr. Murray at the November 2012 SSHAC Workshop 2 (Murray, 2012).

Kinematics of Coastal California Inferred from GPS geodesy
Continuous and campaign GPS observations from several hundred stations from western California and the Pacific Plate were processed by DeMets (2012a) using state-of-the-art procedures and the most recent GPS satellite products to create an up-to-date GPS velocity field for areas of Central California pertinent to the DCPP. The GPS velocity field was transformed to a newly realized frame of reference tied to the Pacific Plate to reveal the pattern of active deformation in areas of Central California west of the San Andreas fault. The preliminary results of the study, which strongly suggested that faults offshore from western California collectively accommodate no more than 3 ± 1 mm/yr of right-lateral long-term slip parallel to the San Andreas fault, were presented by Dr. DeMets at the November 2012 SSHAC Workshop 2 (DeMets, 2012b). Further analysis of regional GPS velocity data by DeMets et al. (2014) suggests that the Pacific plate may deform internally, which implies that rates of dextral shear in the region are slightly lower, accommodating no more than 1.8± 0.6 mm/yr as discussed in *Section 5.1.6*. The results of these analyses are considered in the characterization of the overall tectonic framework of the study region (*Section 5.1*) and for comparison to the slip rate assessed for the Hosgri fault (*Section 8.3.8.4*).

Analysis of Stress and Strain in the Central Coast, California
In 2013 PG&E funded a project to analyze GPS station velocity data and earthquake focal mechanisms in the DCPP vicinity to evaluate the orientations and relative magnitudes of principal strains and stresses (PG&E, 2015b). The primary focus areas of this study include the Irish Hills and adjacent offshore region, Estero Bay, the Hosgri fault (from approximately Point Sal to Point Piedras Blancas), and eastward to the

Oceanic–West Huasna fault and Rinconada fault. The results of this study were presented to the TI Team by N. Lewandowski at the March 2014 SSHAC Workshop 3 (Lewandowski, 2014). The results, which are discussed in more detail in *Section 5.1.6*, include the following:

- The orientation of the maximum compressive principal stress, σ_1, which is a fundamental input to static Coulomb rupture models and dynamic rupture models, including those that provide information on the likelihood for a branching or linked rupture involving the Shoreline and Hosgri faults (e.g., Kame et al., 2003)
- The orientations and relative magnitudes of the principal stresses and strains, which provide information on the current tectonic setting of the DCPP vicinity
- A "stress map" showing the orientations of principal stresses surrounding the site, which is a fundamental data set to include as part of a complete assessment for seismic hazard analysis.

4.3.2.6 California State Mapping Program

Detailed geologic mapping (1:24,000 scale) supported by the STATEMAP element of the National Cooperative Geologic Mapping Program is used extensively by the CGS Seismic Hazard Zonation Program to identify areas where earthquakes are likely to cause liquefaction, landslides, or other ground failures and provides the basic data that enables CGS to improve earthquake ground-shaking estimates, which are integrated into California's building codes. Mapping completed between 2008 and 2013 as part of the STATEMAP program included the following 7.5′ quadrangles in the study region: Morro Bay South, San Luis Obispo, Pismo Beach, Arroyo Grande NE, and Oceano (Wiegers, 2009, 2010, 2011, 2013; Delattre and Wiegers, 2014).

4.3.2.7 PG&E Offshore Seismic Stratigraphy Study

In 2012, PG&E funded a project to map Quaternary stratigraphic features imaged in seismic-reflection data offshore of the DCPP in order to use them to evaluate rates and style of Quaternary fault deformation. This mapping was based on analysis of the USGS high-resolution 2D seismic-reflection data released by Sliter et al. (2010) and the Fugro Point Buchon 3D/2D data set as an aid to better assess the recency, style, and rate of slip on offshore faults.

This analysis has led to a significant improvement in the mapping and understanding of Quaternary stratigraphy in the study area. Several late Quaternary unconformities are identified on the profiles and correlated widely throughout the study area. The depositional setting of the most pronounced and widely correlated unconformities is interpreted based on relationships to surrounding reflectors using a sequence stratigraphic framework. Sea-level lowstand deposits in Estero Bay are recognized in these data as distinctive wedge-shaped sets of clinoforms localized directly beneath the modern shelf break. Similar distinctive clinoform sets buried beneath the outer shelf are interpreted as deposits from older sea-level lowstands. These lowstand deposits underlie and are eroded

by pronounced unconformities that are recognized and correlated widely within the study area.

PG&E (2013a) provides a description of the mapping and assessment of ages of unconformities that are identified throughout the study area. Further analysis and interpretation of these unconformities in the southern Estero Bay and Point Sal regions and their use in constraining the ages of piercing point features across the HFZ are presented in *Section 8.3.4*.

4.3.2.8 LTSP Quaternary Analyses of Fluvial and Marine Terraces in the Los Osos and Edna Valleys

Geologic and geomorphic mapping and analysis of fluvial and marine terraces in the Los Osos and Edna valleys were conducted to provide information to constrain slip rates of the Los Osos fault and other faults along the northeast margin of the San Luis Range. The results of the first phase of this evaluation are presented in PG&E (2013b).

Data from a number of unpublished reports that were completed as part of the LTSP update in 2011 and 2012 were used in the analysis and compilation of figures for this study. These data are listed as follows:

- Ridge line profiles compiled by AMEC (2011) using San Luis Obispo County InSAR data that were created to identify high erosional surfaces within the San Luis Range and were used to evaluate possible uplift rates of the San Luis–Pismo structural block and Los Osos Valley structural block.
- Subsurface data compiled for the Los Osos and Edna valleys that were compiled by AMEC (2011) were evaluated as part of this study, but were not used in any of the analyses because they did not aid in identifying strath surface elevations or origin of terrace deposits. Most of the data included in the subsurface compilation were provided by Tim Cleath (Cleath-Harris Geologists, Inc.). Other data included in the subsurface database are from oil and gas wells, Caltrans wells, and geotechnical studies; some of the data were included in the DCPP LTSP (PG&E, 1988).
- A geologic map GIS database (including geologic units and faults) that was part of a compilation of previously published and some unpublished data (AMEC, 2012a) were used in creation of maps and to guide field studies.
- A reevaluation of shoreline angle elevations on the west side of the Irish Hills based on coastal LiDAR data acquired by PG&E in 2010 was performed by AMEC (2012b). These data were used in hypothesizing correlations of terraces across the Los Osos fault zone. Data from this draft report were superseded where new field data were acquired as part of the field investigations for the PG&E (2013b) study.

Based on preliminary correlation of the highest remnants of marine terraces within Edna Valley to the Late Pliocene warm interval (~3.0 Ma) a long-term uplift rate for the valley was estimated. Less well-constrained data is available for the Los Osos Valley. These preliminary uplift rate estimates are used to evaluate differential uplift across the Los

Osos fault and other structures along the northeastern margin of the San Luis Range (*Section 8.2.2*).

4.3.2.9 San Francisco State University Studies

Aileen Chea conducted preliminary research for a master's thesis under the direction of TI team members Dr. John Caskey (principal thesis advisor) and Kathryn Hanson (thesis committee member). The tasks and objectives of Chea's research were designed to provide additional data to aid in characterization of the Los Osos fault (LOF)—specifically to improve constraints on the relative rates of uplift between the Irish Hills and Los Osos Valley structural blocks.

The work conducted to date focused on two main areas, the western part of the onshore Los Osos fault near the town of Los Osos and the coastal region in and north of the town of Cayucos. Chea's field studies in the area of an elevated Quaternary terrace (informally named the Memorial Park surface), approximately 2 km east of the town of Los Osos, involved surficial mapping and topographic profiling of the terrace surface, as well as soil descriptions and minimum age estimates for the Memorial Park terrace based on relative soil development (see *Section 8.2.2.3*). One of the preliminary results of the investigation is that there is a general lack of well-defined surface scarps along this trace of the LOF in this area, indicating that the LOF may be a blind fault structure in this area.

Preliminary results of Chea's thesis investigations along the approximately 6 km long stretch of coastline northwest of Cayucos are summarized in *Section 8.2.2.2*. The identification of more than one low terrace along this stretch of coast has important implications for (1) evaluating the long-term uplift rate of the Los Osos Valley block, which defines the footwall for the LOF as previously portrayed by Lettis and Hall (1994; see *Section 8.5*), and (2) evaluating evidence for Quaternary activity of the Cambria fault. The new terrace mapping and preferred ages and correlations are discussed in *Section 8.2.2.2*.

5.0 SEISMOTECTONIC SETTING OF THE DIABLO CANYON REGION

This chapter describes the seismotectonic setting of the Diablo Canyon site region, focusing on those aspects of the tectonic and geologic history that help to define the contemporary tectonic setting. In particular, we describe the sequence of tectonic events that gave rise to the location, geometry, and style of active faulting in the region and to the major depositional sequences recognized in the region. We also describe older tectonic processes, such as subduction of the Monterey microplate and Neogene basin formation, that are no longer active processes in the contemporary tectonic setting. The contemporary tectonic setting provides the framework from which to make the following assessments:

- Characterize alternative tectonic models that describe ongoing seismicity and deformation in the site area.
- Identify and characterize the geometry, style, and slip rate of active faults in the site area.
- Evaluate how these active faults may link with one another and/or with other faults that extend beyond the site area during earthquake rupture scenarios.

In this chapter, the terms region, vicinity, and area are used informally, and are not intended to apply to the NRC-defined radial site distance categories (e.g., 320 km, or 200 mi. Site Region; NRC, 2007).

5.1 Tectonic Setting

Diablo Canyon is located along the coastal margin of the San Luis Range in south-central coastal California (Figure 5-1). The site region lies within the right-lateral transform boundary between the Pacific Plate and the Sierra Nevada/Great Valley microplate of the North American Plate. The contemporary plate boundary is a zone of right-lateral strike-slip faults and transpressional deformation over 100 km wide at the latitude of Diablo Canyon, and is generally centered on the San Andreas fault zone. The transform plate boundary initiated approximately 28 million years ago (Ma) (Atwater, 1970) and, for most of its history, developed in a transtensional tectonic setting with the primary location of faulting offshore of south-central coastal California coincident with the development of extensional or transtensional basins.

The change to the contemporary transpressional plate boundary began approximately 8–6 Ma in response to a >20° clockwise rotation in the direction of relative motion between the Pacific and North American plates (Atwater and Stock, 1998; Krijgsman et al., 1999). The plate boundary progressively shifted landward to the present location of the San Andreas fault zone by approximately 5 Ma, coincident with opening of the Gulf of California (Atwater and Stock, 1998). Common to both the transtensional and transpressional environments, movements on the major strike-slip faults accounted for the vast majority of the approximately 52 millimeters per year (mm/yr) of relative motion

across the plate boundary (Titus et al., 2011). However, in the contemporary transpressional setting, in addition to the prominent transform strike-slip faults, contractional structures, such as reverse and reverse-oblique slip faults, are important components of the active tectonics of the plate boundary and the Diablo Canyon site region.

The identified active faults of south-central coastal California are shown on Figure 5-1. As with most of California, the geologic structure of this region results from a long history of tectonic events with superimposed styles and rates of deformation. Many of the active faults in the contemporary tectonic setting are reactivated structures, inherited from one or more previous tectonic regimes, and thus reflect a composite geologic history. For the characterization of seismic sources at Diablo Canyon, it is important to resolve the contemporary style and rate of deformation from the inherited composite history of deformation. The following sections provide a brief summary of the primary tectonic events that influenced the depositional history and origin of faults in the Diablo Canyon area.

5.1.1 Mesozoic Subduction

During the Jurassic and Cretaceous, east-northeast-directed subduction of the Farallon and Kula plates occurred along the western margin of the North American Plate. The Franciscan Complex formed in the accretionary prism above the subduction zone, and sedimentary rocks of the Great Valley sequence were deposited in the forearc basin (Figure 5-2). These two rock units, which were highly deformed during the subduction process, generally constitute “Cretaceous basement” in the Diablo Canyon area. Exhumed Franciscan and ophiolite fragments along the modern coast suggest that the subduction zone was located at or near the modern coastline during this time period.

5.1.2 Cenozoic Transition from Subduction to Transform Plate Margin

During the Cenozoic, the margin of south-central coastal California transitioned from subduction zone tectonic processes to transform plate margin tectonic processes (Atwater, 1970; Dickinson, 1981; Atwater and Stock, 1998; Figure 5-3). This Cenozoic transition is illustrated in detailed tectonic animations by Atwater (2011). Prior to 30 Ma, subduction became increasingly right oblique as the active mid-oceanic ridge (i.e., the East-Pacific rise) separating the Farallon and Pacific plates on its east and west, respectively, approached the trench. Location of the subduction zone migrated westward resulting in growth of the accretionary prism, until becoming situated generally along the Santa Lucia Escarpment offshore of coastal California. Continued deformation and crustal shortening within the overlying “accreted” rocks juxtaposed the older Mesozoic Franciscan Complex and Great Valley sequence rocks along thrust faults. Near Diablo Canyon, these basement rocks are highly folded, faulted and locally imbricated with one another. This period of early Cenozoic subduction during the Paleocene, Eocene, and Oligocene was generally one of nondeposition and/or primarily uplift and erosion in the Diablo Canyon area.

At approximately 28 Ma, the spreading center separating the Farallon Plate from the Pacific Plate approached the subduction zone, and the "narrowing" part of the Farallon plate broke into two smaller microplates along the North American Plate margin, the Monterey microplate at the latitude of Diablo Canyon and the Arguello microplate to the south (Atwater and Stock, 1998). As the North American Plate overrode the spreading center, subduction of the smaller microplates slowed and was replaced by transform faulting along a proto-San Andreas fault (Figure 5-3). The remaining larger Farallon Plate became separated into the Juan de Fuca and Cocos plates to the north and south, respectively, and the transform plate margin progressively grew at an average rate of approximately 4 centimeters per year to the north and south with migration of the Mendocino Triple Junction and Rivera Triple Junction, respectively. Today, the San Andreas transform defines the Pacific Plate–Sierra Nevada/Great Valley microplate boundary for nearly 1,300 km from Cape Mendocino to the Gulf of California (Figure 5-3).

Cessation of subduction and growth of the transform plate margin did not occur seamlessly, but produced many complex geologic structures and features. Of importance to the characterization of seismic sources in the Diablo Canyon area, the cessation of subduction left isolated parts of the sundered Farallon Plate beneath the margin of coastal North America. As described by Atwater and Stock (1998), at approximately 18 Ma the last remnant of the Monterey-Pacific spreading center ceased, and the Monterey microplate became coupled to the northward-migrating Pacific Plate. Northward migration of the now-coupled Pacific Plate and Monterey microplate led to development of dextral faulting along the central California coast, and isolation of part of the Monterey microplate beneath the overriding North American Plate.

The top of the subducted oceanic slab, interpreted as a remnant of the subducted Monterey microplate, is imaged on deep refraction surveys as shown by Howie et al. (1993; Figure 5-4). Current seismicity is concentrated above the subducted slab as shown on Figure 5-4. As described in *Section 5.1.5*, the top of the imaged slab appears continuous and does not appear to be vertically offset or disrupted by crustal faults except possibly beneath the Hosgri fault zone. Thus, as described further in *Sections 5.1.5 and 7.2.1*, the base of the seismogenic crust is generally interpreted to lie at or above the subducted slab, except along the Hosgri fault zone where the fault may penetrate into the subducted slab.

Coeval with the onset of dextral faulting along the central California coast, the Oligocene/early Miocene Morro-Islay volcanic complex (27–22 Ma) was emplaced and nonmarine to shallow marine sediments of the Vaqueros sandstone accumulated locally in the Pismo Basin (Figure 5-5).

From 18 Ma to approximately 5 Ma, the transform margin continued to grow, and the proto–transform fault at the latitude of Diablo Canyon was located primarily along or directly offshore of the coast (Figure 5-3; Dickinson, 1981; Dickinson et al., 2005). During this time, transform faulting also began to step landward (eastward) to the proto-San Andreas fault and produced rotation of the western Transverse Ranges (WTR; Figure

5-6). Rotation of the WTR is discussed further in *Section 5.1.3*. By approximately 5 Ma, the primary transform plate boundary had fully stepped eastward to its current location as the San Andreas fault zone in south-central California (Figure 5-7). As the plate boundary stepped eastward, a large part of the western margin of North America and the underlying Monterey Plate was captured by and began moving northwestward with the Pacific Plate (Figure 5-7).

Many of the faults along the coast of south-central California originally formed during this transitional period of subduction to transform faulting, and eastward transfer of slip from the proto-transform fault along or near the coast to the current landward location of the San Andreas fault zone. In particular, the proto-San Gregorio–San Simeon–Hosgri fault system (abbreviated to San Gregorio–Hosgri fault system below) likely originated during this transition and contributed to initial transform faulting, which was influenced by rotation of the WTR. Tectonic reconstructions of offset features suggest that the fault system accumulated 150–160 km of right-lateral displacement in the past 11 Ma (Figure 5-8; Clark et al., 1984; Dickinson et al., 2005; Langenheim, Jachens, et al., 2012). Most of this slip occurred prior to the landward stepping of the proto-transform fault 5 Ma to the current location of the San Andreas fault zone, suggesting that the proto-San Gregorio–Hosgri fault system accommodated a significant portion of the full plate motion during that time.

5.1.3 Neogene Rotation of Western Transverse Ranges, Basin Formation, and Onset of Transpression in the Diablo Canyon Region

The Neogene tectonic history of the Diablo Canyon region is dominated by distributed deformation associated, in part, with rigid clockwise rotation of the WTR (Lettis et al., 1994, 2004). Episodes and amounts of rotation are reasonably well constrained by paleomagnetic studies (Luyendyk et al., 1985; Hornafius et al., 1986; Luyendyk, 1991). The data show that rotation began in the Miocene (~17–16 Ma) and continued at various rates through the Pliocene and into the Quaternary (Figure 5-6). Rotation of the WTR is inferred to continue to the present (e.g., Meigs and Oskin, 2002) at an angular rotation rate of approximately 6º per million years. Using GPS data, Marshall et al. (2013) show continued contraction within the WTR, with a regional vertical axis rotation rate of approximately 2–2.5° per million years.

As described above, beginning at approximately 22 Ma, the young and buoyant Monterey microplate stalled beneath the coastal margin of the North American Plate. As modeled by Nicholson et al. (1994), once subduction stalled beneath what is now the WTR, the microplate became sutured to and began moving northwestward with the Pacific Plate. This reorganization of dextral plate motion along the western California margin triggered clockwise rotation of the Monterey microplate and the overlying WTR as a large, discrete block. Onderdonk (2007) evaluated the driving mechanisms of vertical-axis rotation using data from the WTR. He concluded that simple force balance considerations and comparison of torque applied to a rotating block indicated that shear forces applied to the base of the WTR are not strong enough to produce the motions and deformation observed at the surface. For the measured dimensions of the WTR and crustal viscosities in

Southern California, stresses transmitted through the upper crust are one to three orders of magnitude stronger than forces generated in the ductile lower crust. Onderdonk (2007) concluded that the kinematics of block rotation within the WTR are primarily controlled by forces within the upper crust rather than a flow field beneath it.

Rotation of the WTR also was accompanied by opening of the onshore and offshore Santa Maria tectonic basins to the north (Nicholson et al., 1994), and also likely opening of the Pismo tectonic basin in the Diablo Canyon area. Paleomagnetic studies document approximately 90° of clockwise rotation of early Miocene rocks in the WTR around an axis near the modern trace of the Garlock fault (Luyendyk et al., 1985), as well as 40°–50° of clockwise rotation of Tertiary rocks in the San Luis Obispo area near Diablo Canyon, north of the WTR (Greenhaus and Cox, 1979; Khan et al., 2001).

Given the magnitude of the paleomagnetic rotations, the crust that underlies the east-west-trending WTR originally was oriented approximately north-south prior to rotation (Figure 5-6). With the onset of rotation, the area north of the WTR experienced a net increase in area (dilation or extension) as the WTR swung away from the rest of California and rotated at higher angles to the azimuth of plate motion. Dilation of the region north of the WTR during the early Neogene rotation is documented by coeval extension of the offshore and onshore Santa Maria basins and the Pismo Basin (Luyendyk, 1991). Basin margin normal and oblique-slip faults accommodated subsidence of the basins. In the Diablo Canyon area, normal and/or oblique-slip faulting on the San Miguelito and Edna faults accommodated tectonic subsidence of the Pismo Basin in the Miocene and early Pliocene (Stanley and Surdam, 1984). The sense of dextral or lateral slip on these basin-bounding faults is not well constrained, and is described further below. Figure 5-5 shows the general locations of these basins and a stratigraphic correlation of deposits within the basins (Hall, 1973; PG&E, 2011; Willingham et al., 2013).

Initial basin sediments of the Rincon Formation were deposited in the Pismo Basin, and the Tranquillon volcanics and nonmarine sediments of the Lospe Formation were deposited in the onshore Santa Maria Basin. Overlying these sediments are thick deposits of deep to shallow marine sediments of the Obispo, Monterey, and Pismo formations in all three basins. Continued rotation eventually brought the WTR approximately normal to the azimuth of plate motion. Further rotation beyond this point progressively decreased the area (contraction) north of the WTR, which Luyendyk (1991) noted could account for the observed transition from regional transtension to transpression in the Santa Maria and Pismo basins in the late Neogene to Quaternary. Rates of basin sedimentation greatly decreased during this time with deposition of the upper Pismo Formation (generally the Squire Member) in the Pismo Basin, the upper Sisquoc Formation in the offshore Santa Maria Basin, and the Foxen Mudstone and Careaga Sandstone in the onshore Santa Maria Basin.

Two general classes of models that relate Neogene extension in the Diablo Canyon region to rotation of the WTR have been proposed. In one class of models, west-northwest-trending structural blocks are assumed to have translated to the northwest

ahead of the rotating WTR, primarily by dextral strike-slip faulting and movement parallel to their long axis with a minimum amount of local rotation (e.g., Luyendyk, 1991). In these models, Neogene basins formed north of the WTR to minimize strain compatibility problems at the margins of the translating blocks. The second class of models assumes that the structural blocks north of the WTR both translated to the northwest and rotated clockwise to accommodate clockwise rotation of the WTR (e.g., Wilson et al., 2005). In these models, relative motions between the structural blocks initially included left-lateral slip as the WTR rotated through the first 45° of motion, and then later relative right-lateral motion as the rotation carried the WTR closer to parallelism with the azimuth of plate motion. These latter models predict a more complex history of Neogene deformation in the Diablo Canyon region.

As shown on Figure 5-6, Neogene rotation of the WTR also occurred during a time of more regional changes in plate motion. Clockwise rotation of the WTR began approximately 17–16 Ma. At this time, resolved motion between the Pacific and North American plates was 33 mm/yr oriented N60°W (Atwater and Stock, 1998; Krijgsman et al., 1999). At approximately 12–10 Ma, the rate of relative plate motion increased to approximately 52 mm/yr, also oriented N60°W. This orientation of plate motion relative to the more northerly trending plate boundary produced regional transtensional strike-slip faulting and contributed to extensional basin formation (i.e., superimposed on the transtension/extension produced by early clockwise rotation of the WTR). The acceleration in plate motion is also believed to have contributed to large dextral slip on the San Gregorio–Hosgri fault system post–11 Ma, as described above. Slip on the Hosgri fault slowed significantly in the Pliocene (Sorlien, Kamerling, and Nicholson, 1999; Sorlien,) as the plate boundary fully stepped landward to its current location at the San Andreas fault at approximately 5 Ma.

In addition, between 8 Ma (Atwater and Stock, 1998) and 5.9 Ma (Cox and Engebretson, 1985; Wilson, 1993; Krijgsman et al., 1999), the azimuth of resolved plate motion between the North American and Pacific plates changed to approximately N37°W (Figure 5-6). This orientation of motion placed the plate boundary under transpression regionally, while at or about the same time (~5–2.5 Ma), continued rotation of the WTR produced localized transpression in the region directly north of the WTR. Near Diablo Canyon, this late Miocene transition to transpression led to folding of the Pismo syncline and possibly also localized reactivation of former basin-margin normal faults such as the San Miguelito and Edna faults as reverse or reverse-right oblique faults. Unconformities within the Pismo Formation show that folding slowed during the late Pliocene. However, gentle folding and local fault offsets within the upper Pismo Formation (Squire Member) show that this period of folding and reactivated faulting continued at least through the late Pliocene. In addition, deposition of the upper Pismo Formation (Squire Member) is locally inset, or “benched”, into the San Luis Range, indicating that uplift and/or sub-aerial emergence of the San Luis Range was initiated by the late Pliocene.

5.1.4 Early to Mid-Pleistocene Deformation of the San Luis Range

During the early to middle Pleistocene (2.6 to ~1 Ma), an important but not well understood transition occurred in the tectonic setting of the Diablo Canyon region. Dextral rates of slip on the Hosgri (Sorlien, Kamerling, and Mayerson, 1999; Sorlien, Nicholson, and Luyendyk, 1999) and West Huasna and Rinconada (Dibblee, 1976) faults all appear to have decreased sometime during the Pliocene into the Quaternary. Folding of the upper Pismo Formation (late Pliocene Squire Member) continued, but the location and orientation of folding is distinct from and more localized than the fold deformation observed in the lower Pismo Formation (late Miocene to early Pliocene Miguelito Member) and older Monterey and Obispo formations. Emergence of the San Luis Range, either by tectonic uplift and/or by regression of the Pliocene high sea-level stand, is documented by deposition of the shallow marine Careaga Sandstone and nonmarine early to middle Pleistocene Paso Robles Formation. Based on these observations, the TI Team infers that slip on the plate boundary may have become more fully localized on the San Andreas fault zone, and rotation of the WTR may have slowed. Slowing of rotation is inferred by reduced rates of dextral slip on those faults that helped to accommodate the latter phase of rotation (e.g., Luyendyk, 1991; Wilson et al., 2005) and is compatible with some estimates of modern rotation rates from geodetic data (Marshall et al., 2013).

5.1.5 Contemporary Tectonic Setting

The contemporary tectonic setting results from current tectonic plate motion superimposed on the structural fabric inherited from the tectonic processes of the Neogene to early Quaternary described above. Large strike-slip faults that accommodated evolution of the transform plate boundary, such as the San Gregorio–Hosgri fault system, West Huasna fault, and Rinconada fault, all have a north-northwest trend similar in orientation to the plate boundary at the time of formation (Figure 5-1). Localized faults and fold axes that originated during transtensional and transpressional deformation related to clockwise rotation of the WTR, in particular those structures east of the Hosgri fault zone, have a more west-northwesterly orientation than the more northerly trending San Gregorio–Hosgri fault system and faults and folds west of the Hosgri fault zone in the offshore Santa Maria Basin.

This interplay of tectonic processes produced several distinct but interacting crustal domains and tectonic structures in the Diablo Canyon region (Figure 5–9). PG&E (1988), Lettis et al. (1994, 2004), and McLaren and Savage (2001) identify the Los Osos domain as a triangular region consisting of northwest-striking reverse, oblique, and dextral-slip faults that border uplifted blocks and subsiding basins within the domain. To the west, the Los Osos domain is bordered by the more northerly trending Hosgri fault zone, which separates the domain from the offshore Santa Maria Basin (PG&E, 1988; Clark et al., 1994; Steritz and Luyendyk, 1994; Lettis et al., 2004). To the south, the Los Osos domain is bordered by the Santa Ynez River fault, which marks the northern boundary of the western Transverse Ranges domain. The structural grain of the western Transverse Ranges is dominantly east-west (Figure 5-9), and some northeast-trending faults, such as the Santa Ynez fault, exhibit evidence for left-lateral displacement (Sylvester and Darrow,

1979; Ford, 1992). On the northeast, the Los Osos domain is bordered by the Oceanic–West Huasna fault system, which separates the domain from the more northerly trending Santa Lucia–San Rafael ranges. Thus, the northwest-trending structural grain of the Los Osos domain is transitional between the west-trending structural grain in the Transverse Ranges to the south, and the north-northwest-trending structural grain of the Santa Lucia–San Rafael ranges to the northeast.

Late Quaternary deformation (1 Ma to present) in the Los Osos domain is characterized by net transpression, accommodated by dextral strike-slip faulting along the eastern and western margins of the domain, and uplift of the fault-bounded ranges within the interior of the domain (Lettis et al., 2004). Transpression within the Los Osos domain and the greater central coast region may be driven by a combination of the following mechanisms (Lettis et al., 2009; PG&E, 2011):

- Continued transpressional deformation along the Pacific Plate–Sierra Nevada/Great Valley microplate boundary as predicted by the N37°W relative plate motion. This transpression resolves into components of dextral slip along faults of the San Andreas fault system and contraction across the broader plate boundary;
- Northward left-restraining transfer of slip from the San Andreas fault zone to the San Gregorio–Hosgri fault zone, across the intervening Rinconada and Oceanic–West Huasna faults (e.g., Hardebeck, 2010). The transfer of slip produces localized crustal shortening along more westerly trending reverse and reverse oblique slip faults; and
- Possible continued clockwise rotation of the WTR, which would continue to impart northeast-directed strain in the region with dextral shear on northwest-oriented faults.

The geomorphology and coastal evolution of south-central California within the Los Osos domain reflects the strong influence of late Quaternary tectonic processes. A well-preserved flight of emergent marine terraces along the coast provides an excellent strain gauge from which Lettis et al. (1994, 2004) have assessed the style, rate, and extent of Quaternary deformation in the domain. These studies show that the region has undergone late Pleistocene transpressional deformation accommodated by both strike-slip and dip-slip faulting, and by block uplift and subsidence. Lettis et al. (1994) and Lettis and Hanson (1992) describe evidence for uplifted blocks within the Los Osos domain as including flights of emergent marine terraces, topographic and structural highs that are bordered by reverse or reverse-oblique slip faults, and the absence (or near absence) of ongoing Quaternary folding within the blocks. Evidence for downdropped or static blocks between the ranges includes substantial Quaternary sedimentation, lack of emergent marine terraces, broad beaches and sand spits, and late Quaternary dune fields (Lettis and Hanson, 1992).

Diablo Canyon is located on the southwestern slope of the Irish Hills in the northern part of the San Luis Range (Figure 5-9). The San Luis Range is a west-northwest-trending topographic and structural high that forms the core of the San Luis–Pismo block within

the Los Osos domain (Lettis et al., 1994). The range is interpreted to have been uplifted approximately as a rigid block during the late Quaternary by reverse slip on the Los Osos fault to the north-northeast, and reverse slip on faults comprising the Southwestern Boundary zone to the south (see *Section 5.3* for further discussion of these structures). Altitudes and ages of the marine terraces on the margin of the San Luis Range show that the range is uplifting at rates of between 0.1 mm/yr to the southeast and 0.2 mm/yr to the northwest, with little or no observable internal deformation (Hanson et al., 1994; PG&E, 2011). The onset of Pleistocene block uplift of the range appears to pre-date the onset of late Pleistocene uplift of the central and southern California Coast Ranges, which was described by Page et al. (1998) as approximately 450 thousand years ago (ka).

Major geologic structures within the range, including the Pismo syncline, which cores the San Luis–Pismo block, and the San Miguelito, Edna, and Pismo faults, do not recognizably deform Quaternary deposits or landforms and do not appear to be active structures in the contemporary tectonic setting (Lettis et al., 1994, 2004). None of these faults appear to deform the marine terrace sequence where they intersect the coastline, and trenches along both the San Miguelito and Edna faults at inland locations show unfaulted late Pleistocene and/or Holocene deposits overlying the fault (PG&E, 1988). The late Miocene–early Pliocene Pismo syncline lies within the crest of the range and is flanked by anticlines on the sides of the range, suggesting that the principal episode of folding ceased by the late Pliocene and is replaced by uplift of the range along bordering reverse or reverse-oblique slip faults. Active faults bordering the San Luis–Pismo block to the northeast, southwest, and west are the Los Osos fault zone, Southwestern Boundary zone (which includes the San Luis Bay fault zone), and Hosgri fault zone, respectively (Figure 5-9). In addition, the recently identified Shoreline fault zone (Hardebeck, 2010; PG&E, 2011) is located near the west-southwestern margin of the San Luis–Pismo block. These faults are described in *Section 5-2*.

The offshore Santa Maria Basin formed primarily during the Miocene (Page et al., 1979; McCullough, 1987; Willingham et al., 2013). The basin is bounded on the east by the Hosgri fault zone and on the west by the Santa Lucia Bank fault zone. Spatially, the central part of the basin at the latitude of Diablo Canyon lacks active faults and folds, except for monoclinal warping directly adjacent to the Hosgri fault zone. The northern part of the basin at the latitude of San Simeon and the southern part of the basin at the latitude of Point Sal have experienced Pliocene and Quaternary reactivation of older Miocene structures (Willingham et al., 2013). These offshore structural features include the Piedras Blancas anticlinorium near San Simeon, and the Queenie, Lompoc, and Purisima structures in the southern part of the basin. In the contemporary tectonic setting, each of these structures represents active folding underlain by reverse or thrust faults that generally dip eastward toward the Hosgri–San Simeon fault zone.

As described earlier, a remnant slab of subducted oceanic crust (the Monterey microplate) stalled beneath the coastal margin of California at the latitude of Diablo Canyon. Deep refraction and reflection profiles from the PG&E/EDGE deep crustal experiment image this gently east-dipping slab of early Miocene oceanic crust beneath the coastal margin (Trehu and Wheeler, 1987; Putzig, 1988; Meltzer and Levander, 1991;

Trehu, 1991; Miller et al., 1992; Howie et al., 1993). Meltzer and Levander (1991) and Howie et al. (1993) interpret the surface of the slab to extend from a depth of approximately 6 km near the continental slope to approximately 16 km depth near the coast, with an easterly dip of approximately 8° (Figure 5-4). Based on all the studies, estimates to the depth of the top of the slab in the Diablo Canyon area range from approximately 12 km to 16 km. Published interpretations show that the top of the slab is not disrupted by apparent faulting or folding from the continental slope eastward to at least the Rinconada fault, although Meltzer and Levander (1991) interpret possible disruption along trend of the Hosgri fault zone (Figure 5-4). At Workshop 1, Dr. W. Mooney presented a reinterpretation of line SJ3 and a proponent model that a large "megaflower" may occur between the West Huasna fault and the Rinconada fault that cuts through the slab to a depth of approximately 25 km, but that the slab does not appear broken beneath the Diablo Canyon area (Mooney, 2011). These observations suggest that current seismogenic deformation in the Diablo Canyon site area is confined to the overlying crust, with the possible exception of the Hosgri fault zone, which may penetrate the slab.

5.1.6 Contemporary Strain Rates and Orientations Based on Geodetic and Seismicity Analysis

Geodetic and seismicity data show that the Los Osos domain is undergoing transpressional dextral shear with localized areas of crustal shortening. A variety of data sets, methods, and alternative models, many of which were presented at the formal workshops, were considered by the TI Team to evaluate the contemporary stress and strain field of the Diablo Canyon region, including the following:

- Analysis of stress and strain from GPS and seismicity data (Lewandowski, 2014, presentation at Workshop 3; and PG&E, 2015b).
- Review of the three published geodetic deformation models presented in UCERF3 (Field et al., 2013), including the rigid block model, the geologic/block model of Zeng and Shen (2014), and the NeoKinema model of Bird and Liu (2007).
- Analysis of fault-based deformation using the NeoKinema model from UCERF3 with specific focus on the Diablo Canyon region (Bird, 2012, presentation at Workshop 2).
- Analysis of regional deformation and kinematics from USGS GPS data (Murray-Moraleda et al., 2011; Murray, 2012, presentation at Workshop 2).
- Analysis of kinematics of central coastal California inferred from GPS geodesy (DeMets, 2012b; presentation at Workshop 2; DeMets et al., 2014).

At Workshop 3, Lewandowski (2014) presented the results of PG&E (2015b) that evaluated the orientation of the maximum compressive stress (σ_1) and maximum shortening strain (d_3) in the Diablo Canyon area. These values were explored by inverting GPS velocity data and earthquake focal mechanisms using several different methods. A GPS velocity field relative to a fixed Pacific Plate as estimated by DeMets (2012a) was used in the analysis. The GPS data were inverted for specific polygonal regions using both the GPSTRN and SSPX algorithms to determine 2D horizontal strain tensors. For

the GPSTRN analysis, polygons are defined by the user; for the SSPX analysis, polygons are generated by an algorithm (either grid-nearest neighbor or Delaunay triangulation). Results of the analysis are shown on Figure 5-10. For the inversion of seismicity data, two focal mechanism data sets were used:

- "Network" mechanisms calculated automatically using the FPFIT algorithm (Reasenberg and Oppenheimer, 1985) from machine phase and hand picks (downloaded from the Northern California Earthquake Data Center website in 2013).
- Focal mechanisms presented in Hardebeck (2010) calculated using the HASH algorithm (Hardebeck and Shearer, 2002).

The focal mechanism data were inverted using both the FLTSLP (L. Guenther and R. Twiss, University of California, Davis; see Appendix D in Guenther, 2004, for user's manual) and SATSI (Hardebeck and Michael, 2006) algorithms. FLTSLP uses a micropolar continuum model for distributed brittle deformation (Twiss et al., 1993; Twiss and Unruh, 1998) as a basis for inverting focal mechanisms for the components of a reduced deformation rate tensor, from which relative contributions of horizontal shearing and crustal shortening or thinning can be evaluated. SATSI determines a best-fit stress tensor for groups of earthquake focal mechanisms using a damped inversion algorithm that minimizes the apparent spatial variability between data groups. Results from the two studies are shown on Figure 5-11. The results from these analyses generally show that the principal orientations of d_3 and σ_1 are relatively consistent at about N15°E, but the results allow for either horizontal plane strain deformation or transpressional deformation with vertical crustal thickening depending on the orientation of faults within the strain field (Figure 5-12). The maximum compressive stress orientation and shortening strain orientation are consistent with distributed dextral shear on N30°W trending faults parallel to the Hosgri fault zone; whereas west-northwest-trending structures within the Irish Hills oriented at a high angle to d_3 or σ_1 are optimally oriented to accommodate reverse slip with crustal shortening and thickening. This thickening may be a result of a local restraining transfer of distributed N30°W dextral shear from faults east-southeast of the Irish Hills to the Hosgri fault zone west of the Irish Hills.

Analysis of regional GPS velocity data generally support low rates of dextral shear and plate normal convergence in the Diablo Canyon region. DeMets (2012b) and DeMets et al (2014) analyzed GPS data from central California specifically to evaluate crustal velocities west of the San Andreas fault zone in the Diablo Canyon region. The general results are shown on Figure 5-13, with the conclusion that the total velocity budget available for faults west of the Oceanic–West Huasna fault zone is 3.4 ± 0.4 mm/yr if the model assumes a rigid Pacific Plate with no internal deformation offshore, or 1.8 ± 0.6 mm/yr if the Pacific Plate deforms internally as indicated by GPS stations on Clarion, Socorro and Guadalupe Islands (DeMets et al., 2014).

Murray (2012; see also Murray-Moraleda et al., 2011) and Bird (2012) modeled the GPS data west of the San Andreas fault zone using discrete block models with slip occurring on faults that define the block boundaries. At Workshop 2, Murray (2012) presented five

models assuming various constraints on slip rates of the San Andreas and Oceanic–West Huasna fault zones, and geometries of the Salinian block and Rinconada–South Cuyama block:

1. A single Salinian block similar to that of McCaffrey (2005).
2. A single Salinian block with slip rate on the San Andreas fault constrained to 34 ± 2 mm/yr.
3. The Oceanic–West Huasna fault as a block boundary defining the eastern edge of the Los Osos domain with an unconstrained slip rate.
4. The Oceanic–West Huasna fault as a block boundary with a slip rate constrained to <1 mm/yr.
5. The Oceanic–West Huasna fault as a block boundary and slip rate on the San Andreas fault constrained to 34 ± 2 mm/yr.

The models generally show resolved dextral slip rate on the Hosgri fault zone from 0.5 to 3 mm/yr, with most models showing 1–2 mm/yr. Example results showing Models 3 and 4 from Murray (2012) are presented on Figure 5-14. The results include an "unconstrained" solution (Model 3; Figure 5-14a) and a "constrained" solution (Model 4; Figure 5-14b) where slip on the Oceanic–West Huasna fault is constrained to be < 1 mm/yr (a geologically reasonable assumption). The estimated Hosgri fault zone slip rate is 0.5 mm/yr for the "unconstrained" Model 3 and 1.7 mm/yr for the "constrained" Model 4.

Bird (2012) presented results at Workshop 2 from the NeoKinema kinematic model showing slip rates of 1.2 mm/yr and 0.14 mm/yr right-lateral for the Hosgri and Shoreline faults, respectively (Figure 5-15). Across the Los Osos Domain, the NeoKinema model result estimates a net shortening rate of approximately 2.3 mm/yr with almost half of this shortening on the Oceanic-West Huasna fault along the northeastern margin of the Los Osos Domain (Figure 5-15).

In summary, results from geodesy and inversions of earthquake focal mechanisms show that the contemporary tectonic setting of the Los Osos domain is one of transpressional dextral shear with localized areas of crustal shortening and thickening, such as within the Irish Hills near Diablo Canyon. Geodetic data provide general constraints on regional crustal velocities west of the Oceanic–West Huasna fault zone of approximately 1–3 mm/yr of dextral shear subparallel to the San Andreas fault zone, with comparable rates of crustal shortening permissible orthogonal to the plate boundary west of the San Andreas fault zone.

5.2 Site Area Faults

This section describes active faults in the Diablo Canyon vicinity that are significant contributors to site-specific seismic hazard at Diablo Canyon based on prior sensitivity analyses (e.g., PG&E, 2011), initial sensitivity results presented at Workshop 1 (Wooddell, 2011; see also *Appendix D*) and final sensitivity analyses presented in *Chapter 14*. Figure 5-16 shows the location of faults in the site area with the distribution of earthquake epicenters from the most recently available relocated seismicity catalog

from Hardebeck (2014a). Primary faults that are significant to seismic hazard at Diablo Canyon include the Hosgri fault zone, the Los Osos fault zone, the San Luis Bay fault within the Southwestern Boundary zone, and the Shoreline fault. *Chapter 6* describes how these primary faults are incorporated into the seismic source model as rupture sources. Additional information on the location, geometry, style of faulting, and slip rate of each of these faults (as well as related faults such as the Wilmar Avenue and Oceano faults that are considered in the source model to sometimes rupture with the primary faults) is provided in *Chapters 7 and 8*. The faults are defined according to their characteristics along the reach that is closest to the DCPP because these are parts that most significantly affect hazard at the site. Faults that are not significant contributors to seismic hazard at the site, such as the Casmalia fault, Oceanic–West Huasna fault, and Rinconada fault, are mentioned but are not described in detail. These less significant faults are captured in the seismic source model as "regional fault sources" using the UCERF3 model results as described in *Chapters 6 and 12*.

Faults shown on Figure 5-16 are compiled from a variety of sources. Offshore faults are compiled from the PG&E LTSP and CCCSIP studies (PG&E, 2013a; PG&E, 2014, Chapter 3). Onshore faults are compiled primarily from Lettis and Hall (1994), Lettis et al. (2004), and PG&E (2014, Chapter 9).

5.2.1 Hosgri Fault Zone

The Hosgri fault zone is the southern part of the larger 410 km long San Gregorio–San Simeon–Hosgri fault system. It is an active transpressional right-slip fault zone that extends southeastward approximately 110 km from a location 6 km offshore Cambria to a point 5 km northwest of Point Pedernales (Hanson et al., 2004). The location of the Hosgri fault zone, which lies offshore for its total length, is known primarily from the interpretation of seismic-reflection data. Two alternative interpretations are presented to explain the structural linkage between the Hosgri and San Simeon faults. PG&E (1988) interpreted the faults to be structurally linked but separated across a zone of transtensional normal faults in a right-releasing step-over based on interpretation of offshore seismic reflection data that was available at the time. Recently acquired offshore bathymetric and seismic-reflection data show the Hosgri and San Simeon faults project towards each other across a zone of shallow bedrock and poor imaging offshore of Cambria. Johnson and Watt (2012) and PG&E (2013a) interpret the two faults to directly connect within this zone of poor imaging (as shown by the dashed line at the north end of Figure 5-16). Alternatively, PG&E (2014, Chapter 4) interprets the Hosgri fault to bend westward south of this zone, and step over to the San Simeon fault across a zone of northwest-trending faults farther to the north. It is clear from both interpretations, however, that the Hosgri and San Simeon faults are part of the same near-coastal system of strike-slip faults that extend from the San Gregorio fault on the north to the southern end of the Hosgri fault on the south. For terminology, we continue traditional usage of both the Hosgri and San Simeon fault zones for ease of reference to existing literature and to avoid confusion.

The Hosgri fault zone was mapped along its entire 110 km length using petroleum industry multichannel seismic-reflection data that imaged the traces to depths of 1.5–3 km beneath the seafloor (PG&E, 1988, 1990a; Willingham et al., 2013). Significant parts of the fault zone, including directly offshore from Diablo Canyon, were remapped using single-channel, high-resolution USGS sparker data (Johnson and Watt, 2012; PG&E, 2013a). The USGS data set provides better near-surface resolution of the fault traces and associated structures but with limited depth of penetration. This more recent mapping shows that the Hosgri fault zone offshore of Diablo Canyon trends approximately N25°W to N30°W and locally is coincident with the shelf break. It also forms the western termination of the offshore bedrock platform associated with uplift of the San Luis–Pismo block (PG&E, 2011, Appendix I; PG&E, 2014, Chapter 3). As mapped from the high-resolution USGS seismic-reflection data set, the Hosgri fault zone consists of multiple traces in a zone up to 2.5 km wide directly offshore of Diablo Canyon (Figure 5-16). The fault traces appear vertical to steeply dipping in the upper few hundred meters of sedimentary section. On the multichannel data, with several seconds of signal penetration, some of the traces have been interpreted to dip steeply to the east below approximately 1 km depth (PG&E, 1988; 1990a; Willingham et al., 2013). As described in *Section 5.4*, focal mechanisms and the distribution of microseismicity along the Hosgri fault zone document nearly pure strike-slip on a near-vertical to steeply (75°) east-dipping fault to a depth of 12 km (Figure 5-17; McLaren and Savage, 2001; PG&E, 2011; Hardebeck, 2013).

The slip rate of the Hosgri–San Simeon fault zone has been evaluated by numerous researchers over the past four decades (summarized in Hanson et al., 2004) and is described in detail in *Section 8.3*. In general, the sources of the estimates of slip rate on the Hosgri fault zone are as follows:

- Geomorphic analysis of onshore deformed marine terraces across the San Simeon fault combined with the assumption (at that time) that the San Simeon and Hosgri faults were structurally linked as part of the same near-coastal system of right-lateral faults (Hanson and Lettis, 1994).
- Structural analysis of slip rate on the Hosgri fault system assuming that slip rate on the fault increases or decreases based on intersecting faults (Hanson et al., 2004).
- Geomorphic analysis of the “cross-Hosgri slope” (Johnson et al., 2014), an offset geomorphic feature located offshore of Point Estero.
- Geomorphic analysis of offset submarine channels observed on 3D and 2D seismic-reflection data in Estero Bay and near Point Sal (PG&E, 2014, Chapter 3).

Combined, these studies provide an estimate of approximately 2 mm/yr of right-lateral slip (*Section 8.3*). This slip rate is consistent with regional geodetic data showing approximately 2 mm/yr of plate-margin lateral shear in the region west of the West Huasna fault (DeMets et al., 2014; *Section 5.1.6*).

As described by Hanson et al. (2004) and Johnson et al. (2014), conceptual tectonic models suggest that the Hosgri–San Simeon fault slip rate should change from north to

south in steps at the intersections of more westerly trending faults. West of the main Hosgri–San Simeon fault zone, and west of the cross-Hosgri slope geomorphic feature, is the Piedras Blancas anticlinorium and the westernmost strands of the Hosgri fault zone (PG&E, 1990b; Johnson et al. 2014). East of the main Hosgri–San Simeon fault zone, within the Los Osos domain (Figure 5-9), are intersecting faults that include the Los Osos, Shoreline, Casmalia, and Lions Head faults, and possibly the Southwest Boundary zone including the San Luis Bay fault (Hanson et al., 2004). Thus the slip rate of the Hosgri–San Simeon fault zone at the San Simeon (Hanson and Lettis, 1994), Point Estero (Johnson et al., 2014), and Estero Bay (PG&E, 2014, Chapter 3) study areas would be considered approximately equal to the slip rate of the Hosgri fault zone directly opposite the DCPP, with differences in slip rate that depend on the relative amounts of slip rate added from the west and subtracted from the east. The Hosgri fault slip rate at the Point Sal study area (PG&E, 2014, Chapter 3), which is located south of the intersections of the Casmalia and Lions Head faults, would be considered less than the slip rate for the Hosgri fault zone directly opposite the DCPP.

5.2.2 Los Osos Fault Zone

The Los Osos fault zone borders the northeastern margin of the San Luis Range (Figures 5-9 and 5-16). The fault generally separates the uplifting San Luis–Pismo block from the more slowly uplifting and locally subsiding Cambria block to the northeast (Lettis et al., 1994). As described by Lettis and Hall (1994) the Los Osos fault zone is a 2 km wide system of discontinuous, subparallel, and en-echelon fault traces extending from an intersection with the Hosgri fault zone in Estero Bay on the north to an intersection with the West Huasna fault southeast of San Luis Obispo, for a distance of over 55 km. Detailed paleoseismic trenching shows that the fault locally displaces Holocene fluvial deposits along the base of the Irish Hills sub-block of the San Luis–Pismo block, and Pleistocene fluvial deposits (Paso Robles Formation[?]) along the Edna sub-block of the San Luis–Pismo block (Lettis and Hall, 1994). Slickenside data show primarily dip slip movement on a southwest-dipping fault plane, and on this basis the fault was characterized as a reverse fault (PG&E, 1988; Lettis and Hall, 1994; Lettis et al., 1994). Based on vertical rates of deformation of marine terraces and fluvial deposits, and an estimated dip of 30°–60°, Lettis and Hall (1994) estimated a net slip rate of 0.2–0.7 mm/yr. Results from new geomorphic lineament and drainage mapping (Baldwin, 2012, presentation at Workshop 2; PG&E, 2014, Chapter 9), interpretation of reprocessed onshore seismic-reflection data (PG&E, 2014, Chapter 7), interpretation of high-resolution offshore seismic-reflection data (PG&E, 2013a), analysis of seismicity data, and structural analysis (PG&E, 2014, Chapters 7 and 9), suggest that the fault dips more steeply to the southwest (45°–70° or possibly steeper), and is likely a reverse or dextral oblique reverse fault that accommodates uplift of the range. The amount of oblique movement likely varies with strike, with more northerly trending parts of the fault accommodating greater amounts of strike slip consistent with the regional stress/stain field. Recent mapping of marine deposits and geomorphic surfaces in the Edna and Los Osos valleys provide additional new information to constrain uplift rates in the footwall block of the Los Osos fault (*Section 8.2.1*; PG&E, 2013b).

5.2.3 Southwestern Boundary Zone and San Luis Bay Fault

The southwestern margin of the San Luis Range is bordered by a complex zone of late Quaternary reverse, oblique-slip, and (possibly) strike-slip faults. These faults in aggregate separate the San Luis–Pismo block from the subsiding Santa Maria Valley block to the southwest (Figure 5-9). The zone of faults is collectively called the Southwestern Boundary zone, and is 4–10 km wide and over 60 km long (Lettis et al., 1994, 2004). The faults generally strike west-northwest and dip moderately to steeply northeast. Principal structures within this fault zone include the following faults: San Luis Bay, Wilmar Avenue, Los Berros, Oceano, and Nipomo (previously mapped as a segment of the Wilmar Avenue fault by PG&E, 1988; Lettis et al., 1994). The cumulative rate of vertical separation across the fault zone, based primarily on deformation of the marine terrace sequence along the coast and southwest side of the range onshore, ranges from approximately 0.1 to 0.3 mm/yr, with each fault generally having a rate of 0.04–0.1 mm/yr (Lettis et al., 1994).

Within the Southwestern Boundary zone, the San Luis Bay fault zone lies closest to the DCPP. The general location of the fault zone is well constrained onshore but is less well constrained offshore both to the east in San Luis Obispo Bay and to the west toward the Hosgri fault zone. Onshore a strand of the fault zone is exposed along Avila Beach Road where it juxtaposes Franciscan basement over the Squire Member of the Pismo Formation and displaces an overlying marine wave-cut platform and associated marine terrace deposits (PG&E, 1990c; Lettis et al., 1994). A fault strand also displaces fluvial deposits at the mouth of San Luis Obispo Creek before extending offshore to the east into San Luis Obispo Bay. Farther east, the fault zone is interpreted to extend to a location offshore of Mallagh Landing where it either dies out or intersects the offshore projection of the San Miguelito fault (Figure 5-16). The fault zone does not extend onshore east of Mallagh Landing, confirming that this is the eastern end of the fault zone.

To the west of Avila Beach, the San Luis Bay fault zone crosses a topographic saddle north of Point San Luis where the fault appears to be blind or is difficult to locate at the surface. Farther west, the fault zone extends beneath the onshore coastal terraces where it deforms the marine terraces across a broad zone. The southern limit of this deformation is marked by the Rattlesnake fault, a discrete fault trace with a vertical separation rate of approximately 0.08 mm/yr. The northern limit of the San Luis Bay fault zone was initially named the Olson fault by PG&E (1990c). The Olson fault was identified based on the interpretation of a step in marine terraces accounting for a vertical separation rate of approximately 0.06 mm/yr coincident with a bedrock fault mapped in the vicinity of Olson Hill. The northern limit of the fault zone is referred to as the Olson Hill deformation zone in later studies (PG&E, 2011, Appendix B), based on the recognition that the terraces are deformed as a monoclinal warp, in contrast to the better-defined Rattlesnake fault, and that the deformation of marine terraces near Olson Hill cannot be attributed to any specific bedrock fault. The cumulative rate of vertical separation across the San Luis Bay fault zone along the outer coast is approximately 0.14 mm/yr.

Offshore to the west, the fault zone is interpreted to extend either to an intersection with the Shoreline fault zone (for a total fault length of 8 km) or across the Shoreline fault zone to an intersection with the Hosgri fault zone (for a total fault length of 16 km). As shown in PG&E (2011, Appendix I), an offshore extension of the San Luis Bay fault to the Hosgri fault zone is indicated by an apparent uplift rate boundary between submerged marine terraces of the Islay and Santa Rosa reef platforms.

5.2.4 Shoreline Fault Zone

The Shoreline fault was originally identified from a seismicity lineament trending approximately N50°W to N60°W offshore and parallel to the coast in the vicinity of the DCPP (Figure 5-18; Hardebeck, 2010). As shown on Figure 5-18, offshore of DCPP to the Point San Luis area, the hypocentral distribution of seismicity forms a nearly vertical alignment that extends to a depth of approximately 8–10 km (Hardebeck, 2013). Along the northern part of the lineament, the hypocentral distribution of seismicity is more diffuse and forms a generally vertical alignment to a depth of approximately 12–15 km. Hardebeck (2013) interprets that to the north the seismicity lineament likely connects with the Hosgri fault zone and to the south the lineament continues south of Point San Luis before dying out.

Subsequent studies using recently acquired multibeam bathymetry identified a prominent ocean bottom lineament in bedrock roughly parallel to the coastline and coincident with the seismicity lineament (Figure 5-19; PG&E, 2011). PG&E (2011) further interpreted the bedrock lineament to be the causative fault producing the seismicity. Based on the bathymetry data, PG&E (2011, Appendix I) also interpreted the spatial (lateral and vertical) position of offshore, submerged marine terraces across the fault to provide an independent geologic/geomorphic assessment of activity (Figure 5-19). Based on the offshore marine terraces, PG&E (2011) concluded that there is little to no observable vertical separation across the fault, but that the extent of lateral slip on the fault could not be constrained. In 2010, 2011 and 2012, PG&E obtained high-resolution 2D and 3D seismic reflection data to better define the northern and southern extent of the “fault,” and to look for independent geologic/geomorphic evidence of activity confirming that the bedrock lineament is, in fact, the causative fault of the seismicity lineament and, if so, to search for evidence to constrain slip rate on the fault (PG&E, 2014, Chapters 2 and 3).

Interpretation of the seismic reflection data show that the bedrock lineament is, in fact, coincident with a subsurface fault that intersects with the Hosgri fault zone northwest of Point Buchon on the north, and extends into San Luis Obispo Bay to the southeast (Figure 5-16). PG&E (2014, Chapter 3) further suggests that the southeastern extent of the fault may extend onshore to an intersection with the Casmalia fault. Along trend, the fault intersects with faults of the Southwestern Boundary zone, including the San Luis Bay, Los Berros, and Oceano faults. Within San Luis Obispo Bay, the 3D seismic data clearly show that the fault displaces sediment of late Quaternary age providing clear geologic evidence of late Quaternary fault activity. PG&E (2014, Chapter 3) interpret that the fault offsets paleo-terrace risers and one or more buried channels crossing the fault in San Luis Obispo Bay in a right-lateral sense. The evidence for amount of right-lateral

displacement and age of the displaced channel are both uncertain, but PG&E (2014, Chapter 3) concludes that a right-lateral slip rate of something greater than zero, with preferred range of 0.07 to 0.12, and range of 0.01 to 0.37 is occurring on the fault (see discussion in *Section 8.4*). Focal mechanisms presented by Hardebeck (2010, 2013) also show that the Shoreline fault zone is primarily a right-lateral fault, but may also accommodate a limited vertical component of slip.

Because the Shoreline fault was initially described as a seismicity lineament, some question has existed regarding whether fault traces observed at the surface were the same faults as the one responsible for the seismicity lineament at depth. Because of this uncertainty, and an acknowledgment that not all surface faults may have been recognized early in the mapping process, PG&E has used several alternative names to describe different parts of the Shoreline fault. These include the Southern Segment; Central Segments C-1, C-2, and C-3; the Northern Segment; the N40W fault; the Point Buchon fault; and the East Branch of the Point Buchon fault. For the purposes of this report, all these traces are now considered to be part of the Shoreline fault zone.

5.3 Regional Seismic Setting

This report section focuses on the aspects of the historical seismicity relevant to establishing the setting of the DCPP. Discussion of the seismicity catalogs used to develop the Diablo Canyon SSC model (e.g., for areal source zones) are presented in *Appendix F* and in later chapters.

Consistent with its tectonic setting, historical seismicity in the DCPP region reflects the dextral transpression between the Pacific plate and Sierra Nevada/Great Valley microplate. The regional distribution of seismicity from 1987 to 2010 from PG&E (PG&E, 2011; McLaren, 2011, presentation at Workshop 1) and from 1987 to 2008 from Hardebeck (2010, 2012c, presentation at Workshop 2) is shown on Figures 5-20 and 5-21, respectively. Seismic activity west of the San Andreas fault zone is concentrated at depths above approximately 12 km and in several areas:

- Within the Santa Lucia Range
- West of the San Simeon area within the active offshore Piedras Blancas anticlinorium
- Along and east of the Hosgri fault zone within the Los Osos domain
- In the southern offshore Santa Maria Basin, west of Point Sal to Point Arguello.

The dense cluster of earthquakes along the Santa Lucia Range consists primarily of aftershocks from the 2003 **M** 6.5 San Simeon earthquake (McLaren et al., 2008). This aftershock sequence constitutes the majority of the earthquakes in the PG&E Catalog (Figure 5-20b). According to McLaren et al. (2008) the aftershock data define a fault plane that projects from approximately 10 km depth to the ground surface near the trace of the Oceanic fault. The focal mechanism of the main shock defines nearly pure reverse displacement on a northeast-dipping fault. The event produced uplift of the Santa Lucia Range and is a potential analog to the type of faulting that may occur along the similar

trending (but oppositely dipping) Los Osos fault bordering the northeastern margin of the San Luis Range (San Luis–Pismo block).

The Lompoc earthquake of 1927, estimated at magnitude (*M*) 7, is the largest event recorded in the south-central coastal California region (Figure 5-22; McLaren and Savage, 2001). The focal mechanism shows nearly pure reverse displacement on a northwest-trending fault plane (the dip being either southwest or northeast). The location of the earthquake is constrained by teleseismic, aftershock, and intensity data to have occurred in the southern offshore region, approximately 25 km west of Point Arguello (Hanks, 1979; PG&E, 1988). The location of the event is within a zone of poorly known faults that splay southeastward from the southern end of the Santa Lucia Bank fault zone offshore of the Point Arguello to Point Pedernales area (Figure 5-22). The closest faults to the epicenter of the Lompoc earthquake were mapped by Sorlien, Nicholson, and Luyendyk (1999) as the West Basin fault and the Southwest Channel fault.

Other moderate magnitude earthquakes in the vicinity of Diablo Canyon include the 1830, 1913, and 1916 *M* 5–5.9 events. As described by McLaren and Savage (2001), these earthquakes did not produce observed surface deformation, but rather, only minor local damage. The 10 km radius circles of uncertainty shown for the 1913 and 1916 earthquakes on Figure 5-22 suggest they could have ruptured the Los Osos, Shoreline, San Luis Bay, or other faults of the Southwestern Boundary zone (PG&E, 2011). For the time-dependent recurrence analysis provided in *Chapter 11*, none of these events are considered to be the most recent "resetting" events for a renewal model. As described in *Chapter 11*, uncertainty in the time since the most recent resetting event on the Hosgri fault and other primary faults was evaluated using available California Mission records since in 1776 for the San Luis Obispo area, and the significant growth of the local population and publication of newspapers in 1850. In other words, the most recent resetting event on the primary faults must have occurred before one of these two dates.

In Estero Bay, Hardebeck (2010; 2012c, presentation at Workshop 2) identifies two northwest-trending, near-vertical seismicity lineaments and one subhorizontal plane (Figure 5-23). It is not known whether these lineaments represent a northerly branch of the Los Osos fault zone across Estero Bay that possibly links to the onshore Cambria fault along the Cambria coastline, or some other possible fault of unknown dimension (Figure 5-16). Seismic-reflection data do not show a structure coincident with the seismicity lineament and, as described in *Section 8.2.2*, recent mapping of marine terraces on opposite sides of the onshore Cambria fault indicate that the fault does not vertically displace late Pleistocene marine terraces. These observations suggest that laterally continuous faults may exist in Estero Bay, but the precise locations, extents and slip rates are not well known. The general characteristics of the seismicity lineaments in Estero Bay are used to help define a local areal source zone (*Section 13.5*).

There are relatively few earthquakes west of the Hosgri fault zone from about the north end of Estero Bay to Point Sal (Figures 5-16, 5-20, and 5-21). This low rate of seismicity west of the Hosgri fault zone is coincident with the apparent lack of observable deformation within the Miocene strata of the offshore Santa Maria Basin described above

(*Section 5.1.5*). The change in rate of seismicity between the very low rates observed west of the Hosgri fault zone and the relatively higher rates east of the fault zone, therefore, is consistent with the truncation of the Los Osos domain by the Hosgri fault zone and the lack of mapped Quaternary faults directly west of the Hosgri fault zone.

Focal mechanisms in south-central coastal California are predominantly reverse and strike-slip (Figure 5-24) and are consistent with dextral transpressional deformation (*Section 5.1.6*; McLaren and Savage, 2001; Hardebeck, 2010, 2013; McLaren, 2011, presentation at Workshop 1). Mechanisms beneath the Santa Lucia Range from the San Simeon earthquake aftershock zone show predominantly reverse motion along west-northwest-trending fault planes. Strike-slip mechanisms are prevalent south of the San Simeon aftershock zone and along the West Huasna fault zone.

There are numerous strike-slip mechanisms along the Hosgri fault zone between Estero Bay and Point San Luis, and directly east of the Hosgri fault zone in Estero Bay, along the Shoreline fault zone, and onshore within the Irish Hills (Figure 5-24). Generally, the mechanisms associated with the Hosgri fault zone have nodal planes that strike more northerly than the northwest-striking focal mechanisms directly east of the Hosgri fault zone. Strike-slip mechanisms along the West Huasna fault zone change from nearly north-south-striking nodal planes east of San Luis Obispo to west-northwest-striking nodal planes north of San Luis Obispo to the southern end of the 2003 San Simeon earthquake aftershock zone.

5.4 Alternative Styles of Active Deformation in the Diablo Canyon Vicinity

Given the available data, two alternative end-member models describe the contemporary tectonic setting of the Diablo Canyon vicinity, and in particular the Irish Hills:

1. Transpressional right shear between the Hosgri and Rinconada fault zones.
2. Northeast-southwest-oriented crustal shortening between the right-lateral Hosgri and West Huasna fault zones.

Transpressional right shear is supported by a variety of observations (Hanson et al., 2004; Lettis et al., 2004):

- Analysis of focal mechanisms that show a mixture of strike-slip, oblique slip, and reverse slip (Hardebeck, 2010; McLaren, 2011, presentation at Workshop 1)
- The San Simeon earthquake and aftershock sequence, which showed both reverse displacement during the mainshock and strike-slip displacement during the aftershock sequence
- Inversion of seismicity and GPS data that show an orientation of σ_1 and d_3 of N15°E ± 5° (Lewandowski, 2014, presentation at Workshop 3; PG&E, 2015b)
- The assessment of individual faults that show both strike-slip and reverse faults are present in the region (Hanson et al., 2004; Lettis et al., 2004).

Figure 5-25 shows a schematic interpretation illustrating transpressional deformation in the Diablo Canyon region from Lettis (2012, presentation at Workshop 2). Transpressional deformation would produce strike-slip, oblique-slip and reverse faulting, with limited, localized crustal thickening. The model would generally support higher dip angles on the oblique-slip and reverse faults. The sense of slip on any one fault depends on the orientation and dip of the fault within the contemporary stress field. As described in *Section 5.1.6*, the orientation of the principal compressional stress axis within the Irish Hills is approximately N15°E, and the sense of predicted slip on faults is shown on Figure 5-12. This would predict primarily reverse or reverse-oblique faulting on the Los Osos fault (partially depending on the local fault strike), reverse faulting on the San Luis Bay fault, and strike-slip faulting on the Hosgri and Shoreline faults.

Alternatively, northeast-southwest-directed crustal shortening with minimal or no strike-slip faulting within the Los Osos domain and, in particular, within the Irish Hills of the San Luis–Pismo block can be supported by an alternative interpretation of the same data and observations. The pure crustal shortening would produce crustal thickening and potentially lower dip angles on the reverse faults. Lettis et al. (1994, 2004), for example, interpret the Los Osos domain as consisting of a series of uplifted structural blocks with little or no internal deformation, separated by subsiding or static blocks. The San Luis–Pismo block is one of the more prominent uplifted blocks in the domain. Lettis et al. (1994, 2004) interpret the block to be bordered by reverse faults along the northeastern and southwestern boundaries, the Los Osos and Southwestern Boundary zones, respectively. Crustal shortening and thickening is suggested by relatively rigid uplift of the block. Hanson et al. (1994) and Lettis et al. (2004) use the spatial distribution of marine terraces along the coastal perimeter of the block to document an uplift rate of 0.1–0.2 mm/yr with no observable deformation of the Pismo syncline or faults within the block (e.g., the San Miguelito and Edna faults and other unnamed faults).

In evaluating these two alternative models, the TI team developed alternative fault models to encompass the epistemic uncertainty in sense of slip and geometry of faults in the Diablo Canyon area. Three alternative models were developed to characterize uncertainty in the downdip geometry of the Hosgri fault zone. These are termed H90, H85, and H75, and are described in *Chapter 7*. Three separate models were developed to characterize faults bounding and underlying the San Luis–Pismo block. These models are also described in *Chapter 7*, and are termed the Outward-Vergent (OV) model, the Southwest-Vergent (SW) model, and the Northeast-Vergent (NE) model.

The OV Model is most representative of the regional transpressional shear tectonic model in which oblique-dextral slip is allowed to occur on the Los Osos fault and other faults of the Southwestern Boundary zone. The OV Model is also the alternative San Luis–Pismo Block fault model most consistent with the preferred interpretation of geologic map, well, and 2D land seismic-reflection data collected and analyzed as part of the CCCSIP studies (PG&E, 2014, Chapter 7; Unruh, 2014, presentation at Workshop 3). The preferred interpretation by PG&E (2014, Chapter 7) is that moderately to steeply dipping faults within and bordering the Irish Hills initially developed within a transtensional basin setting that was subsequently deformed by transpression and shortening. The SW Model

is the most representative of the end-member crustal shortening model, in which uplift of San Luis Range is accommodated by more gently dipping reverse faults and deeper, low-angle detachments at depth. This model is generally similar to the proponent model of Hamilton (2012a; 2012b, presentation at Workshop 2), where the dominant reverse fault under the Irish Hills is a part of the northeast-dipping Southwestern Boundary zone and the Los Osos fault is an antithetic back-thrust. The NE Model shares many characteristics with the SW Model, but differs primarily in treating the Los Osos fault as the primary structure that accommodates uplift of the Irish Hills. In all of these models the Hosgri and Shoreline faults are primarily strike-slip faults. Epistemic uncertainty is captured by the combination of all six models.

During Workshop 2, Hamilton (2012b) presented two tectonic concepts for consideration by the TI Team:

1. The presence of a low-angle northeast-dipping thrust or reverse fault beneath the San Luis Range, termed the IOF/San Luis Range thrust fault. As interpreted by Dr. Hamilton, the fault is responsible for uplift of the San Luis–Pismo block and its up-dip tip would intersect the Shoreline fault at shallow depth directly offshore of Diablo Canyon.
2. The presence of an active east-west-trending fault, termed the "Diablo Cove fault" by Dr. Hamilton, that connects to the west with the Shoreline fault, at depth with the IOF/San Luis Range thrust fault, and underlies the DCPP.

In deliberating the IOF/San Luis Range thrust fault concept, the TI Team considered the merits of the model proposed by Dr. Hamilton and evaluations of the model presented as part of the CCCSIP study (PG&E, 2014, Chapter 12). The TI Team incorporated the general aspects of Dr. Hamilton's model of a northeast-dipping reverse fault beneath the San Luis Range within both the SW and OV fault models. The fault is entirely (SW Model) or partly (OV Model) responsible for uplift of the San Luis–Pismo block. The geometry of the fault (depth and dip) shown in the SW and OV fault models is constrained by available data, including locations of observed fault deformation, dimensions and pattern of uplift (both onshore and offshore) that dictate the required location and dimensions of a fault ramp beneath the range, and onshore seismic-reflection data that (within the quality of the data) help constrain the location and geometry of faults in the upper few hundred meters to 1–2 km (PG&E, 2014, Chapter 7). Thus the OV and SW models capture the epistemic uncertainty associated with a primary reverse fault beneath the San Luis Range responsible for uplift of the San Luis–Pismo block, including the fault concept proposed by Dr. Hamilton. Additional northeast-dipping reverse fault locations and geometries that may underlie the San Luis Range but are not considered sufficiently active to be the primary drivers of uplift of the Irish Hills are accounted for in the local areal source zone (*Section 13.5*). The specific IOF/San Luis Range thrust fault model proposed by Hamilton (2012b, presentation at Workshop 2) was not adopted by the TI Team, based on its disagreement with several of the available data constraints, many of which are discussed in PG&E (2014, Chapter 12).

The TI Team also evaluated the “Diablo Cove fault” as a potential seismic source for the Diablo Canyon SSC model. The evaluation process included an assessment of whether such a fault exists as postulated by Hamilton (2012b, Workshop 2 presentation), and, if so, how the fault may project to seismogenic depth as a potential independent seismic source. PG&E (2014, Chapter 12) provides a thorough evaluation of the data and observations regarding the “Diablo Cove fault.” The report concludes that, although minor faulting is observed in several trench and excavation exposures, a throughgoing, laterally continuous, and active fault extending from the Shoreline fault offshore to a location onshore directly northwest of the DCPP does not have a reasonable technical basis. The TI Team concurs with the conclusions reached by PG&E (2014, Chapter 12) and does not incorporate the “Diablo Cove fault” into the SSC model as an active seismic source.

(a) Simplified Geologic Map

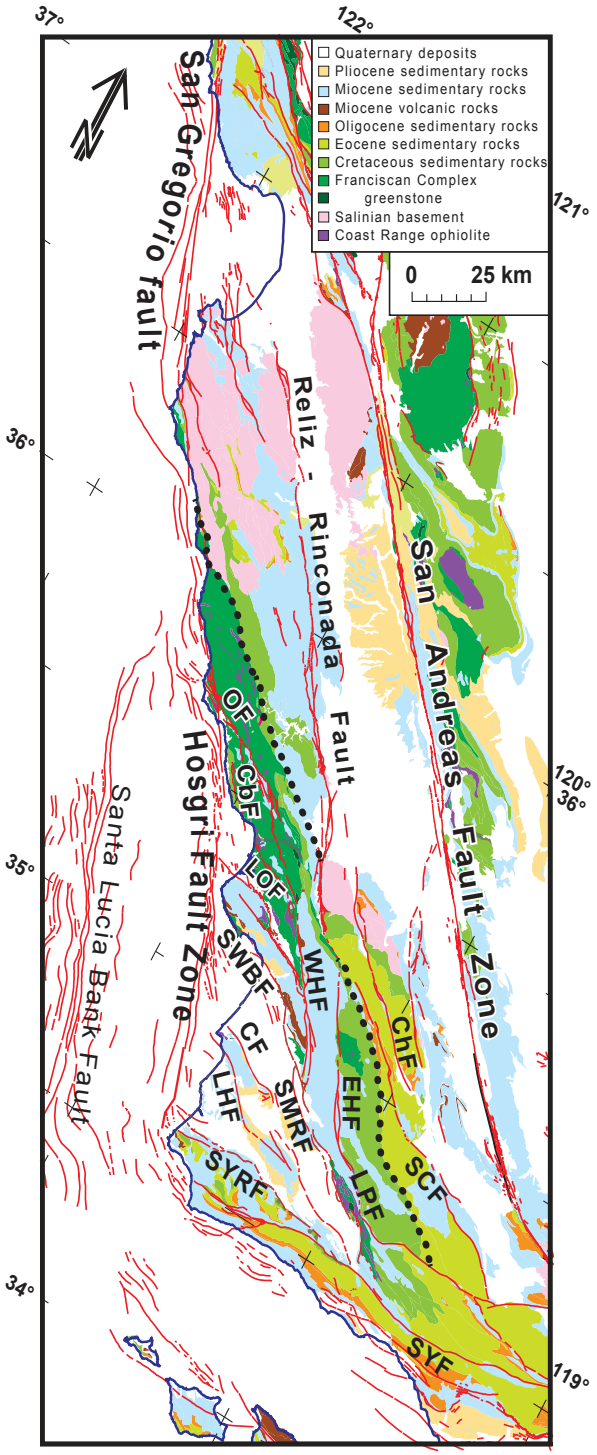

(b) Shaded-Relief Topographic Map

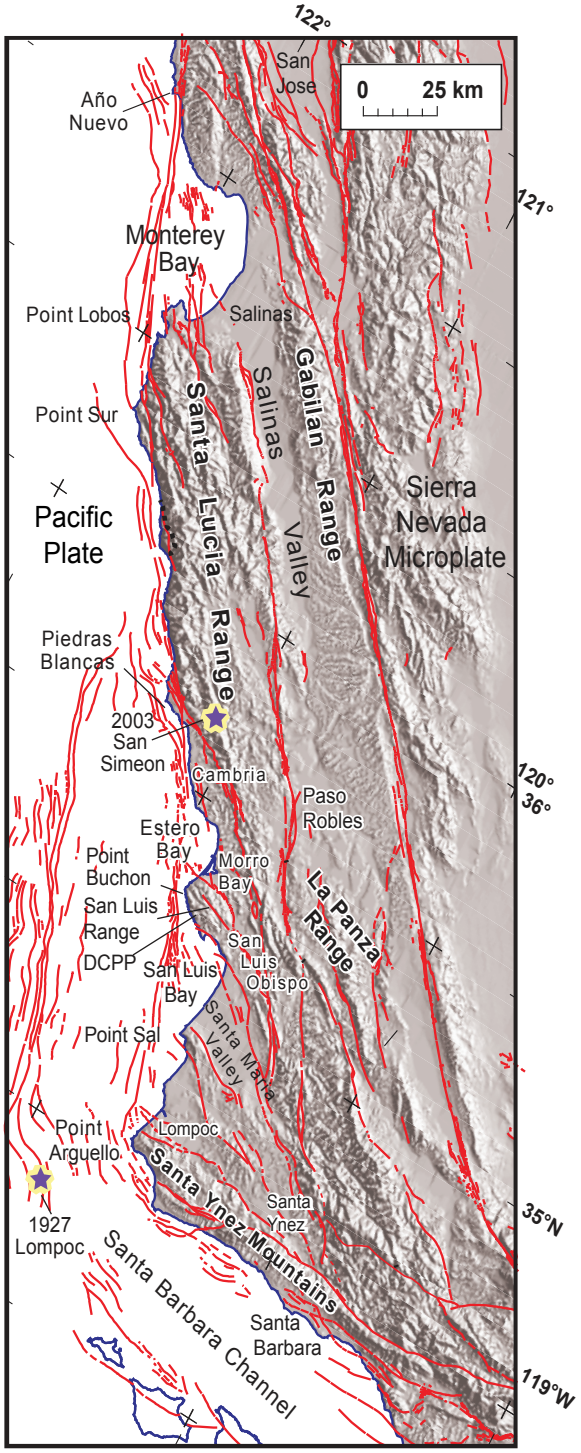

EXPLANATION

Abreviations in Panel (a):

CF - Casmalia fault	OF - Oceanic fault
CbF - Cambria fault	SCF - South Cuyama fault
ChF - Chimineas fault	SMRF - Santa Maria River fault
EHF - East Huasna fault	SWBF - Southwest Boundary fault zone
LHF - Lions Head fault	SYF - Santa Ynez River fault
LOF - Los Osos fault	WHF - West Huasna fault
LPF - Little Pine fault	

Notes:
- Geology in Panel (a) is from Jennings et al. (1977).
- Faults shown as thin red lines in Panels (a) and (b) are modified from Jennings and Bryant (2010).
- Thick dotted line in Panel (a) is the Nacimiento fault.

Sources:
- Modified from Langenheim, Jachens, et al. (2012).
- Jennings et al. (1977).
- Jennings and Bryant (2010).

Simplified Geologic Map and Shaded-Relief Topographic Map of the Central California Coast Region

DCPP SSC REPORT

Pacific Gas and Electric Company | Figure **5-1**

File path: S:\1005\005\Final_Report_Figures\Figure_5-01.ai; Date: 03/11/2015; User: Alex Remar, LCI; Rev.1

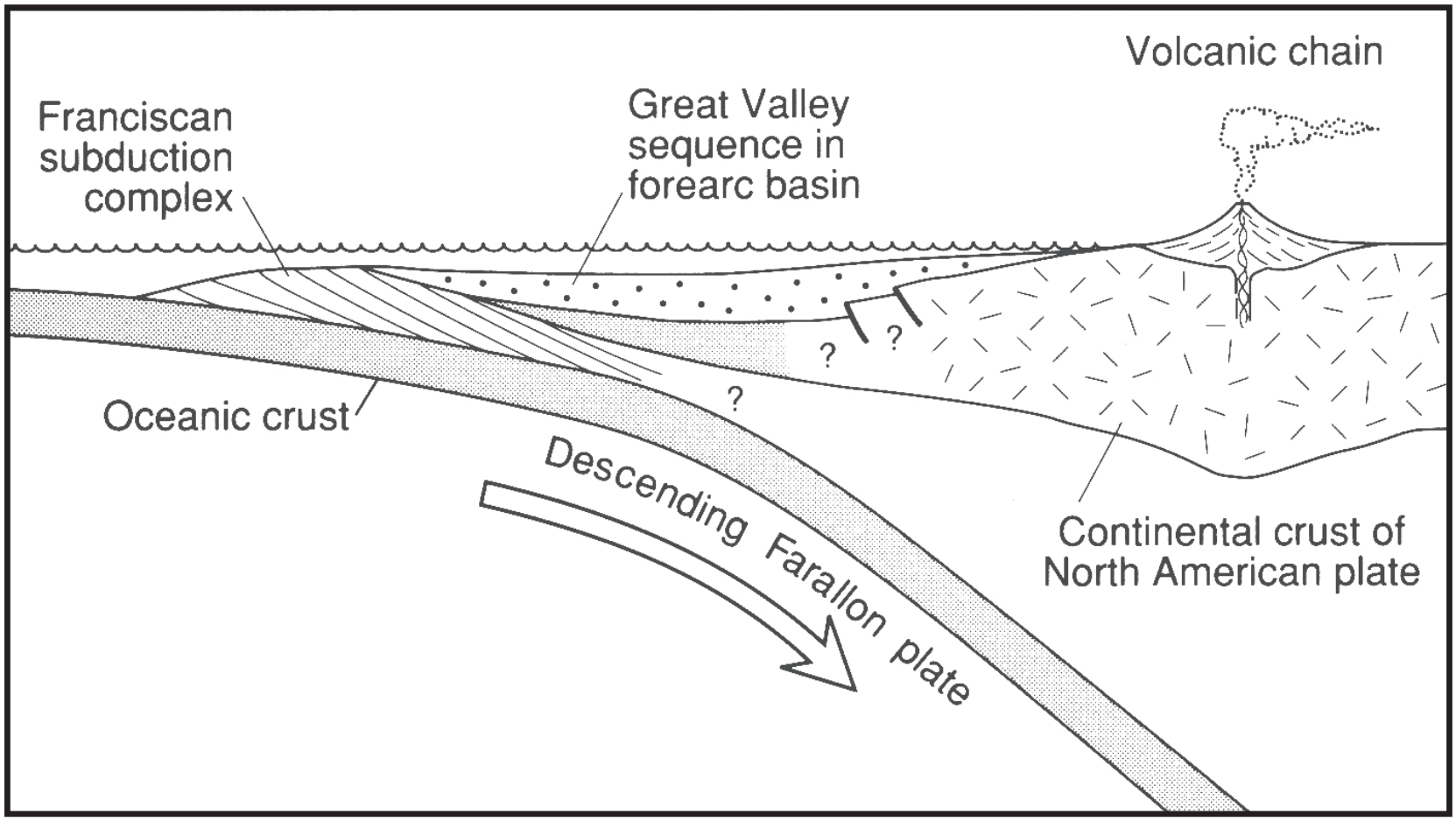

Source: Modified from Dickinson (1981) and Irwin (1990).

Schematic Cross Section of the Convergent North American–Farallon Plate Boundary During Late Mesozoic Franciscan Subduction

DCPP SSC REPORT

Pacific Gas and Electric Company | Figure **5-2**

File path: S:\1005\005\Final_Report_Figures\Figure_5-02.ai; Date: 03/02/2015; User: Alex Remar, LCI; Rev.1

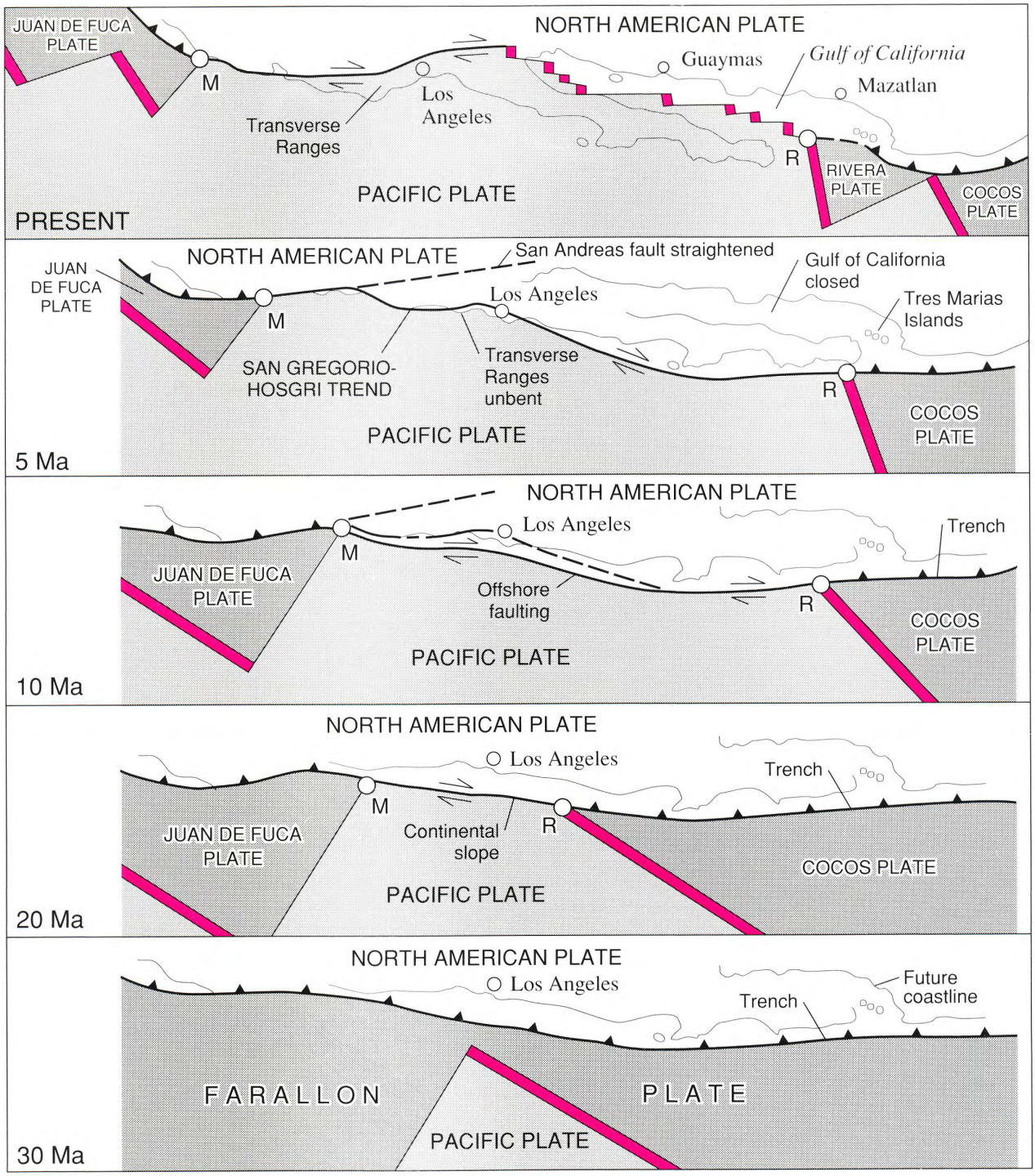

EXPLANATION

Spreading center

Subduction zone, dashed where approximately located. Sawteeth on upper plate

Fault, dashed where approximately located. Arrows indicate direction of relative movement

M Mendocino triple junction

R Rivera triple junction

Source: Modified from Dickinson (1981) in Irwin (1990).

Post–30 Ma Development of the San Andreas Transform Boundary

DCPP SSC REPORT

Pacific Gas and Electric Company

Figure **5-3**

File path: S:\1005\005\Final_Report_Figures\Figure_5-03.ai; Date: 03/02/2015; User: Alex Remar, LCI; Rev.1

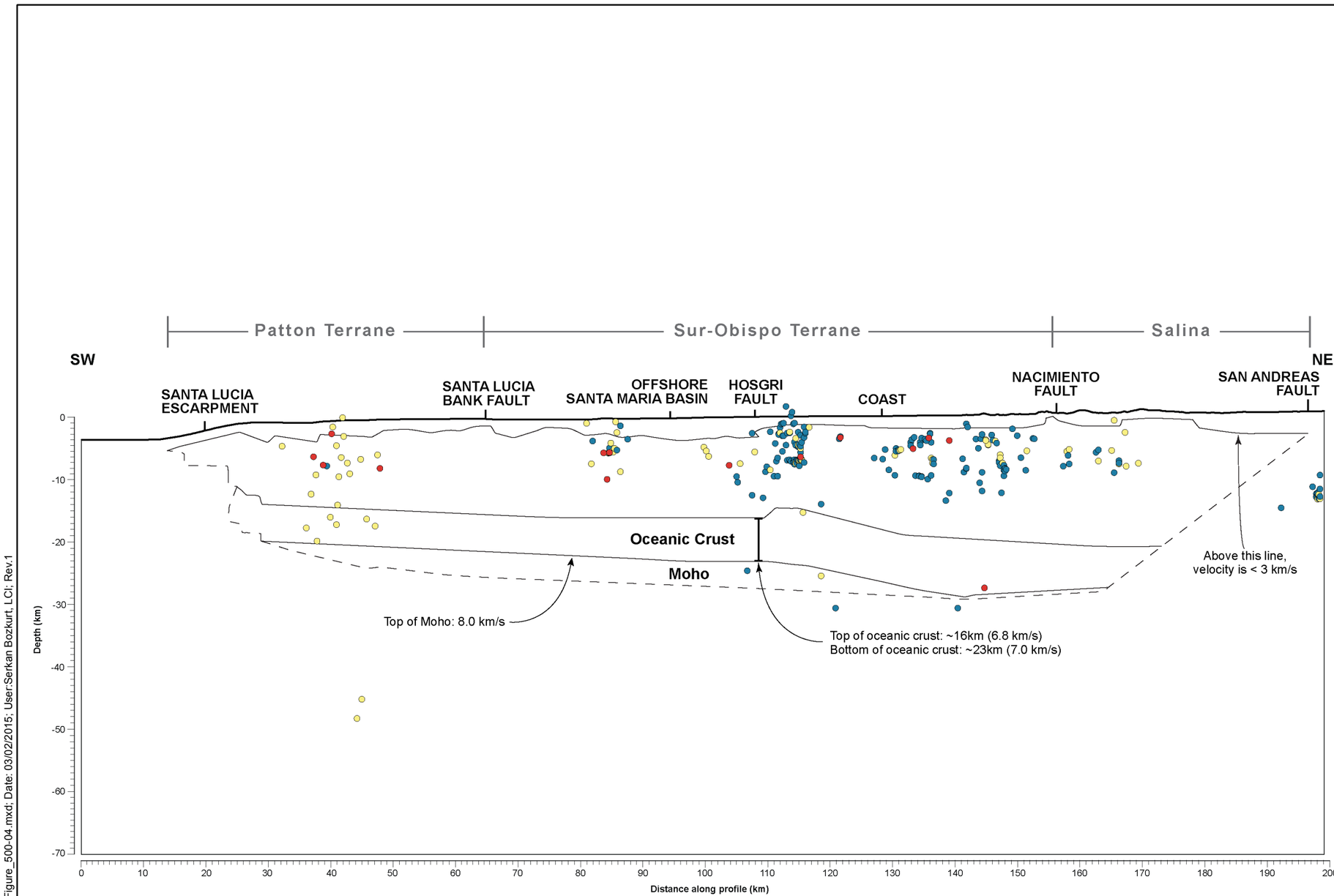

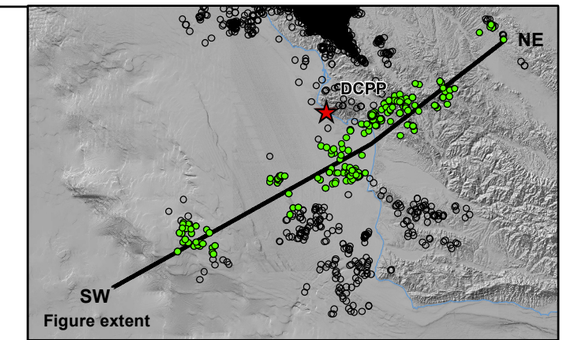

EXPLANATION

Inset Map

- Epicenters within 10 km of the cross section
- Epicenters greater than 10 km from the cross section

Cross Section

Seismicity (Magnitude)

- < 2.0
- 2.0–2.9
- 3.0–4.2

Notes:
- Seismicity shown at 10 km buffer to profile.
- The cross section shows that the majority of seismicity along seismic line PG&E-3 occurs above the subducted oceanic crust.
- Thin black lines in the cross section indicate first order velocity discontinuities. Dashed line indicates limit of data.
- The crustal velocity model from Howie et al. (1993) shown on the cross section was derived from various wide-angle and multichannel seismic and gravity datasets.

Sources:
- Earthquake hypocenters from Hardebeck (2010).
- Crustal velocity model from Howie et al. (1993).

N

0 4 8 mi.
0 8 16 km

Map projection and scale: WGS 84 / UTM Zone 10N, 1:700,000

Deep Crustal Cross Section Along Seismic Line PG&E-3

DCPP SSC REPORT

Pacific Gas and Electric Company

Figure **5-4**

File path: S:\1005\005\Final_Report_Figures\Figure_500-04.mxd; Date: 03/02/2015; User:Serkan Bozkurt, LCI; Rev.1

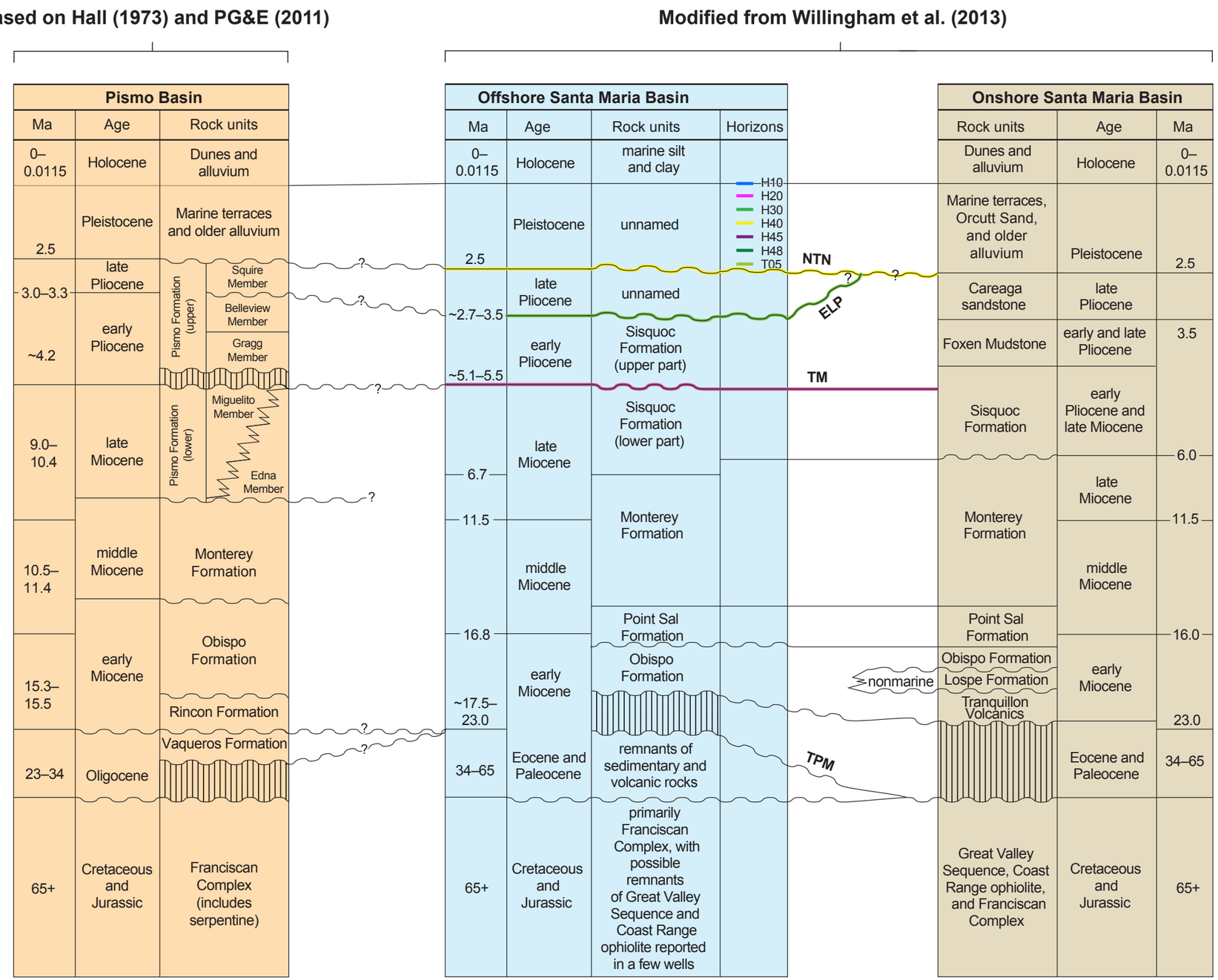

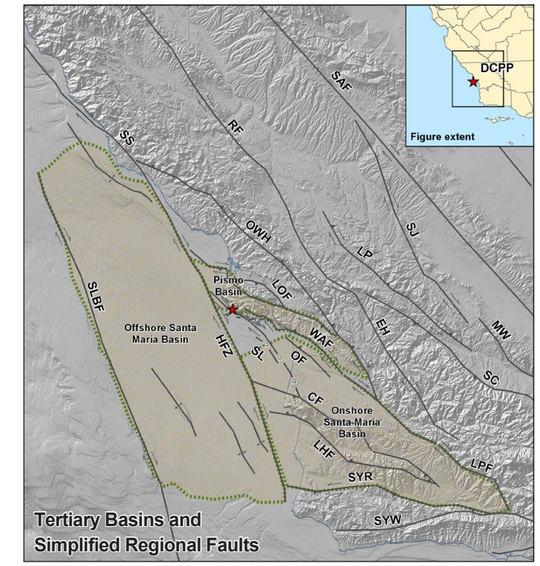

EXPLANATION

Approximate boundary of Tertiary basin

Unconformities

PG&E (2014, Chapter 3)
- H10 - H48 and T05
- NTN = Near top of Neogene unconformity

Willingham et al. (2013)
- ELP = Early–late Pliocene unconformity
- TM = Top of Miocene
- TPM = Top of Pre-Miocene basement

Notes:
- Fault traces modified from the Uniform California Earthquake Rupture Forecast, version 3 (UCERF3), fault model version 3.1 (Field et al, (2013). Generalized trends of active contractional structures in the offshore and the offshore Santa Lucia Bank fault are based on Lettis et al. (2004, Plate 1).
- Fault names in sketch map are as follows: SAF, San Andreas Fault; RF, Rinconada fault; SJ, San Juan fault; MW, Morales (west) fault; LP, La Panza fault; SC, South Cuyama fault; EH, East Huasna fault; OWH, Oceanic-West Huasna fault; SS, San Simeon fault; HFZ, Hosgri fault zone; LOF, Los Osos fault; WAF, Wilmar Avenue fault; LPF, Little Pine fault; OF, Oceano fault; SL, Shoreline fault; CF, Casmalia fault; LHF, Lions Head fault; SYR, Santa Ynez River fault; SYW, Santa Ynez (west) fault; SLBF, Santa Lucia Bank fault.
- Time scales in stratigraphic columns are not linear.

Sources:
- Modified from PG&E (2014, Chapter 3).
- Stratigraphic columns for Santa Maria Basin from Willingham et al. (2013).
- Stratigraphic column for Pismo Basin from PG&E (2011) and Hall (1973).

Generalized Stratigraphic Columns for the Project Study Area

DCPP SSC REPORT

Pacific Gas and Electric Company | Figure **5-5**

File path: S:\1005\005\Final_Report_Figures\Figure_5-05.ai; Date: 03/03/2015; User: Alex Remar, LCI; Rev:1

(a) Transtensional

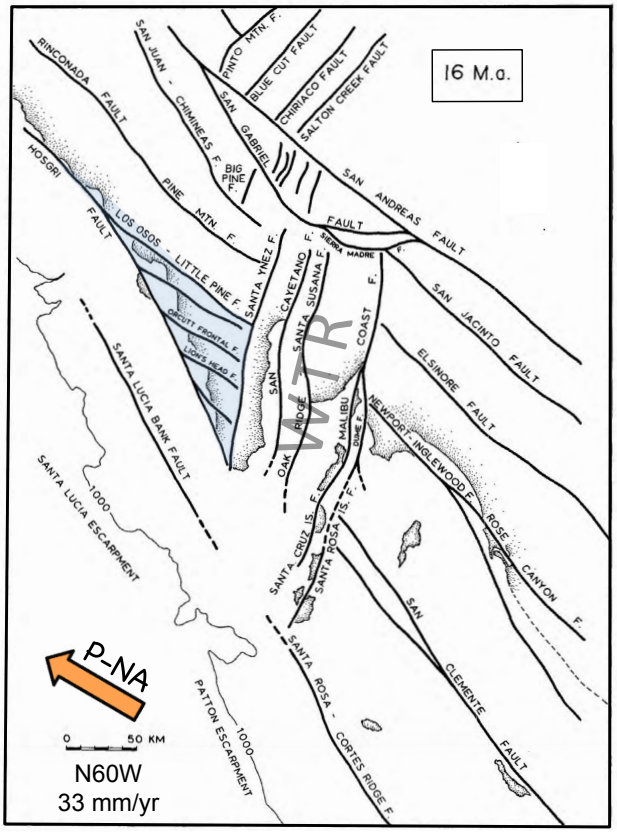

(b) Transtensional (Increased Slip on SGHFZ, 12–10 Ma)

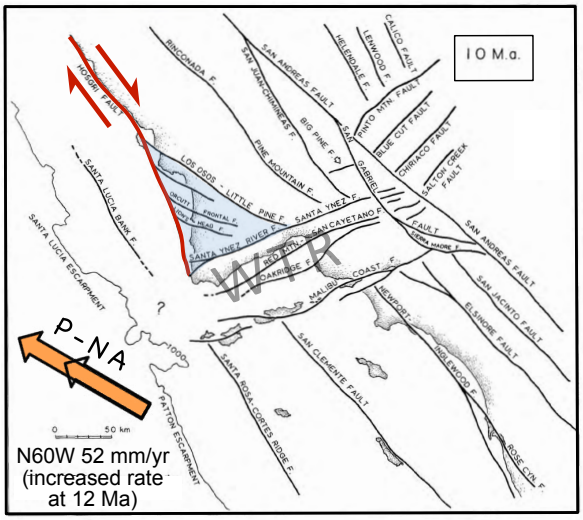

(c) Transpressional (Decreasing Slip on SGHFZ)

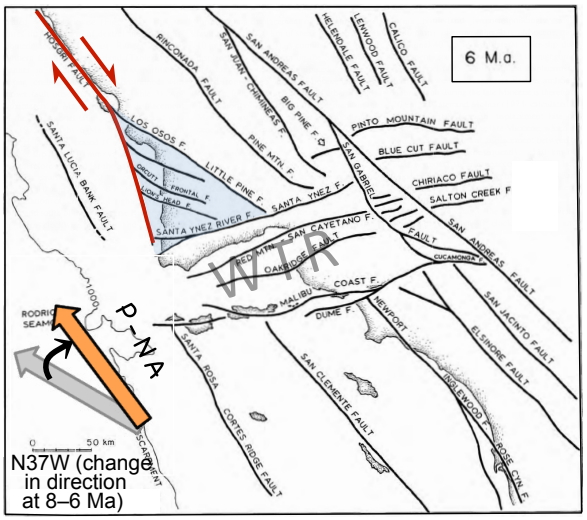

EXPLANATION

WTR Western Transverse Ranges

Sources:
- Resolved motion between the Pacific and North American plates from Atwater and Stock (1998).
- Palinspastic reconstruction of southern California from Hornafius et al. (1986).

Episodes of Rotation of the Western Transverse Ranges and Resolved Pacific-North American Plate Motion

DCPP SSC REPORT

Pacific Gas and Electric Company

Figure **5-6**

File path: S:\1005\005\Final_Report_Figures\Figure_5-06.ai; Date: 03/06/2015; User: Alex Remar, LCI; Rev.1

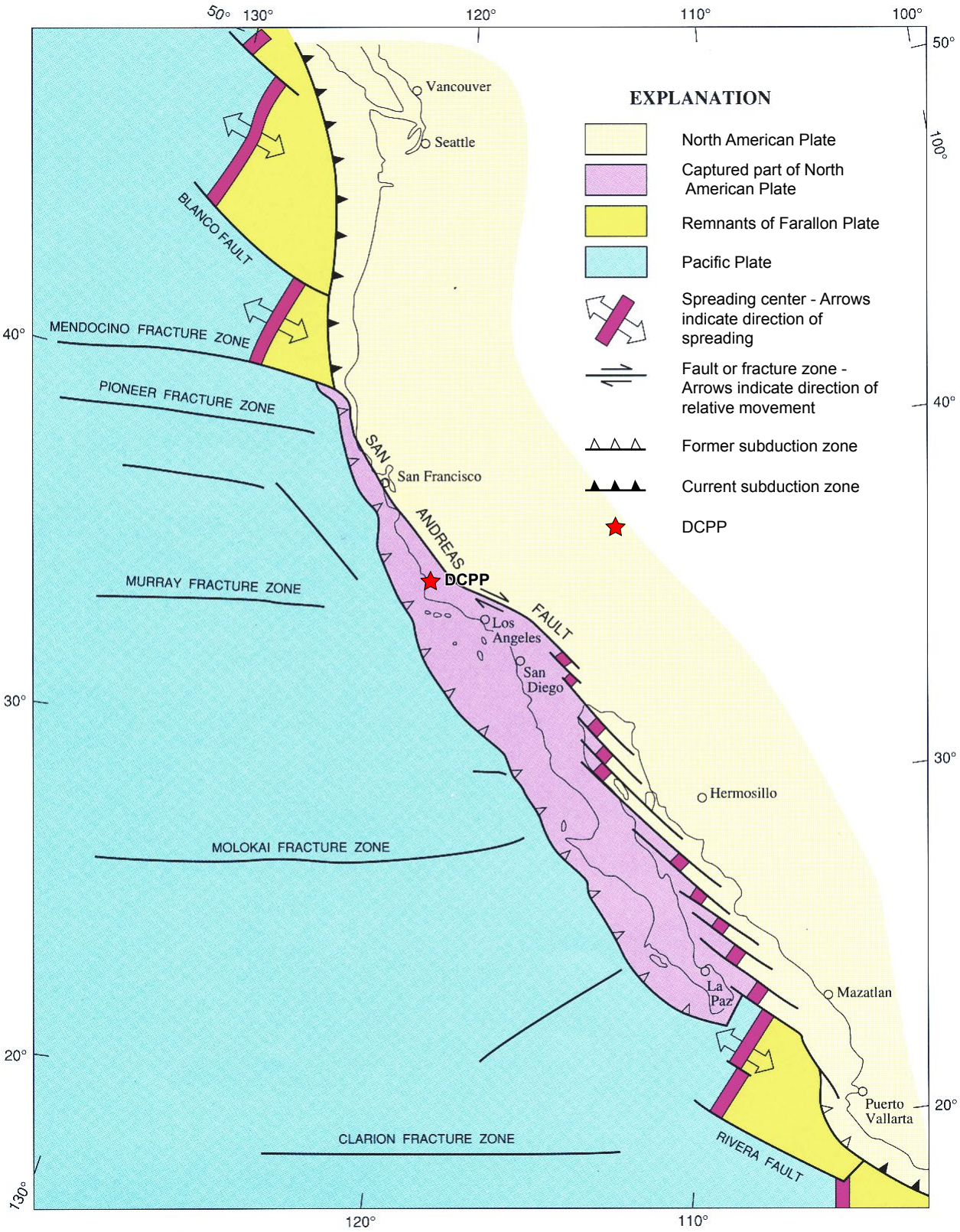

Note: Shown in purple is the part of the North American Plate that has been captured by the Pacific Plate as the transform boundary has stepped landward.

Source: Modified from Moore (1981) in Irwin (1990).

Present-Day Configuration of Tectonic Plates Along the Western Margin of North America

DCPP SSC REPORT

Pacific Gas and Electric Company

Figure **5-7**

File path: S:\1005\005\Final_Report_Figures\Figure_5-07.ai; Date: 02/12/2015; User: Alex Remar, LCI; Rev.1

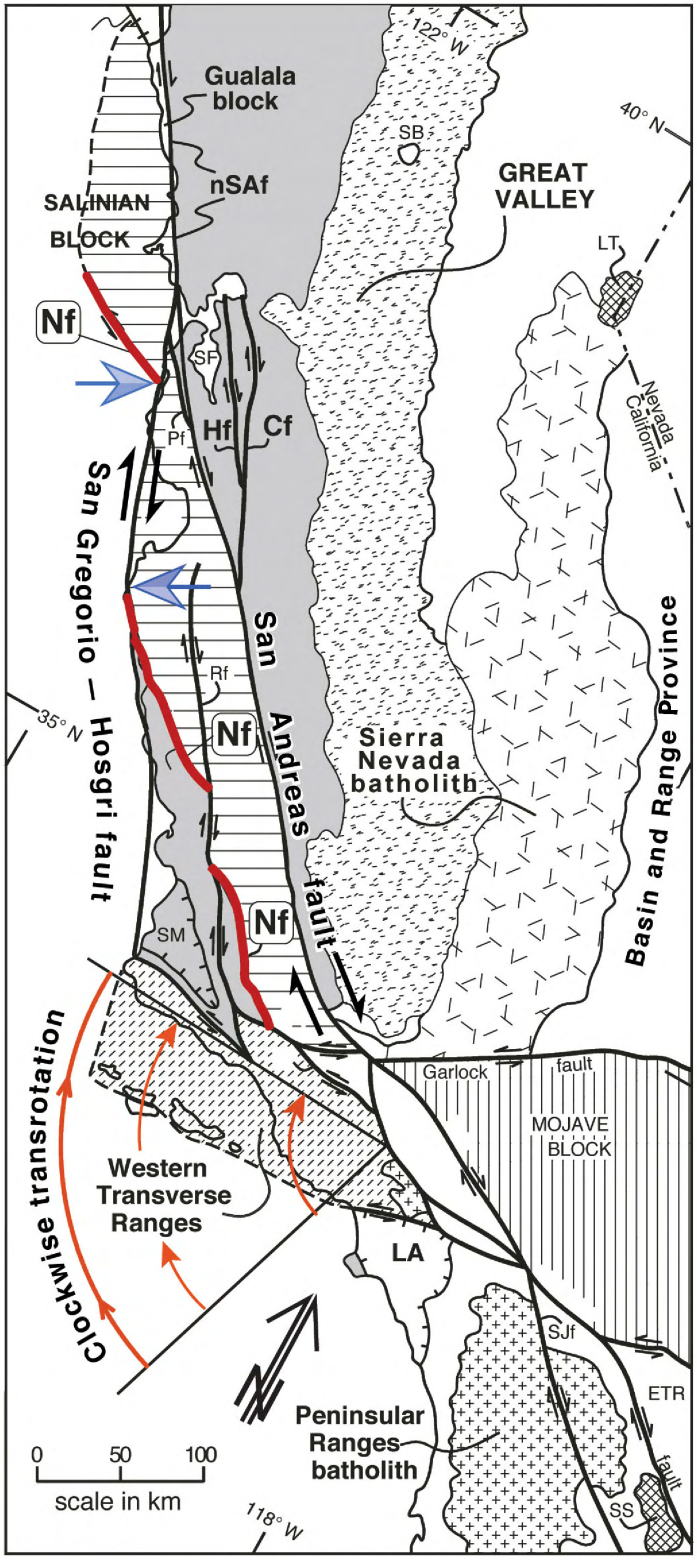

EXPLANATION

- Offset of Mesozoic Nacimiento fault (~150 km; Dickinson et al., 2005)
- Salinian Block
- Franciscan Complex
- Franciscan Complex beneath Western Transverse Ranges

Place Name Abbreviations:

ETR	Eastern Transverse Ranges
LT	Lake Tahoe
SF	San Francisco Bay
SS	Salton Sea
SB	Sutter Butte
SM	Santa Maria Basin

Fault Abbreviations:
(faults shown as heavy lines):

BPf	Big Pine
Cf	Calaveras
nSAf	northern San Andreas
SGf	San Gabriel
SJf	San Jacinto
Hf	Hayward
Nf	Nacimiento
Pf	Pilarcitos
Rf	Rinconada

Source: Modified from Dickinson et al. (2005).

Tectonic Setting of the San Gregorio–Hosgri Fault System and California Coast Ranges

DCPP SSC REPORT

Pacific Gas and Electric Company

Figure **5-8**

File path: S:\1005\005\Final_Report_Figures\Figure_5-08.ai; Date: 02/13/2015; User: Alex Remar, LCI; Rev.1

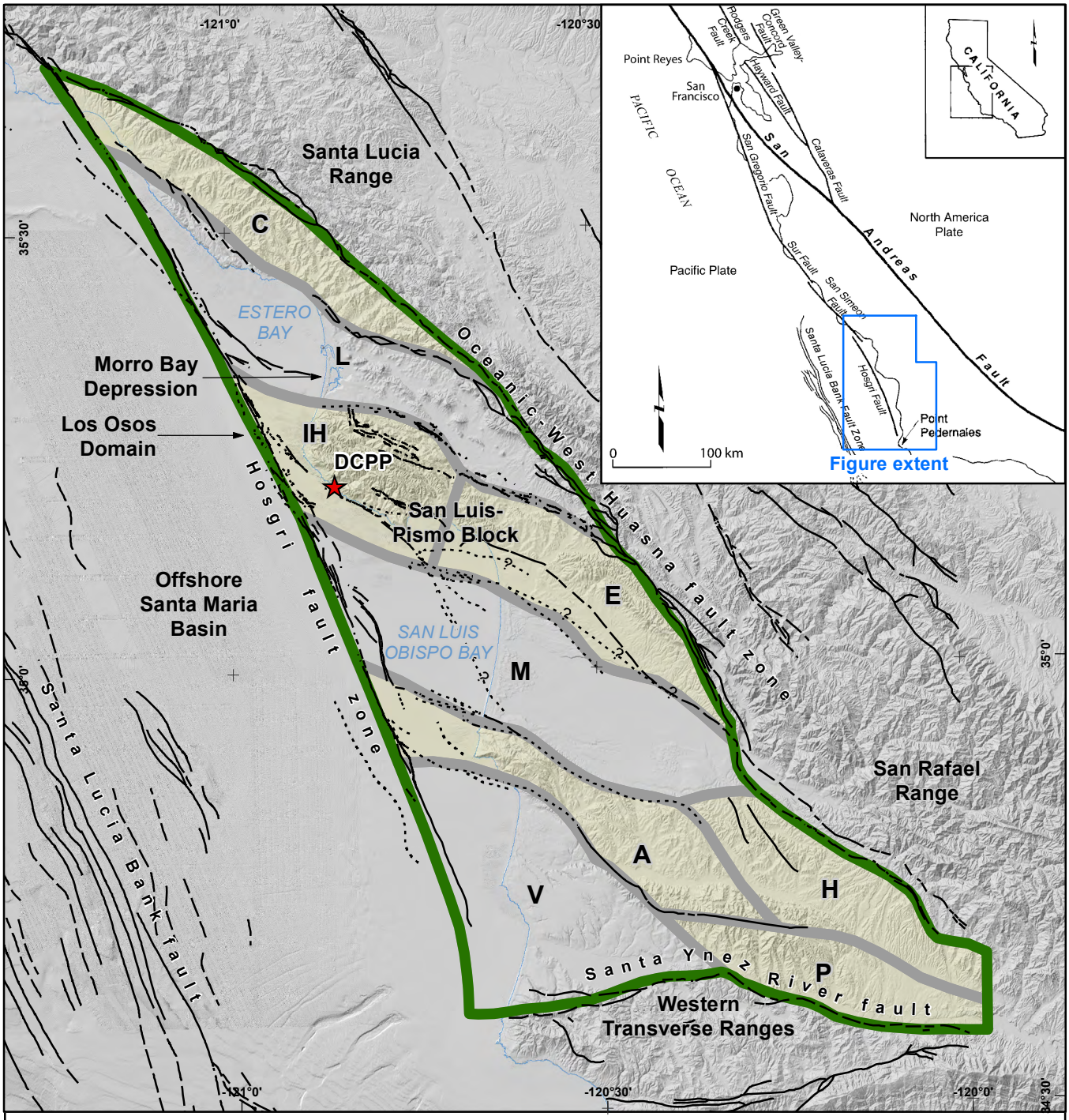

EXPLANATION

Fault: solid where well located, dashed where approximately located, dotted where concealed, short dashed where inferred, queried where existence is uncertain

Uplifted structural blocks within the Los Osos domain, outlined by thick gray line

Boundary outlining Los Osos domain

Diablo Canyon Power Plant site

Structural blocks within the Los Osos domain

A = Casmalia
C = Cambria
E = Edna sub-block
IH = Irish Hills sub-block
H = Solomon Hills
L = Los Osos
M = Santa Maria Valley
P = Purisima
V = Vandenberg/Lompoc

Sources:
- PG&E (1988, 2011, 2013b)
- Regional tectonic sketch map from Hanson et al. (2004)
- AMEC (2011)

N

0 10 20 mi.
0 20 40 km

Map projection and scale: WGS 84 / UTM Zone 10N,1:750,000

Crustal Domains of South-Central Coastal California

DCPP SSC REPORT

Pacific Gas and Electric Company

Figure **5-9**

File path: S:\1005\005\Final_Report_Figures\Figure_500-09.mxd; Date: 03/10/2015; User: Alex Remar, LCI; Rev.1

(a) GPSTRN Results

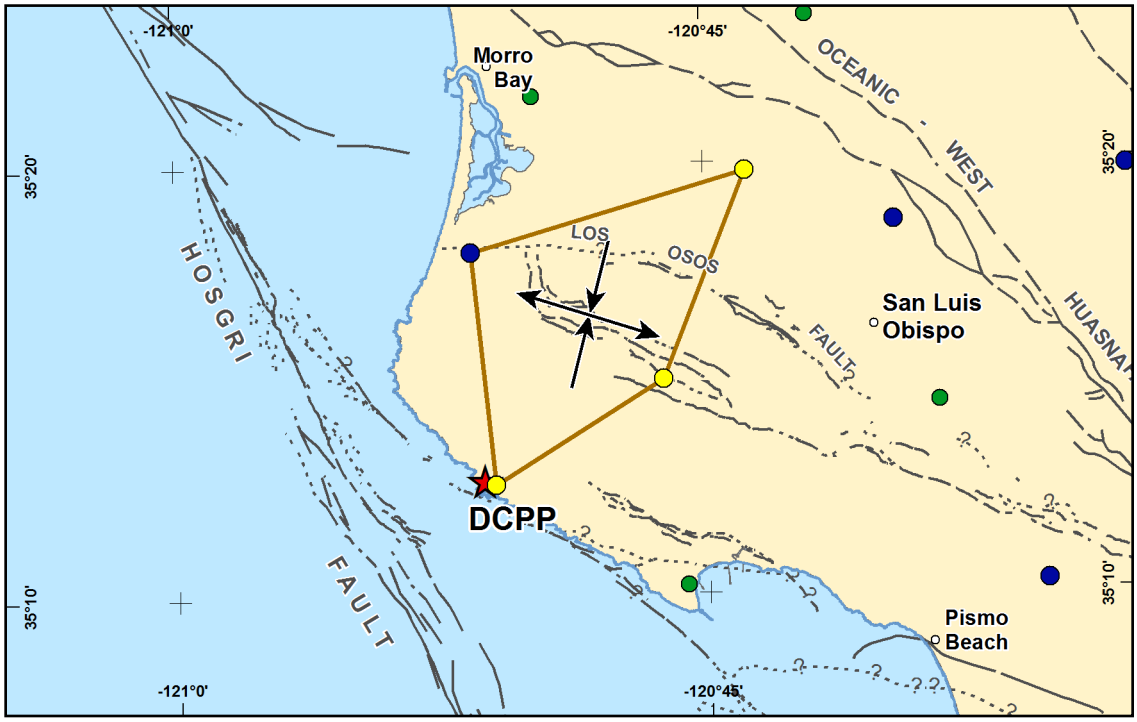

(b) SSPX Results

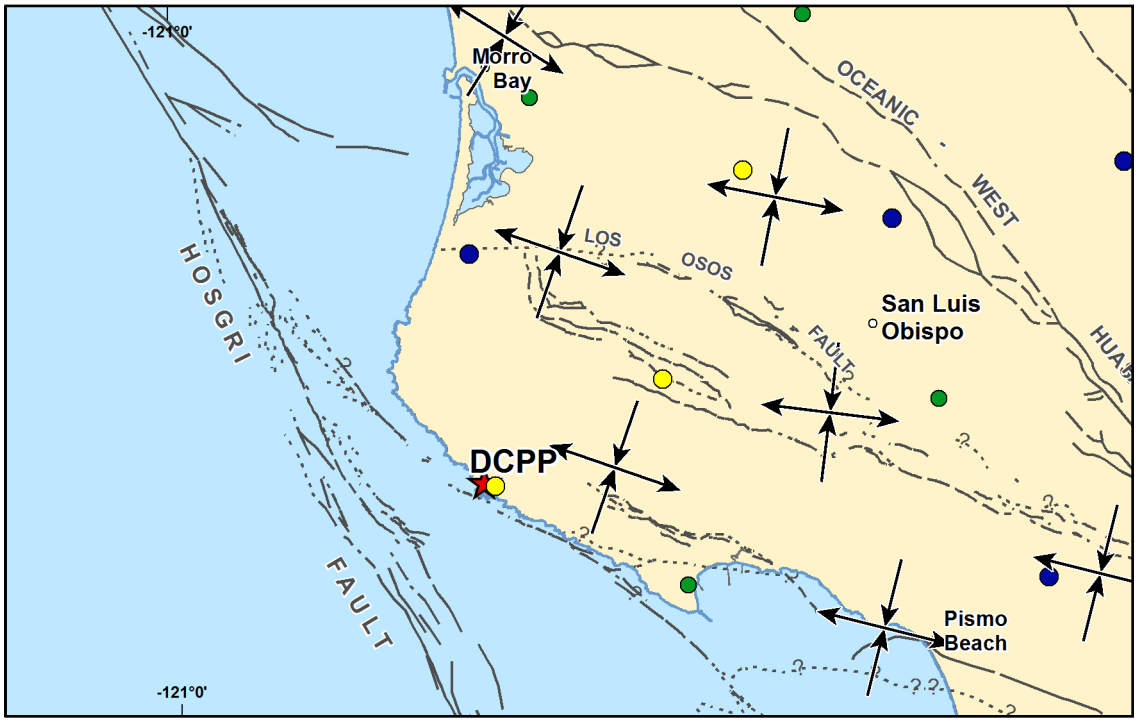

N

0 5 10 mi.

0 10 20 km

Map projection and scale: WGS 84 / UTM Zone 10N, 1:325,000

EXPLANATION

d_1, d_3 — Orientation of principal strain rate axes

GPS Stations

- Continuous
- Campaign
- Semi-Continuous

Note: Brown polygon in Panel (a) shows the four GPS stations used in the GPSTRN inversion.

Sources:
- Modified from Lewandowski (2014).
- Faults from PG&E (2014, Chapter 3).
- GPS data from DeMets (2012a).

Analysis of GPS Data Using the GPSTRN and SSPX Inversion Algorithms

DCPP SSC REPORT

Pacific Gas and Electric Company

Figure **5-10**

File path: S:\1005\005\Final_Report_Figures\Figure_5-10.ai; Date: 03/10/2015; User: Alex Remar, LCI; Rev.1

(a) FLTSLP Results (Strain Inversion)

FPFIT Polygon IHN3

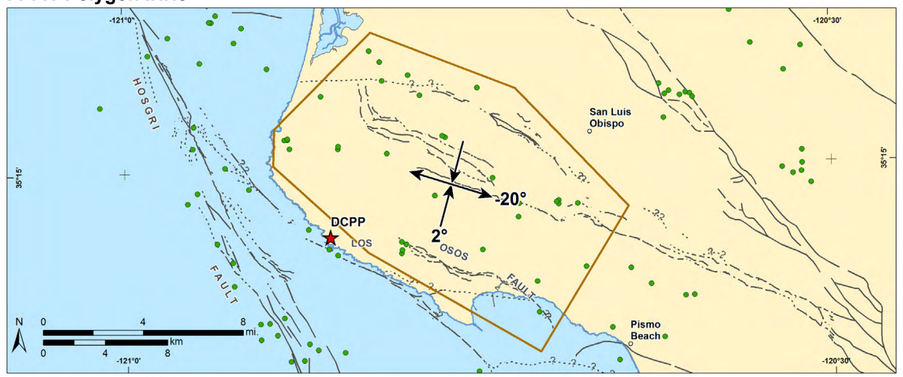

FPFIT Polygon IHN2

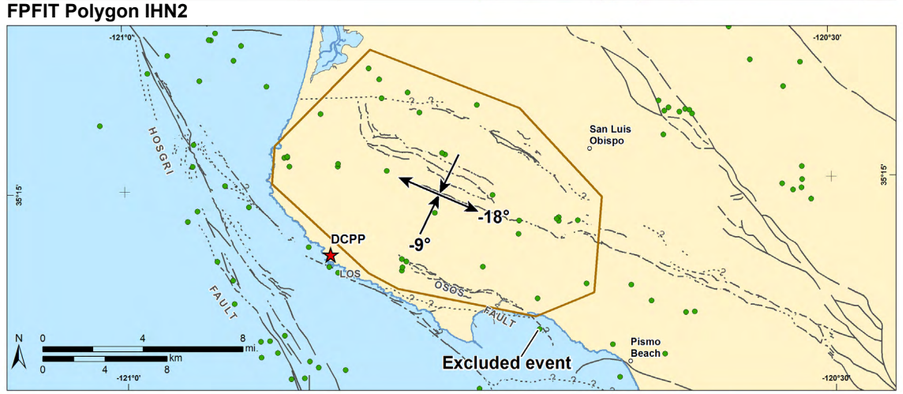

HASH Polygon IRS3

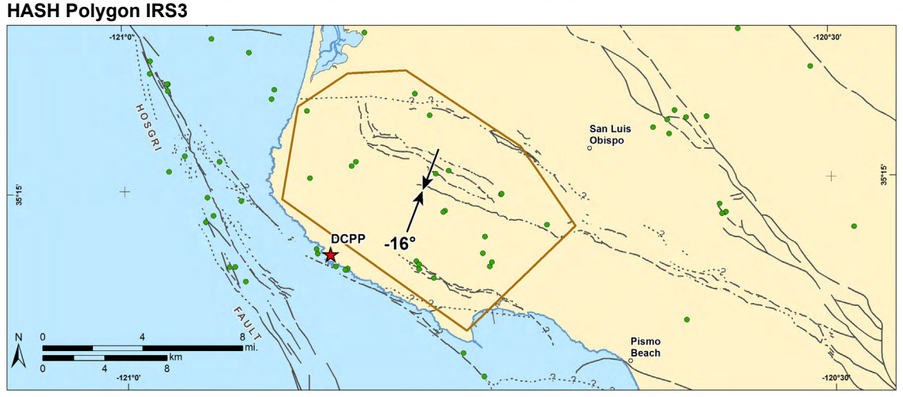

(b) SATSI Results (Stress Inversion)

FPFIT Data

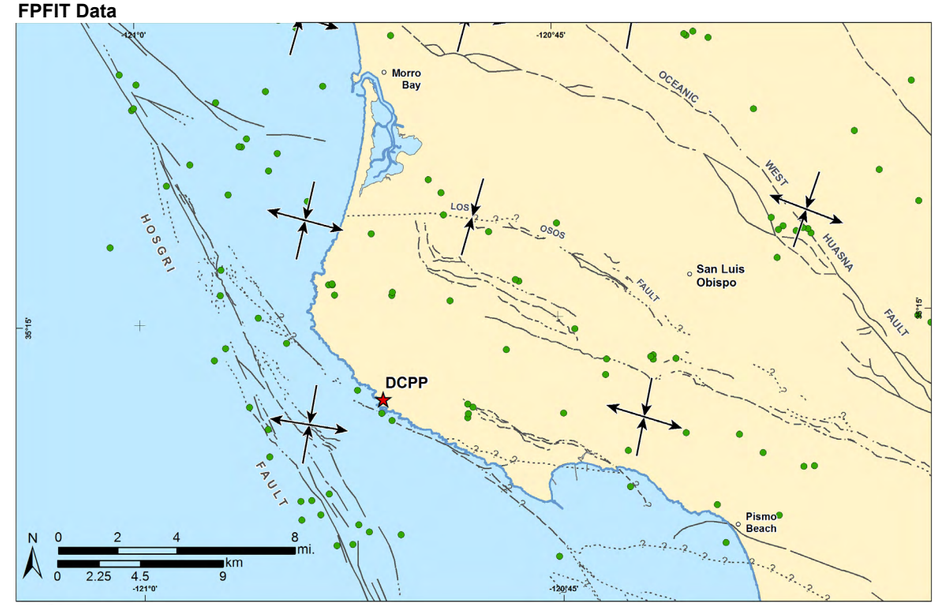

HASH Data

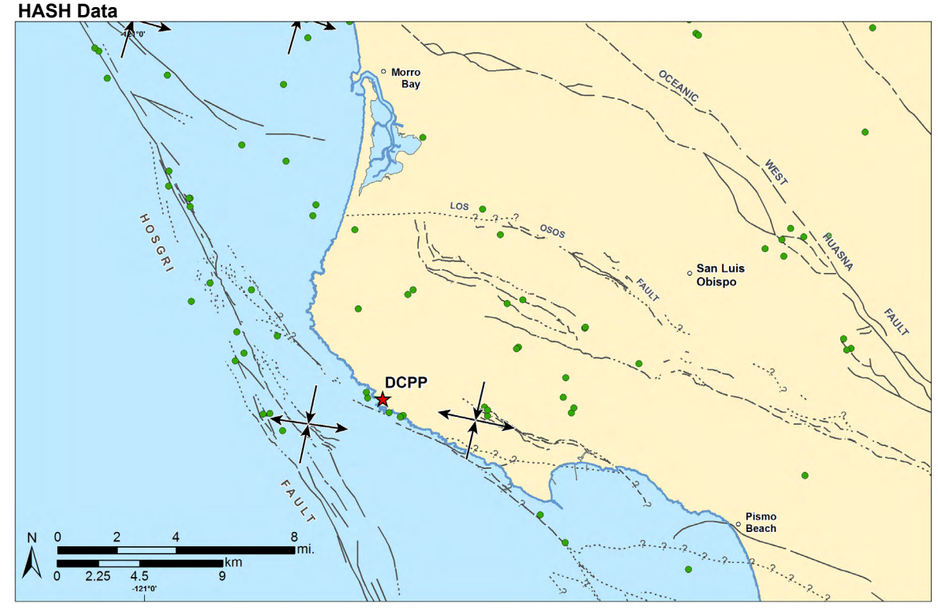

EXPLANATION

$d_1(\sigma_3)$ / $d_3(\sigma_1)$ — Orientation of principal strain rate (or stress) axes, scaled by magnitude

Focal mechanism

Inversion polygon

Notes:
- V is relative contribution of horizontal shearing vs. crustal thickening or thinning, with values closer to 0 indicative of plane strain.
- N is number of focal mechanisms included in inversion.
- In Panel (b), SATSI stress inversions were completed on a 0.1° x 0.1° grid, with a minimum of 8 events per cell. Cells without results had an insufficient number of events for inversion.

Sources:
- Modified from Lewandowski (2014).
- FPFIT focal mechanism data from NCEDC (2013).
- HASH focal mechanism data from Hardebeck (2010).
- Faults from PG&E (2014, Chapter 3).

Analysis of Focal Mechanism Data Using the FLTSLP and SATSI Inversion Algorithms

DCPP SSC REPORT

Pacific Gas and Electric Company

Figure **5-11**

File path: /s/1005/005/Final_Report_Figures/Figure_500-11.ai; Date: 02/12/2015; User: Alex Remar, LCI; Rev. 1

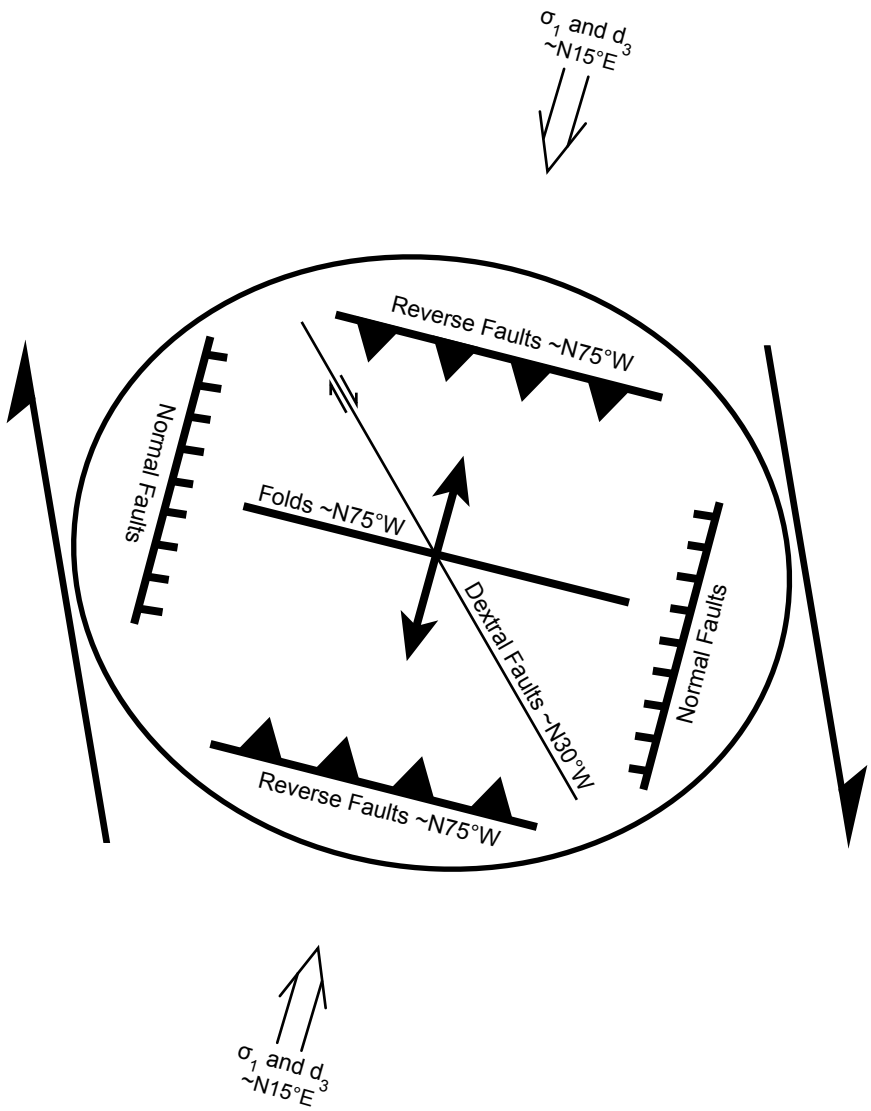

Notes:
- Principal orientation of crustal shortening in the Irish Hills shown at ~N15°E ± 5°.
- Shortening direction calculated from focal mechanism and geodetic data inversion. See PG&E (2015b).

Source: Lewandowski (2014).

Fault Patterns Predicted from Principal Stress and Strain Axes in the Irish Hills

DCPP SSC REPORT

Pacific Gas and Electric Company

Figure **5-12**

File path: S:\1005\005\Final_Report_Figures\Figure_5-12.ai; Date: 03/10/2015; User: Alex Remar, LCI; Rev.1

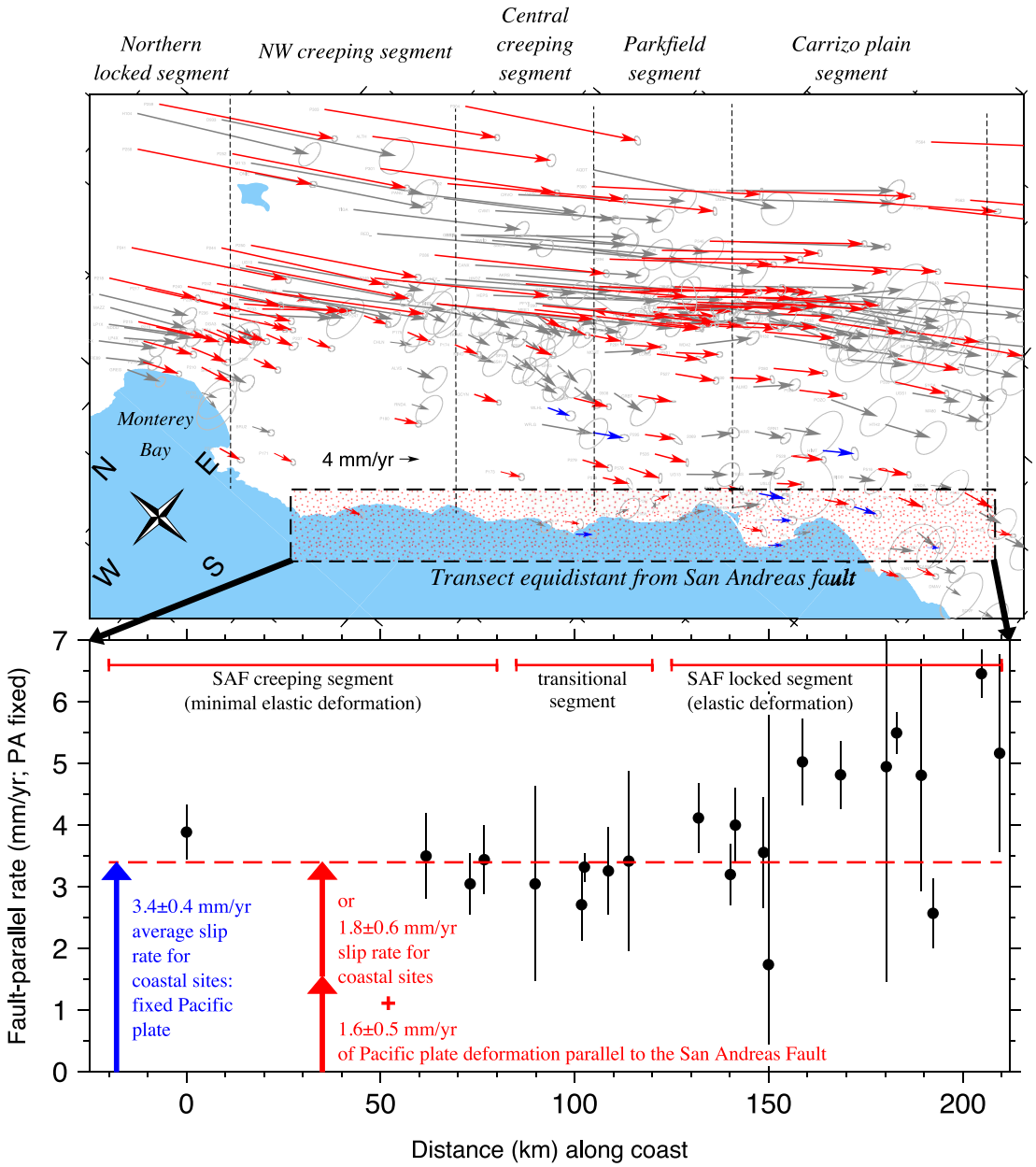

EXPLANATION

- Continuous GPS station
- Campaign USGS station
- USGS semi-continuous GPS station
- Transect equidistant from San Andreas fault

Note: Fault-parallel rates are higher at the southeastern end of the transect (distances of ~125–210 km along the coast) because of the elastic contribution from a locked San Andras fault.

Source: Modified from DeMets et al. (2014).

Synthesis of Fault-Parallel Rates for Stations Within a Coastal Transect Equidistant from the San Andreas Fault

DCPP SSC REPORT

Pacific Gas and Electric Company

Figure **5-13**

File path: S:\1005\005\Final_Report_Figures\Figure_500-13.ai; Date: 03/06/2015; User: Alex Remar, LCI; Rev.1

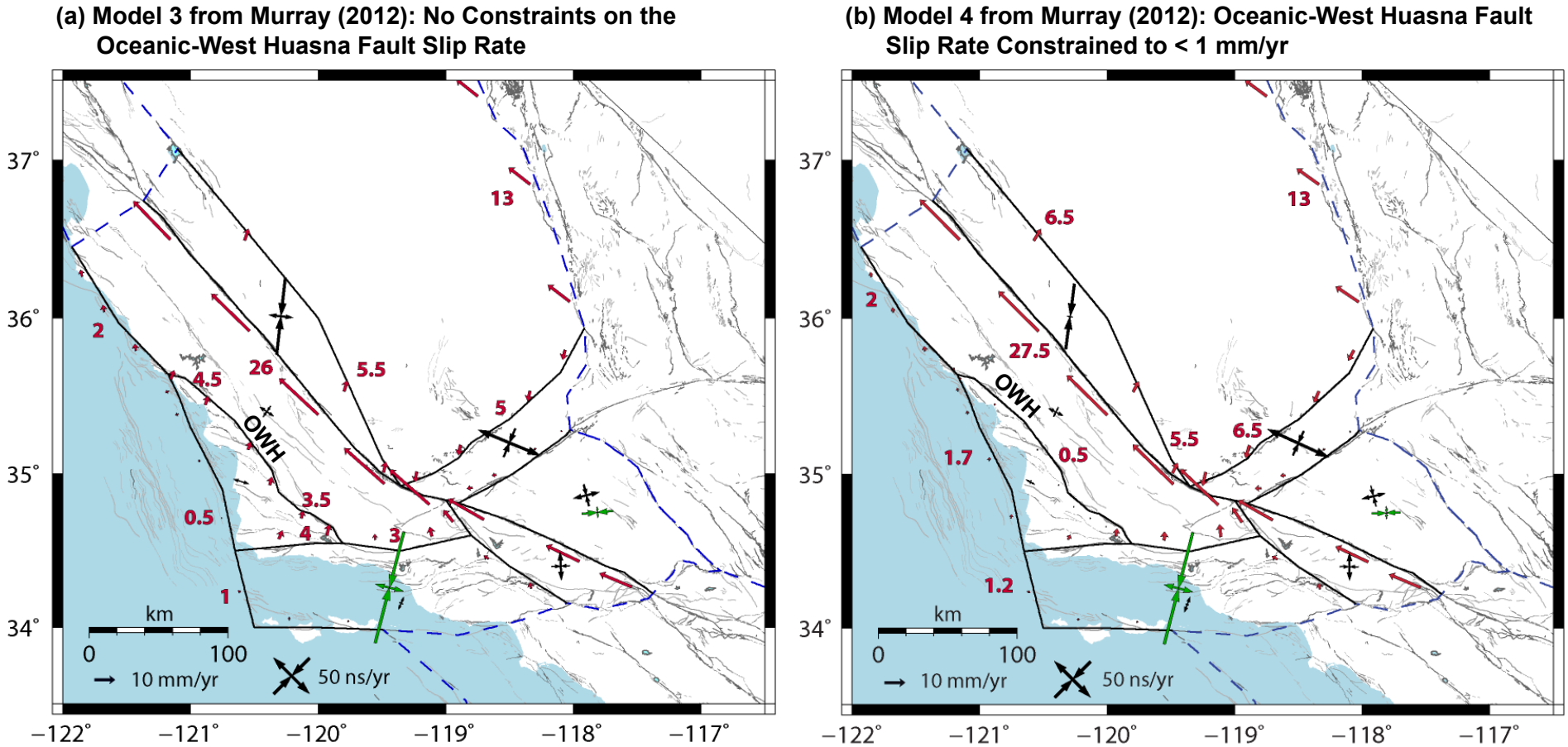

EXPLANATION

- Freely-slipping boundary
- Boundary on which locking is estimated
- OWH — Oceanic-West Huasna fault

Note: Red numbers are slip rate in mm/yr. Sets of green arrows are estimated strain rate tensors. Sets of black arrows are residual strain rate tensors.

Source: Modified from Murray (2012).

Resolved GPS Strain Rates on Tectonic Block Boundaries

DCPP SSC REPORT

Pacific Gas and Electric Company

Figure **5-14**

File path: S:\1005\005\Final_Report_Figures\Figure_500-06.ai; Date: 03/06/2015; User: Alex Remar, LCI; Rev.1

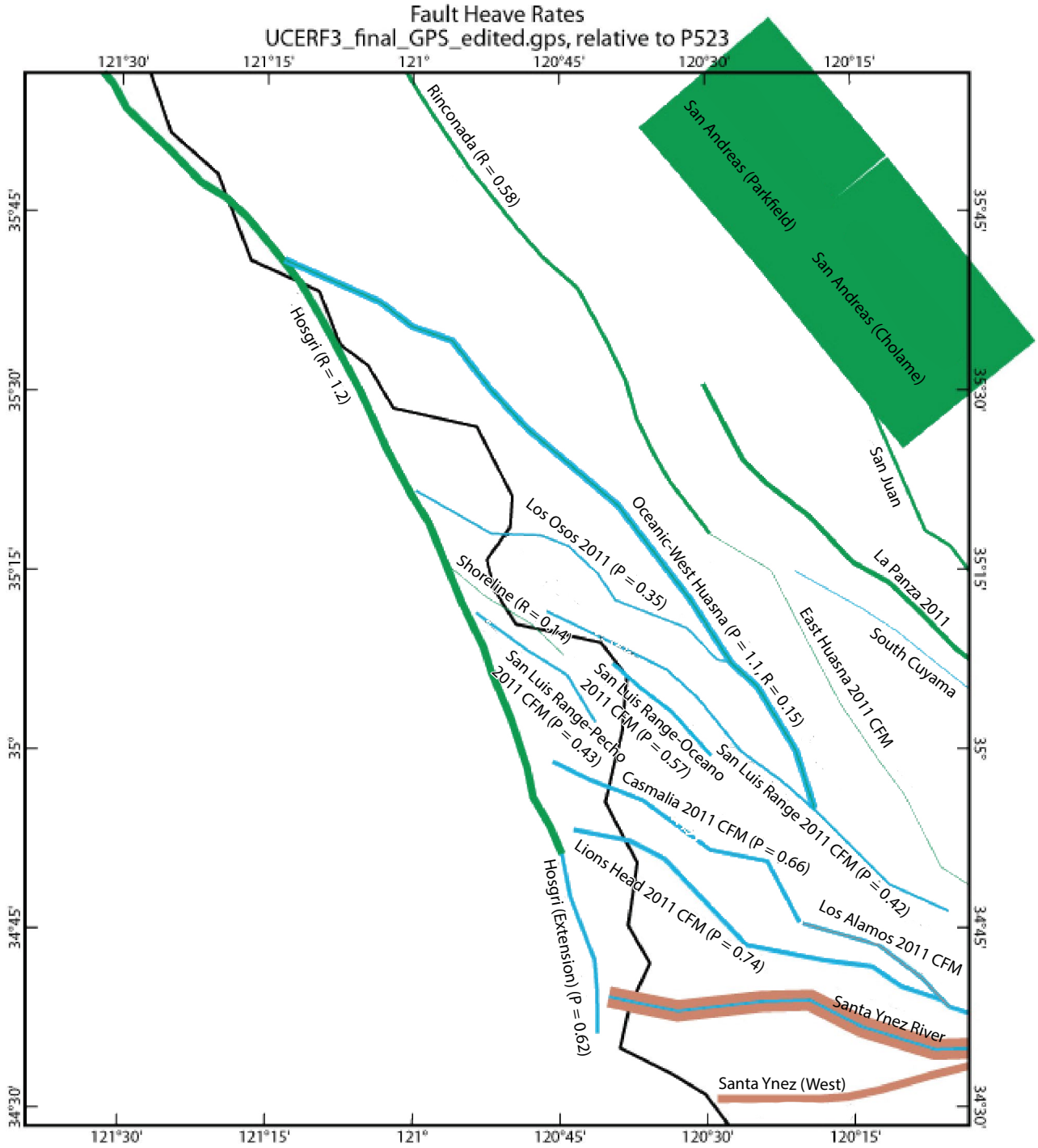

EXPLANATION

- Low-angle thrust plate
- High-angle thrust
- Dextral
- Sinistral
- High-angle normal
- Low-angle normal
- 5 Change in horizontal velocity across fault (mm/a)

Note: Fault widths are scaled by slip (heave) rate.
Sense of slip is coded by color.

Source: Modified from Bird (2012).

Heave Rate Components*
R = right-lateral
L = left-lateral
P = compressional (perpendicular to strike)
* All rates in mm/a.

GPS Strain Rates from the NeoKinema Model in South-Central Coastal California

DCPP SSC REPORT

Pacific Gas and Electric Company

Figure **5-15**

File path: S:\1005\005\Final_Report_Figures\Figure_5-15.ai; Date: 02/13/2015; User: Alex Remar, LCI; Rev.1

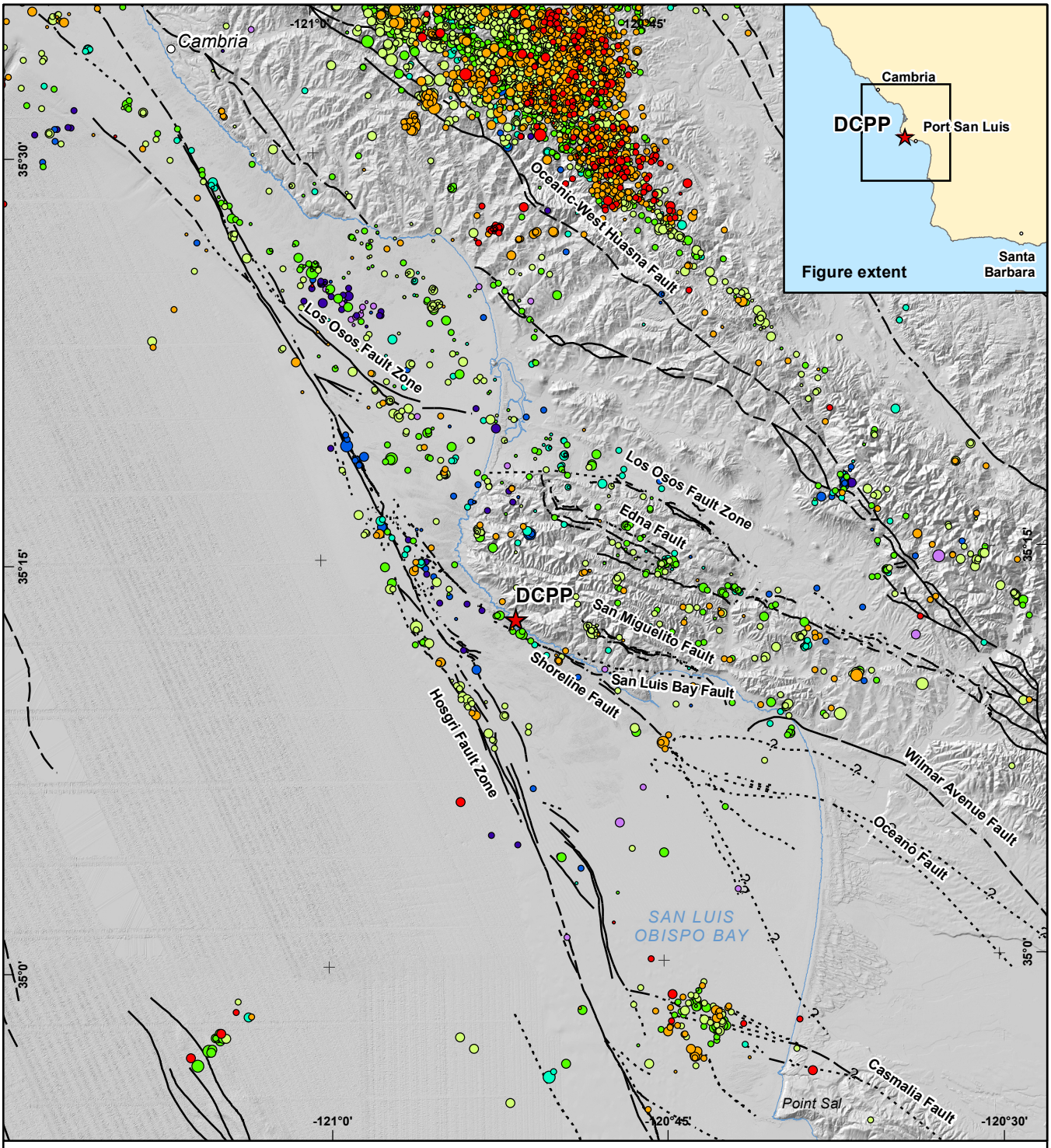

EXPLANATION

Fault, solid where well located, dashed where approximately located, dotted where inferred, queried where existence uncertain

Earthquake Data

Depth (km)

- 0.0–1.9
- 2.0–3.9
- 4.0–5.9
- 6.0–7.9
- 8.0–9.9
- 10.0–11.9
- 12.0–13.9
- 14.0 +

Magnitude

- 0.0–0.9
- 1.0–1.9
- 2.0–2.9
- 3.0–4.1

Note: Quaternary fault traces compiled from Lettis and Hall (1994), Lettis et al. (2004), AMEC (2011), PG&E (2013a; 2014, Chapter 3; 2014, Chapter 9).

Sources:
- Relocated earthquake data from Hardebeck (2014a).
- Project DEM compilation v2013.07.

N

0 4 8 mi.

0 10 20 km

Map projection and scale: WGS 84 / UTM Zone 10N, 1:400,000

Regional Distribution of Seismicity from 1987 to 2013 and Faults in the Site Area

DCPP SSC REPORT

Pacific Gas and Electric Company

Figure **5-16**

File path: S:\1005\005\Final_Report_Figures\Figure_500-16.mxd; Date: 03/10/2015; User: Alex Remar, LCI; Rev.1

(a) Seismicity Map

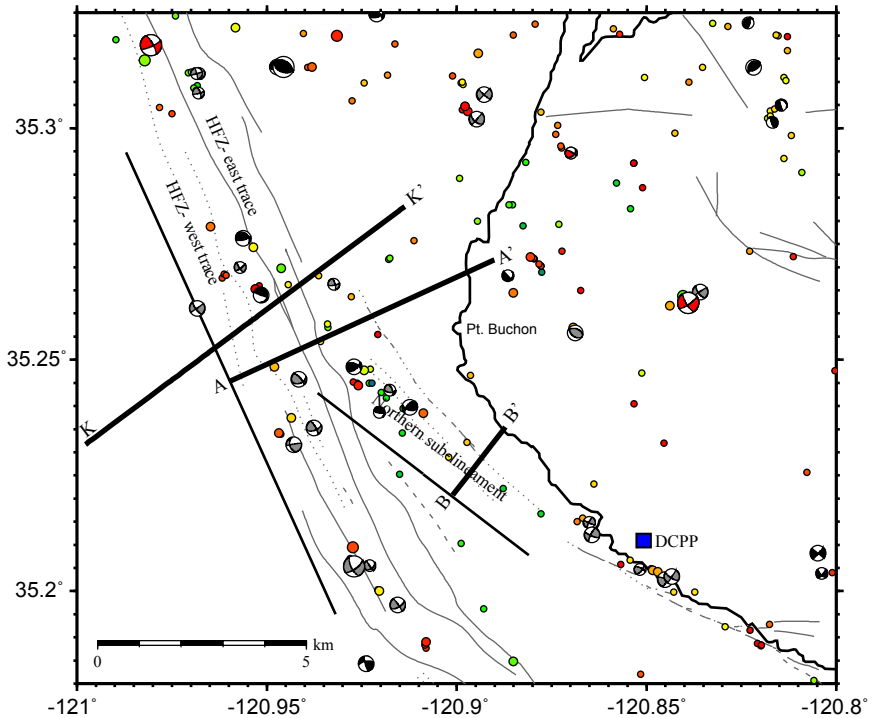

(b) Cross Sections

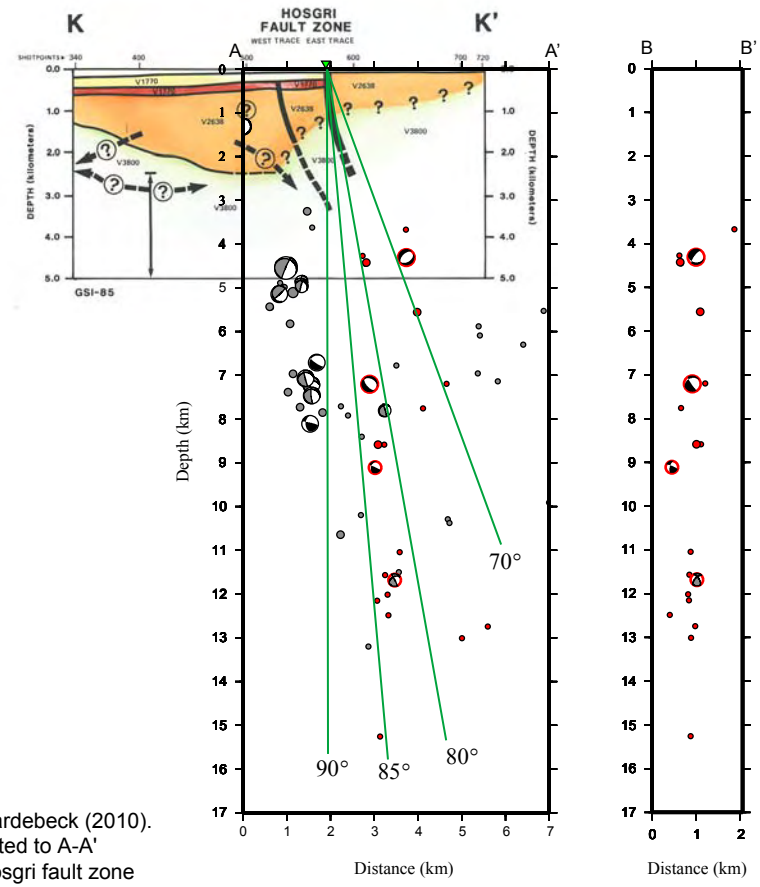

EXPLANATION

Earthquake Magnitudes

- < 2.0
- 2.0–2.99
- 3.0–3.99

depth (km)

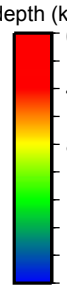

Focal Mechanisms

- <2.0
- 2.0–2.9
- 3.0–3.9
- Hash Quality A,B,C
- Hash Quality D
- FPFIT

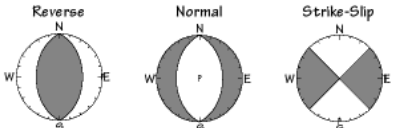

Notes:
- Earthquake relocations in Panels (a) and (b) from Hardebeck (2010). Seismic depth section K-K' (PG&E, 1990a), is projected to A-A' section sub-parallel to Hosgri fault zone. Possible Hosgri fault zone dip angles are shown on Panel (b). Focal mechanisms are from 1-D (FPFIT) and 3-D (HASH) locations. Focal Mechanism symbols are associated with adjacent earthquake locations.
- In Panel (b), northern sub-lineament earthquakes (red dots and red circled focal mechanisms) are shown on both cross sections .

Sources:
- Modified from PG&E (2011).
- Hash Quality A,B,C from Hardebeck (2010) (HASH; Hardebeck and Shearer, 2002).
- Hash Quality D from Hardebeck (2010) (HASH; Hardebeck and Shearer, 2002).
- FPFIT from NCEDC (2010) (FPFIT; Reasenberg and Oppenheimer, 1985).

Seismicity Map and Cross Section A-A' Across the East and West Traces of the HFZ with Interpreted Seismic Depth Section K-K' and Cross Section B-B' Across the Shoreline Fault

DCPP SSC REPORT

Pacific Gas and Electric Company | Figure **5-17**

File path: S:\1005\005\Final_Report_Figures\Figure_5-17.ai; Date: 03/06/2015; User: Alex Remar, LCI; Rev.1

(a) Hardebeck (2010) TomoDD Seismicity Relocations, Map View

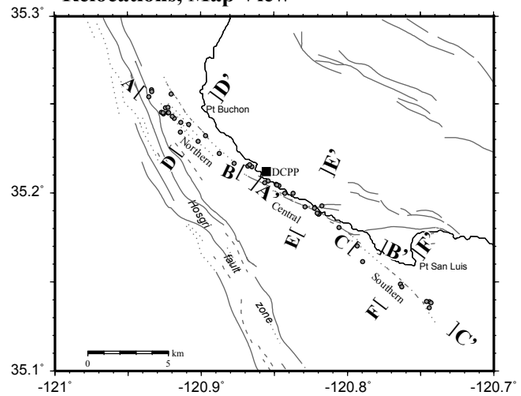

(b) Thurber (2009) TomoDD Seismicity Relocations, Map View

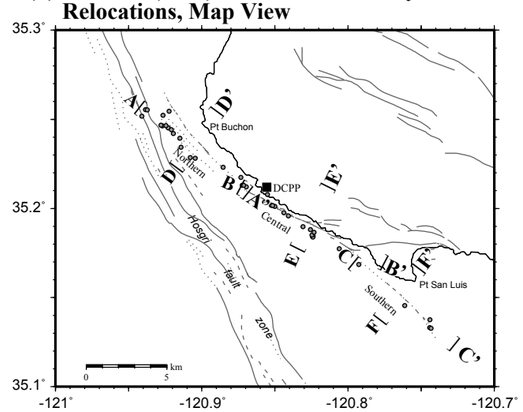

(c) Waldhauser (2009) HypoDD Seismicity Relocations, Map View

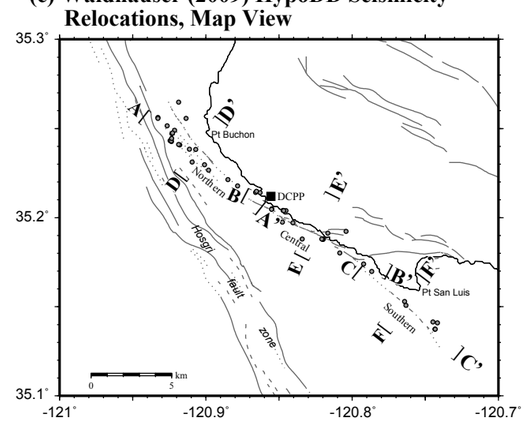

(d) Hardebeck (2010) TomoDD Seismicity Relocations, Cross Section View

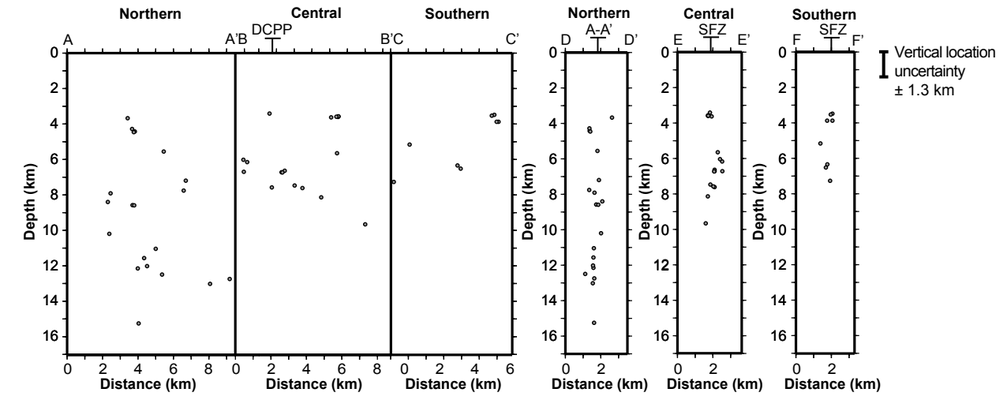

(e) Thurber (2009) TomoDD Seismicity Relocations, Cross Section View

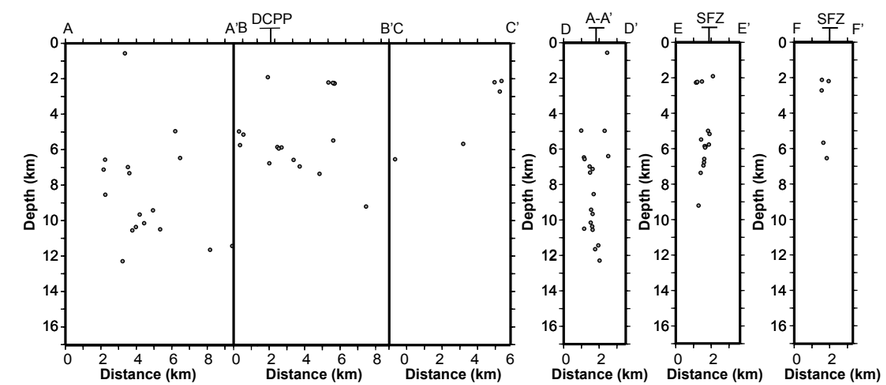

(f) Waldhauser (2009) HypoDD Seismicity Relocations, Cross Section View

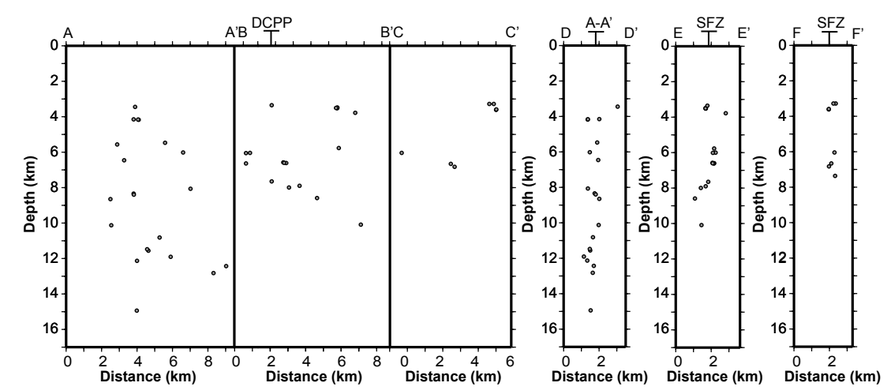

Note: Alternative seismicity relocations from Hardebeck (2010) (Panel a), Thurber (2009) (Panel b) and Waldhauser (2009) (Panel c) are shown for the Shoreline fault. The data are also shown in cross section for each author on Panels (d), (e), and (f), respectively.

Source: Modified from PG&E (2011). Citations for Thurber (2009) and Waldhauser (2009) are provided in PG&E (2011).

Comparison of Shoreline Seismicity Relocations in Map and Cross Section Views

DCPP SSC REPORT

Pacific Gas and Electric Company | Figure **5-18**

File path: S:\1005\005\Final_Report_Figures\Figure_5-18.ai; Date: 03/10/2015; User: Alex Remar; LCI; Rev.1

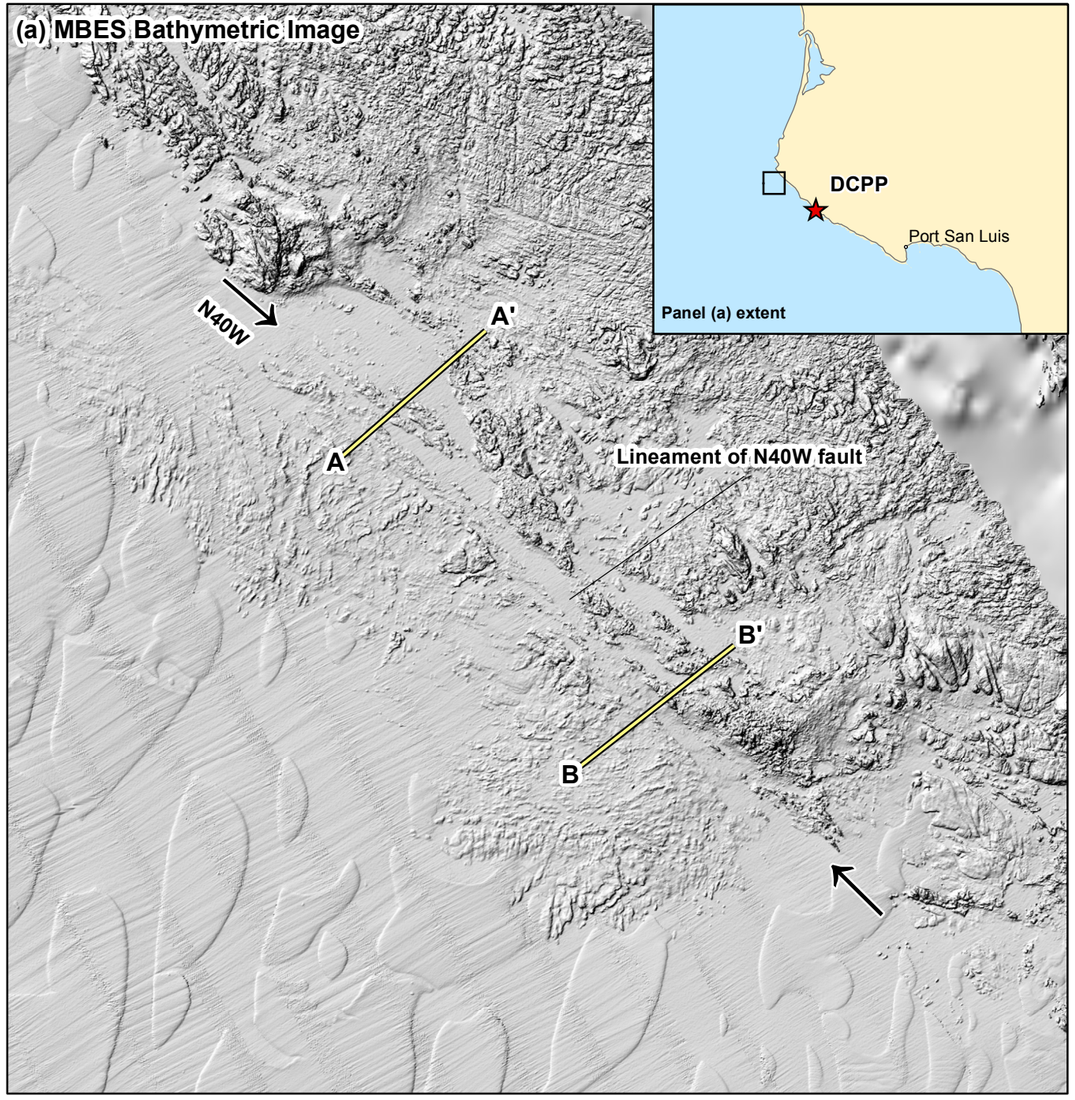

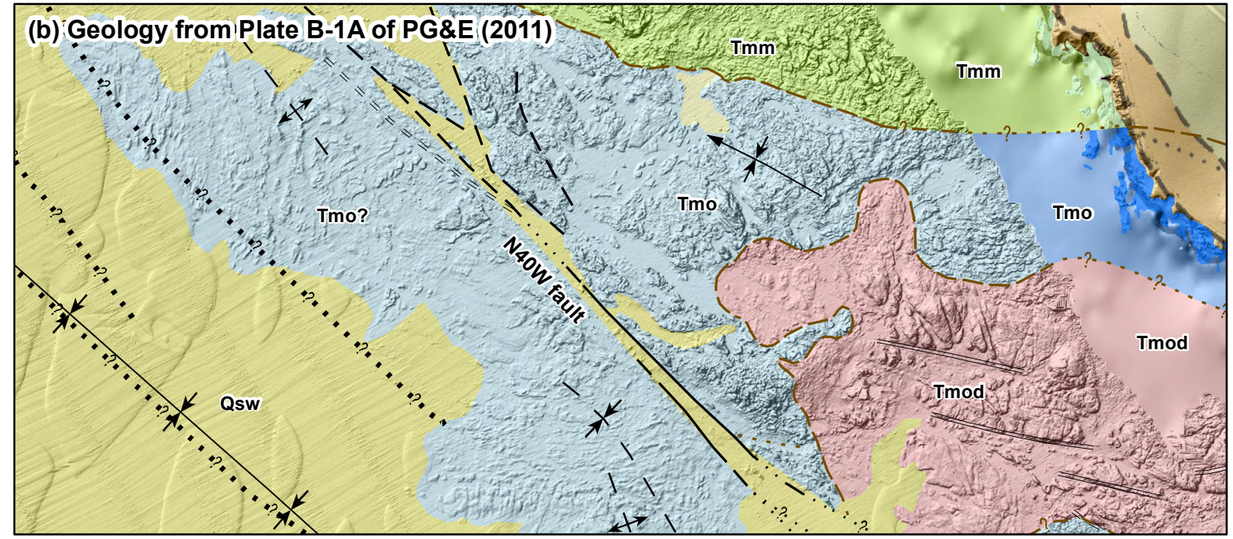

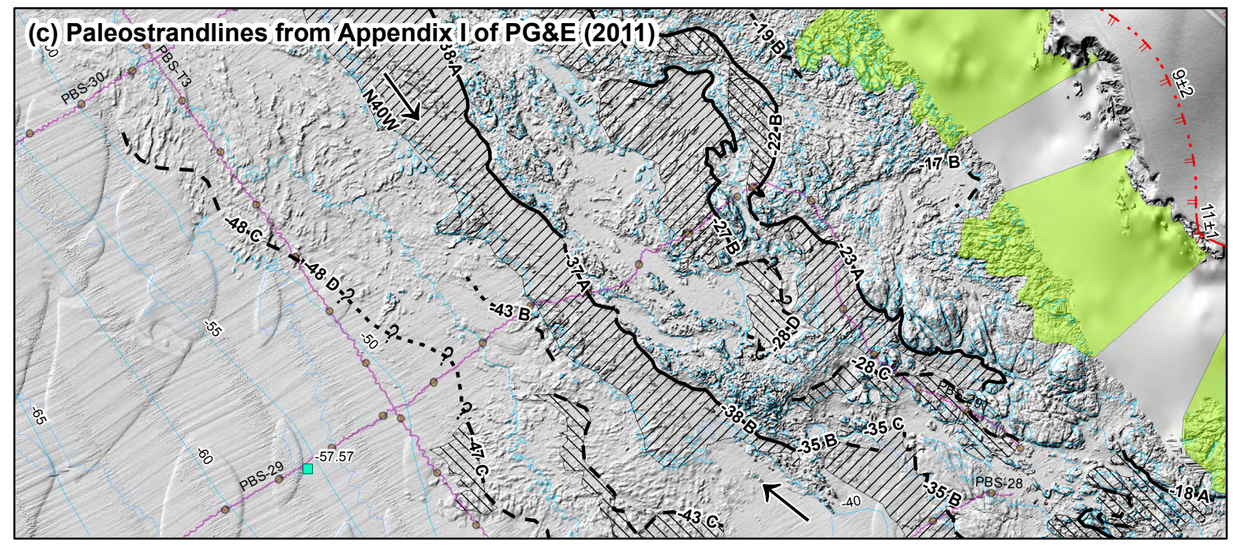

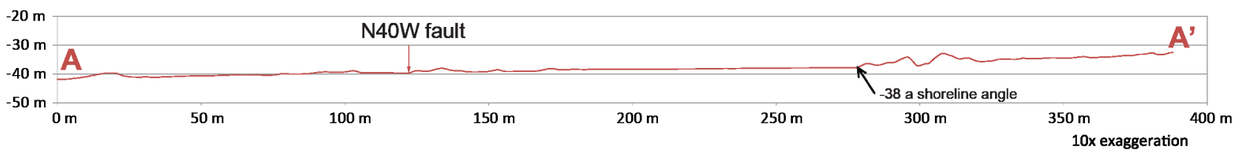

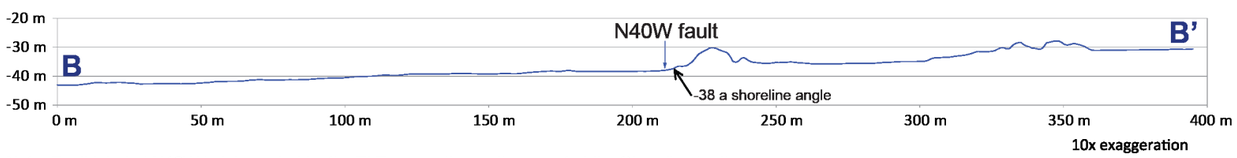

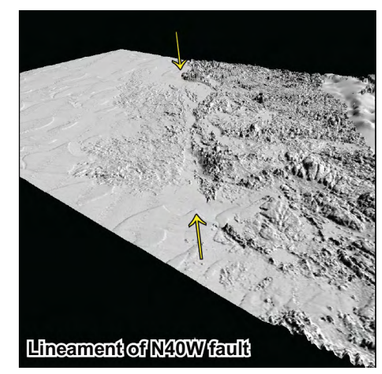

N
0 500 1,000 ft.
0 200 400 m

Map projection and scale: NAD 83 / UTM Zone 10 North, 1:12,000

Note: Fault labeled N40W is interpreted by the TI Team as the northern part of the Shoreline fault zone.

Source: Figure 4-9 of PG&E (2011).

Example Interpretation of Submerged Wave-Cut Platforms from Bathymetric Data

DCPP SSC REPORT

Pacific Gas and Electric Company

Figure **5-19**

File path: S:\1005\005\Final_Report_Figures\Figure_500-19.mxd; Date: 03/06/2015; User: Alex Remar, LCI; Rev.1

(a) Central Coast Region Seismicity

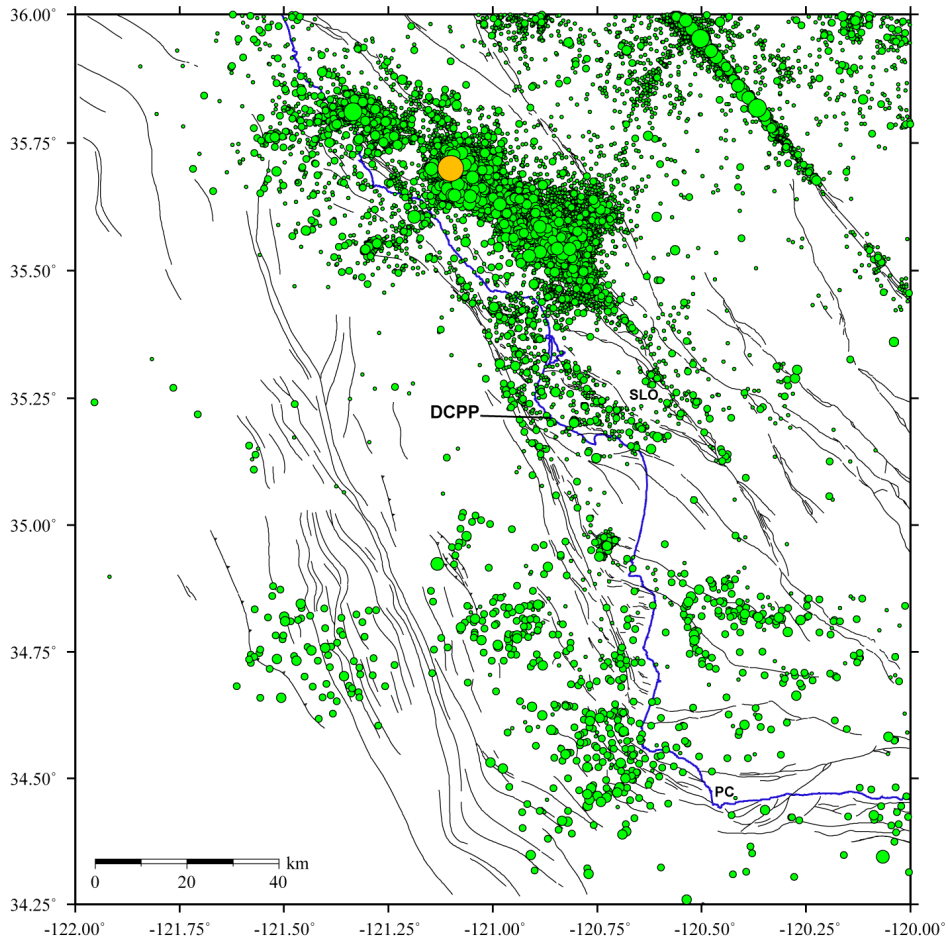

(b) Histogram of Seismicity Through Time

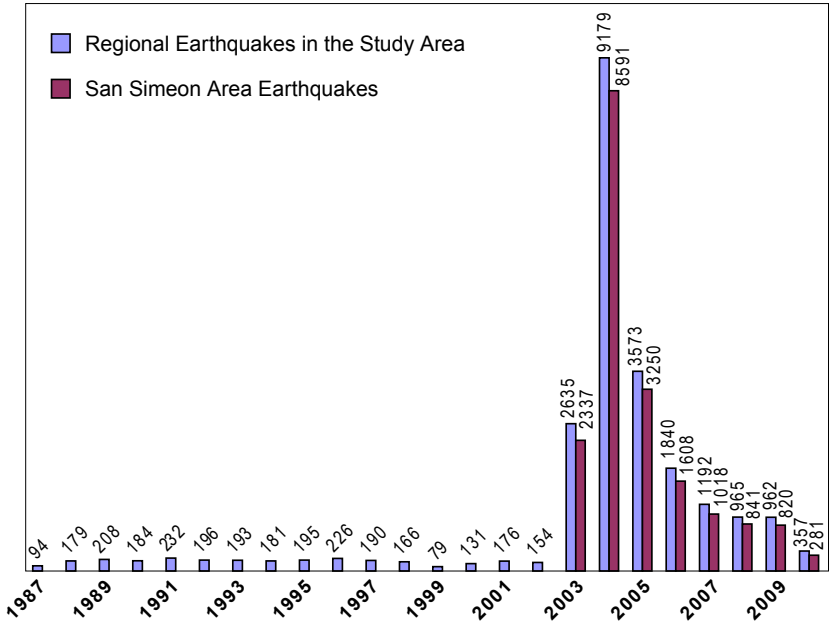

EXPLANATION

Earthquake Magnitudes (NCEDC, 2010)

- < 2.0
- 2.0–2.99
- 3.0–3.99
- 4.0–4.99
- 5.0–5.99
- M6.5 San Simeon Earthquake

Abbreviations in Panel (a)

SLO = San Luis Obispo
PC = Point Conception

Notes:
- Panel (a) shows approximately 23,500 earthquakes in the Central Coast region.
- The histogram in Panel (b) indicates that the majority of earthquakes shown in Panel (a) are aftershocks of the 2003 San Simeon earthquake.
- NCEDC = Northern California Earthquake Data Center.

Source: Modified from PG&E (2011).

Seismicity Recorded by PG&E and the USGS, 1987 though August, 2010

DCPP SSC REPORT

Pacific Gas and Electric Company | Figure **5-20**

File path: S:\1005\005\Final_Report_Figures\Figure_5-20.ai; Date: 03/06/2015; User: Alex Remar, LCI; Rev.1

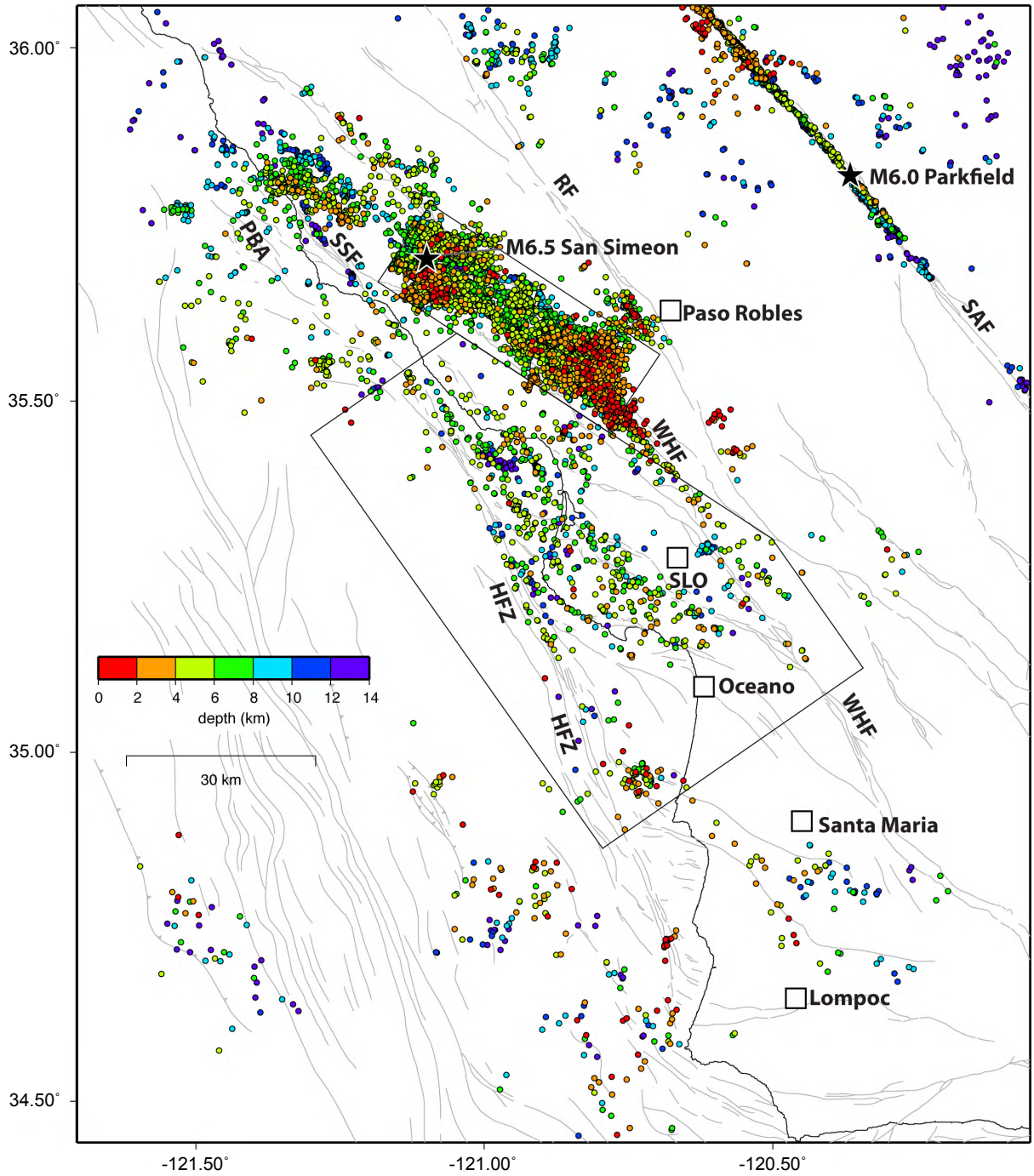

EXPLANATION

Abbreviations

RF	Rinconada fault	PBA	Piedras Blancas anticlinorium
SAF	San Andreas fault	HFZ	Hosgri fault zone
WHF	West Huasna fault	SLO	San Luis Obispo
SSF	San Simeon fault		

Sources:
- Hardebeck (2010).
- PG&E (2011).

Regional Distribution of Seismicity, 1987 through 2008

DCPP SSC REPORT

Pacific Gas and Electric Company

Figure **5-21**

File path: /s/1005/005/Final_Report_Figures/Figure_500-21.ai; Date: 03/06/2015; User: Alex Remar, LCI; Rev. 1

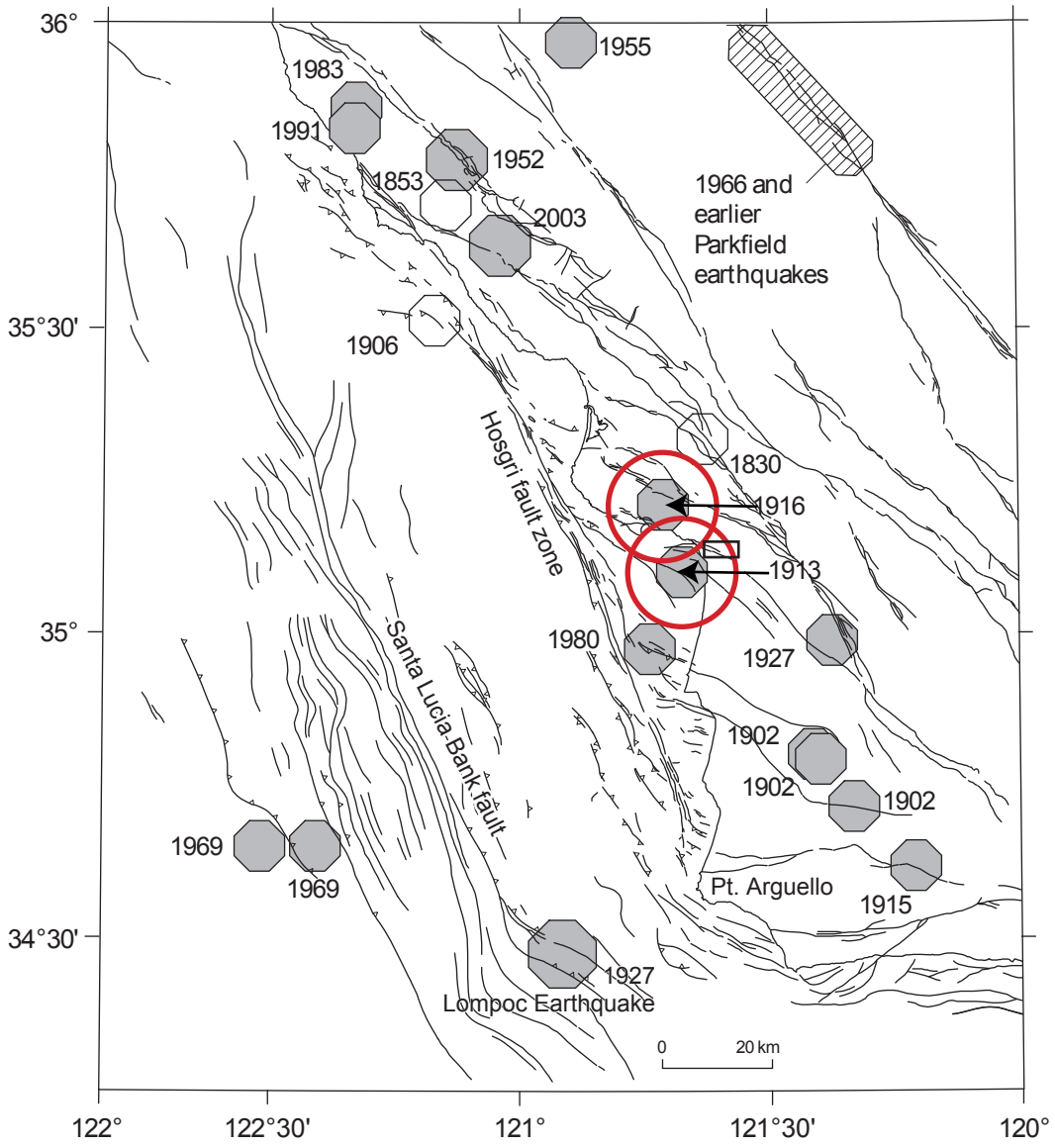

EXPLANATION

Event location that is poorly constrained

Event location that is within 20 km and generally within 10 km

10–km radius of uncertainty

Pismo Beach/Arroyo Grande area northeast of the 1913 earthquake

Magnitudes

5.0 - 5.9

6.0 - 6.9

7.0 - 7.9

Source: Modified from McLaren and Savage (2001); PG&E (2011).

Historical Earthquakes M ≥ 5 Prior to 1987

DCPP SSC REPORT

Pacific Gas and Electric Company

Figure **5-22**

File path: /s/1005/005/Final_Report_Figures/Figure_500-22.ai; Date: 03/06/2015; User: Alex Remar, LCI; Rev. 1

(a) Estero Bay: Relocations and Composite Mechanisms

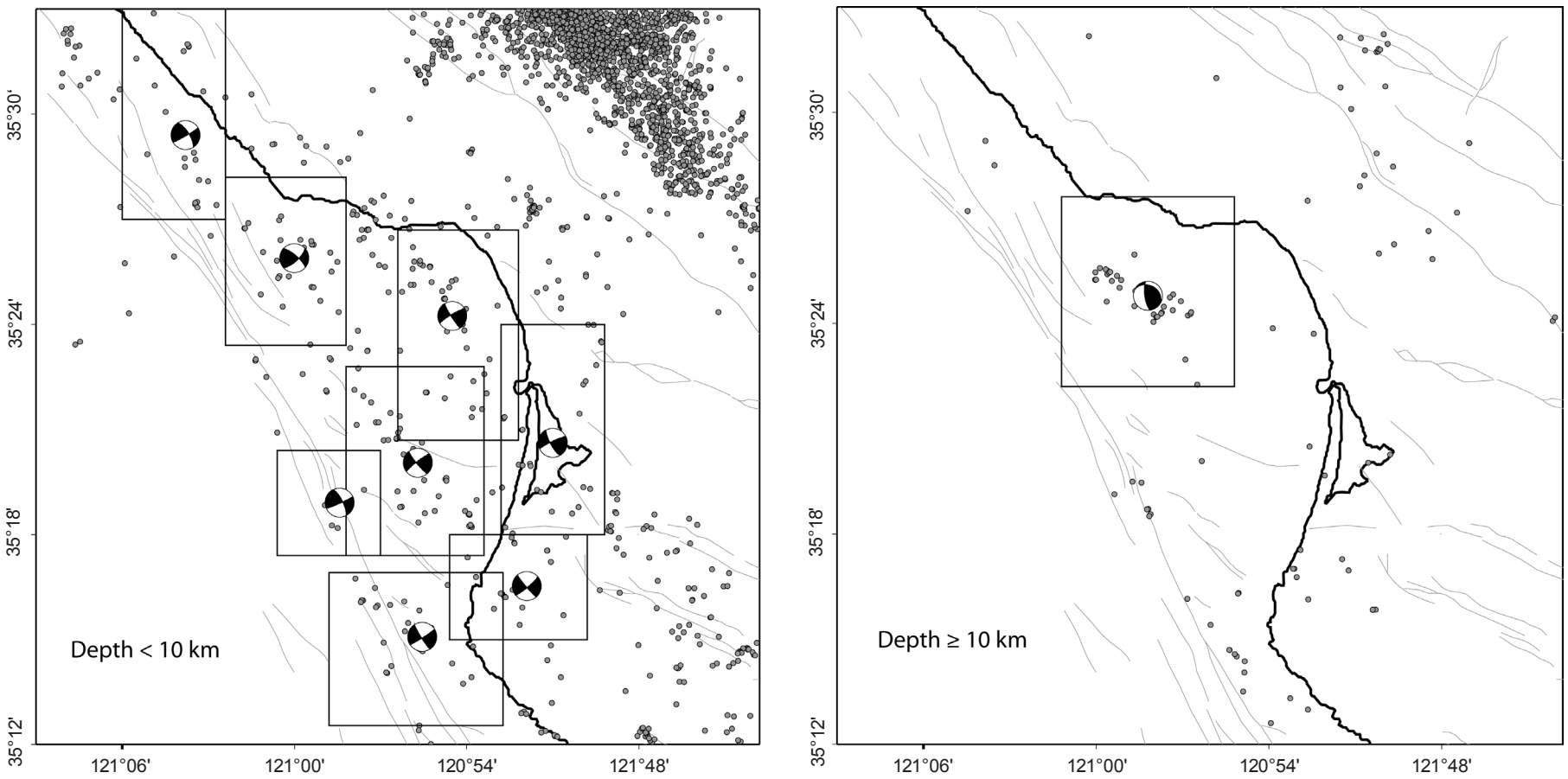

(b) Irish Hills: Relocations and Composite Mechanisms

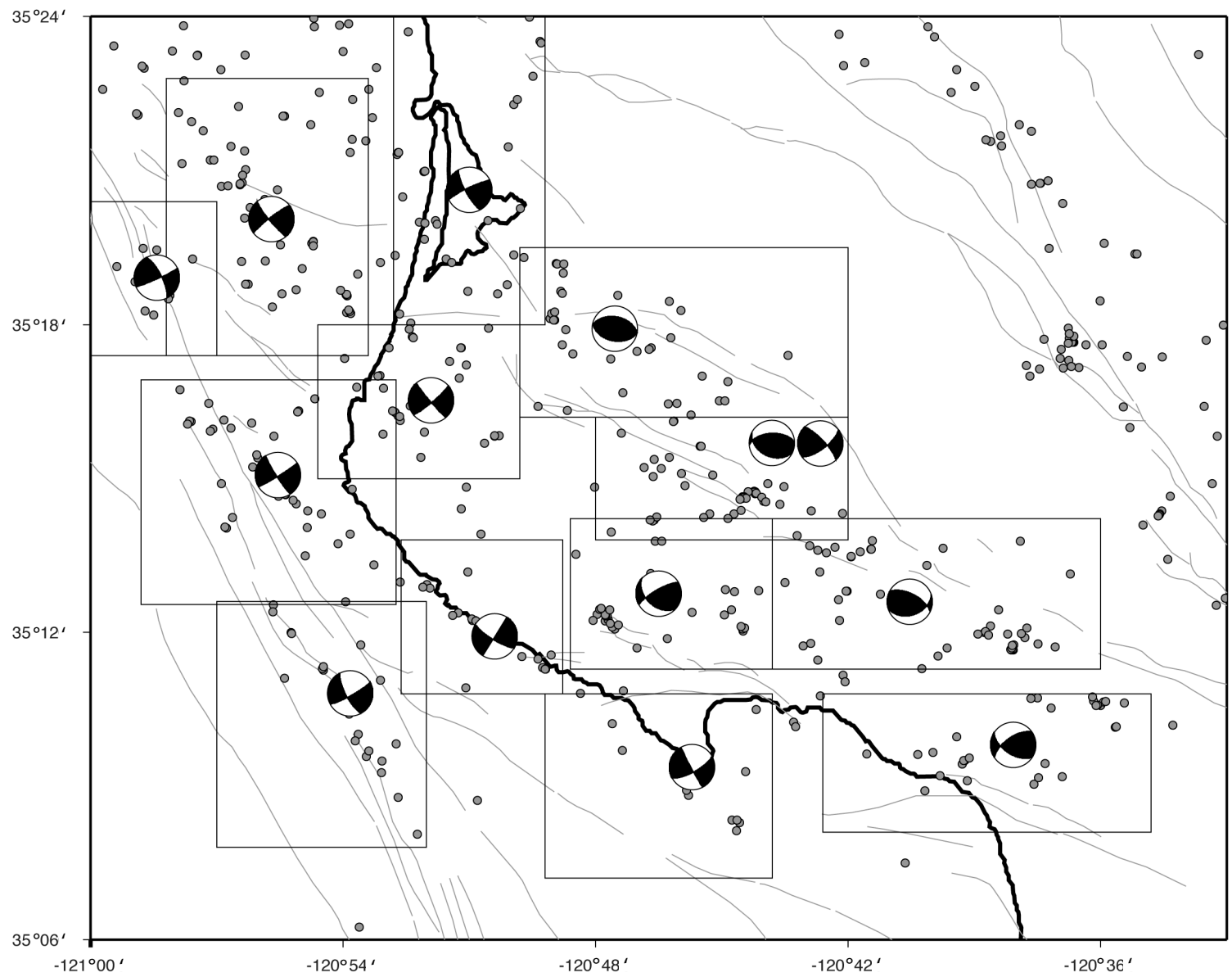

Source: Modified from Hardebeck (2012c).

Seismicity and Focal Mechanism Data from Estero Bay Area and Irish Hills

DCPP SSC REPORT

Pacific Gas and Electric Company

Figure **5-23**

File path: S:\1005\005\Final_Report\Figure_500-23.ai; Date: 03/10/2015; User: Alex Remar, LCI; Rev:1

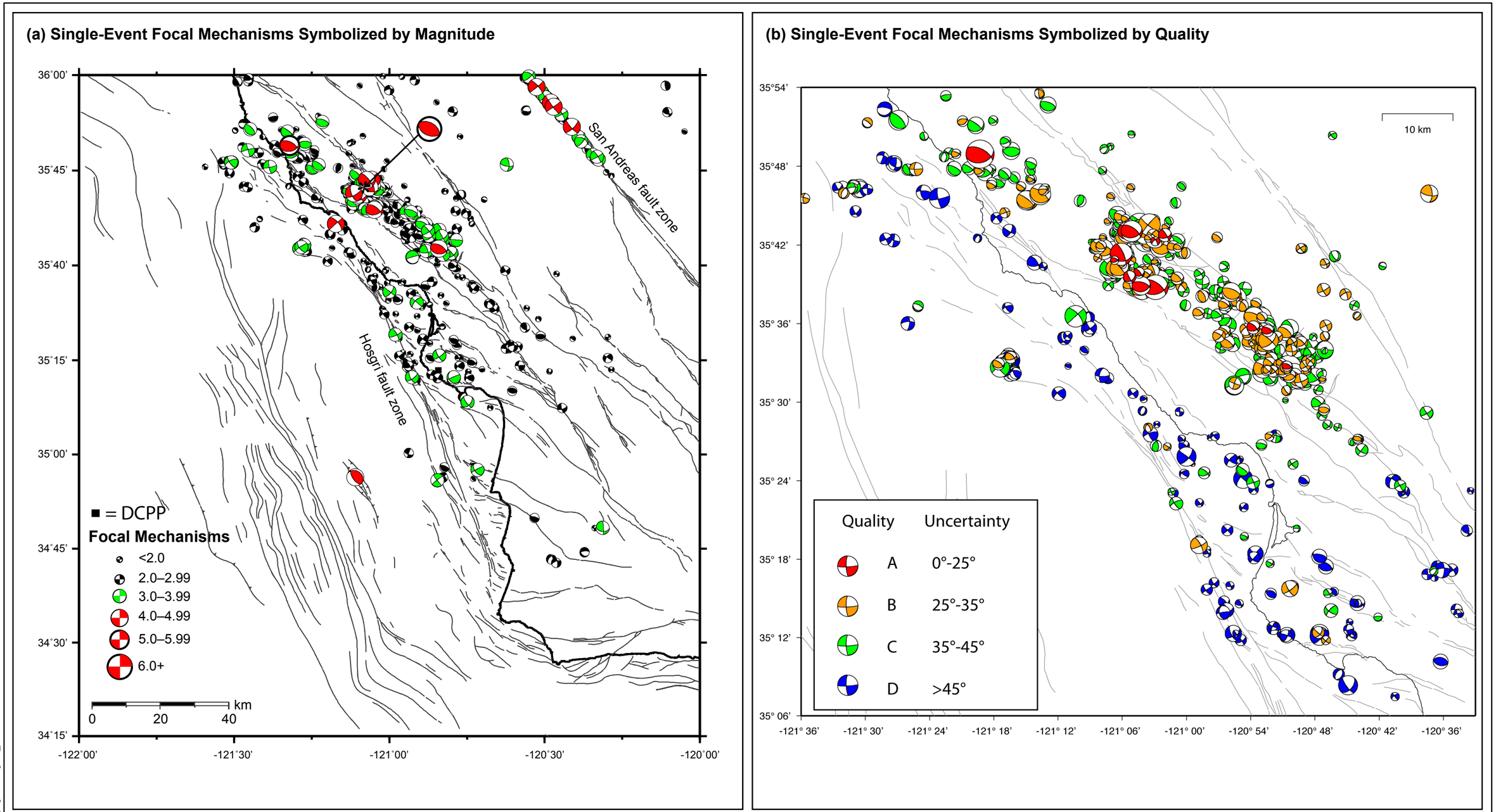

Note: Panels (a) and (b) show single-event focal mechanisms calculated by Hardebeck (2010) for events between 1987 and 2008. The focal mechanisms are symbolized by magnitude and quality on Panels (a) and (b), respectively.

Sources:
- Hardebeck (2010).
- PG&E (2011).

Earthquake Focal Mechanism Data

DCPP SSC REPORT

Pacific Gas and Electric Company

Figure **5-24**

File path: /s/1005/005/Final_Report_Figures/Figure_500-24.ai; Date:03/06/2015; User: Alex Remar; LCI; Rev. 1

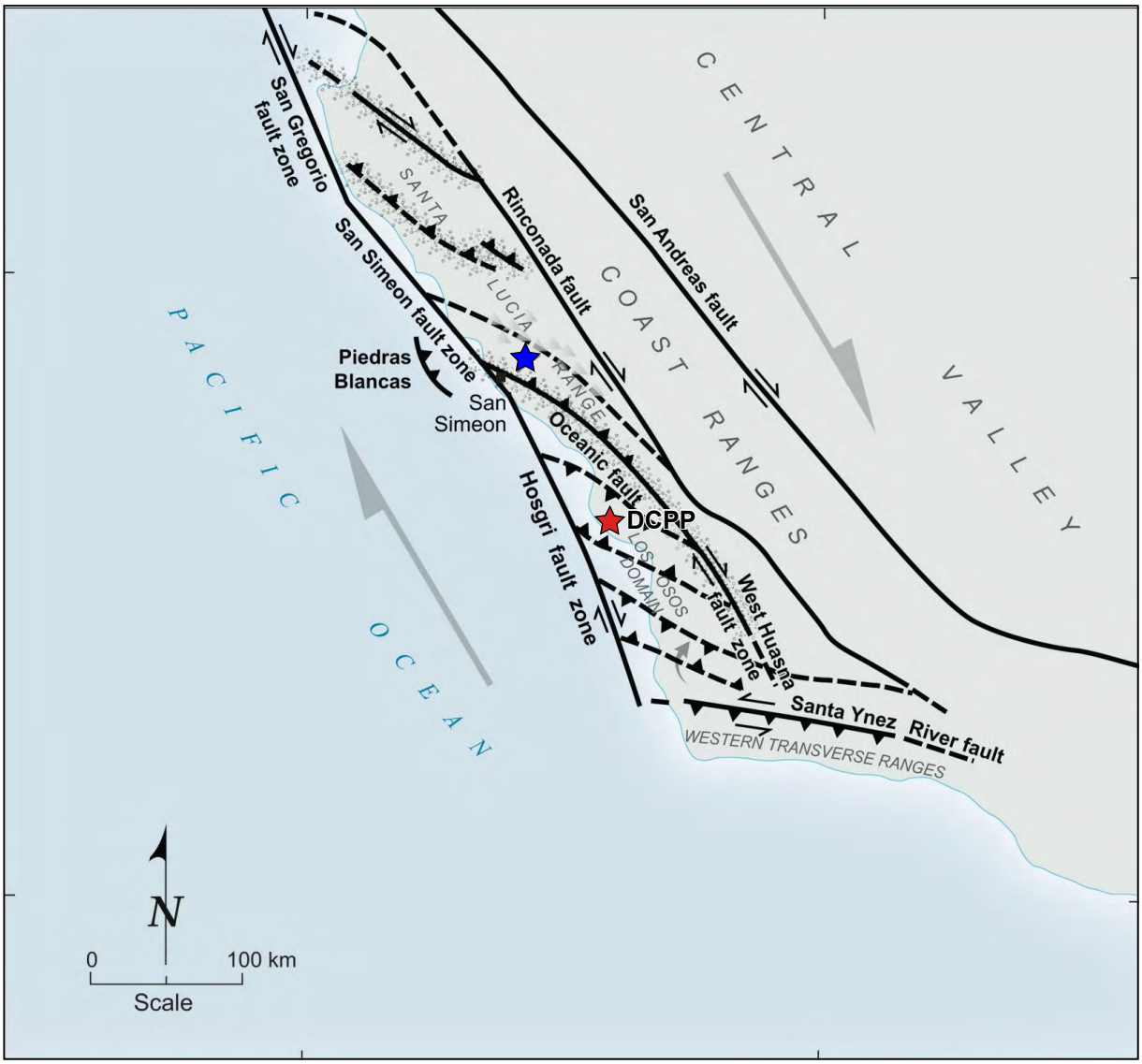

EXPLANATION

- DCPP
- Location of 2003 San Simeon earthquake

Source: Modified from Lettis (2012).

Transpressional Shear Tectonic Model

DCPP SSC REPORT

Pacific Gas and Electric Company

Figure **5-25**

File path: /s/1005/005/Final_Report_Figures/Figure_500-25.ai; Date: 02/13/2015; User: Alex Remar, LCI; Rev. 1

6.0 SEISMIC SOURCE CHARACTERIZATION OVERVIEW

This chapter presents an overview and discussion of the conceptual bases of the seismic source characterization (SSC) model for the Diablo Canyon PSHA. The SSC model consists of sources of earthquakes within the 320 km (200 mi.) DCPP site region.

6.1 Definition and Applicability

The purpose of this overview is to describe the overall logic tree framework for the Diablo Canyon SSC model, the key aspects of the model components, and the technical basis for the modeling approaches that were used to develop the model. The logic tree values and weights for the various parameters are presented in later sections, along with their technical bases. A concise collection of the SSC model inputs is provided in the Hazard Input Document (HID; see *Appendix C*).

For clarification, we define several terms that are used in modeling fault sources as follows:

- *Fault Source*—A piecewise planar source of earthquakes that is a model representation of a geologic fault zone that is seismogenic. Fault zones that are sufficiently active and well defined are included in the SSC model as fault sources. Less active and less well-defined geologic fault zones are included in the SSC model as areal source zones.
- *Primary Fault Source*—A fault source that has been shown to contribute significantly (i.e., approximately defined as contributing greater than a few percent at relevant spectral frequencies and hazard levels) to the seismic hazard at the DCPP. There are four Primary fault sources, all within 12 km of the DCPP at closest source-site distance.
- *Connected Fault Source*—A fault source that connects to a Primary fault source (either directly or via another Connected fault source) in the SSC model.
- *Fault Section*—A portion of a Primary or Connected fault source that is used to define rupture sources. Fault sections are named with two-letter codes.
- *Rupture Source*—A series of adjacent fault sections that are considered capable of hosting a maximum earthquake (i.e., rupture over the entire area of the combined fault sections) and smaller, floating earthquakes (i.e., not confined to a specific section or sections of the rupture source).
- *Regional Fault Sources*—Fault sources within the DCPP site region other than the Primary and Connected fault sources.

6.2 Types of Seismic Sources

The Diablo Canyon SSC model has two types of seismic sources, fault sources and areal sources. Fault sources are piecewise planar sources of earthquakes that are model representations of well-defined geologic fault zones that are seismogenic. In the Diablo Canyon PSHA, a seismogenic fault is defined by the following characteristics:

- Involved in the contemporary tectonic environment.
- Capable of generating moderate-to-large (**M** ≥ 5) earthquakes.
- Worthy of being represented as a fault source that localizes seismicity above the background source zone (represented by the areal source zones; *Section 6.5* and *Chapter 13*).

Geologic and seismologic criteria were used by the TI Team to identify seismogenic faults. Faults that extend to seismogenic depth and displace geomorphic surfaces and deposits that are Quaternary (< 2.6 Ma) in age or that are *causally* associated with **M** ≥ 5 historical earthquakes are judged to be seismogenic. Less diagnostic criteria include an apparent spatial association with a **M** ≥ 5 earthquake or an alignment of seismicity. However, without clear or unequivocal evidence for Quaternary displacement on a fault that extends to seismogenic depth, seismological observations such as these suggest, but do not prove, the presence of a seismogenic fault. Secondary structures, such as back thrusts or splay faults, may have surface expression of Quaternary deformation but are not independent seismogenic faults. These faults may be modeled as secondary faults that rupture with the primary seismogenic fault source. In the Diablo Canyon SSC model, alternative fault geometry models are developed to account for uncertainties in the location and extent of seismogenic faults in the vicinity of the DCPP. Faults that are not identified as being seismogenic (or modeled as secondary structures associated with rupture sources as discussed below in *Section 6.3.3.3*) are represented by virtual faults within the Local areal source zone (*Section 6.5*).

Fault sources are characterized by their location, geometry, depth extent, slip sense, slip rate, magnitude-frequency distribution shape, and probability of occurrence of an earthquake in a given time period. There are four types of fault sources in the Diablo Canyon SSC model, and each type is described in the chapter section noted:

- Primary and Connected fault sources (*Section 6.3*)
- San Andreas fault source (*Section 6.4*)
- UCERF3 regional fault sources (*Section 6.4*)
- Non-UCERF3 regional fault sources (*Section 6.4*)

Areal sources are sources of earthquakes from volumes of crust occurring on non-specified fault planes. Areal sources are characterized with a defined location, crustal thickness, rate of earthquakes, maximum earthquake magnitude (M_{max}), and magnitude-frequency distribution shape. There are three areal source zones in the Diablo Canyon SSC model, named the Regional, Vicinity, and Local areal source zones, with increasing proximity to the DCPP (*Section 6.5* and *Chapter 13*).

Two methods for modeling earthquakes within source zones are used in this study; these are briefly described in *Section 6.5*. For the local source zone in which the DCPP lies, future earthquakes are modeled as occurring on “virtual faults” for which assessments are provided of future earthquake characteristics, such as location, dip, and slip sense (*Section 13.5*). For the regional and vicinity source zones, the earthquakes are modeled as point sources (*Section 13.3* and *Section 13.4*, respectively).

6.3 Primary and Connected Fault Sources

Primary fault sources are four fault sources that contribute most to seismic hazard at the DCPP based on past PSHA analyses (PG&E, 1988, 2011) and as shown by preliminary sensitivity analyses conducted for this study (Wooddell, 2011, presentation at Workshop 1). Primary fault sources include the Hosgri, Shoreline, Los Osos, and San Luis Bay faults. The geologic data that form the basis of their inclusion as fault sources are described in *Section 5.2*.

Connected fault sources are representations of those fault zones that directly connect to the Primary fault sources in the SSC model. In this technical report, we capitalize "Primary" and "Connected" when we are using these terms to refer to fault sources.

Historical earthquakes have shown that fault ruptures may span multiple connected faults and various fault branching relationships. Thus, future ruptures on Primary fault sources may be more complex, involving all or part of adjacent or connected faults, than was considered in previous PSHAs for the DCPP (e.g., PG&E, 1988, 2011). In contrast to earlier PSHAs, the Primary and Connected fault sources in this SSC model are allowed to rupture independently or in various combinations (*Section 6.3.3*). Historical earthquake ruptures in transpressional and transtensional tectonic regimes provide analogs that were used to inform possible rupture source geometries for the Primary and Connected fault sources in the Diablo Canyon SSC model. Selected historical ruptures that the TI Team considered in developing both fault geometry models and rupture sources for these fault sources are listed in Table 6-1 (and discussed below in *Section 6.3.1* and *Section 6.3.3*, respectively). Additional discussion of the relevance of these earthquakes as analogs is provided in *Chapters 7 and 9*.

Table 6-1. Historical Earthquake Ruptures That Are Considered Analogs for Characterizing Rupture Sources in the Diablo Canyon SSC Model

Historical Earthquake	Relevance	Cross-Reference to Additional Discussion

Historical Earthquake	Relevance	Cross-Reference to Additional Discussion
1896 **M** 7.2 Rikuu earthquake, Japan	The 1896 **M** 7.2 Rikuu earthquake, which occurred in the Tohoku district of northern Honshu, Japan, was associated with ~40 km of surface ruptures involving five named reverse faults (Matsuda et al., 1980) Four main surface ruptures, ~36 km long, on the western foot of the Majiru Mountains constitute the main fault zone of the 1896 earthquake. The maximum vertical displacement was ~3.6 m, up on the east. Approximately 6 km of another surface fault, the Kawafune, on the eastern side of the Majiru Mountains also ruptured during the event with the sense of displacement opposite to the main fault, (i.e., the western side was upthrown). Horizontal shortening during the event was ~1–3 m. No strike-slip was observed. The Kawafune fault is considered a subsidiary conjugate fault to the main fault zone.	*Section 9.2*: Example of splay rupture source
1940 **M** 6.9 and 1979 **M** 6.4 Imperial Valley, California	The 1979 **M** 6.4 central Imperial Valley earthquake generated displacements at the ground surface along the Imperial fault, the Brawley fault zone, parts of the Mesquite Basin between these two faults, and a minor structure referred to as the Rico fault (Sharp et al., 1982). The 36 km length of surface rupture on the Imperial fault included approximately the north half of the 1940 trace of surface rupture (60 km length; Sharp et al., 1982; Wesnousky, 2006, 2008). The relative amounts and slip distributions for the coseismic surface ruptures on these two events (Trifunac and Brune, 1970; Sharp et al., 1982; Wesnousky, 2006, 2008; Rockwell and Klinger, 2013) provide insights into the physical parameters that control slip over multiple earthquake cycles.	*Section 9.2*: Example of splay rupture source *Section 10.2*: Example of characteristic and maximum ruptures on a single fault source

Historical Earthquake	Relevance	Cross-Reference to Additional Discussion
1957 **M** 8.1–8.3 Gobi Altay, Mongolia	The Gurvan Bogd Range fault system in Mongolia consists of reverse oblique, strike-slip, and reverse faults that accommodate transpression. This system of faults ruptured in the 1957 **M** 8.1–8.3 Gobi-Altay earthquake (Kurushin et al., 1997). The main rupture of more than 260 km of left-lateral strike-slip occurred along the Bogd fault to the north of the Ih Bogd (3,957 m) and Baga Bogd (3,590 m) massifs (Ritz et al., 2006). An additional 100 km of reverse faulting, distributed on five secondary segments, ruptured simultaneously with the Bogd fault during the 1957 earthquake. These fault segments correspond mainly to thrust faults found at the base of ridges and low hills or 'forebergs" on both margins of the massifs (Florensov and Solonenko, 1965; Kurushin et al. 1997; Bayasgalan et al., 1999). These reverse faults are shortening structures associated with the main Bogd strike-slip fault (Ritz et al., 2006).	*Section 7.4.1*: Possible analog for the Outward-Vergent Fault Geometry Model *Section 9.2.3*: Example of a complex rupture source
1977 M_S 7.3 Caucete, Sierra Pie de Palo, Argentina	Uplift of the Pie de Palo range in Argentina is accommodated by oppositely vergent reverse faults separated by a tear fault (Regnier et al., 1992). The Sierra Pie de Palo was the site of the M_S 7.3 Caucete earthquake in 1977. Regnier et al. (1992) used the morphology of the range, seismicity patterns, and focal mechanisms to define two crustal blocks and an intervening shear zone. Distinct but complex systems of faults were resolved by Regnier et al. (1992) in both the northern and southern blocks. The separation between the two blocks is coincident with a major shear zone crossing the mountain that it is expressed as a deeply eroded canyon. The presence of this shear zone is supported by a concentration of focal mechanism solutions along the shear zone showing the right-lateral strike-slip motion, as well as by regional-scale strike-slip faults identified on satellite images. Kadinsky-Cade and Reilinger (1995) demonstrated that the earthquake was a double event, in that the two shocks occurred 21 s apart and were separated by 65 km along fault strike.	*Section 7.4.3*: Possible analog for the Northeast-Vergent Fault Geometry Model

Historical Earthquake	Relevance	Cross-Reference to Additional Discussion
1992 **M** 7.3 Landers, California	The 1992 **M** 7.3 Landers earthquake was produced by faults within the Eastern California shear zone, an 80 km wide zone of predominantly right-lateral faults. The 1992 earthquake was produced by nearly unilateral northward rupture of five major right-lateral faults and fault segments (Johnson Valley, Landers, Homestead Valley, Emerson, and Camp Rock faults; Sieh et al., 1993; Yeats et al., 1997). Rockwell et al. (2000) showed that the behavior of the fault system during the 1992 Landers earthquake was just one way that these individual faults could be linked within a single rupture, and that successive ruptures do not follow the same path.	*Section 9.2.2*: Example of a splay rupture source
1999 **M** 7.1 Hector Mine, California	The **M** 7.1 Hector Mine earthquake occurred within the Eastern California shear zone (ECSZ) and was accompanied by 48 km of dextral surface rupture. The rupture initiated on an unknown north-trending structure (a splay to a previously mapped but unnamed fault, which is now referred to as the Lavic Lake fault) (Hauksson et al., 2002; Ji et al., 2002). The rupture propagated bi-laterally to the northwest and to the south from the epicentral area. The rupture stepped across the Lavic Lake fault, the Buillion fault, and two minor faults to the south, demonstrating that rupture in the ECSZ can propagate across a series of existing faults that are slightly oblique to the strike of the ECSZ (Treiman et al., 2002). Preliminary data and observations from paleoseismic studies suggest that slip transfer in the penultimate event occurred along different fault elements than in the 1999 event.	*Section 9.2*: Example of a splay rupture source
2002 **M** 7.9 Denali, Alaska	Complex rupture resulting in 341 km of surface rupture on the Susitna Glacier (thrust), Denali (strike-slip) and Totschunda (strike-slip) faults (Crone et al., 2004; Haeussler et al., 2004; Haeussler, 2009). The propagation of the **M** 7.9 rupture from the central Denali fault onto the Totschunda fault has been evaluated to assess dynamic models of fault branching in which the angle of the regional or local pre-stress relative to the orientation of the main fault and branch is thought to play an important role in determining which fault branch is taken.	*Section 9.2*: Example of a complex and linked rupture source

Historical Earthquake	Relevance	Cross-Reference to Additional Discussion
2003 **M** 6.5 San Simeon, California	McLaren et al. (2008) imaged the causative fault (the Oceanic fault) and secondary structures that ruptured during the 2003 **M** 6.5 San Simeon earthquake and related aftershocks, based on analysis of seismological, InSAR, and geologic observations. The primary mainshock structure is a 30 km long NW-striking, NE-dipping thrust fault, which projects to the surface near or to the west of the mapped trace of the Oceanic fault. Two 5–10 km long *en echelon* backthrusts defined by aftershocks and post-seismic uplift seen in InSAR are present on either side of a central area that experienced the highest slip in the mainshock. The well-defined main thrust at the latitude of the epicenter and antithetic backthrust illuminated by the aftershock zone indicate uplift of the Santa Lucia Range as a pop-up block.	*Section 7.4.2*: Possible analog for the Southward-Vergent Fault Geometry Model *Section 9.2*: Possible analog for splay ruptures involving a main thrust and backthrust
2010 **M** 7.2 El Mayor–Cucapah, Mexico	The 2010 **M** 7.2 El Mayor–Cucapah earthquake revealed the existence of a previously unidentified integrated fault system that accommodates oblique strain in Mexico. The fault system, which extends ~120 km from the northern tip of the Gulf of California to the U.S.-Mexico border, is composed of at least seven previously mapped major faults linked by numerous smaller faults. The fault system and rupture is described by Fletcher et al. (2014). Rupture propagated bilaterally and through three distinct kinematic faulting domains having strongly contrasting geomorphologic expression. The rupture involved slip on dextral-normal fault systems having different dip directions as well as cross faults. In the El Mayor–Cucapah surface rupture, slip was activated on faults with several different orientations, and the rake of slip was observed to be directly controlled by the fault strike. Fletcher et al. (2014) hypothesize that different sets of faults within the system may be activated during different earthquakes and that the assembly of fault segments that link together to produce a large-magnitude earthquake may vary in consecutive ruptures.	*Section 9.2*: Example of a complex and splay rupture source

Primary and Connected fault sources in the Diablo Canyon SSC model are listed in Table 6-2 below. The Primary fault sources are divided into two groups: the Hosgri fault sources and other Primary fault sources. The other Primary fault sources are located east of the Hosgri fault zone and are either within or bounding the San Luis–Pismo structural block (SLPB; Lettis et al., 1994). The other Primary fault sources are hereafter referred to

as the SLPB fault sources as shown in Table 6-2. Table 6-2 also shows the group to which the Connected fault sources belong.

Table 6-2. Primary and Connected Fault Sources

Primary Fault Source Name	Group[1]
Hosgri	Hosgri
Los Osos	SLPB
San Luis Bay	SLPB
Shoreline	SLPB
Connected Fault Source Name	**Connected Group[1]**
Foxen Canyon	SLPB
Little Pine	SLPB
Nipomo	SLPB
Oceano	SLPB
Piedras Blancas	Hosgri
San Andreas	Hosgri
San Gregorio	Hosgri
San Miguelito (offshore only)	SLPB
San Simeon	Hosgri
Western Hosgri	Hosgri
Wilmar Avenue–Los Berros	SLPB

[1] Hosgri = Hosgri fault source; SLPB = San Luis–Pismo block fault sources

The SSC for Primary and Connected fault sources is organized into a series of models for each fault parameter that, in combination, describe the Primary fault source characterizations and their logic tree parameterization for hazard calculation. The models are listed in Table 6-3. Most, but not all, of the models are used in the actual hazard calculation. The table indicates whether the models are a part of the hazard calculation; regardless of whether they are part of the hazard calculation, they are steps in the SSC model-building process.

Table 6-3. Models That Comprise the Primary Fault Source Characterization

Model Name	Description	Part of Hazard Calculation?
Fault Geometry	Location, dip, and width of fault sections	Yes
Fault Slip Rate	Slip rate and sense of slip on fault sections	No
Rupture	Combinations of fault sections that may rupture together	Yes
Slip Rate Allocation	Portion of fault slip rate allocated to	Yes

Model Name	Description	Part of Hazard Calculation?
	each rupture source	
Magnitude Distribution	Range and relative rate of earthquake sizes occurring on each rupture source	Yes
Time Dependency	Equivalent Poisson rate of earthquakes on each rupture source	Yes

The SSC logic tree structure for the Primary and Connected fault sources is shown on Figure 6-1. The SSC logic tree is defined as the logic tree that is modeled by the Hazard Analyst for PSHA. Additional logic tree nodes, branches, and weights (e.g., fault slip rate) are part of calculations for information that supports the SSC logic tree. Those additional logic tree branches, or "supporting logic trees," are also presented in this technical report.

The SSC logic tree is constructed such that global assessments applicable to all Primary and Connected fault sources are defined first, followed by more specific assessments applicable to individual rupture sources. The order of the logic tree does not always follow the order of the models shown in Table 6-3. For example, the first nodes of the SSC logic tree describe the Time Dependency Model that accounts for epistemic uncertainty in earthquake recurrence on all Primary and Connected fault sources in the SSC model (Figure 6-1).

The following subsections describe the roles of the models listed in Table 6-3 that make up the SSC model for Primary and Connected faults.

6.3.1 Fault Geometry Models

The Fault Geometry Models (FGMs), which are described in more detail in *Chapter 7*, define the location, dip, depth, and width of fault sections that make up the Primary and Connected fault sources listed in Table 6-2. Uncertainty in fault location, geometry, and depth is accounted for in the SSC model through the combination of FGMs. Three alternative FGMs for the Hosgri fault source and three FGMs for the SLPB fault sources allow the uncertainties in fault location, dip, and connectivity to be correlated among the faults within the SLPB. This attribute acknowledges that in many cases the uncertainty in dip of one fault source is not independent of the dip uncertainty of a nearby fault source, especially if the fault sources likely intersect at depth.

As shown in the matrix in Table 6-4, nine combinations of Hosgri FGMs and SLPB FGMs are possible for the Primary fault sources in the SSC model. Figure 6-1 shows a portion of the logic tree for the combination of the "Hosgri 85 (H85)" FGM and the "Southwest-Vergent (SW)" FGM.

Table 6-4. Fault Geometry Models (FGMs) and Logic Tree Combinations

Hosgri FGMs	SLPB FGMs		
	Outward-Vergent (OV)	Southwest-Vergent (SW)	Northeast-Vergent (NE)
Hosgri 90 (H90)	H90/ OV	H90/ SW	H90/ NE
Hosgri 85 (H85)	H85/ OV	H85/ SW	H85/ NE
Hosgri 75 (H75)	H75/ OV	H75/ SW	H75/ NE

Each Primary and Connected fault source listed in Table 6-2 is divided into sections that are named with unique two-letter codes as shown on Figures 6-2 through 6-6 and as listed in Table 6-5. The fault sections are distinct reaches of each fault source and are simplified traces of the geologic mapped faults. Each fault section is specified to define a unique set of surface coordinates that constitutes the surface location, or updip projection, of a particular reach of a fault source. Not all fault sections are included in every FGM; Figures 6-2, 6-3, and 6-4 show differences between the three SLPB FGMs near the DCPP. Boundaries between fault sections are specified at locations where fault sources intersect in at least one FGM. Fault sections are allowed to rupture together in various combinations, as alternative rupture sources involving sets of fault sections, as described in *Section 9.2*.

Table 6-5. Primary and Connected Fault Section Codes and Descriptions

Code[1]	Fault	Section Description
BE	San Luis Bay	Mallagh Landing to San Luis Hill
BR	San Luis Bay	San Luis Hill to Shoreline fault junction
BW	San Luis Bay	Shoreline fault junction to Hosgri fault junction
FN	Foxen Canyon	Nipomo lineament-Oceano to West Huasna junction
FS	Foxen Canyon	West Huasna junction to Little Pine junction
GN	San Gregorio	Point Ano Nuevo to San Andreas junction
GS	San Gregorio	Point Sur to Point Año Nuevo
HA	Hosgri	Casmalia fault to bend offshore of San Luis Bay fault
HB	Hosgri	Shoreline fault to Western Hosgri fault junction
HC	Hosgri	San Luis Bay (SW) fault to Shoreline fault junction
HD	Hosgri	Western Hosgri to Los Osos fault junction
HE	Hosgri	East path between Casmalia and Shoreline fault junctions
HN	Hosgri	Los Osos fault to offshore of Cambria
HS	Hosgri	Point Arguello to Casmalia fault junction
HW	Hosgri	West path between Casmalia and Shoreline fault junctions
LB	Los Osos	San Luis Obispo Creek Basin—truncated
LC	Los Osos	Morro Bay to Hosgri fault junction
LE	Los Osos	West Huasna fault junction to San Luis Obispo Creek

Code[1]	Fault	Section Description
LM	Los Osos	Southern margin of Morro Bay
LO	Los Osos	San Luis Obispo Creek Basin
LP	Little Pine	West Huasna fault junction to Big Pine–Little Pine junction
LS	Los Osos	San Luis Obispo Creek Basin
LV	Los Osos	San Luis Obispo Creek to Los Osos Valley
MF	San Miguelito offshore	San Luis Obispo Bay to Mallagh Landing
NL	Nipomo	West Huasna fault junction to Arroyo Grande
OF	Oceano	Coastline to Shoreline fault junction
ON	Oceano	West Huasna fault junction to coastline
PB	Piedras Blancas	Western Hosgri to north end Piedras Blancas anticlinorium
PO	Pismo	Wilmar Avenue to Mallagh Landing
SA	San Andreas North	San Gregorio junction to Mendocino Triple Junction
SE	Shoreline	Casmalia fault to Oceano fault junction
SF	Shoreline	Oceano to Wilmar Avenue fault
SH	Shoreline	San Luis Bay fault junction to Hosgri junction
SI	San Simeon	Offshore of Cambria to Oceanic fault junction
SN	San Simeon	Oceanic fault junction to Point Sur
SS	Shoreline	San Luis Bay fault junction to Wilmar Avenue fault junction
WA	Wilmar Avenue	Arroyo Grande to coastline
WB	Wilmar Avenue	Coastline to Shoreline fault
WC	Wilmar Avenue	Coastline to San Miguelito offshore fault
WR	Western Hosgri	Hosgri junction to Piedras Blancas anticlinorium

[1] The coordinates defining the top of these fault sections are provided in the hazard input document (HID; *Appendix C*).

The downdip geometries of the fault sections—including bends, changes in dip, and related changes in width and angular relationships between branching fault sources—are different among FGMs. These values and differences are described in *Chapter 7*.

Preliminary sensitivity analyses presented at Workshop 1 (Wooddell, 2011) showed that variability in the depth of seismogenic faulting has very little effect on hazard at the DCPP. Accordingly, epistemic uncertainty is not characterized for this parameter. The maximum rupture depth is 12 km for all fault sources in the SLPB group, as well as for fault sources in the Hosgri group for events with $\mathbf{M} < 7.4$. For events with $\mathbf{M} \geq 7.4$, the maximum rupture depth for Hosgri group fault sources is 15 km. The 12 and 15 km values are further discussed in *Sections 5.3, 7.2, and 7.3*.

6.3.2 Fault Slip Rate Model

The Fault Slip Rate Model describes the slip rate and its uncertainty for each Primary fault source and certain Connected fault sources. Fault slip rates and their uncertainties are presented as cumulative distribution functions (CDFs) that capture the center, body, and range of technically defensible slip rates. This model is described in *Chapter 8*. The SSC logic tree for Primary and Connected fault sources does not use fault slip rate as direct input to the logic tree (Figure 6-1). Instead, fault slip rate CDFs provide target slip rate budgets that must be accounted for among the various earthquake ruptures modeled to occur on the network of fault sources described in each FGM. In the Diablo Canyon SSC model, this is done by assigning fractions of the fault slip rates to multiple rupture sources that occupy single or multiple fault sections of the FGMs. This process is part of the Rupture Model and is described generally in *Section 6.3.3* and in detail in *Section 9.3*.

6.3.3 Rupture Models

Each FGM has a corresponding Rupture Model that describes the combinations of fault sections that may rupture together. The Rupture Models consist of sets of rupture sources. A rupture source is a series of adjacent fault sections that are considered capable of hosting a maximum earthquake and smaller, floating earthquakes. All rupture sources are considered to occur within each Rupture Model. Thus the rupture sources represent aleatory variability, not epistemic uncertainty, in how earthquake ruptures may span various fault sections. The Rupture Models and rupture sources are defined and described in *Chapter 9*. This section discusses the general characteristics of the approach and the motivations for implementing it.

6.3.3.1 Approach

The rupture model approach, which defines combinations of fault sections spanning multiple named faults, is a deviation from standard fault source characterizations, which typically define fault sources as single or multiple fault sections within a single named fault zone or recognized laterally continuous fault system. The differences between the newer rupture model and standard fault source concepts are presented graphically on Figure 6-7.

In the rupture model approach used for the Diablo Canyon SSC model, the FGMs provide alternative sets of fault geometries and senses of slip, but the combinations of adjacent fault sections that are involved in earthquake rupture are considered independently of the named fault zone. We use the term *rupture topology* to describe the combinations of adjacent fault sections that may rupture in maximum earthquakes (over the entire area of the combined fault sections) and smaller earthquakes (over portions of the fault sections). Each rupture source within a Rupture Model defines a certain rupture topology, and the SSC model proceeds to characterize the slip rate and relative size distribution of earthquakes that may occur on that rupture topology.

6.3.3.2 Motivation

The primary motivation for constructing the Diablo Canyon SSC model with the rupture model approach is that we recognize that there are several branching relationships between fault sections among the Primary and Connected fault sources and that earthquake ruptures near the DCPP may take various pathways through those branching relationships. For example, the Shoreline and Los Osos faults both have branching relationships with the Hosgri fault zone northwest of the DCPP, and the Los Osos and San Luis Bay fault zones likely have a branching relationship at depth beneath the Irish Hills (*Chapter 5*). Recent historical earthquake ruptures that spanned multiple faults and/or crossed various branching relationships include the 1992 Landers, California, and 2002 Denali, Alaska, earthquakes, among others (Table 6-1). Because of the lack of information on past earthquake ruptures in the DCPP vicinity, and the current lack of detailed understanding of what controls rupture pathways and rupture terminations (e.g., Wesnousky, 2006, 2008), the uncertainty in rupture topology is captured through the consideration of various alternative branching relationships (rupture sources) among fault sections in the Diablo Canyon SSC model.

The rupture model approach is a forward modeling method that relies on judgment, simple rules, and simple bookkeeping in its construction. An alternative approach that includes multi-fault and multi-segment ruptures on an interconnected, branching network of fault sources is the inverse modeling approach used in the UCERF3 model for California (Field et al., 2013). That approach, which also requires expert judgment in parameterizing the logic tree branch values and weights that are used to constrain the inversion, has certain advantages and disadvantages over the forward-modeling method used for the Diablo Canyon SSC model. An advantage of the inverse approach is that it provides a measure of objectivity to its solutions—the “grand inversion” algorithm used in the UCERF3 model solves for a set of rupture topologies, earthquake magnitudes, and rates that are permitted within the defined rules of rupture connectivity and that minimize misfits with available constraints on fault parameters such as fault slip rate and paleoseismic data (Page et al., 2013). This type of approach has many advantages over a forward modeling approach for a statewide model, in which model boundary conditions (e.g., an overall target rate of $M \geq 5$ earthquakes) are relatively well constrained.

Some major disadvantages to using an inverse approach apply in cases of a site-specific PSHA where hazard is dominated by low-slip-rate faults, or in the Diablo Canyon situation where details of the Hosgri fault and lesser faults proximal to the site are important. For UCERF3, the vast majority of ruptures in the overall inverse solution are on the San Andreas fault and branching high-slip-rate faults such as the San Jacinto fault in Southern California and the Calaveras and Hayward faults in Northern California. Thus the UCERF3 rupture solution for faults in the DCPP vicinity—including the Hosgri, Los Osos, Shoreline, and San Luis Bay faults—is within the noise of the overall model, and thus the statewide model solution is not sensitive to variability in ruptures on these fault sources. This fact, along with the consistent findings that some of the highest contributors to hazard uncertainty at the DCPP from the SSC model are uncertainties in slip rate and uncertainties in fault dip on local nearby faults (Wooddell, 2011,

presentation at Workshop 1), led to a clear decision by the TI Team not to include the actual UCERF3 model results as a logic tree branch. Because of the dominance of the San Andreas fault solution and other "statewide" parameters to hazard, it was further decided not to propose modifications to the UCERF3 model for use at the DCPP (e.g., by proposing several alternative fault geometry models or by proposing a broader range of target fault slip rates).

The construction of smaller inverse models—models that might have their geographic extent limited to the DCPP site vicinity—was considered by the SSC TI Team but rejected in favor of the forward-modeling rupture model approach. A primary reason for rejecting the construction of a smaller inverse model was that it would have the disadvantage of few constraints on the overall inversion solution. For example, the statewide UCERF3 model has a relatively extensive record of $M \geq 5$ earthquakes that can help determine the overall target earthquake budget. The DCPP site vicinity has extremely few $M \geq 5$ earthquakes. The statewide model—in which hazard is dominated by high-slip-rate faults—includes opportunities to evaluate results against paleoseismic data. Such evaluations are helpful for gaining confidence in the results of this new approach. The available paleoseismic data on the San Simeon fault (Hall et al., 1994), Los Osos fault (Lettis and Hall, 1994), and San Luis Bay fault (Lettis et al., 1994) are few and insufficient to provide meaningful constraints on an inversion. Last, the inverse model approach has the disadvantages of being a new model approach with limited time to gain broad acceptance in the hazard community, and being more difficult than a forward model to dissect and explore from a hazard sensitivity standpoint.

In sum, the SSC TI Team opted for the forward-model approach over an inverse approach, believing it to be more practical to implement for a site-specific PSHA, and more tractable to understand and review what contributes most to hazard uncertainty. It is noted that although regional slip budgets and deformation rates are not formally imposed within the framework of an inverse modeling approach, these data do inform and constrain inputs used in the forward-modeling approach.

6.3.3.3 Rupture Source Types

The Rupture Models describe the number of rupture sources, the fault sections involved in each rupture source, the sense of slip for each fault section in the rupture source, and the *type* of rupture source. The rupture source type is a classification scheme used in the SSC model for PSHA in two ways. First, the rupture source type alerts the Hazard Analyst to conditions that require special treatment in the ground motion characterization (GMC) model. Second, the rupture source type is related to the functional form of earthquake sizes (the magnitude probability density function, or magnitude PDF) that occur on a rupture source (this is described further in *Section 6.3.5*). The four rupture source types are named and described briefly in Table 6-6. Further description of the four types of rupture sources is provided in *Section 9.2.1*.

Table 6-6. Rupture Source Types

Type	Explanation
Characteristic	Rupture source is confined to a single named fault of limited length that has a uniform sense of slip.
Linked	Rupture source includes fault sections of multiple named faults of the same sense of slip.
Complex	Rupture source contains multiple named faults and more than one sense of slip on adjacent fault sections.
Splay	Rupture source includes overlapping faults that rupture simultaneously.

The complex and splay rupture sources require special consideration by the ground motion model regarding how to implement ground motion contributions from multiple portions of the fault rupture (GeoPentech, 2015). For complex rupture sources, where different portions of the rupture source have different senses of slip, two parts are identified: the larger ("primary") part and the smaller ("secondary") part. For splay rupture sources, where there are overlapping portions of the rupture source, resulting in two source-to-site distances, the fault sections are identified as part of either the larger ("main") area or the smaller ("splay") area of the rupture source.

6.3.4 Slip Rate Allocation Models

A Slip Rate Allocation Model describes the slip rate allocated to individual rupture sources in a single Rupture Model. Accordingly, there is one Slip Rate Allocation Model for the Hosgri Rupture Model (that applies to all three Hosgri FGMs) and three Slip Rate Allocation Models for the SLPB Rupture Models, one each for the OV, SW, and NE Rupture Models. The Slip Rate Allocation Models are presented as part of the Rupture Models in *Section 9.3*.

The slip rate of each rupture source represents some fraction of the total fault slip rate determined from the Fault Slip Rate Model for each fault source involved in the rupture (*Section 6.3.2*). Because the Rupture Model contains rupture sources that link across numerous faults with different fault slip rates, the Slip Rate Allocation Model creates a slip rate for each rupture source such that when the contributions from all rupture sources that include a particular fault are summed, the combined slip rate equals the target slip rate budget for that particular fault. The rationale and criteria used to allocate a fraction of the total fault slip rate to individual rupture sources are discussed in *Section 9.3.1*.

For characteristic and linked rupture sources, the slip rate is uniform over the entire rupture source. For complex and splay rupture sources, the slip rates are uniform over each part of the rupture source, but the parts have different slip rates. Slip rates are different for each part (e.g., the *primary* and *secondary* parts) primarily because of the method selected for modeling ground motions for these two rupture source types in the ground motion model (GeoPentech, 2015). The ground motion model requires that for a given complex or splay rupture source, two magnitudes be defined—one each for the larger and smaller parts of the rupture source. In order to have a constant occurrence rate

of the splay and complex earthquake scenarios, the slip rate of the larger fault source (the *main* or *primary* fault for splay and complex cases, respectively) must be greater than the slip rate of the smaller fault source (the *splay* or *secondary* fault for splay and complex cases, respectively) by an amount that is proportional to the estimated seismic moments of each part of the rupture source (*Section 9.3.1*).

Uncertainty in slip rate for each rupture source is handled as epistemic uncertainty in the SSC logic tree with three-point weighted distributions. The three-point weighted distributions are selected from slip rate cumulative distribution functions (CDFs) that are, in turn, calculated based on the fault slip rate CDFs and the fraction of slip rate allocated to each rupture source (*Section 9.3.1*).

6.3.5 Magnitude Distribution Models

A Magnitude Distribution Model (MDM) describes the minimum (M_{min}) and maximum (M_{max}) magnitudes and the relative frequency of earthquake magnitudes from M_{min} through M_{max} that may occur on a rupture source. Four earthquake magnitude-frequency distribution (MFD) functional forms are used in the Diablo Canyon SSC model. These functional forms are herein called magnitude *probability density functions* (magnitude PDFs); the term *MFD* is reserved herein for the distribution of annual rate (in yr^{-1}) plotted against magnitude calculated by combining the magnitude PDF with the rupture source area, slip rate, and bounding magnitudes (M_{min}, M_{max}, and/or characteristic magnitude, M_{char}).

The paucity of information available on past moderate to large earthquake ruptures on the Primary fault sources was considered in developing an approach to constructing MDMs that accounted for both epistemic and aleatory uncertainty. No large earthquakes (**M** 6 or larger) have occurred historically on the Hosgri fault, Shoreline, Los Osos, or San Luis Bay faults (McLaren and Savage, 2001; *Section 5.4*). The paleoseismic data collected on these faults are very limited, with a few estimates of the timing and amount of slip on past earthquakes on the San Simeon fault north of San Simeon (Hall et al., 1994), on the Los Osos fault near San Luis Obispo (Lettis and Hall, 1994), and on the San Luis Bay fault near Avila Beach (Lettis et al., 1994). These paleoseismic records, however, do not have well-constrained or well-determined information about earthquake timing, slip per event, or completeness of the stratigraphic record. In all cases, the number of events captured is very few or is difficult to assess.

The construction of MDMs also considers the geometry of the Primary fault sources. As described in *Chapters 5, 7, and 10*, the best available mapping of the Hosgri–San Simeon–San Gregorio fault zone shows that there is a reasonably well-defined southern end point to the Hosgri Fault near Point Arguello. There are no gaps, step-overs, or sharp double bends in the fault zone between Point Arguello and the northern end of the San Gregorio fault zone at Bolinas Lagoon that are sufficiently large to preclude the possibility of throughgoing earthquake rupture. The Primary faults of the SLPB group—the Shoreline, Los Osos, and San Luis Bay—all appear to have branching relationships with the Hosgri or with one another that also are not sufficiently understood to accurately

model, much less preclude, the continuity of earthquake rupture through the intersections. Likewise, fault geometries and senses of slip along and between the Primary and Connected faults east and west of the Hosgri fault contain relatively abrupt changes in strike, geomorphic expression, and rake, but few are sufficiently large to preclude throughgoing fault rupture based on observations from other segmented strike-slip fault systems (Wesnousky, 2006). These physical characteristics suggest that, in the absence of "behavioral" information on the size and timing of past earthquake ruptures, there is little basis to confidently define specific lengths, or segments, of the faults and rupture sources that are meaningful for narrowly constraining the sizes and relative frequencies of earthquake magnitudes.

6.3.5.1 Approach

Despite the paucity of paleoseismic data, and the lack of historical data and clearly defined fault or rupture segment end points that would limit earthquake rupture, there are alternative models, methods, and empirical observations available to construct models for the earthquake size distribution on the Primary and Connected faults.

The MDMs developed for the Primary and Connected fault sources are derived by assessing possible rupture segmentation of each rupture source, evaluating lengths and areas of possible characteristic and maximum earthquake ruptures, assigning earthquake magnitudes to characteristic and maximum ruptures, and defining magnitude PDFs to characterize the MFDs of earthquakes on the rupture sources. Aspects of the development of the MDMs are described briefly in this section and in greater detail in *Chapter 10*.

Maximum earthquake sizes are subject to epistemic uncertainty but are limited ultimately by the maximum dimensions of the rupture source. Characteristic earthquake rupture dimensions, which are not as clearly constrained, are more challenging to define and defend in the Diablo Canyon SSC model as explained above. The absence of behavioral information or clear segmentation boundaries, however, is not a rationale for precluding characteristic-model behavior as part of the technically defensible range of models. The characteristic earthquake hypothesis—defined herein as the repeated occurrence of earthquakes of similar size over a similar portion of a fault that is much more common than would be predicted from an exponential MFD—appears to apply well to certain continental faults where paleoseismic information can be evaluated (Schwartz and Coppersmith, 1984; Stirling et al., 1996; Ishibe and Shimazaki, 2012), and empirical data from paleoseismic sites on displacement-at-a-point are consistent with the characteristic earthquake hypothesis and would appear to reject an exponential magnitude size distribution for faults (Hecker et al., 2013). We do not suggest that all portions of all faults rupture in characteristic earthquakes, and we recognize that many faults and portions of fault networks that have been modeled with characteristic earthquakes can also be successfully represented with exponential size distributions (Kagan, 1993; Parsons and Geist, 2009; Page et al., 2011). However, as noted by Field et al. (2014) the results of the grand inversion used in UCERF3 have demonstrated challenges with the Gutenberg-Richter hypothesis for individual faults.

The rupture model concept allows for a broad range of earthquake sizes to be present on the Primary and Connected fault sources. Because alternative rupture topologies coexist on the same branching fault network with varying lengths, some rupture sources host maximum earthquakes that approach or exceed the size of historical earthquakes that have occurred on similar types of ruptures observed worldwide, whereas other rupture sources repeatedly produce earthquakes of a much more limited size range.

The MDMs are constructed with the site-specific nature of the PSHA in mind. This arises in two ways: (1) in selecting fault lengths for both maximum and characteristic earthquake ruptures, and (2) in modeling the location of earthquake ruptures in the hazard code for PSHA. Just as the rupture topologies defining the rupture sources are created with the DCPP-specific application in mind, the fault sections and lengths considered to define alternative values of M_{char} on a rupture source are fault sections and lengths nearest to the DCPP. In other words, portions of Connected faults farther from the DCPP that may be considered to define a characteristic rupture are considered less or not at all when compared to portions closer to the DCPP.

Determination of characteristic earthquakes based on fault segmentation has been a durable feature in PSHA (e.g., Schwartz and Coppersmith, 1984), even if it has received much scrutiny (Field et al., 2013). Although we use concepts of fault segmentation to estimate the size of characteristic earthquakes, we acknowledge that there are many instances of earthquake ruptures that do not behave, even in hindsight, according to commonly applied segmentation rules (Table 6-1; Hardebeck, 2012a, presentation at Workshop 2). We believe these instances are accounted for in the SSC model by the following means:

- Having weight on an exponential recurrence distribution for many rupture sources.
- Having a very broad range of characteristic magnitudes on the fault network.
- Allowing the hazard model to “float”—and not fix—earthquake ruptures across the originally postulated fault segment boundaries.

Magnitudes of characteristic and maximum ruptures in the MDMs are calculated from the magnitude-area scaling relation of Hanks and Bakun (2014; HB14). The HB14 relation is a bilinear empirical relation developed from a subset of continental strike-slip earthquakes, mostly from California:

$$\mathbf{M} = \log A + 3.98, \qquad A \leq 537 \text{ km}^2$$

$$\mathbf{M} = 5/4 \log A + 3.30, \qquad A > 537 \text{ km}^2$$

where **M** equals moment magnitude and A equals rupture area in km^2.

The HB14 relation was selected for sole implementation from several alternative candidate empirical magnitude-scaling relations after considering the following:

- The dimensions and style of faulting of the Primary and Connected fault sources yield magnitude estimates that span the magnitude range that appears to be best fit by a bilinear empirical relation.

- The transpressional tectonic setting of the DCPP site is characterized by continental strike-slip faults similar to the type of earthquake ruptures used to develop the empirical relation.
- The hazard results are not sensitive to the choice of empirical relation (Wooddell, 2011, presentation at Workshop 1), which allows for trimming this branch of the logic tree.

A set of proponent models sampled from the range of available models was selected by the TI Team to assess the magnitude PDFs for different types of rupture sources. The set includes the following distributions:

- The truncated exponential, or Gutenberg-Richter, distribution (Gutenberg and Richter, 1944; Kagan, 1993).
- The simplified maximum magnitude distribution (Wesnousky et al., 1983).
- The characteristic earthquake distribution (Youngs and Coppersmith, 1985).
- The recently developed modified characteristic earthquake distribution (WAACY model; *Appendix G*).

These proposed magnitude PDFs, shown graphically on Figure 6-8, provide a broad range that captures uncertainty in the relative earthquake sizes that may occur on the fault sources.

Each rupture source type (Table 6-6) is associated with one or two magnitude PDFs to be used in the hazard calculations. Table 6-7 shows the associations between rupture source type, the applied magnitude PDF(s), and the branch weights used in the SSC logic tree. Discussion of the rationale for the selection and weighting of the various magnitude PDFs for each rupture source type is provided in *Section 10.2.3*.

Table 6-7. Rupture Source Types and Magnitude PDFs

Rupture Source Type	Branch-Weighted Magnitude PDF Branches and Weights
Characteristic and Linked (shorter rupture sources)	Characteristic Earthquake [1.0]
Linked (longer rupture sources)	WAACY [0.8] Truncated Exponential [0.2]
Complex and Splay	Simplified Maximum Magnitude [1.0]

6.3.6 Time Dependency Model

The Time Dependency Model in the SSC applies to the recurrence of moderate to large earthquakes. Near the DCPP it applies to the Primary fault sources and Connected fault sources listed in Table 6-2.

Earthquake recurrence in PSHA is commonly modeled as a time-independent Poisson process. There is growing evidence, however, that earthquake occurrence is too regular on some faults for the Poisson model to be likely (Biasi et al., 2002; Scharer et al., 2009;

Fitzenz et al., 2010). Furthermore, simple elastic rebound theory of elastic strain accumulation and release suggests there is some renewal process involved in earthquake recurrence on individual faults. Thus we find that a non-Poisson model for earthquake occurrence must be considered technically defensible, and thus included in the SSC model. To account for the probability that moderate to large earthquakes on faults do not follow a Poisson process, equivalent Poisson ratios (EPRs) are applied to the Primary and Connected fault source rates. The EPRs are multipliers of the Poisson rate that capture uncertainty in the recurrence functional form, long-term mean recurrence rate of moderate to large earthquakes, coefficient of variation in the recurrence model, and the time elapsed since the most recent event. The methodology and results to derive the equivalent Poisson rates are discussed in detail in *Appendix H. Chapter 11* provides a summary and describes the implementation of EPRs in the SSC logic tree for the Primary and Connected fault sources.

The SSC model incorporates the Time Dependency Model as a global parameter (i.e., it is applicable to all or a group of sources), with a different tree (different branch values and weights) for the Hosgri and SLPB fault source groups (see Figure 6-1 and Table 6-2).

6.4 Regional Fault Sources

There are many active faults within the 320 km (200 mi.) DCPP site region, the distance to which fault activity must be considered in the SSC model. We refer to the fault sources within the DCPP site region other than the Primary and Connected fault sources as *regional* fault sources (*Chapter 12*). Preliminary sensitivity analyses (Wooddell, 2011, presentation at Workshop 1) showed that regional fault sources contribute little to hazard at the DCPP; this was confirmed by sensitivity analyses for the final SSC model (*Chapter 14*). The largest regional fault source, the San Andreas fault source (SAF), located approximately 80 km northeast of Diablo Canyon, represents a few percent of the total hazard at long periods at the hazard levels being evaluated for the DCPP (Wooddell, 2011; *Section 14.2*). Aside from the SAF source, the other regional fault sources contribute less than 1% to hazard *in the aggregate*. The SAF source is described separately from the other regional fault sources in *Chapter 12* because of its relative importance among regional faults and because its geometry allows some simplification of hazard calculation inputs (*Section 12.4*).

Our primary approach for including regional fault sources in the Diablo Canyon SSC model is to rely on the UCERF3 characterizations for these sources (*Sections 12.3 and 12.5*). In cases where regional faults have not been characterized in the UCERF3 but the TI Team decided that they should be included as fault sources, The TI Team constructed simple characterizations (*Section 12.6*).

The UCERF3 model comprehensively included seismic, geological, and geodetic data from active faults in California. The resulting time-independent rupture forecast (Field et al., 2013) has been adopted by the California Earthquake Authority and used to develop the California portion of the 2014 National Seismic Hazard Maps (Petersen et al., 2014).

The methods used to extract SSC parameters from the UCERF3 fault sources for the Diablo Canyon SSC model are described in *Section 12.3*.

For the Diablo Canyon SSC model, the TI Team judges the UCERF3 model to provide a complete accounting of other regional fault sources for the onshore and some offshore areas within the 320 km DCPP site region. The UCERF3 model is judged by the SSC TI Team to be incomplete for offshore fault sources, including faults or late Cenozoic folds west and southwest of the Hosgri fault zone that were identified during the LTSP (Willingham et al., 2013). These include the seismic source of the 1927 Lompoc earthquake (Helmberger et al., 1992; Satake and Somerville, 1992; McLaren and Savage, 2001; *Section 5.3*). Additional offshore fault sources within the DCPP site region not included in the UCERF3 model were characterized based on evaluations of available publications and information (*Section 12.6*).

6.5 Areal Source Zones

Earthquakes occurring off the recognized fault sources within the 320 km DCPP site region are modeled to occur in areal source zones (Figure 6-9). As mentioned in *Section 6.2* and discussed in greater detail in *Chapter 13*, the Diablo Canyon SSC model has two types of areal source zones: those modeled with virtual faults and those modeled as point sources from a grid. The areal source zones are volumes of crust containing faults whose general geometric and sense of slip characteristics are known, but sufficient specific information about activity, extent, and slip rate to model individual fault sources is lacking.

The first method models earthquakes as occurring on a set of subparallel virtual faults, with defined aleatory and epistemic uncertainties in location, rake, dip, and M_{max}. This method is used for the areal source zone that includes the DCPP and adjacent areas. This *host* areal source zone represents an area where the general characteristics of faults are known (to varying degrees of uncertainty) or may be constrained by available information, but where the fault activity and/or slip rate are unresolved. The rates of earthquakes in this areal source zone are determined based on observed seismicity rates and considerations of geologic rates of deformation. More general information about the motivation for the host areal source zone—called the Local areal source zone—is provided in *Section 13.5*.

Two other areal source zones in the Diablo Canyon SSC model—named the Regional and Vicinity source zones—use an alternative method for modeling earthquakes. These source zones represent earthquakes that may occur from faults that are unknown or known but not sufficiently active to be considered as a fault source. The SSC models earthquakes in the vicinity and regional source zones from a set of point sources on regularly spaced grids. This approach is used at greater distances from the DCPP site where less precision is warranted. The rates of earthquakes in the gridded source zones are calculated based on observed and spatially smoothed seismicity rates and model predictions about maximum earthquake size. The gridded areal source zones are described in *Sections 13.3 and 13.4*.

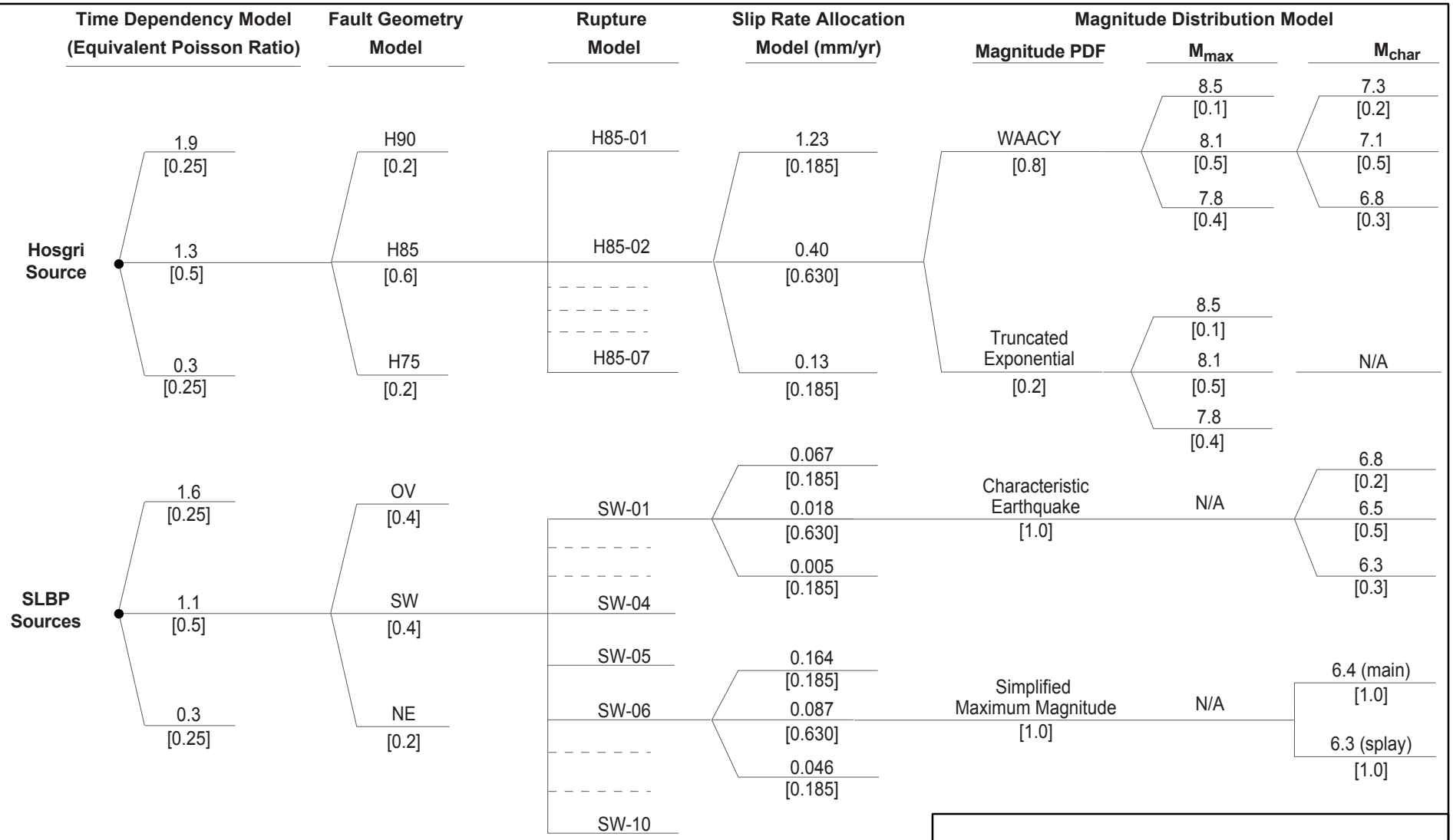

Notes: In the example tree, rupture source H85-02 is a longer *linked* rupture source, so the WAACY and truncated exponential magnitude PDF models are considered. Rupture source SW-01 is a *characteristic* rupture source, so only the Youngs and Coppersmith (1985) characteristic earthquake magnitude PDF is considered. Rupture source SW-06 is a *splay* rupture source, so only the simplified maximum magnitude earthquake magnitude PDF model is considered. See text.

Logic Tree Structure for the Primary and Connected Fault Sources

DCPP SSC REPORT

Pacific Gas and Electric Company

Figure **6-1**

File path: S:\1005\005\Final_Report_Figures\Figure_600-01.ai; Date: 03/10/2015; User: Serkan Bozkurt, LCI; Rev.1

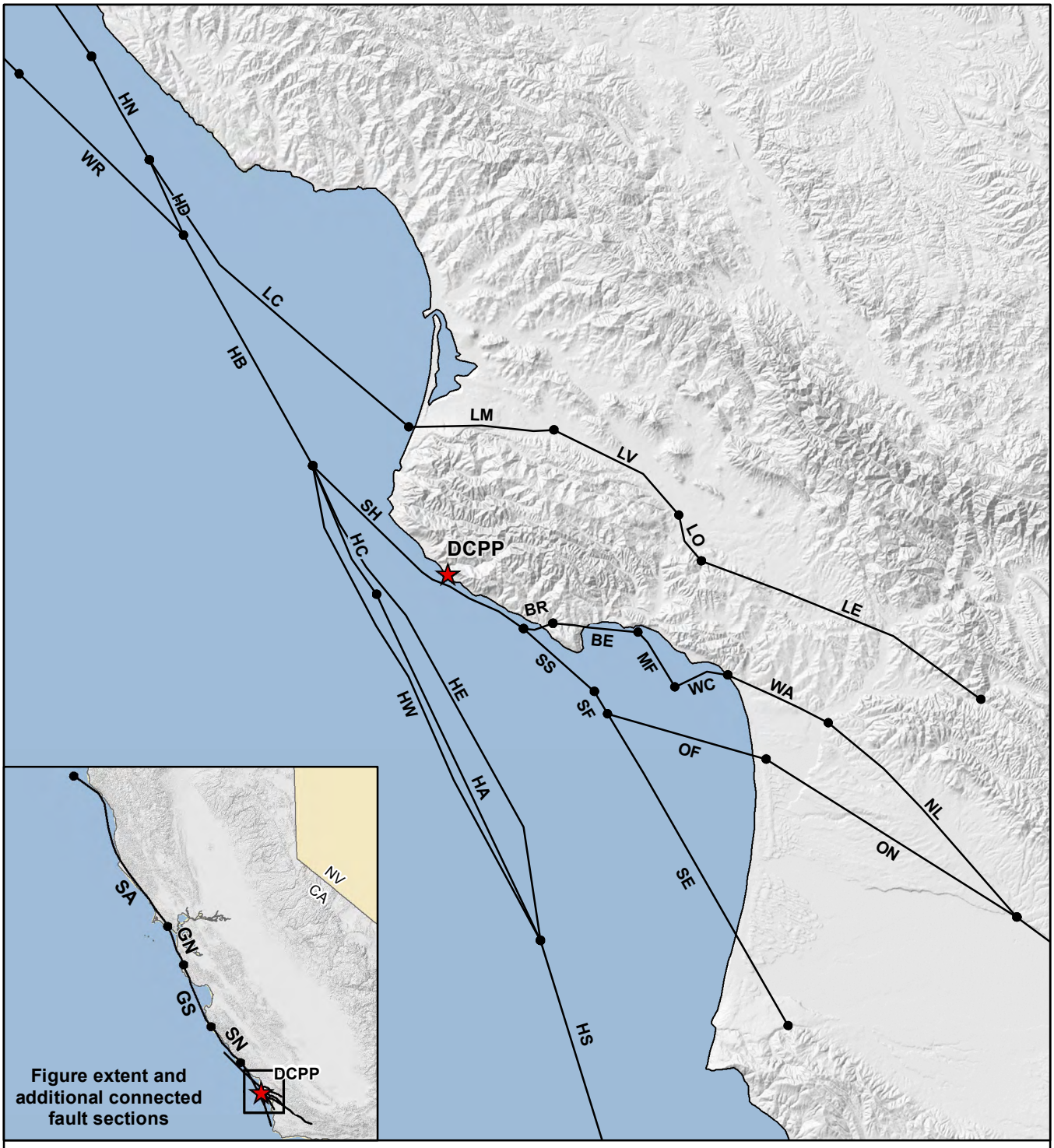

EXPLANATION

★ DCPP site

●——● Fault section, surface trace, or updip surface projection

Note: Two letter fault section codes are defined in Table 6-5 of the report.

N

0 6 12 mi.

0 10 20 km

Map projection and scale: WGS 84 / UTM Zone 10N, 1:400,000

Primary and Connected Fault Sections in the Hosgri and Outward-Vergent (OV) Fault Geometry Model, DCPP Vicinity

DCPP SSC REPORT

Pacific Gas and Electric Company

Figure **6-2**

File path: S:\1005\005\Final_Report_Figures\Figure_600-02.mxd; Date: 02/20/2015; User: serkan, LCI; Rev.1

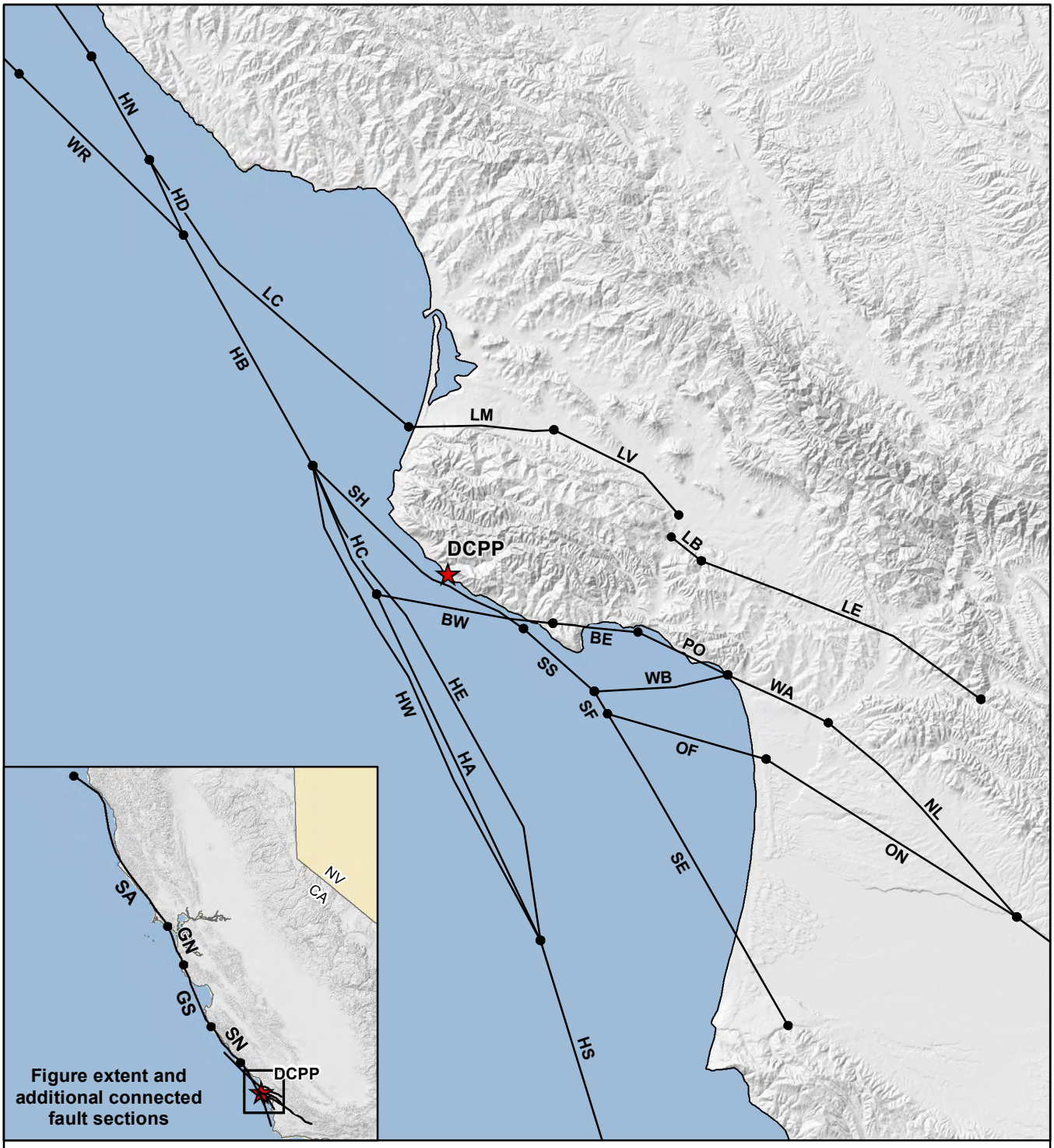

EXPLANATION

★ DCPP site

●——● Fault section, surface trace, or updip surface projection

Note: Two letter fault section codes are defined in Table 6-5 of the report.

N

0 6 12 mi.

0 10 20 km

Map projection and scale: WGS 84 / UTM Zone 10N, 1:400,000

Primary and Connected Fault Sections in the Hosgri and Southwest-Vergent (SW) Fault Geometry Model, DCPP Vicinity

DCPP SSC REPORT

Pacific Gas and Electric Company

Figure **6-3**

File path: S:\1005\005\Final_Report_Figures\Figure_600-03.mxd; Date: 02/20/2015; User: serkan, LCI; Rev.1

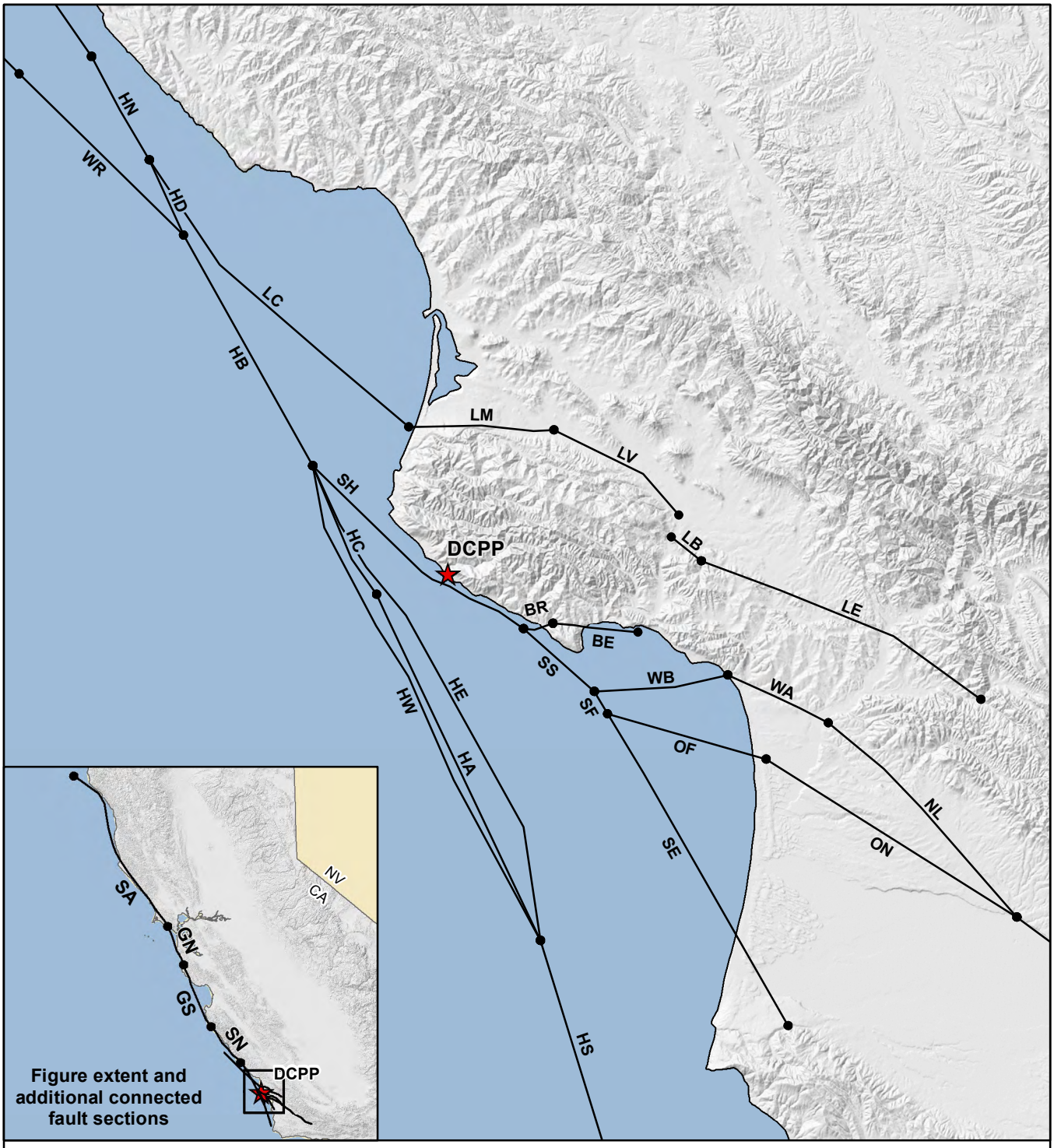

EXPLANATION

★ DCPP site

●——● Fault section, surface trace, or updip surface projection

Note: Two letter fault section codes are defined in Table 6-5 of the report.

N

0 6 12 mi.

0 10 20 km

Map projection and scale: WGS 84 / UTM Zone 10N, 1:400,000

Primary and Connected Fault Sections in the Hosgri and Northeast-Vergent (NE) Fault Geometry Model, DCPP Vicinity

DCPP SSC REPORT

Pacific Gas and Electric Company

Figure **6-4**

File path: S:\1005\005\Final_Report_Figures\Figure_600-04.mxd; Date: 02/20/2015; User: serkan, LCI; Rev.1

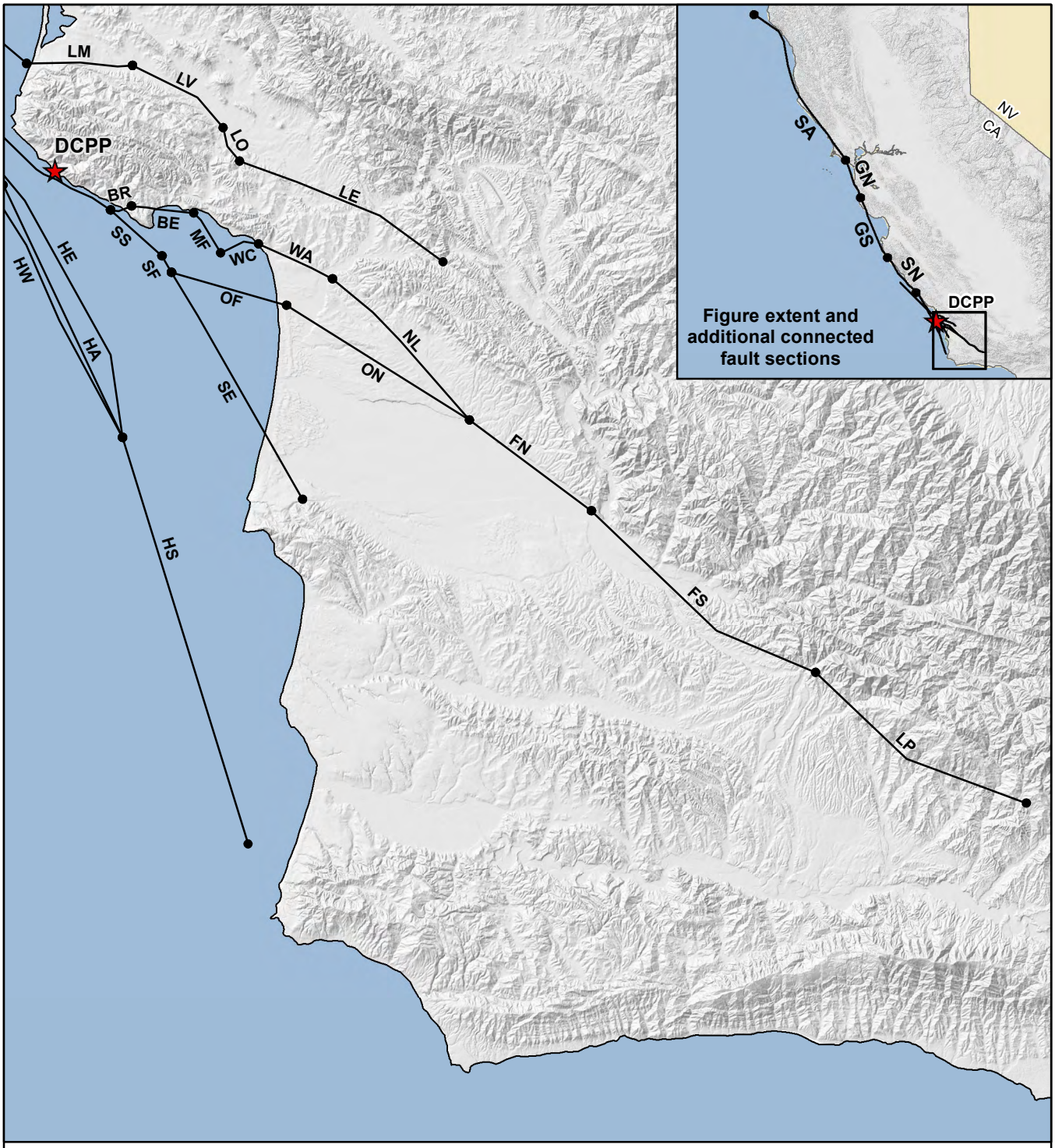

EXPLANATION

★ DCPP site

●——● Fault section, surface trace, or updip surface projection

Notes:
- Outward-Vergent (OV) Fault Geometry Model shown.
- Two letter fault section codes are defined in Table 6-5 of the report.

N

0 6 12 mi.
0 10 20 km

Map projection and scale: WGS 84 / UTM Zone 10N, 1:550,000

Primary and Connected Fault Sections in the Fault Geometry Models, Southern Region

DCPP SSC REPORT

Pacific Gas and Electric Company

Figure **6-5**

File path: S:\1005\005\Final_Report_Figures\Figure_600-05.mxd; Date: 02/20/2015; User: serkan, LCI; Rev.1

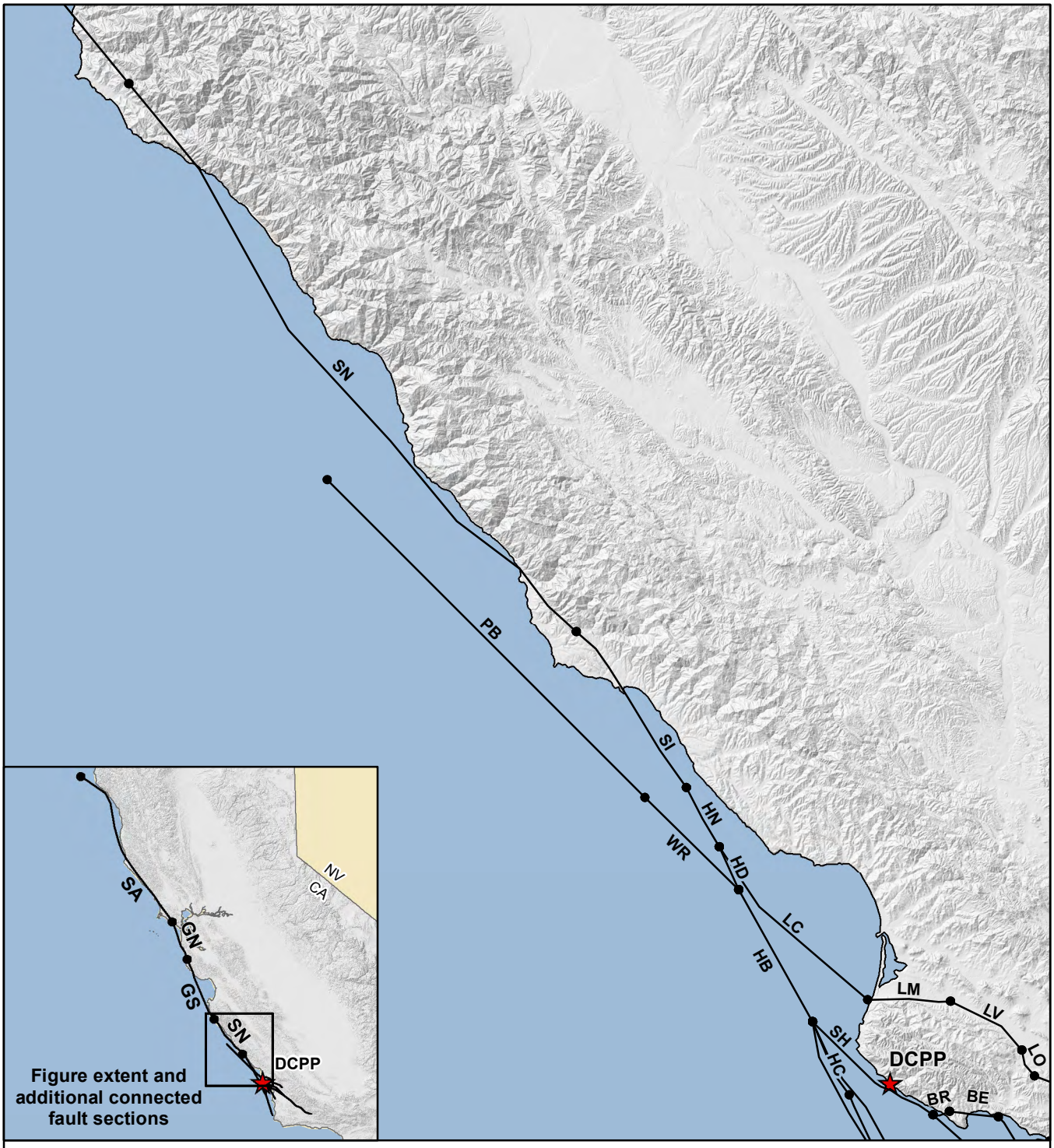

EXPLANATION

★ DCPP site

●——● Fault section, surface trace, or updip surface projection

Notes:
- Outward-Vergent (OV) Fault Geometry Model shown.
- Two letter fault section codes are defined in Table 6-5 of the report.

N

0 6 12 mi.
0 10 20 km

Map projection and scale: WGS 84 / UTM Zone 10N, 1:700,000

Primary and Connected Fault Sections in the Fault Geometry Models, Northern Region

DCPP SSC REPORT

Pacific Gas and Electric Company

Figure **6-6**

File path: S:\1005\005\Final_Report_Figures\Figure_600-06.mxd; Date: 02/20/2015; User: serkan, LCI; Rev.1

(a) Traditional Fault Source Characterization

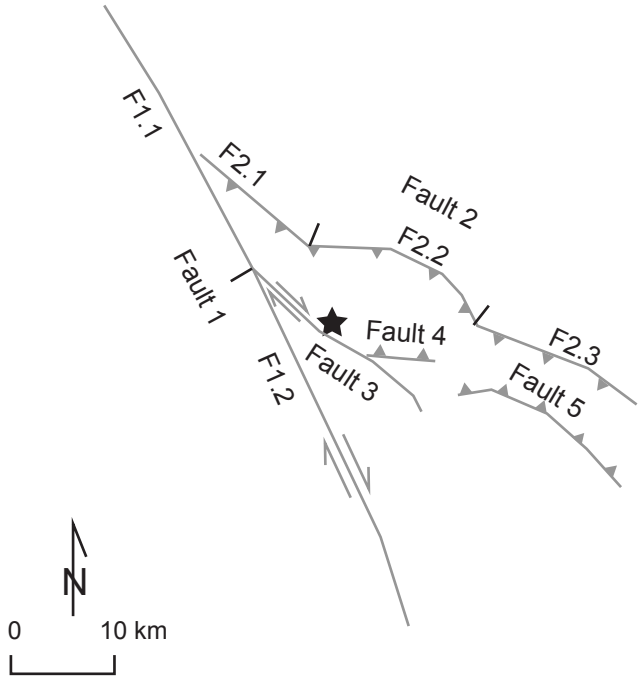

Fault	*Ruptures considered*
Fault 1	F1.1 + F1.2 combined, *or* F1.1 and F1.2, separate
Fault 2	F2.1 + F2.2 + F2.3 combined, *or* F2.1 + F2.2 together, F2.3 separate, *or* F2.1 separate, F2.2 + F2.3 together, *or* F2.1, F2.2, F2.3 each separate
Fault 3	Fault 3 alone
Fault 4	Fault 4 alone
Fault 5	Fault 5 alone

(b) Rupture Source Concept for Fault Source Characterization

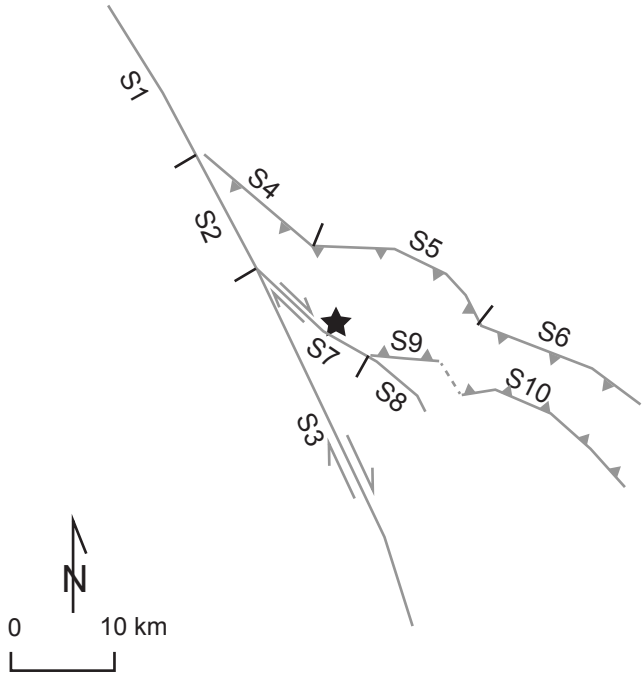

Rupture Sources Considered

S1+S2+S3 *and*
S1+S2+S3+S7 *and*
S1+S2+S7+S8 *and*
S1+S2+S7+S9+S10 *and*
S1+S4+S5+S6 *and*
S7+S8 *and*
S7+S9 *and*
S9 *and*
S9+S10 *and*
S5 *and*
S5+S9 *and*
S4+S5+S6 *and*
S6+S10

EXPLANATION

★ Site

Fault sections: strike-slip (left), reverse (right)

S1 S2 Fault section IDs and section boundary

Differences Between Traditional Fault Source and Rupture Source Concepts

DCPP SSC REPORT

Pacific Gas and Electric Company

Figure **6-7**

File path: S:\1005\005\Final_Report_Figures\Figure_600-07.ai; Date: 02/20/2015; User: Serkan Bozkurt, LCI; Rev.1

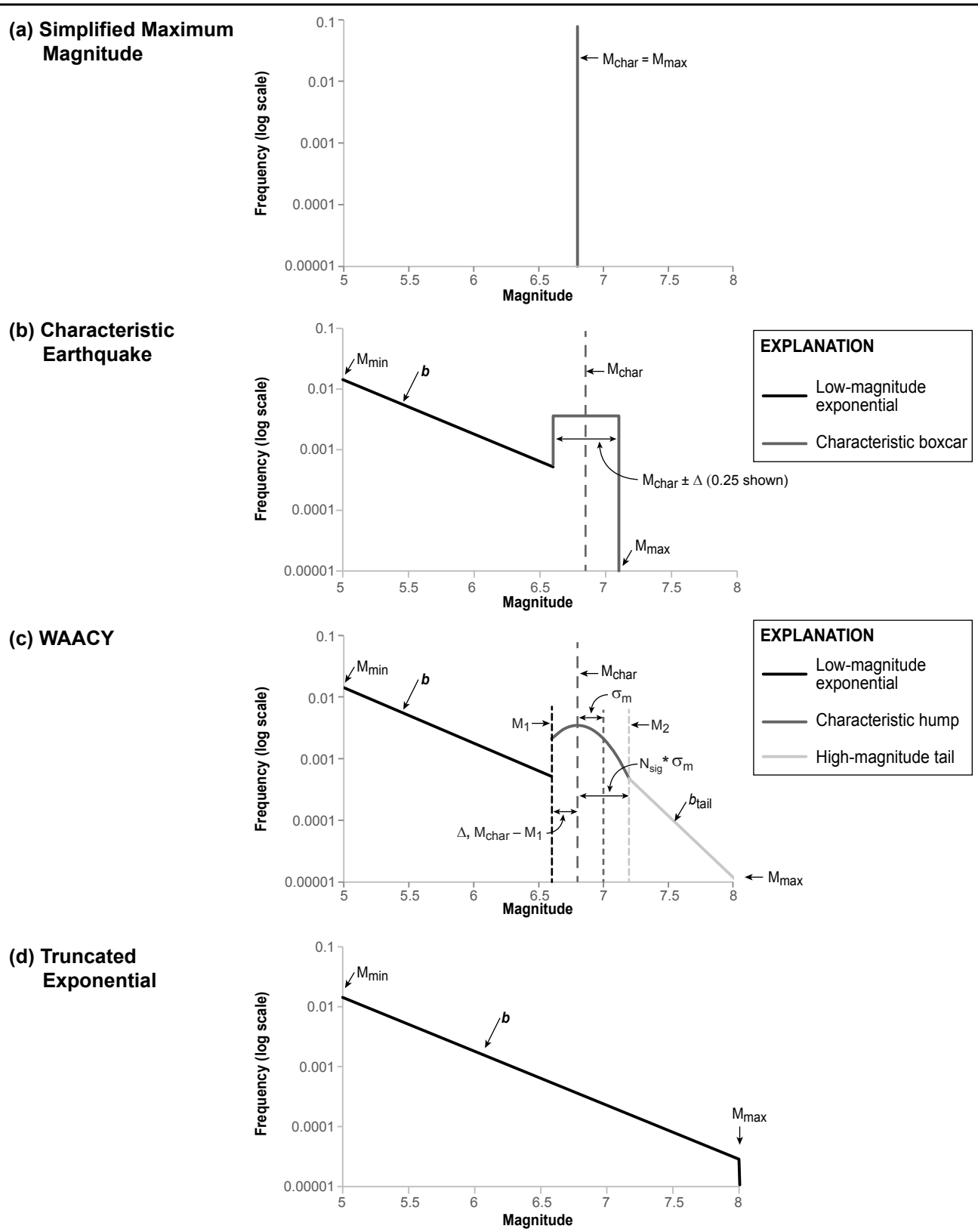

Schematic Diagrams of Magnitude Probability Density Functions Used in the Diablo Canyon SSC Model

DCPP SSC REPORT

Pacific Gas and Electric Company

Figure **6-8**

File path: S:\1005\005\Final_Report_Figures\Figure_600-08.ai; Date: 02/20/2015; User: Serkan Bozkurt, LCI; Rev.1

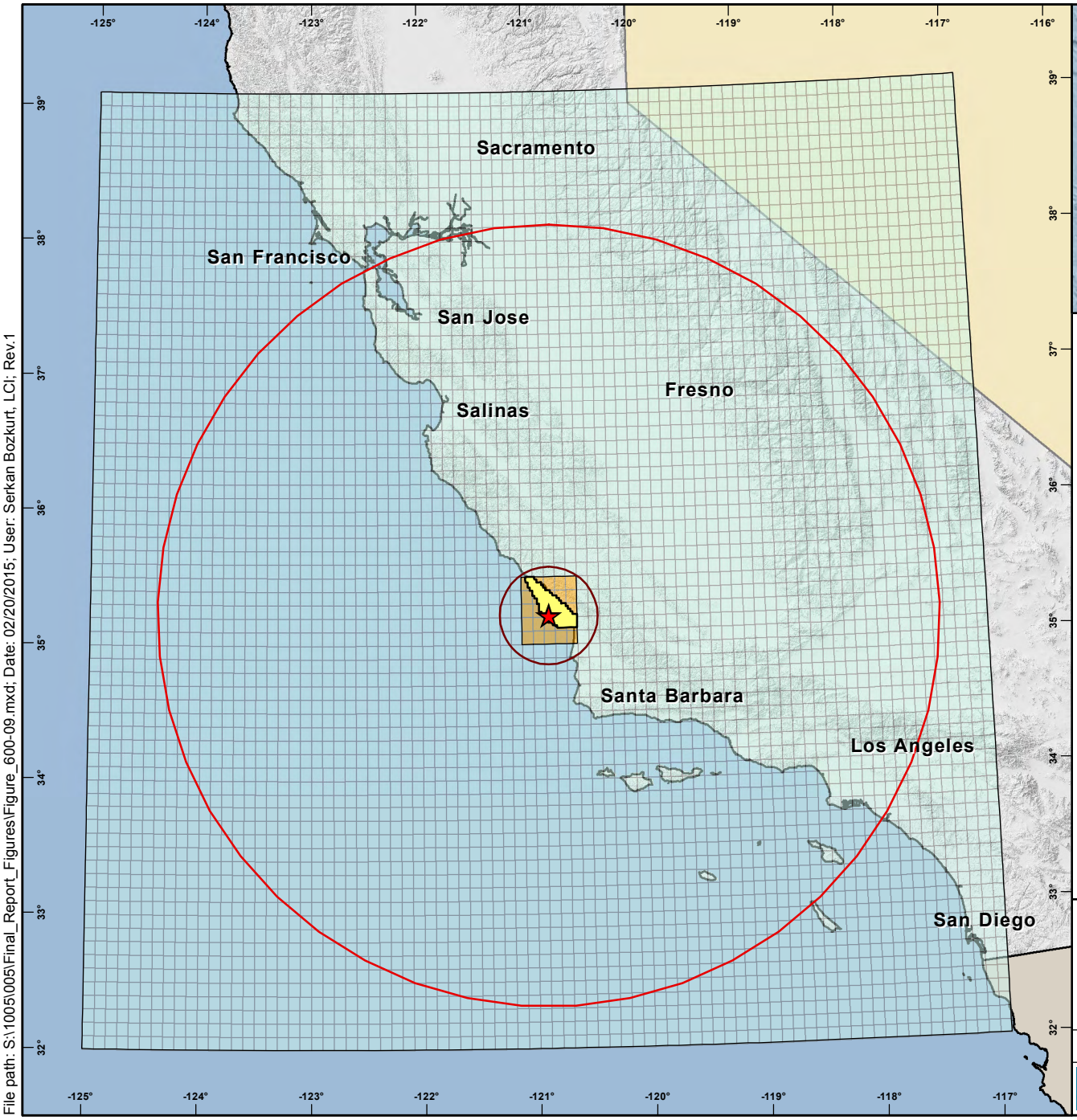

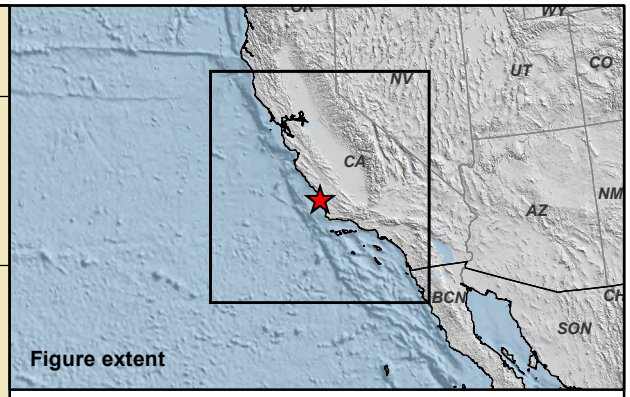

EXPLANATION

- DCPP
- 40 km (25 mi.) DCPP site vicinity boundary
- 320 km (200 mi.) DCPP site region boundary
- Local areal source zone
- Vicinity areal source zone
- Regional areal source zone

Note: 0.1° Grid from the 2008 National Seismic Hazard Mapping Project (NSHMP; Petersen et al., 2008).

N

0 50 100 mi.

0 100 200 km

Map projection and scale: WGS 84 / UTM 10N, 1:5,000,000

Areal Source Zones Used in the Diablo Canyon SSC Model

DCPP SSC REPORT

Pacific Gas and Electric Company | Figure **6-9**

File path: S:\1005\005\Final_Report_Figures\Figure_600-09.mxd; Date: 02/20/2015; User: Serkan Bozkurt, LCI; Rev.1

7.0 FAULT GEOMETRY MODELS

This chapter describes the development of alternative Fault Geometry Models (FGMs) that are used to characterize Primary and Connected fault sources.

7.1 Definition and Applicability

Alternative FGMs are used in this seismic source characterization (SSC) model to capture the range and uncertainty in epistemic assessments related to location and geometry (length, dip, width, connectivity) and style of faulting for Primary and Connected fault sources listed in Table 6-2. Each Primary and Connected fault source listed in Table 6-2 is divided into fault sections that are named with two-letter codes, as listed in Table 6-5 and are shown on maps on Figures 6-5 and 6-6.

The Primary and Connected faults and fault sections are simplified representations of individual faults that are recognized in the Diablo Canyon Power Plant (DCPP) vicinity based on the interpretation of geologic, seismologic, geomorphic, and geophysical data. The location, geometry, and style of faulting for each Primary and Connected fault, including each individual fault section, are based on observations from the actual fault. A map of Quaternary faults in the DCPP vicinity is provided on Plate 7-1.

Epistemic uncertainty in fault location, geometry, and style of faulting is accounted for in the SSC model through the weighted combination of the alternative FGMs (Figure 6-1).

7.2 Approach

The alternative tectonic models described in *Section 5.4* (that are consistent with the available geologic and seismicity data) suggest that different FGMs are viable to explain the interaction between Primary and Connected faults in the study area. The general approach to developing the FGMs involved developing models that were internally consistent with and representative of key aspects of postulated tectonic models, while also capturing the uncertainty and range of values permitted by geologic and seismologic data for specific parameters, such as fault dip and sense of slip.

There are three alternative FGMs for the Hosgri fault source and three alternative FGMs for the San Luis–Pismo block (SLPB) fault sources. Collectively, the weighted FGMs characterize the center, body, and range of viable fault geometry. The FGMs for the Hosgri fault sources primarily address uncertainty in the dip of the Hosgri fault for the reach of the fault adjacent to the DCPP. The three FGMs for the SLPB fault sources reflect the SSC model attribute that the uncertainties in fault location, dip, and connectivity are correlated among the faults within the SLPB. The three Hosgri FGMs and three SLPB FGMs form nine possible FGM combinations for the Primary fault sources in the SSC model (Table 7-1).

Table 7-1. Fault Geometry Models and Logic Tree Combinations

Hosgri FGMs	SLPB FGMs		
	Outward-Vergent (OV)	Southwest-Vergent (SW)	Northeast-Vergent (NE)
Hosgri 90 (H90)	H90/OV	H90/SW	H90/NE
Hosgri 85 (H85)	H85/OV	H85/SW	H85/NE
Hosgri 75 (H75)	H75/OV	H75/SW	H75/NE

The following sections (*Sections 7.2.1 through 7.2.4*) provide a general discussion of the approach used to develop the FGMs. The first two sections describe generic parameters common to all the FGMs: *Section 7.2.1* presents an evaluation of seismogenic thickness, and *Section 7.2.2* presents an evaluation of depth to the top of blind faults. The next two sections describe the approach used to characterize fault geometry (i.e., fault location and dip; *Section 7.2.3*) and style of faulting (i.e., sense of slip; *Section 7.2.4*).

Section 7.3 provides a description of the Hosgri FGMs, focusing on the location and dip of the fault adjacent to the DCPP. *Section 7.4* introduces the three SLPB models, and describes features that are common to the three models. The following subsections describe the unique features of each model (i.e., features that are not common to all three models): the Outward-Vergent (OV; *Section 7.4.1*), Southwest-Vergent (SW; *Section 7.4.2*), and Northeast-Vergent (NE; *Section 7.4.3*) models. For the SLPB FGMs, possible analogs from recent historical fault ruptures are presented to illustrate possible geometric relationships among the faults included in the three FGMs. These analogs from actual earthquake sequences show that each of the FGMs has precedence and is tectonically viable. These analogs also are used to assess possible rupture sources as described in *Section 9.2. Section 7.5* discusses the overall logic tree and weighting of the alternative SLPB FGMs in the SSC model.

7.2.1 Seismogenic Thickness and Depth of Faulting

The thickness of seismogenic crust defines the depth extent of ruptures that release seismic energy important to ground motions. In this SSC model, seismogenic thickness is estimated based primarily on the depth distribution of earthquake hypocenters, and secondarily on consideration of the location of the top of the remnant slab of oceanic crust inferred from deep crustal seismic data, which ranges between 12 km and 16 km in the Diablo Canyon area (*Section 5.1.5*; Figure 5-4).

A measure that is commonly used to estimate seismogenic thickness is the D90 or D95 depth, the depth above which 90% or 95% of earthquakes occur. This approach has been used in other recent SSHAC Level 3 PSHA studies, such as in the Central and Eastern United States (EPRI et al., 2012) and at the Hanford site in eastern Washington (PNNL, 2014). The rationale for using the D90 value is based on physical considerations that suggest that the base of the seismogenic zone occurs near the base of observed focal depths, as reported by the following authors:

- Sibson (1982, 1986) identified the maximum depth of seismogenic faulting as the transition from brittle faulting to plastic flow in the continental crust.
- Scholz (1998) identified the 300°C isotherm as corresponding to the onset of dislocation creep in quartz, which he interprets to control the seismic/aseismic transition zone.
- Tanaka and Ito (2002) and Tanaka (2004) compared high-quality thermal measurements and seismicity depth data to evaluate the concept that temperature is a fundamental parameter for determining seismogenic thickness. The gridded heat flow or geothermal gradient and the D90 value correlate well with each other. The evaluated temperatures for D90 range between 250°C and 450°C, which falls within the typical range for defining the seismogenic zone (e.g., Fagereng and Toy, 2011).

The D90 and D95 values for the DCPP study region were calculated using an areal subset of the Hardebeck (2014a) earthquake catalog. The boundary of the approximately rectangular subset, which is shown on Figure 7-1, was selected to focus on the DCPP vicinity. As shown on Figure 7-1, the subset includes seismicity near the Hosgri and Shoreline faults, the SLPB, Los Osos and Edna Valleys, and offshore in Estero and San Luis Obispo Bays. The northeast corner of the subset boundary is trimmed to exclude seismicity of the 2003 San Simeon earthquake sequence and triggered seismicity of the West Huasna fault (McLaren et al., 2008). As calculated from seismicity within the polygon shown on Figure 7-1, the D90 and D95 values are 10.5 km and 12.6 km, respectively (Figures 7-1 and 7-2). Events at 12 km and deeper, shown in dark blue on Figure 7-1, concentrate near the intersection of the Shoreline and Hosgri faults and in a concentrated area of Estero Bay north of the Los Osos fault.

Sensitivity analyses presented at Workshop 1 (Wooddell, 2011; *Appendix D*) show that variability in depth of seismogenic faulting has very little effect on hazard at the DCPP. Accordingly, epistemic uncertainty is not characterized for this parameter. Based on consideration of the D90 and D95 values in the Diablo Canyon area and the estimated depth to the top of the subducted slab, a single value of 12 km is used for the average depth of faulting for all SLPB fault sources. This value is consistent with the results of inversion of seismic and geodetic data sets from the 2003 moment magnitude (**M**) 6.6 San Simeon earthquake that indicated shallow rupture from 1 km to 10 km depth (Rolandone et al., 2006).

The Hosgri fault geometry is characterized as having a depth of 15 km for earthquakes larger than *M* 7.4, and a depth of 12 km for smaller earthquakes. The greater depth for the Hosgri fault geometry is based on the following considerations:

1. Possible disruption of the slab at the Hosgri fault zone (HFZ) as interpreted by Meltzer and Levander (1991; Figure 5-4), which suggests that ruptures may not be limited by the slab.
2. Observations of mainshock/aftershocks deepening observed during the M 7.3 1992 Landers earthquake (Rolandone et al., 2004)

3. Modeling results show the maximum depth of aftershocks is initially high and decreases with time, suggesting a transient deepening of the brittle-ductile transition depth generated by high strain rates of the main shock (Ben-Zion and Lyakhovsky, 2006)

Rolandone et al. (2004) used seismic data to constrain the change in the depth of the seismic-aseismic transition (which they correlated with $d_{5\%}$, the average depth of the deepest 5% of earthquakes) with time throughout the earthquake cycle. The amplitude (a few kilometers deeper) and duration (a few years) of the depth change were interpreted to be related to a mechanical control on the temporal distribution of deep earthquakes and on the depth of the seismic-aseismic transition. This strain rate dependence was judged to be more important than temperature variations in defining the brittle-ductile boundary.

7.2.2 Depth to Top of Rupture

The Los Osos fault is assumed to be blind along the reach adjacent to the Irish Hills in all three SLPB FGMs based on the absence of a recognizable, continuous surface trace that could accommodate the full vertical separation of the Irish Hills from the Los Osos Valley. Instead, the surface trace consists of a broad zone of distributed minor faults and shears (Plate 7-1), such as those observed in the Cuesta and Ingley trenches (Lettis and Hall, 1994) and localized tilting of the Paso Robles Formation along the range front at the Memorial Park surface, east of the town of Los Osos (see discussion in *Section 8.2.2.3*).

The San Luis Bay fault is also assumed to be blind in all three SLPB FGMs. The San Luis Bay fault was initially recognized from the recognition of multiple surface fault traces west of the city of Avila Beach, each of which accommodates a small fraction of the total vertical separation across the fault zone (PG&E, 1990c; Lettis et al., 1994), and deformation of marine terraces on the outer coast of the Irish Hills at the Rattlesnake fault and Olson fault (Hanson et al., 1994; locations shown on Plate 7-1). As described in *Section 5.2.3*, recent work has shown that deformation of marine terraces is better characterized as a zone of deformation between the Rattlesnake trace and Olson Hill (PG&E, 2011). The TI Team interprets the San Luis Bay fault to be mostly blind based on the absence of a single, continuous surface trace, and the observation that most of the fault deformation is distributed within a zone of approximately 1 to 2 km (Plate 7-1).

For both faults, the depth of the inferred fault tip is uncertain, but is judged to be relatively shallow. Based on the narrowness of the zone of tilting and faulting associated with both faults, the TI Team interprets the fault tip to be non-zero and less than approximately 2 km below the surface. A single value of 1 km for the depth to the top of both fault sources is used for this SSC model. Given the range of technically defensible depths, the TI Team considers uncertainty in the depths of the Los Osos and San Luis Bay fault tips to have relatively little effect on the overall hazard at the DCPP and judges this simplification to be justified.

All other faults in the three SLPB models are assumed to reach the ground surface, including the Shoreline fault. The prominent bathymetric lineaments, scarps, faults

observed in shallow seismic-reflection data, and gas seeps along the Shoreline fault trace show that the fault ruptures to the ground surface.

For all three HFZ models, the HFZ is assessed to reach the ground surface. Similar to the Shoreline fault, the geomorphic expression of the HFZ includes fault scarps, breaks in slope, and bathymetric lineaments showing that the fault ruptures to the seafloor surface. In addition, shallow high-resolution seismic-reflection data show that traces of the HFZ extend to within the upper few meters of the seafloor along most of its length (PG&E, 2013b).

7.2.3 Fault Geometry

The location and downdip geometry of Primary and Connected fault sources are based on consideration of five types of data:

1. Quaternary fault maps based on interpretation of onshore and offshore stratigraphic, structural, and geomorphic data.
2. Geologic mapping of Quaternary geomorphic surfaces (in particular, marine terraces) used to identify the locations of boundaries of active deformation as indicated by different vertical rates of uplift or subsidence.
3. Spatial patterns of both epicenters and hypocenters of microseismicity.
4. Focal mechanism data providing information on style of deformation, which carries implications for fault geometry.
5. Onshore and offshore seismic-reflection data that provide constraints on location and downdip geometry.

A compilation map showing locations and approximate slip rates of Quaternary faults in the study region is provided on Plate 7-1. These fault traces were compiled from numerous studies. Locations, geometry, and slip rate for most offshore faults were compiled from the following studies:

- PG&E (2014, Chapter 3): “Offshore Low-Energy Seismic-Reflection Studies in Estero Bay, San Luis Obispo Bay, and Point Sal Areas.” Fault locations and slip rates interpreted mainly from high-resolution, low-energy 3D and 2D seismic-reflection data, supported by evaluation of high-resolution bathymetric data, older high-energy low-resolution 2D seismic-reflection data, existing well data, and regional magnetic and gravity data.
- PG&E (2013a): “Stratigraphic Framework for Assessment of Fault Activity Offshore of the Central California Coast between Point San Simeon and Point Sal.” Quaternary fault locations and rates of vertical separation interpreted from high-resolution single-channel 2D seismic-reflection data collected by the U.S. Geological Survey (Sliter et al., 2010).
- PG&E (2011): “Report on the Analysis of the Shoreline Fault Zone, Central Coastal California.” Fault location and activity along seismicity alignments interpreted from geomorphic expression in high-resolution multibeam echosounder (MBES) bathymetric data collected by the California State

University Monterey Bay Seafloor Mapping Lab in 2007, 2008, and 2010 (CSUMB,

- 2012) and by the USGS in 2012 (Hartwell et al., 2013).

In the onshore DCPP site area and site vicinity, the original mapping and compilation of Quaternary faults from the LTSP (PG&E, 1988; Lettis et al., 2004) were updated based on a compilation bedrock map (AMEC, 2011) and recent mapping by the California Geological Survey (Wiegers, 2009, 2010, 2011, 2013). Paleoseismic observations that provided evidence for Quaternary activity as previously documented from detailed mapping of trenches, natural and road cut exposures (PG&E, 1988; Lettis et al., 1994; Nitchman and Slemmons, 1994) were supplemented by information from more recent LTSP and AB 1632 mapping programs (PG&E, 2013b; PG&E, 2014, Chapter 9).

The Primary and Connected fault sources are simplified line representations of the actual geologic faults. The mapped traces of the actual faults are shown on Plate 7-1 and a comparison of the fault sources to the mapped fault traces is presented on Figure 7-3. This type of simplification is illustrated by the relationship between the onshore and offshore sections of the Los Osos fault. As shown on Plate 7-1, there is an apparent 4-km wide right step between the onshore and offshore traces of the Los Osos fault. The offshore trace of the fault that splays to the southeast from the HFZ and bends eastward in southern Estero Bay. However, a seismicity alignment beneath Estero Bay that underlies the northern part of the offshore Los Osos fault extends to the southeast, beyond where surface traces of Quaternary faults bend to the east (Hardebeck, 2014b). This structural complexity is associated with several features that suggest it may arrest earthquake ruptures with significant frequency (e.g., step-over width, presence of an actively subsiding basin), and is therefore considered in the definition of rupture sources (*Chapter 9*) and the assessment of magnitude frequency distributions (*Chapter 10*). However, based on comparison to empirical data regarding rupture terminations (e.g., Lettis et al., 2002; Wesnousky, 2008; Wesnousky and Biasi, 2011; Biasi, Parsons, et al., 2013), the TI Team does not consider this step-over to be sufficiently wide to prohibit joint rupture of the onshore and offshore Los Osos fault. Therefore, for the three FGMs, this structural complexity is simplified into a single Connected fault source.

For all three models, the Primary and Connected fault sources are divided into fault sections, as described in *Section 6.1* and shown on Figure 7-3. The fault sections are distinct reaches of each fault source. Each fault section is specified to define a unique set of surface coordinates that constitutes the surface location, or updip projection, of a particular reach of a fault source. Not all fault sections are included in every FGM. Boundaries between fault sections are specified at locations where fault sources intersect in at least one FGM. Two exceptions are discussed below. Fault sections are allowed to rupture together in various combinations, as alternative rupture sources involving sets of fault sections, as described in *Section 9.2*. Each fault section is given a unique two-letter code as shown in Table 6-5.

The two exceptions are defined at locations along a fault where changes in slip rate, or structural complexities are used to define possible endpoints of rupture sources (*Section*

9.2.1.3) or rupture lengths for estimation of characteristic or maximum earthquake magnitude (*Section 10.2.2*). One fault section boundary is defined between the offshore Los Osos fault (LC) and the onshore Los Osos fault (LM) based on differences in interpreted fault behavior within the current tectonic regime. The significant change in fault strike at this boundary suggests that the LC section may accommodate a different sense of slip from the LM section. Variations in the sense of slip are described by the alternative FGMs in *Section 7.4*. In addition, the presence of a step-over and subsiding basin suggests that earthquake ruptures preferentially terminate at this location as described in *Chapters 9 and 10*. A fault section boundary was established at this boundary to account for that possibility.

The other exception was established between the two sections of the Los Osos fault that border the Irish Hills: LM and LV. These sections are distinguished based on differences in evidence for surface faulting and differences in the likely rate of vertical separation across the fault. Section LM is not associated with any surface traces and is interpreted to be completely blind. It also separates the western Irish Hills, which includes strong evidence for active Quaternary uplift, from Morro Bay, which includes evidence suggestive of localized subsidence (as described more completely in *Section 8.5.1*). Section LV is characterized by a broad zone of surface fault traces, with each fault trace exhibiting evidence for little cumulative offset. This reach is associated with secondary evidence for relative uplift of the Irish Hills in the hanging wall of the fault (i.e., geomorphic evidence, but no marine terraces), and geomorphic evidence for uplift of the footwall also, but likely at a lower rate (e.g., marine terraces in the Edna Valley described by PG&E, 2013b).

Figure 7-4 shows a generalized map of uplift rate contours of the SLPB and surrounding area. These uplift patterns represent a primary constraint on location and rate of faulting in the DCPP vicinity. Fault geometries for the Primary and Connected fault sources were considered by the TI Team to be permissible only if slip on the faults will produce this general pattern of vertical deformation. The TI Team recognizes that other mapped faults (and possibly other blind faults) in the SLPB area may be capable of producing moderate to large earthquakes. However, the TI Team judges that the slip rates of these other faults must be sufficiently low so as not to affect the observed uplift rate pattern. This category of other possible faults are considered as part of the areal source zones in the Diablo Canyon SSC model (*Section 6.5* and *Chapter 13*).

The patterns of uplift shown on Figure 7-4 are interpreted to be the surface expression of deformation on faults that dip beneath the San Luis Range (PG&E, 1988; Lettis et al., 1994). The dip of faults that drive uplift of the SLPB are interpreted to correspond to the width of the uplifted area. Each alternative FGM represents a set of internally consistent fault geometries that explains the overall pattern of uplift of the SLPB and surrounding region. Therefore, the dimensions of reverse faults under the SLPB are considered only if they are sufficient (both in width and downdip extent) to be able to accommodate the relatively uniform uplift recorded in the marine terraces along the outer coast of the block. In effect, the variability of dips considered are defined by the width of the range, and the seismogenic thickness.

Models that assume the San Luis Range is uplifting on a primary reverse fault underlying the entire range have dips that are less steep than models that assume the range is uplifting on two oppositely verging structures. Shallow thrust geometries for either the Los Osos or San Luis Bay faults that would extend beyond the width of the range before reaching seismogenic depth, or very steeply dipping faults on both sides of the range that would not satisfy this first-order constraint of uplift of the range, were not included in any of the alternative SLPB models. The dip of individual fault sections—including bends in the fault along its downdip width—are different between each FGM. The full range of fault dip for each of the Primary faults that is consistent with available data is represented by the full set of dips for that Primary fault in each of the three FGMs.

Spatial patterns and alignments of seismicity were carefully reviewed to evaluate the downdip geometry of possible active faults within the site vicinity, particularly within the San Luis Range and Irish Hills close to the DCPP. Seismicity data were most effective in defining the downdip geometry of vertical to near-vertical faults, such as the Hosgri and Shoreline faults (e.g., Hardebeck, 2010, 2013). Microseismicity within the Irish Hills and San Luis Range as a whole is much more diffuse, and, despite attempts to define trends objectively using algorithms such as the optimal anisotropic dynamic clustering (OADC) algorithm (e.g., Hardebeck, 2014b), the TI Team judges that it does not clearly or definitively provide convincing evidence for well-defined fault geometries at depth (*Section 13.5.2*). The ambiguity in association of microseismicity with specific faults within the Irish Hills and adjacent offshore regions of Estero Bay led, in part, to the decision to include a Local areal source zone in the SSC model (*Section 13.5*).

7.2.4 Sense of Slip (Style of Faulting)

Section 5.5 provides a discussion of the seismologic and geologic data that have been used to assess the overall contemporary style of deformation in the DCPP site vicinity and surrounding region. Definitions of various styles of faulting in this SSC model are from Aki and Richards (1980) and are consistent with the definitions used for the ground-motion-characterization models:

- Reverse event (rake of 90° ± 60°; includes what are commonly referred to as reverse oblique events)
- Strike-slip event
  - Right-lateral (rake of 180° ± 30°)
  - Left-lateral (rake of 0° ± 30°)
- Normal event (rake of –90° ± 60°)

The sense of slip on any one fault depends on the orientation and dip of the fault within the contemporary stress field. As described in *Section 5.1.6*, the orientation of the principal compressional stress axis within the Irish Hills is N10–20°E, and the sense of predicted slip on faults is shown on Figure 5-12. This analysis shows that the predicted slip would be primarily reverse faulting on the Los Osos and San Luis Bay faults, and strike-slip faulting on the Hosgri and Shoreline faults.

The HFZ was interpreted by Hanson et al. (2004) to be a convergent right-slip fault in the contemporary tectonic setting based on an integrated analysis of a broad spectrum of data, as follows:

- Shallow high-resolution, seismic-reflection data,
- Deep-penetration seismic-reflection data.
- Geologic and geomorphic data along the Hosgri and San Simeon fault zones.
- The distribution and nature of near-coast seismicity,
- Regional tectonic kinematics.
- Comparison of the HFZ with worldwide strike-slip, oblique-slip, and reverse slip fault zones.

More recent studies using high-resolution seismic-reflection data (Johnson and Watt, 2012; PG&E, 2013a; PG&E, 2014, Chapters 2 and 3) and the distribution of seismicity along the fault (Hardebeck, 2013; Figure 5-17) document nearly pure strike slip on a near-vertical to steeply (~75°) east-dipping fault to a depth of 12 km. Therefore, the sense of slip for the Hosgri fault rupture sources is strike slip.

The sense of slip for the Shoreline fault rupture sources in the SSC model also is strike slip. This assessment reflects the distribution of seismicity and focal mechanisms along the fault (Hardebeck, 2010, 2013; Figure 5-18) and interpretations of high-resolution 3D seismic-reflection data that provide information to assess vertical and horizontal separation of piercing points (PG&E, 2014, Chapters 2 and 3). The best-constrained piercing point for the Shoreline fault, a terrace sequence imaged in the 3D seismic-reflection data in San Luis Obispo Bay, suggests a horizontal-to-vertical (H:V) ratio of approximately 10:1 (see discussion in *Section 8.4*).

The sense of slip for Primary and Connected fault sources in the SLPB group is reverse in all FGM, with a minor component of lateral slip (obliquity) that varies among the three models. Fault sources in the SLPB group accommodate more purely reverse slip the NE and SW Models. The strike-slip component of slip for the San Luis Bay and Los Osos faults is greater in the OV Model. The rake of the San Luis Bay and Los Osos fault sources is described in *Section 8.6.1* and *Section 8.5.1,* respectively.

7.3 Hosgri Fault Zone Geometry Models

This section describes key parameters that are addressed by the Hosgri FGMs:

- Fault location: evaluation of alternative fault maps to define the best-constrained fault source location and range of uncertainty about that location, particularly at the closest approach to the DCPP.
- Fault dip: summary of available constraints on the dip of the HFZ, particularly at the closest approach to the DCPP.
- Fault length: evaluation of the length of the HFZ as a seismic source.

7.3.1 Fault Location Adjacent to the DCPP

Mapping of the HFZ has evolved over time as additional data sets, primarily seismic-reflection survey and improved MBES bathymetry data, have become available (Figure 7-5). The following interpretations for the reach of the HFZ adjacent to the DCPP were examined to evaluate the location and closest approach of the HFZ:

- Willingham et al. (2013): This publication presents the general interpretation of the geometry and location of the HFZ that was presented by PG&E (1988, 1991) based on analysis of high- and low-energy seismic-reflection data from numerous surveys collected for different purposes from the 1970s to 1980s. Faults are mapped as "structural trends" representing a combination of shallow and deep (~2 km) faults.
- Johnson and Watt (2012): This publication presents an interpretation of the near-surface location of traces of the HFZ based on interpretation of high-resolution 2D Sparker seismic-reflection data (800 m spacing) and bathymetry. The faults were mapped at a scale suitable for publication on a 1:35,000 scale map (Watt et al., in preparation), although they were presented at a much smaller scale by Johnson and Watt (2012): Digital fault traces were provided electronically to PG&E as part of a draft offshore geologic map (J. Watt, pers. comm. to H. AbramsonWard, Dec. 10, 2013; see *Section 4.3.2.1* for more detailed description of data sets).
- PG&E (2011): A preliminary interpretation of the near-surface traces of the HFZ, based on the 2D seismic-reflection data and bathymetry sets used by Johnson and Watt as described above, was completed as part of the assessment of the Shoreline fault zone.
- PG&E (2014, Chapter 3): A more comprehensive map of the HFZ is compiled from the mapping performed in conjunction with development of a seismic stratigraphic framework based on analysis of the USGS high-resolution 2D seismic-reflection data released by Sliter et al. (2010; PG&E, 2013a) and interpretation of new 3D and 2D seismic-reflection data collected for PG&E (PG&E, 2014, Chapters 2 and 3).

Several observations pertinent to the assessment of the location and closest distance of the Hosgri fault to the DCPP are made based on the evaluation of these data sets and interpretations:

- The HFZ is the best-imaged and most continuous fault zone in the DCPP site area. In all of the studies, the HFZ near the site is mapped as a distributed zone of faults.
- Locally, strands of the fault zone exhibit seafloor expression, either as erosional fault-line scarps, which generally occur where bedrock is juxtaposed against sediment by the fault, or possibly also as tectonic scarps within young sediment, which are inferred to represent displacement during relatively recent faulting events that ruptured the seafloor. Multiple strands show evidence for Quaternary activity (Figure 7-6).

- The 3D/2D LESS data set shows that the HFZ is more complex near the surface (at depths less than ~400 m) than previously mapped (PG&E, 1988; PG&E, 2011b).
- Despite variations in complexity, most maps of the HFZ show fault traces aligning in three primary zones within the reach directly offshore of the DCPP (Figure 7-7).

We recognize that future earthquakes on the HFZ could occur on any of the three primary fault strands that are mapped in the near surface. In order to capture this aleatory variability in the location of future HFZ ruptures, three near-surface traces are modeled, referred to as the eastern, central, and western traces, which are at distances of 4 km, 5 km, and 6 km, respectively, from the DCPP as shown on Figure 7-7.

7.3.2 Fault Dip

The geometry of the fault zone at depth is inferred primarily from seismicity data. Hardebeck (Workshop 2 presentation, 2012c; 2013) evaluated fault dip from first-motion polarity (Figure 7-8). Evaluations were made using the OADC algorithm and seismicity from the Hardebeck (2010) earthquake catalog. As described in *Appendix F*, alternative earthquake locations were calculated from two different double-difference relocation algorithms, hypoDD (Waldhauser and Ellsworth, 2000) and tomoDD (Zhang and Thurber, 2003). The hypoDD locations were shown to be incompatible with composite first-motion polarities using the OADC algorithm (Figure 7-8a). The analysis using the tomoDD locations did provide a compatible mean solution with a dip of 76°–89° NE. The rake derived from the fit of focal mechanism data is 180° ± 24° (Figure 7-8b; Hardebeck, 2013).

Previous studies (McLaren and Savage, 2001; Hanson et al., 2004; PG&E, 2011) concluded that microseismicity interpreted to be associated with the HFZ is consistent with a steeply dipping to vertical fault to seismogenic depth (e.g., Figure 5-17). Modeling of gravity and magnetic data presented by J. Watt at Workshop 2 also supports a vertical to steeply east-dipping fault in the shallow crust (≤15 km; Watt, 2012). A near-vertical to steeply east-dipping fault was also interpreted by Willingham et al. (2013) based on interpretation of high-energy 2D seismic-reflection data, which images the upper 2–4 km of crust.

For the three Hosgri FGMs, the Hardebeck (2010) tomoDD locations and Hardebeck (2014a) catalog were used to evaluate possible geometries of the three fault traces at depth. To support this evaluation, the TI Team attempted to separate seismicity beneath the surface traces of the Hosgri fault from seismicity to the east. Within San Luis Obispo Bay, seismicity beneath the surface traces of the Hosgri fault forms a near-vertical cloud extending from the surface to approximately 12 km depth. To the north faults within the SLBP merge with the Hosgri (e.g., the Shoreline and Los Osos faults, and seismicity associated with the SLBP overlaps with Hosgri fault seismicity. Figure 7-9 shows seismicity within the DCPP vicinity projected onto a plane perpendicular to the strike of the HFZ. Earthquake hypocenters are shown in color, classified by depth, surrounded by

circles or diamonds that illustrate the approximate uncertainty in hypocentral location. Colored dots are part of the cloud beneath the surface traces of the Hosgri fault and to the west. Diamonds are hypocenters that are:

- part of the Shoreline seismicity alignment (Hardebeck, 2010, 2013) located farther than 2.5 km east of the nearest trace of the Hosgri fault,
- part of the seismicity lineaments within Estero Bay that were discussed by Hardebeck at the Diablo Canyon SSHAC Workshop 3, and associated with strike-slip focal mechanisms (Hardebeck, 2014b), or
- diffuse seismicity to the east.

Plus symbols are hypocenters that do not clearly underlie surface traces of the Hosgri fault (i.e., they are located at relatively shallow depth and more than approximately 1 km east of the nearest Hosgri surface trace, but are located west of the seismicity lineaments described above.

Three alternative geometries are drawn relative to the seismicity beneath the surface traces of the HFZ, as shown on Figure 7-10. These alternative geometries are intended to capture the following information:

- The range of uncertainty indicated by the scatter of hypocenters in the current catalogs.
- The stated uncertainties in hypocentral locations.
- The possibility that systematic errors in hypocentral locations may exist within the current catalogs because of both uncertainty in the crustal velocity model and poor azimuthal coverage (the recordings of these earthquakes come only from onshore).

Figure 7-11 compares the three alternatives and supporting arguments for each. The weights assigned to the three models in the SSC logic tree reflect the judgment of the TI Team regarding the likely geometry of the three surface traces at depth. The preferred model (H85) is given a weight of 0.6 because it provides a reasonable fit to the seismicity and is consistent with the common depth point (CDP) seismic profiles (e.g., Figure 5-17) that show evidence of flower structures along this reach of the HFZ (Willingham et al., 2013). This dip is also most consistent with the mean dip inferred from the tomoDD OADC planar solutions (Hardebeck, 2012c; 2013) (Figure 7-8b). The alternative downdip geometries (H75 and H90), which are each given a weight of 0.2, represent end-member cases that cannot be precluded based on available data. The H75 Model allows for the possibility that there may be a systematic offset of hypocenters from the fault such that the HFZ could lie slightly east of the seismicity that defines the fault zone at depth. Possible future data, such as recordings from ocean bottom seismometers recently installed by PG&E (PG&E, 2014, Chapter 5), could potentially reveal such a systematic offset. In the TI Team evaluation, shallower dips to the HFZ are not consistent with the seismicity data, magnetic data, or seismic-reflection data and are not considered to be technically defensible. The H90 Model represents the opposite end member. This model fits the seismicity data, and approximately corresponds with the maximum dip indicated from the OADC algorithm (Hardebeck, 2012c). It is also less consistent with

interpretation of high-energy seismic-reflection data the fault dips steeply to the east, and that the fault traces at the surface generally converge to a single trace at depth (Willingham et al., 2013).

7.3.3 Fault Length

The Hosgri FGM has one length. The fault extends from the south end of the HFZ as previously mapped by PG&E (1988) and Willingham et al. (2013) north to a point offshore of Cambria where the name changes to the San Simeon fault. The HFZ is directly linked to the San Simeon, San Gregorio, and San Andreas faults to the north, and the north end of the Hosgri FGM is the Mendocino Triple Junction, at the north end of the San Andreas Fault (Figure 7-3). Possible boundaries that would influence rupture propagation on the HFZ and the estimated M_{max} and M_{char} distributions for the HFZ are discussed in *Chapters 9 and 10*, respectively.

7.4 San Luis–Pismo Block Fault Geometry Models

Three alternative FGMs were developed for faults within and bordering the SLPB. These are illustrated in a series of four cross sections developed for each model. The locations of the cross sections, which are drawn perpendicular to the axis of the San Luis Range, were designed to cross key areas of surface data constraints, as numbered on Figure 7-12. The key data constraints are as follows:

1. North end of marine terrace flight (Hanson et al., 1994): The juxtaposition of this evidence for active uplift against evidence for active subsidence beneath Morro Bay, directly to the north, was used by Lettis and Hall (1994) to define the location and slip rate of the Los Osos fault.
2. Memorial Park surface (PG&E, 2013b) and ONSIP Vibroseis Line 204 North (PG&E, 2014, Chapter 7): The Memorial Park surface is a gently sloping terrace of marine or alluvial origin has a very thick soil developed on the surface, suggesting significant antiquity. Where it crosses the approximate projection of the Los Osos fault as mapped by Lettis and Hall (1994) there is no pronounced surface scarp, but the terrace may be warped, suggesting possible deformation by a blind fault (*Section 8.2.2.3*). The ONSIP Vibroseis Line 204 images reflectors within the upper 10,000 ft (~3 km) beneath the northern range front of the Irish Hills and Los Osos Valley beneath the Memorial Park surface. Alignments of truncated reflectors were interpreted by the ONSIP team as possible blind traces of the Los Osos fault, which dip approximately 60° or 75° to the south (Figure 7-14).
3. Bedrock ridge (PG&E, 2014, Chapter 9): A ridge of chert extends northward from the body of the Irish Hills and crosses the zone of faults and lineaments mapped by Lettis and Hall (1994) as the Los Osos fault, indicating the absence of a pronounced active range-front fault.
4. LiDAR analysis of stream channels (PG&E, 2014, Chapter 9): Analysis of streams that cross the range front on the north side of the Irish Hills indicates

equal numbers of right-deflected and left-deflected channels, suggesting low rates or no lateral fault slip.

5. Marine terrace remnants in Edna Valley (PG&E, 2013b): These terraces provide evidence for uplift of the tectonic block that includes the Edna and Los Osos valleys at a low rate.
6. Seismic-reflection data at the Plains Exploration & Production (PXP) facility (PG&E, 2013b): Seismic-reflection data collected across the northern range front of the Edna sub-block of the SLPB image near-vertical fault traces within the eastern part of the Los Osos fault zone.
7. Sea-cliff exposure of the Wilmar Avenue fault (Lettis et al., 1994; Nitchman, 1988; Nitchman and Slemmons, 1994): Faulted marine oxygen-isotope stage (MIS) 5 marine terrace demonstrates the presence of a Quaternary-active surface fault trace. Tilting of terraces indicates that full vertical separation is distributed more broadly than a single fault trace.
8. Rattlesnake trace of San Luis Bay fault (Lettis et al., 1994): An abrupt step in marine terrace platforms and back edges indicates fault surface rupture during the Quaternary that is less than the full vertical separation of the Irish Hills from San Luis Hill.
9. Olson Hill/Green Peak (PG&E, 2011): Approximate northern limit of tilting of marine terrace strandlines. Northwest of this point, the pattern of marine terrace strandlines suggests uniform block uplift (*Section 8.2.2.1*).
10. Marine terrace exposures north of Cayucos (*Section 8.2.2.2*): A sequence of marine terraces provides evidence for low rates of crustal uplift in a tectonic block north of the Los Osos fault.

The following subsections describe the subsurface geometry and relationships of the Primary and Connected fault sources within each model. The downdip geometry of the fault sections—including bends, changes in dip and related changes in width, and angular relationships between branching fault sources—are different between FGMs. The geometry at depth of the faults that bound the uplifting San Luis Range are not well constrained by seismicity or the limited available seismic-reflection data. Consequently, the TI Team considers a range of alternative fault dips such that the fault widths scale approximately with the width of the uplifting range, as described in *Section 7.2.3*. As a result, the dip of the primary fault or faults accommodating the uplift vary along strike as the width of the range changes.

The main difference between the three FGM is the interpretation of which fault primarily drives uplift of the Irish Hills. In the OV Model, uplift of the Irish Hills is driven jointly by the San Luis Bay fault and the Los Osos fault, both of which dip relatively steeply beneath the range. In the SW Model, the primary ramp driving uplift of the Irish Hills is the San Luis Bay fault, which dips moderately to the north and underlies nearly the entire uplifting Irish Hills. In the NE Model, uplift of the Irish Hills is driven primarily by the Los Osos fault, which dips moderately to the south and underlies nearly the entire uplifting Irish Hills. Within each model, the primary fault that drives uplift of the range is considered to extend to the full seismogenic depth of 12 km, and the fault that bounds the

opposite side of the range is considered to branch upward from the primary fault as a backthrust or axial surface. These "secondary" structures may not extend the full thickness of the seismogenic crust. These differences are described in the following subsections. In all three models, the Shoreline fault is a vertical strike-slip fault with a single location and geometry.

7.4.1 Outward-Vergent Model

The concept of the OV Model is that uplift of the SLPB is produced by transpressional right-reverse faulting along the northeastern and southwestern block boundaries (Figure 7-13). As discussed in *Section 5.4*, transpressional right-reverse faulting in the Diablo Canyon region is a viable tectonic model within the center, body, and range of the technically defensible interpretations. The OV Model is most representative of the regional transpressional (dextral) shear tectonic model. The four representative cross sections are shown on Figures 7-15 (cross sections A-A′ and B-B′) and 7-16 (cross sections C-C′ and D-D′). Both the Los Osos and San Luis Bay faults dip beneath the central Irish Hills toward the root zone of the ancestral Edna fault system, which initially developed as a transtensional fault system in the Miocene (see *Section 5.1.3*). The primary fault in the OV Model that accommodates the most strike-slip motion in the present tectonic setting is the Los Osos fault, which splays from the dextral-reverse Oceano–West Huasna fault at the south end of the Edna Valley (Plate 7-1). However, the lack of geomorphic evidence of strike-slip movement along the northern margin of the San Luis Range (i.e., systematically offset drainages, shutter ridges, etc.) suggests that the amount of strike-slip motion on the Los Osos fault is relatively small compared to the reverse component of slip (PG&E, 2014, Chapter 9). The amount of oblique movement likely varies with strike, with more northerly trending parts of the fault accommodating greater amounts of strike slip consistent with the regional stress/stain field (see discussion in *Section 5.1.6*).

To the west, the offshore part of the Los Osos fault (LC) merges with or splays from the HFZ, potentially as a steeply dipping right oblique-slip fault. The component of strike slip on the Irish Hills section of the Los Osos fault may branch from and be accommodated by distributed shear within Estero Bay, where two distinct near-vertical seismicity lineaments have been identified (Hardebeck, 2014b). This distributed deformation in Estero Bay is accounted for in the Local areal source zone (*Section 13.5*). Alternatively, the component of strike slip on the Irish Hills section of the Los Osos fault may step-over northward to the offshore Los Osos fault, thereby accounting for subsidence of Morro Bay as a right-releasing step-over of the dextral component of slip on the Los Osos fault.

Uplift of the Irish Hills is accommodated in the OV Model by two oppositely verging reverse faults: a south 60° dipping Los Osos fault and a north 75° dipping San Luis Bay fault. A blind Los Osos fault that dips 60° to the southwest is consistent with interpretations by the Onshore Seismic Interpretation Project (ONSIP) team of recently collected seismic-reflection data from the Irish Hills and Los Osos Valley (Figure 7-16; PG&E, 2014, Chapter 7). On the north side of the Irish Hills, the Los Osos fault (LM, LV,

and LO) locally may be part of a positive flower structure, with a more steeply dipping Edna fault in the upper several kilometers (Figure 7-17). The LE fault section (Figure 7-15) is assigned a relatively steep dip of 80° in the OV Model based on the inference that it may be the southeastward continuation of an inferred steeply dipping Edna fault. This flower geometry is consistent with possible strain partitioning (Lettis and Hanson, 1991) between range-bounding reverse faults and steeper strike-slip faults within the range.

In the OV Model, the San Luis Bay fault is truncated by the Shoreline fault to the west; thus the top of the fault is progressively deeper to the north along the plunge line of the intersection of the two faults. Uplift of the continental shelf region west of the Shoreline fault, as indicated by the presence of submerged marine terraces (PG&E, 2011, Appendix I), is assumed to be accommodated by distributed deformation produced by additional minor reverse faulting within the Southwestern Boundary zone, a localized restraining bend in the HFZ, and/or possible distributed folding and faulting up-dip of the San Luis Bay fault (represented by the dashed lines on cross section C-C'; Figure 7-15). Because of the absence of a distinct fault evident west of the Shoreline fault, this zone of distributed deformation is incorporated into the Diablo Canyon SSC model as part of the Local areal source zone (*Section 13.5*). To the east, the San Luis Bay fault terminates at Mallagh Landing (on all three SLPB FGMs), where the higher uplift rate of the Irish Hills ends (Figure 7-4), the onshore flight of marine terraces is not disrupted across the trend of the fault (Hanson et al., 1994), and bathymetric data show unbroken Miocene bedding of the Obispo and Monterey formations that precludes a localized fault bend or fault step across the projection of the fault.

Farther to the east, on the south side of the Edna sub-block of the SLPB (shown on Figure 5-9), the Wilmar Avenue fault forms a positive flower splay verging to the south-southwest and rooted into the steeper Los Osos East (LE) fault (cross section OV-AA′, Figure 7-15a). The Oceano fault likely is a northeast-dipping reverse fault that does not intersect the Los Osos fault, assuming that the dip of the Oceano fault is 55° or steeper.

Of the three FGMs, the OV Model is most consistent with the ONSIP preferred interpretation of the geometry of the faults at depth within the Irish Hills. In the ONSIP interpretation (PG&E, 2014, Chapter 7), both the south-dipping Edna fault system and the antithetic north-dipping faults converge downward and merge into a single master fault zone in the upper approximately 9 km depth (Figure 7-17). The geometry of the faults (steep dips and the narrow and deep Obispo-age basin) is suggestive of a negative flower structure, and it is hypothesized that the ancestral basin geometry may be the structural expression of local transtensional deformation in the region during the early Miocene (as described in *Section 5.1.3*). The normal faults associated with the Neogene extensional basin were subsequently reactivated as reverse faults. The Los Osos fault is depicted by the ONSIP mapping team as a range-front structure that dips moderately to steeply south. Projection of dips interpreted from seismic and geologic data suggest that the fault would intersect the base of the seismogenic crust (~12 km) near the Edna fault as shown on Figure 7-17.

These relationships are similar to those observed in analog sandbox models of transtensional basins that are subsequently inverted under transpression. Ustaszewski et al. (2005), for example, found that in models of oblique rift basins formed under transtensional conditions, the primary basin-bounding normal faults form a negative flower structure that roots into the principal displacement zone at the base of the physical model. When the deformation is reversed and the model basins are subjected to transpressional boundary conditions, shortening is accommodated by both reactivation of the normal faults as reverse faults and development of thrust faults that root from or near the principal displacement zone and verge outward from the older extensional basin (Figure 7-18). The Los Osos fault zone may be a blind or buried fault beneath the north-central and northwestern Irish Hills.

Several 2D seismic-reflection profiles were collected in the vicinity of mapped traces of the San Luis Bay fault as part of the ONSIP (PG&E, 2014, Chapter 7). The ONSIP team identified features in this seismic reflection data that they interpreted to possibly be the seismic expression of San Luis Bay fault traces at depth. The ONSIP team interpreted the San Luis Bay fault to be a steeply (65°–85°N, 72°N [avg.]) north-dipping fault with north-side-up structural separation that obliquely crosses the southeastern Irish Hills and probably terminates to the west against the Shoreline fault in the offshore region. However, they acknowledge that imaging quality and depth resolution of reflection data from the southern Irish Hills are relatively low, and interpretations of the San Luis Bay fault zone in the data are very uncertain. Based on our evaluation of the data, the TI Team concurs with the ONSIP team, and judges that the San Luis Bay fault is not well-resolved in the seismic reflection data. Within the Diablo Canyon SSC model, uncertainty in the fault dip is addressed by having a gentler downdip geometry for the fault in the SW Model, *Section 7.4.2*).

7.4.1.1 Possible Analog

The Gurvan Bogd Range fault system in Mongolia provides a general analog for the OV Model. Three discrete ranges bounded by reverse oblique, strike-slip, and reverse faults accommodate transpression within this fault system. This system of faults ruptured in the 1957 **M** 8.3 Gobi-Altay earthquake, which had a left-lateral reverse focal mechanism and occurred in the restraining bend of the Gurvan Bogd fault system (Vassallo et al., 2007). The main rupture of more than 260 km of left-lateral strike slip occurred along the Bogd fault to the north of the Ih Bogd (3,957 m) and Baga Bogd (3,590 m) massifs (Ritz et al., 2006; Figure 7-19). The average horizontal displacement ranged between 3 m and 4 m, with maximum offsets of 5–7 m (Kurushin et al., 1997; Figure 7-20). An additional 100 km of reverse faulting, distributed on five secondary segments, ruptured simultaneously with the Bogd fault during the 1957 earthquake. These fault segments correspond mainly to thrust faults found at the base of ridges and low hills or ‘forebergs” (Florensov and Solonenko, 1965; Kurushin et al. 1997; Bayasgalan et al., 1999). These reverse faults are shortening structures associated with the main Bogd strike-slip fault (Ritz et al., 2006).

Double-verging oblique or reverse faulting occurred on associated segments on both sides of the Ih Bogd Range. The horizontal flat summit (relict of an ancient erosional surface or surfaces) suggests that uplift occurs without major tilting or folding at the mountain scale.

We note that although the faults within and bordering the Irish Hills in the study region (e.g., the Los Osos fault) do not appear to show as much strike-slip displacement in the Quaternary as the Bogd fault, the presence of simultaneously active reverse faults bordering a block showing evidence of relatively uniform uplift is analogous.

7.4.2 Southwest-Vergent Model

The concept of the SW Model is that uplift of the San Luis Range is accommodated primarily by reverse slip on southwest-vergent faults that splay upward from a gently dipping ramp or detachment at depth (Figure 7-21). Given the conceptual nature and uncertainty in the depth of the detachment, however, the Primary faults responsible for uplift of the range are allowed to extend through the seismogenic crust to a depth of 12 km (as discussed earlier in *Section 7.4)* and are not considered to be truncated at shallower depth by a hypothesized detachment, The four representative cross sections illustrating key aspects of this model are shown on Figure 7-22 (A-A′ and B-B′) and Figure 7-23 (C-C′ and D-D′).

In this model, uplift of the Irish Hills sub-block is produced primarily by slip on a north-dipping (45–50°N) San Luis Bay fault (Figures 7-22 and 7-23). The SW Model is included in the Diablo Canyon SSC model as an end-member model for characterizing uncertainty in dip of the San Luis Bay and Los Osos faults. As shown on Profile B-B′ (Figure 7-22), the San Luis Bay fault would intersect the Los Osos fault at a relatively shallow depth of approximately 9 km, based on the relatively gentle 45° dip of the San Luis Bay fault and the relatively steep dip of the Los Osos fault. Because all faults are characterized to extend to the base of the seismogenic crust, at a depth of 12 km, the width of the San Luis Bay fault in this model slightly exceeds the width of the Irish Hills. Dips gentler than 45° are not considered because the widths of these faults would greatly exceed the dimensions of the uplifting range. In the SW Model, the Los Osos fault is modeled as an axial surface or backthrust with sympathetic and generally secondary offset.

In the SW Model, the western part of the San Luis Bay fault (BW) extends across the Shoreline fault zone as a discrete near-surface fault to intersect the HFZ to the west. This extension honors the apparent uplift boundary between the offshore Santa Rosa reef shelf and Islay shelf areas (Figure 7-4) that is inferred from changes in the number and altitudinal spacing of submerged marine terrace platforms, as well as the overall geomorphic expression of the two shelf areas (PG&E, 2011, Appendix I). Uplift of the continental shelf south of the San Luis Bay fault is interpreted to result from distributed deformation above the tip of the detachment south of the San Luis Bay fault and/or by a restraining bend along the HFZ (Section B-B′ on Figure 7-22). The Shoreline fault, which

intersects the southwest-verging faults, extends to seismogenic depth and acts independently to accommodate right-lateral strike slip but little to no vertical deformation.

Uplift of the Edna sub-block is produced by slip along faults of the Southwestern Boundary zone (SWBZ), primarily by the Wilmar Avenue fault and the Oceano fault. These faults dip north at 60° and 45°, respectively (Figure 7-22). The Los Osos East (LE) fault is characterized as an axial surface that dips steeply to the southwest. With an 80° dip, this deformation surface meets the gently dipping Oceano fault and the moderately dipping Wilmar Avenue fault at approximately 8 km depth beneath the range. The Wilmar Avenue and the LE faults both splay upward from a bend in the Oceano fault ramp, creating uplift of the Edna sub-block as a fault-bounded "pop-up" type of structure in the hanging wall of the underlying major ramp/detachment. As noted in the following discussion of a possible analog, these geometric relationships are not unlike the faults that ruptured during the 2003 San Simeon earthquake (McLaren et al., 2008). Minor uplift of the Edna Valley is produced by slip on the deeper part of the Oceano fault, which dips 30° to the northeast. Other faults within the SWBZ, such as the Los Berros fault, are acknowledged to exist but are not explicitly modeled as separate fault sources. Their rate of activity is incorporated into the model on the Wilmar Avenue and Oceano faults (see *Section 8.7*).

Differential rates of slip between individual faults at different structural levels may be accommodated by lateral tear faults and/or lateral ramps between faults (e.g., between the San Luis Bay underlying the Irish Hills sub-block and faults underlying the Edna sub-block [the Wilmar Avenue and Oceano faults]). For example, the possibility of a lateral tear fault between the San Luis Bay fault beneath the Irish Hills sub-block and the Wilmar Avenue fault beneath the Edna sub-block would be roughly aligned along the linear reach of San Luis Obispo Creek through the San Luis Range. Although there is no surface expression of a discrete fault, the presence of a tear fault is suggested by possible structural offsets of Miocene strata across the creek, a subtle change in structural trends across the creek, and an apparent right jog in the Pismo syncline. The existence of these lateral ramps or tear faults as sympathetic or secondary structures is not explicitly included in the model as seismogenic sources. Possible hazard from these zones of deformation is incorporated within the Local areal seismic source zone (*Section 13.5*).

The primary ramps that accommodate uplift of the San Luis Range are interpreted to sole into a basal slip detachment that dips northeast less than 10° beneath the range and the area to the northeast (Figures 7-22 and 7-23). Minor uplift of the Los Osos Valley is accommodated by slip on this detachment, which may intersect the West Huasna fault zone at or below the maximum depth of seismogenic crust. Alternatively, the Morro Rock–Islay intrusions may form a buttress limiting the downdip extent of such a detachment to the northeast. The SW Model does not readily explain the subsidence observed in the Morro Bay area. Possible explanations, such as a localized flat in the geometry of the detachment (as shown on cross section D-D′; Figure 7-23) or deformation off the end of a north-vergent Los Osos fault offshore, do not provide strong, convincing arguments favoring this model. Relative strengths and weaknesses of the SW Model are described as justification for weighting the models in *Section 7.5*.

The SW Model incorporates aspects of conceptual models of ramps below the Irish Hills as initially proposed by Namson and Davis (1990), as well as more recent models such as those presented by Hamilton (2012a and 2012b). The more recent models by Hamilton interpret a northeast-dipping fault beneath the Irish Hills and San Luis Range that has been alternatively named the San Luis Range thrust or San Luis Range/IOF thrust (where IOF is the Inferred Offshore Fault of Nitchman [1988] and Nitchman and Slemmons [1994]). This inferred fault was evaluated by PG&E as part of the CCCSIP report (2014, Chapter 12). Although the concepts behind the fault models are similar, the geometry and dip of faults defined by the SW Model differ in detail from those postulated in these previous studies. Constraints on the locus and rate of uplift within the San Luis Range and adjacent offshore regions, together with patterns of seismicity and new information on fault geometry from the CCCSIP report (PG&E, 2014, Chapters 2, 3, 7, and 9) have been considered in developing the SW Model. Whereas these data are compatible with the SW Model, they do not support (and, in some cases, contradict) the Hamilton (2012a and 2012b) proponent models with regard to location, depth, and importance as the primary uplift boundary along the southwestern margin of the Irish Hills (PG&E, 2014, Chapter 12).

7.4.2.1 Possible Analog

The Oceanic fault and related backthrusts that ruptured during the 2003 **M** 6.5 San Simeon earthquake represent a possible analog for the SW Model. McLaren et al. (2008) image the causative fault and secondary structures that ruptured during this earthquake and related aftershocks based on analysis of seismological, interferometric synthetic aperture radar (InSAR), and geologic observations. The primary mainshock occurred on a 30 km long northwest-striking, northeast-dipping thrust fault, which projects to the surface near the mapped trace of the Oceanic fault (Figure 7-24). On this basis, the Oceanic fault was judged to be the causative structure for the mainshock rupture. Two 5–10 km long en echelon southwest-dipping backthrusts defined by aftershocks and post-seismic uplift seen in InSAR data are present on either side of a central area that experienced the highest slip in the mainshock. The well-defined main thrust at the latitude of the epicenter and antithetic backthrust illuminated by the aftershock sequence indicate uplift of the Santa Lucia Range as a pop-up block. The absence of backthrust features in the central part of the zone suggests range-front uplift by fault-propagation folding, or that backthrusts in the central part were not activated during the mainshock. McLaren et al. (2008) concluded that the simplified model and the changes in the style of faulting with depth are consistent with dextral transpression, but also noted that the simplified model does not account for possible variations in the strike of the main thrust and en echelon faulting in the hanging wall between the northwest and southeast clusters of aftershocks.

7.4.3 Northeast-Vergent Model

The concept of the NE Model is that uplift of the Irish Hills sub-block of the SLPB is accommodated primarily by reverse slip on a northeast-vergent fault, the Los Osos fault

(Figure 7-25). The Los Osos fault soles into a basal detachment at the base of the seismogenic crust beneath the Irish Hills and roots into the HFZ as it approaches the HFZ offshore in Estero Bay. The Los Osos fault and the detachment both underlie regions of uplift (Figure 7-4). This primary northeast-vergent reverse fault does not extend eastward to also underlie the southeastern part of the SLPB, the Edna sub-block, because this would require the existence of a very broad, northeast-vergent detachment beneath San Luis Obispo Bay, a region that has undergone active subsidence in the Quaternary (Figure 7-4). Instead, the Edna sub-block is underlain by a primary southwest-vergent reverse fault that roots into the West Huasna fault, a linkage supported by regional fault mapping (i.e., the surface traces of the West Huasna fault and faults of the SWBZ merge to the southeast), and the proximity of the West Huasna fault to the Edna sub-block (Plate 7-1). The four representative cross sections illustrating key aspects of this model are shown on Figure 7-26 (A-A′ and B-B′) and Figure 7-27 (C-C′ and D-D).

The geometry of the south-vergent faults underlying the Edna sub-block and adjacent eastern Edna Valley is similar to the geometry of the faults as represented by the SW Model, but the dips of the faults are varied to capture additional epistemic uncertainty in the overall geometry of the faults at depth.

The reversal in polarity between the northeast-vergent reverse fault beneath the Irish Hills sub-block and the southwest-vergent reverse fault beneath the Edna sub-block requires a lateral ramp or tear fault between the two sub-blocks, roughly aligned with San Luis Obispo Creek. As noted above for the SW Model, there is no direct evidence of a shear zone or tear fault at the surface in the San Luis Obispo Creek canyon, although the possible jog in the syncline axis is suggestive of lateral offset. Alternatively, the difference in vergence may be localized on a fold or lateral ramp that accommodates distributed right-lateral shear or block rotation. Minor clockwise rotation of the Irish Hills may be indicated by the slight change in the orientation of the structural grain within the Irish Hills sub-block relative to the Edna sub-block, and by paleomagnetic data that show vertical axis clockwise rotation of the Miocene Monterey Formation at Shell Beach (Khan et al., 2001). The paleomagnetic data, however, are from only one location and thus do not provide sufficient coverage to document differential rotation between sub-blocks. Subsidence in the Morro Bay area may be partly explained by the secondary effects of such block rotation.

Uplift of the Irish Hills sub-block and the offshore region near the DCPP is accommodated by slip on the Los Osos fault which is modeled to dip 50° to the south throughout the entire seismogenic crust to a depth of 12 km. This dip is less steep than the range of 55°–80° in the upper 1–2 km interpreted by the ONSIP team from seismic-reflection data (PG&E, 2014, Chapter 7). The shallower dip of 50° satisfies the requirement to produce uniform uplift of the entire Irish Hills sub-block by slip on the Los Osos fault.

The NE Model is an end-member model. Profile D-D′ shows that at the west end of the range, a 50° dip on the Los Osos fault crosses the Shoreline fault at a relatively shallow depth of approximately 9 km. Because the primary faults driving uplift of the Irish Hills

are characterized to extend to the base of the seismogenic crust, at a depth of 12 km, the Los Osos fault here projects across the Shoreline fault and roots into the Hosgri fault. Dips gentler than 50° are not considered because the fault would cross the Shoreline fault at an even shallower depth and would not reach the base of the seismogenic crust before reaching the Hosgri fault.

The San Luis Bay fault in this model is either an axial surface or backthrust. The fault merges with or is truncated to the west by the Shoreline fault and does not extend further west to the HFZ, as it does in the SW Model. Uplift west of the Shoreline fault and north of this intersection is accommodated by slip on the Los Osos fault. Uplift south of this intersection is accommodated by distributed deformation produced by minor reverse faulting within the SWBZ, a left-restraining bend on the HFZ, and/or aseismic slip on the detachment at or below the base of the seismogenic crust (i.e., the detachment the Los Osos fault soles into). This distributed deformation is accounted for in the Local areal source zone (*Section 13.5*).

7.4.3.1 Possible Analogs

A possible analog for this fault model is Sierra Pie de Palo in Argentina. Uplift of the Pie de Palo range is accommodated by oppositely vergent reverse faults separated by a tear fault (Regnier et al., 1992; Figure 7-28). The Sierra Pie de Palo is one of the most seismically active mountain blocks of the Sierras Pampeanas in the San Juan Province of northwestern Argentina and is the site of the M_S 7.3 Caucete earthquake in 1977. Regnier et al. (1992) used the morphology of the range, seismicity patterns, and focal mechanisms to define the two blocks and intervening shear zone. Distinct, but complex, systems of faults were recognized by Regnier et al. (1992) in both the northern and southern blocks. The separation between the two blocks is coincident with a major shear zone crossing the mountain that is expressed as a deeply eroded canyon. The presence of this shear zone is supported by a concentration of focal mechanism solutions along the shear zone showing right-lateral strike-slip motion and by regional-scale strike-slip faults identified on satellite images.

Kadinsky-Cade and Reilinger (1985) also analyzed the 1977 earthquake, which they interpret as M_S 7.4, using leveling data combined with seismic observations. They concluded from the spatial pattern of uplift (~1 m) that accompanied this earthquake that 4 m of slip occurred on a north-south-trending, west-dipping fault with a dip of 35°, a downdip width of 24 km, and a length of 80 km. The top of the fault was at a depth of 17 km. The mainshock was a double event in which the two shocks occurred 21 s apart and were separated by 65 km along the proposed fault strike.

The estimated seismogenic depth/width of the Sierra Pie de Palo structure are significantly greater than what is expected for the SLPB in the vicinity of the DCPP. The potential for oppositely verging structures to coexist and the potential rupture during a single complex earthquake rupture is, however, judged to be a viable hypothesis that is included in the NE Model. The lack of seismological or geomorphic expression of the

shear zone between the two oppositely verging ramps may be due to the low rate of activity in the DCPP region relative to that of the more active Sierra Pie de Palo region.

7.5 SLPB Logic Tree Model Weights

The weights assigned to the three alternative SLPB FGMs in the Primary and Connected fault source characterization logic tree (Figure 6-1) reflect the judgment of the TI Team as to the viability of each individual model as a whole. The representative cross sections for each of the models were constructed to evaluate the relationship of faults along strike and their interaction with other Primary faults, in particular, the Hosgri and Shoreline faults.

The OV and SW models are given equal weight [0.4].

The weight assigned to the OV Model is based on the following observations:

- The model fits the geologic and seismological data supporting transpression within the SLPB.
- The geometry of the faults is consistent with the concept of the development of structures within the range as a Miocene transtensional fault system that has subsequently been reactivated in the contemporary tectonic setting as a transpressional fault system.
- The geometry of the range-front trace of the Los Osos fault, in particular, fits well with sandbox models showing the development of similar reverse faults along transtensional fault systems that subsequently are reactivated during transpressional conditions.
- The OV Model allows for continuity of structures within and bordering the range.
- The OV Model provides an explanation for the presence and development of the Morro Bay subsiding basin.

The OV Model predicts dextral deformation along the axis of the SLPB. However, there is little geologic evidence for active dextral deformation of mapped faults, and the orientation of the range is such that dominantly reverse deformation would be predicted in the current stress/strain regime (Figure 5-12). Uplift of the southwestern part of the Irish Hills (i.e., along the coastline from approximately the DCPP to Point Buchon) is explained in the OV Model by slip on the underlying blind San Luis Bay fault. However, as shown on Figure 7-4, this region of relatively high uplift, and the boundary that separates it from the region of relatively low uplift to the south, both extend offshore to the west of the Shoreline fault. The OV Model does not explain the offshore part of this uplift boundary well, because the San Luis Bay fault is modeled as truncated by the Shoreline fault. Instead of explicitly modeling this uplift boundary as caused by a blind fault, the boundary is modeled as a zone of folding and distributed deformation above the tip of the blind San Luis Bay fault in the OV Model.

The weight assigned to the SW Model is based on the following observations:

- The San Luis Bay fault and faults within the SWBZ are well oriented to accommodate reverse deformation within the current stress-strain regime (Figure 5-12).
- The model, which includes a gently dipping detachment beneath the Edna and Los Osos valleys, is the only model that provides a ramp to explicitly explain uplift, albeit at low rates, within the relatively seismically quiet block between the West Huasna fault and the SLPB.
- The concept of the Los Osos fault as an axial surface or secondary backthrust is supported by the lack of continuous surface expression of faulting observed along the fault in the central part of the Los Osos Valley.
- The geometry and width of the southwest-verging faults relative to the Los Osos backthrust in the Irish Hills is similar to that of the Oceanic fault and related backthrust faults that are inferred to have ruptured during the 2003 San Simeon earthquake.
- The SW Model best explains the pattern of uplift observed in the offshore part of the SLPB between the Shoreline fault and the HFZ (i.e., greater uplift of the Islay Shelf, west of Point Buchon, relative to the lesser uplift of the Santa Rosa Reef Shelf, west of San Luis Hill, is accommodated by the western San Luis Bay fault).

The SW Model, however, does not provide a good explanation for the presence and development of the Morro Bay subsiding basin.

The NE Model is given lower weight [0.2] relative to the OV and SW models. The main reason for the lower weight is that this model predicts a significant through-going, active cross structure that accommodates dextral deformation and is roughly coincident with the San Luis Obispo Creek canyon, for which there is little geologic evidence. Some of the strengths of this model, however, are as follows:

- The Los Osos fault and faults of the SWBZ are well oriented in the current stress regime to accommodate reverse faulting (Figure 5-12).
- Both primary reverse faults are interpreted to root at depth into the primary strike-slip faults that they branch from in map view: The Los Osos fault is interpreted to root into the Hosgri fault at depth beneath the Irish Hills to the southeast of where the two faults merge offshore, and the Oceano/Wilmar Avenue faults are interpreted to root into the West Huasna fault at depth to the northwest of where these faults merge.
- The geometry of the Los Osos fault, together with the detachment that connects it to the Hosgri fault, matches the geometry of the Irish Hills, together with the Santa Rosa Reef, the uplifting part of the shelf to the south and west of San Luis Hill (Figure 7-4).
- Subsiding areas, including San Luis Obispo Bay, Morro Bay, and smaller Quaternary basins adjacent to and north of the Los Osos fault, only occur in the footwalls of the primary reverse faults.

As a whole, uncertainty in the geometries of faults bordering the SLPB is captured by use of the three alternative FGMs. The range and weighted mean values for key geometrical

fault parameters included in the Diablo Canyon SSC model for Primary faults bordering the Irish Hills are presented in tabular form on Figures 7-29 and 7-30. Parameter values for the Los Osos fault are shown on Figure 7-29, and parameter values for the San Luis Bay fault are shown on Figure 7-30.

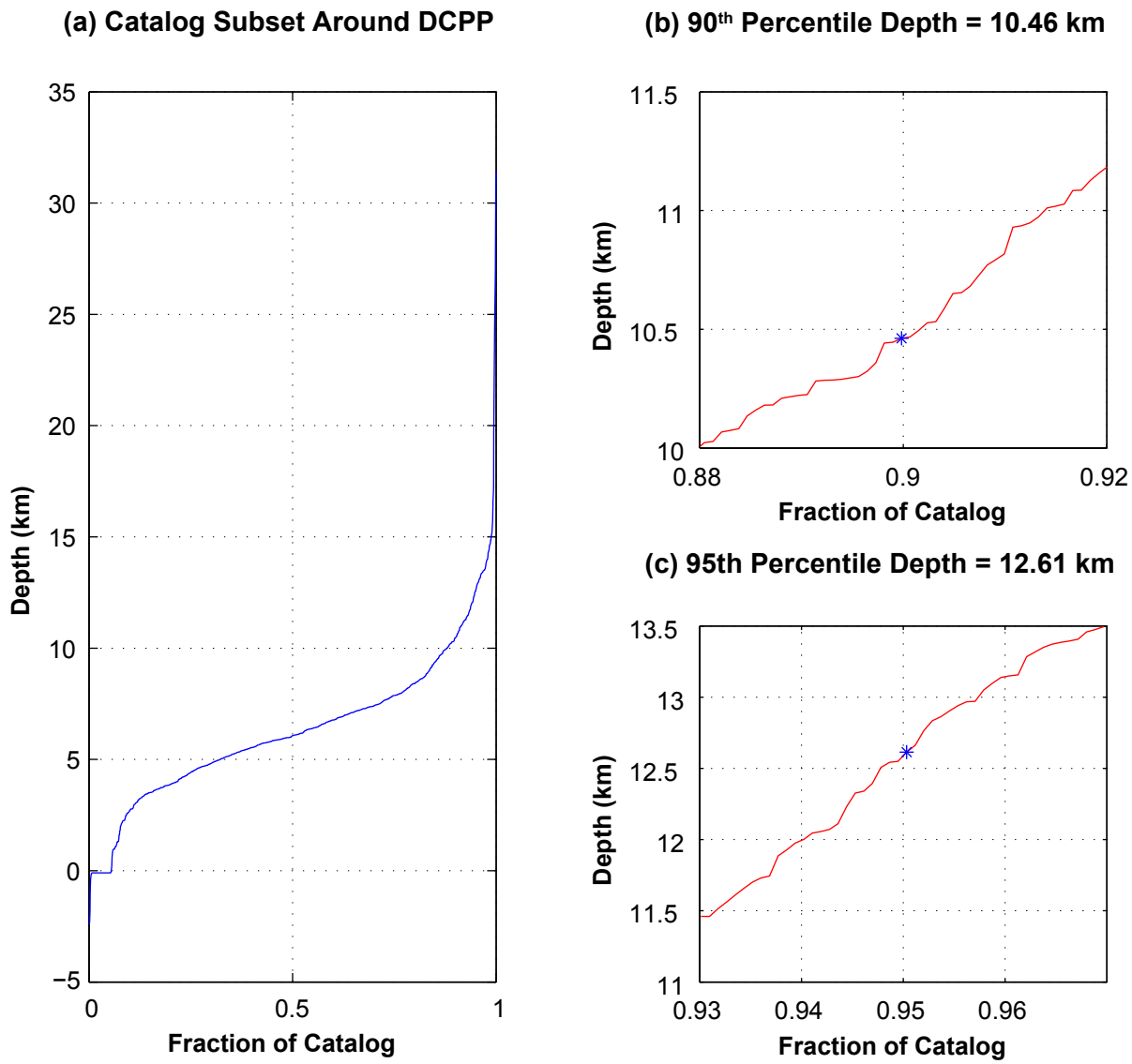

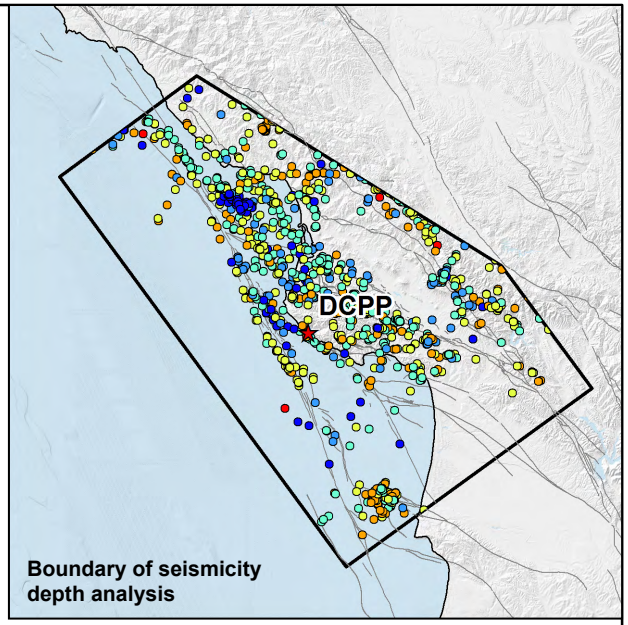

EXPLANATION

Seismicity
depth (km)

0-2 2-4 4-6 6-9 9-12 >12

Note: On Panel (a), minimum depth in catalog subset is 2.41 km and maximum depth is 31.4 km.

Source: Seismicity from Hardebeck (2014a).

CDF Plots Showing Seismicity Distribution with Depth, with D90 and D95 Values on CDF

DCPP SSC REPORT

Pacific Gas and Electric Company | Figure **7-1**

File path: S:\1005\005\Final_Report\Figures\Figure_700-01.ai; Date: 03/10/2015; User: Alex Remar, LCI; Rev.1

(a) Cross Section

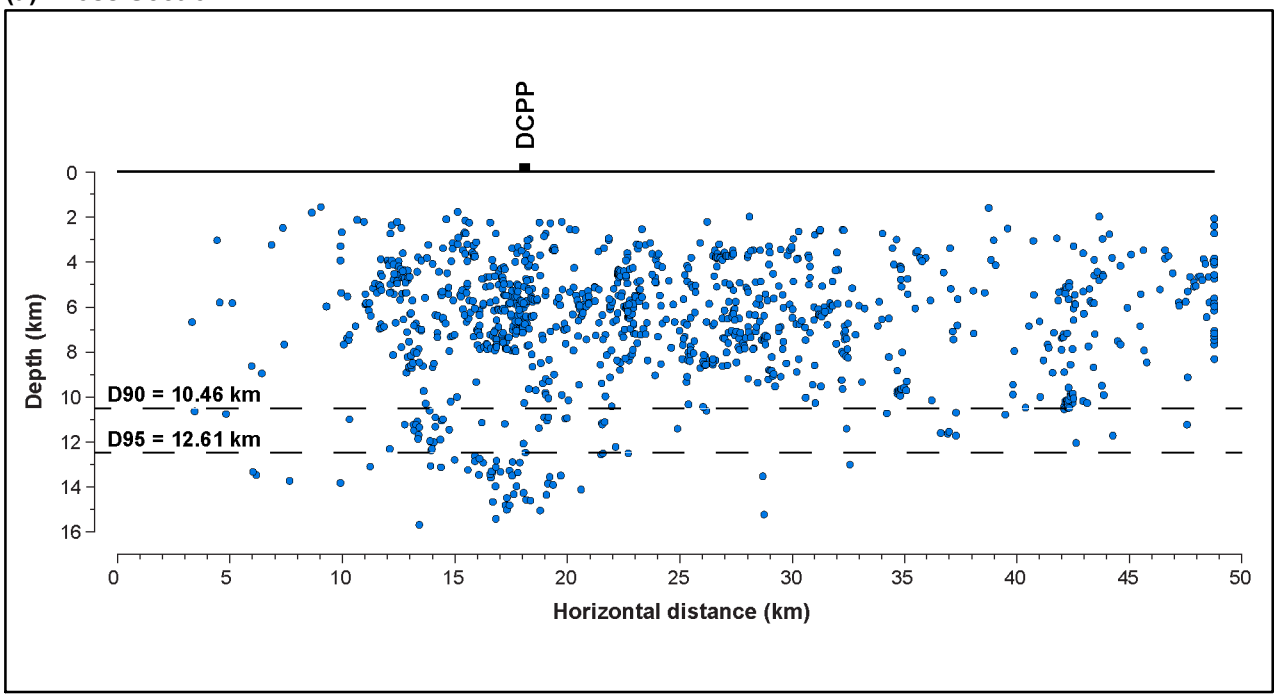

(b) Map

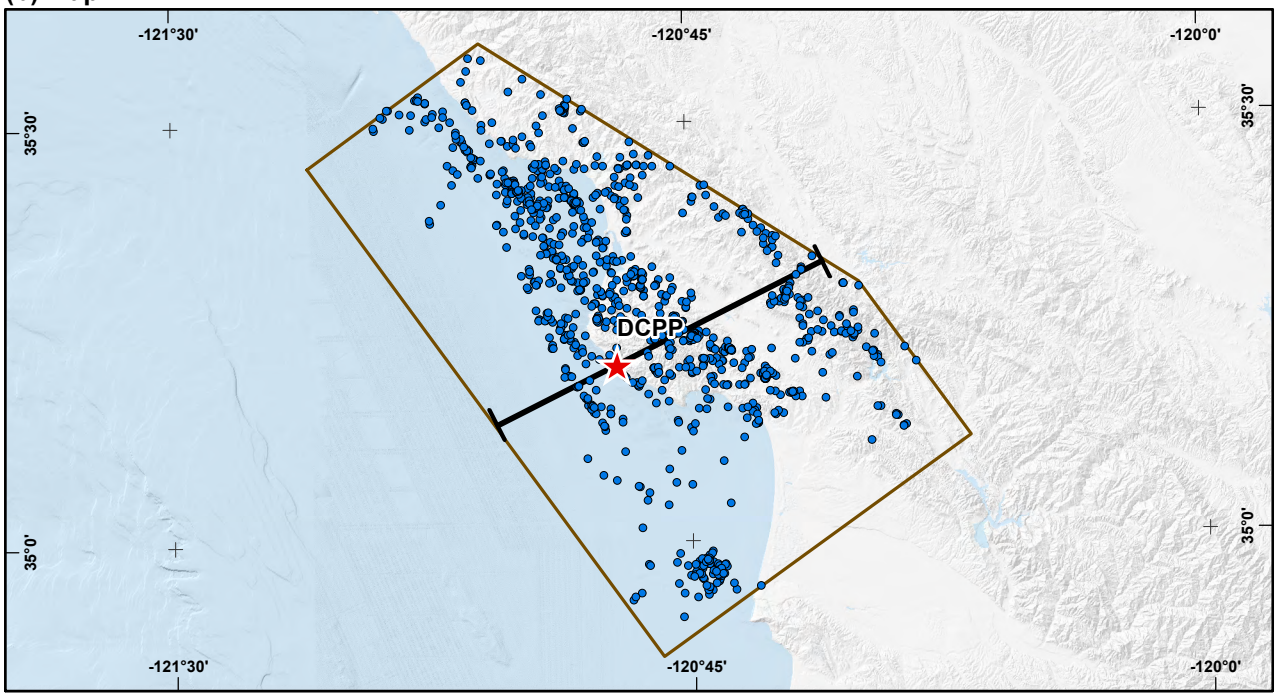

EXPLANATION

- Seismicity (Hardebeck, 2014a)
- Cross section perpendicular to Hosgri fault
- Extent of seismicity projected onto cross section

N

0 8 16 mi

0 10 20 km

Map projection and scale: NAD 83 / UTM Zone 10N, 1:1,000,000

Notes:
- Seismicity projected perpendicularly onto cross section; seismicity beyond cross section projected onto end of cross section.
- Deep seismicity shown between 15 km and 20 km along the profile is mostly from a cluster in northern Estero Bay.
- Extent of seismicity corresponds with boundaries of tomoDD relocations by Hardebeck (2012b).

Cross Section Showing Seismicity Distribution with Depth with D90 and D95 Values

DCPP SSC REPORT

Pacific Gas and Electric Company

Figure **7-2**

File path: S:\1005\005\Final_Report_Figures\Figure_700-02.mxd; Date: 03/10/2015; User: Alex Remar, LCI; Rev.1

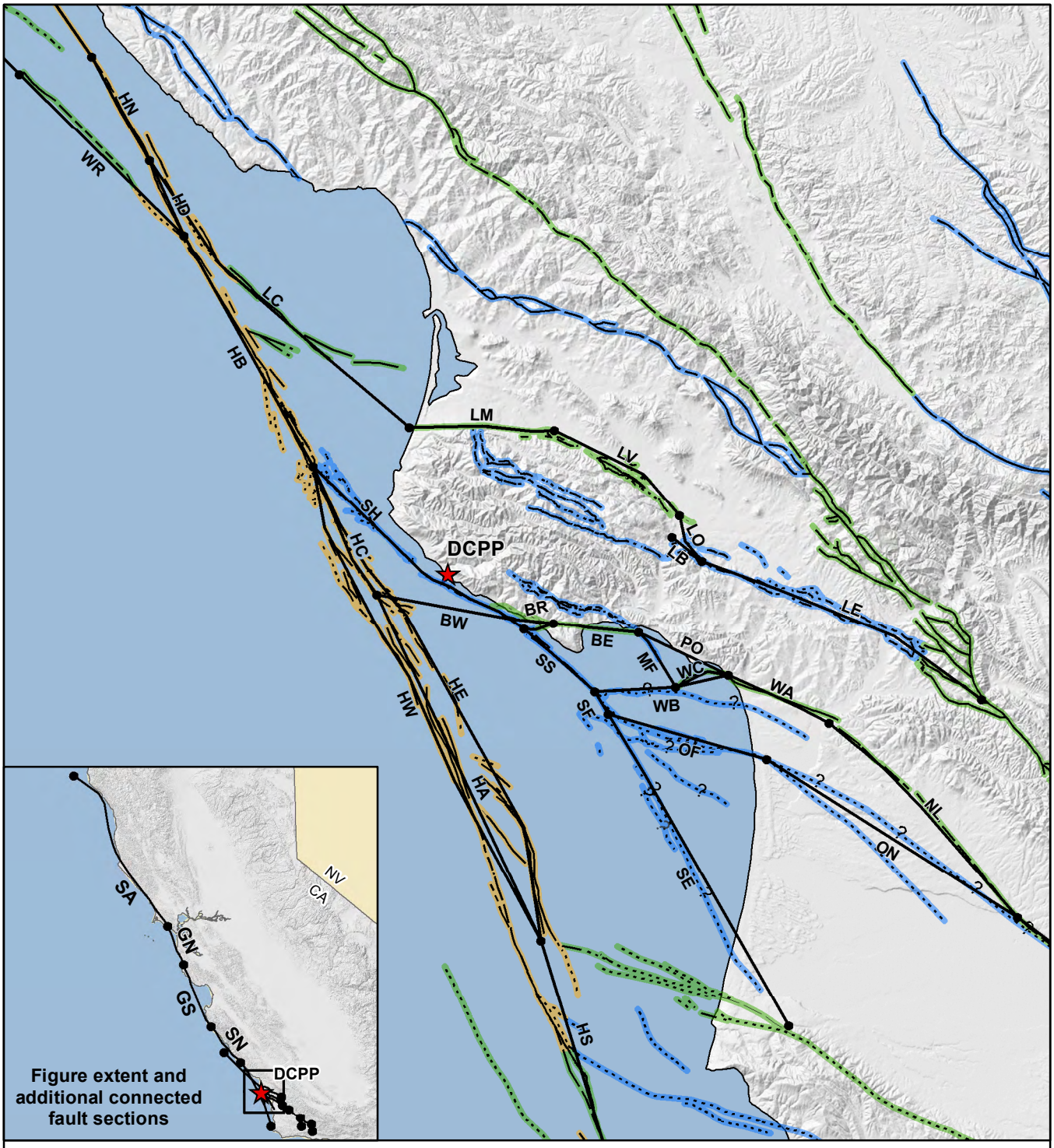

EXPLANATION

DCPP site

Fault source, surface trace,or updip surface projection. Two-letter codes describing sections are explained in Table 6.5.

Quaternary fault trace: solid where well located, dashed where approximately located, offshore faults dotted where buried by undeformed unconformity H10 or older strata, onshore faults dotted where buried, short dashed where inferred, queried where existence is uncertain

Slip Rate

1–5 mm/yr

0.2–1 mm/yr

<0.2 mm/yr

Note: Fault sources are defined as simplified representations of Quaternary fault traces.

N

0 6 12 mi.

0 10 20 km

Map projection and scale: WGS 84 / UTM Zone 10N, 1:400,000

Development of Fault Sources for All FGMs

DCPP SSC REPORT

Pacific Gas and Electric Company

Figure **7-3**

File path: S:\1005\005\Final_Report_Figures\Figure_700-03.mxd; Date: 03/10/2015; User: alex, LCI; Rev.1

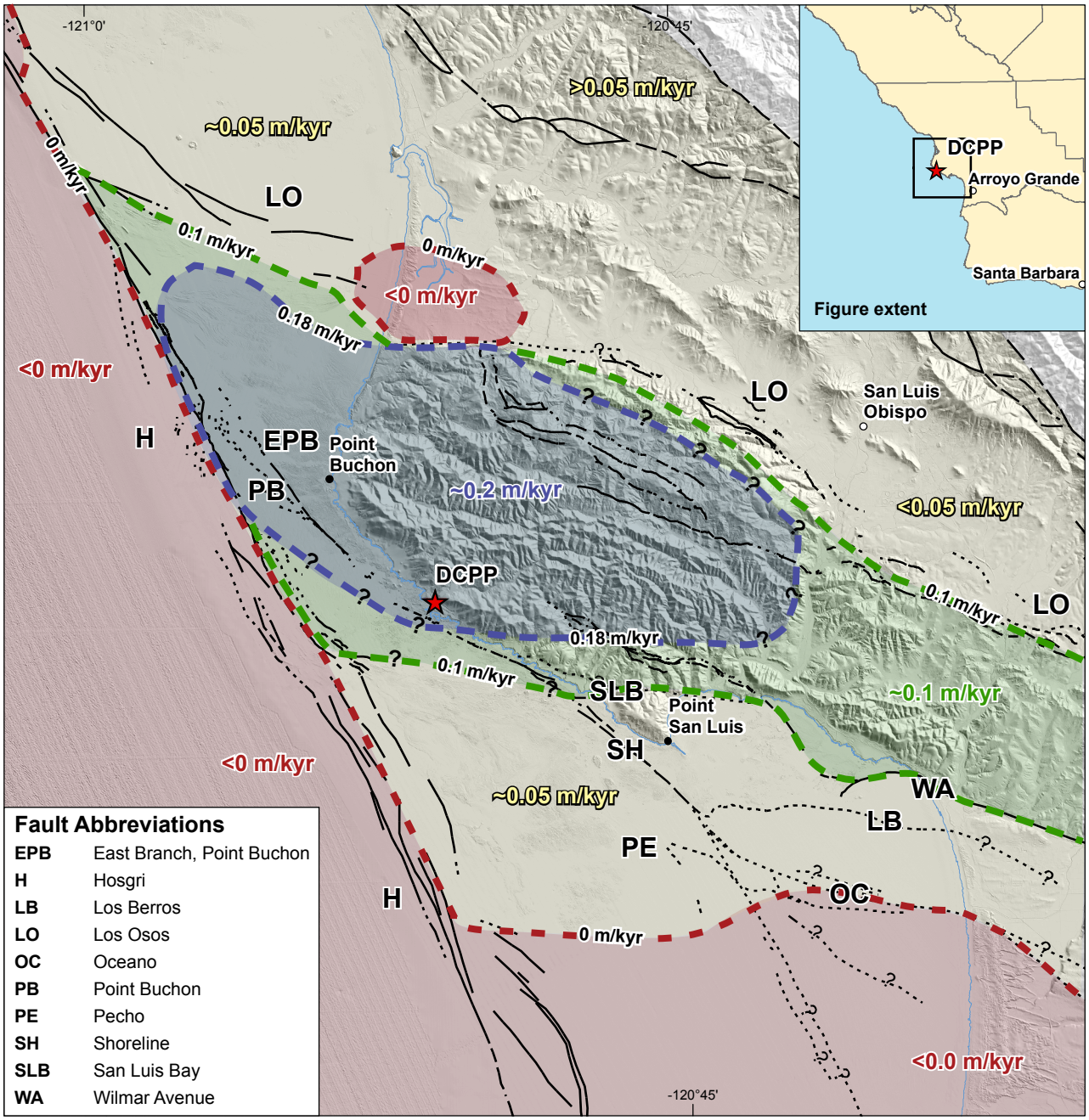

EXPLANATION

Quaternary fault trace: solid where well located, dashed where approximately located, dotted where buried by undeformed unconformity H10 or older strata, short dashed where inferred, queried where existence is uncertain

N

0 4 8 mi.

0 8 16 km

Uplift rate areas (m/kyr)

Areas	Approximate contours
>0.18	0.18
>0.1–0.18	0.1
0–0.1	0
<0	

Note: Approximately located contours of constant late Quaternary uplift rate, in m/kyr, based on information from PG&E (1988; 2013a and b; 2014, Chapter 3) and AMEC (2011). Estimates of approximate generalized uplift rate for each colored region are shown in bold. See discussion in Section 8.2.2 for details.

Map projection and scale: NAD 83 / UTM Zone 10N, 1:250,000

Uplift Rate Contour Map of the San Luis Range Area

DCPP SSC REPORT

Pacific Gas and Electric Company

Figure **7-4**

File path: S:\1005\005\Final_Report_Figures\Figure_700-04.ai; Date: 03/10/2015; User: Alex Remar, LCI; Rev.0

(a) Willingham et al. (2013)

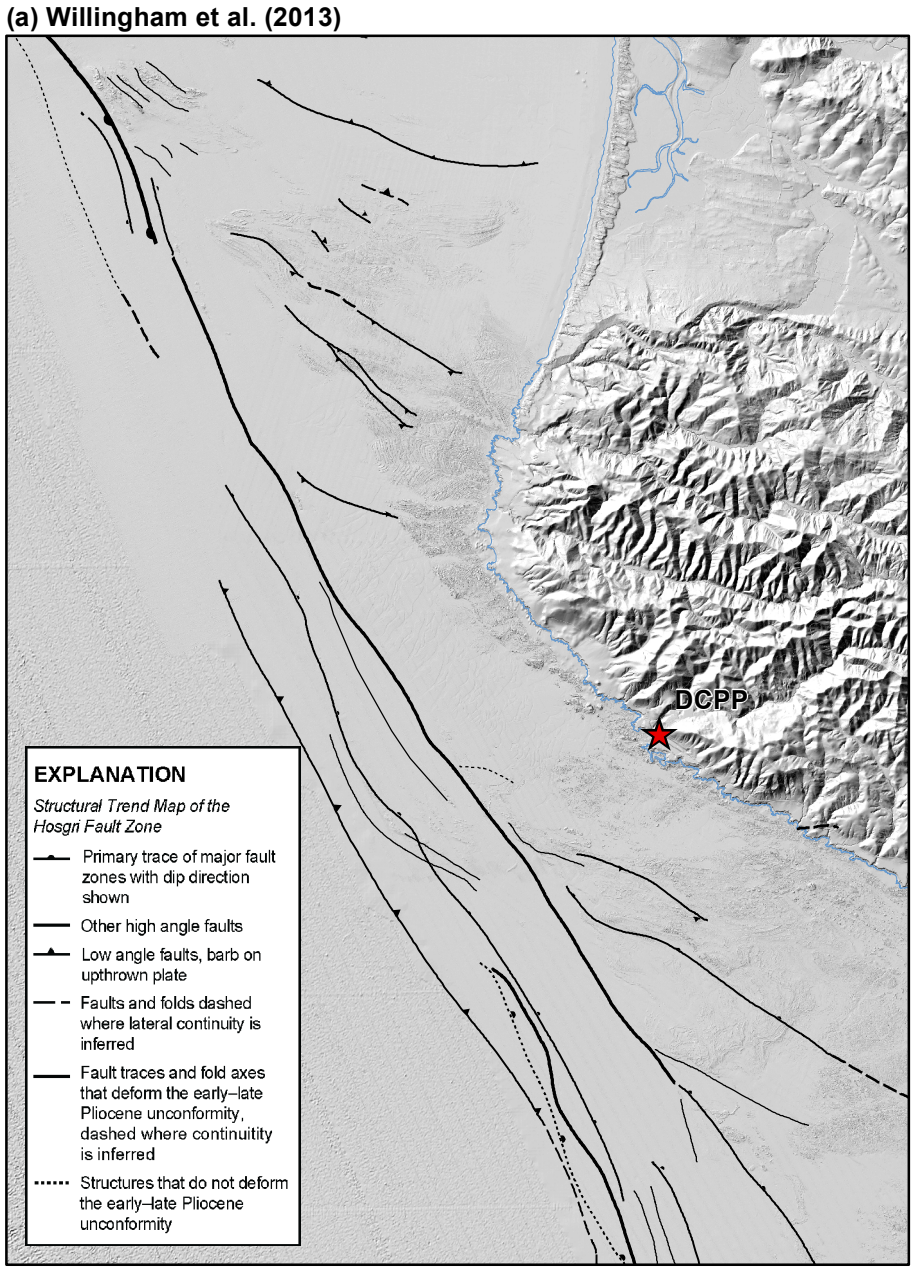

(b) Johnson and Watt (2012)

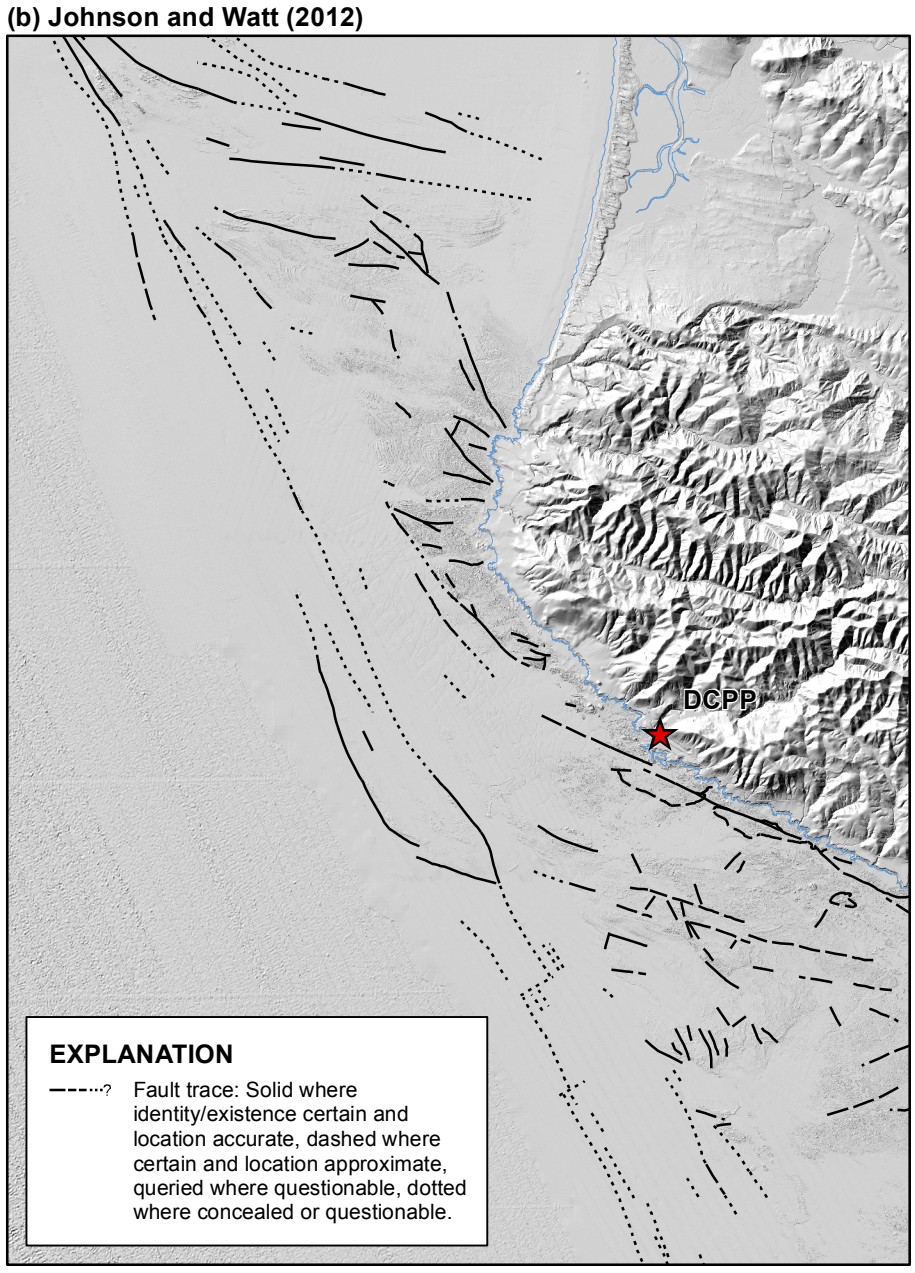

(c) Shoreline Fault Zone Report PG&E (2011)

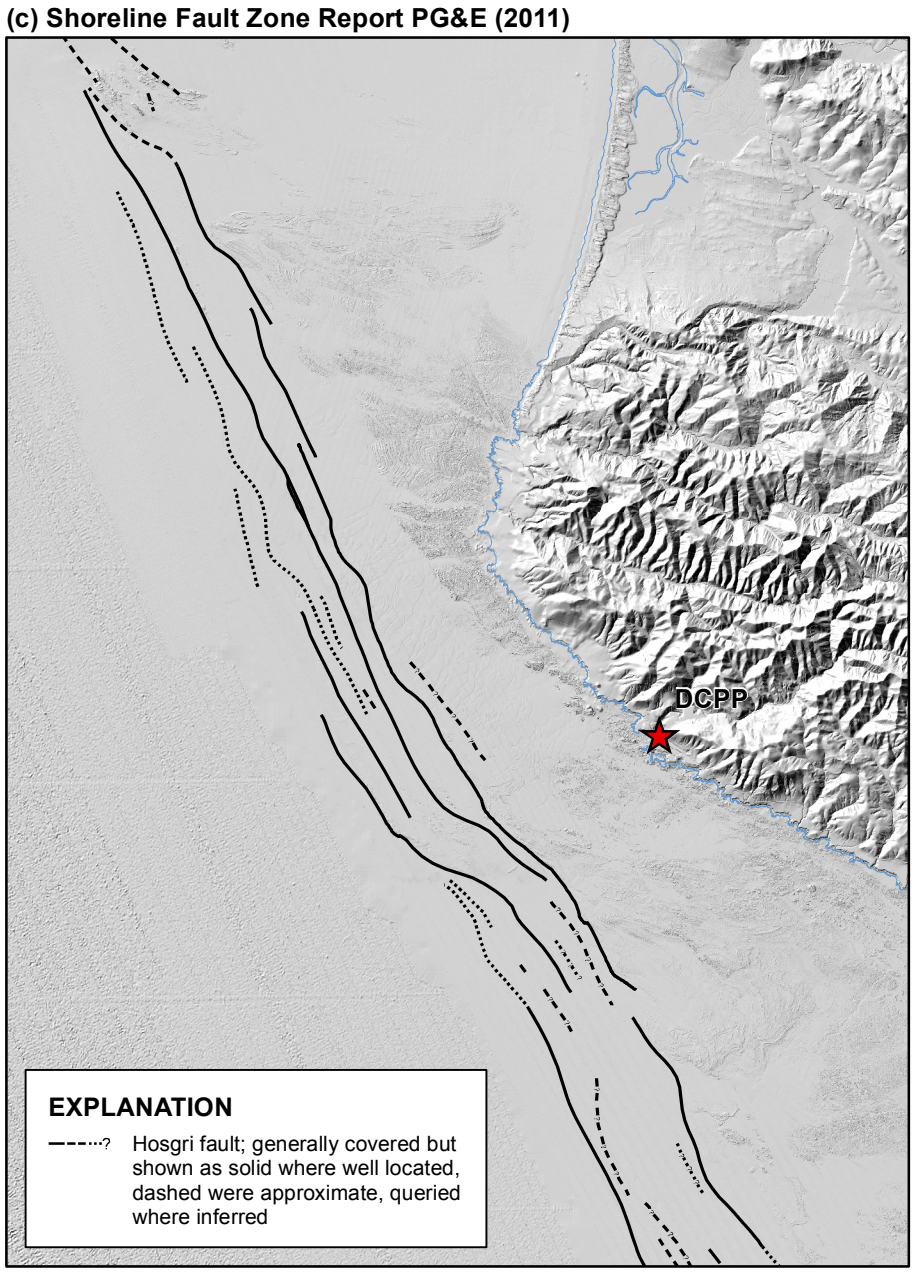

(d) PG&E (2014, Chapter 3)

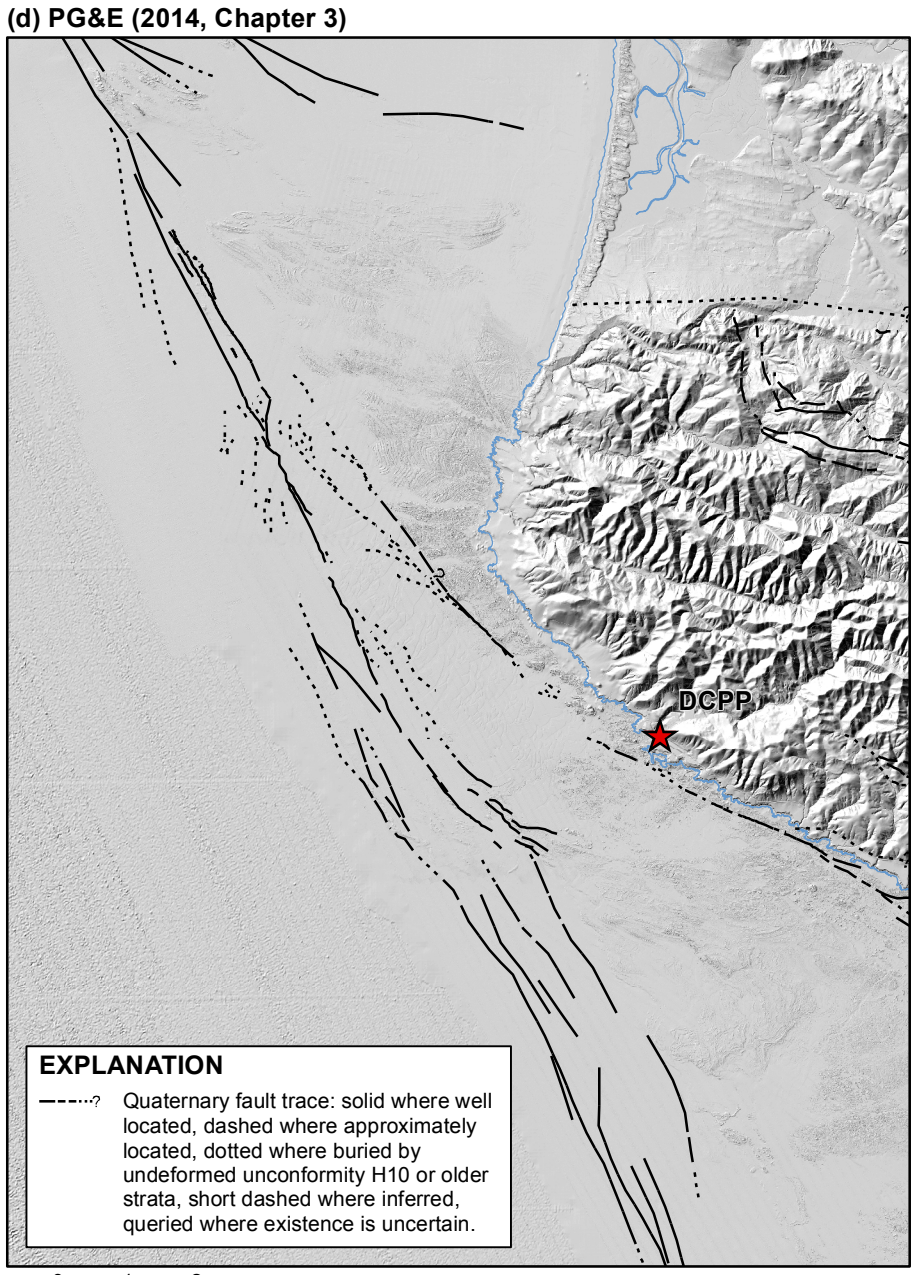

N 0 1 2 mi
0 2 4 km

Map projection and scale: WGS 84 / UTM Zone 10N, 1:175,000

Notes:
- Panel (a): Willingham et al. (2013) show the general interpretation of the geometry and location of the HFZ that was presented by PG&E (1988, 1991) based on analysis of high- and low-energy seismic-reflection data from numerous surveys collected for different purposes from the 1970s to 1980s. Faults are mapped as "structural trends" representing a combination of shallow and deep (~2 km) faults.
- Panel (b): Johnson and Watt (2012) present an interpretation of the near-surface traces of the HFZ from high-resolution 2D Sparker seismic-reflection data (800 m spacing) and bathymetry. Digital faults from Watt et al. (in prep).
- Panel (c): PG&E (2011) present a preliminary interpretation of the near-surface traces of the HFZ, based on the 2D seismic-reflection data and bathymetry sets used by Johnson and Watt as described above.
- Panel (d): PG&E (2014, Chapter 3) present a more comprehensive mapping of the HFZ based on analysis of the USGS high-resolution 2D seismic-reflection data released by Sliter et al. (2010) and new 3D and 2D seismic-reflection data collected for PG&E (PG&E, 2014, Chapters 2 and 3).

Comparison of Hosgri Fault Maps

DCPP SSC REPORT

Pacific Gas and Electric Company | Figure **7-5**

File path: S:\1005\005\Final_Report_Figures\Figure_700-05.mxd; Date: 03/11/2015; User: Alex Remar, LCI; Rev.1

(a) Excerpt of Seismic Line PBS-23

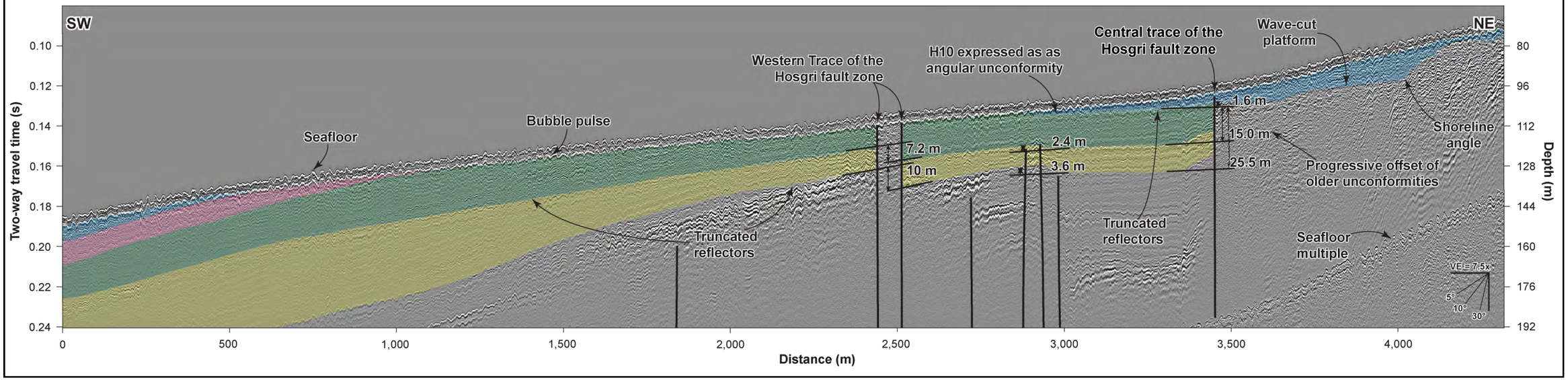

(b) Excerpt of Seismic Line PBS-23 Flattened to Seafloor

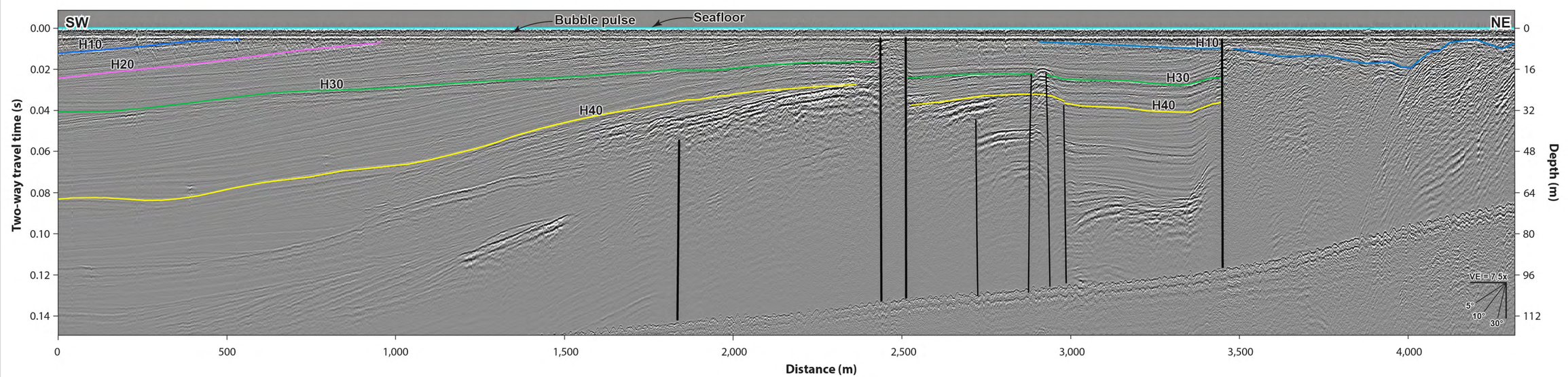

EXPLANATION

- Postglacial transgressive and highstand
- LGM lowstand systems tract
- MIS 3–5 highstand and regressive systems tracts
- MIS 7–8 highstand and regressive systems tracts
- Seafloor
- Unconformity H10
- Unconformity H20
- Unconformity H30
- Unconformity H40
- Location of seismic profile

Note: Deposits from Quaternary sea-level oscillations, systems tracts, are shown with colored shading over the seismic-reflection profile. These systems tracts are bounded by erosional unconformities (H10, H30, and H40) that were developed during Quaternary sea-level transgressions. The preferred ages (Marine Isotope Stages) of these deposits and unconformities are shown here. Uncertainty in these ages is discussed in Section 8.3.4. Vertical separation of key unconformities across fault strands (shown in meters) was estimated using an assumed seismic velocity of 1,600 m/s (PG&E, 2013a).

Sources:
- USGS seismic-reflection data (Sliter et al., 2010).
- Modified from PG&E (2013a) and Gray et al. (2013).

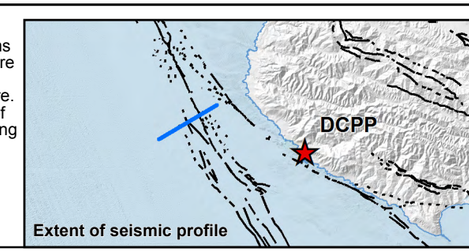

Evidence of Central and Western Hosgri Fault Trace Activity

DCPP SSC REPORT

Pacific Gas and Electric Company

Figure **7-6**

File path: S:\1005\005\Final_Report\Figures\Figure_700-06.ai; Date: 01/21/2015; User: Alex Remar, LCI; Rev.1

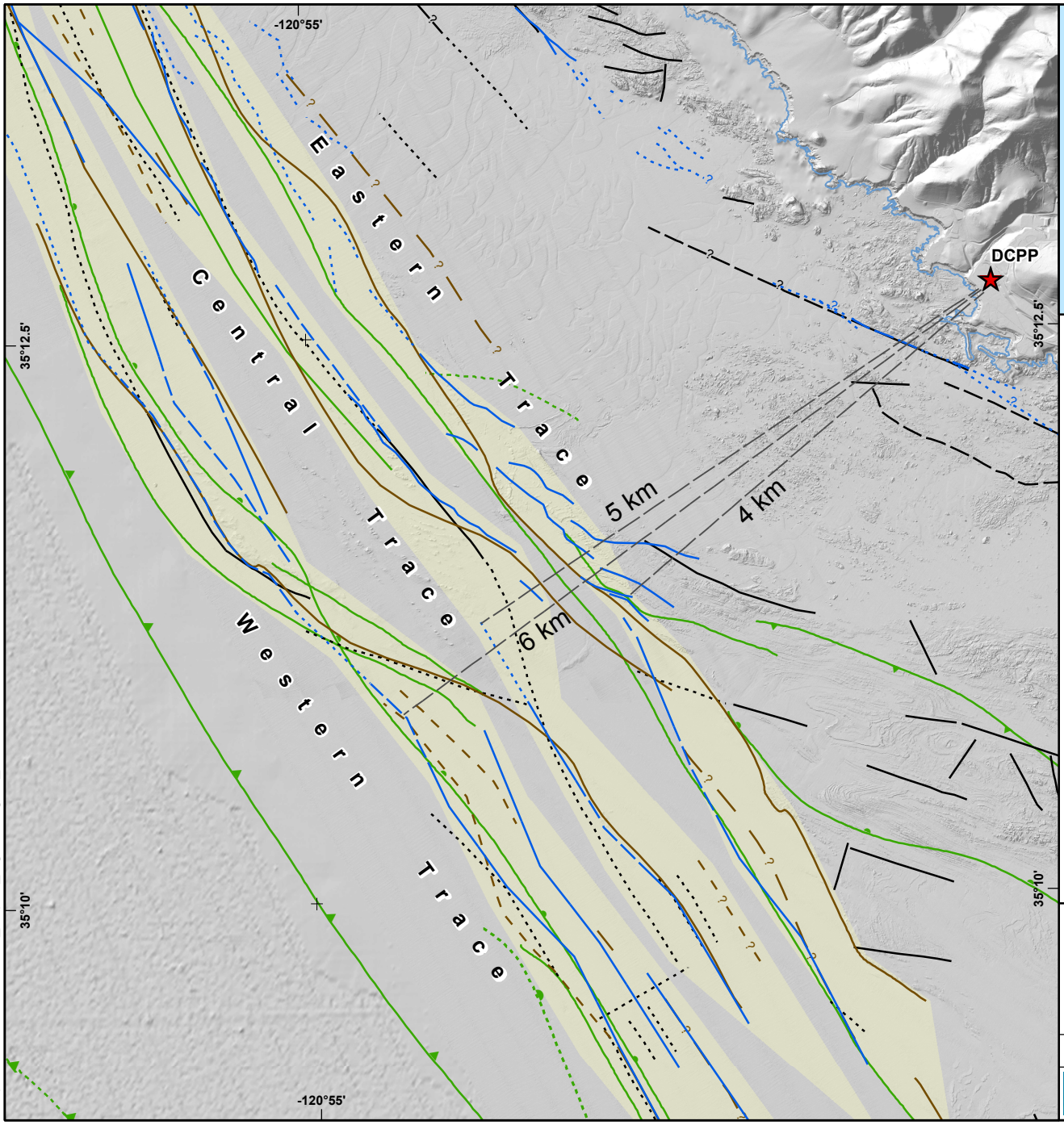

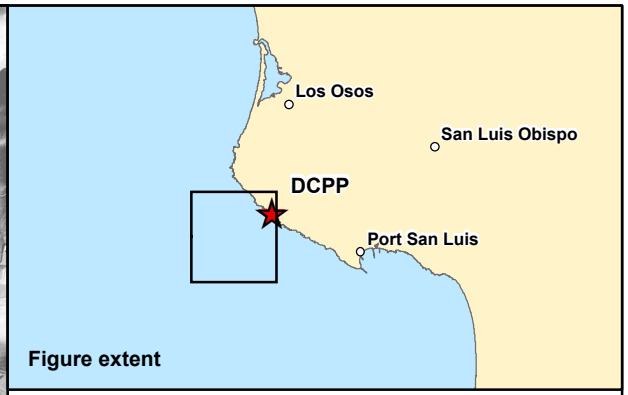

EXPLANATION

Fault trace zone

Quaternary Fault Traces and Sources

PG&E (Plate 7-1 of this report)

PG&E (2011)

Johnson and Watt (2012)

Willingham et al. (2013)

Note: Despite differences in details of individual fault maps, most maps show that offshore of the DCPP the HFZ consists of three traces. Furthermore, these traces generally overlap each other, as illustrated by the fault trace zones shown in beige.

N

0 0.5 1 mi.

0 1 2 km

Map projection and scale: WGS 84 / UTM 10N, 1:50,000

Distances of the Eastern, Central, and Western Hosgri Fault Traces from the DCPP

DCPP SSC REPORT

Pacific Gas and Electric Company

Figure **7-7**

File path: S:\1005\005\Final_Report_Figures\Figure_700-07.mxd; Date: 03/10/2015; User: Alex Remar, LCI; Rev.1

(a) Hosgri (hypoDD)

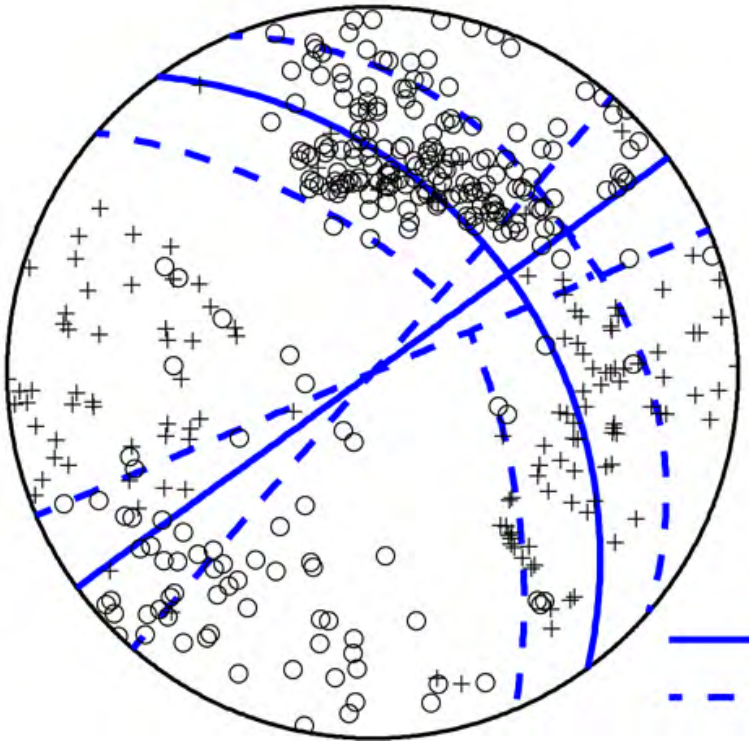

Incompatible with composite first-motion polarities.

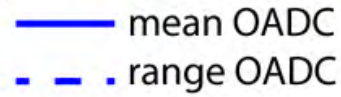

(b) Hosgri (tomoDD)

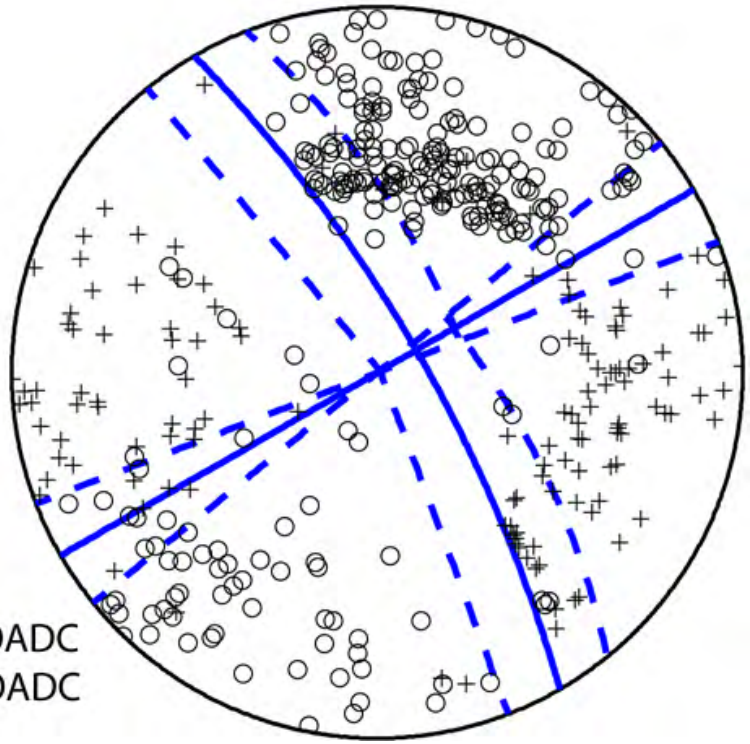

Compatible for mean and steeper dips.
Dip = 76°–89°NE / rake (from FM fit) = 180° ± 24°.

Source: Modified from Hardebeck (2012c).

Hosgri Fault Dip from First-Motion Polarity

DCPP SSC REPORT

Pacific Gas and Electric Company | Figure **7-8**

File path: S:\1005\005\Final_Report\Figures\Figure_700-08.ai; Date: 03/10/2015; User: Alex Remar, LCI; Rev.1

(a) Profile of Seismicity Projected Perpendicular to the Hosgri Fault

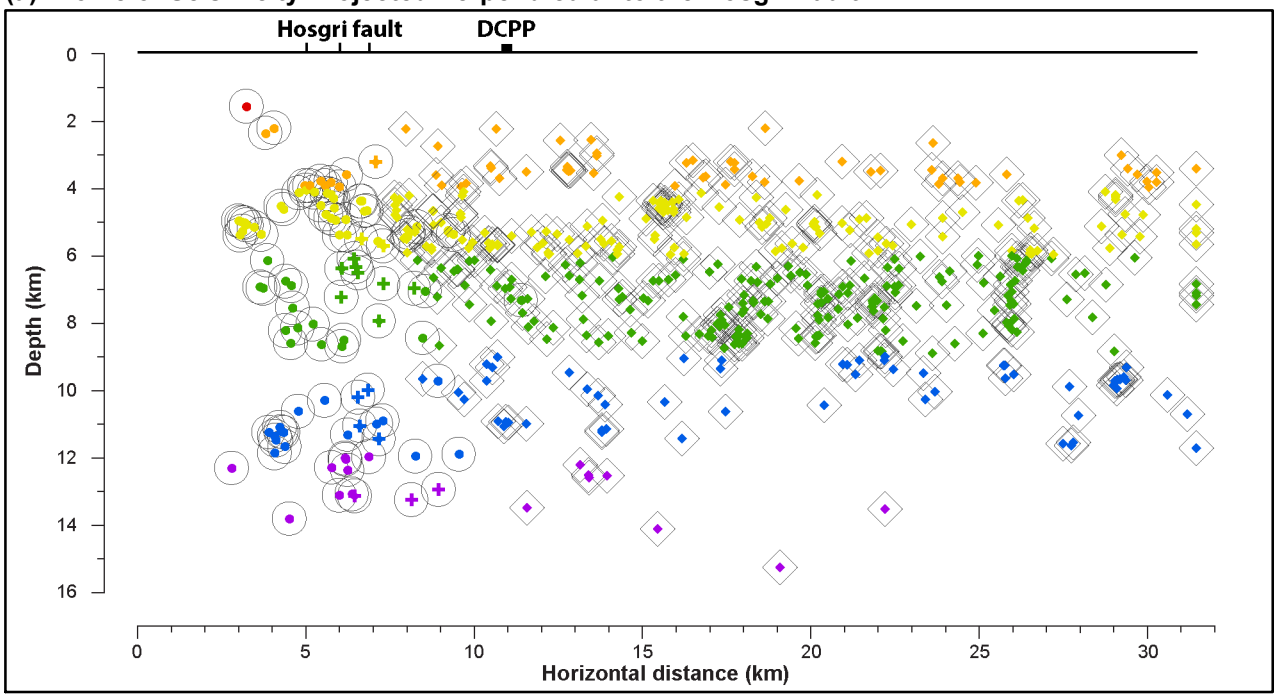

(b) Map of Epicenters

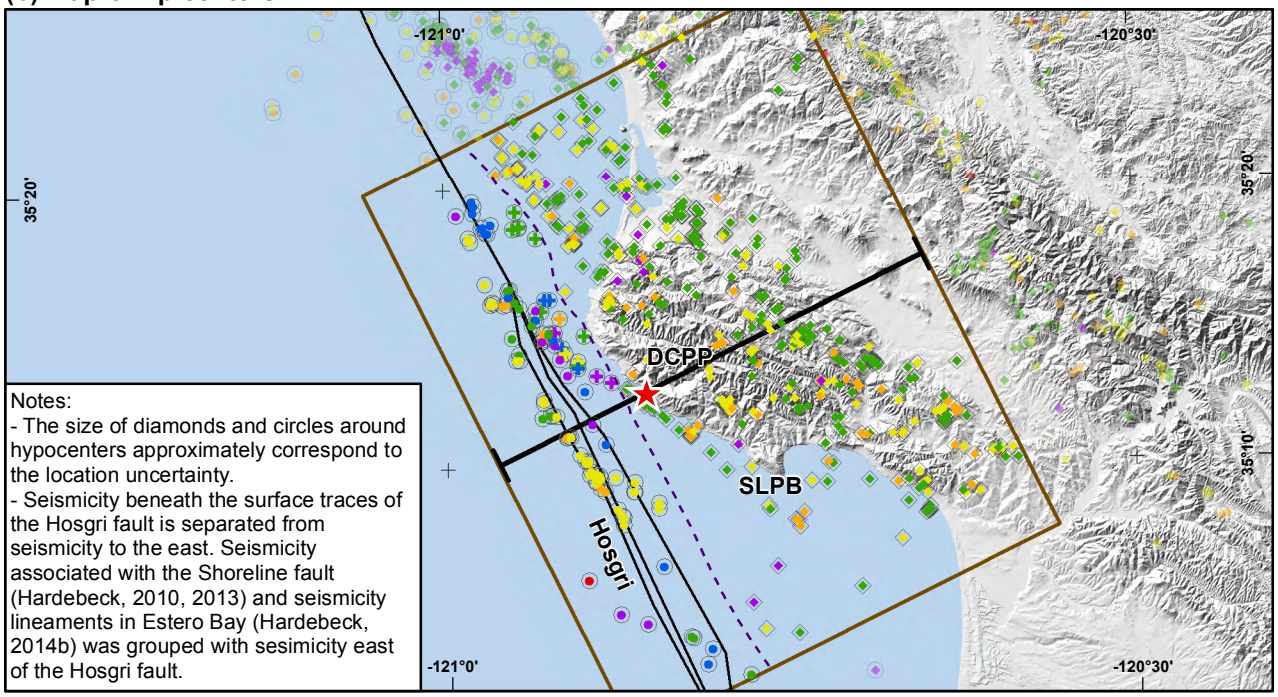

Notes:
- The size of diamonds and circles around hypocenters approximately correspond to the location uncertainty.
- Seismicity beneath the surface traces of the Hosgri fault is separated from seismicity to the east. Seismicity associated with the Shoreline fault (Hardebeck, 2010, 2013) and seismicity lineaments in Estero Bay (Hardebeck, 2014b) was grouped with sesimicity east of the Hosgri fault.

EXPLANATION

- Seismicity of San Luis—Pismo Block
- Seismicity beneath Hosgri fault traces
- Seismicity of intermediate location
- Approximate boundary between Hosgri and non-Hosgri seismicity
- Hosgri fault
- Cross section
- Extent of seismicity projected onto cross section

Seismicity
Depth (km)
- 0–2
- 2–4
- 4–6
- 6–9
- 9–12
- >12

Source: Seismicity from Hardebeck (2014a). Hypocentral locations from the tomoDD double-difference relocation algorithm.

N

0 8 16 mi.

0 10 20 km

Map projection and scale: NAD 83 / UTM Zone 10N, 1:500,000

Seismicity Cross Section Oriented Perpendicular to the Hosgri Fault

DCPP SSC REPORT

Pacific Gas and Electric Company

Figure **7-9**

File path: S:\1005\005\Final_Report_Figures\Figure_700-09.mxd; Date: 03/10/2015; User: Alex Remar, LCI; Rev.1

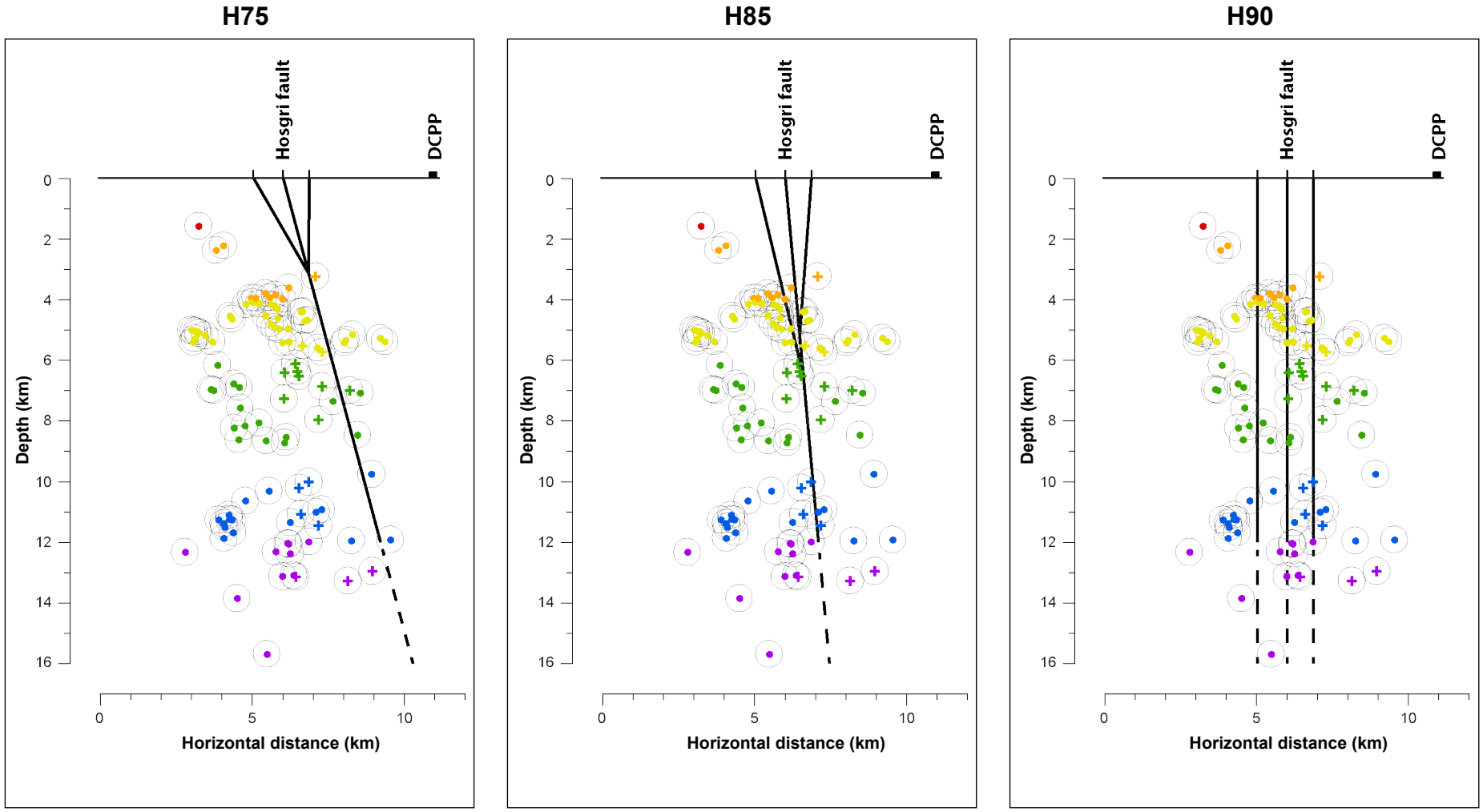

EXPLANATION

- Seismicity along Hosgri fault
- Seismicity of intermediate location
- Hosgri fault
- Cross section
- Extent of seismicity evaluated in cross section

Seismicity (TomoDD 2014)

Depth (km)

- 0–2
- 2–4
- 4–6
- 6–9
- 9–12
- >12

Notes:
- Seismicity from Hardebeck (2014a).
- Seismicity associated with the Shoreline fault, seismicity lineaments in Estero Bay, and diffuse seismicity to the east has been removed as shown on Figure 7-9.
- Circles around symbols represent approximate hypocentral location uncertainty.

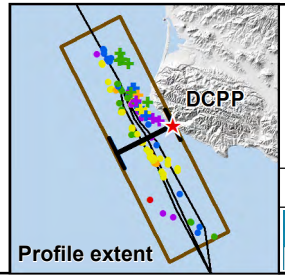

Cross Sections of Hosgri Fault Geometry Models Compared to Seismicity Profiles

DCPP SSC REPORT

Pacific Gas and Electric Company

Figure **7-10**

File path: S:\1005\005\Final_Report\Figures\Figure_700-10.ai; Date: 02/22/2015; User: Alex Remar, LCI; Rev.1

H75 [0.2]

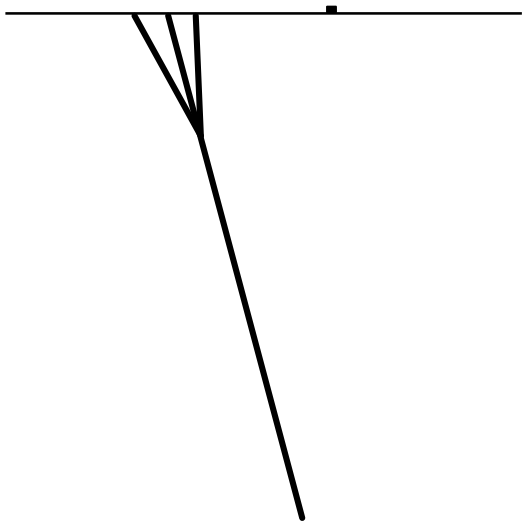

- Central trace dips 75 E, other traces are shallow splays (3 km).
- Locates central trace east of majority of seismicity.
- Approximately corresponds to minimum dip result from OADC (Hardebeck, 2012b).
- Represents limit of technical defensibility from hypocentral location uncertainty and possible systematic offset of hypocenter locations from the fault.

H85 [0.6]

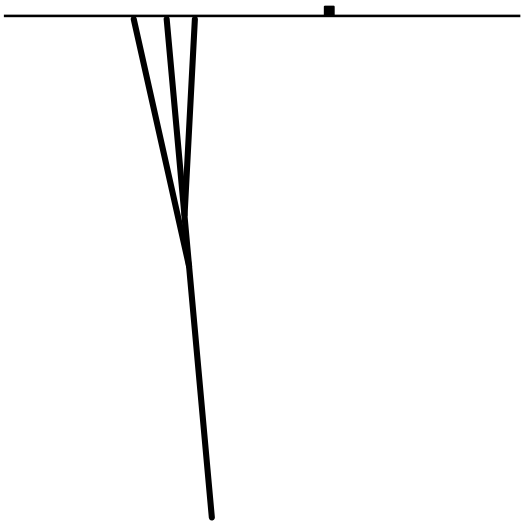

- Central trace dips 85 E, other traces are splays from depth (5 km).
- Within range of OADC solutions (Hardebeck, 2012b).
- Best fit to seismicity.

H90 [0.2]

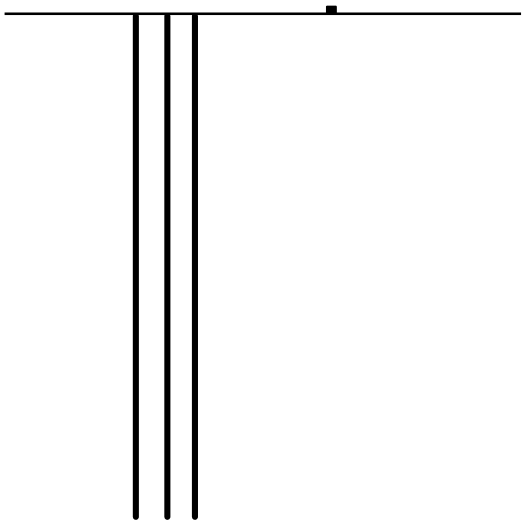

- 3 traces are vertical to base of crust.
- End member case.
- Approximately corresponds to maximum dip from OADC (Hardebeck, 2012b).
- Provides a reasonable fit to seismicity.

Notes:
- Numbers in brackets are model weights assigned to each Hosgri fault geometry model.
- Black box shows approximate location of DCPP.

Hosgri Fault Geometry Models

DCPP SSC REPORT

Pacific Gas and Electric Company | Figure **7-11**

File path: S:\1005\005\Final_Report\Figures\Figure_700-11.ai; Date: 03/10/2015; User: Alex Remar, LCI; Rev.1

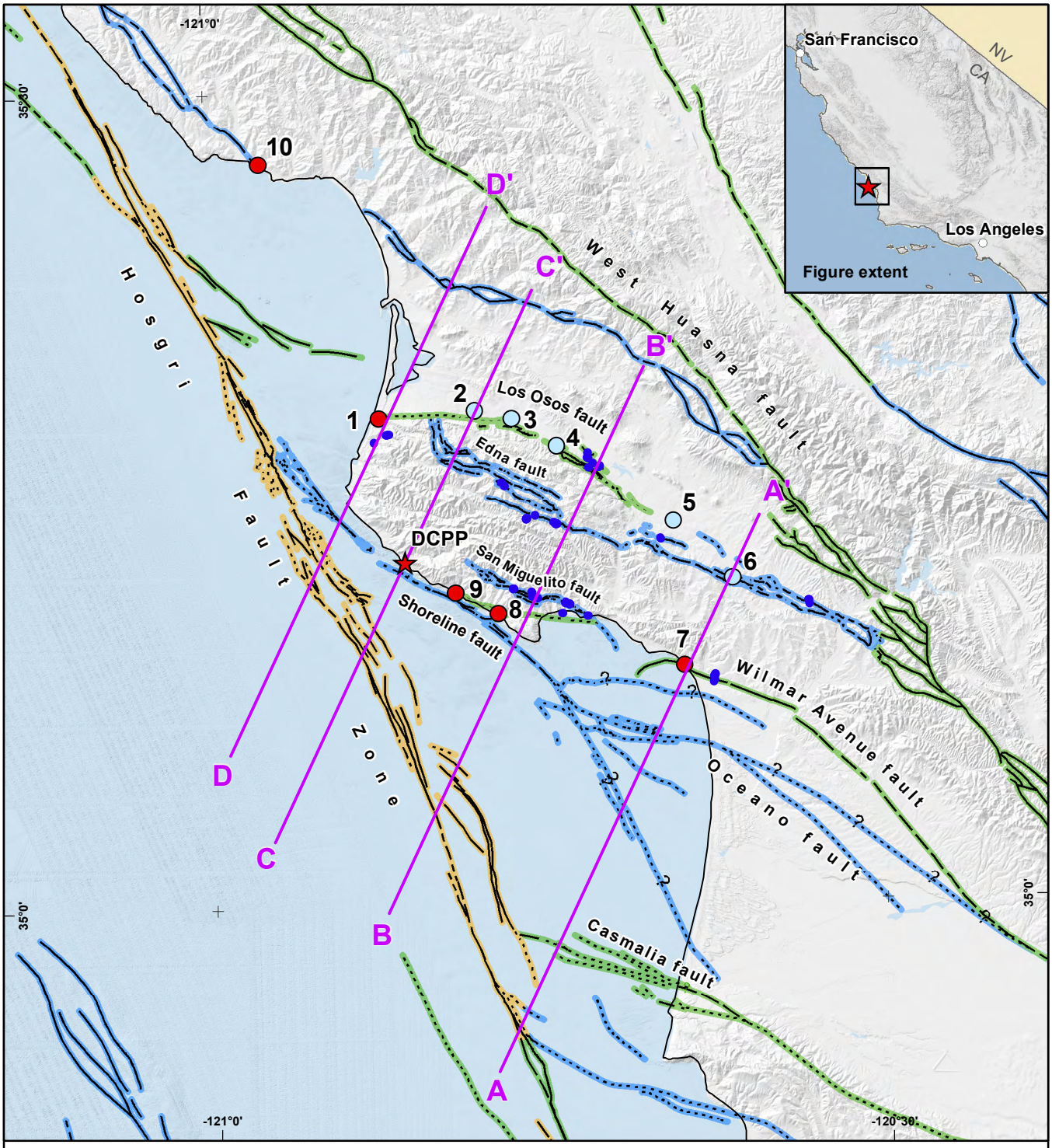

EXPLANATION

Cross section

Quaternary fault trace (see Plate 7-1 or Figure 7-3 for description of line styles)

Slip Rate

1–5 mm/yr

0.2–1 mm/yr

<0.2 mm/yr

Onshore fault activity constraints

Numbers are keyed to descriptions of key data constraints in Section 7.4

Trenches and road logs from LTSP

Deformed marine terrace

New data constraints

N

0 5 10 mi.

0 10 20 km

Map projection and scale: NAD 83 / UTM Zone 10N, 1:400,000

Constraints on Fault Models and Cross Section Locations

DCPP SSC REPORT

Pacific Gas and Electric Company

Figure **7-12**

File path: S:\1005\005\Final_Report_Figures\Figure_700-12.mxd; Date: 02/22/2015; User: Serkan Bozkurt, LCI; Rev.1

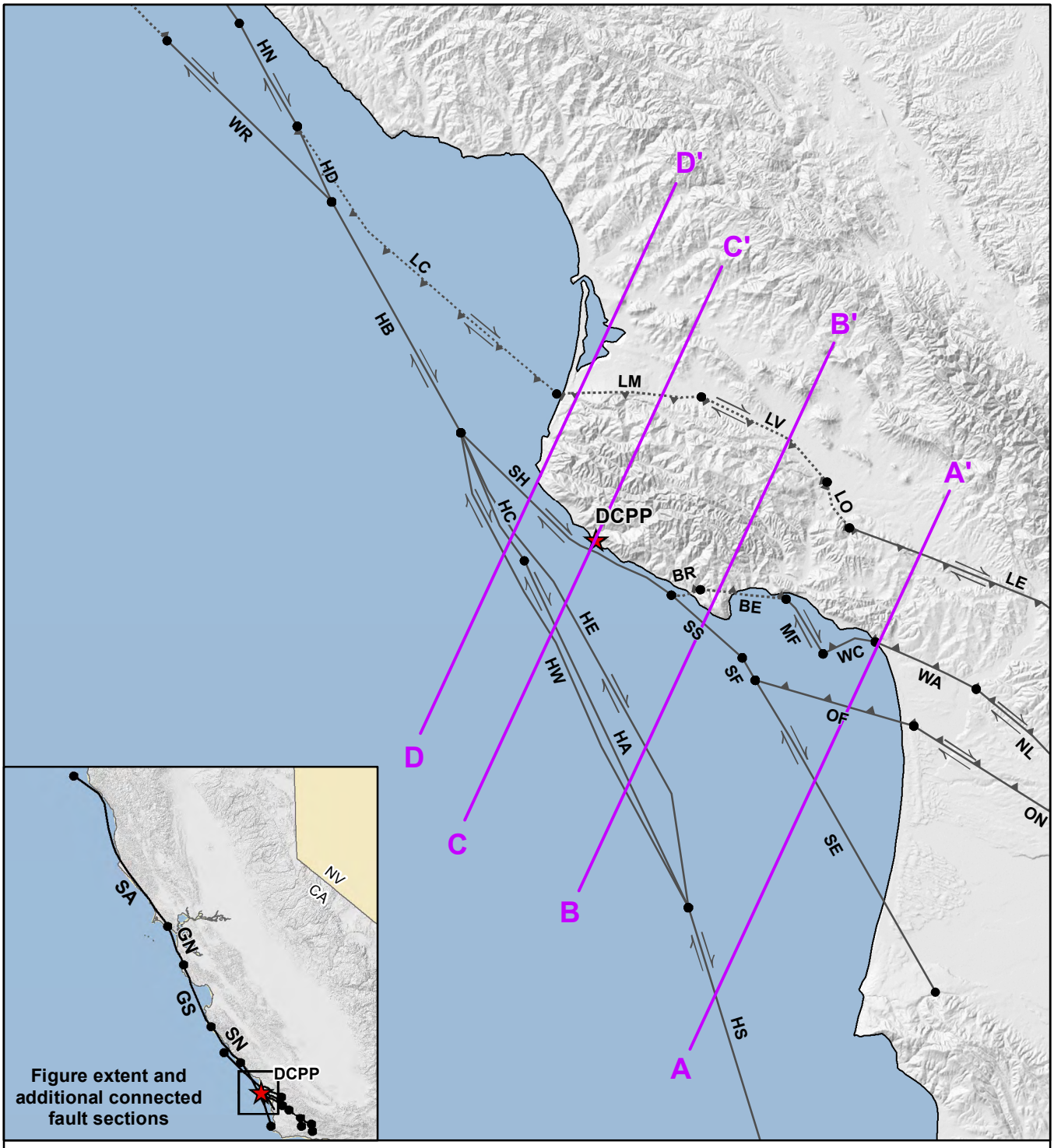

EXPLANATION

Cross section location

Endpoints of fault sections. Two-letter codes describing sections are explained in Table 6-5.

Fault Sources

Fault source; dotted where blind

Strike-slip; arrows indicate direction of slip

Reverse; teeth on upthrown side

Oblique

N

0 6 12 mi.

0 10 20 km

Map projection and scale: WGS 84 / UTM Zone 10N, 1:400,000

Primary and Connected Fault Sources in the Outward-Vergent (OV) Fault Geometry Model, DCPP Vicinity

DCPP SSC REPORT

Pacific Gas and Electric Company

Figure **7-13**

File path: S:\1005\005\Final_Report_Figures\Figure_700-13.mxd; Date: 03/06/2015; User: alex, LCI; Rev.1

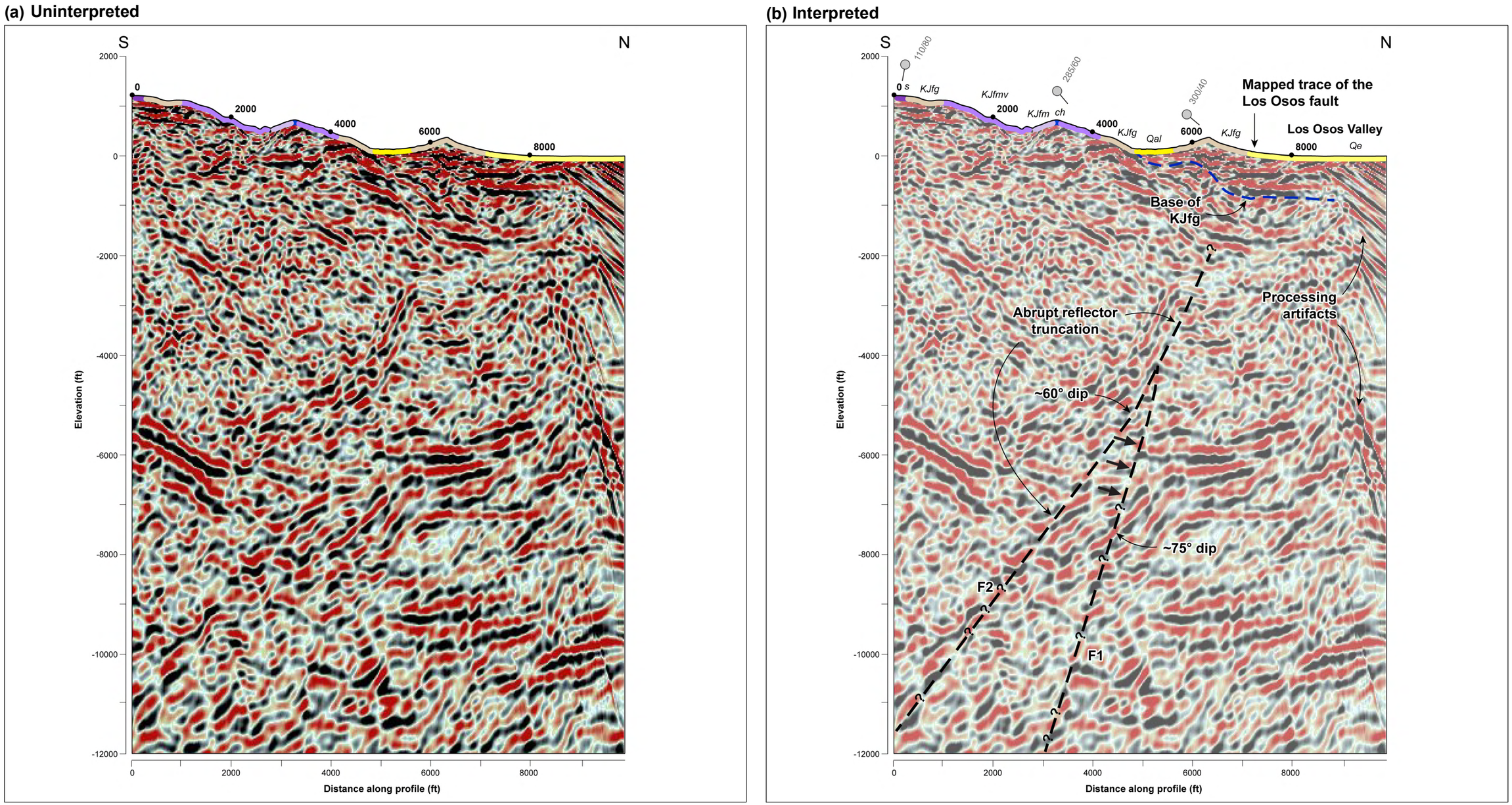

EXPLANATION

Fault: solid where well located, dashed where approximately located, queried where uncertain

Base of KJfg

Arrows marking offset or truncated reflectors

Profile strike/dip

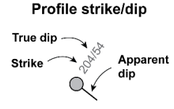

2000 Horizontal distance along seismic line, 2,000 ft increment

Notes:
- Geology along topographic profile from Plate 1 of PG&E (2014, Chapter 7).
- Horizontal offsets are shown along a topographic profile above the seismic line.

Source: Modified from PG&E (2014, Chapter 7).

Vibroseis Line 204 North

DCPP SSC REPORT

Pacific Gas and Electric Company

Figure **7-14**

File path: S:\1005\005\Final_Report_Figures\Figure_700-14.mxd; Date: 02/22/2015; User: Alex Remar, LCI; Rev.1

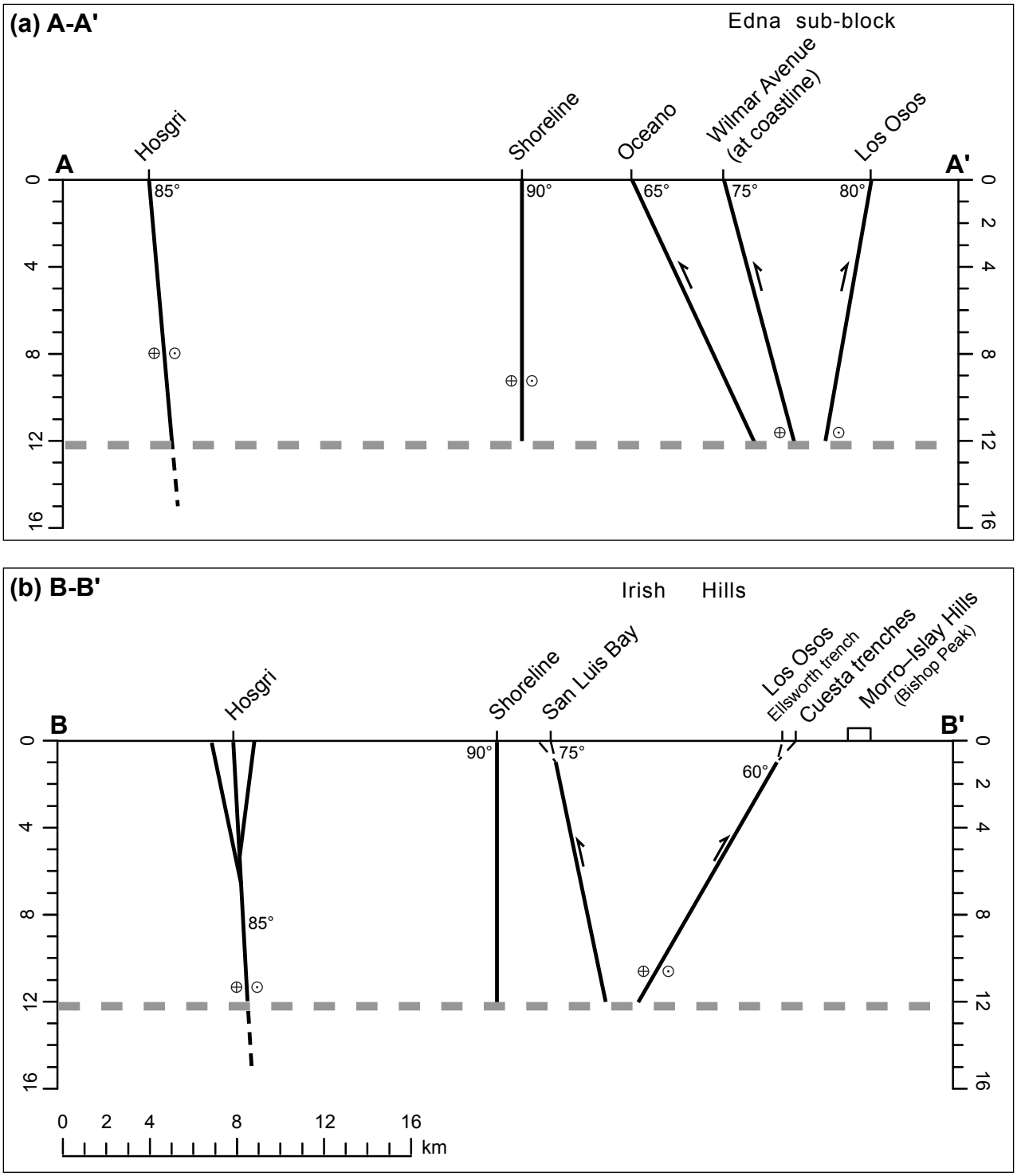

EXPLANATION

Fault; solid where well located, dashed where approximately located; for strike-slip faults, ⊕ is away, ⊙ is toward.

Seismogenic depth (12 km)

Zone of distributed deformation

Notes:
- Relatively steeper dips are characterized for faults bounding the Edna Sub-block because the range is markedly narrower than the Irish Hills.
- Preferred Hosgri FGM shown.

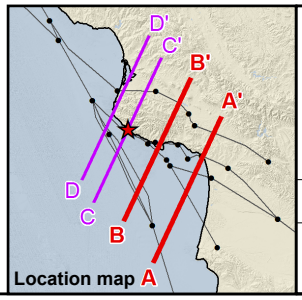

Representative Cross Sections A-A′ and B-B′ in the OV Model

DCPP SSC REPORT

Pacific Gas and Electric Company

Figure **7-15**

File path: S:\1005\005\Final_Report_Figures\Figure_700-15.ai; Date: 02/22/2015; User: Alex Remar, LCI; Rev.1

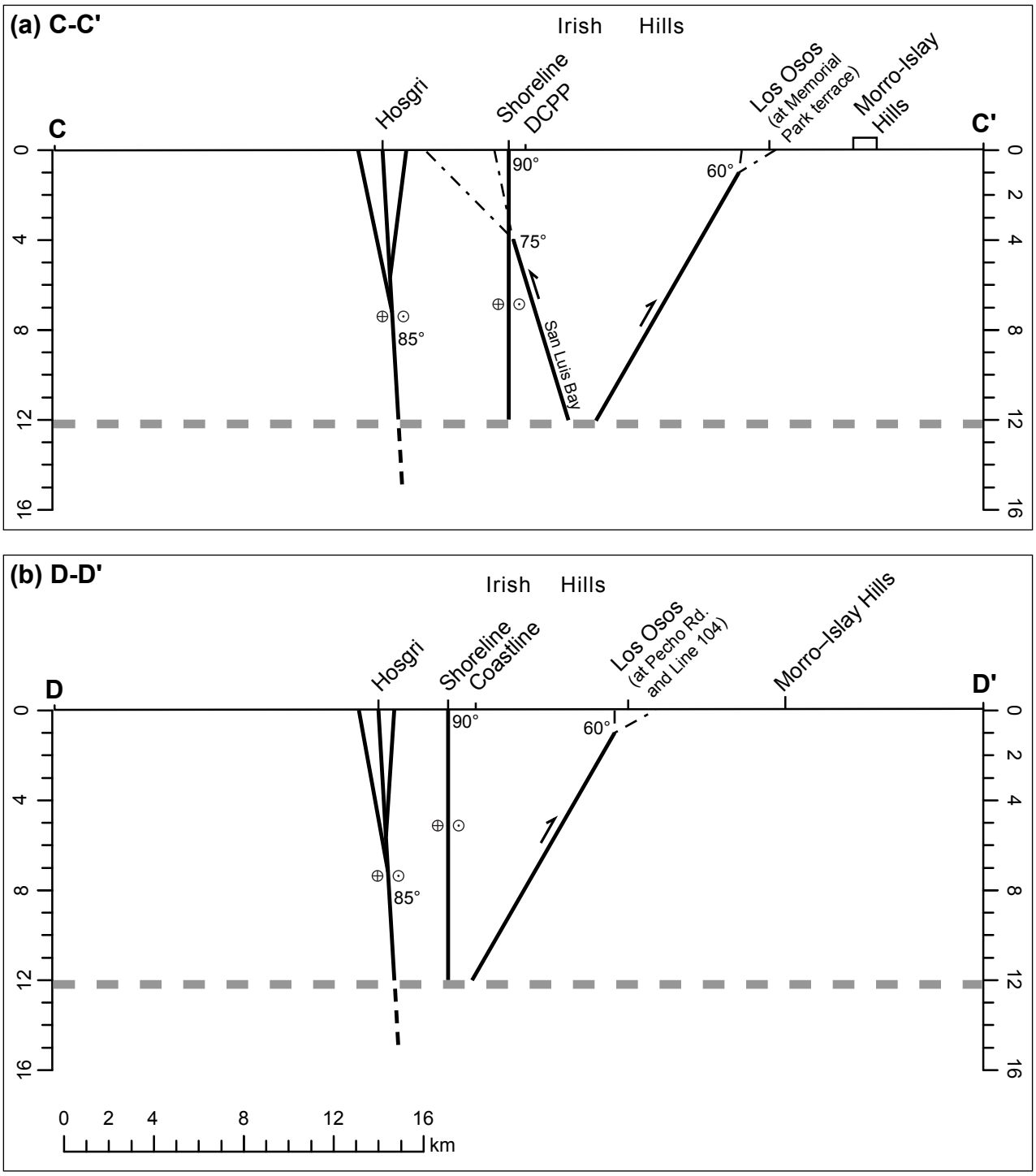

EXPLANATION

Note: Preferred Hosgri FGM shown.

- Fault; solid where well located, dashed where approximately located; for strike-slip faults, ⊕ is away, ⊙ is toward.
- Seismogenic depth (12 km)
- Zone of distributed deformation

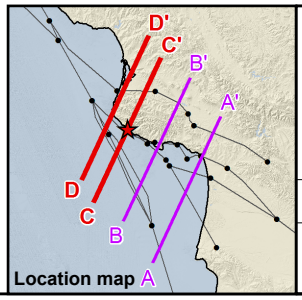

Representative Cross Sections C-C′ and D-D′ in the OV Model

DCPP SSC REPORT

Pacific Gas and Electric Company

Figure **7-16**

File path: S:\1005\005\Final_Report_Figures\Figure_700-16.ai; Date: 03/10/2015; User: Serkan Bozkurt, LCI; Rev.1

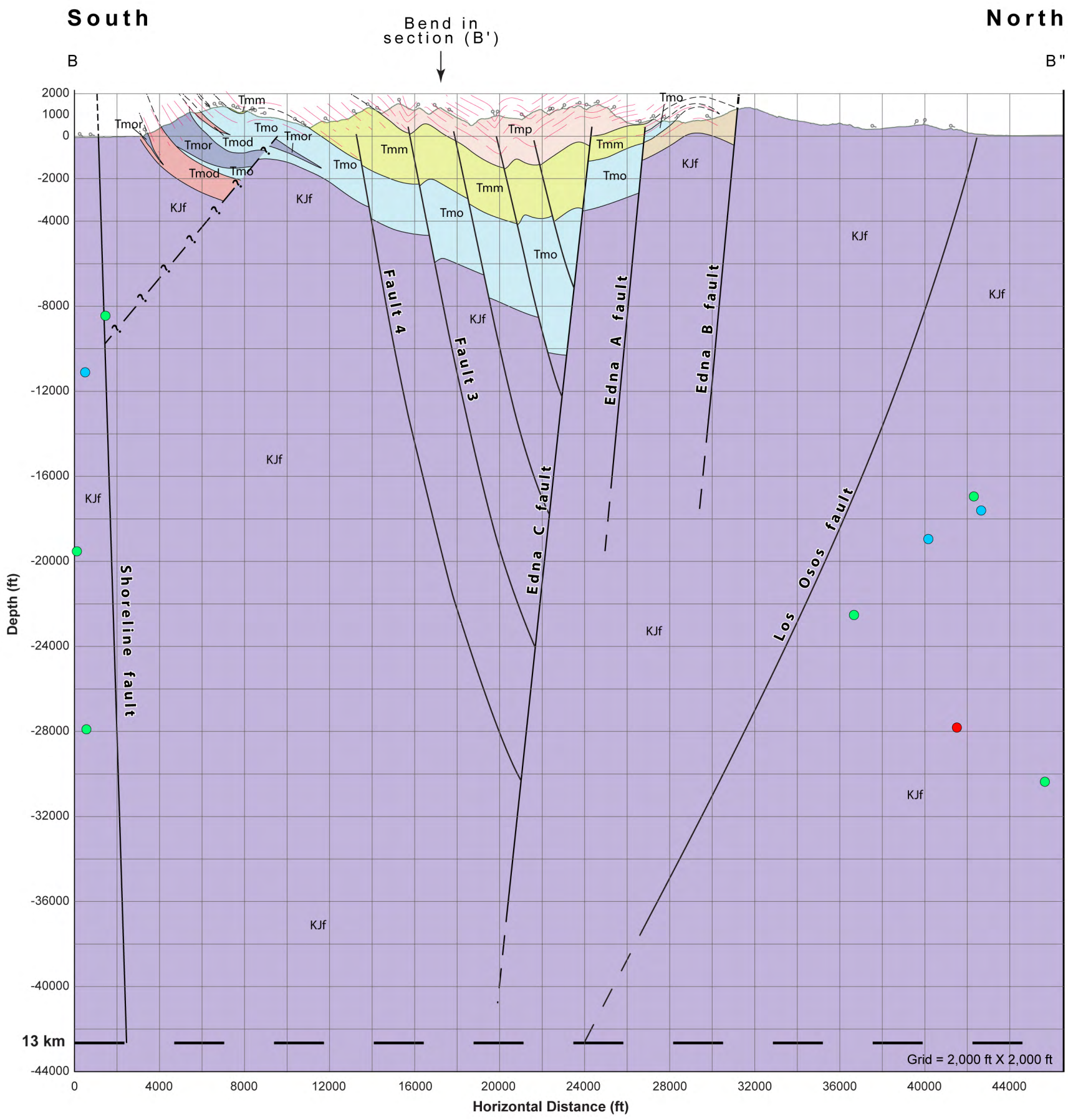

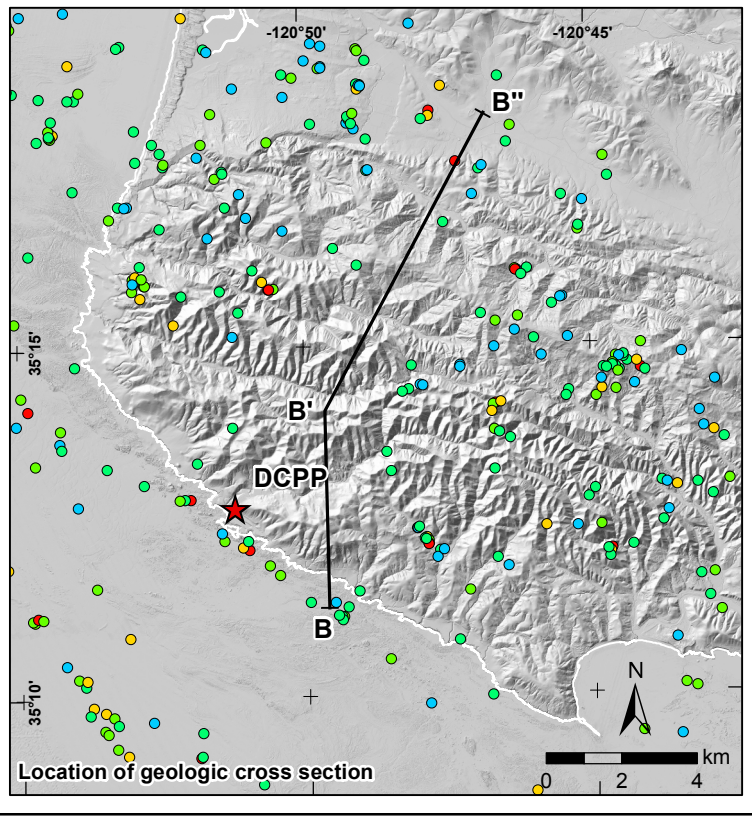

EXPLANATION

Geologic cross section

Seismicity [M]

- 0.00 - 0.49
- 0.50 - 0.99
- 1.00 - 1.49
- 1.50 - 1.99
- 2.00 - 2.49
- 2.50 - 3.50

Geologic Units

Tmpm	Pismo Formation, Miguelito Member
Tmm	Monterey Formation
Tmo	Obispo Formation
Tmod	Obispo diabase
Tmor	Obispo Formation, resistant unit
KJf	Franciscan Complex

Geologic Symbols

- Schematic representation of interpreted fault location
- Form line
- Apparent dip

Notes:
- See Plate 1 of PG&E (2014, Chapter 7) for geologic mapping along cross section.
- The structural cross section shown here was developed by PG&E (2014, Chapter 7) based on interpretation of surficial geologic mapping, seismic-reflection data, and correlation to borings and wells.

Sources:
- Modified from PG&E (2014, Chapter 7).
- Seismicity data from Hardebeck (2014a).

ONSIP Geologic Cross Section B-B"

DCPP SSC REPORT

Pacific Gas and Electric Company

Figure **7-17**

File path: S:\1005\005\Final_Report_Figures\Figure_700-17.mxd; Date: 03/06/2015; User: Alex Remar, LCI; Rev.1

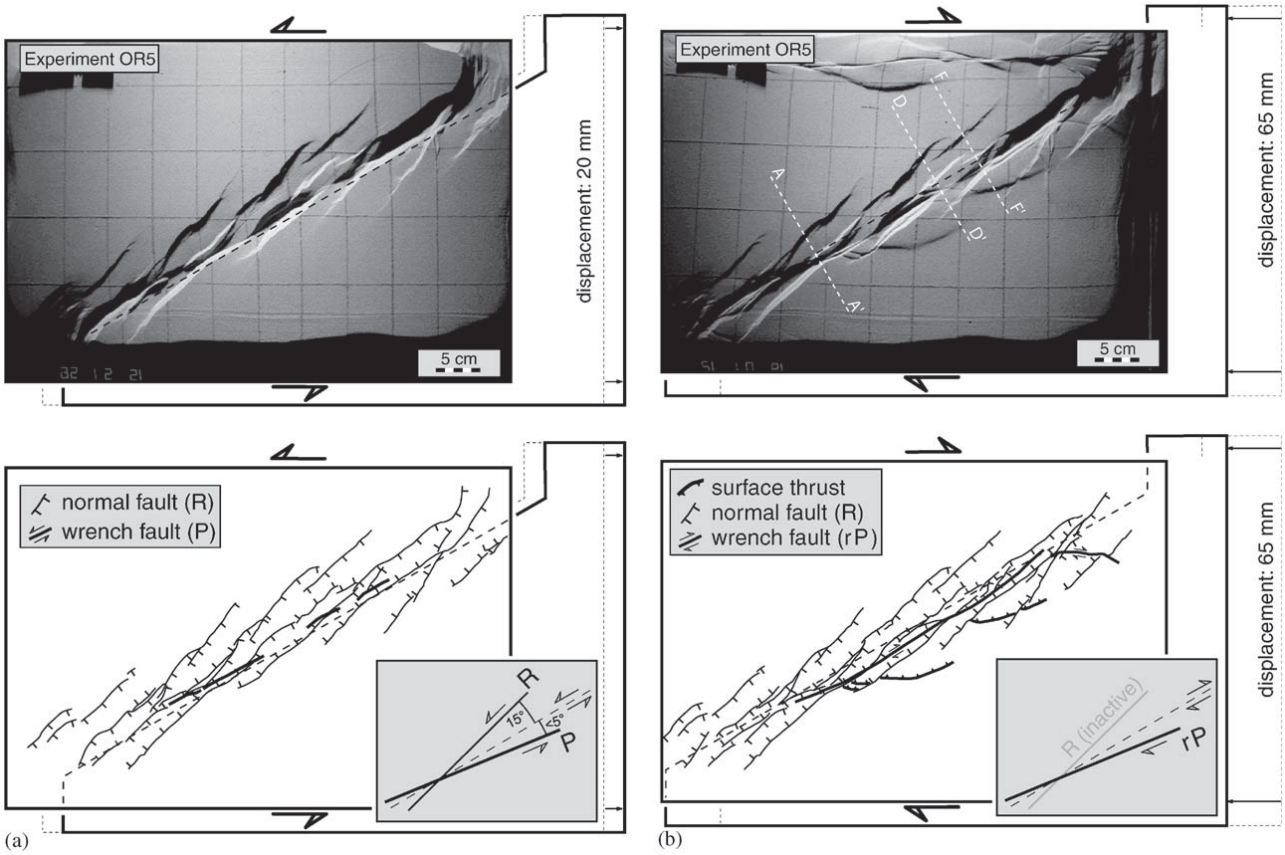

(a) Analog sandbox model of an extensional basin formed under left-lateral transtensional boundary conditions (top left), and subsequently deformed under right-lateral transpressional conditions (top right). Note the right-stepping en echelon pattern of the normal faults formed during sinistral transtension, and development of lobate thrust faults along the margins of the extensional basin system during the later phase of transpression.

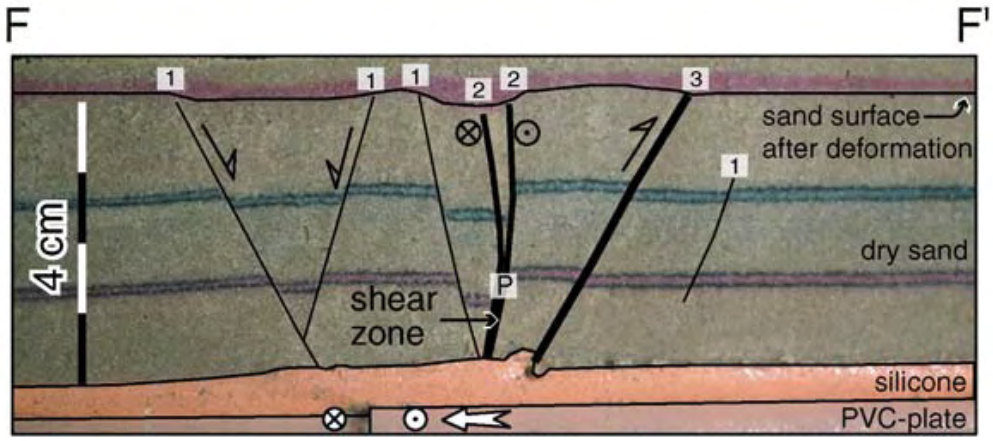

(b) Cross section through the final sandbox model (F-F'; location in upper right figure) showing a late-stage transpressional reverse fault (3) splaying upward from the principal displacement zone at the base of the model.

Sources:
- Images from Ustaszewski et al. (2005).
- Figure modified from PG&E (2014, Chapter 7).

Sandbox Model of a Transtensional Basin Deformed by Transpression

DCPP SSC REPORT

Pacific Gas and Electric Company | Figure **7-18**

File path: S:\1005\005\Final_Report_Figures\Figure_700-18.ai; Date: 03/10/2015; User: Alex Remar, LCI; Rev.1

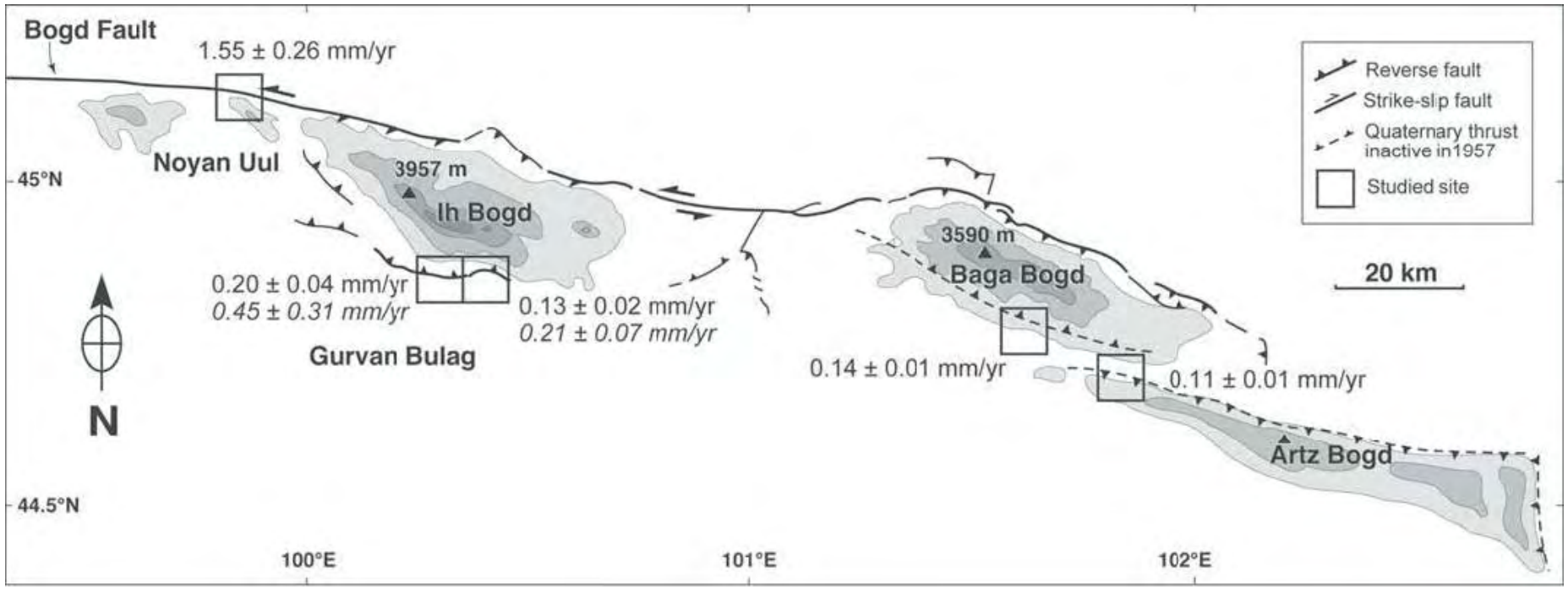

Note: All the slip rates are vertical ones, except at Noyan Uul, and calculated for the Late Pleistocene-Holocene. At Gurvan Bulag, the rates in italics are calculated for the past ~15–20 kyr.

Source: Ritz et al. (2006).

Map Showing the Gurvan Bogd Fault System, Mongolia, and Related Topography

DCPP SSC REPORT

Pacific Gas and Electric Company | Figure **7-19**

File path: S:\1005\005\Final_Report\Figures\Figure_700-19.ai; Date: 12/10/2014; User: Alex Remar, LCI; Rev.1

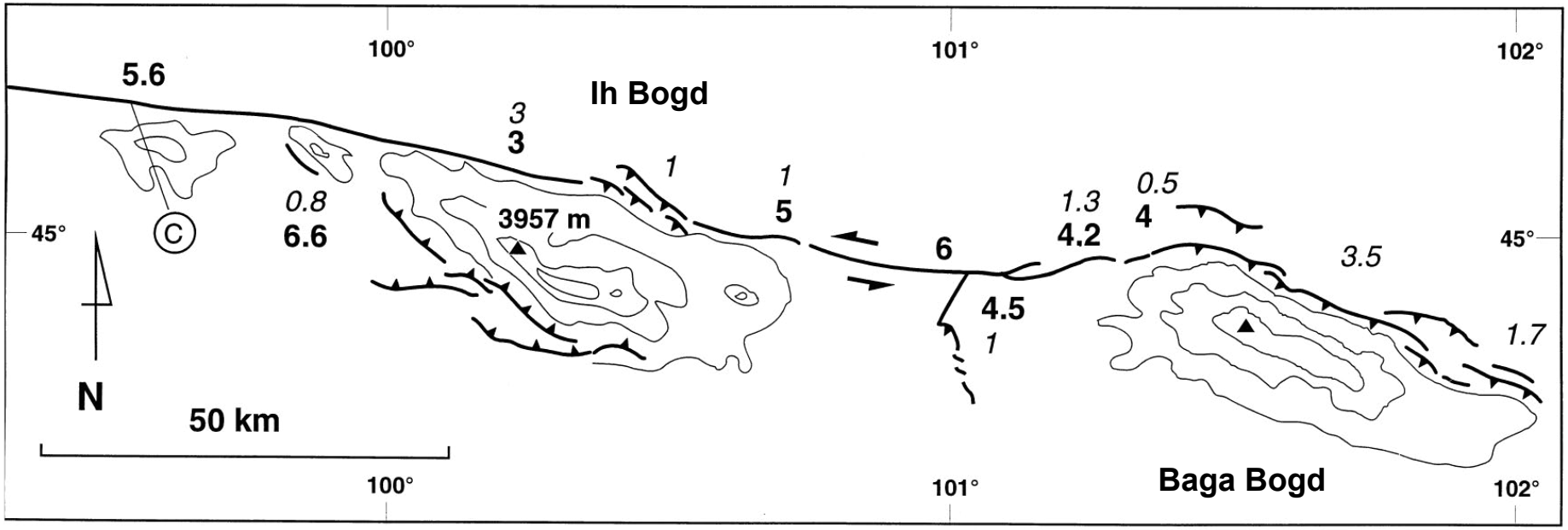

Notes:
- Bold and italic numbers indicate horizontal and vertical displacements in meters, respectively (data from Florensov and Solonenko, 1963).
- Figure was modified from Ritz et al. (1995) to update the spelling of massif names for consistency with other maps (e.g., Figure 7-19).

Source: Ritz et al. (1995).

Simplified Structural Map Showing Diplacements on Faults That Ruptured During the 1957 Gobi-Altay Earthquake, Mongolia

DCPP SSC REPORT

Pacific Gas and Electric Company | Figure **7-20**

File path: S:\1005\005\Final_Report\Figures\Figure_700-20.ai; Date: 02/22/2015; User: Alex Remar, LCI; Rev.1

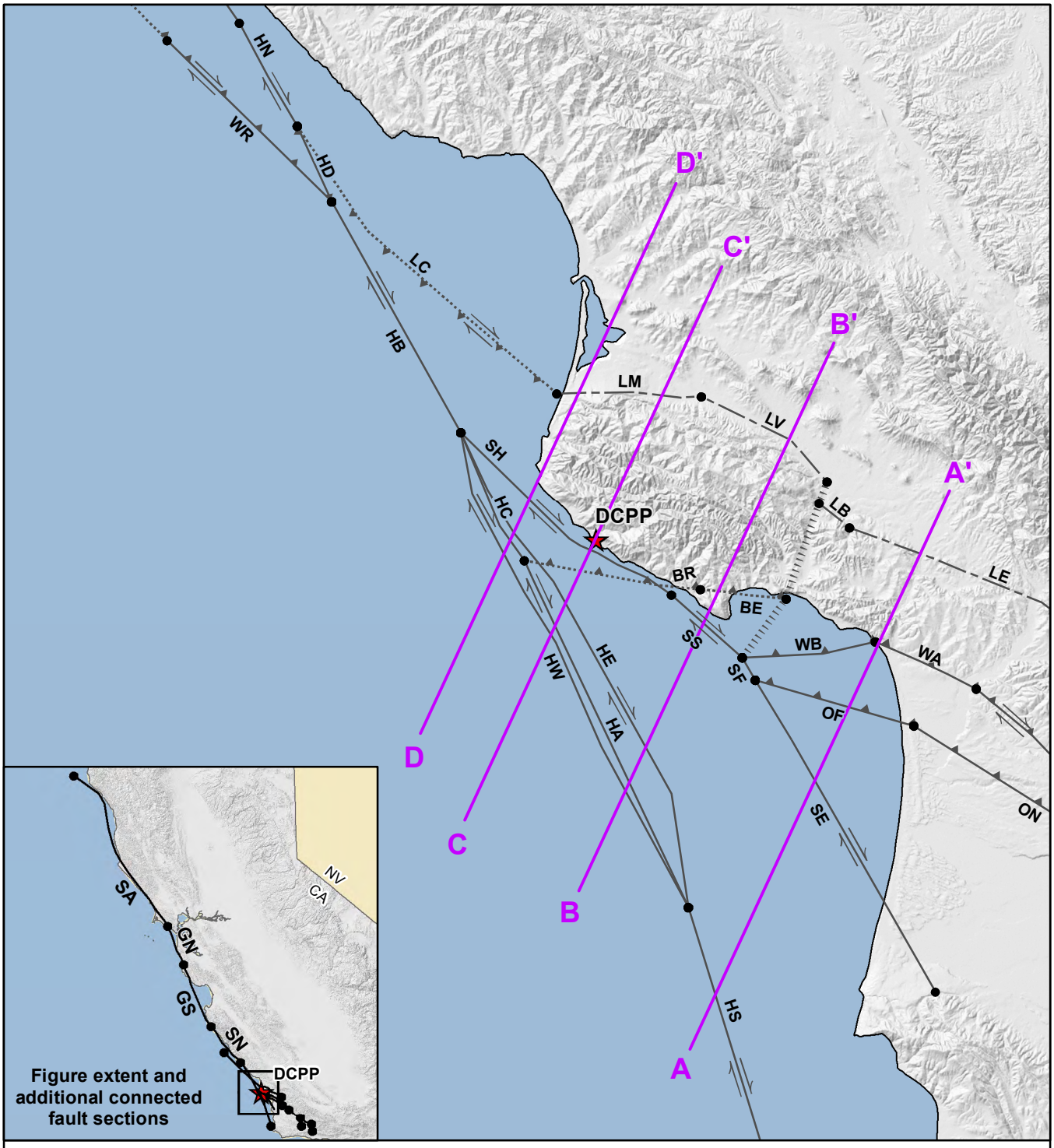

EXPLANATION

Cross section location

Endpoints of fault sections. Two-letter codes describing sections are explained in Table 6-5.

Fault Sources

Fault source; dotted where blind

Strike-slip; arrows indicate direction of slip

Reverse; teeth on upthrown side

Oblique

Axial surface or backthrust

Tear

N

0 6 12 mi.

0 10 20 km

Map projection and scale: WGS 84 / UTM Zone 10N, 1:400,000

Primary and Connected Fault Sources in the Southwest-Vergent (SW) Fault Geometry Model, DCPP Vicinity

DCPP SSC REPORT

Pacific Gas and Electric Company

Figure **7-21**

File path: S:\1005\005\Final_Report_Figures\Figure_700-21.mxd; Date: 03/06/2015; User: alex, LCI; Rev.1

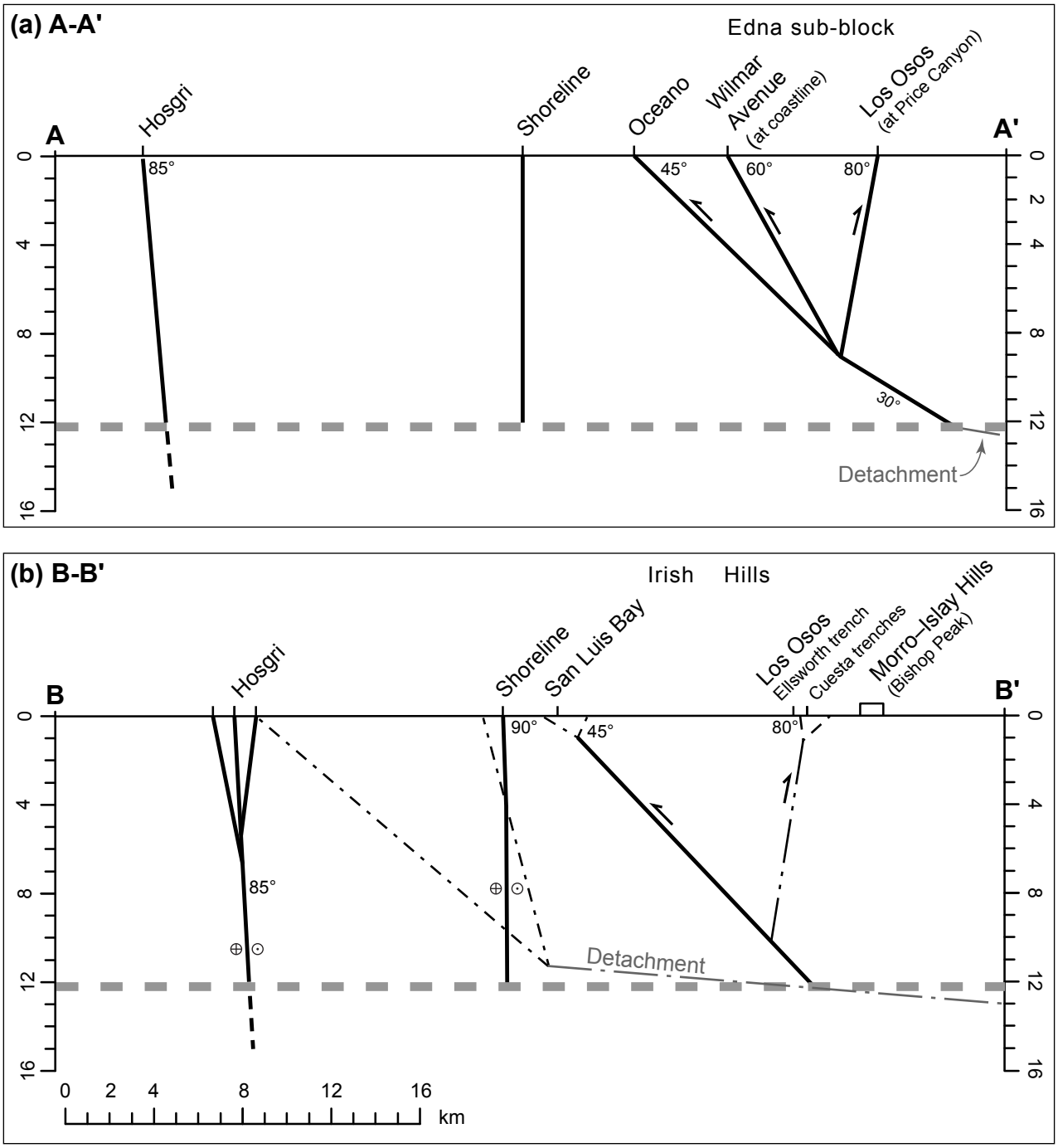

EXPLANATION

- Fault; solid where well located, dashed where approximately located; for strike-slip faults, ⊕ is away, ⊙ is toward.
- Seismogenic depth (12 km)
- Axial Surface or backthrust
- Zone of distributed deformation
- Detachment, nonseismogenic

Notes:
- We recognize that the geometry of the Los Osos fault intersection with the San Luis Bay fault in Panel (b) (Section B-B') does not clearly fit the expected geometry of an axial surface with a change in dip of the underlying reverse fault. The geometry of the San Luis Bay fault has been simplified to allow for a more gently dipping fault (45°) to extend to a seismogenic depth of 12 km.
- Preferred Hosgri FGM shown.

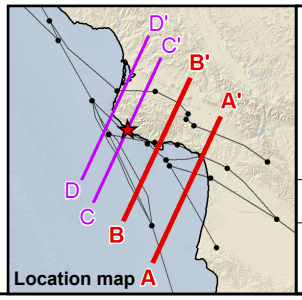

Representative Cross Sections A-A′ and B-B′ in the SW Model

DCPP SSC REPORT

Pacific Gas and Electric Company

Figure **7-22**

File path: S:\1005\005\Final_Report_Figures\Figure_700-22.ai; Date: 03/10/2015; User: Serkan Bozkurt, LCI; Rev.1

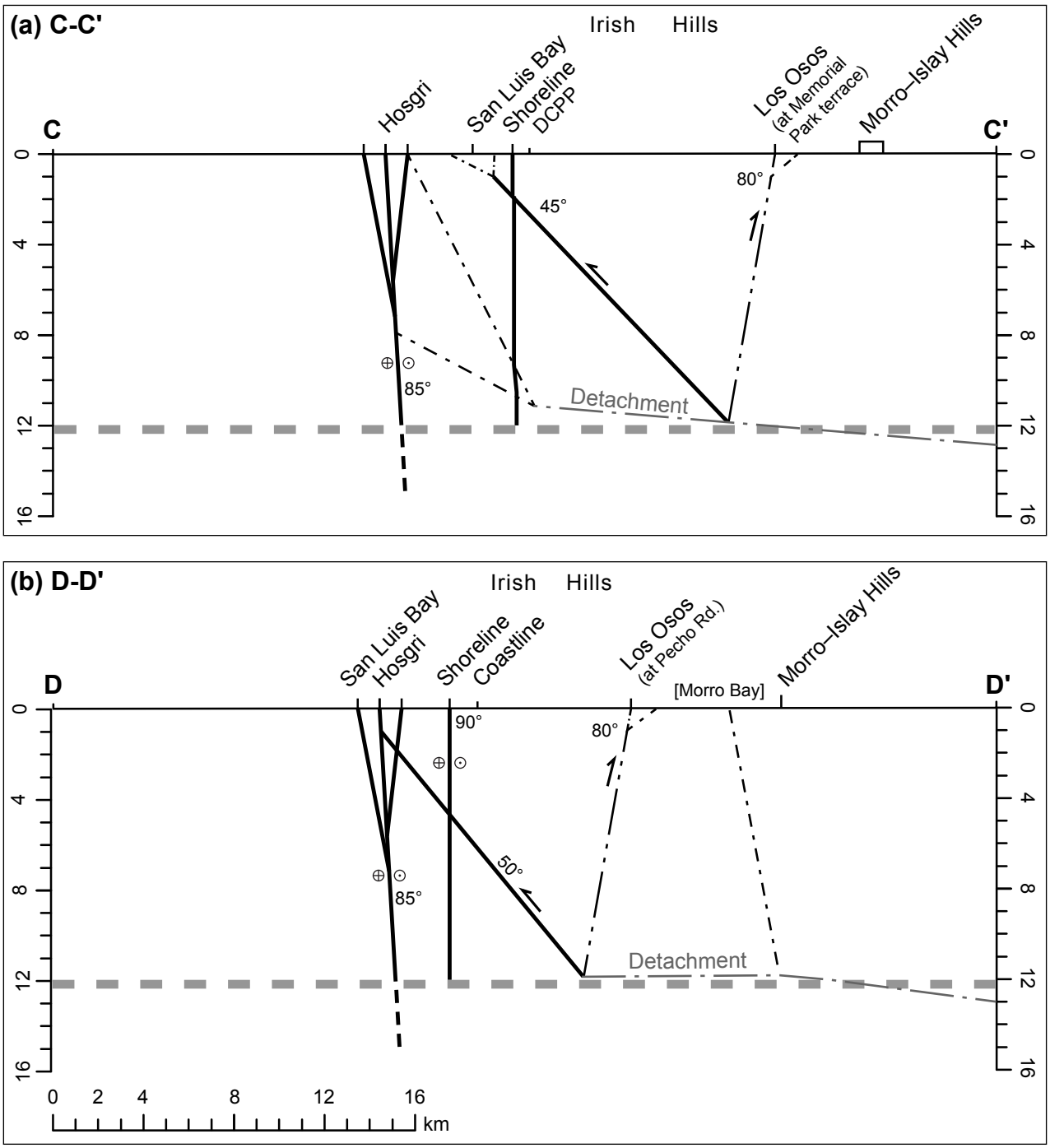

EXPLANATION

- Fault; solid where well located, dashed where approximately located; for strike-slip faults, ⊕ is away, ⊙ is toward.
- Seismogenic depth (12 km)
- Axial Surface or backthrust
- Zone of distributed deformation
- Detachment, nonseismogenic

Note:
- San Luis Bay fault has a slightly steeper dip in Section D-D' than in C-C' because the uplifting range is narrower. Similar to the surface trace of the Los Osos fault, the San Luis Bay fault may splay from the Hosgri fault offshore, suggesting it may steepen as it approaches the Hosgri.
- Preferred Hosgri FGM shown.

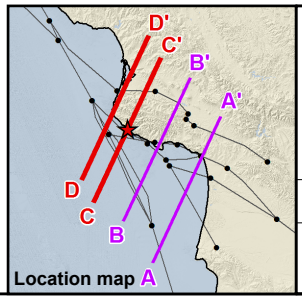

Representative Cross Sections C-C′ and D-D′ in the SW Model

DCPP SSC REPORT

Pacific Gas and Electric Company

Figure **7-23**

File path: S:\1005\005\Final_Report_Figures\Figure_700-23.ai; Date: 03/10/2015; User: Serkan Bozkurt, LCI; Rev.1

(a) Map View

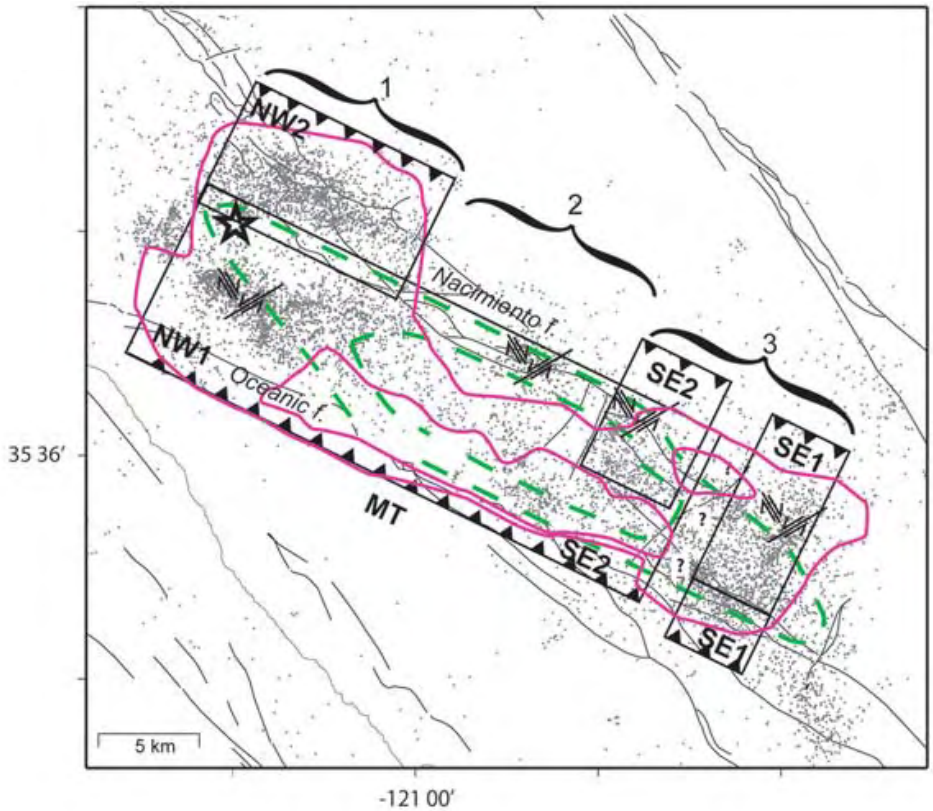

Panels (b)-(d). Schematic cross section views across the three bracketed regions showing surface uplift from InSAR and fault motion at depth

(b) Pop-up block model: Across northwest end of the aftershock zone (bracket 1)

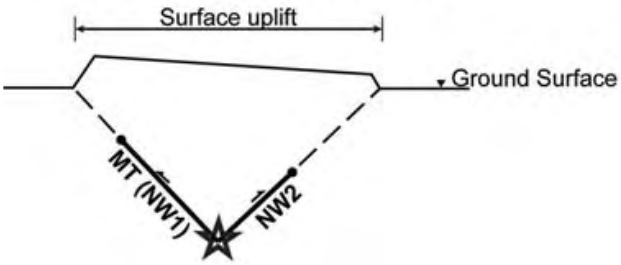

(c) Fault-propagation fold model: Across central section of the aftershock zone (bracket 2)

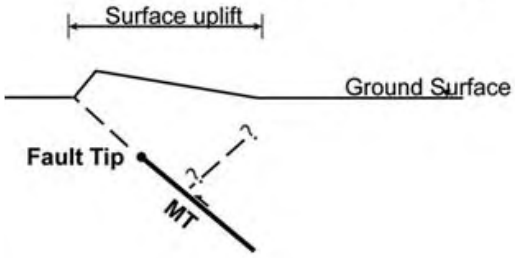

(d) Pop-up block model: Across southeast end of the aftershock zone, near the end of the main thrust (bracket 3)

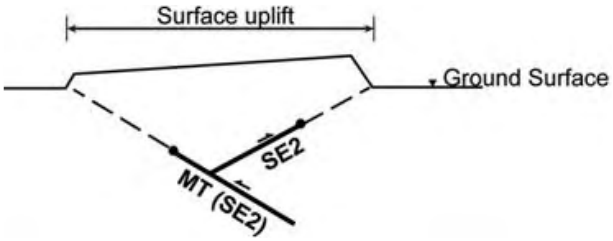

Notes:
- In Panel (a), star represents mainshock, small gray dots are 3D aftershocks, dashed green lines are slip contours (adapted from Ji et al., 2004), and solid pink lines indicate the edge of the range front uplift as mapped from InSAR. Strike-slip fault motion symbols represent the average orientations of the upper parts of clusters in the central and southeastern parts of the aftershock zone.
- MT is the interpreted main thrust plane, NW1. NW2, SE1, and SE2 are interpreted backthrust planes.

Source: Modified from McLaren et al. (2008).

Surface Deformation, Seismicity, and Postulated Fault Ruptures Associated with the 2003 M 6.5 San Simeon Earthquake

DCPP SSC REPORT

Pacific Gas and Electric Company

Figure **7-24**

File path: /s/1005/005/Final_Report_Figures/Figure_700-24.ai; Date: 03/10/2015; User: Brian Greer, LCI; Rev. 1

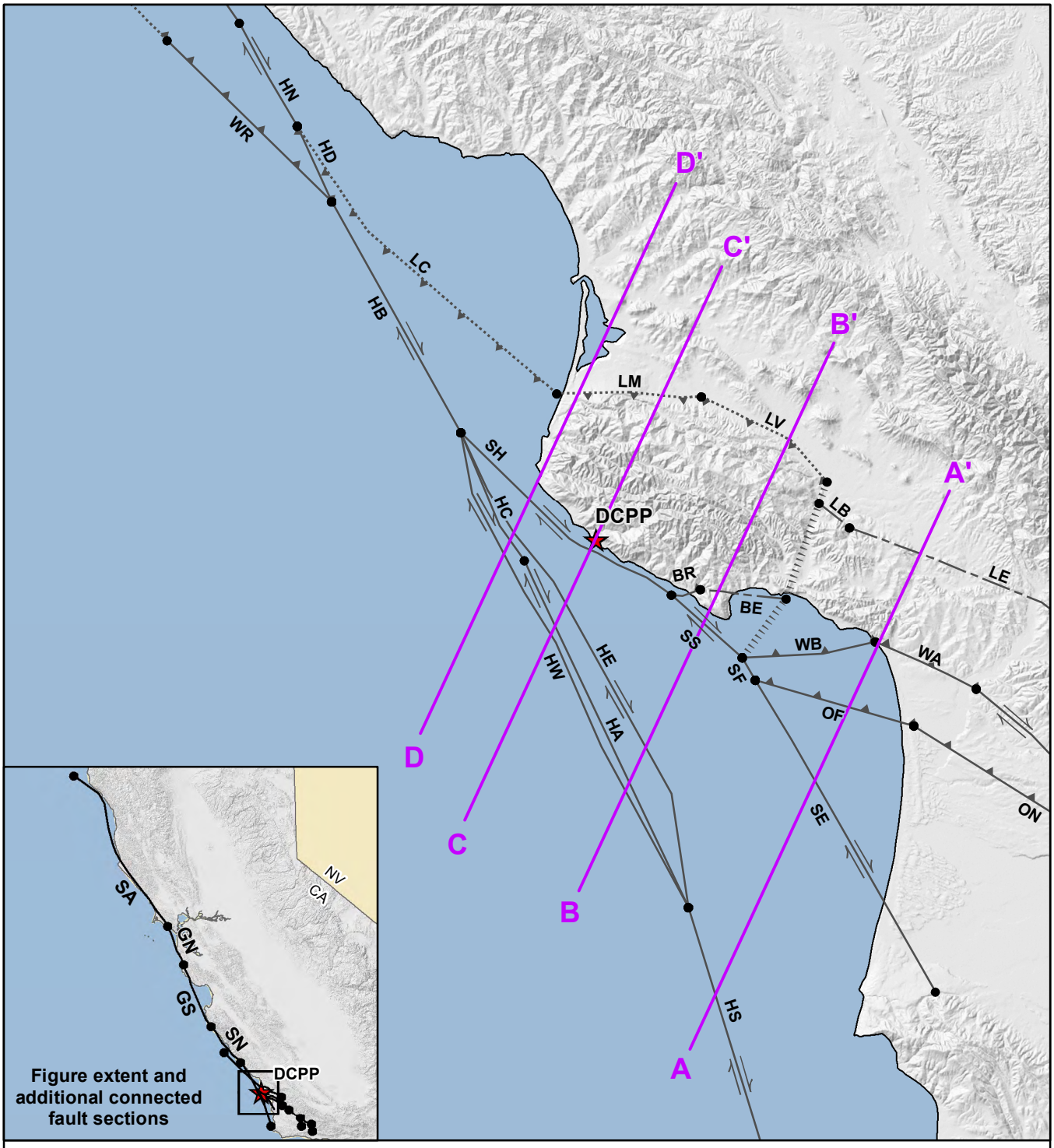

EXPLANATION

Cross section location

Endpoints of fault sections. Two-letter codes describing sections are explained in Table 6-5.

Fault Sources

Fault source; dotted where blind

Strike-slip; arrows indicate direction of slip

Reverse; teeth on upthrown side

Oblique

Axial surface or backthrust

Tear

N

0 6 12 mi.

0 10 20 km

Map projection and scale: WGS 84 / UTM Zone 10N, 1:400,000

Primary and Connected Fault Sources in the Northeast-Vergent (NE) Fault Geometry Model, DCPP Vicinity

DCPP SSC REPORT

Pacific Gas and Electric Company

Figure **7-25**

File path: S:\1005\005\Final_Report_Figures\Figure_700-25.mxd; Date: 03/06/2015; User: alex, LCI; Rev.1

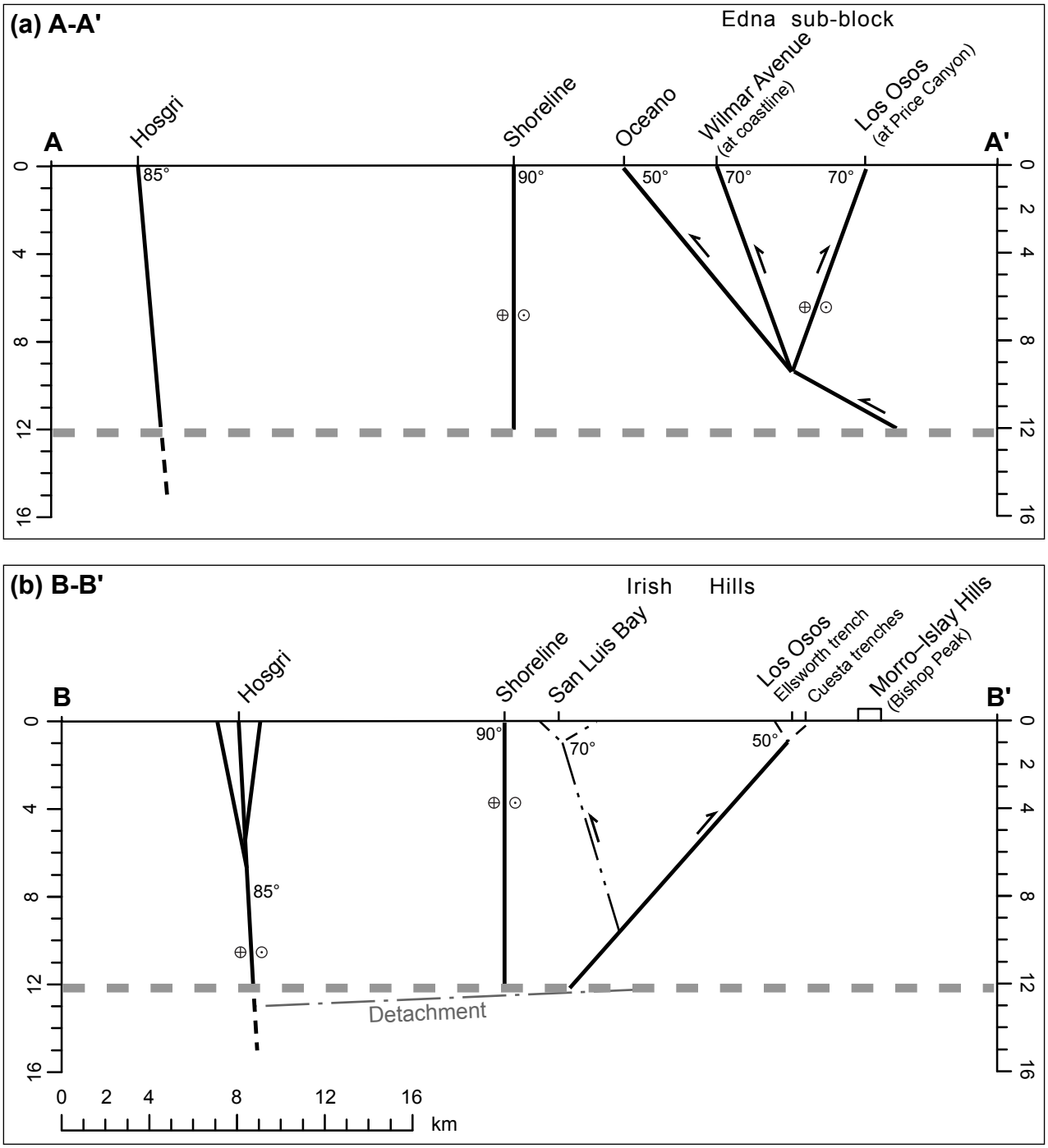

EXPLANATION

- Fault; solid where well located, dashed where approximately located; for strike-slip faults, ⊕ is away, ⊙ is toward.
- Seismogenic depth (12 km)
- Axial Surface or backthrust
- Zone of distributed deformation
- Detachment, nonseismogenic

Notes:
- The TI Team recognizes that the geometry of the San Luis Bay fault intersection with the Los Osos fault in Panel (b) (Section B-B') does not clearly fit the expected geometry of an axial surface with a change in dip of the underlying reverse fault. The geometry of the Los Osos fault has been simplified to allow for a more gently dipping fault (50°) to extend to a seismogenic depth of 12 km.
- Preferred Hosgri FGM shown.

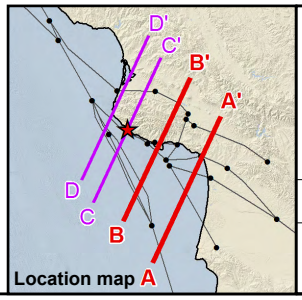

Representative Cross Sections A-A′ and B-B′ in the NE Model

DCPP SSC REPORT

Pacific Gas and Electric Company

Figure **7-26**

File path: S:\1005\005\Final_Report_Figures\Figure_700-26.ai; Date: 03/10/2015; User: Serkan Bozkurt, LCI; Rev.1

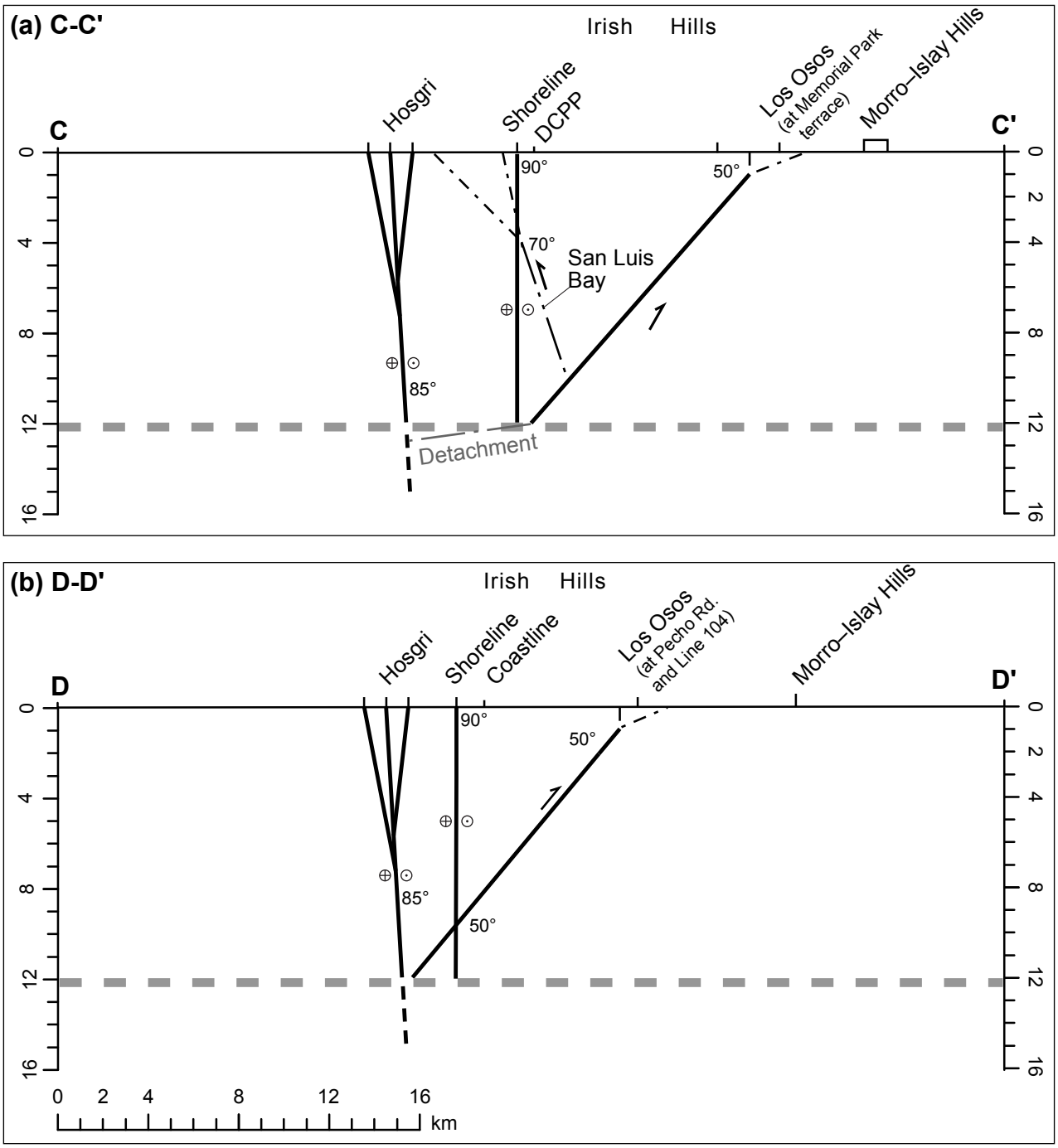

EXPLANATION

- Fault; solid where well located, dashed where approximately located; for strike-slip faults, ⊕ is away, ⊙ is toward.
- Seismogenic depth (12 km)
- Axial Surface or backthrust
- Zone of distributed deformation
- Detachment, nonseismogenic

Note: Preferred Hosgri FGM shown.

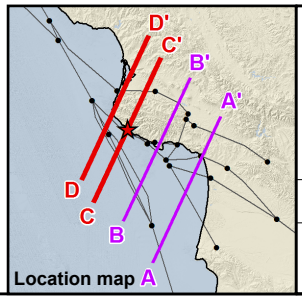

Representative Cross Sections C-C′ and D-D′ in the NE Model

DCPP SSC REPORT

Pacific Gas and Electric Company

Figure **7-27**

File path: S:\1005\005\Final_Report_Figures\Figure_700-27.ai; Date: 03/10/2015; User: Serkan Bozkurt, LCI; Rev.1

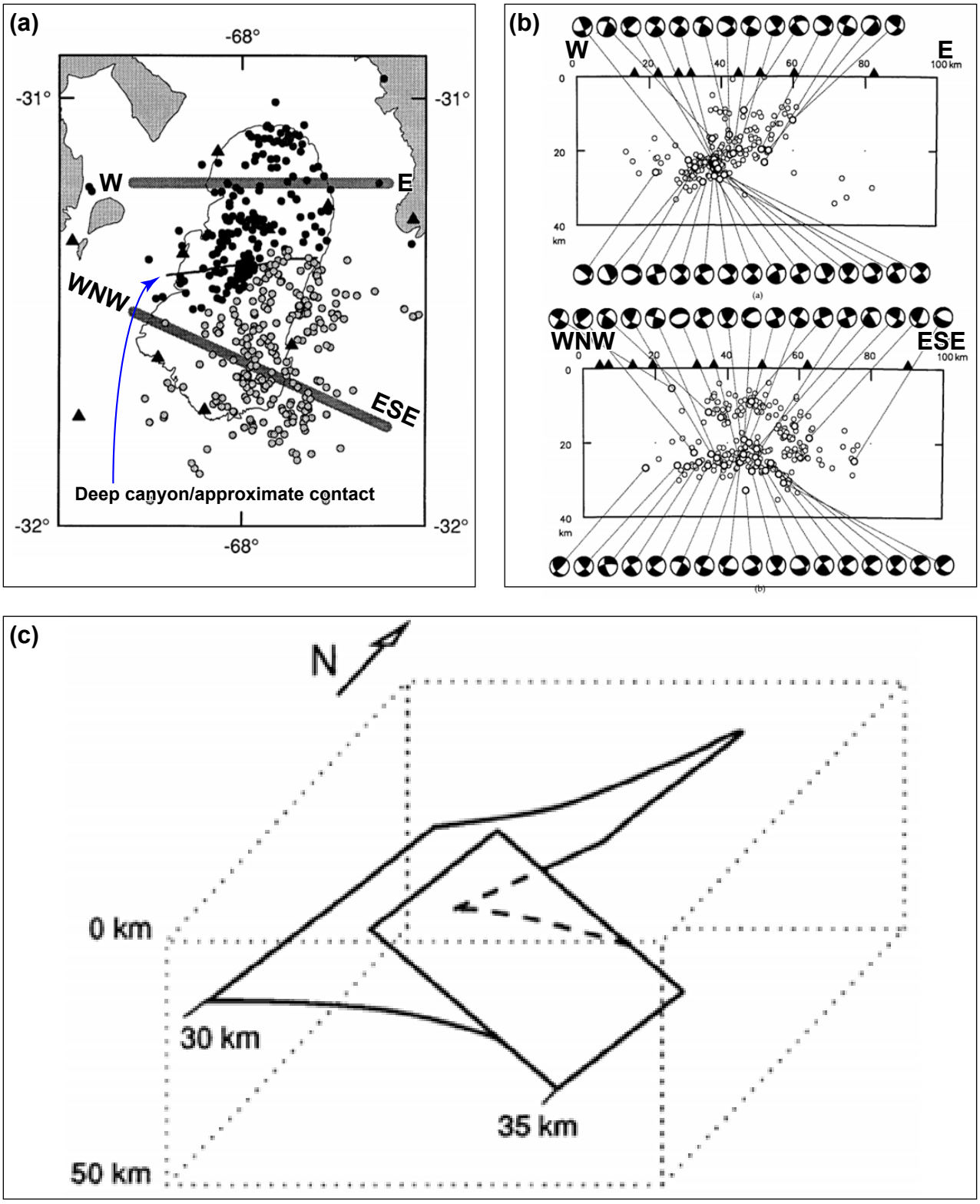

Notes:
- Panel (a) shows two zones of seismicity projected onto cross sections on panel (b).
- Upper cross section of Panel (b) shows seismicity for the northern block.
- Lower cross section of Panel (b) shows seismicity for the southern block.
- Panel (c) shows schematic 3D view of fault geometry inferred from seismicity shown on Panels (a) and (b).

Source: Modified from Regnier et al. (1992).

Postulated Geometry of Faults That Ruptured During the 1977 Caucete Earthquake, Sierra Pie de Palo, Argentina

DCPP SSC REPORT

Pacific Gas and Electric Company

Figure **7-28**

File path: S:\1005\005\Final_Report_Figures\Figure_700-28.ai; Date: 01/22/2015; User: Alex Remar, LCI; Rev.1

Parameter Values, Los Osos Fault

Model	Outward Vergent Weight: 0.4	SW Vergent Weight: 0.4	NE Vergent Weight: 0.2	Range		Weighted mean
Los Osos	LC+LM+LV+LE	LC+LM+LV+LE	LC+LM+LV+LE	Summary		
Dip	60	80	50	50	80	66
Dip Direction	SW	SW	SW			
Style of faulting	RL/R-O	R	R			
Depth to top	1	1	1	1	1	1
Width	13	11	14	11	14	12.4

Outward Vergent

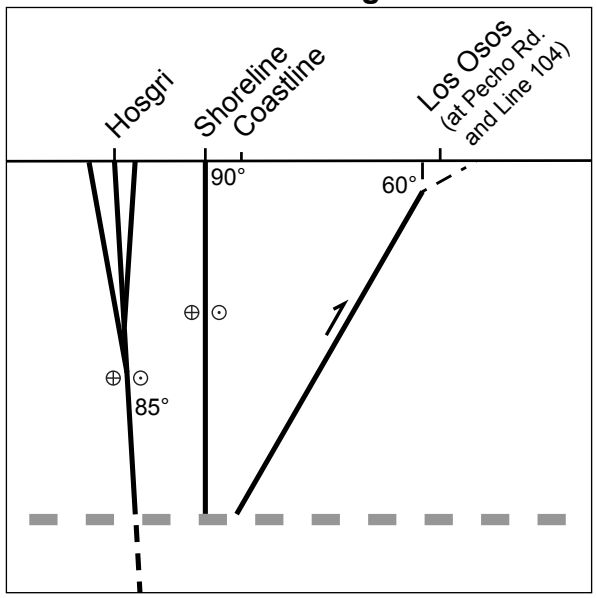

SW Vergent

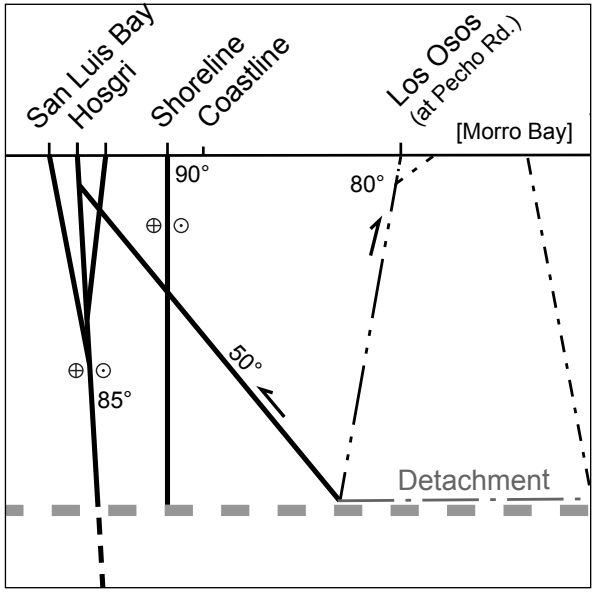

NE Vergent

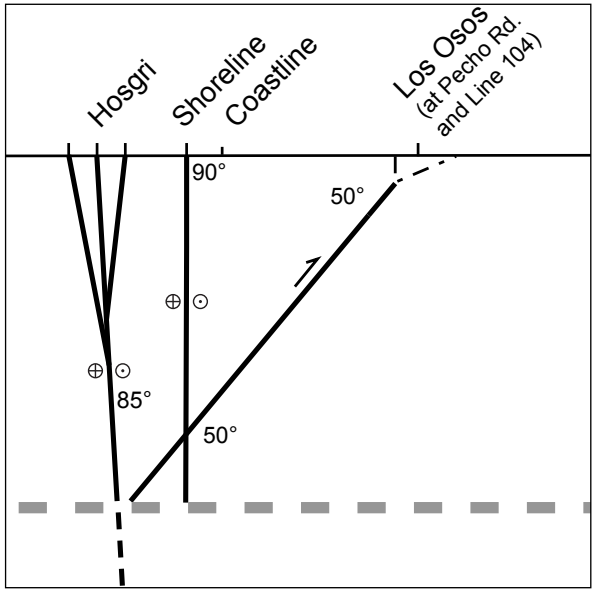

Note: Cross section D-D' shown to illustrate LM section of Los Osos fault, the closest section to the DCPP.

Los Osos Fault Parameter Values

DCPP SSC REPORT

Pacific Gas and Electric Company Figure **7-29**

File path: S:\1005\005\Final_Report\Figures\Figure_700-29.ai; Date: 03/10/2015; User: Alex Remar, LCI; Rev.1

Parameter Values, San Luis Bay Fault

Model	Outward Vergent Weight: 0.4	SW Vergent Weight: 0.4	NE Vergent Weight: 0.2	Range		Weighted mean
San Luis Bay	BR/BO+BE	BR/BO+BE	BR/BO+BE	Summary		
Dip	75	45	70	45	75	62
Dip Direction	N	N	N			
Style of faulting	R	R	R			
Depth to top	1	1	1	1	1	1
Width	11	16	12	11	16	13.6

Outward Vergent

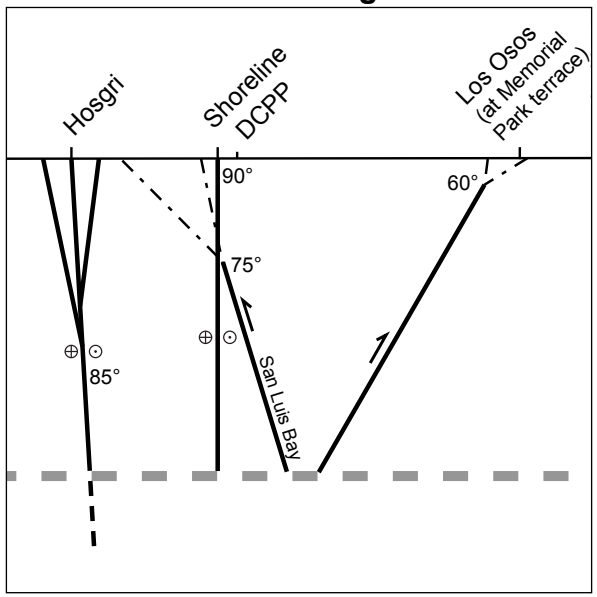

SW Vergent

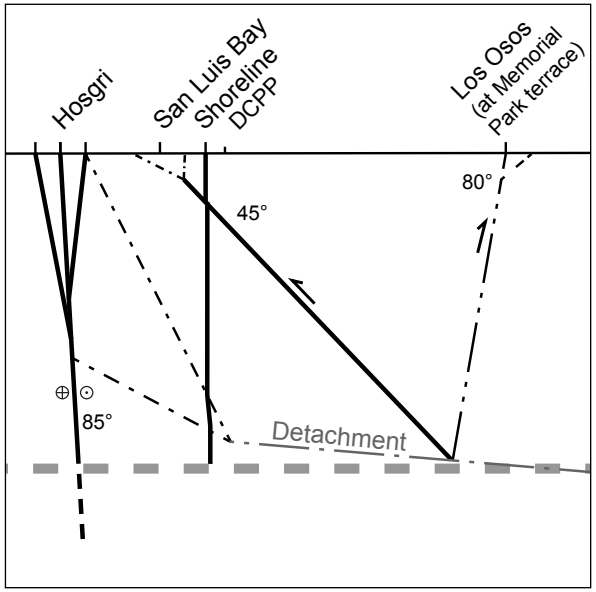

NE Vergent

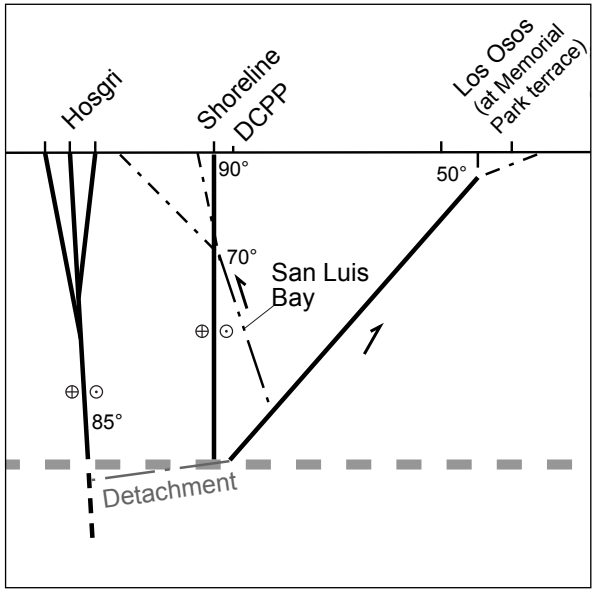

Note: Cross section C-C' shown to illustrate the San Luis Bay fault beneath the DCPP.

San Luis Bay Fault Parameter Values

DCPP SSC REPORT

Pacific Gas and Electric Company | Figure **7-30**

File path: S:\1005\005\Final_Report\Figures\Figure_700-30.ai; Date: 03/10/2015; User: Alex Remar, LCI; Rev.1

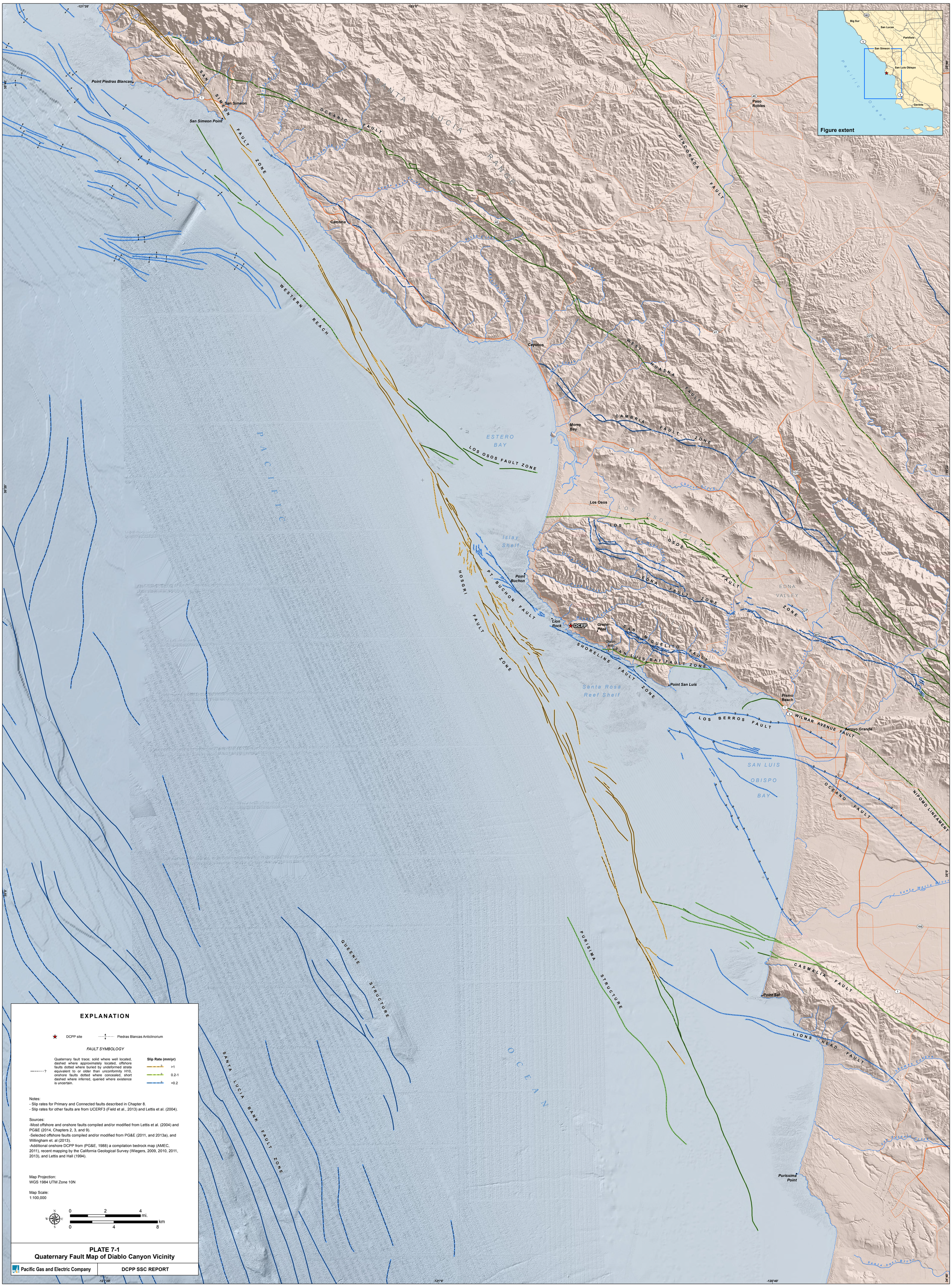

File path: S:\1000\005\Final_Report_Figures\Plate_700-01.mxd; Date: 03/11/2015; User: Serkan Bozkurt, LCI; Rev1

8.0 FAULT SLIP RATE MODEL

This chapter describes the TI Team evaluation of fault slip rates, including an evaluation of slip rate uncertainties, for the Primary and Connected fault sources in the Diablo Canyon SSC model.

8.1 Definition and Applicability

The Fault Slip Rate Model describes the slip rate and its uncertainty for each Primary and Connected fault source (Table 6-2). The SSC model for Primary and Connected fault sources does not use the fault slip rate as direct input to the logic tree (*Section 6.3*). Instead, fractions of the fault slip rates are allocated among various rupture sources that occupy the faults as described as part of the Slip Rate Allocation Model (*Section 9.3*).

8.2 Approach

The Diablo Canyon SSC model requires a characterization of slip rates for Primary faults (i.e., the Hosgri, Shoreline, Los Osos, and San Luis Bay faults), with particular focus on the slip rate uncertainties for the reaches of the faults directly opposite the DCPP. More distant Connected faults that are included in complex or linked rupture sources with the Primary faults (e.g., the Oceano and Wilmar Avenue faults), contribute very little to the total hazard at the DCPP based on sensitivity analyses performed early in the SSHAC study (Wooddell, 2011, presentation at Workshop 1) and final hazard results (*Chapter 14*). Therefore, for the Connected faults a more simple slip rate uncertainty distribution is defined.

Estimation of the net slip, the total amount of slip occurring on a fault, requires information on the style of faulting (also referred to as the sense of slip) and the dip of the fault plane. The assessment of the style of faulting is specific to the fault or rupture source and is based on consideration of local geologic evidence and more regional data regarding the tectonic stress regime and other strain markers. Except for the Hosgri and Shoreline faults, for which there is little uncertainty in the current style of faulting, uncertainty in the style of faulting for other rupture sources is accounted for by alternatives presented in the three fault models. Uncertainty in fault dip is directly linked with the inferred style of faulting, in that low and intermediate values within the range of dip uncertainty are generally correlated with dip-slip (reverse and/or reverse oblique faulting, respectively), and steeper dips are correlated with strike-slip faulting.

Kinematic analyses using inversions of focal mechanisms of earthquakes (*Section 5.1.6*) and regional geologic and tectonic data (*Section 5.1.5*) show that the contemporary tectonic environment of the Irish Hills and surrounding region is generally characterized as one of transpressional strain with a north-northeast orientation of maximum compression. Within this strain regime, faults that strike northwest are favorably oriented to accommodate dextral slip, and more easterly-striking faults (approximately perpendicular to the direction of maximum compression) are favorably oriented to

accommodate reverse slip (Figure 5-12). The rupture sources defined for this study are categorized as strike-slip and reverse faults, following the general definitions used in the ground-motion-prediction equations, in which strike-slip faults have a rake of ≤30°, and reverse (including reverse oblique) faults have a rake of 90° ± 60°.

Net slip is a function of the dip on the fault and can be estimated for different styles of faulting if components of vertical and/or lateral slip are known or can be inferred based on assumptions of ratios of horizontal to vertical slip.

In the site area and site vicinity, the vertical component of slip of most faults is better known or constrained based on uplift rates inferred from mapping and dating of marine terraces (e.g., Hanson et al., 1994) and interpretation of offshore seismic-reflection data (Hanson et al., 2004; Willingham et al., 2013). Recent data and information on onshore uplift rate data that are considered in the assessment of vertical rates of separation on Primary faults within the site vicinity and site area are discussed in *Section 8.2.2*. Offshore 2D and 3D seismic-reflection data collected within the past decade have provided new information from which to measure amounts of vertical stratigraphic separation and, in some cases, the lateral component of slip (e.g., PG&E, 2011; 2013a; 2014, Chapter 3). Geodetic data provide a regional constraint on the slip budget available for the study region. While these data are not used to directly estimate the slip rate for specific faults or rupture sources, they do provide a check on the reasonableness of the estimated slip rate distributions used in the source characterization model.

The slip rate distributions for rupture sources involving faults within the site vicinity are based on the estimated rate along the reach of that fault source closest to the DCPP. It is recognized that slip rate varies along the length of a fault, particularly for long faults such as the San Gregorio–San Simeon–Hosgri fault system. Rupture sources are included in the fault models to accommodate higher slip rates along the fault system north of active faults that branch to the east, including the Shoreline and Los Osos faults. North of the intersection with the Oceano fault, higher slip rates on the San Gregorio–Hosgri fault system are accommodated by ruptures modeled by UCERF3, as discussed in *Section 12.4*.

The following sections describe the approach and data used to develop cumulative distribution functions (CDFs) representing the epistemic uncertainty in the assessment of the net slip rate for Primary and Connected faults included in the rupture sources as defined in *Chapter 7*. For Primary faults, comparisons of slip rate distributions used in previous PSHAs are also provided.

8.2.1 Geologic Slip Rate CDFs

A geologic slip rate, u, is determined from the tectonic displacement of a feature crossing the fault, s, divided by the age of the offset feature, t, or:

$$u = s/t \tag{8-1}$$

Our approach is to represent the parameters s and t using discrete probability density functions (PDFs). As described by Zechar and Frankel (2009), computed slip rates are most accurate when uncertainties in parameters s and t are represented by probability

distributions. This approach allows for consistent reporting of slip rates in terms of mean or median values and probabilistic uncertainties reported as fractiles about the median that represent bounds within which the slip rate is likely to be correct. Zechar and Frankel (2009) consider this method to be more useful than reporting limiting maximum and minimum values, both of which are extremely unlikely to be correct.

The displacement and age PDFs are represented by simple functional forms that allow characterization of minimum (s_{min} or t_{min}) and maximum (s_{max} or t_{max}) values and preferred values (sometimes called "best estimate" values or ranges of values). Three simple and commonly used forms of the PDF are the *triangular*, *trapezoidal*, and *boxcar distributions* (Figure 8-1). A triangular distribution is a PDF characterized by a single preferred value located between a minimum and maximum value. A trapezoidal distribution has a preferred range (plateau) instead of a single preferred value, with the preferred lower and upper values located between the minimum and maximum values. The trapezoidal distribution is commonly used in cases where the resolution of the data is insufficient to prefer a single value over another within a certain range that is narrower than the total uncertainty range. A boxcar distribution, also called a *uniform distribution*, has no preferred value or range of values between the minimum and maximum.

Fault slip rate uncertainties are treated as continuous distributions typically derived from independent and uncorrelated displacement and age PDFs. The slip rate distributions are calculated from these PDFs using Monte-Carlo methods. Ten thousand samples are drawn from each of the displacement and age PDFs to produce 10,000 estimates of slip rate for each offset feature using Equation (8-1). The resulting slip rate is shown graphically as a cumulative distribution function (CDF), and statistical properties of the uncertainty distribution are calculated and tabulated from the CDF, including the arithmetic mean, minimum, maximum, and various cumulative probability levels; these can include 5% and 95% probability values. In some cases, for PDFs describing uncertainty in parts of a total value (e.g., channel offset is measured separately across two strands of a fault zone), a combined CDF is calculated for the total value using the same Monte Carlo technique described above. In other cases, where alternative PDFs are used to describe epistemic uncertainty in a parameter, they are combined by weighting the alternative PDFs (e.g., alternative age models for a channel are considered). All calculations are performed using Microsoft Excel and the built-in Data Analysis Tools

In a logic tree structure, uncertainty distributions are represented by a (small) set of discrete alternatives with assigned probability weights. Miller and Rice (1983) provide a set of discrete approximations for arbitrary continuous probability distributions. Both three- and five-point approximations are used in this study. The Miller and Rice (1983) three- and five-point distributions are given in a table and a plot on Figure 8-2. On the figure, the first column of the table indicates the location of the three- or five-point discrete values for the variable in terms of their cumulative probability levels as illustrated by the purple and green horizontal dashed lines, respectively. The second column lists the probability weights to be assigned to the three or five discrete values of the variable. In other studies, such as the CEUS SSC Project (EPRI et al., 2012), it was judged that the number of decimal points in the probability weights given in Miller and

Rice (1983) could imply too high a degree of precision; therefore, the probability weights were approximated by the values with fewer decimal points. Similar approximations to three decimal points were used in this study, as listed in the third column.

Where there may be several independent or quasi-independent estimates of the same fault slip rate (e.g., multiple channels crossing the Shoreline fault), the multiple sources of information are considered in different ways. If some estimates are of higher quality than others, due mainly to less geologic uncertainty that the interpretation of the feature is robust and that the feature represents a valid marker across the fault zone, then slip rate CDFs are calculated for the high-quality features. Information from the lesser-quality features is considered as possible corroboration of the results. For cases with multiple high-quality features, slip rate CDFs may be combined. One approach for combining results is to use a weighting scheme, with subjective weights based on relative degrees of belief that one of the calculations is a better measurement of the true value than the other(s). This approach has been used in this study to represent the epistemic uncertainty in the slip rate for the section of the fault closest to the DCPP.

A different CDF combination strategy that is not used in this analysis is the calculation of joint probabilities, whereby two or more distributions are combined and used to trim or rescale a “joint” distribution. This type of combination is not used in this analysis because the requirements to perform a joint probability responsibly are not judged to be satisfactorily met for any of the Primary faults in the site area. These requirements include true independence of the measurements, high degrees of belief that all data are robust (i.e., low geologic uncertainty at each site), and the existence of a single “correct” answer (e.g., there is one correct slip rate for all locations and times under consideration). It is expected that the slip rate may vary along the length of the Primary fault sources in this SSC model (in particular the HFZ): therefore, this approach is not appropriate for estimating the epistemic uncertainty in the rate of slip along the target sections closest to the DCPP.

8.2.2 Quaternary Uplift Rate

Emergent marine terraces that are present along most of the south-central California coastline from San Simeon on the north to the Santa Maria Valley on the south are important datums that have been used to evaluate rates and patterns of Quaternary uplift (Hanson et al., 1994). This section discusses new information that has been evaluated to assess uncertainty in tectonic uplift rates in the DCPP region. These uplift rates are used to constrain slip rates of Primary and Connected faults in the study region.

8.2.2.1 San Luis Range

The uplift rates inferred from the correlation and dating of the terraces in the Irish Hills were used to estimate slip rates for faults within and bordering the Irish Hills and San Luis Range (Lettis et al., 1994; Lettis and Hall, 1994). The following are key observations and conclusions from Hanson et al. (1994) regarding the results of marine

terrace investigations that pertain to the evaluation of the rates of vertical deformation for Primary and Connected fault sources:

- A flight of at least 12 elevated marine terraces is present between Morro Bay and the northwestern margin of the Santa Maria Valley.
- The lower two terraces (Q_1 and Q_2) in this sequence are interpreted to correlate to marine oxygen isotope stages (MIS) 5a (80 ka), and 5e (120 ka), respectively, based on 12 uranium-series ages of coral and vertebrate bone samples, 12 amino acid racemization analyses, and 14 paleoclimatic analyses of invertebrate faunal assemblages.
- The ages of the lower two terraces provide local calibration of the terrace sequence for correlation with paleosea-level curves developed from worldwide data.
- For terraces equal to or younger than about 330 ka, estimated terrace ages and uplift rates were assessed by correlating shoreline angle altitude and terrace altitudinal spacing to these curves.
- Uplift rates based on the present altitude of the 120 ka terrace in this region range from approximately 0.06 to 0.23 m/kyr.
- Estimated paleosea level during the ~80 ka highstand in the San Luis Range study area, assuming a +6 m paleosea-level estimate for the ~120 ka terrace and uniform uplift since formation of the ~120 ka terrace, is -4 m ± 1 m (relative to present sea level). This estimate was in good agreement with estimates of -5 ± 2 m (Muhs et al., 1988, 1992) for the altitude of the ~ 80 ka highstand in other coastal California and Baja, California, Mexico, locations.
- Based on assumptions that Q3 and Q4 terraces correlate to MIS 7 and MIS 9 highstands, respectively, and the post-120 ka uplift rate reflects a uniform long-term uplift rate post-MIS 9 (~330 ka), paleosea-level during MIS 7 and MIS 9 is estimated to be -3 ± 4 m and +4 ± 4 m, respectively.

Recent dating and analysis of key localities along the Pacific Coast, including near Cayucos and on San Nicolas Island, suggest that sea level during the latter MIS 5 substages (MIS 5c and 5a) may differ from what was previously used by Hanson et al. (1994) to estimate long-term late Pleistocene uplift rates. In particular, Muhs et al. (2012) suggest that sea level during MIS 5c (ca. 100–105 ka) may have been close to or above the present height (+2 m to +6 m), and sea level during MIS 5a (ca. 80 ka) may have been –11 to –12 m. Extensive reoccupation of the Cayucos MIS 5e platform during MIS 5c, is suggested by these new data (Muhs et al., 2002, 2012; Figure 8-3).

To explore the possibility that the lower terraces in the sequence of terraces mapped along the margins of the Irish Hills are younger than previously estimated, and to evaluate uplift rate at various locations, the Muhs et al. (2012) paleosea-level estimates for MIS 5a and 5c were used, in conjunction with an alternative age model that assumes the Q2 terrace mapped around the southwest margin of the Irish Hills is MIS 5c rather than MIS 5e. Figure 8-4 illustrates the alternative rates of uplift predicted by the two alternative models based on the Q2 terrace elevation data as presented in Hanson et al. (1994). Based strictly on altitudinal spacing, alternative ages of the lower four terraces in

the Irish Hills based on the Muhs et al. (2012) paleosea-level estimates cannot be precluded, but are not preferred for the following reasons:

- Multiple dating approaches that were used to estimate the ages of the marine terraces bordering the San Luis Range (Hanson et al., 1994) strongly support the correlation of the Q1 and Q2 terraces to substages MIS 5a and 5e, respectively.
- Relative altitudinal spacing between terraces within sequences of terraces bordering the San Luis Range is more consistent with expected terrace elevations for the MIS 5 substages, based on dated sequences in the Point Conception region on the northern flank of the Transverse Ranges to the south (Rockwell et al., 1992), and Punta Banda (Muhs et al., 2002).
- Coastal sites along the continental margin are judged by the TI Team to be a better analog for the DCPP site than the San Nicolas Island, where response to glacial hydro-isostatic adjustments may differ significantly due to differences in the relative areas of continental shelf and land between the two settings.

The estimated ages and paleo–sea level of terraces in the study region as outlined in Hanson et al. (1994) and resulting estimated uplift rates are therefore given high weight [0.8] in assessing long-term deformation rates associated with structures within and bordering the San Luis Range. Low weight [0.2] is given to higher uplift rates based on alternative correlations permitted by the estimated ages and paleosea-level model outlined by Muhs et al. (2012). The range in uplift rates shown on Figure 8-5 was calculated using the same terrace Q2 shoreline angle elevation (for minimum, maximum, and preferred range), combined with alternative age/paleosea-level assessments. The resulting combined PDF describing uncertainty in the uplift the Irish Hills is shown on Figure 8-6.

8.2.2.2 Cayucos Study Area

The age of the first emergent marine terrace at Cayucos was long considered to be approximately 120 ka (MIS 5e) based on dating of coral and faunal assemblage data (Hanson et al., 1994 and references cited therein). Muhs et al. (2002, 2004) note that the presence of corals of two different ages, approximately 105 ka and approximately 120 ka, on both the Cayucos terrace (also described by Stein et al., 1991) and the Nestor terrace at Point Loma in Southern California explains a previously enigmatic mixture of extralimital warm-water and cool-water mollusks in terrace sediments at these localities (Figure 8-7). Muhs et al. (2002) postulate that a relatively high sea level with cool waters may have “captured” the terrace, or at least the outer (seaward) part of the terrace that initially formed during the 120 ka sea-level highstand. Muhs et al. (2012) provides further support for this hypothesis based on more recent dating of terraces on San Nicolas Island (Figure 8-3). The bimodal age distribution of fossils from three sites, the Cayucos terrace, the Nestor terrace at Point Loma, and terrace 2b on San Nicolas Island, are explained by cliff retreat and platform reoccupation of the approximately 120 ka marine terrace by a younger highstand approximately 100 ka. Muhs et al. (2012) state that unlike on San Nicolas Island, neither Point Loma or Cayucos has fragments of the older (~120 ka) terrace at slightly higher elevations, and that in these areas of low uplift rate, only one

terrace may be preserved. Kern and Rockwell (1992) do recognize slightly higher abrasion platform remnants at Point Loma, which they correlate to MIS 7. The correlation of platforms older than the Nestor terrace to MIS 7 and MIS 9 at Point Loma are based on the good agreement between the present elevation of those platform remnants and the predicted elevations using the uplift rate determined for the Nestor terrace.

Remnants of a previously unrecognized higher terrace are preserved along the coast in the Cayucos area between Ellysly Creek and Cayucos (Figure 8-8). Terraces with shoreline angle elevations approximately 13 ± 1 m above sea level are preserved both west and east of Ellysly Creek (Figure 8-9). This terrace is mapped across the Cambria fault with no change in elevation, and also within the town of Cayucos. The 13 ± 1 m terrace west of Ellysly Creek was identified as the Tripod terrace by Weber (1983) and correlated to the second emergent marine terrace east of the San Simeon fault zone near San Simeon Point (Weber, 1983; Hanson et al., 1994). Based on relative soil profile development amongst the terraces preserved near San Simeon, the Tripod terrace was interpreted to correlate to MIS 5e (~120 ka; Rockwell et al., 1994).

The lowest emergent terrace at Cayucos, which has traditionally been referred to as the Cayucos terrace, has a shoreline angle of approximately 7-8 m, and platform exposures in the modern sea cliff as high as 5 m (Muhs et al., 2002). Sample locations described by Muhs et al. (2002) and Hanson et al. (1994) are shown on panel a of Figure 8-8. The generalized inner edge of the Cayucos terrace as shown by Muhs et al. (2002) encompasses both the 7-8 m inner edge and the previously unmapped 13 ± 1 m inner edge.

Independent dating of the higher 13 ± 1 m terrace east of the Cambria fault is not available, but possible correlation of that terrace to the San Simeon area and soil geomorphic relationships described by Rockwell et al. (1994) for the San Simeon terraces suggest that this terrace correlates to the MIS 5e terrace. The relative soil profile development in the ~13 m terrace at locality R062012B is generally consistent with that of the Tripod terrace soil at San Simeon based on preliminary observations of members of the TI Team (J. Caskey and K. Hanson; Figure 8-9). Assuming that the 13 ± 1 m terrace at Cayucos formed during the MIS 5e (~120 ka) sea-level highstand with a paleosea level of 6 ± 2 m, a late Pleistocene uplift rate of 0.06 ± 0.01 m/kyr is estimated. At this rate the MIS 5c terrace (~100–105 ka), which is currently +7–8 m above present sea level, would have been uplifted between 5 m and 7.5 m. This suggests that paleosea-level during the MIS 5c highstand was at or close to modern sea level. These observations are consistent with the -2 ± 2 m estimated paleosea-level suggested for this highstand by Muhs et al. (1988). This value was used by Rockwell et al. (1992) and Hanson et al. (1994) to check ages and average uplift rates for terraces at Point Conception. These observations are less consistent with the range (+2 to +6 m for the ~100 ka) estimated from San Nicolas Island data (Muhs et al., 2012).

An alternative uplift rate on the order of 0.035 ± 0.25 m/kyr is estimated from correlation of the Cayucos terrace to MIS 5c with an initial elevation of approximately +2 m to +6 m,

as described by the alternative paleosea-level model proposed by Muhs et al. (2012). This uplift rate, combined with a paleosea-level estimate of 6 ± 2 m would predict the MIS 5e terrace at an elevation of approximately 10 ± 5 m. Although this range includes the elevation of the 13 ± 1 m terrace at Cayucos, the alternative model proposed by Muhs et al. generally predicts the MIS 5e terrace to be at a lower elevation.

8.2.2.3 Los Osos and Edna Valleys Study Area

Recent work identified remnants of surfaces underlain by marine deposits within the Edna Valley (PG&E, 2013b). The surfaces are mapped at elevations of 40 m, 55 m, 70 m, and 80 m (Figure 8-10). Some of these localities (40 m and 80 m terraces) had been previously mapped as the Pliocene Squire Member of the Pismo Formation (Hall, 1973). PG&E (2013b) speculated that if the terrace surfaces represented a flight of terraces and the lowest of the terraces was formed 3 Ma, the uplift rate in the Edna valley would be at a minimum 0.006 mm/yr. Subsequent attempts to date clasts and sediment within the marine deposits underlying the 40 m terrace surface at one location (Jespersen Road cut exposure) using cosmogenic nuclide ($^{26}Al/^{10}Be$) dating methods were not successful in dating the marine sediments. The results indicated that the sediments currently exposed in this road cut had been deeply buried and exposed by erosion within the past approximately 30,000 to 40,000 years (30–40 kyr, Bierman, 2013).

If it assumed that the marine sediments identified within Edna Valley at an elevation of 80 m above mean sea level formed during the Pliocene warm interval (3.3–3.0 Ma) and that eustatic sea level at approximately 2.95 Ma was 22 ± 10 m (95% confidence interval) or 22 ± 5 m (68% confidence interval (Miller et al., 2012), a long-term uplift rate for the Edna Valley is estimated to range from approximately 0.02 m/kyr to 0.03 m/kyr. Given the erosional nature of the surfaces associated with these marine terrace deposits, it is possible that the long-term uplift rate could be higher. Alternatively, if the marine deposits formed during an earlier Pliocene highstand, the long-term uplift rate would be lower. While a correlation to the late Pliocene warm interval highstand is reasonable, the TI Team acknowledges that in the absence of direct dating, the correlation is speculative.

In the Los Osos Valley, there is a paucity of convincing marine terraces, and most of the terraces identified are of uncertain origin (PG&E, 2013b). The most distinct surface is located directly east of where Los Osos Creek meets the range front (Figure 8-10). At this location the surface is partially occupied by the Los Osos Valley Memorial Park, and is therefore, informally referred to as the Memorial Park surface (MPS). The deposits associated with the Memorial Park surface were mapped as Paso Robles Formation by Hall (1973) and as fluvial gravels overlain by aeolian sands by Lettis and Hall (1994).

The Memorial Park surface outboard of the range front, is relatively flat with a shallow (< 1°) dip to the north-northeast: the subhorizontal part of the terrace ranges from an elevation of about 38–40 m near the range front to about 23 m at the northern distal margin (Figure 8-11). Within approximately 200 to 300 m of the range front the surface appears to steepen to between approximately 6–8.5 degrees. Subtle, fan-shaped cones as indicated by the topographic contours suggest a colluvial mantle of unknown thickness

may overlie parts of the surface adjacent to the range front. However, similar dips of 8 °N were recorded in the underlying Paso Robles Formation unit (Hall, 1973). It is uncertain what was the original deposition dip of the units. It is possible that the increased slope of the surface and dip of the Paso Robles Formation sediments is tectonically tilted due to movement on a blind Los Osos fault. The surface outboard of the range is moderately dissected with gullies prominent along the northeastern flank.

The origin and post-depositional history of the Memorial Park surface is not certain, but appears to represent depositional and erosional processes over a significant period of time. Field relationships from an exposure along Los Osos Valley Road indicate that fluvial gravel is incised into aeolian sand (PG&E, 2013b). This relationship is consistent with deposition of aeolian deposits and subsequent erosion by a fluvial stream, similar to that observed to the west in the present-day flat-floored Los Osos Creek valley, which abuts a dune field (Figure 8-11). The flat surface may reflect post-depositional nonmarine erosional (lateral fluvial or alluvial erosion) processes. Alternatively the surface may have formed by wave erosion in a lagoonal embayment.

The deposits underlying the surface appear to have been deposited by a fluvial and or alluvial fan system emanating from a drainage through what is now a windgap. The wind gap appears to represent an ancestral channel of the Los Osos Creek. The size and character of Los Osos Creek and its associated floodplain is markedly different up and down stream of the windgap (located near the middle of the map). The abrupt change in character of the valley suggests a greater antiquity of the channel upstream of the windgap, inferring that at one time the ancestral Los Osos Creek crossed the rangefront through the wind gap depositing sediments that comprise the Memorial Park terrace.

A strongly developed soil formed within the deposits is exposed in the northern roadcut along Los Osos Valley road adjacent to the Memorial Park facilities (Location 12268HS06 on Figure 8-11), Coarse to some very coarse columnar prismatic peds and some very coarse subangular blocky peds with many and distinct to prominent clay films on ped faces were observed over an interval at least 40–50 cm thick at a depth of approximately 1.5–2 m below the terrace surface. Pedogenic clay appears to extend to greater depth, but the total depth and character of the soil at this locality is obscured by slope wash. The upper part of the soil has been disturbed by construction of a road and due to the amount of slope cover, steepness of the cut and proximity to traffic areas, excavation of the cut and a more complete description of the soil at this locality has not been undertaken. Based on the preliminary observations of the thickness and depth of the strongly developed textural B horizon, and comparison to soils described in a similar coastal marine environment at San Simeon (e.g., Rockwell et al., 1994), PG&E (2013b) concluded that the soil suggested a considerable antiquity to the surface, in excess of 100 ka—and likely in excess of 200–300 ka.

A more detailed soil profile development description was conducted by John Caskey and Aileen Chea in a road-cut along Los Osos Valley Road near the eastern margin of the Memorial Park terrace (Location -SP1 on Figure 8-11; a soil profile description is provided in Attachment E-4 of *Appendix E*). The soil description features (e.g. ped

development, clay film descriptions, etc), secondary pedogenic clay accumulation amount and depth, described at this location are similar to those of the Oso marine terrace believed to be MIS 7 age of approximately 200–230 ka (Rockwell et al., 1994; Figure 8-12). As mentioned above the east-northeast flank of the Memorial Park terrace is more degraded and incised by headward eroding drainages, and has a surface elevation that is greater than 8 m lower than the western margin of the terrace. Qualitative observations of the soil exposed in a road-cut near the topographic high along the western margin of the terrace (Location 12268HS06 described above) suggest the depth of secondary pedogenic clay accumulation as well as soil structure could be more strongly developed than what was described at Location -SP1. Variation in soil development across the surface could be related to differing erosion rates across the surface, variations in parent material, or both. These observations are somewhat speculative, but suggest that the Memorial Park surface is older than MIS 7 (the age of the Oso marine terrace at San Simeon interpreted by Rockwell et al., 1994 and Hanson and Lettis, 1994).

Based on the available information regarding the stratigraphy, soil structure, and geomorphic setting of Memorial Park surface, the TI Team judges it to be older than MIS 7 (~210 ka) and possibly as old as MIS 11 (~400 ka). If the terrace was planated during MIS 11 and eustatic sea level was as high as +13 m during that highstand (Roberts et al., 2012), the resulting uplift rate of between 0.05 m/kyr and 0.06 m/kyr is reasonable and consistent with the estimated rate of uplift at Cayucos, which is described above (*Section 8.2.1.2*).

8.3 Hosgri Fault

The Hosgri fault slip rate has been the focus of considerable research since the fault was first identified as a significant structure within the offshore Santa Maria Basin by Wolf and Wagner (1970) and Hoskins and Griffiths (1971). Hanson et al. (2004) summarized investigations conducted as part of the LTSP (PG&E, 1988) studies regarding the style and rate of Quaternary deformation of the Hosgri fault zone (HFZ). The conclusions of these studies were that the HFZ is a convergent right-slip (transpressional) fault having a late Quaternary slip rate of 1–3 mm/yr (see *Section 5.2.1*).

More recent offshore studies conducted as part of the ongoing PG&E LTSP, PG&E/USGS CRADA, and AB 1632 research programs (see *Chapter 4.0*) provide additional information to assess the style and rate of Quaternary deformation of the Hosgri fault, particularly along the reach of the fault zone closest to the DCPP. The results of these studies (Johnson and Watt, 2012; PG&E, 2013a; PG&E, 2014, Chapter 3) generally confirm the LTSP conclusion that the Hosgri fault is predominantly a right-lateral strike-slip fault in the contemporary tectonic environment (PG&E, 1988; Hanson et al., 2004; Willingham et al., 2013). As described in *Section 5.2.1*, interpretation of bathymetric and 2D seismic-reflection data collected along the offshore San Simeon and Hosgri faults indicates that there is a relatively continuous trace linking the two fault zones in Estero Bay (Johnson and Watt, 2012; PG&E, 2013a).

The locations of study sites for characterizing Quaternary slip rate of the Hosgri fault relative to the DCPP are shown on the map on Figure 8-13. The slip rate estimated for the onshore San Simeon fault (Hanson and Lettis, 1994), which was previously used as a constraint for the assessment of horizontal slip on the Hosgri fault by PG&E (1988) and Hanson et al. (2004), remains a viable estimate of the slip rate for the HFZ north of Estero Bay. Within the northern part of Estero Bay near Point Estero, Johnson et al. (2014) have identified a geomorphic feature that they refer to as the cross-Hosgri slope (CHS) and from which they have estimated a latest Pleistocene-Holocene slip rate.

The western branch of the Hosgri fault intersects the main active trace of the fault in Estero Bay to the south of the CHS. Possible contributions of slip from the western branch of the HFZ to the primary fault zone have been estimated from analysis of folding within the Piedras Blancas anticlinorium (PG&E, 1990b). Interpretation of offset channels imaged in high-resolution 2D and 3D seismic-reflection data collected across the Hosgri fault in two other locations, southern Estero Bay and south of Point Sal, are used to constrain long-term slip rates along the Hosgri fault north and south of the DCPP (PG&E, 2014, Chapter 3).

Sections 8.3.1, 8.3.2, 8.3.5, and 8.3.6 describe key data from both onshore studies at San Simeon and offshore localities where piercing points that can be used to directly assess offsets across the Hosgri fault. Possible contribution to slip rate from the Piedras Blancas anticlinorium is described in *Section 8.3.3*. Given that the interpretation of offshore seismic stratigraphy is a key aspect of estimating slip rate from laterally displaced offshore channels, *Section 8.3.4* provides a discussion of the age constraints for these offshore piercing points. *Section 8.3.7* summarizes how the slip rate data from these various locations are used to develop a slip rate distribution for the HFZ along the reach closest to the DCPP. *Section 8.3.8* compares the resulting five-point slip rate distribution to slip rates proposed by others based on geologic and geodetic data.

8.3.1 Onshore San Simeon Slip Rate Estimate

Detailed paleoseismic trenching and marine terrace investigations conducted as part of the LTSP investigations in the late 1980s provided constraints on the style and rate of Quaternary deformation along the southern part of the onshore San Simeon fault zone. The LTSP investigations focused on the southern part of the fault zone where the zone of late Quaternary deformation is relatively narrow and where flights of marine terraces are present on both sides of the fault zone. Field mapping was supplemented with more than 100 boreholes and numerous trench and soil pit excavations to delineate the altitude and distribution of terrace remnants that typically are buried by younger aeolian and fluvial deposits. The results of the PG&E LTSP investigations are described in detail by Hall et al. (1994) and Hanson and Lettis (1994).

The best-constrained late Quaternary slip rate for the southern onshore San Simeon fault is based on the offset Oso marine terrace, which is estimated to be approximately 210 ka (MIS 7; Hanson and Lettis, 1994). The location and the elevation of the Oso strandline on each side of the fault zone are both tightly constrained by field mapping and subsurface

data from boreholes, soil test pits, and exploration pits (Figure 8-14). As described in detail by Hanson and Lettis (1994), a key aspect of the analysis of the lateral offset of strandlines across the HFZ was the assessment of the paleogeography of the coastline (in particular, the presence and size of a paleoheadland/bay adjacent to the fault) during earlier sea-level highstands. During development of the Oso terrace, a small headland likely was present on the shoreline southwest of the San Simeon fault zone. The maximum size of this headland was estimated by comparing the geometry of the Oso (Qo) terrace to that of modern headland/bay shorelines. The strandline geometry of the Qo terrace, which is well constrained on both sides of the fault zone, shows that, if a headland/bay coastline configuration occurred, the bay must have been less than 250 m wide. Because headlands typically are no longer than the maximum width of the adjacent bay, 250 m is also probably a maximum length for the adjacent Oso terrace headland. Stratigraphy exposed in soil test pits on the northeast side of the fault, which is suggestive of deposition in a more open coastal environment rather than a quiet bay or lagoon, also provides supporting evidence that a large headland was not present during development of the Oso terrace.

The correlation and ages of marine terraces across the San Simeon fault zone, particularly the Oso terrace, which is the key marine terrace, are critical to the assessment of a long-term Pleistocene slip rate for the southern onshore San Simeon fault zone. More recent research regarding the timing and paleo–sea level during Pleistocene highstands along the California margin (e.g., Muhs et al., 2002, 2012) was reviewed to ensure that the correlation and age of the Oso terrace are reliable, because that terrace provides the best-constrained offset measurement. The conclusion of this analysis is that the basis for the correlation of terrace remnants across the San Simeon fault zone and age of Oso terrace is robust. This assessment is based on multiple lines of evidence, as follows:

- Geomorphic preservation and position of the Oso terrace remnants on both sides of the fault are similar in that the narrow, laterally discontinuous remnants are bordered by broader, more laterally continuous and well-expressed terraces.
- Analysis of the properties in soils developed in the marine terraces on both sides of the San Simeon fault (based on a suite of seven soil and stratigraphic parameters) favor the correlation and ages reported by Hanson et al. (1994) and Hanson and Lettis (1994). Similarities in clay distribution with depth for the sequences of terraces, in particular, provide strong evidence to correlate individual terraces. Differences in the relative amounts and locations of mean clay accumulation observed in soils formed in the San Simeon, Tripod, and Oso terraces are consistent with ages of 80–105 ka, 120 ka, and 210 ka, respectively (Rockwell et al., 1994).
- Relative altitudinal spacing between terraces within sequences of terraces on both sides of the fault is consistent with expected terrace elevations, based on dated sequences bordering the San Luis Range (Hanson et al., 1994), the Point Conception region in the western Transverse Ranges to the south (Rockwell et al., 1992), and Punta Banda (Muhs et al., 2002). The terrace spacing at San Simeon is

poorly fit using recently estimated paleo–sea levels for MIS 5 highstands based on marine terraces studies on San Nicholas Island (Muhs et al., 2012; Figure 8-15).

PDFs that show uncertainty in the displacement and age parameters used to estimate a post-Oso terrace slip rate for the San Simeon fault zone are shown on Figure 8-16. Estimates of lateral offset of the Oso strandline as reported by Hanson and Lettis (1994) range from 150 m to 550 m (panels a and b of Figure 8-16). This range encompasses uncertainty in both the projection of the back edge of the Oso terrace into the Hosgri fault and the shape and size of the paleo-headland that was present when the terrace formed (Figure 8-14). The lower preferred offset of 300 m is based on the current separation of the two piercing points (designated by black triangles) on each side of the Hosgri fault; the upper preferred offset of 450 m is based on this apparent offset and the presence of an assumed small (150 m) headland. Considering the 150–550 m range of lateral offset and the 11–15 m vertical separation of the Oso terrace, the approximate horizontal to vertical (H:V) offset ratio ranges from 10:1 to 50:1; this H:V ratio supports the Hosgri as a strike-slip fault with a low rake (Hanson and Lettis, 1994).

Hanson and Lettis (1994) infer the age of the Oso marine terrace to be MIS 7 (~210 ka). Based on a recent synthesis of all available sea level and coral data, Compton (2011) shows that there were three substage highstands during MIS 7 between 243 ka and 190 ka. The highest period of sea level during the latter part of MIS 7 occurred in the time between approximately 225 ka and 191 ka. Different paleosea-level estimates suggest peaks near or above present level between approximately 215 ka and 195 ka. These two ages are used as the upper and lower limits of the preferred age. The resulting trapezoidal age PDF is shown graphically in panel c, and the justification for this distribution is summarized in panel d of Figure 8-16.

A slip rate CDF calculated based on the inputs described above is shown in panel e of Figure 8-16. The CDF curve plots the cumulative probability (from 0 to 1) that the slip rate is less than or equal to the specified value in millimeters per year. The mean slip rate and certain probability values drawn from the CDF are tabulated in panel f of Figure 8-16. The mean slip rate for the onshore San Simeon fault zone is 1.8 mm/yr. The extreme-low-probability minimum and maximum slip rates based on the weighted age model are 0.7 and 2.8 mm/yr. The 90% confidence limit slip rate ranges from 1.0 mm/yr to 2.4 mm/yr (5% and 95% cumulative probability, respectively).

Slip rate estimates based on other marine terraces and deflected drainages as documented by Hanson and Lettis (1994), are less well constrained and hence broader. With the exception of the rates based on very poorly constrained piercing points for the younger Tripod and San Simeon terraces as described by Hanson and Lettis (1994), the values generally are consistent with the San Simeon slip rate CDF. The resulting late Quaternary slip rate CDF is similar to the minimum Holocene slip of 1–3 mm/yr that Hall et al. (1994) report based on offset fluvial deposits exposed in several trench excavations at the Airport Creek trench locality. The estimated Holocene slip rate at the Airport Creek site is based largely on the slip across a single fault strand, and thus there is some likelihood that it does not capture the total slip across the fault zone. Hall et al. (1994) note, however,

that comparison of the estimated slip rate based on mapping of marine terraces provides a long-term check on the reasonableness of the best-constrained Holocene slip rate from the main strand based on trench data. The consistency between the results suggest that almost all of the late Quaternary slip rate across the San Simeon fault zone at the latitude of Airport Creek have been concentrated on the faults exposed in the trenches, which is consistent with the lack of geomorphic expression of additional active fault traces.

8.3.2 Point Estero Slip Rate Estimate

In the Point Estero study area, Johnson et al. (2014) observed an approximately 265 m wide, 8 m high geomorphic feature in multibeam echosounding (MBES) data that crosses the primary strand of the HFZ between Morro Bay and Point San Simeon (Figure 8-17). As mentioned in *Section 8.3*, Johnson et al. (2014) name this feature the cross-Hosgri slope (CHS) and interpret the feature as a shoreface of a latest Pleistocene sand spit. This feature consists of post–Last Glacial Maximum (LGM) sandy sediment, and extends southeastward from a pronounced outcrop of bedrock on the seafloor west of the primary traces of the Hosgri fault. The entire feature, including both the top and bottom of the slope, rises approximately 6 m from west to east before bending southward parallel to the coastline and becoming more irregular. The feature slopes 1.6°–2.0° to the south and is bounded to the north and south by relatively flat areas that slope approximately 0.4°–0.6° to the south.

Johnson et al. (2014) interpret the feature to have formed slightly below sea level during the post-LGM transgression. They explain the slope of the feature as a result of interplay between depositional processes and sea-level rise. According to their model, during the Younger Dryas stadial (~12.8–11.5 ka), the CHS shoreface existed seaward of a sandbar that completely enclosed a lagoon. During meltwater pulse 1B, directly after the Younger Dryas stadial, sea level rose rapidly and the shoreface was drowned. The drowning likely began with the west end where the sediment supply was starved. This drowning would have preserved the submarine section of the CHS while the sub-aerially exposed section continued to be eroded (Johnson et al., 2014).

Using slope maps and slope-normal profiles spaced 12.5 m apart, and given an estimated age of the submersion and preservation of the lower CHS break, Johnson et al. (2014) interpret a lateral slip rate of 2.6 ± 0.9 mm/yr for the primary strand of the Hosgri. Johnson et al. (2014) measured offset of the CHS by defining upper and lower slope breaks on each slope-normal profile in the MBES data, choosing subsets of the slope break picks west and east of the primary strand of the HFZ, and performing a linear regression of points within the subset on each side of the fault. These regressions (west and east) were projected to the fault, and offset was measured between regression lines along the fault. Using a high-resolution multibeam bathymetry data set collected by the USGS specifically to characterize possible fault deformation of this feature (Hartwell et al., 2013), Johnson et al. (2014) estimate a lateral offset of 30.3 ± 9.4 m and 20.5 ± 8.0 m across the lower and upper slope breaks, respectively (values given as mean and two standard deviations). Johnson et al. (2014) also performed an identical analysis of the CHS using an existing high-resolution MBES data set collected by the Seafloor Mapping

Lab at California State University, Monterey Bay (CSUMB), and estimated lateral offset 43.8 ± 10.4 m and 15.4 ± 5.6 m across the lower and upper slope breaks, respectively. They note, however, that the CSUMB (2012) bathymetry is part of a regional data set that was collected along tracklines oblique to the CHS, and therefore, they favor the offset measurements developed from the USGS data set. The inferred younger age of the upper slope break and the presence of geomorphic indicators that it has been modified led Johnson et al. (2014) to consider the offset across the upper slope break a weaker measurement than the offset across the lower slope break. Consequently they do not report a lateral slip rate estimate derived from the upper slope break value.

The PDFs shown on Figure 8-18 were developed by the TI Team to represent uncertainty in the displacement and age parameters presented by Johnson et al. (2014), and are used to calculate a CDF for Hosgri slip rate at the site. Estimates of lateral offset of the lower slope break are used by the TI Team to define an offset PDF (panels a and b of Figure 8-18). As shown on Figure 12(b) in the article by Johnson et al. (2014), offset estimates range from approximately 15 m to 43 m at the 1% and 99% confidence limit, respectively. This range exceeds the two standard deviations reported by Johnson et al. (2014) that address the scatter in the data points regressed, which are shown as colored dots on Figure 8-17. The preferred offset range of 26–35 m approximately represents the one standard deviation range reported by Johnson et al. (2014) and encompasses the reported mean offset value of 30.3 m.

Johnson et al. (2014) interpret the lower slope break to have been submerged and likely preserved at approximately 12 ± 0.5 ka, approximately corresponding to uncertainty in the timing of the end of the Younger Dryas stadial (Stanford et al., 2011). This preferred age and reported uncertainty are used to construct a triangular age PDF shown graphically on panel c of Figure 8-18.

A slip rate CDF was calculated based on the input parameters described above and is shown on panel e of Figure 8-18. The mean slip rate and certain probability values drawn from the CDF are also provided on Figure 8-18. The mean slip rate for the HFZ at this site is 2.5 mm/yr. The extreme low-probability minimum and maximum slip rates based on the offset and age model are 1.3 mm/yr and 3.6 mm/yr, respectively. The 90% confidence limit slip rate ranges from 1.6 mm/yr to 3.3 mm/yr (5% and 95% cumulative probability, respectively).

8.3.3 Piedras Blancas Anticlinorium/West Hosgri Slip Rate Constraints

The Piedras Blancas anticlinorium is a northwest-trending structural and basement high west of the San Simeon fault zone (Figure 8-13). The Piedras Blancas anticlinorium is within the apex of a broad, regional left-restraining bend in the San Simeon-Hosgri fault system. The fault system progressively changes trend from about N23°W along the coast near the DCPP to N40°W along the San Simeon fault zone north of Ragged Point. The kinematics of restraining bends along regional strike-slip fault systems predict that localized compression will result within the bend. Many of the folds and faults within the Piedras Blancas anticlinorium deform post–Miocene strata, and Pliocene to early

Quaternary strata are absent, indicating active late Cenozoic compression in the region. Active compression is supported by the occurrence of microseismicity, principally within the central and northern parts of the anticlinorium (McLaren and Savage, 2001), and by late Quaternary uplift of marine terraces along the coast from Ragged Point to Point San Simeon (Weber, 1983; Hanson et al., 1994).

Whether there is a contribution to slip along the HFZ from shortening within the Piedras Blancas anticlinorium was addressed during the LTSP studies (PG&E, 1990b). As noted in the response to NRC Question GSG-13, the question indirectly considers whether strain on the HFZ "partitions" northward into a tangential (strike-slip) component on the San Simeon fault zone and a normal (dip-slip or convergent) component from compression in the Piedras Blancas anticlinorium. If local strain partitioning (Lettis and Hanson, 1991) occurs, an estimate of slip rate and sense of slip on the HFZ should combine the rates and orientations of slip along the San Simeon fault zone and across the Piedras Blancas anticlinorium.

PG&E (1990b) estimated the rates of east-vergent and west-vergent crustal shortening within the Piedras Blancas anticlinorium by restoring the amount of deformation recorded by the top of Miocene (5.3 Ma) unconformity. The cumulative shortening from this analysis was 0.9 km. This indicates a post–5.3 Ma shortening rate of approximately 0.17 mm/yr. Based on the resolution of this rate onto a 30° dipping fault and the conservative assumption that all of this slip translates to strike-slip on the western trace of the HFZ, which is nearly parallel to the strike of the folds within the anticlinorium, a 0.2 mm/yr slip rate is assigned to both the Piedras Blancas anticlinorium and the western branch of the HFZ.

The results of more recent mapping of Quaternary stratigraphy and faulting on the continental shelf based primarily on interpretation of high-resolution 2D seismic-reflection profiles collected from Point San Simeon to southern San Luis Obispo Bay in 2008 and 2009 by the U.S. Geological Survey (USGS; Sliter et al., 2010) provide additional information on possible contributions from fault strands west of the primary active trace of the Hosgri–San Simeon fault (PG&E, 2013a). This study showed that the western branch of the HFZ diverges from the primary HFZ near the convergence with the Los Osos fault zone (Figure 8-13). Faults at depth on the western branch do not deform unconformities H30 or younger, which are discussed below in *Section 8.3.4*. Unconformity H30 is interpreted as the transgressive surface developed between the MIS 6 lowstand and the MIS 5e highstand. Its age is estimated to range from approximately 135 ka to 125 ka. It is distributed widely above the shelf break in San Luis Obispo and Estero bays. In contrast to evidence for several meters of deformation of the same unconformities across the primary strands of the HFZ, these observations indicate that the western branch has a very low slip rate. Given the resolution of the seismic reflection data at the Hosgri fault crossings and the inferred age of unfaulted unconformities, the lack of deformation suggests the slip rate would be considerably less than 0.2 mm/yr.

8.3.4 Age Constraints on Channels Buried Beneath Continental Shelf

Buried channels are offset by the Hosgri fault at two study sites offshore of the DCPP, the southern Estero Bay site and the Point Sal site, which are described in *Sections 8.3.5 and 8.3.6* (Figure 8-13). At both sites, the channels are buried beneath a stratigraphic sequence punctuated by numerous unconformities that are locally erosional and locally paraconformable. These shallow reflectors record episodes of deposition on the outer continental shelf separated by periods of nondeposition and erosion. The shallowest unconformities at both sites are part of a sequence of regional unconformities that were identified and mapped beneath the outer continental shelf by PG&E (2013a).

8.3.4.1 Upper Pleistocene Sequence Stratigraphy

Between Point Sal and Point San Simeon, the continental shelf is characterized by local regions of rocky seafloor offshore of uplifting blocks (dominantly the Casmalia block at Point Sal, the San Luis–Pismo block at Point Buchon, and rocky regions north of Estero Bay) and intervening regions of smooth seafloor that are underlain by marine sediment that buries bedrock in San Luis Obispo Bay, Estero Bay, and the outer continental shelf. The sedimentary sections beneath the outer continental shelf in Estero Bay and west of the Irish Hills contain distinctive sedimentary prisms that thin both landward and seaward. Sediments within these prisms consist of clinoforms that downlap onto underlying depositional surfaces and are overlain by erosional surfaces that extend landward into Estero Bay and San Luis Obispo Bay, where they merge with the erosional bedrock surface where the sedimentary section laps onto rock. Examples of these sedimentary prisms are shown on Figure 8-19. These features are interpreted in a sequence stratigraphic framework as stacked highstand and lowstand-to-transgressive system tracts that were deposited during late Quaternary sea-level oscillations (PG&E, 2013a).

A first-order chronology for the study area succession, which was first developed by PG&E (2013a), has been refined by the SSHAC TI Team using additional analog studies. The general framework of multiple stacked highstand and lowstand-to-transgressive system tracts documented by PG&E (2013a) is consistent with the findings of previous workers (e.g., Lobo and Ridente, 2014) that demonstrate that the stratigraphy of Quaternary continental margins is ruled by cyclical deposition that can be confidently related to high-amplitude sea-level oscillations. Several studies have shown that the middle to upper Pleistocene (i.e., 500–700 ka) stratigraphy displays a main sequence stratigraphic pattern characterized by the dominance of 100 ka glacial cyclicity, in which major transgressive surfaces result from abrupt rises in sea level at the termination of 100 ka glacial cycles (Chiocci et al., 1997; Ridente et al., 2008; McHugh et al., 2010; Lobo and Ridente, 2014; Figures 8-20 and 8-21).

Three key shallow unconformities that separate systems tracts in the shallow stratigraphy of the outer shelf were mapped to extend regionally both along the shelf edge and eastward across the shelf. Unconformities H10, H30, and H40 were interpreted as transgressive surfaces that developed following the three most recent sea-level lowstands, MIS 2, MIS 6, and MIS 8, respectively (Figure 8-20; PG&E, 2013a). Two deeper

transgressive unconformities, H45 and H48, were subsequently recognized in Estero Bay, west of the Irish Hills, and on deeper records from San Luis Obispo Bay (PG&E, 2014, Chapter 3; Figure 8-22). PG&E (2014, Chapter 3) could not correlate these deeper unconformities regionally as confidently as the shallow ones due to limitations in imaging of the USGS sparker profiles. As a result, the ages of these two unconformities are less well constrained, but it is likely that they were developed during transgressions following prior lowstands between MIS 10 and MIS 16 (PG&E, 2014, Chapter 3; Figure 8-21).

In the western part of the Point Sal study area, west of the Hosgri fault, the shallow stratigraphic section consists of relatively uniform gently dipping reflectors of the continental shelf that are punctuated by at least five unconformities, each of which is locally associated with erosion and truncation of underlying reflectors (Figure 8-23). The two shallowest unconformities are parts of the regional unconformities H10 and H30 and were correlated on intersecting 2D profiles and within the 3D volume by PG&E (2014, Chapter 3). The deeper unconformities were subsequently identified and mapped by the TI Team and are associated with erosion into underlying strata at locations where sufficient deformation has occurred to uplift and tilt or fold the section, such as the left side of Figure 8-23. Based on this evidence for erosion close to maximum sea-level lowstand depths, the character of the reflections, and the spacing of unconformities, we interpret the deeper unconformities as parts of the deeper regional unconformities H40, H45, and H48 (Figure 8-20).

The recognition by PG&E (2014, Chapter 3) of five separate sequences separated by six shelf-wide unconformities in the study area is consistent with the findings of sequence stratigraphic investigations of other Quaternary shelf margins. Rabineau et al. (2006) inferred paleoshoreline positions from deposits of five separate lowstands in the Gulf of Lions and interpreted them to result from the last five glacial terminations (the ends of the past five 100 kyr cycles). Reis et al. (2013) also recognized at least five distinct sequences that they interpreted to result from five separate sea-level cycles on the continental shelf off of Rio De Janeiro, Brazil. Ridente et al. (2012) recognized six sequence boundaries that bound five distinct depositional sequences beneath the shelf offshore of the west coast of Italy. They interpreted these to record episodic deposition and erosion during the past five complete sea-level cycles.

8.3.4.2 Shelf Progradation Following the Mid-Pleistocene Transition

Although they are now buried beneath sediments of the continental shelf, the channels recognized in the Estero Bay and Point Sal study areas are interpreted to have developed on the paleo–continental slope based on their great depth (PG&E, 2014, Chapter 3). In the western part of the Estero Bay study area, the deep part of the stratigraphic section is characterized by relatively uniform slope-parallel reflectors, consistent with a relatively low-energy continental slope environment. The boundary between this section and the overlying continental shelf stratigraphy is mapped as unconformity T05 (Figure 8-22). Over much of the western Estero Bay study area, unconformity T05 dips uniformly westward, parallel to underlying reflectors, but it is buried by downlapping reflectors that

constitute the prograding sedimentary prism of the continental shelf beneath unconformity H48 (PG&E, 2014, Chapter 3). In the Point Sal study area, the boundary between shallow stratigraphy of the continental shelf and the deeper stratigraphic section of the continental slope appears erosive instead of depositional; the TI Team interprets this erosive unconformity to be part of unconformity H48, which may have removed the surface of downlap that would be equivalent to unconformity T05 at this site (Figure 8-23).

The marked progradation of the shelf in Estero Bay that accompanied the burial of the channels was interpreted by PG&E (2014, Chapter 3) to result from the mid-Pleistocene Transition (MPT), a global climatic transition from relatively frequent low-amplitude 41 kyr sea-level cycles to relatively infrequent high-amplitude 100 kyr sea-level cycles (Bintanja and van de Wal, 2008). Oxygen isotope records compiled by Lisiecki and Raymo (2005) suggest that this transition affected the magnitude of extreme lowstands more than extreme highstands, and that the MIS 16 sea-level lowstand was the first of a series of lowstands that were significantly deeper than any prior lowstand (Figure 8-21). It is likely that this extreme lowstand exposed a much greater portion of the shelf to sub-aerial erosion than earlier lowstands, and it led to a brief period of significant shelf progradation as lowstand deposits were graded to a much lower sea level than had occurred during previous lowstands.

Although the transition from slope to shelf environment in the western part of the Point Sal study area was not discussed by PG&E (2014, Chapter 3), the TI Team considers it likely that the extreme sea-level lowstand that led to shelf progradation suggested by the stratigraphy at Estero Bay may have also caused the pronounced erosional unconformity and shelf progradation at Point Sal (Figure 8-23). Therefore, it is possible that shelf expansion at the end of the MPT led to burial of the continental slope strata in the western parts of both the Estero Bay and Point Sal study areas.

Other shelf margins exhibit distinctive changes in sedimentary architecture that have been attributed to the change in amplitude of sea-level oscillations during the MPT. For example, architectural changes associated with the MPT have been described for shelf margins in the Gulf of Lion (Rabineau et al., 2005, 2006), the Adriatic Sea (Maselli et al., 2010), and in the Alboran Sea (Lobo et al., 2008). In the South Evoikos Gulf in the Aegean Sea in Greece, Anastasakis and Piper (2013) studied an exceptionally well-preserved progradational sequence containing lowstand deposits from MIS 2 to MIS 16, which they tentatively extended as far back as MIS 38 based on correlation with the benthic $\delta^{18}O$ record. This sequence shows that clinoforms of smaller amplitude and volume were deposited before the 100 ka cyclic progradational units, and that the clinoform wedge associated with the MIS 16 lowstand is significantly thicker and shows evidence for progradation much farther seaward than other middle to late Quaternary lowstands.

8.3.4.3 Characterization of Uncertainty in Channel Ages

In both the Estero Bay and Point Sal study areas, channels offset by the Hosgri fault are buried beneath a pronounced unconformity that separates relatively continuous unchannelized reflectors that are punctuated by regional unconformities of the outer continental shelf, from the underlying stratigraphy that is incised by submarine channels that descend the paleo–continental slope (Figures 8-22 and 8-23). An interpretation of the ages of buried channels at the two sites is provided by PG&E (2014, Chapter 3). The TI Team has further evaluated the sequence of unconformities to better constrain the uncertainty in age of the unconformities that both underlie and overlie the buried channels, and thereby better constrain the minimum, preferred, and maximum age of the channels, as discussed above.

Within the Estero Bay study area, the TI Team age model is very similar to the one developed by PG&E (2014, Chapter 3), but it incorporates additional uncertainty, particularly on the low end of the age range. Within the San Luis Obispo Bay study area, the TI Team age model differs significantly from the one presented by PG&E (2014, Chapter 3) because it is based on the recognition of three additional unconformities within the stratigraphic section above Channel F, which were not incorporated into the PG&E age model. The TI Team considers each of these to have been developed during separate sea-level cycles based on evidence for erosion into underlying strata locally associated with these unconformities, and the similarity in thickness of stratigraphic intervals between them and between the shallower unconformities, H10 and H30. Based on these new observations, the TI Team judged that the low end of the age range in the model presented by PG&E (2014, Chapter 3) is not technically defensible. Instead of accepting the previous age models for Channel DBw-Ee1-De at Estero Bay and Channel Fw3-Fe3 at Point Sal, the TI Team developed the age model presented below to describe uncertainty in the ages of the buried channels at both sites.

A PDF describing uncertainty in channel ages for the two sites is illustrated in the bottom part of Figure 8-21. This PDF consists of a high-probability trapezoid that represents the most likely age range for the channels, and two triangular distributions that represent the low end and high end of the range of possible ages.

The TI Team considers the most likely age of channel abandonment at the Estero Bay and Point Sal study areas to be shortly before a period of shelf progradation that likely accompanied the onset of extreme lowstands at the end of the MPT, and the onset of 100 ka glacial cycles. The regional unconformities, H10, H30, H40, H45, and H48, which are locally associated with significant erosion into underlying strata on the continental shelf, are each interpreted to be caused by transgressions at the terminations of 100 kyr glacial cycles. This consideration is used to define the high-probability trapezoid at the center of the PDF. A weight of 0.8 is assigned to this trapezoid based on the strength of the evidence supporting this age range.

The low end of the high-probability trapezoid is defined to be 535 ka, the approximate age of the MIS 14 lowstand, based on the recognition that at least five significant erosive unconformities are present within the succession that buries the channels at both sites,

and the interpretation that these represent at least five major glacial terminations, corresponding with those that followed the MIS 2, MIS 6, MIS 8, MIS 10, and MIS 12 lowstands (Figure 8-21). A preferred range of 630–800 ka is defined based on the interpretation that the extreme lowstand during MIS 16 (~630 ka) is the most likely cause of shelf progradation in the two study areas, and the recognition that the channels are separated from the progradational surface (T05 in Estero Bay and the pronounced erosive unconformity at Point Sal) by relatively uninterrupted reflectors (Figures 8-22 and 8-23), indicating that some delay likely occurred between channel abandonment and shelf progradation. The high end of the high-probability trapezoid is somewhat arbitrarily defined as 1 Ma. This reflects an interpretation that the channels were likely abandoned shortly before shelf progradation; it also acknowledges uncertainty in the timing of shelf progradation at each site. Although there is no hard evidence to assign this boundary of probability, it is required to separate the high-probability trapezoid from a low-probability tail on the older side. Given the great age of this boundary, small differences (±100 ka) have very little effect on the calculated fault slip rate.

A minimum age is assessed from an alternative interpretation that the ages of unconformities H10, H30, H40, H45, and H48 may relate to the subordinate 20 ka glacial sea-level cycle instead of the major 100 ka cycle. This alternative interpretation is based on the possibility that these transgressive surfaces do not represent extreme sea-level minima, and they may have developed during intermediate lowstands. This alternative model is illustrated as the 'Minimum' age model on Figure 8-20. Within this alternative model, we interpret the following:

- H10 corresponds to the transgression following the LGM, approximately 19–7 ka.
- H30 is interpreted to result from the transgression that followed the MIS 4 stadial lowstand, approximately 60 ka.
- H40 is interpreted to result from the transgression that followed the MIS 6 glacial maximum (~130 ka).
- H45 is interpreted to result from the transgression that followed the MIS 6f stadial lowstand (~180 ka).
- H48 is interpreted to result from the transgression that followed the MIS 8 glacial maximum (~240 ka).
- The progradational surface (T05 in Estero Bay and the pronounced boundary at Point Sal) is interpreted to result from the MIS 8 sea-level lowstand (~240–280 ka).

The minimum age for channel activity is therefore considered to be during the preceding lowstand, MIS 10, and the minimum age of channel abandonment is defined to be 335 ka, the age of the transgression associated with the glacial termination at the end of MIS 10 (Figure 8-21). The minimum age of 335 ka is used to define the lowest point in a triangular probability distribution that represents the low end of the range of uncertainty in the age of channel abandonment. The probability increases uniformly from the low point to a maximum at 535 ka, which corresponds to the low end of the preferred age range (discussed above; Figure 8-21). This triangular distribution is assigned a low weight of 0.1 based on a number of observations that suggest that the alternative

minimum unconformity age model is unlikely to be correct, although it cannot be precluded with available data.

The depths of paleo–shelf breaks, defined morphologically as the break in slope between a gently sloping outer shelf and a steeper upper continental slope, provide approximate indicators of paleo–sea levels during past lowstands. The paleo-shelf breaks within unconformities H30, H45, and H48 are well below the water depths characterized for the MIS 4, MIS 6f, and MIS 8 stadial lowstands (Figure 8-20). Paleo–shelf breaks associated with unconformities H10 and H30 occur more than 1 km west of the paleo–shelf break associated with unconformity H40 (Figure 8-19; Figure 6-3 in PG&E, 2014, Chapter 3) suggesting that the shelf was substantially wider and the sea level was substantially lower during the lowstands preceding H10 and H30 than the lowstand preceding H40. This relationship is consistent with the preferred unconformity age model, whereby the lowstands that preceded unconformities H10 and H30 (MIS 2 and MIS 6, respectively) were associated with significantly lower sea levels than the lowstand that preceded unconformity H40 (MIS 8; Figure 8-20). In contrast, the alternative minimum age model described above and illustrated on Figure 8-20, would predict the paleo–shelf break associated with unconformity H30 to be located significantly landward of those associated with unconformities H10 and H40 because sea level during the MIS 4 stadial lowstand was not nearly as low as it was during the MIS 2 and MIS 6 lowstands. The relative positions of paleo–shelf breaks associated with unconformities H10, H30 and H40 strongly supports the preferred age model and contradicts the relationships that would be predicted by the alternative model (Figure 8-20).

The limiting maximum possible age of channel abandonment is not well defined. An absolute limiting maximum age is defined by the ages of surfaces that underlie the channels, the early–late Pliocene unconformity (ELP; Willingham et al., 2013) at Estero Bay, and the erosional bedrock surface at Point Sal (Figure 8-23). The shallowest unconformity recognized throughout the offshore Santa Maria Basin is described by Willingham et al. (2013) as the ELP. Near the Point Sal study area, a shallower unconformity was recognized by PG&E (2014, Chapter 3) in deep-penetration high-energy seismic-reflection data and was named the near-top-of-Neogene unconformity (NTN). This surface laps onto and merges with the ELP near the HFZ. The age of this surface is estimated to be at most 2.5 Ma (PG&E, 2014, Chapter 3). As described above, the channels are interpreted to have been abandoned shortly before—and perhaps because of—shelf progradation at the end of the MPT. To characterize this uncertainty, the high end in the range of uncertainty in channel age models is defined as a triangular probability distribution that decreases uniformly with age to a maximum value of 2.5 Ma.

8.3.5 Southern Estero Bay Slip Rate Estimate

In the Estero Bay study area, the HFZ consists mainly of two dominant subparallel fault strands, faults labeled 10001 and 10006 on Figure 8-24 (PG&E, 2014, Chapter 3), with minor secondary strands to the northeast and southwest. Within this area, the HFZ marks a boundary between active tectonic uplift to the east (as indicated by the thin sedimentary cover and erosional surface of bedrock characterizing much of the continental shelf) and

minor subsidence to the west (as indicated by the accumulation and preservation of the shelf-edge sedimentary prisms described above in *Section 8.3.4* and shown on Figure 8-19). A high-resolution 3D seismic-reflection volume was collected along the eastern strand of the fault, and a series of high-resolution 2D seismic-reflection profiles were collected parallel to and oblique to the fault to supplement the existing high-resolution profiles collected largely perpendicular to the fault by the USGS in 2008 and 2009 (PG&E, 2014, Chapter 3). Based on the interpretation of these data, PG&E (2014, Chapter 3) identified multiple channel segments in upper continental slope sediments within the southern Estero Bay study area (Figure 8-24).

Of the channels observed east of the HFZ, PG&E (2014, Chapter 3) identified only one, Channel Complex De, as a viable strain marker because it may be correlated across the eastern trace (fault 11006). Channel Complex De descends to the west and is offset to the north by fault 11006, where it appears to correlate with Channel Ee1 between the two primary fault traces (Figure 8-25; see Plate 3 in PG&E, 2014, Chapter 3). Based on correlation of the thalwegs of Channel Ee1 to Channel Complex De, PG&E (2014, Chapter 3) estimated a right-lateral separation of 260 ± 60 m and a vertical separation of 40 ± 8 m, down to the west, across fault 11006 (Figure 8-25).

PG&E (2014, Chapter 3) interpreted the combined Channels De and Ee1 ("Channel De-Ee1") as the upstream reach of a continuous channel that descended the continental slope and did not end abruptly at the Hosgri fault. Active uplift of both the block between fault strands, which is incised by Channel Ee1, and the block to the east, which is incised by Channel De, is supported by truncation of reflectors at the seafloor, indicating erosion at the seafloor, likely due to wave activity during late Quaternary lowstands (Figure 8-26; PG&E, 2014, Chapter 3). Uplift east of the fault was also inferred by vertical separation of unconformities H10, H30, and H40 as imaged on USGS seismic-reflection profiles to the south of this channel (PG&E, 2013a). The Channel De thalweg slopes down to the west from a depth of approximately 132 m to 140 m, and the Channel Ee1 thalweg slopes down to the west from approximately 180 m to 204 m (Plate 3 of PG&E, 2014, Chapter 3). These depths range from slightly below to well below the maximum depth interpreted for late Quaternary sea-level lowstands (Waelbroeck et al., 2002; Figure 8-20). Restoring uplift implies that this channel was initially carved at a greater depth, indicating that it was developed in a continental slope environment or incised into the outer shelf. The recognition by PG&E (2014, Chapter 3) that this channel was carved to depths below the shelf suggests that Channel De-Ee1 represents the headward reaches of a channel that very likely extended downslope to the west. If so, the thalweg of this entire channel would be too deep to have been removed by erosion during Quaternary sea-level lowstands. Therefore, the segment of this channel that extends west of the HFZ must be located beneath the shelf-margin stratigraphic sequences described in Section 8.3.4, which bury the continental slope sediments and are graded to paleosea-level lowstands (Figure 8-19).

PG&E (2014, Chapter 3) interprets the combined Channel De-Ee1 to increase in width and depth of incision as it approaches the western strand of the HFZ, from approximately 470 m wide and 30 m deep at the east end of Channel De to approximately 510 m wide

and 45 m deep at the west end of Channel Ee1, adjacent to the fault (Figure 8-26). Given that the western strand of the Hosgri fault is a significant uplift boundary, it is likely that this channel geometry changes significantly where it crosses the fault. However, the TI Team considers it unlikely that a channel of this size in a continental slope environment would end abruptly where it meets the fault. Instead, we expect that the downstream extension of the channel would be preserved in the stratigraphy of the upper continental slope west of the fault.

The potential for imaging channels west of the HFZ is significantly limited by the resolution and line spacing of 2D seismic-reflection profiles in this area. Channels are clearly evident in the deeper part of the USGS sparker profile PBS-T2, approximately 2.6 km west of the fault (Figure 8-27). Potential evidence for channels is much less clear in the 2D boomer profiles collected closer to the fault. This evidence is limited to reflector truncations, subtle sloping reflectors along channel margins, a minor distinction in reflective character of the channel fill relative to the surrounding strata, and a relatively high-amplitude reflection from the channel thalweg[1]. Evidence for channels on any single 2D boomer profile is weak, but the persistence of these features on several profiles along a similar trend and at a similar depth provides confidence that buried channels are imaged (Figure 8-27).

As described by PG&E (2014, Chapter 3), of the channels imaged west of the HFZ, three extend far enough upslope to the east, and are incised deeply enough to suggest that they may correlate to channel segments east of the HFZ. Restoring approximately 850 m of slip on the western trace (fault 10001) aligns each of these three channels (DAw, DBw, and DCw; Figure 8-24) with candidate upgradient extensions east of the fault. This restoration suggests that Channel DBw is the downgradient extension of Channel De-Ee1.

Precise constraints on the amount of offset were initially measured by PG&E (2014, Chapter 3) from the offset thalwegs of Channel DBw from Channel Ee1, and slightly broadened by the TI Team (Figure 8-25). Two sources of uncertainty in the offset of this channel were identified by PG&E (2014, Chapter 3). The first is uncertainty in the projection of the channel thalweg from where it is mapped on each side of the fault to where it intersects the fault. The second is based on the mapping of Channel DBw itself. Channel DBw is not as well imaged near fault 10001, as it is farther from the fault (Figure 8-27). On the nearest profile to the fault, two channel-like features were recognized that could represent the upslope extension of Channel DBw. The southern channel-like feature appears more likely to be the upslope continuation of Channel DBw because it is shallower than the channel thalweg imaged in profiles to the west, continuing a trend of sloping up to the east. The northern channel-like feature is also viable but is considered less likely to be correct because it would require the channel to jog sharply to the north between seismic profiles, and it would require the channel

[1] The higher amplitude reflection of channel thalwegs may result from the potential presence of relatively coarse sediment along the channel thalweg, and may also be augmented by gas potentially trapped within this sediment.

thalweg to step down to the east approximately 25 m relative to the adjacent profile (Figure 8-25).

The limits of uncertainty in the projection of Channel Ee1 to the fault also include the consideration that the northern bend observed in the channel may be a result of near-fault deformation and does not represent the original geometry of the channel. Therefore, uncertainty in the thalweg offset measurement is large. The best estimate of horizontal offset across the primary trace of the HFZ (fault 10001) is between approximately 770 m and 1,050 m. Based on the uncertainties described above, the maximum horizontal offset is 1,730 m and the minimum is 450 m (Figure 8-25). The vertical separation is 100 ± 25 m, down to the west.

A slip rate CDF is calculated for combined Channels DBw, Ee1, and De ("Channel DBw-Ee1-De") across the HFZ based on the inputs described above. Offset across the western strand of the HFZ is combined with offset across the eastern strand using the trapezoidal probability distributions shown in panel a of Figure 8-28. The probable age of Channel DBw-Ee1-De and the associated uncertainty are characterized by the age model described above in Section 8.3.4 and illustrated on Figure 8-21. A slip rate CDF calculated based on these is shown in panel e of Figure 8-28. The weighted mean slip rate for the HFZ is 1.7 mm/yr. The extreme-low-probability minimum and maximum slip rates are 0.3 mm/yr and 5.3 mm/yr, respectively. The 90% confidence limit slip rate ranges from 0.8 mm/yr to 2.9 mm/yr (5% and 95% cumulative probability, respectively).

8.3.6 Point Sal Slip Rate Estimate

Seismic-reflection data collected from the outer continental shelf adjacent to Point Sal image buried channels east of, within, and west of the HFZ, which locally consists of two primary strands and numerous additional minor strands within the central block between them (Figure 8-29). PG&E (2014, Chapter 3) identified seven possible channels or channel complexes within the 3D data set with varying degrees of confidence. Several of the features identified by PG&E (2014, Chapter 3) as possible channels lack clearly incised margins, and alternatively, could be interpreted as synclines. In addition, most possible channels were identified on only one side of the fault zone, or within it. Only one channel complex (Channel Complex F) was confidently correlated by PG&E (2014, Chapter 3) across the entire HFZ (Figure 8-29). The margins of this channel clearly truncate surrounding reflectors, indicating that this channel was incised into surrounding stratigraphy (Figure 8-30). The thalwegs of channels within Channel Complex F, therefore, were considered to be high-quality piercing points and were used by PG&E (2014, Chapter 3) to estimate offset across the HFZ with greater confidence than other channels. The TI Team assessment focuses only on channel thalwegs within Channel Complex F due to ambiguity in the interpretation of other possible channels and the absence of clear correlations across the HFZ.

East of the HFZ, at least three inset channels (Fe1, Fe2, and Fe3) were identified within Channel Complex F, indicating at least three episodes of channel incision and refilling (Figure 8-30; PG&E, 2014, Chapter 3). West of the fault, seismic imaging of the channels

is less clear, but at least three separate channels (Fw1, Fw2, and Fw3) were identified (Figure 8-23). Only the youngest of these, Fw3, was completely mapped and contoured by PG&E (2014, Chapter 3) because it is the best imaged and most closely related to Channel Complex F east of the fault. The older channels, Fw2 and Fw1, occur progressively farther northward, and were only locally imaged in the 3D volume, which limited the potential for mapping them completely (Figure 8-23). PG&E (2014, Chapter 3) also mapped a surface in the central block between the eastern and western strands of the HFZ, which was interpreted as part of Channel Complex F and is named Fc. However, this surface is not clearly incised, and is located within a growing syncline, suggesting it may not be a channel at all. Given the vertical separation of shallow stratigraphic horizons across the eastern and western strands of the fault, the central part of Channel Complex F may have subsided beneath the depth of imaging within the central block. Because of this uncertainty, the TI Team assessment of offset across the fault does not rely on Channel Fc.

Channel Complex F was interpreted by PG&E (2014, Chapter 3) as a continuous channel system that experienced multiple episodes of activity. Similar to Estero Bay, channels in the eastern block, east of the HFZ, appear to have undergone tectonic uplift, as indicated by reflector truncations associated with unconformity H10 overlying the channels and the bedrock to the southeast (Figure 8-30). Relatively less uplift is indicated directly north of the channels, where a thin sliver of sediment is preserved between unconformities H30 and H10. The thalwegs of Channels Fe1 through Fe3 are incised to depths of at least 135 m and 175 m, respectively, which is deeper than the maximum depth of Quaternary sea-level lowstands, approximately 125 m (Figure 8-20). No surfaces were imaged within the channel fill that grade to lowstand sea-level depths. Based on the depth of Channel F thalwegs both east of the fault and to the west, PG&E (2014, Chapter 3) concluded that Channel Complex F is graded to a base level far below lowstand sea levels. No shoreline or submarine fan was imaged within the stratigraphy across the fault from the Channel Fe complex. The TI Team concurs that, together, these observations support the interpretation of a continuous channel system across the HFZ, uninterrupted by shoreline features such as beaches or deltas.

The TI Team estimated offset across the HFZ by projecting the Channel Fe3 and Fw3 thalwegs from their nearest mapped location to the western strand of the fault (Figure 8-31). A preferred range of 625 ± 25 m is estimated by projecting the thalwegs across the data gaps directly along the trend of thalwegs within the nearest reaches of the channels. Minimum and maximum estimates of 350 m and 830 m, respectively, are estimated from incorporating uncertainty in channel sinuosity into the thalweg projections, as suggested by the approximate curvature of bends within Channel Fe3, to the east (Figure 8-29). The preferred offset assessment described here is the same as that interpreted by PG&E, but the TI Team considers more uncertainty than that reported by PG&E (2014, Chapter 3). PG&E (2014, Chapter 3) also presents an alternative correlation of Channel Fe1 east of the HFZ with the correlation of Channel Fw3 west of the HFZ. Although this correlation is not supported by the channel stratigraphy, it cannot be ruled out because the material filling Channel Fw3 is not sufficiently imaged to preclude inset channels. Therefore, the

fault offset indicated by this alternative interpretation, approximately 525 m, is incorporated into the range defined here. Similarly, the range defined here encompasses the combined offsets across the east strand (from Channel Fe3 to Channel Fc1), approximately 435 ± 55 m, and the west strand (from Channel Fc1 to Channel Fw3), approximately 200 ± 50 m, reported by PG&E (2014, Chapter 3).

A slip rate CDF is calculated for Channel Fw3-Fe3 across the HFZ based on the inputs described above. Offset across the HFZ modeled using the trapezoidal probability distribution shown in panel a of Figure 8-32. The probable age of Channel Fw3-Fe3 and the associated uncertainty are characterized by the age model described above in Section 8.3.4 and illustrated on Figure 8-21. The slip rate CDF calculated based on these is shown on panel e of Figure 8-32. The mean slip rate calculated for the HFZ at Point Sal is 0.8 mm/yr. The extreme low-probability minimum and maximum slip rates based on the weighted age model are 0.2 mm/yr and 2.1 mm/yr, respectively. The 90% confidence limit slip rate ranges from 0.4 mm/yr to 1.3 mm/yr (5% and 95% cumulative probability, respectively).

The correlation of Channel Fe1 to Channel Fw1 by the TI Team provides an additional offset measurement that can be used to corroborate the slip rate implied by the offset and uncertainty in Channel Fw3-Fe3. The thalweg of Channel Fw1 is located approximately 1.6 km northwest of the projection of Channel Fe1, as measured parallel to the western strand of the Hosgri fault (Figure 8-29). Although the ages of these channels are not known, an estimated age of approximately 2 Ma is suggested by stratigraphic relationships, indicating that Fw1 is significantly older than Fw3, and is younger than the erosional top of bedrock, which is estimated to be 2.5 Ma or less at this location (PG&E, 2014, Chapter 3). These very rough estimates suggest a slip rate close to 0.8 mm/yr for the fault, indicating that both the younger and older channel offsets can be explained with a uniform slip rate for the HFZ.

8.3.7 Development of a Hosgri Fault CDF

A CDF is calculated to characterize the slip rate of the HFZ directly offshore of the DCPP site. This CDF incorporates information from the four primary slip rate sites described above: San Simeon, Point Estero, Estero Bay, and Point Sal. Slip rate CDFs developed for each of these sites describe epistemic uncertainty in the slip rate at the site. However, the HFZ slip rate at a particular site may differ from the HFZ slip rate directly offshore of the DCPP site. Kinematic linkage with active faults that merge with the HFZ suggest that the HFZ slip rate changes along strike, and likely decreases to the south until eventually reaching zero at the south end of the fault (Hanson et al., 2004). However, the amount and precise location that the HFZ slip rate changes where it intersects active faults are not known. Therefore, instead of attempting to quantify the likely amount or rate of slip rate change between sites where the HFZ slip rate is constrained and the DCPP, the TI Team incorporated this uncertainty into their weighting scheme for the applicability of each site-specific CDF to the reach of the HFZ offshore of the DCPP.

The slip rate CDF for the HFZ at the DCPP site is a weighted average of the slip rate CDFs calculated for the slip rate at each of these four sites. The weight assigned to each site represents the judgment of the TI Team regarding how well the slip rate calculated at each site represents the slip rate of the Hosgri fault at the DCPP, with primary consideration given to the quality of the slip rate constraint, the age of the constraint, and the distance of the site from the DCPP. Each of the four individual CDFs are shown together with the final weighted Hosgri fault CDF on Figure 8-33. The weights for each site are as follows:

- San Simeon [0.3]
- Point Estero [0.2]
- Estero Bay [0.3]
- Point Sal [0.2]

The San Simeon slip rate CDF is assigned a weight of [0.3]. We consider the San Simeon slip rate study to be the best characterization of slip rate anywhere on the Hosgri–San Simeon fault zone. Although significant uncertainty in the offset amount exists, primarily due to uncertainty in paleogeographic reconstruction, there is very little uncertainty in the age of the Oso marine terrace (see Section 8.3-1). This tightly constrained age estimate is reflected in the relatively steep CDF for the San Simeon site (Figure 8-33). The San Simeon slip rate site is the farthest of the four from the DCPP, located approximately 60 km to the northwest (Figure 8-13). Therefore, despite the high confidence in the quality of the slip rate constraint, the weight assigned to this slip rate being representative of the rate along the section of the Hosgri fault adjacent to the DCPP is lowered to account for the uncertainty in how much the slip rate on the fault may change along strike between the San Simeon site and the DCPP.

The Point Estero slip rate CDF is assigned a weight of [0.2]. Although the offset feature (the cross-Hosgri slope [CHS]) provides a shorter-term (Holocene) slip rate that may better represent the current rate of slip and the site is somewhat closer to the DCPP, located approximately 40 km to the northwest, the relatively lower weight assigned to this site reflects the TI Team's judgment regarding the quality of this feature as a well-constrained piercing point and potential underestimation of the uncertainty in the amount of offset. To be a valid piercing point, a feature must be isolated in space and time, so that the original geometry of the feature at a known time can be reconstructed, and fault deformation of the feature can be distinguished from other processes. For the CHS, significant uncertainties exist in the original geometry of the feature and the time that the feature stabilized (or was abandoned). The slope itself includes erosional hollows near the top and depositional lobes near the bottom, suggesting it has been modified by slumping and, perhaps, incision by submarine currents (Figure 8-17). Slope break measurements from the top and the bottom of the slope include steps and bulges that appear to be associated with these slumps, suggesting that the top and bottom of the slope have both been modified since it was formed. Given the likelihood that the feature is composed of saturated sand and has undergone multiple earthquake ruptures and associated strong ground motion, some slope failures or lateral spreading can be expected.

As shown on Figure 8-17, only a subset of slope break measurements was used by Johnson et al. (2014) to characterize offset of the CHS feature. It is not clear that the subset used to measure offset best represents the original geometry of the feature. The part of the slope directly east of the fault appears to have degraded, and the slope may have widened, moving the lower slope break farther south than its original position. The slope break points that are east of the fault and are used to measure offset, shown as blue circles on Figure 8-17, are significantly farther from the top of the slope than the slope break points from the steeper, and likely more intact, part of the slope farther to the east. Regressing different subsets or the entire collection of measurements yields markedly different estimates of offset.

The age at which the CHS stabilized also is uncertain. The depositional model described by Johnson et al. (2014) implies that the feature was abandoned shortly after the Younger Dryas stadial approximately 12 ka, when rapid sea-level rise associated with meltwater pulse 1B flooded the feature and isolated it from the effects of wave erosion. Based on the rate of sea-level rise during this period, estimated to be approximately 130–150 centimeters per century (Stanford et al., 2011), and the height of the slope, approximately 7–9 m high, both the top and bottom of the slope would be isolated from the effects of wave erosion within less than one millennium of each other.

Although the top of the slope was likely subject to modification by wave erosion for a longer duration than the base of the slope, as described by Johnson et al. (2014), both slope breaks were likely isolated from wave erosion for similar durations (i.e., on the order of 11 ka and 12 ka, respectively), suggesting that active fault deformation should have displaced both slope breaks by approximately the same amount. The fact that the offsets calculated for the two slope breaks are quite different (20.5 ± 8.0 m for the upper slope break and 30.3 ± 9.4 m for the lower slope break) suggests that either the slope breaks do not represent the original geometry of the feature (as described in the previous paragraph) or that the age model for abandonment of the feature is incorrect, or both. Because of these uncertainties, the slip rate characterized by Johnson et al. (2014) is incorporated into the SSC model but is assigned a weight of [0.2].

The Estero Bay slip rate CDF is assigned a weight of [0.3]. The Estero Bay slip rate site is the closest of the four sites to the DCPP, located approximately 15 km to the northwest, which suggests that it most closely approximates slip rate on the HFZ at the DCPP. As described above, estimates of channel ages and the amount of channel offset are moderately well constrained (see *Sections 8.3-4 and 8.3-5*). However, uncertainty exists in the interpretation of channels west of the fault. The data quality west of the HFZ is significantly lower than the data quality east of the fault, and it is possible that the features interpreted as channels on the 2D boomer data near the fault are not channels at all. If so, it is possible that continuous channels were never incised between the fault and the channels imaged farther to the west on USGS line PBS-T2, or that the channels are there and are not imaged by the boomer data. Despite the channels' proximity to the DCPP and the relatively well-founded basis for age estimates, a weight of only [0.3] is assigned because of this epistemic uncertainty in the validity of channel locations west of the fault.

The Point Sal CDF slip rate is assigned a weight of [0.2]. Channel F at Point Sal is very well imaged, and there is very little uncertainty in channel correlation across the fault zone (see *Section 8.3-6*). Age estimates for the channel are moderately well constrained (see *Section 8.3-4*). However, the Point Sal site is located approximately 35 km south of the DCPP. Between the Point Sal site and the DCPP, the reverse to reverse oblique faults of the Southwestern Boundary zone (SWBZ), as well as the Casmalia and Lions Head faults, branch from the HFZ, and each of these faults is likely associated with a decrease in slip rate along the HFZ (Hanson et al., 2004; *Section 5.2.1*). The moderately high confidence in the slip rate constraint is balanced by the distance of the Point Sal study site from the DCPP and the presence of active faults that branch from the Hosgri and likely reduce the slip rate of the HFZ.

8.3.8 Equivalent Five-Point Distribution and Comparison to Other Studies

The weighted slip rate CDF for the Hosgri fault is represented by the black line as shown on Figure 8-33. The five-point discrete representation of this continuous probability distribution, which is provided in the associated table, ranges from 0.6 mm/yr to 3.1 mm/yr, with a weighted average value of 1.7 mm/yr.

The slip rate estimates used in previous PG&E seismic hazard analyses (PG&E, 1988, 2004, 2011) are compared to the UCERF2 and UCERF3 characterizations in the following sections.

8.3.8.1 Previous PG&E Studies

The slip rate estimated for the Hosgri fault source in the Diablo Canyon LTSP (PG&E, 1988) study varied depending on the style of faulting. The strike-slip branch, which was given the highest weight at that time and which has been given a weight of 1.0 in subsequent PSHAs (PG&E, 2004, 2011), used the following slip rate distribution, resulting in a weighted mean slip rate of 2.25 mm/yr:

- 0.5 mm/yr [0.1]
- 1 mm/yr [0.4]
- 3 mm/yr [0.4]
- 6 mm/yr [0.1]

The 2004 SSC update for the ISFSI mainly involved revising the Hosgri fault characterization to be primarily strike-slip based on new data that rejected the reverse and reverse oblique alternatives that were included in the SSC logic trees in the 1988 LTSP study.

The source parameters for the Hosgri fault used in the analysis of the Shoreline fault (PG&E, 2011) were mostly unchanged from the LTSP Final Report (PG&E, 1988), but some minor modifications to the depth to bottom of rupture, style of faulting (oblique-slip and reverse branches are not viable based on more recent information and analyses), and

dip were included. The range of slip rate values used for the strike-slip fault geometry in the PG&E (1988) study was used in this analysis.

8.3.8.2 UCERF2

The Uniform California Earthquake Rupture Forecast, Version 2 (UCERF2), Deformation Model 4 characterized the combined Hosgri–San Simeon fault as a strike-slip fault with a slip rate of 2.5 mm/yr along its entire length.

8.3.8.3 UCERF3

The Uniform California Earthquake Rupture Forecast, Version 3 (UCERF3) deformation model describes slip rates of faults included in the statewide model. The deformation model incorporates a geologic model plus three geodetic models, each of which is constrained at sites where paleoseismic slip rates are known. Slip rates for the Hosgri–San Simeon–San Gregorio fault system characterized by each of these four models are presented in Table 8-1. For the part of the fault nearest the DCPP, the slip rates characterized by UCERF3 range from 0.83 mm/yr to 1.5 mm/yr.

Table 8-1. UCERF3 Modeled Slip Rates

Fault	Geodetic Model			Geologic Model
	Zeng	NeoKinema	Average Block Model	
San Gregorio Fault (north)	3.94	3.97	2.1–2.2 (N) 1.5 (S)	7.0
San Gregorio Fault (south)	2.73	1,22	1.5–2 (N) 1–1.25 (S)	3.0
Hosgri (San Simeon)	0.83	1.18	2.16	2.5
Hosgri (near DCPP)	0.83	1.18	~1.5	1.5
Hosgri (south)	0.83	1.18	1.23	1.5
Hosgri (extension)	0.43	0.94	1.39 to 0.76 (N to S)	0.6

8.3.8.4 DeMets Analysis of GPS Velocity Data

As discussed in Section 5.2.6, the analysis of regional GPS velocity data generally supports low rates of dextral shear and plate normal convergence in the Diablo Canyon region. DeMets (2012a) analyzed GPS data from Central California specifically to evaluate crustal velocities west of the San Andreas fault in the Diablo Canyon region. The conclusion of this study is that the total velocity budget available for faults west of the West Huasna–Oceanic fault zone is 2–4 mm/yr if the model assumes a rigid Pacific Plate with no internal deformation offshore, or 0.5–2.5 mm/yr if the Pacific Plate deforms

internally as indicated by GPS stations on Clarion, Socorro, and Guadalupe Islands (DeMets et al., 2014).

8.4 Shoreline Fault

The Shoreline fault zone lies entirely offshore (Figure 8-34), making it difficult to develop direct quantitative estimates for rate and sense of slip. The Shoreline fault was initially recognized based on an alignment of microseismicity directly offshore of the coastline of the Irish Hills (Hardebeck, 2010). Subsequent offshore studies conducted as part of the ongoing PG&E LTSP, PG&E/USGS CRADA, and CCCSIP research programs (see *Chapter 4.0*) have provided additional information to assess the style and rate of Quaternary deformation of the Shoreline fault.

The first comprehensive SSC logic tree of the Shoreline fault was published by PG&E in 2011. Analysis of the data available at the time showed the Shoreline fault to be primarily a right-lateral fault with a limited vertical component of slip, based on three primary lines of evidence (PG&E, 2011):

1. Focal mechanisms that indicate strike-slip motion on a vertical fault.
2. A very steep fault dip inferred from seismicity data and the linear geologic expression of the fault on the seafloor.
3. Constraints on maximum vertical displacement of Pleistocene submerged wave-cut platforms.

This conclusion has been supported by analysis of additional high-resolution 2D and 3D seismic data (PG&E, 2014, Chapters 2 and 3) and subsequent analysis of seismicity data (Hardebeck, 2012c, 2013).

Multibeam echosounder (MBES) bathymetric data that were available at the time of the initial SSC of the Shoreline fault (PG&E, 2011) were examined to identify piercing points (i.e., potentially datable geomorphic features such as paleostrandlines or channel thalwegs on both sides of the fault zone that could be used to constrain cumulative slip and slip rate). No geomorphic features that could be used reliably as lateral offset markers were identified based on detailed examination of these data. In the absence of more direct information, PG&E (2011) used four lines of reasoning to provide constraints on the minimum, maximum, and preferred values for slip rate:

1. Comparison to the Hosgri fault.
2. Seismicity rate.
3. Observed vertical separation of submerged wave-cut platforms.
4. Postulated lateral separation of magnetic anomalies.

These analyses provide estimates of slip rate ranging from 0.05 mm/yr to 1 mm/yr, with a preferred range between 0.1 mm/yr and 0.3 mm/yr. It was noted, however, that a slip rate of zero could not be precluded, based on the data available at that time.

Interpretations of new high-resolution 3D seismic-reflection data acquired in San Luis Obispo Bay provide additional information to evaluate mapped patterns and structural

relationships between the Shoreline fault and faults within the SWBZ (i.e., the Oceano, and Los Berros faults; Figure 8-35). PG&E (2014, Chapter 3) estimated slip rates for the Shoreline fault in San Luis Obispo Bay based on constraints on the amount that buried submarine channels are offset where they cross the fault, and on the measured offset of scalloped terrace risers within a sequence of terraces imaged by 3D seismic-reflection data and interpreted by PG&E (2014, Chapter 3) as buried paleoshorelines. These slip rate constraints are located south of the intersections of the Shoreline fault with active faults of the SWBZ. Similar to the Hosgri fault (*Section 8.3*), tectonic and kinematic models suggest that the slip rate of the Shoreline fault increases to the north of intersections with active reverse faults that branch from the east. Therefore, the slip rate of the Shoreline fault opposite the DCPP is likely to be greater than the slip rate estimates from piercing points in San Luis Obispo Bay. The TI Team approach to characterizing the slip rate of the Shoreline fault opposite the DCPP considers the amount that may be contributed to the fault from SWBZ faults that branch from the east as added to the slip rate of the fault in San Luis Obispo Bay.

The analysis of available offshore data that provide information on the slip sense and slip rate of the Shoreline fault is discussed in *Sections 8.4.1 through 8.4.4*. As described in Chapter 3 of PG&E (2014), numerous buried channels are imaged across the Shoreline fault in the 3D seismic-reflection survey in San Luis Obispo Bay (Figure 8-35). Given the limitations of data resolution (horizontal resolution is nominally 3.2 m), however, it is unlikely that channels that were abandoned at the end of the LGM lowstand (~19 ka; Stanford et al., 2011) provide a tight constraint on slip rate. Therefore, the discussions below include only the channels or terraces with evidence to suggest they are older than the LGM. Section 8.4.1 describes the offset terrace sequence near the southeastern edge of the 3D volume. Section 8.4.2 describes Channel I, and Section 8.4.3 describes Channel A. Section 8.4.4 provides data and analysis to support evaluation of how much vertical separation occurs across the Shoreline fault west of the Irish Hills, which is north of the intersection with faults of the SWBZ. Section 8.4.5 summarizes how these data are used to develop a slip rate distribution for the Shoreline fault along the reach closest to the DCPP. Section 8.4.6 compares the resulting five-point slip rate distribution to slip rates proposed by others based on geologic and geodetic data.

8.4.1 Terrace Sequence Slip Rate Estimate

A sequence of buried terraces are imaged within the sedimentary section beneath the seafloor near the southeastern edge of the 3D seismic-reflection survey in San Luis Obispo Bay. As mapped by PG&E (2014, Chapter 3), these features consist of broad, relatively flat surfaces separated by relatively steep slopes (risers) that range from as little as 2–3 m to 12 m high. The risers between the flat surfaces are clearly evident in time slices as scalloped boundaries between reflectors of different amplitude (Figure 8-36). These features were interpreted by PG&E (2014, Chapter 3) as paleoshorelines carved by small-scale sea-level fluctuations during a longer period of net sea-level regression. However, other viable interpretations of their origin also exist. They may be meander scars on the margins of a lowstand fluvial system. The broad curves of the terrace risers

are morphologically quite similar to low terrace risers present along the margins of the modern Santa Maria River, directly onshore to the east. Alternatively, these features are morphologically similar to some channels and lakes observed in modern deltas, suggesting that the features may be part of a more complex shoreline system consisting of both deposition and erosion. Due to this uncertainty in the genesis of these features, we describe them with the morphologic terms “terrace” and “riser” for the purposes of this report.

Two buried terrace risers within this sequence are imaged crossing the Shoreline fault zone (Figure 8-36). The intersections between the risers and terraces were mapped at depths of 84 m and 92 m. PG&E (2014, Chapter 3) interpreted right-lateral offset of both terrace risers (described as paleostrandlines) across the Shoreline fault to be approximately 10 m with minimum and maximum values of 3.4 m and 15.4 m estimated from the pixel dimensions in time slices of 3.4 m, and an assumed 2-pixel uncertainty. PG&E (2014, Chapter 3) measured 1 m of vertical separation of the terrace surface across the Shoreline fault, with a range of 0.8–1.6 m.

The TI Team concurs with the offset amounts estimated by PG&E (2014, Chapter 3). A preferred offset of approximately 10 m is estimated from correlating the central dark reflector in a light-dark-light triplet across the fault (Figure 8-36). A lower bound is estimated from an alternative correlation of the light reflector that marks the north side of this triplet east of the fault, with the light reflector that marks the south side of this triplet west of the fault. An upper bound is estimated by adding the inferred offset from an apparent jog in the terrace riser approximately 25 m northeast of the fault to the preferred offset, based on the consideration that the jog may be due to displacement on a secondary strand of the fault. The range in the ratio of horizontal-to-vertical slip suggested by these offsets, which is from approximately 2:1 to 19:1 with a preferred value of approximately 10:1, demonstrates that the Shoreline fault is a low-rake and dominantly right-lateral strike-slip fault in the southern San Luis Obispo Bay study area, and the lateral slip rate is a good approximation of the net slip rate. The proximity and similarity in offset amount suggest that the two terraces formed over a time span that is short relative to their absolute ages, indicating that the two terraces can be treated as a single strain marker for purposes of the slip rate evaluation.

The ages of the terraces are estimated from stratigraphic constraints and consideration of late Quaternary sea-level curves. Seismic-reflection profiles from the USGS sparker data (Figure 8-37) and the 3D volume show that the terrace sequence is buried by strata that are below unconformity H30, which is correlated to the MIS 6–5 transgression (*Section 8.3.4.1*). PG&E (2014, Chapter 3) interpreted the same stratigraphic unit and the terrace sequence to overlie unconformity H40, which is correlated to the MIS 8–7 transition. However, the TI Team considers the stratigraphic relationship with unconformity H40 to be less certain, and considers it possible that unconformity H40 continues to rise to the east, parallel to overlying reflectors, from the limit of mapping on the left side of Figure 8-37. This alternative interpretation acknowledges limitations in the seismic stratigraphic mapping by PG&E (2013a) and would imply that terrace sequence may be older than unconformity H40. Given the interpretation that the terrace sequence represents a series

of shorelines or fluvial terraces, the terraces must have formed either at or above sea level. Therefore, viable ages for the terraces are times prior to unconformity H30 when sea level was either at the approximate depths of the terraces, or below them. The terrace sequence is probably subsiding at a low rate, as suggested by the accumulation of marine sediment from multiple sea-level cycles over the terraces. This observation suggests that little to no correction for tectonic uplift rate of the terraces is necessary for comparison to paleosea levels, and using their current elevation as an upper bound of viable paleosea levels captures the full range of possible terrace ages.

Figure 8-38 shows the reconstructed sea-level curve from Waelbroeck et al. (2002) and the stacked oxygen isotope ($\delta^{18}O$) curve from Lisiecki and Raymo (2005) scaled to match geologic constraints on LGM sea level. Horizontal lines are drawn at –84 m and –92 m, the approximate depths of the bases of the terrace risers. Allowable terrace ages correspond to parts of the sea-level curve below these lines. Trapezoidal-age PDFs are shown on the lower portion of the figure with the corresponding points that define the minimum, maximum, and preferred lower and upper values plotted from selection of parts of the sea-level curves that fall below the terrace riser depths. These PDFs and the weights associated with each of them represent the TI Team assessment of the likelihood that the terraces formed during the corresponding lowstands. A minimum age of MIS 4 is allowed, but it is assigned a very low weight of [0.05] based on the possibility that the terraces were developed during the lowstand directly prior to the H30 transgression, and the possibility that unconformity H30 developed at the end of MIS 4 (as described in Section 8.3.4.1). An alternative age of MIS 6 is assigned a higher weight of [0.3] and is estimated from the same stratigraphic relationship and the preferred age of unconformity H30. The most probable age of the terrace sequence is MIS 8, and it is assigned a weight of [0.55], based on the likelihood that unconformity H40 postdates the terrace sequence but was not identified within the stratigraphic sequence that buries the terraces. A limiting maximum age of the terrace sequence is not constrained. However, MIS 10 and earlier lowstands are judged to be unlikely ages of terrace formation due to the absence of additional strata and unconformities that bury the terraces. Therefore, the upper part of the uncertainty distribution is modeled as a triangular PDF, with the highest probability during MIS 10 and decreasing probability with age to a maximum of MIS 16 (~630 ka).

Figure 8-39 shows PDFs that indicate uncertainty in the displacement and age parameters used to estimate the slip rate of the Shoreline fault from the offset terrace riser. A trapezoidal offset PDF was constructed to characterize uncertainty in displacement with minimum and maximum values of 3.4 m and 15.4 m, respectively, and preferred lower and upper values of 9.5 m and 10.5 m, respectively (Figure 8-39). This uncertainty distribution reflects a strong preference for an offset amount close to the preferred value of 10 m. The wide range of uncertainty reflected by the maximum and minimum values incorporates uncertainty from a variety of sources:

- Uncertainty in the slope of the shoreline, acknowledging that some of the apparent lateral separation may be due to vertical separation of a sloping surface.
- Alternative viable cross-fault correlations.
- The potential presence of a secondary fault trace.

- Limitations in data resolution.

Uncertainty in the age of the terrace sequence is modeled as described in the previous paragraph.

A slip rate CDF calculated based on the inputs described above is shown on Figure 8-39. The mean slip rates and certain probability values drawn from the CDFs are also provided. The weighted age mean slip rate for the Shoreline fault zone at the location of the terrace sequence is 0.05 mm/yr. The extreme-low-probability minimum and maximum slip rates are 0.01 and 0.24 mm/yr. The 90% confidence limit slip rate ranges from 0.02 mm/yr to 0.09 mm/yr.

8.4.2 Channel I Slip Rate Estimate

In the southeastern part of the 3D seismic-reflection survey area, Channel I is incised into bedrock and generally trends northeast-southwest (Figure 8-35). The channel ranges in width from approximately 50 m to 115 m and is incised approximately 5–15 m into the surrounding bedrock. At its downstream limit, Channel I extends to the southwestern edge of the 3D survey and remains incised into bedrock at a depth of approximately 110 m below modern sea level. At its upstream limit, Channel I branches from Channel F at its intersection with the Oceano fault at a depth of approximately 50–60 m below modern sea level. Farther upstream, the combined Channels F and I become narrower in the hanging wall of the Oceano fault (PG&E, 2014, Chapter 3).

Where Channel I crosses the Shoreline fault, it is poorly imaged on profiles and time slices of amplitude data, but is relatively well imaged on the smoothed similarity attribute[2] of the top of bedrock surface developed by PG&E (2014, Chapter 3; Figure 8-40). Along this reach, the channel is approximately 110 m wide and is incised approximately 11 m below the bedrock surface, which occurs at a depth of approximately 80 m below modern sea level. PG&E (2014, Chapter 3) mapped and interpreted a sequence of upper Pleistocene coastal or marginal marine sediments that lap onto bedrock in the southeastern part of the 3D survey area. At the Shoreline fault, PG&E (2014, Chapter 3) interpreted Channel I to be incised through this upper Pleistocene unit. However, a seismic-reflection profile across the channel directly upstream of the crossing shows that the channel is buried by these deposits (Figure 8-40e). The upper Pleistocene unit is overlain by unconformity H10, and the low-amplitude postglacial marine transgressive and highstand strata that bury unconformity H10. PG&E (2014, Chapter 3) interpreted the margins of this channel and the thalweg to be offset by 1 m within an uncertainty of 0–6 m (the approximate width of two pixels in time slices).

---

[2] The smoothed similarity attribute measures the filtered trace-to-trace agreement of the recorded seismic waveform over a user-specified correlation window, initially set to 10 ms (5 ms above and below each recorded event) and subsequently reduced to a 5 ms comparison window (2.5 ms above and below each recorded event) to improve the imaging of channel fill. Within a 3D volume, areas of flat or laterally continuous reflections (bedding) manifest as zones of strong similarity, while localized discontinuities such as faults and paleochannel margins manifest as zones lacking any trace-to-trace similarity (PG&E, 2014, Chapter 3).

The TI Team reassessed the seismic-reflection data at the intersection of Channel I and the Shoreline fault and concluded that it is likely that Channel I is offset by the Shoreline fault, and that uncertainty in the amount of offset is greater than that reported by PG&E (2014, Chapter 3). The TI Team assessment of offset and uncertainty is estimated from the magnitude of apparent right-lateral steps in the margins of Channel I that are coincident with the Shoreline fault, as illustrated on Figure 8-40c. The channel is likely offset between approximately 6 m and 12 m; 6 m is approximately the magnitude of one of the right-lateral steps in the southern channel margin within the Shoreline fault zone, and 12 m corresponds with a preferred high estimate of offset of the northern margin, and is close to the combined value of two steps in the southern margin (measured conservatively). A minimum offset of 0 m is allowed because there is no clear evidence in amplitude data or smoothed similarity for channel fill to be faulted, and the magnitude of steps in the channel margin at the Shoreline fault is similar to the magnitude of steps that occur elsewhere along the channel. A maximum credible offset of 18 m corresponds with a preferred high estimate of 12 m, plus an additional 6 m uncertainty to account for the fact that these offsets are estimated from smoothed similarity data of the interpreted bedrock surface, and therefore may incorporate some smoothing relative to raw amplitude data. This estimate of maximum credible offset exceeds the magnitude of observed steps in both channel margins.

The age of channel abandonment must be known in order to calculate the rate of fault deformation that produced the observed steps in the channel margin. Viable ages for activity of Channel I and modification of the channel margins include only those periods when sea level was lower than the intersection of the Shoreline fault with Channel I. Channels may have reached maximum incision during the maximum sea-level lowstands, but their margins (the most precise strain gauges) would likely be exposed to weathering and slope failure processes until they were buried (as sea level rose above them).

PG&E (2014, Chapter 3) initially interpreted the age of Channel I to be highly uncertain, ranging from a minimum of approximately 20 ka (the LGM) to a maximum of 1.4 Ma. The TI Team refined this range based on stratigraphic relationships shown on a profile that crosses Channel I downstream of the fault crossing, near the southwestern boundary of the 3D survey (Figure 8-41c). Here, Channel I is incised through some of the strata that overlie the bedrock surface, but it is clearly buried by unconformity H30 and possibly older marine unconformities as well.

A minimum age of Channel I is considered to be during the MIS 4 lowstand. This age would be correct if unconformity H30 were developed during the transgression from MIS 4 to MIS 3, which is the minimum possible age of unconformity H30 (as described in Section 8.3.4.1), and Channel I were active during the preceding lowstand. The likely timing of channel abandonment is considered to be late during the MIS 4 lowstand because the channel was most likely abandoned due to sea level rise at the end of the lowstand. A trapezoidal probability distribution describing this assessment is shown on Figure 8-42b and in the schematic on Figure 8-37. A weight of [0.2] is assigned to the MIS 4 age alternative based on the strength of evidence suggesting that unconformity H30 is older than MIS4.

A preferred age for abandonment of Channel I is considered to be late during MIS 6. This age would be correct if unconformity H30 were developed during the transgression from MIS 6 to MIS 5, which is the most likely age for that unconformity (see Section 8.3.4.1), and if Channel I were abandoned late during the preceding lowstand. A trapezoidal probability distribution describing this assessment is shown on Figure 8-42b. A weight of [0.6] is assigned to the MIS 6 age alternative based on the strength of evidence suggesting that unconformity H30 was developed during the transgression from MIS 6 to MIS 5 (*Section 8.3.4.1*).

Uncertainty in the upper end of possible ages for Channel I is based on the consideration that Channel I may substantially predate unconformity H30. This consideration is represented by a triangular PDF that covers a range that includes multiple sea-level lowstands from MIS 8 to MIS 12. A minimum age of 240 ka is assigned to the MIS 8–12 age alternative based on the approximate time that sea level flooded the intersection of the Shoreline fault with Channel I during the MIS 8–7 transgression. A preferred range is considered to be near the end of the MIS 8 lowstand. A maximum age of 420 ka, corresponding to the maximum depth of the MIS 12 lowstand, is assigned based on the recognition that the southwestern part of Channel I appears to be located within an area of relative subsidence, as indicated by the accumulation of strata that bury it, and the TI Team judgment that more strata would exist between Channel I and unconformity H30 if it were substantially older. This admittedly arbitrary limit is justified due to the fact that differences in age between lowstands older than MIS 12 have very little effect on the slip rate at the Channel I crossing. The MIS 8–12 age alternative is assigned a weight of [0.2] based on the thin interval of reflectors between Channel I and unconformity H30 (Figure 8-41b).

A slip rate CDF calculated based on the inputs described above is shown on Figure 8-42. The mean slip rates and certain probability values drawn from the CDFs are also provided. The weighted age mean slip rate for the Shoreline fault zone at the Channel I crossing is 0.07 mm/yr. The extreme low-probability minimum and maximum slip rates are 0.00 mm/yr and 0.29 mm/yr, respectively. The 90% confidence limit slip rate ranges from 0.01 mm/yr to 0.18 mm/yr.

8.4.3 Channel A Slip Rate Estimate

Channel A is part of a system of interweaving buried channels that traverse the continental shelf from north to south in the western part of the 3D survey area and that includes Channels A, B, C, D, and E (Figure 8-35). Based on their proximity and trends, these channels appear to represent ancestral channels of San Luis Obispo Creek that were active during Quaternary sea-level lowstands (PG&E, 2014, Chapter 3). Channel A varies significantly in width, ranging approximately 70–230 m wide, and is incised approximately 10–20 m into the bedrock surface. PG&E (2014, Chapter 3) interpreted Channel A as a nested channel complex that includes a smaller, inset channel that is incised into the fill of the larger bedrock channel.

Channel A crosses the Shoreline fault in the northwestern part of the 3D survey area, approximately at the location where the Oceano fault merges with the Shoreline fault (Figure 8-35). PG&E (2014, Chapter 3) interpreted Channel A to be clearly offset, based on a lineament imaged within the channel fill in smoothed similarity time slices, and they reported offsets of 20 ± 10 m, 30 ± 10 m, and 40 ± 10 m of the northwestern channel margin, the channel thalweg, and the southeastern channel margins, respectively. The smaller inset channel was interpreted to be not offset. The offsets reported by PG&E (2014, Chapter 3) for the north channel margin, thalweg, and south channel margin were primarily based on conservative interpretations of derivative data (i.e., seismic attributes, and contouring of interpreted horizons) and relied less directly on the primary data (seismic amplitude).

The TI Team reassessed the seismic-reflection data at the intersection of Channel A and the Shoreline fault and concluded that it is likely that Channel A is offset by the Shoreline fault, but that the offset amount is significantly less than that reported by PG&E, and that uncertainty in the amount of offset is greater than that reported by PG&E (2014, Chapter 3). Figure 8-43 shows a time slice and profile of amplitude data from the high-resolution 3D seismic-reflection volume where Channel A crosses the Shoreline fault. The locations of channel margins and the Shoreline fault shown on Figure 8-43 were interpreted by the TI Team based on examination of numerous time slices of amplitude and smoothed similarity data and profiles of amplitude data. These images suggest that the channel fill is offset by the Shoreline fault. However, the amount of offset is less clear. The channel floor is interpreted to be too broad for the thalweg to provide a high-precision piercing point, but the channel margins are clearly imaged in time slices. Therefore, offset of the channel margins is considered the most reliable deformation marker associated with Channel A. Similarly, the inset channel reported by PG&E (2014, Chapter 3) is not well resolved by the seismic-reflection data, and therefore, is not used as a strain marker to constrain offset.

Enlarged images of time slices are shown in panels c, d, e, and f on the right-hand side of Figure 8-43. The preferred offset measurements are shown on the interpreted versions of these panels. The Shoreline fault intersects the north margin of Channel A at the location of a small gully in the channel margin (Figure 8-43d), requiring offset to be estimated by projecting the channel margin toward the fault trace from either side. Based on these projections, the TI Team interprets the north channel margin to be offset approximately 6 m, and up to 13 m based on uncertainty in the mapping and geomorphic variability of the channel margin. We judge that greater offsets, including the 20 ± 10 m reported by PG&E (2014, Chapter 3) are not supported by the data.

As shown in Figure 8-43f, the TI Team interprets approximately 8 m offset of the south channel margin. An alternative correlation of the channel margin east of the fault to a high-amplitude black-to-white couplet of reflectors within the channel fill west of the fault suggests a maximum offset of 15 m for the south channel margin. The larger offset of the southern channel margin reported by PG&E (2014, Chapter 3) coincides with a jog to the right in the channel margin. If this jog had been caused by 40 ± 10 m of fault slip after the channel was abandoned, the jog would be parallel to the fault, and be

approximately the length of the scale bar in Figure 8-43f. Instead, the jog is not parallel to the fault, and is relatively rounded, suggesting it was eroded by flows within the channel. Therefore, we interpret this jog to have been developed while the channel was still active, based on the rounded nature of the channel margin around the jog.

The magnitude of the steps in both margins of Channel A suggests a preferred offset amount of 7 m ± 3 m. However, based on the limitations of resolution in the 3D volume, and on the observed geomorphic variability of the channel margins, a maximum estimate of approximately 15 m cannot be ruled out. Similarly, an interpretation of no offset is also allowed by the data.

The age of channel abandonment must be known to calculate the rate of fault deformation that produced the observed steps in the channel margin. Viable ages for activity of Channel A and modification of the channel margins include only those periods when sea level was lower than the intersection of the Shoreline fault with Channel A, approximately 60 m below modern sea level. Channels may have reached maximum incision during the maximum sea-level lowstands, but their margins (the most precise strain gauges) would likely be exposed to weathering and slope failure processes until they were buried (as sea level rose above them). Therefore, the TI Team considers the likely age of channel abandonment to be near the end of a sea-level lowstand that reached a greater depth than the intersection of the Shoreline fault with Channel A. Although it is clear that Channel A was active during a Quaternary sea-level lowstand, it is uncertain which lowstand was the most recent period of activity.

PG&E (2014, Chapter 3) describes a wide range of possible ages of Channel A. As shown on Figure 7-45 of that chapter, possible ages of Channel A are considered to range from the MIS 2 to MIS 1 transgression (as young as approximately 10 ka) to approximately 1.4 Ma, the end of the Mid-Pleistocene Transition (MPT). A preferred age of MIS 8, 10, or 12 is reported for Channel A (pages 126–129 of PG&E, 2014, Chapter 3) based on a number of observations, including the following:

- Crosscutting relationships that indicate Channel A is older than Channels B and C (Figure 8-44).
- A tentative correlation to MIS 12, during which sea level fell particularly low for an unusually long duration (Figure 8-38).
- A tentative, and admittedly unlikely, correlation to a possible channel incised into bedrock beneath unconformity H30 imaged west of the 3D volume on USGS Sparker line PBS-319.
- The occurrence of a minor bulge in unconformity H40 near the location that the unconformity laps onto bedrock, which may have been a sandbar formed near the mouth of Channel F or A when the channel was active, thereby tying the age of the channel to the age of the unconformity.

The TI Team concurs with PG&E (2014, Chapter 3) that the crosscutting relationships among Channels A, B, and C provide a robust constraint on the relative ages of the channels. Figure 8-44 shows an amplitude time slice of the area directly upstream (north) of the location where Channel A crosses the Shoreline fault, illustrating parts of Channels

A, B, and C. As shown in this time slice, Channel C clearly crosscuts both Channels B and A, and Channel B also crosscuts Channel A. These crosscutting relationships indicate that Channel A is the oldest of the three, Channel B is of intermediate age, and Channel C is the youngest. However, it is less certain whether the channels may have been active during a single sea-level lowstand, or must have been active during separate lowstands, and which lowstand corresponds to which channel. The TI Team judges that the tentative correlations used by PG&E to develop alternative preferred ages of Channel A do not provide robust constraints on the channel age.

The TI Team examined the 3D and 2D seismic-reflection data to re-evaluate stratigraphic relationships between Channel A and adjacent channels, and re-evaluated the stratigraphic and tectonic context of Channel A in order to refine the previous age model and better describe the most likely age and range of possible ages of the channel. The TI Team uses two lines of evidence to estimate which lowstand represents the most recent activity of Channel A: (1) crosscutting relationships within the submarine San Luis Obispo Creek channel system and (2) differences in depth of incision.

Near the northern extent of the 3D volume, Channels A, B, and C are imaged in a seismic-reflection profile taken approximately parallel to the strike of SWBZ faults and to structural contours on the top of rock (Figure 8-45). At this location, the channels are eroded into a region of active uplift in the hanging walls of the Los Berros and Oceano faults. Marine terraces preserved on Point San Luis, approximately 3 km to the northwest, indicate that this area is uplifting at a constant rate of approximately 0.06 mm/yr (Hanson et al., 1994). It is likely that the channels were graded to a similar base level, as Quaternary sea-level curves indicate that the past five major lowstands all reached similar depths (Waelbroeck et al., 2002; Figure 8-20). The streams that carved these channels presumably had similar stream power, as they originate from the same drainage source, San Luis Obispo Creek, and the drainage area has probably not evolved much to its present state over the expected age range of the three channels (i.e., the past several sea-level cycles). Given their close spatial proximity, it is also likely that the lithology of rock underlying each of the three channels is similar. If each of these assumptions is correct, then the three channels should all be incised similar amounts relative to the surrounding surface. Apparent differences in depth of incision may result from older channels becoming abandoned and uplifted, exposing their original channel margins to wave erosion during subsequent marine transgressions and regressions.

As shown on Figure 8-45b, Channel C is incised approximately 18–19 m, Channel B is incised approximately 16 m, and Channel A is incised approximately 12 m into the surrounding bedrock. The decreased depth of incision corresponding with increased channel age indicated by crosscutting relationships supports the interpretation that older channels are gradually removed by tectonic uplift and erosion. If each of the channels was initially incised to the same depth, and erosion rate matches the tectonic uplift rate of 0.06 mm/yr, then these differences suggest that Channel B is approximately 40 ka older than Channel C, and that Channel A is approximately 70 ka older than Channel B. These relationships suggest an age model in which Channel C was carved during MIS 2, Channel B was carved during MIS 4, and Channel A was carved during MIS 6.

Regardless of the precise uplift rate and erosion rate, the large difference in depth of incision between Channels A and C, which presumably were carved by the same creek at a similar distance from the coast, suggests that Channel A is substantially older than Channel C and was likely carved during a prior sea-level lowstand.

The TI Team developed an age model to estimate the age of Channel A based on the information described above. The age model only considers sea-level lowstands deeper than 60 m. For each lowstand, probability distributions are defined as asymmetric trapezoids that favor periods late in a lowstand as the likely age of channel abandonment. Three periods of channel occupation are considered: MIS 2, MIS 6, and a broad distribution encompassing MIS 8–12. This probability distribution is illustrated schematically relative to paleosea-level curves on Figure 8-38, and is shown in detail on Figure 8-46c.

The MIS 2 age alternative is included because it cannot be completely ruled out; however, it is assigned a low weight of [0.1] based on the multiple lines of evidence described above that suggest Channel A was abandoned during a prior sea-level lowstand. A minimum possible age of 11 ka for Channel A margin is set by the age sea level rose above the 0.072 s time slice (~58 m depth). The precise age of 11 ka corresponds with the low end of the uncertainty distribution in the Stanford et al. (2011) postglacial sea-level curve. The low end of the preferred range is estimated to be 11.5 ka from the preferred timing of sea level rise above the time slice (Stanford et al., 2011). The high end of the preferred range is estimated to be 20 ka from the onset of sea level rise following the MIS 2 lowstand (Stanford et al., 2011). A limiting maximum age of 75 ka is selected as the onset of the MIS 4 lowstand from Waelbroeck et al. (2002).

The MIS 6 age alternative is preferred and assigned a weight of [0.7] based on the observation that Channel A is crosscut by Channels B and C and therefore must be older than they are (Figure 8-44), and based on the greater depth of incision of Channel C, which suggests it is likely a full sea-level cycle younger than Channel A (as described above and illustrated on Figure 8-45). A minimum age for this distribution of 125 ka is assigned from the minimum age of the MIS 6–5 transgression from the uncertainty band reported by Waelbroeck et al. (2002). A preferred range of 132–135 ka is estimated from the preferred and maximum age of the MIS 6–5 transgression. A maximum age of 190 ka is estimated from the onset of MIS 6 lowstand (Waelbroeck et al., 2002).

The MIS 8–12 age alternative is intended to represent a broad range spanning numerous sea-level lowstands and reaching the maximum possible age of the channel. Possible ages within MIS 8 and earlier lowstands have less direct impact on slip rate, so the precise shape of the MIS 8–12 trapezoid is less important. Also, the paleo–sea levels are less well constrained by geologic record (e.g., the difference between the Lisiecki and Raymo [2005] and Waelbroeck et al. [2002] curves during MIS 11; Figure 8-38), so additional uncertainty is built into possible ages. The MIS 8–12 alternative is assigned a low weight of [0.2] based on the judgment of the TI Team that the difference in depth of incision between Channel A and Channel C would likely be greater if Channel A were 240 ka or older. A minimum age for this alternative is estimated to be 240 ka, the age that the

MIS 8–7 transgression elevated sea level above the 0.072 ms time slice. A preferred range of 245–250 ka is estimated from the onset of the MIS 8–7 transgression and the maximum MIS 8 lowstand (Waelbroeck et al., 2002). A maximum age of 420 ka, corresponding with the maximum MIS 12 lowstand, is estimated based on the TI Team judgment that a channel this old would be completely removed by erosion in the northern part of the 3D survey area. At the rate of 0.06 mm/yr presented by Hanson et al. (1994), the amount of uplift that has occurred on the shelf offshore of Point San Luis is approximately 8 m since MIS 6, 15 m since MIS 8, 20 m since MIS 10, and 25 m since MIS 12.

This age model overlaps significantly with the one presented by PG&E (2014, Chapter 3). However, the preferred age range and maximum allowed channel age are both reduced in the TI Team age model relative to the previous model based on the evidence described above for preservation of incised channels within a tectonically uplifting block.

A slip rate CDF calculated based on the inputs described above is shown on Figure 8-46. The mean slip rates and certain probability values drawn from the CDF are also provided. The weighted-age mean slip rate for the Shoreline fault zone at the Channel A crossing is 0.07 mm/yr. The extreme low-probability minimum and maximum slip rates are 0.00 mm/yr and 1.17 mm/yr, respectively. The 90% confidence limit slip rate ranges from 0.01 to 0.23 mm/yr.

8.4.4 Development of Slip Rate CDF

Two approaches are used to estimate components of horizontal and vertical slip rate for the Shoreline fault. As outlined in *Sections 8.4.1, 8.4.2, and 8.4.3*, offset channels and terrace features interpreted from high-resolution 3D seismic-reflection data in San Luis Obispo Bay are used to directly measure lateral—and in one case, vertical—components of slip across the Shoreline fault south of the intersections of the major structures of the SWBZ. This assessment is described in *Section 8.4.4.1*. The estimated slip rate along this part of the Shoreline fault is assumed to represent the minimum slip rate for the Shoreline fault adjacent to the DCPP.

Similar piercing point features are not identified along the Shoreline fault north of the intersections of the SWBZ structures. The second approach, described in *Section 8.4.4.2*, relies on geometric and structural relationships to estimate the maximum amount of slip that may be transferred to the Shoreline fault from SWBZ structures. The slip rate CDF for the Shoreline fault at the DCPP site is described in *Section 8.4.4.3*.

8.4.4.1 Assessment of Slip Rate for Southern Part of Shoreline Fault

Of the three features used to measure slip on the southern part of the Shoreline fault, within San Luis Obispo Bay, the offset terrace sequence provides the best constraint. The intersection of the terrace riser with the Shoreline fault imaged on Figure 8-36 provides the clearest image of an offset feature and represents the least ambiguous interpretation of the three sites. Variability in the channel margins at the Channel A and I sites, due either to lower-quality images or to geomorphic variability, suggests that the two channel sites

represent lower quality slip rate constraints. The age of the offset terrace sequence is also reasonably well constrained due to clear stratigraphic relationships with unconformities H10 and H30, whose ages are reasonably well understood. Because of the quality of the piercing point, the slip rate calculated from the offset terrace sequence is considered to represent the slip rate of the southern part of the Shoreline fault. The slip rates calculated from Channels A and I are used to corroborate the assessment of the offset terrace sequence. Table 8-2 presents a comparison of the slip rates calculated from the three sites.

Table 8-2. Slip Rates Calculated from the Shoreline Fault in San Luis Obispo Bay

Summary Statistics	Terrace Sequence Slip Rate	Channel A Slip Rate	Channel I Slip Rate
Mean	0.05	0.07	0.07
Min	0.01	0.001	0.001
Max	0.24	1.17	0.29
0.05	0.02	0.01	0.01
0.1	0.02	0.02	0.02
0.2	0.03	0.02	0.03
0.5	0.04	0.04	0.06
0.8	0.06	0.07	0.10
0.9	0.07	0.09	0.14
0.95	0.09	0.23	0.18

As shown in Table 8-2, the slip rate calculated from the offset terrace sequence is allowed by the range of slip rates assessed from the two other sites. The similarity in mean slip rates for all three sites, despite the alternative approaches to estimating ages of the features, suggests that the analyses are robust.

8.4.4.2 Estimate of Dextral Slip Rate Contributed from the Southwestern Boundary Zone

North of the three piercing points in San Luis Obispo Bay, faults of the SWBZ merge with or intersect the Shoreline fault, including the Oceano, Los Berros, and San Luis Bay faults. At least one of these faults, the Oceano fault, does not cross the Shoreline fault (Figure 8-34). The northward curve in the Oceano fault east of its intersection with the Shoreline fault, and the counterclockwise bend in the Shoreline fault to the north of the Oceano-Shoreline intersection suggests that the faults may interact kinematically. This relationship suggests that slip from SWBZ faults may be transferred to Shoreline fault, thereby increasing the slip rate of the Shoreline fault to the north relative to its slip rate in San Luis Obispo Bay. Other observations also suggest that the slip rate of the Shoreline fault may be greater to the north of the intersection with the SWBZ faults than it is to the south:

- Greater proximity of the northern part of the Shoreline fault to the Hosgri fault, the most active fault in the region, suggests that it may be more active than the southern part, and
- Increased microseismicity along the northern part of the fault suggests it may be more active.

This section describes a kinematic model to predict the amount of SWBZ deformation that may be resolved as dextral slip on the northern part of the Shoreline fault. Although some details of the model (e.g., vertical separation predicted across the Shoreline fault) are inconsistent with other available data for the Shoreline fault, and therefore, are not incorporated into the SSC model, the TI Team considers this approach to characterizing the increase in slip rate, and the amount of dextral slip predicted by the model for the northern part of the Shoreline fault to be appropriate.

This section includes the following discussions:

- The rate of slip on the SWBZ as a whole.
- Resolution of the component of right-lateral slip that is parallel to the Shoreline fault offshore of the Irish Hills.
- The possible rate of vertical separation that may be occurring on the northern part of the Shoreline fault.
- The estimate of Shoreline-parallel slip that may be transferred to the Shoreline fault from the SWBZ.

Slip Rate of SWBZ

The SWBZ is interpreted to accommodate purely reverse deformation. Dextral oblique slip on SWBZ faults transferring dextral slip to the Shoreline fault is not considered separately for the following reasons:

- Dextral slip on SWBZ faults is incompatible with regional stress/strain regime.
- Where observed (on the San Luis Bay fault), kinematic indicators of strain (slickenlines) are compatible with reverse or reverse left-oblique slip.

The combined slip rate of all the structures of the SWBZ is assessed from the difference in uplift rate of the Irish Hills and the subsidence rate of San Luis Obispo Bay, and from consideration of the mean dip of faults within the SWBZ as a whole (Figure 8-47). The uplift rate of the Irish Hills is assessed from the elevations and ages of marine terraces mapped along the coastline by Hanson et al. (1994) and from consideration of two alternative models for paleo–sea levels, the Hanson et al. (1994) model and the Muhs et al. (2012) model, as described in Section 8.2.2. Based on this assessment, uncertainty in the uplift rate of the Irish Hills ranges from 0.15 mm/yr to 0.35 mm/yr, but the most likely rate is between approximately 0.18 and 0.23 mm/yr (see Section 8.2.2; Figure 8-6).

Subsidence of the central part of San Luis Obispo Bay is inferred from the thick accumulation of sediments over bedrock in the southern part of the 3D survey area and to the south. This accumulation and preservation of sediments from multiple sea-level cycles stand in contrast to the rocky shelf offshore of the uplifting Irish Hills, which is

generally bare or covered by a thin veneer of sediment. Subsidence of San Luis Obispo Bay is estimated to range from 0 to –0.1 mm/yr. A minimum of 0 is set based on the recognition that subsidence and accommodation has occurred, and a maximum of –0.1 mm/yr is estimated from the maximum observed vertical separation of 13 m down to the east of unconformity H30 across the Hosgri fault, and a preferred age of 130 ka for the unconformity. A preferred slip rate range between –0.01 mm/yr and –0.08 mm/yr is established based on the range of variability in vertical separation of H30 and H10 across the HFZ in San Luis Obispo Bay. A mean dip-slip rate for all structures of the SWBZ is estimated by resolving the vertical separation rate onto a dipping fault. A broad distribution of possible fault dips for reverse faults is considered because all SWBZ structures are being averaged and represented by single fault, and no dip information exists for most of the SWBZ faults. The mean dip is considered to range from a minimum of 35° to a maximum of 75°, with a preferred range between 45° and 60°.

A slip rate CDF calculated based on the inputs described above is shown on Figure 8-47. The mean slip rate and certain probability values drawn from the CDF are also provided. The weighted mean slip rate for the SWBZ is 0.34 mm/yr. The extreme-low-probability minimum and maximum slip rates are 0.19 mm/yr and 0.64 mm/yr. The 90% confidence limit slip rate ranges from 0.24 mm/yr to 0.46 mm/yr.

Resolution of Component of SWBZ Slip Rate Parallel to Shoreline Fault

Based on the angle of intersection between the SWBZ and Shoreline faults, the resolved component of right-lateral, Shoreline-parallel slip rate may be estimated. This estimate is a limiting maximum for the amount that the slip rate of the Shoreline fault could be increased due to interaction with the SWBZ. The horizontal shortening may not be fully or even partially resolved on discrete faults such as the Shoreline fault. A diagram illustrating the geometric relationship between the SWBZ and Shoreline faults and the approach to estimating maximum change in Shoreline slip rate is shown on Figure —8-48.

From Figure 8-47, the SWBZ net slip rate, SWr (which approximately equals the dip-slip rate) is calculated as

$$\mathrm{SWr} = {}^{\mathrm{SWv}}/_{\sin\delta} \tag{8-2}$$

And the horizontal slip rate (i.e., shortening), SWh, is

$$\mathrm{SWh} = {}^{\mathrm{SWv}}/_{\tan\delta} \tag{8-3}$$

The component of the horizontal slip rate that is parallel to the Shoreline fault, SWsp, is a function of the angle of intersection between the SWBZ and Shoreline faults (Figure 8-48) and is calculated as

$$\mathrm{SWsp} = \mathrm{SWh}(\sin\beta) \tag{8-4}$$

Substituting Equation (8-3) into Equation (8-4) yields

$$\mathrm{SWsp} = \mathrm{SWv}\frac{\sin\beta}{\tan\delta} \tag{8-5}$$

Figure 8-48 shows the input parameters, including a range of values for δ and β (panel b), used to estimate the rate of slip on the SWBZ and the resolved Shoreline-parallel component. The values of the intersection angle, β, are based on assessment of the general strike of the SWBZ as indicated in the regional fault map (Figure 8-34). The dips represent a broad range of plausible values for the SWBZ faults at shallow depth (as described above and shown on Figure 8-47). The result of the evaluation, the resolved Shoreline-parallel component of shortening, is plotted as a slip rate CDF (dashed line) on panel a of Figure 8-49.

The maximum increase in slip rate on the Shoreline fault north of the SWBZ due to a transfer of slip is provided by Equation (8-5). This would be correct if all the slip from the SWBZ, and associated uplift of the hanging wall, were transferred to the Shoreline fault zone (i.e., if the SWBZ ended at the Shoreline fault zone). However, uplift of the range does not end at the Shoreline fault, but instead extends westward to the Hosgri fault, as indicated by the presence of an uplifted and eroded rocky shelf offshore of the Irish Hills between the Shoreline fault and the Hosgri fault (Figure7-4). Therefore, the amount of SWBZ slip that is transferred to the Shoreline fault must be substantially less than the maximum. The minimum increase in slip rate is zero if the SWBZ slip is not at all resolved onto the Shoreline fault as localized slip (e.g., it may be resolved as broadly distributed fold deformation).

The presence or absence of vertical offset across the Shoreline fault north of the intersection with SWBZ structures provides a means to evaluate what fraction of the SWBZ slip rate is resolved onto the Shoreline fault as localized offset. The constraints on vertical separation across the Shoreline fault north of its intersection with the SWBZ are described below.

Constraints on Vertical Separation Rate Offshore of Irish Hills

As part of the initial SSC of the Shoreline fault, PG&E examined high-resolution MBES bathymetry and 2D seismic-reflection data and identified suites of submerged wave-cut platforms on the continental shelf offshore of the Irish Hills (PG&E, 2011). The wider terraces that crosscut bedrock structure were interpreted to have been carved during paleosea-level stillstands during or prior to MIS 3, 4, or 5, depending on their depth (PG&E, 2011, Appendix I). At four sites, submerged strandlines, wave-cut platforms, or both were mapped across the surface trace of the fault. Examples of these are shown on Figure 5-19. At each location, possible vertical separation across the fault since the platform was developed was estimated from projection of the wave-cut platform from opposite sides of the fault trace. The greatest credible vertical separation at each location was estimated based on the amount of uncertainty in this projection, and included consideration of the surface roughness and the amount of bedrock erosion that may have occurred since the platform was developed. At three of these sites, no vertical separation of the wave-cut platform was observed, within uncertainty of 1.5 m for two of the sites and 2 m for the third. At the fourth site, directly south of the DCPP, vertical separation of the wave-cut platform was estimated to be 0 or 1 m, east side up, within an uncertainty of 2.5 m.

High-resolution 3D and 2D seismic-reflection data collected northwest of the DCPP provide detailed imaging of the Point Buchon fault, the northern part of the Shoreline fault zone, and the marine sediment that buries it. Figure 8-50 shows an example 2D seismic-reflection profile across both primary branches of the Point Buchon fault. As shown on this figure, no vertical separation of the bedrock surface is observed across either strand of the fault, within an uncertainty of ±0.8 m for the Point Buchon fault, and an uncertainty of ±1.6 m for the East Branch of the Point Buchon fault. A detailed map of the bedrock surface above the fault trace developed from the 3D seismic-reflection volume along the Point Buchon fault shows no systematic vertical separation across the fault within a depth range from approximately 70 m to 40 m (PG&E, 2014, Chapter 2). The age of this surface is estimated from the timing of sea level rise across this part of the shelf during the post-LGM transgression to be approximately 10.5 ± 2 ka (Stanford et al., 2011).

The observations summarized above are used to constrain the possible vertical separation rate across the Shoreline fault within the reach directly offshore of the DCPP. Two age models are considered to assess the possible rate of vertical separation. The first, which we name the MIS 3–5 age model, is based on the assessment presented by PG&E (2011) that the wave-cut platforms that cross the Shoreline fault were developed during the period of falling sea level between the MIS 5 highstand and the MIS 2 lowstand. This age model is assigned a weight of [0.6], which reflects the TI Team assessment that it is more likely to be correct than the alternative model, but it also acknowledges uncertainty in the interpretation of the origin of these erosive surfaces, recognizing that many of the wave-cut platforms are quite rough and their back edges, or paleo–sea cliffs, are subdued. If the MIS 3–5 age model is correct, the allowable vertical separation rates across the Shoreline fault range from 0 to 0.04 mm/yr, with a maximum rate based on an inferred 2 m offset post MIS 3 highstand (50 ka). Although it is possible that no vertical separation of wave-cut platforms has occurred, consistent with the observations described above, this approach assumes that they are, because vertical separation across the northern Shoreline fault is required in this model for dextral slip rate to be transferred from the SWBZ to the Shoreline fault. Consequently, a zero probability is assigned to a vertical separation rate of 0 mm/yr. A preferred range of 0.004–0.02 mm/yr, corresponding with 10% to 50% of the maximum, is established from the assumption that vertical separation across the Shoreline fault does occur, but is not observed from the strain marker.

The second age model is called the post-LGM age model. This model, which is assigned a weight of [0.4], accounts for the possibility that many of the wave-cut platforms mapped by PG&E (2011, Appendix I) do not represent long-lived stillstands, and may instead be erosional surfaces developed during the last transgression. These relatively flat surfaces may have been planated during relatively short-lived pauses between meltwater pulses during the last transgression, or they may represent pockets of bedrock that are relatively more erosive than the surrounding parts of the shelf, or other processes. If the post-LGM age model is correct, the allowable vertical separation rates across the Shoreline fault offshore of the DCPP range of 0–0.22 mm/yr, with a maximum rate based on an inferred 2 m offset since 9 ka. A preferred range of 0.022–0.11 mm/yr,

corresponding with 10% to 50% of the maximum, is established from the model assumption that vertical separation across the Shoreline fault does occur, but is not observed from the strain markers. These two age models, and the associated vertical separation constraints are shown on Figure 8-49b.

Assessment of Amount of SWBZ Slip Rate Contributed to Northern Shoreline Fault
As described above, a kinematic model in which deformation of the SWBZ is resolved onto the Shoreline fault as discrete fault slip predicts that both dextral slip and vertical separation would be added to the Shoreline fault north of its intersection with the SWBZ. The constraints on vertical separation across the Shoreline fault, which are shown on Figure 8-49b, indicate that a small fraction of the vertical component of SWBZ slip (the vertical separation rate) may be resolved onto the Shoreline fault. This fraction is used to estimate the amount of Shoreline-parallel slip (SWsp) that is resolved onto the Shoreline fault. The ratio of vertical slip rate across the northern part of the Shoreline fault to the SWBZ vertical slip rate is assumed to be proportional to the ratio of dextral slip rate that is added to the Shoreline fault to the Shoreline-parallel component calculated for the SWBZ (see proportion illustrated on Figure 8-49). A CDF representing the amount of the Shoreline-parallel component of SWBZ slip that is added to the dextral slip rate of the Shoreline fault is shown as a blue line on the plot on Figure 8-49a.

The simple kinematic model described above provides an approach to estimate the amount of dextral slip rate increase on the northern part of the Shoreline fault relative to the southern part. For the reasons given above, the TI Team judges that some increase in slip rate on the northern part of the Shoreline fault compared to the southern part is probable. The TI Team recognizes that the kinematic model used to estimate the increase in dextral slip rate also predicts higher rates of vertical separation across the northern Shoreline fault, resulting in estimates of a net slip vector that are inconsistent with other observations. For example, the preferred increase in dextral slip rate calculated from the simple kinematic model also suggests a vertical separation rate that would classify the northern Shoreline fault as an oblique-slip fault, with an almost 1:1 ratio of right-lateral slip and northeast-side up dip slip. This resulting estimate of the net slip vector contradicts other observations that suggest that the northern Shoreline fault is dominantly a dextral fault. These observations include the following:

- Submerged wave-cut platforms that cross the fault trace are not deformed, within the resolution of multibeam bathymetric or seismic-reflection data (PG&E, 2011).
- Dextral focal mechanisms align with (and were initially used to characterize) the Shoreline fault (Hardebeck, 2010, 2013).
- The fault is approximately vertical (*Section 5.2.4*; Hardebeck, 2010, 2013), which is unfavorable for a fault with a significant component of reverse deformation.

Based on the observations listed above, the TI Team does not incorporate the vertical component of slip predicted by this kinematic model, and only incorporates the dextral component into our slip rate assessment for the Shoreline fault source. The TI Team considers it appropriate to use the kinematic model to increase the slip rate on the northern part of the Shoreline fault despite this shortcoming for lack of a preferred

alternative method that honors the geologic slip rate data constraints and first-order kinematic constraints of block movement. The TI Team judges that the estimated rate of dextral slip rate increase on the northern Shoreline fault compared to the southern part of the Shoreline fault is sufficiently small (~0.02 mm/yr for the preferred rate increase) such that refining this number to make a more compatible kinematic model would not have a meaningful impact on the overall hazard to the DCPP.

8.4.4.3 Shoreline Fault Slip Rate at the DCPP

A slip rate CDF for the Shoreline fault is presented on the plot on Figure 8-51. This CDF, shown in black, was developed by adding slip from the SWBZ to the slip rate of the southern part of the Shoreline fault. The amount of Shoreline-parallel SWBZ slip permitted by constraints on vertical separation across the Shoreline fault is represented by the CDF shown in blue on the plot. The slip rate for the southern part of the Shoreline fault, south of the intersection with structures of the SWBZ, is represented by the CDF developed from the offset terrace riser, which is shown in lavender on the plot. The weighted-age mean slip rate for the Shoreline fault zone at DCPP is 0.07 mm/yr. The extreme low-probability minimum and maximum slip rates are 0.01 mm/yr and 0.34 mm/yr, respectively. The 90% confidence limit slip rate ranges from 0.03 to 0.15 mm/yr.

8.4.5 Equivalent Five-Point Distribution and Comparison to Other Studies

The weighted slip rate CDF for the Shoreline fault is represented by the black line on Figure 8-51. The five-point discrete representation of this continuous probability distribution, which is provided in the associated table on the figure, ranges from 0.03 mm/yr to 0.16 mm/yr, with a weighted average value of 0.07 mm/yr.

For comparison slip rate estimates used in previous hazard analyses, PG&E (2011) and UCERF3 (Field et al., 2013), are briefly outlined. The slip rate estimated for the Shoreline fault source in the PG&E (2011) report on the Shoreline fault zone ranged from 0.05 mm/yr to 1 mm/yr, with a preferred range between 0.1 mm/yr and 0.6 mm/yr and a weighted mean slip rate of approximately 0.29 mm/yr. This characterization was represented by the following five-point distribution with corresponding weights: 0.05 mm/yr [0.1]; 0.1 mm/yr [0.35]; 0.3 mm/yr [0.35]; 0.6 mm/yr [0.15]; and 1.0 mm/yr [0.05].

The target Shoreline fault slip rates characterized by UCERF3 deformation models are as follows (Field et al., 2013):

- Zeng: 0.09 mm/yr
- Bird (NeoKinema): 0.3–0.4 mm/yr
- Average block model: 0.08 mm/yr
- Geologic model: 0.1 mm/yr

The solution slip rates that result from the UCERF3 grand inversion range from 0.07 mm/yr to 0.42 mm/yr, with a weighted mean of 0.16 mm/yr (Field et al., 2013).

8.5 Los Osos Fault

The Los Osos fault was characterized by PG&E (1988) as a complex reverse fault along the northeastern margin of the San Luis Range that separates the uplifting range from the relatively stable or subsiding Cambria structural block to the northeast (Lettis and Hall, 1994; Lettis et al., 1994). Rates of vertical separation were estimated from detailed mapping of marine terraces in the uplifting San Luis–Pismo block and from vertical separation of fluvial deposits observed in paleoseismic trenches (Lettis and Hall, 1994). The altitudes and ages of terraces between Morro Bay and Green Peak (south of the DCPP) show that the Irish Hills sub-block of the San Luis Range is uplifting at a rate of between approximately 0.19 ± 0.03 mm/yr and 0.23 ± 0.02 mm/yr (Hanson et al., 1994). A long-term dip-slip rate of 0.2 mm/yr to 0.7 mm/yr was estimated for the part of the fault closest to the DCPP, based on assumed fault dips of 30° and 60° (i.e., the Irish Hills segment; Lettis et al., 1994).

New data are available, particularly related to evaluating long-term uplift of the Los Osos and Edna valleys and local subsidence in the vicinity of Morro Bay. As described in Section 8.2.2, an alternative uplift model based on a newly proposed paleosea-level model for California terraces (e.g., Muhs et al., 2012) is also being considered (Figure 8-5). These data provide additional constraints to evaluate differential rates of vertical separation across the northeastern margin of the San Luis Range. The uplift data, along with alternative fault dips assigned to the Los Osos fault in the three different fault models (*Section 7.4*), are used to estimate slip rate CDFs for the Los Osos fault as described below.

8.5.1 Information on Slip Sense and Slip Rate

The net Los Osos slip rate is estimated from several PDFs and CDFs of the dip-slip rate, and fault rake and is resolved on planes defined by the three fault models. The dip-slip rate is estimated with two components: the differential uplift or vertical rate of the Irish Hills and San Luis Range, and the fault dip. The differential uplift or vertical rate of the Irish Hills and San Luis Range is determined from the uplift rate PDF of the hanging wall and the net uplift and subsidence rate PDF of the footwall. The slip rate of the Los Osos fault is calculated for the part of the fault closest to the DCPP. Therefore, the hanging-wall uplift PDF for the Los Osos fault is considered to be equivalent to the uplift rate PDF for the Irish Hills, which is shown on Figure 8-6.

In order to evaluate the differential uplift rate of the Irish Hills, the relative motion of the footwall is also assessed. Unlike the hanging wall, the footwall rate is characterized differently for the three fault models. For the NE Model, the rate of subsidence of Morro Bay, which lies adjacent to the reach of the fault zone closest to the DCPP, is used to estimate the footwall vertical rate. Because the subsided Morro Bay area is an isolated depression, the majority of the Los Osos fault does not experience a similar Morro Bay footwall subsidence rate; therefore, different data are used to estimate a limiting rate for the OV and SW models. For these two models, the uplift rate of the Los Osos and Edna valleys is used to constrain the footwall rate.

For the NE Model, the trapezoidal distribution representing the Morro Bay subsidence rate (Figure 8-52) is primarily based on water and test well data from groundwater and saltwater intrusion studies (Lettis and Hall, 1994; Cleath & Associates, 2003). The Morro Bay groundwater basin is interpreted to be filled with a thick sequence of Quaternary terrestrial deposits. Two key datums are identified from interpretation of these data. The shallowest and youngest datum is a clay layer recognized by Cleath & Associates (2003), which they name AT2 and correlate widely within the basin (Figure 8-54). A second key datum is the unconformity at the base of Quaternary deposits/top-of-Pliocene marine sediments (interpreted to be equivalent to the Careaga Formation; Figures 8-53 and 8-54). From these data, the top of the AT2 clay is observed at a depth of up to –50 m, and the top of the underlying marine sediments (Careaga Sandstone) is at a maximum depth of approximately –150 m. The TI Team considers the minimum allowable subsidence rate to be –0.02 mm/yr based on the assumption that Quaternary terrestrial deposits in the Morro Bay groundwater basin, which would necessarily have been deposited at elevations above the maximum Quaternary sea-level lowstands (approx. –125 to 150 m), have subsided at least 50 m to a depth of –200 m in the past 2.5 Ma. This age defines the beginning of the Quaternary and is the estimated age of the Careaga Sandstone (Lettis and Hall, 1994). The lower preferred value of –0.06 mm/yr is based on the assumption that the Quaternary terrestrial deposits have subsided 150 m over the past 2.5 Ma. The upper preferred value of –0.1 mm/yr assumes that the AT2 clay aquitard formed during the MIS 11 (~400 ka) highstand (at a paleo–sea level of approx. 10 m, Waelbroeck et al., 2002) and has subsequently experienced 40 m of subsidence to a mean depth of approximately 30 m (approx. –100 m on Figure 8-54). The maximum value considered is –0.20 mm/yr, based on the judgment of the TI Team that the subsidence rate of the Morro Bay groundwater basin, a localized crustal depression on the order of 5 km long, does not exceed the uplift rate of the Irish Hills, an uplifting rigid block on the order of 20 km long. If the maximum subsidence rate of –0.20 mm/yr had occurred throughout the Pleistocene, the depth to the bottom of the basin would be 500 m.

For the OV and SW models, the trapezoidal distribution of the uplift rate of Los Osos and Edna valleys is used to assess the footwall uplift rate, with values considered in this distribution based on recent and unpublished marine terrace mapping data (Figure 8-10; see *Section 8.2.2*). The minimum uplift rate considered in the distribution is no uplift, and the maximum value of 0.07 mm/yr is based on correlation of the 13 ± 1 m terrace remnant at Cayucos to MIS 5e (paleo–sea level +6 m). The lower preferred value of 0.02 mm/yr is consistent with correlation of marine deposits and terrace platforms mapped at elevations of 80 m in Edna Valley (PG&E, 2013b) to the late Pliocene warm interval (~3.3–3.0 Ma, paleo–sea level of +22 ± 10 m). The upper preferred estimate of 0.05 mm/yr is consistent with the possible correlation of the Memorial Park surface (current elevation of ~33 m) to MIS 11 (~400 ka; paleo–sea level of ~10–13 m) (*Section 8.2.2.3*). The lower and upper preferred rates are also consistent with the range of uplift inferred from correlation of the 7–8 m Cayucos terrace to MIS 5c and the age and paleo–sea level estimates of Muhs et al. (2012; described in *Section 8.2.2*).

To calculate the differential uplift rate across the fault, the subsidence or uplift rate PDF for the footwall (subsidence rate for the NE Model; uplift rate for the OV and SW models) was subtracted from the uplift rate of the hanging wall (Figure 8-6). The CDFs representative of the vertical separation rates rates for the three fault models are shown on Figure 8-55. Given the inferred subsidence of the footwall in the NE Model compared to the uplift of the footwall in the OV and SW models, the differential uplift associated with the NE Model is larger than the OV and SW models.

The dip-slip rate of the Los Osos fault was calculated for each of the fault models from the vertical rate and with the dips characterized for the Los Osos fault of 60°, 80°, and 50° for the OV, SW, and NE models, respectively (*Section 7.4*). The lateral and net slip rates were calculated for the Los Osos fault by considering the dip-slip rates and PDFs of the fault rake developed for each of the three fault models. The general west-northwest strike of the fault relative to the direction of principal strain axes inferred from geodetic and microseismicity data suggests that it accommodates dominantly reverse deformation, although a minor amount of dextral shear may also be accommodated (See discussion in Section 8.2 and Figure 5-12). This general result is supported by analyses of modern drainages that are not deflected where they cross the northern range front of the Irish Hills where traces of the Los Osos fault have been mapped (Baldwin, 2011). The distributions for rake shown on Figure 8-56 reflect a higher probability of oblique slip for the OV Model and reverse slip for the SW and NE models as discussed in *Section 7.2.4.*

8.5.2 Development of Slip Rate CDFs

Lateral and net slip rate CDFs were calculated based on the dip-slip rate and fault rake distributions developed for each of the fault models and are shown on Figures 8-57, 8-58, and 8-59. The mean slip rate and certain probability values drawn from the CDFs are also provided on these figures.

For the OV Model (Figure 8-57), the mean net slip rate is 0.26 mm/yr. The extreme low-probability minimum and maximum net slip rates based on the dip-slip rate and fault rake models are 0.12 mm/yr and 0.61 mm/yr, respectively. The 90% confidence limit slip rate ranges from 0.17 mm/yr to 0.39 mm/yr (5% and 95% cumulative probability, respectively).

For the SW Model (Figure 8-58), the mean net slip rate is 0.19 mm/yr. The extreme low-probability minimum and maximum net slip rates based on the dip-slip rate and fault rake models are 0.1 mm/yr and 0.36 mm/yr, respectively. The 90% confidence limit slip rate ranges from 0.13 mm/yr to 0.27 mm/yr (5% and 95% cumulative probability, respectively).

For the NE Model (Figure 8-59), the mean net slip rate is 0.42 mm/yr. The extreme low-probability minimum and maximum net slip rates based on the dip-slip rate and fault rake models are 0.25 mm/yr and 0.75 mm/yr, respectively. The 90% confidence limit slip rate ranges from 0.31 mm/yr to 0.55 mm/yr (5% and 95% cumulative probability, respectively).

8.5.3 Equivalent Five-Point Distribution and Comparison to Other Studies

A summary figure showing slip rate CDFs for the three models is provided on Figure 8-60. The five-point discrete representations of these continuous probability distributions are provided on the associated table. These values vary among the three fault models. For the OV Model, the five-point distribution ranges from a minimum of 0.16 mm/yr to a maximum of 0.41 mm/yr with a weighted average value of 0.26 mm/yr. For the SW Model, the five-point distribution ranges from a minimum of 0.13 mm/yr to a maximum of 0.28 mm/yr with a weighted average value of 0.19 mm/yr. For the NE Model, the five-point distribution ranges from a minimum of 0.30 to a maximum of 0.56 with a weighted average value of 0.42 mm/yr.

The slip rate estimated for the Los Osos fault source in the Diablo Canyon LTSP (1988) study varied depending on the style of faulting. Two alternatives were considered:

- Reverse or thrust faulting [0.9] with a dip distribution of 60° [0.7] and 30° [0.3].
- Oblique-slip faulting [0.1] with a dip distribution of 75° [0.8] and 45° [0.2].

The vertical component of the slip rate for both alternatives was 0.2 mm/yr [0.6] and 0.4 mm/yr [0.4]. For the oblique-slip case, a horizontal component of slip was assumed directly from the definition of an oblique-slip fault used in the analysis (a range in the H/V ratio from 2:1 to 1:2). Values of 0.1 mm/yr and 0.2 mm/yr for vertical rates of 0.2 mm/yr and 0.4 mm/yr, respectively, were used.

The source parameters for the Los Osos fault used in the analysis of the Shoreline fault (PG&E, 2011) were modified from the LTSP Final Report (PG&E, 1988) as follows:

- The LTSP Final Report (PG&E, 1988) heavily weighted reverse slip [0.9] over oblique slip [0.1] for the Los Osos fault zone. In the Shoreline fault PSHA, a higher weight was given to oblique slip [0.7] over reverse slip [0.3].
- Estimated values for the average dip of the Los Osos fault zone varied between 30° and 75° southwest based on the assumed model for sense of slip in the LTSP Final Report (PG&E, 1988). The logic tree for the Shoreline fault PSHA defines the dip of the Los Osos fault zone source with branch values [and weights] of 75° [0.2], 60° [0.5], and 45° [0.3] southwest. The shallowest fault dip (30°) used in the LTSP Final Report (PG&E, 1988) is not supported by more recent studies that suggest the Los Osos fault is a more steeply dipping reverse or oblique-slip fault.
- The weights on the slip rates were modified, with higher weight given to 0.4 v [0.6] and 0.2 v [0.4] for the reverse-slip case; and 0.4 v, 0.2 h [0.6], and 0.2 v, 0.1 h [0.4] for the oblique slip case.

The Uniform California Earthquake Rupture Forecast, Version 2 (UCERF2) modeled the Los Osos fault as a reverse fault (rake of 90°) with a long-term slip rate of 0.5 mm/yr (Field et al., 2008).

The target Los Osos fault slip rates characterized by UCERF3 deformation models range from 0.15 mm/yr to 0.39 mm/yr, with a weighted average of 0.33 mm/yr (Field et al.,

2013). The solution slip rates that result from the UCERF3 grand inversion range from 0.15 mm/yr to 0.38 mm/yr and result in a weighted mean of 0.28 mm/yr (Field et al., 2013).

8.6 San Luis Bay Fault

The San Luis Bay fault (including both the Rattlesnake and Olson traces as identified by PG&E, 1988) is the northernmost fault within the complex zone of faulting that borders the southwest margin of the San Luis Range. The San Luis Bay fault was characterized by PG&E (1988) as a reverse fault along the southern margin of the Irish Hills, with a net slip rate of 0.08–0.20 mm/yr (based on a vertical separation rate of 0.07–0.12 mm/yr and a range in fault dip of 40°–70°; PG&E, 1988; Lettis et al., 1994). Rates of vertical separation were estimated from detailed mapping of marine terraces along the southern flank of the uplifting San Luis Range (Hanson et al., 1994; Lettis et al., 1994). In the preliminary characterization of the Shoreline fault zone (PG&E, 2011), possible connections of the San Luis Bay and the Shoreline fault allowed for oblique slip on the linked faults.

New data pertinent to the assessment of the style of faulting and slip rate of the San Luis Bay fault are available, particularly related to the geometry of the fault in the subsurface and the nature of deformation in the near surface based on interpretation of seismic-reflection data (PG&E, 2014, Chapters 7 and 9). Furthermore, as described in Section 8.2.2, an alternative uplift model based on a newly proposed paleosea-level model for California terraces (e.g., Muhs et al., 2012), is being considered. These data, along with alternative fault dips assigned to the San Luis Bay fault in the three different fault models (Section 7.4), are used to estimate slip rate CDFs for the San Luis Bay fault as described below.

8.6.1 Information on Slip Sense and Slip Rate

Similar to the approach used to assess the differential vertical separation rate across the Los Osos fault (Section 8.5), a differential vertical rate is estimated for the San Luis Bay fault based on rates of uplift of the hanging-wall and footwall blocks as inferred from the elevation of the Q2 marine terrace. The range of possible uplift rates are estimated based on the two alternative age/paleosea-level models considered for the Irish Hills (i.e., the Hanson et al. [1994] uplift model [0.8] and the Muhs et al. [2012] uplift model [0.2]).

The range in uncertainty in the uplift rate of the hanging-wall block for the two uplift models is described in Section 8.2.2.1 (Figure 8-5). A PDF describing uncertainty in the hanging wall uplift rate is presented in Figure 8-6. The distribution used for the footwall block (San Luis Hill rate) reflects the range of values allowed by correlation of the Q2 terrace (elevation of 13 ± 1 m) to either MIS 5e (125–120 ka, paleo–sea level of 6 ± 2 m) [0.8] or MIS 5c (~100 ka, paleo–sea level of + 2 to +6 m) [0.2]. The probability distributions and resulting range in uplift rate for the footwall of the San Luis Bay fault are presented on Figure 8-61.

The San Luis Bay fault is interpreted to accommodate predominantly reverse deformation because the fault strikes approximately east-west, which is approximately perpendicular to the direction of maximum compression inferred from inversion of focal mechanisms and geodetic data (*Section 5.1.6*). The TI Team judges that a minor component of lateral slip is also possible based on uncertainty in the resolution of principal strain axes and the strike of the fault. A minor component of left-oblique slip is suggested by slickenlines observed on a surface trace of the fault exposed in a roadcut west of the mouth of San Luis Obispo Creek. A minor component of right-oblique slip is suggested by potential linkage with the dextral Shoreline fault (Figure 8-34). Given these uncertainties, and consideration that the effect on net slip rate is the same for either right or left oblique slip, the TI Team considers uncertainty in the rake to be symmetrical, and considers the rake of the San Luis Bay fault to be 90°±20°.

8.6.2 Development of Slip Rate CDFs

Uncertainties in the dip and rake of the San Luis Bay fault, which lead to variation in net slip rate estimates, are accounted for in the three fault models. Figures 8-62, 8-63, and 8-64 show the input values and resulting net slip rate CDFs calculated for the San Luis fault in the OV, SW, and NE fault models, respectively.

The dip-slip rate of the San Luis Bay fault was calculated for each of the fault models from the vertical rate and the San Luis Bay fault dips of 75°, 45°, and 70° for the OV, SW, and NE models, respectively (*Section 7-4*). The lateral and net slip rates were calculated for the San Luis Bay fault by considering the dip-slip rates and a single PDF of fault rake applied to San Luis Bay fault in all three fault models. The PDF of fault rake is a uniform distribution from 70° to 110°.

8.6.3 Equivalent Five-Point Distribution and Comparison to Other Studies

A summary figure showing comparisons of slip rate CDFs for the three models is provided on Figure 8-65. The five-point discrete representations of these continuous probability distributions are provided on the associated table. These values vary among the three fault models. For the OV Model, the five-point distribution ranges from a minimum of 0.09 mm/yr to a maximum of 0.25 mm/yr with a weighted average value of 0.16 mm/yr. For the SW Model, the five-point distribution ranges from a minimum of 0.13 mm/yr to a maximum of 0.34 mm/yr with a weighted average value of 0.22 mm/yr. For the NE Model, the five-point distribution ranges from a minimum of 0.10 to a maximum of 0.25 with a weighted average value of 0.16 mm/yr.

The slip rate estimated for the San Luis Bay fault source, which was modeled as a reverse fault [1.0] with a dip of 70° north [0.8] or 40° north [0.2] in the Diablo Canyon LTSP study (PG&E, 1988), was based on a vertical rate of 0.07 mm/yr [0.6] or 0.11 mm/yr [0.4].

The source parameters for the San Luis Bay fault used in the analysis of the Shoreline fault (PG&E, 2011) were modified from the LTSP Final Report (PG&E, 1988) as follows:

- Two rupture scenarios were considered for the San Luis Bay fault source. One rupture scenario treats the San Luis Bay fault zone as an independent source of earthquakes [0.7]. The other rupture scenario considers the San Luis Bay fault zone to be kinematically linked to ruptures on the Shoreline fault zone [0.3].
- Based on the updated evaluation of the San Luis Bay fault and its possible intersection with the Los Osos fault at depth beneath the Irish Hills, the branch values [and weights] for dip of the San Luis Bay fault were changed to be 50° north [0.2], 70° north [0.4], and 80° north [0.4].
- Instead of a weight of 1.0 given to a reverse sense of slip for the independent San Luis Bay fault source, equal weight was given to oblique and reverse mechanisms.
- The slip rates (mm/yr) assigned to the two alternative senses of slip when the San Luis Bay fault was modeled as an independent source were 0.14 v [0.8] and 0.08 v [0.2] for the reverse model [0.5], and 0.14 v/0.07 h [0.8] and 0.08 v/ 0.04 h [0.2] for the oblique model.

The Uniform California Earthquake Rupture Forecast, Version 2 (UCERF2), Deformation Model 4 included the San Luis Bay fault as part of a fault source named the "San Luis Range S margin" fault source that was modeled as a reverse fault (rake of 90°) with a long-term slip rate of 0.2 ± 0.1 mm/yr (Field et al., 2008).

The updated assessment in UCERF3 included the San Luis Bay fault as part of the Community fault model 3.2. Target slip rates for the San Luis Bay fault within the four deformation models range from 0.09 mm/yr to 0.18 mm/yr with a weighted average of 0.12 mm/yr (Field et al., 2013). The solution slip rates that result from the UCERF3 grand inversion range from 0.07 mm/yr to 0.18 mm/yr with a weighted average of 0.12 mm/yr (Field et al., 2013).

8.7 Other Site Vicinity Faults

Slip rates assigned to other faults within the San Luis–Pismo Block that lie at greater distances from the DCPP than the key faults described in the previous sections are discussed below. These include the Wilmar Avenue and Oceano faults, which are included in various rupture sources described in *Chapter 9.0*.

8.7.1 Wilmar Avenue Fault

The Wilmar Avenue fault was characterized by PG&E (1988) as a northwest-trending, northeast-dipping reverse fault along the southwestern boundary of the San Luis Range. At the type locality sea-cliff exposure, the Wilmar Avenue fault displaces the lowest emergent marine terrace, which is interpreted to be 120 ka based on analyses of faunal assemblages (Hanson et al., 1994). The platform has a 6.4 m vertical separation across the fault, but may be as little as 4.3 m due to uncertainties in the possible reoccupation and erosion of the terrace during a later sea-level stand. Based on a range in fault dip of

45°–70° and a range in vertical separation of 4.3–6.4 m of this terrace, the Wilmar Avenue fault at this location has an average late Pleistocene net slip rate of 0.04–0.08 mm/yr (PG&E, 1988; Lettis et al., 1994). A similar net slip rate is estimated for the fault at the Farmboy quarry site approximately 2 km to the southeast of the sea cliff exposure.

Sensitivity analyses have consistently shown that the Wilmar Avenue fault does not contribute significantly to hazard at the DCPP (PG&E, 2011, Chapter 6; Wooddell, 2011, presentation at Workshop 1). Because of this, the TI Team characterized the slip rate of the Wilmar Avenue fault conservatively for the SSC model, and instead focused on other parameters that are more hazard significant. The slip rate assigned to the Wilmar Avenue fault varies depending on the fault model. For the SW- and NE-Vergent models, where the Wilmar Avenue fault is included as purely a reverse fault rupture source, the weighted mean slip rates for the fault source are 0.21 mm/yr and 0.20 mm/yr, respectively. For the OV Model, where the fault is assumed to have a right-oblique component of slip, the weighted mean slip rate is 0.24 mm/yr.

8.7.2 Oceano Fault

The Oceano fault was characterized by PG&E (1988) as a northwest-trending reverse fault recognized northwest of the town of Santa Maria and in the offshore San Luis Obispo Bay region, based on interpretation of onshore and offshore seismic-reflection data. The geometry and cumulative displacement of the fault were inferred from subsurface geophysical and well data. This fault, which lies along the northern margin of the onshore Santa Maria Basin is the southernmost structure within the Southwestern Boundary zone as defined by PG&E (1988). Additional possible faults (unnamed) between the Oceano fault and the Nipomo lineament (Wilmar Avenue fault) were identified by PG&E (1988) and Hanson et al. (1994) based on postulated steps or warps in the top of bedrock beneath the Nipomo Mesa. The DWR (2002) follows the nomenclature of Hall (1978, 1981, 1982) in referring to that zone of faulting as the Santa Maria River fault. The Santa Maria fault as mapped by the DWR (2002) extends from offshore near Oceano across the Nipomo Mesa and along the eastern margin of the onshore Santa Maria Basin. The Oceano fault and traces of the Santa Maria River fault are shown to merge near the coast, where the location of the fault is constrained by its intersection with the Madonna Construction Company's Oceano 1 oil well at a depth of 1,000 ft (330 m).

Estimates of the slip rate along the onshore reach of the Oceano fault were based on vertical separation of marine deposits of probable Pliocene or possibly early Pleistocene age (PG&E, 1988; Lettis et al. 1994). Oil well data from the Nipomo Mesa area show that the vertical separation of an unconformity at the top of what was inferred to be the Pliocene Foxen Formation is between 77 m and 126 m (PG&E, 1988; Plate 3 of Hanson et al., 1994). The age of this unconformity was not known. Using an estimated age of 1–2 Ma for the unconformity and an assumed fault dip of between 40° and 65° yielded a net slip rate of 0.04–0.20 mm/yr for the fault in the Nipomo Mesa area (Lettis et al., 1994). The DWR (2002) shows a similar 76–100 m of vertical stratigraphic separation of the base of the Tertiary Careaga Formation across the Oceano fault beneath the central part

of the Nipomo Mesa, and a cumulative vertical separation of approximately 129–172 m across both the Oceano and Santa Maria fault traces. Using an age of approximately 3.7–2.7 Ma for the age of this contact (Willingham et al., 2013; PG&E, 2014) yields maximum vertical rates of 0.05–0.06 mm/yr.

It was noted by PG&E (1988) that the long-term rate appeared to decrease toward the northwest end of the fault where data from water wells along the coastline suggest that the top of the Foxen Formation has approximately 27 m of vertical stratigraphic separation. Using the same age and fault dip data as above yields a net post-Pliocene slip rate of 0.01–0.04 mm/yr for the Oceano fault at the coast (Lettis et al., 1994). DWR (2002) also cites a similar vertical offset (27 m) of the base of the Squire Member/Pismo Formation and the base of the Careaga Formation where the Oceano and Santa Maria River faults merge at the coastline. Using the 2.7 Ma minimum estimated age of the top of the Careaga Formation (Willingham et al., 2013; PG&E, 2014, Chapter 3) yields a vertical rate of offset of 0.01 mm/yr.

The results of the LESS study (PG&E, 2014, Chapter 3) indicate that the Oceano fault zone has a preferred reverse-slip rate of approximately 0.1 mm/yr, within a range of 0.0–0.25 mm/yr. The estimated vertical offsets were based primarily on bedrock channel thalweg profiles. With the exception of Channels B and F, the preferred vertical separation of 1–2 m are less than or equal to the stated uncertainty in thalweg profiles. The LESS report also states that there is evidence for little or no surface fault rupture and associated vertical separation on the Oceano fault within most of the study area since the pre-Holocene MIS 2–1 sea-level transgression, although minor offset of the H10 unconformity is possible in the southeastern part of the study area.

Sensitivity analyses have consistently shown that the Oceano fault does not contribute significantly to hazard at the DCPP (PG&E, 2011, Chapter 6; Wooddell, 2011, presentation at Workshop1). Because of this, the TI Team characterized the slip rate of the Oceano fault conservatively for the SSC model, and instead focused on other parameters that are more hazard significant. The slip rate assigned to the Wilmar Avenue fault is 0.15 mm/yr.

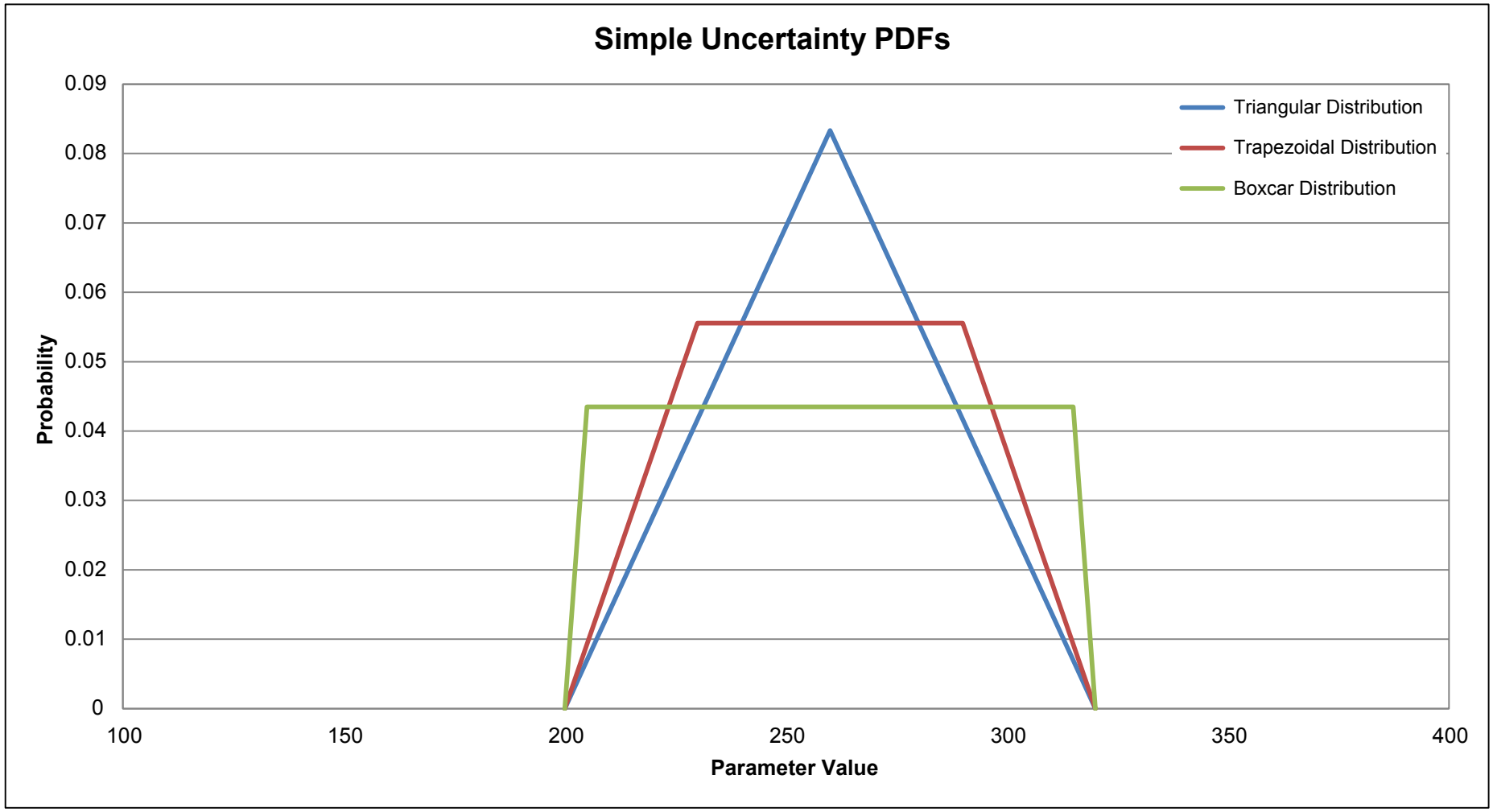

Note: Schematic depiction of common probability density function (PDF) forms used to describe uncertainty in parameters such as offset and age of a feature for use in calculating slip rate.

Example of Simple Uncertainty PDFs, Including the Triangular, Trapezoidal, and Boxcar Distributions

DCPP SSC REPORT

Pacific Gas and Electric Company | Figure **8-1**

File path: S:\1005\005\Final_Report\Figure_800-01.ai; Date: 03/11/2015; User: Alex Remar, LCI; Rev.1

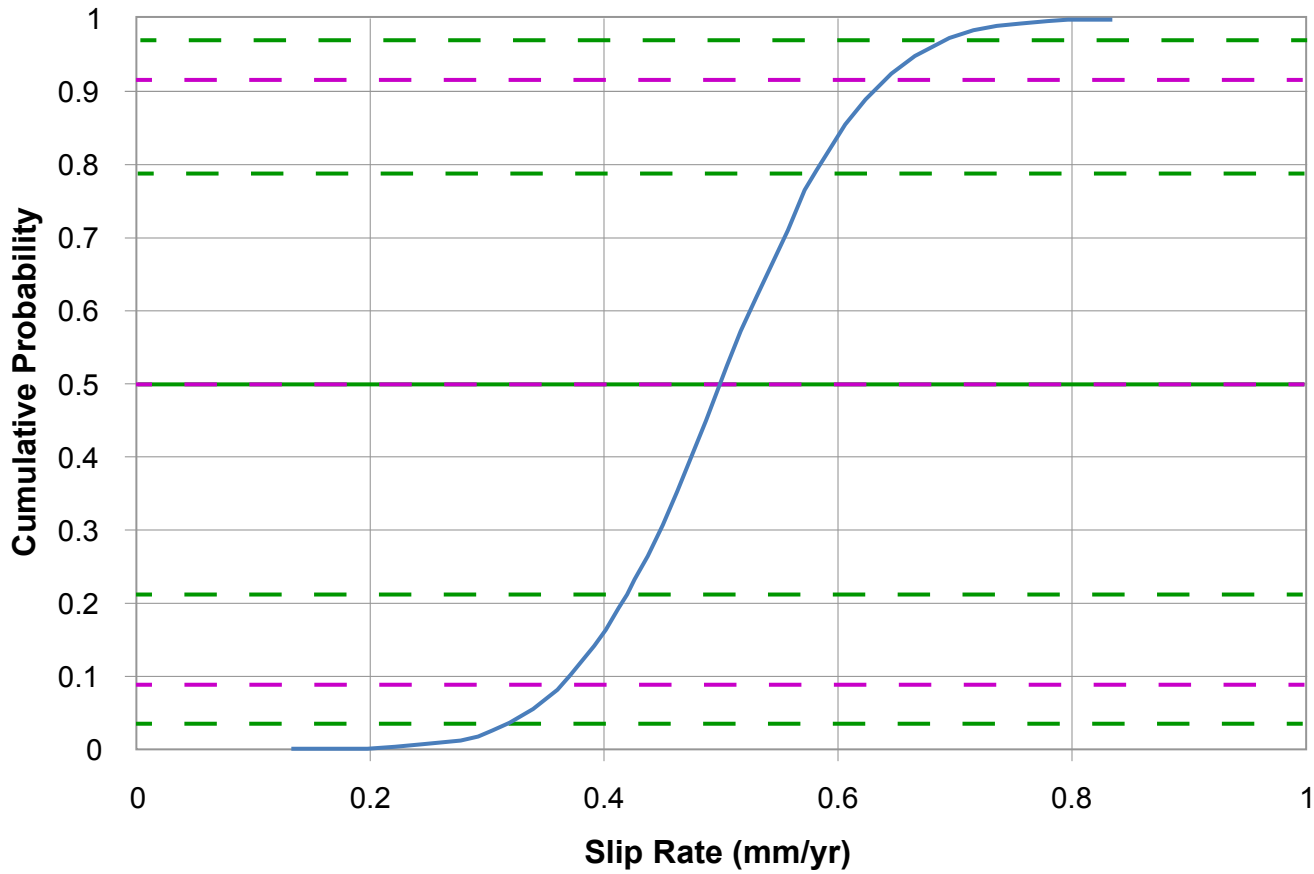

Cumulative Probability Level of Continuous Distribution	Assigned Probability Weight	Modified Probability Weight
3-Point Approximation		
0.084669	0.247614	0.248
0.500000	0.504771	0.504
0.915331	0.247614	0.248
5-Point Approximation		
0.034893	0.101080	0.101
0.211702	0.244290	0.244
0.500000	0.309260	0.310
0.788298	0.244290	0.244
0.965107	0.101080	0.101

EXPLANATION

- Cumulative probability level of continuous distribution, 5-point approximation
- Cumulative probability level of continuous distribution, 3-point approximation
- Continuous probability distribution

Miller and Rice (1983) Discrete 3- and 5-Point Approximations to a Continuous Probability Distribution

DCPP SSC REPORT

Pacific Gas and Electric Company

Figure **8-2**

File path: S:\1005\005\Final_Report_Figures\Figure_800-02.ai; Date: 02/05/2015; User: Alex Remar, LCI; Rev.1

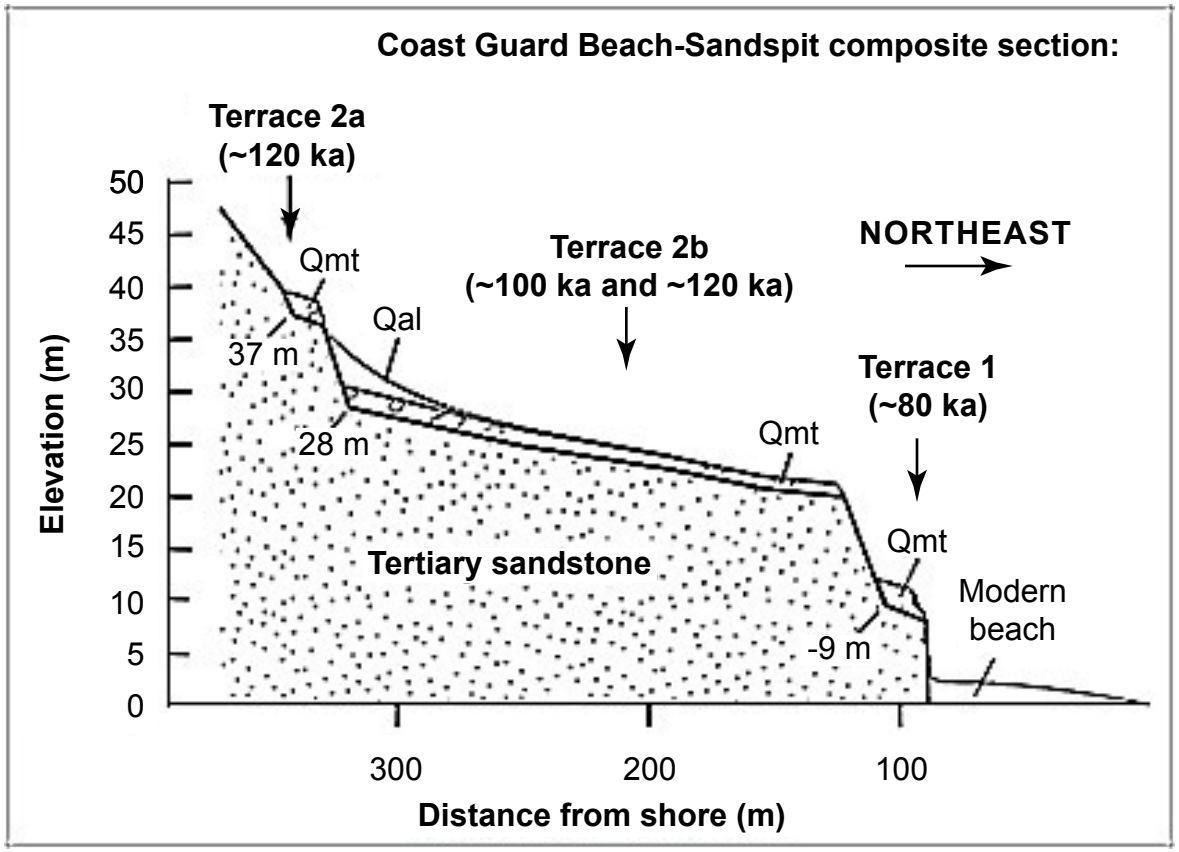

Note: Marine terrace cross section from a transect across terraces 2a, 2b, and 1 on San Nicolas Island. Qmt: marine terrace deposit; Qal: alluvium. Based on U-series ages of individual corals and faunal thermal aspects, these terraces are correlated to MIS 5a (~80 ka), 5c (~100 ka), and 5e (~120 ka).

Source: Muhs et al. (2012).

MIS 5 Marine Terrace Sequence, San Nicolas Island, California

DCPP SSC REPORT

Pacific Gas and Electric Company

Figure **8-3**

File path: S:\1005S\1005\005\Final_Report_Figures\Figure_800_03.ai; Date: 02/03/2015; User: Alex Remar LCI; Rev.0

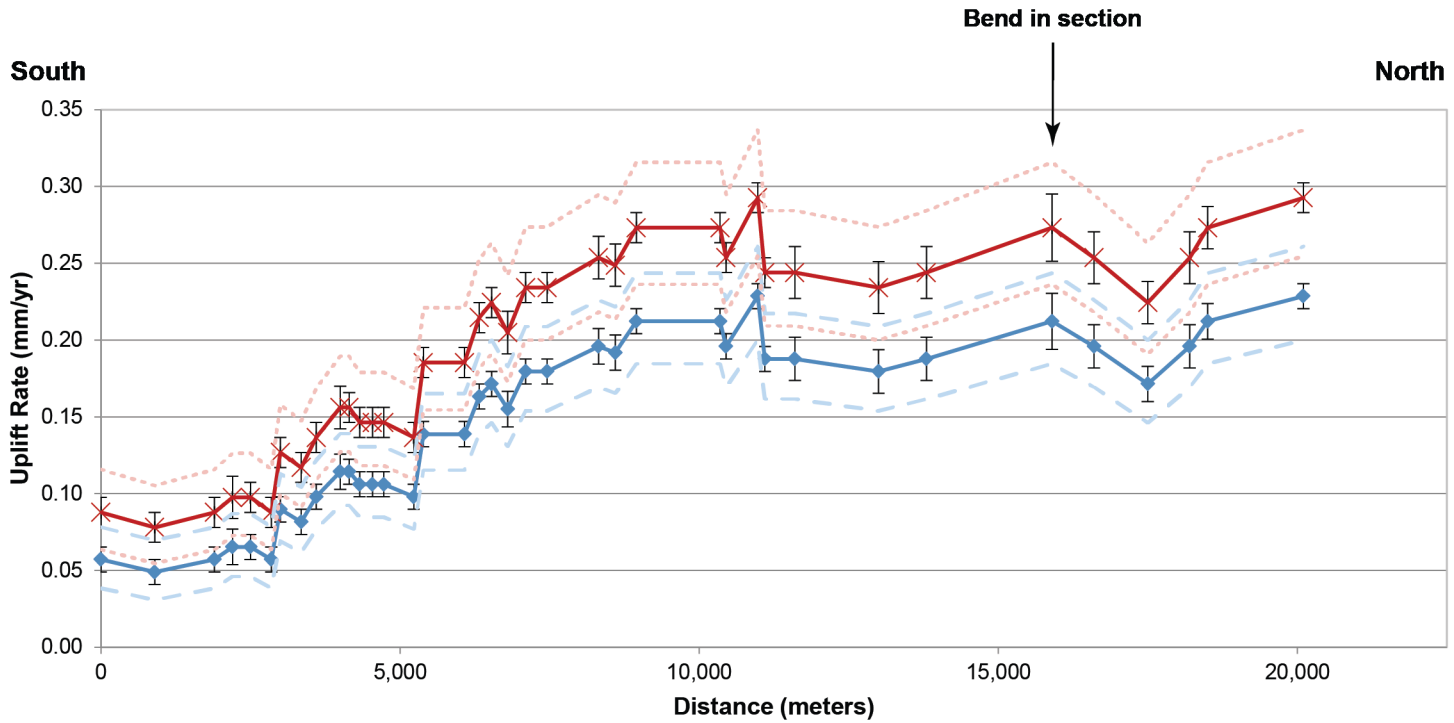

EXPLANATION

- Age and paleosea-level model (Hanson et al.,1994)
- Alternative age and paleo-sea-level model (Muhs et al., 2012)
- Uncertainty in uplift rate based on field measurements
- Minimum and maximum uplift rate based on uncertainty in paleosea-level and initial elevation (Hanson et al., 1994)
- Minimum and maximum uplift rate based on uncertainty in paleosea-level and initial elevation (Muhs et al., 2012)

Note: Shore-parallel profiles showing comparison of uplift rates from the second emergent terrace (Q2) shoreline angle elevations in the Irish Hills based on alternative paleosea-level models. The Q2 terrace in the Hanson et al. (1994) model (blue line) is correlated to the MIS 5e highstand, with an initial elevation of +6 ± 2 m approximately 120 ka. In the Muhs et al. (2012) model (red line), the Q2 terrace is correlated to MIS 5c, with an initial elevation of +4 ± 2 m approximately 100 ka.

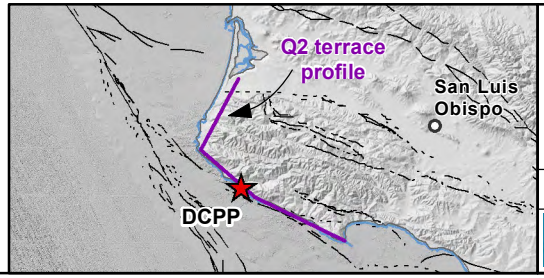

Comparison of Marine Terrace Uplift Rates on the Irish Hills Coastline from Alternative Paleosea-Level Models

DCPP SSC REPORT

Pacific Gas and Electric Company

Figure **8-4**

File path: S:\1005\005\Final_Report_Figures\Figure_800-04.mxd; Date: 02/27/2015; User: Alex Remar, LCI; Rev.1

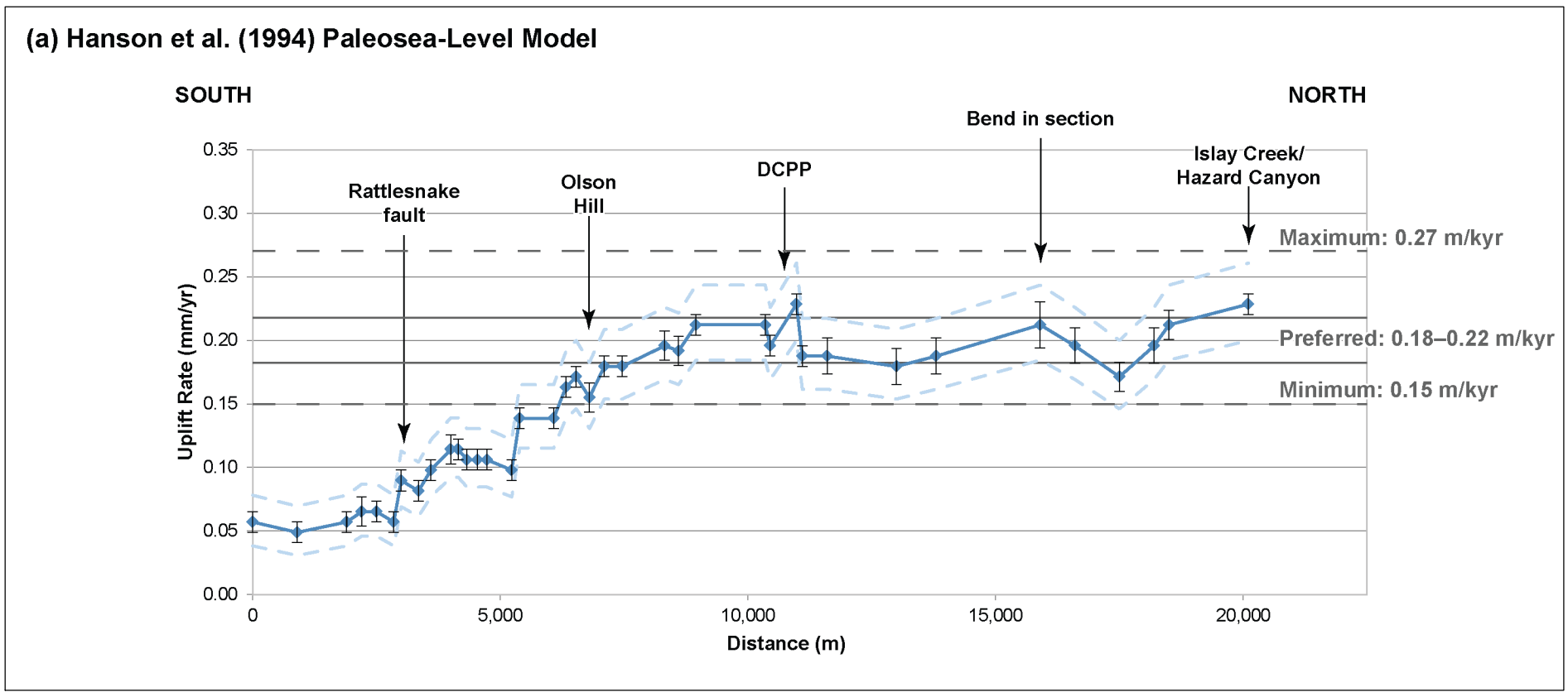

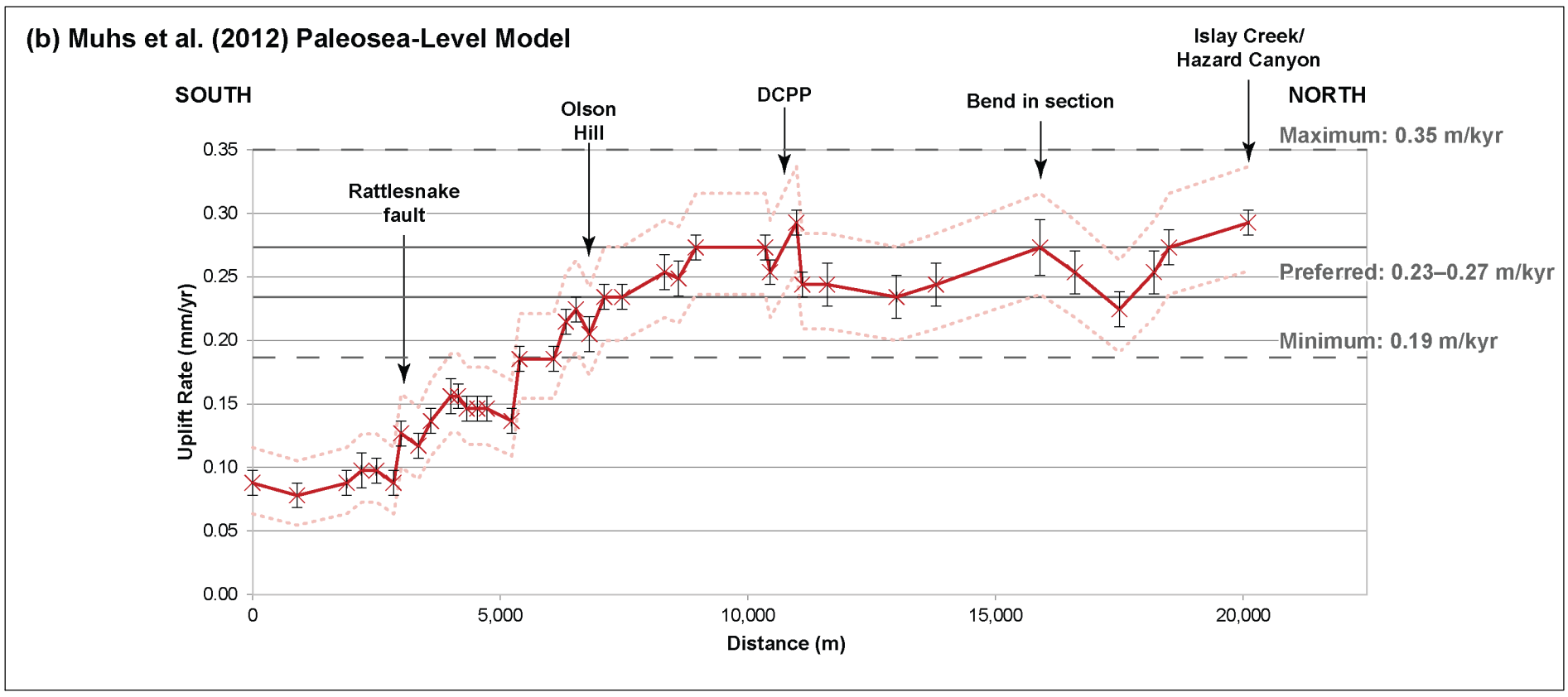

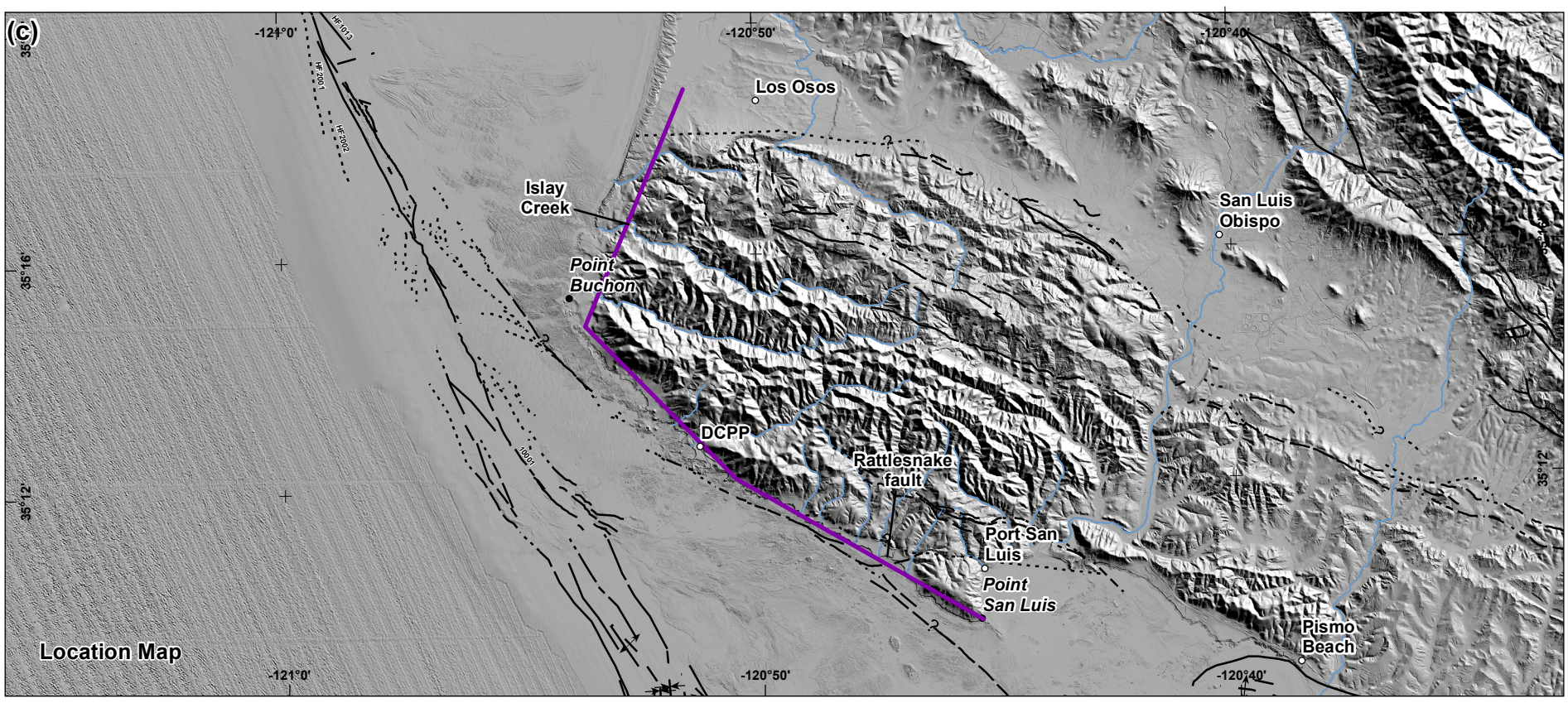

EXPLANATION

- Q2 rate–Hanson et al. (1994) age/paleosea-level model
- Q2 rate–Muhs et al. (2012) age/paleosea-level model
- Q2 terrace profile
- Fault, solid where well located, dashed where approximately located, dotted where buried by undeformed strata of H10 or older, queried where existence uncertain

Note: Uplift rate estimates for the Irish Hills are based on the mapped elevations of the Q2 terrace shoreline angles and alternative models for age and paleosea level. Panel (a) shows preferred uplift rates and bounding values estimated from the Hanson et al. (1994) paleosea-level model. Panel (b) shows preferred uplift rates and bounding values estimated from the Muhs et al. (2012) paleosea-level model.

Sources:
- Hanson et al. (1994).
- Muhs et al. (2012).

N

0 1 2 mi.
0 2 4 km

Map projection and scale: WGS 84 / UTM Zone 10N, 1:200,000

Irish Hills –
Alternative Uplift Rate Models

DCPP SSC REPORT

Pacific Gas and Electric Company

Figure **8-5**

File path: S:\1005\005\Final_Report_Figures\Figure_800-05.mxd; Date: 03/11/2015; User: Alex Remar, LCI; Rev.1

(a) Hanging Wall Uplift Rate PDFs

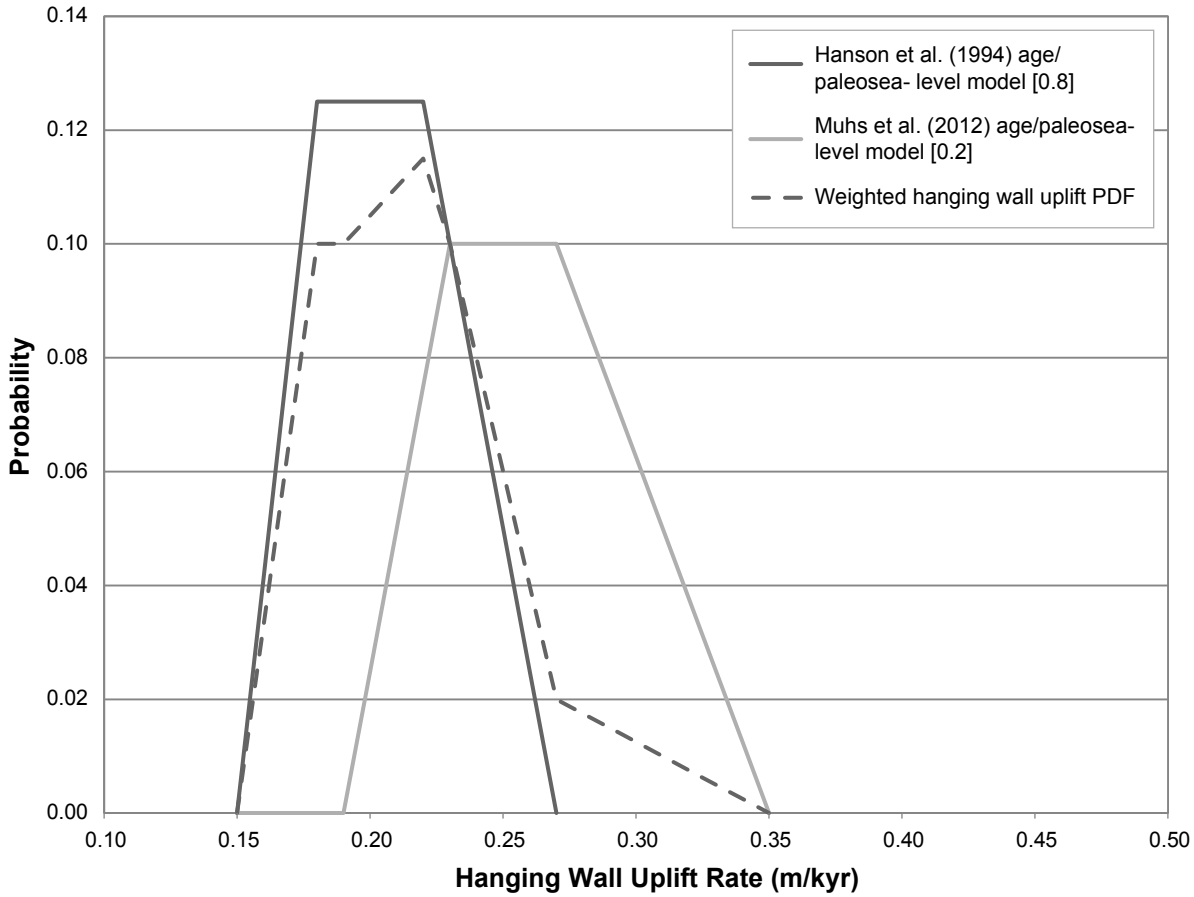

(b) Justification for Hanging Wall Uplift Rate PDFs

Hanson et al. (1994) Age Model [0.8]		
Value	**Uplift Rate (m/kyr)**	**Basis**
Min.	0.15	Enveloping minimum of uncertainty in strandline elevation
Preferred	0.18	Preferred Q2 marine terrace age of MIS 5e (~120-125 ka)
Preferred	0.22	
Max.	0.27	Enveloping maximum of uncertainty in strandline elevation

Muhs et al. (2012) Age Model [0.2]		
Value	**Uplift Rate (m/kyr)**	**Basis**
Min.	0.19	Enveloping minimum of uncertainty in strandline elevation
Preferred	0.23	Preferred Q2 marine terrace age of MIS 5c (~100 ka)
Preferred	0.27	
Max.	0.35	Enveloping maximum of uncertainty in strandline elevation

Notes:
- Numbers in brackets are weights assigned to each age model.
- PDF for uplift rate of the Irish Hills based on the weighted combination of the Hanson et al. (1994) paleosea-level model [weight of 0.8] and the Muhs et al. (2012) paleosea-level model [weight of 0.2].

Irish Hills Uplift Rate PDFs

DCPP SSC REPORT

Pacific Gas and Electric Company

Figure **8-6**

File path: S:\1005\005\Final_Report_Figures\Figure_800-06.ai; Date: 03/11/2015; User: Alex Remar, LCI; Rev.1

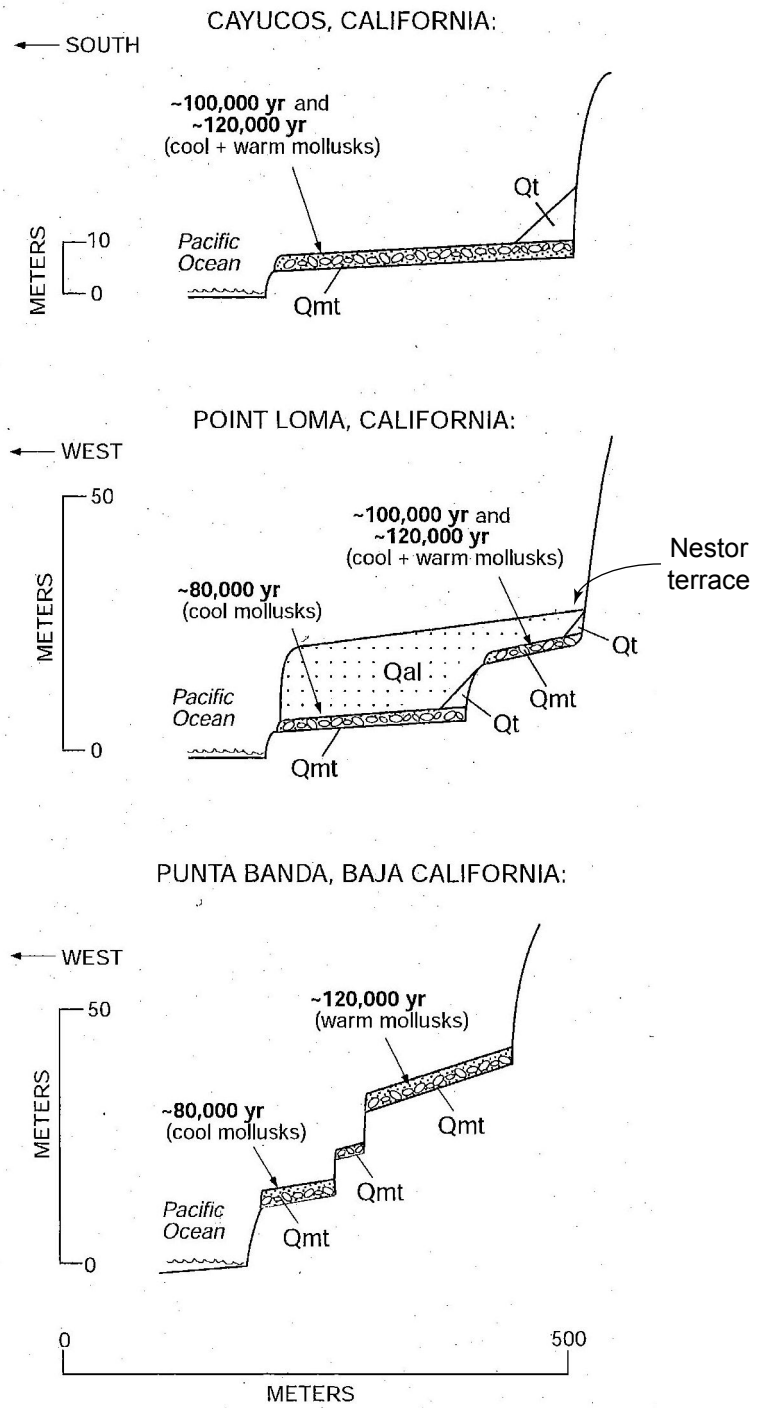

EXPLANATION

Qal	Quaternary alluvium
Qmt	Quaternary marine terrace deposits
Qt	Quaternary talus

Note: Shore-normal profiles of low terraces at Cayucos and Point Loma, California and Punta Banda, Baja California, showing average U-series ages of individual corals and faunal thermal aspects. Abbreviations for deposits: Qal, alluvium; Qt, talus and other colluvial deposits; Qmt, marine terrace deposits. From data in Muhs et al. (2002).

Source: Muhs et al. (2004)

MIS 5 Marine Terrace Sequences at Cayucos, Point Loma, and Punta Banda, California

DCPP SSC REPORT

Pacific Gas and Electric Company

Figure **8-7**

File path: S:\1005\005\Final_Report_Figures\Figure_800-07.ai; Date: 02/05/2015; User: Alex Remar, LCI; Rev.1

(a) Map of Sample Locations

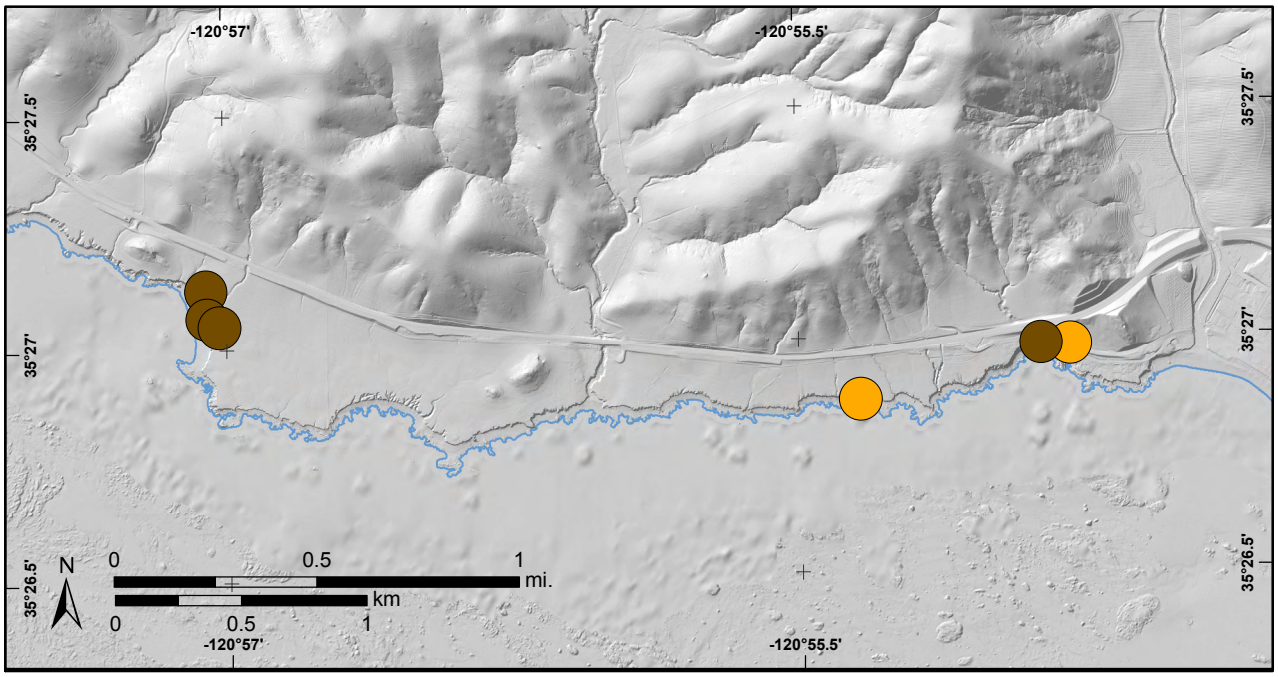

(b) Map of Bedrock Elevation Measurements

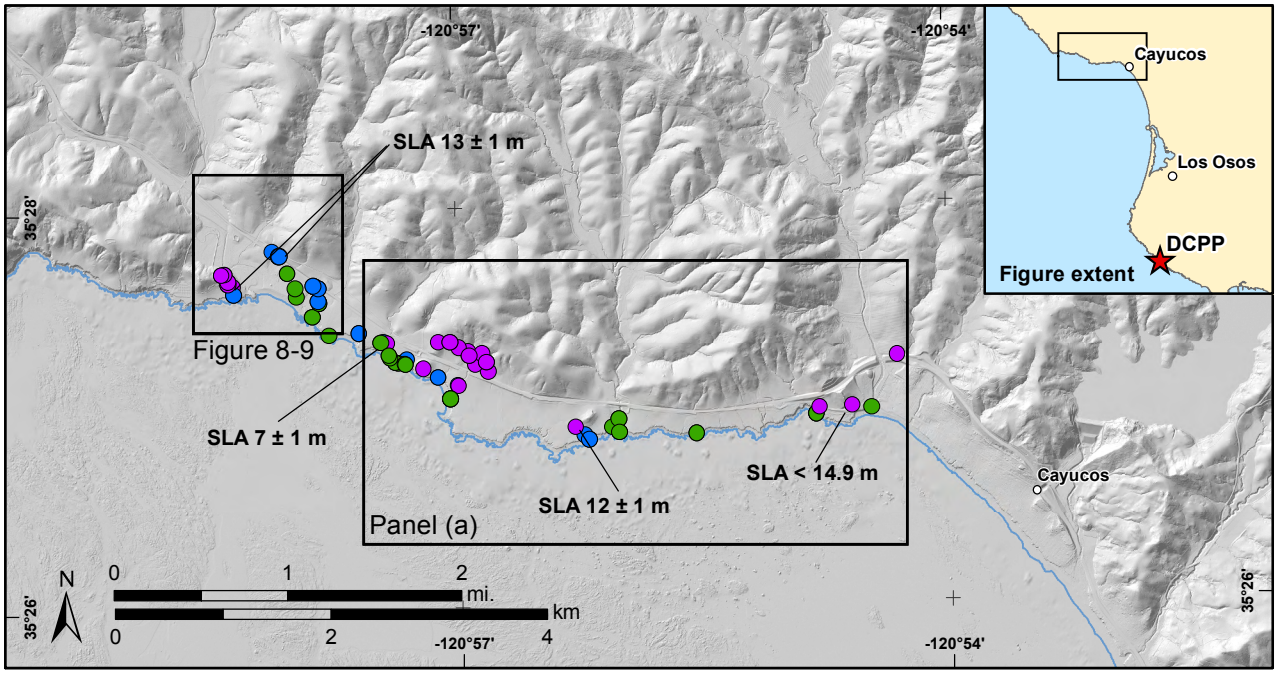

EXPLANATION

Measured bedrock elevation

- First emergent terrace (3-7 m)
- Second emergent terrace (8-14 m)
- Uplands (15-55 m)
- SLA Shoreline angle elevation and uncertainty

Sample locations

- Hanson et al. (1994)
- Muhs et al. (2002)

Map projection and scale: NAD 83 / UTM Zone 10N

Notes:
- Panel (a) is a map showing locations where samples from the first emergent terrace at Cayucos were collected for U-series dating and assessment of faunal thermal aspects.
- Panel (b) is a map showing locations where elevations of bedrock were measured and post-processed using Trimble GPS equipment and processing software. These observations are used to constrain the shoreline angle elevations of two low emergent terraces along the coast near Cayucos, California.

Marine Terrace Observations, Cayucos Study Area

DCPP SSC REPORT

Pacific Gas and Electric Company

Figure **8-8**

File path: S:\1005\005\Final_Report_Figures\Figure_800-08.mxd; Date: 02/25/2015; User: Alex Remar, LCI; Rev.1

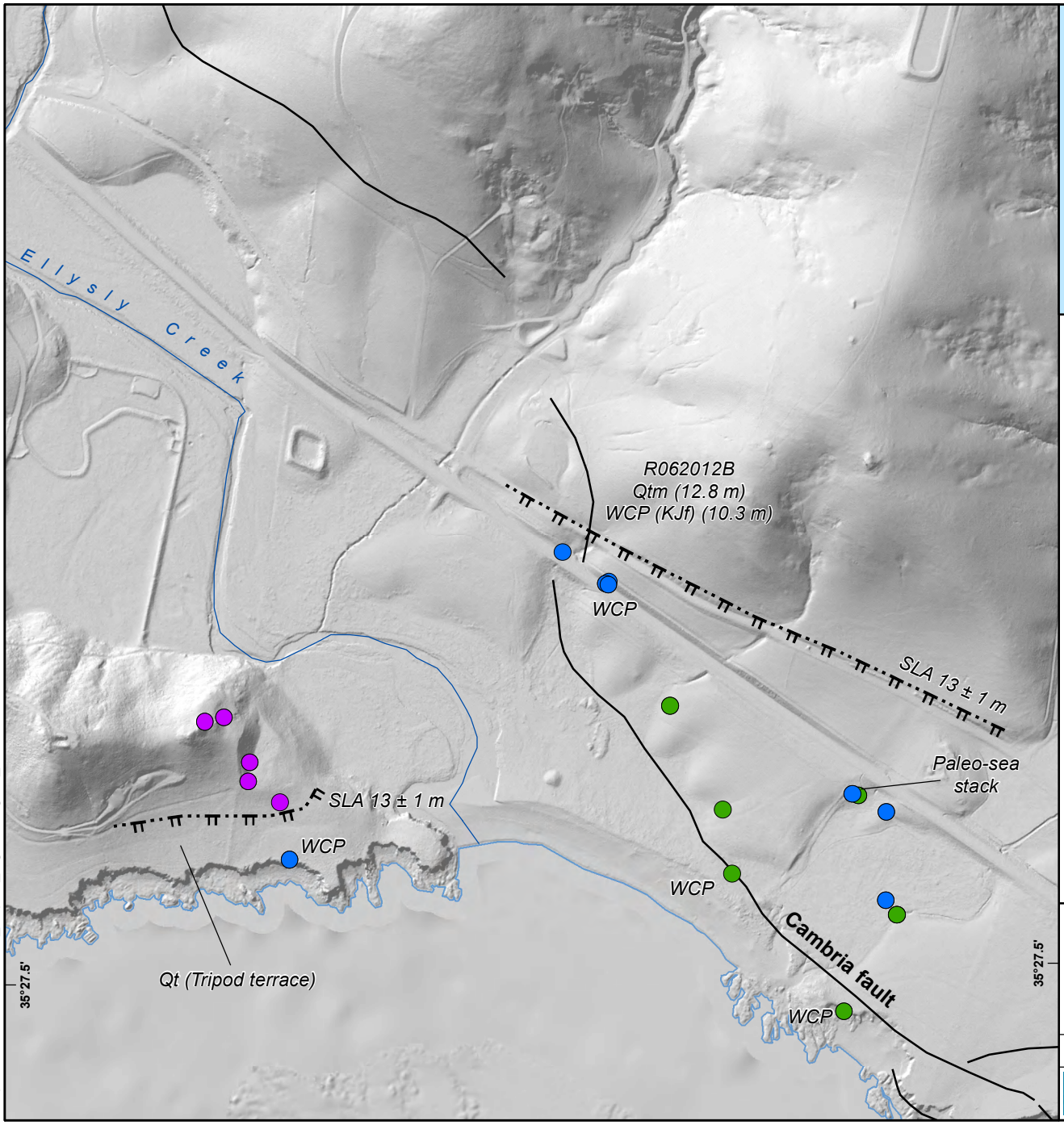

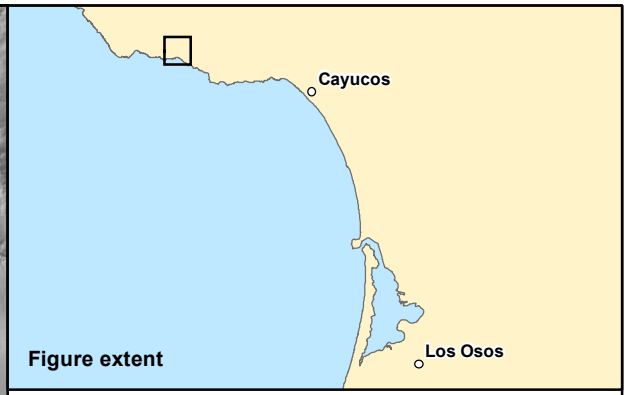

EXPLANATION

Measured bedrock elevation

- First emergent terrace (3-7 m)
- Second emergent terrace (8-14 m)
- Uplands (15-55 m)
- Fault (Rosenberg, 2011)
- Poorly constrained marine terrace strandline

SLA	Shoreline angle
WCP	Wave-cut platform
Qtm	Quaternary marine deposits
KJf	Franciscan complex

Note: Location of inner edge and shoreline angle elevation of 13 ± 1 m terrace remnants in the vicinity of Ellysly Creek inferred from topography and projections from localities where wave-cut platform elevations were measured.

N

0 500 1,000 ft.

0 200 400 m

Map projection and scale: WGS 84 / UTM 10N, 1:8,000

Marine Terrace Observations, Ellysly Creek

DCPP SSC REPORT

Pacific Gas and Electric Company

Figure **8-9**

File path: S:\1005\005\Final_Report_Figures\Figure_800-09.mxd; Date: 02/25/2015; User: Alex Remar, LCI; Rev.1

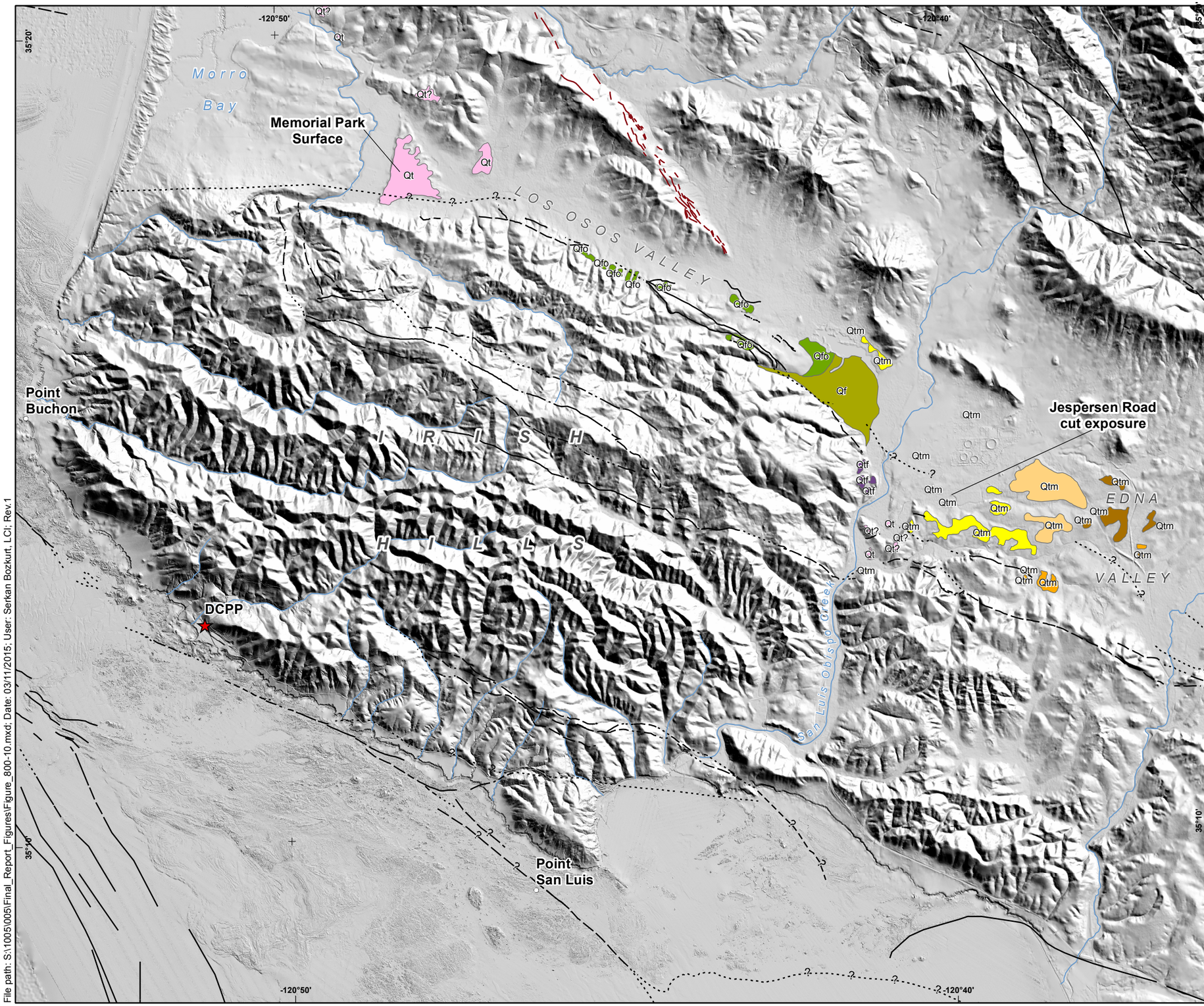

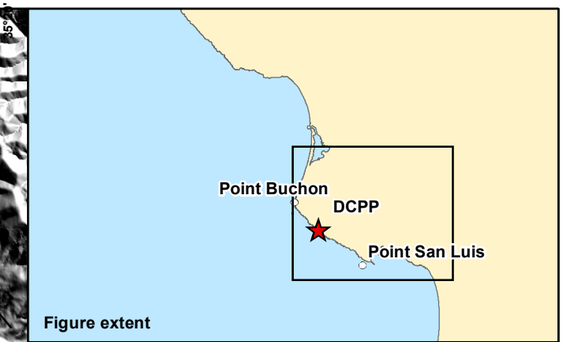

EXPLANATION

Quaternary fault trace; solid where well located, dashed where approximately located, offshore faults dotted where buried by undeformed strata equivalent to or older than unconformity H10, onshore faults dotted where concealed, short dashed where inferred, queried where existence is uncertain

Lineament

Geomorphic Units (queried where uncertain)

- Qf — Quaternary fan
- Qfo — Quaternary fan, old
- Qt — Quaternary terrace or surface, undifferentiated
- Qtm — Terrace remnant or erosional surface underlain by marine sediments (color coded by elevation)
  - 30-40 m
  - > 40-50 m
  - > 50-60 m
  - > 60-80 m
  - > 80-100 m

Source: Terrace and lineament mapping from PG&E (2013b).

Note: Faults from Plate 7-1.

N

0 1 2 mi.

0 2 4 km

Map projection and scale: WGS 84 / UTM Zone 10N, 1:90,000

Edna Valley and Los Osos Valley Quaternary Terraces and Surfaces

DCPP SSC REPORT

Pacific Gas and Electric Company

Figure **8-10**

File path: S:\1005\005\Final_Report_Figures\Figure_800-10.mxd; Date: 03/11/2015; User: Serkan Bozkurt, LCi; Rev.1

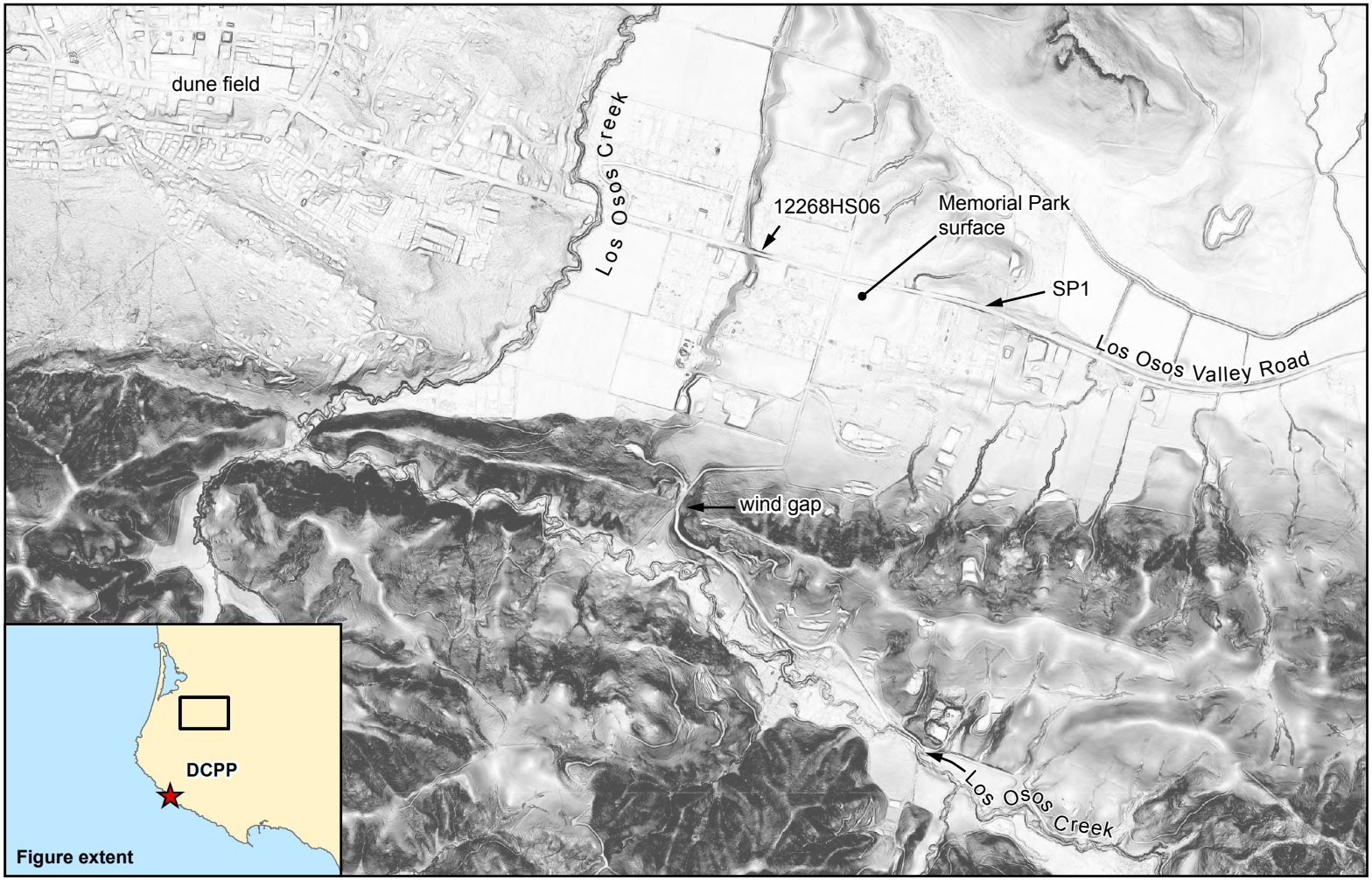

N

0 0.5 1 mi.

0 0.5 1 km

Note: Slope map showing the lower reach of Los Osos Creek and the Memorial Park surface. Note the change in size and character of Los Osos Creek and its associated floodplain up- and downstream of the wind gap (located near the middle of the map). The abrupt change in character of the valley suggests a greater antiquity of the channel upstream of the wind gap, inferring that at one time the ancestral Los Osos Creek crossed the range front through the wind gap, depositing sediments that make up the Memorial Park surface.

Slope Map Illustrating the Relationship Between the Memorial Park Surface and Inferred Location of Ancestral Los Osos Creek Through Wind Gap

DCPP SSC REPORT

Pacific Gas and Electric Company | Figure **8-11**

File path: S:\1005\005\Final_Report_Figures\Figure_8-11.ai; Date: 03/11/2015; User: Alex Remar, LCI; Rev.1

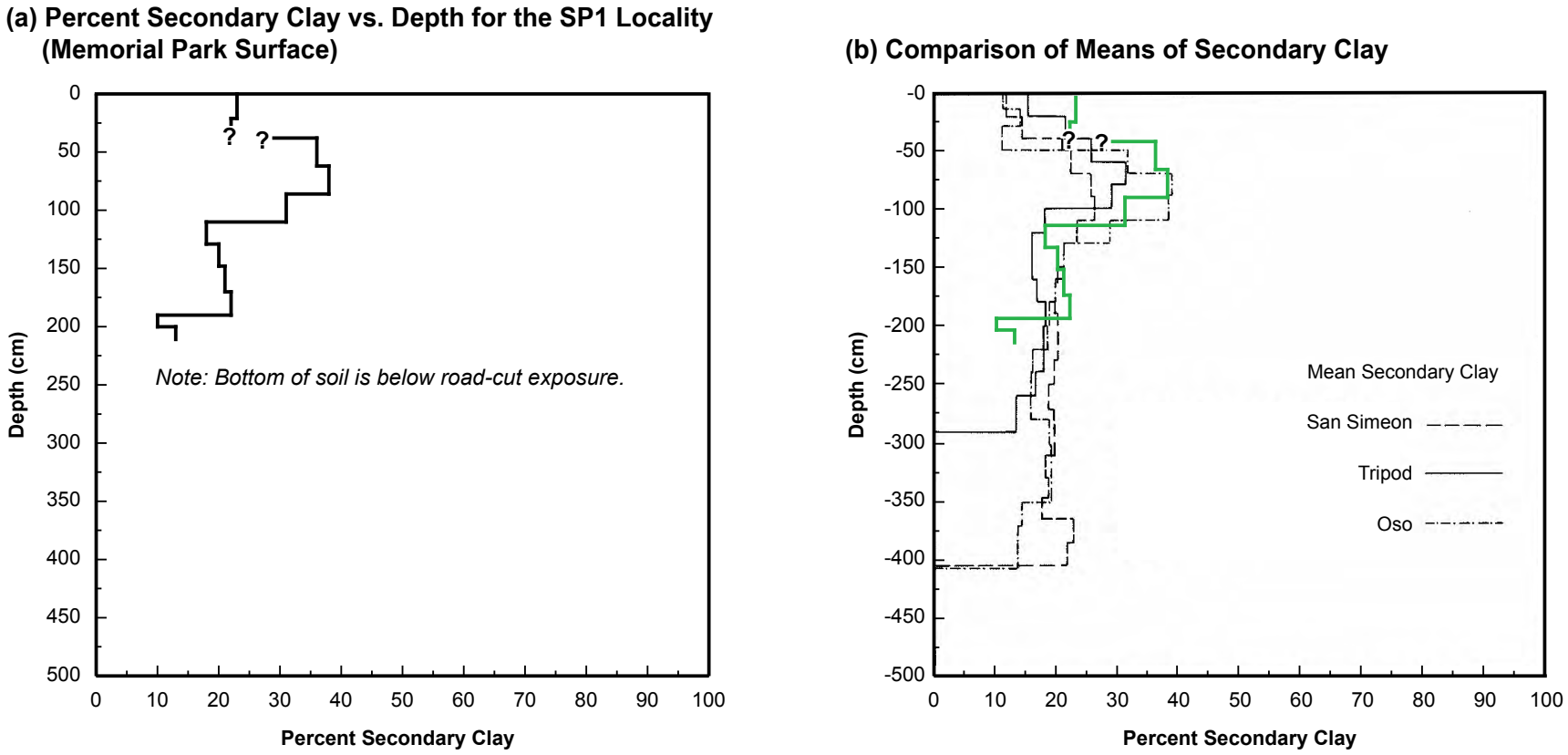

Notes:
- Panel (a) shows a depth profile of secondary clay from the Memorial Park surface (SP1 locality).
- Panel (b) compares SP1 depth profile (green line; this study) to mean depth profiles of secondary clay from the San Simeon, Tripod, and Oso marine terraces at San Simeon (from Rockwell et al., 1994).

Comparison of Clay Profile Data: Memorial Park Surface (SP1) and Marine Terraces at San Simeon

DCPP SSC REPORT

Pacific Gas and Electric Company | Figure **8-12**

File path: S:\1005\005\Final_Report_Figures\Figure_8-12.ai; Date: 02/24/2015; User: Alex Remar, LCI; Rev.1

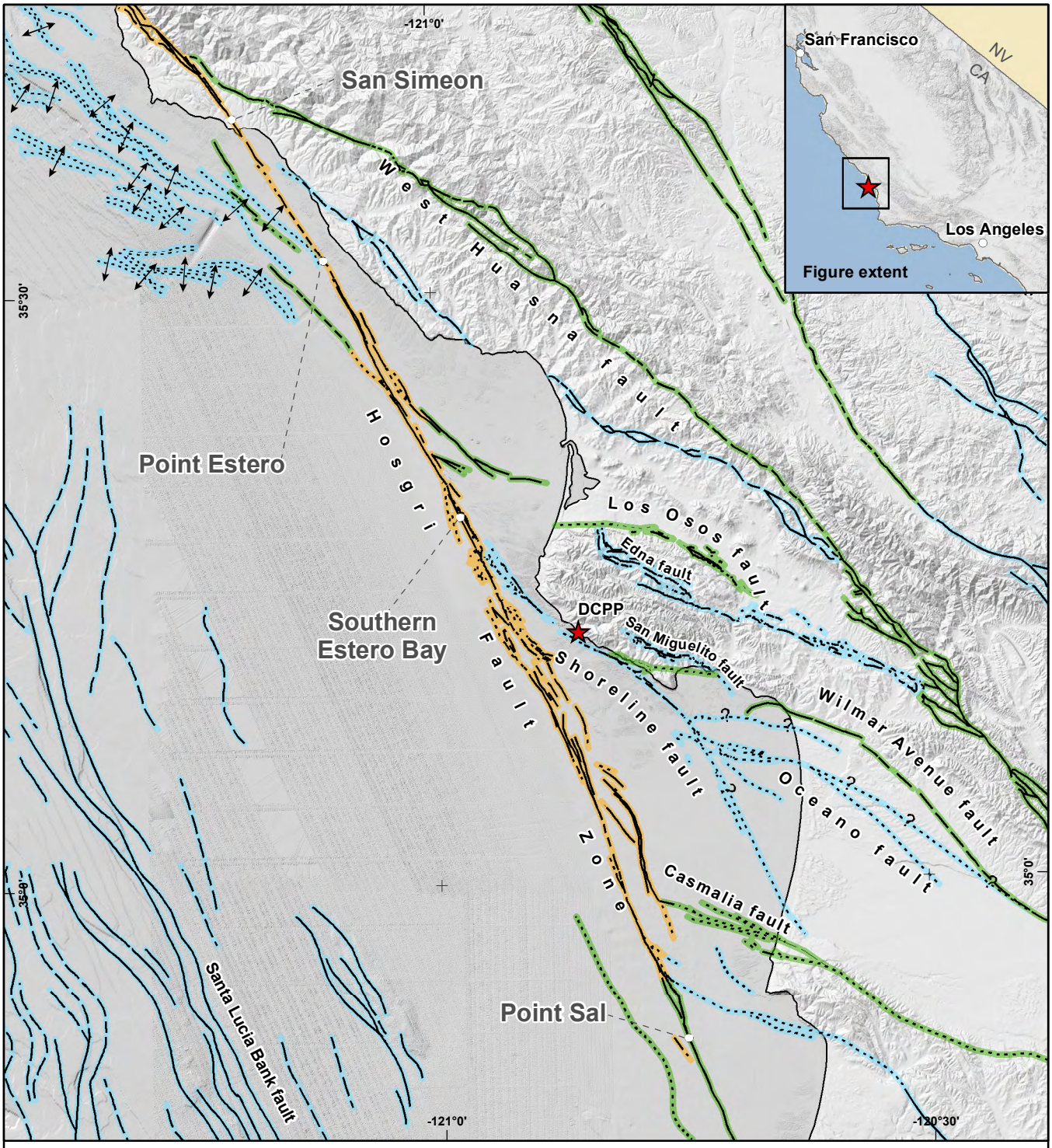

EXPLANATION

Quaternary fault trace; solid where well located, dashed where approximately located, offshore faults dotted where buried by undeformed H10 strata, onshore faults dotted where buried, short dashed where inferred, queried where existence is uncertain

Folds of the Piedras Blancas Anticlinorium

Slip Rate

1–5 mm/yr

0.2–1 mm/yr

<0.2 mm/yr

N

0 5 10 mi.

0 10 20 km

Map projection and scale: NAD 83 / UTM Zone 10N, 1:550,000

Hosgri Fault Slip Rate Sites

DCPP SSC REPORT

Pacific Gas and Electric Company

Figure **8-13**

File path: S:\1005\005\Final_Report_Figures\Figure_800-13.mxd; Date: 02/27/2015; User: Alex Remar, LCI; Rev.1

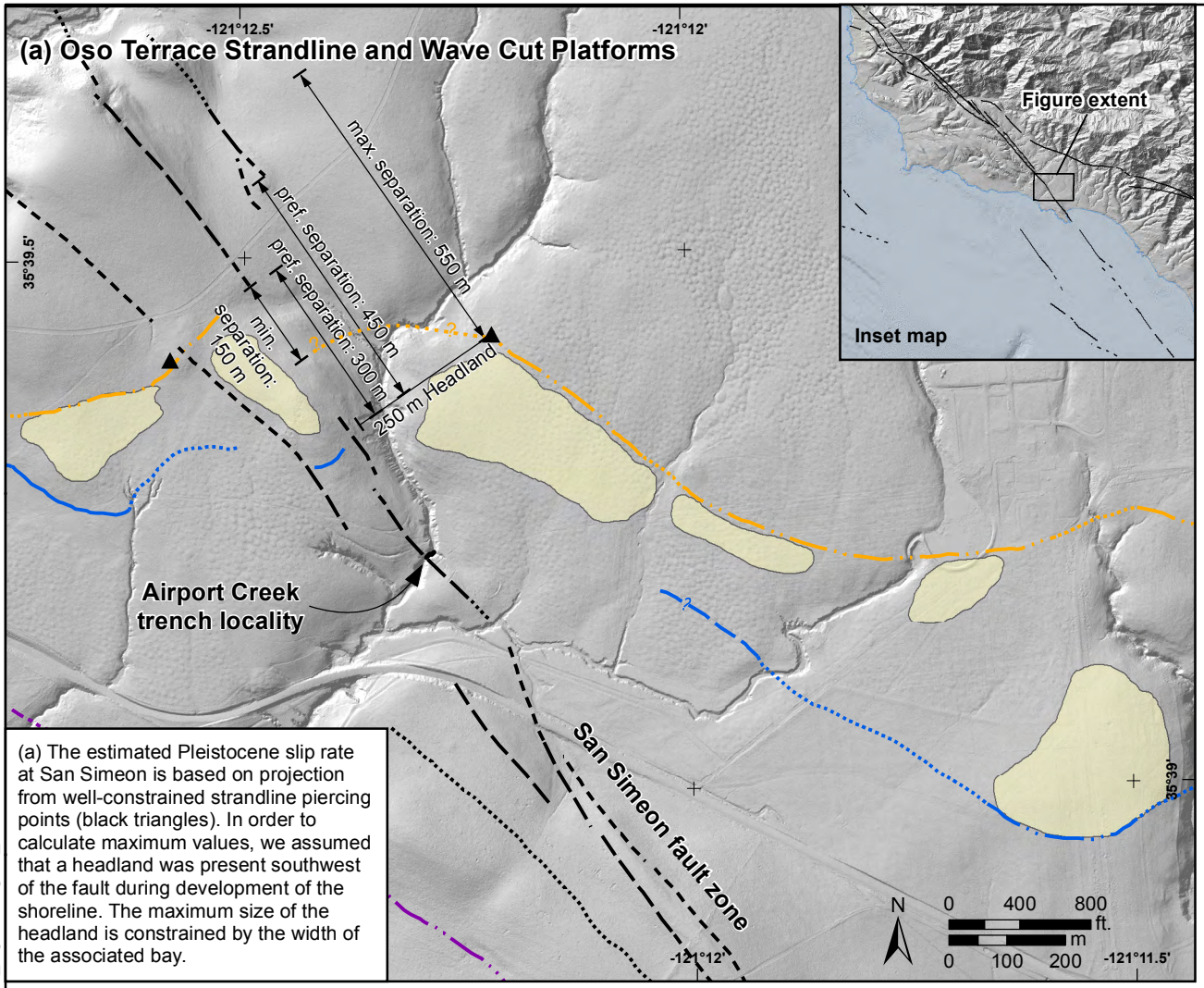

(a) The estimated Pleistocene slip rate at San Simeon is based on projection from well-constrained strandline piercing points (black triangles). In order to calculate maximum values, we assumed that a headland was present southwest of the fault during development of the shoreline. The maximum size of the headland is constrained by the width of the associated bay.

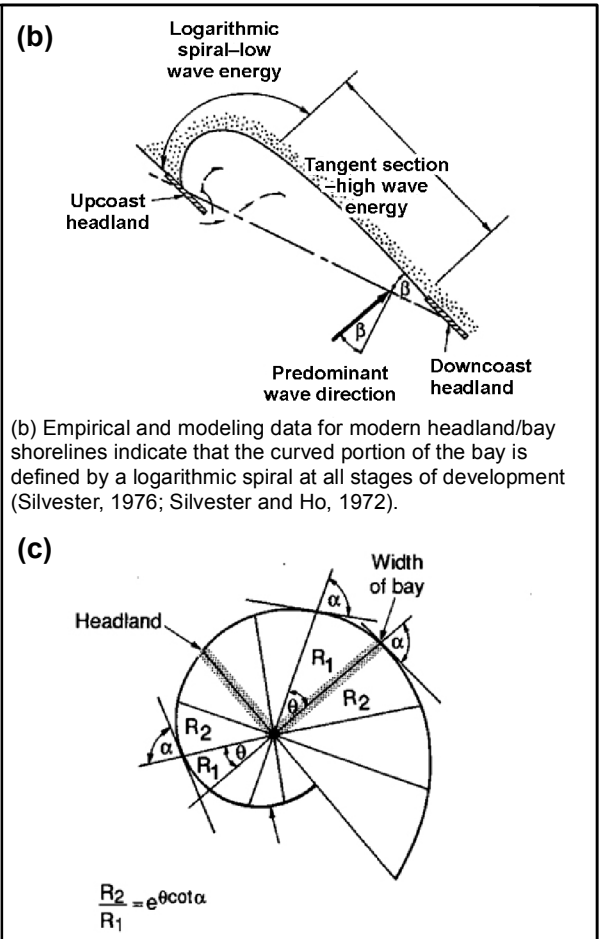

(b) Empirical and modeling data for modern headland/bay shorelines indicate that the curved portion of the bay is defined by a logarithmic spiral at all stages of development (Silvester, 1976; Silvester and Ho, 1972).

(c) Yasso (1965) noted that the center of the best-fit log spiral is near the headland and that the radius (R) of the curvature increases with distance from the headland. Thus, the length of a headland generally will not exceed the width of the bay.

EXPLANATION

Fault from Hanson and Lettis (1994); solid where location certain, dashed where approximate, short dashed where concealed, dotted where inferred

Strandline

Oso Terrace (MIS 7)

Tripod Terrace (MIS 5e)

San Simeon Terrace (MIS 5a)

Marine terrace platform

Piercing point

Note: Strandlines are solid where well located, dotted where eroded, double dotted and dashed where buried or less well located, dashed and queried where existence is uncertain.

Source: Hanson and Lettis (1994).

Map of Oso Terrace Strandline and Offset Projections

DCPP SSC REPORT

Pacific Gas and Electric Company

Figure **8-14**

File path: S:\1005\005\Final_Report_Figures\Figure_800-14.mxd; Date: 03/11/2015; User: Alex Remar, LCI; Rev.1

(a) West of San Simeon Fault

(b) East of San Simeon Fault

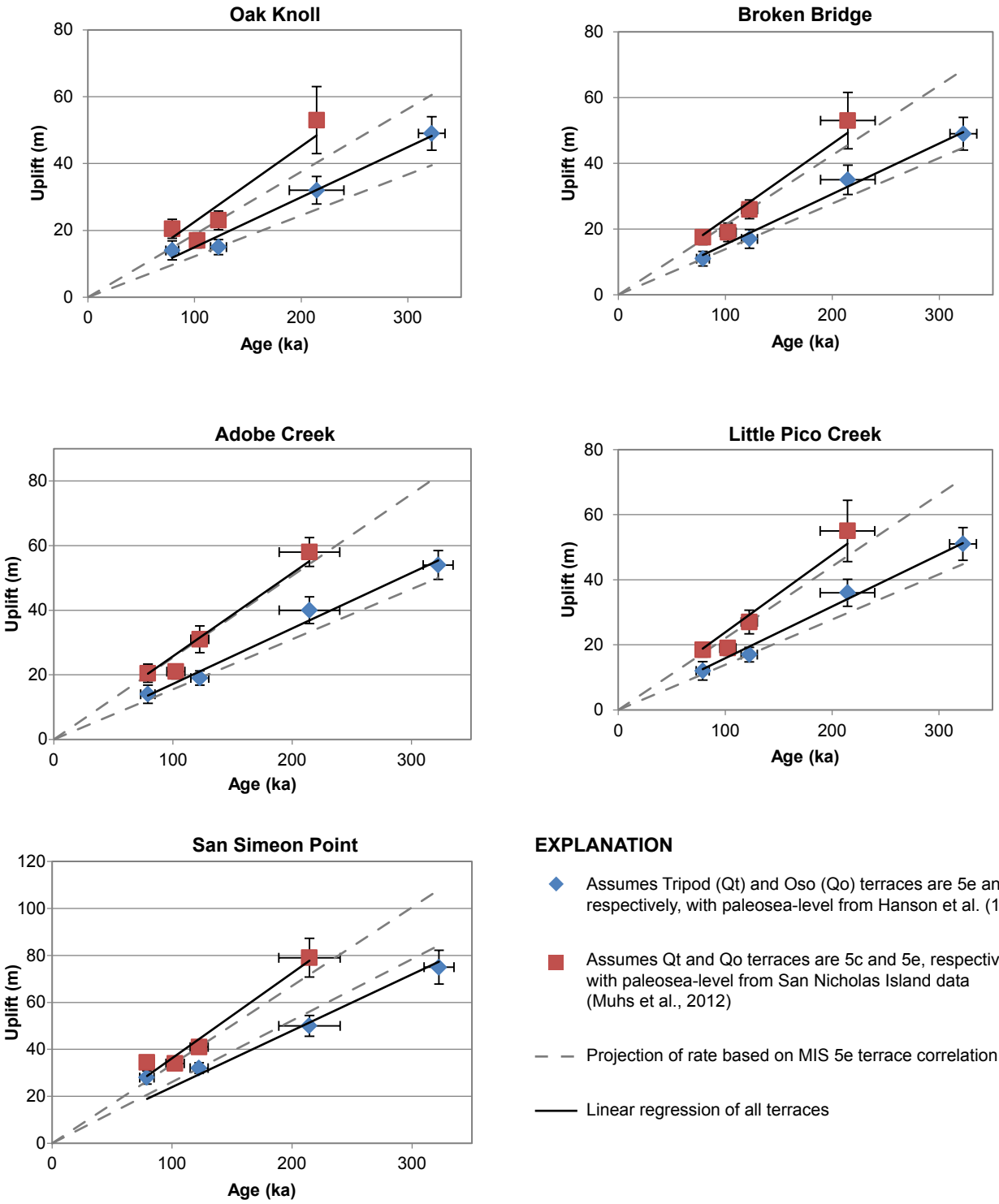

EXPLANATION

- ◆ Assumes Tripod (Qt) and Oso (Qo) terraces are 5e and 7, respectively, with paleosea-level from Hanson et al. (1994)
- ■ Assumes Qt and Qo terraces are 5c and 5e, respectively, with paleosea-level from San Nicholas Island data (Muhs et al., 2012)
- – – Projection of rate based on MIS 5e terrace correlation
- —— Linear regression of all terraces

Note: Terrace elevation data is from Hanson et al. (1994); marine isotope stage ages used to develop plots are MIS 5a (79 ± 6 ka), MIS 5c (102.5 ± 7.5 ka), MIS 5e (122.5 ± 7.5), MIS 7 (214.5 ± 25.5 ka), and MIS 9 (322.5 ± 12.5 ka).

Sources:
- Hanson et al. (1994).
- Muhs et al. (2012).

Alternative Correlations and Paleosea-Level Models Used to Evaluate Ages of San Simeon Marine Terraces

DCPP SSC REPORT

Pacific Gas and Electric Company

Figure **8-15**

File path: S:\1005\005\Final_Report_Figures\Figure_800-15.ai; Date: 02/23/2015; User: Alex Remar, LCI; Rev.1

(a) Offset PDF

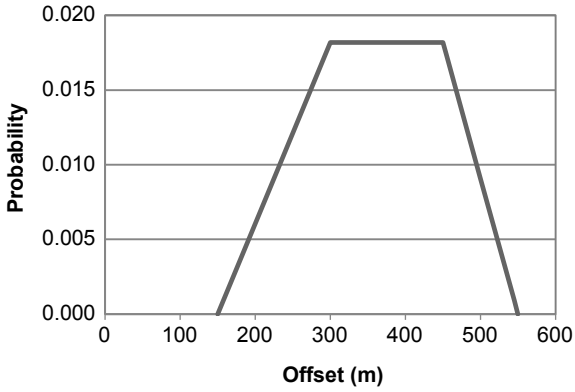

(b) Justification for Offset PDF

Value	Offset (m)	Basis
Min.	150	Uncertainty in the projection of the terrace back edge and the shape and size of the paleoheadland present during terrace formation
Preferred	300	Current separation of two piercing points on either side of the HFZ
Preferred	450	Apparent piercing point offset and presence of assumed small headland
Max.	550	Uncertainty in the projection of the terrace back edge and the shape and size of the paleoheadland present during terrace formation

(c) Age PDF

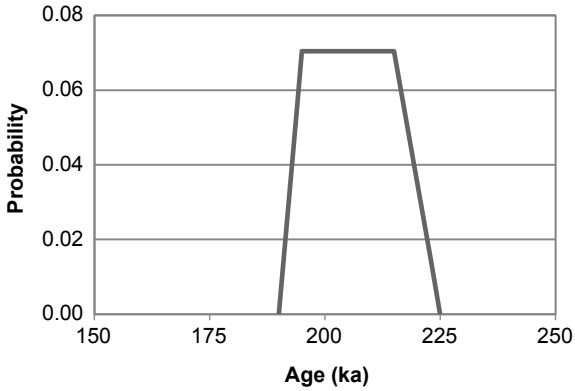

(d) Justification for Age PDF

Value	Age (ka)	Basis
Min.	190	Youngest substage highstand within MIS 7 (Compton, 2011)
Preferred	195	Inferred MIS 7 age of the terrace (Hanson and Lettis, 1994)
Preferred	215	
Max.	225	Oldest substage highstand within MIS 7 (Compton, 2011)

(e) Slip Rate CDF

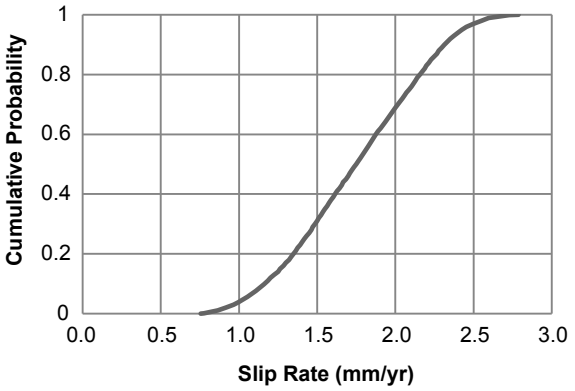

(f) Summary Statistics

Cumulative Probability	Slip Rate (mm/yr)
0.05	1.0
0.1	1.2
0.2	1.4
0.5	1.8
0.8	2.2
0.9	2.3
0.95	2.4
Min.	0.7
Max.	2.8
Mean	**1.8**

Note: Probability distributions used to describe uncertainty in offset (Panels (a) and (b)) and age (Panels (c) and (d)) of the Oso Terrace strandline, and used by the TI Team to calculate a slip rate CDF for the HFZ at San Simeon.

Oso Terrace:
Offset and Age PDFs, CDF, and Summary Statistics for San Simeon Slip Rate

DCPP SSC REPORT

Pacific Gas and Electric Company

Figure **8-16**

File path: S:\1005\005\Final_Report\Figures\Figure_800-16.ai; Date: 02/19/2015; User: Alex Remar, LCi; Rev.1

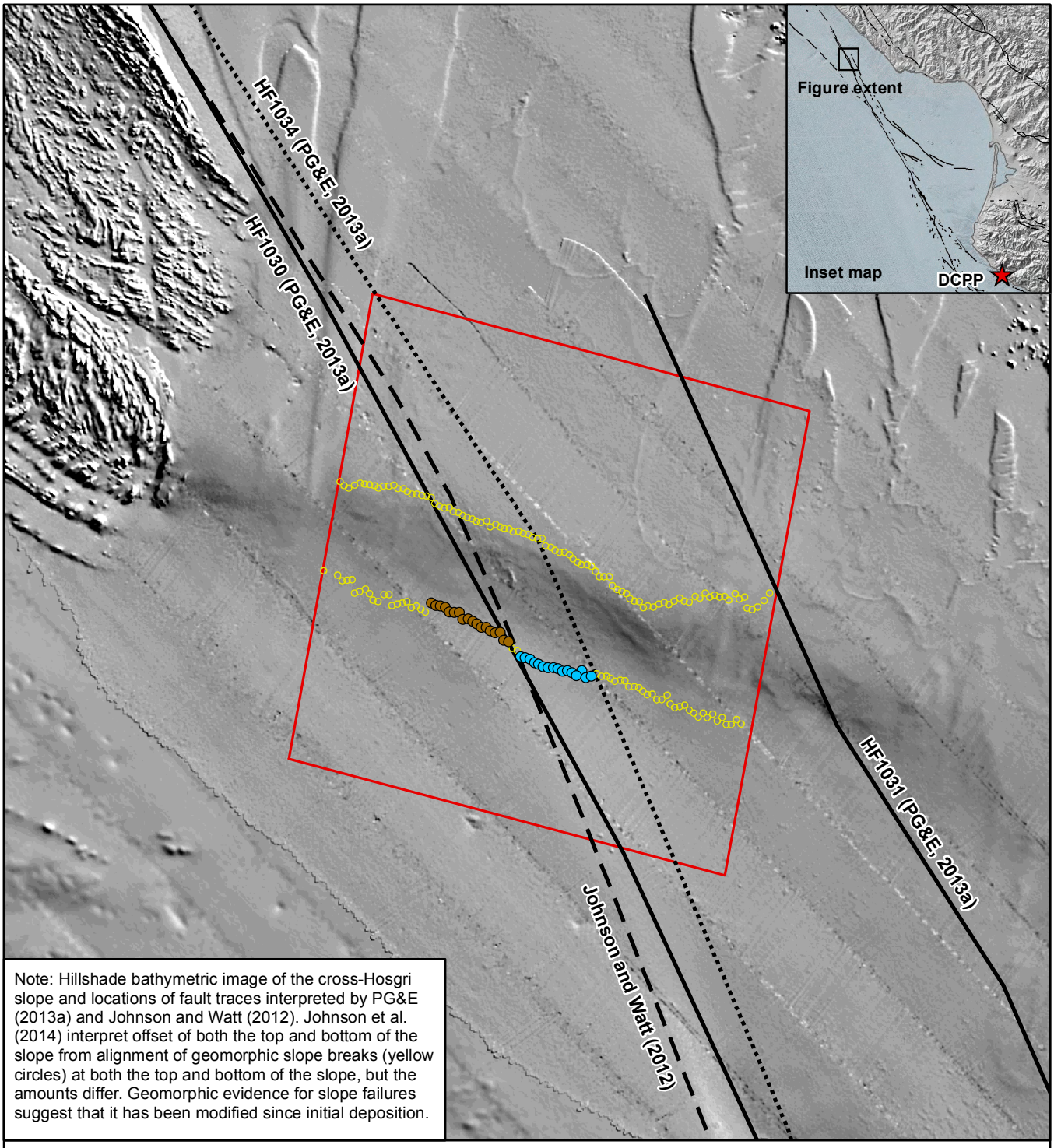

Note: Hillshade bathymetric image of the cross-Hosgri slope and locations of fault traces interpreted by PG&E (2013a) and Johnson and Watt (2012). Johnson et al. (2014) interpret offset of both the top and bottom of the slope from alignment of geomorphic slope breaks (yellow circles) at both the top and bottom of the slope, but the amounts differ. Geomorphic evidence for slope failures suggest that it has been modified since initial deposition.

EXPLANATION

Geomorphic interpretation from Johnson et al. (2014)

- Slope break picks on bathymetric profiles
- Lower slope break picks linearly regressed west of the dashed HFZ trace
- Lower slope break picks linearly regressed east of the dashed HFZ trace
- Bathymetric profile extent

Faults

- HFZ trace (PG&E, 2013a): solid where well located, dotted where concealed
- HFZ trace (Johnson and Watt, 2012)

N

0 1,000 2,000 ft.

0 400 800 m

Map projection and scale: NAD 83 / UTM Zone 10N, 1:15,000

Map of the Cross-Hosgri Slope

DCPP SSC REPORT

Pacific Gas and Electric Company

Figure **8-17**

File path: S:\1005\005\Final_Report_Figures\Figure_800-17.mxd; Date: 03/11/2015; User: Serkan Bozkurt, LCI; Rev.1

(a) Offset PDF

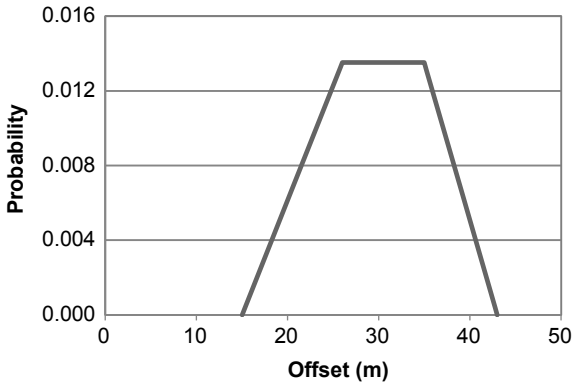

(b) Justification for Offset PDF

Value	Offset (m)	Basis
Min	15	~1% confidence limit
Preferred	26	Mean minus 1σ
Preferred	35	Mean plus 1σ
Max	43	~99% confidence limit reported in Johnson et al. (2014)

(c) Age PDF

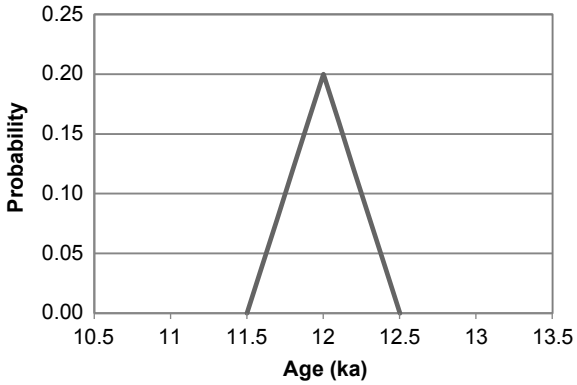

(d) Justification for Age PDF

Value	Age (ka)	Basis
Min	11.5	Age of Younger Dryas stadial reported by Johnson et al. (2014) is 12 ± 0.5 ka
Preferred	12	
Max	12.5	

(e) Slip Rate CDF

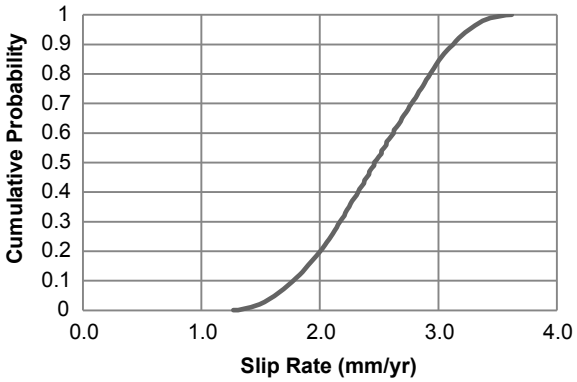

(f) Summary Statistics

Cumulative Probability	Slip Rate (mm/yr)
0.05	1.6
0.1	1.8
0.2	2.0
0.5	2.5
0.8	2.9
0.9	3.1
0.95	3.3
Min.	1.3
Max.	3.6
Mean	**2.5**

Notes:
- Probability distributions used to describe uncertainty in offset (Panels (a) and (b)) and age (Panels (c) and (d)) based on the descriptions provided in Johnson et al. (2014), and used by the TI Team to calculate a slip rate CDF for the HFZ at the cross-Hosgri slope.
- In Panel (b), offset of base of slope taken from Figure 12(b) of Johnson et al. (2014).

Cross-Hosgri Slope: Offset and Age PDFs, CDF, Summary Statistics, and Mean Slip Rate

DCPP SSC REPORT

Pacific Gas and Electric Company

Figure **8-18**

File path: S:\1005\005\Final_Report\Figures\Figure_800-18.ai; Date: 02/27/2015; User: Serkan Bozkurt, LCI; Rev.1

(a) Uninterpreted Profile Flattened to Seafloor

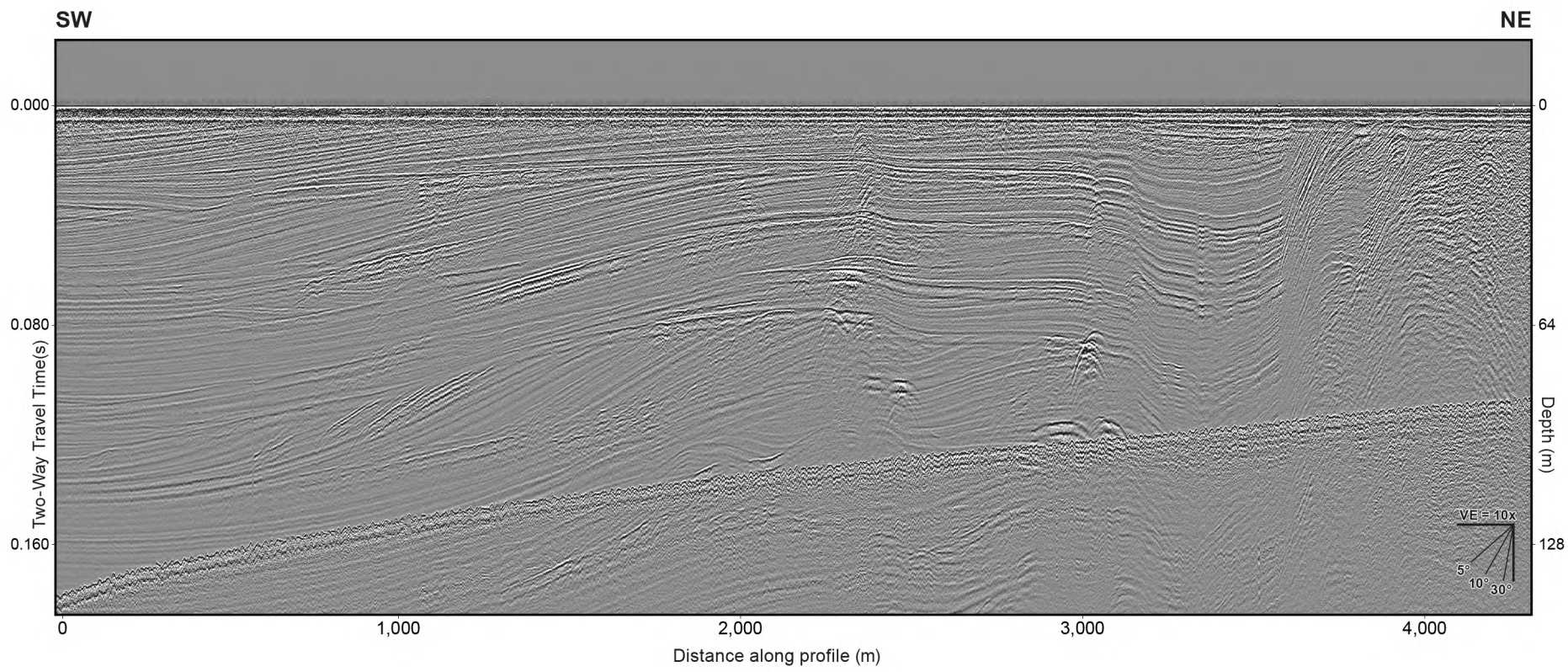

(b) Interpreted

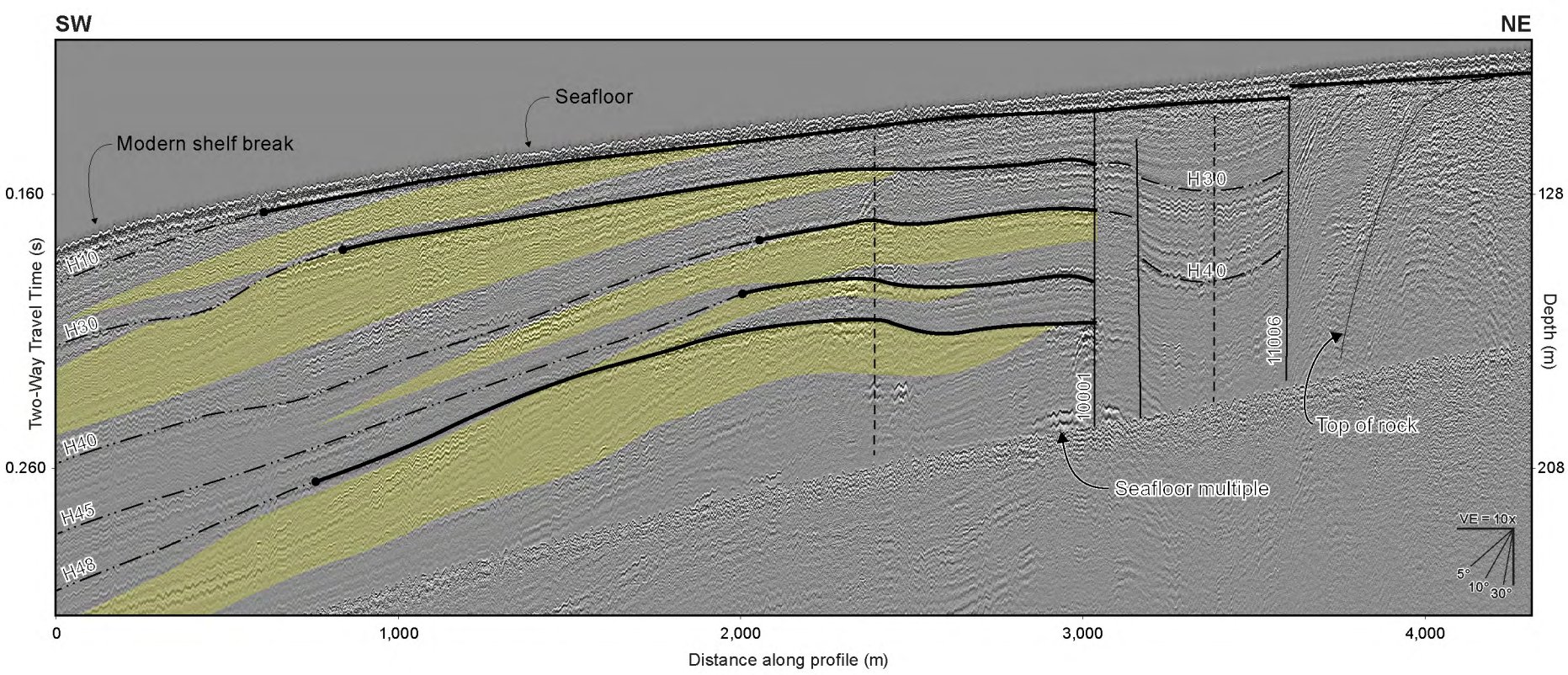

EXPLANATION

- Regional unconformities
- Fault: solid where well located, dashed where approximately located, dotted where inferred, queried where existence uncertain
- Top of shelf margin sedimentary prism, dot indicates approximate depth of lowstand
- Shelf margin sedimentary prisms
- Location of seismic profile
- PG&E 3D survey extent
- PG&E 2D survey trackline
- USGS survey trackline

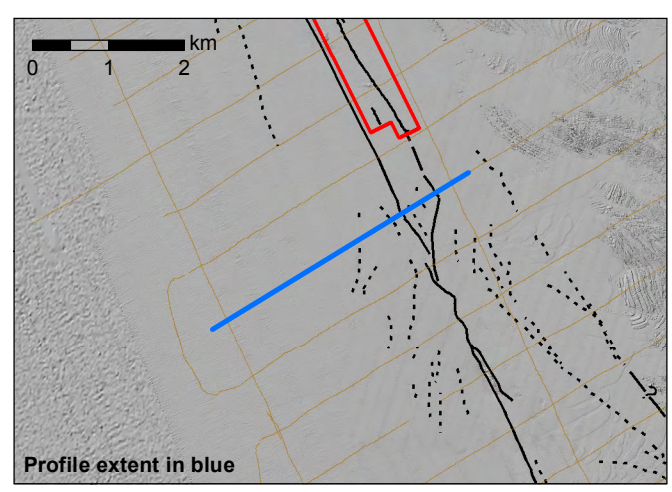

Notes:
- Distinctive sedimentary prisms are localized beneath the outer continental shelf (highlighted in yellow) that thin both landward and seaward and consist of seaward-sloping clinoforms. These are interpreted as the remnants of lowstand and highstand/regressive systems tracts. The erosive upper boundary of these prisms (heavy black lines) are interpreted as the most seaward parts of shelf-wide erosion surfaces developed during past sea-level transgressions. Black dots at the western ends of these surfaces mark the paleo-shelf breaks, the approximate positions of lowstand shorelines prior to the transgressions.
- Depth values on seismic profile assume a velocity of 1,600 m/s.

Sources:
- USGS seismic-reflection data (Sliter et al., 2010).
- 2D/3D seismic-reflection data from PG&E (2014, Chapters 2 and 3).

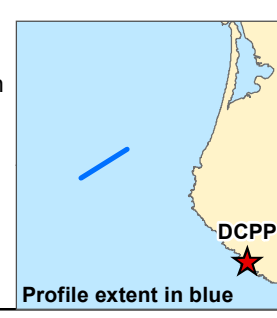

Excerpt of Profile PBS-34 Showing Regional Transgressive Unconformities and Sequence Stratigraphic Interpretation

DCPP SSC REPORT

Pacific Gas and Electric Company

Figure **8-19**

File path: S:\1005\005\Final_Report_Figures\Figure_800-19.mxd; Date: 03/11/2015; User: alex, LCI; Rev.1

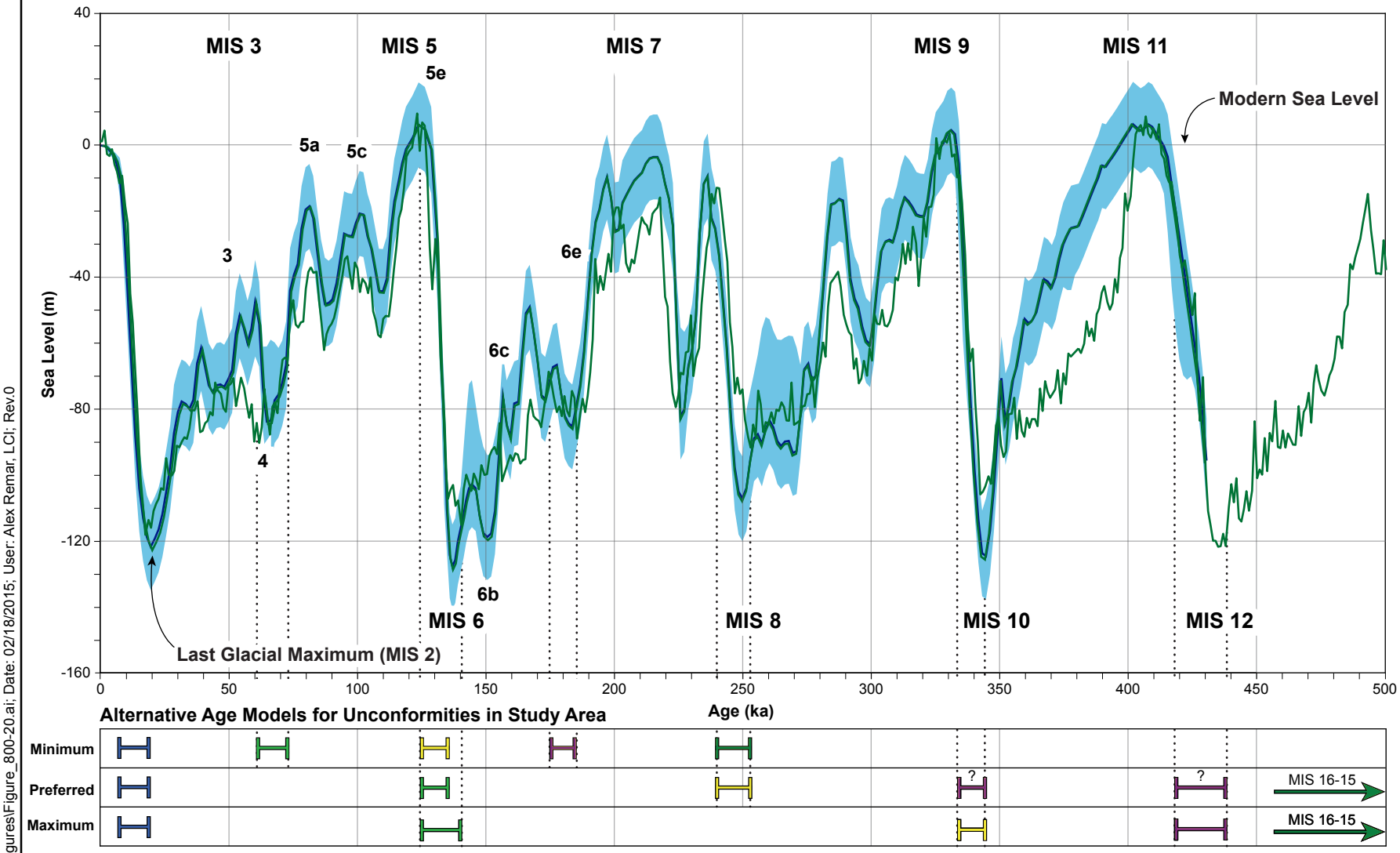

EXPLANATION

MIS Marine oxygen isotope stage

6c Marine oxygen isotope substage

Waelbroeck et al. (2002)

Lisiecki and Raymo (2005)

UNCONFORMITIES

H10 H30 H40 H45 H48

Notes:

- Waelbroeck et al. (2002) use regressions established from relative sea-level (RSL) coral terrace data and benthic foraminifera oxygen isotope data calibrated to sea temperature data from the North Atlantic and equatorial Pacific to create a composite RSL curve for past climatic cycles. Shaded region is confidence interval.
- Lisiecki and Raymo (2005) use 57 globally distributed $\delta^{18}O$ records to compile a 5.3 Myr record. Scaled to sea level by Carlson (2008).
- Uncertainty in the ages of regional unconformities H10, H30, H40, H45 and H48 is captured through alternative age models, which are developed from correlation to paleosea-level curves.

Age Model for Quaternary Unconformities

DCPP SSC REPORT

Pacific Gas and Electric Company

Figure **8-20**

File path: S:\1005\005\Final_Report\Figures\Figure_800-20.ai; Date: 02/18/2015; User: Alex Remar, LCI; Rev.0

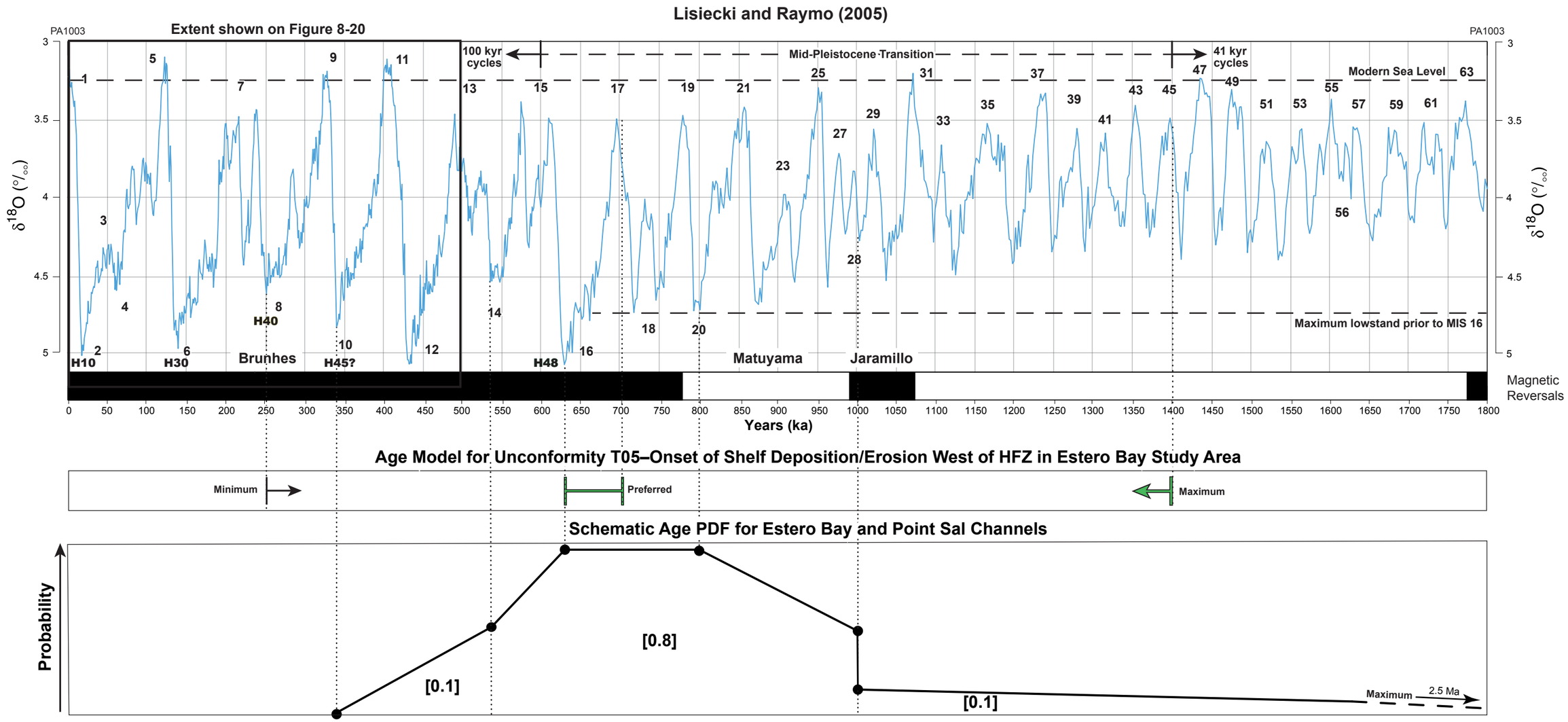

Notes:

- Uncertainty in the ages of buried channels at both Point Sal and Estero Bay is described by the PDF illustrated at the bottom of the figure. The channel age assessment is based on their stratigraphic position beneath unconformities H10, H30, H40, H45, and H45, and the recognition that they were abandoned prior to a significant episode of shelf widening. The preferred unconformity ages are shown adjacent to the sea level curve from Lisiecki and Raymo (2005) at the top of the figure. The most likely age of the channels is assessed from the interpretation that the episode of shelf widening resulted from an increase in amplitude of sea-level oscillations at the end of the mid-Pleistocene Transition.
- Lisiecki and Raymo (2005) use 57 globally distributed $\delta^{18}O$ records to compile a 5.3 Myr record of sea-level fluctuations.
- Timing of mid-Pleistocene Transition from Bintanja and van de Wal (2008).

Age Model for Unconformity T05 and Age Constraints on Channels in Estero Bay and Point Sal

DCPP SSC REPORT

Pacific Gas and Electric Company

Figure **8-21**

File path: S:\1005\005\Final_Report\Figures\Figure_800-21.ai; Date: 03/11/2015; User: Serkan Bozkurt, LCI; Rev.0

(a) Uninterpreted Profile Flattened to Seafloor

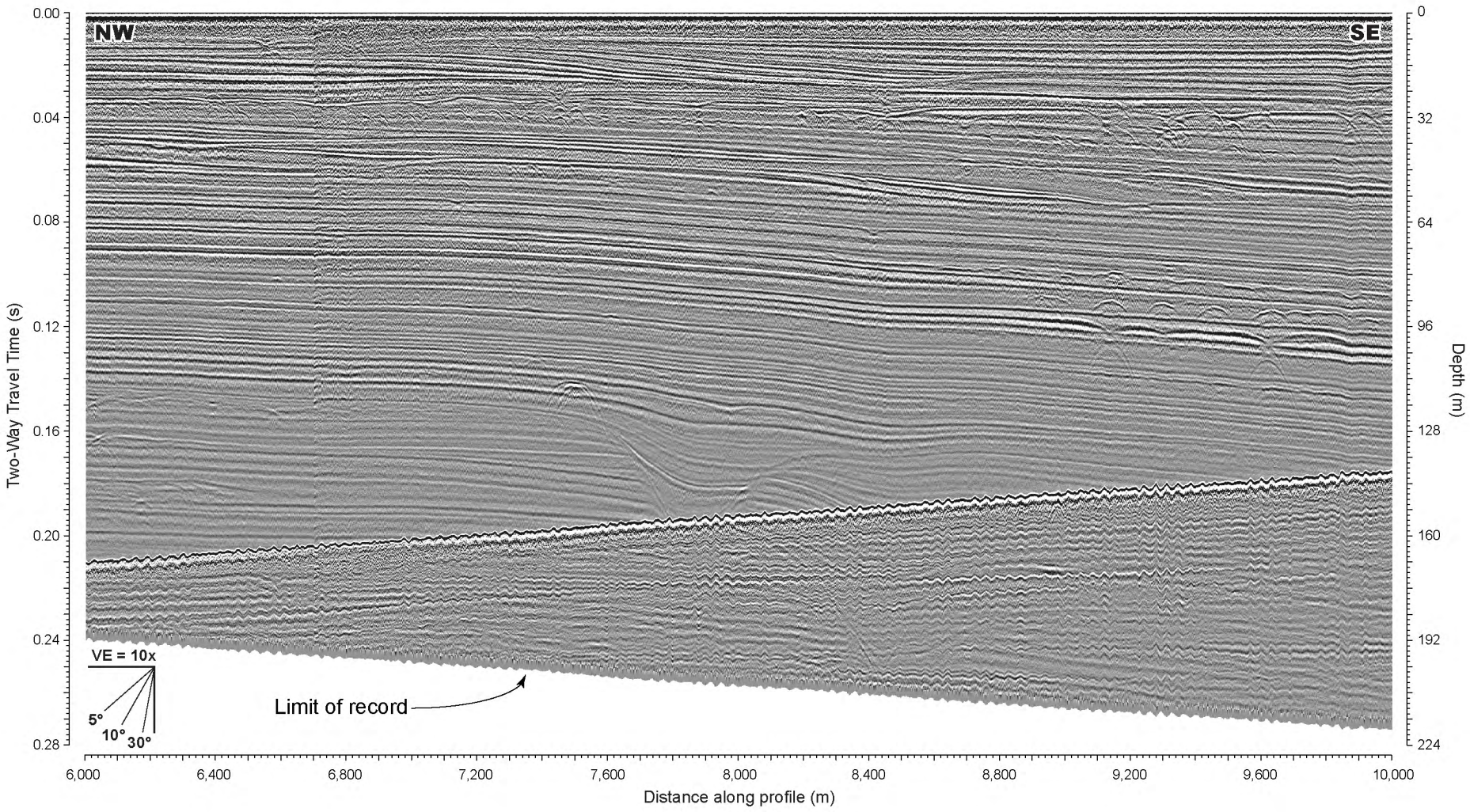

(b) Interpreted

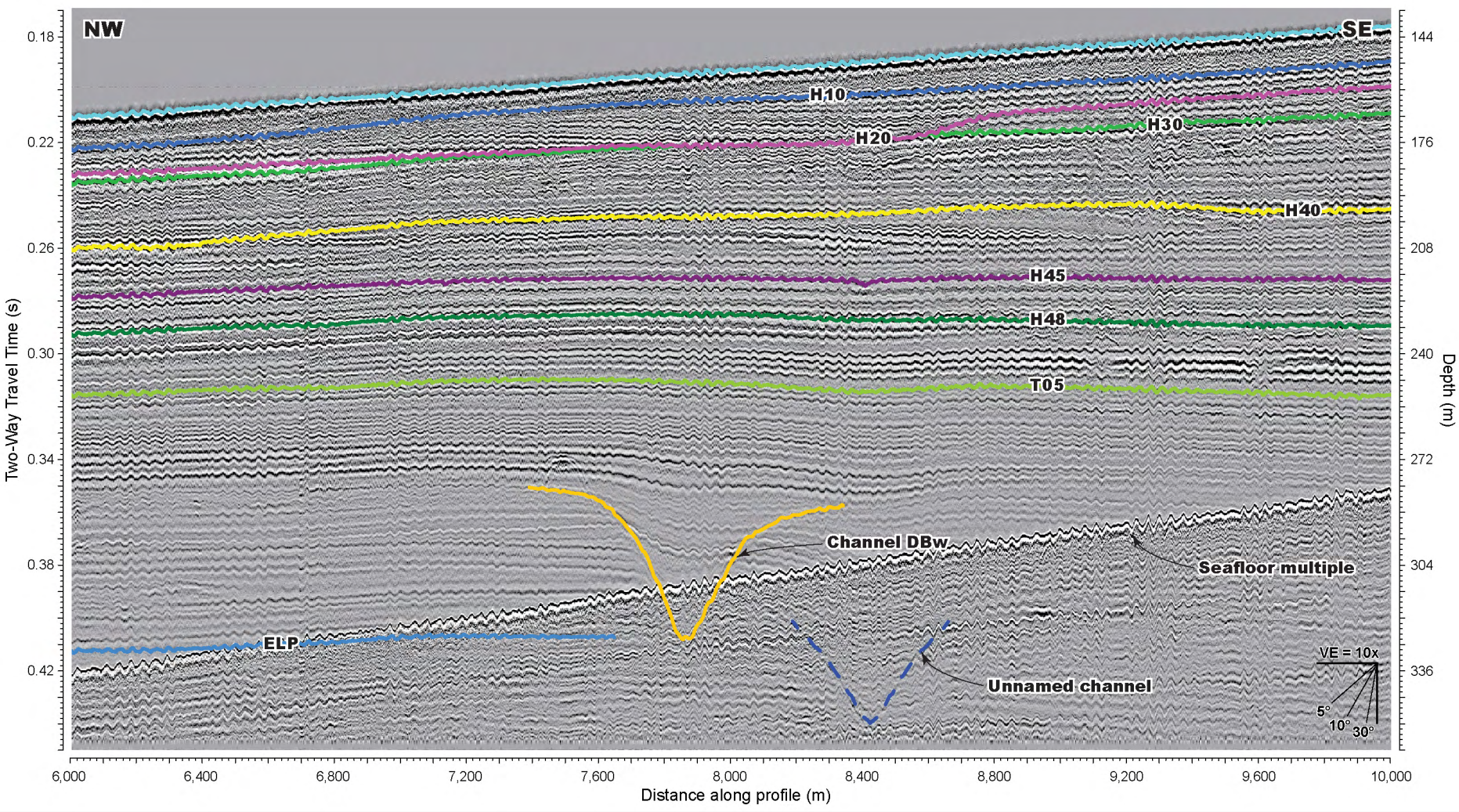

EXPLANATION

- Seafloor
- Unconformity H10
- Unconformity H20
- Unconformity H30
- Unconformity H40
- Unconformity H45
- Unconformity H48
- Unconformity T05
- Unconformity ELP
- Channel DBw
- Unnamed channels; approximately located
- Fault, solid where well located, dashed where approximately located, dotted where inferred
- Location of seismic profile
- PG&E 3D survey extent

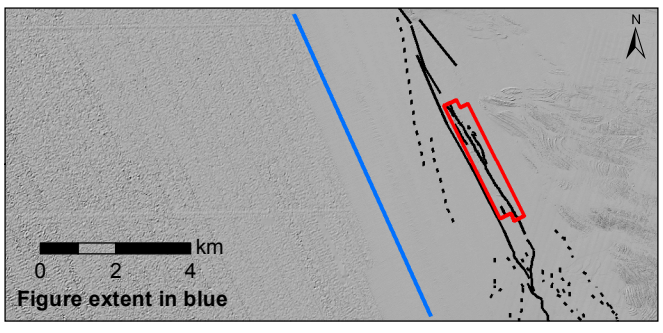

Notes:
- The age of channel DBw in Estero Bay is constrained to be older than unconformity T05, which separates a shelf margin depositional sequence punctuated by unconformities H10, H30, H40, H45, and H48 from relatively uniform strata of the upper continental slope. The channel is younger than the early-late Pliocene unconformity (ELP), which was interpreted by Willingham et al. (2013) to be between 2.8 and 3.5 Ma.
- Channels recognized by V-shaped truncations underlying reflections, and by "sagging" reflections of channel fill.
- Depth values on seismic profile assume a seismic velocity of 1,600 m/s.

Source: USGS seismic-reflection data (Sliter et al., 2010).

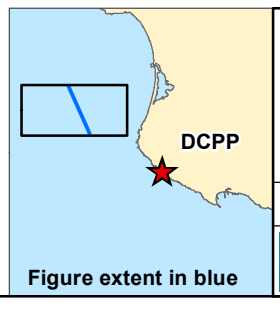

Excerpt of Profile PBS-T2 Showing Channels Deep in Stratigraphy West of the HFZ in Estero Bay

DCPP SSC REPORT

Pacific Gas and Electric Company

Figure **8-22**

File path: S:\1005\005\Final_Report_Figures\Figure_800-22.mxd; Date: 03/11/2015; User: Alex Remar, LCI; Rev.1

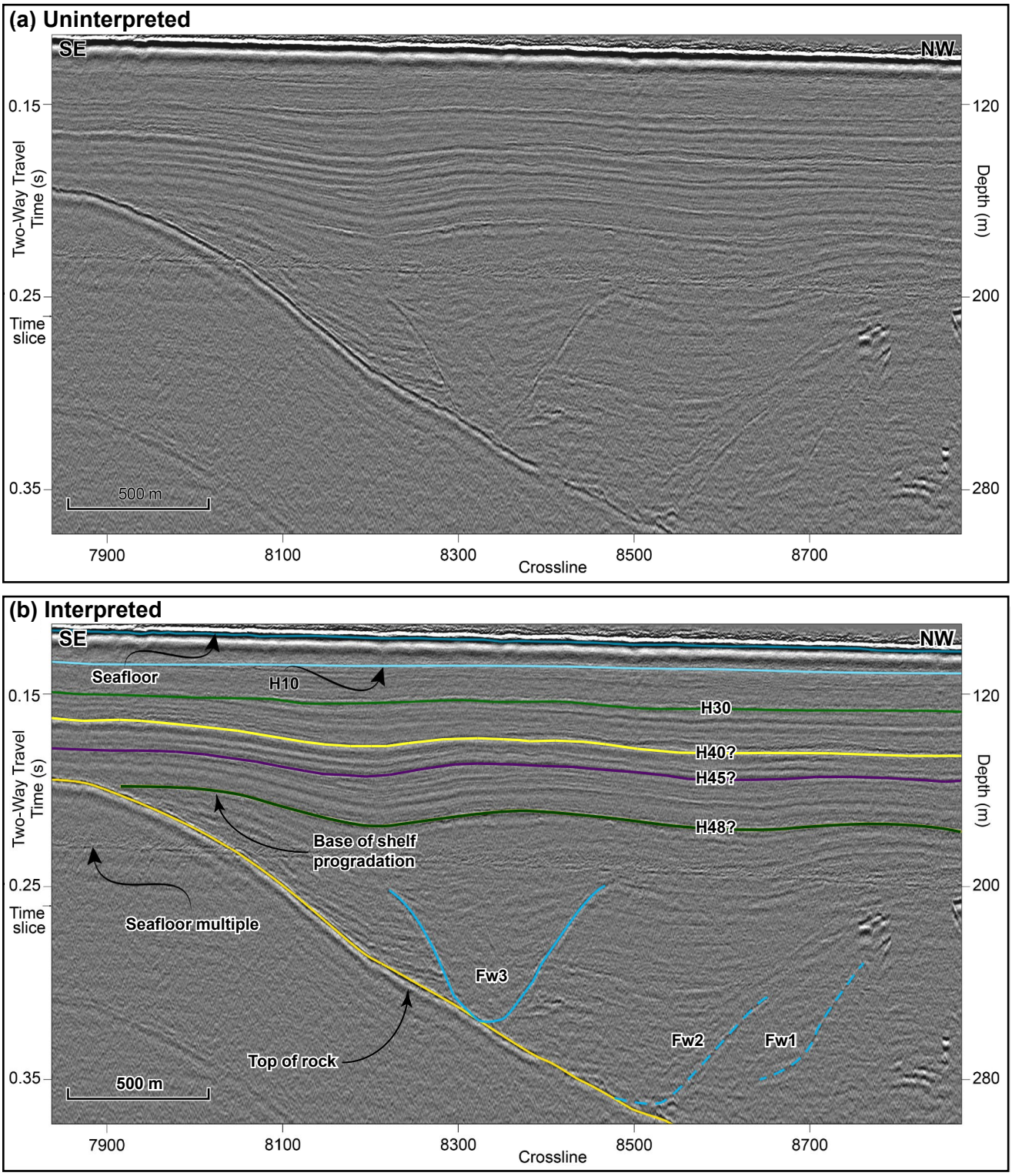

EXPLANATION

- Seafloor
- Unconformity H10
- Unconformity H30
- Unconformity H40
- Unconformity H45
- Unconformity H48
- Top of rock
- Channel F margin
- 2012 Point Sal 3D high-resolution survey extent

Note: The ages of Channels Fw1, Fw2, and Fw3 at the Point Sal study area are all constrained to be older than unconformity H48 and younger than the erosional top of rock, which was interpreted by PG&E (2014, Chapter 3) to be up to 2.5 Ma.

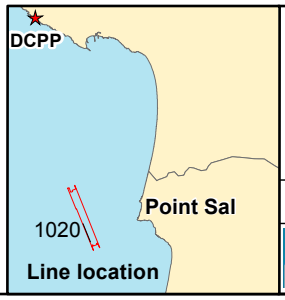

Excerpt of Line 1020 Showing Channel F West of the HFZ in the Point Sal Study Area

DCPP SSC Report

Pacific Gas and Electric Company

Figure **8-23**

File path: S:\1005\005\Final_Report\Figures\Figure_800-23.ai; Date: 02/07/2015; User: Alex Remar, LCI; Rev.1

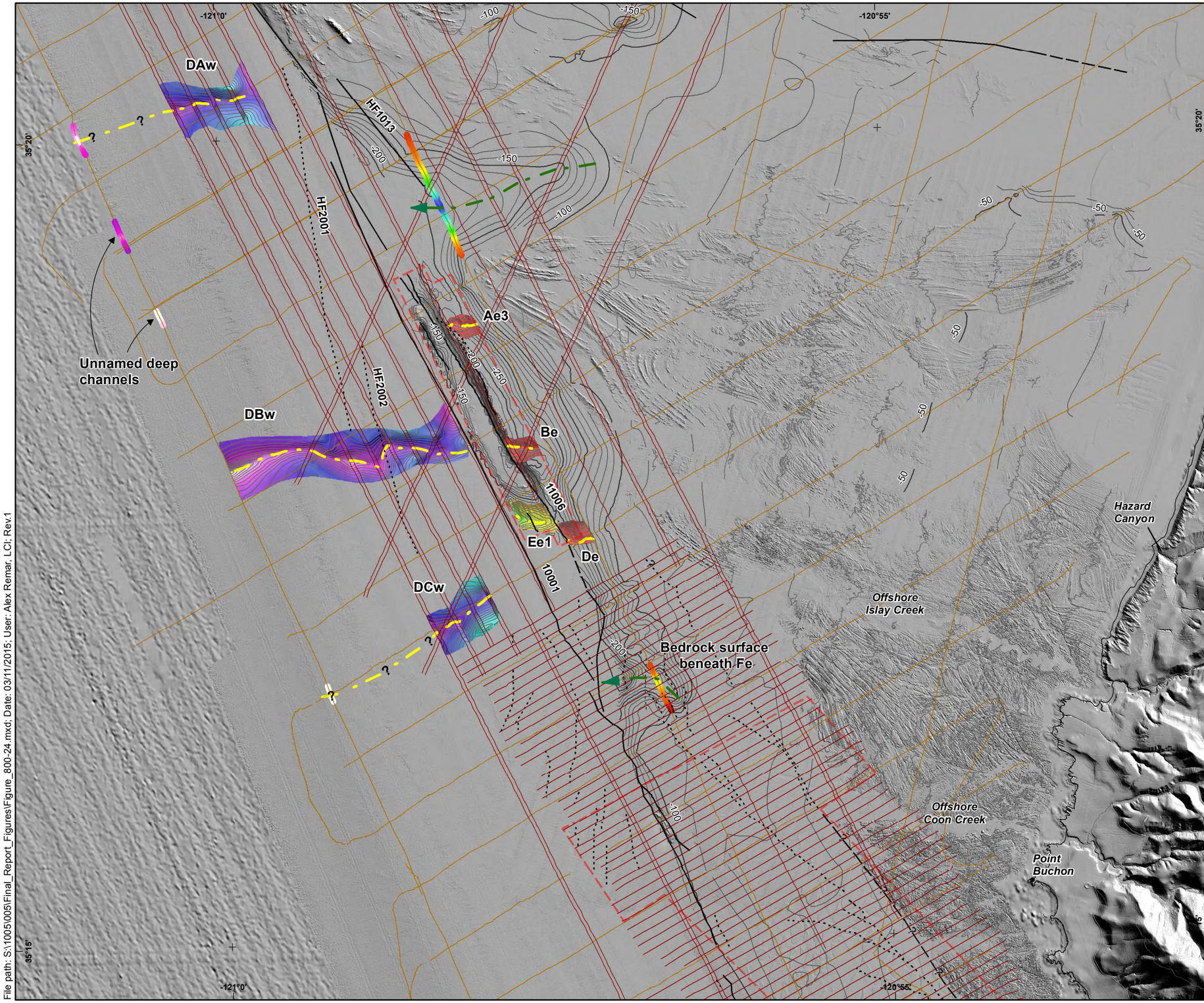

EXPLANATION

- Fault, solid where well located, dashed where approximately located, dotted where inferred, queried where existence uncertain (from Plate 7-1)
- Slope channel thalweg mapped from seismic-reflection data
- Approximate direction of slope channel inferred from contours on top of pre-Quaternary rock
- Structure contours on bedrock surface are on 10 m intervals, heavy contours are 50 m
- USGS 2D survey trackline
- PG&E 2D survey trackline
- PG&E 3D survey extent

Channel Depth

130 ms (~100 m)

440 ms (~350 m)

Notes:
- Dextral separation of the buried Channel DBw-Ee1-De across strands of the HFZ is assessed from (1) uncertainty in the projection of channel thalwegs from the nearest well-imaged location, (2) consideration of possible tectonic deflection of Channel Ee1 east of fault 10001, and (3) consideration of evidence for two alternative upstream locations of Channel DBw west of fault 10001.
- See Figure 8-13 for location of study area.
- Contours within channels mapped from seismic data are on 5 ms intervals.

Source: Modified from PG&E (2014, Chapter 3).

N

0 0.5 1 mi.

0 1 2 km

Map projection and scale: WGS 84 / UTM Zone 10N, 1:45,000

Map of Channels, Faults, and Bedrock Surface on Shelf, Estero Bay Study Area

DCPP SSC REPORT

Pacific Gas and Electric Company

Figure **8-24**

File path: S:\10005\005\Final_Report_Figures\Figure_800-24.mxd; Date: 03/11/2015; User: Alex Remar, LCI; Rev.1

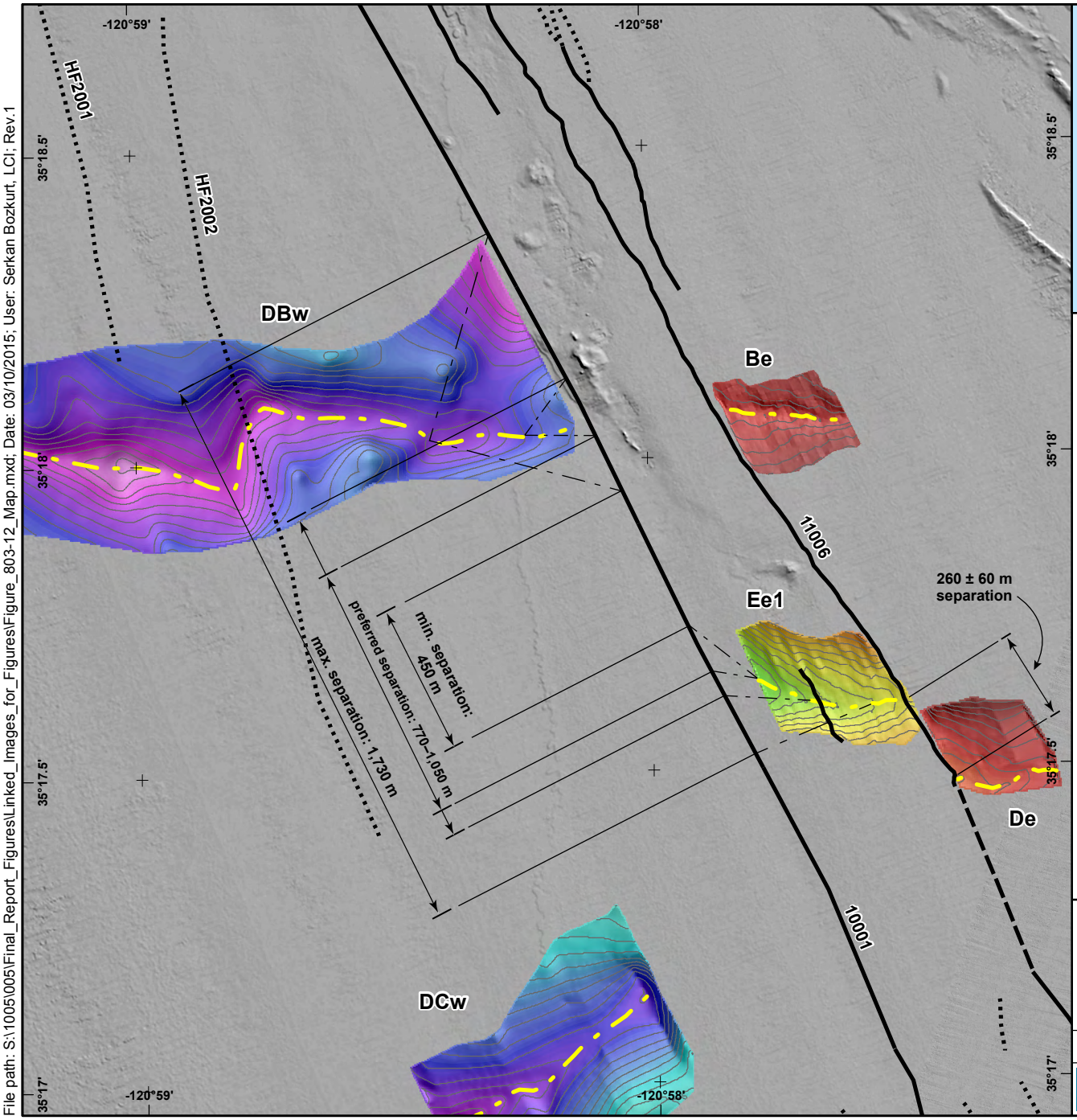

EXPLANATION

Fault, solid where well located, dashed where approximately located, dotted where inferred

Interpreted Thalwegs

Slope channel thalweg mapped from seismic–reflection data

Alternative thalweg projection

Channel Depth

130 ms (~100 m)

440 ms (~350 m)

Notes:
- Dextral separation of the buried Channel DBw-Ee1-De across strands of the HFZ is assessed from (1) uncertainty in the projection of channel thalwegs from the nearest well-imaged location, (2) consideration of possible tectonic deflection of Channel Ee1 east of fault 10001, and (3) consideration of evidence for two alternative upstream locations of Channel DBw west of fault 10001.
- See Figure 8-13 for location of study area.
- Contours within channels mapped from seismic data are on 5 ms intervals.

Source: Modified from PG&E (2014, Chapter 3).

N

0 1,000 2,000 ft.

0 400 800 m

Map projection and scale: WGS 84 / UTM 10N, 1:18,000

Estero Bay: Piercing Point DBw-Ee1-De Separation and Uncertainty

DCPP SSC REPORT

Pacific Gas and Electric Company

Figure **8-25**

File path: S:\1005\005\Final_Report_Figures\Linked_Images_for_Figures\Figure_803-12_Map.mxd; Date: 03/10/2015; User: Serkan Bozkurt, LCI; Rev.1

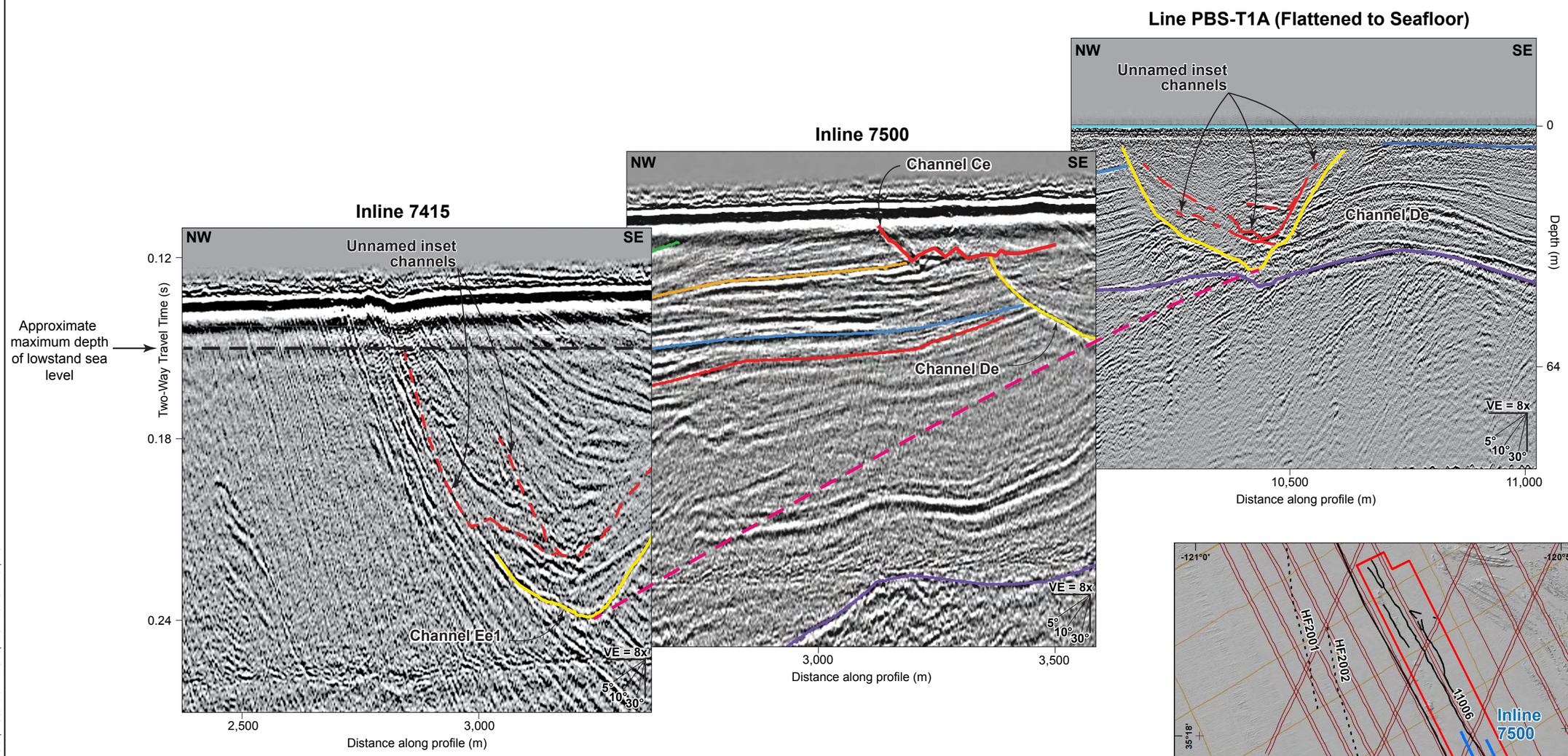

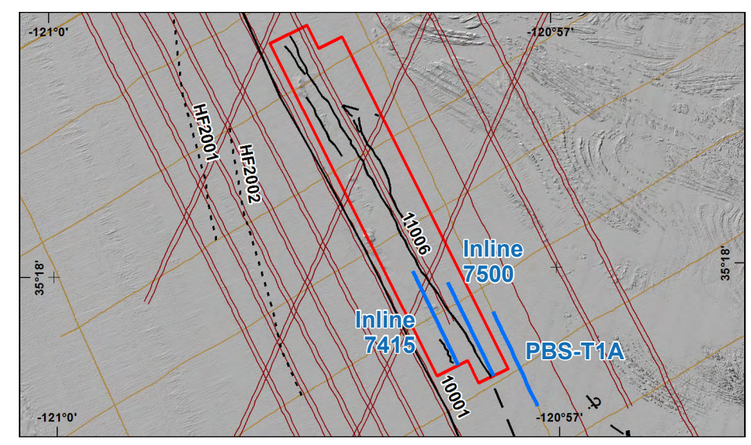

EXPLANATION

- Seafloor
- Unconformity H10
- Unconformity T30
- Unconformity T50
- Unconformity T70
- Top of pre-Quaternary rock
- Channel De, Channel Ee
- Unnamed inset channels
- Fault, solid where well located, dashed where approximately located, dotted where inferred, queried where existence uncertain
- Location of seismic profile
- PG&E 3D survey extent
- PG&E 2D survey trackline
- USGS survey trackline
- Channel thalweg correlation

Notes:
- Seismic images from the 2D USGS sparker data (right panel) and the 3D seismic-reflection volume (two left panels) illustrate the similarity in size and width of two correlative channel segments: Channel De, east of the HFZ, and Channel Ee1, between strands of the HFZ. The channel is incised too deeply to be a lowstand channel that traversed the continental shelf, and therefore, it must have been graded to greater depths on the continental slope. Channel Ce (central panel) crosscuts Channel De adjacent to the fault at shallow depth, suggesting that Channel Ce may have originated later as a subaerial lowstand channel. No traces of Channel Ce were found west of the HFZ.
- See Figure 8-13 for location of study area.
- Depth values on seismic profile assume a velocity of 1,600 m/s.
- Unnamed inset channels are not correlated between the three profiles illustrated due to gaps in data coverage.
- All profiles displayed at 8x vertical exaggeration.

Source: Modified from PG&E (2014, Chapter 3).

N
0 0.5 1 mi.
0 1 2 km

Map scale: 1:54,000
Map projection: WGS 84 / UTM Zone 10N

Fence Diagram Showing Correlation of Channels De and Ee

DCPP SSC REPORT

Pacific Gas and Electric Company

Figure **8-26**

File path: S:\1005\005\Final_Report_Figures\Figure_800-26.ai; Date: 03/11/2015; Alex Remar: LCI; Rev.1

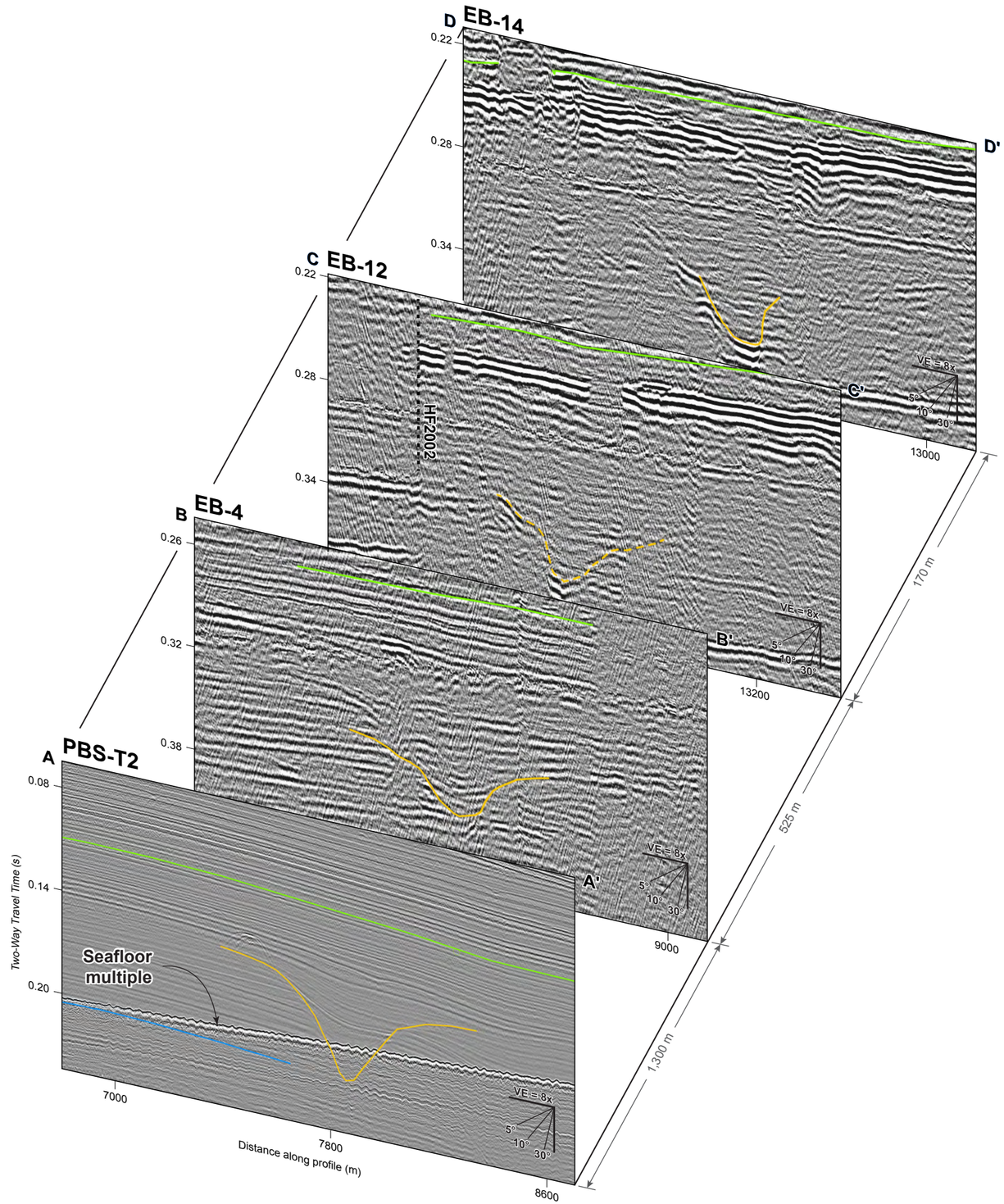

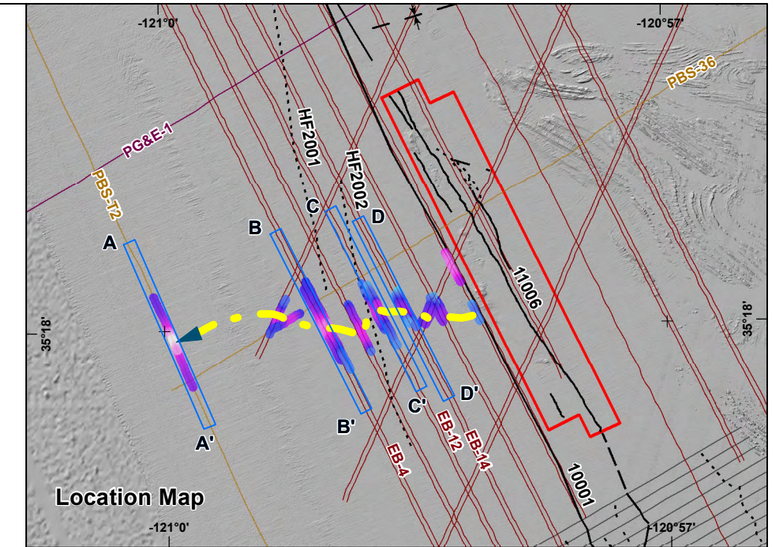

EXPLANATION

- Unconformity T05
- Unconformity ELP
- Channel DBw
- Location of seismic profile
- PG&E 3D survey extent
- PG&E 2D survey trackline
- USGS survey trackline
- PG&E deep crustal survey trackline
- Fault, solid where well located, dashed where approximately located, dotted where inferred, queried where existence uncertain
- Slope channel thalweg mapped from seismic-reflection data

Channel Depth

130 ms (~100 m)

440 ms (~350 m)

Notes:
- See Figure 8-13 for location of study area.
- Depth values on seismic profile assume a velocity of 1,600 m/s.
- USGS profile PBS-T2 is shown flattened to seafloor.
- All profiles displayed at 8x vertical exaggeration.
- The early-late Pliocene unconformity (ELP) was mapped regionally by Willingham et al. (2013). It is mapped onto USGS 2D profile PBS-T2 based on the direct intersection with line PG&E-1, which was the basis for section C-C' in Willingham et al. (2013).
- Excerpts of 2D profiles west of the fault show the variability in seismic imaging of Channel DBw west of the HFZ. Key stratigraphic markers that bracket Channel DBw and constrain its age are shown on the USGS sparker profile PBS-T2 (lower left frame).

Source: Modified from PG&E (2014, Chapter 3).

N 0 0.5 1 mi. 0 1 2 km

Map projection and scale: WGS 84 / UTM Zone 10N, 1:54,000

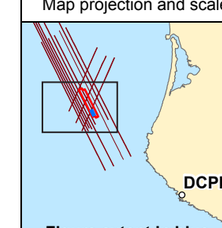

Figure extent in blue

Interpreted Fence Diagram Showing Channel DBw West of the HFZ

DCPP SSC REPORT

Pacific Gas and Electric Company

Figure **8-27**

File path: S:\1005\005\Final_Report_Figures\Figure_800-27.ai; Date: 03/11/2015; Serkan Bozkurt: LCI; Rev.1

(a) Offset PDF

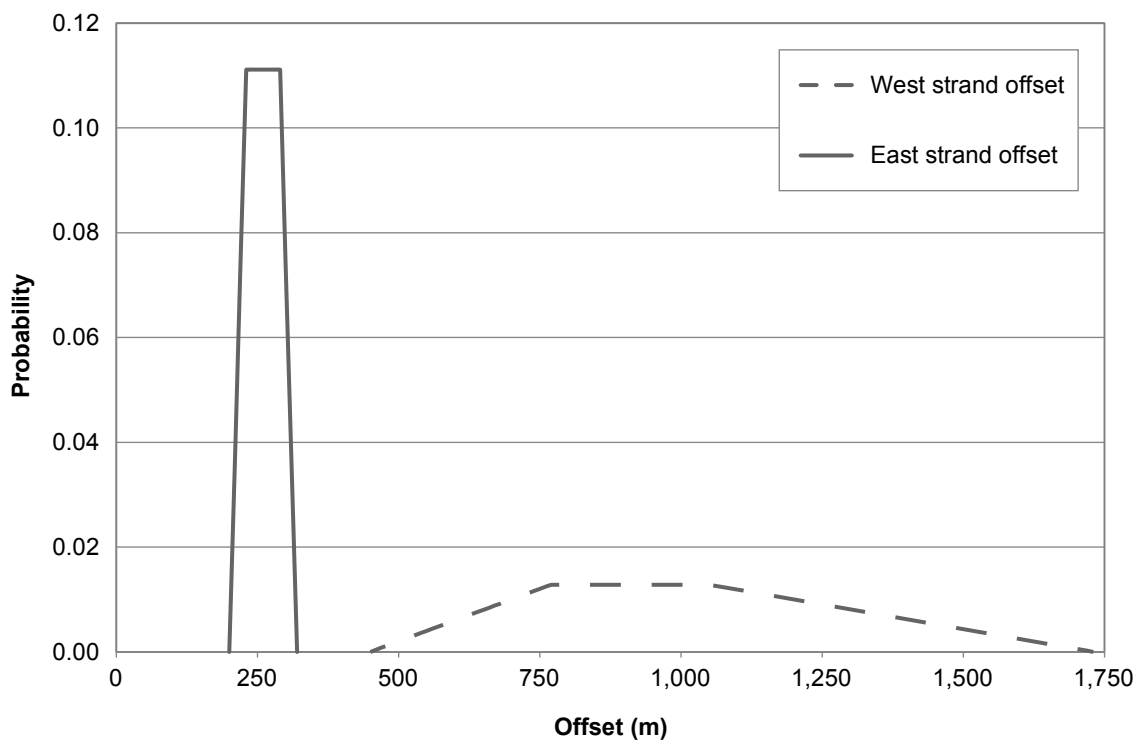

(b) Justification for offset PDF

Value	West Strand Offset (m)	Basis
Min.	450	South margin of the shallow channel-like feature and the limits of uncertainty in the projection of Channel Ee1
Preferred	770	Range estimated from direct projection of Channel Ee1 and margins of shallow channel-like feature west of fault 10001
Preferred	1,050	
Max.	1,730	North margin of the deep channel- like feature and the limits of uncertainty in the projection of Channel Ee1

Value	East Strand Offset (m)	Basis
Min.	200	Estimated from incorporating uncertainty in projections
Preferred	230	Range estimated from the direct projection of Channel Ee1 and De thalwegs
Preferred	290	
Max.	320	Estimated from incorporating uncertainty in projections

(c) Age PDF

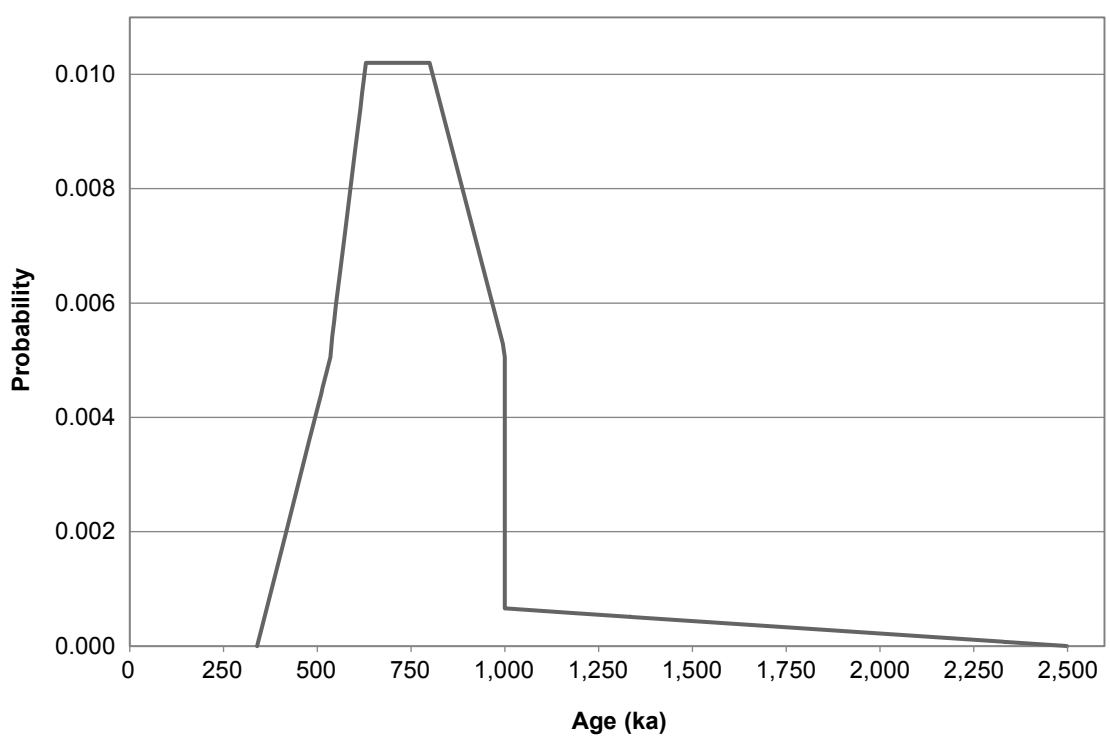

(d) Justification for Age PDF

Value	Age (ka)	Basis
Min	340	MIS 10; youngest age of overlying unconformity
Pref. Low End	535	MIS 14; ≥5 transgressive uncon. in strata above channel
Preferred	630	MIS 16; probable end of MPT
Preferred	800	MIS 20; shelf progradation deeper sea level during late stage MPT
Pref. High End	1,000	High end of uncertainty in shelf progadation
Max.	2,500	Max. age of NTN unconformity (PG&E, 2014 Chapter 3)

(e) Slip Rate CDF

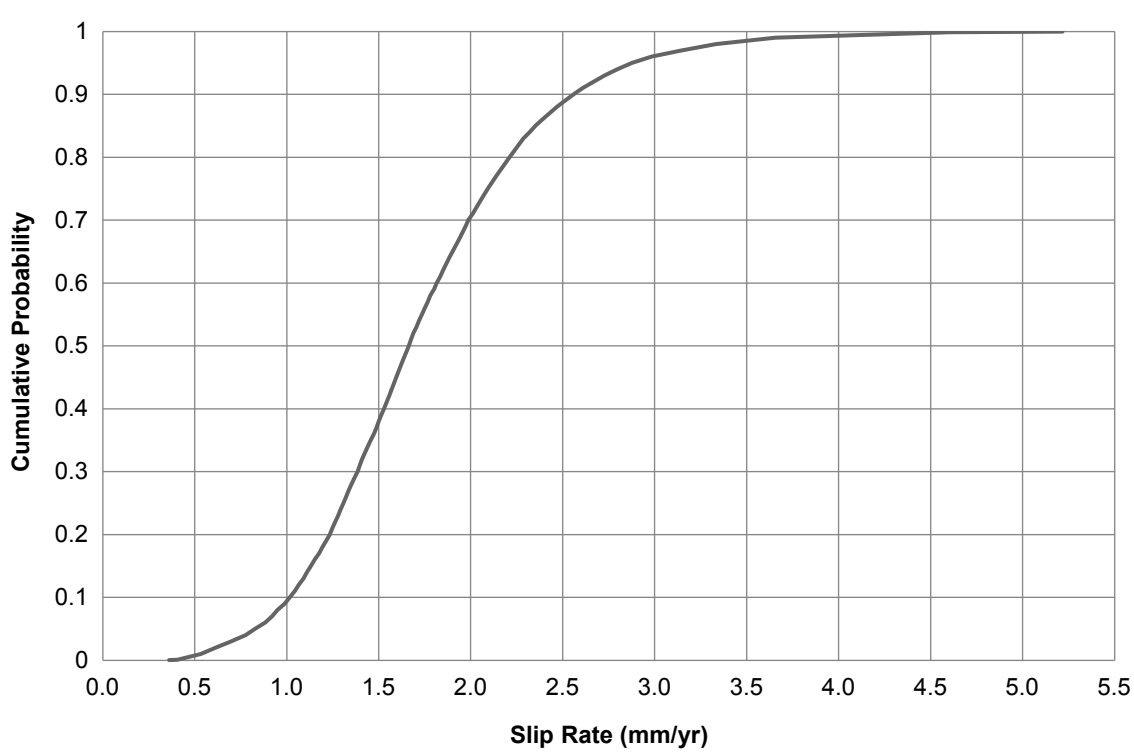

(f) Summary Statistics

Cumulative Probability	Slip Rate (mm/yr)
0.05	0.8
0.1	1.0
0.2	1.2
0.5	1.7
0.8	2.2
0.9	2.6
0.95	2.9
Minimum	0.3
Maximum	5.3
Mean	1.7

EXPLANATION

MPT: Mid-Pleistocene Transition
NTN: Near-Top Neogene unconformity

Note: Probability distributions used to describe uncertainty in offset (Panels (a) and (b)) and age (Panels (c) and (d)) of the correlated Channel DBw-Ee1-De, and used by the TI Team to calculate a slip rate CDF for the HFZ in the Estero Bay study area (Panel (e)). Refer to Figure 8-21 for a more complete description of the justification for the age PDF.

Offset and Age PDFs, Slip Rate CDF, and Summary Statistics for Estero Bay Channels

DCPP SSC REPORT

Pacific Gas and Electric Company

Figure **8-28**

File path: S:\1005\005\Final_Report\Figures\Figure_800-28.ai; Date: 03/11/2015; User: Alex Remar, LCI; Rev.1

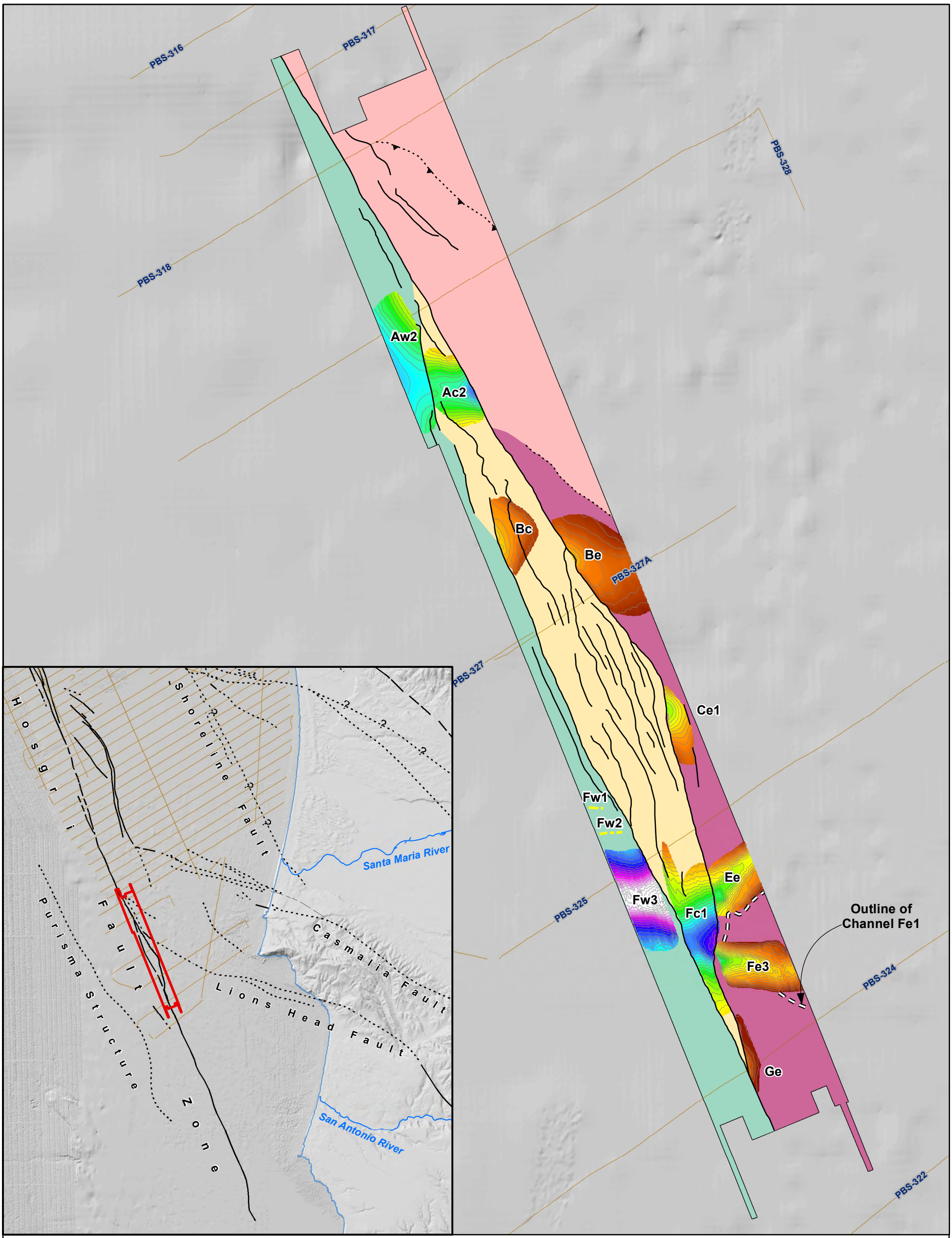

EXPLANATION

- Slope channel thalweg mapped from seismic-reflection data (locations approximate)
- USGS 2D survey trackline
- Fault, dashed where inferred, barbs on upthrown side of reverse fault
- Outline of Channel Fe1
- 2012 Point Sal 3D high-resolution survey extent
- Central Block
- Eastern Block South
- Eastern Block North (Point Sal block)
- Western Block (Santa Maria Basin)

Channel Depth: 342 ms (~274 m) – 127 ms (~102 m)

Note: Outline of Point Sal 3D seismic-reflection volume showing locations of tectonic blocks faults, and features interpreted by PG&E (2014, Chapter 3) as possible paleochannels.
Source: Modified from PG&E (2014, Chapter 3).

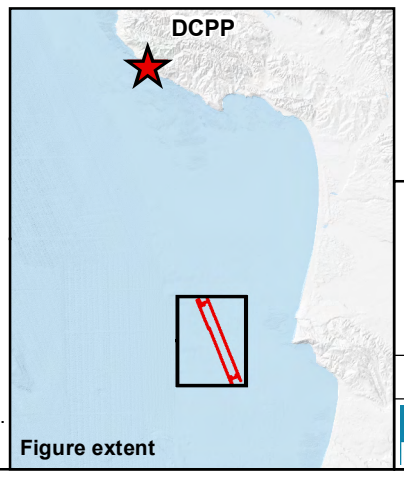

N

0 0.5 1 mi.
0 1 2 km

Map projection and scale: WGS 84 / UTM Zone 10N, 1:33,000

Locations of Possible Paleochannels Interpreted from Point Sal 3D Data

DCPP SSC REPORT

Pacific Gas and Electric Company

Figure **8-29**

File path: S:\1005\005\Final_Report_Figures\Figure_800-29.mxd; Date: 03/11/2015; User: Alex Remar, LCI; Rev:1

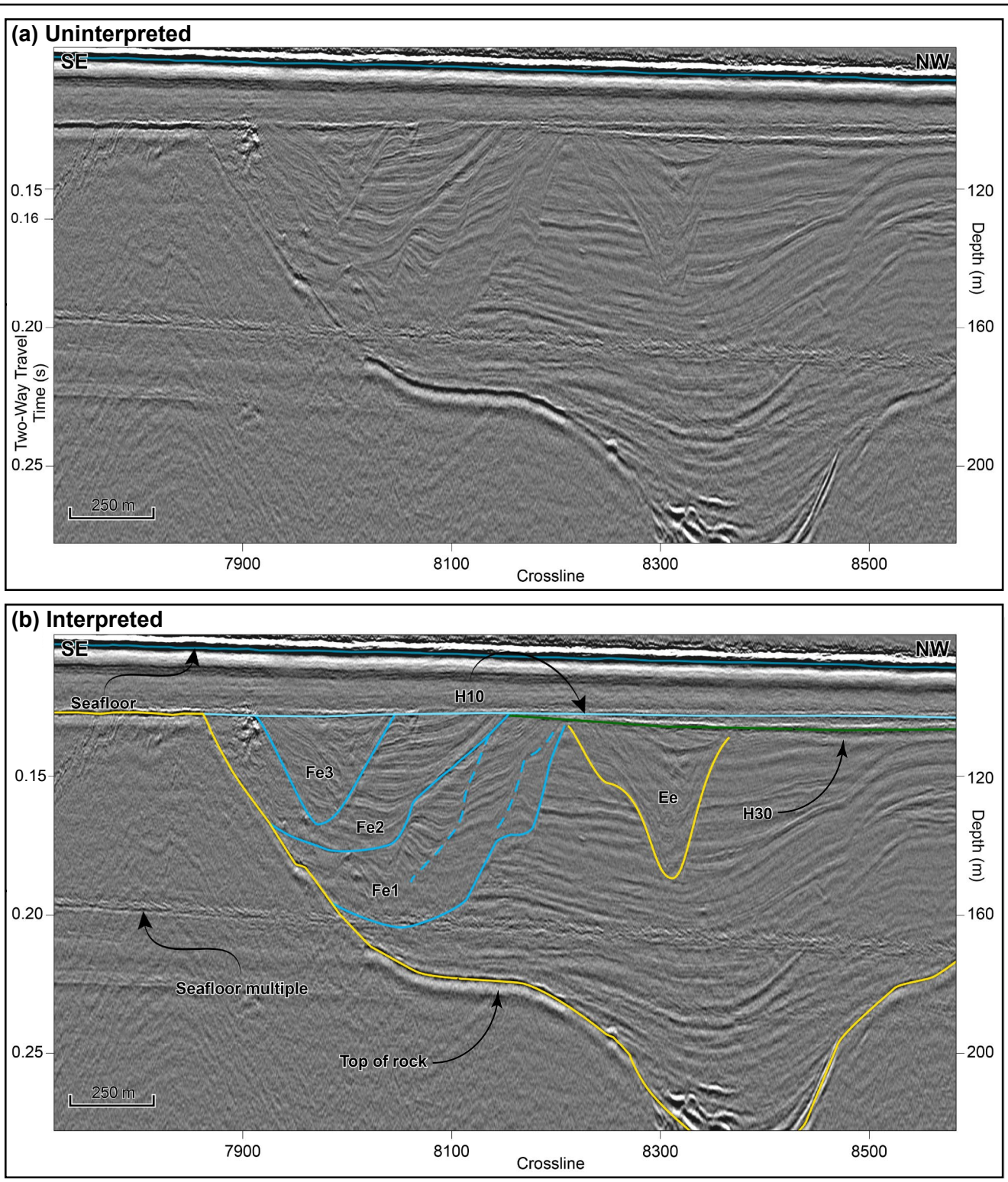

EXPLANATION

- Seafloor
- H10 unconformity
- H30 unconformity
- Top of rock
- Channel E margin
- Channel F margin
- 2012 Point Sal 3D high-resolution survey extent

Source: Modified from PG&E (2014, Chapter 3).

Note: Channels within Channel Complex F are incised too deeply to be fluvial channels that traversed the continental shelf and graded to lowstand sea levels. Therefore, they must have been graded to greater depths on the continental slope.

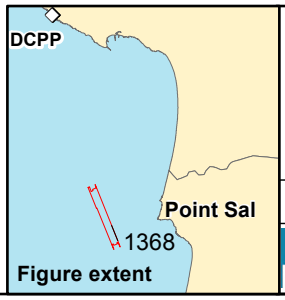

Excerpt of Line 1368 Showing Channel Complex F East of the HFZ in the Point Sal Study Area

DCPP SSC REPORT

Pacific Gas and Electric Company

Figure **8-30**

File path: S:\1005\005\Final_Report\Figures\Figure_800-30.ai; Date: 02/25/2015; User: Alex Remar, LCI; Rev.1

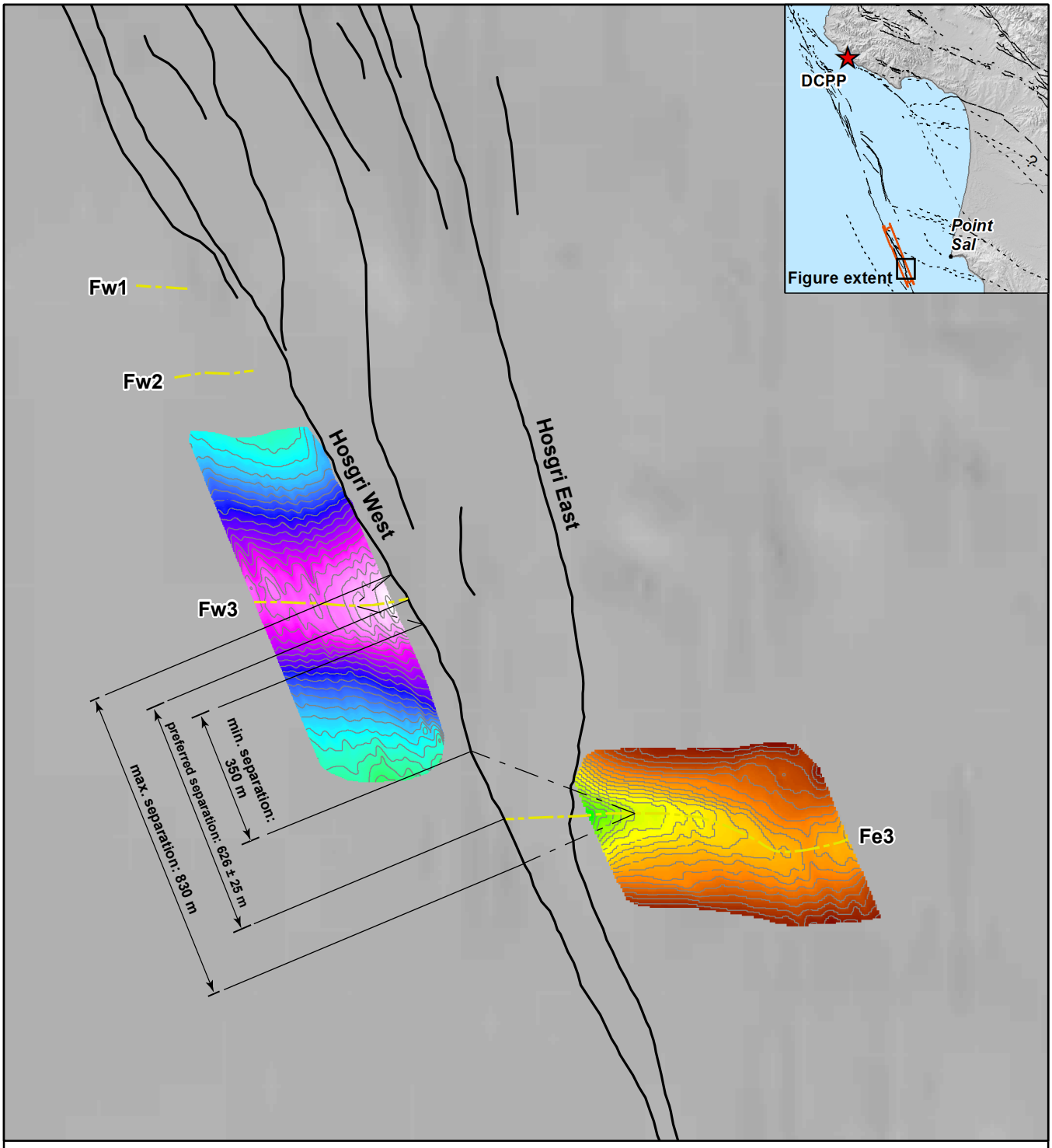

EXPLANATION

- Fault (PG&E, 2014, Chapter 3)
- Slope channel thalweg mapped from seismic-reflection data; Fw1 and Fw2 thalweg locations approximate
- Alternative thalweg projection
- 2012 Point Sal 3D high-resolution survey extent

Channel Depth

340 ms (~272 m)

126 ms (-101 m)

N

0 1,000 2,000 ft.

0 400 800 m

Map projection and scale: NAD 83 / UTM Zone 10N, 1:15,000

Note: Dextral separation of the buried channel Fw3-Fe3 across strands of the HFZ is assessed from uncertainty in the projection of channel thalwegs from the nearest well-imaged location. Source: Modified from PG&E (2014, Chapter 3).

Point Sal Channel F Separation and Uncertainty

DCPP SSC REPORT

Pacific Gas and Electric Company

Figure **8-31**

File path: S:\1005\005\Final_Report_Figures\Figure_800-31.ai; Date: 02/26/2015; User: Alex Remar, LCI; Rev.1

(a) Offset PDF

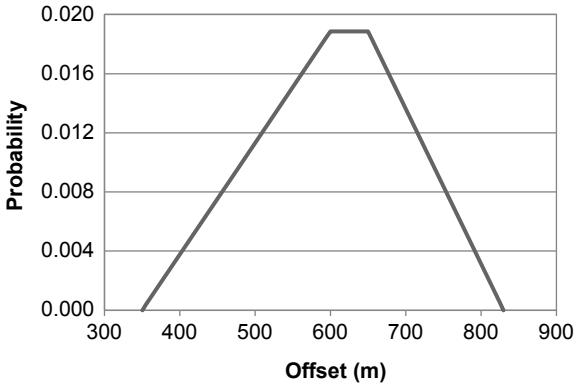

(b) Justification for Offset PDF

Value	Offset (m)	Basis
Min.	350	Estimated from incorporating uncertainty in channel sinuosity into projections
Preferred	600	Projection of thalwegs across data gaps directly along the thalweg trends
Preferred	650	
Max.	830	Estimated from incorporating uncertainty in channel sinuosity into projections

(c) Age PDF

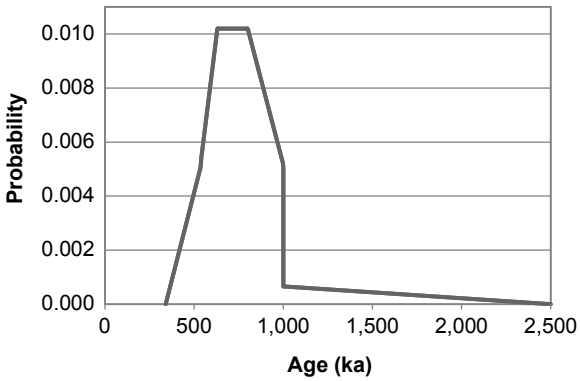

(d) Justification for Age PDF

Value	Offset (m)	Basis
Min.	340	MIS 10; youngest age of overlying unconformity
Pref. Low End	535	MIS 14; ≥5 transgressive unconformities in strata above channel
Preferred	630	MIS 16; probable end of MPT
Preferred	800	MIS 20; shelf progradation and/or deeper sea level during late stage MPT
Pref. High End	1,000	High end of uncertainty in shelf progradation
Max.	2,500	Max age of NTN unconformity (PG&E, 2014, Chapter 3)

(e) Slip Rate CDF

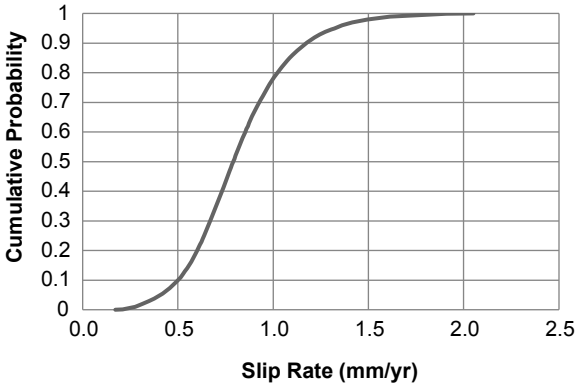

(f) Summary Statistics

Cumulative Probability	Slip Rate (mm/yr)
0.05	0.4
0.1	0.5
0.2	0.6
0.5	0.8
0.8	1.0
0.9	1.2
0.95	1.3
Min.	0.2
Max.	2.1
Mean	**0.8**

Note: Probability distributions used to describe uncertainty in offset (Panels (a) and (b)) and age (Panels (c) and (d)) of the correlated Channel Fw3-Fe3, and used by the TI Team to calculate a slip rate CDF for the HFZ in the Point Sal study area (Panel (e)). Refer to Figure 8-21 for a more complete description of the justification for the age PDF.

Offset and Age PDFs, Slip Rate CDF, and Summary Statistics for Offset Channels at Point Sal Study Area

DCPP SSC REPORT

Pacific Gas and Electric Company

Figure **8-32**

File path: S:\1005\005\Final_Report\Figures\Figure_800-32.ai; Date: 02/26/2015; User: Alex Remar, LCI; Rev.1

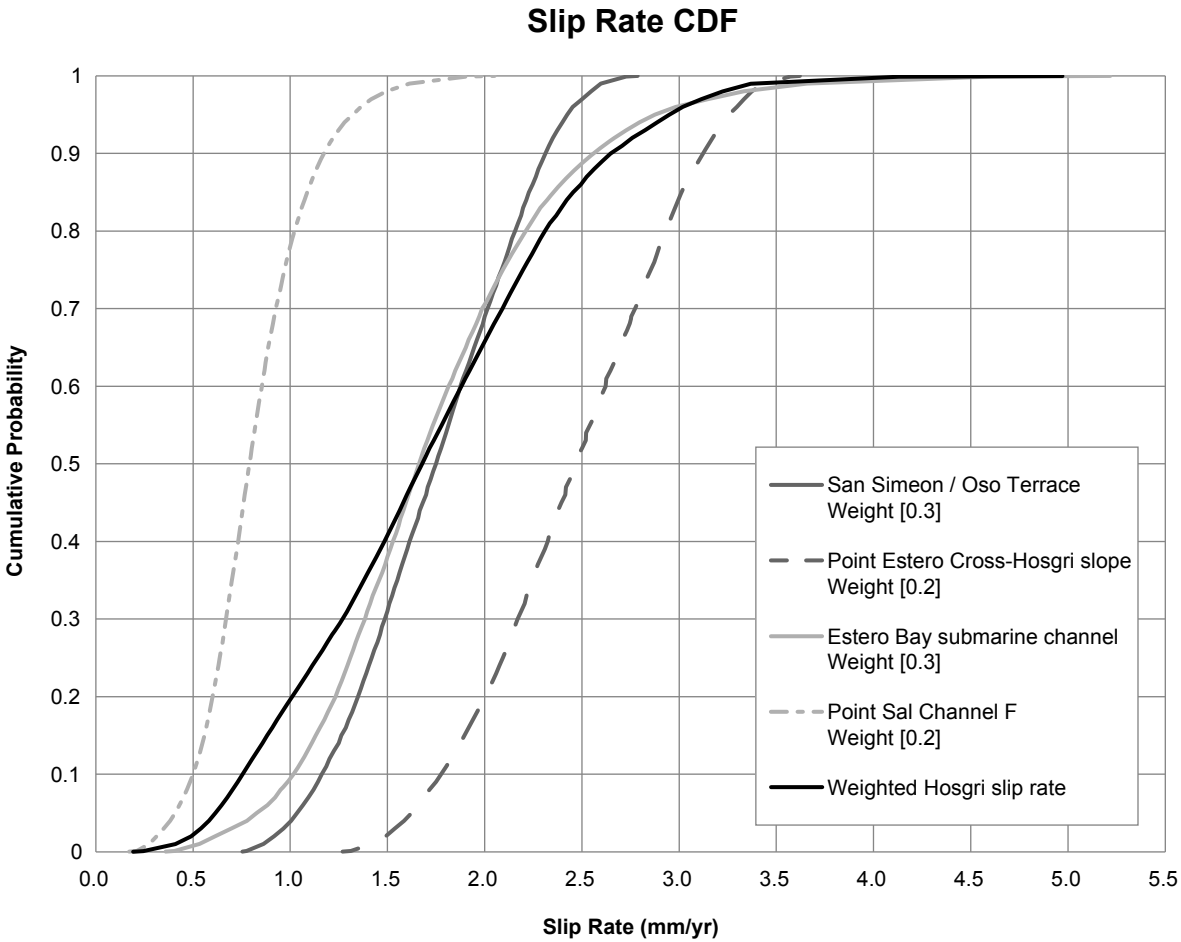

5-Point Distribution		
Percentile	**Slip Rate (mm/yr)**	**Weight**
0.034893	0.6	0.101
0.211702	1	0.244
0.5	1.7	0.309
0.788298	2.3	0.244
0.965107	3.1	0.101
Weighted Mean	**1.7**	

Note: The Hosgri slip rate CDF is calculated from the weighted combination of slip rate CDFs developed for each of the four Hosgri slip rate sites.

Hosgri Slip Rate CDF Compilation and Selection of 5-Point Distribution

DCPP SSC REPORT

Pacific Gas and Electric Company | Figure **8-33**

File path: S:\1005\005\Final_Report\Figures\Figure_800-33.ai; Date: 02/26/2015; User: Alex Remar, LCI; Rev.1

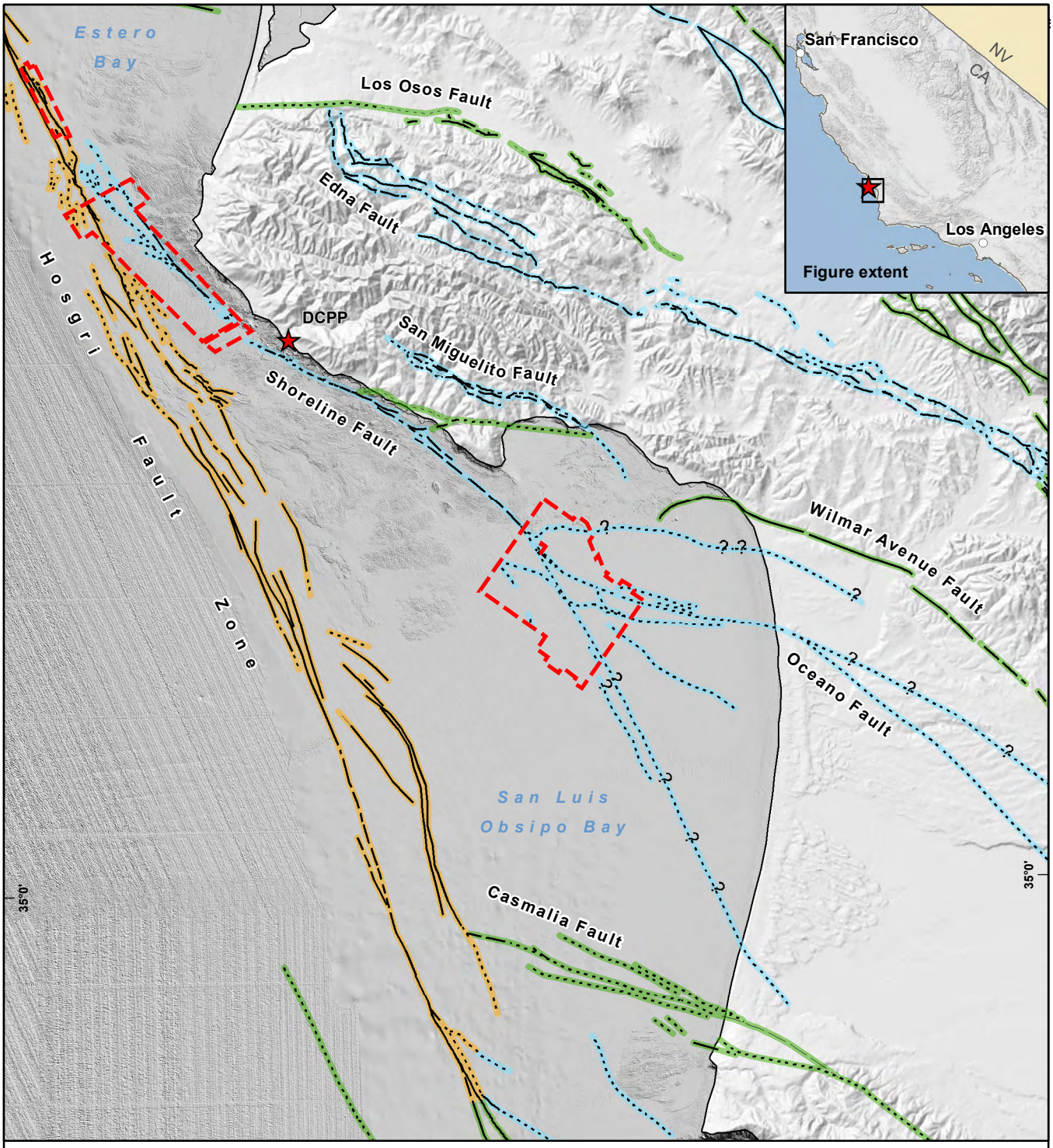

EXPLANATION

3D seismic-reflection survey extent

Quaternary fault trace: solid where well located, dashed where approximately located, offshore faults dotted where buried by undeformed unconformity H10 or older strata, onshore faults dotted where buried, short dashed where inferred, queried where existence is uncertain

Slip Rate

1–5 mm/yr

0.2–1 mm/yr

< 0.2 mm/yr

N

0 2.5 5 mi.

0 5 10 km

Map projection and scale: NAD 83 / UTM Zone 10N, 1:250,000

Overview Map of the Shoreline Fault

DCPP SSC REPORT

Pacific Gas and Electric Company

Figure **8-34**

File path: S:\1005\005\Final_Report_Figures\Figure_800-34.mxd; Date: 03/11/2015; User: Alex Remar, LCI; Rev.1

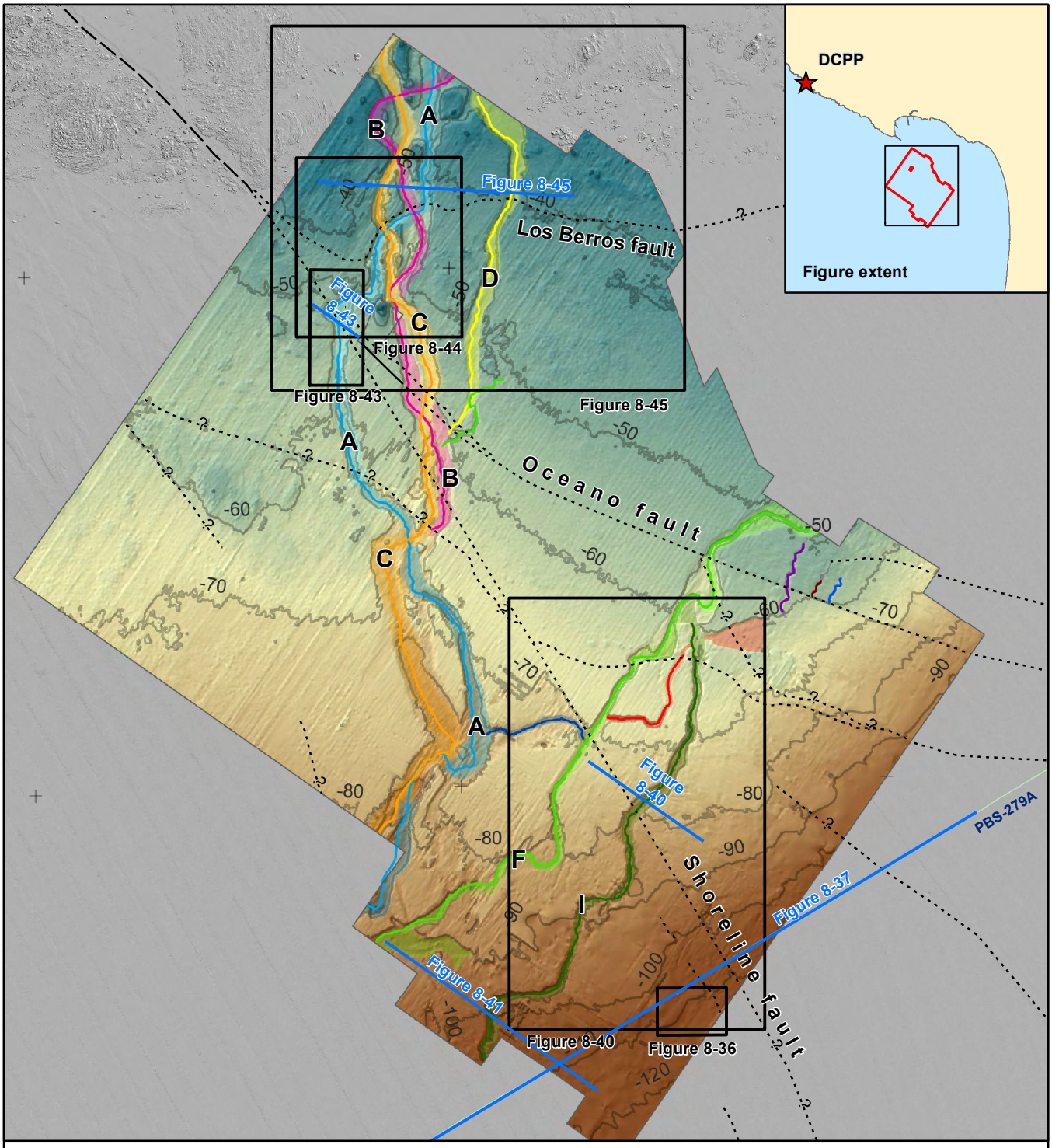

EXPLANATION

Quaternary fault trace: solid where well located, dashed where approximately located, dotted where buried by undeformed unconformity H10 or older strata, short dashed where inferred, queried where existence is uncertain

Figure extent of seismic profile

Figure extent

Notes:
- Channels mapped by PG&E (2014, Chapter 3) shown in various colors, letter indicated.
- Base map from PG&E (2014, Chapter 3). Blue to brown shading indicates increasing depth. Contours indicate depth below sea level in meters.

N

0 0.5 1 mi
0 1 2 km

Map projection and scale: NAD 83 / UTM Zone 10N, 1:42,000

Shaded Relief Image of the Bedrock Surface Interpreted from 3D Seismic-Reflection Data in San Luis Obispo Bay Study Area, Showing Faults, Channels, and Figure Extents

DCPP SSC REPORT

Pacific Gas and Electric Company

Figure **8-35**

File path: S:\1005\005\Final_Report_Figures\Figure_800-35.mxd; Date: 02/27/2015; User: Alex Remar, LCI; Rev.1

(a) Amplitude Time Slice at 119.3 ms

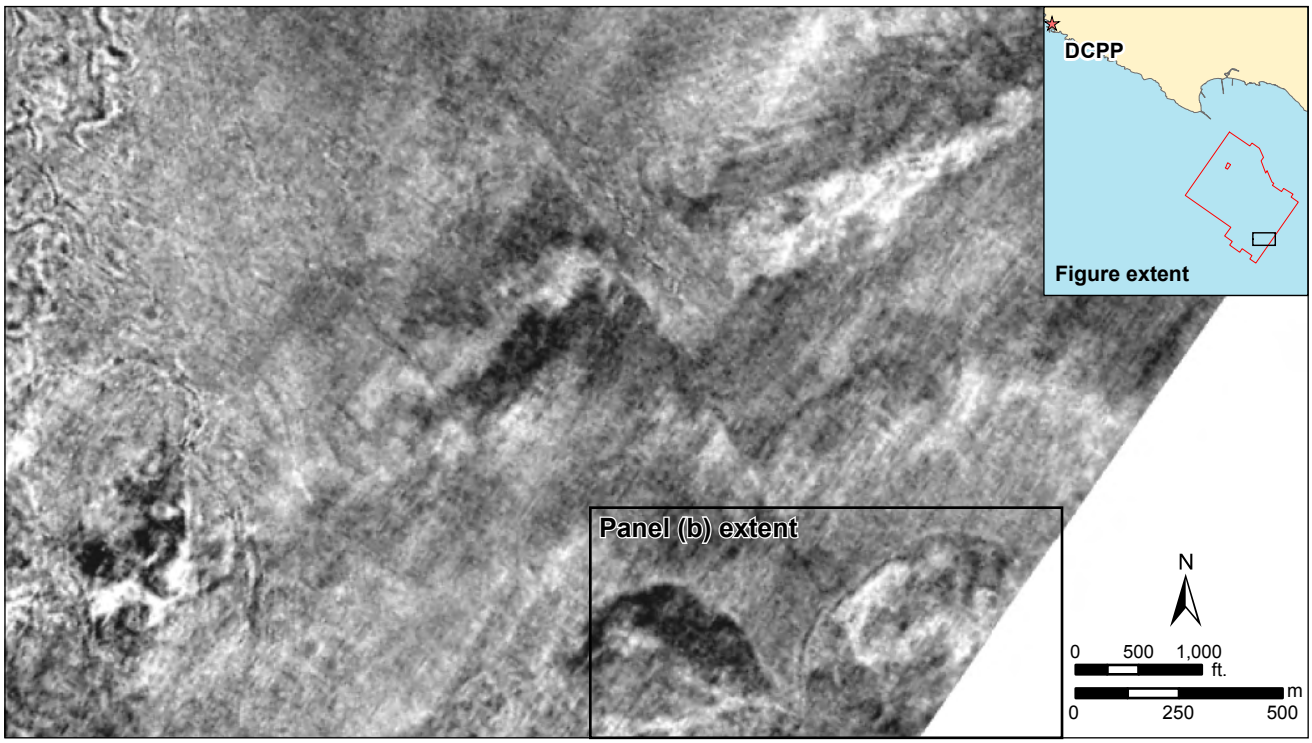

(b) Amplitude Time Slice at 119.3 ms and Shoreline Fault and Offset Terrace Riser

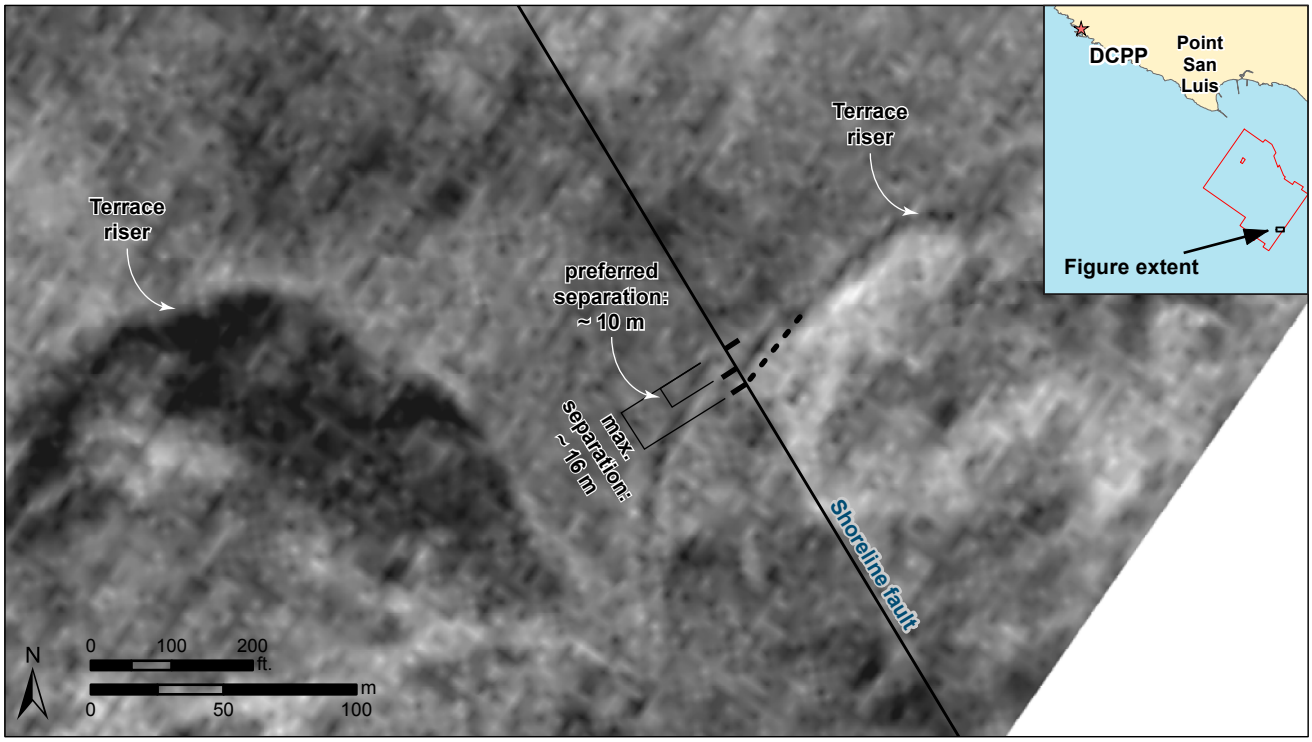

EXPLANATION

Shoreline fault

San Luis Obispo Bay 3D survey extent

Notes:
- Alternative correlations of reflectors across the Shoreline fault are used to assess uncertainty in lateral separation. A maximum dextral separation of 16 m is estimated from considering a minor apparent jog in the terrace riser northeast of the Shoreline fault as offset on a secondary strand that is part of the total fault separation.
- See Figure 8-35 for figure location.

Source: 3D seismic-reflection data from PG&E (2014, Chapters 2 and 3).

Map projection: WGS 84 / UTM Zone 10N

Time Slice at 119.3 ms Showing Terrace Riser and Assessment of Offset Across Shoreline Fault

DCPP SSC REPORT

Pacific Gas and Electric Company

Figure **8-36**

File path: S:\1005\ Figure_800-36.ai; Date: 03/11/2015; User: Serkan Bozkurt, LCI; Rev.1

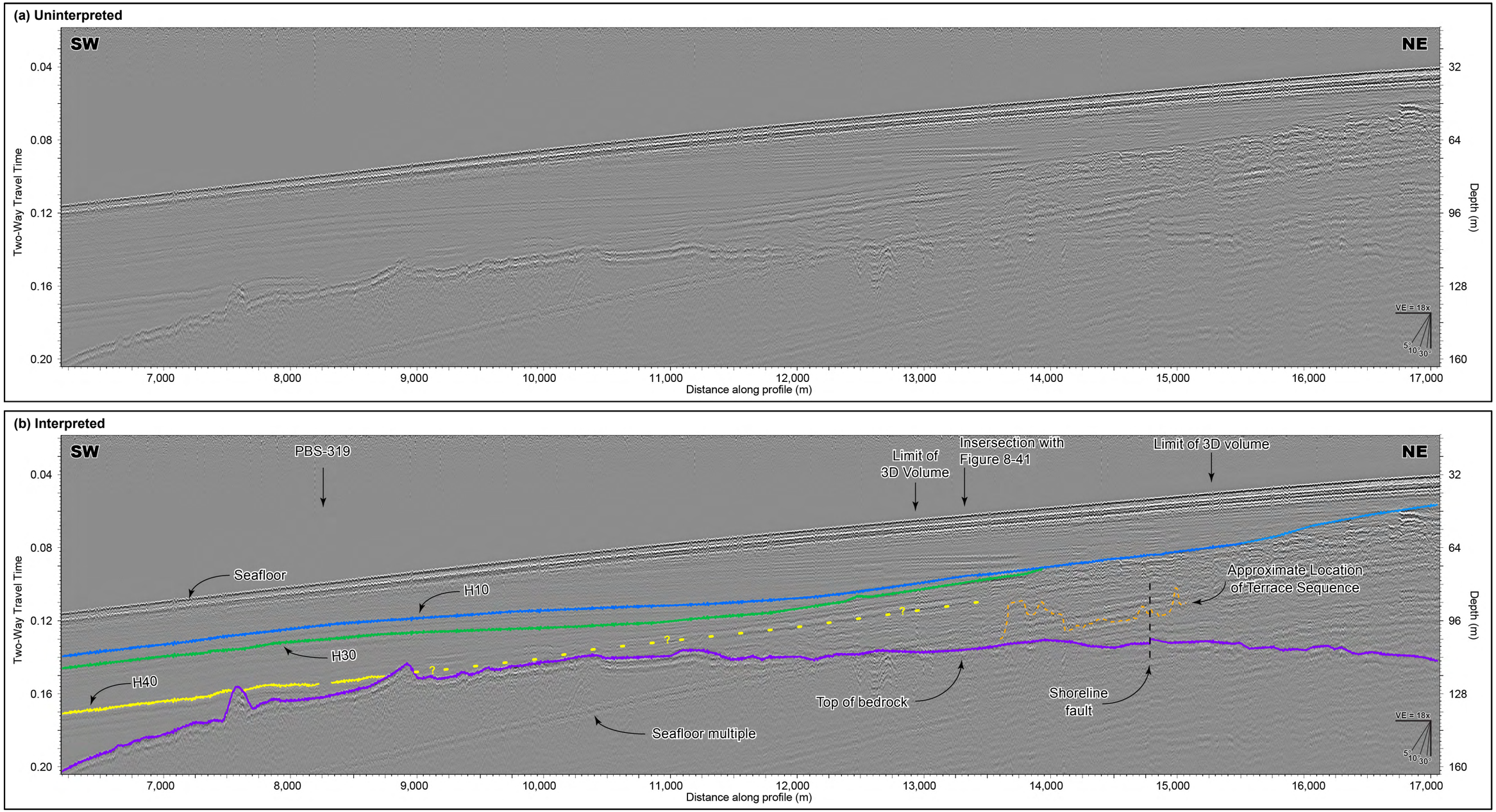

EXPLANATION

- Unconformity H10 (PG&E, 2013a)
- Unconformity H30 (PG&E, 2013a)
- Unconformity H40 (PG&E, 2013a)
- Plausible landward extension of unconformity H40
- Top of bedrock (modified from PG&E, 2013a)
- Approximate location of terrace sequence (PG&E, 2014, Chapter 3)
- San Luis Obispo Bay 3D survey extent

Notes:
- Unconformity H40 as mapped by PG&E (2013a) with moderate confidence is shown as a solid line. A viable extension to the northeast (yellow dots) is postulated by the TI Team. The age of the terrace sequence is constrained to be older than unconformity H30, and likely is older than unconformity H40.
- Depth values on seismic profile assume a velocity of 1,600 m/s.
- See Figure 8-35 for figure location.

Source: 2D seismic-reflection data from Sliter et al. (2010).

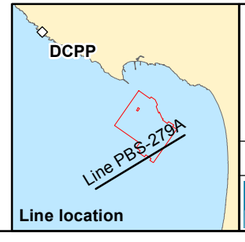

Excerpt of Line PBS-279A Showing Stratigraphic Context of Terrace Sequence

DCPP SSC REPORT

Pacific Gas and Electric Company

Figure **8-37**

File path: S:\1005\005\Final_Report\Figures\Figure_800-37.ai; Date: 02/26/2015; User: Alex Remar, LCI; Rev.1

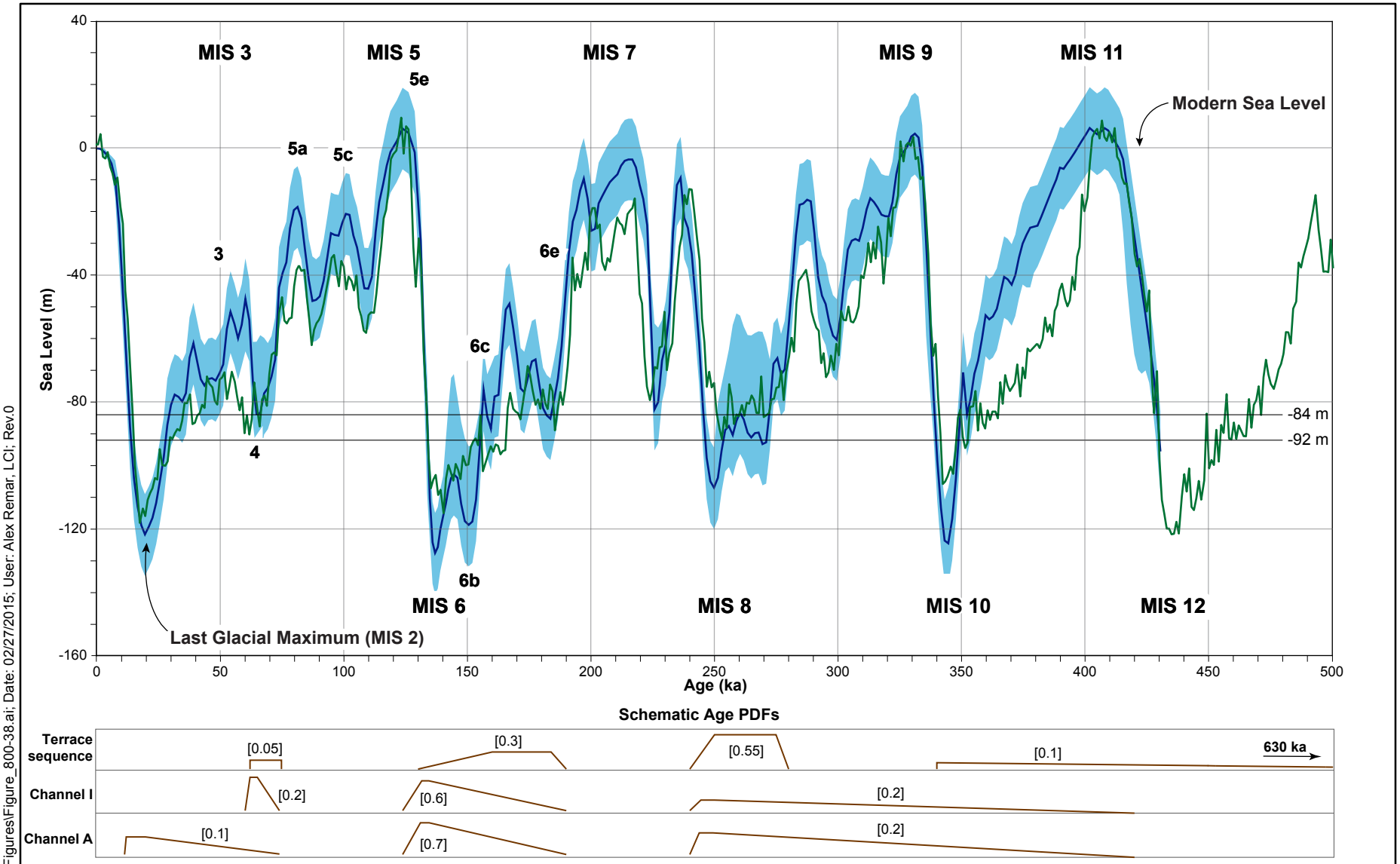

EXPLANATION

MIS Marine oxygen isotope stage

6c Marine oxygen isotope substage

Waelbroeck et al. (2002)

Lisiecki and Raymo (2005)

Notes:
- Uncertainty in the ages of the terrace sequence, Channel I, and Channel A are assessed from correlation to Quaternary sea-level curves. See text for detailed explanation.
- Numbers in brackets are weights assigned to each age alternative.
- Waelbroeck et al. (2002) relative sea-level (RSL) curve from δ18O data scaled to sea-level with coral terrace data. Shaded region is confidence interval.
- Lisiecki and Raymo (2005) use 57 globally distributed δ18O records to compile a 5.3 Myr record. Scaled to sea level by Carlson (2008).

Late Quaternary Sea-Level Curves and Age Models for Terrace Sequence, Channel I, and Channel A

DCPP SSC REPORT

Pacific Gas and Electric Company

Figure **8-38**

File path: S:\1005\005\Final_Report\Figures\Figure_800-38.ai; Date: 02/27/2015; User: Alex Remar, LCI; Rev.0

(a) Offset PDF

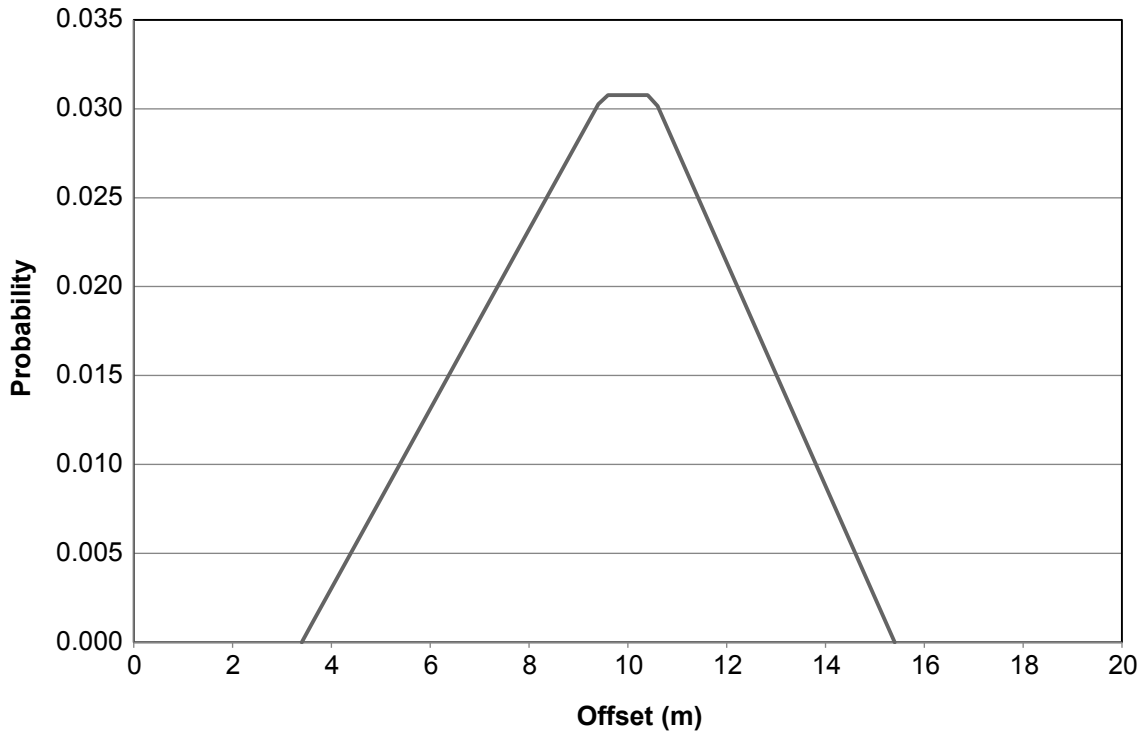

(b) Justification for Offset PDF

Value	Offset (m)	Basis
Min.	3.4	Minimum allowable offset based on uncertainty
Preferred	9.5	Observed offset of 10 m
Preferred	10.5	
Max.	15.4	Maximum allowable offset based on uncertainty

(c) Age PDF

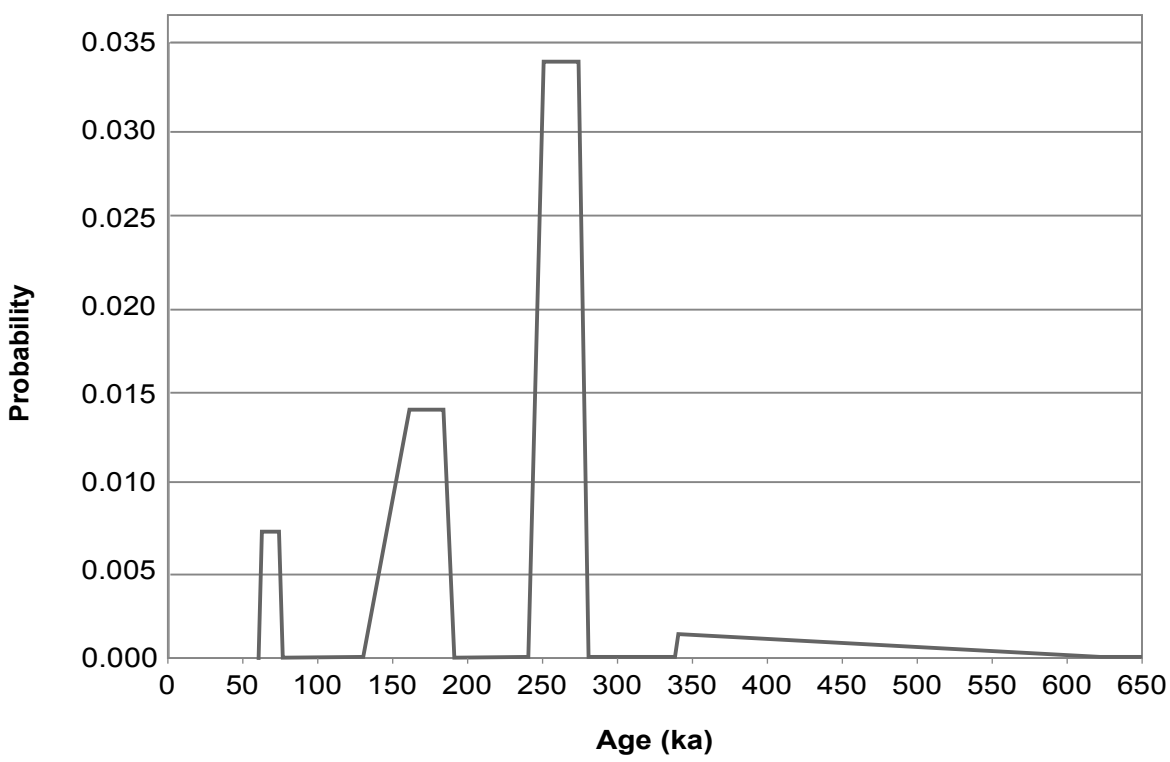

(d) Justification for Age PDF

MIS 4 [0.05]		
Value	**Age (ka)**	**Basis**
Min.	62	Uniform age distribution of MIS 4 lowstand
Max.	75	

MIS 6 [0.3]		
Value	**Age (ka)**	**Basis**
Min.	130	Age of MIS 6–5 transgression
Preferred	160	Age of small sea level fluctuations through -84 m and -92 m depth
Preferred	185	
Max.	190	Onset of MIS 6 lowstand

MIS 6 [0.3]		
Value	**Age (ka)**	**Basis**
Min.	240	Age of MIS 8–7 transgression
Preferred	250	Maximum MIS 8 lowstand
Preferred	275	
Max.	280	Onset of MIS 8 lowstand

MIS 10–16 [0.1]		
Value	**Age (ka)**	**Basis**
Min.	340	Minimum age of MIS 10 lowstand
Preferred	340	Maximum depth of MIS 10 lowstand
Max.	630	Maximum depth of MIS 16 lowstand

(e) Slip Rate CDF

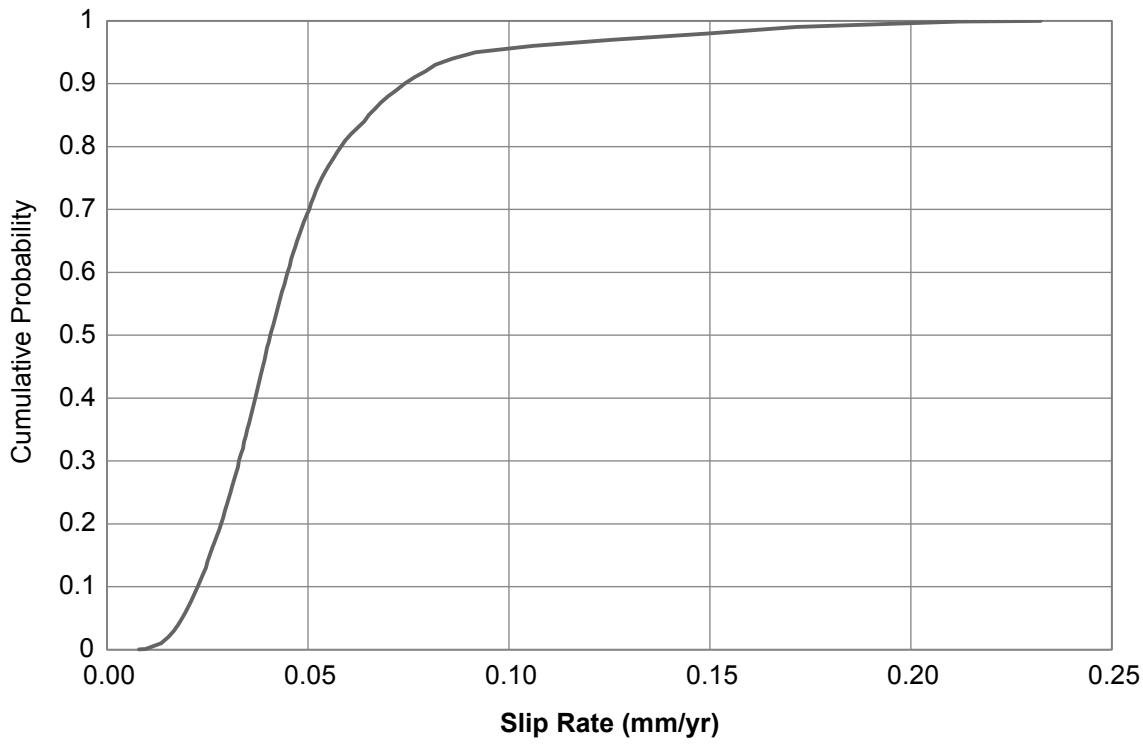

(f) Summary Statistics

Cumulative Probability	Slip Rate (mm/yr)
0.05	0.02
0.1	0.02
0.2	0.03
0.5	0.04
0.8	0.06
0.9	0.07
0.95	0.09
Minimum	0.01
Maximum	0.24
Mean	**0.05**

Notes:
- Numbers in brackets in Panel (d) are weights assigned to each age model.
- Onset of lowstand is defined as the age that sea level passed below terrace risers.
- Probability distributions used to describe uncertainty in offset (Panels (a) and (b)) and age (Panels (c) and (d)) of the terrace riser, and used by the TI Team to calculate a slip rate CDF for the Shoreline fault at the location of the offset terrace sequence.

PDFs of Uncertainty in Offset and Age of Terrace Riser, and Slip Rate CDF

DCPP SSC REPORT

Pacific Gas and Electric Company

Figure **8-39**

File path: S:\1005\005\Final_Report\Figures\Figure_800-39.ai; Date: 02/26/2015; User: Alex Remar, LCI; Rev.1

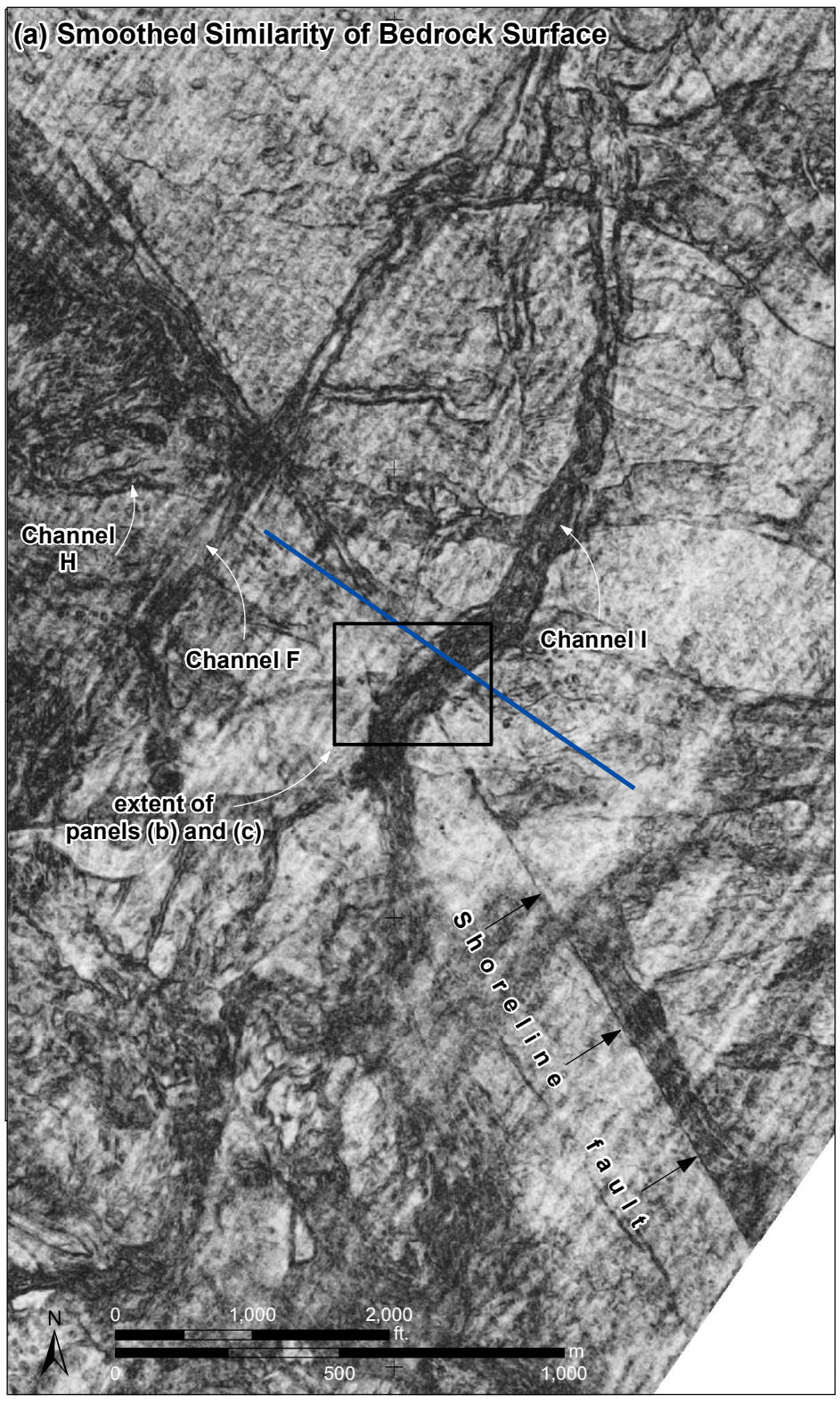

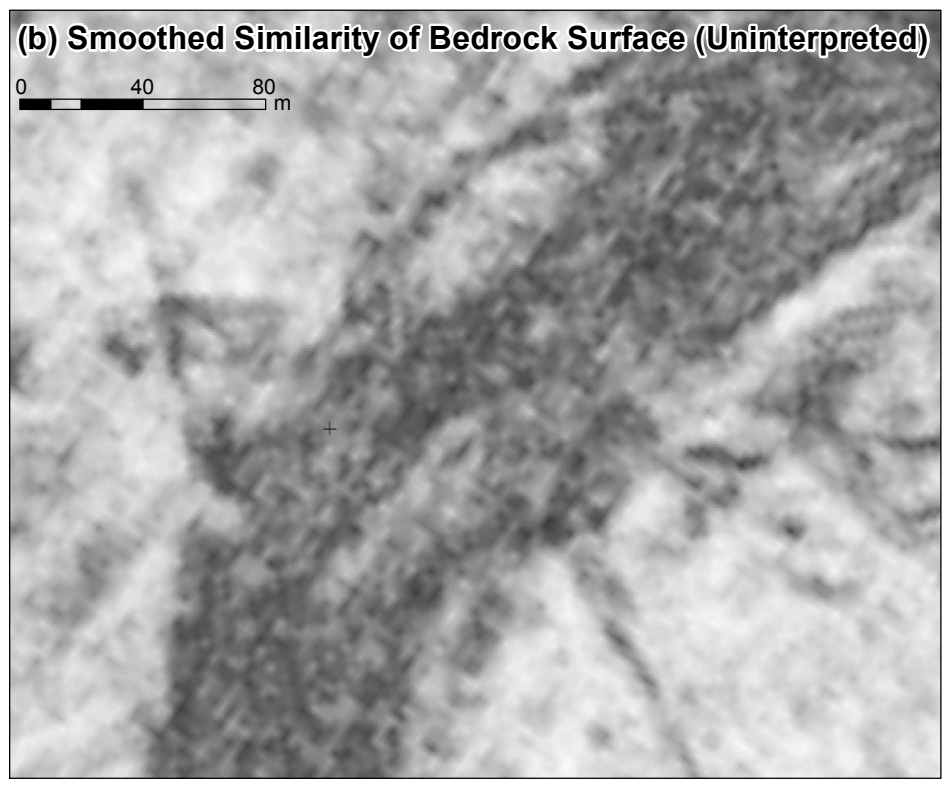

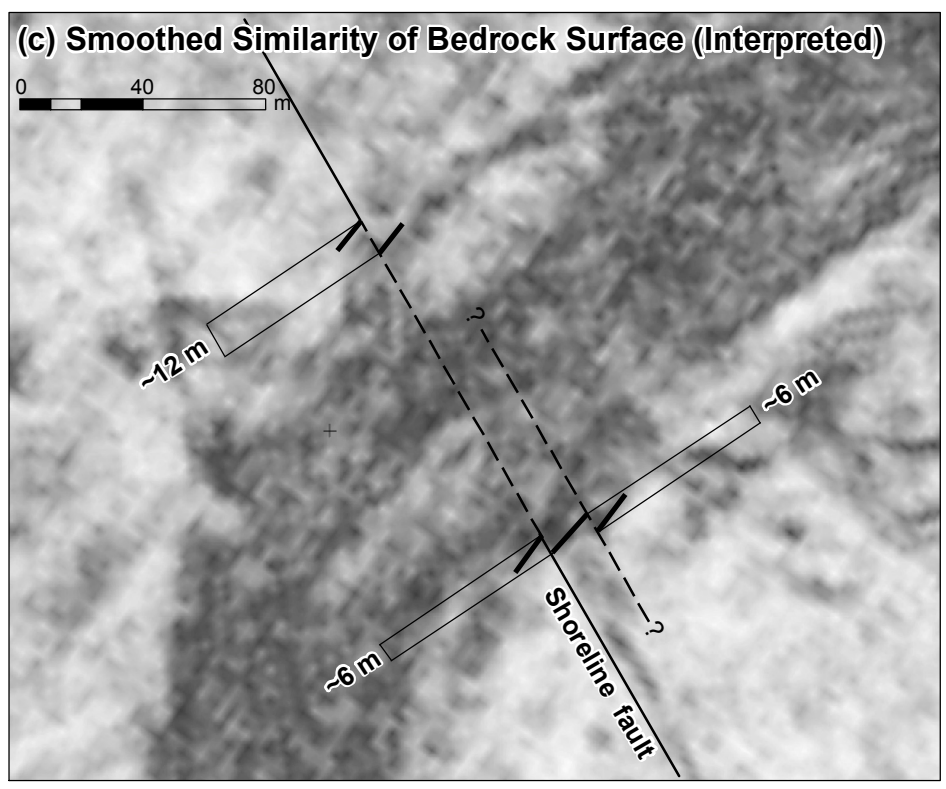

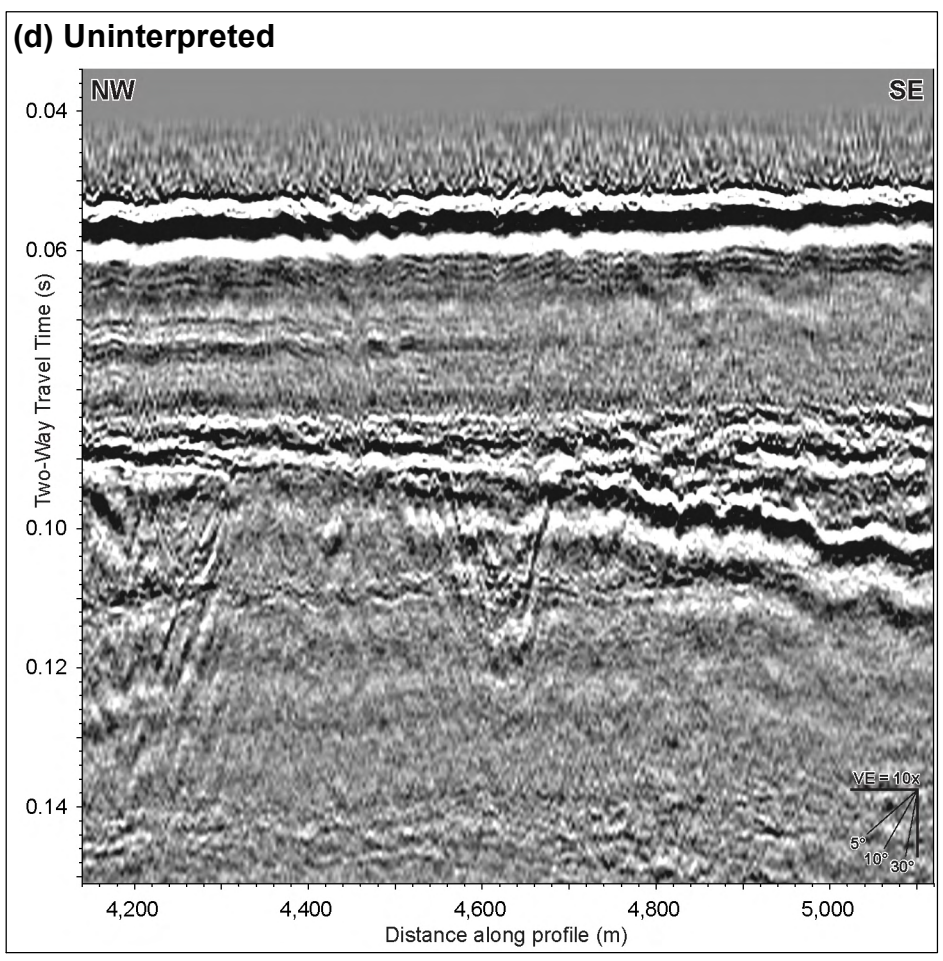

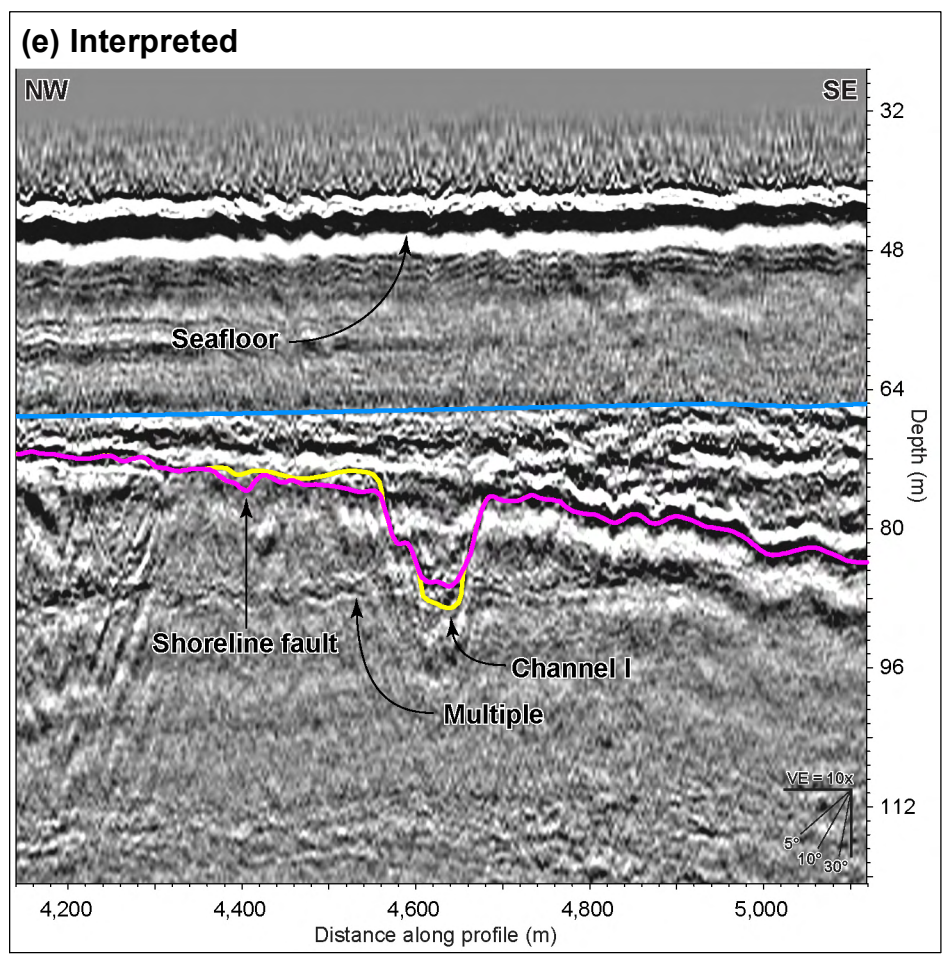

EXPLANATION

- H10 (PG&E, 2014, Chapter 3)
- Top of rock (from PG&E, 2014, Chapter 3)
- Top of rock (alternative interpretation by TI Team)
- Location of seismic profile
- 3D survey extent

Notes:
- Panel (a) is a smoothed similarity attribute extracted along the surface of bedrock mapped from 3D seismic-reflection data.
- Panels (b) and (c) show dextral separation of the margins of Channel I across the Shoreline fault is assessed from the smoothed similarity data.
- Panels (d) and (e) are seismic-reflection profiles at the intersection of Channel I and the Shoreline fault show that Channel I is buried by strata older than unconformity H10.
- See Figure 8-35 for figure location.
- Depth values on seismic profile assume a velocity of 1,600 m/s.

Source: 3D seismic-reflection data from PG&E (2014, Chapter 2 and Chapter 3).

Map projection and scale: WGS 84 / UTM Zone 10N, 1:15,000

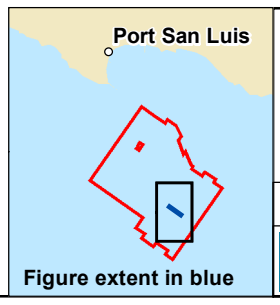

Smoothed Similarity of Bedrock Surface and Crossline 1276 Showing Channel I Intersection with Shoreline Fault

DCPP SSC REPORT

Pacific Gas and Electric Company

Figure **8-40**

File path: S:\1005\005\Final_Report_Figures\Figure_800-40.mxd; Date: 03/11/2015; User: Alex Remar, LCI; Rev:1

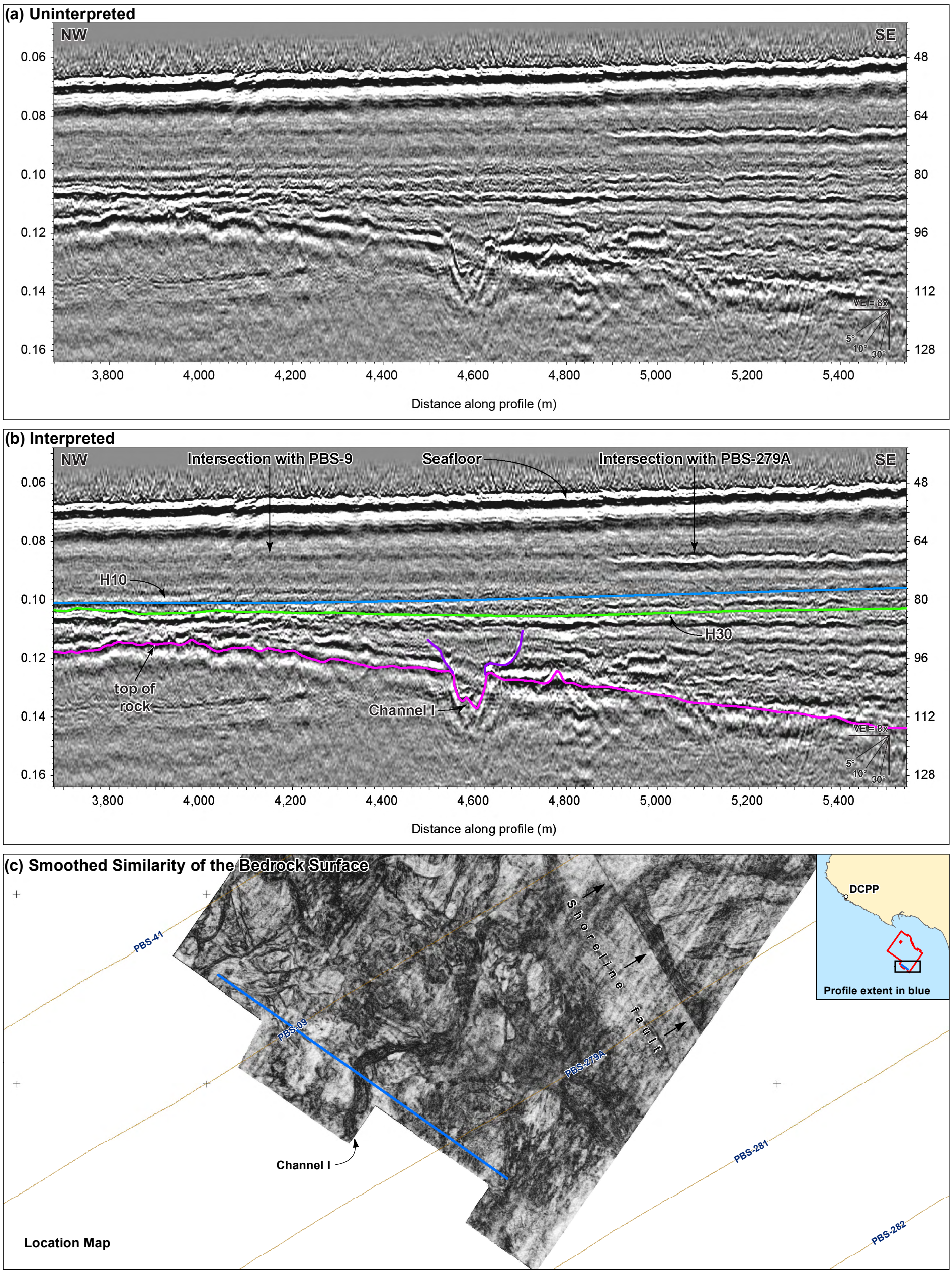

EXPLANATION

- Top of rock (PG&E, 2014, Chapter 3)
- H10 (PG&E, 2014, Chapter 3)
- H30 (this study)
- Base of Channel I
- Location of seismic profile
- USGS 2D survey trackline

Notes:
- Channel I is constrained to be older than unconformity H30, and possibly older unconformities as well.
- See Figure 8-35 for figure location.
- Depth values on seismic profile assume a velocity of 1,600 m/s.

Sources:
- 3D seismic-reflection data from PG&E (2014, Chapters 2 and 3).
- USGS 2D tracklines from Sliter et al. (2010).

N

0 0.25 0.5 mi.
0 0.5 1 km

Map projection and scale: WGS 84 / UTM Zone 10N, 1:20,000

Smoothed Similarity of Bedrock Surface and Crossline 672 Showing Stratigraphic Constraints on Age of Channel I

DCPP SSC REPORT

Pacific Gas and Electric Company

Figure **8-41**

File path: S:\1005\005\Final_Report_Figures\Figure_800-41.mxd; Date: 03/11/2015; User: Alex Remar, LCI; Rev.1

(a) Offset (m)

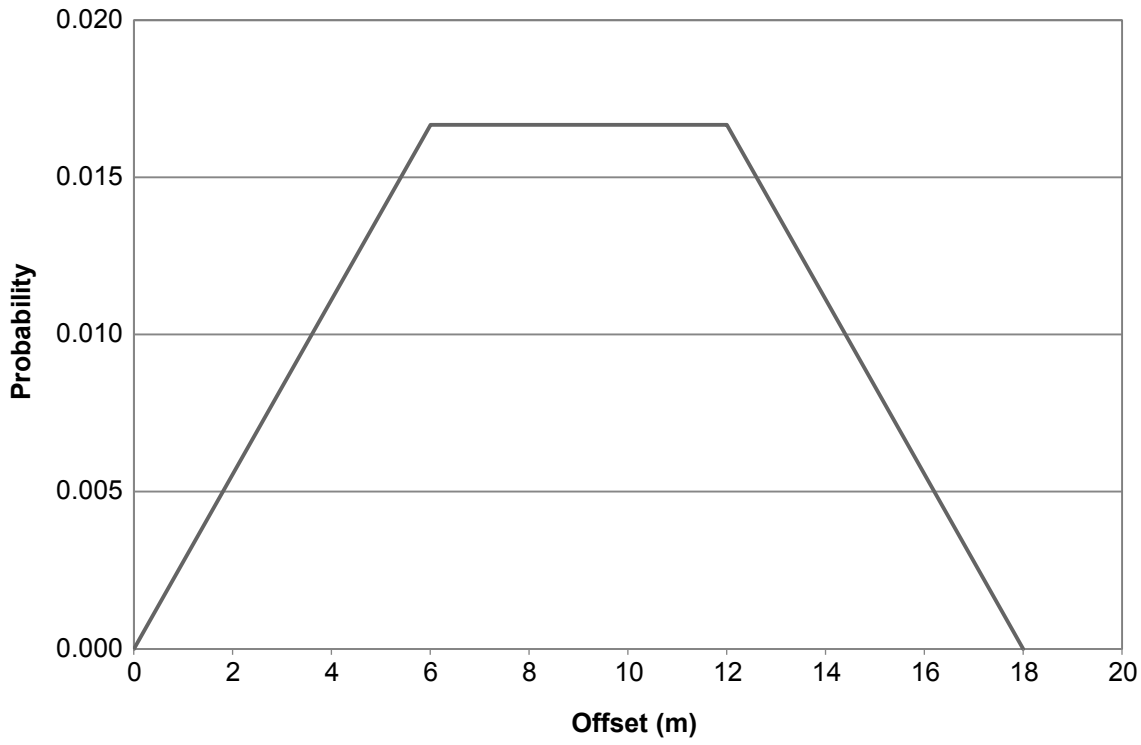

(b) Justification for Offset PDF

Value	Offset (m)	Basis
Min.	0	Interpretation of no offset credible
Preferred	6	Observed offset of 9 m ± 3 m
Preferred	12	
Max.	18	Exceeds observed channel offsets. Additional 6 m uncertainty accounts for smoothing in similarity data

(c) Age PDF

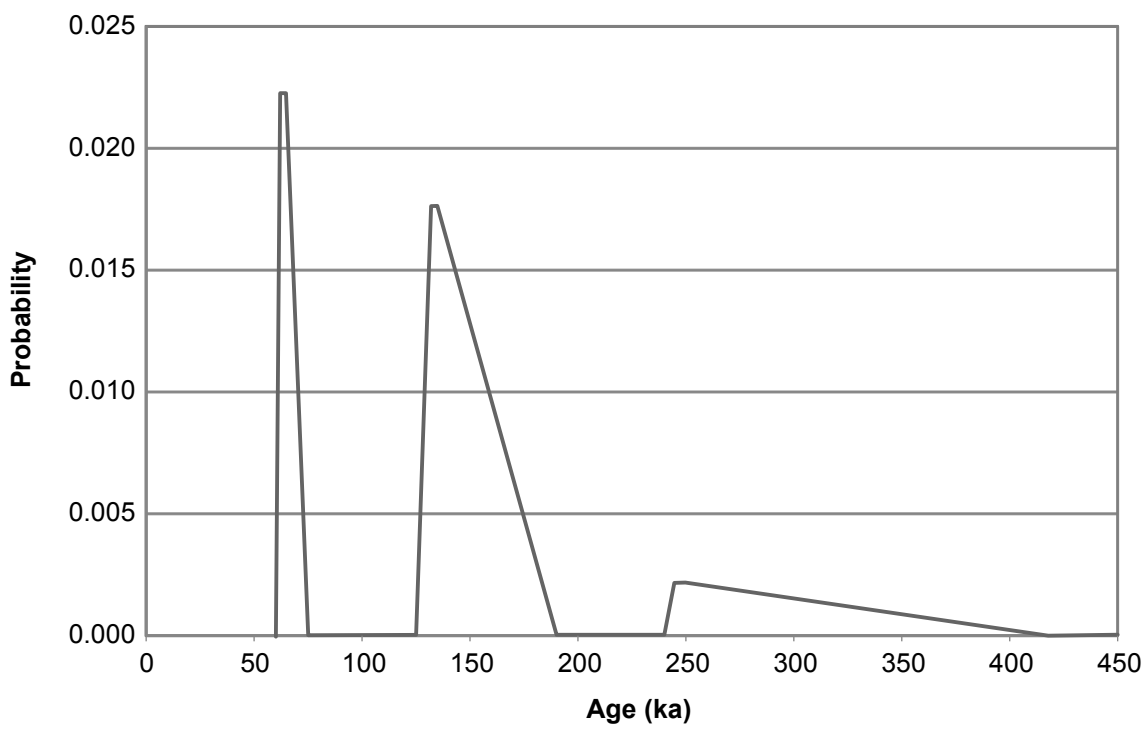

(d) Justification for Age PDF

MIS 4 [0.2]		
Value	**Age (ka)**	**Basis–H30 marks end of MIS 4**
Min.	60	Minimum possible age of H30
Preferred	62	Preferred age of MIS 4–3 transgression
Preferred	65	Maximum age of MIS 4 lowstand
Max.	75	Onset of MIS 4 lowstand

MIS 6 [0.6]		
Value	**Age (ka)**	**Basis–H30 marks end of MIS 6**
Min.	125	Minimum possible age of MIS 6–5 transgression
Preferred	132	Preferred age of MIS 6–5 transgression
Preferred	135	Maximum depth of MIS 6 lowstand
Max.	190	Onset of MIS 6 lowstand

MIS 8–12 [0.2]		
Value	**Age (ka)**	**Basis–Channel significantly pre-dates H30**
Min.	240	Minimum age of MIS 8–7 transgression
Preferred	245	Onset of MIS 8–7 transgression
Preferred	250	Maximum depth of MIS 8 lowstand
Max.	420	End of MIS 12 lowstand

(e) Slip Rate CDF

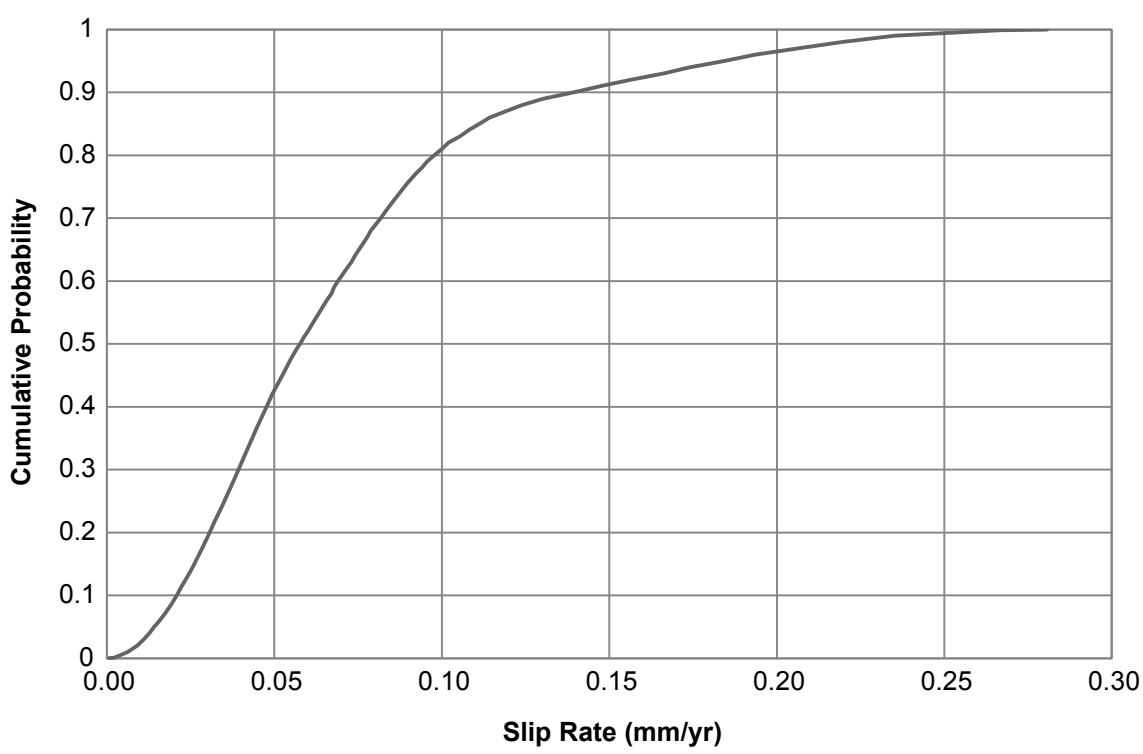

(f) Summary Statistics

Cumulative Probability	Slip Rate (mm/yr)
0.05	0.01
0.1	0.02
0.2	0.03
0.5	0.06
0.8	0.10
0.9	0.14
0.95	0.18
Minimum	0.00
Maximum	0.29
Mean	**0.07**

Notes:
- Probability distributions used to describe uncertainty in offset (Panels (a) and (b)) and age (Panels (c) and (d)) of Channel I, and used by the TI Team to calculate a slip rate CDF for the Shoreline fault at Channel I.
- Numbers in brackets in Panel (d) are weights assigned to each age model.
- Uncertainty in timing of lowstands from Waelbroeck et al. (2002).

PDFs of Uncertainty in Offset and Age of Channel I, and Slip Rate CDF

DCPP SSC REPORT

Pacific Gas and Electric Company

Figure **8-42**

File path: S:\1005\005\Final_Report\Figures\Figure_800-42.ai; Date: 02/26/2015; User: Alex Remar, LCI; Rev.1

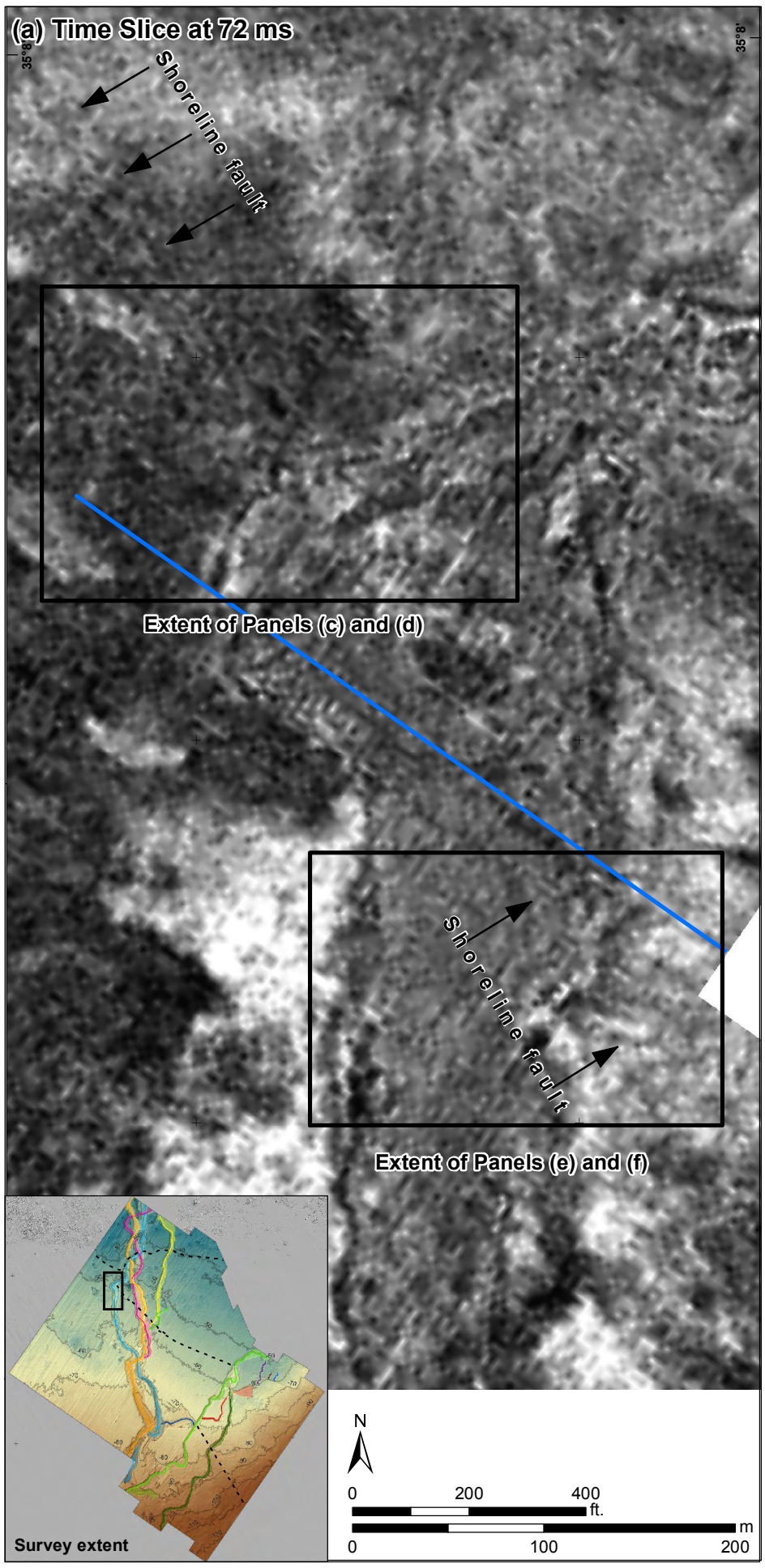

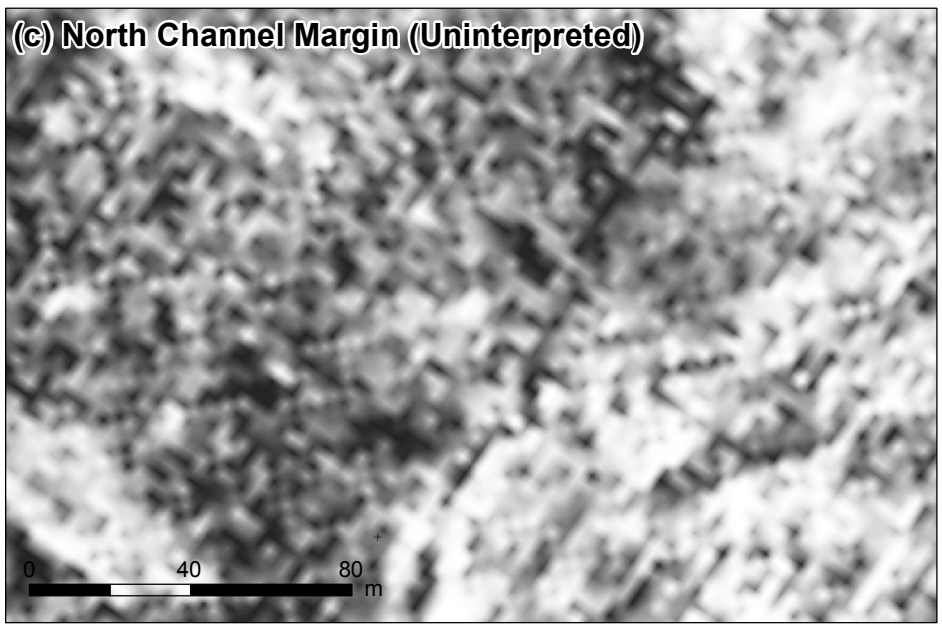

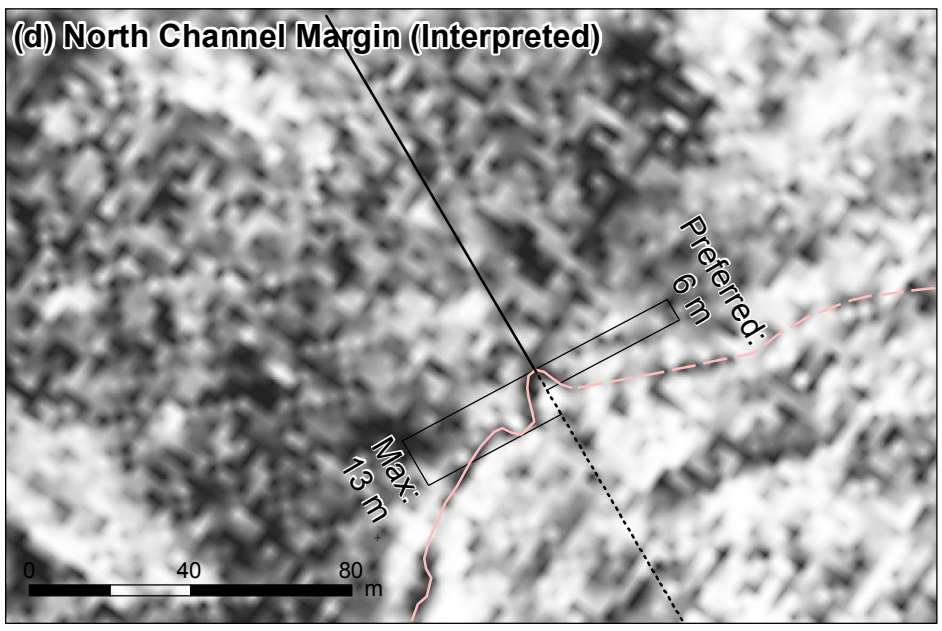

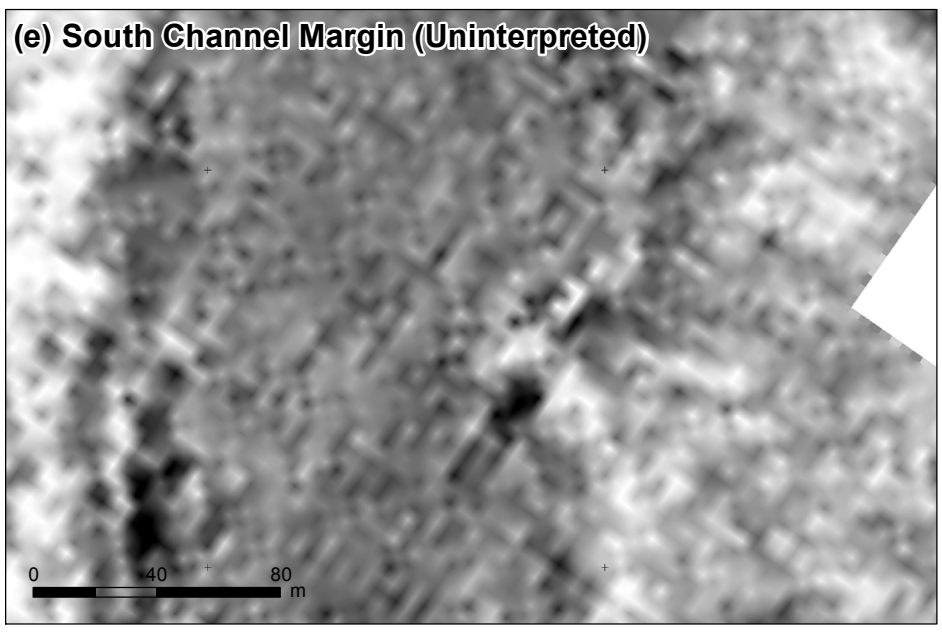

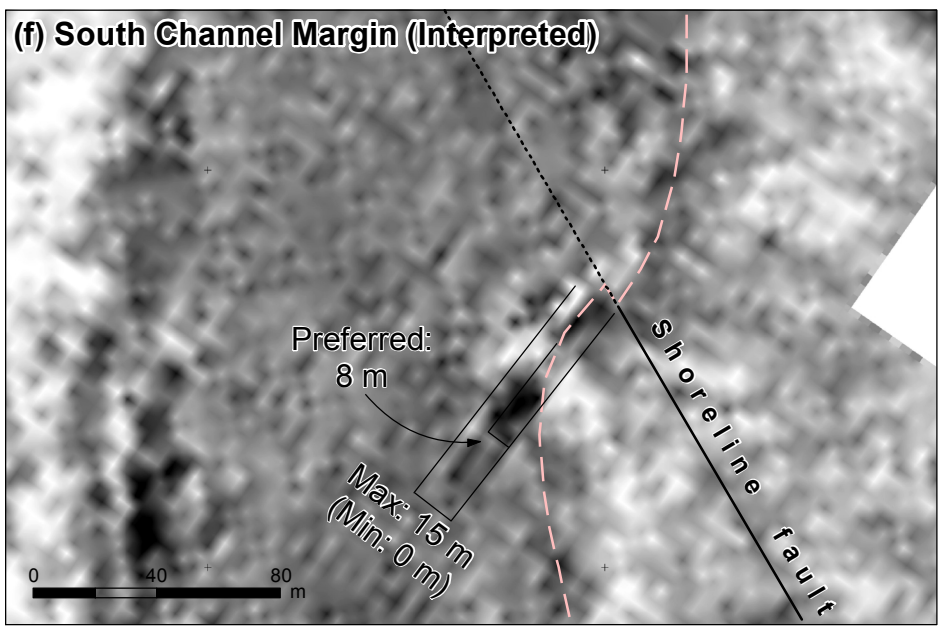

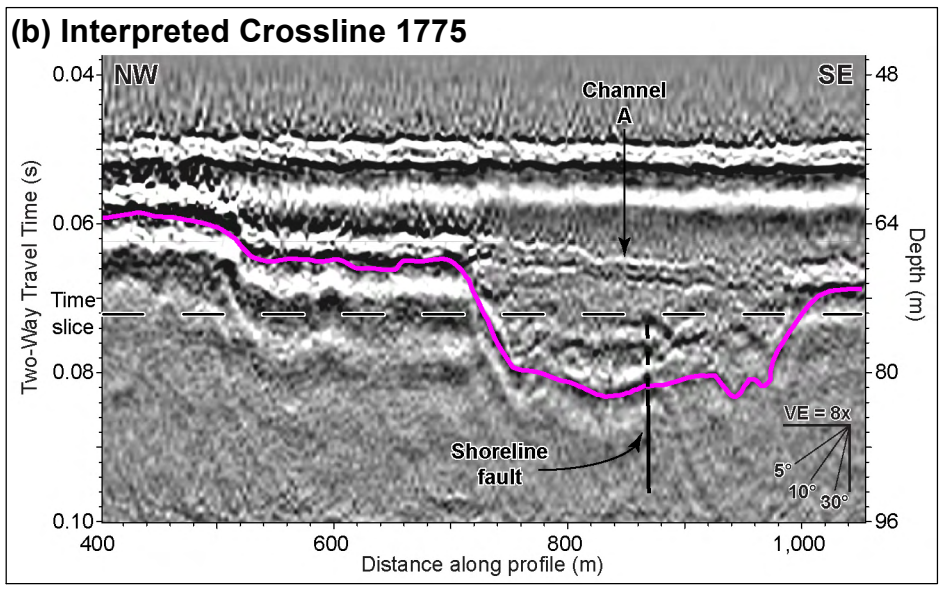

EXPLANATION

- Channel margin, solid where well located, dashed where approximate
- Top of rock (modified from PG&E, 2014, Chapter 3)
- Location of seismic profile
- Depth of time slice
- 3D survey extent

Notes:
- Enlargements of time slices are used to assess uncertainty in dextral fault displacement where the Shoreline fault intersects the margins of Channel A. The TI Team interpreted the channel margins, shown as pink lines, from detailed mapping on profiles and time slices from the 3D seismic-reflection volume.
- See Figure 8-35 for figure location.
- Depth values on seismic profile assume a velocity of 1,600 m/s.

Source: 3D seismic-reflection data from PG&E (2014, Chapter 3).

Map projection and scale: WGS 84 / UTM Zone 10N

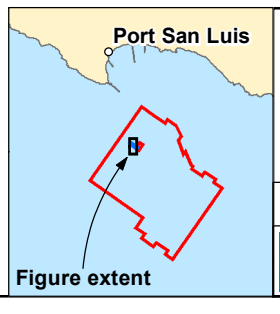

Time Slice at 72 ms and Crossline 1775 Showing Channel A Intersection with Shoreline Fault

DCPP SSC REPORT

Pacific Gas and Electric Company

Figure **8-43**

File path: S:\1005\005\Final_Report_Figures\Figure_800-43.mxd; Date: 03/11/2015; User: Alex Remar, LCI; Rev.1

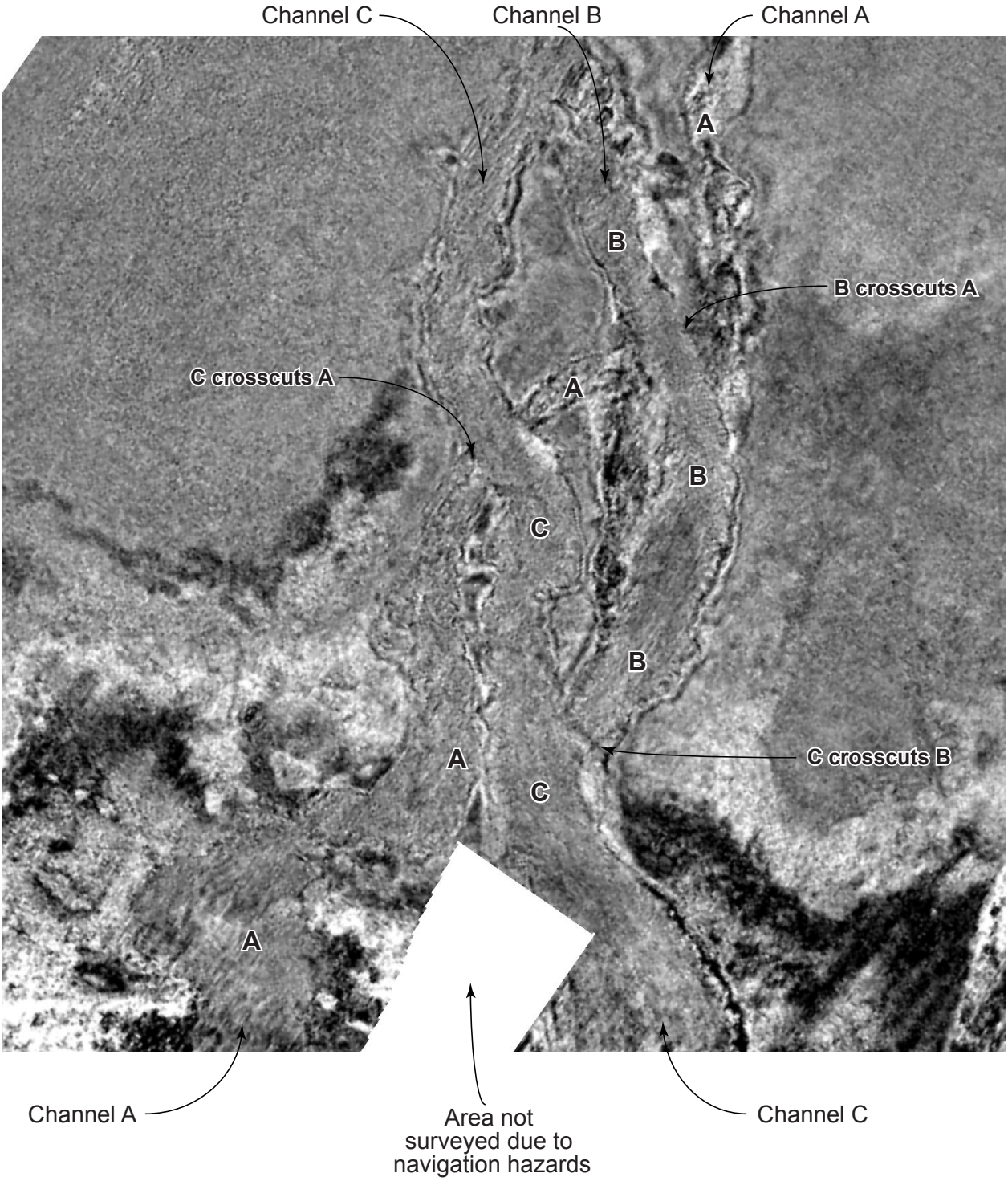

Note:
- See Figure 8-35 for location of figure.
- Crosscutting relationships show that among channels in the offshore San Luis Obispo Creek system, Channel C is the youngest and Channel A is the oldest of the three channels imaged. Channels D and E are not imaged in this time slice.

Source: 3D seismic-reflection data from PG&E (2014, Chapters 2 and 3).

Time Slice at 66.3 ms Showing Crosscutting Relationships Between Channels A, B, and C

DCPP SSC REPORT

Pacific Gas and Electric Company

Figure **8-44**

File path: S:\1005\005\Final_Report_Figures\Figure_800-44.ai; Date: 03/11/2015; User: Alex Remar, LCI; Rev.1

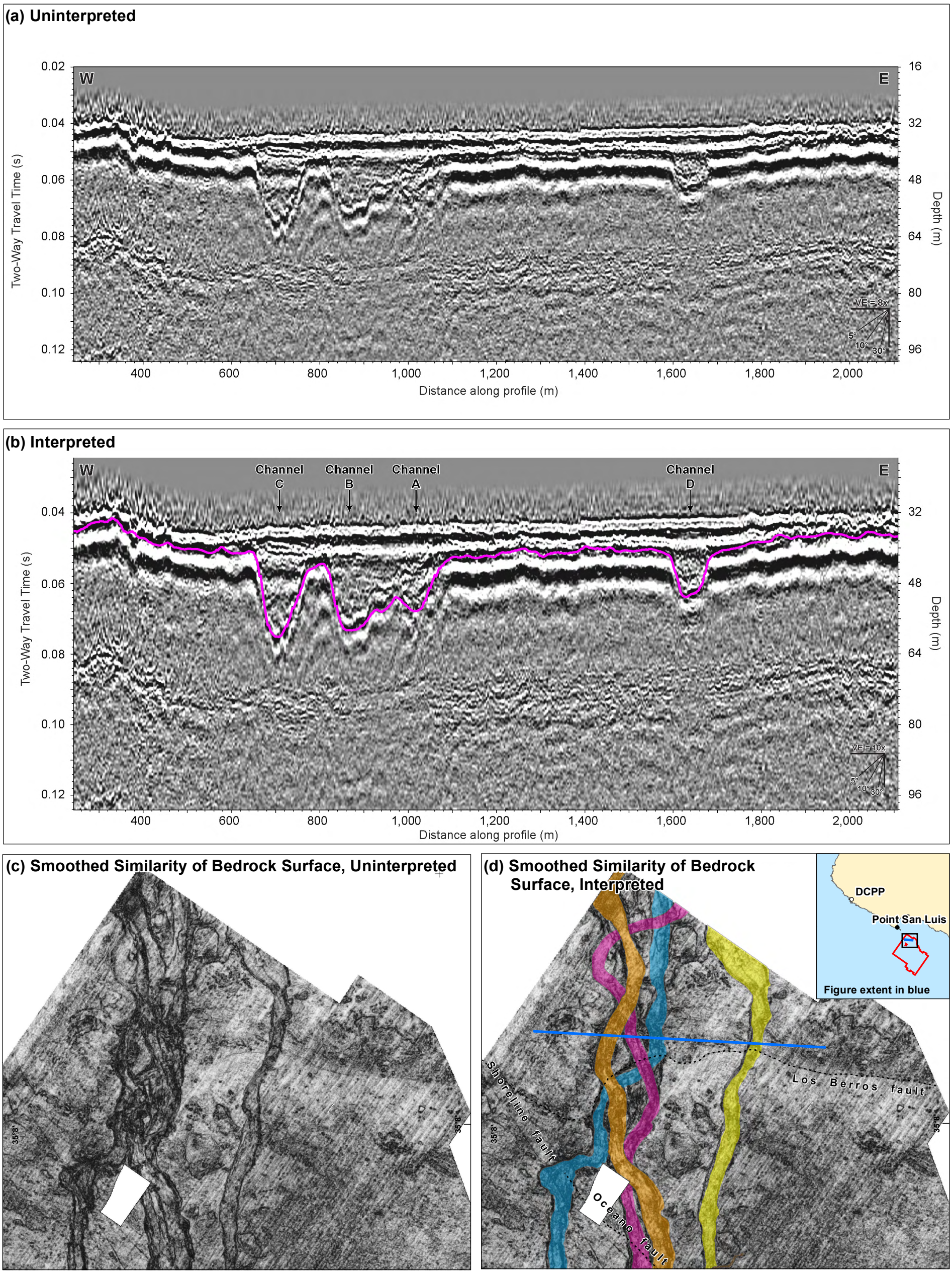

EXPLANATION

- Quaternary fault trace buried by undeformed unconformity H10 or older strata
- Top of rock
- Location of seismic profile
- Approximate contours on top of bedrock, 5 m interval

Channel Name

A, B, C, D

Notes:
- Panels (a) and (b) show profiles across buried channels at a similar distance from the coast within the uplifting hanging wall of the Oceano and Los Berros faults. Channel A is incised approximately 18-19 m, Channel B is incised approximately 16 m, and Channel A is incised approximately 12 m relative to the surrounding bedrock surface. Differences in depth of incision suggest that Channel A is significantly older than Channel C. See text of Section 8.4.3 for more explanation.
- See Figure 8-35 for figure location.
- Depth values on seismic profile assume a velocity of 1,600 m/s.

Source: 3D seismic-reflection data from PG&E (2014, Chapters 2 and 3).

Map projection and scale: WGS 84 / UTM Zone 10N, 1:24,000

Profile Showing Differences in Depth of Incision in Upper Reaches of Channels A, B, and C

DCPP SSC REPORT

Pacific Gas and Electric Company

Figure **8-45**

File path: S:\1005\005\Final_Report_Figures\Figure_800-45.mxd; Date: 03/11/2015; User: Alex Remar, LCI; Rev.1

(a) Offset PDF

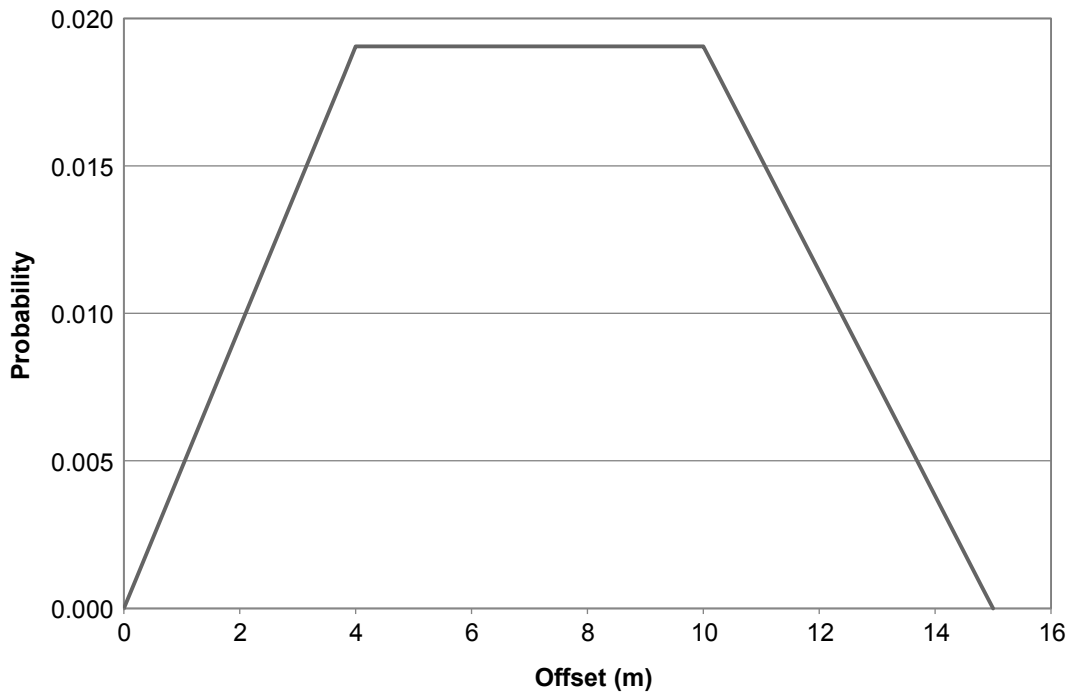

(b) Justification for Offset PDF

Value	Offset (m)	Basis
Min.	0	Interpretation of no offset credible
Preferred	4	Observed offset of 7 m ± 3 m
Preferred	10	
Max.	15	Exceeds observed channel offsets. Additional 5 m uncertainty accounts for poor resolution of channel margins.

(c) Age PDF

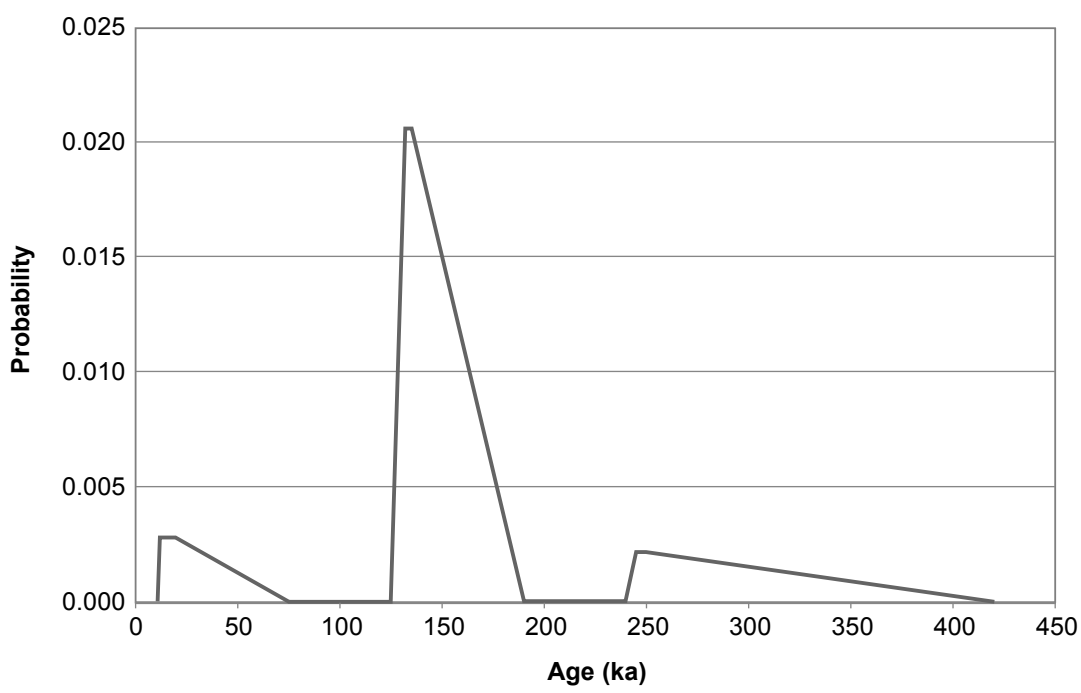

(d) Justification for Age PDF

MIS 2 [0.1]		
Value	**Age (ka)**	**Basis–Channels A, B, and C all active during MIS 2**
Min.	11	Minimum possible timing of sea level rise above ~58 m depth
Preferred	11.5	Most likely timing of sea level rise above ~58 m depth
Preferred	20	Onset of sea level rise following MIS 2 lowstand
Max.	75	Onset of MIS 4 lowstand

MIS 6 [0.7]		
Value	**Age (ka)**	**Basis–Channel A is one full sea level cycle older than Channel C**
Min.	125	Minimum possible age of MIS 6–5 transgression
Preferred	132	Most likely age of MIS 6–5 transgression
Preferred	135	Maximum depth of MIS 6 lowstand
Max.	190	Onset of MIS 6 lowstand

MIS 8–12 [0.2]		
Value	**Age (ka)**	**Basis–Channels A, B, and C were active during separate low stands**
Min.	240	Age of sea level rise above ~58 m during MIS 8–7 transgression
Preferred	245	Onset of MIS 8–7 transgression
Preferred	250	Maximum MIS 8 lowstand
Max.	420	Maximum MIS 12 lowstand

(e) Slip Rate CDF

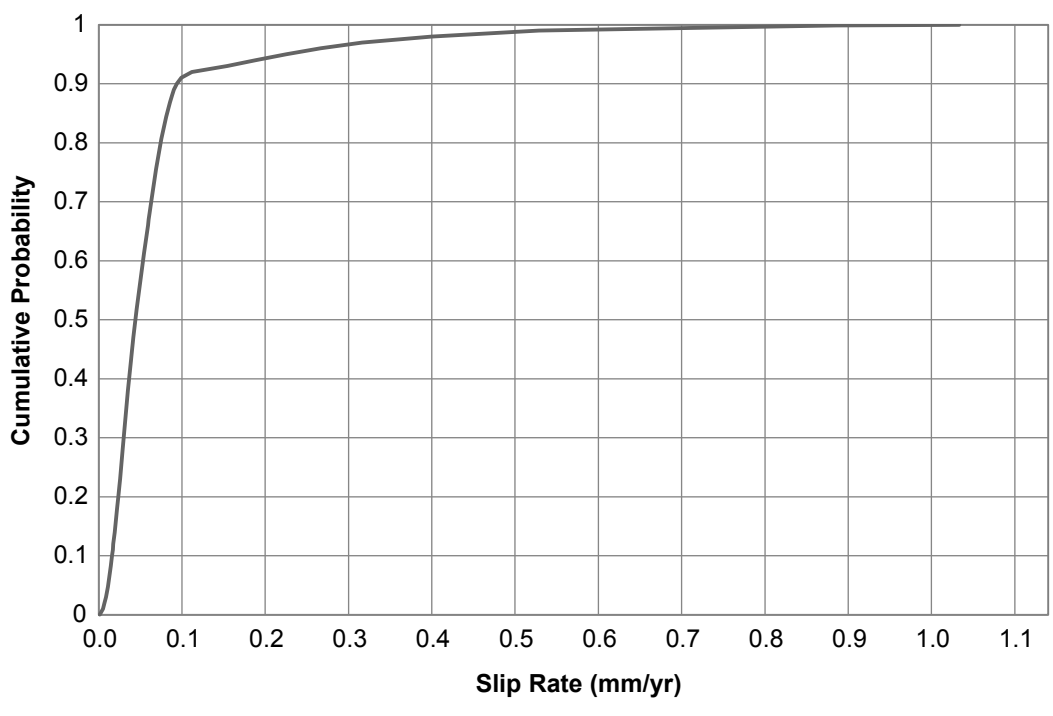

(f) Summary Statistics

Cumulative Probability	Slip Rate (mm/yr)
0.05	0.01
0.1	0.02
0.2	0.02
0.5	0.04
0.8	0.07
0.9	0.09
0.95	0.23
Minimum	0.00
Maximum	1.17
Mean	**0.07**

Notes:
- Numbers in brackets in Panel (d) are weights assigned to each age model.
- Uncertainty in timing of MIS 4 and 6 lowstands from Waelbroeck et al. (2002); uncertainty in timing of MIS 2 from Stanford et al. (2011).
- Probability distributions used to describe uncertainty in offset (Panels (a) and (b)) and age (Panels (c) and (d)) of the margins of Channel A, and used by the TI Team to calculate a slip rate CDF for the Shoreline fault at the intersection with Channel A.

PDFs of Uncertainty in Offset and Age of Channel A, and Slip Rate CDF

DCPP SSC REPORT

Pacific Gas and Electric Company

Figure **8-46**

File path: S:\1005\005\Final_Report\Figures\Figure_800-46.ai; Date: 02/26/2015; User: Alex Remar, LCI; Rev.1

(a) Uplift Rate PDFs

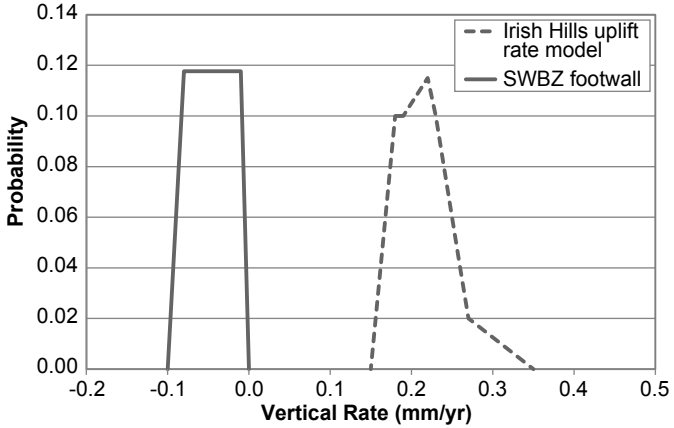

(c) Slip Rate CDF

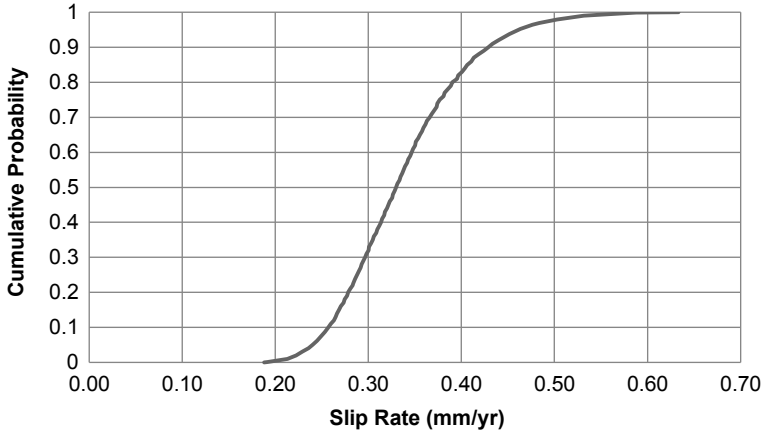

(b) Justification for Subsidence Rate of the SWBZ Footwall

Value	Vertical Rate (m/kyr)	Basis
Min.	-0.10	Max. 13 m vertical separation down to the east of H30 across the HFZ in San Luis Obispo Bay
Preferred	-0.08	Range of subsidence based on variability in vertical separation of H10 and H30 across the HFZ in San Luis Obispo Bay
Preferred	-0.01	
Max.	0	Min. possible rate based on accommodation and deposition between transgressive unconformities

(d) Summary Statistics

Cumulative Probability	SWBZ Slip Rate
0.05	0.24
0.1	0.26
0.2	0.28
0.5	0.33
0.8	0.39
0.9	0.43
0.95	0.46
Minimum	0.19
Maximum	0.64
Mean	**0.34**

Notes:
- Probability distributions used to describe uncertainty in vertical separation rate between the Irish Hills in the hanging wall of the SWBZ and San Luis Obispo Bay in the footwall of the SWBZ (Panels (a) and (b)) used by the TI Team to calculate a generalized slip rate CDF for the entire SWBZ.
- The Irish Hills uplift rate model is described in Section 8.2-2 and shown on Figure 8-6.
- Mean dip of SWBZ characterized as 45° to 60° +15°/-10°.
- Vertical separation measurements across the HFZ are from PG&E (2013b).

PDFs of Uncertainty in Vertical Rate of the SWBZ, and Slip Rate CDF

DCPP SSC REPORT

Pacific Gas and Electric Company | Figure **8-47**

File path: S:\1005\005\Final_Report\Figures\Figure_800-47.ai; Date: 03/11/2015; User: Alex Remar, LCI; Rev.1

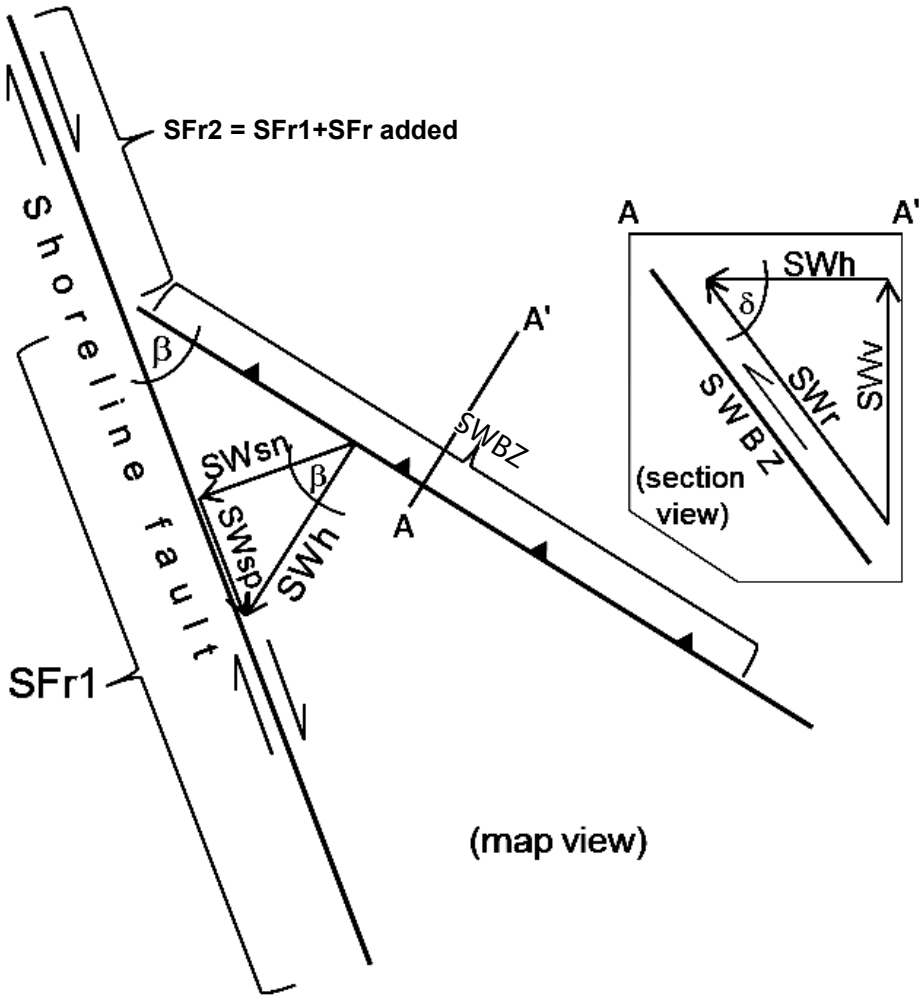

Symbols and Abbrevitions	
β	Angle between SWBZ and Shoreline fault strikes characterized as 40°–45° ± 5°
δ	Dip (SWBZ) characterized as 45°–60° + 15° / -10°
SWBZ slip rate components	
SWv	Vertical
SWr	Net (and dip slip)
SWh	Horizontal (shortening)
SWsn	Shoreline-normal
SWsp	Shoreline-parallel
Shoreline fault slip rate	
SFr1	Net (and ≅ horizontal), south of the SWBZ intersection
SFr2	Net (and ≅ horizontal), north of the SWBZ intersection
SFr added	Amount of slip rate added to the Shoreline fault from the SWBZ (= SFr2 - SFr1), where SFr added is greater than zero and less than SWsp

Note: Geometric relationships between the generalized SWBZ and the Shoreline fault are used to calculate the fraction of the SWBZ slip rate that is parallel to the Shoreline fault.

Resolution of Shoreline-Parallel Component of the Southwest Boundary Zone Slip Rate

DCPP SSC REPORT

Pacific Gas and Electric Company

Figure **8-48**

File path: S:\1005\005\Final_Report_Figures\Figure_800-48.ai; Date: 02/26/2015; User: Alex Remar, LCI; Rev.1

(a) Slip Rate CDFs

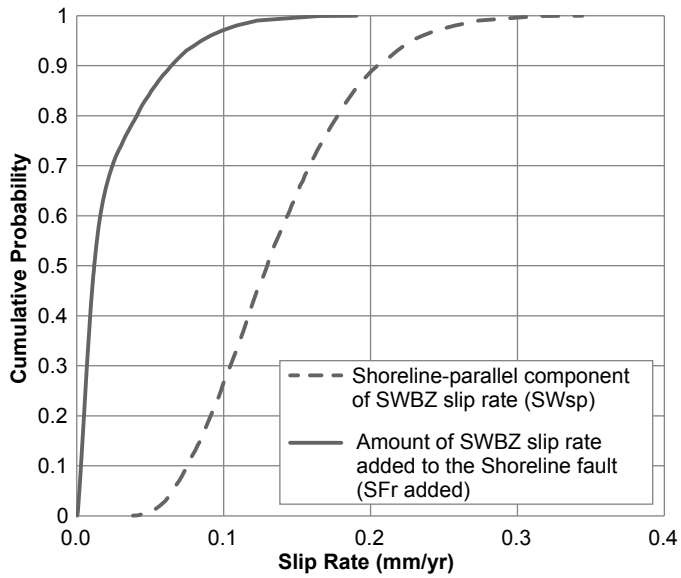

Slip Rate (mm/yr)		
Cumulative Probability	SWsp	SFr added
0.05	0.07	0.00
0.1	0.08	0.00
0.2	0.09	0.00
0.5	0.13	0.01
0.8	0.18	0.04
0.9	0.20	0.06
0.95	0.23	0.08
Minimum	0.04	0.00
Maximum	0.35	0.19
Mean	**0.14**	**0.02**

$$\frac{SFr\ added}{SWsp} = \frac{SFv}{SWv}$$

Sfv Vertical separation rate across northern Shoreline fault

(b) Shoreline Fault Vertical Separation Rate PDF

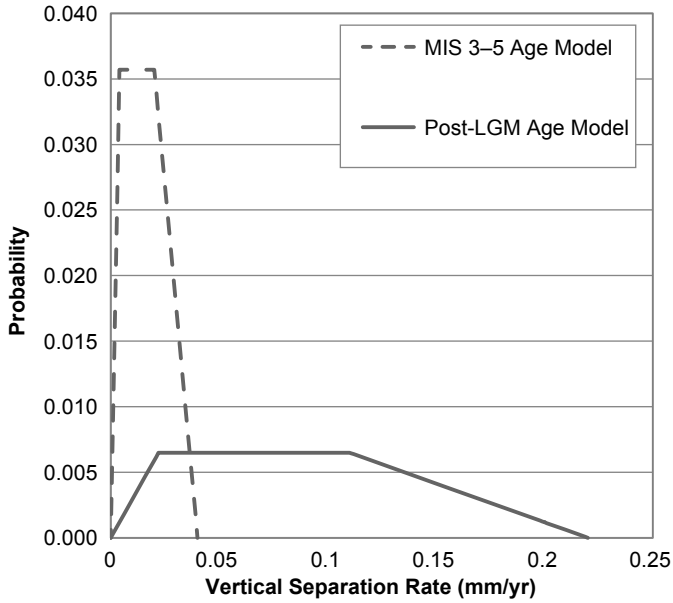

MIS 3–5 Age Model [0.6]		
Value	Vertical Separation Rate (mm/yr)	Basis
Min.	0	Observed separation
Preferred	0.004	10% of maximum
Preferred	0.02	50% of maximum
Max.	0.04	Maximum separation (2 m) in 50 ka

Post-LGM Age Model [0.4]		
Value	Vertical Separation Rate (mm/yr)	Basis
Min.	0	Observed separation
Preferred	0.022	10% of maximum
Preferred	0.11	50% of maximum
Max.	0.22	Maximum separation (2 m) in 9 ka

Note: Constraints on vertical separation across the northern Shoreline fault are used to assess the fraction of the Shoreline fault-parallel SWBZ slip rate (dashed line in Panel (a)) that is contributed to the Shoreline fault (solid line in Panel (a)). Panel (b) illustrates the assessment of possible rates of vertical separation across the northern Shoreline fault from submerged wave-cut platforms (PG&E, 2011) and uncertainty in the ages of the platforms. Although no vertical separation of wave-cut platforms was observed, this value is assigned a probability of 0 because vertical separation across the northern Shoreline fault is required in this model for dextral slip rate to be transferred from the SWBZ to the Shoreline fault.

Assessment of the Amount of SWBZ Slip Rate Contributed to the Northern Shoreline Fault

DCPP SSC REPORT

Pacific Gas and Electric Company

Figure **8-49**

File path: S:\1005\005\Final_Report_Figures\Figure_800-49.ai; Date: 02/26/2015; User: Alex Remar, LCI; Rev.1

(a) Uninterpreted

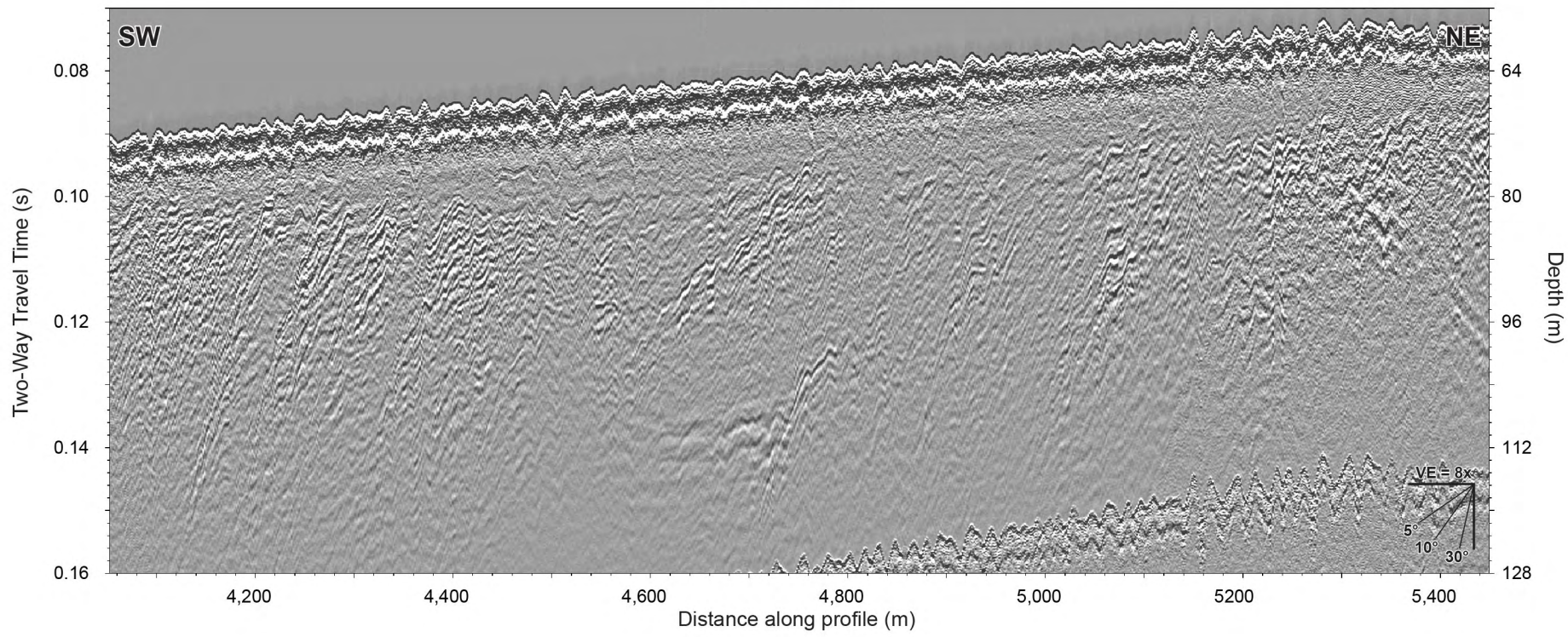

(b) Interpreted Profile Flattened to Seafloor

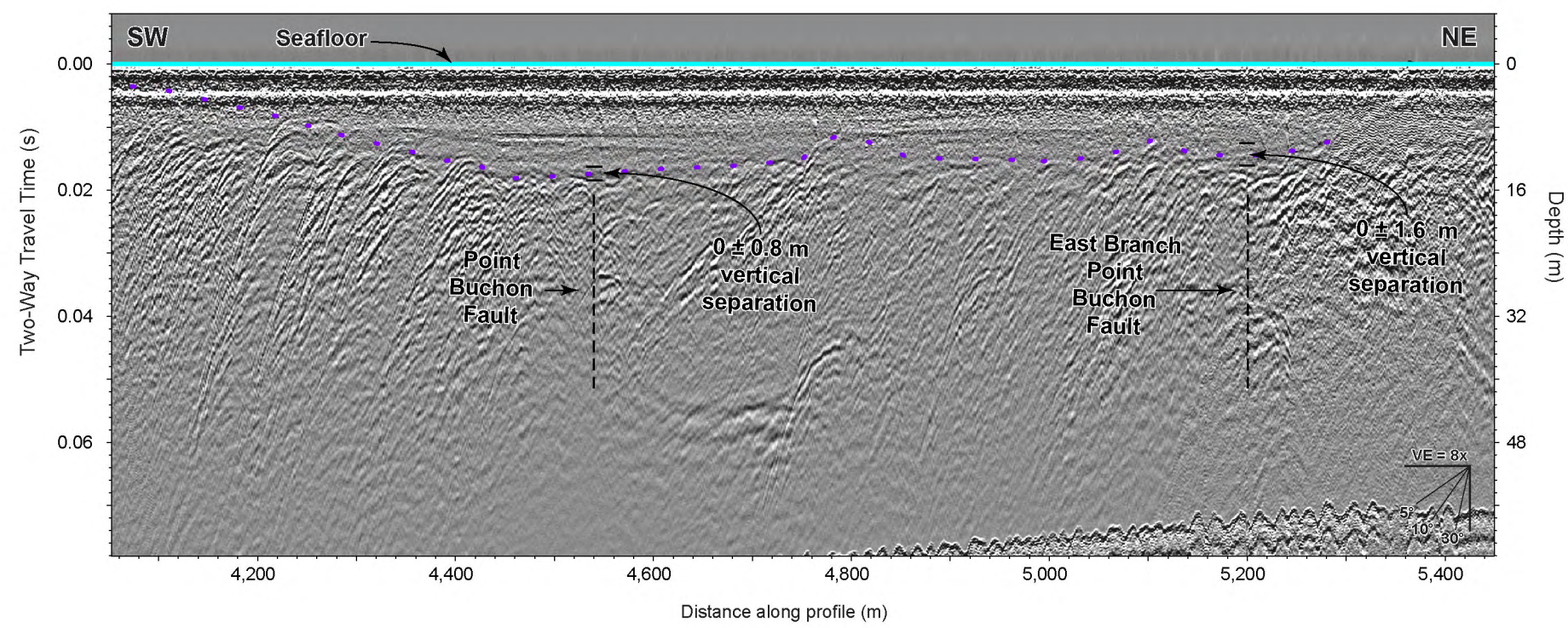

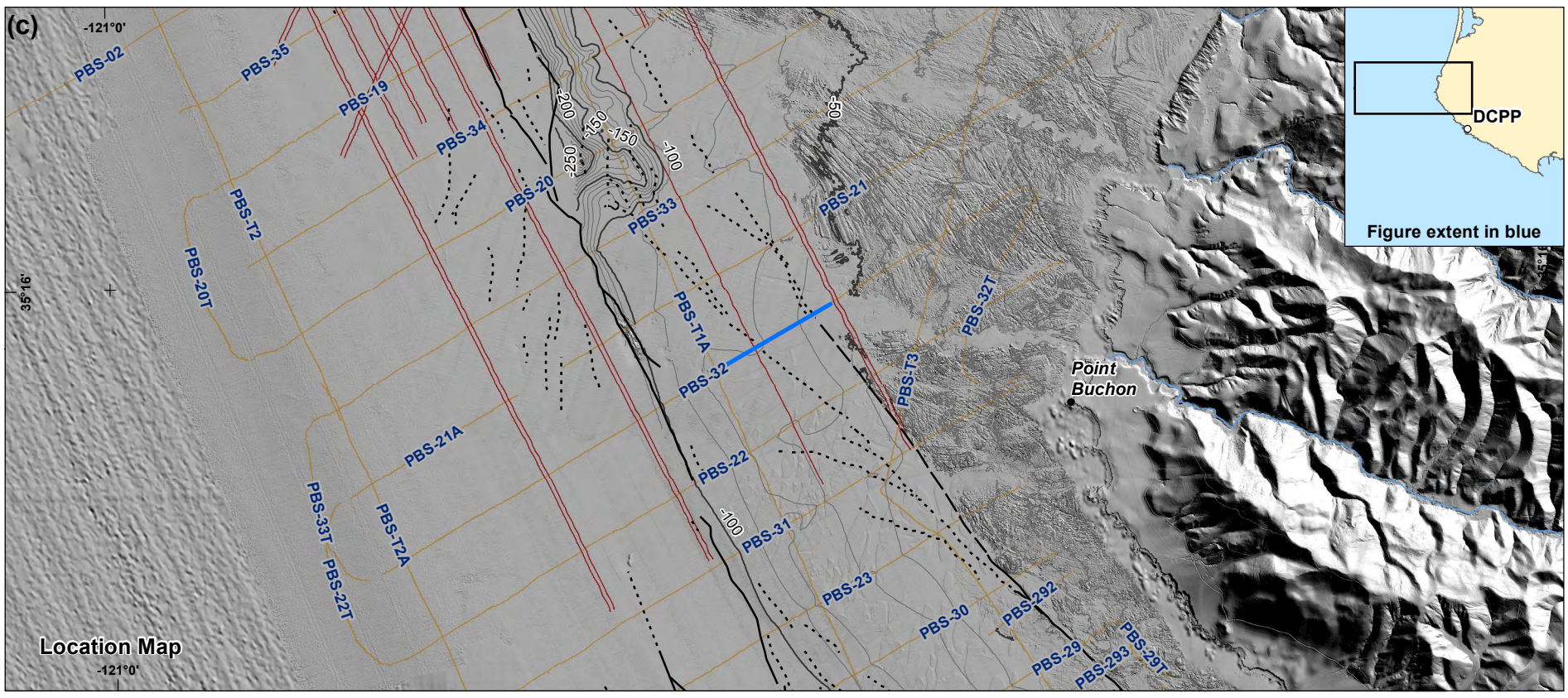

EXPLANATION

- Quaternary fault trace: solid where well located, dashed where approximately located, dotted where buried by undeformed unconformity H10 or older strata, short dashed where inferred, queried where existence is uncertain
- PG&E 2D survey trackline
- USGS survey trackline
- Location of seismic profile
- Top of rock

Notes:
- No vertical separation is observed in the top of bedrock surface or in overlying stratigraphy across the northern part of the Shoreline fault (the Point Buchon fault and the east branch of the Point Buchon fault). Uncertainty is assessed from variability in the top of bedrock (Panels (a) and (b)).
- Depth values on seismic profile assume a velocity of 1,600 m/s.
- Horizontal black bars in Panel (b) above traces of the Point Buchon fault are approximate limits of uncertainty in vertical separation across the fault.
- A 10 m structure contour interval is shown in Panel (c), heavy contours are 50 m. Bathymetric contours are used in regions where bedrock is exposed at the seafloor.

Sources:
- 2D seismic-reflection data (Sliter et al., 2010).
- Bedrock contours from PG&E (2014, Chapter 3).

N

0 1 2 mi.

0 2 4 km

Map projection and scale: WGS 84 / UTM Zone 10N, 1:60,000

Excerpt of Seismic-Reflection Profile PBS-32 and Contours of Bedrock Surface Showing Absence of Vertical Separation Across the Point Buchon Fault

DCPP SSC REPORT

Pacific Gas and Electric Company

Figure **8-50**

File path: S:\1005\005\Final_Report_Figures\Figure_800-50.mxd; Date: 02/27/2015; User: Serkan Bozkurt, LCI; Rev.1

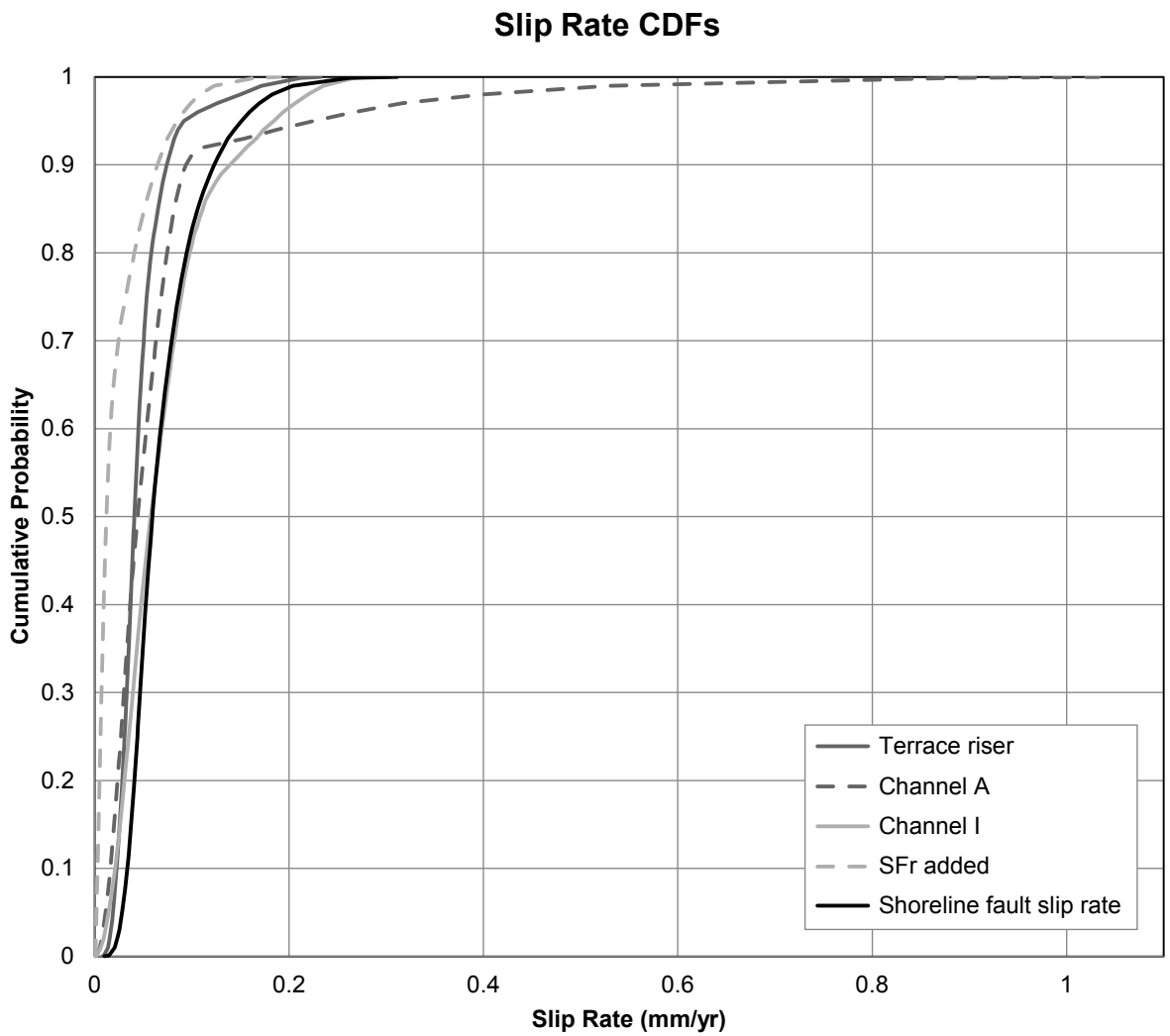

5-Point Distribution		
Percentile	**Slip Rate (mm/yr)**	**Weight**
0.034893	0.03	0.101
0.211702	0.04	0.244
0.5	0.06	0.309
0.788298	0.09	0.244
0.965107	0.16	0.101
Weighted Mean	**0.07**	

Note: The slip rate CDF for the Shoreline fault (solid black line) is calculated by adding the rate of Shoreline-parallel dextral slip contributed from the SWBZ (SFr added) to the slip rate CDF calculated from the terrace riser slip rate site (solid dark grey line). Slip rate CDFs calculated for the Channel A (dashed dark grey line) and Channel I (solid light grey line) slip rate sites are shown for comparison.

Shoreline Fault Slip Rate at the DCPP

DCPP SSC REPORT

Pacific Gas and Electric Company | Figure **8-51**

File path: S:\1005\005\Final_Report\Figures\Figure_800-51.ai; Date: 02/26/2015; User: Alex Remar, LCI; Rev.1

(a) Footwall Uplift Rate PDFs

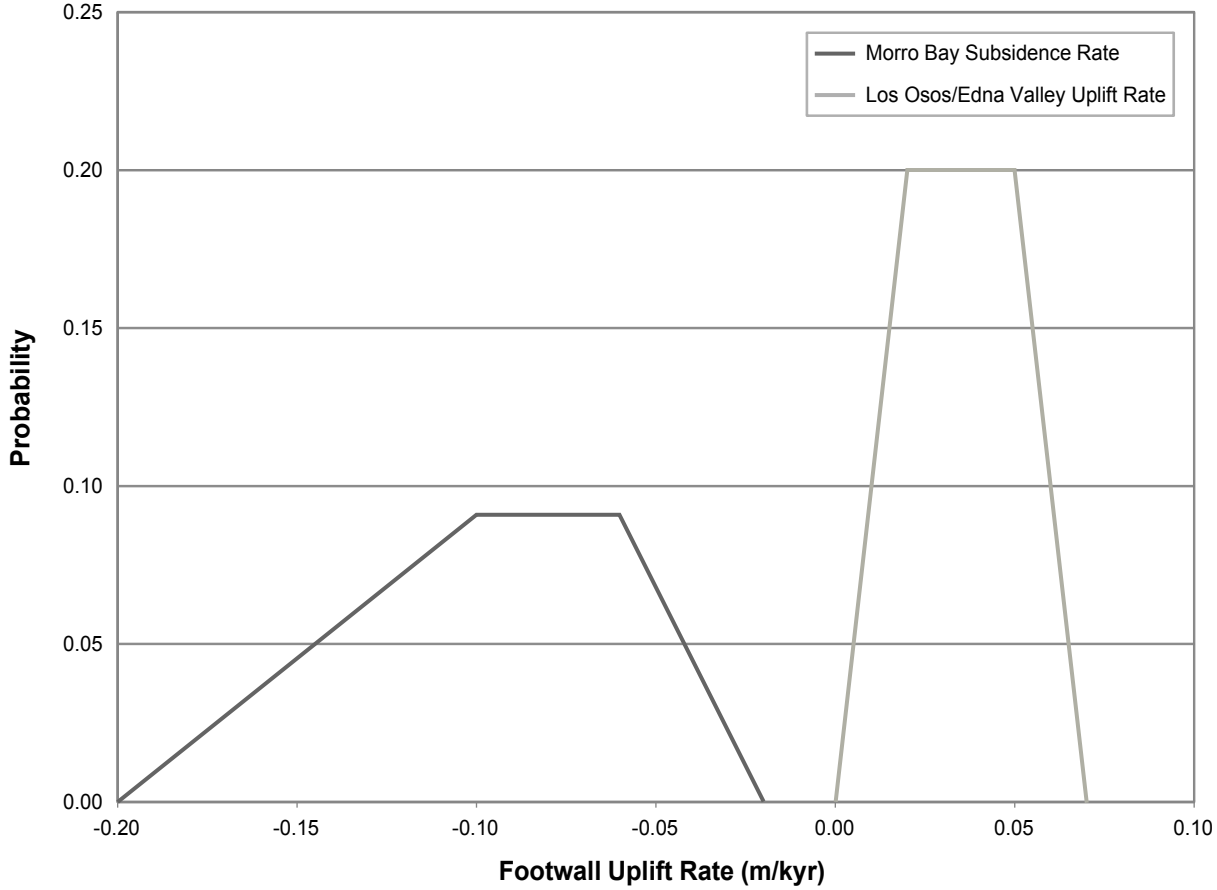

(b) Justification for Footwall Uplift Rate PDFs

Morro Bay Subsidence Rate		
Value	**Uplift Rate (m/kyr)**	**Basis**
Min.	-0.02	Q terrestrial deposits subsided ≥ 50 m to -200 m in past 2.5 Ma
Preferred	-0.06	Q terrestrial deposits subsided 150 m to -200 m in past 2.5 Ma
Preferred	-0.10	AT2 clay subsided 40 m from initial elevation of 10 m during MIS 11
Max.	-0.20	TI Team judgment that the subsidence rate of this minor basin does not exceed the uplift rate of the Irish Hills

Los Osos/Edna Valley Uplift Rate		
Value	**Uplift Rate (m/kyr)**	**Basis**
Min.	0	No uplift of Los Osos and Edna Valleys
Preferred	0.02	Estimated late Pliocene age (~3.3-3.0 Ma) of marine deposits at 80 m elevation in Edna Valley
Preferred	0.05	Correlation of Memorial Park terrace to MIS 11
Max.	0.07	Correlation of the 13 ± 1 m Cayucos terrace remnant to MIS 5e

Note: PDFs for uncetainty in the vertical deformation rate of the footwall of the Los Osos fault. The Quaternary subsidence rate of the Morro Bay region (dark gray line) is used in the NE Model. The Quaternary uplift rate of other parts of the Los Osos Valley and Edna Valleys (light gray line) are used in the SW and OV Models. See Section 8.5.1 for more explanation.

Los Osos Fault – Footwall Uplift Rate PDFs

DCPP SSC REPORT

Pacific Gas and Electric Company | Figure **8-52**

File path: S:\1005\005\Final_Report_Figures\Figure_800-52.ai; Date: 03/11/2015; User: Alex Remar, LCI; Rev.1

(a) Interpreted Cross Section Through the Morro Bay Groundwater Basin

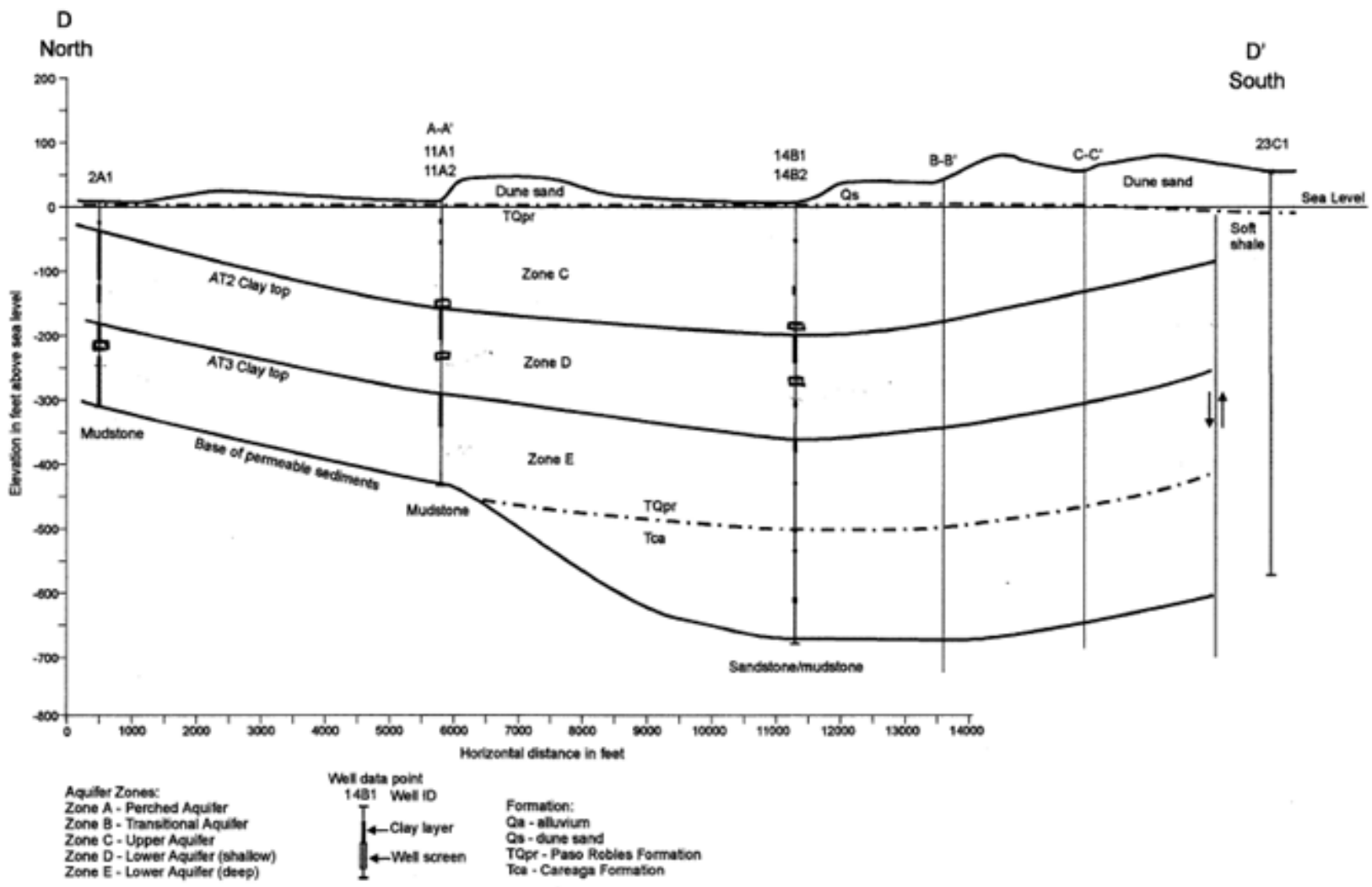

(b) Structure Contour Map of the Top of the AT2 Clay Layer

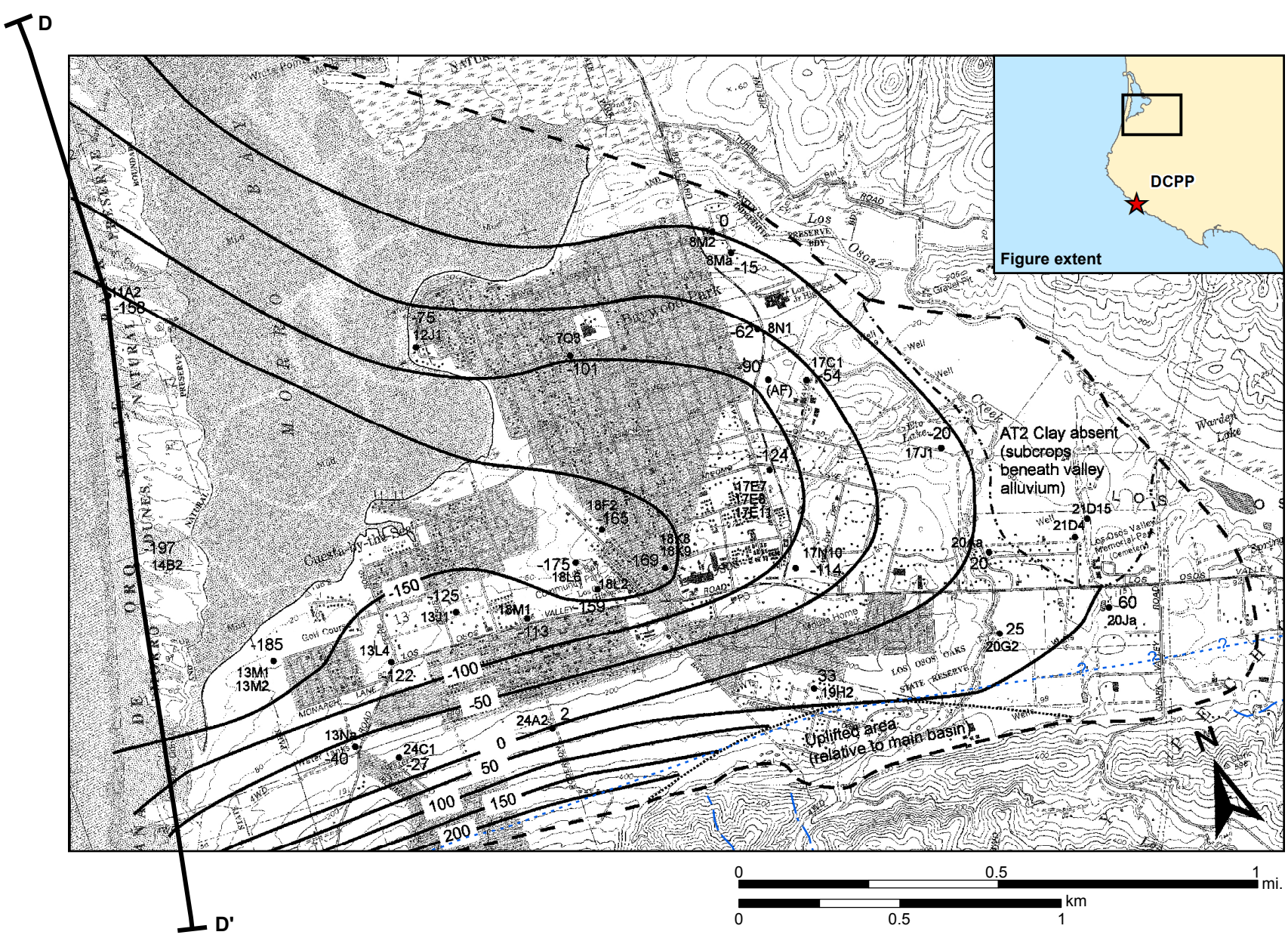

EXPLANATION

- Cross section D-D'
- Elevation contour on base of permeable sediments in feet above sea-level.
- Approximate basin limits
- Fault mapped in this study; dashed where approximately located, dotted where inferred, queried where existence uncertain

Note: Key marker horizons within the Morro Bay groundwater basin as mapped by Cleath & Associates (2003) are shown in profile in Panel (a). Panel (b) shows a structure contour map of the top of the shallowest key horizon, the AT2 clay.

Source: Modified from Cleath & Associates (2003).

Cross Section and Structure Contour Map of AT2 Horizon in the Morro Bay Area

DCPP SSC REPORT

Pacific Gas and Electric Company

Figure **8-53**

File path: S:\1005\005\Final_Report\Figures\Figure_800-53.ai; Date: 03/10/2015; User: Serkan Bozkurt, LCI; Rev.1

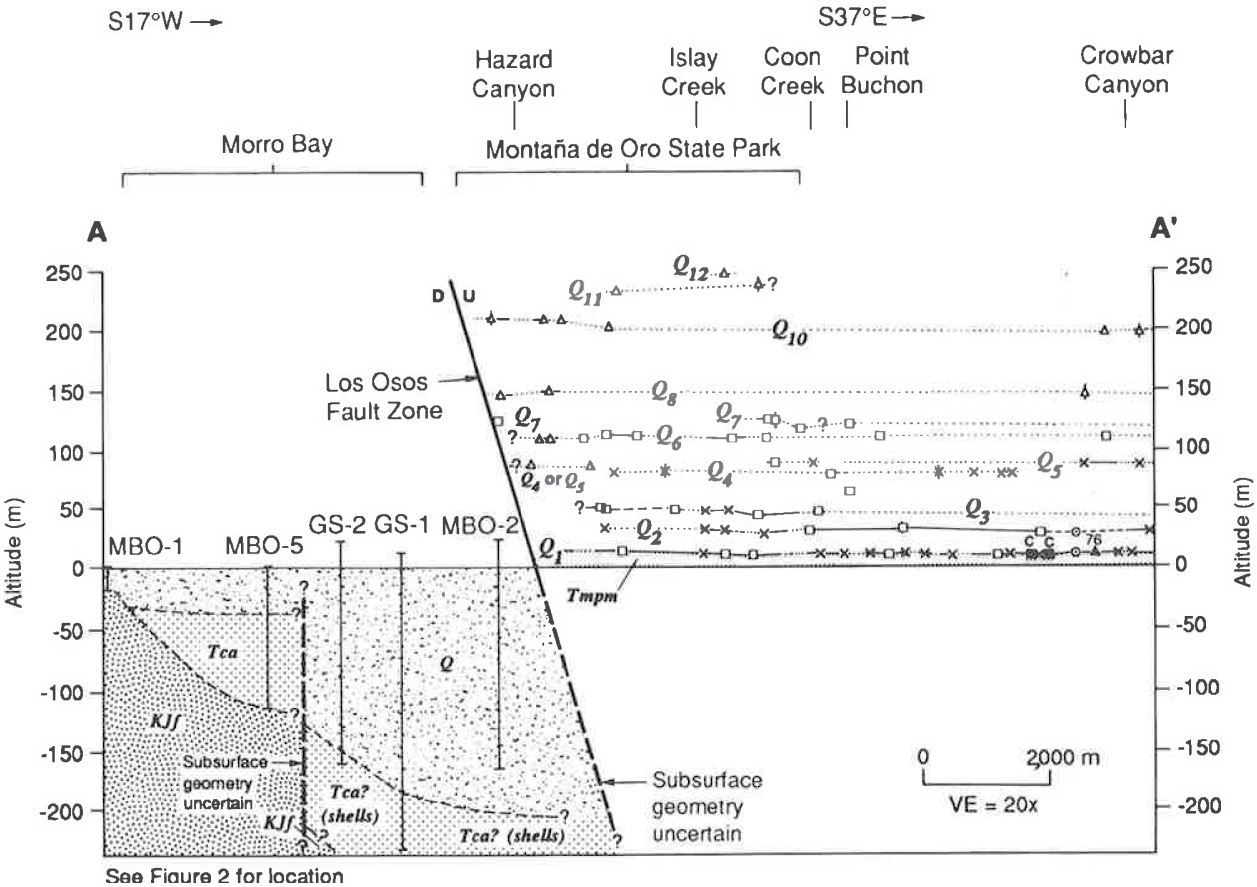

EXPLANATION

- Altitude of shoreline angle: solid where well constrained, dashed where concealed, dotted where eroded
- × Exposed shoreline angle
- ⊙ Projection from borehole
- □ Projection from exposure of wave-cut platform (WCP)
- + From trench logs
- △ Altitude estimated from 1:24,000 scale map (± 40 ft)
- △ Altitude estimated from 1:24,000 scale map (± 20 ft)
- ○ Altitude estimated from 1:2000 scale map (± 10 ft) (error in altitude is contained within the size of the symbols except where shown by the vertical bar)
- ▼ Wave-cut platform
- ■ Faunal assemblage: w = warm (inferred age 120 ka), c = cool (inferred age 80 or 105 ka)
- ● Coral U-series age (ka)
- ▲ Bone U-series age (ka)
- U/D Fault: dashed where uncertain, dotted where inferred; U = up, D = down
- Well

Marine Terrace	Oxygen Isotope Stage (Shackelton and Opdyde, 1973)	Age
Q_1	Substage 5a	80 ka
Q_{1a}	Substage 5c	105 ka
Q_2	Substage 5e	120 ka
Q_3	Stage 7	210 ka
Q_4	Stage 9	330 ka
Q_5	Stage 11	430 ka
Q_6	Stage 13	480 ka
Q_{7-13}	Stage 15 or older	≥560 ka

- Q Quaternary deposits
- Tca Careaga Sandstone - Pliocene
- Tmpm Miguelito Member, Pismo Formation - Pliocene
- KJf Franciscan Complex - Cretaceous-Jurassic

Source: Modified from Lettis and Hall (1994).

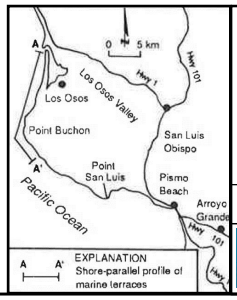

Subsurface Data from Morro Bay Used to Constrain the Rate of Footwall Deformation for the Los Osos Fault – NE Fault Model

DCPP SSC REPORT

Pacific Gas and Electric Company

Figure **8-54**

File path: S:\1005\005\Final_Report\Figures\Figure_800-54.ai; Date: 02/26/2015; User: Alex Remar, LCI; Rev.1

(a) Differential Uplift Rate CDFs

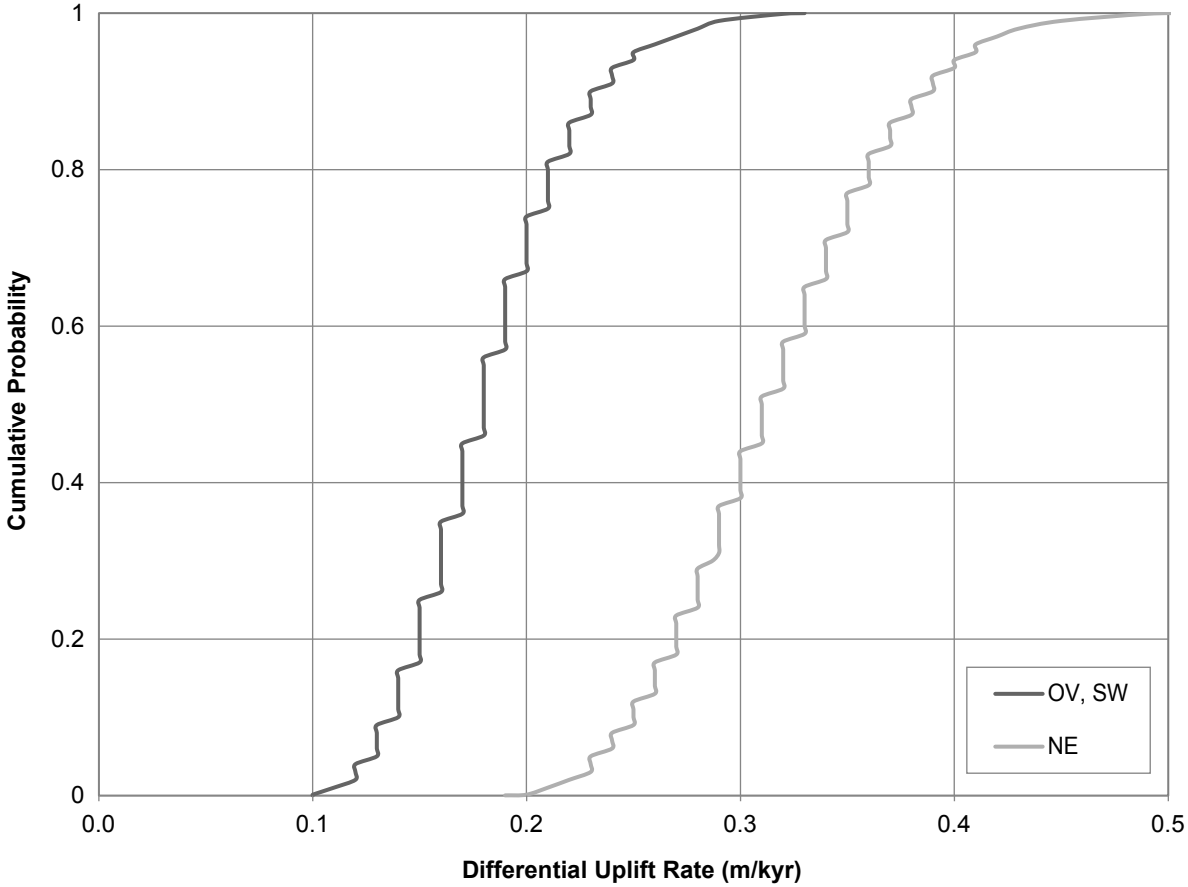

(b) Summary Statistics

Differential Uplift Rate (m/kyr)		
Cumulative Probability	**NE Model**	**OV, SW Models**
0.05	0.23	0.13
0.1	0.25	0.14
0.2	0.27	0.15
0.5	0.31	0.18
0.8	0.36	0.21
0.9	0.39	0.23
0.95	0.41	0.25
Min.	0.19	0.10
Max.	0.52	0.33
Mean	**0.32**	**0.18**

Note: Differential uplift of the hanging wall and the footwall of the Los Osos fault is used to calculate the vertical separation rate, which is shown for the three fault models in Panel (a). Steps in the CDFs result from the 0.01 mm/yr slip rate bin size sampled for Monte Carlo calculations (which is described in Section 8.2.1). Net slip rate of the fault is calculated from these separation rates and the fault dip associated with each model.

Los Osos Fault Differential Uplift CDFs for OV, SW, and NE Fault Models

DCPP SSC REPORT

Pacific Gas and Electric Company Figure **8-55**

File path: S:\1005\005\Final_Report_Figures\Figure_800-55.ai; Date: 02/26/2015; User: Alex Remar, LCI; Rev.1

(a) Rake PDFs

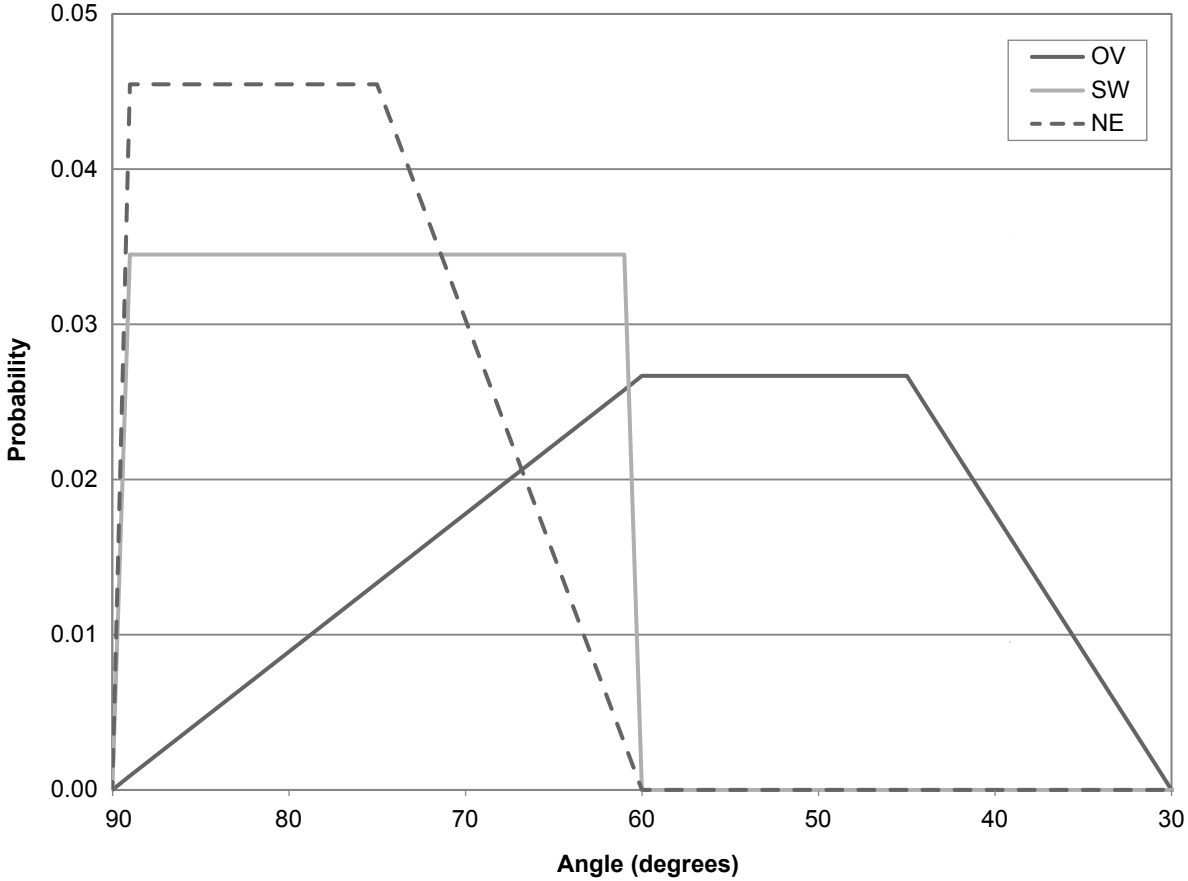

(b) Rake (Degrees)

Value	OV Model	SW Model	NE Model
Min.	90	90	90
Preferred	60	89	89
Preferred	45	61	75
Max.	30	60	60

Note: Probability distributions for the rake of the Los Osos fault in each of the three fault models. These distributions reflect the concept that in the OV Model, the Los Osos fault may accommodate relatively more oblique slip, whereas in the SW and NE Models, the Los Osos fault likely accommodates dominantly reverse slip.

Los Osos Fault Rake PDFs for OV, SW, and NE Fault Models

DCPP SSC REPORT

Pacific Gas and Electric Company | Figure **8-56**

File path: S:\1005\005\Final_Report_Figures\Figure_800-56.ai; Date: 02/26/2015; User: Alex Remar, LCI; Rev.1

(a) Calculation of Net Slip Rate CDF

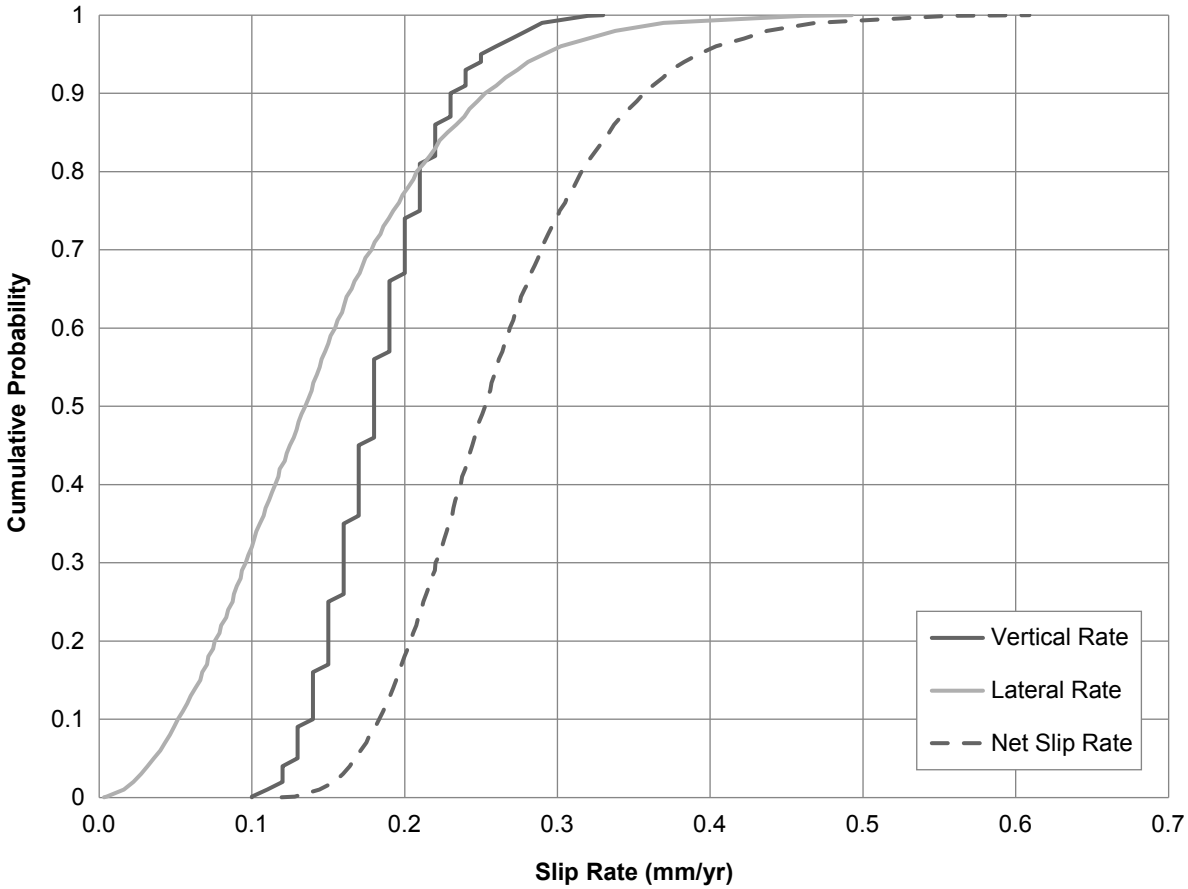

(b) Summary Statistics

Cumulative Probability	Vertical Rate (mm/yr)	Lateral Rate (mm/yr)	Net Slip Rate (mm/yr)
0.05	0.13	0.04	0.17
0.1	0.14	0.05	0.18
0.2	0.15	0.08	0.20
0.5	0.18	0.13	0.25
0.8	0.21	0.21	0.32
0.9	0.23	0.25	0.36
0.95	0.25	0.29	0.39
Min.	0.10	0.00	0.12
Max.	0.33	0.49	0.61
Mean	**0.18**	**0.15**	**0.26**

Note: A net slip rate CDF for the Los Osos fault in the OV Model was calculated from the vertical separation rate (from Figure 8-55), a modeled dip of 60 degrees, and a lateral slip rate calculated from the rake distribution shown on Figure 8-56. Steps in the vertical rate CDF result from the 0.01 mm/yr slip rate bin size sampled for Monte Carlo calculations (which is described in Section 8.2.1).

Los Osos Fault Net Slip Rate CDF for OV Model

DCPP SSC REPORT

Pacific Gas and Electric Company | Figure **8-57**

File path: S:\1005\005\Final_Report_Figures\Figure_805-57.ai; Date: 02/26/2015; User: Alex Remar, LCI; Rev.1

(a) Calculation of Net Slip Rate CDF

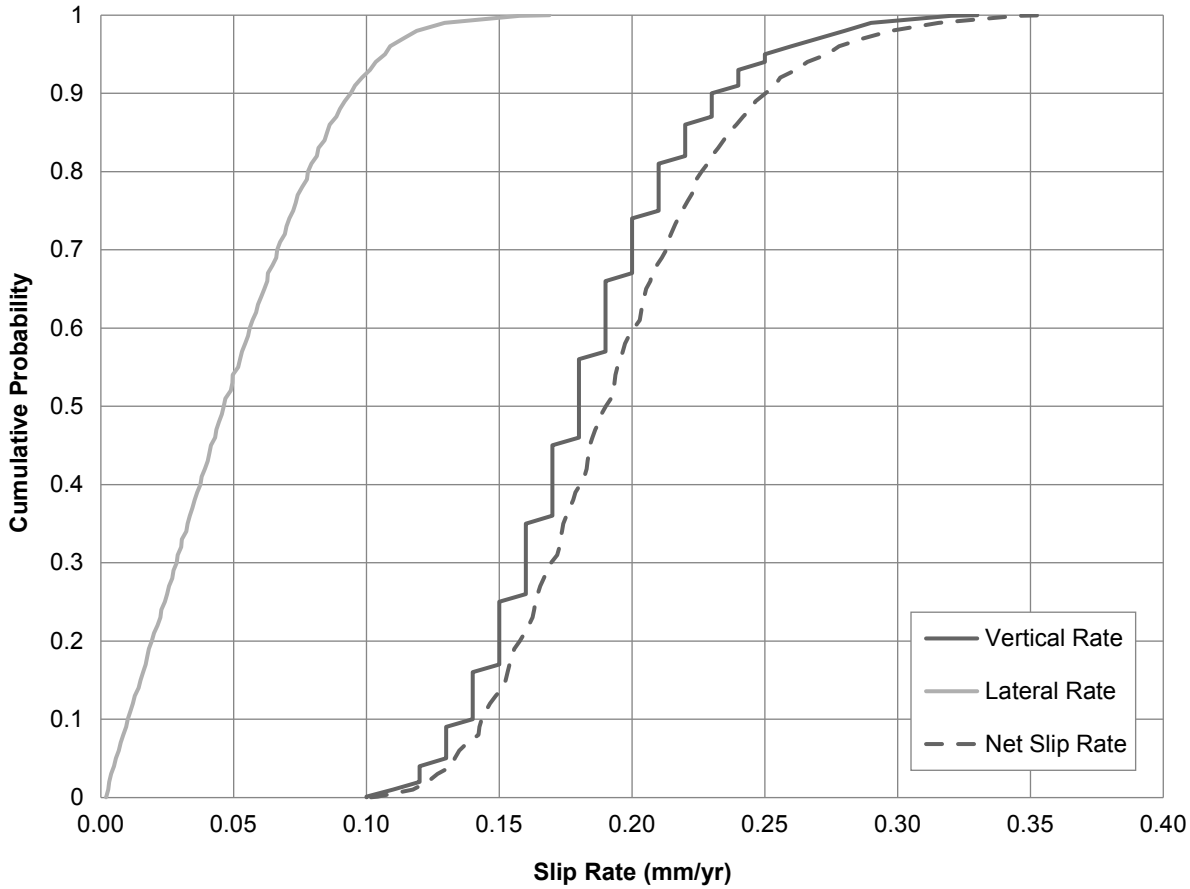

(b) Summary Statistics

Cumulative Probability	Vertical Rate (mm/yr)	Lateral Rate (mm/yr)	Net Slip Rate (mm/yr)
0.05	0.13	0.01	0.13
0.1	0.14	0.01	0.14
0.2	0.15	0.02	0.16
0.5	0.18	0.05	0.19
0.8	0.21	0.08	0.23
0.9	0.23	0.09	0.25
0.95	0.25	0.11	0.27
Min.	0.10	0.00	0.10
Max.	0.33	0.17	0.36
Mean	**0.18**	**0.05**	**0.19**

Note: A net slip rate CDF for the Los Osos fault in the SW Model was calculated from the vertical separation rate (from Figure 8-55), a modeled dip of 80 degrees, and a lateral slip rate calculated from the rake distribution shown on Figure 8-56. Steps in the vertical rate CDF result from the 0.01 mm/yr slip rate bin size sampled for Monte Carlo calculations (which is described in Section 8.2.1).

Los Osos Fault Net Slip Rate CDF for SW Model

DCPP SSC REPORT

Pacific Gas and Electric Company | Figure **8-58**

File path: S:\1005\005\Final_Report_Figures\Figure_800-58.ai; Date: 03/11/2015; User: Alex Remar, LCI; Rev.1

(a) Calculation of Net Slip Rate CDF

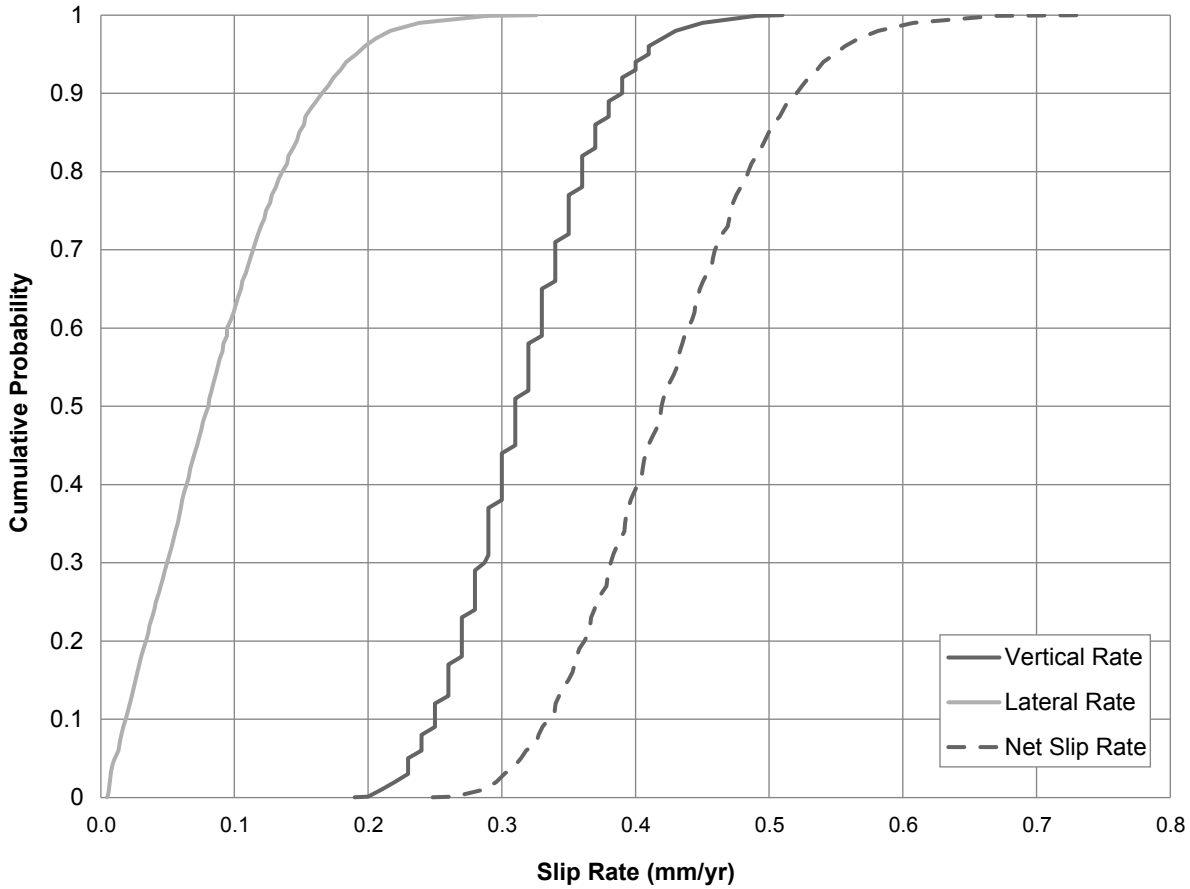

(b) Summary Statistics

Cumulative Probability	Vertical Rate (mm/yr)	Lateral Rate (mm/yr)	Net Slip Rate (mm/yr)
0.05	0.23	0.01	0.31
0.1	0.25	0.02	0.33
0.2	0.27	0.03	0.36
0.5	0.31	0.08	0.42
0.8	0.36	0.14	0.48
0.9	0.39	0.17	0.52
0.95	0.41	0.19	0.55
Min.	0.19	0.00	0.25
Max.	0.52	0.33	0.75
Mean	**0.32**	**0.09**	**0.42**

Note: A net slip rate CDF for the Los Osos fault in the NE Model was calculated from the vertical separation rate (from Figure 8-55), a modeled dip of 50 degrees, and a lateral slip rate calculated from the rake distribution shown on Figure 8-56. Steps in the vertical rate CDF result from the 0.01 mm/yr slip rate bin size sampled for Monte Carlo calculations (which is described in Section 8.2.1).

Los Osos Fault Net Slip Rate CDF for NE Model

DCPP SSC REPORT

Pacific Gas and Electric Company | Figure **8-59**

File path: S:\1005\005\Final_Report_Figures\Figure_800-59.ai; Date: 02/26/2015; User: Alex Remar, LCI; Rev.1

(a) Net Slip Rate CDFs

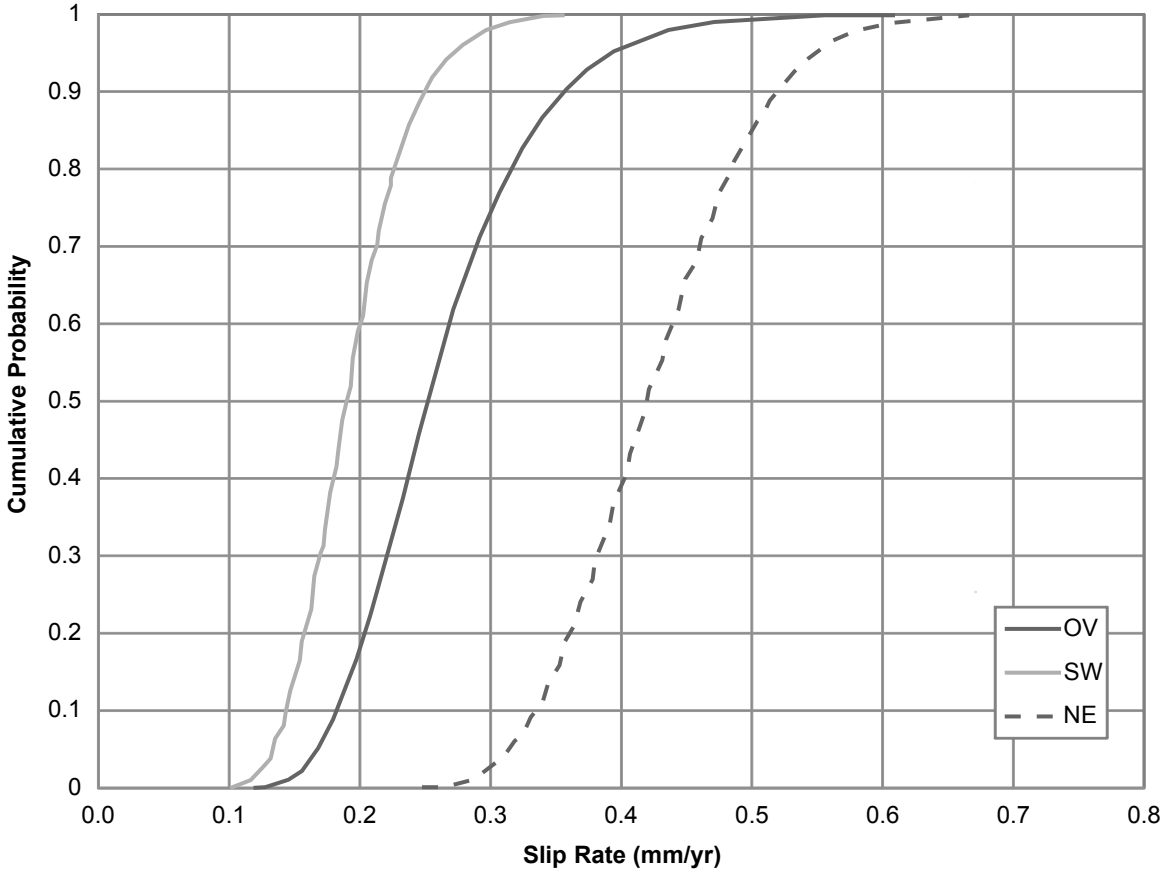

(b) 5-Point Distribution

Percentile	OV Slip Rate (mm/yr)	SW Slip Rate (mm/yr)	NE Slip Rate (mm/yr)	Weight
0.034893	0.16	0.13	0.30	0.101
0.211702	0.21	0.16	0.37	0.244
0.5	0.25	0.19	0.42	0.309
0.788298	0.31	0.22	0.48	0.244
0.965107	0.41	0.28	0.56	0.101
Weighted Mean	**0.26**	**0.19**	**0.42**	

Comparison of Los Osos CDFs for OV, SW, and NE Models

DCPP SSC REPORT

Pacific Gas and Electric Company

Figure **8-60**

File path: S:\1005\005\Final_Report_Figures\Figure_800-60.ai; Date: 02/26/2015; User: Alex Remar, LCI; Rev.1

(a) Footwall Uplift Rate PDFs

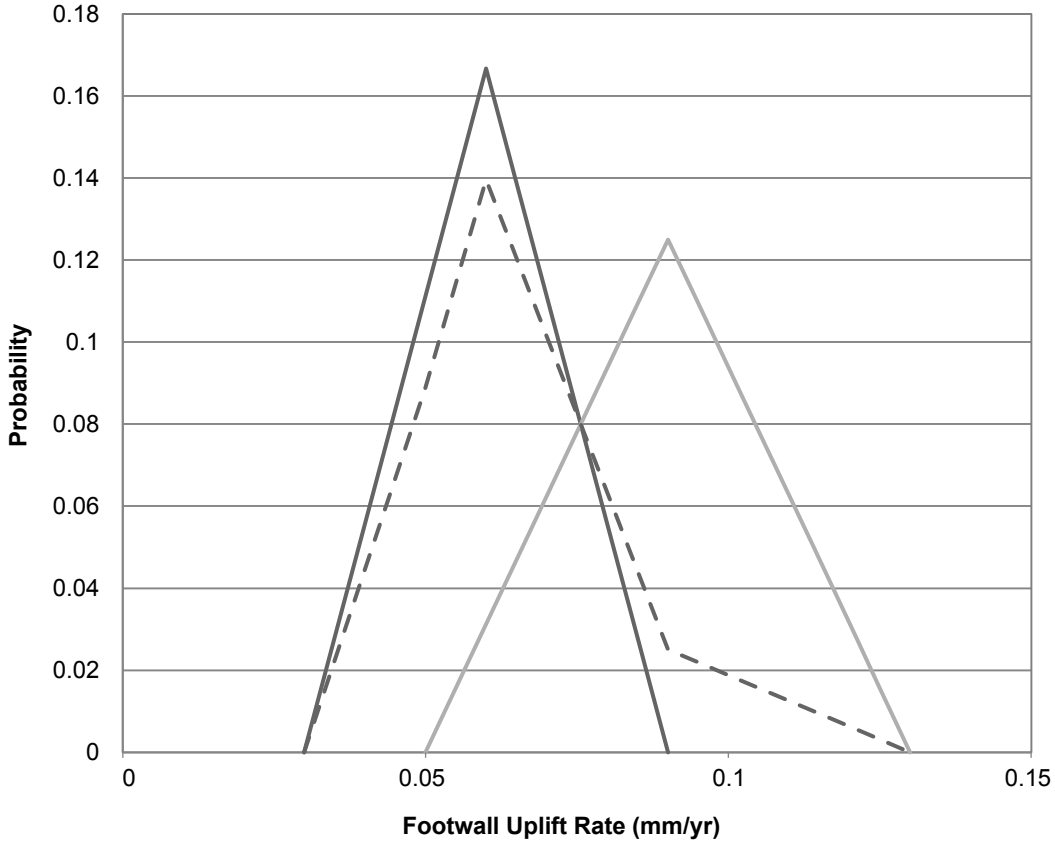

EXPLANATION

- Hanson et al. (1994) age/paleosea-level model [0.8]
- Muhs et al. (2012) age/paleosea-level model [0.2]
- Weighted hanging wall uplift PDF

Notes:
- Footwall uplift rate of the San Luis Bay fault is characterized from marine terrace uplift rates at San Luis Hill, which are shown on Figure 8-5.
- Numbers in brackets are weights assigned to each age model.

(b) Justification for Footwall Uplift Rate PDFs

Hanson et al. (1994) Age Model [0.8]		
	Uplift Rate (m/kyr)	Basis
Min.	0.03	Enveloping minimum of uncertainty in strandline elevation
Preferred	0.06	Preferred Q2 marine terrace age of MIS 5e (~120-125 ka)
Max.	0.09	Enveloping maximum of uncertainty in strandline elevation

Muhs et al. (2012) Age Model [0.2]		
	Uplift Rate (m/kyr)	Basis
Min.	0.05	Enveloping minimum of uncertainty in strandline elevation
Preferred	0.09	Preferred Q2 marine terrace age of MIS 5c (~100 ka)
Max.	0.13	Enveloping maximum of uncertainty in strandline elevation

San Luis Bay Fault – Footwall Uplift Rate PDFs

DCPP SSC REPORT

Pacific Gas and Electric Company

Figure **8-61**

File path: S:\1005\005\Final_Report_Figures\Figure_800-61.ai; Date: 02/23/2014; User: Alex Remar, LCI; Rev.1

(a) Calculation of Net Slip Rate CDF

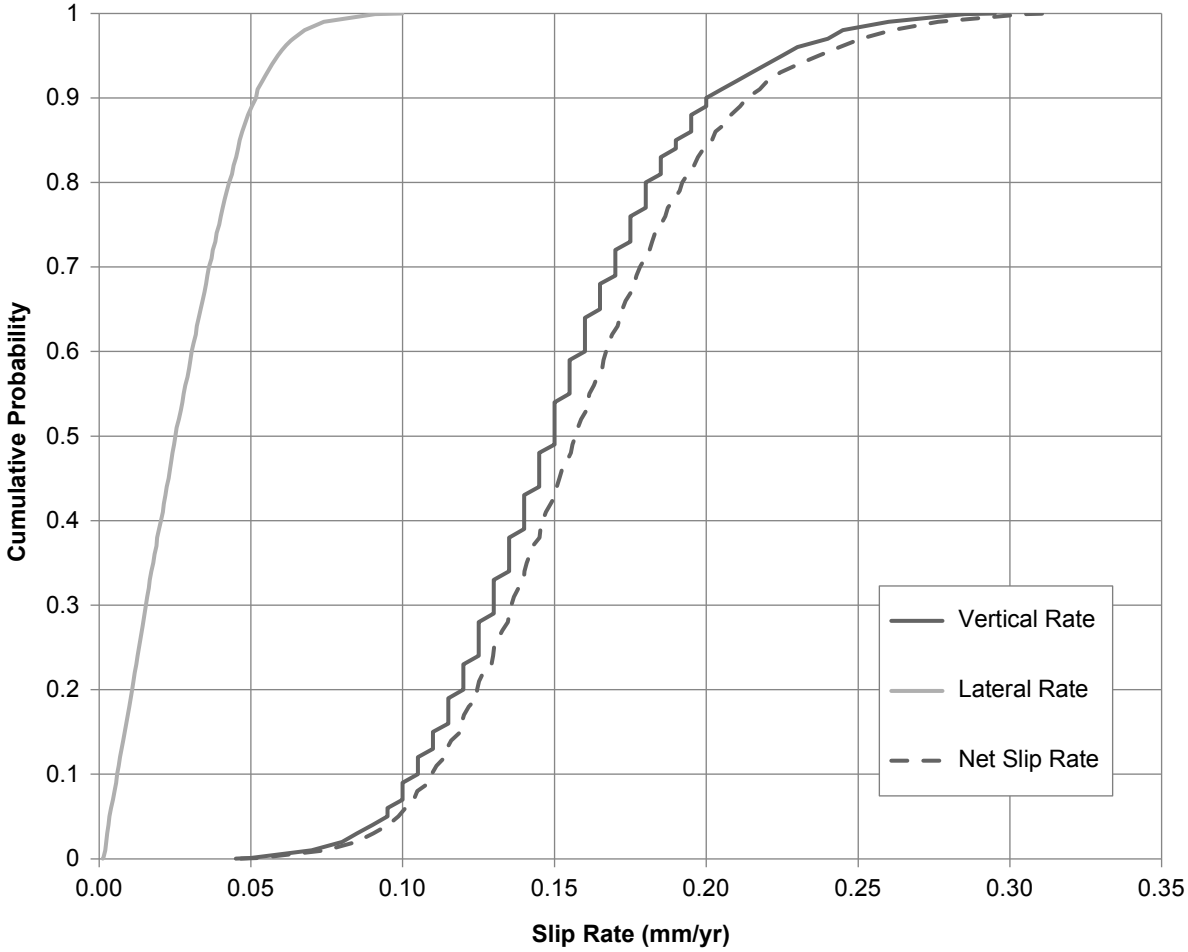

(a) Summary Statistics

Cumulative Probability	Vertical Rate (mm/yr)	Lateral Rate (mm/yr)	Net Slip Rate (mm/yr)
0.05	0.10	0.00	0.10
0.1	0.11	0.01	0.11
0.2	0.12	0.01	0.12
0.5	0.15	0.03	0.16
0.8	0.18	0.04	0.19
0.9	0.20	0.05	0.21
0.95	0.23	0.06	0.24
Min	0.04	0.00	0.04
Max	0.30	0.10	0.32
Mean	**0.15**	**0.03**	**0.16**

Note: A net slip rate CDF for the San Luis Bay fault in the OV Model was calculated from the vertical separation rate (calculated by subtracting the uplift rate of the footwall on Figure 8-61 from the uplift rate of the hanging wall on Figure 8-6), a modeled dip of 75 degrees, and a lateral slip rate calculated from a uniform probability probability distribution in rake between 70 and 110 degrees. Steps in the vertical rate CDF result from the 0.01 mm/yr slip rate bin size sampled for Monte Carlo calculations (which is described in Section 8.2.1).

San Luis Bay Fault
Net Slip Rate CDF for OV Model

DCPP SSC REPORT

Pacific Gas and Electric Company | Figure **8-62**

File path: S:\1005\005\Final_Report\Figures\Figure_800-62.ai; Date: 02/24/2015; User: Alex Remar, LCI; Rev.1

(a) Calculation of Net Slip Rate CDF

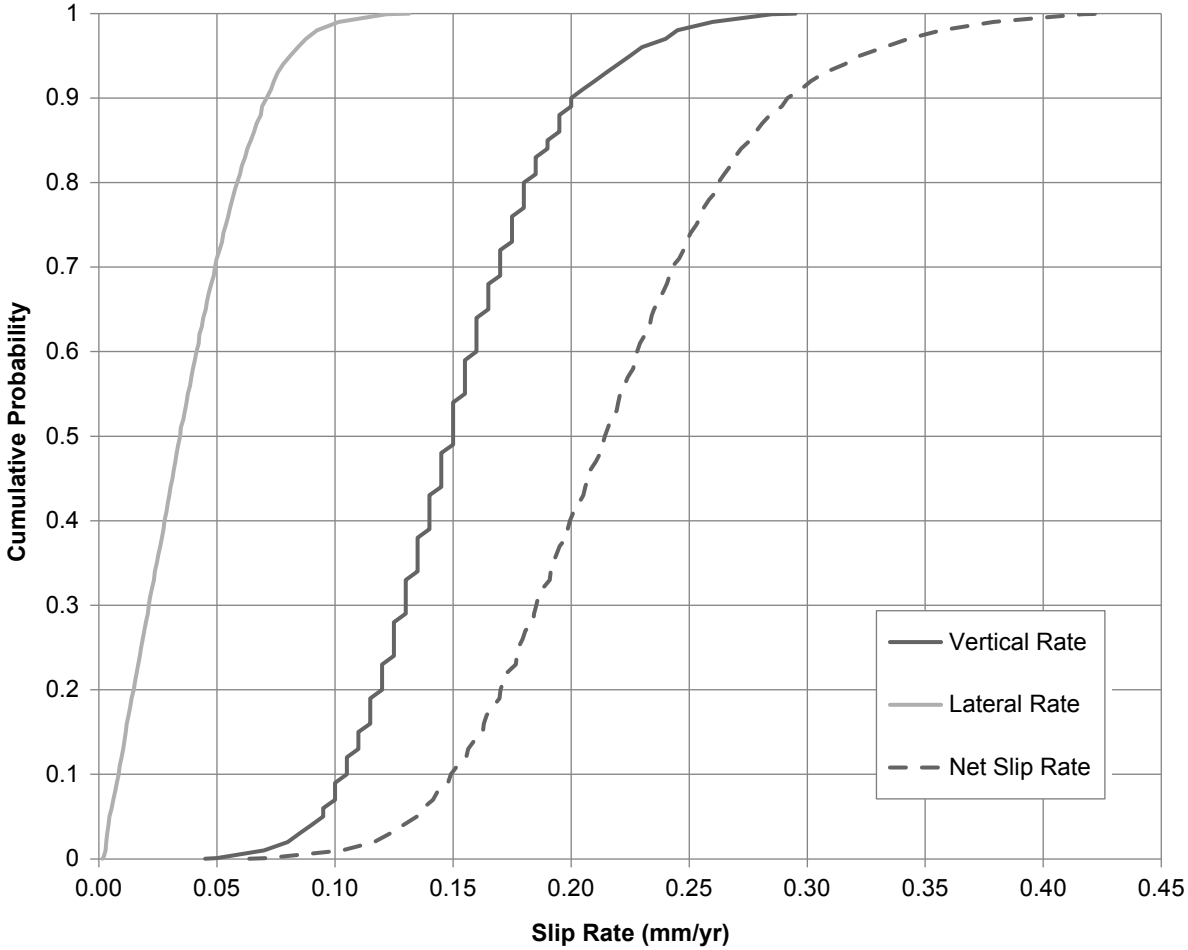

(b) Summary Statistics

Cumulative Probability	Vertical Rate (mm/yr)	Lateral Rate (mm/yr)	Net Slip Rate (mm/yr)
0.05	0.10	0.00	0.13
0.1	0.11	0.01	0.15
0.2	0.12	0.01	0.17
0.5	0.15	0.03	0.21
0.8	0.18	0.06	0.26
0.9	0.20	0.07	0.29
0.95	0.23	0.08	0.32
Min	0.04	0.00	0.06
Max	0.30	0.14	0.43
Mean	**0.15**	**0.04**	**0.22**

Note: A net slip rate CDF for the San Luis Bay fault in the SW Model was calculated from the vertical separation rate (calculated by subtracting the uplift rate of the footwall on Figure 8-61 from the uplift rate of the hanging wall on Figure 8-6), a modeled dip of 45 degrees, and a lateral slip rate calculated from a uniform probability probability distribution in rake between 70 and 110 degrees. Steps in the vertical rate CDF result from the 0.01 mm/yr slip rate bin size sampled for Monte Carlo calculations (which is described in Section 8.2.1).

San Luis Bay Fault
Net Slip Rate CDF for SW Model

DCPP SSC REPORT

Pacific Gas and Electric Company | Figure **8-63**

File path: S:\1005\005\Final_Report\Figures\Figure_800-63.ai; Date: 02/24/2015; User: Alex Remar, LCI; Rev.1

(a) Calculation of Net Slip Rate CDF

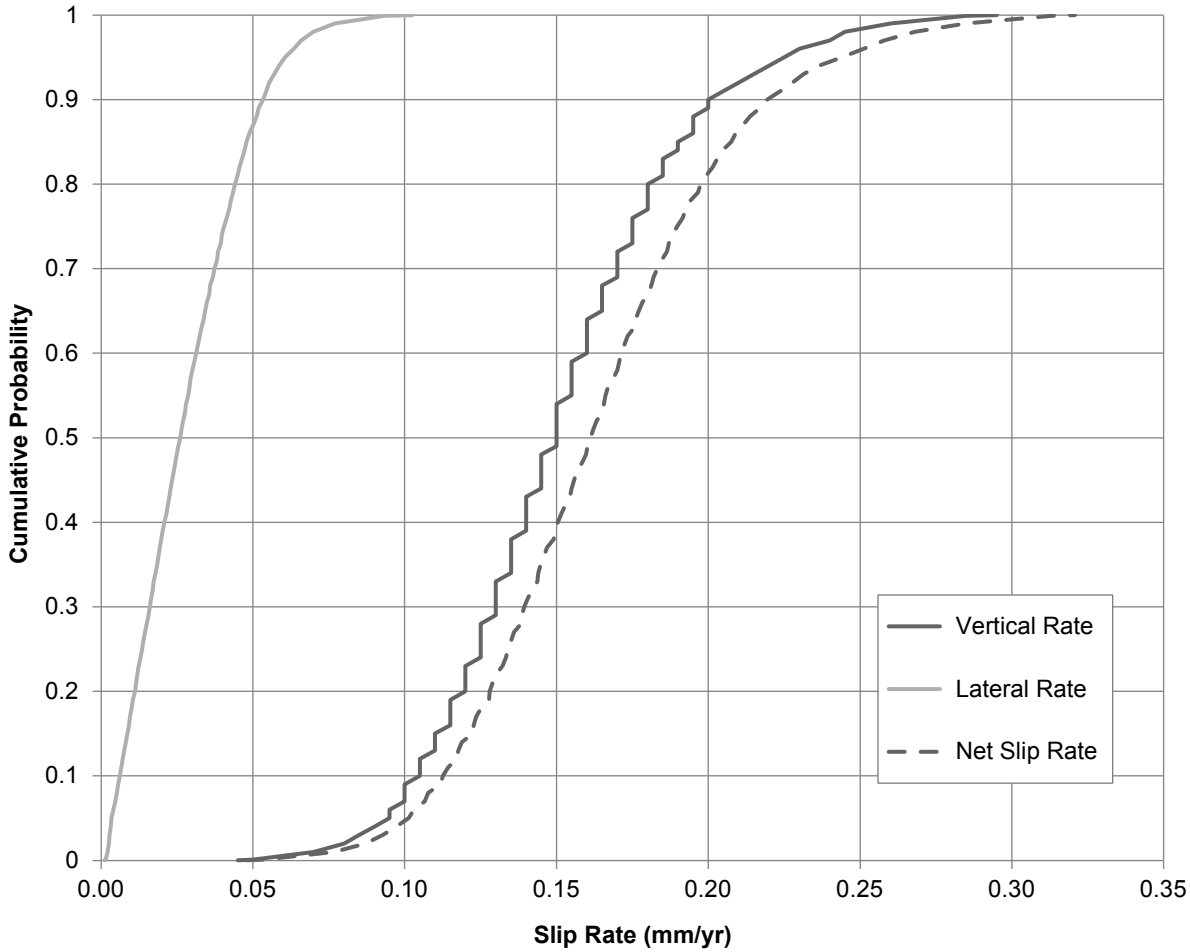

(b) Summary Statistics

Cumulative Probability	Vertical Rate (mm/yr)	Lateral Rate (mm/yr)	Net Slip Rate (mm/yr)
0.05	0.10	0.00	0.10
0.1	0.11	0.01	0.11
0.2	0.12	0.01	0.13
0.5	0.15	0.03	0.16
0.8	0.18	0.04	0.20
0.9	0.20	0.05	0.22
0.95	0.23	0.06	0.24
Min	0.04	0.00	0.04
Max	0.30	0.10	0.32
Mean	**0.15**	**0.03**	**0.16**

Note: A net slip rate CDF for the San Luis Bay fault in the NE Model was calculated from the vertical separation rate (calculated by subtracting the uplift rate of the footwall on Figure 8-61 from the uplift rate of the hanging wall on Figure 8-6), a modeled dip of 70 degrees, and a lateral slip rate calculated from a uniform probability probability distribution in rake between 70 and 110 degrees. Steps in the vertical rate CDF result from the 0.01 mm/yr slip rate bin size sampled for Monte Carlo calculations (which is described in Section 8.2.1).

San Luis Bay Fault
Net Slip Rate CDF for NE Model

DCPP SSC REPORT

Pacific Gas and Electric Company | Figure **8-64**

File path: S:\1005\005\Final_Report\Figures\Figure_800-64.ai; Date: 02/24/2015; User: Alex Remar, LCI; Rev.1

(a) Net Slip Rate CDFs

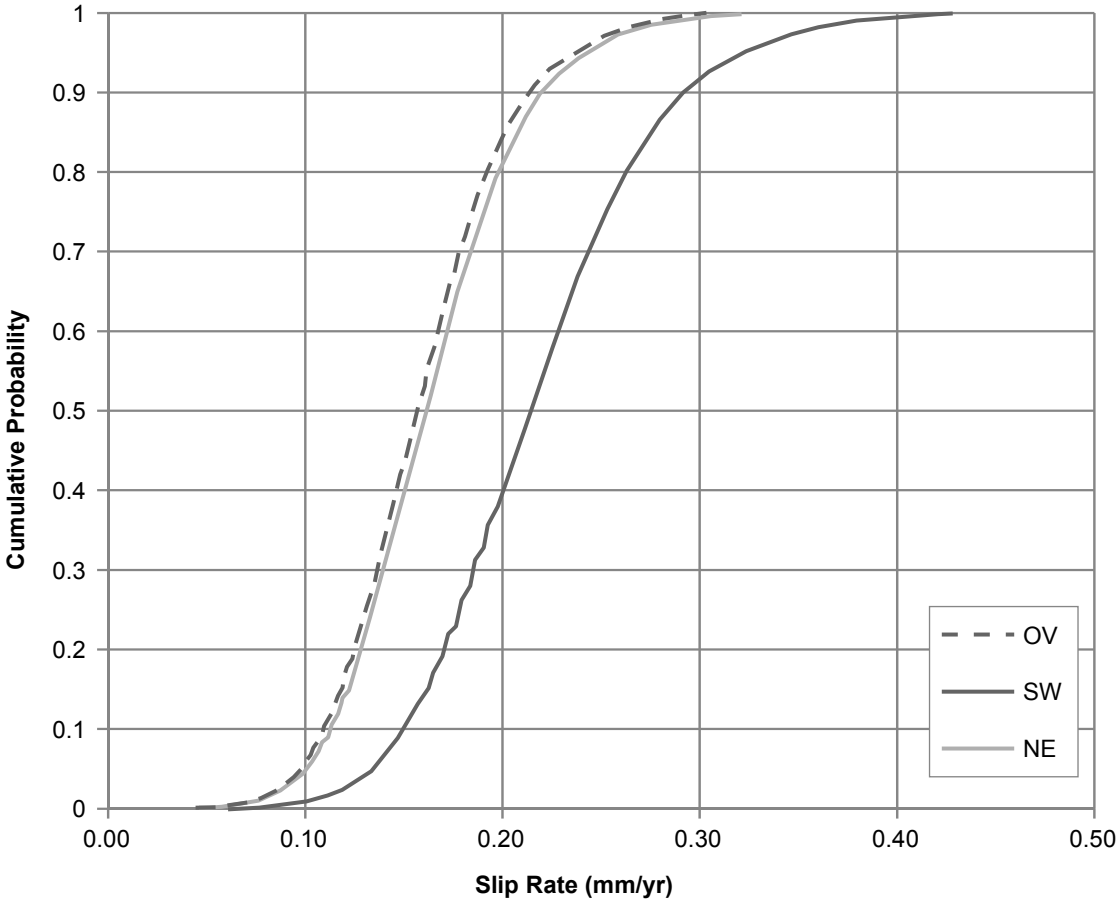

(b) 5-Point Distributions

Percentile	OV Slip Rate (mm/yr)	SW Slip Rate (mm/yr)	NE Slip Rate (mm/yr)	Weight
0.034893	0.09	0.13	0.10	0.101
0.211702	0.13	0.17	0.13	0.244
0.5	0.16	0.21	0.16	0.309
0.788298	0.19	0.26	0.20	0.244
0.965107	0.25	0.34	0.25	0.101
Weighted Mean	0.16	0.22	0.16	

Note: Steps in CDFs result from the 0.01 mm/yr slip rate bin size sampled for Monte Carlo calculations (which are described in Section 8.2.1).

Comparison of San Luis Bay CDFs for OV, SW, and NE Models

DCPP SSC REPORT

Pacific Gas and Electric Company | Figure **8-65**

File path: S:\1005\005\Final_Report_Figures\Figure_800-65.ai; Date: 02/26/2015; User: Alex Remar, LCI; Rev.1

9.0 RUPTURE MODELS

Recent continental earthquakes (e.g., 1992 Landers, California; 1999 Hector Mine, California; 2002 Denali, Alaska; 2010 El Mayor–Cucapah, Mexico) have demonstrated that large-magnitude earthquakes are not always simple ruptures involving a single fault (Wesnousky, 2008). Some historical ruptures have involved multiple faults having a similar sense of slip within a single fault system (1992 Landers earthquake, Madden and Pollard, 2012), secondary faults (1999 Hector Mine earthquake, Treiman et al., 2002), and in some cases, multiple faults having differing styles of faulting (2002 Denali earthquake, Haeussler et al., 2004; 2010 El Mayor–Cucapah earthquake, Fletcher et al., 2014). Without behavioral information to identify the segments or faults that have ruptured together in past earthquakes, it is difficult to define specific locations, magnitudes, and rates of future earthquake ruptures.

Alternative models to estimate the lengths of future ruptures were discussed during Workshop 2; these included fault segmentation models, multi-fault rupture models, and the inversion approach used recently in the UCERF3 model (Page et al., 2014). The TI Team evaluated these different approaches and judged that the uncertainty due to the lack of knowledge on segmentation and fault complexity may be greater than previously considered in earlier Diablo Canyon SSC models (i.e., PG&E, 1988; 2011) and that this greater uncertainty in modeling future ruptures should be captured and integrated into the Diablo Canyon SSC model. As described in *Sections 6.3.3 and 6.3.4*, the Diablo Canyon SSC model uses the construction of Rupture Models—consisting of separate rupture sources—to capture the range of viable rupture scenarios, and Slip Rate Allocation Models to allocate a fraction of the total fault slip rate to individual rupture sources. The methodology and results of the Rupture Models and the Slip Rate Allocation Models are presented in this chapter.

9.1 Applicability to the SSC Model

As discussed in *Chapter 6*, each of the Fault Geometry Models (FGMs) defined in *Chapter 7* has a corresponding Rupture Model that describes a set of *rupture sources* that may occur. The rupture-source framework used in the Diablo Canyon SSC model captures epistemic uncertainty and aleatory variability as follows:

1. The Rupture Models represent different logic-tree branches that (together with branches for the rupture-source slip rates and various magnitude PDF models) collectively sample and represent the range of epistemic uncertainty in the slip budget and the way that slip budget is distributed spatially and with respect to magnitude and style of faulting.
2. The collection of rupture sources (and their respective magnitude PDFs) within each Rupture Model is designed to capture the corresponding aleatory variability in magnitude (and rupture dimensions) and distance to the site.

A *rupture source* is a series or combination of fault sections that are considered capable of hosting a maximum earthquake (i.e., rupture over the entire area of the combined fault

sections) and smaller, floating (i.e., not confined to specific section or sections of the rupture source) earthquakes. The different rupture sources within each Rupture Model are all considered to occur and as such they are developed to capture potential aleatory variability in the style and extent of future ruptures in the network of Primary and Connected faults. It can be argued that the selection of the alternative rupture scenarios may include epistemic uncertainty in that the set of Rupture Sources may not be inclusive of all possible ruptures that could occur and that others might develop a different set of rupture sources to which they assign different slip rates. However, the selected set of rupture sources chosen for the Diablo Canyon SSC Model are judged by the TI Team to capture the center, body, and range of technically defensible ruptures that could occur on Primary fault sources on the sections of the fault closest to the DCPP.

The characterization of the individual rupture sources is not unlike the characterization of fault sources in the more traditional manner in which the geometry of the fault source is used to evaluate the potential size of future ruptures, a slip rate is assigned to the fault source, and a recurrence model is used to develop a recurrence curve that expresses aleatory variability in the magnitudes (and rupture dimensions) of possible earthquakes on the fault. The Rupture Model differs from this approach in that it acknowledges that larger, more complex ruptures do occur in similar types of fault networks and that allowing for such ruptures better captures the full range of likely rupture scenarios.

All rupture sources occur within each Rupture Model. In other words, the TI Team has chosen to model the rupture sources as aleatory variability in the SSC logic tree, not epistemic uncertainty. Four Rupture Models were developed—one for the three Hosgri FGMs and three for the San Luis–Pismo Block (SLPB) FGMs. The Rupture Models and the number of rupture sources in each Rupture Model are listed in Table 9-1. All three Hosgri FGMs have the same Rupture Model. Each SLPB FGM has a distinct Rupture Model: the Outward-Vergent (OV) Model, the Southwest-Vergent (SW) Model, and the Northeast-Vergent (NE) Model. Maps of the rupture sources for the Hosgri Rupture Model are provided on Plate 9-1. The three rows on Plate 9-1 show the same rupture sources on the three Hosgri FGMs with the different fault dips. Maps of rupture sources for the three SLPB Rupture Models are provided on Plate 9-2.

Table 9-1. Rupture Models and Number of Rupture Sources

Rupture Models	Rupture Sources
Hosgri (all three FGMs)	8
Outward-Vergent (OV)	10
Southwest-Vergent (SW)	10
Northeast-Vergent (NE)	11

Each rupture source has alternative slip rate values and weights, which represent epistemic uncertainty in the slip assigned to that rupture source. The weighted means of the slip rates assigned to the rupture sources sum to capture the weighted mean fault slip rates for the Primary and Connected faults as described in *Chapter 8*.

The following sections present the Rupture Model (*Section 9.2*) and Slip Rate Allocation Model (*Section 9.3*) methodologies and results, including a summary of the key aspects of each rupture source and demonstrations of how the Slip Rate Allocation Models reproduce fault slip rates.

9.2 Diablo Canyon SSC Rupture Models

In developing the Rupture Models for the Diablo Canyon SSC, the TI Team started with the FGMs defined in *Chapter 7*. These FGMs provide the framework for considering future ruptures that could occur given the overall geometry, connectivity, and sense of slip of the Primary and Connected faults near the Diablo Canyon Power Plant (DCPP). As described in *Chapter 6*, the Rupture Models are specific to the Primary fault sources (Hosgri, Shoreline, Los Osos, and San Luis Bay faults) and Connected fault sources (e.g., Wilmar Avenue, Oceano, and San Simeon faults; Table 6-2).

Rupture source geometries define alternative rupture topologies and are drawn to capture the maximum permissible rupture on that topology. The geometrical and seismological characteristics of historical earthquake ruptures are used to evaluate possible types of future ruptures that could occur on faults within each FGM (*Section 6.3.3*). Examples of historical ruptures from other regions that are possible analogs for each FGM are described in *Chapter 7*. Rupture Models are collections of rupture sources selected to capture variability in distance, magnitude, and style of potential ruptures near the DCPP. The TI Team acknowledges that the set of rupture sources defined within a Rupture Model is not inclusive of all possible rupture scenarios. However, the set is defined to capture the range of viable ruptures on Primary and Connected faults that could contribute significantly to hazard at the DCPP.

9.2.1 Methodology to Develop Rupture Sources

The four Rupture Models (one each for the Hosgri, OV, SW and NE Fault Geometry Models) describe the number of rupture sources, the fault sections involved in each rupture source, the sense of slip for each fault section in the rupture source, and the type of rupture source.

9.2.1.1 Types of Rupture Sources

Four types of rupture sources are defined for use in the Diablo Canyon SSC: characteristic, linked, complex, and splay. These four types are described briefly below and summarized in Table 9-2 (which is a copy of Table 6-6 and is shown again here for ease of reference). The rupture source types are treated differently in the PSHA based on how the ground motions from such ruptures are calculated in the GMC model (GeoPentech, 2015). Schematic drawings of each rupture source type are shown on Figure 9-1.

Table 9-2. Rupture Source Types

Type	Explanation
Characteristic	A rupture source that is confined to a single named fault of limited length that has a uniform sense of slip
Linked	A rupture source that includes fault sections of multiple named faults having the same sense of slip
Complex	A rupture source that contains multiple faults and more than one sense of slip on adjacent fault sections
Splay	A rupture source that includes branching faults that form two source planes having the same sense of slip

Characteristic rupture source types are rupture sources that are confined to a single named fault (Figure 9-1a). Characteristic type rupture sources are not to be confused with characteristic earthquakes (M_{char}) as defined for use in applying a magnitude PDF (*Section 6.3.5* and *Chapter 10*). These rupture sources have a limited length and a uniform sense of slip. Characteristic type rupture sources included in the Diablo Canyon SSC model are generally 100 km or less in length. Characteristic rupture sources do not require special consideration for modeling ground motions (GeoPentech, 2015).

Linked rupture source types are rupture sources that include fault sections from multiple named faults with the same sense of slip (Figure 9-1b). These rupture sources vary in total length, but they are commonly several hundred kilometers long. Linked rupture sources do not require special consideration for modeling ground motions (GeoPentech, 2015).

Complex rupture source types are rupture sources that contain multiple named faults and more than one sense of slip on adjacent fault sections (Figure 9-1c). The total length involved in a complex rupture source varies from tens to hundreds of kilometers. Ground motions modeled from complex rupture sources are treated in a specific manner within the GMC model; namely, the rupture source is divided into separate parts according to slip sense (GeoPentech, 2015). The complex rupture sources thus are divided into two rupture planes—a *primary* part and a *secondary* part—that contribute to ground motions with different geometries, source-to-site distances, slip senses, and magnitudes. The primary part is defined as the part of the rupture source with the larger rupture area. The secondary part of the rupture source has a smaller rupture area. The GMC model specifies that the median ground motions from a complex rupture source are equal to the square root of the sum of the squares (SRSS) of the median ground motions of each part (GeoPentech, 2015).

Splay rupture source types are rupture sources that include branching faults that form two source planes both in map view and cross section. Examples of strike-slip and reverse splay ruptures are shown on Figure 9-1d. The total length involved in a splay rupture source varies from tens to hundreds of kilometers. Similar to complex rupture sources, ground motions calculated from splay rupture sources are treated in a specific manner by the GMC model, namely, the rupture source is divided into separate parts (GeoPentech,

2015). The *main* part of the splay rupture source is defined as the contiguous rupture plane with the larger area, and the *splay* part of the source has the smaller area (Figure 9-1d). The main and splay parts each contribute to ground motions with different geometries, source-to-site distances, and magnitudes. The median ground motions from a splay rupture source are calculated by the identical SRSS method used for the complex rupture sources described above.

9.2.1.2 Definition of Rupture Topology

The topologies for rupture sources for each FGM are developed by the TI Team based on consideration of historical earthquake ruptures that may be analogous to the ruptures in the Diablo Canyon region (see representative examples described in *Section 9.2.1.5* and Table 6-1) and a few simple rules. The downdip geometry of each rupture source is defined by the FGM to which it belongs. The rules and guidelines used to develop the rupture sources are presented below.

- Rupture sources are defined to have a uniform slip rate along their entire length for characteristic and linked ruptures. The slip rates assigned to both the main fault as well the secondary fault in complex or splay ruptures are uniform over their respective fault planes, although the slip rates for each part are different. Changes in fault slip rate from fault section to fault section are accommodated by "layering" rupture sources, so that a fault section that is known to have a higher slip rate than a neighboring fault section may host additional rupture source(s) to account for the change in slip rate. In this way, some ends of rupture sources are defined at locations where fault slip rate changes.
- Faults located within 5 km or less (including their downdip geometry) of one another may be part of the same rupture source. However, faults are not necessarily part of the same rupture source simply because they are located within 5 km or less of one another.
- Fault sections within a rupture source do not necessarily have the same rake or sense of slip. In the SSC model, complex rupture sources are defined with two different slip senses.
- Fault sections that intersect with an obtuse angle (>90°) may be part of the same rupture source. Fault sections with surface traces that intersect at acute angles are not part of the same rupture source, with the exception of a splay rupture source involving the Hosgri and Shoreline faults, in which both obtuse and acute angles between fault sections are part of the same rupture source.

9.2.1.3 Rupture Source Endpoints

In the Diablo Canyon SSC model, rupture sources end at three types of features:

- Ends of fault sources.
- Fault source branch points.
- Locations where fault slip rate changes.

While the TI Team recognized that many historical ruptures have an endpoint at a major step or bend (Wesnousky, 2006), this criteria was not used explicitly to define the ends of rupture sources for the DCPP model. As explained above, fault steps or abrupt bends less than 5 km were not used as criteria to end a rupture source. Such bends, however, were considered for developing the length scales of characteristic earthquakes (*Section 10.2*).

Endpoints of rupture sources may be considered "segment boundaries" in the traditional sense (e.g., Schwartz and Coppersmith, 1984; Field et al., 2009) because earthquakes on a rupture source may not rupture past them. However, rupture sources sometimes span points identified as endpoints for other rupture sources (Plates 9-1 and 9-2). This is similar to the modeling of multi-segment ruptures (e.g., Field et al., 2009), wherein some ends of fault sections are effectively "soft" segment boundaries that are commonly, but not always, the endpoints of large earthquake ruptures.

The most common feature used to define the endpoint of a rupture source is the end of a Primary or Connected fault source (Plates 9-1 and 9-2), such as the following:

- The north end of the Hosgri fault source at the north end of the northern San Andreas fault source (fault section SA; at the Mendocino Triple Junction).
- The south end of the Hosgri fault source offshore of Point Arguello (fault section HS).
- The north end of the fault source underlying the Piedras Blancas fold belt (fault section PB).
- The southeast end of the Little Pine fault source (fault section LP).

Fault source branch points are also used to define endpoints of some rupture sources. Empirical studies of historical earthquakes suggest that branch points (i.e., fault-to-fault ruptures of branching faults) may arrest ruptures more frequently than other points along a fault (e.g., Biasi, Parsons, et al., 2013). Wesnousky and Biasi (2011) and Biasi, Parsons, et al. (2013) observed that fault-to-fault ruptures are particularly less likely when the faults in question have different senses of slip. The following fault source intersections are examples of key branch points used to define endpoints of rupture sources:

- **Hosgri–San Andreas.** Whereas many rupture sources involving the Hosgri fault source continue onto the northern San Andreas fault and end at the Mendocino Triple Junction, several rupture sources end at the north end of the San Gregorio fault source (fault section GN), where it branches from the San Andreas fault in Bolinas. This boundary coincides with a pull-apart basin and a major change in fault slip rate between the northern San Gregorio and San Andreas faults. This boundary is considered in developing length scales for M_{max} earthquakes on Hosgri rupture sources.
- **Shoreline-Hosgri.** Some, but not all, of the rupture sources involving the northern Shoreline fault source (fault section SH) end at the intersection with the Hosgri fault source. This boundary is set based on two observations: (1) the slip rate of the Hosgri fault zone (HFZ) greatly exceeds that of the Shoreline fault, and (2) the results of recent 2D dynamic modeling suggest that propagation of Hosgri slip onto the Shoreline fault is unlikely (Kame et al., 2003; Somerville, 2011).

- **Shoreline-Casmalia.** All rupture sources involving the southern portion of the Shoreline fault source (fault section SE) terminate at the intersection with the Casmalia fault near Point Sal. This boundary coincides with a change in slip sense. The Casmalia fault source is a part of the regional fault sources (*Chapter 12*).
- **Los Osos–Hosgri.** Most, but not all, of the rupture sources involving the offshore portion of the Los Osos fault source (fault section LC) end to the northwest at the intersection with the Hosgri fault source, where changes occur in both slip sense and slip rate.
- **Los Osos–West Huasna.** All rupture sources involving the eastern portion of the Los Osos fault source (fault section LE) terminate at the intersection with the Oceanic–West Huasna fault zone. Changes in fault strike and slip rate occur at this location. The Oceanic–West Huasna fault source is a part of the regional fault sources (*Chapter 12*).
- **San Luis Bay–Hosgri.** These fault sources only intersect in the SW Model. Most, but not all, of the rupture sources involving the San Luis Bay fault source in this FGM end to the west at the intersection with the Hosgri fault source (fault section BW), where changes occur in both slip sense and slip rate.
- **Oceano–Shoreline.** Some, but not all, of the rupture sources involving the Oceano fault source end to the north at the intersection of the northern portion of the Oceano fault source (fault section OF) with the Shoreline fault source where changes occur in slip sense and slip rate.

Locations where slip rate is known or inferred to change along a fault are also used to define endpoints of rupture sources. Where slip rate of a fault increases, additional rupture sources are "layered" over one another to account for this change. In the Diablo Canyon SSC model, endpoints of rupture sources are defined to accommodate slip rate changes at the boundary between the Irish Hills and adjacent sub-blocks of the San Luis–Pismo Range, and at two locations where branching faults merge with the HFZ, as follows:

- **Boundaries of Irish Hills.** Uplifted marine terraces indicate that the Irish Hills sub-block of the SLPB is uplifting at a rate of approximately 0.2 mm/yr and that the adjacent Edna sub-block is uplifting at a rate of approximately 0.1 mm/yr (see Figure 7-4 and discussion in *Section 8.2.2*). This difference in uplift rate suggests that the slip rate of faults driving the uplift also differs between the sub-blocks. Some of the rupture sources involving the San Luis Bay and Los Osos fault sources end at the boundary between the Irish Hills and Edna sub-blocks to account for this difference.
- **Slip rate changes along Hosgri fault zone.** Within the Diablo Canyon SSC model, the slip rate of the HFZ is inferred to increase northward of locations where active faults merge with it. Some, but not all, of this increased slip rate is modeled by rupture sources that involve joint rupture of the Hosgri fault source with the branching fault source (e.g., the Hosgri and Shoreline fault sources). The remainder of the slip rate increase is accounted for by additional "layered" rupture

sources that extend from the fault intersection northward to the end of the Hosgri fault source.

9.2.1.4 Definition of Rupture Models

Rupture Models are sets of rupture sources that are selected to capture aleatory variability in distance, magnitude and style of potential ruptures near the DCPP. The TI Team has developed the Rupture Models to capture this variability with a relatively small number of rupture sources. The selection of rupture sources was informed through careful review of historical analogs and salient elements of the selected rupture topologies are supported by observations that they have occurred elsewhere during actual earthquakes. Although additional rupture topologies are possible, the TI Team judged that the set of rupture sources within each Rupture Model, when combined with the Magnitude Distribution Models in *Chapter 10*, effectively captures the center, body, and range of viable ruptures on Primary and Connected faults that could contribute significantly to hazard at the DCPP. The TI Team judged that adding additional rupture sources to any of the Rupture Models beyond those shown on Plates 9.1 and 9.2 would not significantly add to the variability in distance, magnitude, and style of potential ruptures considered near the DCPP.

The characterization of rupture sources involving the Shoreline fault in the OV Model illustrates this approach (Plate 9-2, top row). Potential rupture sources involving the Shoreline fault all have the same source-to-site distance, but incorporate variability in rupture topology by including the following features:

- A relatively short strike-slip rupture source (OV-01).
- A very long strike-slip rupture source that hosts moderate to large-magnitude earthquakes (OV-02).
- A relatively short, complex rupture source that includes a portion rupturing with reverse slip (OV-03).
- A much longer complex rupture source that involves multiple strike-slip and reverse-slip fault sections and that hosts large-magnitude earthquakes (OV-04).
- A splay rupture source with contemporaneous rupture of the Shoreline and Hosgri fault sources (H-05; Plate 9-1).

9.2.1.5 Rupture Event Analogs

Several historical earthquake ruptures are discussed below as analogs for specific rupture sources that are incorporated into the Rupture Models. The following historical earthquake ruptures are described in this section:

- 1896 **M** 7.2 Rikuu earthquake, Japan
- 1940 **M** 6.9 and 1979 **M** 6.4 Imperial Valley earthquakes, Southern California
- 1992 **M** 7.3 Landers earthquake, California
- 1999 **M** 7.1 Hector Mine earthquake, California
- 2002 **M** 7.9 Denali earthquake, Alaska

- 2010 **M** 7.2 El Mayor–Cucapah earthquake, Mexico

Other historical ruptures that occurred on fault systems are also used as analogs for the alternative FGMs for the SLPB, as described in *Chapter 7*. These historical events are useful analogs for splay and complex rupture sources:

- 1957 **M** 8.3 Gobi-Altay earthquake, Mongolia (*Section 7.4.1.1*)
- 2003 **M** 6.5 San Simeon earthquake, California (*Section 7.4.2.1*)
- 1977 M_S 7.3 Caucete earthquake, Sierra Pie de Palo, Argentina (*Section 7.4.3.1*)

Somerville (2011) studied branching rupture on strike-slip faults; he evaluated scenarios in which rupture begins on a main fault and branches onto a splay fault—regardless of whether it continues on the main fault past the branch point. Observations from six events were compared with the predictions of the Kame et al. (2003) model that shows the propensity of an earthquake rupture to follow a fault branch as a function of the preexisting stress state, branch angle, and incoming rupture velocity at the branch location. The results of the Somerville (2011) study suggest that some fault geometries may not be as favorable for rupture propagation, including the specific case of rupture on the HFZ north of the DCPP propagating to the south and branching onto the Shoreline fault. Although the TI Team considered this result in developing the rupture sources, it was not considered adequate to preclude the possibility of the specific rupture topology that included joint rupture of the Hosgri and Shoreline faults.

*1896 **M** 7.2 Rikuu Earthquake, Japan*

The 1896 **M** 7.2 Rikuu earthquake, which occurred in the Tohoku district of northern Honshu, Japan, was an intraplate event associated with approximately 40 km of surface ruptures involving five named reverse faults (Matsuda et al., 1980; Figure 9-2). Four main surface ruptures, approximately 36 km long, on the western foot of the Majiru Mountains constitute the main fault zone of the 1896 earthquake. The maximum vertical displacement was approximately 3.6 m, up on the east. Approximately 6 km of another surface fault, the Kawafune fault, on the eastern side of the Majiru Mountains, also ruptured during the event, with the opposite sense of vertical displacement (i.e., the western side was upthrown). The maximum vertical displacement on the Kawafune fault was 2 m. Horizontal shortening during the 1896 event was approximately 1–3 m. No strike slip was observed. The Kawafune fault is considered a subsidiary conjugate fault to the main fault zone.

Matsuda et al. (1980) summarized the following observations regarding the surface ruptures that occurred during this event. The concept of discontinuous jumping and migration of the fault trace of the reverse fault away from the mountains is applicable to this fault system. Older, less active Quaternary faults are located on the mountain side of the 1896 surface rupture. The 1896 surface faulting occurred along the topographically well-defined Quaternary active faults. Locally, vertical displacements observed on the present alluvial fan exceed the displacements that occurred during the 1896 event, implying the occurrence of at least one similar event in the Holocene period prior to 1896

(Matsuda et al., 1980). The average vertical displacement rate during the past approximately 23 ka is estimated to be 0.2–0.3 mm/yr.

The dip angle of the fault was estimated from fault outcrops, the ratio of vertical displacement to horizontal shortening, and the relation between the bend of the fault trace and topography. The angle obtained was variable, ranging from almost vertical to less than 20°; this variability was attributed to local differences in the thickness of unconsolidated alluvial deposits. The dip angle of the fault in the basement rocks is estimated to be approximately 45°E.

*1940 **M** 6.9 (El Centro) and 1979 **M** 6.4 Imperial Valley Earthquakes, Southern California*

The Imperial fault, which extends southward from Brawley, California, into Mexico, was the site of surface-rupturing earthquakes in 1940 and 1979 (Figure 9-3). The Imperial fault is a rather simple 60 km long ridge-ridge transform fault within the San Andreas–Gulf of California transform system (Sharp et al., 1982; Yeats et al., 1997). During the 1940 event, a 60 km long surface rupture was formed, which is the entire known length of the fault. The maximum recorded displacement of 7.0 m occurred approximately 2 km northwest of the U.S.-Mexico border, with an average slip of 5.5 m for that approximately 3 km-long section of the fault directly north of the border (Rockwell and Klinger, 2013). The sense of movement was almost pure strike slip (Trifunac and Brune, 1970), with no vertical displacement observed.

During the 1979 event, the same section of fault ruptured on the U.S. side of the border, but with no observed surface rupture in Mexico. A 36 km long surface rupture formed with a maximum slip of 0.6–0.78 m. The displacement pattern of the two earthquakes was very similar on the U.S. side, typically within a few tens of centimeters. The similarity of the two slip distributions along the northern half of the fault and the coincidence of the location of steep gradients in slip in both the 1940 and 1979 earthquakes may indicate the persistence of a segment boundary (Sieh, 1996; Yeats et al., 1997).

Geologic, geodetic, and geophysical investigations provide tight constraints on the fault and on the kinematics and dynamics of the fault rupture of the 1979 earthquake. Yeats et al. (1997) summarized the key observations as follows:

- The hypocenter of the event was determined to be on or near the Imperial fault at a depth of approximately 10 km and at a point a few kilometers south of the U.S.-Mexico border.
- Aftershocks were concentrated north of the border in a volume of crust within a few kilometers of the northern tip of the fault. This concentration reflects the failure of a number of small faults in the step-over region between the Imperial and Superstition Hills faults.
- The largest aftershock, which occurred within eight hours of the main event, was produced by left-lateral subsurface rupture of a northeast-trending 10 km long fault directly north of the Imperial fault.

- Surficial ruptures associated with the 1979 earthquake were all north of the U.S.-Mexico border, 10–45 km northwest of the hypocenter. Most of the ruptures were on the Imperial fault (dextral offsets up to 50 cm), but minor dip-slip displacement occurred on the northern part of the fault where it forms the southwestern margin of the Mesquite graben and along the Brawley fault, a splay the forms the northeastern margin of the graben.
- Analysis of near-field geodetic measurements and strong-ground-motion data also required a concentration of dextral slip well north of the Border, tens of kilometers north of the hypocenter (Hartzell and Helmberger, 1982; Hartzell and Heaton, 1983; Archuleta, 1984). These data also suggest that the magnitude of the maximum slip at depth is 2–3 m, several times greater than slip values across the surficial trace of the fault.
- Subsequent slippage along the Imperial fault in the months and years following the 1979 earthquake reduced considerably the discrepancy between the coseismic surface and subsurface offsets but did not completely eliminate it.

The 1979 rupture of the Brawley fault zone is an example of a rupture splay as defined for this study. Rupture in the 1979 Imperial Valley earthquake branched at the junction of the Imperial and Brawley faults, and surface and subsurface rupture proceeded on both faults (Archuleta, 1984). As described by Sharp et al. (1982), the Brawley fault zone east of the northern section of the Imperial fault ruptured discontinuously along multiple strands over a length of 13.1 km. The faulting extended approximately 0.9 km northward and 1.8 km southward beyond the limits of recognized faulting identified from an earthquake swarm in 1975. Displacement in the Brawley fault zone was dominantly vertical, similar to but smaller than and opposite in sense to that on the northern section of the Imperial fault. However, there were several sites along the Brawley fault zone where cultural features were also displaced right-laterally during the earthquake.

*1992 **M** 7.3 Landers Earthquake, California*

The **M** 7.3 Landers earthquake, which occurred on 28 June 1992, resulted from the rupture of several major and many minor right-lateral faults within the southern part of the Eastern California shear zone (ECSZ), an 80 km wide zone of active predominantly right-lateral strike-slip faults, historical geodetic strain, and abundant seismicity (Sieh et al., 1993). The 1992 event was produced by nearly unilateral, northward rupture of five major right-lateral faults and fault segments: Johnson Valley, Landers (also referred to as Kickapoo), Homestead Valley, Emerson, and Camp Rock faults (Sieh et al., 1993; Figure 9-4). Sowers et al. (1994) describe the geometry of the fault zone where the rupture—which was propagating northward along the Johnson Valley fault—extended onto the Kickapoo fault, a pre-1992 fault best interpreted as the northward continuation of the Southern Johnson Valley fault. The rupture crossed three extensional step-overs (one from the Johnson Valley fault to the Homestead Valley fault along the Landers/Kickapoo fault, another from the Homestead Valley fault to the Emerson fault, and a third complex releasing step-over near the north end of the rupture from the Emerson fault to the Camp Rock fault) (Figure 9-4b).

Sieh et al. (1993) note that the large surficial offsets (as great as 6 m) and a relatively short rupture length are consistent with seismological calculations of a high stress drop (200 bars), which is in turn consistent with an apparently long recurrence interval for these faults. Paleoseismology of the Johnson Valley, Kickappo, and Homestead Valley faults shows that the return period for large surface rupturing events in this part of the ECSZ is in the range of 5–15 thousand years and that previous events along the Johnson Valley and Kickapoo faults were different and involved different fault segments than did the 1992 event (Rockwell et al., 2000). The data also show evidence for temporal clustering of large (?) earthquakes on faults trenched in the southwestern Mojave desert, with the most recent sequence including the 1992 Landers earthquake in the late Holocene (0–1 ka) preceded by clusters in the early (8–9 ka) and middle (5–6 ka) Holocene, and possibly the latest Pleistocene (~15 ka).

Subsequent studies using linear-elastic quasi-static mechanical models of faults involved in the **M** 7.3 Landers earthquake were conducted by Madden and Pollard (2012) to test the influence of fault continuity, dip, and strike on fault slip and the perturbed stress field in regions of complex surface deformation and dense aftershock activity. In addition to providing insight into aftershock behavior, the Madden and Pollard (2012) study provided information to resolve better the subsurface fault geometry along the complex Landers rupture.

1999 ***M*** *7.1 Hector Mine, California*

The 1999 **M** 7.1 Hector Mine earthquake occurred within the Mojave Desert portion of the Eastern California shear zone (ECSZ) and was accompanied by 48 km of dextral surface rupture (Treiman et al., 2002) (Figure 9-5). The 1999 Hector Mine earthquake was unexpected in that it occurred on a fault that had not been considered to have Holocene activity or to be significant in the ECSZ, and the amount of slip was larger than would be predicted based on the length of the fault. The complex rupture stepped across the Lavic Lake fault, the Bullion fault, and two minor faults to the south, demonstrating that rupture in the ECSZ can propagate across a series of existing faults that are slightly oblique to the strike of the ECSZ. Analysis of interferometric synthetic aperture radar (InSAR) and global positioning systems (GPS) observations (Simons et al., 2002) and inversions of strong motion, teleseismic, geodetic, and surface offset data also showed the inferred geometry to be spatially complex, with multiple strands (Hauksson et al., 2002; Ji et al., 2002; Jónsson et al., 2002; Kaverina et al., 2002).

The rupture initiated on an unknown north-trending structure (a splay to a previously mapped but unnamed fault, which is now referred to as the Lavic Lake fault) (Hauksson et al., 2002; Ji et al., 2002). The rupture propagated bi-laterally to the northwest and to the south from the epicentral area. South of the epicenter, the rupture merged into the southern portion of the Bullion fault zone and continued southeastward along the East- and West Bullion faults.

Principal surface rupture (as much as 5.25 ± 0.85 m dextral slip), occurred on the Lavic fault approximately 4 km south of the epicenter in the Bullion Mountains. Vertical slip was a secondary component and was variable; within the Bullion Mountains vertical slip

was generally more west side down, whereas to the north and south vertical slip was more east side down.

Based on preliminary paleoseismic data, Treiman et al. (2002) suggest that slip transfer in the penultimate event on the Lavic Lake and Bullion faults did not occur on the same fault elements.

*2002 **M** 7.9 Denali Earthquake, Alaska*

The 3 November 2002 **M** 7.9 Denali earthquake resulted in a complex 341 km long surface rupture involving the Susitna Glacier (thrust), Denali (strike-slip), and Totschunda (strike-slip) faults (Figure 9-6). Detailed mapping of the rupture indicated direct connections between adjacent faults, such that the rupture was continuous despite the geometric variability of the fault surface; the two fault intersections did not appear to significantly impede the rupture that propagated through them (Haeussler et al., 2004; Figure 9-7).

The rupture initiated on the previously unrecognized Susitna Glacier thrust and proceeded from west to east along 48 km of that fault, with an average dip slip of 4 m estimated from scarp heights (Eberhart-Phillips et al., 2003; Crone et al., 2004; Haeussler et al., 2004; Haeussler, 2009). Field and seismological data suggest that the Susitna Glacier fault is part of a large positive flower structure associated with northwest-directed transpressive deformation on the Denali fault (Crone et al., 2004). Rupture then occurred along 226 km of the Denali fault, where right-lateral slip at the surface averaged 4.5–5.1 m and reached a maximum of 8.8 m (Haeussler et al., 2004). The rupture then progressed southeasterly another 66 km along the Totschunda fault, where right-lateral offsets average approximately 1.7 m (Haeussler et al., 2004).

The propagation of the **M** 7.9 rupture from the central Denali fault onto the Totschunda fault has been evaluated to assess dynamic models of fault branching, in which the angle of the regional or local prestress relative to the orientation of the main fault and branch is thought to play an important role in determining which fault branch is taken (Schwartz et al., 2012). Paleoseismic data show significant differences timing of the pre-2002 ruptures on the eastern Denali and Totschunda with elapse time on the eastern Denali fault being considerably shorter in duration. Schwartz et al. (2012) propose that differences in accumulated strain on fault segments, which express differences in elapsed time since the most recent event , was an important control on the branching direction.

*2010 **M** 7.2 El Mayor–Cucapah Earthquake, Mexico*

The 4 April 2010 **M** 7.2 El Mayor–Cucapah earthquake occurred within a fault system that accommodates oblique strain in northern Mexico. The fault system, which extends approximately 120 km from the northern tip of the Gulf of California to the U.S.-Mexico border, is composed of at least seven major faults linked by numerous smaller faults (Figure 9-8) some of which were unnamed and some unmapped prior to the earthquake. The fault system and rupture are described by Fletcher et al. (2014). Prior to the earthquake, it was not recognized that the major previously mapped individual faults had the physical links required for them to behave as a single fault system capable of

producing a major earthquake. Rupture initiated on the central part of the zone near a north-striking fault and then propagated bilaterally through three distinct kinematic faulting domains having strongly contrasting geomorphologic expression. The rupture involved slip on dextral-normal fault systems having different dip directions as well as cross faults.

Southeast of the epicenter, a broad region of distributed deformation (fracturing, liquefaction, and discontinuous fault rupture) was controlled by a buried southwest-dipping, dextral-normal fault system that extends for approximately 53 km across the southern Colorado River delta. Northwest of the epicenter, the sense of vertical slip reverses as the rupture propagated approximately 55 km through multiple strands of an imbricate stack of east-dipping dextral-normal faults in the Sierra Cucapah. Some coseismic slip also was partitioned onto the west-dipping Laguna Salada fault, which extends parallel to the main rupture and defines the western margin of the Sierra Cucapah. In the northwestern (Yuha Desert) domain, rupture terminated on several north-northeast-striking cross faults, with minor offset (<8 cm) that cut uplifted and folded sediments of the northern Colorado River in the Yuha Desert.

In the El Mayor–Cucapah surface rupture, slip was activated on faults with several different orientations, and the rake of slip was observed to be directly controlled by the fault strike. Fault segments having end-member kinematics of either pure-normal or dextral slip are rare relative to those exhibiting oblique-slip kinematics; from this, Fletcher et al. (2014) conclude that the overall slip direction is more westerly than the average trend (312°) of the rupture. The presence of low-angle detachments that appear to control large segments of the surface rupture is thought to have played an important role in transferring slip through the fault network. Fletcher et al. (2014) hypothesize that different sets of faults within the system may be activated during different earthquakes and that the assembly of fault segments that link together to produce a large-magnitude earthquake may vary in consecutive ruptures.

9.2.2 Hosgri Fault Rupture Model

As described in *Chapter 7*, the three Hosgri FGMs are differentiated primarily based on the geometry and dip of the fault zone at depth, which impacts the source-to-site distance. A single Hosgri fault Rupture Model is used for all three FGMs, with rupture sources described in Table 9-3 and shown for the different FGMs on Plate 9-1. Linked and splay rupture sources involving the Hosgri and Shoreline fault sources are included with the Hosgri Rupture Model. Complex rupture sources involving the Hosgri fault source and the Los Osos or San Luis Bay fault sources are included with the SLPB Rupture Models (*Sections 9.2.3 through 9.2.5*).

The Hosgri Rupture Model consists mostly of linked rupture sources, such that in the largest ruptures, the Hosgri fault ruptures with the San Simeon, San Gregorio, and northern San Andreas faults from offshore Point Arguello in the south, to the Mendocino Triple Junction (MTJ) in the north (Plate 9-1). Rupture sources H-01 through H-03 were developed to account for aleatory variability in the distance of future ruptures on the

Hosgri fault source from the DCPP. These sources are identical in length, extending from the south end of the Hosgri fault to the MTJ, but they occupy different strands of the fault zone directly west of the DCPP with different dips. In rupture source H-04, a complex rupture source, the maximum Hosgri rupture includes the western Hosgri fault section (WR) with strike-slip motion and the Piedras Blancas fault section (PB) with a reverse sense of slip. Rupture source H-08 is a characteristic rupture source of the Piedras Blancas reverse source that provides an alternative rupture topology for that reverse fault source. In rupture source H-05, a splay rupture source, the maximum Hosgri fault source ruptures as the primary fault, together with the Shoreline fault source, as the splay fault. Rupture sources H-06 and H-07 were developed to account for higher slip rate of the Hosgri fault north of its intersection with the Shoreline and Los Osos faults, respectively. These rupture sources are added to the Diablo Canyon SSC model so that the full slip rate of branching faults may be added to the HFZ north of the intersections where those faults merge with the HFZ (*Section 9.4*).

Table 9-3. Hosgri Fault Rupture Model

Rupture Source Number	Type	Description	Fault Sections[1] (closest section to the DCPP in bold)	Sense of Slip
H-01	Linked	Hosgri (Central trace) to MTJ[2]	HS+**HA**+HC+HB+HD+HN+SI+SN+GS+GN+SA	Strike slip
H-02	Linked	Hosgri (West trace) to MTJ	HS+**HW**+HB+HD+HN+SI+SN+GS+GN+SA	Strike slip
H-03	Linked	Hosgri (East trace) to MTJ	HS+**HE**+HB+HD+HN+SI+SN+GS+GN+SA	Strike slip
H-04	Complex	Hosgri (Central trace) with Piedras Blancas	HS+**HA**+HC+HB+WR (primary fault); PB (secondary fault)	Primary = strike slip Secondary = reverse
H-05	Splay	Shoreline with Hosgri (Central trace) to Bolinas	HS+**HA**+HC+HB+HD+HN+SI+SN+GS+GN (main fault); SE+SS+**SH** (splay fault)	Strike slip
H-06[3]	Linked	Hosgri north of the Shoreline fault intersection	**HB**+HD+HN+SI+SN+GS+GN+SA	Strike slip
H-07[3]	Linked	Hosgri north of the Los Osos fault intersection	**HN**+SI+SN+GS+GN+SA	Strike slip
H-08[3]	Characteristic	Piedras Blancas	**PB**	Reverse

[1] Two-letter codes are explained in Table 6-5 and on Plate 9-1.
[2] MTJ = Mendocino Triple Junction
[3] Same downdip geometry is used for all three Hosgri FGMs.

- **H-01.** Rupture source H-01 is a linked rupture source that represents ruptures on the primary active central trace of the HFZ. Thus it occupies the central trace of the HFZ west of the DCPP and extends from the MTJ in the north to the south end of the Hosgri fault offshore of Point Arguello.
- **H-02.** Rupture source H-02 is a linked rupture source that represents ruptures on the western trace of the HFZ. It extends from the MTJ in the north to the south end of the HFZ offshore of Point Arguello.
- **H-03.** Rupture source H-03 is a linked rupture source that represents ruptures on the eastern trace of the Hosgri, and the likely minimum source-to-site distance. It extends from the MTJ in the north to the south end of the Hosgri fault offshore of Point Arguello.
- **H-04.** Rupture source H-04 is a complex rupture that incorporates contractional deformation of the Piedras Blancas (PB) reverse fault and dextral deformation of the western reach of the Hosgri fault (WR) and the central strand of the Hosgri fault west of the DCPP (HA and HC). A historical analog for this rupture topology is the 2002 Denali, Alaska, earthquake (*Section 9.2.1.5*). The north end of this rupture source is fixed at the north end of PB because no active faults are mapped within 5 km of the north end of PB, and because very long ruptures on the Hosgri fault are already included in this Rupture Model as rupture sources H-01, H-02, and H-03. To the south, the rupture source extends to the south end of the Hosgri fault offshore of Point Arguello.
- **H-05.** Rupture source H-05 is a splay rupture that represents scenario earthquakes that rupture the Hosgri fault (as the main fault plane) together with the Shoreline fault (as the splay fault plane). Analogous historical earthquakes that involved joint rupture of a main fault together with a splay fault include the 1979 Imperial Valley, California, the 1995 Kobe, Japan, and the 1992 Landers, California, earthquakes (Somerville, 2011; *Section 9.2.1.5*). 2D dynamic modeling suggests that propagation of Hosgri slip onto the Shoreline fault is unlikely (Kame et al., 2003). Despite the possibly unfavorable geometry, this rupture source is included in the Hosgri Rupture Model to account for the incomplete understanding of dynamic rupture propagation, and because the Kame et al. (2003) result does not preclude ruptures that may initiate on the Shoreline fault and then propagate onto the Hosgri fault. The Hosgri fault source included in this rupture source extends from the north end of the San Gregorio fault zone (where it intersects the northern San Andreas fault) in Bolinas to the south end of the Hosgri fault source offshore of Point Arguello. The entire Shoreline fault source is also included, from its north end at the intersection with the Hosgri fault to its south end at the intersection with the Casmalia fault.
- **H-06.** Rupture source H-06 is a linked rupture source that extends from the Hosgri–Shoreline fault intersection north to the MTJ. This source is developed to account for the additional slip rate that is added to the Hosgri fault source north of the intersection with the Shoreline fault source.
- **H-07.** Rupture source H-07 is a linked rupture source that extends from the intersection of the Hosgri and the Los Osos faults north to the MTJ. This source is

developed to account for the additional slip rate that is added to the Hosgri fault source north of the intersection with the Los Osos fault source.

9.2.3 Outward-Vergent Rupture Model

The OV Rupture Model consists of 10 rupture sources as shown on Plate 9-2 and described in Table 9-4. The OV Rupture Model includes ruptures of the Los Osos, San Luis Bay, and Shoreline fault sources, and their Connected SLPB fault sources. Splay rupture sources involving only the Shoreline and Hosgri fault sources are tracked as part of the Hosgri Rupture Model.

Rupture sources OV-01 through OV-04 describe various ways that the Shoreline fault may or may not rupture with adjacent faults. The first two rupture sources (OV-01 and OV-02) were developed to encompass uncertainty in whether the Shoreline fault ruptures jointly with the Hosgri fault. The third and fourth rupture sources (OV-03 and OV-04) involve joint rupture of the Shoreline fault with the San Luis Bay fault. The distinction is that the OV-04 source also includes Connected faults that extend the rupture source to the southeast and northwest such that it may host very large earthquakes. Rupture sources OV-05 through OV-08 were developed to describe variability in rupture topology of faults primarily responsible for uplifting the Irish Hills. Rupture sources OV-09 and OV-10 are included to balance the slip rate on Connected faults.

Table 9-4. Outward-Vergent (OV) Rupture Model

Rupture Source Number	Type	Description	Fault Sections[1] (closest section to the DCPP in bold)	Sense of Slip
OV-01	Characteristic	Shoreline	SE+SF+SS+**SH**	Strike slip
OV-02	Linked	Shoreline and Hosgri	SE+SF+SS+**SH**+HB+HD+HN+SI+SN+GS+GN+SA	Strike slip
OV-03	Complex	Shoreline with San Luis Bay	**SH** (primary fault); BE+BR (secondary fault)	Primary = reverse Secondary = strike slip
OV-04	Complex	Shoreline and Hosgri with San Luis Bay and SWBZ[2]	**SH**+HB+HD+HN+SI+SN+GS+GN (primary fault); LP+FS+FN+NL+WA+WC+MF+BE+BR (secondary fault)	Primary = strike slip Secondary= reverse
OV-05	Characteristic	San Luis Bay	BE+**BR**	Reverse
OV-06	Splay	San Luis Bay with Los Osos	LO+LV+**LM** (main fault); BE+**BR** (splay fault)	Reverse
OV-07	Characteristic	Los Osos	LE+LO+LV+**LM**+LC	Reverse oblique

Rupture Source Number	Type	Description	Fault Sections[1] (closest section to the DCPP in bold)	Sense of Slip
OV-08	Complex	Los Osos with Hosgri	HN+SI+SN+GS+GN (primary fault); LO+LV+**LM**+LC (secondary fault)	Primary = strike slip Secondary = reverse oblique
OV-09	Linked	Oceano and SWBZ[2]	LP+FS+FN+ON+**OF**	Reverse oblique
OV-10	Characteristic	Wilmar Avenue	NL+WA+**WC**	Reverse oblique

[1] Two-letter codes are explained in Table 6-5 and on Plate 9-2.
[2] SWBZ = Southwestern Boundary zone of faults. The SWBZ includes the Little Pine and Foxen Canyon faults and the Nipomo lineament, as well as the San Luis Bay, Wilmar Avenue, and Oceano faults, which are specified by name in this table.

- **OV-01.** Rupture source OV-01 is a characteristic rupture source of the entire Shoreline fault source. The north end of this rupture source is the intersection with the Hosgri fault. The south end of the Shoreline fault source at the intersection with the Casmalia fault is the south end of the rupture.
- **OV-02.** Rupture source OV-02 is a linked rupture source that includes the Shoreline fault source and the Hosgri fault source north of its intersection with the Shoreline fault source. Its north end is the northern San Andreas fault source at the MTJ. An approximate historical analog for this rupture source is the 2002 Denali, Alaska, earthquake (Eberhart-Phillips et al., 2003; Haeussler et al., 2004; *Section 9.2.1.5*). At its eastern extent, the Denali earthquake rupture propagated southeastward onto the lower-slip-rate Totschunda fault instead of continuing eastward on the main Denali fault (Schwartz et al., 2012). Although the angular relationship of the Shoreline-Hosgri intersection is the opposite of that of the Totschunda-Denali intersection, the OV-02 rupture source allows such events to occur near the DCPP.
- **OV-03.** Rupture source OV-03 is a complex rupture source that includes the northern part of the strike-slip Shoreline fault source as the primary rupture plane, and the reverse San Luis Bay fault source as the secondary rupture plane. This rupture source captures the possibility that the northern part of the Shoreline fault source and the entire San Luis Bay fault source rupture together in repeated earthquakes that uplift the southern portion of the Irish Hills and accommodate dextral shear within the SLPB.
- **OV-04.** Rupture source OV-04 is a complex rupture source that includes numerous fault sources. The rupture source incorporates the northern part of the strike-slip Shoreline fault together with the strike-slip Hosgri fault and linked strike-slip faults that extend northward to the north end of the San Gregorio fault source. The rupture source also involves secondary reverse slip on faults of the

SWBZ, including the San Luis Bay, Wilmar Avenue, Nipomo, Foxen Canyon, and Little Pine fault sources. Although the Nipomo Lineament is steeply dipping in the model, and is vertical at the south end (Plate 9-2), for this rupture source it is presumed to be capable of being involved in a through-going, primarily reverse rupture with the Foxen Canyon fault to the south. In this rupture source, the offshore continuation of the San Miguelito fault (fault section MF) is a tear fault linking the San Luis Bay and Wilmar Avenue faults across eastern San Luis Obispo Bay.

- **OV-05.** Rupture source OV-05 is a characteristic rupture source of the entire San Luis Bay fault source. The west end of this rupture source is the intersection of the San Luis Bay fault with the Shoreline fault. The east end of the rupture source is located at the east end of the San Luis Bay fault, where geologic map constraints suggest there is a 2–5 km step-over south-southeast to the Wilmar Avenue fault, and the uplift rate of the San Luis Range decreases from approximately 0.2 mm/yr (in the Irish Hills sub-block) to approximately 0.1 mm/yr (in the Edna sub-block; Figure 7-4).
- **OV-06.** Rupture source OV-06 is a splay rupture source that involves reverse rupture of the San Luis Bay and Los Osos fault sources jointly. The Los Osos fault is the larger, main rupture plane and the San Luis Bay is the smaller splay rupture plane. Historical analogs that involved coseismic rupture of an oppositely verging main thrust and backthrust include the 2003 San Simeon, California, earthquake (McLaren et al., 2008; *Section 7.4.2.1*) and the 1896 Rikuu, Japan, earthquake (Matsuda et al., 1980; *Section 9.2.1.5*). The rationale for defining the ends of the rupture source on the San Luis Bay fault is identical to that described above for rupture source OV-05. The ends of the rupture source on the Los Osos fault are selected to scale approximately with the geometry of the Irish Hills sub-block. This rupture source also serves to account for the higher slip rate of the Los Osos fault where it borders the Irish Hills sub-block (with its higher uplift rate) (fault sections LM, LV, and LO) relative to the part that borders the Edna sub-block (with its lower uplift rate) (fault section LE).
- **OV-07.** Rupture source OV-07 is a characteristic rupture source that includes reverse oblique rupture of the entire Los Osos fault from its offshore intersection with the Hosgri fault to its intersection with the West Huasna fault. This rupture source accounts for the plausible mode of behavior for the Los Osos fault rupturing in its entirety or in part along its “named” extent along the northern margin of the San Luis Range, without joint rupture with adjacent faults.
- **OV-08.** Rupture source OV-08 is a complex rupture that includes primary strike-slip ruptures on the Hosgri fault source and secondary reverse oblique ruptures on the offshore and Irish Hills portion of the Los Osos fault source. The strike-slip part of the rupture extends from the Los Osos fault intersection to the north end of the San Gregorio fault.
- **OV-09.** Rupture source OV-09 is a linked rupture source that includes reverse oblique slip of the Oceano fault with Connected faults of the SWBZ to the southeast, including the Foxen Canyon and Little Pine faults. This rupture source

is included in the OV Rupture Model to account for the fraction of slip rate on the Oceano fault that is not included in other rupture sources (*Section 9.3.3*).

- **OV-10.** Rupture source OV-10 is a characteristic rupture source that includes reverse slip on the Wilmar Avenue fault and Nipomo lineament. It extends from the west end of the Wilmar Avenue fault in San Luis Obispo Bay to the intersection of the Nipomo lineament with the Oceano fault to the south. This rupture source is included in the OV Rupture Model to account for the fraction of slip rate on the Wilmar Avenue fault that is not included in other rupture sources (*Section 9.3.3*).

9.2.4 Southwest-Vergent Rupture Model

The SW Rupture Model consists of 10 rupture sources as shown on Plate 9-2 and described in Table 9-5. Like the OV Rupture Model, the SW Rupture Model describes all ruptures that include the Los Osos and San Luis Bay fault sources and Connected fault sources. Splay rupture sources involving only the Shoreline and Hosgri fault sources are tracked as part of the Hosgri Rupture Model. Linked and complex rupture sources involving the Shoreline and other SLPB fault sources are tracked as part of the SW Rupture Model.

Rupture sources SW-01 through SW-03 were developed to describe various ways that the Shoreline fault may or may not link to connecting faults during future ruptures. The first rupture source (SW-01) involves only the Shoreline fault. The second rupture (OV-02) allows for rupture of the Shoreline fault with the Hosgri fault. The third rupture source (SW-03) involves joint rupture of the Shoreline fault with the Oceano fault and Connected faults of the SWBZ to the southeast. Rupture sources SW-04 through SW-07 were developed to describe variability in ruptures involving the San Luis Bay fault, which is the primary fault responsible for uplifting the Irish Hills in the SW Model. Rupture sources SW-08 through SW-10 are included to balance the slip rate on Connected faults.

Table 9-5. Southwest-Vergent (SW) Rupture Model

Rupture Source Number	Type	Description	Fault Sections[1] (closest section to the DCPP in bold)	Sense of Slip
SW-01	Characteristic	Shoreline	SE+SF+SS+**SH**	Strike slip
SW-02	Linked	Shoreline and Hosgri	SE+SF+SS+**SH**+HB+HD+HN +SI+SN+GS+GN+SA	Strike slip
SW-03	Complex	Shoreline with Oceano and SWBZ[2]	LP+FS+FN+ON+OF (primary fault); SF+SS+**SH** (secondary fault)	Primary = reverse Secondary = strike slip

Rupture Source Number	Type	Description	Fault Sections[1] (closest section to the DCPP in bold)	Sense of Slip
SW-04	Complex	San Luis Bay with Hosgri	HC+HB+HD+HN+SI+SN+GS +GN (primary fault); BE+**BW** (secondary fault)	Primary = strike slip Secondary = reverse
SW-05	Characteristic	San Luis Bay	BE+**BW**	Reverse
SW-06	Splay	San Luis Bay with Los Osos	BE+**BW** (main fault); LV+**LM** (splay fault)	Reverse
SW-07	Linked	San Luis Bay, Wilmar Avenue, and SWBZ[2]	LP+FS+FN+NL+WA+PO+BE+**BW**	Reverse
SW-08	Complex	Los Osos offshore with Hosgri	HN+SI+SN+GS+GN (primary fault); **LC** (secondary fault)	Primary = strike slip Secondary = reverse oblique
SW-09	Linked	Oceano and SWBZ[2]	LP+FS+FN+ON+**OF**	Reverse
SW-10	Splay	Wilmar Avenue with Los Osos East	NL+WA+**WB** (main fault); LE+**LB** (splay fault)	Reverse

[1] Two-letter codes are explained in Table 6-5 and on Plate 9-2.
[2] SWBZ = Southwestern Boundary zone of faults. The SWBZ includes the Little Pine and Foxen Canyon faults and the Nipomo lineament, as well as the San Luis Bay, Wilmar Avenue, and Oceano faults, which are specified by name in this table.

- **SW-01.** Rupture source SW-01 is a characteristic rupture source of the entire Shoreline fault source. The north end of this rupture source is the intersection with the Hosgri fault source. The south end the rupture source is the south end of the Shoreline fault source, at the intersection with the Casmalia fault source.
- **SW-02.** Rupture source SW-02 is a linked rupture source that includes both the Shoreline and Hosgri fault sources. Ruptures are allowed to float freely across their intersection. It extends from the north end of the San Andreas fault at the MTJ to the south end of the Shoreline fault source. An historical analog for this rupture topology is the 2002 Denali, Alaska, earthquake (Eberhart-Phillips et al., 2003, *Section 9.2.1.5*). At its eastern extent, this rupture propagated southeastward onto the less active Totschunda fault instead of continuing eastward on the main Denali fault (Haeussler et al., 2004; Schwartz et al., 2012). Similarly, rupture source SW-02 represents ruptures that occur jointly on the more active Hosgri fault source and the less active Shoreline fault source.

- **SW-03.** Rupture source SW-03 is a linked complex rupture source that includes the northern part of the Shoreline fault source, the Oceano fault source, and Connected faults of the SWBZ to the southeast, including the Foxen Canyon and Little Pine fault sources. This is a complex rupture source that jointly incorporates reverse slip on the Oceano, Foxen Canyon, and Little Pine fault sources, and strike slip on the Shoreline fault source. The rupture source extends from the north end of the Shoreline fault source at the intersection with the Hosgri fault source, to the southeast end of the Little Pine fault source.
- **SW-04.** Rupture source SW-04 is a linked complex rupture source that includes the San Luis Bay fault source and the northern part of the Hosgri fault source, north of its intersection with the San Luis Bay fault source. The rupture source incorporates strike slip on the Hosgri fault source and reverse slip on the San Luis Bay fault source. The north end of this rupture source is the north end of the San Andreas fault at the MTJ. The east end is the east end of the San Luis Bay fault source, where geologic map constraints suggest there is a 2–5 km step-over to the Wilmar Avenue fault, and the uplift rate decreases between the Irish Hills sub-block and the Edna sub-block of the SLPB (Figure 7-4). An historical analog for this rupture topology is the 2002 Denali, Alaska, earthquake. This earthquake was dominantly a strike-slip rupture of the Denali fault, but also included joint rupture of the Susitna Glacier thrust fault (Eberhart-Phillips et al., 2003; *Section 9.2.1.5*).
- **SW-05.** Rupture source SW-05 is a characteristic rupture source of the entire San Luis Bay fault source. The west end of this characteristic rupture source is the intersection with the Hosgri fault source. The east end of the rupture source is located at east end of the San Luis Bay fault source, where geologic map constraints suggest there is a 2–5 km step-over to the Wilmar Avenue fault, and the uplift rate decreases between the Irish Hills sub-block and the Edna sub-block of the SLPB (Figure 7-4).
- **SW-06.** Rupture source SW-06 is a splay rupture source that includes reverse rupture of the San Luis Bay and Los Osos fault sources jointly. The San Luis Bay fault is the primary rupture plane and the Los Osos fault source is the secondary rupture plane. Historical analogs for this rupture source that involved coseismic rupture of an oppositely verging main thrust and backthrust include the 2003 San Simeon, California, earthquake (McLaren et al., 2008; *Section 7.4.2.1*) and the 1896 Rikuu, Japan, earthquake (Matsuda et al., 1980;*Section 9.2.1.5*). The endpoints of the rupture source are selected to scale approximately with the geometry of the Irish Hills, thereby accounting for the higher slip rate of the Los Osos and San Luis Bay faults where they border the Irish Hills relative to the parts that border the Edna sub-block.
- **SW-07.** Rupture source SW-07 is a linked rupture source that includes numerous faults of the SWBZ that could plausibly fail together in a large reverse-slip earthquake. This linked rupture source involves reverse slip on the San Luis Bay, Wilmar Avenue, Nipomo Lineament, Foxen Canyon, and Little Pine fault sources. The west end of the rupture source is the intersection of the San Luis Bay fault source and the Hosgri fault source, and the east end is the southeast end of the

Little Pine fault source. Although the Nipomo Lineament is steeply dipping in the model, and is vertical at the south end (Plate 9-2), for this rupture source it is presumed to be capable of being involved in a through-going, primarily reverse rupture with the Foxen Canyon fault to the south. An historical analog for this rupture topology is the 1999 Chi-Chi, Taiwan, earthquake (Lin et al., 2001).

- **SW-08.** Rupture source SW-08 is a linked complex rupture source that includes rupture of the offshore part of the Los Osos fault source extending onto the Hosgri fault source north of the intersection. This rupture source involves reverse oblique rupture of the offshore part of the Los Osos fault source (LC) and strike-slip rupture of the Hosgri fault source and linked strike-slip faults to the north. The north end of the rupture source is the north end of the San Andreas fault source at the MTJ. The south end of the rupture is the point where the Los Osos fault is inferred to extend onshore where fault mapping suggests the presence of an approximately 5 km wide subsiding basin or step-over in the fault trace. An historical analog for this rupture topology is the 2002 Denali, Alaska, earthquake. This earthquake was dominantly a strike-slip rupture of the Denali fault, but also included joint rupture of the Susitna Glacier thrust fault (Eberhart-Phillips et al., 2003; *Section 9.2.1.5*).
- **SW-09.** Rupture source SW-09 is a linked rupture source that includes reverse slip of the Oceano fault source with Connected faults of the SWBZ to the southeast, including the Foxen Canyon and Little Pine fault sources. The rupture source extends from the intersection of the Oceano and Shoreline fault sources to the southeast end of the Little Pine fault source. This rupture source is included in the SW Model to account for slip rate of the Oceano fault that is not included in other rupture sources.
- **SW-10.** Rupture source SW-10 is a splay rupture source that includes reverse rupture of the Wilmar Avenue and Los Osos East fault sources jointly. The Wilmar Avenue fault source is the primary rupture plane, and the Los Osos East fault source is the secondary rupture plane. Historical analogs for this rupture source that involved coseismic rupture of oppositely verging main thrust and backthrust include the 2003 San Simeon, California, earthquake (McLaren et al., 2008; *Section 7.4.2.1*) and the 1896 Rikuu, Japan, earthquake (Matsuda et al., 1980; *Section 9.2.1.5*).

9.2.5 Northeast-Vergent Rupture Model

The NE Rupture Model consists of 11 rupture sources as shown on Plate 9-2 and described in Table 9-6. As with the OV and SW Models, the NE Model describes all ruptures that include the Los Osos and San Luis Bay fault sources and Connected fault sources. Splay rupture sources involving only the Shoreline and Hosgri fault sources are tracked as part of the Hosgri Rupture Model. Linked and complex rupture sources involving the Shoreline and other SLPB fault sources are tracked as part of the NE Model.

Rupture sources NE-01 through NE-04 were developed to describe various ways that the Shoreline fault source may or may not link to connecting faults in future ruptures. The

first rupture source (NE-01) involves only the Shoreline fault. The second rupture (NE-02) allows for rupture of the Shoreline fault with the Hosgri fault. The third and fourth rupture sources (NE-03 and NE-04) describe alternative possible linkages between the Shoreline fault source and faults of the SWBZ. Rupture sources NE-05 through NE-08, and NE-11 were developed to describe variability in rupture topology involving the Los Osos fault source, which is the primary fault responsible for uplifting the Irish Hills in the NE Model. Rupture sources NE-09 and NE-10 are included to balance the slip rate on Connected faults.

Table 9-6. Northeast-Vergent (NE) Rupture Model

Rupture Source Number	Type	Description	Fault Sections[1] (closest section to the DCPP in bold)	Sense of Slip
NE-01	Characteristic	Shoreline	SE+SF+SS+**SH**	Strike slip
NE-02	Linked	Shoreline and Hosgri	SE+SF+SS+**SH**+HB+HD+HN+SI +SN+GS+GN+SA	Strike slip
NE-03	Complex	Shoreline with San Luis Bay	**SH** (primary fault); BE+BR (secondary fault)	Primary = strike slip Secondary = reverse
NE-04	Complex	Shoreline and Hosgri with Oceano and SWBZ[2]	SF+SS+**SH**+HB+HD+HN+SI +SN+GS+GN (primary fault); LP+FS+FN+ON+OF (secondary fault)	Primary = strike slip Secondary = reverse
NE-05	Characteristic	Los Osos, Irish Hills	LV+**LM**	Reverse
NE-06	Splay	Los Osos with San Luis Bay	LV+**LM** (main fault); BE+**BR** (splay fault)	Reverse
NE-07	Splay	Los Osos with Wilmar Avenue and SWBZ	LP+FS+FN+NL+WA+**WB** (main fault); LV+**LM**+LC (splay fault)	Reverse
NE-08	Complex	Los Osos with Hosgri	HN+SI+SN+GS+GN (primary fault); LV+**LM**+LC (secondary fault)	Primary = strike slip Secondary = reverse
NE-09	Linked	Oceano and SWBZ	LP+FS+FN+ON+**OF**	Reverse
NE-10	Splay	Wilmar Avenue with Los Osos East	**WA**+WB (main fault); LE+**LB** (splay fault)	Reverse

Rupture Source Number	Type	Description	Fault Sections[1] (closest section to the DCPP in bold)	Sense of Slip
NE-11	Characteristic	Los Osos, Irish Hills and Offshore	LV+**LM**+LC	Reverse

[1] Two-letter codes are explained on Table 6-5 and on Plate 9-2.
[2] SWBZ = Southwestern Boundary zone of faults. The SWBZ includes the Little Pine and Foxen Canyon faults and the Nipomo lineament, as well as the San Luis Bay, Wilmar Avenue, and Oceano faults, which are specified by name in this table.

- **NE-01.** Rupture source NE-01 is a characteristic rupture source of the entire Shoreline fault source. The north end of the rupture source is the intersection with the Hosgri fault source. The south end the rupture source is the south end of the Shoreline fault source, at the intersection with the Casmalia fault source.
- **NE-02.** Rupture source NE-02 is a linked rupture source that includes both the Shoreline and Hosgri fault sources. Ruptures are allowed to float freely across their intersection. The rupture source extends from the north end of the San Andreas fault at the MTJ to the south end of the Shoreline fault at its intersection with the Casmalia fault source. An historical analog for this rupture topology is the 2002 Denali, Alaska, earthquake (Eberhart-Phillips et al., 2003; *Section 9.2.1.5*). At its eastern extent, this rupture propagated southeastward onto the less active Totschunda fault instead of continuing eastward on the main Denali fault (Haeussler et al., 2004; Schwartz et al., 2012). Similarly, rupture source NE-02 represents ruptures that occur jointly on the more active Hosgri fault and the less active Shoreline fault.
- **NE-03.** Rupture source NE-03 is a characteristic rupture source that includes the northern part of the Shoreline fault source and the entire San Luis Bay fault source. Only the shallow part of the Shoreline fault source, above the intersection with the San Luis Bay fault plane at depth, is involved in the rupture source. This is a complex rupture source that jointly incorporates reverse slip on the San Luis Bay fault source and strike slip on the Shoreline fault source. The rupture source extends from the north end of the Shoreline fault source at the intersection with the Hosgri fault source to the east end of the San Luis Bay fault source, where it ends at the tear between the hanging walls of the Los Osos fault source and the Oceano fault source in the NE Model.
- **NE-04.** Rupture source NE-04 is a linked complex rupture source that includes the northern part of the Shoreline fault source, the Oceano fault source, and Connected faults of the SWBZ to the southeast, including the Foxen Canyon and Little Pine fault sources. The Oceano fault is the most likely potential linkage between the Shoreline fault and the SWBZ because the San Luis Bay fault is not a dominant structure in the NE Model. Consequently, rupture source NE-04 is significantly longer than NE-03. This is a complex rupture source that jointly

incorporates reverse slip on the Oceano, Foxen Canyon, and Little Pine fault sources and strike slip on the Shoreline fault source. The rupture source extends from the north end of the Shoreline fault source at the intersection with the Hosgri fault source to the southeast end of the Little Pine fault source.

- **NE-05 and NE-11.** These two characteristic rupture sources involve the Los Osos fault. The concept behind rupture source NE-05 is that the most active part of the Los Osos fault, the primary structure driving uplift of the Irish Hills in the NE Model, may rupture independently from adjacent faults. This characteristic rupture source involves reverse slip of only the sections of the Los Osos fault source that underlie the Irish Hills (fault sections LM and LV). The west end of this rupture source is the intersection with the offshore Los Osos fault source (fault section LC), where geologic mapping and the presence of the actively subsiding Morro Bay basin suggest there may be an approximately 5 km right step-over in the fault trace that could inhibit the propagation of some future ruptures. The east end of both of these rupture sources is the east end of the moderately south-dipping Los Osos fault source, and it is marked by a tear or lateral ramp between the Los Osos fault source and the north-dipping Oceano fault source. Rupture source NE-11 includes the Irish Hills portion of the fault source (fault sections LM and LV) and the offshore portion of the Los Osos fault (fault section LC), to model the future ruptures that do not terminate at or in the Morro Bay basin step-over in the fault trace.
- **NE-06.** Rupture source NE-06 is a splay rupture source that includes reverse rupture of the San Luis Bay and Los Osos faults jointly. The Los Osos fault is the primary rupture plane, and the San Luis Bay is the secondary rupture plane. Historical analogs for this rupture source that involved coseismic rupture of oppositely verging main thrust and backthrust include the 2003 San Simeon, California, earthquake (McLaren et al., 2008; *Section 7.4.2.1*) and the 1896 Rikuu, Japan, earthquake (Matsuda et al., 1980; *Section 9.2.1.5*). The rationale for defining the ends of the rupture source on the Los Osos fault source is identical to that described above for rupture source NE-05. The width of the San Luis Bay fault backthrust is also defined to scale with the width of the Los Osos main thrust.
- **NE-07.** The concept behind this splay rupture source is that numerous faults that underlie and drive uplift of the SLPB could plausibly fail together in a large reverse-slip earthquake. This rupture source involves reverse slip on the Wilmar Avenue, Nipomo Lineament, Foxen Canyon, and Little Pine fault sources, and reverse slip on the smaller (secondary) Irish Hills and offshore portions of the Los Osos fault. Although the Nipomo Lineament is steeply dipping in the model, and is vertical at the south end (Plate 9-2), for this rupture source it is presumed to be capable of being involved in a through-going, primarily reverse rupture with the Foxen Canyon fault to the south. The change in vergence from the primary SW faults to the secondary NE faults reflects rupture on principal reverse fault ramps driving uplift of the SLPB in the NE Model. An historical analog for this splay rupture topology is the 1977 Caucete, Argentina, earthquake (*Section 7.4.3.1*).

- **NE-08.** Rupture source NE-08 is a complex rupture source that allows the Los Osos fault source to rupture jointly with the Hosgri fault source north of the fault intersection. This rupture source involves reverse oblique rupture of the Los Osos fault source (fault sections LV, LM, and LC) and strike-slip rupture of the Hosgri fault source and linked strike slip fault sources to the north. The rupture source extends from the north end of the San Andreas fault source, at the MTJ, to the east end of Los Osos fault section LV, at the tear or lateral ramp between the Los Osos and Oceano fault sources.
- **NE-09.** Rupture source NE-09 is a linked rupture source that includes reverse slip on the Oceano fault source with Connected faults of the SWBZ to the southeast, including the Foxen Canyon and Little Pine fault sources. The rupture source extends from the intersection of the Oceano and Shoreline fault sources to the southeast end of the Little Pine fault source. This rupture source is included in the NE Rupture Model to account for slip rate of the Oceano fault that is not included in other rupture sources.
- **NE-10.** Rupture source NE-10 is a splay rupture source that includes reverse rupture of both the Wilmar Avenue and Los Osos East fault sources jointly. The Wilmar Avenue fault source is the primary rupture plane, and the Los Osos East fault source is the secondary rupture plane. Historical analogs for this rupture source that involved coseismic rupture of oppositely verging main thrust and backthrust include the 2003 San Simeon, California, earthquake (McLaren et al., 2008; *Section 7.4.2.1*) and the 1896 Rikuu, Japan, earthquake (Matsuda et al., 1980; *Section 9.2.1.5*).

9.3 Slip Rate Allocation Model

After developing a set of rupture sources, the second piece in developing Rupture Models for use in the PSHA is to assign a slip rate to each rupture source (*Section 6.3.4*), which ultimately will be used to develop earthquake recurrence rates for the Primary and Connected fault sources. A Slip Rate Allocation Model describes the slip rate allocated to individual rupture sources in a single Rupture Model. Accordingly, there is one Slip Rate Allocation Model for the Hosgri Rupture Model (that applies to all three Hosgri FGMs) and three Slip Rate Allocation Models for the SLPB Rupture Models—one each for the OV, SW, and NE Rupture Models.

9.3.1 Slip Rate Allocation Methodology

The slip rate of each rupture source represents some fraction of the total fault slip rate determined from the Fault Slip Rate Model (*Chapter 8*) for each fault source involved in the rupture. Because the Rupture Model contains rupture sources that link across numerous faults with different fault slip rates, the Slip Rate Allocation Model creates a slip rate for each rupture source such that, when the contributions from all rupture sources including a particular fault are summed, the combined slip rate equals the target slip rate budget for that particular fault for that particular Rupture Model.

The methodology for subdividing the fault slip rate into fractions requires consideration of both the mean slip rate *m* and the uncertainty distribution in slip rate (standard deviation *s* and variance $s^2 = v$). The methodology for developing the mean slip rates for each rupture source is straightforward, as the mean slip rates of all rupture sources involving a particular fault section must sum to the target mean fault slip rate for that fault section:

$$m_T = \sum_{i=1}^{n} m_i \tag{9-1}$$

where m_T is the target mean fault slip rate for a given fault section, and m_i is the mean slip rate for one of *n* rupture sources that occupy that fault section. The value of each mean rupture source slip rate is simply the target mean fault slip rate times the fraction allocated to that rupture source a_i:

$$m_i = a_i(m_T) \tag{9-2}$$

For characteristic and linked rupture sources, the slip rate is uniform over the entire rupture source. For complex and splay rupture sources, two slip rates are defined as required by the method of calculating ground motions from these rupture source types (*Section 9.2.1.1*). A greater slip rate is assigned to the primary or main part of the rupture source relative to the secondary or splay part of the rupture source. The slip rate is greater by an amount that is proportional to the estimated seismic moments divided by the areas of each part, such that the scenario primary+secondary or main+splay earthquakes have the same occurrence rate.

The ratio of primary to secondary (or main to splay) slip rates is calculated using the following steps. First, the moment magnitudes of each part are estimated using the magnitude-area relation of Hanks and Bakun (2014; see *Chapter 10*):

$$\mathbf{M} = \log(A) + 3.98; A < 537\ km^2 \tag{9-3a}$$

$$\mathbf{M} = {}^{5}/_{4} \log(A) + 3.30; A \geq 537\ km^2 \tag{9-3b}$$

Scalar seismic moments (in dyne-cm) for each part are derived from the definition of moment magnitude (Hanks and Kanamori, 1979):

$$Log\ M_O = {}^{3}/_{2}\,\mathbf{M} + 16.05 \tag{9-4}$$

The ratio of seismic moments from the primary (*p*) and secondary (*s*) parts is related to the ratio of estimated displacements d_p and d_s of each part using the definition of seismic moment (Aki, 1966):

$$\frac{M_{o,p}}{M_{o,s}} = \frac{\mu A_p d_p}{\mu A_s d_s} \tag{9-5}$$

After rearranging and canceling the shear modulus μ, the ratio of displacements is

$$\frac{d_p}{d_s} = \frac{A_s M_{o,p}}{A_p M_{o,s}} \tag{9-6}$$

Because we define the complex and splay rupture sources to have a single occurrence rate for both the primary and secondary parts, the ratio of displacements in Equation (9-6) is equivalent to the ratio of slip rates. For complex and splay rupture sources where multiple rupture scenarios are involved with different frequencies (*Chapter 10*), the average slip rate ratio is used for the Slip Rate Allocation Models.

Figure 9-9 shows an example of the slip rate allocation approach. Panel (a) of Figure 9-9 shows the fault sections in a mock FGM (generally based on the configuration of faults surrounding the DCPP) and fault slip rates, which are scaled by line width and with values in arbitrary units placed in parentheses. The figure shows a Los Osos–like fault source consisting of fault sections S4, S5, and S6 that has a fault slip rate of 3 units. Rupture sources that are considered with this conceptual FGM are listed on the right side of Figure 9-9a. The three rupture sources that include fault section S5 are indicated by a bracket and in bold font.

Panel (b) on Figure 9-9 shows the slip rate allocation methodology for the mean slip rate for fault section S5. In the example, three rupture sources include fault section S5. The rupture source $i = 1$ on the left consists of fault sections S4, S5, and S6, and represents a characteristic, single-fault rupture source (Table 9-2) where the source ends at a change in slip sense and slip rate to the northwest and at the end of the fault to the southeast. A slip rate of $m_1 = 1.5$ units is allocated to this source, representing $a_1 = 0.5$ (i.e., 50%) of the target mean fault slip rate $m_T = 3$ units. The middle rupture source $i = 2$ on Figure 9-9b shows a splay rupture source (Table 9-2 and *Section 9.2.1.1*) involving the "main" fault section S5 (on the same Los Osos–like fault source) and the "splay" fault section S9 (on the oppositely dipping San Luis Bay–like fault source). A mean slip rate of $m_2 = 1.0$ unit is allocated to fault section S5, representing $a_2 = 0.33$ of the target mean fault slip rate for fault section S5. Because this is a splay rupture source, which ruptures in the Diablo Canyon SSC model as a scenario rupture with a single occurrence rate and set of magnitudes, the slip rate on splay fault section S9 is less—by a ratio of 0.9 in the example.

The right-hand rupture source $i = 3$ on Figure 9-9b shows a complex rupture source consisting of "primary" reverse fault sections S5 and S4 and "secondary" strike-slip fault section S1 (*Section 9.2.1.1*). This rupture source, which spans multiple faults with different slip rates and changes sense of slip along strike, has a slip rate of $m_3 = 0.5$ unit on fault section S5, representing $a_3 = 0.17$ of its total fault slip rate. The shorter, strike-slip portion of the complex rupture source has a lower slip rate—0.3 unit in the example. The 0.3-unit slip rate represents approximately 4% of the total fault slip rate of 7 units for fault section S1. The sum of the mean rupture source slip rates involving fault section S5 allocated between the three rupture sources—1.5+1.0+0.5—equals the 3 units target slip rate for the S5 fault section.

The fraction of total fault slip rate a_i allocated to each rupture source is based on two primary considerations. First, the slip rate that can be allocated to a rupture source cannot exceed the slip rates of any fault involved in the rupture source. Second, it is important to assess which rupture sources are more or less likely to perform the greatest amount of

displacement of the crust over an extended period of time (a time period spanning many earthquake cycles). This assessment may be based on the relative simplicity or complexity of a rupture source topology (and an implicit assumption that relatively simple source topologies are more efficient at deforming the crust), or on the degree to which the rupture topology is favored based on empirical observations (e.g., Wesnousky, 2006, 2008; Biasi, Parsons, et al., 2013) or simple dynamic rupture models (e.g., Kame et al., 2003; Lozos et al., 2011). In the case of the Hosgri fault source, where different rupture sources follow different mapped strands of the Hosgri fault zone, the assessment of how to allocate slip rate among the different strands is based on stratigraphic and geomorphic evidence.

The methodology for allocating slip rate uncertainty affects how the Diablo Canyon SSC model handles epistemic and aleatory uncertainties. Aleatory variability is introduced to the SSC logic tree through the rupture source concept, where all rupture sources may occur and thus contribute to the model. The uncertainties in the slip rate for each rupture source, however, are treated through epistemic uncertainty with logic tree branch values and weights (Figure 6-1). Because of the simplicity of the logic tree and because of the approximate nature of slip rate allocation, the slip rate branch values are treated independently (i.e., they are not correlated) between rupture sources. For example, if two rupture sources each have slip rate distributions with three branch values and weights, there are six unique paths through the logic tree for different combinations of slip rates. This aspect of the model lessens the need to strictly defend the relative allocation of slip rate between rupture sources, because the relative allocation of slip rate can vary considerably depending on the path through the logic tree.

The methodology for allocating slip rate uncertainty consists of the following five steps:

1. Fitting the target fault slip rate cumulative distribution function (CDF; *Chapter 8*) to a standard functional form with a defined mean and variance.
2. Subdividing the mean and variance into the allocated parts based on the allocations of the mean (described above).
3. Creating rupture source slip rate CDFs using the allocated mean and variance values.
4. Extracting three-point distributions (branch values and weights) from the rupture source CDFs following published methodology (Keefer and Bodily, 1983).
5. Verifying that the three-point distributions, when propagated through all paths in the logic tree, reasonably represent the original fault slip rate CDF.

The mean (m), standard deviation (s), and variance ($v = s^2$) values were calculated from the discrete fault slip rate outputs resulting from the Monte-Carlo analyses (*Chapter 8*). Normal and lognormal CDFs constructed from these parameters were compared to the Monte-Carlo derived slip rate CDFs. Lognormal distributions were selected for fitting the slip rate data because they were found to have a satisfactory fit and have the advantage of retaining positive values at all probability levels. For the lognormal distribution fit, m and v are related to the mean (μ) and standard deviation (σ) of the natural logarithms of the slip rates by

$$m = e^{(\mu+\sigma^2/2)} \tag{9-7}$$

$$v = e^{(2\mu+\sigma^2)}\left(e^{\sigma^2} - 1\right) \tag{9-8}$$

Similar to the means (Equations 9-1 and 9-2), the variance (v_i) values of each rupture source *i* were calculated by multiplying the fraction allocated to the rupture source (a_i) by the variance of the target slip rate CDF (v_T):

$$v_i = a_i(v_T) \tag{9-9}$$

Because the slip rates are treated in the logic tree as independent variables, the target variance equals the sum of the variances of each rupture source:

$$v_T = \sum_{i=1}^{n} v_i \tag{9-10}$$

From the allocated mean and variance values m_i and v_i, lognormal CDFs are constructed to represent each rupture source slip rate. From these lognormal CDFs, a three-point approximation using the method of Keefer and Bodily (1983) was used as shown on Table 9-7. These three-point distribution values and weights are direct inputs to the SSC logic tree.

Table 9-7. Three-Point Approximation Method of Keefer and Bodily (1983)

Percentile	Weight
0.95	0.185
0.50	0.630
0.05	0.185

The weighted mean of the three-point distribution for each rupture source is checked against the allocated mean slip rate to ensure that the three-point approximation method is accurately capturing the target mean slip rate. Minor adjustments to the mean and/or variance of the lognormal fit to the slip rate CDFs were made in some cases to minimize any discrepancies.

The final step is to verify that the three-point distributions for each rupture source, when combined through the various paths through the logic tree, adequately reconstruct the original slip rate CDFs. These fits were deemed satisfactory based on visual inspection and do a good job of sampling from the center, body, and range of the slip rate uncertainty as represented by the slip rate CDFs.

9.3.2 Hosgri Slip Rate Allocation Model

Five rupture sources—H-01, H-02, H-03, H-04, and H-05—include sections of the Hosgri fault source located closest to the DCPP (Plate 9-1). Two additional rupture sources—H-06 and H-07—include sections of the Hosgri fault source northwest of the DCPP and are intended to account for probable increases in the rate of right-lateral strike

slip north of intersections with faults branching from the east (e.g., the Shoreline and Los Osos faults; see *Section 9.4*). Rupture source H-08 is a characteristic rupture source for the PB fault source, and is summed with rupture source H-04 to capture the PB fault source target slip rate.

9.3.2.1 Allocation of the Mean Slip Rate

Table 9-8 presents the mean slip rate allocations for all rupture sources involving the Hosgri fault source, expressed both in units of mm/yr and in percentage of total target slip rate.

Table 9-8. Mean Slip Rate Allocation for the Hosgri Rupture Sources

Rupture Source	Hosgri Fault Source[1]		Shoreline Fault Source[2]		Piedras Blancas Source[3]		Hosgri Source North of DCPP[4]	
	Rate (mm/yr)	% of total	Rate (mm/yr)	% of total	Rate (mm/yr)	% of total	Rate (mm/yr)	% of total
H-01	0.92	54%					0.92	--
H-02	0.50	29%					0.50	--
H-03	0.10	6%					0.10	--
H-04	0.10	6%			0.058	29%		
H-05	0.08	5%	0.016	23%			0.08	--
H-06							0.03	--
H-07							0.07	--
H-08					0.142	71%		
Totals	1.7	100%	0.016	23%	0.20	100%	1.7	--

Note: See Plate 9-1 for rupture sources and fault section locations.
[1] For the HA, HW, and HE fault sections.
[2] For the SH fault section.
[3] For the PB fault section.
[4] For the HN and SI fault sections.

The Slip Rate Allocation Model for the Hosgri Rupture Model requires that the weighted mean slip rates of the first five Hosgri rupture sources sum to 1.7 mm/yr, the weighted mean slip rate for the Hosgri fault source opposite the DCPP (Table 9-8; see *Section 8.3.8*). In addition, rupture sources H-04 and H-08, which include the Piedras Blancas fault source, sum to 0.2 mm/yr (*Section 8.3.3*). Rupture source H-05, the splay rupture source that includes the Hosgri and Shoreline fault sources, contributes 0.016 mm/yr to the Shoreline fault slip rate, representing approximately 23% of the total target weighted mean slip rate of 0.07 mm/yr (*Section 8.4.5*). The two columns on the right side of Table 9-8 show the sum of slip rate for the Hosgri fault source on sections HN and SI, north of the DCPP between approximately Point Estero and San Simeon. The slip rates from rupture sources H-06 and H-07 are added to the total, but the rupture source H-04 slip rate is removed, as that rupture source follows the western reach of the Hosgri fault

source and extends to the Piedras Blancas fault source (Plate 9-1). Additional slip rate on the Hosgri fault source north of the DCPP is added in the Slip Rate Allocation Models for the SLPB Rupture Models; the value of 1.7 mm/yr is the contribution to the Hosgri slip rate north of the DCPP from the Hosgri Slip Rate Allocation Model. The effective slip rate of the Hosgri fault source north of the DCPP is discussed in *Section 9.4* below.

The mean slip rates for the five Hosgri rupture sources that involve the section of the fault adjacent to the DCPP, including a summary table justifying the allocated rates, are shown in Table 9-9.

Table 9-9. Mean Slip Rate Allocation for the Hosgri Rupture Sources Opposite the DCPP

Rupture Source (and Location Opposite the DCPP)	Mean Slip Rate (mm/yr)	Fraction of Total	Explanation
H-01 (Central strand)	0.92	0.54	One of three rupture sources (H-01, H04, and H-05) occupying the central strand whose sum should equal ~65% of the total fault slip rate, consistent with the strongest geomorphic expression and largest vertical separation of a late Quaternary marker horizon. The fraction of the total for the central strand that is not allocated to H-01 (~11%) is allocated to H-04 and H-05 ruptures.
H-02 (Western strand)	0.5	0.29	~30% of the total rate; consistent with moderate geomorphic expression and moderate vertical separation of a late Quaternary marker horizon.
H-03 (Eastern strand)	0.1	0.06	~5% of the total rate; consistent with the poorest geomorphic expression and least vertical separation of a late Quaternary marker horizon.
H-04 (Central strand; complex rupture with western reach of the Hosgri and Piedras Blancas)	0.1	0.06	Limited by the slip rate of the western reach of the Hosgri fault and assumed rate of the Piedras Blancas fault source.
H-05 (Central strand; splay rupture with the Hosgri and Shoreline fault sources)	0.08	0.05	Limited by the slip rate of the Shoreline fault, the relative slip rate of the Hosgri and Shoreline faults given the splay rupture scenario, and the alternative rupture sources involving the Shoreline fault.
Total	1.7	1.0	Equal to the weighted mean slip rate of the Hosgri fault source for the reach opposite the DCPP.

The Hosgri rupture sources occupy three locations opposite the DCPP, representing the width of the Hosgri fault zone mapped near the DCPP and the identification of multiple fault strands. The three locations in the Hosgri FGMs include the relatively well-defined western and central strands and the less-well-defined eastern strand (*Section 7.3.1*). As discussed in *Chapters 5 and 7* and in *Section 9.2.2*, the Diablo Canyon SSC model considers all three strands to be possible locations of future surface-fault rupture, so the location of the Hosgri fault source is expressed as aleatory variability, not epistemic uncertainty. Rupture sources H-01, H-04, and H-05 occur on the central strand, rupture source H-02 is on the western strand, and H-03 is on the eastern strand.

Based on a geologic and geomorphic assessment of the Hosgri fault zone, the central strand appears to have the highest slip rate of the three; the western strand has a significantly lower rate; and the eastern strand, which is a discontinuous trace and is not as well expressed geomorphically, has the lowest rate. Using relative amounts of vertical separation on a late Quaternary unconformity as a proxy for relative lateral (and net) slip rate, it is estimated that the central trace accounts for approximately 65% of the total slip rate, with the western strand approximately 30%, and the eastern strand approximately 5%. Based on these percentages and the total weighted mean slip rate of 1.7 mm/yr, the mean slip rates of the rupture sources can be estimated. Rupture source H-02, located on the western strand, receives a slip rate of 0.5 mm/yr (29.4% of the total), and rupture source H-03, located on the eastern strand, receives a slip rate of 0.1 mm/yr (5.9% of the total; Table 9-9).

The remaining 1.1 mm/yr of the mean Hosgri slip rate is on the central strand of the Hosgri fault source and is divided among the H-01, H-04, and H-05 rupture sources. This allocation is based on considerations such as slip rates on other faults involved in the rupture sources and a qualitative assessment of the rupture sources that are more optimally configured to slip at a higher rate than others. Rupture source H-04 includes the central Hosgri fault source (HC) opposite the DCPP, the western reach of the Hosgri fault source offshore of Cambria (WR), and a northeast-dipping reverse fault source representing the Piedras Blancas fold belt (PB). The estimated slip rate of the western reach of the Hosgri and Piedras Blancas fault sources is approximately 0.2 mm/yr (*Section 8.3.3*). Half of this total, 0.1 mm/yr, or approximately 6 % of the total Hosgri slip rate, is assigned to the primary Hosgri part of the rupture source, with 0.058 mm/yr remaining for the Piedras Blancas rupture source (Table 9-8). The remaining 1.0 mm/yr is divided between rupture source H-01, which continues south and north over the Hosgri–San Simeon–San Gregorio fault system, and rupture source H-05, which represents the splay case of simultaneous rupture of the Hosgri and Shoreline fault sources. Given that the slip rate allocated to rupture source H-05 is limited by the lower slip rate of the Shoreline fault, and considering the results of 2D dynamic modeling that suggest propagation of Hosgri slip onto the Shoreline fault is unlikely (Kame et al., 2003; Somerville, 2011), the amount of Hosgri slip rate allocated to this rupture source is 0.08 mm/yr, or approximately 5% of the total Hosgri slip rate. After accounting for slip partitioned to the central trace for H-04 and H-05 ruptures (~0.18 mm/yr or 11% of the

Hosgri slip rate), this leaves 0.92 mm/yr slip rate, or approximately 54% of the total Hosgri slip rate at a location opposite the DCPP, for the rupture source H-01 (Table 9-9).

9.3.2.2 Hosgri Rupture Source Slip Rates for the SSC Logic Tree

The SSC logic tree three-point slip rate distributions and weights for the Hosgri rupture sources were calculated following the method explained in *Section 9.3.1* and are shown in Table 9-10. A graphical representation of the slip rate allocation is presented on Figure 9-10 for the rupture sources that make up the Hosgri fault slip rate for the reach opposite the DCPP. The slip rate CDF from *Section 8.3.7* is shown on Figure 9-10a, along with normal and lognormal distribution fits. As discussed in *Section 9.3.1*, the lognormal fit was adopted for use as it provided a satisfactory fit to the data and retains positive values at all probability levels. The slip rate CDFs for the Hosgri rupture sources H-01 through H-05 are on Figure 9-10b. The discrete CDF of all weighted logic tree branch combinations is shown against the slip rate CDF on Figure 9-10c.

Table 9-10. Hosgri Rupture Model Slip Rates in the SSC Logic Tree

Rupture Source* No.	Slip Rate (mm/yr)	Weight	Rupture Source No.	Slip Rate (mm/yr)	Weight
H-01	1.93	0.185	H-05†	0.29	0.185
	0.81	0.630		0.04	0.630
	0.34	0.185		0.005	0.185
H-02	1.23	0.185	H-06	0.13	0.185
	0.40	0.630		0.01	0.630
	0.13	0.185		0.001	0.185
H-03	0.35	0.185	H-07	0.27	0.185
	0.05	0.630		0.03	0.630
	0.01	0.185		0.004	0.185
H-04†	0.35	0.185	H-08	0.25	0.185
	0.05	0.630		0.13	0.630
	0.01	0.185		0.07	0.185

* Slip rates are applicable to all three Hosgri Rupture Models.
† Complex or splay rupture type. Tabulated slip rate values are for the primary or main source.

9.3.3 OV Slip Rate Allocation Model

The OV Rupture Model contains 10 rupture sources (Plate 9-2):

- OV-01, OV-02, OV-03, and OV-04 involve the Shoreline fault source.
- OV-03, OV-04, OV-05, and OV-06 involve the San Luis Bay fault source.
- OV-06, OV-07, and OV-08 involve the Los Osos fault source.

- OV-09 and OV-10 involve Connected faults southeast of the DCPP, not within the Primary fault sources. OV-09 involves the Oceano fault, and OV-10 involves the Wilmar Avenue fault.

9.3.3.1 Allocation of the Mean Slip Rate—OV Model

Table 9-11 presents the mean slip rate allocations for all OV rupture sources, expressed in units of mm/yr and in percent of total target slip rate. The table includes the rupture source H-05 from the Hosgri Rupture Model to show its contribution to the Shoreline fault source slip rate.

Table 9-11. Mean Slip Rate Allocation for the OV Rupture Sources

	Shoreline Fault Source[1]		San Luis Bay Fault Source[2]		Los Osos Fault Source[3]		Wilmar Avenue Fault Source		Oceano Fault Source	
Source	Rate (mm/yr)	% of total	Rate (mm/yr)	% of total	Rate (mm/yr)	% of total	Rate (mm/yr)	% of total	Rate (mm/yr)	% of total
H-05	0.016	23%								
OV-01	0.017	24%								
OV-02	0.015	21%								
OV-03	0.012	17%	0.010	6%						
OV-04	0.010	14%	0.004	3%			0.004	2%		
OV-05			0.102	64%						
OV-06			0.044	28%	0.06	23%				
OV-07					0.12	46%				
OV-08					0.08	31%				
OV-09									0.15	100%
OV-10							0.236	98%		
Totals	0.07	100% *	0.16	100% *	0.26	100%	0.24	100%	0.15	100%

Note: See Plate 9-2 for rupture sources and fault section locations.
[1] For the SH fault section.
[2] For the BE and BR fault sections.
[3] For the LV and LM fault sections.
* Rounding to the nearest percent results in apparent rounding error of the total.

The OV Slip Rate Allocation Model requires that the weighted mean slip rates of the rupture sources including the northern portion of the Shoreline fault (fault section SH) sum to 0.07 mm/yr, the weighted mean slip rate for the Shoreline fault source opposite the DCPP (Table 9-11; *Section 8.4*). The splay rupture source H-05 contributes approximately 23% to the total, and an additional 45% of the total is divided approximately evenly between rupture sources OV-01 and OV-02. The 68% allocation to strike-slip-only ruptures involving the Shoreline fault indicates a preference that the fault

slips either alone or as a part of the Hosgri fault source accommodating dextral shear, which the TI Team judges to be the most consistent with the findings of Biasi, Parsons, et al. (2013) that fault-to-fault jumps most frequently occur with the same sense of slip. The remaining slip rate is allocated approximately evenly between the shorter (OV-03) and longer (OV-04) complex ruptures whereby the Shoreline fault source ruptures as part of multi-fault complex ruptures involving both strike-slip motion and reverse or reverse oblique motion. This indicates a less-preferred mode of rupture whereby the Shoreline fault source ruptures as part of multi-fault complex rupture involving both strike-slip motion and reverse or reverse oblique motion, again consistent with historical ruptures as documented by Biasi, Parsons, et al. (2013).

The four rupture sources in the OV Model that accommodate the 0.16 mm/yr target slip rate of the San Luis Bay fault can be divided into rupture sources that are reverse-only (OV-05 and OV-06) and complex rupture sources with a dominant strike-slip component (OV-03 and OV-04; Table 9-11). Approximately 92% of the slip rate is allocated to reverse-only rupture sources, with most of that slip rate involved in characteristic San Luis Bay fault–only earthquakes rather than as splay ruptures with the Los Osos fault source. The 92% majority is supported by the findings of Biasi, Parsons, et al. (2013) as stated above. The preference for single-segment ruptures is somewhat driven by necessity to achieve the slip-rate balancing objective, but may be supported by the judgment that the single segment rupture represents the least complex rupture topology and therefore may be mechanically more favorable. The remaining (less than 10%) slip rate is divided between the shorter (OV-03) and longer (OV-04) complex rupture sources, with the fraction of slip rate available to the San Luis Bay fault total being limited by the amounts that may be allocated to the Shoreline fault source.

The Los Osos fault slip rate in the OV Model has a target mean slip rate of 0.26 mm/yr and is accommodated by three rupture sources (Table 9-11). Approximately half of the total slip rate is accommodated by a Los Osos–only rupture topology (OV-07), with lesser amounts allocated to complex ruptures involving the Hosgri fault (OV-08) and splay ruptures whereby the Los Osos fault is the main fault and the San Luis Bay fault is the splay fault (OV-06). The basis for these allocations follow the same general principals as outlined above, with a preference for having a higher frequency of ruptures with a single sense of slip, and a second preference for simpler rupture topologies.

For the Oceano and Wilmar Avenue fault slip rates, the OV Model has these faults essentially slipping in their entirety by linked or characteristic rupture sources (Table 9-11). Only approximately 2% of the target slip rate for the Oceano fault is accommodated by the complex rupture source OV-04; this amount is limited by the Slip Rate Allocation Model for the Shoreline fault source.

9.3.3.2 OV Rupture Source Slip Rates for the SSC Logic Tree

The SSC logic tree three-point slip rate distributions and weights for the OV rupture sources, calculated following the method explained in *Section 9.3.1*, are shown in Table 9-12. Graphical representations of the slip rate allocation for rupture sources that make up

the Shoreline, San Luis Bay, and Los Osos fault sources are presented on Figures 9-10, 9-11, and 9-12, respectively. On each figure, the slip rate CDFs from *Sections 8.4, 8.5, and 8.6* are shown on panel (a), along with normal and lognormal distribution fits. The slip rate CDFs for the rupture sources that make up each fault source are shown on panel (b). The discrete CDF of all weighted logic tree branch combinations is shown against the fault slip rate CDFs on panel (c).

Table 9-12. OV Rupture Model Slip Rates in the SSC Logic Tree

Rupture Source No.	Slip Rate (mm/yr)	Weight	Rupture Source No.	Slip Rate (mm/yr)	Weight
OV-01	0.051	0.185	OV-06*	0.125	0.185
	0.012	0.630		0.054	0.630
	0.003	0.185		0.023	0.185
OV-02	0.046	0.185	OV-07	0.212	0.185
	0.010	0.630		0.114	0.630
	0.002	0.185		0.061	0.185
OV-03*	0.039	0.185	OV-08†	0.155	0.185
	0.007	0.630		0.074	0.630
	0.001	0.185		0.035	0.185
OV-04*	0.034	0.185	OV-09	0.241	0.185
	0.006	0.630		0.144	0.630
	0.001	0.185		0.086	0.185
OV-05	0.165	0.185	OV-10	0.331	0.185
	0.098	0.630		0.230	0.630
	0.058	0.185		0.160	0.185

Note: See Plate 9-2 for rupture sources and fault section locations.
* Complex or splay rupture type. Tabulated slip rate values are for the primary or main source.
† Complex rupture source including the Hosgri fault north of the DCPP. Slip rates are shown for the Los Osos part of the rupture.

9.3.4 SW Slip Rate Allocation Model

The SW Rupture Model contains 10 rupture sources (Plate 9-2):

- SW-01, SW-02, SW-03 involve the Shoreline fault source.
- SW-04, SW-05, SW-06 and SW-07 involve the San Luis Bay fault source.
- SW-06 involves the Los Osos fault sections bordering the Irish Hills.
- SW-08 and SW-10 involve the offshore and eastern sections of the Los Osos fault, respectively
- SW-09 does not include any portion of a Primary fault source but does involve the Oceano and other connected faults.

9.3.4.1 Allocation of the Mean Slip Rate—SW Model

Table 9-13 presents the mean slip rate allocations for all SW rupture sources, expressed both in units of mm/yr and in percentage of the total target slip rate. The table includes the rupture source H-05 from the Hosgri Rupture Model to show its contribution to the Shoreline fault source slip rate.

Table 9-13. Mean Slip Rate Allocation for the SW Rupture Sources

	Shoreline Fault Source[1]		San Luis Bay Fault Source[2]		Los Osos Fault Source[3]		Wilmar Avenue Fault Source		Oceano Fault Source	
Source	Rate (mm/yr)	% of total	Rate (mm/yr)	% of total	Rate (mm/yr)	% of total	Rate (mm/yr)	% of total	Rate (mm/yr)	% of total
H-05	0.016	23%								
SW-01	0.023	33%								
SW-02	0.020	29%								
SW-03	0.011	16%							0.025	17%
SW-04			0.016	7%						
SW-05			0.060	27%						
SW-06			0.094	43%	0.086	45%				
SW-07			0.050	23%			0.05	24%		
SW-08					(0.2)†					
SW-09									0.125	83%
SW-10							0.16	76%		
Totals	0.07	100% *	0.22	100%	0.086	45%‡	0.21	100%	0.15	100%

Note: See Plate 9-2 for rupture sources and fault section locations.
[1] For the SH fault section.
[2] For the BE and BW fault sections.
[3] For the LV and LM fault sections.
* Rounding to the nearest percent results in an apparent rounding error of the total.
† The value in parentheses in SW-08 is for the offshore Los Osos fault section (LC); it is not added to the total for the Los Osos (LV and LM) column.
‡ The Los Osos fault source in the SW Model is a backthrust branching off the San Luis Bay fault. The 45% total signifies a 45% seismic coupling for the fault in the model.

The SW Slip Rate Allocation Model has four rupture sources that accommodate the 0.07 mm/yr mean slip rate of the northern portion of the Shoreline fault (fault section SH; Table 9-13). Approximately 85% of the total slip rate is accommodated by the splay rupture source H-05, characteristic Shoreline-only rupture source (SW-01), and linked Shoreline-Hosgri rupture source (SW-02). The higher total percentage allocated to strike-slip-only rupture sources compared to the OV Slip Rate Allocation Model is consistent with the general view of the FGMs that the OV Model accommodates more dextral shear and obliquity on its Primary and Connected fault sources compared to the SW and NE

Models. A remaining 16% of the Shoreline fault slip rate is accommodated by the complex rupture topology SW-03 involving the reverse Oceano fault source and strike-slip Shoreline fault source (Plate 9-2).

The four rupture sources in the SW Model that accommodate the 0.22 mm/yr slip rate of the San Luis Bay fault include three reverse-only rupture sources that accommodate 93% of the total slip rate and one complex rupture source (SW-04) involving the San Luis Bay and Hosgri fault sources that accommodates the remaining 7% (Table 9-13). Most of the reverse slip is in shorter characteristic rupture topologies (SW-05 and SW-06), but approximately a quarter of the total slip rate is accommodated in longer linked rupture topologies involving the Wilmar Avenue fault source and other faults to the southeast (SW-07). The splay rupture source SW-06 involves the San Luis Bay fault source as the main rupture plane, with the Los Osos fault as the splay.

The Los Osos fault source adjacent to the Irish Hills (fault sections LM and LV) has only one rupture source—the splay rupture source SW-06—accommodating seismogenic slip on the fault (Table 9-13). The total slip rate assigned to the Los Osos fault of 0.086 mm/yr is approximately 45% of the geologic rate of slip of 0.19 mm/yr attributed to the Los Osos fault in the SW Model (*Section 8.5*). This is comparable to a statement that the Los Osos fault does not slip entirely during the release of seismic strain energy, with the *coupling coefficient*, or ratio of the rate of slip that occurs in earthquakes to the total rate of slip, equal to 0.45 (cf. McCaffrey, 1997; Field et al., 2013). This coupling coefficient of less than one is an expression of the SW Model that characterizes the Los Osos fault either as a backthrust or as a fold axial surface with minor faulting that is subordinate to the main north- and northeast-dipping reverse faults. Such secondary deformation was likely seen during the 2003 San Simeon earthquake (McLaren et al., 2008) and 1999 ChiChi, Taiwan, earthquakes (Graveleau et al., 2014). In the SW Model, slip on the Los Osos fault accommodates uplift of the northeastern margin of the San Luis Range, but this is accommodated through a combination of aseismic folding and/or secondary faulting and coupled seismogenic faulting. The resulting value of 45% in Table 9-13 is deemed acceptable by the TI Team based on its judgment that, in the SW Model, the Los Osos fault is not a main, seismogenic fault. There is no precision implied by the 45% number, and adjusting the number higher or lower would have minimal consequences to the overall hazard model. Epistemic uncertainty in the correct value for coupling is expressed by the range in slip rates in Table 9-12, whereby various rupture source slip rate combinations can result in higher and lower implied seismic coupling.

The Oceano and Wilmar Avenue fault slip rates have two rupture sources contributing to the fault slip rates (Table 9-13). The complex rupture source SW-03 contributes 17% to the 0.15 mm/yr total slip rate for the Oceano fault, with the contribution from this source limited by the Shoreline fault source slip rate. Linked rupture source SW-09 accommodates the remaining 83% of the Oceano fault slip rate. Linked rupture source SW-07 contributes approximately a quarter of the 0.21 mm/yr total slip rate for the Wilmar Avenue fault, and splay rupture source SW-10 accommodates the remaining slip rate through joint rupture with the eastern portion of the Los Osos fault.

9.3.4.2 SW Rupture Source Slip Rates for the SSC Logic Tree

The SSC logic tree three-point slip rate distributions and weights for the SW rupture sources, calculated following the method explained in *Section 9.3.1*, are shown in Table 9-14. Graphical representations of the slip rate allocation for the San Luis Bay fault source is presented on Figure 9-13. The results for the San Luis Bay fault were chosen for graphical display due to its prominence in the SW Model as the primary thrust ramp beneath the Irish Hills. Figure 9-13 shows the slip rate CDF from *Section 8.6*, along with the normal and lognormal distribution fits on panel (a). The slip rate CDFs for the rupture sources that make up each fault source are on panel (b). The discrete CDF of all weighted logic tree branch combinations is shown against the slip rate CDF on panel (c).

Table 9-14. SW Rupture Model Slip Rates in the SSC Logic Tree

Rupture Source No.	Slip Rate (mm/yr)	Weight	Rupture Source No.	Slip Rate (mm/yr)	Weight
SW-01	0.065	0.185	SW-06*	0.164	0.185
	0.017	0.630		0.087	0.630
	0.005	0.185		0.046	0.185
SW-02	0.058	0.185	SW-07	0.102	0.185
	0.014	0.630		0.044	0.630
	0.004	0.185		0.019	0.185
SW-03*	0.062	0.185	SW-08†	0.326	0.185
	0.020	0.630		0.186	0.630
	0.006	0.185		0.106	0.185
SW-04†	0.044	0.185	SW-09	0.208	0.185
	0.012	0.630		0.119	0.630
	0.003	0.185		0.068	0.185
SW-05	0.117	0.185	SW-10*	0.214	0.185
	0.054	0.630		0.154	0.630
	0.025	0.185		0.111	0.185

* Complex or splay rupture type. Tabulated slip rate values are for the primary or main source.
† Complex rupture source including the Hosgri north of the DCPP. Slip rates are shown for the San Luis Bay part of the rupture for SW-04, and for the Los Osos offshore (LC) part of the rupture for SW-08.

9.3.5 NE Slip Rate Allocation Model

The NE Rupture Model contains 11 rupture sources (Plate 9-2):

- NE-01, NE-02, NE-03, and NE-04 involve the Shoreline fault source.
- NE-05, NE-06, NE-07, NE-08, and NE-11involve the Los Osos fault sections bordering the Irish Hills.
- NE-03 and NE-06 involve the San Luis Bay fault source.
- NE-09 and NE-10 do not include any portion of a Primary fault source but do involve the Oceano and other Connected faults (NE-09) or the Wilmar Avenue fault source and the eastern part of the Los Osos fault source (NE-10).

9.3.5.1 Allocation of the Mean Slip Rate—NE Model

Table 9-15 presents the mean slip rate allocations for all NE rupture sources, expressed both in units of mm/yr and in percentage of the total target slip rate. The table includes the rupture source H-05 from the Hosgri Rupture Model to show its contribution to the Shoreline fault source slip rate.

Table 9-15. Mean Slip Rate Allocation for the NE Rupture Sources

	Shoreline Fault Source[1]		San Luis Bay Fault Source[2]		Los Osos Fault Source[3]		Wilmar Avenue Fault Source		Oceano Fault Source	
Source	Rate (mm/yr)	% of total	Rate (mm/yr)	% of total	Rate (mm/yr)	% of total	Rate (mm/yr)	% of total	Rate (mm/yr)	% of total
H-05	0.016	23%								
NE-01	0.019	27%								
NE-02	0.015	21%								
NE-03	0.012	17%	0.009	6%						
NE-04	0.008	11%							0.004	3%
NE-05					0.110	26%				
NE-06			0.083	52%	0.110	26%				
NE-07					0.041	10%	0.08	40%		
NE-08					0.060	14%				

Source	Shoreline Fault Source[1]		San Luis Bay Fault Source[2]		Los Osos Fault Source[3]		Wilmar Avenue Fault Source		Oceano Fault Source	
	Rate (mm/yr)	% of total	Rate (mm/yr)	% of total	Rate (mm/yr)	% of total	Rate (mm/yr)	% of total	Rate (mm/yr)	% of total
NE-09									0.146	97%
NE-10							0.12	60%		
NE-11					0.100	24%				
Totals	0.07	100%*	0.092	57%*‡	0.42	100%	0.20	100%	0.15	100%

Note: See Plate 9-2 for rupture sources and fault section locations.
[1] For the SH fault section.
[2] For the BE and BR fault sections.
[3] For the LV and LM fault sections.
* Rounding to the nearest percent results in an apparent rounding error of the total.
‡ The San Luis Bay fault source in the NE Model is a backthrust branching off the Los Osos fault. The 57% total signifies a 57% seismic coupling for the fault in the model.

The NE Slip Rate Allocation Model has five rupture sources that accommodate the 0.07 mm/yr mean slip rate of the northern portion of the Shoreline fault (fault section SH; Table 9-15). Approximately 71% of the total slip rate is accommodated by splay rupture source H-05, characteristic Shoreline-only rupture source (SW-01), and linked Shoreline-Hosgri rupture source (SW-02). The remaining 28% of the Shoreline fault slip rate is accommodated by the complex rupture topologies NE-03 (involving the northern portion of the Shoreline fault and the reverse San Luis Bay fault), and NE-04 (involving the Shoreline and reverse Oceano fault sources).

Five rupture sources in the NE Model accommodate the 0.42 mm/yr slip rate of the Los Osos fault, the principal thrust ramp underlying the Irish Hills in this FGM (*Section 8.5*). Approximately 86% of the Los Osos fault slip rate is accommodated by reverse-only topologies, including two characteristic rupture source alternatives (NE-05 and NE-11) and splay rupture source NE-06, wherein the San Luis Bay fault ruptures as a splay (Table 9-15). The minority allocation (10% of the total) is for splay rupture source NE-07, which ruptures along the entire San Luis Range with a change in vergence between the Irish Hills and the rest of the range to the southeast (Plate 9-2). The relative allocation favoring the simpler rupture topologies over the more complex topologies is based on the TI Team's judgment that simpler topologies are likely more favorable mechanically and, therefore, would occur with greater frequency. The remaining 14% of Los Osos fault slip rate is allocated to the complex rupture source NE-08, wherein the Los Osos fault ruptures as a secondary fault to the primary strike-slip Hosgri fault source north of the Los Osos–Hosgri fault intersection. This low percent is consistent with the findings of

Biasi, Parsons, et al. (2013) that historical ruptures that change sense of slip are relatively rare compared to multi-segment ruptures with the same sense of slip.

The San Luis Bay fault source has only two rupture sources in the NE Rupture Model—the complex rupture source NE-03 and the splay rupture source NE-06. Combined, these rupture sources accommodate approximately 0.09 mm/yr of seismogenic slip rate on the fault, or approximately 57% of the 0.16 mm/yr slip rate attributed to the San Luis Bay fault in the NE Model (Table 9-15; *Section 8.6*). Similar to the Los Osos fault in the SW Rupture Model (*Section 9.3.4*), the San Luis Bay fault in the NE Model is considered a secondary backthrust or fold axial surface with minor faulting that branches from the larger south- to southwest-dipping Los Osos fault. Thus, the implied seismic coupling coefficient of 0.57 in the results (Table 9-15) reflects the TI Team's judgment that the slip rate allocated to rupture sources on the San Luis Bay fault in the NE Model should be less than the geologic slip rate because the total rate would be accommodated partially as non-seismogenic deformation. Similar to the Los Osos fault in the SW Model (*Section 9.3.4*), there is no precision implied by the 57% number, and adjusting the number higher or lower would have minimal consequences to the overall hazard model. Epistemic uncertainty in the correct value for coupling is expressed by the range in slip rates in Table 9-16, whereby various rupture source slip rate combinations can result in higher and lower implied seismic coupling.

The Oceano and Wilmar Avenue fault slip rates have two rupture sources contributing to the fault slip rates (Table 9-15). The complex rupture source NE-04 contributes 3% to the total for the Oceano fault, with the contribution from this source limited by the Shoreline fault source slip rate. Linked rupture source NE-09 accommodates the remaining 97% of the Oceano fault slip rate. Splay rupture source NE-07 contributes approximately 40% of the total slip rate for the Wilmar Avenue fault, and splay rupture source NE-10 accommodates the remaining slip rate through joint rupture with the eastern portion of the Los Osos fault (Plate 9-2).

9.3.5.2 NE Rupture Source Slip Rates for the SSC Logic Tree

The SSC logic tree three-point slip rate distributions and weights for the NE rupture sources, calculated following the method explained in *Section 9.3.1*, are shown in Table 9-16. Graphical representations of the slip rate allocation for the Los Osos fault source are presented on Figure 9-14. The results for the Los Osos fault were chosen for graphical display due to its prominence in the NE Model as the primary thrust ramp beneath the Irish Hills. Figure 9-14 shows the slip rate CDF from *Section 8.5*, along with the normal and lognormal distribution fits. The slip rate CDFs for the rupture sources that make up each fault source are also shown.

Table 9-16. NE Rupture Model Slip Rates in the SSC Logic Tree

Rupture Source No.	Slip Rate (mm/yr)	Weight	Rupture Source No.	Slip Rate (mm/yr)	Weight
NE-01	0.056	0.185	NE-07†	0.120	0.185
	0.013	0.630		0.077	0.630
	0.003	0.185		0.049	0.185
NE-02	0.046	0.185	NE-08‡	0.112	0.185
	0.010	0.630		0.056	0.630
	0.002	0.185		0.028	0.185
NE-03†	0.039	0.185	NE-09	0.235	0.185
	0.007	0.630		0.140	0.630
	0.001	0.185		0.083	0.185
NE-04‡	0.028	0.185	NE-10†	0.168	0.185
	0.004	0.630		0.116	0.630
	0.001	0.185		0.081	0.185
NE-05	0.179	0.185	NE-11	0.166	0.185
	0.106	0.630		0.096	0.630
	0.062	0.185		0.055	0.185
NE-06†	0.179	0.185			
	0.106	0.630			
	0.062	0.185			

† Complex or splay rupture type. Tabulated slip rate values are for the primary or main source.
‡ Complex rupture source including the Hosgri north of the DCPP. Slip rates are shown for the Los Osos part of the rupture.

9.4 Slip Rate of the Hosgri Fault North of the DCPP

The Hosgri Rupture Models have the property that slip rate on the Hosgri fault source increases from south to north. This is consistent with the kinematic model for an increase in slip rate on the fault source from its south end offshore Point Arguello to the north end of the San Gregorio fault near Bolinas (*Chapter 5*; *Section 8.3*). The Hosgri Slip Rate Allocation Model maintains a 1.7 mm/yr slip rate on the Hosgri fault source for the portion of the fault directly opposite the DCPP, and includes two rupture sources—H-06 and H-07—that increase slip rate north of the DCPP (Plate 9-1 and *Section 9.3.2*). The three SLPB Rupture Models include additional rupture sources that involve the Hosgri fault source north of the DCPP (Plate 9-2), but the three Slip Rate Allocation Models differ in how and by what amount the slip rates increase. Table 9-17 summarizes the slip rate on the Hosgri fault sections HN and SI—the sections between the intersection with the Los Osos fault source to the south and the Oceanic–West Huasna fault source to the north—after the Hosgri and SLPB rupture sources are combined.

Table 9-17. Hosgri Slip Rate Allocation North of the DCPP (Evaluated for Fault Sections HN and SI)

Fault Sources	Hosgri + OV Models		Hosgri + SW Models		Hosgri + NE Models	
	Rate (mm/yr)	% of total	Rate (mm/yr)	% of total	Rate (mm/yr)	% of total
Hosgri fault source, DCPP	1.70	91%	1.70	91%	1.70	91%
Western reach, Hosgri fault	–0.10	–5%	–0.10	–5%	–0.10	–5%
Shoreline fault source	0.07	4%	0.07	4%	0.07	4%
Los Osos fault source	0.20	10%	0.20	10%	0.20	10%
Total target	1.87	100%	1.87	100%	1.87	100%
Rupture Sources	**Hosgri + OV Models**		**Hosgri + SW Models**		**Hosgri + NE Models**	
	Rate (mm/yr)	**% of total**	**Rate (mm/yr)**	**% of total**	**Rate (mm/yr)**	**% of total**
H-01 to H-03; H-05	1.60	86%	1.60	86%	1.60	86%
H-06	0.03	2%	0.03	2%	0.03	2%
H-07	0.07	4%	0.07	4%	0.07	4%
OV-02, SW-02, NE-02	0.02	1%	0.02	1%	0.02	1%
OV-04, SW-04, NE-04	0.01	<1%	0.06	3%	0.01	<1%
OV-08, SW-08, NE-08	0.17	9%	0.61	33%	0.13	7%
Totals	1.90	102%†	2.39	128%†	1.85†	99%†

See Plate 9-2 for rupture sources and fault section locations.
[1] For the SH fault section.
[2] For the BE and BR fault sections.
[3] For the LV and LM fault sections.
† Rounding of slip rates or percentages results in apparent rounding error of total.

The upper part of Table 9-17 contains the estimate for the Hosgri fault slip rate near fault sections HN and SI. This total slip rate equals the Hosgri slip rate opposite the DCPP, plus the slip rates of the Shoreline fault and the offshore Los Osos fault, minus the estimated slip rate of the western reach of the Hosgri fault (fault section WR) that gets transferred to the Piedras Blancas fault source. The total—1.87 mm/yr—should be considered an approximate target that is intended to capture a poorly constrained increase in slip rate from south-to-north on the Hosgri fault source. The negative value for the Western reach is not the fault section's slip rate, but rather represents the amount of right-

lateral strike-slip that is transferred from the main Hosgri–San Simeon fault zone to the Piedras Blancas anticlinorium to the west (cf. Johnson et al., 2014; *Section 5.2.1*).

The lower part of Table 9-17 contains the sums of the rupture sources that pass through fault sections HN and SI for the three SLPB Rupture Models. The rupture sources equal the Hosgri sources that pass through these sections (H-01 to H-03 and H-05 to H-07; Plate 9-1), plus the –02, –04, and –08 rupture sources (Plate 9-2). The sums for the OV and NE models are within a few percent of the target slip rate. The sum for the SW Model—approximately 2.4 mm/yr—exceeds the target by approximately 28%. This exceedance is mostly due to the nature of the complex rupture source SW-08, wherein the primary Hosgri rupture planes have a slip rate of approximately 0.6 mm/yr, and the secondary offshore Los Osos rupture plane has a slip rate at the target 0.2 mm/yr. The higher-than-target slip rate on the Hosgri fault north of the DCPP does not meaningfully affect the hazard results for the DCPP, as initial sensitivities (Wooddell, 2011, presentation at Workshop 1) and final hazard sensitivities (*Chapter 14*) show that Connected fault sources more distant from the DCPP have a small contribution to hazard at the ground motions of interest.

Finally, we note that the slip rate increase on the Hosgri fault source north of fault section SI (north of the intersection with the Oceanic–West Huasna fault) is accommodated through the regional fault sources, which is described in *Chapter 12*.

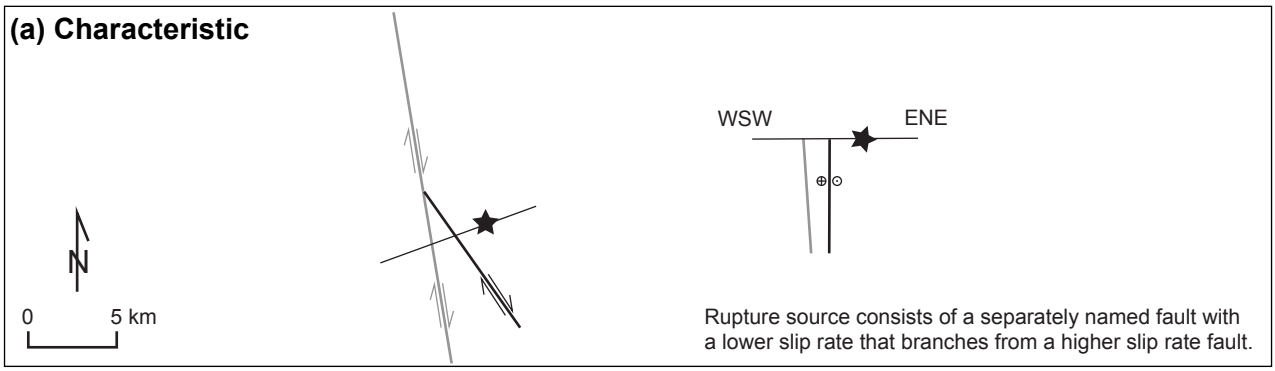

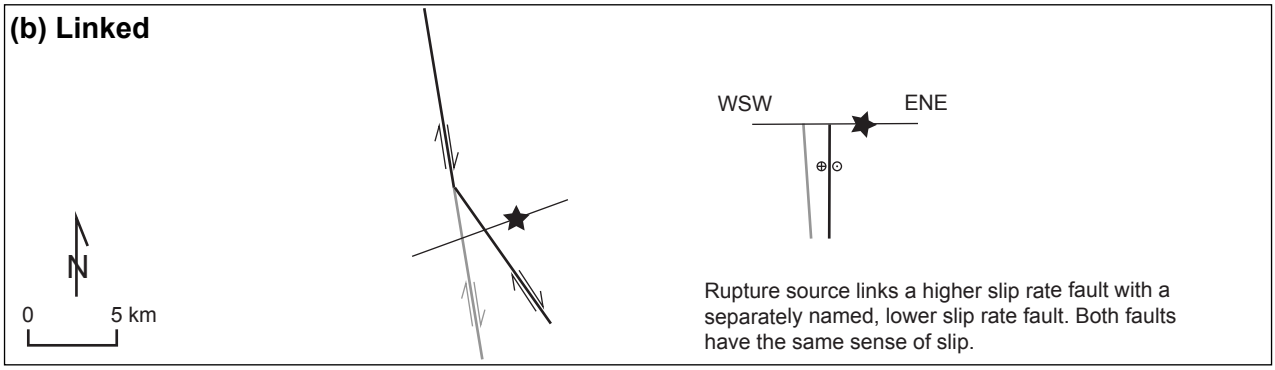

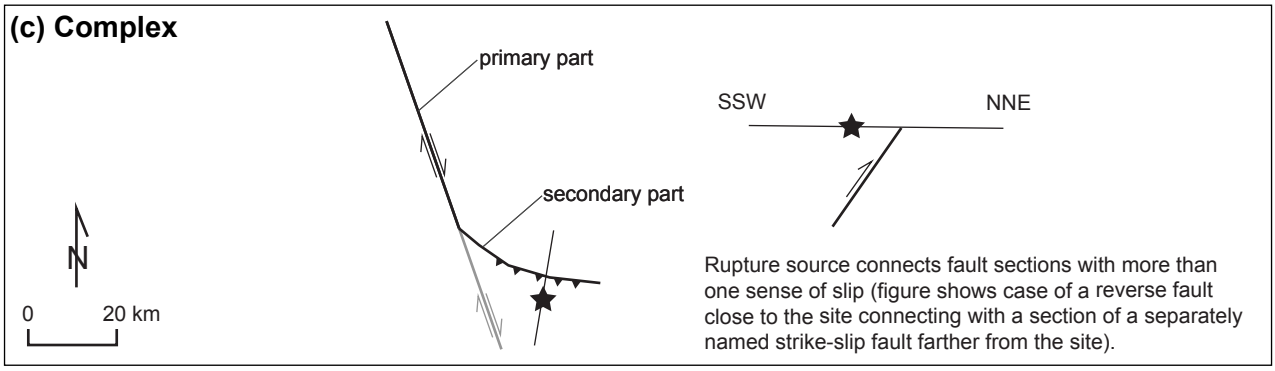

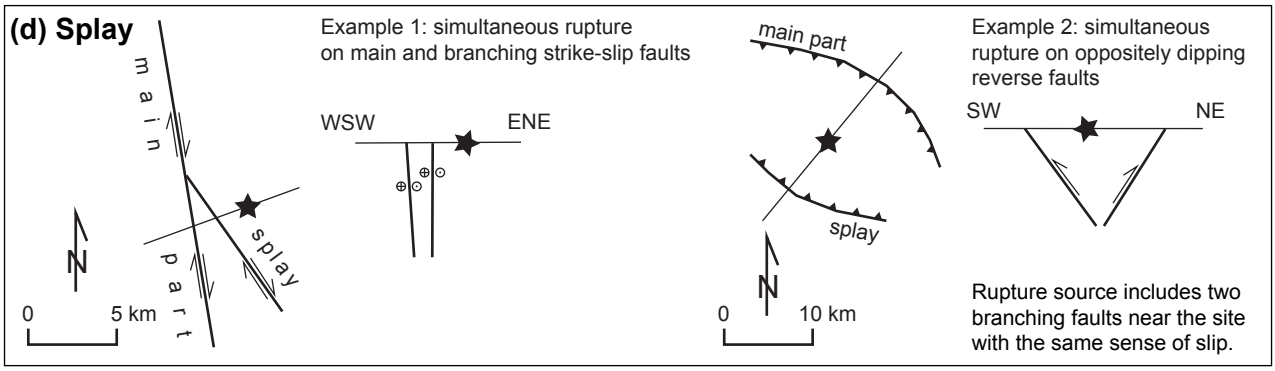

EXPLANATION

- Site
- Fault section in rupture source
- Fault section not in rupture source
- Map view: strike-slip (left), reverse (right)
- Cross-section view: strike-slip (left), reverse (right)

Rupture Source Types Used in the Diablo Canyon SSC Model

DCPP SSC REPORT

Pacific Gas and Electric Company

Figure **9-1**

File path: S:\1005\005\Final_Report_Figures\Figure_900-01.ai; Date: 02/20/2015; User: Alex Remar, LCI; Rev.1

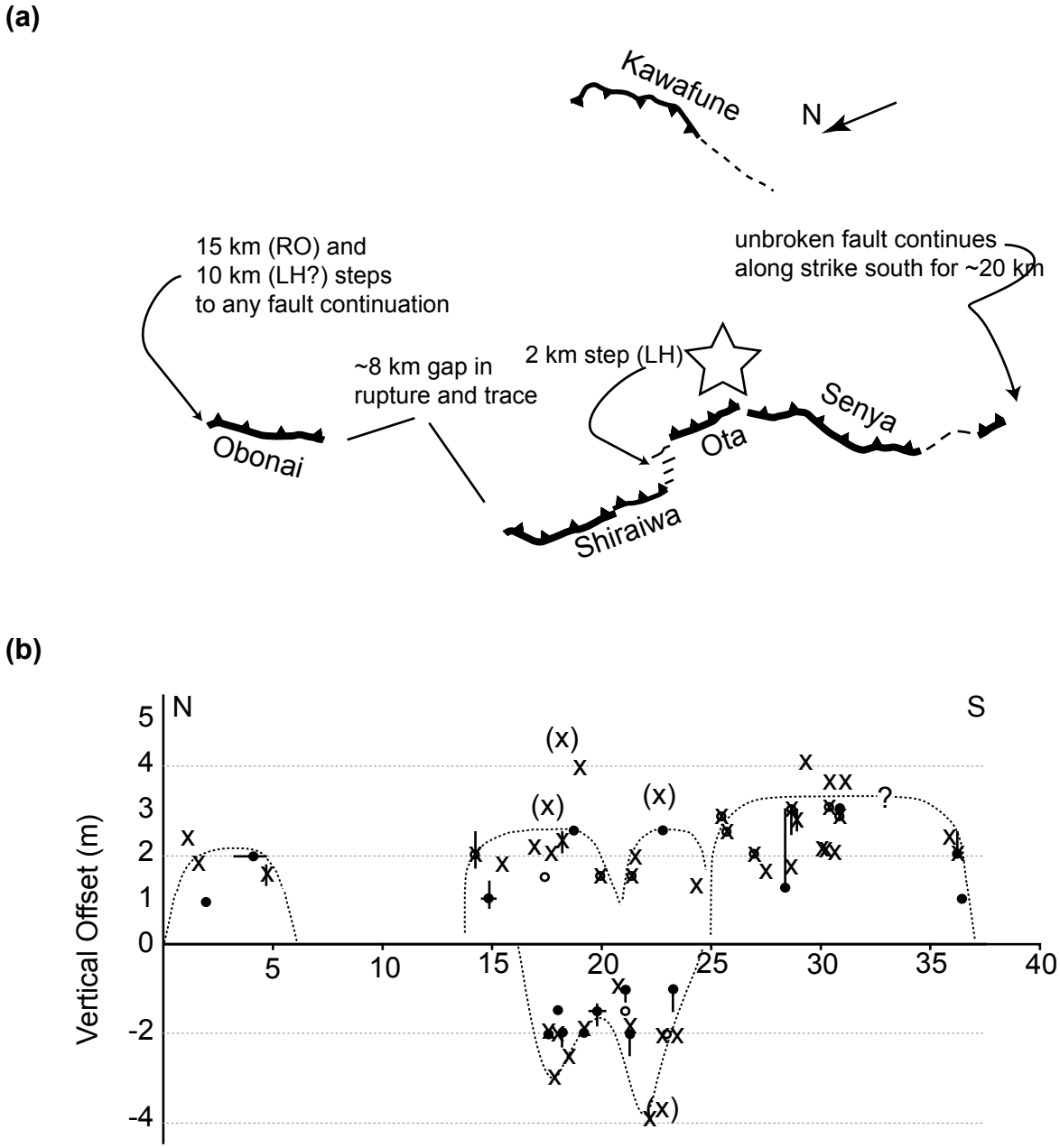

EXPLANATION

- ● After Yamasaki (1896) and Imamura (1913) as cited by Matsuda et al. (1980)
- ○ Observed by local people
- X Value obtained from topographic profiles, with pre-1896 displacements shown in parentheses

Notes:
-Star in Panel (a) shows earthquake epicenter
-Abbreviations in Panel (a): RO = Right Oblique; LH = Left step, Hanging wall
- Panel (b) shows vertical offset along faults on the western foot of Mahiru Mountains (positive values) and the Kawafune fault on the eastern foot (negative vaules); adopted from Matsuda et al. (1980).

Modified from Wesnousky (2008, electronic supplement, Section 1).

Surface Rupture Map for the 1896 Rikuu Earthquake, Japan

DCPP SSC REPORT

Pacific Gas and Electric Company

Figure **9-2**

File path: S:\1005\005\Final_Report_Figures\Figure_900-02.ai; Date: 03/11/2015; User: Alex Remar, LCI; Rev.1

(a) 1940 Imperial Valley (El Centro) Earthquake Rupture

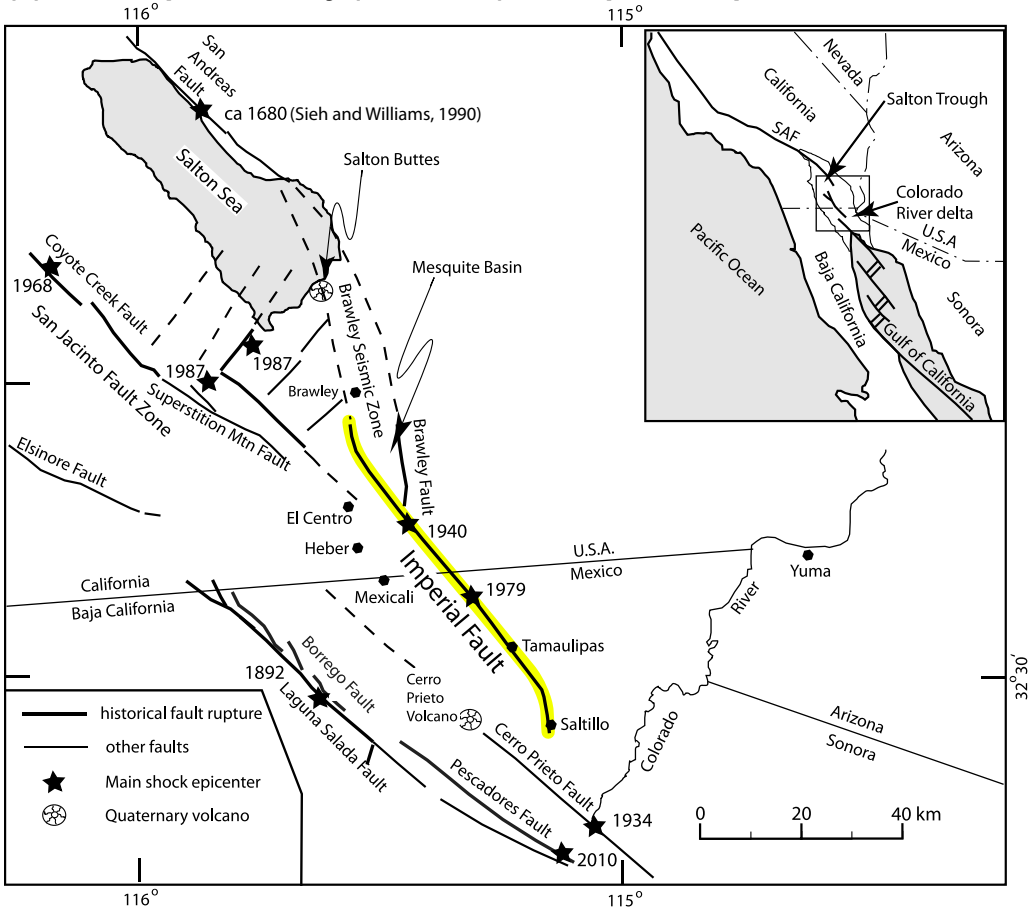

(b) 1979 Imperial Valley Earthquake Rupture

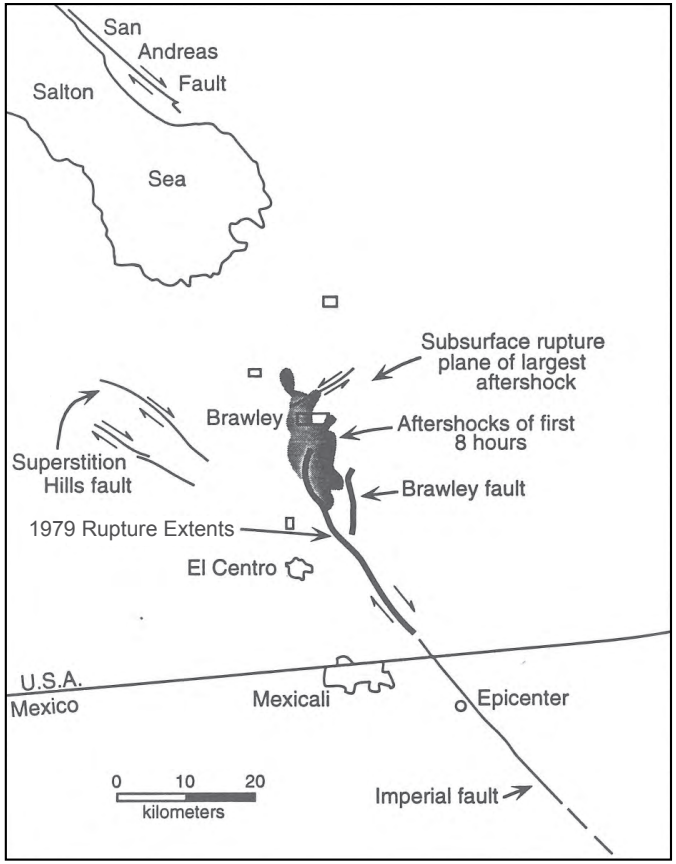

Sources:
- Panel (a) modified from Rockwell and Klinger (2013).
- Panel (b) modified from Yeats et al. (1997).

Surface Rupture Maps for the 1940 and 1979 Imperial Valley Earthquakes, California

DCPP SSC REPORT

Pacific Gas and Electric Company | Figure **9-3**

File path: S:\1005\005\Final_Report\Figures\Figure_900-03.ai; Date: 12/22/2014; User: Alex Remar, LCI; Rev.0

(a) Surface Rupture Map and Faults of the Eastern California Shear Zone

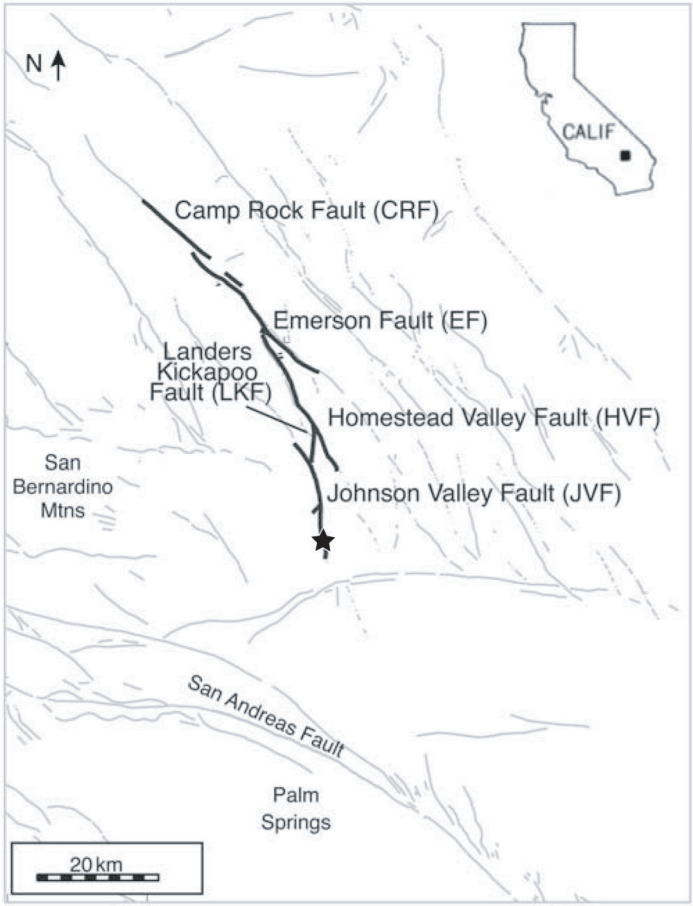

(b) Surface Displacement Profile

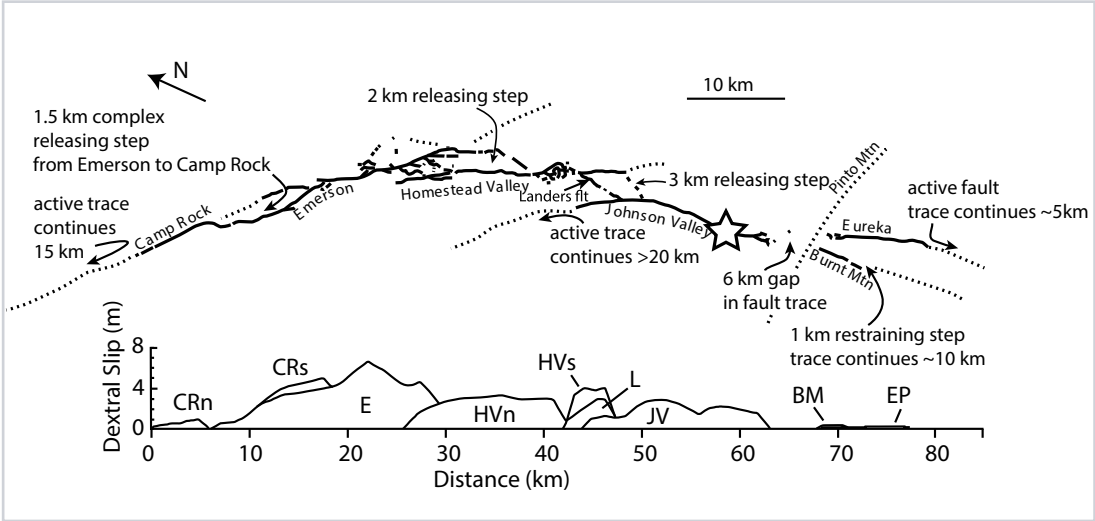

Abbreviations

CRn	= Camp Rock north	L	= Landers
CRs	= Camp Rock south	JV	= Johnson Valley
E	= Emerson	BM	= Burnt Mountain
HVn	= Homestead Valley north	EP	= Eureka Peak
HVs	= Homestead Valley south		

Notes:
- In panel (a), black lines are faults involved in the 28 June 1992 Landers earthquake; gray lines are other faults in the Eastern California shear zone; star shows epicenter; adapted from Langenheim and Jachens (2002) as cited by Madden and Pollard (2012).
- Panel (b) shows distribution of dextral surficial slip along faults.

Sources:
- Panel (a) modified from Madden and Pollard (2012).
- Panel (b) modified from Wesnousky (2008, electronic supplement, Section 1).

Surface Rupture Map and Displacement Profile for the 1992 Landers Earthquake, California

DCPP SSC REPORT

Pacific Gas and Electric Company | Figure **9-4**

File path: S:\1005\005\Final_Report\Figures\Figure_900-04.ai; Date: 02/20/2015; User: Alex Remar, LCI; Rev.1

(a)

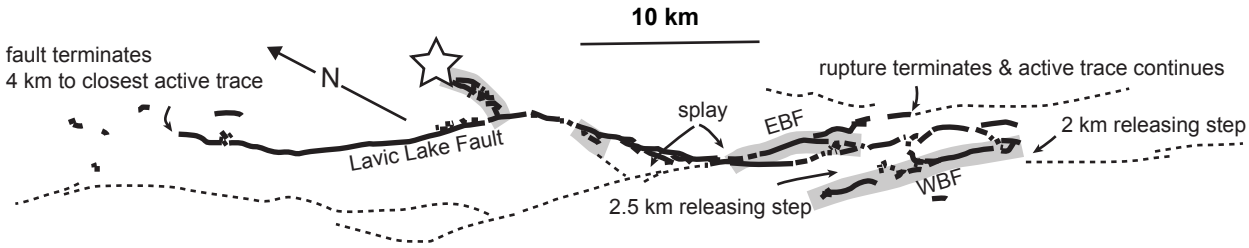

(b)

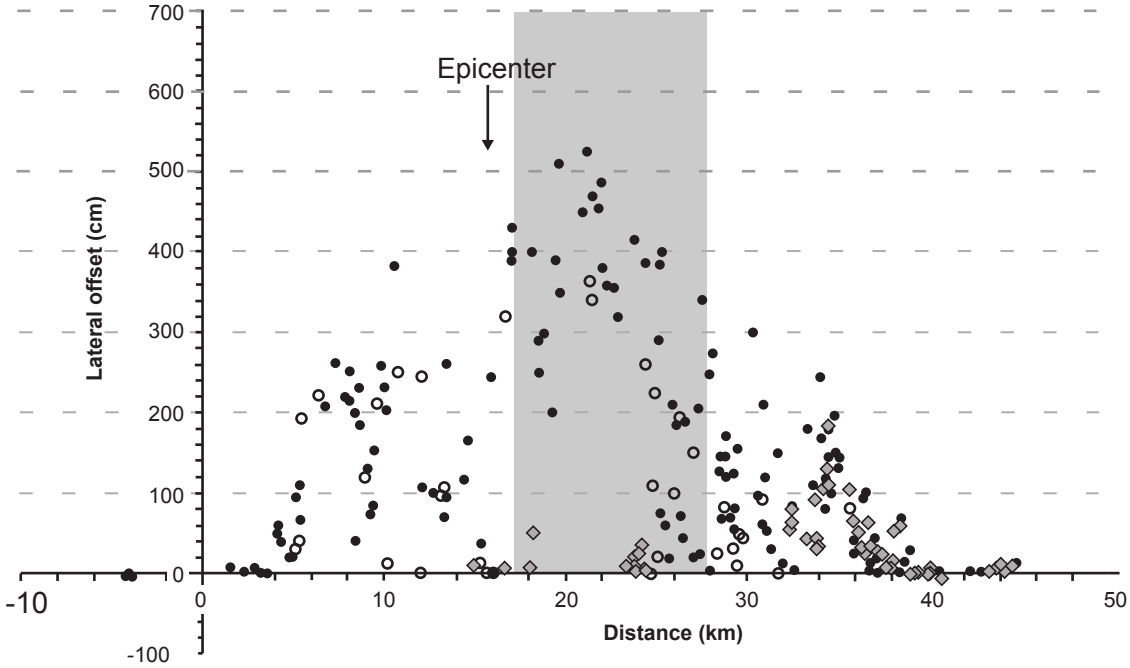

EXPLANATION

- ● Offset measures along main trace
- ○ Minimum estimates
- ◇ Measures on secondary structures in shaded areas

WBF West Bullion fault

EBF East Bullion fault

Notes:
- Star in Panel (a) shows earthquake epicenter.
- Shaded area in Panel (a) shows faults with surface rupture.
- Mapping in Panel (a) from Treiman et al. (2002).
- Lateral offsets in Panel (b) from Treiman et al. (2002).

Source: Modified from Wesnousky (2008, Electronic Supplement, Section 1).

Surface Rupture Map for the 1999 Hector Mine Earthquake, California

DCPP SSC REPORT

Pacific Gas and Electric Company

Figure **9-5**

File path: S:\1005\005\Final_Report_Figures\Figure_900-05.ai; Date: 03/11/2015; User: Alex Remar, LCI; Rev.1

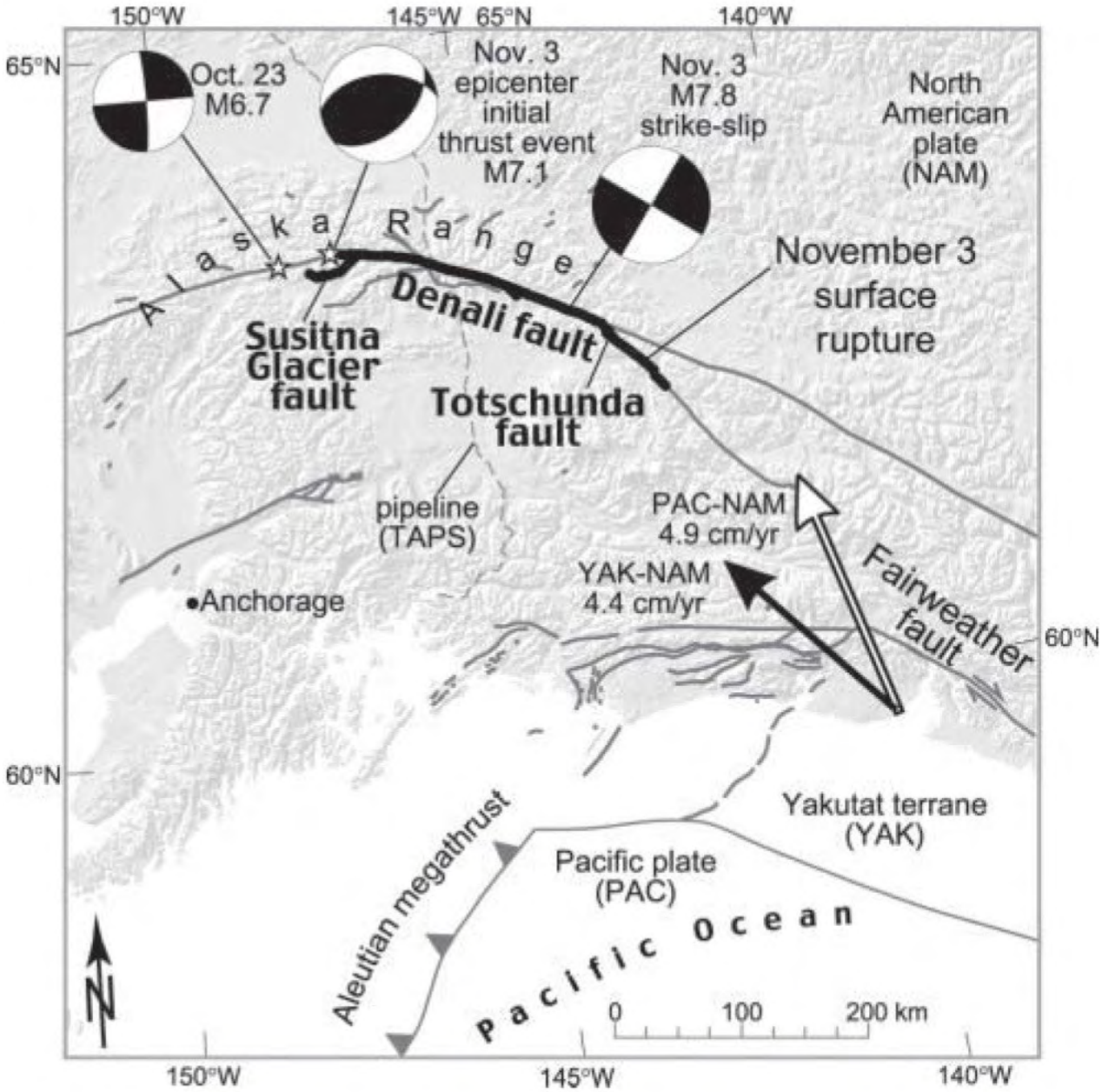

EXPLANATION

TAPS = Trans-Alaska Pipeline system
PAC-NAM = Pacific-North America relative plate motion (direction and rate indicated)
YAK-NAM = Yakutat-North America relative plate motion (direction and rate indicated)

Notes:
- White arrow shows relative motion between Pacific Plate and North American Plate (DeMets et al., 1994).
- Thick black lines show Denali fault earthquake surface rupture; gray lines show active faults (Plafker et al., 1994).
- Locations of 23 October and 3 November 2002 epicenters shown as stars.
- Solid black arrow is GPS-measured motion of Yakutat relative to Fairbanks, Alaska (Fletcher and Freymueller, 1999).
- References are as cited by Haeussler et al. (2004).

Source: Haeussler et al. (2004).

Tectonic Setting and Surface Rupture Map for the 2002 Denali Earthquake, Alaska

DCPP SSC REPORT

Pacific Gas and Electric Company

Figure **9-6**

File path: S:\1005\005\Final_Report_Figures\Figure_900-06.ai; Date: 02/20/2015; User: Alex Remar, LCI; Rev.1

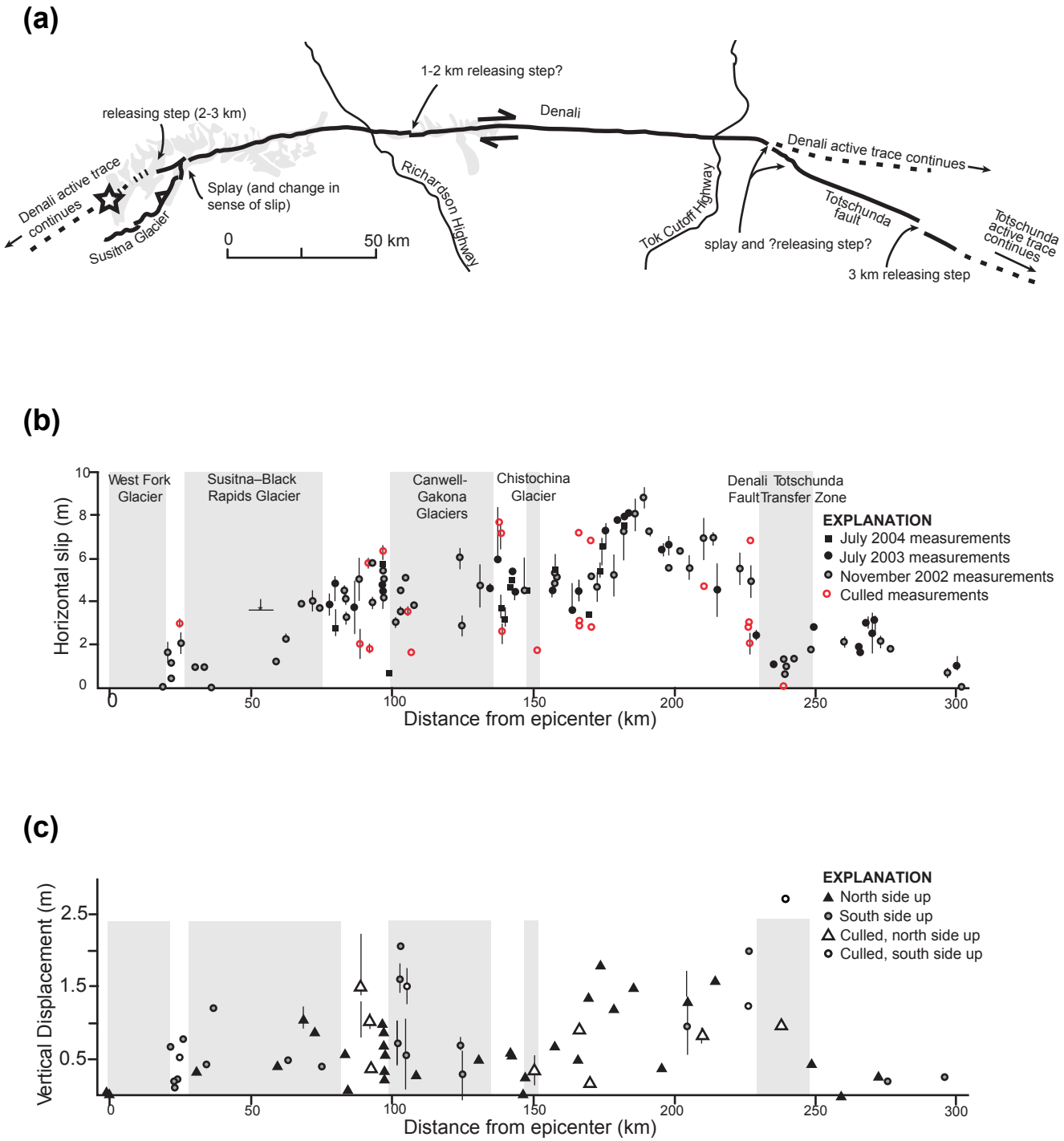

Source: Wesnousky (2008, electronic supplement, Section 1).

Horizontal and Vertical Slip Measurements for the 2002 Denali Earthquake, Alaska

DCPP SSC REPORT

Pacific Gas and Electric Company

Figure **9-7**

File path: S:\1005\005\Final_Report_Figures\Figure_900-07.ai; Date: 02/20/2015; User: Alex Remar, LCI; Rev.1

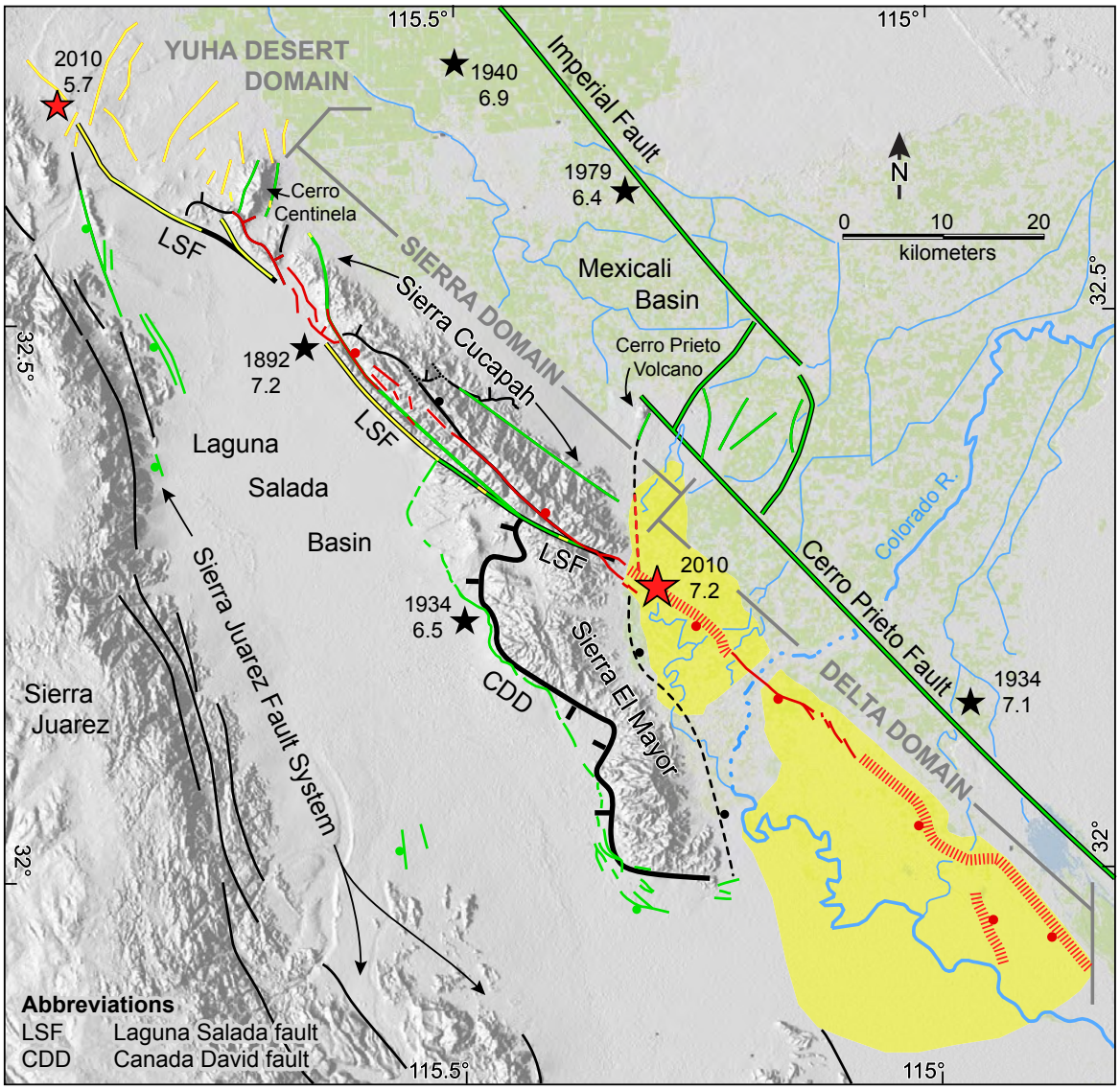

EXPLANATION

- Main shock epicenter
- Epicenter of historical earthquake
- Initial fault to rupture in the earthquake sequence
- Coseismic surface-fault rupture (≥ 0.5 m) mapped from pre- and post-event lidar (light detection and ranging) data
- Coseismic surface-fault rupture (≥ 0.5 m) mapped from synthetic aperture radar interferometry
- Coseismic surface-fault rupture (< 0.5 m) mapped from pre- and post-event lidar data
- Quaternary fault
- Older (late Quaternary) surface-fault rupture
- Dominant active fault (controls topography and accommodates most plate-margin shearing)
- Approximate limits of distributed liquefaction and surface failure

Note:
Modified from Fletcher et al. (2014, their Figure 3). Map shows the main shock epicenter of the 2010 M 7.2 El Mayor–Cucapah (EMC) earthquake sequence, surface-fault rupture, historical and prehistoric earthquakes and surface-fault ruptures, and other Quaternary faults. The three macroscopic domains of the surface rupture include the Yuda Desert, Sierra, and Delta domains. The EMC rupture activated slip on seven different faults that exist between two dominant fault systems that control topography and accommodate most plate margin shearing (e.g., Mueller and Rockwell, 1991; Bennett et al., 1996; Genrich et al., 1997; Axen and Fletcher, 1998). These include the Cerro Prieto–Imperial system and the Laguna Salada (LSF)–Canada David (CDD) fault system. Green patterns in the base map show active farmlands in the Imperial and Mexicali Valleys. Shaded-relief map is produced from Shuttle Radar Topography Mission data. More details of the tectonic setting and the 2010 earthquake are in Fletcher et al. (2014).

Surface Rupture Map for the 2010 El Mayor–Cucapah Earthquake, Mexico

DCPP SSC REPORT

Pacific Gas and Electric Company

Figure **9-8**

File path: /s/1005/005/Final_Report_Figures/Figure_900-08.ai; Date: 02/20/2015; User: Brian Greer, LCI; Rev. 1

(a) Mock FGM Fault Sections and Fault Slip Rates

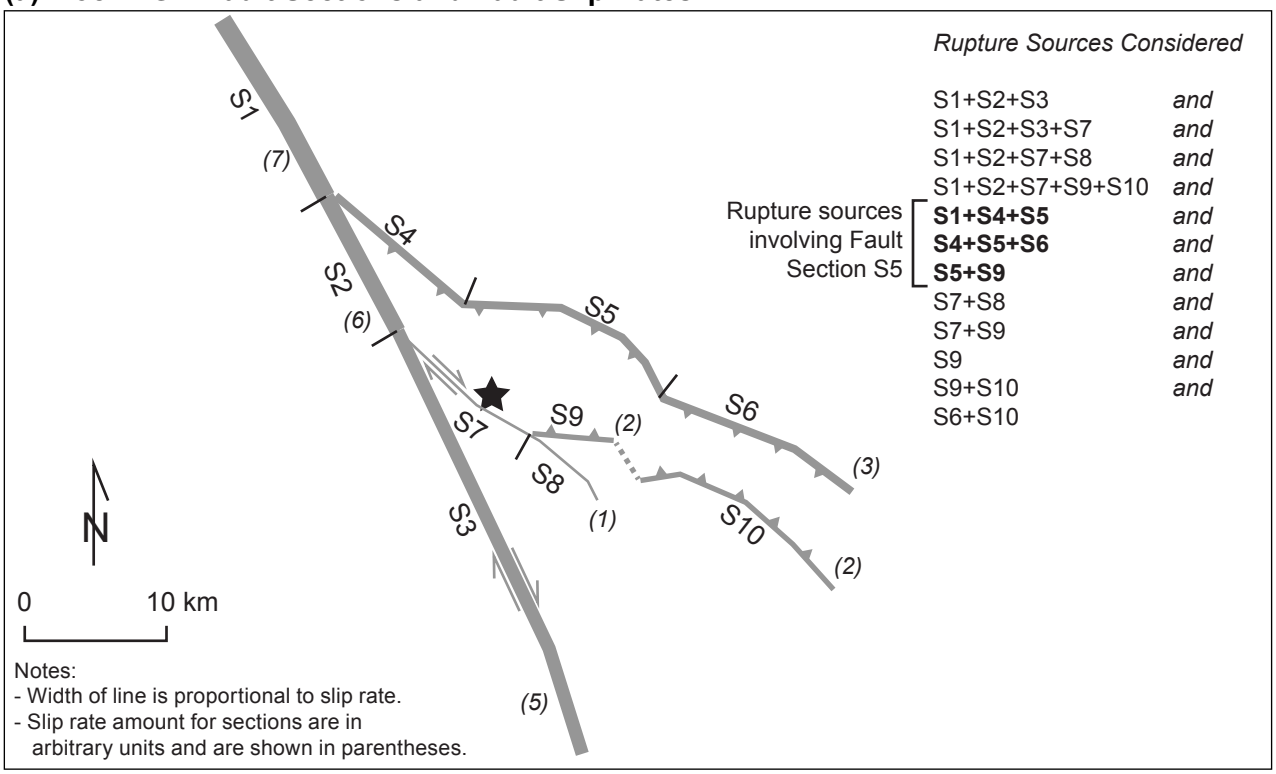

Notes:
- Width of line is proportional to slip rate.
- Slip rate amount for sections are in arbitrary units and are shown in parentheses.

(b) Slip Rate Allocation Methodology for Mean Slip Rate, Fault Section S5

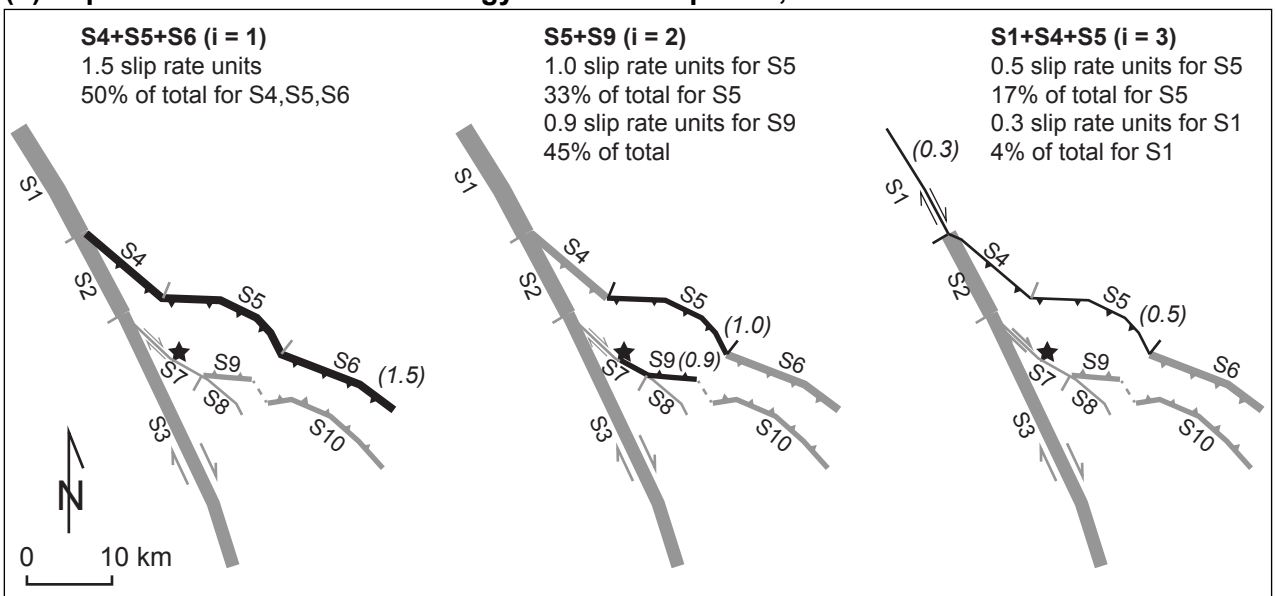

Notes:
- Black lines indicate fault rupture.
- i value designates each rupture source involving fault section S5. The sum of the slip rates in all three scenarios equals the target mean slip rate for fault section S5 (see equation 9-1).

EXPLANATION

- ★ Site
- Fault sections: strike-slip (left), reverse (right)
- (3) (1) Fault section slip rate, with the value in parentheses, and the width of the line proportional to the slip rate.
- S1 S2 Fault section IDs and section boundary

Slip Rate Allocation Model Concept

DCPP SSC REPORT

Pacific Gas and Electric Company

Figure **9-9**

File path: S:\1005\005\Final_Report_Figures\Figure_900-09.ai; Date: 12/22/2014; User: Alex Remar, LCI; Rev.1

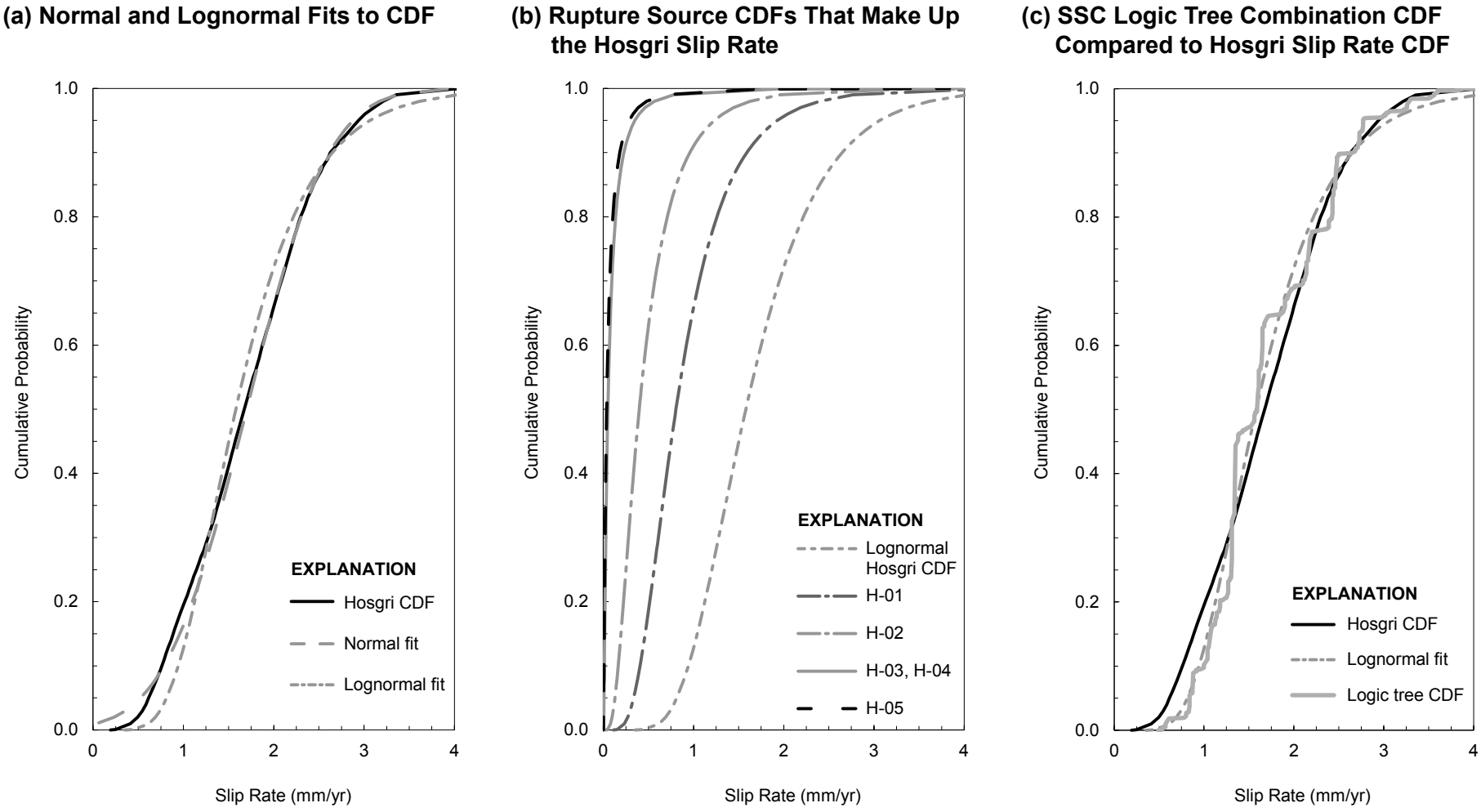

Note: In Panel (b), individual rupture source CDFs sum to the Lognormal CDF.

Slip Rate Allocation for the Hosgri Slip Rate CDF

DCPP SSC REPORT

Pacific Gas and Electric Company | Figure **9-10**

File path: S:\1005\005\Final_Report\Figures\Figure_900-10.ai; Date: 12/22/2014; User: Alex Remar, LCI; Rev.1

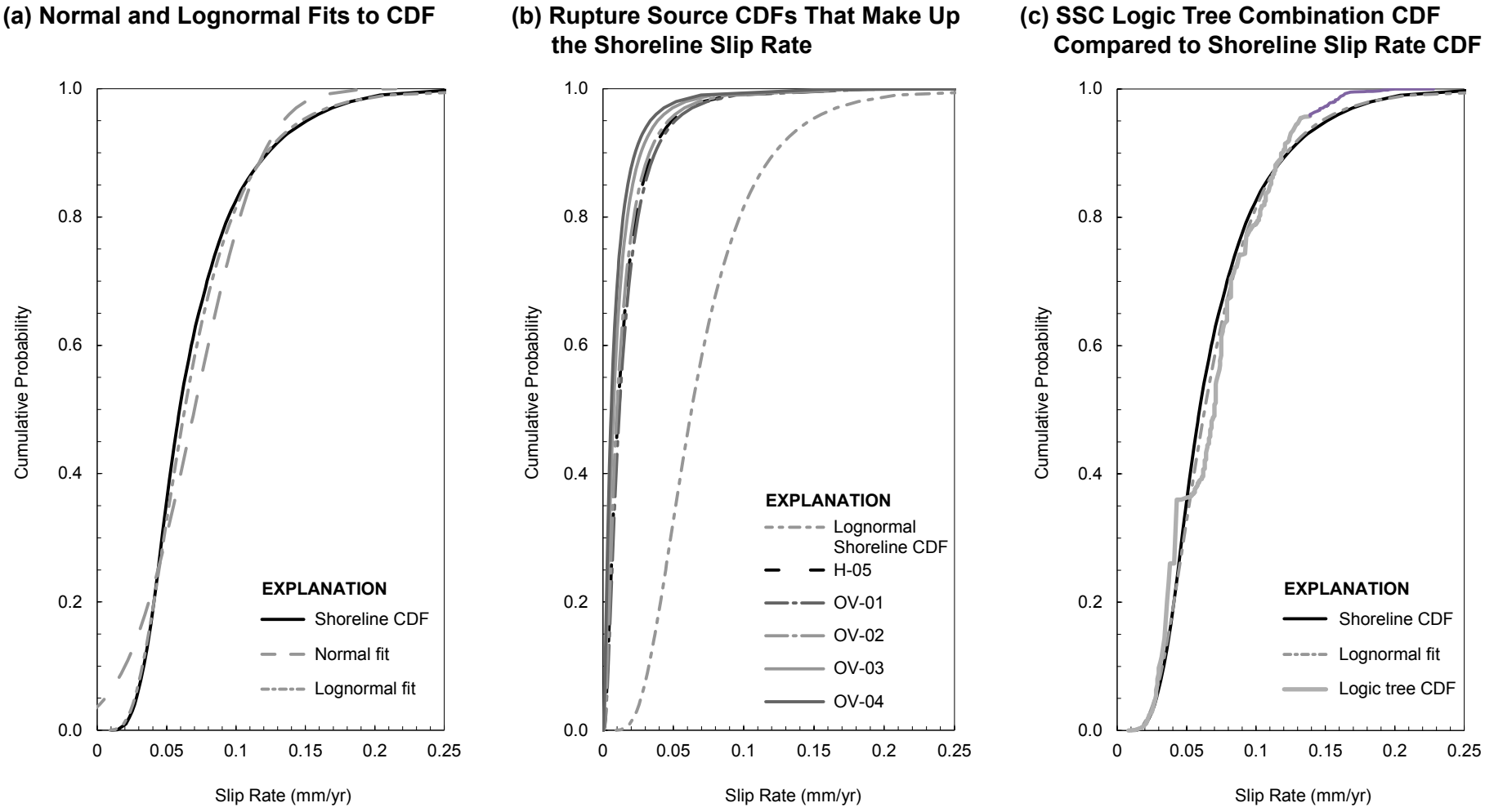

Note: In Panel (b), individual rupture source CDFs sum to the Lognormal CDF.

Slip Rate Allocation for the Shoreline Slip Rate CDF (OV Model)

DCPP SSC REPORT

Pacific Gas and Electric Company | Figure **9-11**

File path: S:\1005\005\Final_Report\Figures\Figure_900-11.ai; Date: 03/10/2015; User: Serkan Bozkurt, LCI; Rev.1

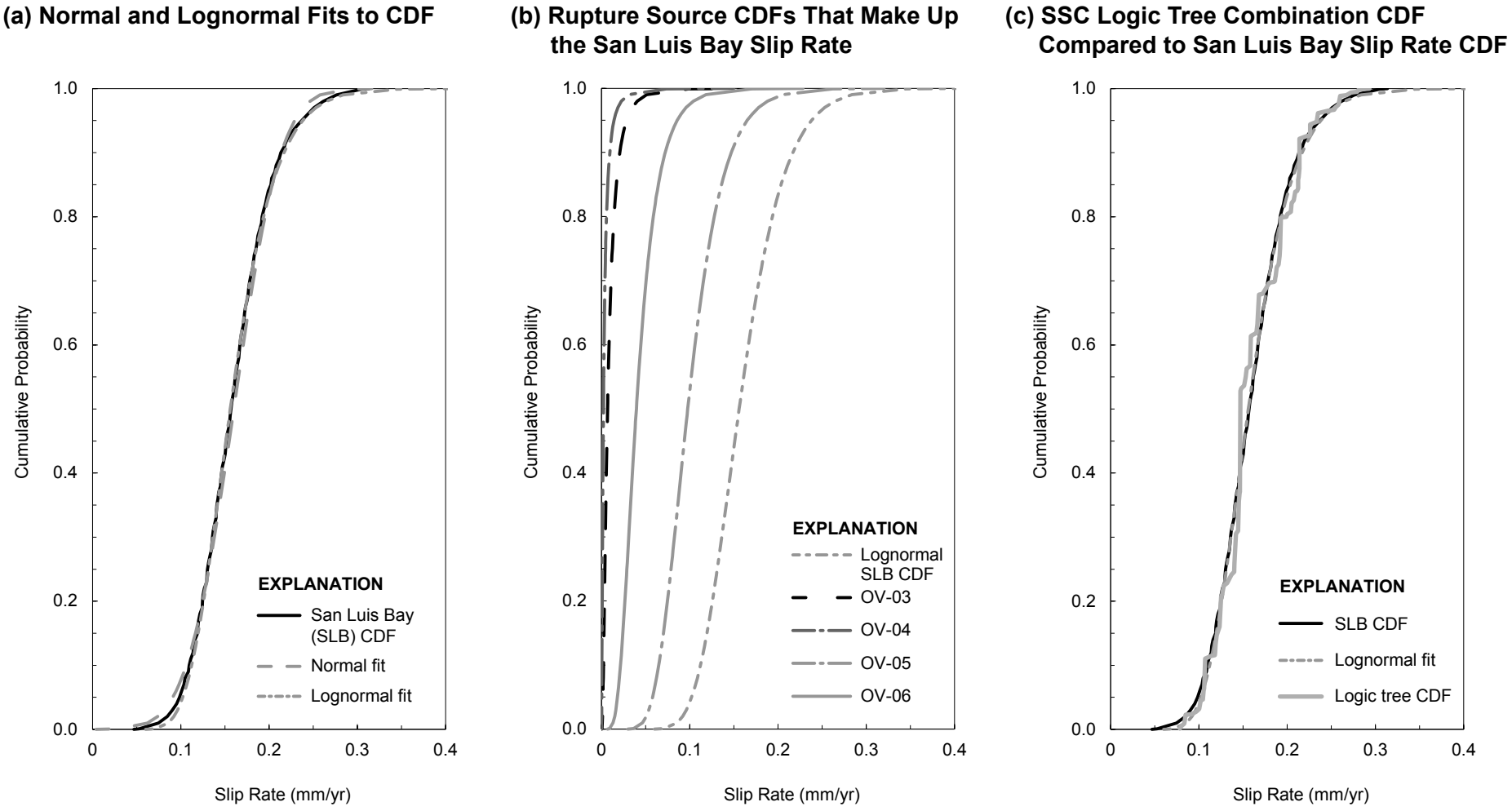

Note: In Panel (b), individual rupture source CDFs sum to the Lognormal CDF.

Slip Rate Allocation for the San Luis Bay Slip Rate CDF (OV Model)

DCPP SSC REPORT

Pacific Gas and Electric Company | Figure **9-12**

File path: S:\1005\005\Final_Report\Figures\Figure_900-12.ai; Date: 02/20/2015; User: Alex Remar, LCI; Rev.1

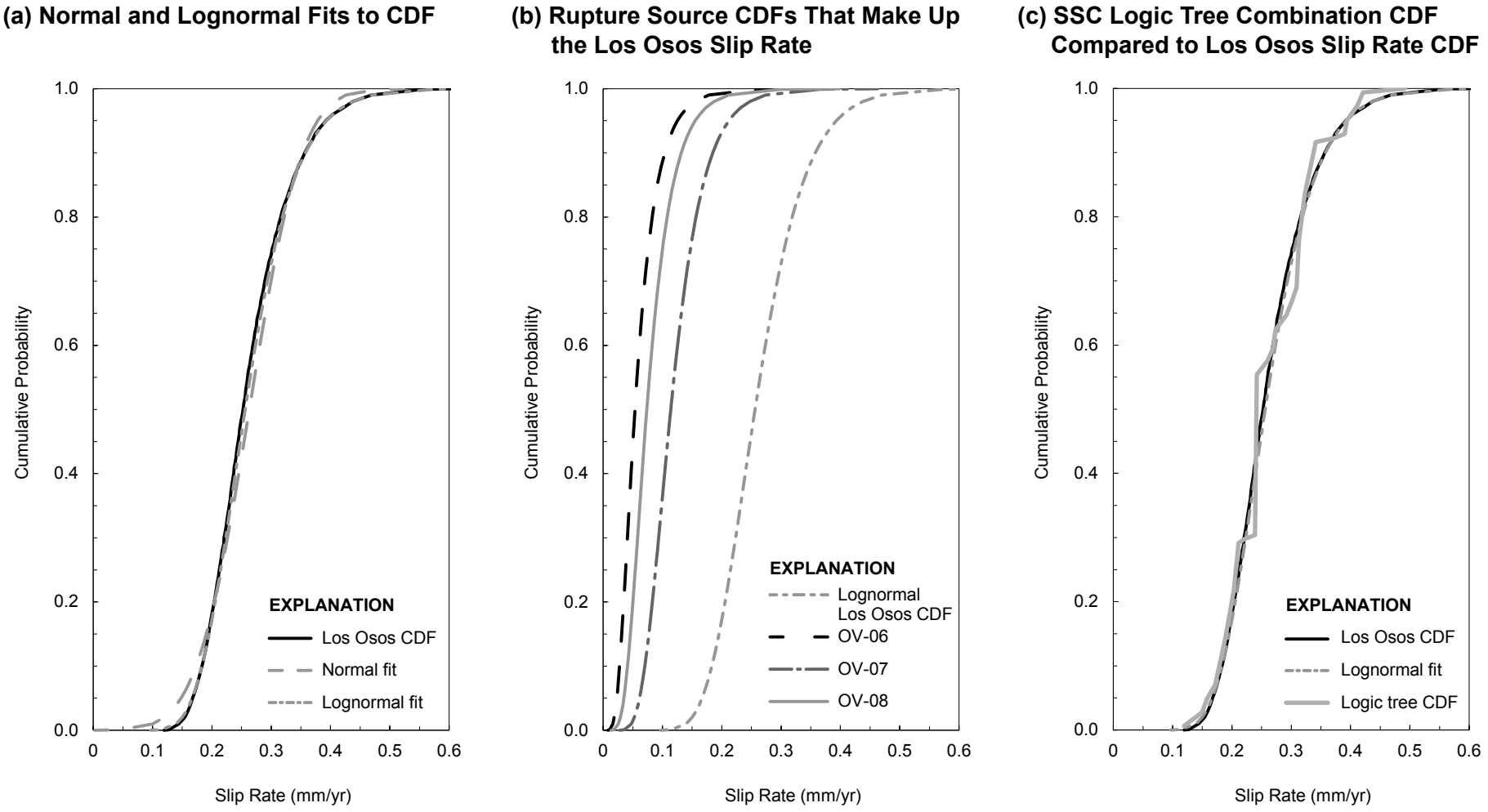

Note: In Panel (b), individual rupture source CDFs sum to the Lognormal CDF.

Slip Rate Allocation for the Los Osos Slip Rate CDF (OV Model)

DCPP SSC REPORT

Pacific Gas and Electric Company | Figure **9-13**

File path: S:\1005\005\Final_Report\Figures\Figure_900-13.ai; Date: 02/20/2015; User: Alex Remar, LCI; Rev.1

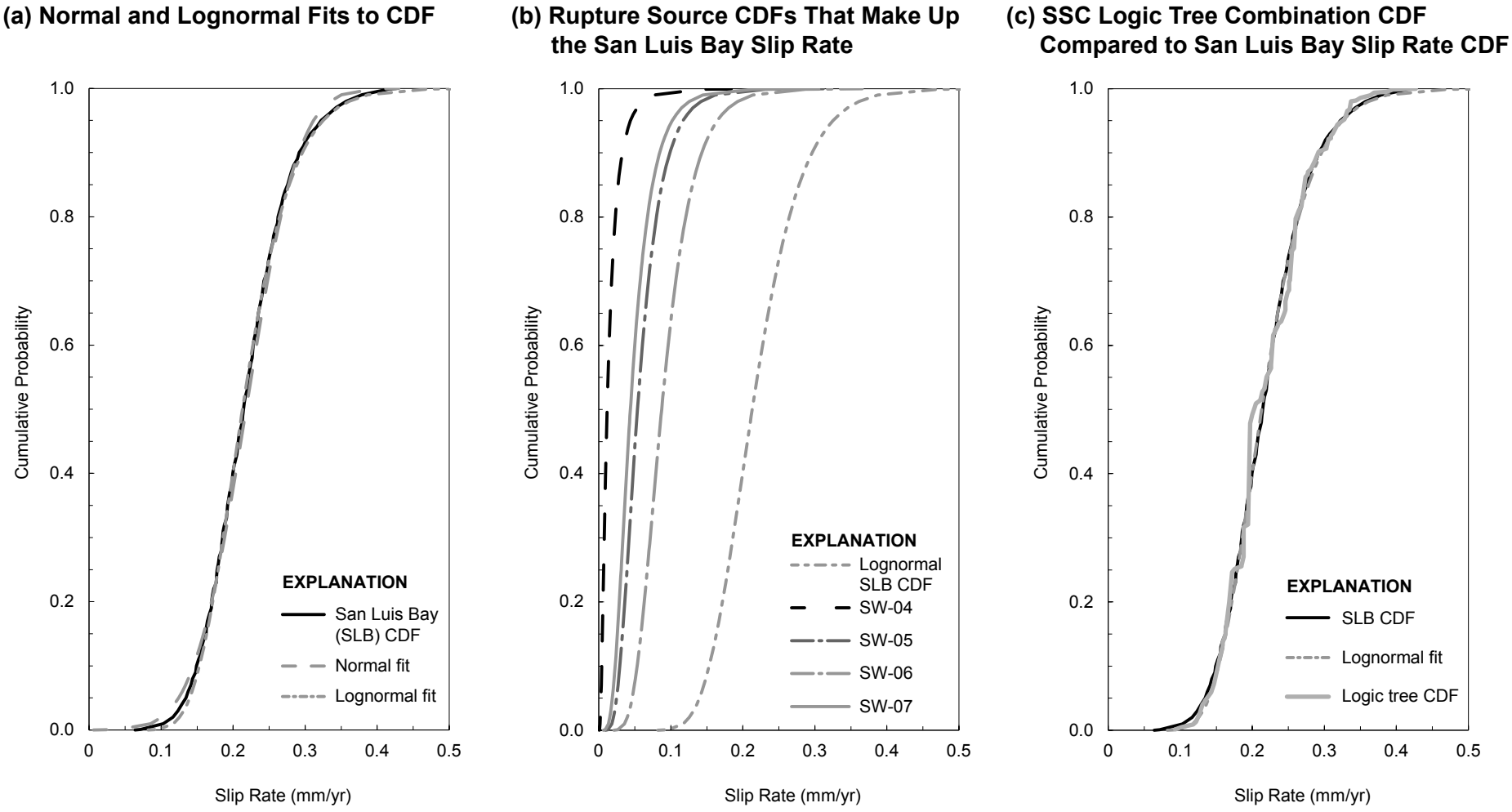

Note: In Panel (b), individual rupture source CDFs sum to the Lognormal CDF.

Slip Rate Allocation for the San Luis Bay Slip Rate CDF (SW Model)

DCPP SSC REPORT

Pacific Gas and Electric Company | Figure **9-14**

File path: S:\1005\005\Final_Report\Figures\Figure_900-14.ai; Date: 02/20/2015; User: Alex Remar, LCI; Rev.1

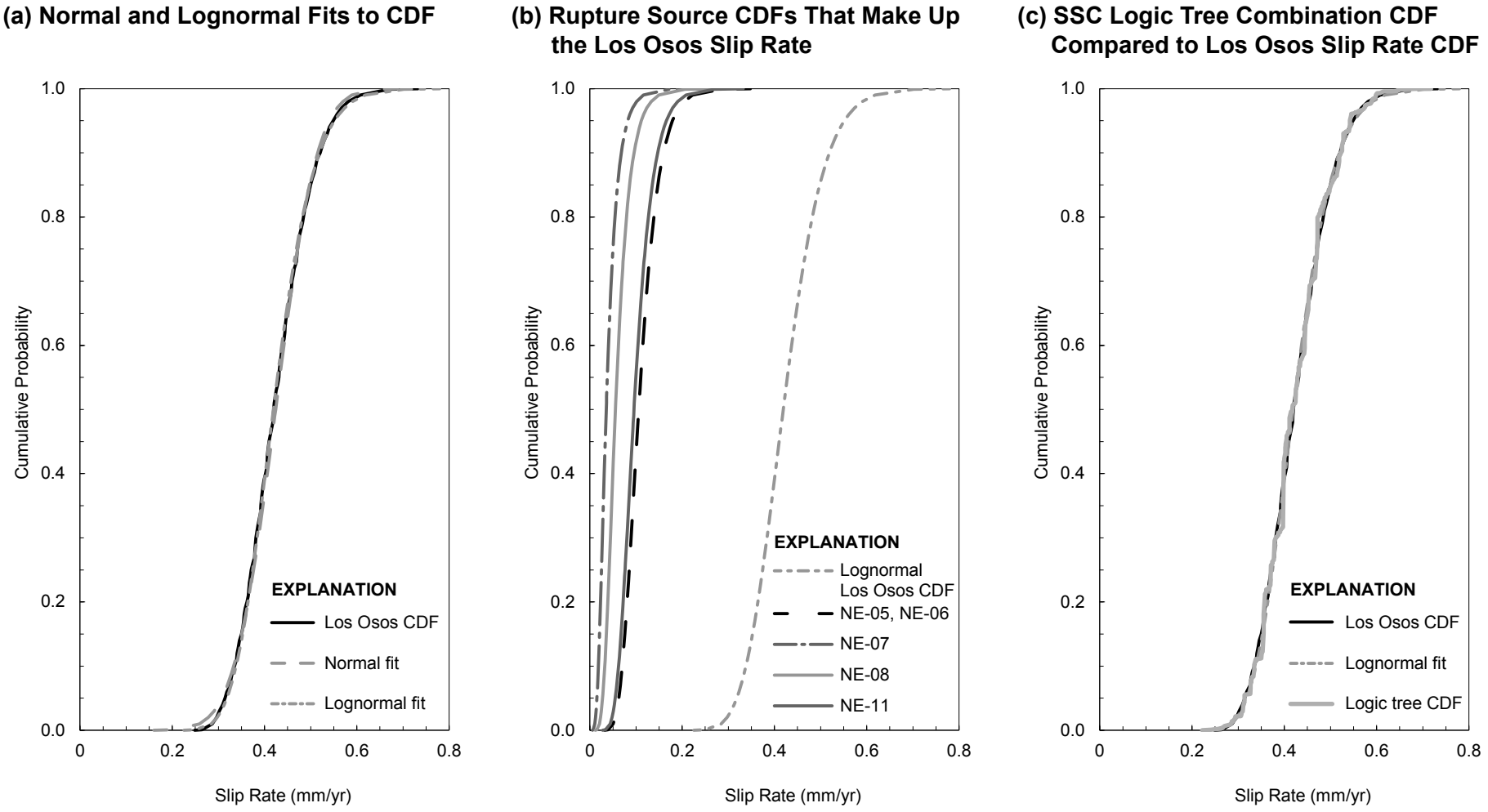

Note: In Panel (b), individual rupture source CDFs sum to the Lognormal CDF.

Slip Rate Allocation for the Los Osos Slip Rate CDF (NE Model)

DCPP SSC REPORT

Pacific Gas and Electric Company | Figure **9-15**

File path: S:\1005\005\Final_Report\Figures\Figure_900-15.ai; Date: 02/20/2015; User: Alex Remar, LCI; Rev.1

	-01 Linked, Hosgri (Central Trace)	-02 Linked, Hosgri (Western Trace)	-03 Linked, Hosgri (Eastern Trace)	-04 Complex, Hosgri (Central Trace) and Piedras Blancas	-05 Splay, Hosgri (Central Trace) and Shoreline
H75	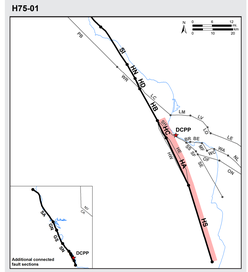	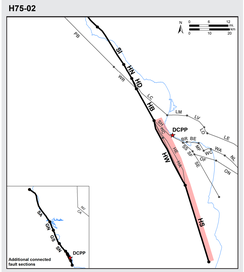	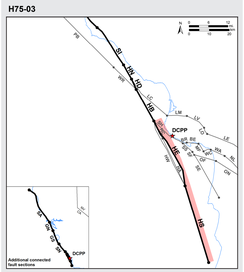	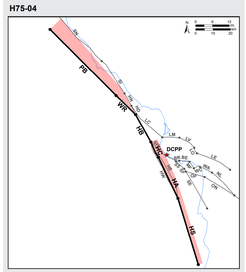	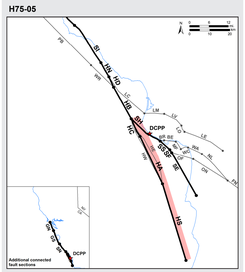
H85	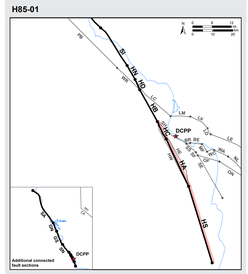	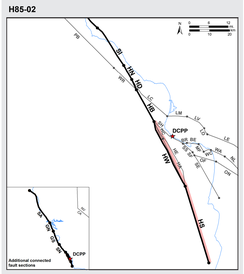	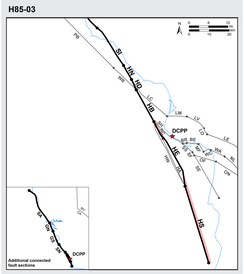	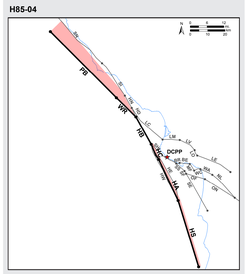	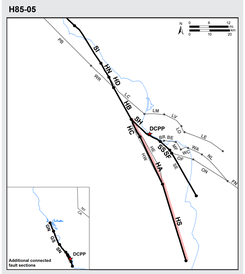
H90	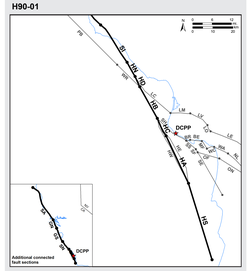	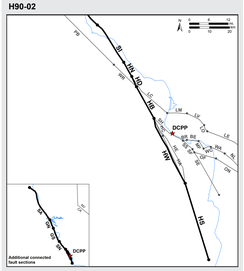	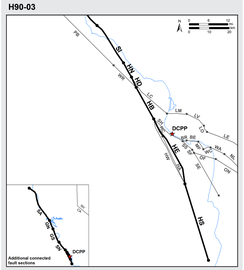	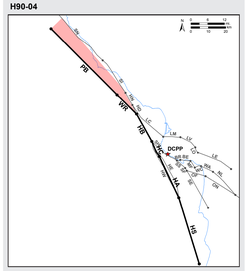	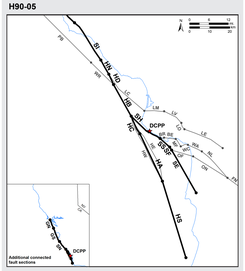

H75/H85/H90

-06 Linked, Hosgri, North of Shoreline Fault Intersection	-07 Linked, Hosgri, North of Los Osos Fault Intersection	-08 Characteristic, Piedras Blancas
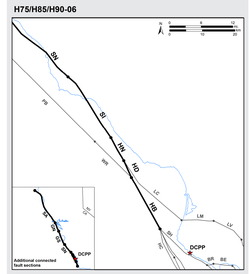	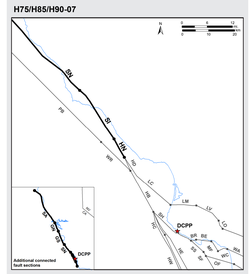	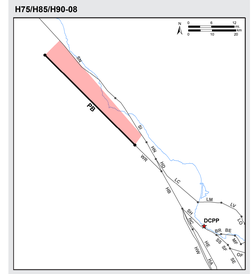

PRIMARY AND CONNECTED FAULT SECTION CODES AND DESCRIPTIONS

Code*	Fault	Section Description
BE	San Luis Bay	Mallagh Landing to San Luis Hill
BR	San Luis Bay	San Luis Hill to Shoreline fault junction
BW	San Luis Bay	Shoreline fault junction to Hosgri fault junction
FN	Foxen Canyon	Oceano fault junction to West Huasna fault junction
FS	Foxen Canyon	West Huasna junction to Little Pine junction
GN	San Gregorio	Point Ano Nuevo to San Andreas junction
GS	San Gregorio	Point Sur to Point Ano Nuevo
HA	Hosgri	Casmalia fault to bend offshore of San Luis Bay fault
HB	Hosgri	Shoreline fault to Western Hosgri fault junction
HC	Hosgri	San Luis Bay (SVN) fault to Shoreline fault junction
HD	Hosgri	Western Hosgri to Los Osos fault junction
HE	Hosgri	East path between Casmalia and Shoreline fault junctions
HN	Hosgri	Los Osos fault to offshore of Cambria
HS	Hosgri	Point Arguello to Casmalia fault junction
HW	Hosgri	West path between Casmalia and Shoreline fault junctions
LB	Los Osos	San Luis Obispo Creek basin (truncated)
LC	Los Osos	Morro Bay to Hosgri fault junction
LE	Los Osos	West Huasna fault junction to San Luis Obispo Creek
LM	Los Osos	Southern margin of Morro Bay
LO	Los Osos	San Luis Obispo Creek basin
LP	Little Pine	West Huasna junction to Big Pine–Little Pine junction
LS	Los Osos	San Luis Obispo Creek basin
LV	Los Osos	San Luis Obispo Creek to Los Osos Valley
MF	San Miguelito offshore	San Luis Obispo Bay to Mallagh Landing
NL	Nipomo	West Huasna fault junction to Arroyo Grande
OF	Oceano	Coastline to Shoreline fault junction
ON	Oceano	West Huasna fault junction to coastline
PB	Piedras Blancas	Western Hosgri to north end Piedras Blancas anticlinorium
PO	Pismo	Wilmar Ave. to Mallagh Landing
SA	San Andreas North	San Gregorio junction to Mendocino Triple Junction
SE	Shoreline	Casmalia fault to Oceano fault junction
SF	Shoreline	Oceano to Wilmar Avenue fault
SH	Shoreline	San Luis Bay fault junction to Hosgri junction
SI	San Simeon	Offshore of Cambria to Oceanic fault junction
SN	San Simeon	Oceanic fault junction to Point Sur
SS	Shoreline	San Luis Bay fault junction to Wilmar Avenue fault junction
WA	Wilmar Avenue	Arroyo Grande to coastline
WB	Wilmar Avenue	Coastline to Shoreline fault
WC	Wilmar Avenue	Coastline to San Miguelito offshore fault
WR	Western Hosgri	Hosgri junction to Piedras Blancas anticlinorium

*The coordinates defining the top of these fault sections are provided in the HID (Appendix D).

EXPLANATION

Rupture source at surface

Surface projection of dipping rupture source

Fault section not involved in surface rupture

Coastline

Notes:
- Map projection, WGS 84 / UTM Zone 10N.
- From Section HB to the north, Hosgri fault section dips are 90 degrees for all Hosgri fault models.

PLATE 9-1
Hosgri Rupture Sources

Pacific Gas and Electric Company

DCPP SSC REPORT

File path: S:\GIS\DCPP\Final_Report_Figures\Plate_9\H-Linkl.mxd Date: 5/20/2015 User: Crew

	-01 Characteristic, Shoreline	-02 Linked, Shoreline and Hosgri	-03 Complex, Shorter Rupture Length	-04 Complex, Longer Rupture Length	-05 Characteristic, Shorter Reverse Rupture of Irish Hills	-06 Splay, Pop-up of Irish Hills	-07 Longer Reverse Rupture of Irish Hills	-08 Complex, Los Osos and Hosgri	-09 Linked, Oceano, Foxen Canyon, and Little Pine	-10 Reverse Ruptures of Eastern San Luis Range	-11 Characteristic, Irish Hills and Offshore Los Osos
Outward-Vergent	OV/SW/NE-01	OV/SW/NE-02	OV-03	OV-04	OV-05	OV-06	OV-07 (Characteristic)	OV-08	OV-09	OV-10 (Characteristic)	
Southwest-Vergent	OV/SW/NE-01	OV/SW/NE-02	SW-03	SW-04	SW-05	SW-06	SW-07 (Linked)	SW-08	SW-09	SW-10 (Splay)	
Northeast-Vergent	OV/SW/NE-01	OV/SW/NE-02	NE-03	NE-04	NE-05	NE-06	NE-07 (Splay)	NE-08	NE-09	NE-10 (Splay)	NE-11

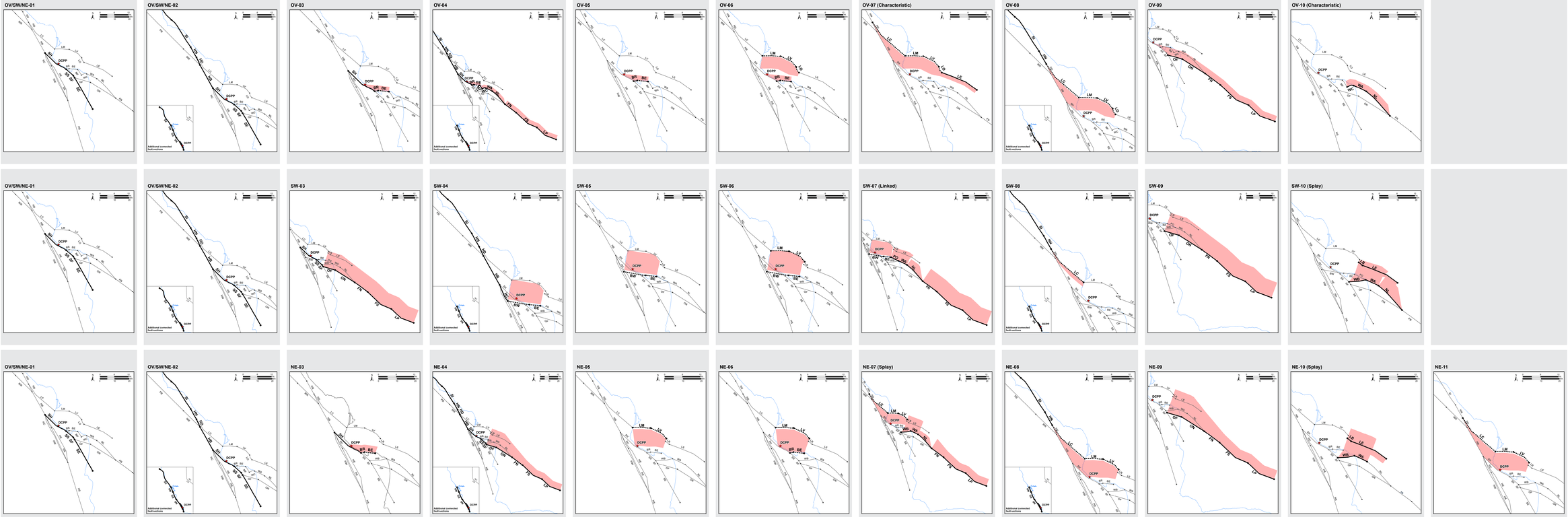

PRIMARY AND CONNECTED FAULT SECTION CODES AND DESCRIPTIONS

Code*	Fault	Section Description
BE	San Luis Bay	Malaga Landing to San Luis Hill
BR	San Luis Bay	San Luis Hill to Shoreline fault junction
BW	San Luis Bay	Shoreline fault junction to Hosgri fault junction
FN	Foxen Canyon	Oceano fault junction to West Huasna fault junction
FS	Foxen Canyon	West Huasna junction to Little Pine junction
GN	San Gregorio	Point Ano Nuevo to San Andreas junction
GS	San Gregorio	Point Sur to Point Ano Nuevo
HA	Hosgri	Casmalia fault to bend offshore of San Luis Bay fault
HB	Hosgri	Shoreline fault to Western Hosgri fault junction
HC	Hosgri	San Luis Bay (SW) fault to Shoreline fault junction
HD	Hosgri	Western Hosgri to Los Osos fault junction
HE	Hosgri	East path between Casmalia and Shoreline fault junctions
HN	Hosgri	Los Osos fault to offshore of Cambria
HS	Hosgri	Point Arguello to Casmalia fault junction
HW	Hosgri	West path between Casmalia and Shoreline fault junctions
LB	Los Osos	San Luis Obispo Creek basin (truncated)
LC	Los Osos	Morro Bay to Hosgri fault junction
LE	Los Osos	West Huasna fault junction to San Luis Obispo Creek
LM	Los Osos	Southern margin of Morro Bay
LO	Los Osos	San Luis Obispo Creek basin
LP	Little Pine	West Huasna junction to Big Pine–Little Pine junction
LS	Los Osos	San Luis Obispo Creek basin
LV	Los Osos	San Luis Obispo Creek to Los Osos Valley
MF	San Miguelito offshore	San Luis Obispo Bay to Malaga Landing
NL	Nipomo	West Huasna fault junction to Arroyo Grande
OF	Oceano	Coastline to Shoreline fault junction
ON	Oceano	West Huasna fault junction to coastline
PB	Piedras Blancas	Western Hosgri to north end Piedras Blancas anticlinorium
PO	Pismo	Wilmar Ave. to Malaga Landing
SA	San Andreas North	San Gregorio junction to Mendocino Triple Junction
SE	Shoreline	Casmalia fault to Oceano fault junction
SF	Shoreline	Oceano to Wilmar Avenue fault
SH	Shoreline	San Luis Bay fault junction to Hosgri junction
SI	San Simeon	Offshore of Cambria to Oceano fault junction
SN	San Simeon	Oceanic fault junction to Point Sur
SS	Shoreline	San Luis Bay fault junction to Wilmar Avenue fault junction
WA	Wilmar Avenue	Arroyo Grande to coastline
WB	Wilmar Avenue	Coastline to Shoreline fault
WC	Wilmar Avenue	Coastline to San Miguelito offshore fault
WR	Western Hosgri	Hosgri junction to Piedras Blancas anticlinorium

*The coordinates defining the top of these fault sections are provided in the HID (Appendix D).

EXPLANATION

- Rupture source at surface
- Updip surface projection of buried rupture source
- Fault section not involved in surface rupture
- Surface projection of dipping rupture source
- Coastline

Note: Map projection; WGS 84 / UTM Zone 10N.

PLATE 9-2
San Luis–Pismo Block Rupture Sources

Pacific Gas and Electric Company | DCPP SSC REPORT

10.0 MAGNITUDE DISTRIBUTION MODELS

This section provides a discussion of the alternative models used to assess the Magnitude Distribution Models (MDMs) for the rupture sources in each Rupture Model that are used to assess fault-section-specific Magnitude Frequency Distributions (MFDs) in the Diablo Canyon seismic source characterization (SSC) model.

10.1 Definition and Applicability

The MDMs describe the minimum and maximum magnitudes and relative frequency of earthquake magnitudes between the minimum and maximum that are allowed to occur on the rupture sources in each Rupture Model. The generic functional forms of the MDMs are herein called magnitude *probability density functions* (PDFs). The *magnitude-frequency distribution*, or MFD, defines the shape of the recurrence curve as it expresses the annual frequency (in yr^{-1}) of various magnitude earthquakes up to the maximum for a given rupture source or fault source. The MFD for a rupture source is calculated by combining the magnitude PDF(s) and associated bounding magnitudes (M_{min}, M_{max}, and/or characteristic magnitude, M_{char}) with the rupture source area and slip rate from the Slip Rate Allocation Model. The MFD for a fault source is calculated by aggregating all rupture-source MFDs that are located on a given fault section. The approach used to define the rupture-source MDMs and fault-source MFDs is outlined in *Section 10.2*.

10.2 Approach

The MDM for each Rupture Model is derived using the following process:

- Assessing possible fault segmentation of each rupture source.
- Evaluating lengths and areas of characteristic and maximum earthquake ruptures.
- Assigning magnitudes for characteristic and maximum ruptures based on empirical magnitude-scaling relations.
- Defining magnitude PDFs to characterize the relative size distributions of earthquakes on the rupture sources.

The magnitude PDF(s) and associated bounding magnitudes (M_{min}, M_{max}, and/or characteristic magnitude, M_{char}) is then combined with slip rates for each rupture source to create rupture source MFDs. The aggregated results from the rupture sources at specific locations on the fault sources (i.e., at a point on a specific fault section) allow creation of fault-section-specific MFDs.

Details of the methodology to develop the MDMs are provided as follows:

- *Section 10.2.1* describes the magnitude PDFs used to construct the MDMs.
- *Section 10.2.2* describes the approach used to select values for minimum (M_{min}), characteristic (M_{char}), and maximum (M_{max}) magnitudes that are required for the magnitude PDFs. This includes an assessment of fault segmentation to derive characteristic and maximum rupture areas and discussion of alternative

magnitude-scaling relations that were considered in estimating M_{char} and M_{max} values.

- *Section 10.2.3* describes the application of magnitude PDFs to rupture sources and the consequent logic tree implementations.
- *Section 10.2.4* describes the calculation of MFDs at specific points on fault sources to evaluate the Diablo Canyon SSC model and compare it to other SSC models.

10.2.1 Candidate Magnitude PDF Models

Historical and paleoseismic data are not sufficient to characterize earthquake magnitudes and rates that give rise to significant ground motions in the Diablo Canyon Power Plant (DCPP) area. In the absence of historical information, four magnitude PDFs are used in the Diablo Canyon SSC model to describe aleatory variability in magnitudes from the fault sources. These models require selection of M_{max} and/or M_{char} values to populate the magnitude PDFs. Epistemic uncertainty in M_{max} and M_{char} is incorporated through alternative logic tree values and weights.

The four magnitude PDFs used in the SSC model (truncated exponential, simplified maximum magnitude, characteristic earthquake, and WAACY) are described briefly in Table 10-1. Schematic diagrams of the magnitude PDFs are shown on Figure 10-1. The magnitude PDFs are described in slightly more detail below in *Sections 10.2.1.1 through 10.2.1.4.*

Table 10-1. Magnitude PDFs Used in the Diablo Canyon SSC Model

Magnitude PDF Name	Explanation
Truncated Exponential	From Gutenberg and Richter (1944). The magnitude PDF is a doubly truncated exponential distribution. Parameters are M_{min}, M_{max}, and *b*-value.
Simplified Maximum Magnitude	From Wesnousky et al. (1983). The magnitude PDF is a delta function with $M_{min} = M_{char} = M_{max}$.
Characteristic Earthquake	From Youngs and Coppersmith (1985). The magnitude PDF has two components: a characteristic portion and a low-magnitude exponential portion. The characteristic portion is a uniform distribution, centered on M_{char} with a half-width ΔM. Low-magnitude portion is a doubly truncated exponential distribution from M_{min} to $M_{char} - \Delta M$ and with a uniform *b*-value. M_{max} is $M_{char} + \Delta M$. Parameters are M_{min}, *b*, M_{char}, ΔM, and percent of the total moment rate in the low-magnitude tail.

Magnitude PDF Name	Explanation
WAACY	From Wooddell and Abrahamson (2013) and Abrahamson (2014) (*Appendix G*). The magnitude PDF has three components: a characteristic portion, a low-magnitude exponential portion, and a high-magnitude exponential "tail." The characteristic portion is a Gaussian distribution with a mean of M_{char}, standard deviation σ_{char}, and range from M_1 to M_2, where $M_1 = M_{char} - \Delta M$ and $M_2 = M_{char} + \sigma_{char}N_{sig}$, with N_{sig} representing a multiple of standard deviations. The low-magnitude portion fits a doubly truncated exponential distribution from M_{min} to M_1 with a slope of -*b*. The high-magnitude tail fits a doubly truncated exponential distribution from M_2 to M_{max} and a *b*-value of b_{tail}. Parameters are M_{min}, *b*, M_{char}, ΔM, σ_{char}, N_{sig}, b_{tail}, M_{max}, and percent of the total moment rate in the low-magnitude portion, F1.

10.2.1.1 Truncated Exponential Model

The truncated exponential model is characterized by a doubly truncated exponential distribution (Cornell and Vanmarcke, 1969) based on the exponential relation between earthquake frequency and magnitude noted for crustal volumes by Gutenberg and Richter (1944). A schematic representation is shown on panel (a) of Figure 10-1. The range of magnitudes is between M_{min} and M_{max}, where $M_{min} = 5.0$ and M_{max} is defined with epistemic uncertainty in the logic tree with branch values and weights. The slope of the exponential is consistent with a fixed *b*-value of 1.0 based on assessments of fault *b*-values in Page et al. (2011) and Stirling et al. (1996).

10.2.1.2 Simplified Maximum Magnitude Model

The simplified maximum magnitude model puts 100% of the moment rate on a single magnitude such that $M_{min} = M_{char} = M_{max}$. Smaller magnitudes occurring on the fault are assumed to be dependent events (mostly aftershocks; Wesnousky et al., 1983). The magnitude PDF is a delta function with a peak at $M_{char,}$ as illustrated on panel (b) of Figure 10-1. Recognizing that it is common practice in probabilistic seismic hazard analysis (PSHA) to implement the maximum moment model with uncertainty in the characteristic magnitude (e.g., as aleatory variability using a normal distribution centered on M_{char}, or as epistemic uncertainty using a three-point approximation of an equivalent normal distribution), we use the term *simplified* maximum magnitude model to emphasize that the prescribed magnitude PDF is a delta function. The simplified maximum magnitude model is used in the Diablo Canyon SSC model for complex and splay rupture sources, which represent scenario large earthquakes that involve simultaneous rupture on more than one fault plane. Each scenario earthquake consists of a pair of earthquake magnitudes (i.e., magnitudes for the primary and secondary rupture planes in a complex rupture source, or magnitudes for the main and splay rupture planes for a splay rupture source). Aleatory magnitude variability is introduced by involving more than one scenario earthquake pair, whereby the relative frequency of the scenario

earthquake pair is defined. The identification of the earthquake scenarios and their relative frequencies are discussed below in *Sections 10.3 through 10.6*.

The simplified maximum magnitude model allows for tractable bookkeeping for complex and splay rupture sources, which are defined as a series of scenario earthquakes, each with a single occurrence rate (*Section 9.3.1*).

10.2.1.3 Characteristic Earthquake Model

The characteristic earthquake model of Youngs and Coppersmith (1985) is illustrated graphically on panel (c) of Figure 10-1. The magnitude PDF has two components: a characteristic portion and a low-magnitude exponential portion. The characteristic portion of the magnitude PDF is a uniform distribution (or "boxcar") centered on M_{char} and with a half-width of ΔM. The low-magnitude portion fits a doubly truncated exponential distribution from M_{min} to $M_{char} - \Delta M$ and a slope of $-b$. The relative sizes of the exponential and boxcar portions are set by fixing the moment rate of the low-magnitude tail. For the SSC logic tree, the shape of the characteristic earthquake magnitude PDF is relatively fixed following Youngs and Coppersmith (1985) and subsequent years of model implementation in engineering practice, with $M_{min} = 5.0$, $\Delta M = 0.25$, and 6% of the total moment rate allocated to the low-magnitude tail. M_{char} is defined with epistemic uncertainty in the logic tree with branch values and weights. b is fixed to equal 1.0 in accordance with the assessments of Page et al. (2011) and Stirling et al. (1996).

10.2.1.4 WAACY Model

The WAACY model (named for authors Wooddell, Abrahamson, Acevedo-Cabrera, and Youngs) is a recently introduced magnitude PDF that combines concepts of the characteristic earthquake and truncated exponential models (*Appendix G*). It is used to characterize earthquake occurrence on sources that are too long for reasonable application of the characteristic earthquake model, and that could infrequently host earthquakes significantly larger than hypothesized characteristic events on shorter portions of the source. In the WAACY magnitude PDF, characteristic earthquakes of magnitude M_{char} occur with greater frequency than would be predicted from an exponential distribution with an M_{max} value that is based on the longest multi-segment or multi-fault ruptures that could occur on the rupture source.

The motivation for developing the WAACY magnitude PDF comes from two considerations:

1. In tectonic settings such as coastal California, multi-fault or multi-segment ruptures, even if relatively unlikely, need to be considered in SSC models for PSHA (Field et al., 2013).
2. Based on paleoseismic data, the coefficient of variation (CV), or the standard deviation divided by the mean, of surface-fault displacements at single points is significantly less than predicted from faults modeled with Gutenberg-Richter-like exponential MFDs (Hecker et al., 2013). The maximum slip-at-a-point CV

determined from Hecker et al. (2013) is used to constrain the allowable implementations of the WAACY model.

Thus the WAACY model is proposed to satisfy a need for a magnitude PDF that permits broad aleatory variability in magnitude yet remains consistent with paleoseismic data that may preclude the simpler truncated exponential magnitude distribution. While we recognize that the WAACY model contains many parameters and has not been implemented in seismic hazard analysis previously, the TI Team believes that the advantages of including it in the Diablo Canyon SSC model outweigh these disadvantages, and that it will provide better representation of aleatory and epistemic uncertainty in earthquake magnitudes that may occur on the Primary and Connected faults.

As outlined in Table 10-1, the WAACY magnitude PDF has three components: a characteristic portion, a low-magnitude exponential portion, and a high-magnitude tail. These components and the terms introduced below are shown graphically on Panel (d) of Figure 10-1. The characteristic portion is a Gaussian distribution with a mean of M_{char}, standard deviation σ_{char}, and range from M_1 to M_2, where $M_1 = M_{char} - \Delta M$ and $M_2 = M_{char} + \sigma_{char}N_{sig}$, with N_{sig} representing a multiple of standard deviations. The low-magnitude portion fits a doubly truncated exponential distribution from M_{min} to M_1 and a slope of -*b*. The high-magnitude tail fits a doubly truncated exponential distribution from M_2 to M_{max} with a *b*-value of b_{tail}.

The parameters are M_{min}, *b*, M_{char}, ΔM, σ_{char}, N_{sig}, b_{tail}, M_{max}, and F1 (Table 10-1). For the SSC logic tree, certain parameters are fixed that reflect standard of practice for earthquake engineering or have been shown to be relatively insensitive to the CV constraint or to hazard (*Appendix G*). Simplified parameters and their values are M_{min} = 5.0, b = 1.0, ΔM = 0.25, σ_{char} = 0.2, and N_{sig} = 1.5.

The WAACY magnitude PDF is designed to incorporate a range of large magnitudes (i.e., those between M_{char} and M_{max}) while also adhering to the constraint that the resulting MFD predicts slip-at-a-point values that have a CV equal to or less than 0.55 (Hecker et al., 2013; *Appendix G*). As such, only certain combinations of M_{char}, M_{max}, b_{tail}, and F1 are permissible. In the SSC model, the logic tree values and weights of the non-fixed WAACY parameters b_{tail} and F1, and their correlations with M_{char} and M_{max} combinations, are shown on Figure 10-2 and described in *Appendix G*. The justification for using the WAACY model is presented in *Section 10.2.3*, and the M_{char} and M_{max} combinations defined for the rupture sources are presented in *Sections 10.3 through 10.6*.

10.2.2 Selection of Values for Characteristic and Maximum Magnitudes

This section describes the approach to selecting values for M_{char} and/or M_{max} that are required for applying the magnitude PDFs to rupture sources.

10.2.2.1 Segmentation Concepts

The term *fault segment* has been defined in various ways, depending on the context in which it is used. For SSC, the term has traditionally been used to describe a length or section of a fault believed to rupture in its entirety or with other segments in a single event (e.g., Schwartz and Coppersmith, 1984, 1986). Segmentation refers to dividing a fault into expected rupture extents based on geologic, mechanical, or dynamic considerations. This approach has been employed by many recent PSHAs, including UCERF2 (Field et al., 2008) and previous studies for the DCPP (PG&E, 1988, 2011).

The idea that future ruptures will be restricted to fault segments that can be identified in advance by geologists has been questioned by many researchers (e.g., Kagan, 1993; Jackson and Kagan, 2011). Others have argued that fault segmentation is not an appropriate model for describing earthquake behavior (e.g., Hardebeck, 2012a, presentation at Workshop 2). Strict segmentation is not observed in historic ground-rupturing earthquakes. Several recent earthquakes ruptured across boundaries that many geologists would likely consider to be segment boundaries (e.g., 1992 **M** 7.3 Landers, California; 2002 **M** 7.9 Denali, Alaska; 2010 **M** 7.2 El Mayor Cucapah, Mexico, described in *Section 9.2.1.5*). Because of these concerns, the current trend in seismic hazard assessment is toward "relaxing" segment boundaries and allowing multi-segment and multi-fault ruptures. The UCERF3 model (Field et al., 2013) relaxed segment boundaries to a greater degree than previous models and incorporated multi-fault rupture under modest continuity requirements, including across gaps between faults of less than 5 km.

Despite concerns about its validity as a model for earthquake rupture behavior, fault segmentation remains within the range of the technically defensible models for estimating the dimensions of future ruptures (e.g., dePolo, 2012; Schwartz, 2012), especially on faults with paleoseismic data helping to characterize past rupture behavior. The concept that earthquake ruptures terminate at certain locations along a fault more often than at a random location along a fault is supported by recent empirical studies and dynamic models.

Detailed studies of historical earthquake surface ruptures have shown that ruptures preferentially terminate at geometric irregularities along a fault trace. Based on analysis of strike-slip earthquakes, Wesnousky (2006, 2008) found that surface rupture endpoints commonly occur at fault step-overs greater than 1 km wide. Of the 21 ruptures he studies, 16, or 76%, had at least one endpoint at a step-over, and 7, or 33%, had both ends at step-overs. Only 5, or 24%, were not at all associated with a step-over. In other words, over half of the rupture endpoints (23 of 42) occurred at locations that could have been identified by geologists before the earthquakes. Similar relationships are found in smaller samples of reverse and normal faults (Biasi, Parsons, et al., 2013).

Dynamic rupture models (e.g., Lozos et al., 2011) suggest that wider step-overs are more likely to arrest rupture than narrower ones. This prediction is supported to an extent by empirical data, which include no step-overs wider than 4 km (Wesnousky, 2008) or 5 km (Lettis et al., 2002), although Wesnousky (2008) found that among step-overs less than 4

km wide, there was no relationship between step-over width and likelihood of arresting rupture. The results of dynamic models also suggest that fault bends tend to arrest ruptures if they rotate a fault out of a favored alignment relative to the regional stress direction (Lozos et al., 2011). Trend changes affect the rupture energy balance, with kinetic energy during rupture lost to extra friction, rock damage, dilational and compressional changes in topography, and redistribution of elastic energy (Biasi, 2012).

In the Diablo Canyon SSC model, the geometric complexities of a fault are used to estimate rupture lengths, as empirical data suggest that these types of features are commonly associated with rupture terminations. These complexities are used to define *soft segment boundaries*, a term we define herein as short reaches along a fault where ruptures are more likely to terminate than elsewhere along the fault. Where they are more pronounced (i.e., where fault traces bend more abruptly, other active faults intersect, or evidence for a change in uplift or subsidence rate is localized), the soft segment boundaries are considered to be *stronger* (i.e., more likely to terminate ruptures). The relative strength or magnitude of such features is used as one criterion to define two tiers of soft-segment boundaries, as described below in *Section 10.2.2.2*. These soft segment boundaries are used to define rupture lengths to characterize alternative candidate M_{char} and M_{max} values.

Uncertainty in the validity of the segmentation concept, and/or its applicability to the Primary and Connected faults in the Diablo Canyon vicinity, is incorporated into the SSC model in the following ways:

- Using the truncated exponential magnitude PDF, which does not consider characteristic rupture lengths.
- Considering the epistemic uncertainty in M_{max} values. Each Rupture Model includes rupture sources with at least some weight on M_{max} values that bypass essentially all proposed segment boundaries (i.e., there is some probability of ruptures involving one or more of the Primary fault sources that are linked with rupture of the Hosgri, San Gregorio and San Andreas faults to the Mendocino Triple Junction)
- Allowing earthquake magnitudes that result in rupture areas less than the maximum rupture source area to float along the rupture source.
- Including alternative rupture sources in each Rupture Model, which contributes aleatory variability in rupture length and magnitude.

We note that the representation of faults as segmented or not is not the end goal of the SSC, but rather a device with which to develop a suite of credible rupture magnitudes, rates, and configurations for ground motion estimation.

10.2.2.2 Selection of Characteristic and Maximum Rupture Lengths

Characteristic and maximum earthquake magnitudes are estimated for each rupture source based on consideration of geometric length scales informed by fault activity, geometry, and branching relationships. This section describes the soft segment

boundaries that are used to define these length scales. Epistemic uncertainty in M_{char} and M_{max} is incorporated into the logic tree by considering a variety of length scales.

As this is a site-specific SSC model, the motivation for estimating alternative M_{char} and M_{max} values on the rupture sources is to capture the uncertainty in earthquake magnitudes at close distances to the DCPP that result in substantially different ground motions at the plant. Therefore, length scales between soft segment boundaries used to estimate alternative values for M_{max} and M_{char} focus on the reaches of the rupture sources adjacent to the DCPP. Soft segment boundaries defined along the rupture sources farther from the DCPP are more widely spaced because increments of magnitude correspond to length increments of tens, then hundreds, of kilometers. For example, there is little value in exploring differences between proposed segments of 400 km and 450 km because the magnitudes will be essentially equal.

Features along rupture sources are considered potential soft segment boundaries where pronounced fault geometric and mechanical complexities occur, or where pronounced slip rate changes are known or suspected. Soft segment boundaries are classified into tiers based on the magnitude of the feature (e.g., width of the step-over, sharpness of fault bend) and geologic evidence for uplift or subsidence localized around the complexity.

Two tiers of soft segment boundaries are considered. “First-tier” segment boundaries are used to define epistemic alternatives in M_{max}. They are also used to constrain an upper bound for epistemic uncertainty in M_{char}. First-tier segment boundaries are characterized by significant known or suspected changes in fault slip rate, as well as by the following mechanical qualities:

- The fault trace bends sharply.
- The trace has complexity, such as multiple secondary structures at high angles to the primary structure.
- There is geologic evidence for subsidence or uplift at a scale large enough to suggest a mechanical disruption in the fault plane at seismogenic depths.
- The scale of bend or step-over is likely to affect the mechanics of rupture at seismogenic depths.
- Faults join the main trace in a way that suggests ongoing disruption of the main fault.
- Dip-slip focal mechanisms are concentrated in a short reach of a strike-slip fault.

An example of a first-tier segment boundary is the intersection of the San Simeon and Oceanic faults north of San Simeon Point (Figure 10-3). The Oceanic fault is an active reverse- to oblique-slip fault that was the source of the 2003 **M** 6.5 San Simeon earthquake (McLaren et al., 2008). The slip rate of the Oceanic fault characterized by UCERF3 is 0.7 mm/yr (Field et al., 2013), which represents a significant fraction of the approximately 1–3 mm/yr slip rate of the San Simeon fault (*Section 8.3.1*). Numerous Quaternary faults splay westward from the main trace of the San Simeon fault near where the surface trace of the Oceanic fault merges from the east (Figure 10-3). The main trace of the San Simeon fault also jogs sharply to the left, suggesting the presence of a restraining step-over approximately 1–2 km wide. Geomorphic assessment of the region

around this fault intersection suggests that tectonic uplift may be localized around this restraining step-over.

Detailed mapping of warped marine terraces directly south of this intersection documents a relatively higher uplift rate localized adjacent to the San Simeon fault that gradually decreases to the west. Hanson and Lettis (1994) interpreted these warped marine terraces as evidence for the potential presence of blind southwest-vergent reverse faults that splay from the San Simeon fault. The rugged topography of the Santa Lucia Range to the north of the Oceanic fault and east of the San Simeon fault suggests active tectonic uplift and contrasts sharply with the relatively subdued topography of the region to the west. The 1991 M_L 5.1 Ragged Point earthquake directly north of this fault intersection had a reverse to reverse-oblique focal mechanism (McLaren and Savage, 2001; Hardebeck, 2010), providing additional evidence to suggest the presence of a restraining step that affects the San Simeon fault at seismogenic depth.

"Second-tier" segment boundaries are used to define alternative length scales to describe epistemic uncertainty in M_{char}, and to define scenario magnitudes for complex and splay rupture sources. For many characteristic rupture sources, the maximum earthquake magnitude allowed on the rupture source is defined by a second-tier segment boundary. However, other rupture sources allow ruptures to pass the same boundaries. Second-tier boundaries are associated with many of the same types of features as first-tier boundaries, but the features are less well developed. Second-tier segment boundaries are characterized by a minor change in fault slip rate and/or by the following mechanical qualities:

- Fault bends are less pronounced than with first-tier boundaries.
- The fault or fault zone may have complexity, but individual traces are generally approximately on trend with the main fault trace.
- Fault bends and step-overs are associated only with minor topographic expression, or localized evidence for uplift or subsidence that occurs at a small scale.
- The activity of faults intersecting the main trace is low compared to that of the main trace itself.

Soft segment boundaries do not predict the locations of rupture terminations precisely. Changes in fault structures observed at more detailed mapping scales commonly are gradational and many of the features used to define a segment boundary occur over a finite distance along a fault, or within a volume around a fault intersection, bend, or step-over. These observations suggest that although a segment boundary may function to arrest rupture, there is uncertainty in precisely where the rupture will terminate.

As described above, because the Diablo Canyon SSC model is a site-specific assessment, the primary goal of the MDM is to characterize the distribution of earthquake magnitudes that may occur along the reaches of fault sources nearest the DCPP. The approximate locations of soft segment boundaries are used to estimate characteristic and maximum rupture lengths. However, in order to account for uncertainty in the precise locations and sizes of potential segment boundaries, earthquake ruptures are allowed to float freely along characteristic and linked rupture sources when they rupture a length that is shorter

than the full length of the rupture source. For complex and splay rupture sources, aleatory uncertainty in earthquake magnitude is based on multiple estimates of rupture lengths for both primary (main) and secondary (splay) ruptures that "grow" outward from the point where the two faults join.

Potential soft segment boundaries considered in the Diablo Canyon SSC model for the purposes of estimating M_{char} or M_{max}, or both are described below in *Section 10.3* for the Hosgri magnitude model, *Section 10.4* for the Outward-Vergent magnitude model, *Section 10.5* for the Southwest-Vergent magnitude model, and *Section 10.6* for the Northeast-Vergent magnitude model.

10.2.2.3 Magnitude-Area Relations

Magnitudes of characteristic and maximum ruptures are estimated using empirical magnitude-area scaling relations, a standard method for SSC studies (e.g., PG&E, 1988; WGCEP, 2003; Field et al., 2008, 2013). The TI Team's general approach to capture magnitude uncertainty, given the lack of historical and paleoseismic data, is to characterize uncertainty in M_{char} and M_{max} through a wide range of alternative rupture lengths instead of through a comprehensive selection of alternative magnitude-scaling relations that are approximately equivalent. The range of magnitudes predicted by any single magnitude-scaling relation for the alternative rupture lengths considered in the Diablo Canyon SSC model is much greater than the range of magnitudes predicted for any single rupture length (or area) from a suite of magnitude-scaling relations.

The TI Team considered various magnitude-scaling relations during the evaluation phase of the Diablo Canyon SSC study, including scaling relations for both magnitude length and magnitude area developed for a variety of slip types and tectonic environments (e.g., Wells and Coppersmith, 1994; Hanks and Bakun, 2002, 2008, 2014; the Ellsworth "B" relation of the WGCEP, 2003; Manighetti et al., 2007; Wesnousky, 2008; Shaw, 2009, 2013; Leonard, 2010; Yen and Ma, 2011; Stirling et al., 2013). An initial decision was made to consider only magnitude-area relations, and to exclude magnitude-length relations. The decision was based on two considerations:

1. There is a more direct physical scaling between seismic moment and rupture area than between seismic moment and rupture length.
2. Magnitude-area relations provide more direct application for the PSHA code used to model ground motions at the DCPP site, which develops MFDs and source-to-site distances based on total rupture source area and magnitude-area relations.

Figure 10-4 shows alternative magnitude-area relations considered for the Diablo Canyon SSC model, divided into data and relations developed for strike-slip environments (panel a) and data and relations developed for reverse or reverse oblique environments (panel b). Both slip types are relevant to the Diablo Canyon SSC model; although the greatest contributor to hazard at the DCPP is the strike-slip Hosgri fault, contributions from moderate- to high-angle reverse to reverse oblique faults are not insignificant as shown in *Section 14.2*.

For the strike-slip relations (Figure 10-4a), the data set from Hanks and Bakun (2008) is shown along with the following relations:

- Ellsworth "B" from the WGCEP (2003), abbreviated as EB03.
- Hanks and Bakun (2002, 2008), abbreviated as HB02 and HB08.
- Hanks and Bakun (2014), abbreviated as HB14.
- Shaw (2009) as implemented by Shaw (2013), abbreviated as S09′.
- Wells and Coppersmith (1994) strike-slip earthquake subset, abbreviated as WC94, ss.

Of the candidate models, the EB03 relation stands apart in the magnitude range $5 \leq \mathbf{M} \leq 6.8$ because of its intercept value of 4.2 instead of approximately 4 used by the others (specifically 3.98 per WC94 and HB02). Although the TI Team acknowledges the rationale provided by the WGCEP (2003)—that aftershock patterns used to estimate rupture area for most earthquakes in the database may systematically overestimate the true rupture areas, especially for the lower magnitude ranges—we reject the EB03 relation for use in the Diablo Canyon SSC because it does not provide a good estimate of the data mean for the currently available strike-slip earthquakes in the range $\mathbf{M} \leq 6.8$. We note that there is more variability in the Next Generation Attenuation West 2 "flat file" (abbreviated as NGA-W2 on Figure 10-4; Ancheta et al., 2013), which is the basis for the current ground-motion-prediction equations, than either the HB08 magnitude-area or the YM 11 data sets. Although not essential to our model selection, we appreciate the inherent consistency between magnitude-area relations used for estimating earthquake sizes on fault sources and source dimensions associated with earthquake magnitudes used to model ground motions. The misfit of the EB03 relation to earthquakes in the lower magnitude range is especially relevant for the DCPP, as earthquakes in the range $6 \leq \mathbf{M} \leq 7$ at close distances dominate the ground motion hazard (*Chapter 14*).

The log-linear WC94 relation deviates from the other candidate models at approximately **M** 7.3, above which the mean prediction underlies all but one event (Figure 10-4a). Although the underestimation of magnitude in the high magnitude range is less relevant for hazard at the DCPP, it nevertheless is rejected for use in the SSC logic tree. Of the remaining candidate models, the TI Team judged that the recently published bilinear HB14 relation provides a reasonable visual (and statistical) fit to the available data at all magnitude ranges, and lies between the other models with acceptable fits (HB02, HB08, and S09′) for the largest rupture dimensions considered in the SSC model. Based on the minimal differences in predicted magnitude and the other approaches to including uncertainty in magnitude in the SSC model (described below), we adopt the HB14 relation with full weight for estimating magnitudes of strike-slip rupture sources. The bilinear HB14 relation is

$$\mathbf{M} = \log_{10}A + 3.98,\ A < 537\ \text{km}^2 \qquad (10\text{-}1a)$$

$$\mathbf{M} = 5/4\ \log_{10}A + 3.30,\ A \geq 537\ \text{km}^2 \qquad (10\text{-}1b)$$

For the reverse- and reverse-oblique-slip relations (Figure 10-4b), the data sets from the NGA-W2 flat file (reverse and reverse oblique events; Ancheta et al., 2013) and Yen and Ma (2011; reverse events) are shown along with the following relations:

- Hanks and Bakun (2014; HB14).
- Leonard (2010) dip-slip relation, abbreviated as L10.
- The New Zealand relation used by Stirling et al. (2008) and described by Stirling et al. (2013), abbreviated as NZ08.
- Wells and Coppersmith (1994) reverse earthquake relation, abbreviated as WC94,r.
- Yen and Ma (2011) dip-slip relation, abbreviated as YM11.

Of the candidate models, the NZ08 relation is consistently higher than other relations across all magnitude ranges, and especially in the **M** > 6 range (Figure 10-4b). It also plots above the data mean based on visual inspection. The NZ08 model, which is fit to a data set with rupture dimensions derived from seismic waveform (duration) data and assumed aspect ratios rather than aftershock dimensions (Webb et al., 1999), may not be directly comparable to most of the data in the NGA West2 flat file. Similarly, the YM11 relation is fit to data with an "effective" rupture area (their A_e) based on inspection of finite fault inversion results rather than aftershock dimensions (Yen and Ma, 2011). Inspection of the YM11 data points and log-linear fit compared to the NGA-W2 data points for reverse and reverse oblique earthquakes suggests there may be a systematic difference due to methodology that could render these two data sets incompatible.

On the other hand, we note that the L10 and HB14 relations provide reasonably good fits to the NGA-W2 data (Figure 10-4b), particularly over the interval relevant to the Diablo Canyon SSC model (i.e., maximum dimensions of reverse and reverse-oblique rupture sources on the order of $A \leq 2{,}000$ km^2). Because the differences in predicted magnitude between the L10 and HB14 relations are minimal, and based on the other aspects of our approach to include uncertainty in magnitude in the SSC model (described below), the TI Team also adopts the HB14 relation with full weight for estimating magnitudes of reverse and reverse-oblique rupture sources (i.e., Equation 10-1). Our selection of the HB14 magnitude-area relation with full weight for use applied to all slip types in the SSC model is based on the simplicity in using a single model, its goodness of fit to a data set that is most compatible with the ground motion model (the NGA-W2 data), and the lack of magnitude-scaling precision required in our model approach. Our rejection of alternative magnitude-scaling relations is not a commentary on the authors' arguments for the appropriate physics of magnitude scaling (e.g., Webb et al., 1999; Shaw, 2009; Yen and Ma, 2011).

Implementation of the HB14 magnitude-area relation to derive M_{char} and M_{max} values is straightforward. Characteristic earthquake magnitudes are based on the characteristic rupture lengths times the maximum fault widths, assuming a 12 km maximum rupture depth inferred for all fault sources from analysis of the D90 or D95 values from historical microseismicity and consideration of the estimated depth to the top of the subducted slab (*Section 7.2.1*). From these rupture areas, the M_{char} values are selected from Equation (10-

1) and rounded to the nearest tenth of a magnitude unit. Maximum magnitudes are based on the maximum rupture lengths times the maximum fault widths, assuming a 12 km maximum rupture depth for the San Luis–Pismo block (SLPB) fault sections and a potential greater 15 km rupture depth for some large-magnitude Hosgri fault ruptures as outlined in *Section 7.2.1*. A maximum depth of 15 km is used for all Hosgri M_{max} ruptures or scenario ruptures where the Hosgri portions have magnitudes greater than **M** 7.4, which exceeds the highest Hosgri M_{char} earthquake. From these estimated maximum rupture areas, the M_{max} values are selected from Equation (10-1), rounded to the nearest tenth, and increased by 0.1 magnitude unit. The addition of the 0.1 magnitude unit from the best-estimate magnitude predicted from HB14 is to account for aleatory variability in M_{max} given the rupture dimension and given that M_{max} represents the largest possible earthquake to occur on a given rupture source. The 0.1 magnitude unit addition is less than typical standard deviations of the data reported for regressions (e.g., Wells and Coppersmith, 1994), but the TI team considers this simplification to be justified by sensitivity analyses presented at the SSHAC Workshop 2 (Gregor, 2012), which show that uncertainties in fault length (which are direct proxies for M_{max} in the analyses) have very small impacts on the total hazard at the DCPP for the ranges of lengths considered in the Diablo Canyon SSC model. The TI Team considers this approach to be appropriate given the broad sampling of aleatory variability in magnitude achieved through the use of rupture models, and the broad sampling of epistemic uncertainty regarding the correct maximum rupture length to use.

10.2.3 Application of Magnitude PDFs to Rupture Sources

Each rupture source in the Rupture Models is assigned to one of three rupture-source categories that defines the magnitude PDF(s) to be used in the hazard calculations. These categories are shown schematically on Figure 10-5. Table 10-2 shows the categories, relevant magnitude PDFs, and branch weights.

Table 10-2. Rupture-Source Categories and Magnitude PDFs

Rupture-Source Magnitude PDF Category	Magnitude PDF Branches and Weights
A	Characteristic Earthquake [1.0]
B	WAACY [0.8] Truncated Exponential [0.2]
C	Simplified maximum magnitude [1.0]

Characteristic and linked rupture sources with no fundamental difference in scale between characteristic and maximum rupture lengths are classified as Category A (Table 10-2). For these rupture sources, relatively large earthquakes (i.e., characteristic earthquakes) that rupture nearly the entire length of the rupture source are interpreted to occur with greater frequency than would be predicted by an exponential MFD. In the Diablo Canyon SSC model, these rupture sources range from approximately 15 km to nearly 100 km in length. For Category A rupture sources, full weight is given to the characteristic earthquake magnitude PDF. The 0.5 magnitude unit width of the

characteristic "boxcar" represents aleatory variability of the characteristic earthquake magnitude (Figure 10-1 and *Section 10.2.1.3*). The TI Team considers this aleatory variability to represent a combination of the following:

- Variability in estimated rupture area of the characteristic earthquake, given the approximate definitions of the soft segmentation points used to define the characteristic ruptures.
- Magnitude variability, given the estimated rupture area.

The uniform distribution for the characteristic portion of the magnitude PDF shown on Figure 10-1 follows the original shape defined by the authors (Youngs and Coppersmith, 1985). The TI Team selected this boxcar shape, instead of a Gaussian distribution for the characteristic portion, which was used by the WGCEP (2003) and has been adopted for the WAACY model, because the boxcar shape has been used in standard engineering practice since publication of the model in 1985. In addition, the TI Team acknowledges the uncertainty in estimates of the magnitude of characteristic earthquakes, considering the absence of historical or paleoseismic events and lack of clearly defined segment boundaries on the Primary and Connected faults in the DCPP area. Thus the TI Team judges that a central M_{char} value is not appreciably preferred over magnitudes slightly above or below the central value. The adoption of the boxcar is representative of this additional uncertainty and is motivated by practical purposes for hazard analysis. It is not, meant to be a strict endorsement of the implied earthquake phenomenon of the boxcar, whereby the M_{max} value occurs at an equal frequency as the best-estimate M_{char} value, but a slightly greater magnitude (M_{max} + 0.1) does not occur.

No weight is given to the truncated exponential magnitude PDF for Category A rupture sources based on consideration of the following:

- Results of other hazard studies that demonstrated observed seismicity within narrow corridors around fault sources similar to the Type A rupture sources in the Diablo Canyon SSC model does not provide a reasonable fit with earthquake frequencies predicted from fault slip rates using the exponential model (e.g., Youngs et al., 1992: PNNL, 2014).
- Analysis of fault-specific data that shows that the truncated exponential distribution does not agree with paleoseismic observations of slip at a point (Hecker et al., 2013).

The TI Team judged that the truncated exponential magnitude PDF relation for faults is most compatible with the historical recognition in California of the connectivity of faults and the potential for multi-segment and multi-fault ruptures that yield rare maximum earthquakes that greatly exceed the magnitudes of relatively more frequent hypothesized "characteristic" ruptures.

Category B comprises linked rupture sources with length scales under consideration for M_{max} values that are appreciably longer than length scales under consideration for M_{char} values (Table 10-2). In other words, Category B rupture sources are recognized as having a maximum rupture length that is several multiples of the longest hypothesized

characteristic earthquake rupture length. In the Diablo Canyon SSC model, these rupture sources are longer than approximately 100 km and range to more than 700 km long. Characteristic rupture lengths hypothesized for these rupture sources range up to approximately 130 km (*Sections 10.3 through 10.6*). Magnitude distributions for Category B rupture sources are defined by a combination of the truncated exponential magnitude PDF (weight of 0.2) and the WAACY magnitude PDF (weight of 0.8). The greater weight given to the WAACY model than to the exponential model is due to the finding by Hecker et al. (2013) that slip-at-a point paleoseismic data have coefficients of variation that appear incompatible with the truncated exponential relation. Furthermore, the TI Team has determined that the WAACY model provides a reasonable means of constraining the relative rates of the largest multi-fault earthquake ruptures and more frequent characteristic ruptures. The logic tree implementation of the WAACY magnitude PDF is described more completely in *Appendix G, Section 10.2.1.4* and on Figure 10-2. The weight given to the truncated exponential magnitude PDF for Category B rupture sources is based on its acceptance as a method for characterizing faults in PSHA (Cornell and Vanmarcke, 1969) and the arguments that it is a simple, two-parameter model that captures a broad range of magnitudes on long rupture sources and that cannot be rejected by, and is arguably compatible with, paleoseismic and seismicity data near active faults (Kagan, 1993; Parsons and Geist, 2009; Page et al., 2011). However, as noted by Field et al. (2014), the results of the grand inversion used in UCERF3 have demonstrated challenges with the Gutenberg-Richter hypothesis for individual faults.

Category C comprises splay and complex rupture sources. Category C sources give full weight to the simplified maximum magnitude model (Table 10-2). Category C rupture sources are characterized differently from Category A and B rupture sources in that epistemic uncertainty in magnitudes is not explicitly modeled. The complex and splay ruptures are interpreted to be relatively large and rare scenario events compared to the range of earthquake sizes considered to occur on other rupture sources, as represented by the low magnitude tail in the characteristic earthquake, WAACY, and truncated exponential MFDs. Category C sources have one or more hypothesized scenarios involving single magnitudes for the primary and secondary rupture planes (for complex rupture sources) or the main and splay rupture planes (for splay rupture sources; Figure 10-5c). Aleatory magnitude variability is introduced by involving more than one scenario earthquake pair, whereby the relative frequency of the scenario earthquake pair is defined. The earthquake scenarios and their relative frequencies are discussed below in *Sections 10.3 through 10.6*.

10.2.4 Model Evaluation—MFDs at Points

In this section we describe how rupture source magnitude PDFs are combined into net activity rates (and MFDs) at points on SSC faults. Activity rates at points are of interest for two reasons. First, they provide estimates of earthquake magnitudes and their rates at the closest distances to the site, because they represent the subset of events with the least attenuated ground motions. Second, they provide a method to evaluate the total rate of

earthquakes occurring on a network of rupture sources. Given the Rupture Model construct, whereby rupture sources are not confined to single faults or fault systems, the activity rates at points on the fault network provide a way to understand the combined effect of many rupture source "layers" on a portion of a fault.

A comparable strategy to evaluate the grand inversion results is used by the UCERF3 model (Field et al., 2013) with the "participation MFDs." Faults interconnect in the Diablo Canyon SSC and in UCERF3 models in such a way that there is no longer a simple meaning to the idea of a fault-source MFD. Slip rates and MFDs vary along fault sources, and do not generally follow any simple fault-source MFD functional form. By converting SSC rupture-source MFDs to fault source MFDs at points, results can be compared to equivalent "participation rate" estimates from UCERF3.

10.2.4.1 Estimating Fault Activity at Points

As described in *Section 10.2.3*, each rupture source is assigned a magnitude PDF category (Table 10-2) corresponding to a recognized model of earthquake magnitude distribution on a fault. When combined with rupture-source slip rate, the rupture source activity rate, or MFD, can be calculated. The actual activity rate at a given point on a fault source is the combined rate of all rupture sources that include that point. Rupture-source MFDs cannot be summed directly because the earthquakes they characterize are considered to float along the rupture source (i.e., they occur up and down the source), and different rupture sources include different combinations of fault sections. Only a fraction of earthquakes represented by rupture-source MFDs involve the point of interest. On the other hand, rupture-source MFDs reduced to contributions at a point can be summed to calculate the earthquake rate of the fault source at the point.

10.2.4.2 Geometric Reduction Approach

To estimate the fraction of events in a rupture-source MFD that pass a given point, we must make some simplifying assumptions. First, we assume that earthquakes on linked and characteristic rupture sources occur randomly within the source (i.e., they float, as described in *Section 10.2.2.2*). This provides a geometric basis for the reduction and avoids stronger assumptions about segmentation or relative frequency. Second, we assume that earthquake rupture length L is a known function of magnitude and source downdip width W. We use the HB14 magnitude-area relation (Equation 10-1), where the rupture area $A = L*W$. $N_S(L)$ will mean the rate of ruptures of length L for the source as a whole, and $N_X(L)$ will refer to the rate that involve an observer at point X. If L_S is the length of a generic fault source, L/L_S is the fraction of the source occupied by an earthquake rupture of length L, and $(1–L/Ls)$ is the fraction of the fault source not involved in the event. Under this simplified rupture and source geometry, $N_S(L)$ is reduced by the factor $(1-L/L_S)$ to obtain $N_X(L)$.

This approximation overestimates the reduction when L is greater than the distance from the observation point to the end of the fault. Let the observation point X be a given point in the range $0 \leq x \leq L_S$, x increasing to the right, with $x = 0$ coinciding with the left end of

the source. Length $R_l = \{X\text{-}L, \text{ if } L < X; \text{ and } 0 \text{ otherwise}\}$ is the length to the left of X that cannot be spanned by a rupture of length L. Length $R_r = \{L_S - (X+L) \text{ if } L_S > (X+L); \text{ and } 0 \text{ otherwise}\}$ is the length in excess of L to the right of X. The fraction of the fault source where rupture L can occur on a source of total length L_S without passing point X is the geometric reduction rate G_r:

$$G_r = (R_l + R_r) / L_S \tag{10-2}$$

Gr is a reduction in the sense of reducing the MFD at X by the fraction that could have occurred up or down the fault without involving X. Numerically the number of events of length L observed at X is related to the total by

$$N_X(L) = N_S(L)*(1 - G_r) \tag{10-3}$$

For example, if a fault source is 100 km long and the observation point is at X = 80 km, then a rupture 10 km could occur on most of the source without passing X. R_l =70 km and R_r = 10 km, and $G_r = (R_l + R_r)/L_S$ = 0.8. If $L \geq 20$ km, $R_r = 0$, and there is no place to the right of X where the rupture would fit. For $L \geq 80$ km, the rupture will not fit on either side of X and thus cannot occur on the source without involving the observation point. $R_r = R_l = 0$, $G_r = 0$, and $N_X(L) = N_S(L)$.

Figure 10-6 shows the rate reduction $G_r(L)$ for two points located on a 400 km long fault source. For the case $X = 40$ km from the end (in red), ruptures $L<40$ km can occur on either side of X. For ruptures L ≥ 40 km long and $M \geq 6.7$, $R_l = 0$.

This changes the rate of decrease in G_r and causes an inflection point in the plot. An observation point at $X = 100$ km from the end (in blue) shows a change in rate reduction near M 7.2 (corresponding to a rupture 100 km by 12 km). A second inflection point in Gr for $X = 100$ occurs near M 7.8; this break corresponds to $L = 300$ km, beyond which $G_r = 0$.

The geometric reduction affects the four magnitude PDF shapes differently. This point is developed on Figure 10-7. On these plots, $N_S(L)$ is shown in red, $N_X(L)$ is shown in blue, both on a logarithmic scale, $X = 40$ km and $L_S = 400$ km. As mentioned above, **M** is an implicit function of L. The exponential MFD with a b value of 1.0 and slip rate of 1 mm/yr on Figure 10-7a brings out a perhaps unexpected relationship between $N_S(L)$ and $N_X(L)$. For magnitudes with $L < 40$ km, the geometric reduction rate exactly matches the exponential decrease in $N_S(L)$. This match occurs because of the exponential relationship between magnitude and moment, which depends linearly on L. The result is that as long as there is room for L on both sides of X the magnitude-frequency distribution at X will be uniform. For longer ruptures the reduction rate decreases, and relatively more of the earthquake ruptures pass the observation point. This causes a gentle downward deflection in the point MFD for larger magnitudes. A second downward deflection occurs when ruptures exceed 360 km and $G_r = 0$ for longer ruptures.

The simplified maximum magnitude MFD with a slip rate of 1 mm/yr (Figure 10-7b) does not have a range of magnitudes, and therefore follows a different reduction. Specifically, the reduction is zero if the observation point is inside the rupture, and 1.0 if

it is not. On Figure 10-7c a characteristic MFD is considered with a slip rate of 1 mm/yr. The exponential portion of the distribution reduces as described for Figure 10-7a, including the small downward deflection as ruptures exceed 40 km in length. The flat characteristic portion of $N_S(L)$ maps to a relative increase in frequency in $N_X(L)$. The resulting point MFD has the property that the most likely event is also the largest. This can be understood by reference to the flat portion of the input distribution. Among equally frequent characteristic events, the largest will also be the longest, and thus the most likely to include the observation point. The WAACY MFD with a slip rate of 1 mm/yr observed at a point (Figure 10-7d) is a predictable hybrid, with an initial flat magnitude distribution, an increase across the characteristic "hump," then a decrease in the high-magnitude tail. Comparable transformations of fault MFDs to point MFDs for the truncated exponential and characteristic earthquake magnitude PDFs are presented by Hecker et al. (2013).

A second adjustment must be applied to each rupture-source MFD so that the total displacement at the observation point matches the assigned rupture-source slip rate. The rate of events times the displacement per event has to account for all of the slip rate in the rupture source if all the slip rate is seismogenic. This adjustment has the effect of raising or lowering the entire MFDs. Adjusted rates $N_X(L)$ at points are then summed across all rupture sources that pass X to obtain the total MFDs predicted by the SSC source model.

For final comparisons we add one further complexity by summing adjusted source MFDs across their respective logic tree weights for input parameters. The results are discussed in *Section 10.7*.

10.3 Hosgri Magnitude Distribution Model

This section presents the TI Team's assessment of the MDM for the Hosgri Rupture Model, which proceeds as follows:

1. We describe the potential segment boundaries that are used to calculate rupture lengths and alternative estimates of key magnitudes, including M_{char} and M_{max} for characteristic and linked rupture sources, and scenario magnitudes for complex and splay rupture sources.
2. We assign rupture source categories to characteristic and linked rupture sources and we represent epistemic uncertainty by considering alternative values and weights for M_{char} and M_{max} that are required to define the magnitude PDFs.
3. We present earthquake scenario magnitudes and frequencies for complex and splay rupture sources.

Table 10-3 provides potential segment boundaries used to estimate characteristic and maximum rupture lengths in the Hosgri MDM.

Table 10-3. Segment Boundaries Used in the Hosgri Magnitude Distribution Model

Segment Boundary*	Tier	Rupture Sources	Explanation

Segment Boundary*	Tier	Rupture Sources	Explanation
SA	First	H-01, H-02, H-03, H-05, H-06, H-07	North end of the San Andreas fault at the Mendocino Triple Junction.
SA, GN	First	H-01, H-02, H-03, H-05, H-06, H-07	Bolinas: Junction of the San Gregorio and San Andreas faults: marked slip rate change between the San Andreas and San Gregorio faults, actively subsiding basin between the faults (Bruns et al., 2002; Ryan et al., 2008).
GS, SN	First	H-01, H-02, H-03, H-05, H-06, H-07	Point Sur: Left-restraining step-over of 1–4 km (Dickinson et al., 2004) near junction of active Quaternary faults that branch east of the San Gregorio fault (Jennings and Bryant, 2010).
SN, SI	First	H-01, H-02, H-03, H-05, H-06, H-07	San Simeon: Junction of the San Simeon and Oceanic faults associated with a left-restraining step-over of 1–2 km, localized uplift, and occurrence of reverse focal mechanisms adjacent to the strike-slip fault (see references cited in *Section 10.2.2.2*).
HN, HD	Second	H-01, H-02, H-03, H-05, H-06, H-07	Junction of the Hosgri fault with the Los Osos fault to the east and the western reach of the Hosgri fault to the west. Marks the northern boundary of the reach dominated by the uplifting SLPB to the east and subsidence to the west. Also associated with a minor right step-over and subsiding basin to the east (described by Johnson and Watt, 2012, as a Lazy Z bend).
HS, HA	Second	H-01, H-02, H-03, H-04, H-05	Junction of the Hosgri and Casmalia faults, associated with localized uplift east of the Hosgri fault, and narrow subsiding basin to the south of the block bounded by the Casmalia and Lions Head faults (PG&E, 2014, Chapter 3).
HS	First	H-01, H-02, H-03, H-04, H-05	South end of the Hosgri fault at Point Arguello (Plate 7-1).
PB**	First	H-04, H-08	North end of the Piedras Blancas anticlinorium (Willingham et al., 2013).
PB, WR**	Second	H-04, H-08	Junction of the western reach of the Hosgri fault with the Piedras Blancas anticlinorium (PG&E, 2013a).
HC, HA**	Second	H-04	Potential junction of the offshore San Luis Bay fault with the Hosgri fault, associated with a minor left bend in the Hosgri fault and a minor change in uplift rate east of the Hosgri fault (PG&E, 2011).
HB, HW,	--	H-05	Junction of the Shoreline and Hosgri faults. Not considered to arrest rupture in H-05 but

Segment Boundary*	Tier	Rupture Sources	Explanation
HC, HE**			required for modeling the splay scenarios.
SH, SS**	Second	H-05	Junction of the San Luis Bay and Shoreline faults, associated with a change in uplift rate north of the San Luis Bay fault (PG&E, 2011) and likely an increase in slip rate on the Shoreline fault to the north (*Section 8.4.4.2*).
SF, SE**	Second	H-05	Junction of the Oceano and Shoreline faults, likely associated with an increase in slip rate on the Shoreline fault north of the junction (*Section 8.4.4.2*).
SE**	Second	H-05	Postulated southeast end of the Shoreline fault at the Casmalia fault junction (*Section 9.2.1.3*).

* Soft segment boundaries apply to all three Hosgri Rupture Models (H75, H85, and H90).
** Soft segment boundaries used to characterize magnitudes on secondary faults in complex and splay rupture sources.

Table 10-4 provides an assessment of the appropriate functional form for magnitude PDFs used to describe earthquake rates for characteristic and linked rupture sources. As described in *Section 10.2.3*, these functional forms are assigned based on consideration of the lengths of postulated characteristic ruptures relative to the full length of the rupture source. In the Diablo Canyon SSC model, characteristic and linked rupture sources that are less than approximately 100 km long are Category A, and those that are greater than approximately 100 km long are Category B. Alternative epistemic logic tree branch values and weights for M_{char} and M_{max} assessed for these rupture sources are also provided in Table 10-4. The rupture lengths used to estimate alternative values of M_{char} or M_{max}, or both, are shown graphically on Figures 10-8 through 10-15. As described in *Section 10.2.2*, alternative magnitude estimates incorporate a wide range of uncertainty in M_{char} and M_{max} to account for a lack of historical or paleoseismic information to characterize earthquake size and frequency. Weights for alternative magnitude estimates are assessed based on the relative strength of the segment boundaries that are used to define them, and the number of potential segment boundaries that would be ruptured through for a particular rupture length.

Table 10-4. Hosgri MDM Magnitude PDF Categories and Key Magnitude Parameters—Linked and Characteristic Rupture Sources

Rupture Source No.*	Type	Description (Faults)	Magnitude PDF Category	M_{char}	M_{char} Weight	M_{max}	M_{max} Weight
H-01	Linked	Hosgri (Central trace) to MTJ**	B	7.3	0.2	8.5	0.1
				7.1	0.5	8.1	0.5
				6.8	0.3	7.8	0.4
H-02	Linked	Hosgri (West	B	7.3	0.2	8.5	0.1

Rupture Source No.*	Type	Description (Faults)	Magnitude PDF Category	M_{char}	M_{char} Weight	M_{max}	M_{max} Weight
		trace) to MTJ		7.1	0.5	8.1	0.5
				6.8	0.3	7.8	0.4
H-03	Linked	Hosgri (East trace) to MTJ	B	7.3	0.2	8.5	0.1
				7.1	0.5	8.1	0.5
				6.8	0.3	7.8	0.4
H-06	Linked	Hosgri north of the Shoreline fault intersection	B	7.3	0.3	8.4	0.1
				6.8	0.5	8.0	0.9
				6.6	0.2	-	-
H-07	Linked	Hosgri north of the Los Osos fault intersection	B	7.2	0.5	8.4	0.1
				6.6	0.5	8.0	0.9
H-08	Characteristic	Piedras Blancas	A	6.9	0.5	N/A	N/A
				6.6	0.5	N/A	N/A

* Parameters apply to all three Hosgri Rupture Models (H75, H85, and H90).
MTJ = Mendocino Triple Junction; N/A = not applicable

Table 10-5 provides relative frequencies of scenario events for complex and splay rupture sources that involve the Hosgri fault source. Relative frequencies of paired-magnitude events involving primary (or main) and secondary (or splay) faults are assessed based on the relative strength of the segment or soft-segment boundaries that are used to define them and consideration of the expected magnitude-frequency scaling for relatively rare complex or splay ruptures. As a general approach, large-magnitude scenario earthquakes are judged to occur less frequently than smaller-magnitude earthquakes.

Table 10-5. Hosgri MDM Magnitudes and Scenario Frequencies for Complex and Splay Rupture Sources

Rupture Source No.*	Type	Description (Faults)	Primary or Main Magnitude	Secondary or Splay Magnitude	Scenario Frequency
H-04	Complex	Hosgri (primary) with Piedras Blancas (secondary)	7.2	6.9	50%
			7.0	6.6	50%
H-05	Splay	Hosgri, Central trace (main); Shoreline (splay)	8.0	6.8	10%
			7.7	6.5	40%
			7.1	6.3	50%

* Parameters apply to all three Hosgri Rupture Models (H75, H85, and H90).

10.4 Outward-Vergent Magnitude Distribution Model

This section presents the TI Team's assessment of the MDM for the Outward-Vergent Rupture Model, which proceeds as follows:

1. We describe the potential segment boundaries that are used to calculate rupture lengths and alternative estimates of key magnitudes, including M_{char} and M_{max} for characteristic and linked rupture sources, and scenario magnitudes for complex and splay rupture sources.
2. We assign rupture source categories to characteristic and linked rupture sources and we represent epistemic uncertainty by considering alternative values and weights for M_{char} and M_{max} that are required to define the magnitude PDFs.
3. We present earthquake scenario magnitudes and frequencies for complex and splay rupture sources.

Table 10-6 provides potential segment boundaries used to estimate characteristic and maximum rupture lengths in the Outward-Vergent MDM. Locations of boundaries are shown on Plate 9-2.

Table 10-6. Segment Boundaries Used in the Outward-Vergent Magnitude Distribution Model

Segment Boundary	Tier	Rupture Sources	Explanation
SH-HB	First/ second	OV-01 (Fig. 10-16) OV-02 (Fig. 10-17) OV-03 (Fig. 10-18)	Junction of the Shoreline and Hosgri faults associated with a marked difference in slip rate between the two faults. Dynamic rupture models suggest Hosgri ruptures are unlikely to propagate onto the Shoreline fault (Kame et al., 2003; Somerville, 2011).
SH, SS, BR	Second	OV-01 (Fig.10-16) OV-03* (Fig.10-18) OV-04* (Fig.10-19) OV-05 (Fig.10-20) OV-06 (Fig.10-21)	Junction of the San Luis Bay and Shoreline faults, associated with a change in uplift rate to the east of the Shoreline fault (PG&E, 2011) and likely an increase in slip rate on the Shoreline fault to the north *(Section 8.4.4.2*).
SF, SE, OF	Second	OV-01 (Fig. 10-16) OV-02 (Fig. 10-17) OV-09 (Fig. 10-24)	Junction of the Oceano and Shoreline faults, likely associated with an increase in slip rate on the Shoreline fault to the north of the intersection and a change in uplift rate to the east of the Shoreline fault (*Section 8.4.4.2*).
SE	First	OV-01 (Fig. 10-16) OV-02 (Fig. 10-17)	Postulated southeast end of the Shoreline fault at the junction with the Casmalia fault (*Section 9.2.1.3*; PG&E, 2014, Chapter 3).

Segment Boundary	Tier	Rupture Sources	Explanation
SA	First	OV-02 (Fig. 10-17)	North end of the San Andreas fault at the Mendocino Triple Junction.
SA, GN	First	OV-02 (Fig. 10-17) OV-04 (Fig. 10-19); OV-08 (Fig. 10-23)	Bolinas: Junction of the San Gregorio and San Andreas faults: marked slip rate change between the San Andreas and San Gregorio faults, actively subsiding basin between the faults (Bruns et al., 2002; Ryan et al., 2008).
GS, SN	First	OV-02 (Fig. 10-17) OV-04 (Fig. 10-19) OV-08 (Fig. 10-23)	Point Sur: Left-restraining step-over of 1–4 km (Dickinson et al., 2004) near junction of active Quaternary faults that branch east of the San Gregorio fault (Jennings and Bryant, 2010).
SN, SI	First	OV-02 (Fig. 10-17) OV-04 (Fig. 10-19) OV-08 (Fig. 10-23)	San Simeon: Junction of the San Simeon and Oceanic faults associated with a left-restraining step-over of 1–2 km, localized uplift, and occurrence of reverse focal mechanisms adjacent to the strike-slip fault (see references cited in *Section 10.2.2.2*).
BE, MF	Second	OV-03 (Fig. 10-18) OV-05 (Fig. 10-20) OV-06 (Fig. 10-21)	East end of the San Luis Bay fault at the junction with the San Miguelito fault, associated with a probable change in slip rate between the two faults and a boundary of uplift between the Irish Hills and Edna sub-blocks of the SLPB (*Section 9.2.1.3*).
LP	First	OV-04 (Fig. 10-19) OV-09 (Fig. 10-24)	Southeast end of the Little Pine fault.
FS, FN	Second	OV-04 (Fig. 10-19) OV-09 (Fig. 10-24)	Junction of the West Huasna and Foxen Canyon faults, associated with a probable change in slip rate on the Foxen Canyon fault.
WA, NL	Second	OV-04 (Fig. 10-19) OV-10 (Fig. 10-25)	Bend in the Wilmar Avenue fault/Nipomo lineament at Arroyo Grande, associated with a likely change in rate and sense of slip between the two faults. Borehole data suggest the presence of a localized Quaternary basin (AMEC, 2011).
LC, LM	Second	OV-06 (Fig. 10-21) OV-07 (Fig. 10-22)	Junction between onshore and offshore traces of the Los Osos fault at Montaña de Oro State Park, associated with a probable change in rate and sense of slip between the two traces and a right step of

Segment Boundary	Tier	Rupture Sources	Explanation
			approximately 5 km across the subsiding Morro Bay Basin (Plate 7-1 and *Section 7.2.3*). Not considered a first-tier soft segment boundary because reverse faults may incorporate larger step-overs than strike-slip faults (Biasi, Parsons, et al., 2013).
LO, LE	Second	OV-06 (Fig. 10-21) OV-07 (Fig. 10-22) OV-08 (Fig. 10-23)	Los Osos fault at San Luis Obispo Creek, the boundary between the Irish Hills and Edna sub-blocks of the SLPB. Differential uplift rate of the two sub-blocks suggests a difference in slip rate of the Los Osos fault across this boundary (Lettis and Hall, 1994).
LE	First	OV-07 (Fig. 10-22)	East end of the Los Osos fault at junction with the West Huasna fault (Lettis and Hall, 1994), associated with a probable difference in rate and sense of slip between the two faults.
LC, HN, HD	Second	OV-07 (Fig. 10-22) OV-08* (Fig. 10-23)	West end of the Los Osos fault at junction with the Hosgri fault, associated with a pronounced difference in rate and sense of slip between the two faults (*Sections 8.3 and 8.5.1*).
LM, LV	Second	OV-08 (Fig. 10-23)	Boundary between the Morro Bay reach and Los Osos Valley reach of the Los Osos fault, associated with a minor bend in the fault strike and a change in footwall subsidence rate between the actively subsiding Morro Bay Basin and the relatively stable or slowly uplifting Los Osos Valley (*Section 8.5.1*).
ON, FN, NL	Second	OV-09 (Fig. 10-24) OV-10 (Fig. 10-25)	Junction of the Nipomo lineament with the Oceano and Foxen Canyon faults, associated with a probable difference in slip rate between the Foxen Canyon and Oceano faults.

* For rupture sources indicated with an asterisk, the potential segment boundary represents the location where the sense of slip changes for a complex rupture source or the branch point between the main and splay rupture planes for a splay rupture source.

Table 10-7 provides an assessment of the appropriate functional form for magnitude PDFs used to describe earthquake rates for characteristic and linked rupture sources. Alternative epistemic logic tree branch values and weights for M_{char} and M_{max} assessed

for these rupture sources are also provided in Table 10-7. The rupture lengths used to estimate alternative values of M_{char} or M_{max}, or both, are shown graphically on Figures 10-16 through 10-25. As described in *Section 10.2.2*, alternative magnitude estimates incorporate a wide range of uncertainty in M_{char} and M_{max} to account for a lack of historical or paleoseismic information to characterize earthquake size and frequency. Weights for alternative magnitude estimates are assessed from the relative strength of the segment boundaries that are used to define them, and the number of potential segment boundaries that would be ruptured through for a particular rupture length.

Table 10-7. Outward-Vergent MDM Magnitude PDF Categories and Key Magnitude Parameters—Linked and Characteristic Rupture Sources

Rupture Source No.	Type	Description (Faults)	Magnitude PDF Category	M_{char}	M_{char} Weight	M_{max}	M_{max} Weight
OV-01	Characteristic	Shoreline	A	6.8	0.2	N/A	N/A
				6.5	0.5	N/A	N/A
				6.3	0.3	N/A	N/A
OV-02	Linked	Shoreline and Hosgri	B	7.0	0.2	8.4	0.1
				6.8	0.5	8.1	0.5
				6.5	0.3	7.7	0.4
OV-05	Characteristic	San Luis Bay	A	6.1	0.5	N/A	N/A
				6.0	0.5	N/A	N/A
OV-07	Characteristic	Los Osos	A	7.0	0.2	N/A	N/A
				6.8	0.5	N/A	N/A
				6.4	0.3	N/A	N/A
OV-09	Linked	Oceano and SWBZ	A	7.2	0.2	N/A	N/A
				6.8	0.3	N/A	N/A
				6.7	0.5	N/A	N/A
OV-10	Characteristic	Wilmar Avenue and Nipomo	A	6.5	0.5	N/A	N/A
				6.2	0.5	N/A	N/A

N/A = not applicable; SWBZ = Southwestern Boundary zone

Table 10-8 provides aleatory scenario magnitudes and relative frequencies on primary (or main) and secondary (or splay) faults for use in complex and splay rupture sources. Relative frequencies of magnitude estimates are assessed based on the relative strength of the segment boundaries that are used to define them, and a simple magnitude-frequency scaling that suggests large magnitude earthquakes are less frequent than small magnitude earthquakes.

Table 10-8. Outward-Vergent MDM Magnitudes and Scenario Frequencies for Complex and Splay Rupture Sources

Rupture Source No.	Type	Description (Faults)	Primary or Main Magnitude	Secondary or Splay Magnitude	Scenario Frequency
OV-03	Complex	Shoreline (primary) and San Luis Bay (secondary)	6.3	6.1	100%
OV-04	Complex	Shoreline (primary), San Luis Bay and SWBZ (secondary)	8.0	7.2	10%
			7.5	6.9	40%
			7.0	6.5	50%
OV-06	Splay	Los Osos (main) and San Luis Bay (splay)	6.4	6.1	100%
OV-08	Complex	Los Osos (secondary) and Hosgri (primary)	7.9	6.8	10%
			7.4	6.8	40%
			6.6	6.6	50%

SWBZ = Southwestern Boundary zone

10.5 Southwest-Vergent Magnitude Distribution Model

This section presents the TI Team's assessment of the MDM for the Southwest-Vergent Rupture Model, which proceeds as follows:

1. We describe the potential segment boundaries that are used to calculate rupture lengths and alternative estimates of key magnitudes, including M_{char} and M_{max} for characteristic and linked rupture sources, and scenario magnitudes for complex and splay rupture sources.
2. We assign rupture source categories to characteristic and linked rupture sources and we represent epistemic uncertainty by considering alternative values and weights for M_{char} and M_{max} that are required to define the magnitude PDFs.
3. We present earthquake scenario magnitudes and frequencies for complex and splay rupture sources.

Table 10-9 provides potential segment boundaries used to estimate characteristic and maximum rupture lengths in the Southwest-Vergent MDM. Locations of boundaries are shown on Plate 9-2.

Table 10-9. Segment Boundaries Used in the Southwest-Vergent Magnitude Distribution Model

Segment Boundary	Tier	Rupture Sources	Explanation

Segment Boundary	Tier	Rupture Sources	Explanation
SH-HB	First/ second	SW-01 (Fig.10-16) SW-02 (Fig. 10-17) SW-03 (Fig. 10-26)	Junction of the Shoreline and Hosgri faults associated with a marked difference in slip rate between the two faults. Dynamic rupture models suggest Hosgri ruptures are unlikely to propagate onto the Shoreline fault (Kame et al., 2003; Somerville, 2011).
SH, SS, BR, BW	Second	SW-01 (Fig. 10-16, SW-06 (Fig. 10-29)	Junction of the San Luis Bay and Shoreline faults, associated with a change in uplift rate to the east of the Shoreline fault (PG&E, 2011) and likely an increase in slip rate on the Shoreline fault to the north (*Section 8.4.4.2*).
SF, SE, OF	Second	SW-01 (Fig. 10-16) SW-02 (Fig. 10-17) SW-03*(Fig. 10-26) SW-09 (Fig. 10-32)	Junction of the Oceano and Shoreline faults, likely associated with an increase in slip rate on the Shoreline fault to the north of the intersection and a change in uplift rate to the east of the Shoreline fault (*Section 8.4.4.2*).
SE	First	SW-01 (Fig. 10-16) SW-02 (Fig. 10-17)	Postulated southeast end of the Shoreline fault at the junction with the Casmalia fault (*Section 9.2.1.3*; PG&E, 2014, Chapter 3).
SA	First	SW-02 (Fig. 10-17)	North end of the San Andreas Fault at the Mendocino Triple Junction.
SA, GN	First	SW-02 (Fig. 10-17) SW-04 (Fig. 10-27) SW-08 (Fig. 10-31)	Bolinas: Junction of the San Gregorio and San Andreas faults: marked slip rate change between the San Andreas and San Gregorio faults, actively subsiding basin between the faults (Bruns et al., 2002; Ryan et al., 2008).
GS, SN	First	SW-02 (Fig. 10-17) SW-04 (Fig. 10-27) SW-08 (Fig. 10-31)	Point Sur: Left-restraining step-over of 1–4 km (Dickinson et al., 2004) near junction of active Quaternary faults that branch east of the San Gregorio fault (Jennings and Bryant, 2010).
GS, SN	First	SW-02 (Fig. 10-17) SW-04 (Fig. 10-27) SW-08 (Fig. 10-31)	San Simeon: Junction of the San Simeon and Oceanic faults associated with a left-restraining step-over of 1–2 km, localized uplift, and occurrence of reverse focal mechanisms adjacent to the strike-slip fault (see references cited in *Section 10.2.2.2*).
BE, MF	Second	SW-04 (Fig. 10-27) SW-05 (Fig. 10-28) SW-06 (Fig. 10-29) SW-07 (Fig. 10-30)	East end of the San Luis Bay fault at the junction with the San Miguelito fault, associated with probable change in slip rate between the two faults and a boundary of uplift between the Irish Hills and Edna sub-blocks of the SLPB (*Section 9.2.1.3*).
BW, HC, HA	First/ Second	SW-04* (Fig. 10-27) SW-06 (Fig. 10-29) SW-07 (Fig. 10-30)	Intersection of the San Luis Bay and Hosgri faults, associated with pronounced difference in style and rate of slip between the two faults. Used as limit of rupture length for M_{max} on linked southwest-vergent reverse faults in SW-

Segment Boundary	Tier	Rupture Sources	Explanation
			07 but not considered to arrest rupture in the complex rupture source SW-04.
LP	First	SW-03 (Fig. 10-26) SW-07 (Fig. 10-30) SW-09 (Fig. 10-32)	Southeast end of the Little Pine fault.
BE, BW	Second	SW-06 (Fig. 10-29)	Approximately half the length of the San Luis Bay fault, where the Shoreline fault crosses the San Luis Bay fault.
FS, FN	Second	SW-07 (Fig. 10-30) SW-09 (Fig. 10-32)	Junction of the West Huasna and Foxen Canyon faults, associated with probable change in slip rate on the Foxen Canyon fault.
WA, NL	Second	SW-07 (Fig. 10-30)	Bend in the Wilmar Avenue fault/Nipomo lineament at Arroyo Grande, associated with a likely change in rate and sense of slip between the two faults. Borehole data suggest the presence of a localized Quaternary basin (AMEC, 2011).
LC, LM	Second	SW-06 (Fig. 10-29) SW-08 (Fig. 10-31)	Junction between onshore and offshore traces of the Los Osos fault at Montaña de Oro State Park, associated with a probable change in rate and sense of slip between the two traces and a right step of approximately 5 km across the subsiding Morro Bay Basin (Plate 7-1 and *Section 7.2.3*). Not considered a first-tier soft segment boundary because reverse faults may incorporate larger step-overs than strike-slip faults (Biasi, Parsons, et al., 2013).
LV, LB	Second	SW-06 (Fig. 10-29) SW-10 (Fig. 10-33)	Los Osos fault at San Luis Obispo Creek, the boundary between the Irish Hills and Edna sub-blocks of the SLPB. Differential uplift rate of the two sub-blocks suggests a difference in slip rate of the Los Osos fault across this boundary (Lettis and Hall, 1994).
LE	Second	SW-10 (Fig. 10-33)	East end of the Los Osos fault at junction with the West Huasna fault (Lettis and Hall, 1994), associated with a probable difference in rate and sense of slip between the two faults.
LC, HN, HD	Second	SW-08* (Fig. 10-31)	West end of the Los Osos fault at the junction with the Hosgri fault, associated with a pronounced difference in rate and sense of slip between the two faults (*Sections 8.3 and 8.5.1*).
WB, SS, SF	Second	SW-10 (Fig. 10-33)	West end of the Wilmar Avenue at the junction with the Shoreline fault, likely associated with an increase in slip rate of the Shoreline fault to the north of the intersection and a change in uplift rate to the east of the Shoreline fault

Segment Boundary	Tier	Rupture Sources	Explanation
			across the Wilmar Avenue fault (*Section 8.4*).
ON, FN, NL	Second	SW-09 (Fig. 10-32) SW-10 (Fig. 10-33)	Junction of the Nipomo lineament with the Oceano and Foxen Canyon faults, associated with a probable difference in slip rate between the Foxen Canyon and Oceano faults.

* For rupture sources indicated with an asterisk, the potential segment boundary represents the location where the sense of slip changes for a complex rupture source or the branch point between the main and splay rupture planes for a splay rupture source.

Table 10-10 provides an assessment of the appropriate functional form for magnitude PDFs used to describe earthquake rates for characteristic and linked rupture sources. Alternative epistemic logic tree branch values and weights for M_{char} and M_{max} assessed for these rupture sources are also provided in Table 10-10. The rupture lengths used to estimate alternative values of M_{char} or M_{max}, or both, are shown graphically on Figures 10-16, 10-17, and 10-26 through 10-33. As described in *Section 10.2.2*, alternative magnitude estimates incorporate a wide range of uncertainty in M_{char} and M_{max} to account for a lack of historical or paleoseismic information to characterize earthquake size and frequency. Weights for alternative magnitude estimates are assessed from the relative strength of the segment boundaries that are used to define them, and the number of potential segment boundaries that would be ruptured through for a particular rupture length.

Table 10-10. Southwest-Vergent MDM Magnitude PDF Categories and Key Magnitude Parameters—Linked and Characteristic Rupture Sources

Rupture Source No.	Type	Description (Faults)	Magnitude PDF Category	M_{char}	M_{char} Weight	M_{max}	M_{max} Weight
SW-01	Characteristic	Shoreline	A	6.8	0.2	N/A	-
				6.5	0.5	-	-
				6.3	0.3	-	-
SW-02	Linked	Shoreline and Hosgri	B	7.0	0.2	8.4	0.1
				6.8	0.5	8.1	0.5
				6.5	0.3	7.7	0.4
SW-05	Characteristic	San Luis Bay	A	6.4	0.6	N/A	-
				6.2	0.4	-	-
SW-07	Linked	San Luis Bay and SWBZ	B	7.0	0.2	7.4	1.0
				6.7	0.5	-	-
				6.4	0.3	-	-
SW-09	Linked	Oceano and	A	7.3	0.2	N/A	-

Rupture Source No.	Type	Description (Faults)	Magnitude PDF Category	M_{char}	M_{char} Weight	M_{max}	M_{max} Weight
				7.0	0.3	-	-
				6.8	0.5	-	-

N/A = not applicable; SWBZ = Southwestern Boundary zone

Table 10-11 provides aleatory scenario magnitudes and relative frequencies on primary (or main) and secondary (or splay) faults for use in complex and splay rupture sources. Relative frequencies of magnitude estimates are assessed based on the relative strength of the segment boundaries that are used to define them, and a simple magnitude-frequency scaling that suggests large magnitude earthquakes are less frequent than small magnitude earthquakes.

Table 10-11. Southwest-Vergent MDM Key Magnitude Parameters for Complex and Splay Rupture Sources

Rupture Source No.	Type	Description (Faults)	Primary or Main Magnitude	Secondary or Splay Magnitude	Scenario Frequency
SW-03	Complex	Oceano and SWBZ (primary) with Shoreline (secondary)	7.3	6.5	50%
		Shoreline (primary) with Oceano (secondary)	6.5	6.3	50%
SW-04	Complex	Hosgri (primary) and San Luis Bay (secondary) and	8.0	6.4	10%
			7.5	6.4	40%
			6.9	6.4	50%
SW-06	Splay	San Luis Bay (main) and Los Osos (splay)	6.4	6.4	100%
SW-08	Complex	Hosgri (primary) and Los Osos Offshore (secondary)	7.9	6.5	10%
			7.4	6.5	40%
			6.6	6.5	50%
SW-10	Splay	Wilmar Avenue (main) and Los Osos east (splay)	6.6	6.3	100%

SWBZ = Southwestern Boundary zone

10.6 Northeast-Vergent Magnitude Distribution Model

This section presents the TI Team's assessment of the MDM for the Northeast-Vergent Rupture Model, which proceeds as follows:

1. We describe the potential segment boundaries that are used to calculate rupture lengths and alternative estimates of key magnitudes, including M_{char} and M_{max} for characteristic and linked rupture sources, and scenario magnitudes for complex and splay rupture sources.
2. We assign rupture source categories to characteristic and linked rupture sources and we represent epistemic uncertainty by considering alternative values and weights for M_{char} and M_{max} that are required to define the magnitude PDFs.
3. We present earthquake scenario magnitudes and frequencies for complex and splay rupture sources.

Table 10-12 provides potential segment boundaries used to estimate characteristic and maximum rupture lengths in the Northeast-Vergent MDM. Locations of boundaries are shown on Plate 9-2.

Table 10-12. Segment Boundaries Used in the Northeast-Vergent Magnitude Distribution Model

Segment Boundary	Tier	Rupture Sources	Explanation
SH-HB	First/ second	NE-01 (Fig. 10-16) NE-02 (Fig. 10-17);	Junction of the Shoreline and Hosgri faults associated with a marked difference in slip rate between the two faults. Dynamic rupture models suggest Hosgri ruptures are unlikely to propagate onto the Shoreline fault (Kame et al., 2003; Somerville, 2011).
SH, SS, BR	Second	NE-01 (Fig. 10-16) NE-03* (Fig. 10-34) NE-06 (Fig. 10-37)	Junction of the San Luis Bay and Shoreline faults, associated with a change in uplift rate to the east of the Shoreline fault (PG&E, 2011) and likely an increase in slip rate on the Shoreline fault to the north (*Section 8.4.4.2*).
SF, SE, OF	Second	NE-01 (Fig. 10-16) NE-02 (Fig. 10-17) NE-04* (Fig. 10-35, NE-09 (Fig. 10-40)	Junction of the Oceano and Shoreline faults, likely associated with an increase in slip rate on the Shoreline fault to the north of the intersection and a change in uplift rate to the east of the Shoreline fault (*Section 8.4.4.2*).
SE	First	NE-01 (Fig. 10-16) NE-02 (Fig. 10-17)	Postulated southeast end of the Shoreline fault at the junction with the Casmalia fault (*Section 9.2.1.3*; PG&E, 2014, Chapter 3).
SA	First	NE-02 (Fig. 10-17)	North end of the San Andreas fault at the Mendocino Triple Junction.
SA, GN	First	NE-02 (Fig. 10-17), NE-04 (Fig. 10-35) NE-08 (Fig. 10-39)	Bolinas: Junction of the San Gregorio and San Andreas faults: marked slip rate change between the San Andreas and San Gregorio faults, actively subsiding basin between the

Segment Boundary	Tier	Rupture Sources	Explanation
			faults (Bruns et al., 2002; Ryan et al., 2008).
GS, SN	First	NE-02 (Fig. 10-17) NE-04 (Fig. 10-35) NE-08 (Fig. 10-39)	Point Sur: Left-restraining step-over of 1–4 km (Dickinson et al., 2004) near junction of active Quaternary faults that branch east of the San Gregorio fault (Jennings and Bryant, 2010).
GS, SN	First	NE-02 (Fig. 10-17) NE04 (Fig. 10-35) NE-08 (Fig. 10-39)	San Simeon: Junction of the San Simeon and Oceanic faults associated with a left-restraining step-over of 1–2 km, localized uplift, and occurrence of reverse focal mechanisms adjacent to the strike-slip fault (see references cited in *Section 10.2.2.2*).
BE, MF	Second	NE-03 (Fig. 10-34) NE-06 (Fig. 10-29)	East end of the San Luis Bay fault at the junction with the San Miguelito fault, associated with probable change in slip rate between the two faults and a boundary of uplift between the Irish Hills and Edna sub-blocks of the SLPB (*Section 9.2.1.3*).
LP	First	NE-04 (Fig. 10-35) NE-07 (Fig. 10-38) NE-09 (Fig. 10-40)	Southeast end of the Little Pine fault.
FS, FN	Second	NE-04 (Fig. 10-35) NE-07 (Fig. 10-38), NE-09 (Fig. 10-40)	Junction of the West Huasna and Foxen Canyon faults, associated with probable change in slip rate on the Foxen Canyon fault.
WB, SS, SF	Second	NE-07* (Fig. 10-38) NE-10 (Fig. 10-41)	West end of the Wilmar Avenue fault at the junction with the Shoreline fault, likely associated with an increase in slip rate of the Shoreline fault to the north of the intersection and a change in uplift rate to the east of the Shoreline fault across the Wilmar Avenue fault (*Section 8.4*).
WA, NL	Second	NE-10 (Fig. 10-41)	Bend in the Wilmar Avenue fault/Nipomo lineament at Arroyo Grande, associated with a likely change in rate and sense of slip between the two faults. Borehole data suggest the presence of a localized Quaternary basin (AMEC, 2011).
LC, LM	Second	NE-05 (Fig. 10-36) NE-06 (Fig. 10-37) NE-07 (Fig. 10-38) NE-11 (Fig. 10-42)	Junction between onshore and offshore traces of the Los Osos fault at Montaña de Oro State Park, associated with a probable change in rate and sense of slip between the two traces and a right step of approximately 5 km across the subsiding Morro Bay Basin (Plate 7-1 and *Section 7.2.3*). Not considered a first-tier soft segment boundary because reverse faults may incorporate larger step-overs than strike-slip faults (Biasi, Parsons, et al., 2013).
LV, LB	Second	NE-05 (Fig. 10-36)	Los Osos fault at San Luis Obispo Creek, the

Segment Boundary	Tier	Rupture Sources	Explanation
		NE-06 (Fig. 10-37), NE-07* (Fig. 10-38) NE-08 (Fig. 10-39) NE-10 (Fig. 10-41) NE-11 (Fig. 10-42)	boundary between the Irish Hills and Edna sub-blocks of the SLPB. Differential uplift rate of the two sub-blocks suggests a difference in slip rate of the Los Osos fault across this boundary (Lettis and Hall, 1994).
LE	Second	NE-10 (Fig. 10-41)	East end of the Los Osos fault at junction with the West Huasna fault (Lettis and Hall, 1994), associated with a probable difference in rate and sense of slip between the two faults.
LC, HN, HD	Second	NE-07 (Fig. 10-38) NE-08* (Fig. 10-39) NE-11 (Fig. 10-42)	West end of the Los Osos fault at junction with the Hosgri fault, associated with a pronounced difference in rate and sense of slip between the two faults (*Sections 8.3 and 8.5.1*).
LM, LV	Second	NE-05 (Fig. 10-36) NE-08 (Fig. 10-39) NE-11 (Fig. 10-42)	Boundary between the Morro Bay reach and Los Osos Valley reach of the Los Osos fault, associated with a minor bend in the fault strike and a change in footwall subsidence rate between the actively subsiding Morro Bay Basin and the relatively stable or slowly uplifting Los Osos Valley (*Section 8.5.1*).
ON, FN, NL	Second	NE-04 (Fig. 10-35) NE-09 (Fig. 10-40)	Junction of the Nipomo lineament with the Oceano and Foxen Canyon faults, associated with a probable difference in slip rate between the Foxen Canyon and Oceano faults.

* For rupture sources indicated with an asterisk, the potential segment boundary represents the location where the sense of slip changes for a complex rupture source or the branch point between the main and splay rupture planes for a splay rupture source.

Table 10-13 provides an assessment of the appropriate functional form for magnitude PDFs used to describe earthquake rates for characteristic and linked rupture sources. Alternative epistemic logic tree branch values and weights for M_{char} and M_{max} assessed for these rupture sources are also provided in Table 10-13. The rupture lengths used to estimate alternative values of M_{char} or M_{max}, or both, are shown graphically on Figures 10-16, 10-17, and 10-34 through 10-42. As described in *Section 10.2.2*, alternative magnitude estimates incorporate a wide range of uncertainty in M_{char} and M_{max} to account for a lack of historical or paleoseismic information to characterize earthquake size and frequency. Weights for alternative magnitude estimates are assessed from the relative strength of the segment boundaries that are used to define them, and the number of potential segment boundaries that would be ruptured through for a particular rupture length.

Table 10-13. Northeast-Vergent MDM Magnitude PDF Categories and Key Magnitude Parameters—Linked and Characteristic Rupture Sources

Rupture Source	Type	Description (Faults)	Magnitude PDF	M_{char}	M_{char} Weight	M_{max}	M_{max} Weight

No.			Category				
NE-01	Characteristic	Shoreline	A	6.8	0.2	N/A	-
				6.5	0.5	-	-
				6.3	0.3	-	-
NE-02	Linked	Shoreline and Hosgri	B	7.0	0.2	8.4	0.1
				6.8	0.5	8.1	0.5
				6.5	0.3	7.7	0.4
NE-05	Characteristic	Los Osos Irish Hills	A	6.4	0.6	N/A	-
				6.1	0.4	-	-
NE-09	Linked	Oceano and SWBZ	A	7.3	0.2	N/A	-
				7.0	0.3	-	-
				6.8	0.5	-	-
NE-11	Characteristic	Los Osos Irish Hills and offshore	A	6.8	0.2	N/A	-
				6.4	0.6	-	-
				6.1	0.2	-	-

N/A = not applicable; SWBZ = Southwestern Boundary zone

Table 10-14 provides aleatory scenario magnitudes and relative frequencies for primary (or main) and secondary (or splay) faults for use in complex and splay rupture sources. Relative frequencies of magnitude estimates are assessed based on the relative strength of the segment boundaries that are used to define them, and a simple magnitude-frequency scaling that suggests large magnitude earthquakes are less frequent than small magnitude earthquakes.

Table 10-14. Northeast-Vergent MDM Magnitudes and Scenario Frequencies for Complex and Splay Rupture Sources

Rupture Source No.	Type	Description (Faults)	Primary or Main Magnitude	Secondary or Splay Magnitude	Scenario Frequency
NE-03	Complex	Shoreline (primary) and San Luis Bay (secondary)	6.3	6.1	100%
NE-04	Complex	Shoreline (primary) Oceano and SWBZ (secondary)	8.0	7.3	10%
			7.5	7.0	40%
			7.0	6.8	50%
NE-06	Splay	Los Osos (main) and San Luis Bay (splay)	6.4	6.1	100%

Rupture Source No.	Type	Description (Faults)	Primary or Main Magnitude	Secondary or Splay Magnitude	Scenario Frequency
NE-07	Splay	Los Osos (splay), Wilmar Avenue and SWBZ (main)	7.2	6.8	50%
			6.8	6.4	50%
NE-08	Complex	Hosgri (primary) and Los Osos (secondary)	7.9	6.8	10%
			7.4	6.8	40%
			6.6	6.7	50%
NE-10	Splay	Wilmar Avenue (main) and Los Osos east (splay)	6.5	6.3	100%

SWBZ = Southwestern Boundary zone

10.7 Magnitude-Frequency Distributions for Specific Points on the Primary Faults

This section discusses fault MFDs at points on Primary faults closest to the DCPP.

In *Section 10.2.4*, the process for geometric reduction of fault-source MFDs to point MFDs was explained for single sets of parameters for each distribution. In the SSC logic tree, however, most sources have a range of possible parametric settings. Thus the actual MFD for each fault source must combine individual contributions, represented by the different paths through the SSC logic tree for each rupture source. For example, the Hosgri fault source H-01 includes three slip rates, two magnitude PDFs, three maximum magnitudes, and three characteristic magnitudes: 3×2×3×3 = 54 permutations, each with its combined weight. The individual source MFD contributions and their weighted sum are shown on Figure 10-43. The DCPP is 65 km from the south end of H-01, and its total length is 740 km. The HB14 magnitude-area relation (Equation 10-1) has been used to estimate rupture length for the geometric reduction. In practice, the results do not materially depend on the magnitude-area relation. The net rupture-source MFD after weighting all contributions (thick black line on Figure 10-43) favors the transformed WAACY shape (which gets a weight of 0.8 compared to 0.2 for the truncated exponential magnitude PDF), but it is widened by the range of M_{char} values. The cumulative MFD for the rupture source is shown as a dashed black line. Each rupture source is distilled to a single point source MFD and cumulative distribution in this fashion.

Fault-source MFDs are constructed by summing the contributions of each individual rupture source, as presented in *Sections 10.7.1 through 10.7.4*. The MFD results for the Hosgri fault source, which is applicable for all three Hosgri Fault Geometry Models (FGMs), is presented in *Section 10.7.1*. We present representative MFD results for the other Primary faults in following subsections, showing results using the Outward-Vergent

FGM for the Shoreline fault source (*Section 10.7.2*), Los Osos fault source (*Section 10.7.3*), and San Luis Bay fault source (*Section 10.7.4*). We also show results using the Northeast-Vergent FGM (NE Model) for the Los Osos fault source, and using the Southwest-Vergent FGM (SW Model) for the San Luis Bay fault source, so that results may be compared between FGMs where those faults are modeled as both completely independent fault sources (OV Model) and where each fault is modeled as the principal reverse fault underlying the Irish Hills (NE Model and SW Model for Los Osos and San Luis Bay faults, respectively).

10.7.1 Hosgri Fault Source

A complete set of MFDs for the Hosgri fault source is shown on Figure 10-44 as they would be observed to pass a point on the fault offshore from the DCPP. A geometric reduction rate (*Section 10.2.4*) has been applied to all fault sources. Rupture source H-01 is repeated with plotting conventions and line styles from Figure 10-43. Figure 10-44 is in some sense the culmination of the Diablo Canyon SSC for the Hosgri fault, since it shows all sources producing earthquakes at the nearest point on the fault to the DCPP. Note that plot scales can vary from source to source. Differences in slip rate among the three Hosgri strands cause systematic commensurate differences in the levels (annual rates) of MFDs, with the eastern strand rupture source (H-03) having the lowest allocated slip rate. We note that the H85 series of Hosgri rupture source MFDs are shown on Figures 10-43 to 10-45 because the dip differences in H75 and H90 do not affect rupture source and summed MFDs. Rupture sources H-04 and H-05, which are characterized using the simplified maximum magnitude PDF, are shown as vertical lines at the scenario earthquake magnitudes as a plotting device, but their actual rates are given by the green circles and gray squares corresponding to the tops of individual line segments. On these plots, the two symbols—green circles and gray squares—correspond to the two "subevents" that combine to form a complex or splay rupture source. Green lines and circles correspond to the subevents occurring on the *subject* fault—that is, the fault that is the subject of the plot (i.e., the Hosgri for Figure 10-44). The gray lines and squares correspond to the subevents occurring on the *companion* (or "other") fault source involved in the complex or splay rupture. In the case of H-04, the gray square shows the magnitude and rate of the reverse Piedras Blancas source rupture (Plate 9-1). In the case of H-05, the gray square shows the magnitude and rate of the Shoreline fault source rupture. By design, the rates of the subject – companion subevent pairs are equal. The cumulative MFD (dashed black line) corresponds to the subevents on the subject fault only. Reflecting the maximum magnitude nature of the magnitude PDFs, the cumulative MFD line plots at a constant rate up to M_{char}=M_{max}, and is zero for magnitudes greater than M_{max}. There is no visible solid black line (summed incremental rate) on the plots for rupture sources H-04 and H-05because the rate of earthquake magnitudes is zero except at M_{max}.

The summed MFD at the nearest point to the DCPP on the Hosgri sources is shown on Figure 10-45. The results show the dominant contribution of the WAACY magnitude PDF used in rupture sources H-01, H-02, and H-03 to the overall Hosgri fault source

MFD. Superimposed on the summed incremental MFD are higher peaks created by the addition of the scenario magnitudes from the complex H-04 and splay H-05 rupture sources. The magnitudes shown are those for the subevents on the Hosgri fault source. The cumulative MFD for the Hosgri fault source shows a break in slope near **M** 7.0, corresponding to the characteristic magnitudes in the model. A second break occurs at approximately **M** 8.0, above which maximum earthquakes are permissible but, due to the low epistemic weight on the highest alternative M_{max} values (Table 10-4) and the form of the WAACY magnitude PDF that favors high *b* values for the high-magnitude tail (Figures 10-1 and 10-5), their rates are very low.

To evaluate the resulting Hosgri fault MFD, we compare it with corresponding UCERF3 subsection participation rates for the subsection of the Hosgri source closest to the DCPP (Figure 10-46; Field et al., 2013). For this we extract the rates of occurrence of individual ruptures in the UCERF3 inversion solution (red stars on Figure 10-46), and sum them to create a summed incremental MFD (blue line on Figure 10-46; see *Chapter 12* for details). UCERF3 solution MFDs are expected to differ in detail because the constructive process used in the Diablo Canyon SSC incorporates more geologic and fault-specific information to characterize earthquake size distributions, rather than the broader rules and constraints (such as solving for the statewide rate of $M \geq 5$ earthquakes) included in the more general UCERF3 inversion (Field et al., 2013; Page et al., 2014).

A comparison of Figures 10-45 and 10-46 suggests that the incremental earthquake rates are broadly similar. First, we note that the mean Hosgri fault source slip rate in the Diablo Canyon SSC model of 1.7 mm/yr (*Section 8.3.8*) compares favorably to the UCERF3 solution slip rate of the Hosgri fault section of approximately 1.5 mm/yr (Field et al., 2013), and thus both the pattern and rates of earthquakes predicted from the two models are comparable. The Diablo Canyon SSC incremental MFD has relatively higher rates within the range of M_{char} values, $6.9 < \mathbf{M} < 7.3$, and relatively low rates at magnitudes greater than approximately **M** 7.7 (Figure 10-45). The UCERF3 incremental MFD predicts relatively more of the largest events up to approximately magnitude *M* 8.1 (Figure 10-46). To some extent this could reflect greater connectivity among faults in the UCERF3 fault model, or an inversion constraint that favors a more even rate of earthquake magnitudes locally in order to satisfy the state-wide earthquake rate target (and thus help suppress the state-wide "bulge" in $6 < M < 7$ earthquakes documented by Field et al. 2008).

10.7.2 Shoreline Fault Source

A complete set of rupture source MFDs for the Shoreline fault source as observed at a point nearest the DCPP are shown on Figure 10-47 (for the Outward-Vergent Model). Rupture source OV-01 is characteristic (Category A rupture source; Table 10-2), OV-02 reflects the portion of the Shoreline fault source that participates with the longer Hosgri source resulting in a Category B rupture source (modeled with either truncated exponential or WAACY magnitude PDFs), and the other rupture sources (OV-03, OV-04, and H-05) are complex or splay sources with simplified maximum magnitude PDFs. The green and gray symbols on the complex and splay rupture sources are comparable to

those described for the Hosgri fault source results above in *Section 10.7.1*, with the green symbol representing the subevent on the subject fault (in this case, the Shoreline fault source) and the gray symbol representing the companion fault source subevent. For rupture source H-05, the splay rupture source with a main Hosgri fault source subevent and a splay Shoreline fault source subevent (Plate 9-1), a comparison between Figures 10-44 and 10-47 shows the same subevent pairs and the same rates, but the symbols for the subject (green) and companion (gray) subevents are switched.

The Shoreline fault source point MFD (Figure 10-48) is shaped by the one long, continuous source MFD, OV-02. The point contributions from the complex and splay rupture sources—shown as circles at or near the tops of sharp peaks in the summed incremental earthquake rate curve, result in a stepped pattern in the cumulative earthquake rate curve. As in Figure 10-45 for the Hosgri fault, we note that the magnitudes on Figure 10-48 plotted for the complex and splay rupture sources represent only the Shoreline subevent magnitude; other faults also contribute to the ground motions from these types of sources. The overall shape of the fault source MFD reflects a decreasing likelihood in earthquake magnitude from approximately **M** 6.3 to **M** 8.0, above which the MFD suggests the annual rate of **M** > 8 is less than 10^{-7}. The Shoreline fault source point MFD earthquake rates observed at the DCPP are an order of magnitude or more lower than on the Hosgri fault, consistent with the difference in fault slip rate.

10.7.3 Los Osos Fault Source

A complete set of rupture source point MFDs for the Los Osos fault source in the Outward-Vergent Model are shown on Figure 10-49. The observation point is on the LM section of the Los Osos fault source, at the uplift rate boundary between the Irish Hills and Morro Bay (e.g., Plate 9-2). Three rupture sources contribute to the fault source, including characteristic rupture source OV-07, splay rupture source OV-06, and complex rupture source OV-08. For rupture source OV-06, the companion subevents (in gray) are on the San Luis Bay fault source. For rupture source OV-08, the companion subevents are on the Hosgri fault source north of the Los Osos-Hosgri fault junction (Plate 9-2). The summed incremental earthquake rate on Figure 10-50 is shaped by the characteristic MFD from rupture source OV-07, with peaks corresponding to the Los Osos subevent magnitudes superimposed on the smoother characteristic shape. The plot shows an increased rate of earthquakes above **M** 6.2, and an upper limit of **M** 7.25 from the upper limit of source OV-07. The complex ruptures from rupture source OV-08 include companion subevent magnitudes up to **M** 7.9 on the Hosgri fault, so the range of magnitudes associated with earthquakes on the Los Osos fault in the OV Model is broader than indicated on Figure 10-50.

The five individual rupture source point MFDs contributing to the Los Osos fault source in the Northeast-Vergent FGM are shown on Figure 10-51. Characteristic rupture sources NE-05 and NE-11 contribute half of the moment rate to the MFD (Table 9-15), with additional contributions from splay and complex rupture sources NE-06, NE-07, and NE-08. The companion subevents shown in gray are for the San Luis Bay (NE-06), the Wilmar Avenue and faults along strike to the southeast (NE-07), and the Hosgri fault

(NE-08; Plate 9-2). The shape of the summed incremental earthquake rate on the Los Osos fault (NE Model) is formed by the two characteristic rupture sources, with peaks at the magnitudes from the splay and complex rupture sources (Figure 10-52). The plot shows an increased rate of earthquakes above **M** 5.8, and an upper limit of **M** 7.05 from NE-11. As with the Los Osos fault in the OV Model, the companion magnitudes from splay and complex ruptures are not included on the plot on Figure 10-52, but magnitudes up to **M** 7.9 are associated with earthquakes on the Los Osos fault source.

A comparison of the summed incremental and cumulative MFDs between the OV (Figure 10-50) and NE (Figure 10-52) models shows general similarities, but with a greater rate of **M** ≥ 5 and **M** ≥ 6 earthquakes in the NE Model and a comparable rate of **M** ≥ 6.5 earthquakes between the two models. The plots show a greater number of **M** ≥ 7 earthquakes in the OV Model, which is mainly due to the differences in the M_{char} values of OV-07 (which include up to **M** 7.0) compared to those of NE-11 (up to **M** 6.8).

10.7.4 San Luis Bay Fault Source

A complete set of rupture source point MFDs for the San Luis Bay fault source in the Outward-Vergent FGM are shown on Figure 10-53. The observation point is on the BE section of the San Luis Bay fault source, at the intersection with the Shoreline fault (Plate 9-2). Four rupture sources contribute to the San Luis Bay fault source in the OV Model, with most of the moment rate (~90%) contributed by the characteristic OV-05 and splay OV-06 rupture sources, and a minor amount from the complex OV-03 and OV-04 rupture sources. The companion subevents for rupture sources OV-06, OV-03, and OV-04 are on the Los Osos, Shoreline, and Hosgri fault sources, respectively (Plate 9-2). In all cases, the companion subevents are the larger (primary or main) parts of the scenario ruptures.

The summed incremental and cumulative earthquake rates for the San Luis Bay fault (OV Model) are shown on Figure 10-54. The summed incremental earthquake rate line is continuous from **M** 5 to **M** 6.35, the largest magnitude for the characteristic OV-05 rupture source. The geometric reduction of the exponential part of the characteristic earthquake magnitude PDF in rupture source OV-05 trends downward at smaller magnitudes because the observation point closest to the DCPP is near the west end of the fault. The cumulative earthquake rate curve shows a stepped pattern from **M** 6.35 to **M** 7.2 with steps corresponding to scenario subevent magnitudes on the San Luis Bay fault source. Similar to the cases with the Los Osos fault, the complex ruptures from rupture source OV-04 include companion subevent magnitudes up to **M** 8.0 on the Hosgri fault, so the range of magnitudes associated with earthquakes on the San Luis Bay fault in the OV Model is broader than indicated on Figure 10-53.

Four individual rupture source point MFDs make up the San Luis Bay fault source for the Southwest-Vergent FGM (Figure 10-55). The point location for the Southwest-Vergent Model is located on the offshore fault section BW (Plate 9-2). The majority of the moment rate is contributed by splay rupture source SW-06, characteristic rupture source SW-05, and linked rupture source SW-07 (Table 9-13). A minor moment rate contributor is complex rupture source SW-04. The companion subevent magnitudes for complex

rupture source SW-04 and splay rupture source SW-06 are all greater than the subevent magnitudes for the San Luis Bay fault (Figure 10-55).

The summed incremental and cumulative earthquake rates for the San Luis Bay fault source in the SW Model are on Figure 10-56. The summed incremental rate curve is shaped by the characteristic MFD from source SW-05, the WAACY MFD from source SW-07, and the subevent magnitudes for the two maximum magnitude MFDs that form a peak at **M** 6.4. The complex ruptures from rupture source SW-04 include companion subevent magnitudes up to **M** 8.0 on the Hosgri fault, so the range of magnitudes associated with earthquakes on the San Luis Bay fault in the SW Model is broader than indicated on Figure 10-56.

A comparison of the summed incremental and cumulative MFDs between the OV (Figure 10-54) and SW (Figure 10-56) models for the San Luis Bay fault source shows general similarities. The OV and SW models show comparable rates of **M** ≥ 5 and **M** ≥ 6 earthquakes, but the SW Model has higher rates of **M** ≥ 6.5 and **M** ≥ 7.0 earthquakes. The higher rates of larger magnitudes in the SW Model compared to the OV Model is a result of two factors. First, the MFD plot for the San Luis Bay fault in the SW Model includes the WAACY magnitude PDF model for SW-07 and its M_{max} = **M** 7.4. Second, the San Luis Bay fault has a higher weighted mean slip rate in the SW Model (0.22 mm/yr) compared to the OV Model (0.16 mm/yr, *Section 8.6.3*). Both models include companion subevent magnitudes on the Hosgri fault zone that are **M** ≥ 8.0.

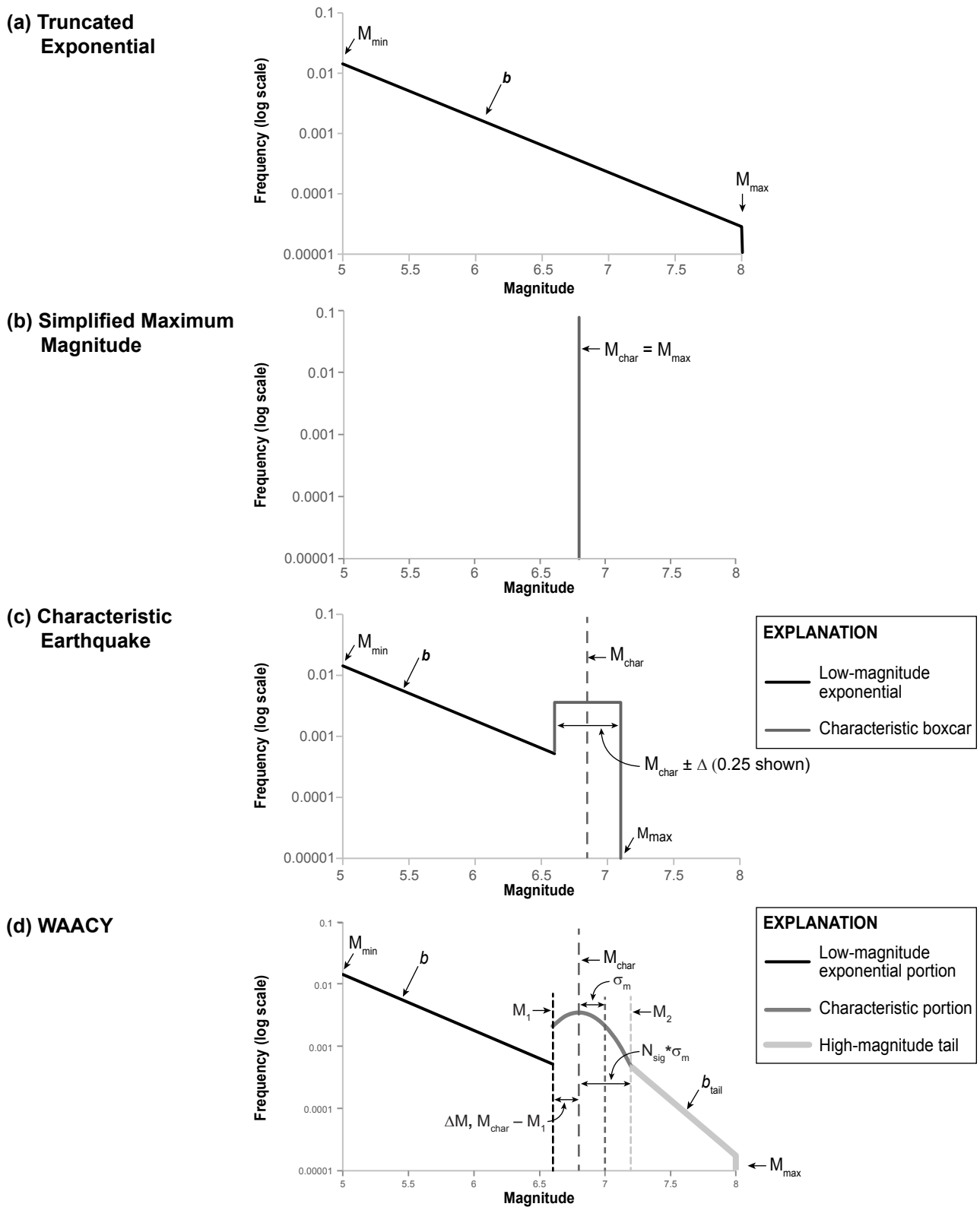

Schematic Diagrams of Magnitude Probability Density Functions Used in the Diablo Canyon SSC Model

DCPP SSC REPORT

Pacific Gas and Electric Company

Figure **10-1**

File path: S:\1005\005\Final_Report_Figures\Figure_1000-01.ai; Date: 03/04/2015; User: Serkan Bozkurt, LCI; Rev.1

Magnitude Range	Group	Percent Moment Rate, Low-Magnitude Exponential Portion	*b*-Value, High-Magnitude Tail
M_{char} = 6.5 ± 0.2, M_{max} = 7.5 ± 0.2 or M_{char} = 7.0 ± 0.2, M_{max} = 7.5 ± 0.2 or M_{char} = 7.3, M_{max} = 8.0 ± 0.2	GROUP (A)	12% [0.2] 6% [0.35] 3% [0.45]	3 [0.35] 2 [0.35] 1 [0.30]
M_{char} = 7.0 ± 0.2, M_{max} = 8.0 ± 0.2 or M_{char} = 7.3, M_{max} = 8.3–8.5	GROUP (B)	12% [0.1] 6% [0.4] 3% [0.5]	3 [0.45] 2 [0.35] 1 [0.2]
M_{char} = 6.5 ± 0.2, M_{max} = 8.0 ± 0.2 or M_{char} = 6.5 ± 0.2, M_{max} = 8.3–8.5 or M_{char} = 7.0 ± 0.2, M_{max} = 8.3–8.5	GROUP (C)	12% [0.2] 6% [0.35] 3% [0.45]	3 [0.7] 2 [0.3] 1 [0.0]

Note: WAACY magnitude PDF parameters are shown on Figure G-1 and defined in the text. The logic trees specify values and weights for the two non-fixed WAACY parameters to be used with specific M_{char}, M_{max} combinations based on their proximity to one of 8 combinations tested in the parametric studies. The magnitude pair groups and associated logic tree parameter weights shown on this figure were constructed based on an earlier version of the parametric study results shown on Figures G-2 to G-4 and in *Attachment G-1*. Differences between the current and earlier results are minor such that changes in group assignments or logic tree branch weights to better match the current results would have negligible effects on the overall results.

Logic Trees for the Non-Fixed Parameters in the WAACY Magnitude PDF Model

DCPP SSC REPORT

Pacific Gas and Electric Company

Figure **10-2**

File path: S:\1005\005\Final_Report_Figures\Figure_10-02.ai; Date:03/06/2015; User: Alex Remar, LCI; Rev.1

EXPLANATION

Epicenter, 1991 Ragged Point Earthquake (McLaren and Savage, 2001)

Quaternary fault trace; solid where well located, dashed where approximately located, offshore faults dotted where buried by undeformed equivalent to or older than unconformity H10 onshore faults dotted where concealed, short dashed where inferred, queried where existence is uncertain.

Slip Rate (mm/yr)

>1

0.2-1

0 2 4 mi.

0 2 4 km

Map projection and scale: WGS 84 / UTM Zone 10N, 1:130,000

Fault Trace Complexity at the Intersection of the Oceanic and San Simeon Faults

DCPP SSC REPORT

Pacific Gas and Electric Company

Figure **10-3**

File path: S:\1005\005\Final_Report_Figures\Figure_1000-03.mxd; Date: 03/06/2015; User: Serkan Bozkurt, LCI; Rev.1

(a) Comparison of Magnitude-Area Relations Considered for Continental Strike-Slip Faults

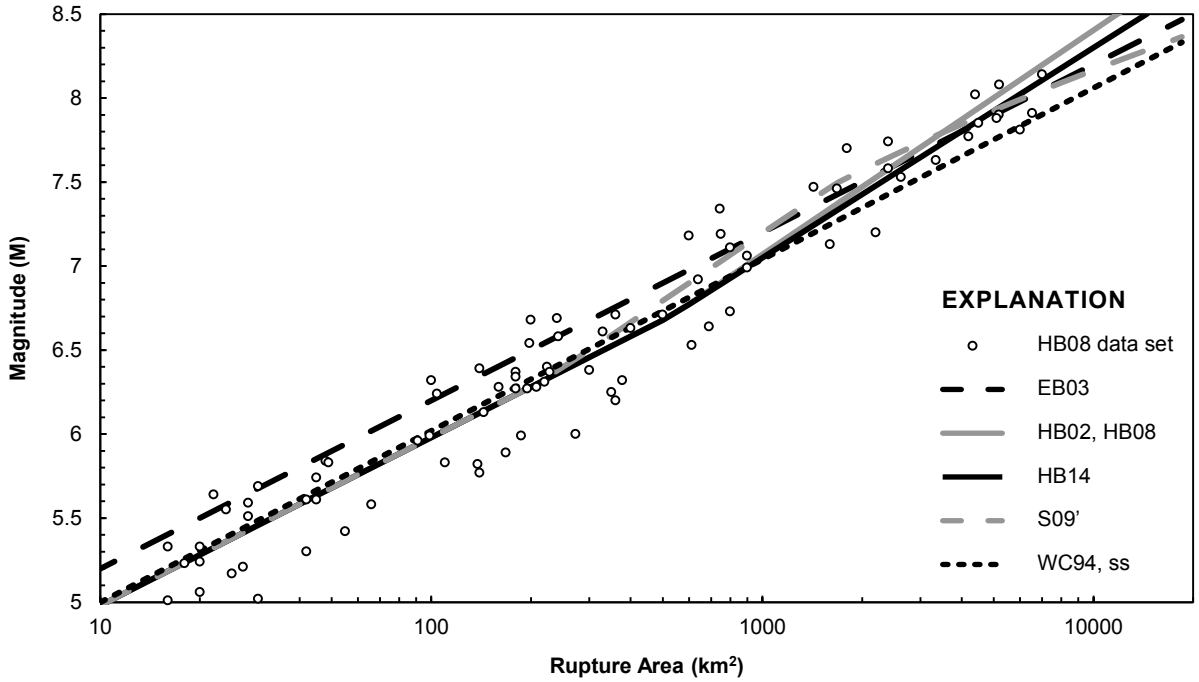

(b) Comparison of Magnitude-Area Relations Considered for Continental Reverse-Slip Faults and Reverse-Oblique-Slip Faults

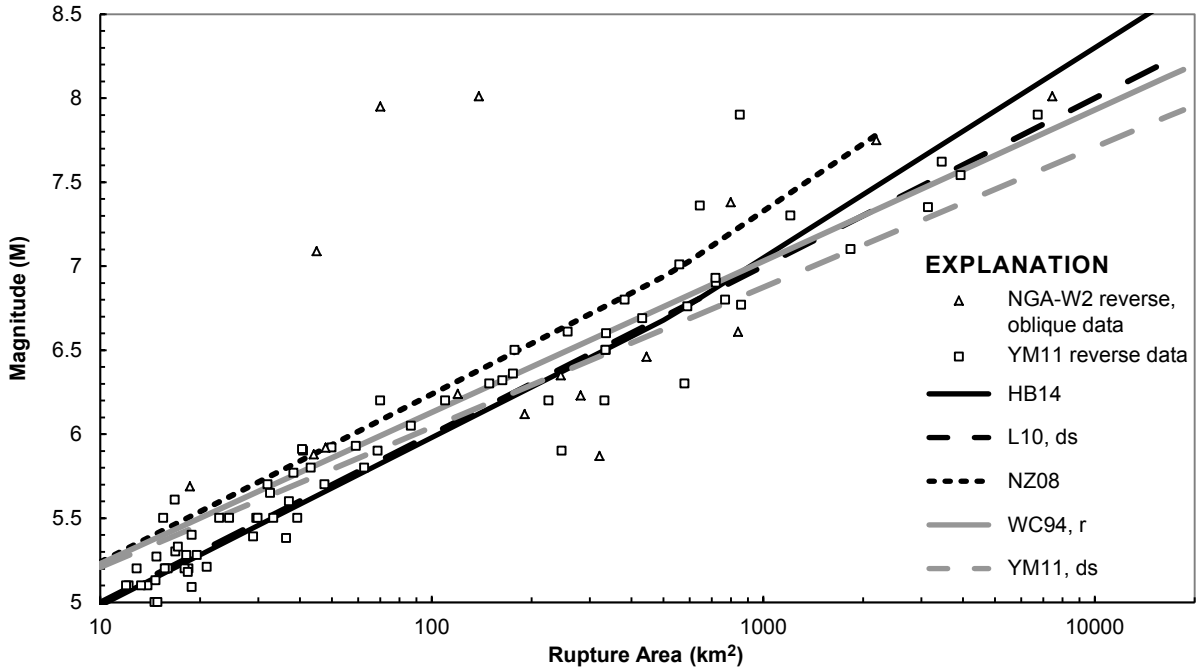

ABBREVIATIONS

EB03	Ellsworth-B relation (Equation 4.5b in WGCEP, 2003)
HB02	Hanks and Bakun (2002)
HB08	Hanks and Bakun (2008)
HB14	Hanks and Bakun (2014)
L10	Leonard (2010); ds = dip-slip relation
NGA-W2	Next Generation Attenuation West 2 flat file (Ancheta et al., 2013)
NZ08	New Zealand relation cited in Stirling et al. (2008, 2013); maximum width of 19 km shown
S09'	Implementation of Shaw (2009) per Shaw (2013); maximum width of 15 km shown
YM11	Yen and Ma (2011); ds = dip-slip relation
WC94	Wells and Coppersmith (1994); ss = strike-slip relation; r = reverse relation

Magnitude-Scaling Relations Considered in the Diablo Canyon SSC Model

DCPP SSC REPORT

Pacific Gas and Electric Company

Figure **10-4**

File path: S:\1005\005\Final_Report_Figures\Figure_10-04.ai; Date:03/11/2015; User: Alex.Remar, LCI; Rev.1

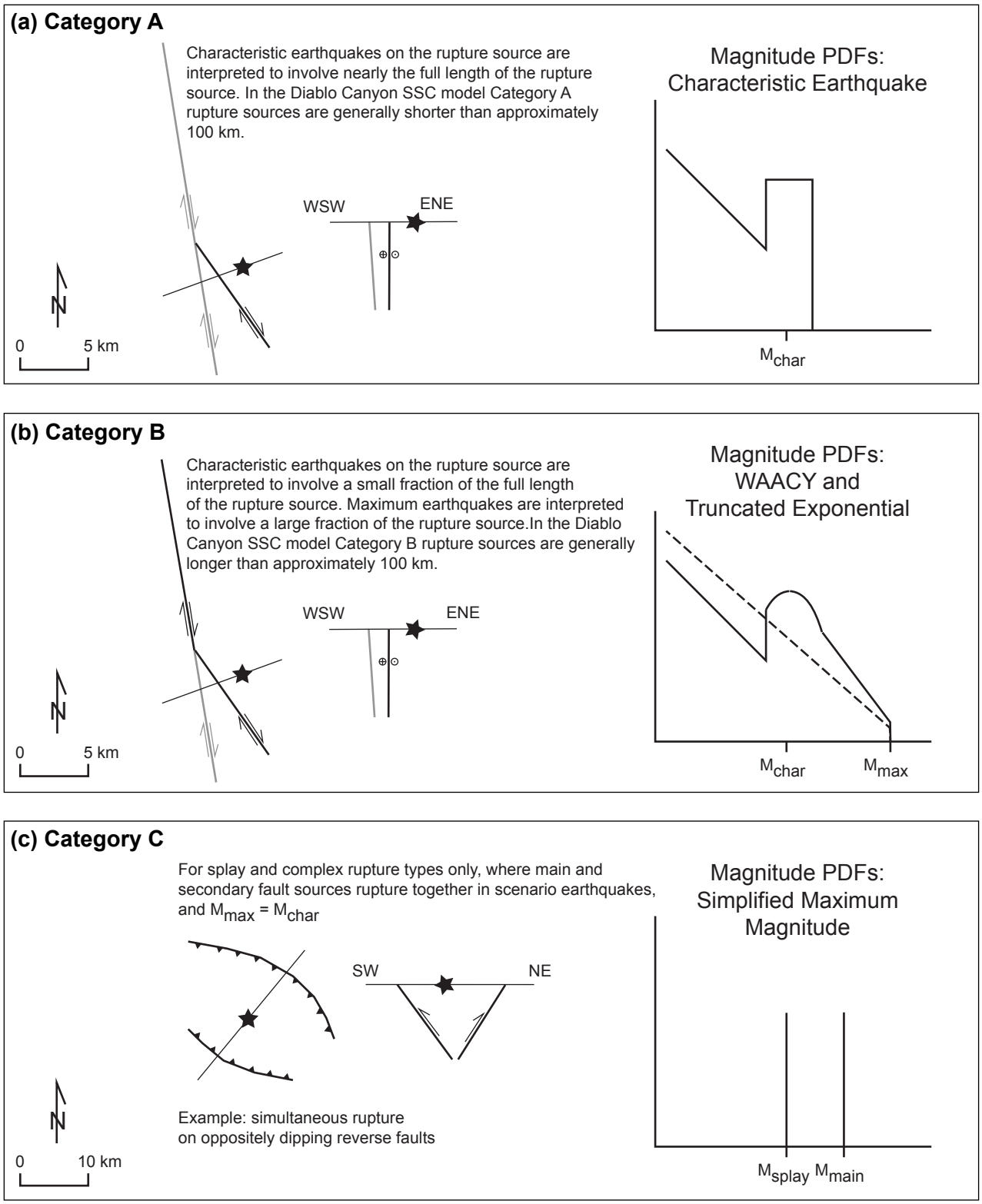

EXPLANATION

- Site
- Fault section in rupture source
- Fault section not in rupture source
- Map view: strike-slip (left), reverse (right)
- Cross section view: strike-slip (left), reverse (right)

Schematic Diagrams of Category A, B, and C Rupture Sources

DCPP SSC REPORT

Pacific Gas and Electric Company

Figure **10-5**

File path: S:\1005\005\Final_Report_Figures\Figure_10-05.ai; Date:03/10/2015; User: Alex Remar, LCI; Rev.1

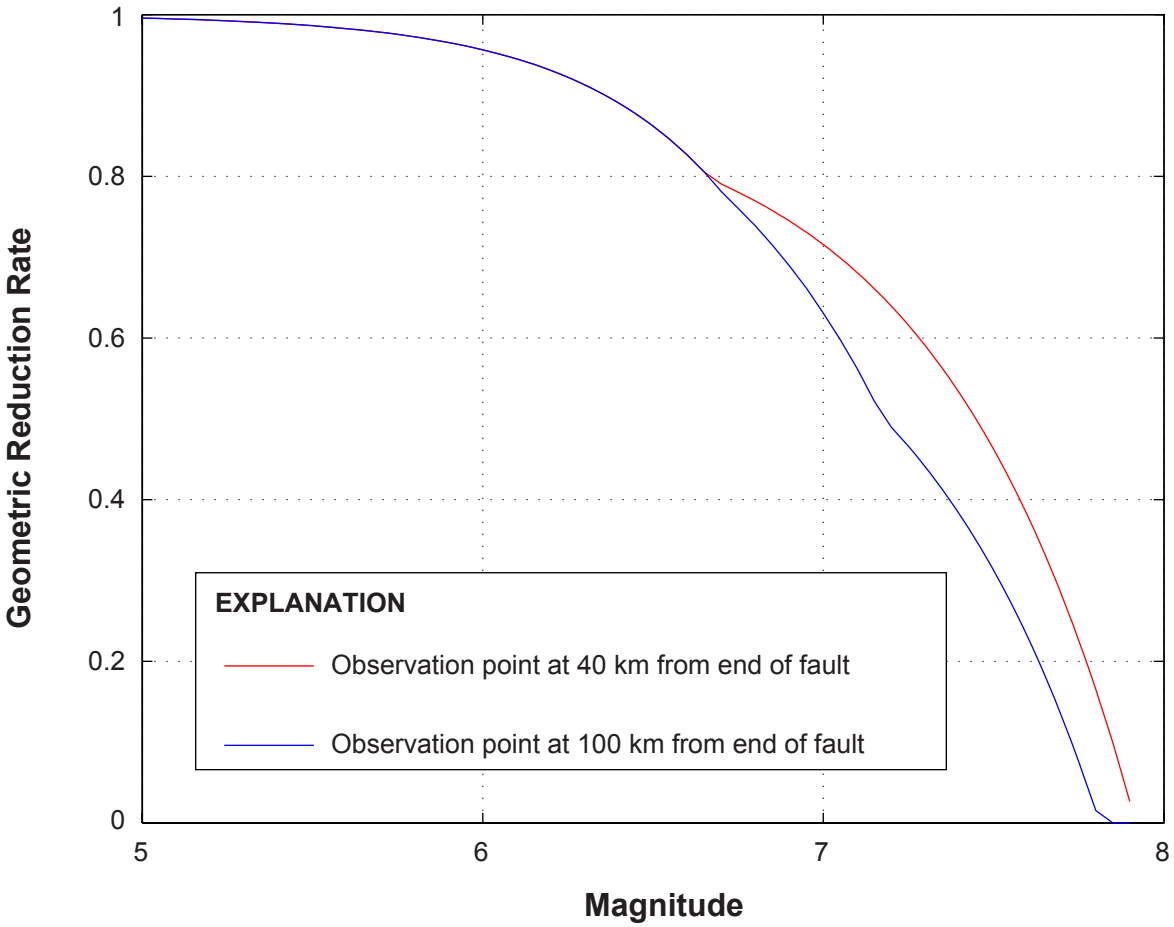

Note: Geometric reduction rate for a fault source 400 km long and observation points 40 km and 100 km from the end. Inflections in rate reduction curves occur at magnitudes where floating earthquakes can no longer fit between the observation point and the near end of the fault source.

Geometric Reduction Rate for Magnitude-Frequency Distributions at Points along a Fault

DCPP SSC REPORT

Pacific Gas and Electric Company | Figure **10-6**

File path: S:\1005\005\Final_Report_Figures\Figure_10-06.ai; Date:03/11/2015; User: Serkan Bozkurt, LCI; Rev.1

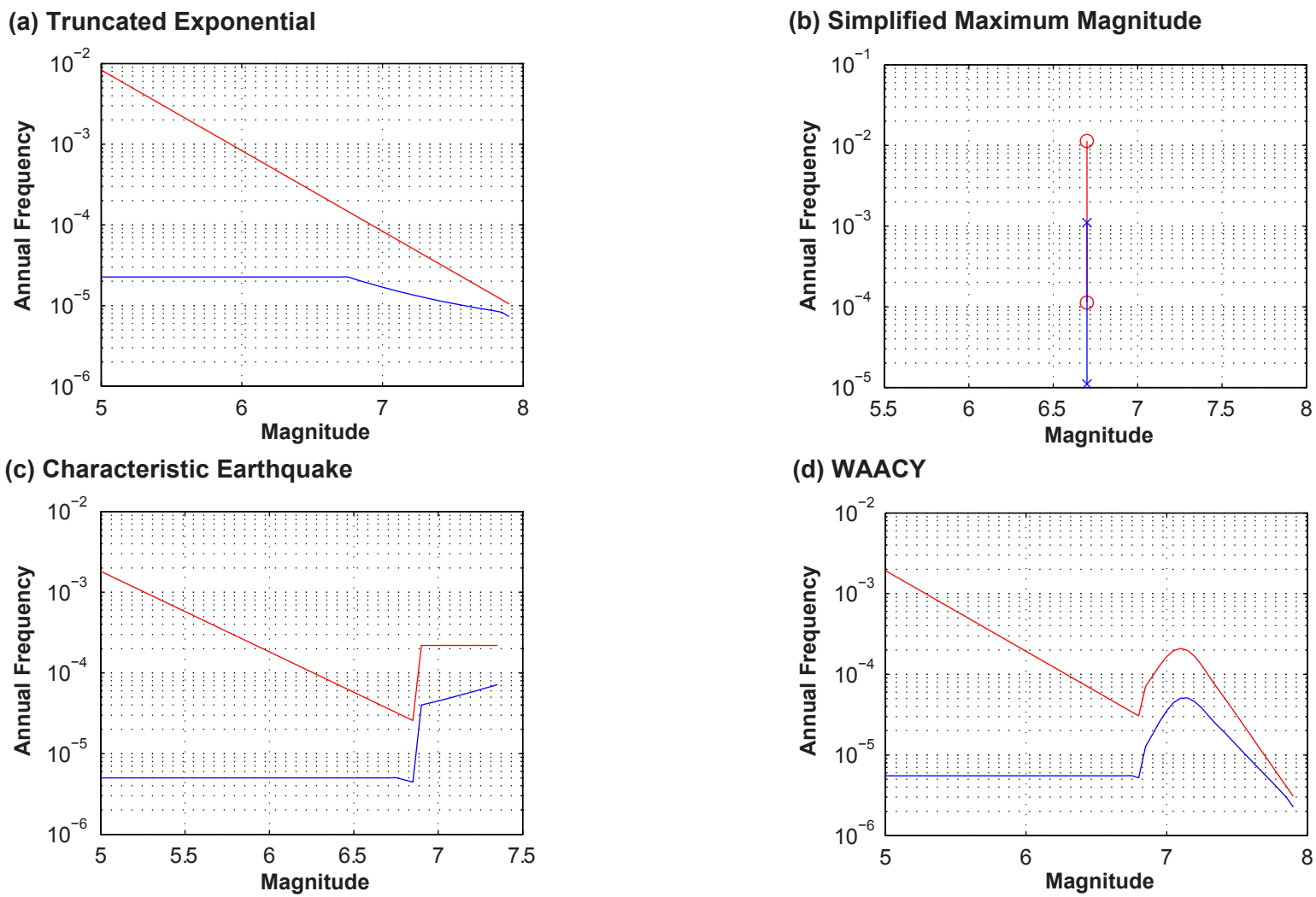

Note: The geometric reduction at a point (Figure 10-6) is applied to the four magnitude PDFs of the SSC model. Red lines are MFDs for a fault source 400 km long slipping at 1 mm/yr. Blue lines are MFDs at a point 40 km from the end of the fault. Earthquakes at all magnitudes defined in the magnitude PDFs are assumed to float—to the extent possible—on the fault source.

Magnitude-Frequency Distributions for a Fault vs. a Point on a Fault

DCPP SSC REPORT

Pacific Gas and Electric Company | Figure **10-7**

File path: S:\1005\005\Final_Report_Figures\Figure_10-07.ai; Date:03/06/2015; User: Alex Remar, LCI; Rev.1

(a) M_{max}

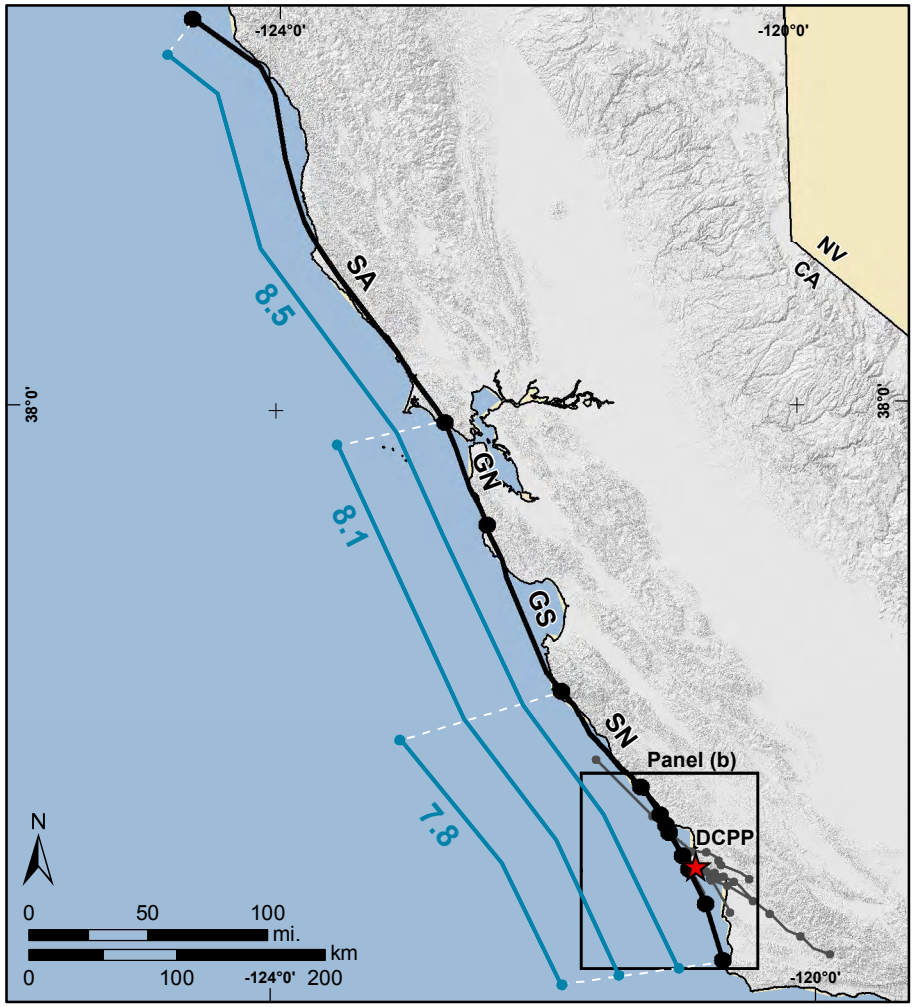

Map projection and scale: WGS 1984 UTM Zone 10N, 1:5,100,000

(b) M_{char}

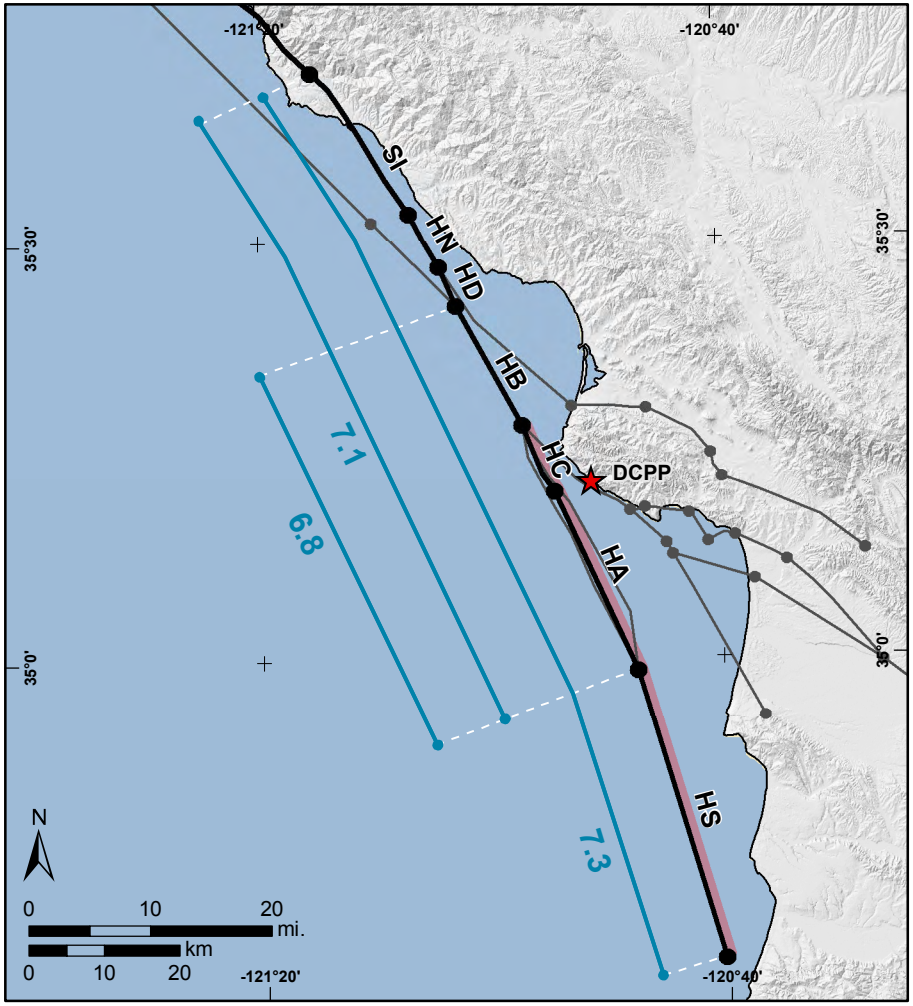

Map projection and scale: WGS 1984 UTM Zone 10N, 1:1,000,000

EXPLANATION

- Length scale used for magnitude estimates
- Rupture source at surface
- Other fault section
- Surface projection of dipping rupture source

Notes:
- No shading is shown for vertical faults.
- Two-letter fault section codes are explained in Table 6-5 and on Plates 9-1 and 9-2.

Alternative Estimates of M_{max} and M_{char} for Rupture Source H-01

DCPP SSC REPORT

Pacific Gas and Electric Company Figure **10-8**

File path: S:\1005\005\Final_Report_Figures\Figure_1000-08.mxd; Date: 02/25/2015; User: Serkan Bozkurt, LCI; Rev.1

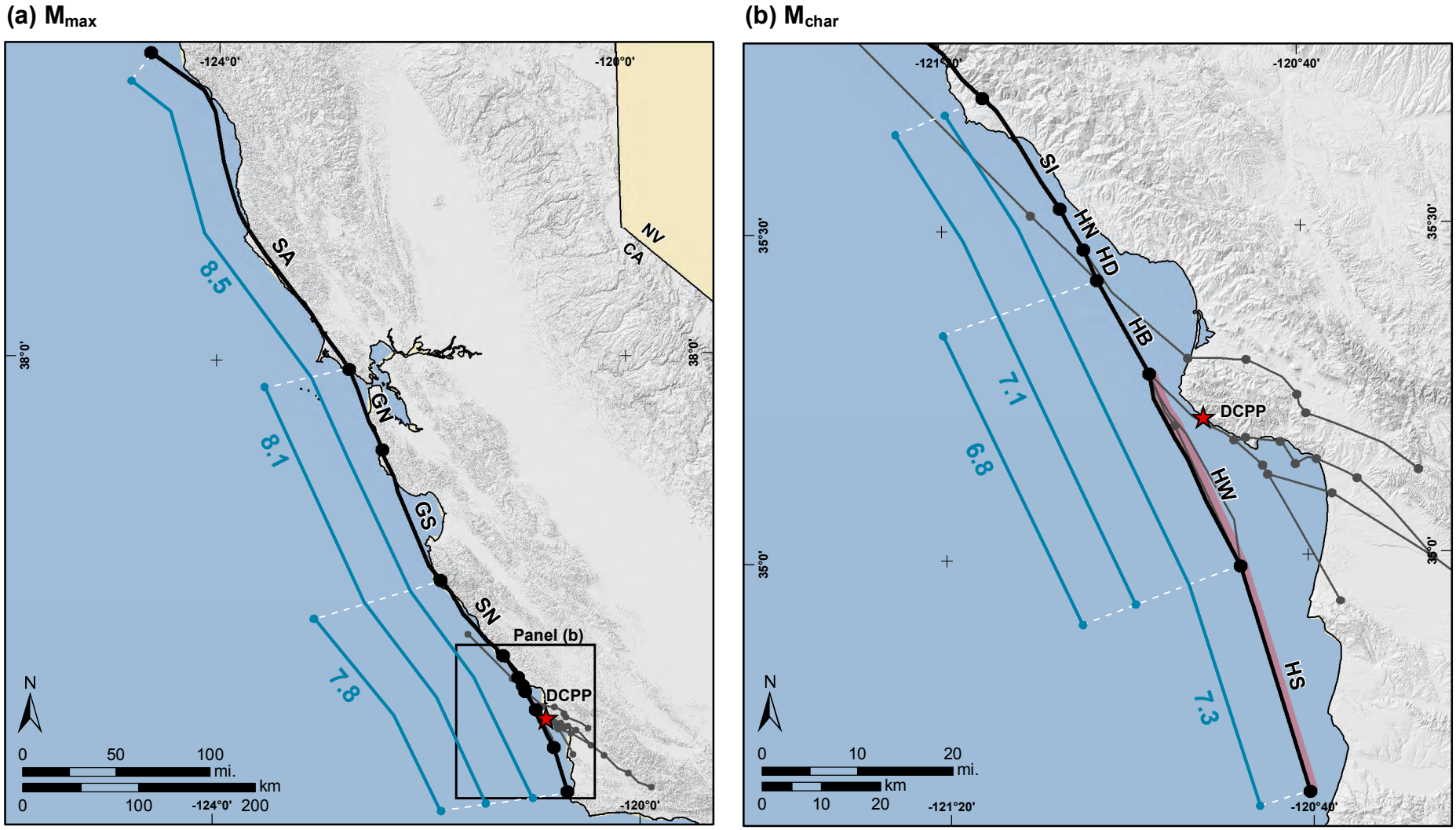

Map projection and scale: WGS 1984 UTM Zone 10N, 1:5,100,000

Map projection and scale: WGS 1984 UTM Zone 10N, 1:1,000,000

EXPLANATION

- Length scale used for magnitude estimates
- Rupture source at surface
- Other fault section
- Surface projection of dipping rupture source

Notes:
- No shading is shown for vertical faults.
- Two-letter fault section codes are explained in Table 6-5 and on Plates 9-1 and 9-2.

Alternative Estimates of M_{max} and M_{char} for Rupture Source H-02

DCPP SSC REPORT

Pacific Gas and Electric Company | Figure **10-9**

File path: S:\1005\005\Final_Report_Figures\Figure_1000-09.mxd; Date: 02/25/2015; User: Serkan Bozkurt, LCI; Rev.1

(a) M_{max}

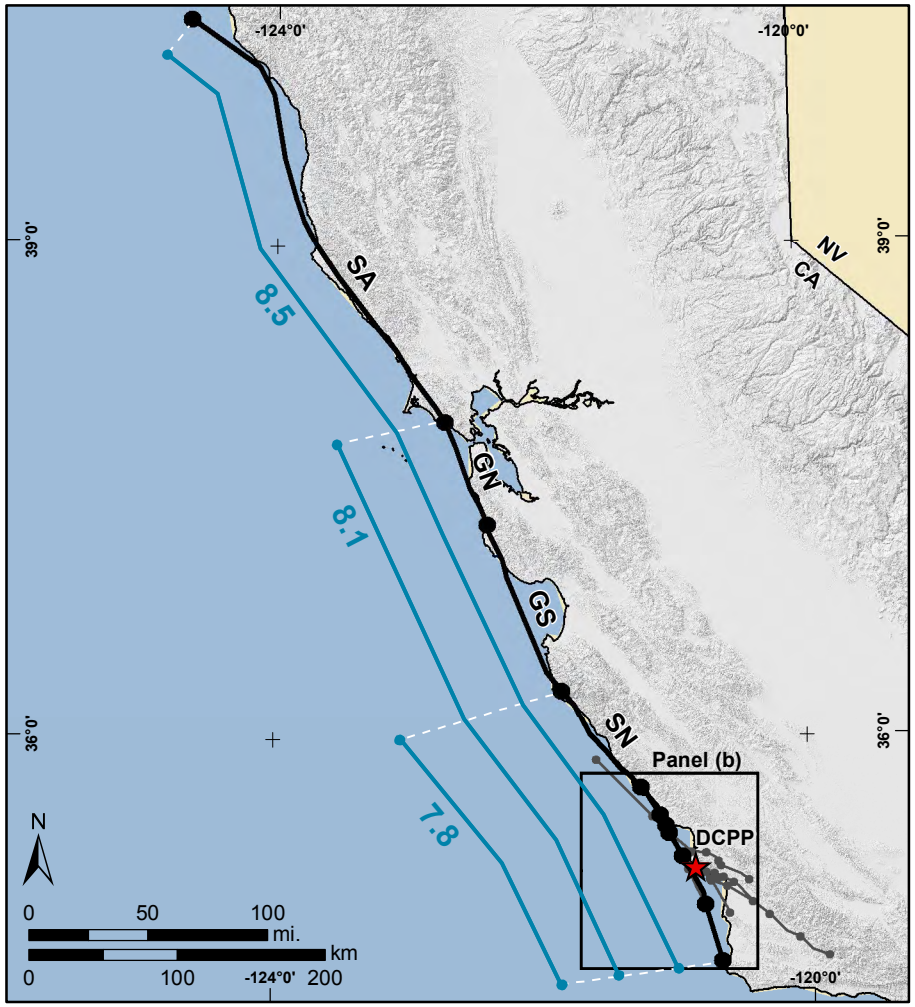

Map projection and scale: WGS 1984 UTM Zone 10N, 1:5,100,000

(b) M_{char}

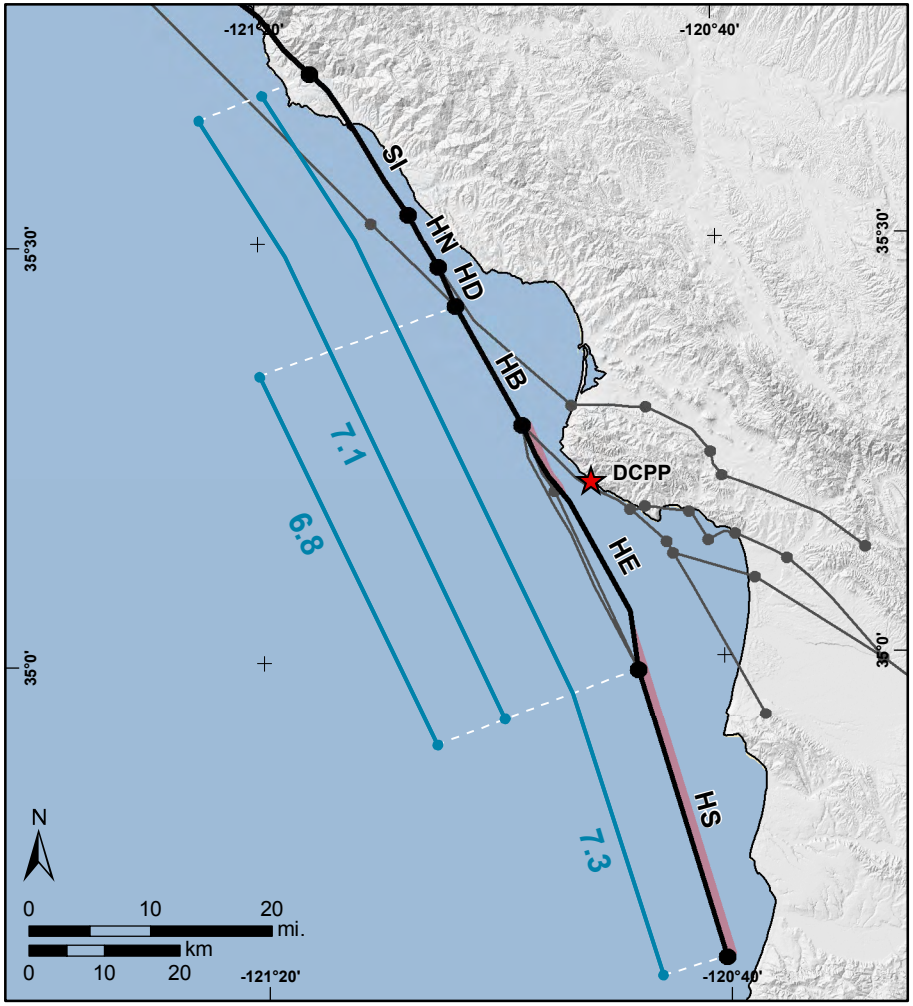

Map projection and scale: WGS 1984 UTM Zone 10N, 1:1,000,000

EXPLANATION

- Length scale used for magnitude estimates
- Rupture source at surface
- Other fault section
- Surface projection of dipping rupture source

Notes:
- No shading is shown for vertical faults.
- Two-letter fault section codes are explained in Table 6-5 and on Plates 9-1 and 9-2.

Alternative Estimates of M_{max} and M_{char} for Rupture Source H-03

DCPP SSC REPORT

Pacific Gas and Electric Company | Figure **10-10**

File path: S:\1005\005\Final_Report_Figures\Figure_1000-10.mxd; Date: 02/25/2015; User: Serkan Bozkurt, LCI; Rev.1

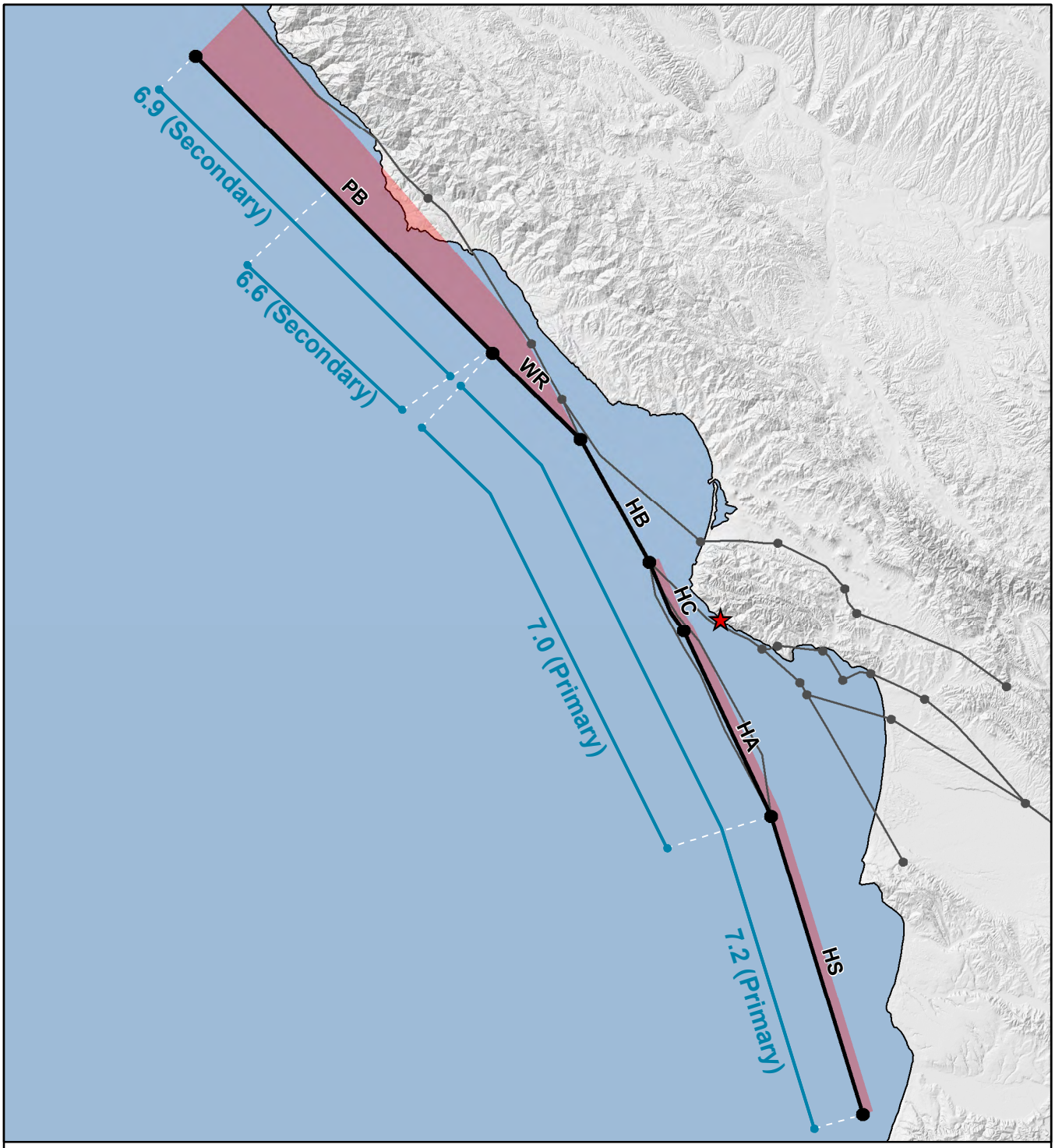

EXPLANATION

- Length scale used for magnitude estimates
- Rupture source at surface
- Other fault section
- Surface projection of dipping rupture source

Notes:
- No shading is shown for vertical faults.
- Two-letter fault section codes are explained in Table 6-5 and on Plates 9-1 and 9-2.
- Two scenario magnitude pairs are shown. See Table 10-5.

N

0 6 12 mi.
0 10 20 km

Map projection and scale: WGS 1984 UTM Zone 10N, 1:750,000

Alternative Estimates of Primary and Secondary Rupture-Plane Magnitudes for Rupture Source H-04

DCPP SSC REPORT

Pacific Gas and Electric Company

Figure **10-11**

File path: S:\1005\005\Final_Report_Figures\Figure_1000-11.mxd; Date: 02/26/2015; User: Serkan Bozkurt, LCI; Rev.1

(a) Magnitudes for Main Rupture Plane

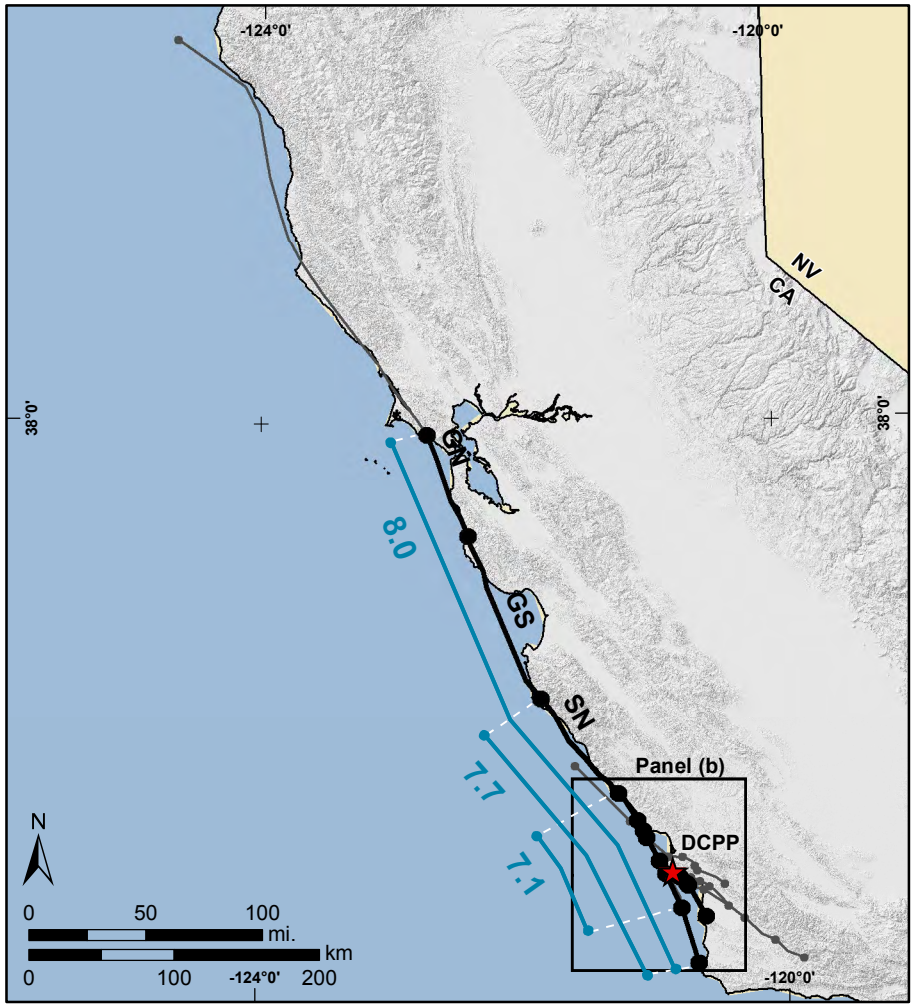

Map projection and scale: WGS 1984 UTM Zone 10N, 1:5,200,000

(b) Magnitudes for Splay Rupture Plane

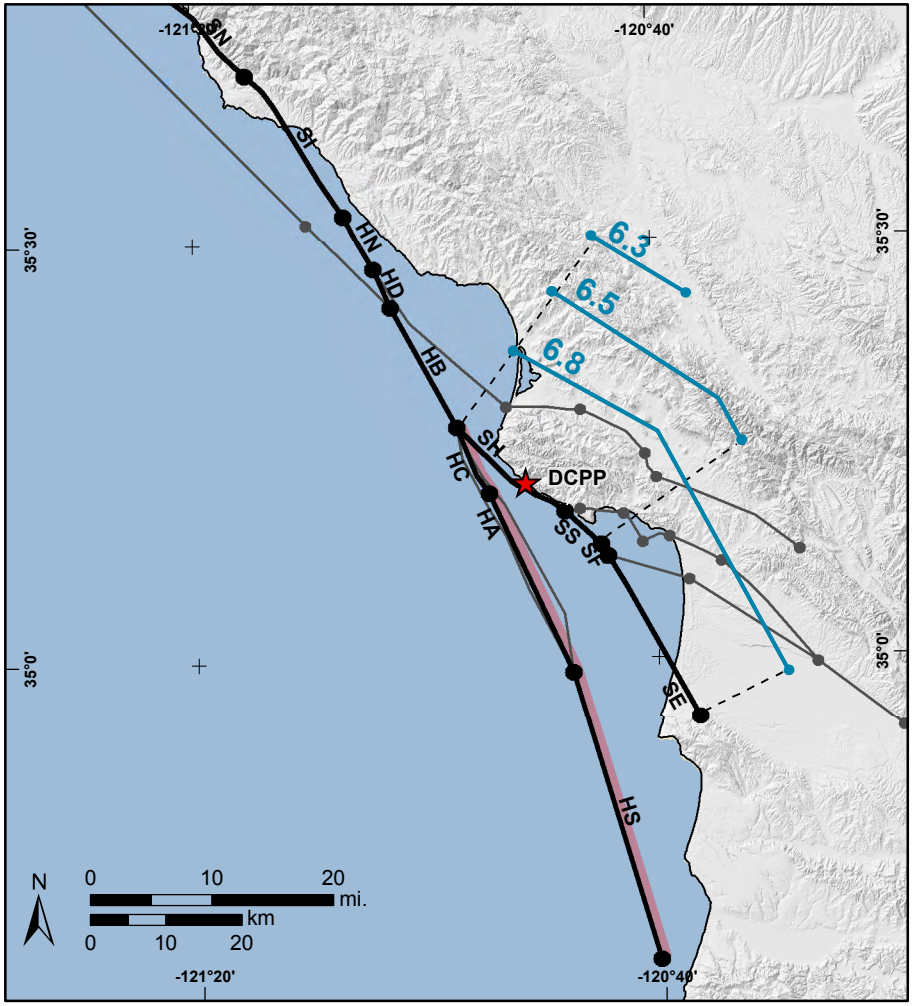

Map projection and scale: WGS 1984 UTM Zone 10N, 1:1,000,000

EXPLANATION

- Length scale used for magnitude estimates
- Rupture source at surface
- Other fault section
- Surface projection of dipping rupture source

Notes:
- No shading is shown for vertical faults.
- Two-letter fault section codes are explained in Table 6-5 and on Plates 9-1 and 9-2.
- Three scenario magnitude pairs are shown. See Table 10-5.

Alternative Estimates of Main and Splay Rupture-Plane Magnitudes for Rupture Source H-05

DCPP SSC REPORT

Pacific Gas and Electric Company Figure **10-12**

File path: S:\1005\005\Final_Report_Figures\Figure_1000-12.mxd; Date: 02/25/2015; User: Serkan Bozkurt, LCI; Rev.1

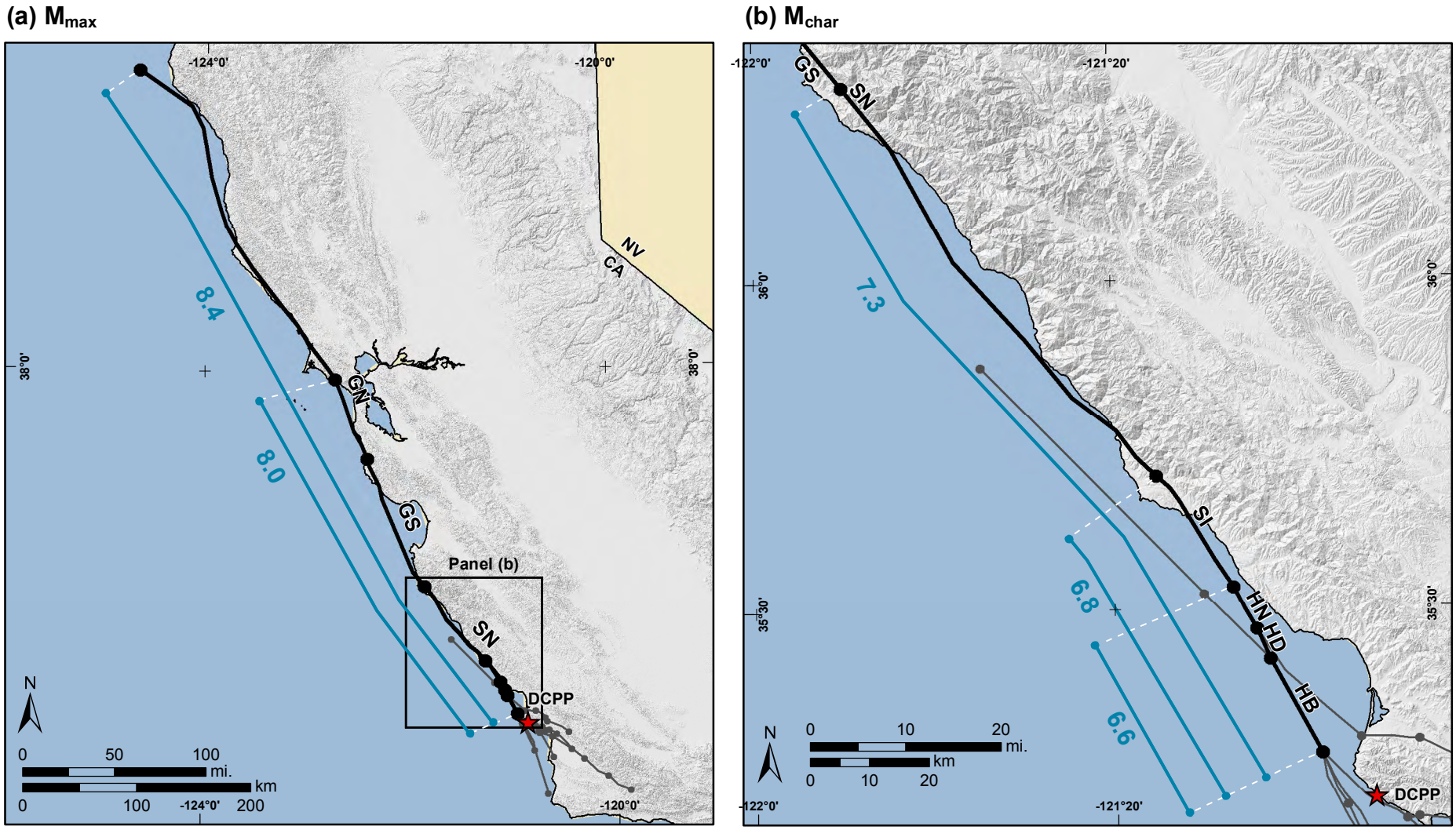

Map projection and scale: WGS 1984 UTM Zone 10N, 1:5,200,000

Map projection and scale: WGS 1984 UTM Zone 10N, 1:1,000,000

EXPLANATION

- Length scale used for magnitude estimates
- Rupture source at surface
- Other fault section

Notes:
- No shading is shown for vertical faults.
- Two-letter fault section codes are explained in Table 6-5 and on Plates 9-1 and 9-2.

Alternative Estimates of M_{max} and M_{char} for Rupture Source H-06

DCPP SSC REPORT

Pacific Gas and Electric Company | Figure **10-13**

File path: S:\1005\005\Final_Report_Figures\Figure_1000-13.mxd; Date: 02/25/2015; User: Serkan Bozkurt, LCI; Rev.1

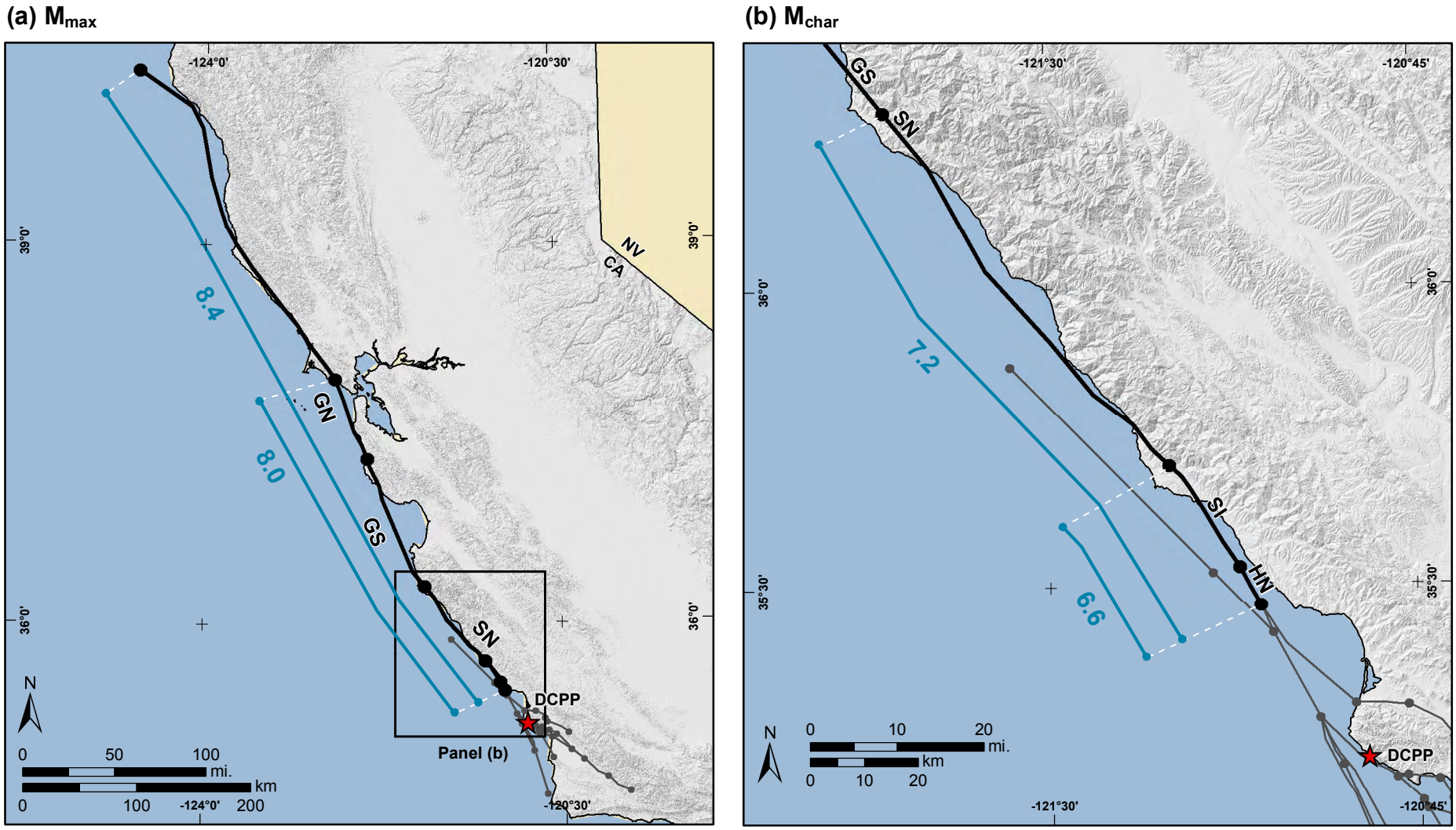

Map projection and scale: WGS 1984 UTM Zone 10N, 1:5,200,000

Map projection and scale: WGS 1984 UTM Zone 10N, 1:1,100,000

EXPLANATION

- Length scale used for magnitude estimates
- Rupture source at surface
- Other fault section

Notes:
- No shading is shown for vertical faults.
- Two-letter fault section codes are explained in Table 6-5 and on Plates 9-1 and 9-2.

Alternative Estimates of M_{max} and M_{char} for Rupture Source H-07

DCPP SSC REPORT

Pacific Gas and Electric Company Figure **10-14**

File path: S:\1005\005\Final_Report_Figures\Figure_1000-14.mxd; Date: 12/30/2014; User: Serkan Bozkurt, LCI; Rev.1

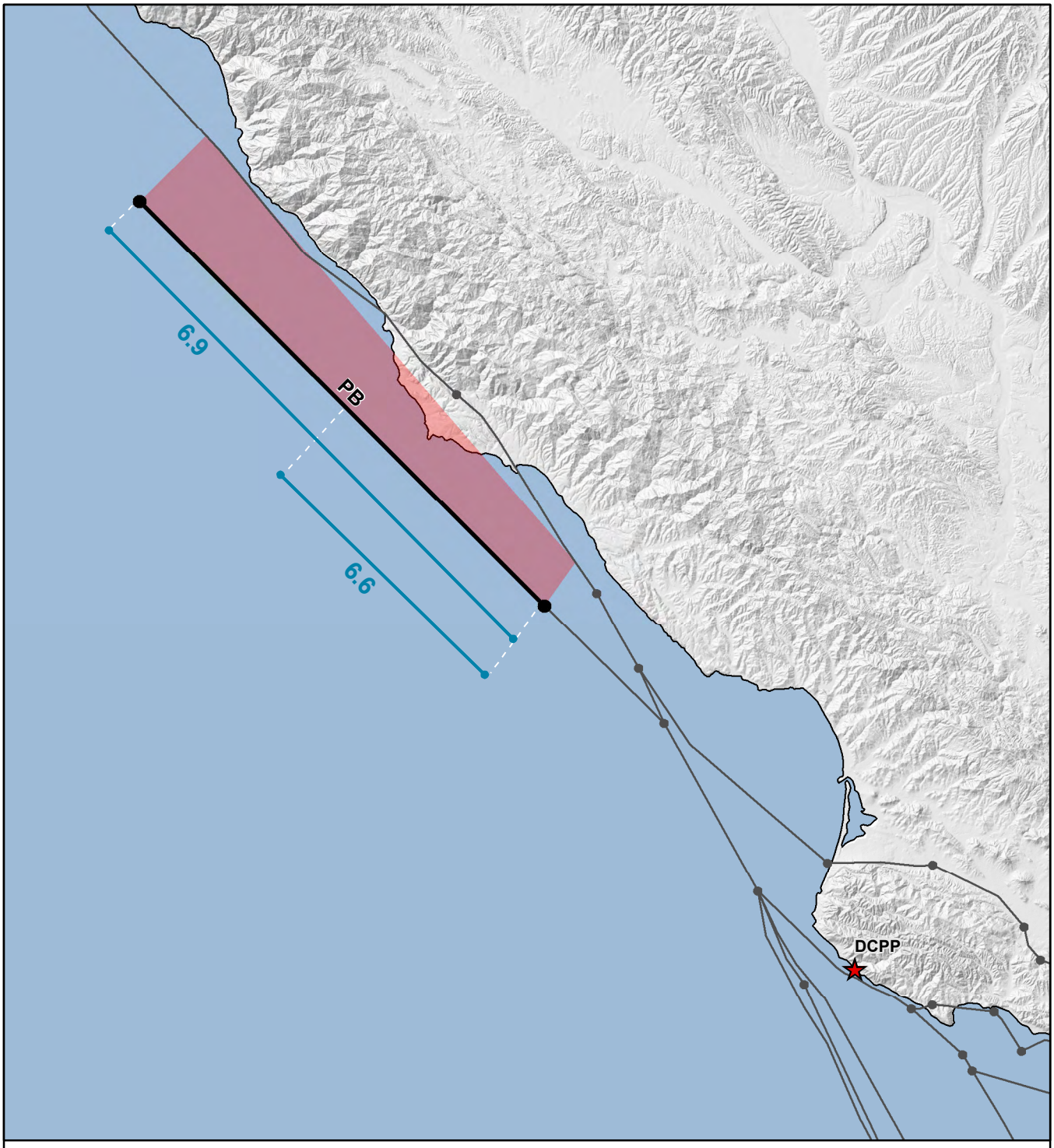

EXPLANATION

- Length scale used for magnitude estimates
- Rupture source at surface
- Other fault section
- Surface projection of dipping rupture source

Note: Two-letter fault section codes are explained in Table 6-5 and on Plates 9-1 and 9-2.

N

0 6 12 mi.

0 10 20 km

Map projection and scale: WGS 1984 UTM Zone 10N, 1:550,000

Alternative Estimates of M_{char} for Rupture Source H-08

DCPP SSC REPORT

Pacific Gas and Electric Company

Figure **10-15**

File path: S:\1005\005\Final_Report_Figures\Figure_1000-15.mxd; Date: 02/26/2015; User: Serkan Bozkurt, LCI; Rev.1

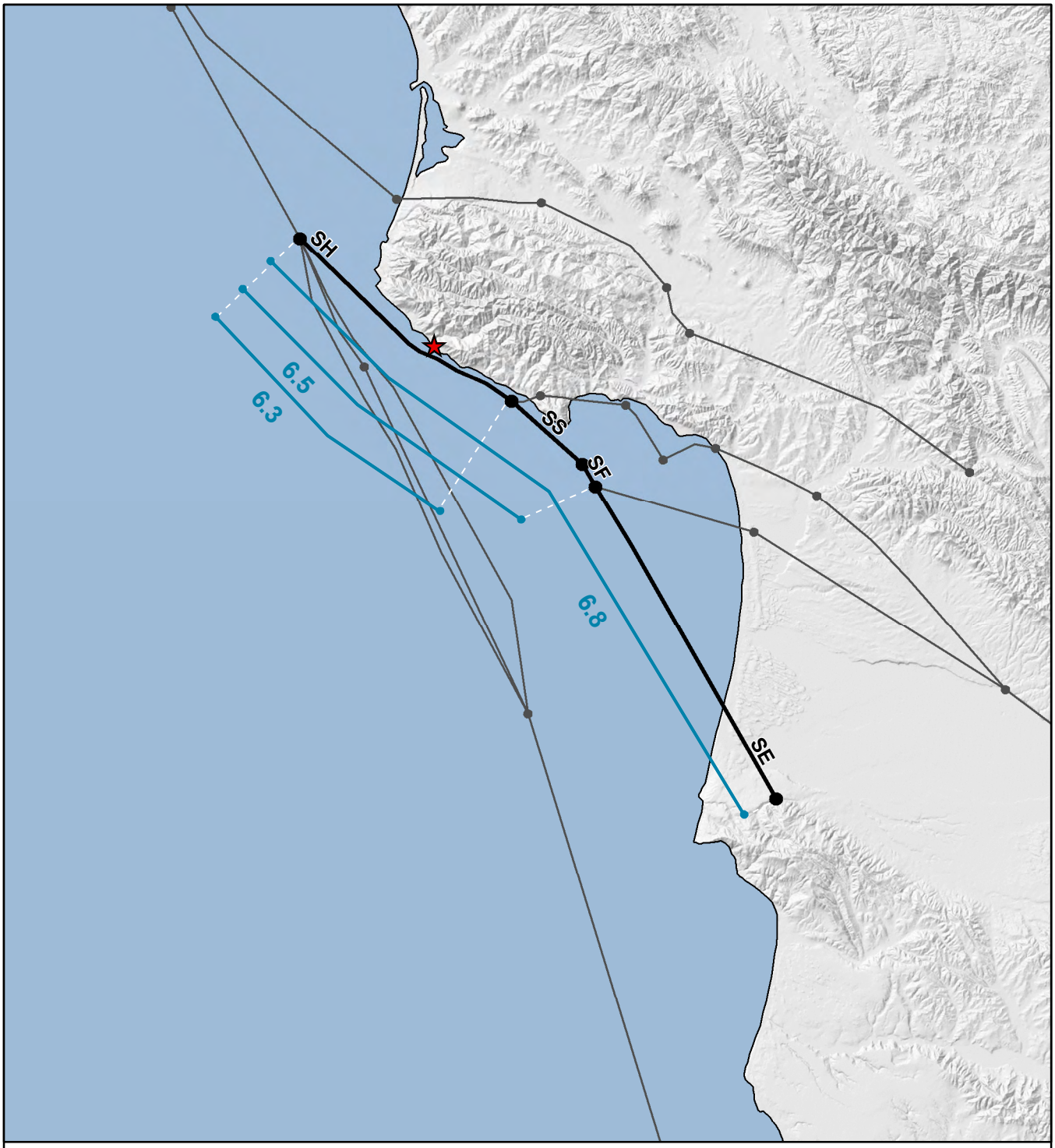

EXPLANATION

- Length scale used for magnitude estimates
- Rupture source at surface
- Other fault section

Notes:
- No shading is shown for vertical faults.
- Two-letter fault section codes are explained in Table 6-5 and on Plates 9-1 and 9-2.

N

0 6 12 mi.
0 10 20 km

Map projection and scale: WGS 1984 UTM Zone 10N, 1:400,000

Alternative Estimates of M_{char} for Rupture Sources OV-01, SW-01, and NE-01

DCPP SSC REPORT

Pacific Gas and Electric Company

Figure **10-16**

File path: S:\1005\005\Final_Report_Figures\Figure_1000-16.mxd; Date: 02/25/2015; User: Serkan Bozkurt, LCI; Rev.1

(a) M_{max}

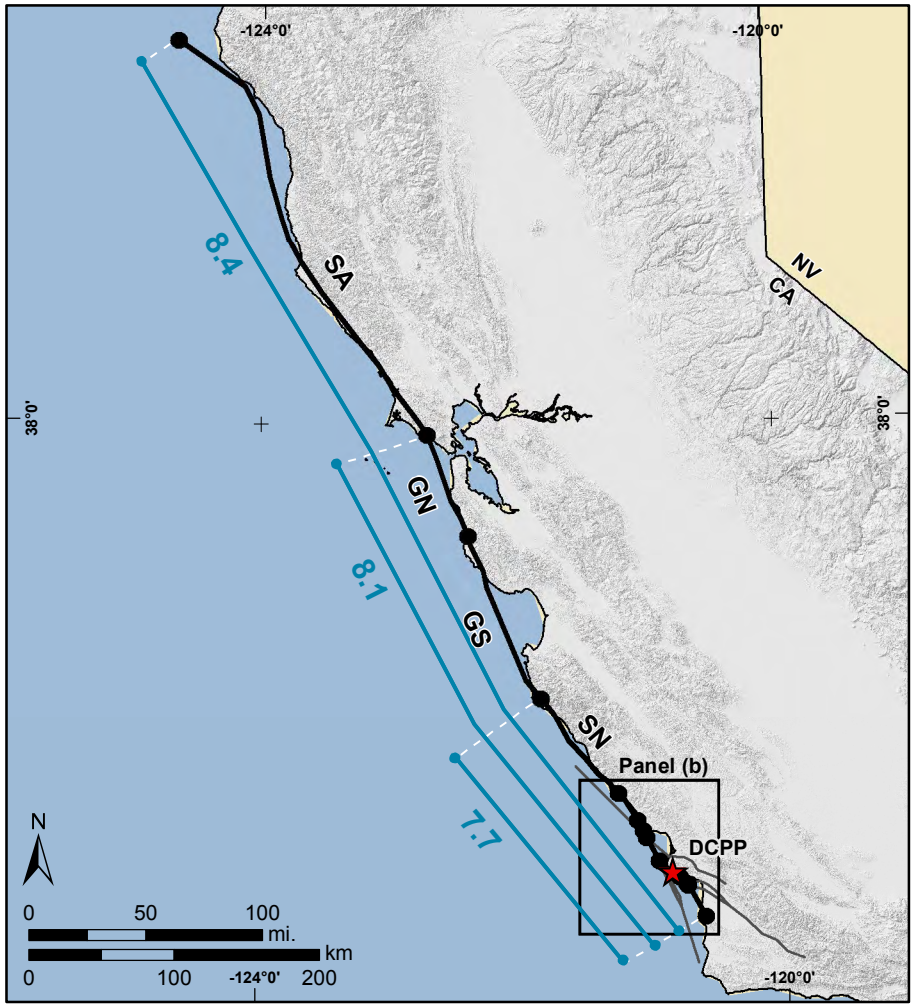

Map projection and scale: WGS 1984 UTM Zone 10N, 1:5,200,000

(b) M_{char}

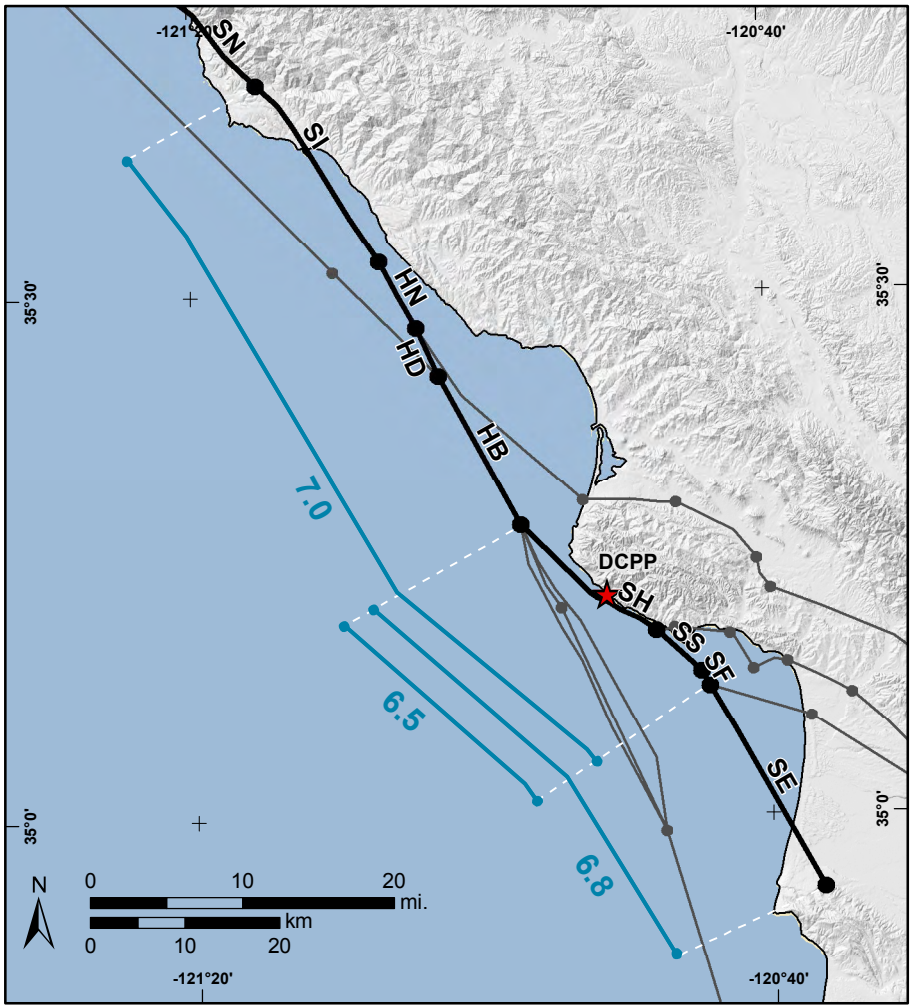

Map projection and scale: WGS 1984 UTM Zone 10N, 1:800,000

EXPLANATION

- Length scale used for magnitude estimates
- Rupture source at surface
- Other fault section

Notes:
- No shading is shown for vertical faults.
- Two-letter fault section codes are explained in Table 6-5 and on Plates 9-1 and 9-2.

Alternative Estimates of M_{max} and M_{char} for Rupture Sources OV-02, SW-02, and NE-02

DCPP SSC REPORT

Pacific Gas and Electric Company | Figure **10-17**

File path: S:\1005\005\Final_Report_Figures\Figure_1000-17.mxd; Date: 02/25/2015; User: Serkan Bozkurt, LCI; Rev.1

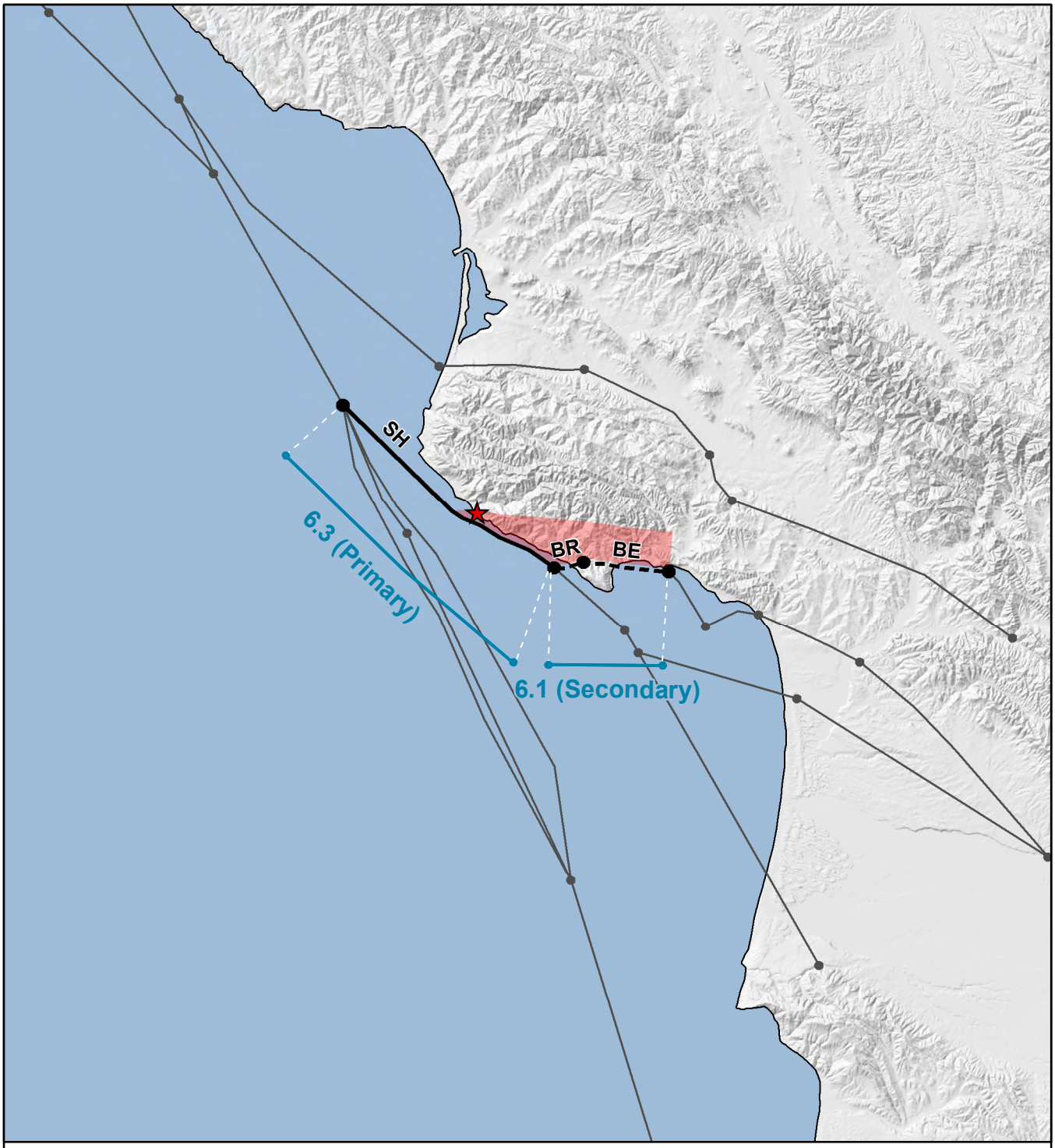

EXPLANATION

- Length scale used for magnitude estimates
- Rupture source at surface
- Updip surface projection of buried rupture source
- Other fault section
- Surface projection of dipping rupture source

Notes:
- No shading is shown for vertical faults.
- Two-letter fault section codes are explained in Table 6-5 and on Plates 9-1 and 9-2.

N

0 6 12 mi.
0 10 20 km

Map projection and scale: WGS 1984 UTM Zone 10N, 1:400,000

Estimates of Primary and Secondary Rupture-Plane Magnitudes for Rupture Source OV-03

DCPP SSC REPORT

Pacific Gas and Electric Company

Figure **10-18**

File path: S:\1005\005\Final_Report_Figures\Figure_1000-18.mxd; Date: 02/26/2015; User: Serkan Bozkurt, LCI; Rev.1

(a) Magnitudes for Primary Rupture Plane

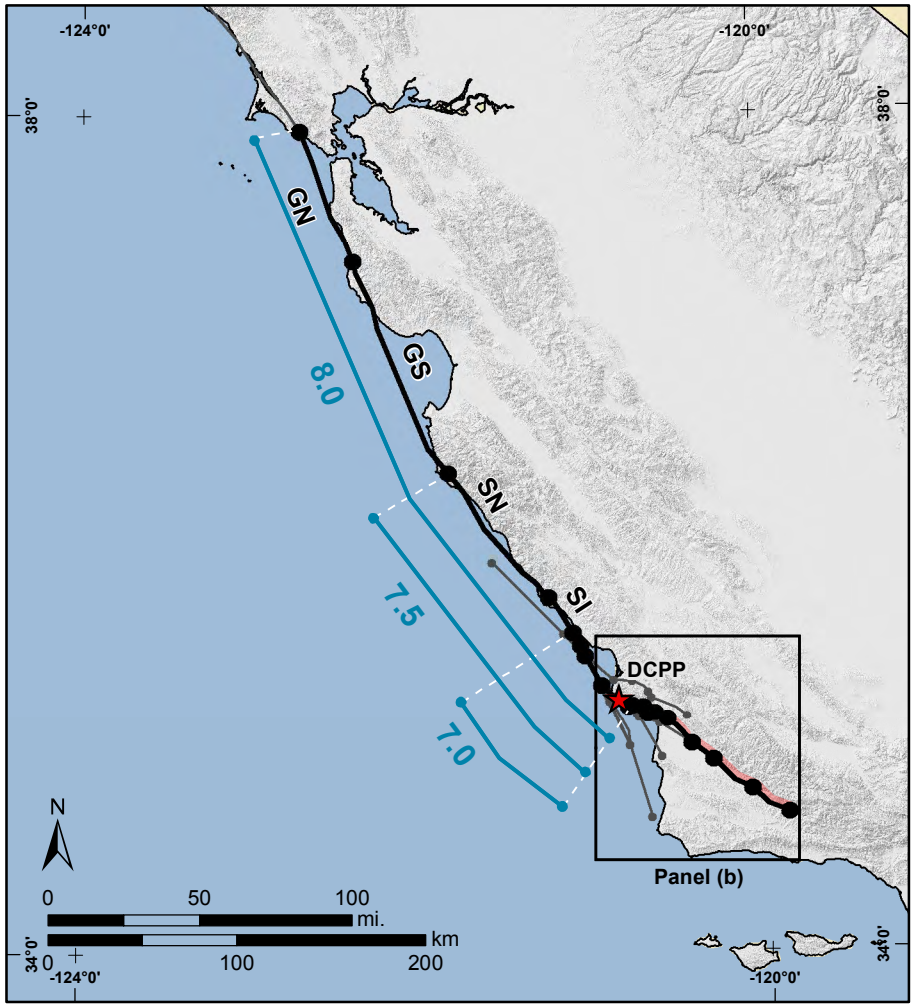

Map projection and scale: WGS 1984 UTM Zone 10N, 1:4,000,000

(b) Magnitudes for Secondary Rupture Plane

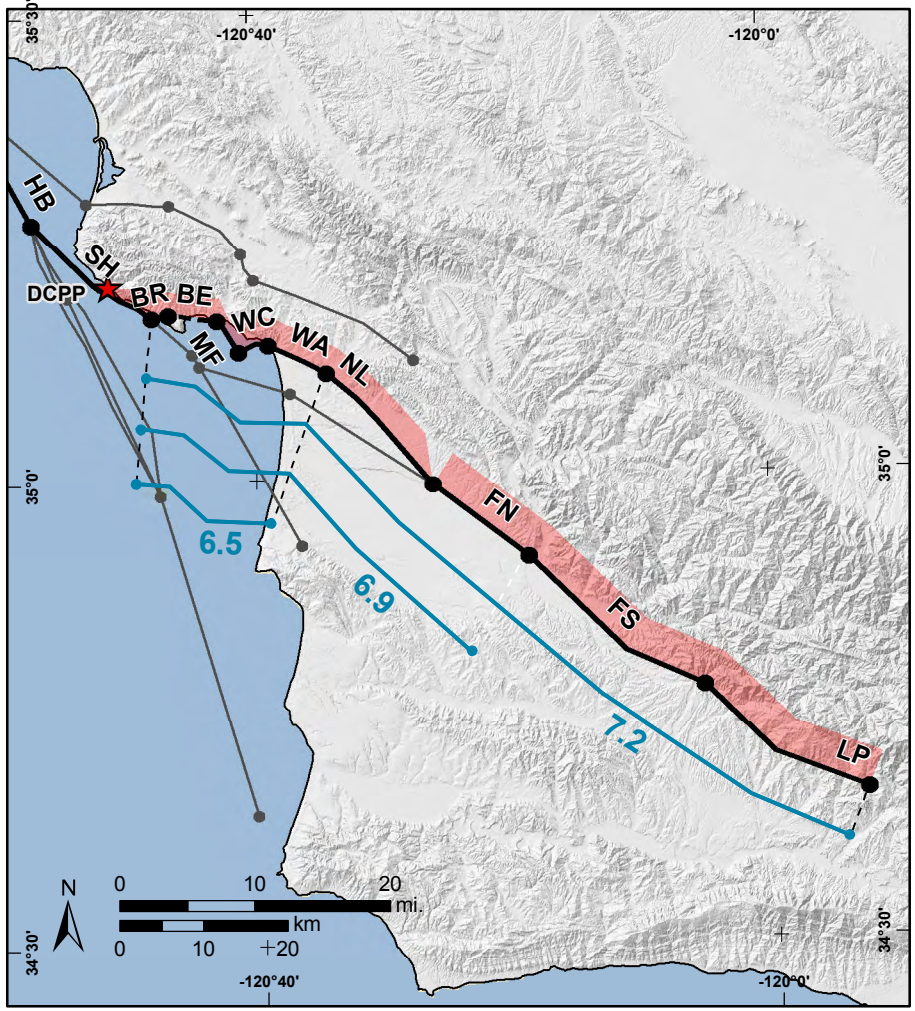

Map projection and scale: WGS 1984 UTM Zone 10N, 1:900,000

EXPLANATION

- Length scale used for magnitude estimates
- Rupture source at surface
- Updip surface projection of buried rupture source
- Other fault section
- Surface projection of dipping rupture source

Notes:
- No shading is shown for vertical faults.
- Two-letter fault section codes are explained in Table 6-5 and on Plates 9-1 and 9-2.
- Three scenario magnitude pairs are shown. See Table 10-8.

Alternative Estimates of Primary and Secondary Rupture-Plane Magnitudes for Rupture Source OV-04

DCPP SSC REPORT

Pacific Gas and Electric Company | Figure **10-19**

File path: S:\1005\005\Final_Report_Figures\Figure_1000-19.mxd; Date: 02/26/2015; User: Serkan Bozkurt, LCI; Rev.1

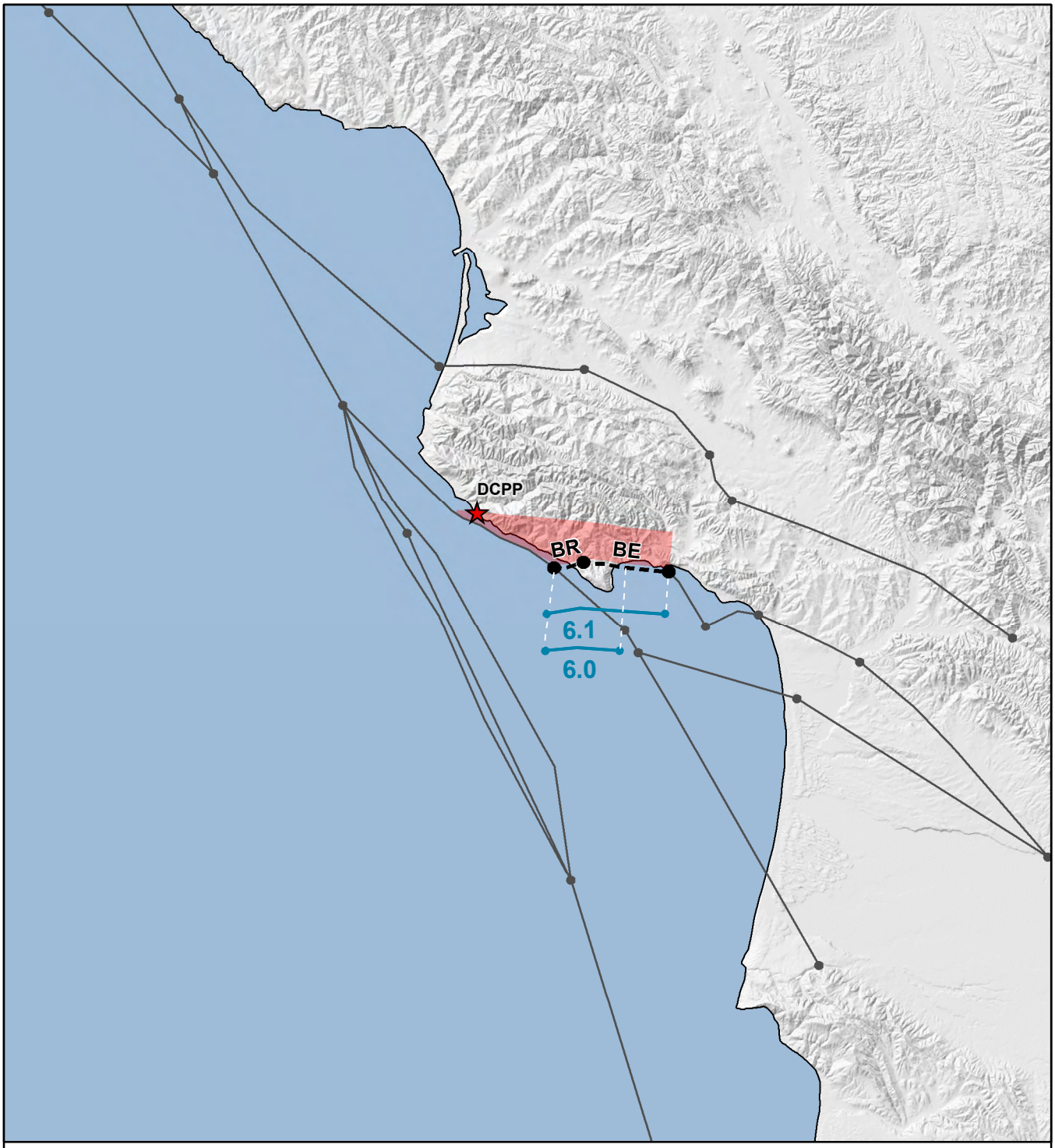

EXPLANATION

- Length scale used for magnitude estimates
- Updip surface projection of buried rupture source
- Other fault section
- Surface projection of dipping rupture source

Note: Two-letter fault section codes are explained in Table 6-5 and on Plates 9-1 and 9-2.

N

0 6 12 mi.

0 10 20 km

Map projection and scale: WGS 1984 UTM Zone 10N, 1:400,000

Alternative Estimates of M_{char} for Rupture Source OV-05

DCPP SSC REPORT

Pacific Gas and Electric Company

Figure **10-20**

File path: S:\1005\005\Final_Report_Figures\Figure_1000-20.mxd; Date: 02/25/2015; User: Serkan Bozkurt, LCI; Rev.1

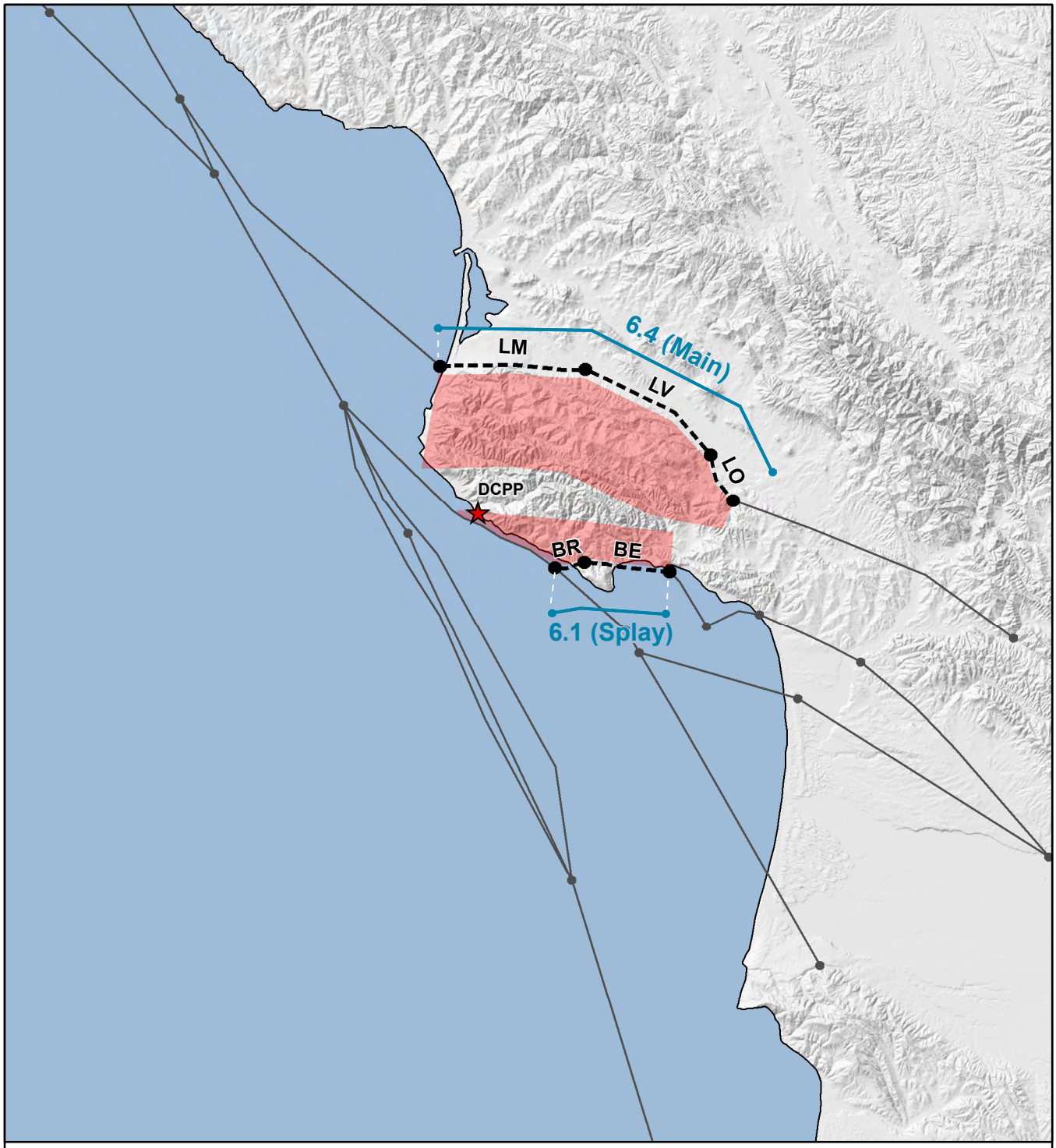

EXPLANATION

- Length scale used for magnitude estimates
- Updip surface projection of buried rupture source
- Other fault section
- Surface projection of dipping rupture source

Note: Two-letter fault section codes are explained in Table 6-5 and on Plates 9-1 and 9-2.

N

0 6 12 mi.

0 10 20 km

Map projection and scale: WGS 1984 UTM Zone 10N, 1:400,000

Estimates of Main and Splay Rupture-Plane Magnitudes for Rupture Source OV-06

DCPP SSC REPORT

Pacific Gas and Electric Company

Figure **10-21**

File path: S:\1005\005\Final_Report_Figures\Figure_1000-21.mxd; Date: 02/25/2015; User: Serkan Bozkurt, LCI; Rev.1

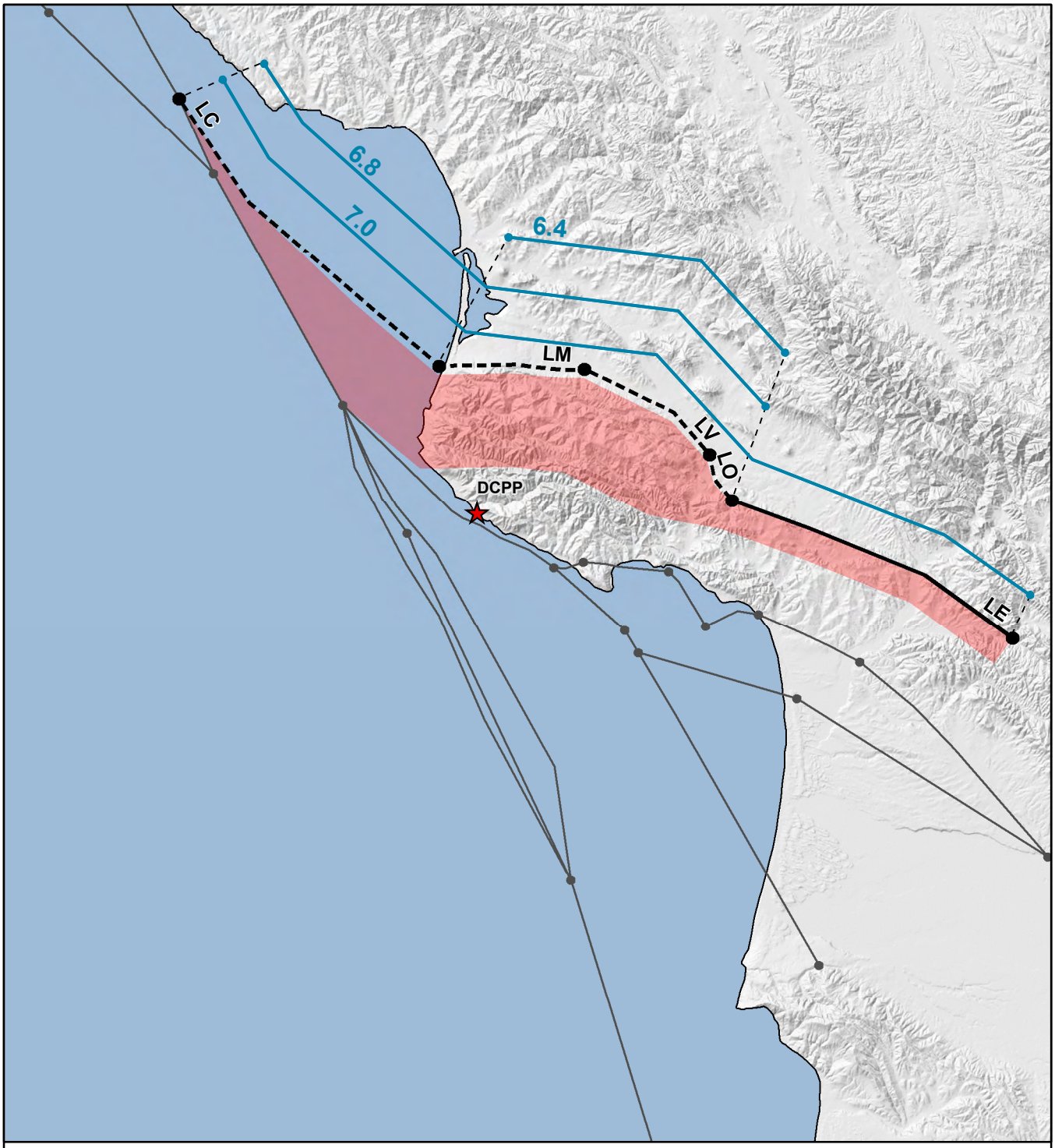

EXPLANATION

- Length scale used for magnitude estimates
- Rupture source at surface
- Updip surface projection of buried rupture source
- Other fault section
- Surface projection of dipping rupture source

Note: Two-letter fault section codes are explained in Table 6-5 and on Plates 9-1 and 9-2.

N

0 6 12 mi.

0 10 20 km

Map projection and scale: WGS 1984 UTM Zone 10N, 1:400,000

Alternative Estimates of M_{char} for Rupture Source OV-07

DCPP SSC REPORT

Pacific Gas and Electric Company

Figure **10-22**

File path: S:\1005\005\Final_Report_Figures\Figure_1000-22.mxd; Date: 02/26/2015; User: Serkan Bozkurt, LCI; Rev.1

(a) Magnitudes for Primary Rupture Plane

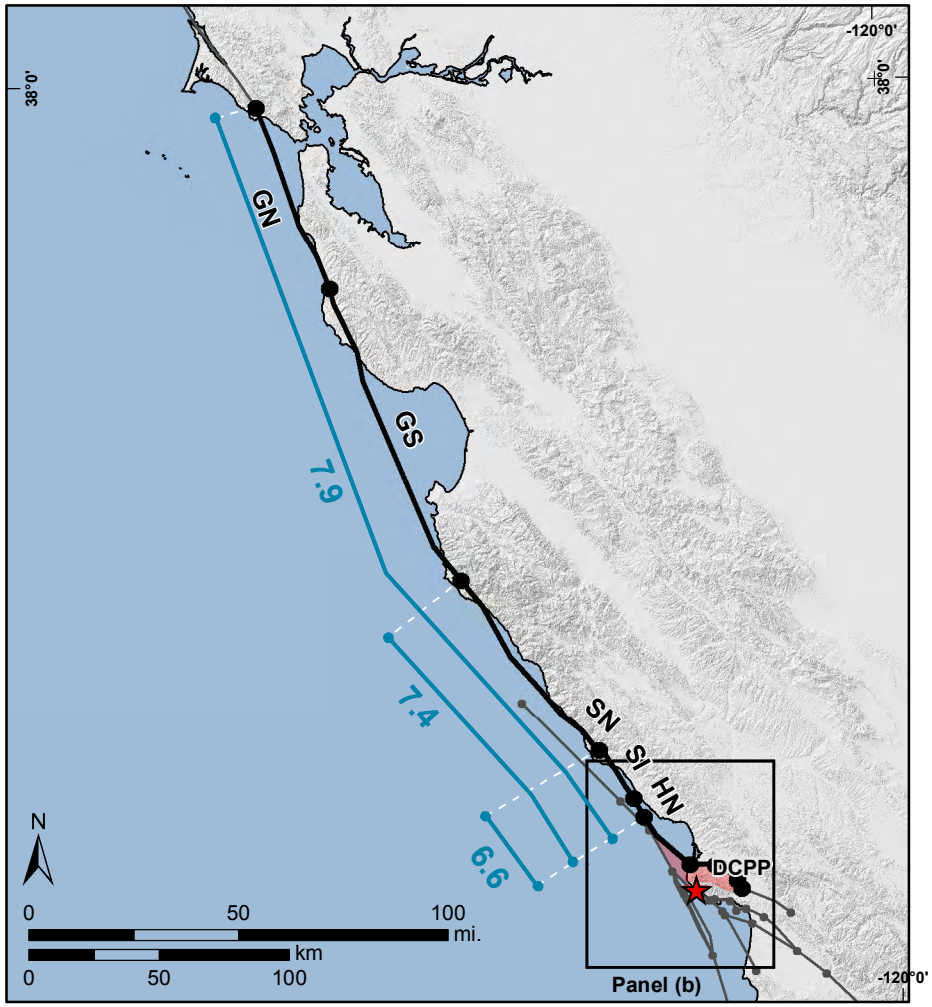

Map projection and scale: WGS 1984 UTM Zone 10N, 1:2,900,000

(b) Magnitudes for Secondary Rupture Plane

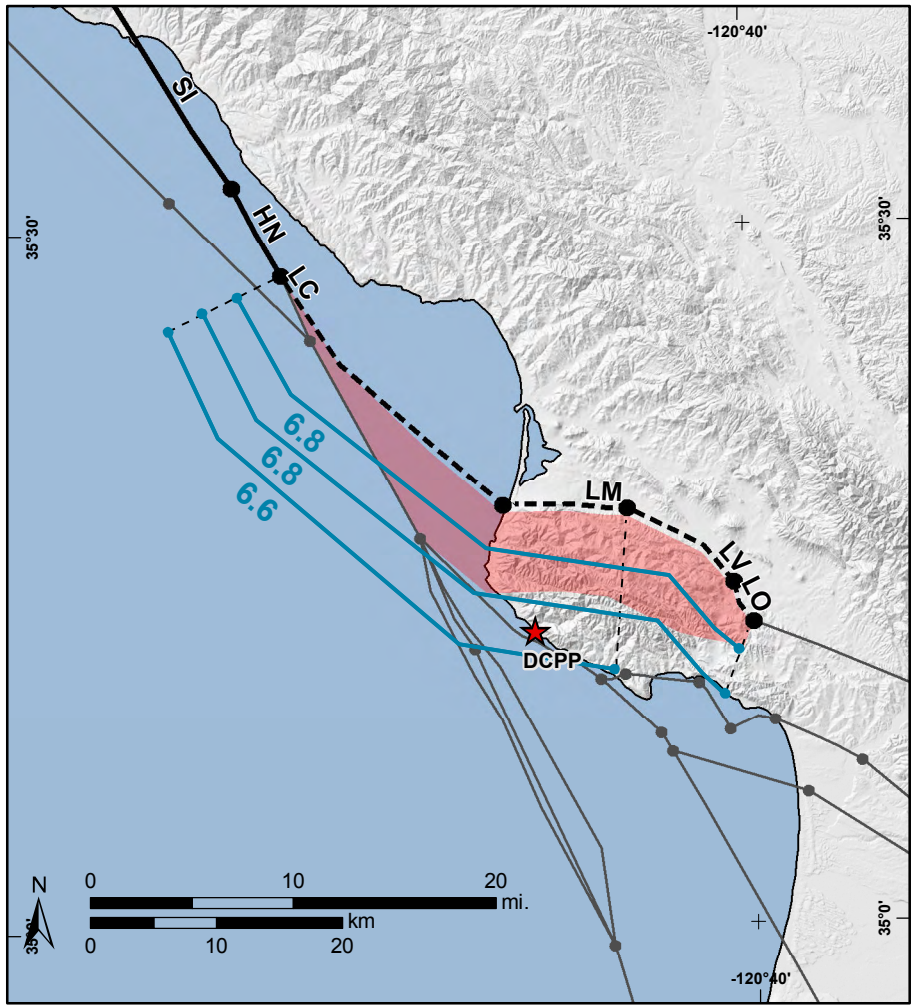

Map projection and scale: WGS 1984 UTM Zone 10N, 1:600,000

EXPLANATION

- Length scale used for magnitude estimates
- Rupture source at surface
- Updip surface projection of buried rupture source
- Other fault section
- Surface projection of dipping rupture source

Notes:
- No shading is shown for vertical faults.
- Two-letter fault section codes are explained in Table 6-5 and on Plates 9-1 and 9-2.
- Three scenario magnitude pairs are shown. See Table 10-8.

Alternative Estimates of Primary and Secondary Rupture-Plane Magnitudes for Rupture Source OV-08

DCPP SSC REPORT

Pacific Gas and Electric Company Figure **10-23**

File path: S:\1005\005\Final_Report_Figures\Figure_1000-23.mxd; Date: 02/26/2015; User: Serkan Bozkurt, LCI; Rev.1

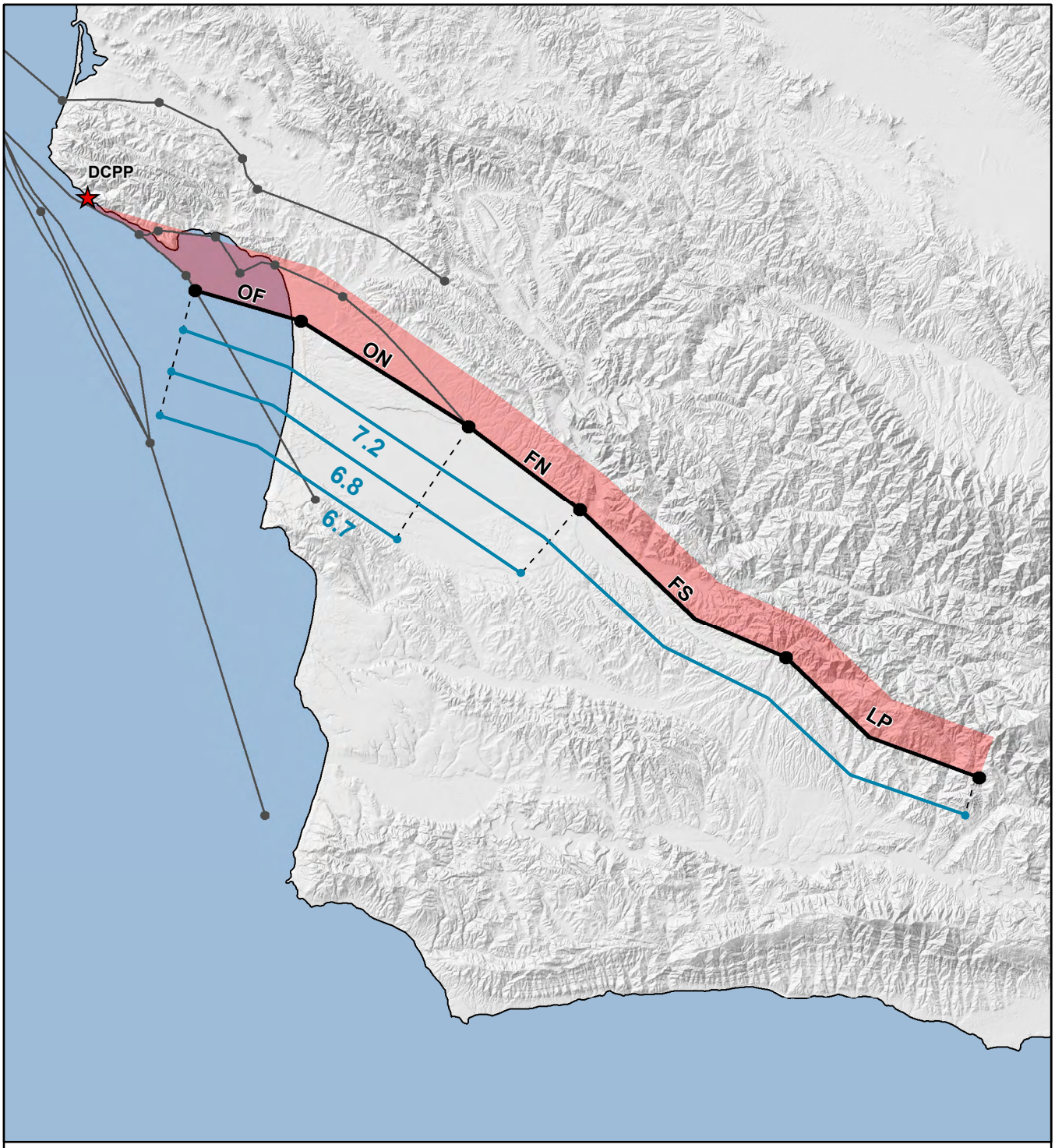

EXPLANATION

- Length scale used for magnitude estimates
- Rupture source at surface
- Other fault section
- Surface projection of dipping rupture source

Note: Two-letter fault section codes are explained in Table 6-5 and on Plates 9-1 and 9-2.

N

0 6 12 mi.

0 10 20 km

Map projection and scale: WGS 1984 UTM Zone 10N, 1:11,000,000

Alternative Estimates of M_{char} for Rupture Source OV-09

DCPP SSC REPORT

Pacific Gas and Electric Company

Figure **10-24**

File path: S:\1005\005\Final_Report_Figures\Figure_1000-24.mxd; Date: 03/11/2015; User: Serkan Bozkurt, LCI; Rev.1

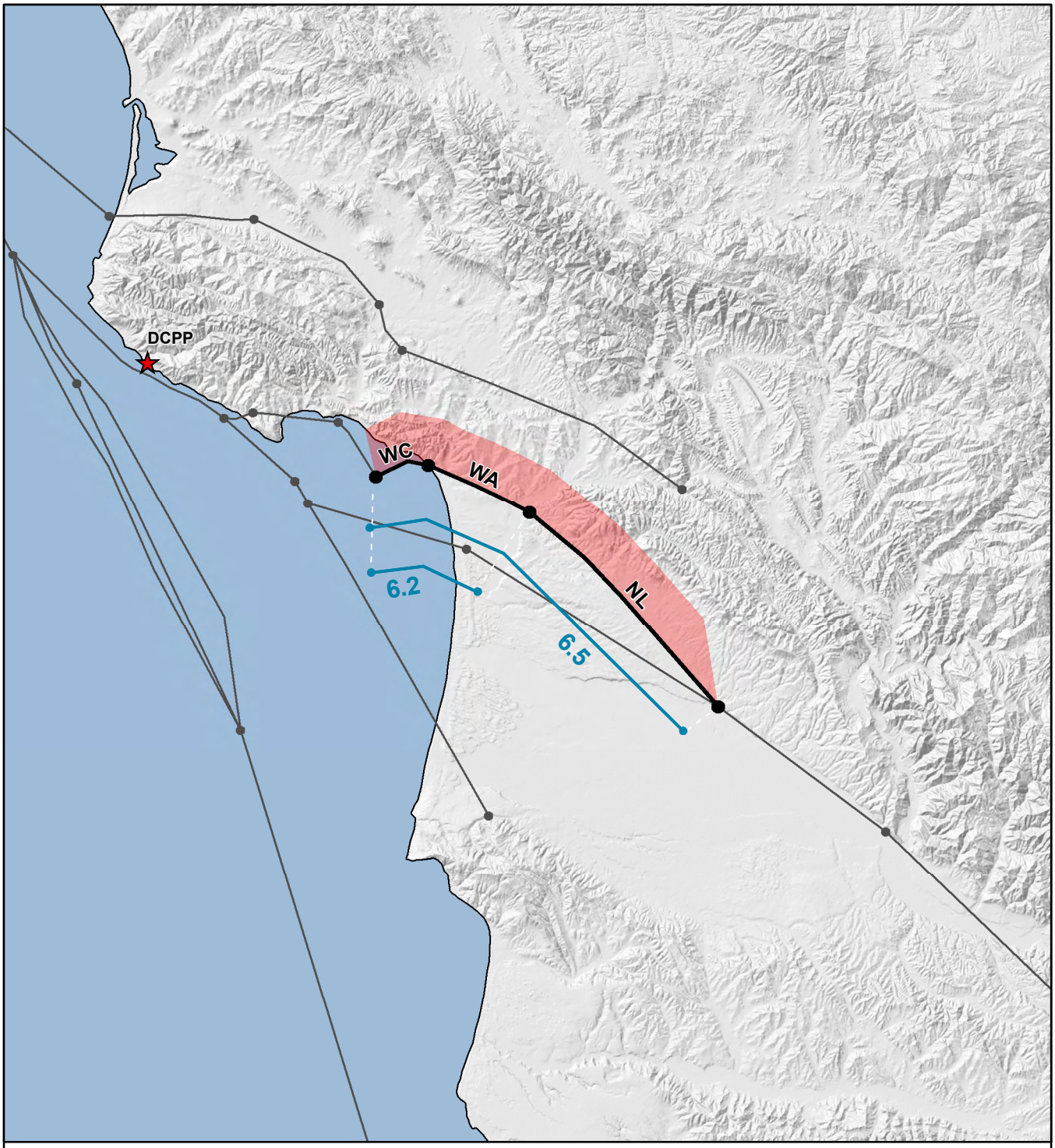

EXPLANATION

- Length scale used for magnitude estimates
- Rupture source at surface
- Other fault section
- Surface projection of dipping rupture source

Note: Two-letter fault section codes are explained in Table 6-5 and on Plates 9-1 and 9-2.

N

0 6 12 mi.

0 10 20 km

Map projection and scale: WGS 1984 UTM Zone 10N, 1:400,000

Alternative Estimates of M_{char} for Rupture Source OV-10

DCPP SSC REPORT

Pacific Gas and Electric Company

Figure **10-25**

File path: S:\1005\005\Final_Report_Figures\Figure_1000-25.mxd; Date: 03/11/2015; User: Serkan Bozkurt, LCI; Rev.1

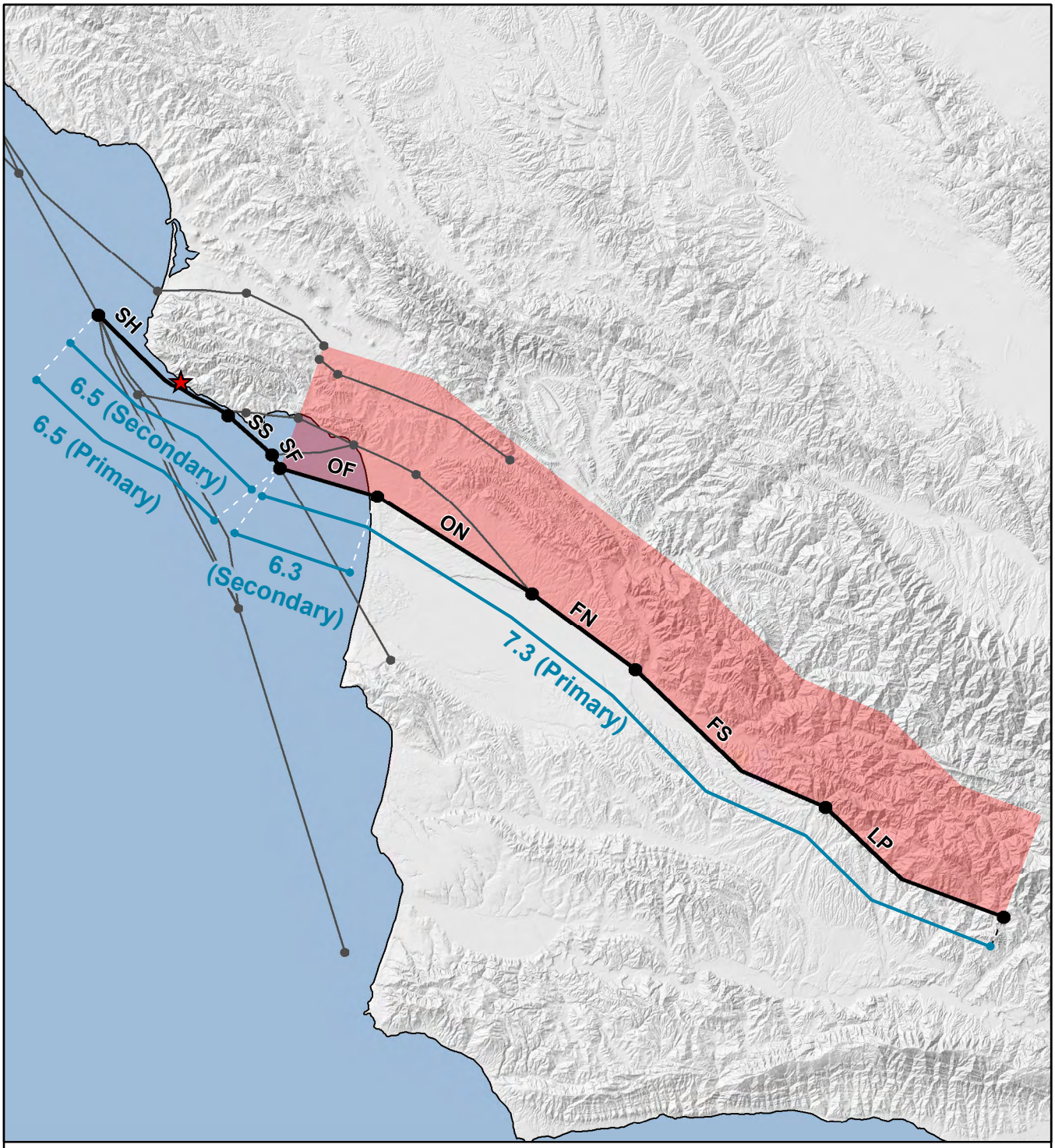

EXPLANATION

- Length scale used for magnitude estimates
- Rupture source at surface
- Other fault section
- Surface projection of dipping rupture source

Notes:
- No shading is shown for vertical faults.
- Two-letter fault section codes are explained in Table 6-5 and on Plates 9-1 and 9-2.
- Two scenario magnitude pairs are shown. See Table 10-11.

N

0 6 12 mi.
0 10 20 km

Map projection and scale: WGS 84 / UTM Zone 10N,1:650,000

Alternative Estimates of Primary and Secondary Rupture-Plane Magnitudes for Rupture Source SW-03

DCPP SSC REPORT

Pacific Gas and Electric Company

Figure **10-26**

File path: S:\1005\005\Final_Report_Figures\Figure_1000-26.mxd; Date: 02/26/2015; User: Serkan Bozkurt, LCI; Rev.1

(a) Magnitudes for Primary Rupture Plane

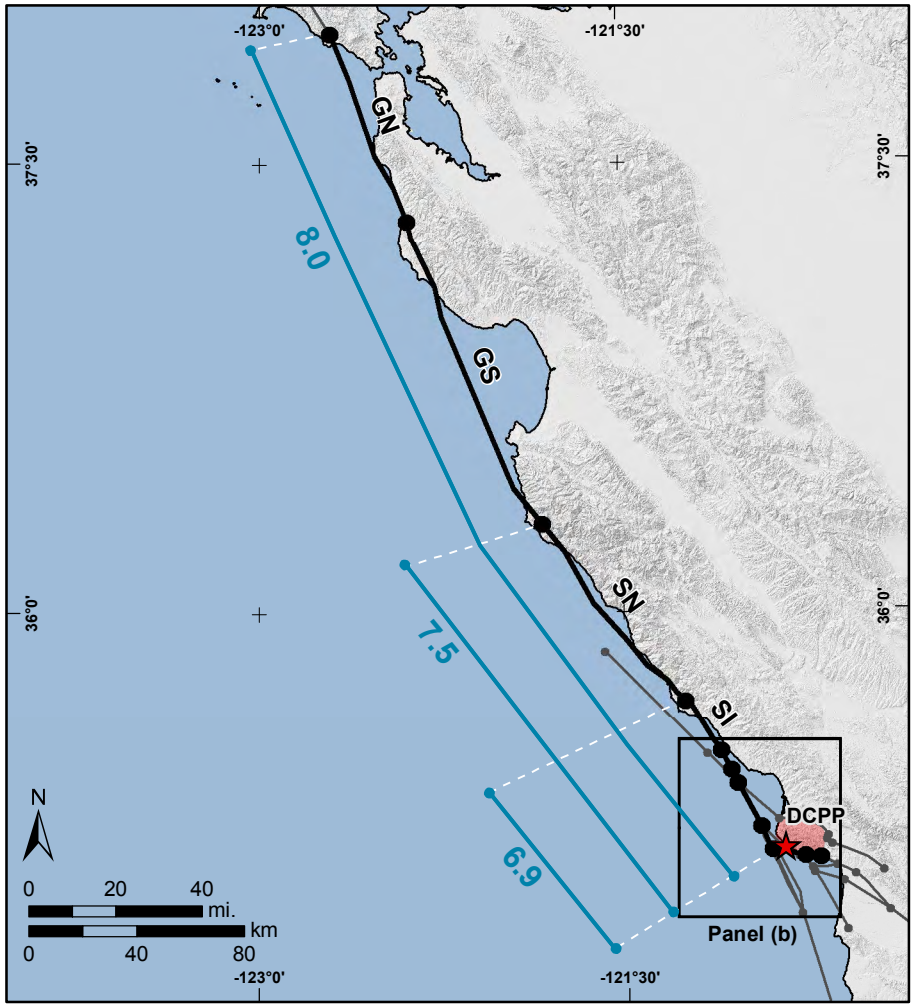

Map projection and scale: WGS 1984 UTM Zone 10N, 1:2,800,000

(b) Magnitudes for Secondary Rupture Plane

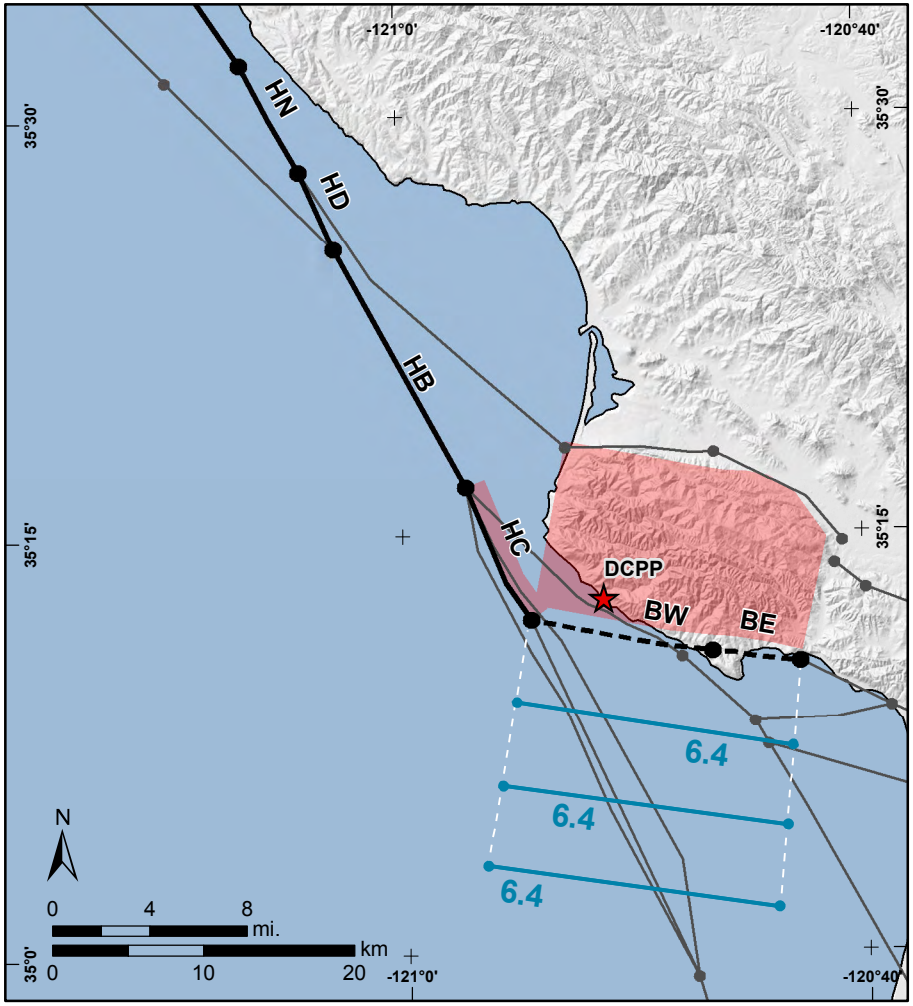

Map projection and scale: WGS 1984 UTM Zone 10N, 1:500,000

EXPLANATION

- Length scale used for magnitude estimates
- Rupture source at surface
- Updip surface projection of buried rupture source
- Other fault section
- Surface projection of dipping rupture source

Notes:
- No shading is shown for vertical faults.
- Two-letter fault section codes are explained in Table 6-5 and on Plates 9-1 and 9-2.
- Three scenario magnitude pairs are shown. See Table 10-11.

Alternative Estimates of Primary and Secondary Rupture-Plane Magnitudes for Rupture Source SW-04

DCPP SSC REPORT

Pacific Gas and Electric Company | Figure **10-27**

File path: S:\1005\005\Final_Report_Figures\Figure_1000-27.mxd; Date: 02/26/2015; User: Serkan Bozkurt, LCI; Rev.1

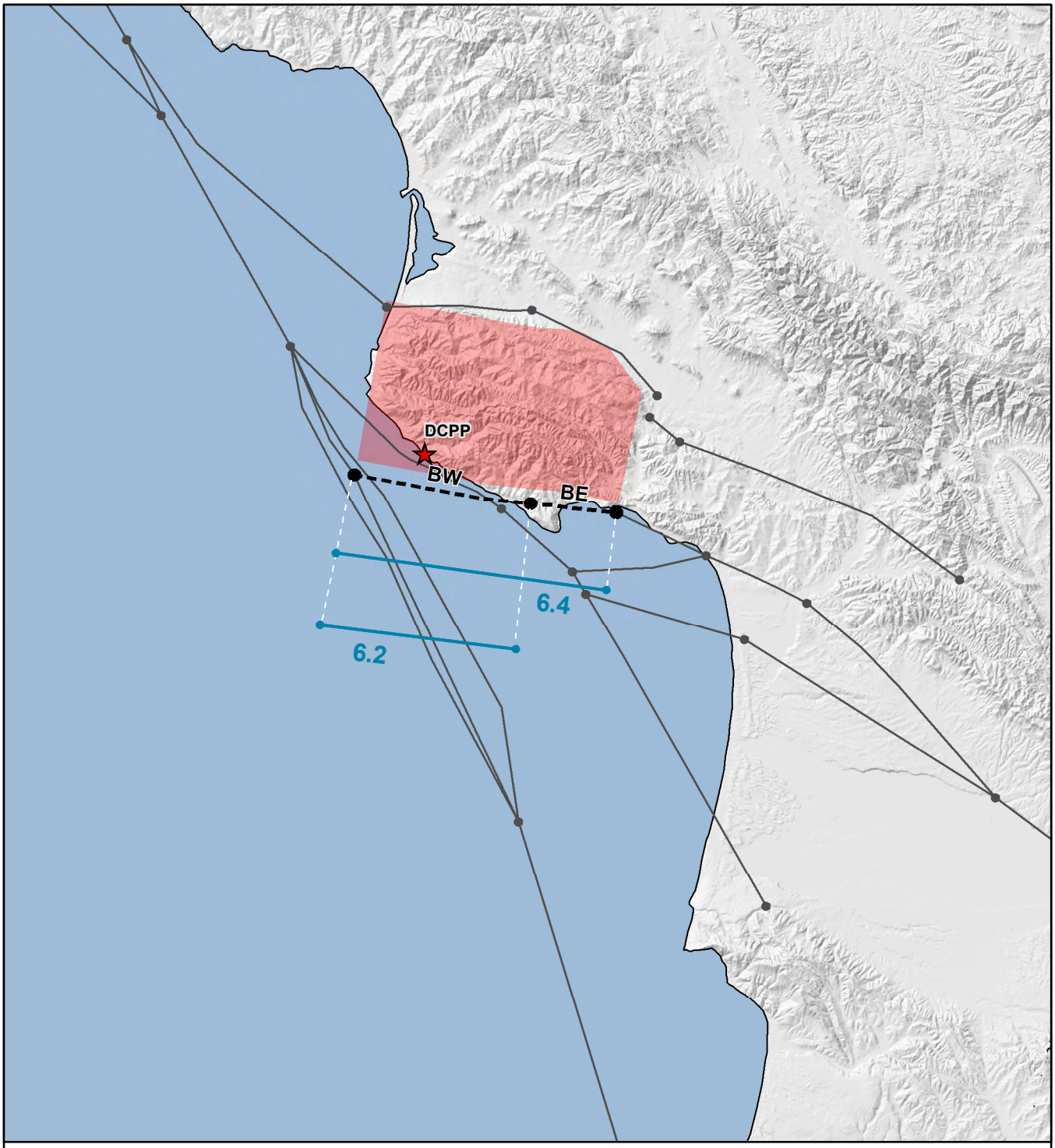

EXPLANATION

- Length scale used for magnitude estimates
- Updip surface projection of buried rupture source
- Other fault section
- Surface projection of dipping rupture source

Note: Two-letter fault section codes are explained in Table 6-5 and on Plates 9-1 and 9-2.

N

0 6 12 mi.

0 10 20 km

Map projection and scale: WGS 1984 UTM Zone 10N, 1:400,000

Alternative Estimates of M_{char} for Rupture Source SW-05

DCPP SSC REPORT

Pacific Gas and Electric Company

Figure **10-28**

File path: S:\1005\005\Final_Report_Figures\Figure_1000-28.mxd; Date: 02/26/2015; User: Serkan Bozkurt, LCI; Rev.1

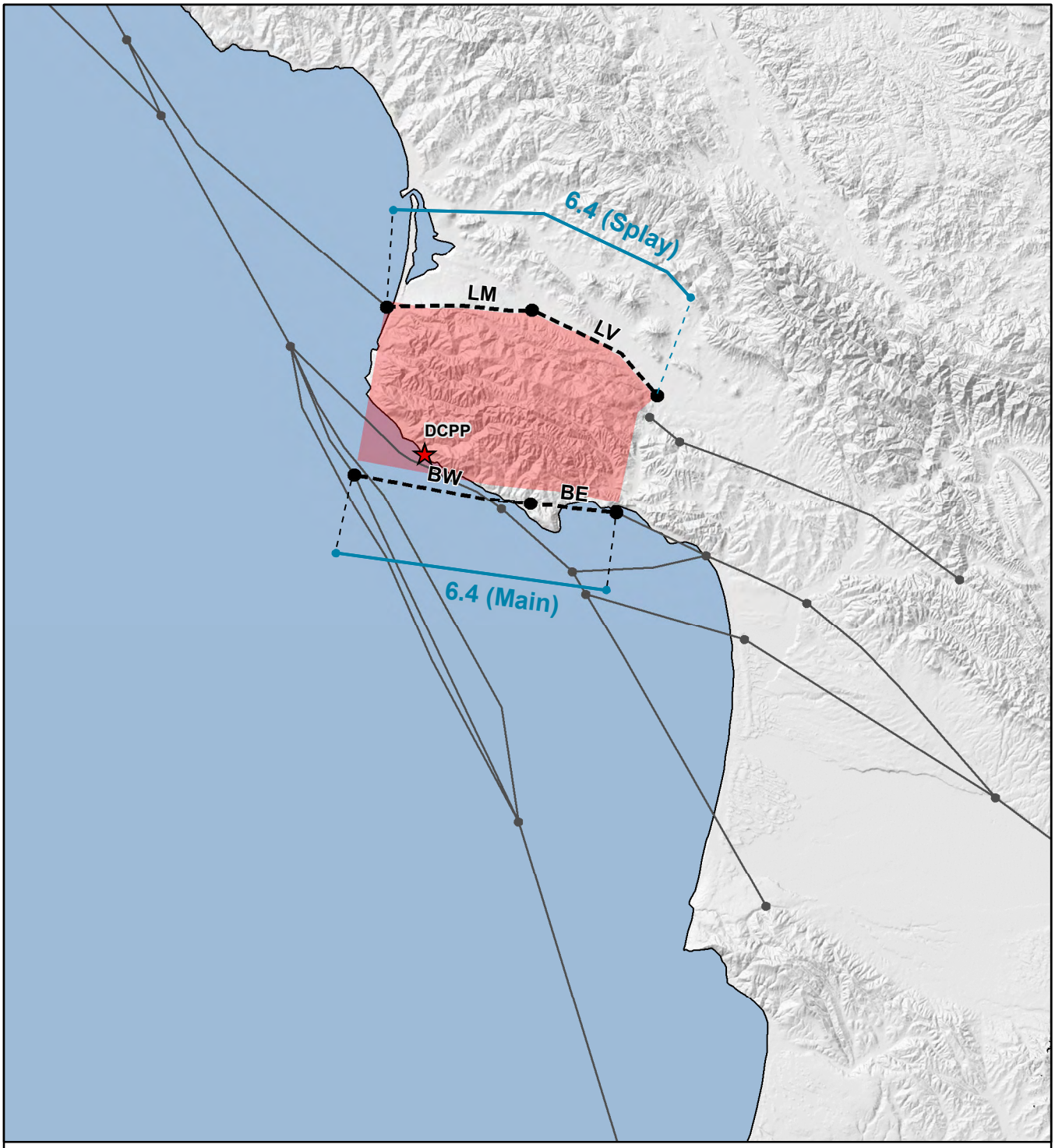

EXPLANATION

- Length scale used for magnitude estimates
- Updip surface projection of buried rupture source
- Other fault section
- Surface projection of dipping rupture source

Note: Two-letter fault section codes are explained in Table 6-5 and on Plates 9-1 and 9-2.

N

0 6 12 mi.

0 10 20 km

Map projection and scale: WGS 1984 UTM Zone 10N, 1:400,000

Estimates of Main and Splay Rupture-Plane Magnitudes for Rupture Source SW-06

DCPP SSC REPORT

Pacific Gas and Electric Company

Figure **10-29**

File path: S:\1005\005\Final_Report_Figures\Figure_1000-29.mxd; Date: 02/26/2015; User: Serkan Bozkurt, LCI; Rev.1

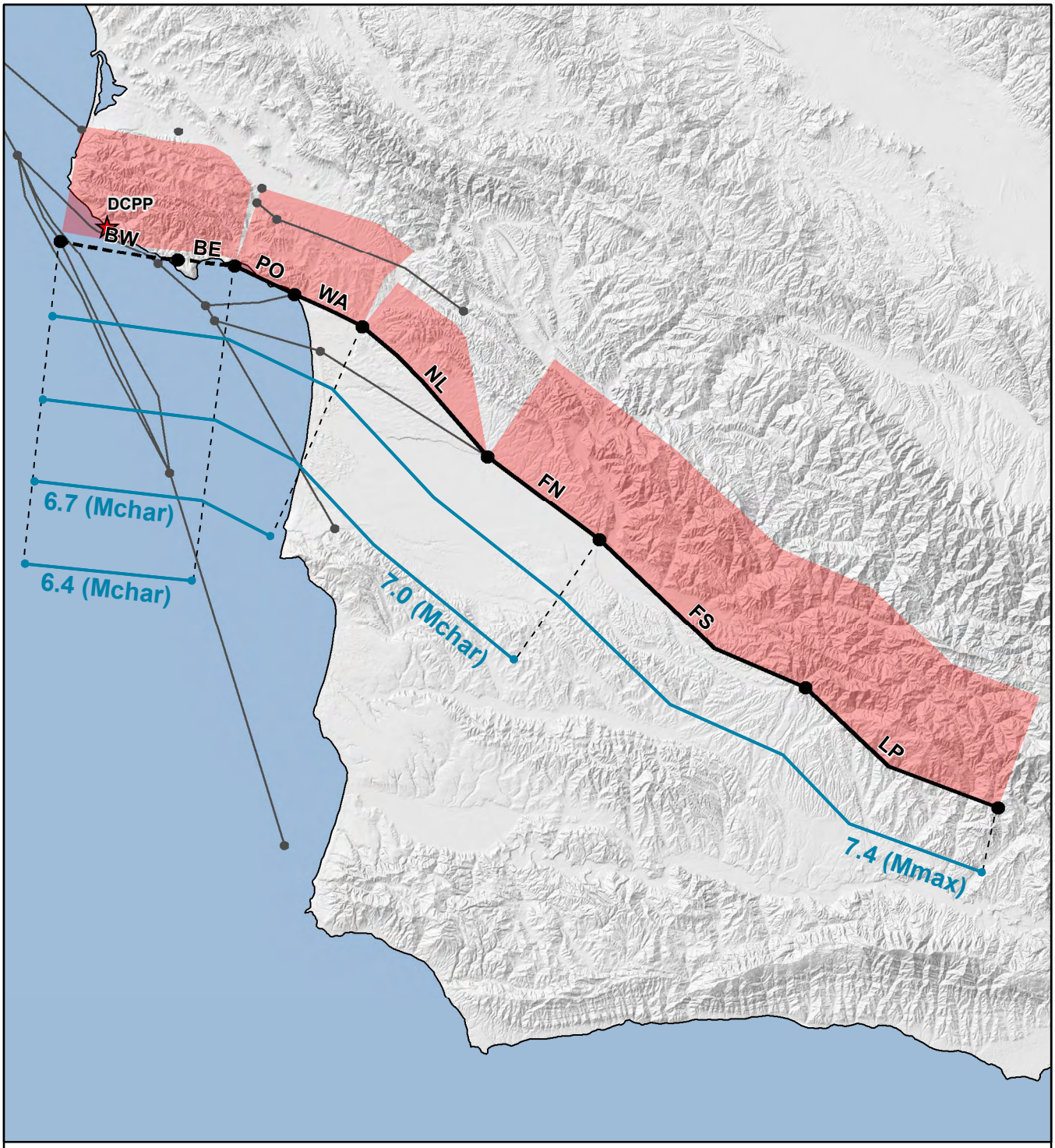

EXPLANATION

- Length scale used for magnitude estimates
- Rupture source at surface
- Updip surface projection of buried rupture source
- Other fault section
- Surface projection of dipping rupture source

Note: Two-letter fault section codes are explained in Table 6-5 and on Plates 9-1 and 9-2.

N

0 6 12 mi.

0 10 20 km

Map projection and scale: WGS 1984 UTM Zone 10N, 1:600,000

Alternative Estimates of M_{max} and M_{char} for Rupture Source SW-07

DCPP SSC REPORT

Pacific Gas and Electric Company

Figure **10-30**

File path: S:\1005\005\Final_Report_Figures\Figure_1000-30.mxd; Date: 02/26/2015; User: Serkan Bozkurt, LCI; Rev.1

(a) Magnitudes for Primary Rupture Plane

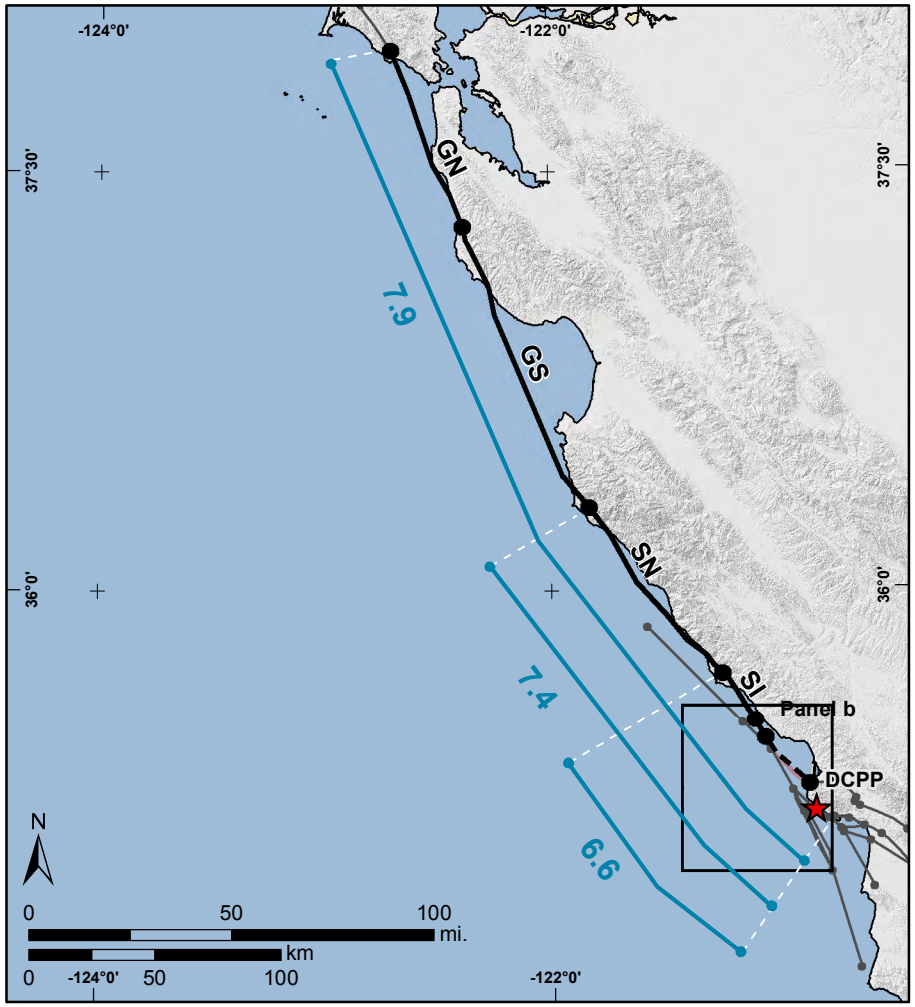

Map projection and scale: WGS 1984 UTM Zone 10N, 1:3,000,000

(b) Magnitudes for Secondary Rupture Plane

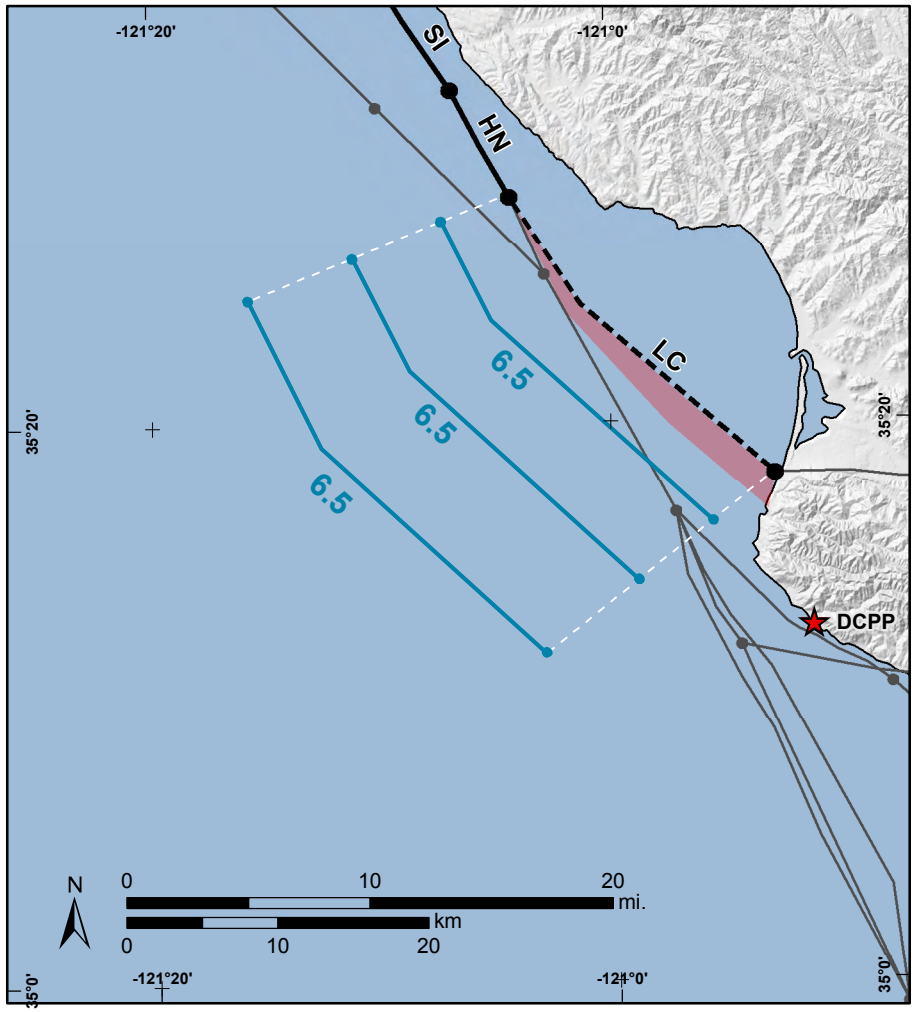

Map projection and scale: WGS 1984 UTM Zone 10N, 1:500,000

EXPLANATION

- Length scale used for magnitude estimates
- Rupture source at surface
- Updip surface projection of buried rupture source
- Other fault section
- Surface projection of dipping rupture source

Notes:
- No shading is shown for vertical faults.
- Two-letter fault section codes are explained in Table 6-5 and on Plates 9-1 and 9-2.
- Three scenario magnitude pairs are shown. See Table 10-11.

Alternative Estimates of Primary and Secondary Rupture-Plane Magnitudes for Rupture Source SW-08

DCPP SSC REPORT

Pacific Gas and Electric Company | Figure **10-31**

File path: S:\1005\005\Final_Report_Figures\Figure_1000-31.mxd; Date: 02/26/2015; User: Serkan Bozkurt, LCI; Rev.1

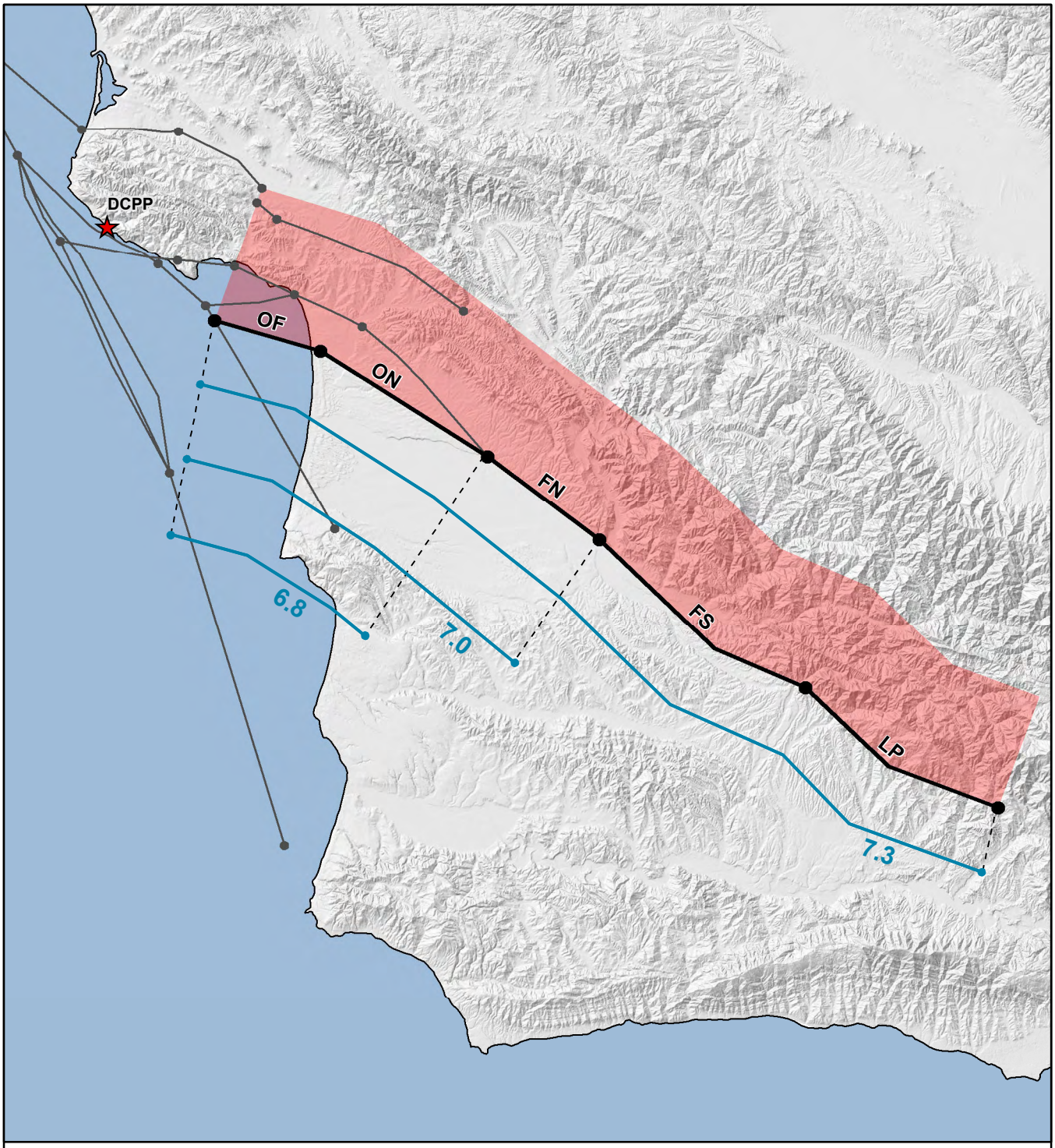

EXPLANATION

- Length scale used for magnitude estimates
- Rupture source at surface
- Other fault section
- Surface projection of dipping rupture source

Note: Two-letter fault section codes are explained in Table 6-5 and on Plates 9-1 and 9-2.

N

0 6 12 mi.

0 10 20 km

Map projection and scale: WGS 1984 UTM Zone 10N, 1:600,000

Alternative Estimates of M_{char} for Rupture Source SW-09

DCPP SSC REPORT

Pacific Gas and Electric Company

Figure **10-32**

File path: S:\1005\005\Final_Report_Figures\Figure_1000-32.mxd; Date: 02/26/2015; User: Serkan Bozkurt, LCI; Rev.1

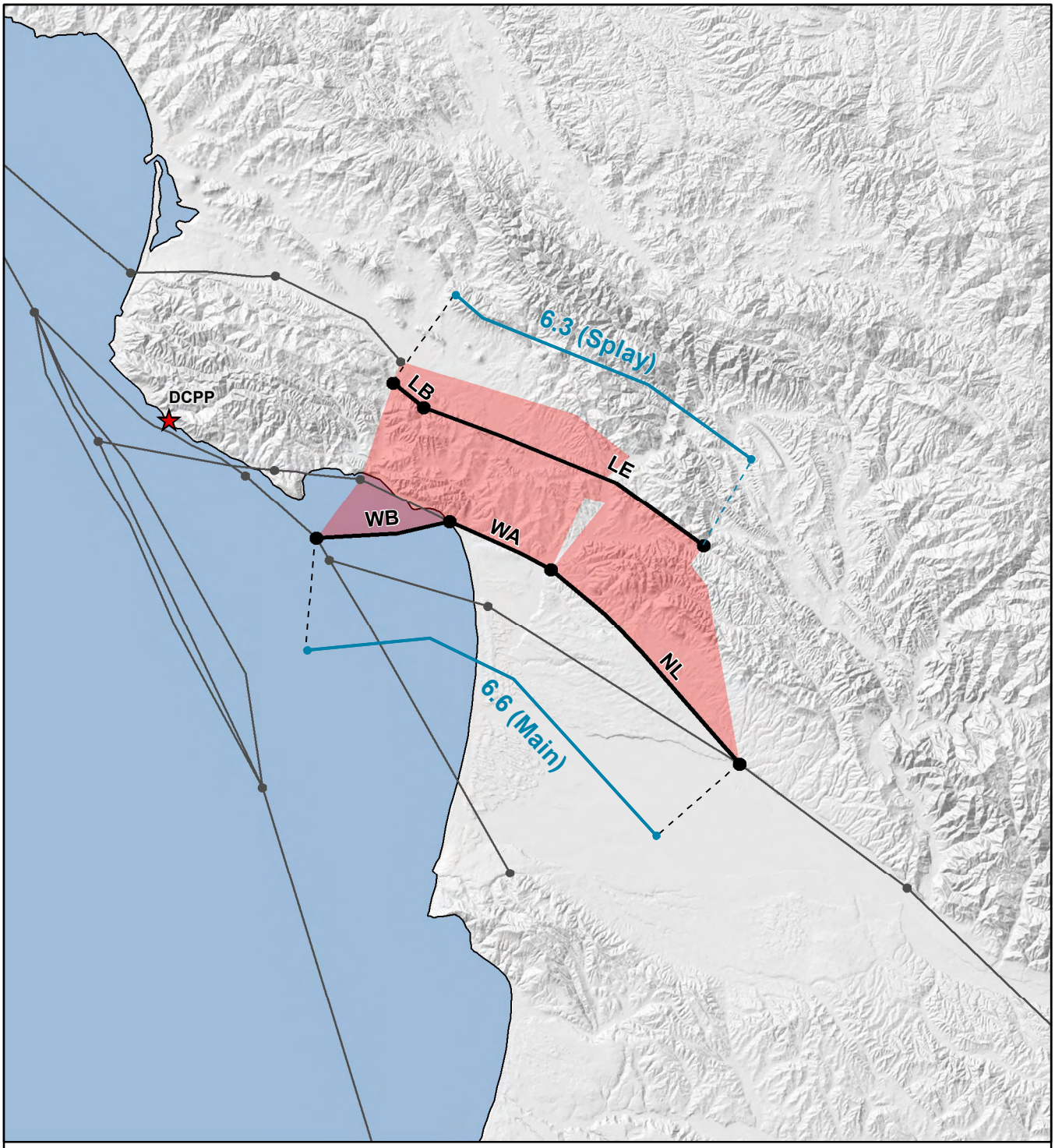

EXPLANATION

- Length scale used for magnitude estimates
- Rupture source at surface
- Other fault section
- Surface projection of dipping rupture source

Note: Two-letter fault section codes are explained in Table 6-5 and on Plates 9-1 and 9-2.

N

0 6 12 mi.

0 10 20 km

Map projection and scale: WGS 1984 UTM Zone 10N, 1:400,000

Estimates of Main and Splay Rupture-Plane Magnitudes for Rupture Source SW-10

DCPP SSC REPORT

Pacific Gas and Electric Company

Figure **10-33**

File path: S:\1005\005\Final_Report_Figures\Figure_1000-33.mxd; Date: 02/26/2015; User: Serkan Bozkurt, LCI; Rev.1

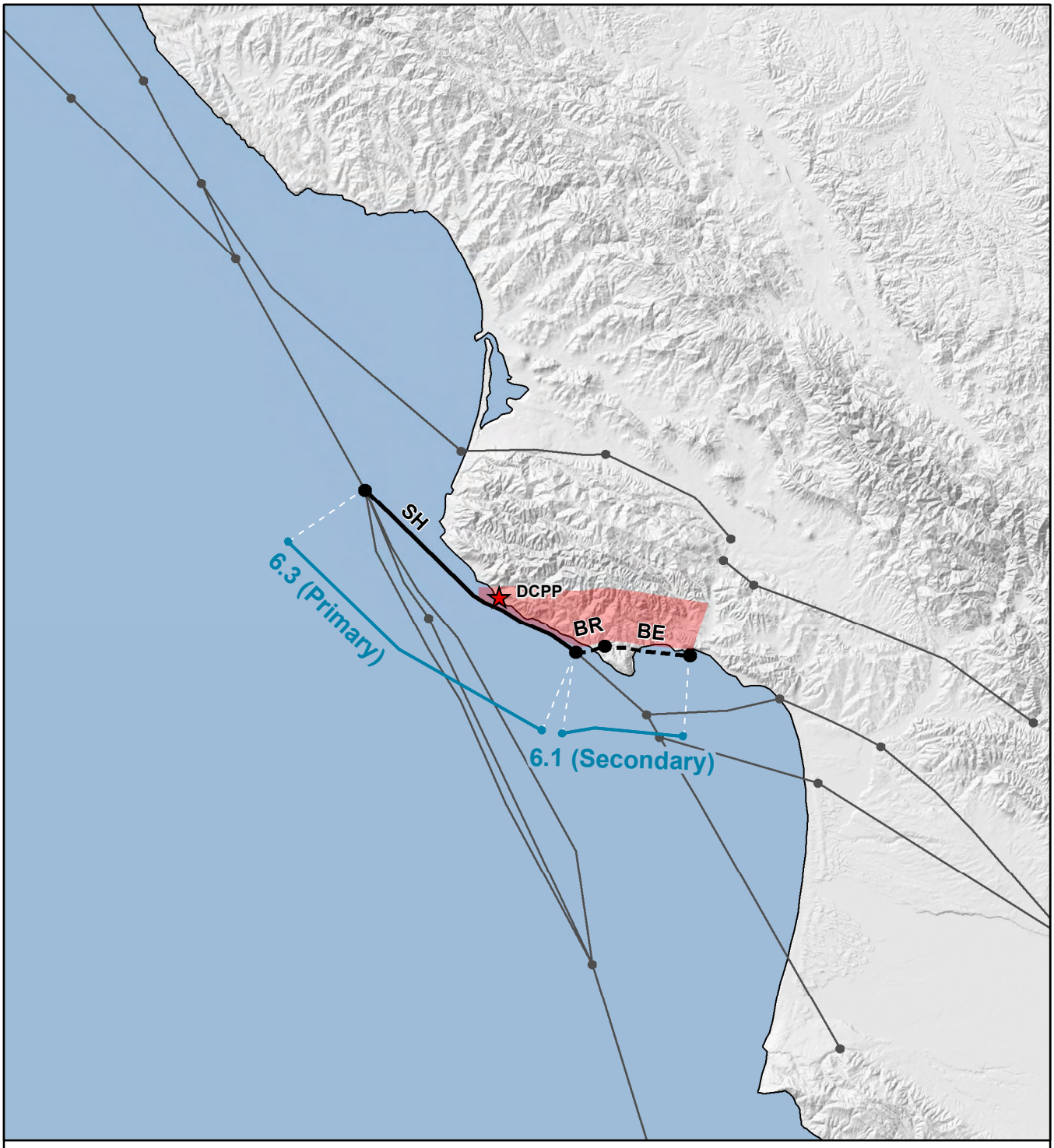

EXPLANATION

- Length scale used for magnitude estimates
- Rupture source at surface
- Updip surface projection of buried rupture source
- Other fault section
- Surface projection of dipping rupture source

Notes:
- No shading is shown for vertical faults.
- Two-letter fault section codes are explained in Table 6-5 and on Plates 9-1 and 9-2.

N

0 6 12 mi.
0 10 20 km

Map projection and scale: WGS 1984 UTM Zone 10N, 1:400,000

Estimates of Primary and Secondary Rupture-Plane Magnitudes for Rupture Source NE-03

DCPP SSC REPORT

Pacific Gas and Electric Company

Figure **10-34**

File path: S:\1005\005\Final_Report_Figures\Figure_1000-34.mxd; Date: 02/26/2015; User: Serkan Bozkurt, LCI; Rev.1

(a) Magnitudes for Primary Rupture Plane

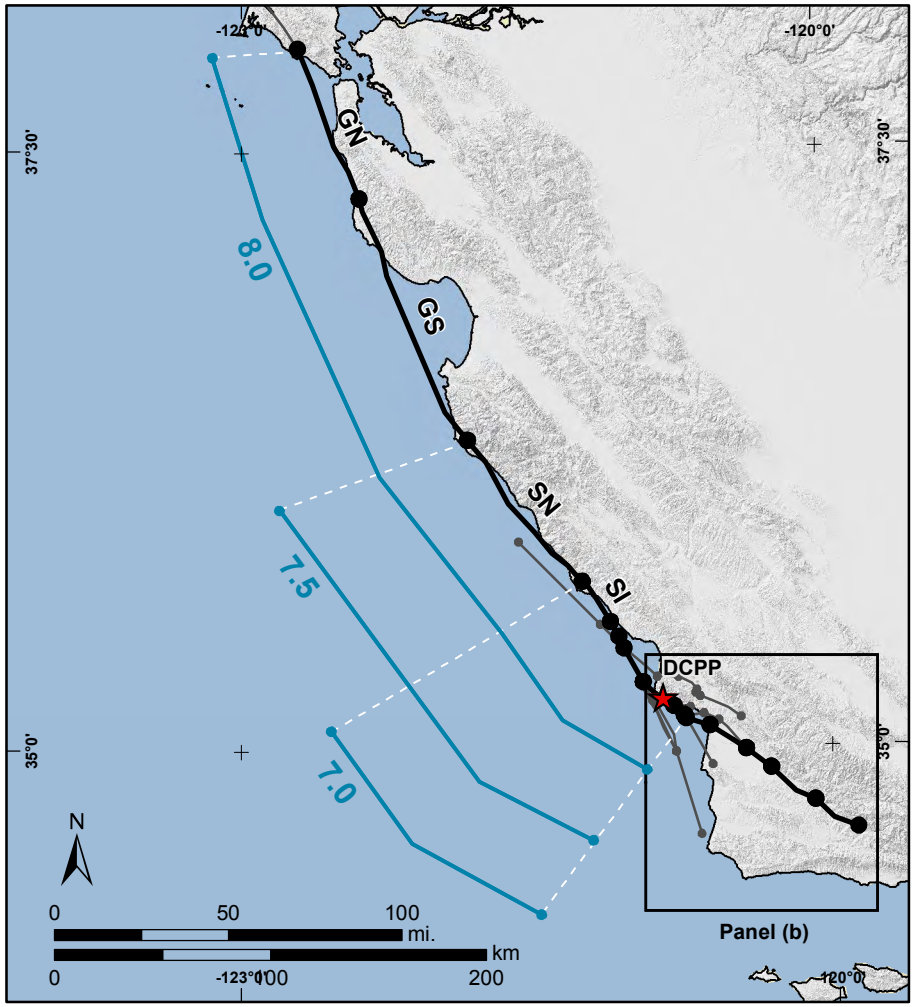

Map projection and scale: WGS 1984 UTM Zone 10N, 1:3,500,000

(b) Magnitudes for Secondary Rupture Plane

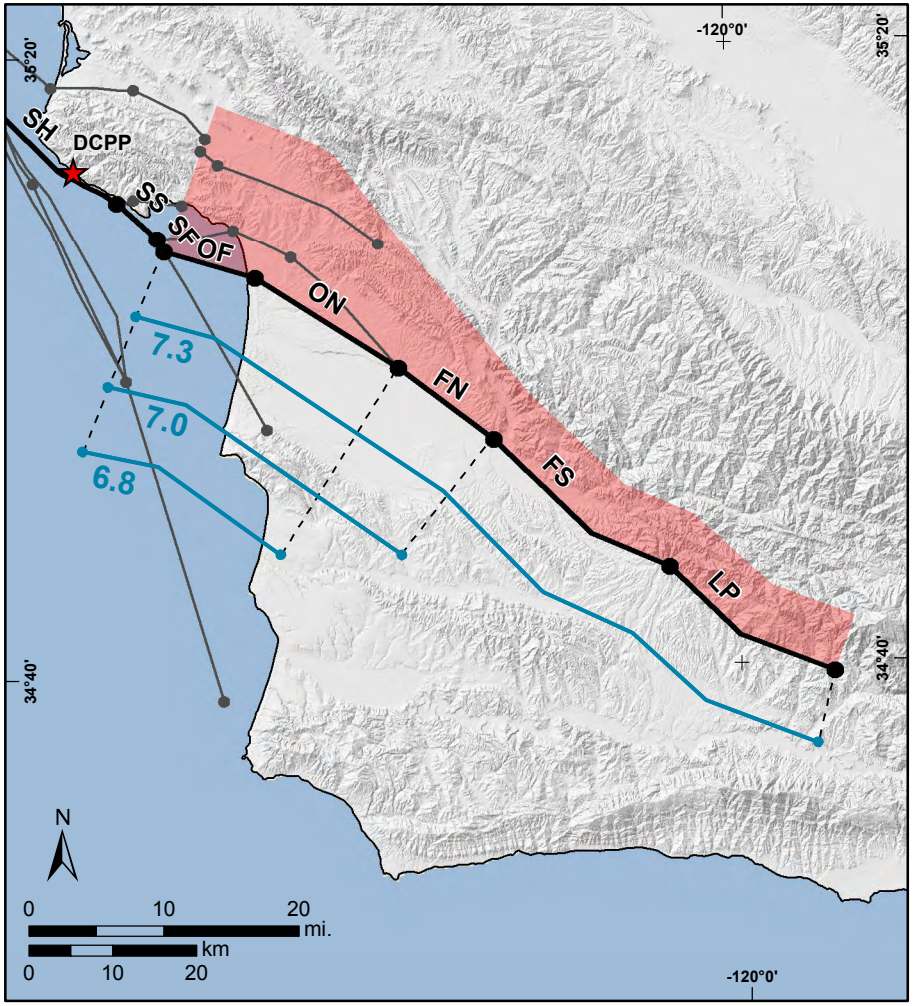

Map projection and scale: WGS 1984 UTM Zone 10N, 1:900,000

EXPLANATION

- Length scale used for magnitude estimates
- Rupture source at surface
- Other fault section
- Surface projection of dipping rupture source

Notes:
- No shading is shown for vertical faults.
- Two-letter fault section codes are explained in Table 6-5 and on Plates 9-1 and 9-2.
- Three scenario magnitude pairs shown. See Table 10-14.

Alternative Estimates of Primary and Secondary Rupture-Plane Magnitudes for Rupture Source NE-04

DCPP SSC REPORT

Pacific Gas and Electric Company | Figure **10-35**

File path: S:\1005\005\Final_Report_Figures\Figure_1000-35.mxd; Date: 02/26/2015; User: Serkan Bozkurt, LCI; Rev.1

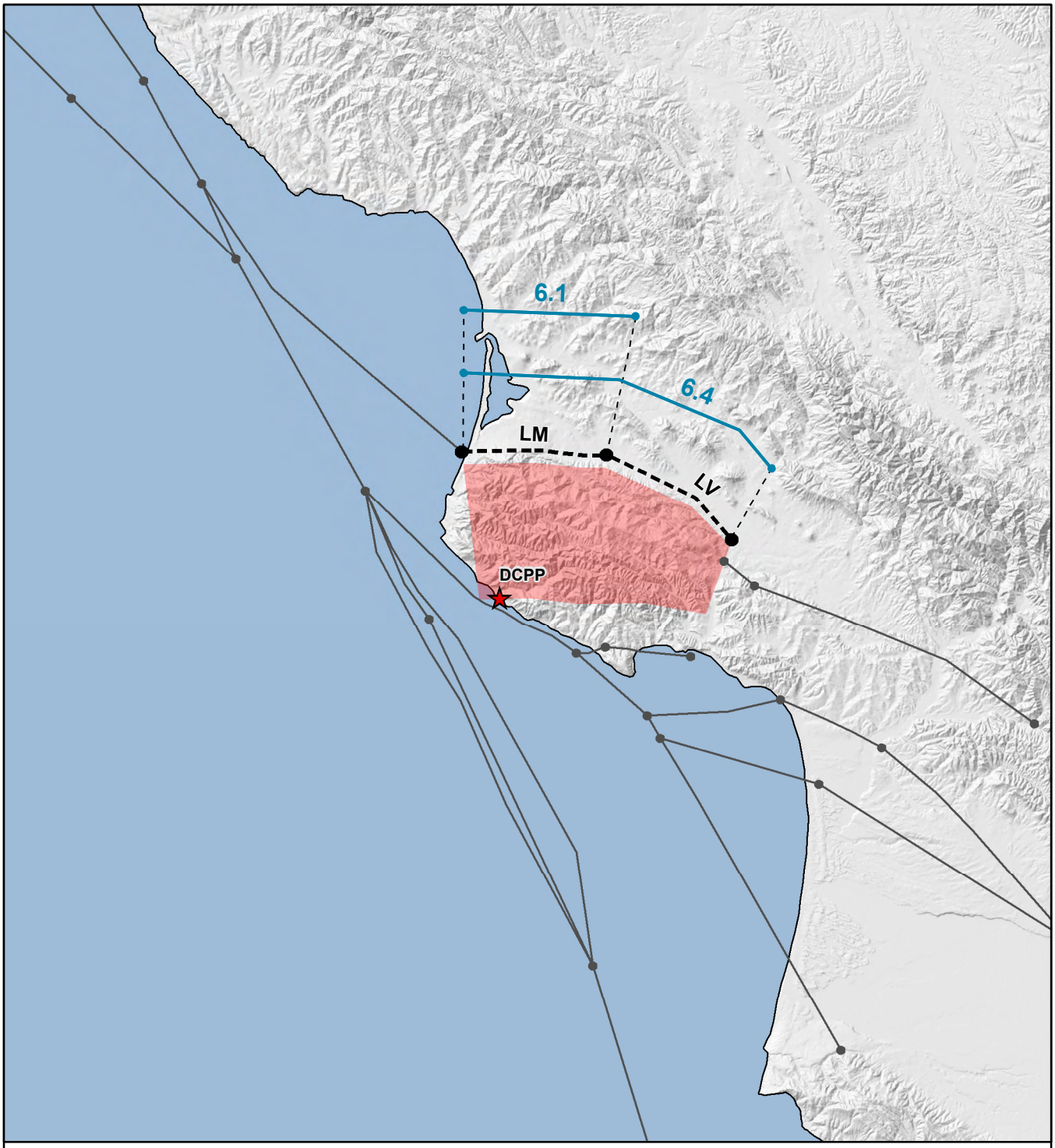

EXPLANATION

- Length scale used for magnitude estimates
- Updip surface projection of buried rupture source
- Other fault section
- Surface projection of dipping rupture source

Note: Two-letter fault section codes are explained in Table 6-5 and on Plates 9-1 and 9-2.

N

0 6 12 mi.

0 10 20 km

Map projection and scale: WGS 1984 UTM Zone 10N, 1:400,000

Alternative Estimates of M_{char} for Rupture Source NE-05

DCPP SSC REPORT

Pacific Gas and Electric Company

Figure **10-36**

File path: S:\1005\005\Final_Report_Figures\Figure_1000-36.mxd; Date: 02/26/2015; User: Serkan Bozkurt, LCI; Rev.1

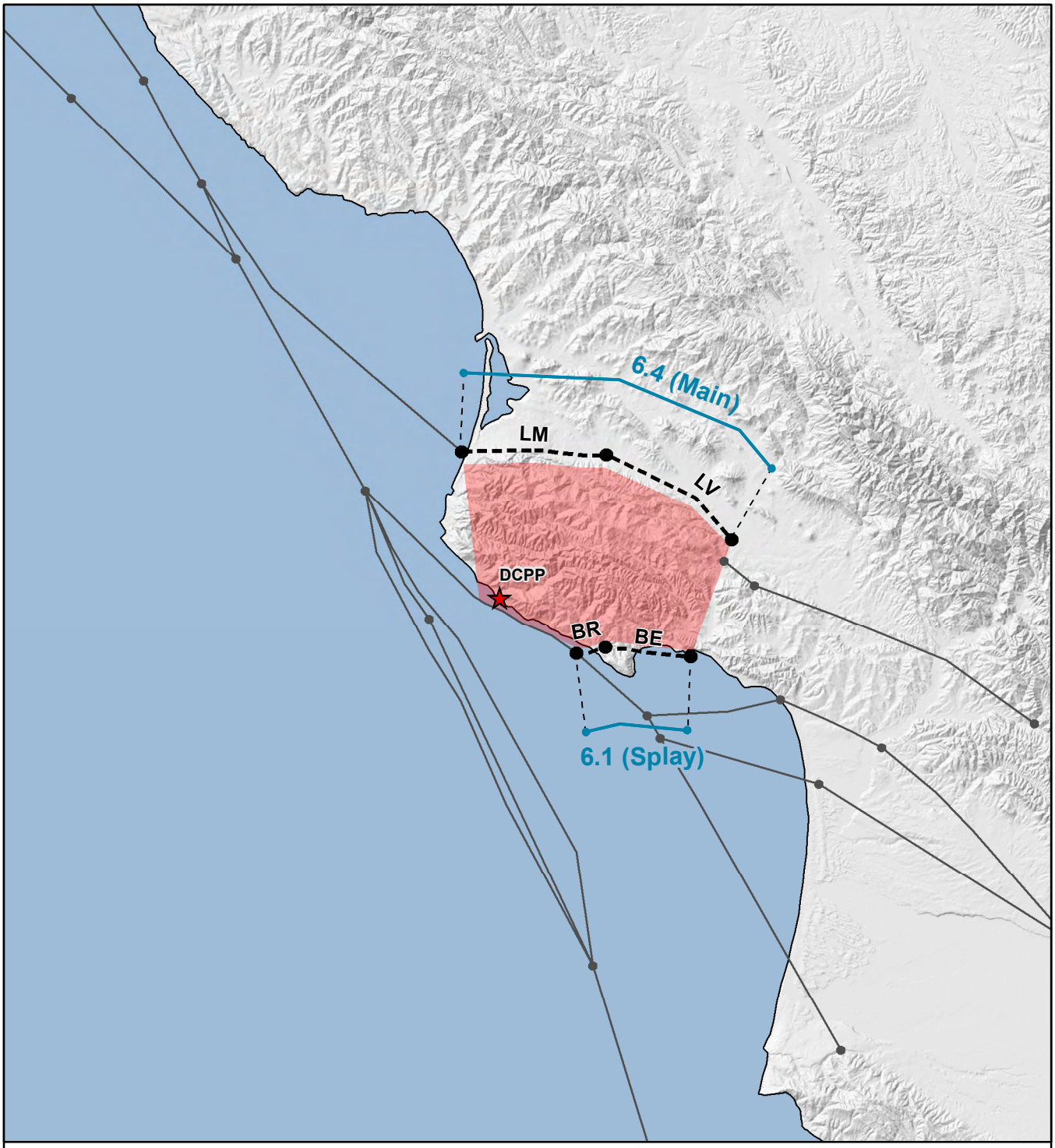

EXPLANATION

- Length scale used for magnitude estimates
- Updip surface projection of buried rupture source
- Other fault section
- Surface projection of dipping rupture source

Note: Two-letter fault section codes are explained in Table 6-5 and on Plates 9-1 and 9-2.

N

0 6 12 mi.

0 10 20 km

Map projection and scale: WGS 1984 UTM Zone 10N, 1:400,000

Estimates of Main and Splay Rupture-Plane Magnitudes for Rupture Source NE-06

DCPP SSC REPORT

Pacific Gas and Electric Company

Figure **10-37**

File path: S:\1005\005\Final_Report_Figures\Figure_1000-37.mxd; Date: 12/31/2014; User: Serkan Bozkurt, LCI; Rev.1

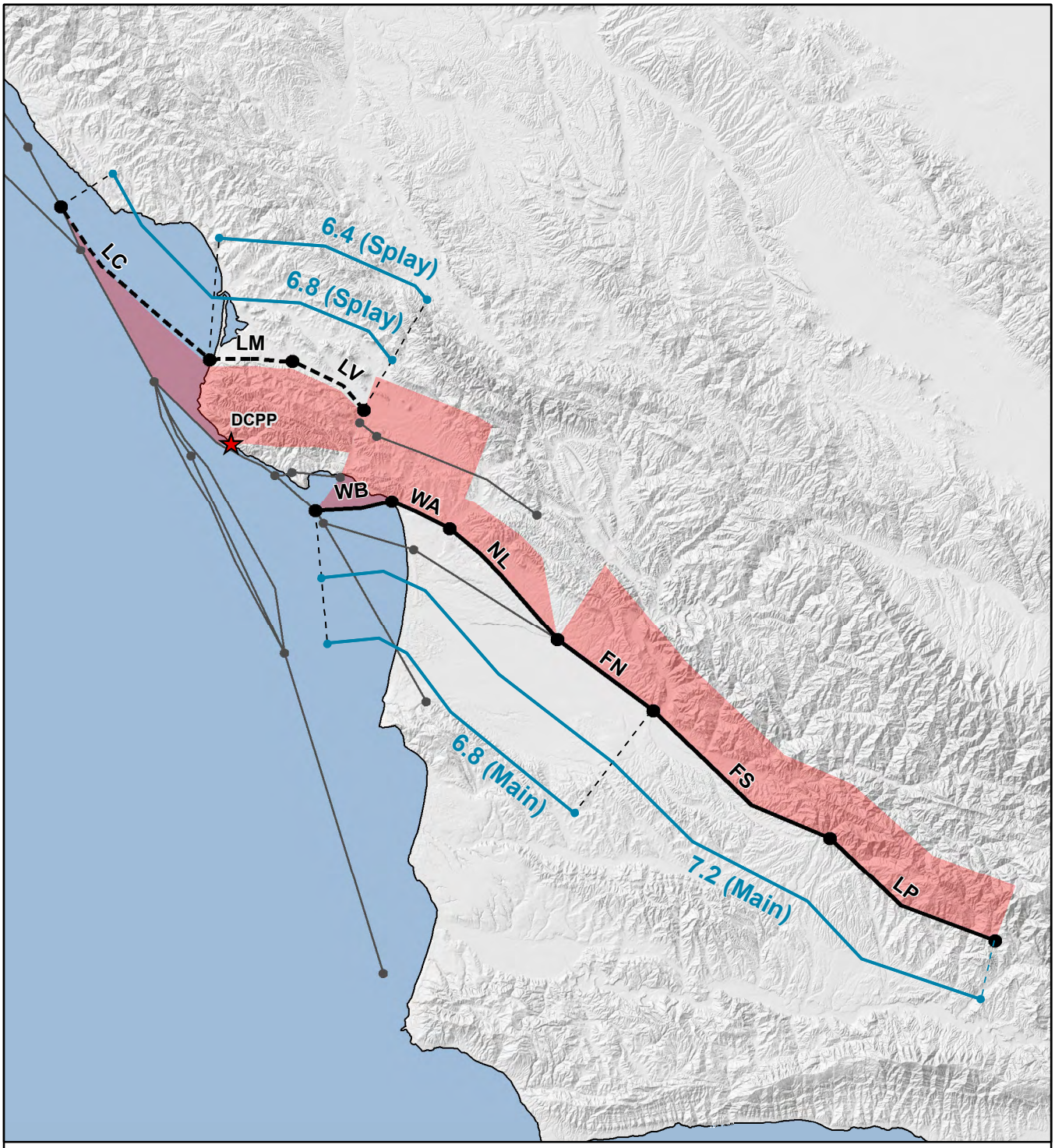

EXPLANATION

- Length scale used for magnitude estimates
- Rupture source at surface
- Updip surface projection of buried rupture source
- Other fault section
- Surface projection of dipping rupture source

Notes:
- Two-letter fault section codes are explained in Table 6-5 and on Plates 9-1 and 9-2.
- Two scenario magnitude pairs are shown. See Table 10-14.

N

0 6 12 mi.
0 10 20 km

Map projection and scale: WGS 1984 UTM Zone 10N, 1:700,000

Alternative Estimates of Main and Splay Rupture-Plane Magnitudes for Rupture Source NE-07

DCPP SSC REPORT

Pacific Gas and Electric Company

Figure **10-38**

File path: S:\1005\005\Final_Report_Figures\Figure_1000-38.mxd; Date: 02/26/2015; User: Serkan Bozkurt, LCI; Rev.1

(a) Magnitudes for Primary Rupture Plane

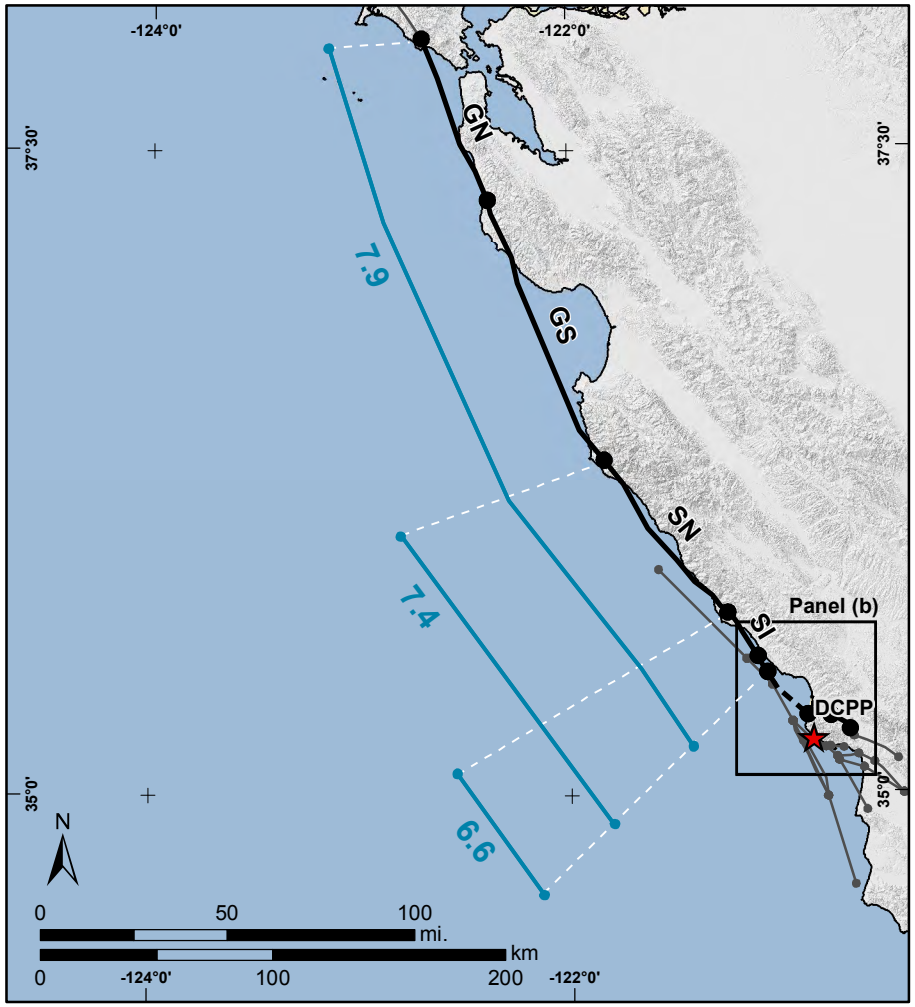

Map projection and scale: WGS 1984 UTM Zone 10N, 1:3,250,000

(b) Magnitudes for Secondary Rupture Plane

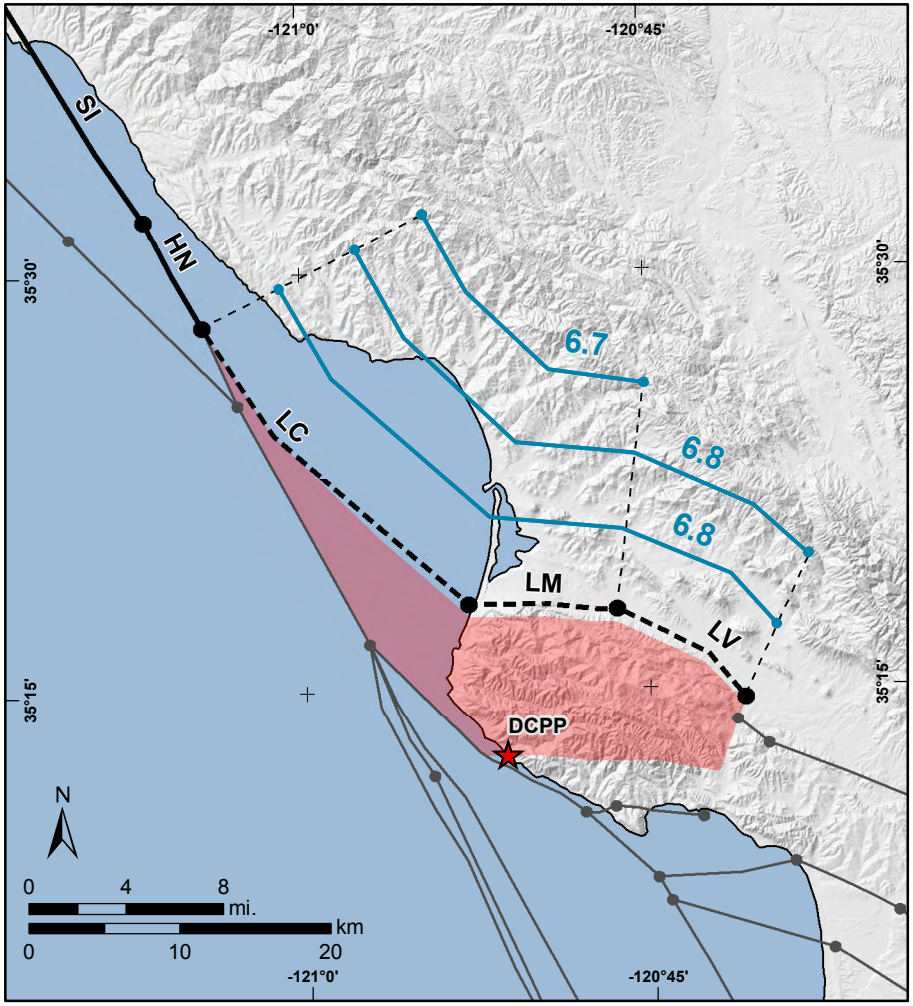

Map projection and scale: WGS 1984 UTM Zone 10N, 1:500,000

EXPLANATION

- Length scale used for magnitude estimates
- Rupture source at surface
- Updip surface projection of buried rupture source
- Other fault section
- Surface projection of dipping rupture source

Notes:
- No shading is shown for vertical faults.
- Two-letter fault section codes are explained in Table 6-5 and on Plates 9-1 and 9-2.
- Three scenario magnitude pairs are shown. See Table 10-14.

Alternative Estimates of Primary and Secondary Rupture-Plane Magnitudes for Rupture Source NE-08

DCPP SSC REPORT

Pacific Gas and Electric Company | Figure **10-39**

File path: S:\1005\005\Final_Report_Figures\Figure_1000-39.mxd; Date: 02/26/2015; User: Serkan Bozkurt, LCI; Rev.1

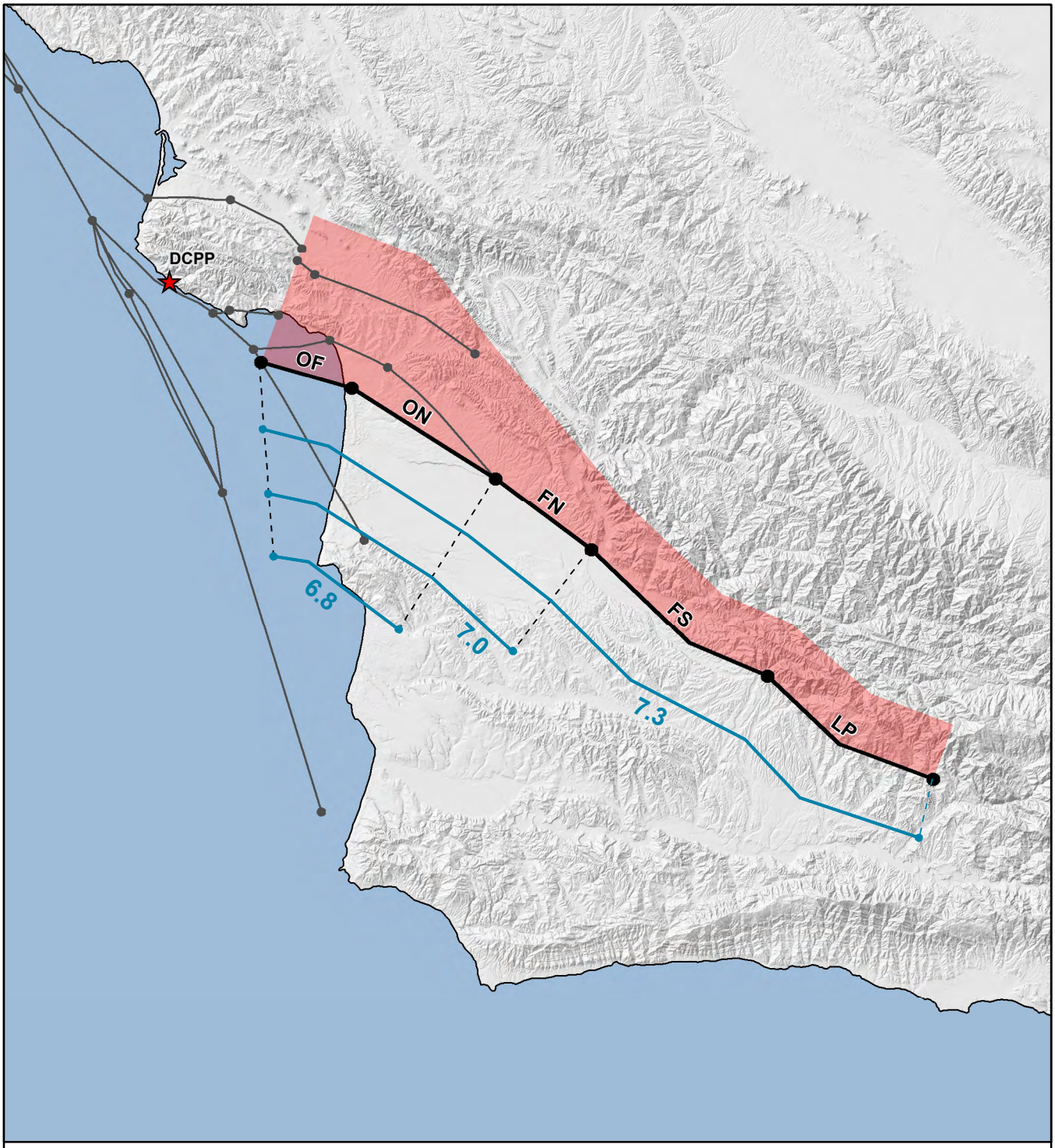

EXPLANATION

- Length scale used for magnitude estimates
- Rupture source at surface
- Other fault section
- Surface projection of dipping rupture source

Note: Two-letter fault section codes are explained in Table 6-5 and on Plates 9-1 and 9-2.

N

0 6 12 mi.

0 10 20 km

Map projection and scale: WGS 1984 UTM Zone 10N, 1:700,000

Alternative Estimates of M_{char} for Rupture Source NE-09

DCPP SSC REPORT

Pacific Gas and Electric Company

Figure **10-40**

File path: S:\1005\005\Final_Report_Figures\Figure_1000-40.mxd; Date: 02/26/2015; User: Serkan Bozkurt, LCI; Rev.1

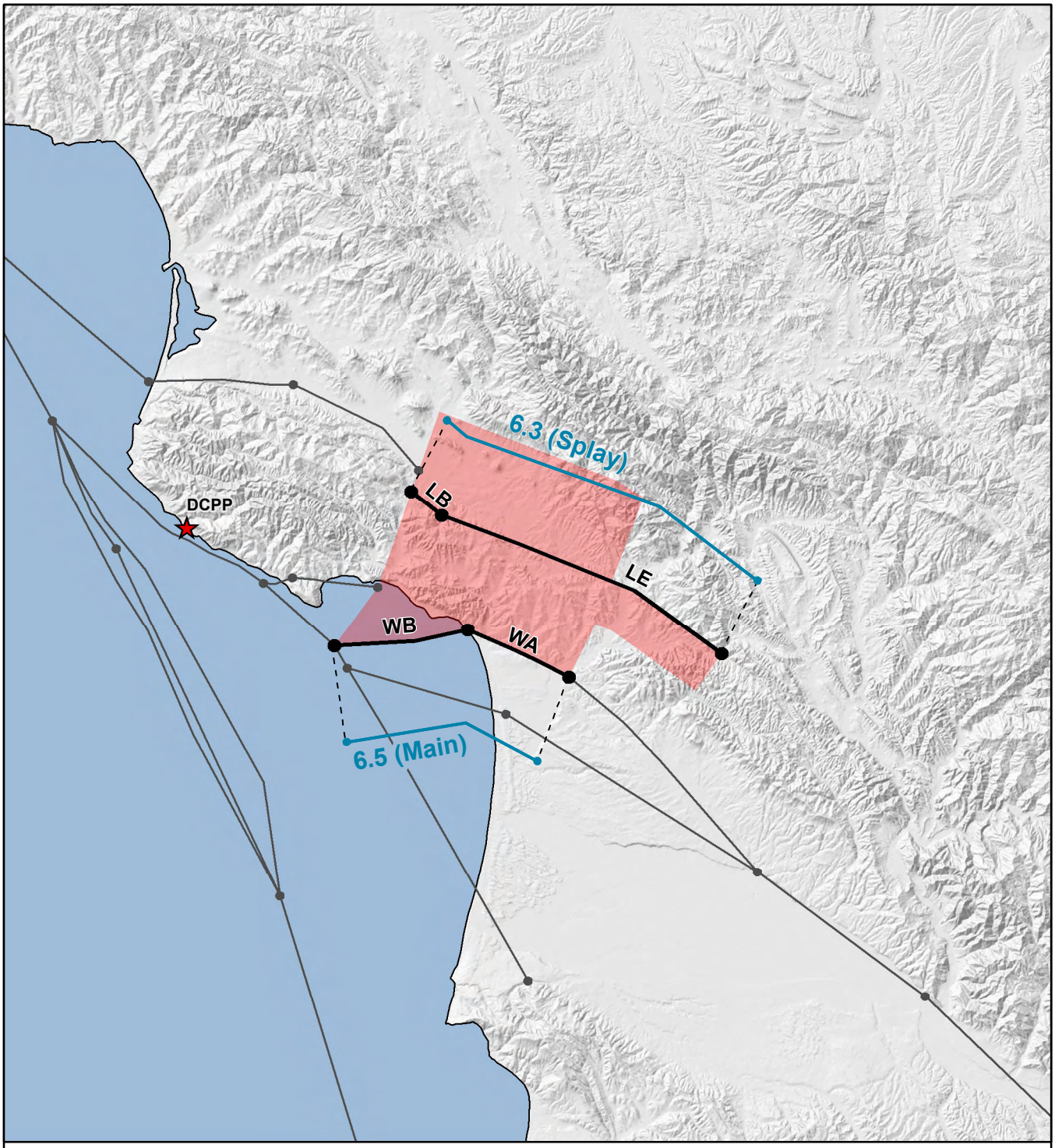

EXPLANATION

- Length scale used for magnitude estimates
- Rupture source at surface
- Other fault section
- Surface projection of dipping rupture source

Notes: Two-letter fault section codes are explained in Table 6-5 and on Plates 9-1 and 9-2.

N

0 6 12 mi.

0 10 20 km

Map projection and scale: WGS 1984 UTM Zone 10N, 1:400,000

Estimates of Main and Splay Rupture-Plane Magnitudes for Rupture Source NE-10

DCPP SSC REPORT

Pacific Gas and Electric Company

Figure **10-41**

File path: S:\1005\005\Final_Report_Figures\Figure_1000-41.mxd; Date: 02/26/2015; User: Serkan Bozkurt, LCI; Rev.1

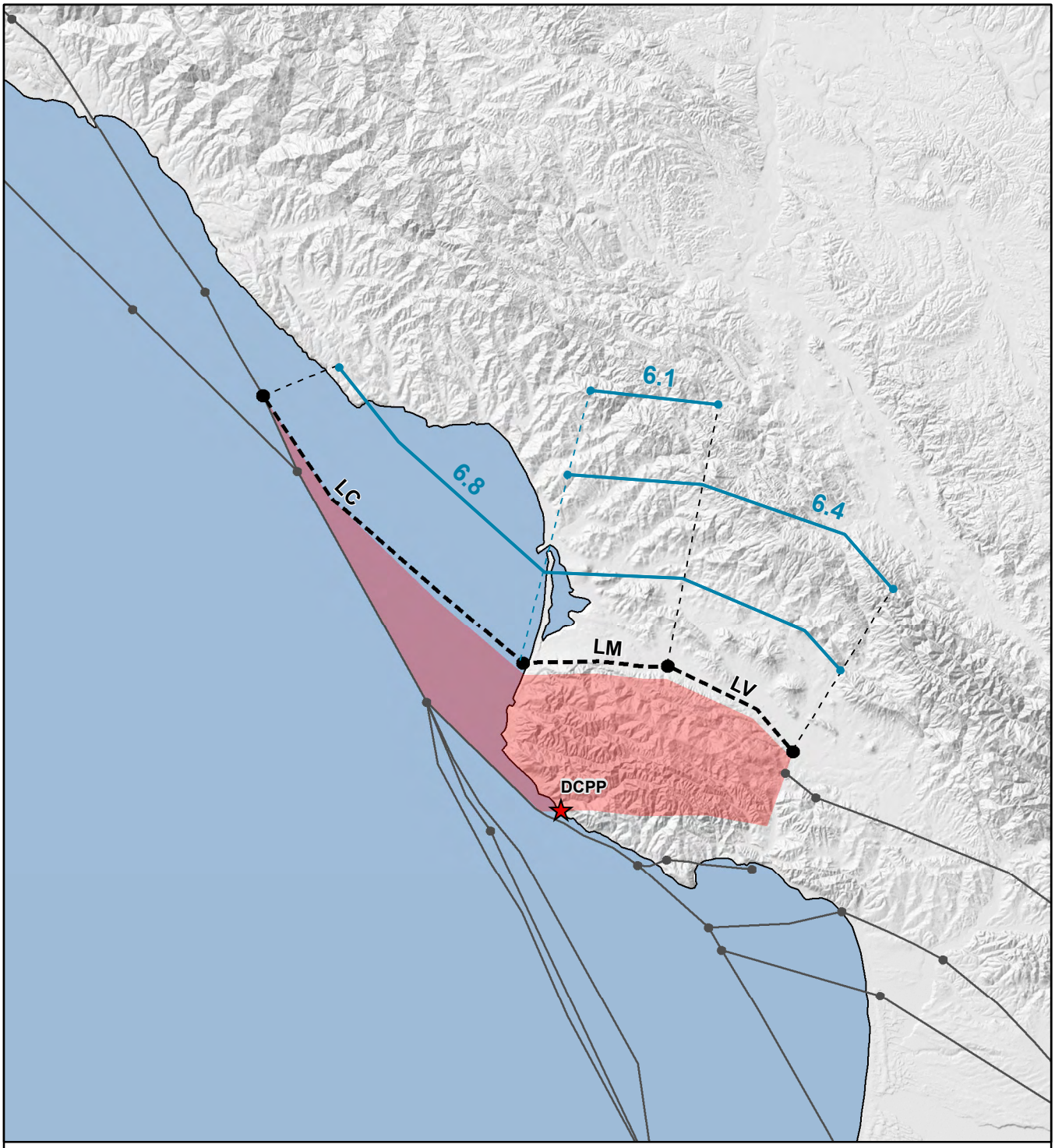

EXPLANATION

- Length scale used for magnitude estimates
- Updip surface projection of buried rupture source
- Other fault section
- Surface projection of dipping rupture source

Note: Two-letter fault section codes are explained in Table 6-5 and on Plates 9-1 and 9-2.

N

0 6 12 mi.

0 10 20 km

Map projection and scale: WGS 1984 UTM Zone 10N, 1:400,000

Alternative Estimates of M_{char} for Rupture Source NE-11

DCPP SSC REPORT

Pacific Gas and Electric Company

Figure **10-42**

File path: S:\1005\005\Final_Report_Figures\Figure_1000-42.mxd; Date: 02/26/2015; User: Serkan Bozkurt, LCI; Rev.1

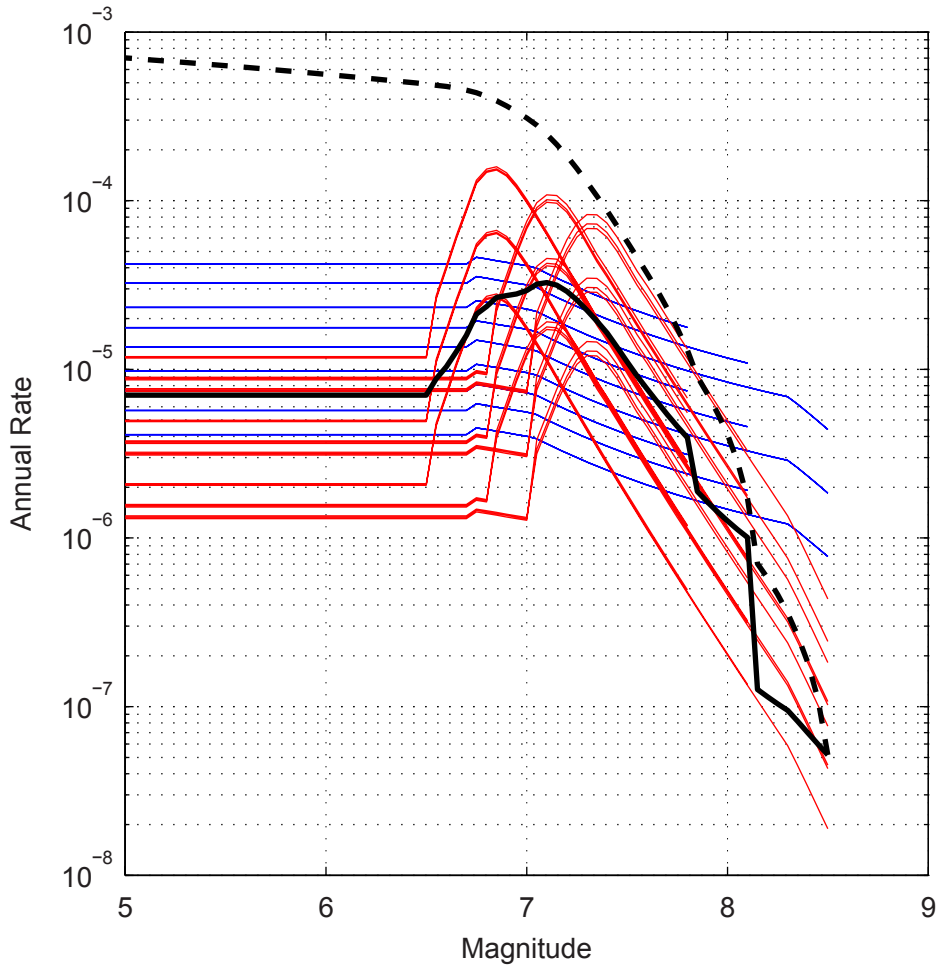

EXPLANATION

- WAACY model, incremental earthquake rate
- Exponential model, incremental earthquake rate
- Summed incremental earthquake rate
- Cumulative earthquake rate

Note: The point MFD for Hosgri rupture source H-01 has 54 contributions, each representing a separate path through the SSC logic tree. These contributions are shown as separate red and blue lines. Many of these lines overprint. After weighting each, they are summed to an incremental rupture source "point" MFD (solid black line). The corresponding cumulative MFD is shown as a dashed line. Magnitude bin size is 0.05.

Individual Logic-Tree Path and Weighted-Sum "Point" MFDs, Hosgri Rupture Source H-01

DCPP SSC REPORT

Pacific Gas and Electric Company

Figure **10-43**

File path: /s/1005/005/Final_Report_Figures/Figure_1000-07_10-43.ai; Date: 02/26/2015; User: Serkan Bozkurt, LCI; Rev. 1

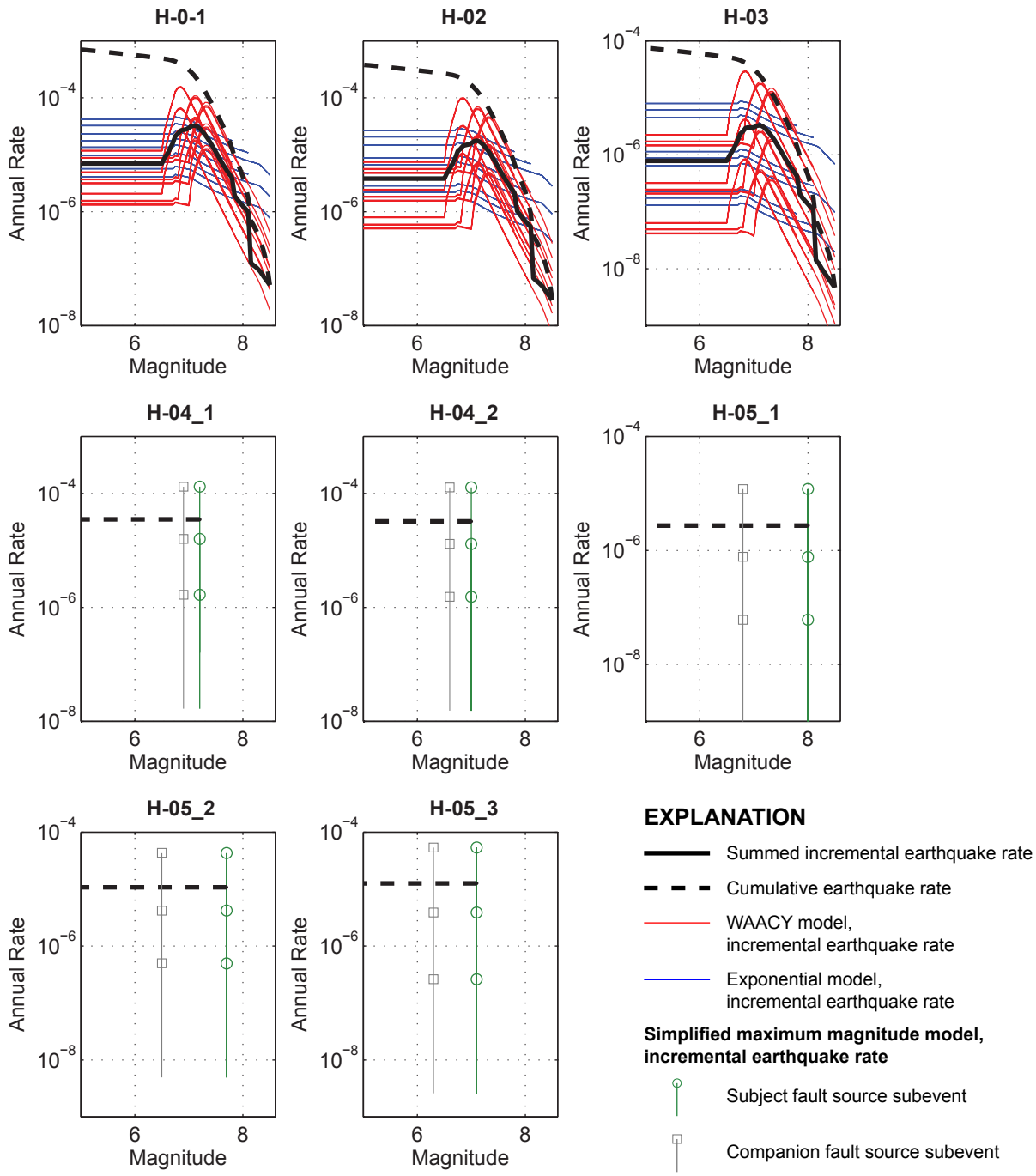

Note: The MFD for the Hosgri fault source, calculated for a point nearest the DCPP, has contributions from five rupture sources. The MFDs from rupture sources H-01, H-02, and H-03 consist of individual contributions from WAACY (red) and exponential (blue) magnitude PDFs. The graph for H-01 is repeated from Figure 10-43. The MFDs from rupture sources H-04 and H-05 consist of contributions from alternative complex (H-04) and splay (H-05) scenarios with simplified maximum magnitude PDFs. As each complex and splay scenario consists of two subevents (a primary and secondary or main and splay), the green circles show the magnitudes for the subevent on the Hosgri source and the grey squares show the magnitudes for the "companion" subevent. By design, the rates for both subevents are the same. The vertical lines through the circles and squares are for visualization only. The solid black lines are the summed incremental MFDs, and the dashed black lines are the cumulative MFDs. Magnitude bin size is 0.05.

Rupture-Source MFDs Contributing to the Hosgri Fault Source "Point" MFD

DCPP SSC REPORT

Pacific Gas and Electric Company

Figure **10-44**

File path: /s/1005/005/Final_Report_Figures/Figure_1000-44.ai; Date: 02/26/2015; User: Serkan Bozkurt, LCI; Rev. 1

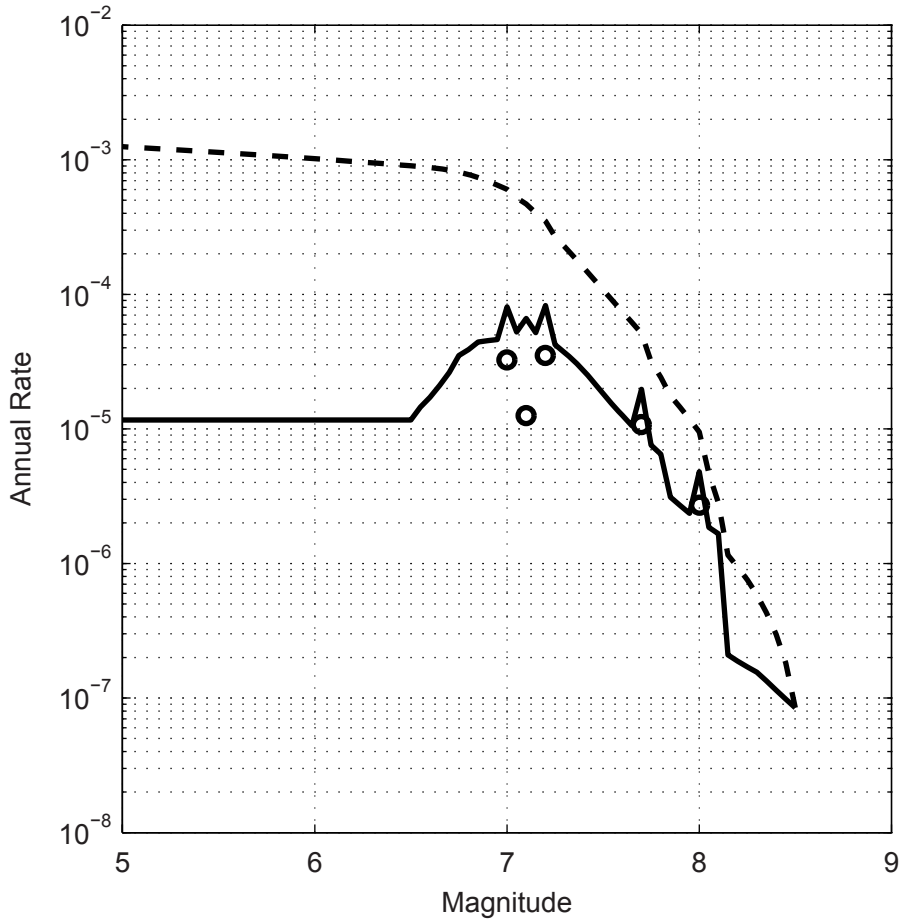

EXPLANATION

- Single-magnitude contribution from simplified maximum magnitude PDF rupture source (magnitude of subevent on the subject fault shown)
- Summed incremental earthquake rate
- Cumulative earthquake rate

Note: The MFD for the Hosgri fault source for a point nearest the DCPP is shown on this figure. The incremental (black line) and cumulative (dashed line) earthquake rates are summed from the rupture source MFDs presented on Figure 10-44. Circles represent the rates of earthquakes at the Hosgri subevent magnitudes contributed from rupture sources H-04 (two scenarios) and H-05 (three scenarios). Magnitude bin size is 0.05.

Hosgri Fault MFD, Summed Incremental and Cumulative Earthquake Rates at a Point Nearest to the DCPP

DCPP SSC REPORT

Pacific Gas and Electric Company

Figure **10-45**

File path: /s/1005/005/Final_Report_Figures/Figure_1000-45.ai; Date: 02/26/2015; User: Serkan Bozkurt, LCI; Rev. 1

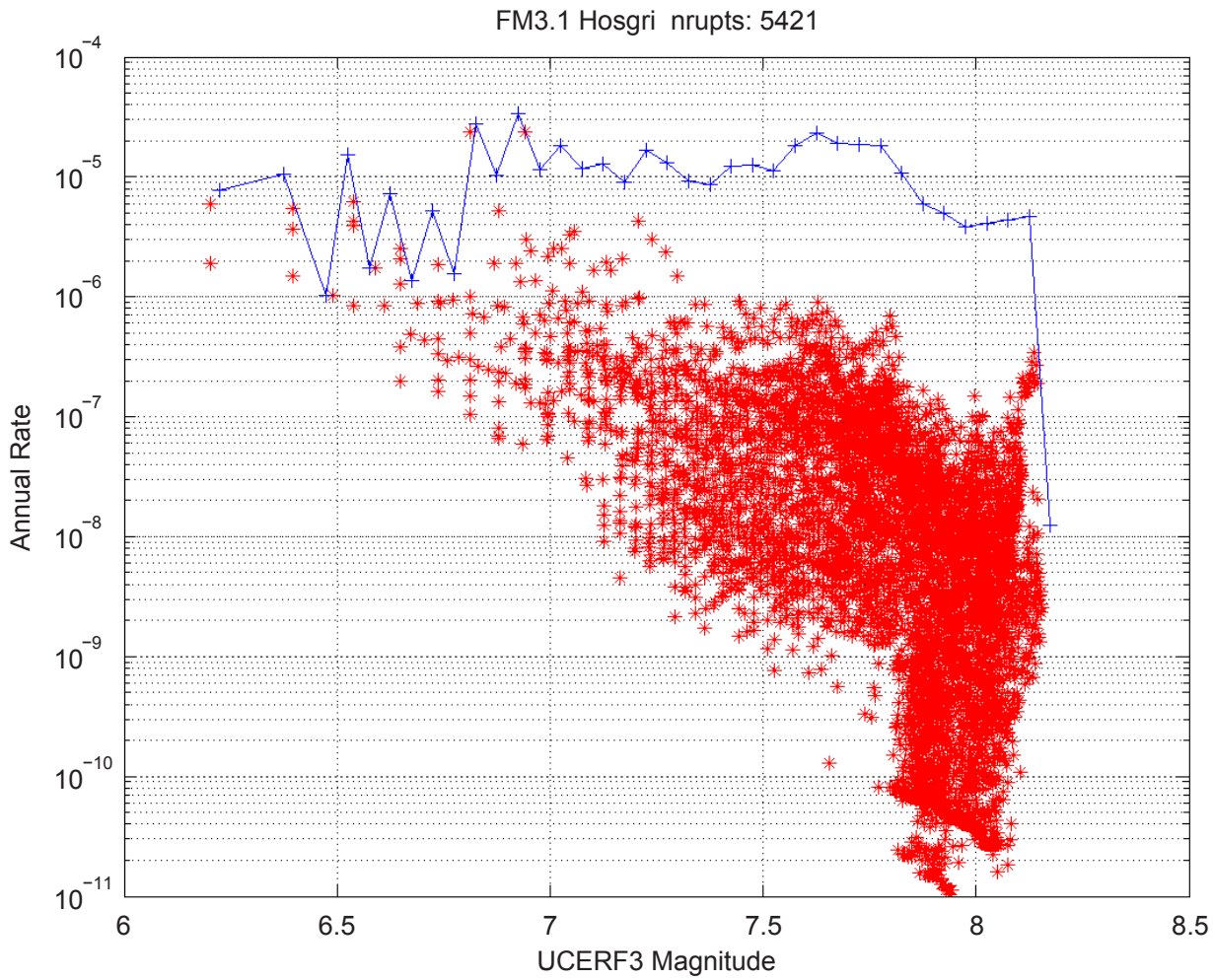

EXPLANATION

Individual rupture rates

Summed incremental earthquake rate

Notes: UCERF3, Fault Model 3.1, mean branch solution.
See Chapter 12 for details about UCERF3 rupture sets.
Magnitude bin size is 0.05.

Subsection (Point) Participation Rate for the Hosgri Fault Nearest the DCPP from the UCERF3 Inversion

DCPP SSC REPORT

Pacific Gas and Electric Company

Figure **10-46**

File path: /s/1005/005/Final_Report_Figures/Figure_1000-46.ai; Date: 02/26/2015; User: Serkan Bozkurt, LCI; Rev. 1

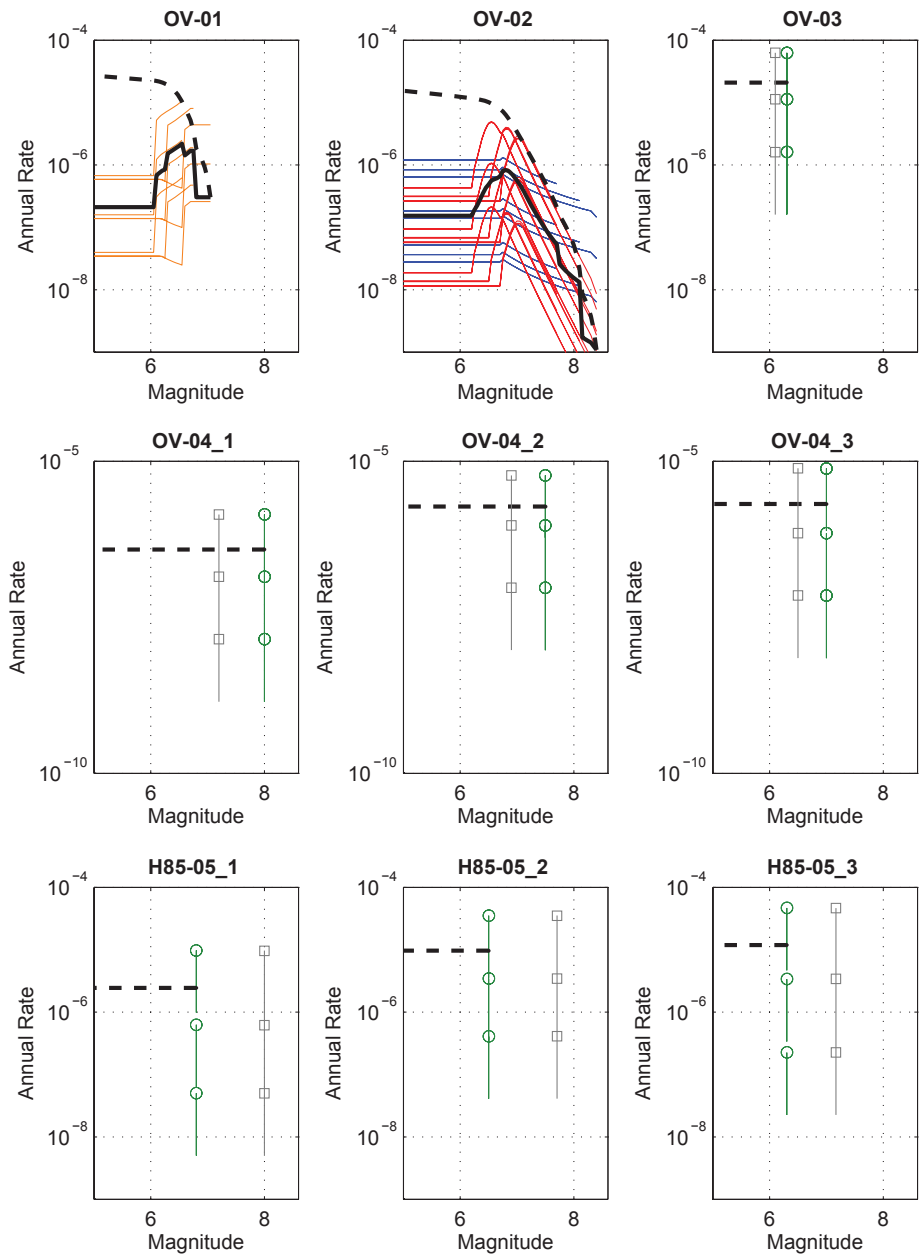

EXPLANATION

- WAACY model, incremental earthquake rate
- Exponential model, incremental earthquake rate
- Characteristic model, incremental earthquake rate
- Summed incremental earthquake rate
- Cumulative earthquake rate

Simplified maximum magnitude model, incremental earthquake rate

- Subject fault source subevent
- Companion fault source subevent

Note: The MFD for the Shoreline fault source (Outward-Vergent model), calculated for a point nearest the DCPP, has contributions from five rupture sources. The MFD from rupture source OV-01 consists of individual contributions from characteristic magnitude PDFs. The MFD from rupture source OV-02 consists of individual contributions from WAACY (red) and exponential (blue) magnitude PDFs. The MFDs from rupture sources OV-03, OV-04, and H-05 consist of contributions from alternative complex (OV-03 and OV-04) and splay (H-05) scenarios with simplified maximum magnitude PDFs. As each complex and splay scenario consists of two subevents (a primary and secondary or main and splay), the green circles show the magnitudes for the subevent on the Shoreline source and the grey squares show the magnitudes for the "companion" subevent. By design, the rates for both subevents are the same. The vertical lines through the circles and squares are for visualization only. The solid black lines are the summed incremental MFDs, and the dashed black lines are the cumulative MFDs. Magnitude bin size is 0.05.

Rupture-Source MFDs Contributing to the Shoreline Fault Source (OV Model) "Point" MFD

DCPP SSC REPORT

Pacific Gas and Electric Company

Figure **10-47**

File path: /s/1005/005/Final_Report_Figures/Figure_1000-47.ai; Date: 02/26/2015; User: Serkan Bozkurt, LCI; Rev. 1

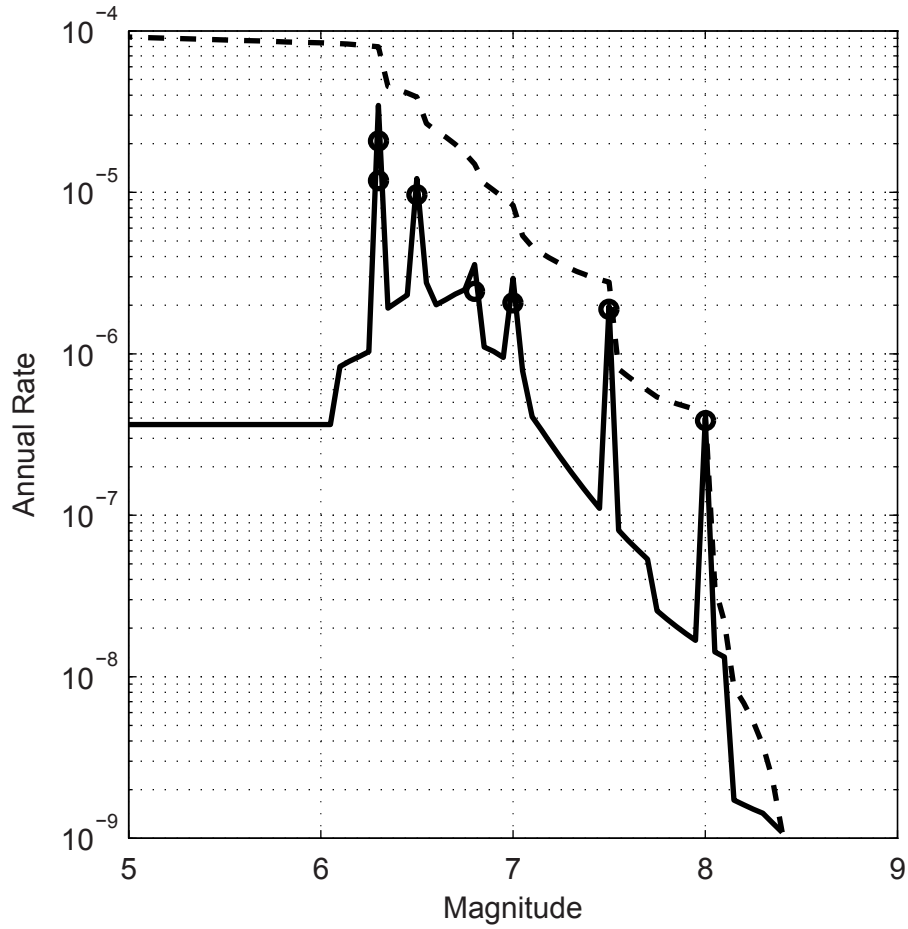

EXPLANATION

- Single-magnitude contribution from simplified maximum magnitude PDF rupture source (magnitude of subevent on the subject fault shown)
- Summed incremental earthquake rate
- Cumulative earthquake rate

Note: The MFD for the Shoreline fault source (Outward-Vergent Model) for a point nearest the DCPP is shown on this figure. The incremental (black line) and cumulative (dashed line) earthquake rates are summed from the rupture source MFDs presented on Figure 10-47. Circles represent the rates of earthquakes (at the Shoreline subevent magnitudes) contributed from rupture sources OV-03 (one scenario), OV-04 (three scenarios) and H-05 (three scenarios). Magnitude bin size is 0.05.

Shoreline Fault (OV Model) MFD, Summed Incremental and Cumulative Earthquake Rates at a Point Nearest the DCPP

DCPP SSC REPORT

Pacific Gas and Electric Company

Figure **10-48**

File path: /s/1005/005/Final_Report_Figures/Figure_1000-48.ai; Date: 02/26/2015; User: Serkan Bozkurt, LCI; Rev. 1

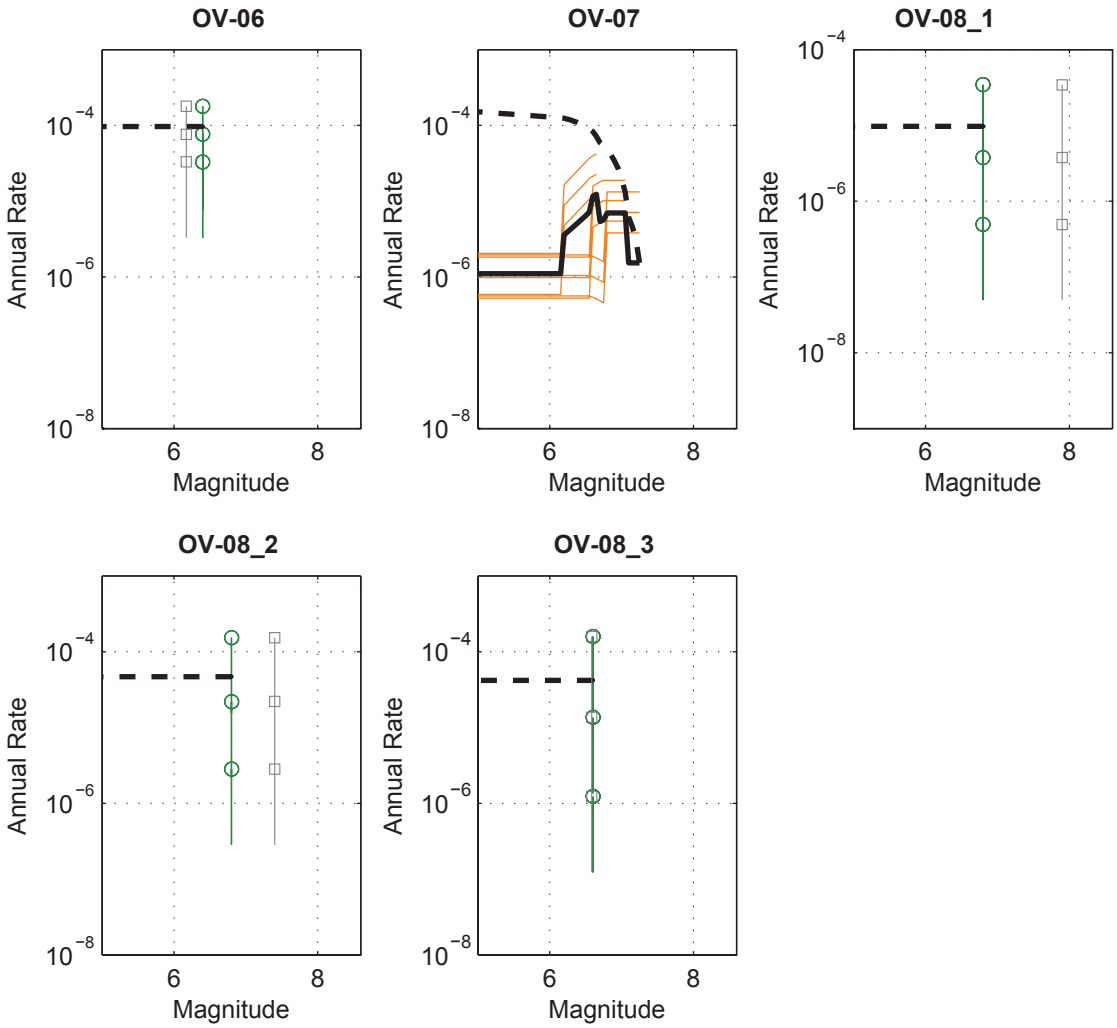

EXPLANATION

Summed incremental earthquake rate

Cumulative earthquake rate

Characteristic model, incremental earthquake rate

Simplified maximum magnitude model, incremental earthquake rate

Subject fault source subevent

Companion fault source subevent

Note: The MFD for the Los Osos fault source (Outward-Vergent Model), calculated for a point nearest the DCPP, has contributions from three rupture sources. The MFD from rupture source OV-07 consists of individual contributions from characteristic magnitude PDFs. The MFDs from rupture sources OV-06 and OV-08 consist of contributions from alternative splay (OV-06) and complex (OV-08) scenarios with simplified maximum magnitude PDFs. As each splay and complex scenario consists of two subevents (a main and splay or primary and secondary), the green circles show the magnitudes for the subevent on the Los Osos fault source and the grey squares show the magnitudes for the “companion” subevent. By design, the rates for both subevents are the same. The vertical lines through the circles and squares are for visualization only. The solid black lines are the summed incremental MFDs, and the dashed black lines are the cumulative MFDs. Magnitude bin size is 0.05.

Rupture-Source MFDs Contributing to the Los Osos Fault Source (OV Model) "Point" MFD

DCPP SSC REPORT

Pacific Gas and Electric Company

Figure **10-49**

File path: /s/1005/005/Final_Report_Figures/Figure_1000-49.ai; Date: 02/26/2015; User: Serkan Bozkurt, LCI; Rev. 1

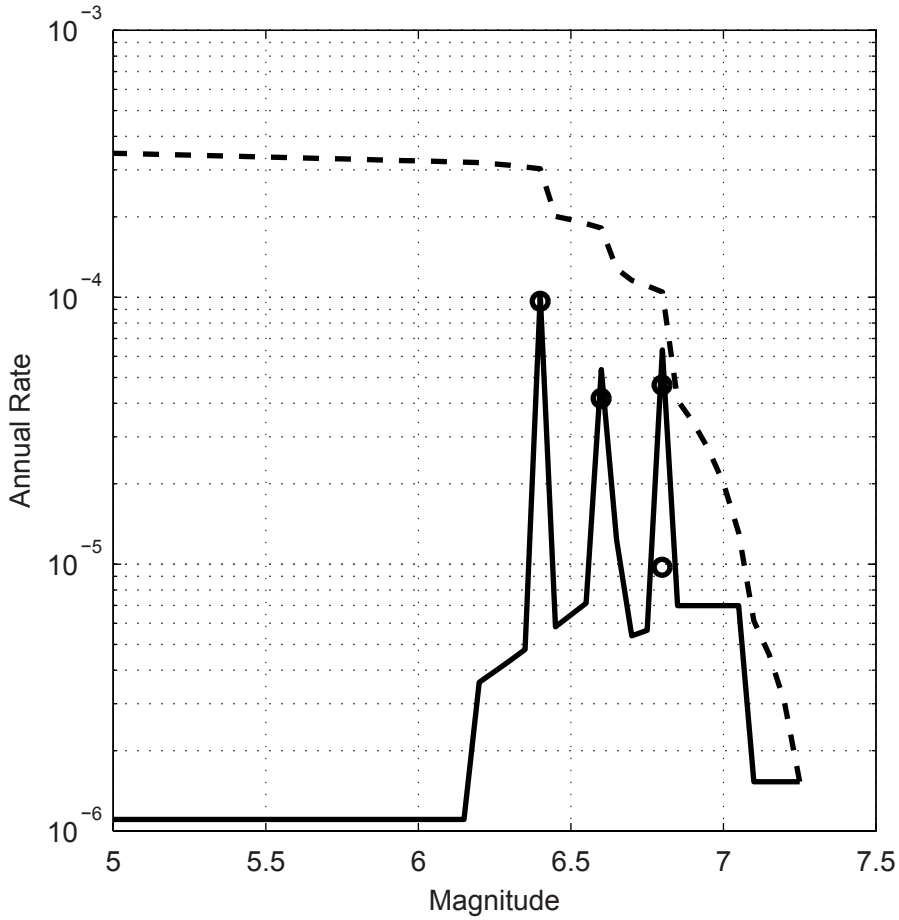

EXPLANATION

- Single-magnitude contribution from simplified maximum magnitude PDF rupture source (magnitude of subevent on the subject fault shown)
- Summed incremental earthquake rate
- Cumulative earthquake rate

Note: The MFD for the Los Osos fault source (Outward-Vergent Model) for a point nearest the DCPP is shown on this figure. The incremental (black line) and cumulative (dashed line) earthquake rates are summed from the rupture source MFDs presented on Figure 10-49. Circles represent the rates of earthquakes (at the Los Osos subevent magnitudes) contributed from rupture sources OV-06 (one scenario) and OV-08 (three scenarios). Magnitude bin size is 0.05.

Los Osos Fault (OV Model) MFD, Summed Incremental and Cumulative Earthquake Rates at a Point Nearest the DCPP

DCPP SSC REPORT

Pacific Gas and Electric Company

Figure **10-50**

File path: /s/1005/005/Final_Report_Figures/Figure_1000-50.ai; Date: 02/26/2015; User: Serkan Bozkurt, LCI; Rev. 1

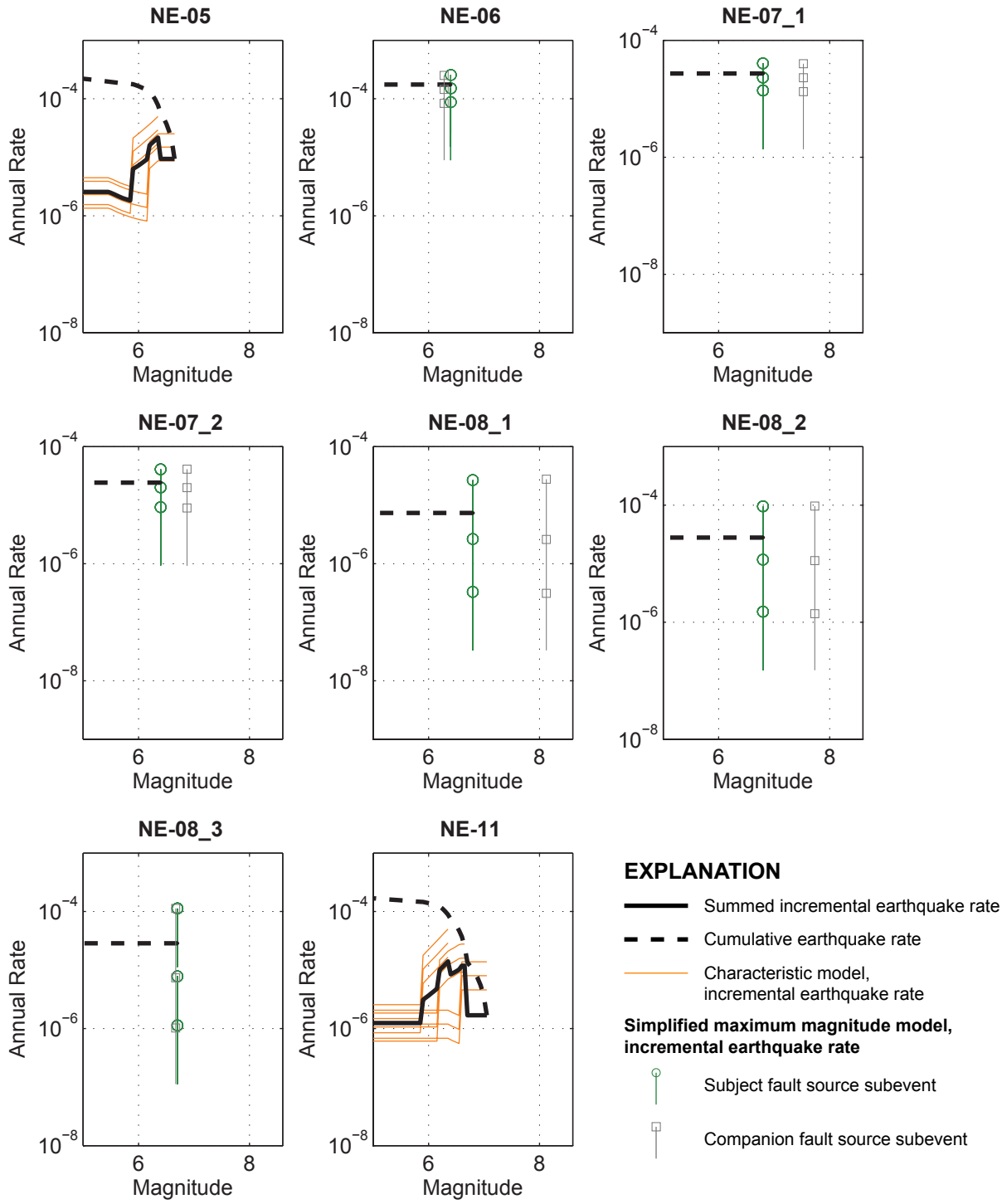

Note: The MFD for the Los Osos fault source (Northeast-Vergent Model), calculated for a point nearest the DCPP, has contributions from four rupture sources. The MFD from rupture source NE-05 consists of individual contributions from characteristic magnitude PDFs. The MFDs from rupture sources NE-06, NE-07, and NE-08 consist of contributions from alternative splay (NE-06, NE-07) and complex (NE-08) scenarios with simplified maximum magnitude PDFs. As each splay and complex scenario consists of two subevents (a main and splay or primary and secondary), the green circles show the magnitudes for the subevent on the Los Osos fault source and the grey squares show the magnitudes for the "companion" subevent. By design, the rates for both subevents are the same. The vertical lines through the circles and squares are for visualization only. The solid black lines are the summed incremental MFDs, and the dashed black lines are the cumulative MFDs. Magnitude bin size is 0.05.

Rupture-Source MFDs Contributing to the Los Osos Fault Source (NE Model) "Point" MFD

DCPP SSC REPORT

Pacific Gas and Electric Company

Figure **10-51**

File path: /s/1005/005/Final_Report_Figures/Figure_1000-51.ai; Date: 02/26/2015; User: Serkan Bozkurt, LCI; Rev. 1

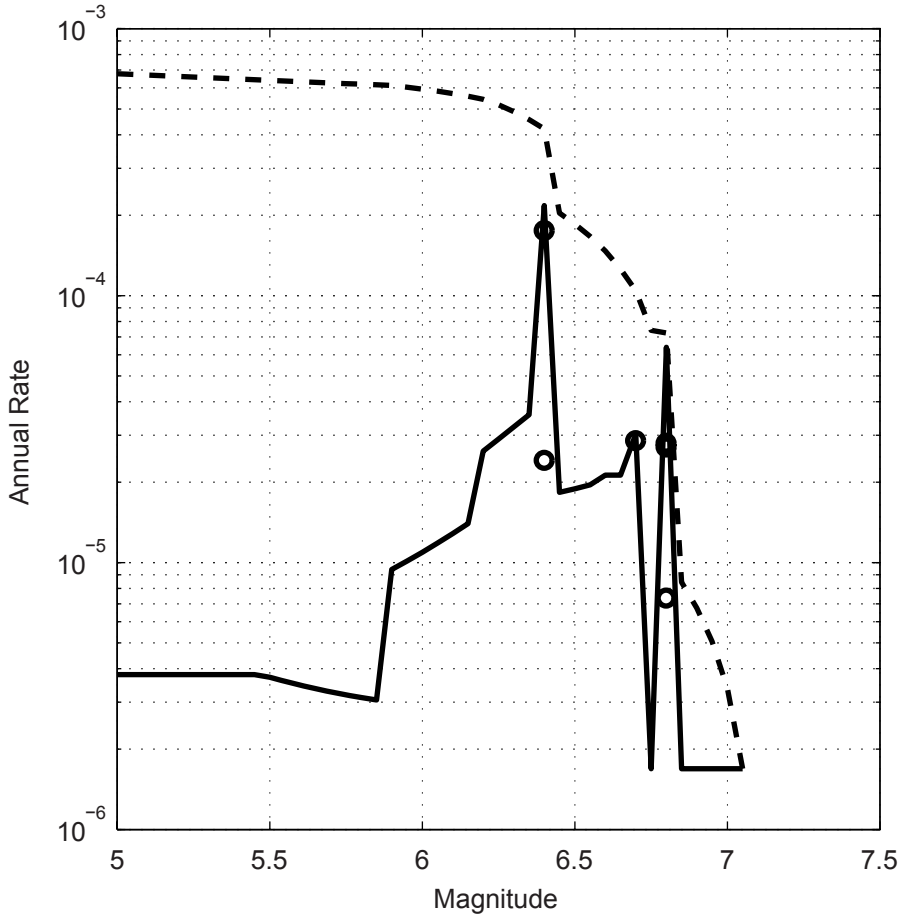

EXPLANATION

- Single-magnitude contribution from simplified maximum magnitude PDF rupture source (magnitude of subevent on the subject fault shown)
- Summed incremental earthquake rate
- Cumulative earthquake rate

Note: The MFD for the Los Osos fault source (Northeast-Vergent Model) for a point nearest the DCPP is shown on this figure. The incremental (black line) and cumulative (dashed line) earthquake rates are summed from the rupture source MFDs presented on Figure 10-51. Circles represent the rates of earthquakes (at the Los Osos subevent magnitudes) contributed from rupture sources NE-06 (one scenario), NE-07 (two scenarios), and NE-08 (three scenarios). Magnitude bin size is 0.05.

Los Osos Fault (NE Model) MFD, Summed Incremental and Cumulative Earthquake Rates at a Point Nearest the DCPP

DCPP SSC REPORT

Pacific Gas and Electric Company

Figure **10-52**

File path: /s/1005/005/Final_Report_Figures/Figure_1000-52.ai; Date: 02/26/2015; User: Serkan Bozkurt, LCI; Rev. 1

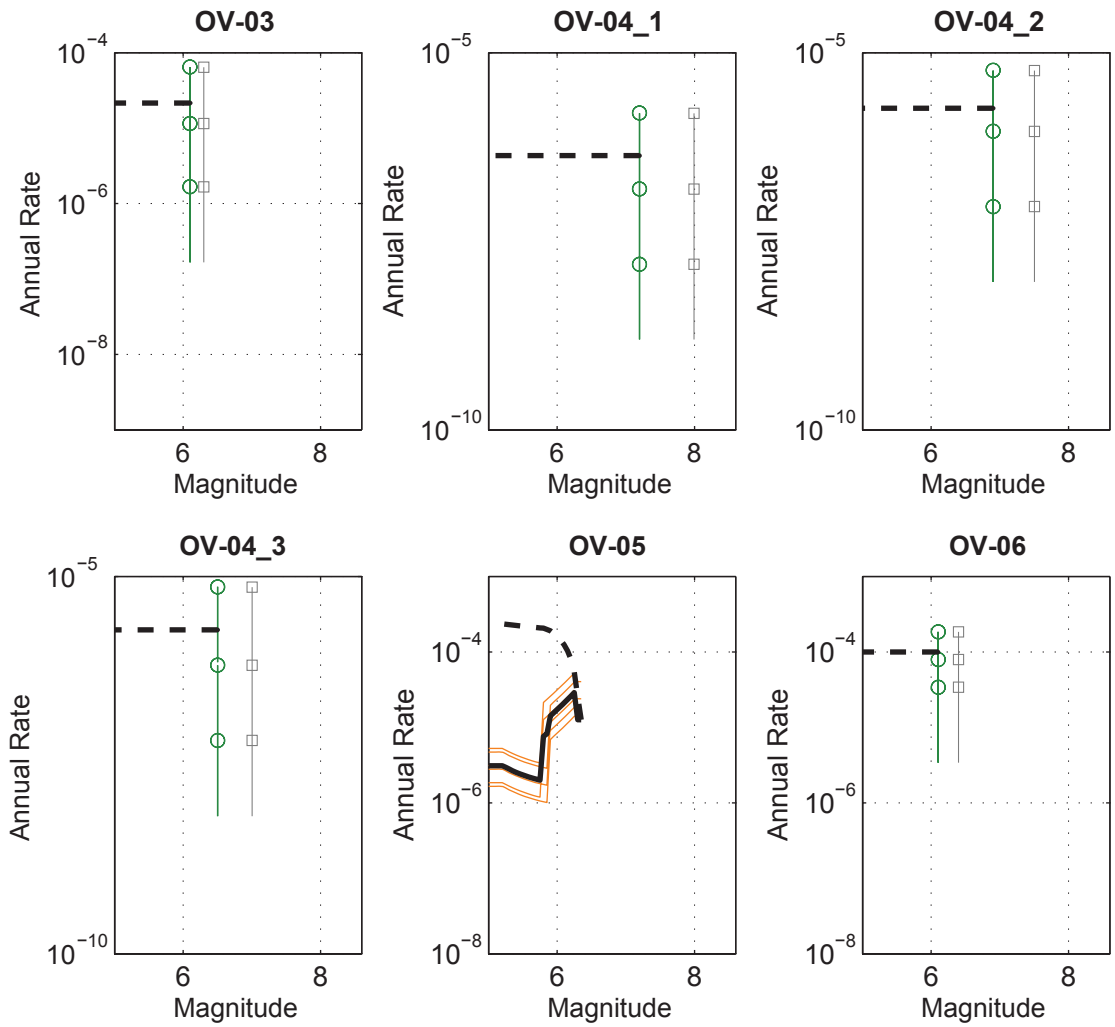

EXPLANATION

Summed incremental earthquake rate

Cumulative earthquake rate

Characteristic model, incremental earthquake rate

Simplified maximum magnitude model, incremental earthquake rate

Subject fault source subevent

Companion fault source subevent

Note: The MFD for the San Luis Bay fault source (Outward-Vergent Model), calculated for a point nearest the DCPP, has contributions from four rupture sources. The MFD from rupture source OV-05 consists of individual contributions from characteristic magnitude PDFs. The MFDs from rupture sources OV-03, OV-04, and OV-06 consist of contributions from alternative complex (OV-03, OV-04) and splay (OV-06) scenarios with simplified maximum magnitude PDFs. As each complex and splay scenario consists of two subevents (a primary and secondary or main and splay), the green circles show the magnitudes for the subevent on the San Luis Bay fault source and the grey squares show the magnitudes for the "companion" subevent. By design, the rates for both subevents are the same. The vertical lines through the circles and squares are for visualization only. The solid black lines are the summed incremental MFDs, and the dashed black lines are the cumulative MFDs. Magnitude bin size is 0.05.

Rupture-Source MFDs Contributing to the San Luis Bay Fault Source (OV Model) "Point" MFD

DCPP SSC REPORT

Pacific Gas and Electric Company

Figure **10-53**

File path: /s/1005/005/Final_Report_Figures/Figure_1000-53.ai; Date: 02/26/2015; User: Serkan Bozkurt, LCI; Rev. 1

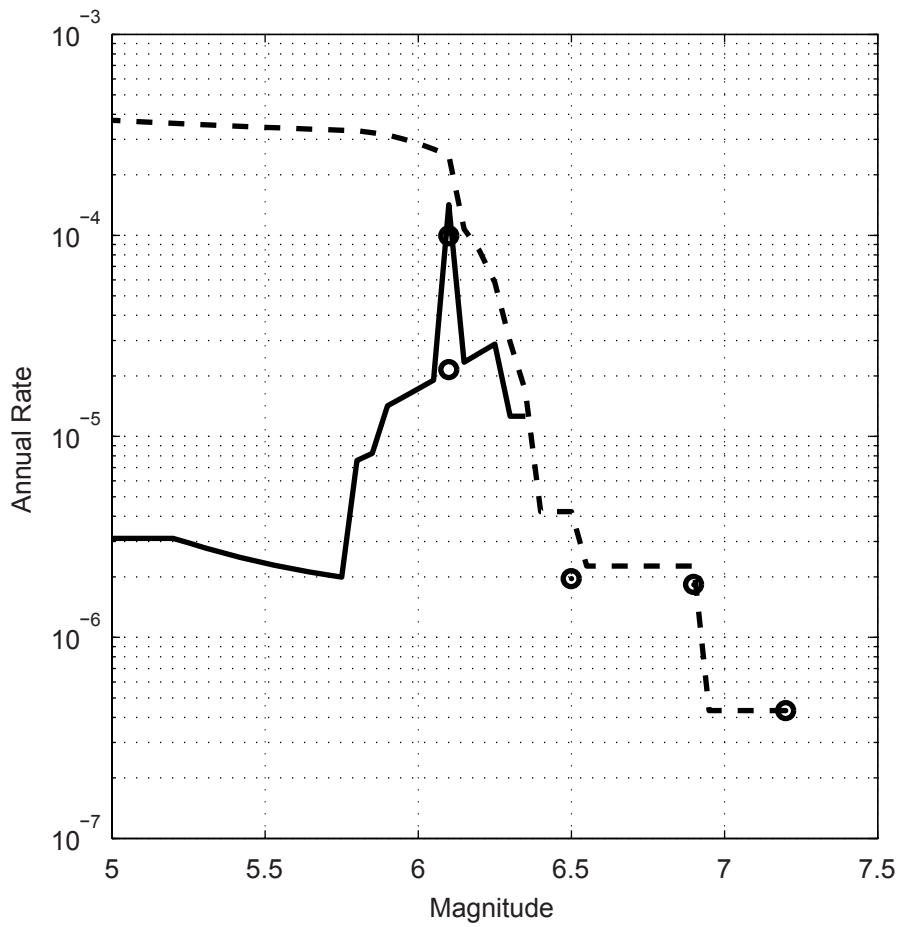

EXPLANATION

- Single-magnitude contribution from simplified maximum magnitude PDF rupture source (magnitude of subevent on the subject fault shown)
- Summed incremental earthquake rate
- Cumulative earthquake rate

Note: The MFD for the San Luis Bay fault source (Outward-Vergent Model) for a point nearest the DCPP is shown on this figure. The incremental (black line) and cumulative (dashed line) earthquake rates are summed from the rupture source MFDs presented on Figure 10-53. Circles represent the rates of earthquakes (at the San Luis Bay subevent magnitudes) contributed from rupture sources OV-03 (one scenario), OV-04 (two scenarios), and OV-06 (one scenario). Magnitude bin size is 0.05.

San Luis Bay Fault (OV Model) MFD, Summed Incremental and Cumulative Earthquake Rates at a Point Nearest the DCPP

DCPP SSC REPORT

Pacific Gas and Electric Company

Figure **10-54**

File path: /s/1005/005/Final_Report_Figures/Figure_1000-54.ai; Date: 02/26/2015; User: Serkan Bozkurt, LCI; Rev. 1

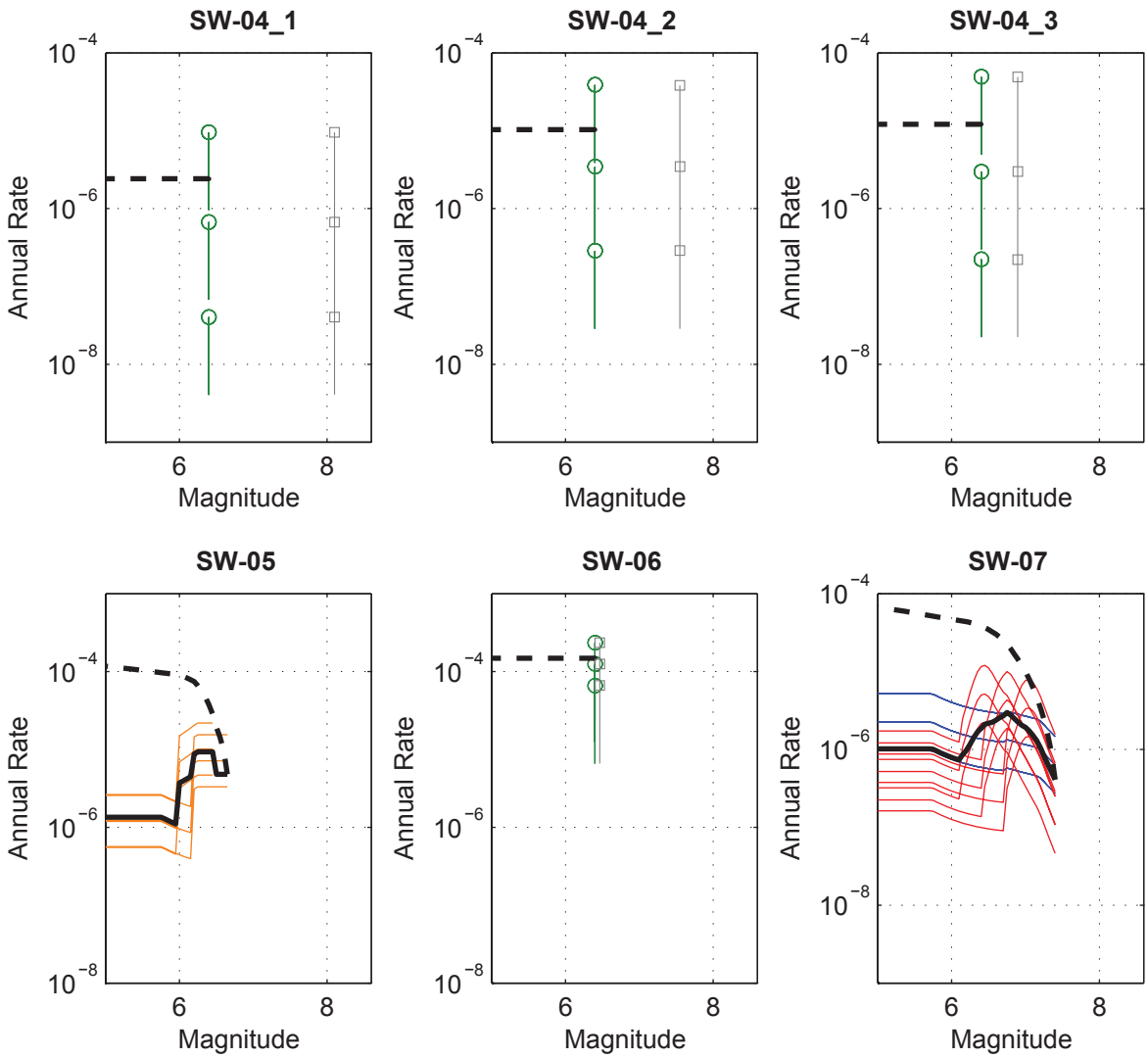

EXPLANATION

- WAACY model, incremental earthquake rate
- Exponential model, incremental earthquake rate
- Characteristic model, incremental earthquake rate
- Summed incremental earthquake rate
- Cumulative earthquake rate

Simplified maximum magnitude model, incremental earthquake rate

- Subject fault source subevent
- Companion fault source subevent

Note: The MFD for the San Luis Bay fault source (Southwest-Vergent Model), calculated for a point nearest the DCPP, has contributions from four rupture sources. The MFD from rupture source SW-05 consists of individual contributions from characteristic magnitude PDFs (orange lines). The MFD from rupture source SW-07 consists of individual contributions from WAACY (red) and exponential (blue) magnitude PDFs. The MFDs from rupture sources SW-04 and SW-06 consist of contributions from alternative complex (SW-04) and splay (SW-06) scenarios with simplified maximum magnitude PDFs. As each complex and splay scenario consists of two subevents (a primary and secondary or main and splay), the green circles show the magnitudes for the subevent on the San Luis Bay fault source and the grey squares show the magnitudes for the “companion” subevent. By design, the rates for both subevents are the same. The vertical lines through the circles and squares are for visualization only. The solid black lines are the summed incremental MFDs, and the dashed black lines are the cumulative MFDs. Magnitude bin size is 0.05.

Rupture-Source MFDs Contributing to the San Luis Bay Fault Source (SW Model) "Point" MFD

DCPP SSC REPORT

Pacific Gas and Electric Company

Figure **10-55**

File path: /s/1005/005/Final_Report_Figures/Figure_1000-55.ai; Date: 02/26/2015; User: Serkan Bozkurt, LCI; Rev. 1

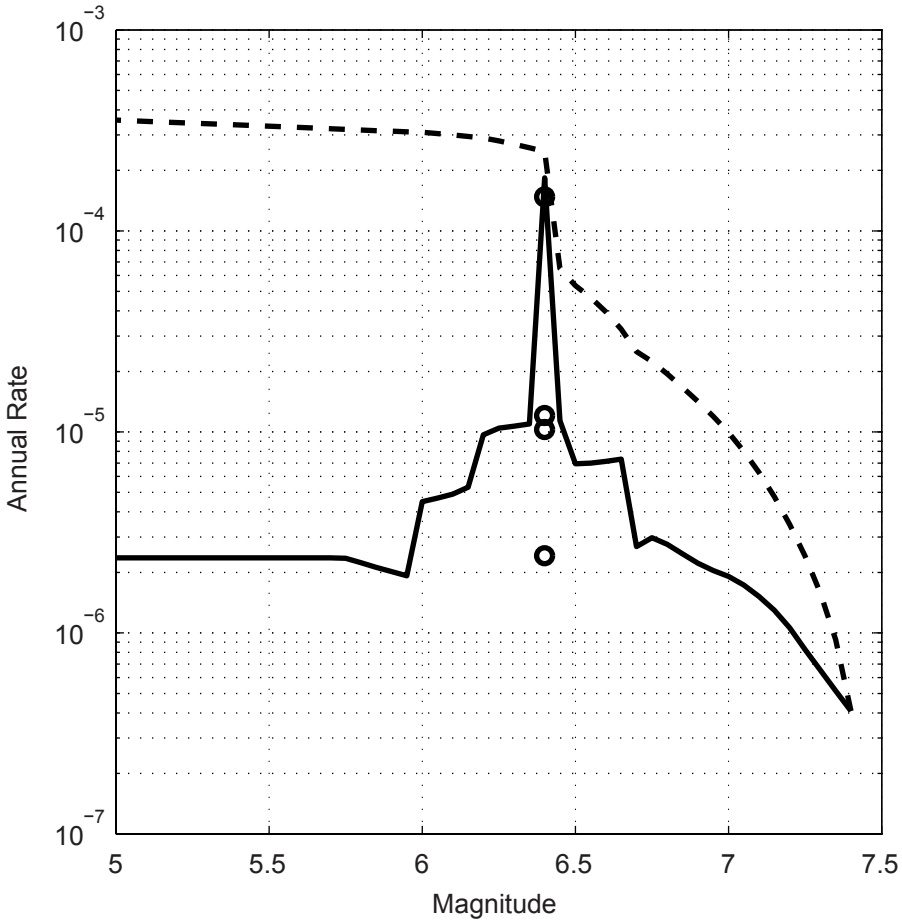

EXPLANATION

- Single-magnitude contribution from simplified maximum magnitude PDF rupture source (magnitude of subevent on the subject fault shown)
- Summed incremental earthquake rate
- Cumulative earthquake rate

Note: The MFD for the San Luis Bay fault source (Southwest-Vergent Model) for a point nearest the DCPP is shown on this figure. The incremental (black line) and cumulative (dashed line) earthquake rates are summed from the rupture source MFDs presented on Figure 10-55. Circles represent the rates of earthquakes (at the San Luis Bay subevent magnitudes) contributed from rupture sources SW-04 (three scenarios) and SW-06 (one scenario). Magnitude bin size is 0.05.

San Luis Bay Fault (SW Model) MFD, Summed Incremental and Cumulative Earthquake Rates at a Point Nearest the DCPP

DCPP SSC REPORT

Pacific Gas and Electric Company

Figure **10-56**

File path: /s/1005/005/Final_Report_Figures/Figure_100056.ai; Date: 02/26/2015; User: Serkan Bozkurt, LCI; Rev. 1

11.0 TIME DEPENDENCY MODEL

Earthquake recurrence models describe the probability distribution of the time between earthquakes of hazard significance on a particular fault. Recurrence models are used to characterize the probability of occurrence of an earthquake in a forecast window of interest. The forecast window is normally shorter than the earthquake recurrence interval, so the only cases considered are those in which zero or one event will occur in the forecast window. Few data constrain the shape and parameters of recurrence models for Primary and Connected faults. This condition is reflected in the Diablo Canyon SSC model by including alternative time dependent recurrence models and a full range of parametric uncertainties. Time dependent recurrence models are considered because studies of paleoseismic records on well-studied faults in California find them to be technically defensible characterizations of the timing of earthquakes in the state.

Recurrence models can be either time-independent or time-dependent. For a time-independent model, earthquakes occur randomly in time when viewed over a long interval; this corresponds to a Poisson process. The time intervals between earthquakes distributed randomly in time (i.e., the recurrence model) are characterized by an exponential distribution. The probability of earthquake occurrence in a forecast window for an exponential distribution is constant because randomness in time of a Poisson process means that there is no predictive advantage in knowing when the last earthquake occurred. Time-dependent earthquake recurrence models have a variety of shapes, although the most common models include a single maximum and a somewhat extended right tail. Three such distributions are considered in the Diablo Canyon SSC model.

The Poisson model has a long history of application in probabilistic seismic hazard assessment (e.g., Cornell, 1968; Cornell and Winterstein, 1988). The corresponding exponential model for earthquake occurrence is attractive because it is characterized by a single parameter, the long-term mean event rate. Time-dependent recurrence distributions are more complicated than the exponential distribution, requiring two or more parameters for their description. When few data constrain the earthquake recurrence model, a rigorous defense of a more complicated recurrence model cannot be offered on the basis of relative improvement of the fit to the data. At the same time, the limited nature of available data for project area faults cannot be offered as evidence against time-dependent earthquake recurrence, especially when physical processes of strain accumulation and release at the site are similar to other places in California with better data.

11.1 Definition and Applicability

The time-independent seismic hazard at the Diablo Canyon Power Plant (DCPP) is determined by the fault geometries, rupture-source slip rates and magnitude-frequency relations set out in *Chapters 9 and 10*. The earthquake occurrence rates can be interpreted as the Poisson-equivalent hazard for the DCPP. Earthquake recurrence within the rupture-source magnitude-frequency distributions is random in time, and the rate of events is

adjusted to total to the rupture-source slip rate. Since the Poisson model is used in baseline hazard calculation, time dependence is implemented using a factor that can be applied to the earthquake rate that raises (or, in principle, could lower) hazard. This factor is called the equivalent Poisson ratio, or EPR. The EPR is calculated on a per-fault and per-slip-rate basis.

11.2 Approach

Very limited data constrain earthquake recurrence rates for the Primary and Connected faults of the SSC model. In this section available constraints are reviewed, with their ranges of uncertainty. Key data from the DCPP region are needed for fault slip rates and the time since the most recent earthquake. Other constraints are introduced in the form of bounding values to complete the EPR estimates. Then the method for estimating EPRs is reviewed. A more detailed explanation focused on the method itself is given in *Appendix H*. EPR estimation is introduced as a generalization of more familiar methods from conditional probability estimation. Generalization is necessary because recurrence intervals or times since the most recent event (MRE) for any of the Primary DCPP faults are known only in terms of uncertain ranges. The EPR for the San Andreas fault (SAF) source is developed as a special case. The SAF is given special attention because it is the largest and highest slip-rate fault among the regional sources near the DCPP (*Chapter 12*), and because the time since its most recent event (*tMRE*) is near or has exceeded its mean recurrence time. Yet despite of the size of the SAF and the relatively long time since the last event, hazard sensitivity results show that it has only a small effect on hazard at the DCPP at the ground motions of interest (*Chapter 14*) because of its high source-to-site distance.

11.2.1 DCPP Regional Data and Estimation of Equivalent Poisson Ratios

This section provides a review of the data available to constrain inputs to the EPR estimates.

Paleoseismic findings have been reported on the Los Osos and San Simeon faults. Lettis and Hall (1994) report on several trenches excavated to study the Los Osos fault. The fault trace is discontinuous along strike and irregular in expression in the trenches. A trench at the Ingley site (Lettis and Hall, 1994, p.94) shows fault activity offsetting late Pleistocene alluvium. Above the faulted layer are deposits that are warped and pinch out laterally toward the fault, although they do not actually cross the fault. The warped layer included wood samples with radiocarbon ages of 2,500 years before present (2.5 ^{14}C kyr BP). Assuming that the samples accurately date the layer, and that the warping can be associated with fault activity, a maximum *tMRE* of 2,500 years ago (2.5 ka) can be inferred for that trace of the Los Osos fault.

In a second exposure, low-angle faults displace a soil horizon thought to be 13–18 ka. Four prominent shears with 0.5–2.0 m offsets are described, with displacements averaging 1.0 m (Lettis and Hall, 1994, p.96). Dating relations indicate that the youngest offset postdates 1.8 ^{14}C kyr BP. The low-angle faults are interpreted be secondary to the

main Los Osos fault at depth. Considering both exposures together, the available data for the Los Osos fault suggest a recurrence interval of approximately 3–4.5 kyr, displacements at a point of 0.5–2.0 m, and most recent activity sometime after 1.8 ka. It should be noted that the Los Osos fault is considered to be blind in the SSC, so events recorded as surface ruptures on the secondary splays exposed in the trenches may underrepresent the number of events that occurred on the fault plane at depth. Consequently, the recurrence interval for the Los Osos fault developed from strict use of the paleoseismic data may overestimate the actual recurrence interval of the fault, or equivalently, underestimate the rate of ground-rupturing earthquakes.

Trenching on the San Simeon fault near San Simeon exposed vertical strike-slip displacements with net slips of 1–2 m per event and a recurrence interval between 265 and 2,000 years, with a best-constrained recurrence interval of between 600 and 1,800 years (Hall et al., 1994, p.183). The San Simeon fault splits into multiple active splays, but the main splays investigated in trenches are thought to capture the majority of recent fault activity. The San Simeon fault paleoseismic sites are approximately 58 km north of the DCPP, so displacements and rates may not be same as for the Hosgri fault near the DCPP.

The paleoseismic investigations on the Los Osos and San Simeon faults sampled only a few recent events, providing useful reference points in evaluating assumptions about displacement and recurrence in the EPR method. But neither investigation provided data that constrains rupture rates or displacements per event to a degree that would alter the more generic treatment undertaken in this chapter.

On the Hosgri or Shoreline faults near the DCPP, no relevant recurrence or displacement-per-event data are available. New detailed 3D seismic images and high-resolution bathymetry were examined for discrete offsets or evidence of scarp freshness that might relate to recency of activity. Even where the faults are well exposed, the resolution was not sufficient to identify individual offsets or relevant features. It is conceivable that data that resolve these features may be collected in the future using low-energy seismic profiling, side-scan sonar, or similar technologies, but for now such data are not available. Similarly, on the San Luis Bay fault, no data are available relating to the recency of activity.

The minimum value of time since the most recent event, $T_{\min}$, influences the EPR when $T_{\min}$ is more than a few percent of the long-term mean recurrence interval. Two values are adopted for the SSC. The primary reference date used is the founding of the Spanish mission at San Luis Obispo in 1772. The founding of the mission at San Luis Obispo together with the lack of reported earthquakes in mission documents provides a rationale for setting $T_{\min}$ = 242 yr. Toppozada et al. (1981) detail the history of the Spanish missions as they relate to significant earthquakes in California. Missions were sensitive to strong ground motions. An earthquake in 1800 damaged missions in San Juan Capistrano, 80 km away, and in San Diego; Salisbury et al. (2012) have associated this earthquake with the San Jacinto fault. An earthquake in 1812 on the SAF 85 km away from San Juan Capistrano caused additional damage and some fatalities. A few weeks later, a second

large earthquake on the SAF caused extensive damage in Ventura, Santa Barbara, and elsewhere (Toppozada et al., 2002). In the same interval, no damaging events were reported affecting the mission at San Luis Obispo. Since other quasi-continuous records (baptisms, marriages) from Mission San Luis Obispo survived from the time of the mission founding, and missions were in communication with one another, it is likely that a damaging event would have been noted. Also, by 1812, Mission San Miguel had been established approximately 37 miles north on the coastal California route (in 1797), and a chapel had been opened in Avila Bay (in 1808). Considering the extent of this network, the lack of any damage reports in documents from the San Luis Obispo mission make it unlikely that an earthquake of *M* 6.5 or larger occurred on DCPP Primary and Connected faults since 1772.

With some weight, a secondary, and more secure, value of $T_{\min}$ is the establishment of San Luis Obispo as a regional center. By the early 1870s, road and rail connections were opened to the rest of California, and the first newspaper was established. Separately, Felzer (2013b) estimates that the seismic catalog for the central coast of California is likely to be complete to *M* 6.5 beginning in 1870. Since San Luis Obispo was a regional center by this time, it is likely that the local catalog is complete to lower magnitudes. For final EPR estimates, to account for this epistemic uncertainty, we assign [0.8] weight to EPR estimates using the founding of the San Luis Obispo mission ($T_{\min}$ = 242 years), and [0.2] weight on $T_{\min}$ = 144 years associated with the founding of San Luis Obispo itself. Assigned weights reflect the TI Team assessment of the relative merits of evidence for the two dates of catalog completeness for ground-rupturing earthquakes on DCPP Primary and Connected faults.

11.2.2 Conditional Probability of an Earthquake

The conditional probability (CP) of an earthquake refers to the probability that it will occur in a forecast interval T_f given that it has not occurred up to time *t.* For SSC calculations, a forecast interval of T_f = 30 years is used. The results do not depend materially on the forecast interval because the EPR is relative to a Poisson forecast of the same width. In the CP calculation, time $t = 0$ refers to the moment after the last large earthquake on the fault of interest. The equation for the CP is

$$CP(t, T_f) = \frac{F(T_f + t) - F(t)}{1 - F(t)} \tag{11-1}$$

where *F(t)* is the cumulative distribution function (CDF) of a probability density function (PDF) *f(t)* that describes earthquake recurrence. The CP equation (Equation 1) is shown graphically on Figure 11-1 for two recurrence model functional forms. The CP is the ratio of the area in the forecast period (dark shading) to the total area to the right of *t* (sum of shaded areas).

Figure 11-1 shows that the CP depends on the shape of the recurrence model. On Figure 11-1a is the exponential PDF:

$$f_{exp}(t; \lambda) = \lambda e^{-\lambda t} \tag{11-2}$$

with cumulative distribution

$$F_{exp}(t;\ \lambda) = 1 - e^{-\lambda t} \tag{11-3}$$

Parameter λ is the mean annual rate of events when t is in years. On Figure 11-1, rates have been normalized to a long-term rate of 1.0 (so $\lambda = 1.0$). The CP for an exponential earthquake recurrence model, combining Equations (11-1), (11-2), and (11-3), is

$$CP_{exp}(t, T_f) = 1 - \ e^{-\lambda T_f} \ \approx \ \lambda T_f \tag{11-4}$$

where the last approximation applies when λT_f is small compared to 1. Equation (11-4) shows that the exponential recurrence model, which corresponds to a Poisson distribution of events randomly in time, does not depend on time and, for T_f small compared to $1/\lambda$, is approximately equal to the annual earthquake rate multiplied by the forecast period.

On Figure 11-1b, a lognormal PDF is shown as an example of the three time-dependent recurrence models considered. This distribution is commonly used to model paleoseismic earthquake recurrence (Fitzenz et al., 2010; Biasi, 2013). The lognormal probability distribution characterizes random variables whose logarithms are normally distributed with parameters $\{\mu, \sigma\}$, where μ is the mean log of interval lengths and σ^2 is the variance. The lognormal PDF is given by

$$f_{LN}(t; \mu, \sigma) = \frac{1}{t\sigma\sqrt{2\pi}} e^{\frac{-(\ln(t)-\mu)^2}{2\sigma^2}} \tag{11-5}$$

The CDF of the lognormal distribution is

$$F_{LN}(t; \mu, \sigma) = \frac{1}{2} + \frac{1}{2}\mathrm{erf}\left(\frac{\ln(t)-\mu}{\sigma\sqrt{2}}\right), \tag{11-6}$$

where *erf(.)* is the error function. Substitution of $F_{LN}(t;\mu,\sigma)$ into Equation (11-1) would confirm that the lognormal CP is time-dependent. The lognormal distribution has two necessary qualities for modeling earthquake occurrence. First, the lognormal distribution is restricted in domain to positive numbers. Every interval between earthquakes is positive, so the distribution describing intervals cannot allow a negative range. Second, it has an asymmetric right tail that allows it to fit the occasional, longer-than-average recurrence interval that is commonly observed in paleoseismic data.

Lognormal parameters μ and σ are related to the long-term mean recurrence rate λ by

$$1/\lambda = \exp(\mu + \sigma^2/2) \tag{11-7}$$

The arithmetic coefficient of variation (CV) for the lognormal distribution does not depend on mean parameter μ and is given by

$$CV = \sqrt{e^{\sigma^2} - 1} \tag{11-8}$$

$f_{LN}(t)$ approaches 0 as t approaches 0. Physically, this means that the lognormal distribution probability is smallest just after the previous event. The lognormal CP depends on time, being less than the exponential distribution rate for small t and the same

long-term rate, but approximately 1.5 times $CP_{\exp}$ for the values of t and T_f used on Figure 11-1. This variation in CP is the basis of the EPR. For the Diablo Canyon SSC model, because the times of the MREs are uncertain for the Primary and Connected fault sources, *tMRE* is incorporated as a range in estimating the EPR. Details on how this range is implemented are given later in this chapter.

The functional form in time dependence is also unknown. To sample the range of uncertainties, two other distributions are considered besides the lognormal: the Brownian passage time (BPT) model and the Weibull distribution. The BPT model of earthquake recurrence (Ellsworth et al., 1999; Matthews et al., 2002; WGCEP, 2003) models recurrence in terms of a secular loading rate around which are random Gaussian deviations representing local strain increases or decreases. The BPT PDF can be formulated in terms of two variables, η and α, as follows:

$$f_{BPT}(t;\ \eta, a) = \left(\frac{\eta}{2\pi a^2 t^3}\right)^{\frac{1}{2}} exp\left(\frac{(t-\eta)^2}{2a^2\eta t}\right) \tag{11-9}$$

Variable η parameterizes the secular loading rate. Numerically, η is the arithmetic mean of the interval lengths and is equal to the reciprocal of λ from the exponential distribution. Parameter α is called the aperiodicity by Matthews et al. (2002), but numerically it is equal to the CV. The BPT model can have a wider variety of shapes than the lognormal distribution, but the two are similar for parameters likely to come from paleoseismic data.

The Weibull distribution is sometimes applied to forecast probabilities of a large earthquake because of its more common use in modeling time-to-failure rates in mechanical or engineered systems. The PDF for Weibull random variables and $t \geq 0$ is

$$f_{Wbl}(t;\ \nu, k) = \frac{k}{\nu}\left(\frac{t}{\nu}\right)^{k-1} \exp\left(-\left(\frac{t}{\nu}\right)^{k}\right) \tag{11-10}$$

Parameter ν governs the width of the distribution. Comparison of the Weibull cumulative distribution,

$$F_{Wbl}(t;\ \nu, k) = 1 - \exp(-\left(\frac{t}{\nu}\right)^{k}) \tag{11-11}$$

to Equation (11-3) shows that parameter k controls the shape of the Weibull distribution relative to an exponential. For $k = 1$, the Weibull distribution reduces to the exponential distribution. For $k > 0$, the failure rate for the Weibull distribution increases monotonically with time.

11.2.3 Development of Equivalent Poisson Ratios

EPRs can be estimated by generalizing the ratios of the conditional probability introduced in *Section 11.2.2*. The conditional probability ratio (CPR) is the ratio of the CP for a given recurrence model PDF and CV divided by the corresponding time-independent (exponential distribution) CP. The CPR is a mathematical construct that can be calculated for any pair of long-term mean (LTM) and *tMRE* without reference to the likelihood of either. Figure 11-2 shows CPRs for four values of CV and the lognormal model; for each

discrete pair (*LTM, tMRE*) in the four plots, we divide the 30-year lognormal CP (CP_{LN}) by its corresponding 30-year value under the exponential distribution (CP_{exp}). LTM and *tMRE* axes have been chosen looking ahead to the relevant range for the Hosgri fault, but the axes can be rescaled to other ranges by dividing both by the same value. Contours on Figure 11-2 are generally similar among the four plots, although the location of the maximum values varies relative to the diagonal (*LTM = tMRE*) depending on CV. Maximum values of the CPR do depend on CV, however. This is because distributions with larger CVs are less informative (spread across a wider range). Conversely, CPRs can become large for narrow PDFs that model more regular earthquake recurrence.

The EPR is extracted from the CPR by using probabilities distributions for *LTM*, *tMRE*, and *CV* to weight among CPR values and to focus on its likely range. The EPR estimate is developed from Figure 11-2 in two steps. First, not all values of LTM are equally probable. The Hosgri fault is not considered likely to produce larger average slip-per-event earthquakes than, for example, the San Andreas fault. Average displacements in the two largest known SAF earthquakes were 4.3 m and 4.45 m for the 1857 and 1906 events, respectively (Biasi, Weldon, and Dawson, 2013). Dividing 4.5 m by the Hosgri fault slip rate of 1.7 mm/yr (*Chapter 8*) gives a mean recurrence of 2,650 years. Larger average displacement-per-event (DPE) values are considered possible at a low probability, but they are not as likely as smaller values. On the other hand, if the Hosgri fault fails in 0.5 m per event (m/event) average displacements, the LTM will be about 300 years. On Figure 11-3 we plot the DPE distribution applied to the Hosgri fault for estimation of the EPR, along with its corresponding LTM distributions for three fault slip rates. The DPE plot expresses uniform probabilities for displacements from 1.5 to 3.0 m/event, with values from 0.5 to 5.0 m/event allowed. Little definite information on DPE is available, so the flat central part of the DPE is instead intended to be geologically defensible and otherwise nonprescriptive. The LTM distributions on Figure 11-3 use slip rates of 0.7, 1.7, and 2.7 mm/yr from the respective 8.5%, 50%, and 91.5% points of the Hosgri fault cumulative slip rate distribution from *Chapter 8* (Figure 8-33). Each distribution has the same shape but different widths in calendar years. *Appendix H* explores the sensitivity of EPR to DPE and finds that EPR is not sensitive for reasonable ranges of DPE.

The probable range of *tMRE* on Figure 11-2 can also be restricted. We note first that the likely range of *tMRE* is a function of *LTM.* Qualitatively, it should be unlikely that a process with a short mean recurrence interval would produce a long open interval. This notion is implemented in probability by the survivor function:

$$S(t|LTM) = 1 - F(t)$$

$S(t|LTM)$ gives the probability that an event characterized by CDF $F(t)$ will not have occurred by time t. $S(t)$ is plotted on Figure 11-4 for three values of LTM using $F_{LN}(t)$ and assuming a CV of 0.6.

The joint probability of *LTM* and *tMRE* is used to select more and less probable values of CPR. A value of the joint probability weighting is calculated for each cell of the corresponding plot on Figure 11-2. Contours of the joint probability surface are shown on Figure 11-5. Numerically, the values in Figure 11-5 have been renormalized by the peak

value of the surface so the relative areas of weighting can be read directly from the contours. The unnormalized weighting is used in all calculations. To obtain relative weights for CPR values, the CPR surface is sorted from largest to smallest. The weighting surface is sorted in the same order, and weight is then summed beginning from the largest CPR value. Since weightings of probable ranges of CPR are applied at this point, the result is a distribution of EPR (Figure 11-6) in the form of a complimentary cumulative probability distribution. The examples on Figures 11-5 and 11-6 assume T_{min} = 0 and T_{min} = 242 yr. Stars on Figure 11-6 mark EPR values at 8.5%, 50%, and 91.5% points in the distribution. These probability levels are adopted to summarize the EPR distribution in subsequent steps and in order to use weightings by Miller and Rice (1983) to calculate weighted mean estimates of EPR. Miller and Rice (1983) weights are, respectively, [0.25, 0.5, 0.25]. Results in Figure 11-6 are for *CV*=0.6. Similar results are constructed for each value of CV having non-zero weight. Other details on the implementation of weights to obtain EPR estimates are given in *Appendix H*.

The final step in estimating EPR for a given fault slip rate and recurrence model functional form is to weight the per-CV EPR estimates by the probabilities of each CV. Little is known about the CV of the Hosgri or other Primary and Connected faults of the SSC. However, nothing about these faults suggests that they would be exceptional when compared to the range of recurrence CVs observed for other California faults. To ensure that the center, body and range of CV values were considered, CV values were estimated for the best available records from California paleoseismic sites. Results from 12 from sites in California and one from New Zealand are shown on Figure 11-7. All records have at least seven events, so CV estimates are reasonably well resolved. Data are from Weldon et al. (2013), Rockwell et al. (2014), Berryman et al. (2012), and Scharer (2013). Sites *Hog2* and *Mystic* are on the San Jacinto fault; *Coachella* and *Burro* represent the southern San Andreas fault; *Pitman*, *Wrightwood*, *Pallett Creek*, and *Frazier* are from the central San Andreas fault; *Arano* and *Vedanta* represent the northern San Andreas fault; *Tyson* is on the Hayward fault; and *Hokuri* is a 24-event record from the South Alpine fault, South Island, New Zealand. The value *Burro 9 ev* is an alternate for *Burro* that assumes that no events are missing in the Burro Flat record. To estimate CVs, sample event sequences are drawn in order from earthquake date distributions, respecting reported dating uncertainties, as described in Biasi (2013). The *CV* for each sampled sequence is calculated as the sample standard deviation of the interval lengths divided by the mean. Values shown in Figure 11-7 are averages from hundreds of random event realizations per site. Figure 11-7 shows that CV estimates from best-studied strike-slip sites are distributed around 0.6, with a range from 0.38 to 0.76. These sites are unlikely to capture the full range of CV for strike-slip faults, and all sites on Figure 11-7 are on higher slip-rate faults than the Primary and Connected faults of the SSC. Therefore CV weights used for EPR estimation are centered on the observed CV range, but given a wider allowed distribution from 0.3 to 1.0.

EPR values computed over a range of CVs are shown on Figure 11-8 for three values of Hosgri fault slip rate and T_{min} = 242 yr. Three-point distribution estimates are seen to increase as the *CV* decreases. This occurs because the corresponding time-dependent

distributions for smaller *CV* values are narrower and concentrate probability to a greater degree than the time-independent (Poisson) rate that makes up the CPR denominator. Dotted lines in Figure 11-8 are the weighted mean EPR estimates computed by multiplying the CV weights by the respective per-CV EPR value and summing the result. Weighted mean EPR estimates are seen to increase with fault slip rate. This occurs because the relative improbability of an open period of 242 years increases with slip rate, thus increasing the underlying conditional probability ratios. CV weights are also applied to the respective 8.5%, 50%, and 91.5% EPR estimate points to calculate the range of EPR. Results are compiled in Table 11-1 for three Hosgri fault slip rates, three recurrence PDF functional forms, and minimum open intervals T_{min} of 144 and 242 years.

Table 11-1. Hosgri Fault Equivalent Poisson Ratios for Three Slip Rates, Three Recurrence Models, and Two Minimum Open Intervals

Recurrence PDF	Slip Rate (mm/yr)	T_{min} (yr)	8.5% EPR	50% EPR	91.5% EPR	Weighted Mean EPR
LN	1.7	242	0.39	1.35	1.85	1.24
LN	0.7	242	0.15	1.18	1.86	1.09
LN	2.7	242	0.58	1.46	1.84	1.33
LN	1.7	144	0.24	1.24	1.84	1.14
LN	0.7	144	0.10	1.12	1.86	1.05
LN	2.7	144	0.38	1.32	1.82	1.21
BPT	1.7	242	0.42	1.35	1.81	1.23
BPT	0.7	242	0.14	1.20	1.81	1.09
BPT	2.7	242	0.63	1.44	1.79	1.33
BPT	1.7	144	0.25	1.25	1.80	1.14
BPT	0.7	144	0.07	1.15	1.81	1.04
BPT	2.7	144	0.40	1.32	1.78	1.21
WBL	1.7	242	0.59	1.08	1.92	1.17
WBL	0.7	242	0.48	0.95	1.80	1.04
WBL	2.7	242	0.68	1.18	1.98	1.25
WBL	1.7	144	0.51	1.00	1.84	1.09
WBL	0.7	144	0.44	0.92	1.77	1.01
WBL	2.7	144	0.58	1.06	1.85	1.14

11.2.4 Evaluation of Recurrence Model Functional Forms

Figure 11-9 shows a comparison of Hosgri fault EPRs for the three time-dependent distributions introduced in *Section 11.2.2*. Three distributions are used to explore the range of EPRs across a reasonable alternative set of recurrence models. Weighted-mean and three-point distribution values are similar between the lognormal and BPT models. In the range of CV values considered for the Hosgri fault (Figure 11-8), the lognormal and

BPT distributions themselves have similar shapes. The Weibull distribution differs primarily in its shape for short intervals, decreasing more rapidly than the other two distributions for small values of *tMRE*. This shape detail is a manifestation of the genetic relationship between the Weibull and exponential distributions. The Weibull weighted-mean EPR of 1.7 (Table 11-1) is somewhat smaller than the means of 1.24 and 1.23 for the lognormal and BPT distributions, respectively. Table 11-1 shows that this relative relationship is maintained for $T_{\min}$ = 144 yr.

11.2.5 Equivalent Poisson Ratios for Primary and Connected Faults

EPR estimates for Primary and Connected faults are listed in Tables 11-1 and 11-2. A comparison of Hosgri fault EPRs between cases with $T_{\min}$ = 242 yr and those with $T_{\min}$ = 144 yr shows that the weighted-mean EPR is lower by roughly 8% with $T_{\min}$ = 144 yr. Smaller values of $T_{\min}$ include more of the low hazard period early in the reloading phase of the presumed cycle. Hosgri fault weighted-mean EPRs are greater than 1.0 because T_{min} = 242 yr covers a significant fraction of the recurrence interval for reasonable slips per event on the Hosgri fault.

EPR estimates for Primary faults of the San Luis–Pismo block (SLPB), the Los Osos, San Luis Bay, and Shoreline faults, are given in Table 11-2. Inspection of the EPRs shows that all cases the weighted mean EPRs are close to 1.0 and similar in their three-point distributions. Entries have been rounded to hundredths, so slight differences may exist between apparently identical rows. Compared to the Hosgri fault, slip rates are uniformly lower, so recurrence intervals (RIs) are longer and $T_{\min}$ is a smaller fraction of the recurrence interval. Weighted-mean EPRs approach 1.0 as $T_{\min}/RI$ approaches zero. As observed with the Hosgri fault, the lognormal and BPT results are similar, and the Weibull estimates are lower by a few percent. Because the differences between recurrence model functional forms are small, the results for all three models are shown only for the Los Osos fault. EPRs vary systematically with slip rate, with the highest values for the highest slip-rate cases. Slip rates and $T_{\min}$ are similar between the Los Osos, Shoreline, and San Luis Bay faults, so the EPR estimates are similar also.

Table 11-2. SLPB Fault Equivalent Poisson Individual Estimates

Fault, Geometry	Recurrence PDF	Slip Rate (mm/yr)	tMRE Min (yr)	8.5% EPR	50% EPR	91.5% EPR	Weighted Mean EPR
Los Osos, OV	LN	0.26	242	0.26	1.16	1.54	1.03
Los Osos, OV	LN	0.18	242	0.24	1.16	1.54	1.02
Los Osos, OV	LN	0.36	242	0.29	1.17	1.53	1.04
Los Osos, OV	LN	0.26	144	0.21	1.15	1.54	1.01
Los Osos, OV	LN	0.18	144	0.20	1.15	1.54	1.01
Los Osos, OV	LN	0.36	144	0.23	1.15	1.53	1.02
Los Osos, OV	BPT	0.26	242	0.24	1.16	1.56	1.03
Los Osos, OV	BPT	0.18	242	0.20	1.16	1.56	1.02

Fault, Geometry	Recurrence PDF	Slip Rate (mm/yr)	tMRE Min (yr)	8.5% EPR	50% EPR	91.5% EPR	Weighted Mean EPR
Los Osos, OV	BPT	0.36	242	0.27	1.17	1.56	1.04
Los Osos, OV	WBL	0.26	242	0.64	0.96	1.44	1.00
Los Osos, OV	WBL	0.18	242	0.64	0.96	1.45	1.00
Los Osos, OV	WBL	0.36	242	0.65	0.96	1.44	1.00
Los Osos, SW	LN	0.19	242	0.24	1.16	1.54	1.03
Los Osos, SW	LN	0.14	242	0.22	1.16	1.54	1.02
Los Osos, SW	LN	0.26	242	0.26	1.17	1.54	1.04
Los Osos, NE	LN	0.42	242	0.31	1.18	1.53	1.05
Los Osos, NE	LN	0.33	242	0.28	1.17	1.53	1.04
Los Osos, NE	LN	0.53	242	0.34	1.19	1.53	1.06
San Luis Bay, OV	LN	0.16	242	0.23	1.16	1.54	1.02
San Luis Bay, OV	LN	0.11	242	0.22	0.16	1.54	1.02
San Luis Bay, OV	LN	0.22	242	0.25	1.16	1.54	1.03
San Luis Bay, SW	LN	0.21	242	0.25	1.16	1.54	1.03
San Luis Bay, SW	LN	0.15	242	0.23	1.16	1.54	1.02
San Luis Bay, SW	LN	0.30	242	0.28	1.17	1.54	1.04
San Luis Bay, NE	LN	0.16	242	0.23	1.16	1.54	1.02
San Luis Bay, NE	LN	0.11	242	0.22	1.16	1.54	1.02
San Luis Bay, NE	LN	0.23	242	0.26	1.17	1.54	1.03
Shoreline	LN	0.07	242	0.09	1.16	1.62	1.01
Shoreline	LN	0.03	242	0.09	1.16	1.62	1.00
Shoreline	LN	0.13	242	0.11	1.16	1.61	1.01

11.2.6 Equivalent Poisson Ratios for Regional Faults

For purposes of applying EPRs, regional faults are categorized as SAF sources and non-SAF sources. The SAF is treated separately because of its high slip rate and relatively short average recurrence interval. Non-SAF faults are different because recurrence rates are lower, which reduces their hazard significance, the time since their most recent events vary from fault to fault, and in general little is known about dates of their MREs.

The SAF case requires some adapting of the EPR methodology because it has a known *tMRE*, the January 1857 Fort Tejon earthquake. This rupture extended from north of Parkfield southeast for 330–350 km, with an average displacement of 4.45 m (Biasi, Weldon, and Dawson, 2013). Biasi (2013) reports an LTM recurrence interval of 114.7

years, with a 95% range from 64.1 to 205.1 years using the paleoseismic record from the Carrizo segment at Bidart Fan (Akçiz et al., 2010).

Having a known *tMRE* changes the EPR formulation for *tMRE* from $tMRE > T_{min}$ to $tMRE = T_0$, an equality constraint with a single value. Thus, instead of developing weights for the whole range $tMRE > T_{min}$, the weighting considers a single vertical column on Figure 11-6. Numerically, the weighting becomes the conditional distribution of LTM given $tMRE = T_0$. Uncertainty in the SAF EPR estimate is explored using three candidate DPE models and the lognormal recurrence model (Figure 11-10). Model SAF1 reflects likely displacements if average recurrence is in the range of 100–165 years, with some lesser probabilities outside that range. This model is arguably most consistent with paleoseismic observations. Model SAF2 is an extreme case for the SAF, emphasizing the smallest range of displacements. Model SAF3 gives no preference to average DPEs from 1 to 5 m, in effect picking up the extreme parts of SAF1 and SAF2 in one model. Weighted-mean EPRs for SAF1, SAF2, and SAF3 and the lognormal model are 1.34, 1.11, and 1.19, respectively. Corresponding values for the BPT and Weibull models are given in Table 11-3. EPR estimates are similar between the three recurrence PDFs, with the Weibull model a few percent higher for all cases. Lower EPR values for DPE models SAF2 and SAF3 are caused by including significant weight in their low displacement ranges. Among the three DPE models, SAF1 was considered most realistic, and used for the SAF EPR calculation. Weighted mean EPR values for model SAF1 from the three recurrence models were averaged to obtain net EPR estimate of 1.35 (Table 11-3).

For non-SAF regional fault sources we do not apply an EPR. First, the SAF is unique among faults in the DCPP region in terms of its slip rate and potential to host frequent large events. The *tMRE* of the SAF is at or beyond its nominal recurrence interval, so an EPR reflecting time dependence is consistent with the particular knowledge we have about the fault. A similar level of knowledge is not available for the non-SAF regional faults. In addition, hazard sensitivity results find that these faults are not hazard significant to the DCPP at the ground motions of interest (Wooddell, 2011, presentation at Workshop 1; *Chapter 14*). As a result, EPRs are not applied for other regional faults.

Table 11-3. San Andreas Fault Equivalent Poisson Individual Estimates

Recurrence PDF	DPE	8.5% EPR	50% EPR	91.5% EPR	Weighted Mean EPR
Lognormal	SAF1	0.99	1.42	1.52	1.34
Lognormal	SAF2	0.57	1.20	1.47	1.11
Lognormal	SAF3	0.57	1.33	1.51	1.19
BPT	SAF1	1.05	1.37	1.46	1.32
BPT	SAF2	0.66	1.21	1.42	1.12
BPT	SAF3	0.66	1.31	1.46	1.19
WBL	SAF1	1.18	1.41	1.55	1.39
WBL	SAF2	0.58	1.44	1.55	1.26

Recurrence PDF	DPE	8.5% EPR	50% EPR	91.5% EPR	Weighted Mean EPR
WBL	SAF3	0.58	1.39	1.55	1.23
Lognormal	SAF 1,2,3	0.71	1.32	1.50	1.21
BPT	SAF 1,2,3	0.79	1.30	1.45	1.21
WBL	SAF 1,2,3	0.78	1.42	1.55	1.29
Net SAF EPR	SAF1	1.07	1.40	1.51	1.35

11.2.7 Other Processes Affecting Recurrence

For the SSC model, other processes were considered that could affect the likelihood of an earthquake in the DCPP region. Stress transfer between ruptures sometimes seems to affect the timing of events elsewhere. In practice current understanding of whether or how it affects rupture probabilities is incomplete. Stress communication from the 1992 Landers rupture is considered likely to have triggered the 1999 Hector Mine event (Pollitz and Sacks, 2002). Given the very long recurrence intervals on the faults involved, it is improbable that the two earthquakes were only coincidentally close in time. Another potentially similar sequence occurred in the central Nevada seismic belt, involving multiple earthquakes separated over four decades from 1915 to 1954 (Bell et al., 2004). In both of these examples, the first earthquake can be recognized (in hindsight) as part of a linked sequence. In the DCPP region the only significant recent rupture was the 2003 San Simeon event. Mechanically, this rupture could affect the Oceanic-West Huasna fault system, but whether or how it could affect Primary faults in or adjacent to the SLPB is not known. Since explicit EPRs have been constructed for the Primary and Connected faults to reflect their time dependence, we have not attempted further adjustments for stress communication processes. In the event of a rupture on a more proximal fault, such as the reach of the Hosgri fault north of Estero Bay, reconsidering stress communication is recommended.

A more difficult case to evaluate is the possibility that current seismicity in Central California is artificially low because of a stress shadow from the SAF events in 1857 and 1906 (Harris and Simpson, 1996; Felzer and Brodsky, 2005). Comparison of paleoseismic records on the southern SAF (Scharer et al., 2014; Biasi and Weldon, 2009) indicates that the 1857 event was larger than most known to occur on the fault. It is also clear that the current open interval along the southern SAF since 1857 is very unusual, given its history up to 1857. Regardless of how large regional events affect probabilities on other faults, the direct impact on hazard reduces to a relative time dependence. The TI Team considers the EPR estimates to capture epistemic uncertainty in time dependence for the hazard estimates from the Primary and Connected faults.

11.3 Logic Tree

The Time Dependency Model in the SSC applies to the recurrence of moderate to large earthquakes. EPRs are applied to the Primary and Connected fault sources and to the SAF source.

The exponential model plus the three time-dependent models are considered to represent the center, body, and range of earthquake recurrence distributions. Based on primary literature sources, the lognormal, Brownian Passage Time, and Weibull models together reasonably approximate the center and body of models used in California and internationally where long records of paleoseismic events are available (Fitzenz et al., 2010; Matthews et al., 2002; Ellsworth et al., 1999; Berryman et al., 2012; Biasi, 2013). There is no information in the SSC model on which to prefer any model over the others. Addressing the center first, when these three distributions are fit to long paleoseismic records, their shapes are very similar, and inferences from them do not materially differ. For intervals short compared to the long-term mean, the range property of these time-dependent distributions is supported the Weibull distribution. For small *CVs* in the range considered, the Weibull distribution increases most rapidly for short times after the most recent event, which can give rise to large conditional probability ratios. As the *CV* approaches 1.0, the Weibull distribution mathematically approaches the exponential model. Thus the Weibull spans the continuum from a time-dependent to a time-independent model. Extreme influences of the Weibull model on the EPR estimate are moderated by low weights on their corresponding CVs. For intervals long compared to the long-term mean, the range of recurrence behavior is supported in these three models by the fact that their asymptotes diverge from one another (Matthews et al., 2002). The BPT model settles asymptotically to the time-independent earthquake occurrence rate, the lognormal hazard declines below the time-independent rate, and the Weibull hazard increases without bound. None of these asymptotes control EPR estimates because the probability of a given time since the most recent event is effectively capped by their respective survivor functions. The use of the survivor function to weight the range of likely *tMRE* values strongly moderates the dependence of EPR estimates on the recurrence model functional form.

The Diablo Canyon SSC model applies the Time Dependency Model as a set of global parameters with different logic trees (different branch values and weights) for the Hosgri fault source group, SLPB fault source group (Figure 6-1), and SAF source (*Chapter 12*). The recommended logic tree values and weights are provided in Table 11-4. EPRs are considered to apply to the Hosgri fault as a whole instead of individual rupture sources that occupy the fault source. Therefore, EPR is considered a global parameter and is the first branch of the logic tree. Similarly, fault sources of the SLPB are considered to be part of a regional network such that EPRs apply to all rupture sources that occupy the fault sources, and EPR is characterized as the first branch of the logic tree.

Table 11-4. EPR Values for Hazard Calculation

Fault Source	EPR	Weight
Hosgri (H90, H85, H75)	1.9	0.25
	1.3	0.5
	0.3	0.25
Weighted Mean, Hosgri:	1.2	
SLPBs (OV, SW, and NE)	1.6	0.25
	1.1	0.5
	0.3	0.25
Weighted Mean, SLPBs:	1.0	
San Andreas fault zone (SAF)	1.5	0.25
	1.4	0.50
	1.1	0.25
Weighted Mean, SAF:	1.35	

11.3.1 Poisson or Non-Poisson Earthquake Distributions

In the SSC model logic tree, the distinction between Poisson versus non-Poisson temporal distributions is captured in the range of the EPR estimates. An EPR weighted-mean value of 1.0 corresponds to the Poisson hazard rate. For the Hosgri fault, the weighted mean is greater than 1.0, commensurate with the probabilistic consequences of the historical constraint on $T_{\min}$. The range of EPR values considered in the logic tree encompasses the Poisson hazard rate (Table 11-4). Therefore, even though the SSC logic tree does not include a branch for a Poisson model for recurrence (i.e., Figure 6-1), the uncertainty in the Time Dependency Model encompasses time independent, Poisson behavior.

11.3.2 Equivalent Poisson Ratios for Logic Tree Application

The evaluation of alternative models for time-dependent earthquake recurrence represents the best approach to evaluating non-Poisson recurrence behavior that the TI Team is aware of. Individual results from these analyses are shown in Tables 11-1, 11-2, and 11-3. However, it is acknowledged that other factors could contribute to earthquake recurrence beside those that are accounted for in the renewal models. Recognizing that the EPRs developed in this chapter are only approximately modeling uncertainty in recurrence behavior, the TI Team selected the EPR values in Table 11-4 to be representative of the means and ranges in Tables 11-1, 11-2, and 11-3 based on inspection and judgment instead of resorting to a more elaborate system of weighted sums. Each case is discussed below. For each, the mean and branch values consider the three recurrence models equally. For the Hosgri and SLPB fault cases, the longer time of 242 years since the most recent large event is emphasized.

For the Hosgri fault EPR logic tree, the weighted mean of 1.2 is used to approximately represent the more precise weighted mean values in Table 11-1. The Hosgri fault source logic tree branches are assigned values of 0.3, 1.3, and 1.9, with weights of [0.25], [0.5], and [0.25], respectively, likewise to represent the range of estimates in Table 11-1. The TI Team recognizes that the high branch value of 1.9 exceeds the 91.5% probability value for all but two cases in Table 11-1, but the TI Team judged that this high value provided some additional (though slight) margin for recurrence behavior uncertainty not captured in the recurrence models. These values apply equally across Hosgri dip uncertainty cases, and for all rupture source slip rate branch combinations. Although the EPR results do correlate with slip rate (Table 11-1), the TI Team judged that additional complexity in the SSC model to introduce a correlation between EPR values and rupture source slip rates was not worth the resulting slight difference in model uncertainty.

Estimates for SLPB faults average slightly greater than 1.0 in lognormal and BPT estimates, and very near 1.0 for the Weibull cases (Table 11-2). The TI Team judged that the variability in the EPR results was small for the range of slip rates evaluated, so a single logic tree could be applied to all SLPB rupture sources. Logic tree branch values of 0.3, 1.1, and 1.6 are assigned, with weights of [0.25], [0.5], and [0.25], respectively (Table 11-4). The weighted-mean EPR is 1.0, which is equivalent to Poisson recurrence behavior.

The SAF EPR is unique in that all three points in its summary distribution are greater than 1.0 (values of 1.1, 1.4, and 1.5, at weights of 0.25, 0.50, and 0.25, respectively; Table 11-4). The EPR weighted mean of 1.35 and its individual values thus reflect the fact that the *tMRE* for the SAF is at or beyond its mean recurrence. The application of the SAF EPR in the SSC Model logic tree is discussed in *Section 12.4*.

11.4 Summary

The EPR method provides a framework within which to estimate relative time dependence on faults that lack sufficient data for a direct estimate. The use of EPRs improves the range of fault behavior that is modeled in the Diablo Canyon SSC. A side effect of including non-Poisson fault behavior as a new term in the SSC model is that seismic hazard from affected faults is increased by inclusion of the EPR. This result conforms to the expectation that hazard should be elevated if it has been a long time since the most recent earthquake on a hazard-significant fault.

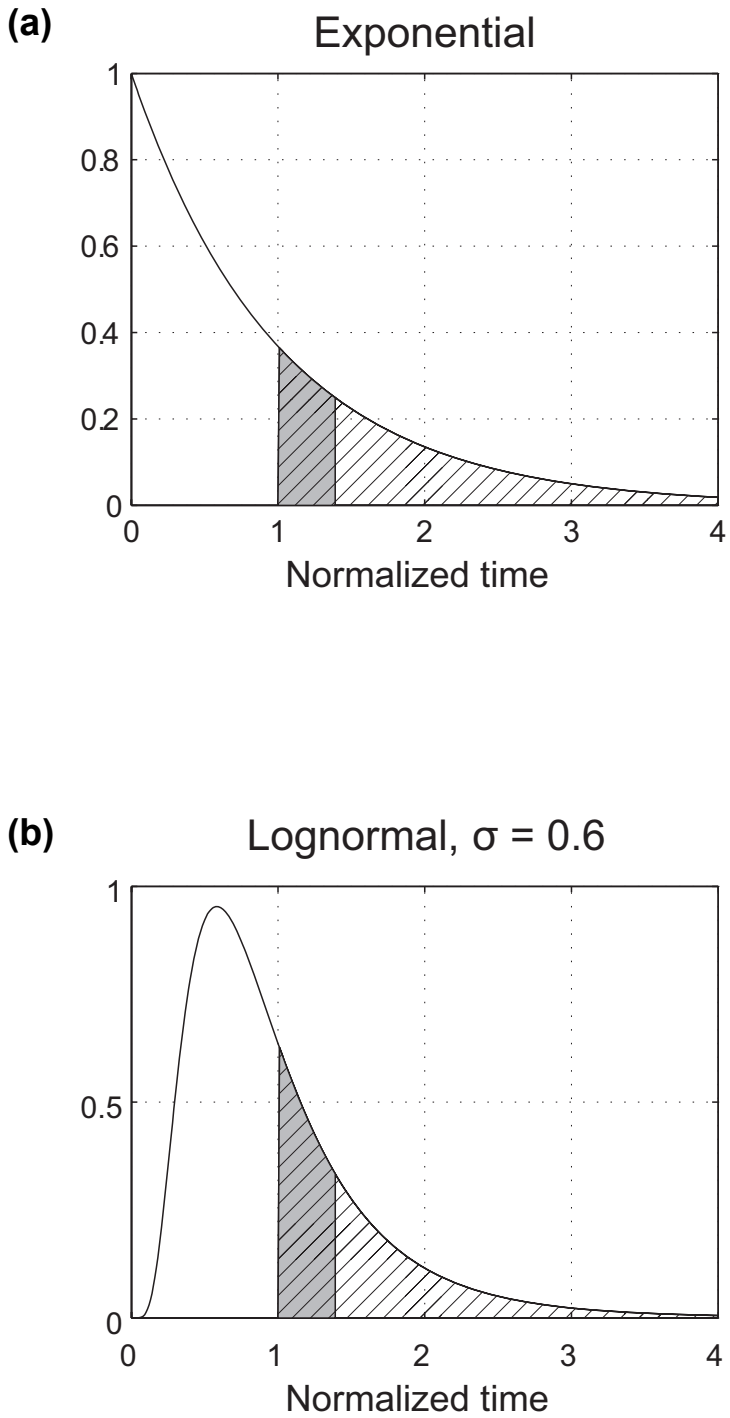

EXPLANATION

Area of forecast period

Total area

Conditional Probability Calculation Illustrated for Exponential and Lognormal Recurrence Probability Distributions with Equal Long-Term Mean Rates

DCPP SSC REPORT

Pacific Gas and Electric Company

Figure **11-1**

File path: /s/1005/005/Final_Report_Figures/Figure_1100_01.ai; Date: 02/23/2015; User: Alex Remar, LCI; Rev. 1

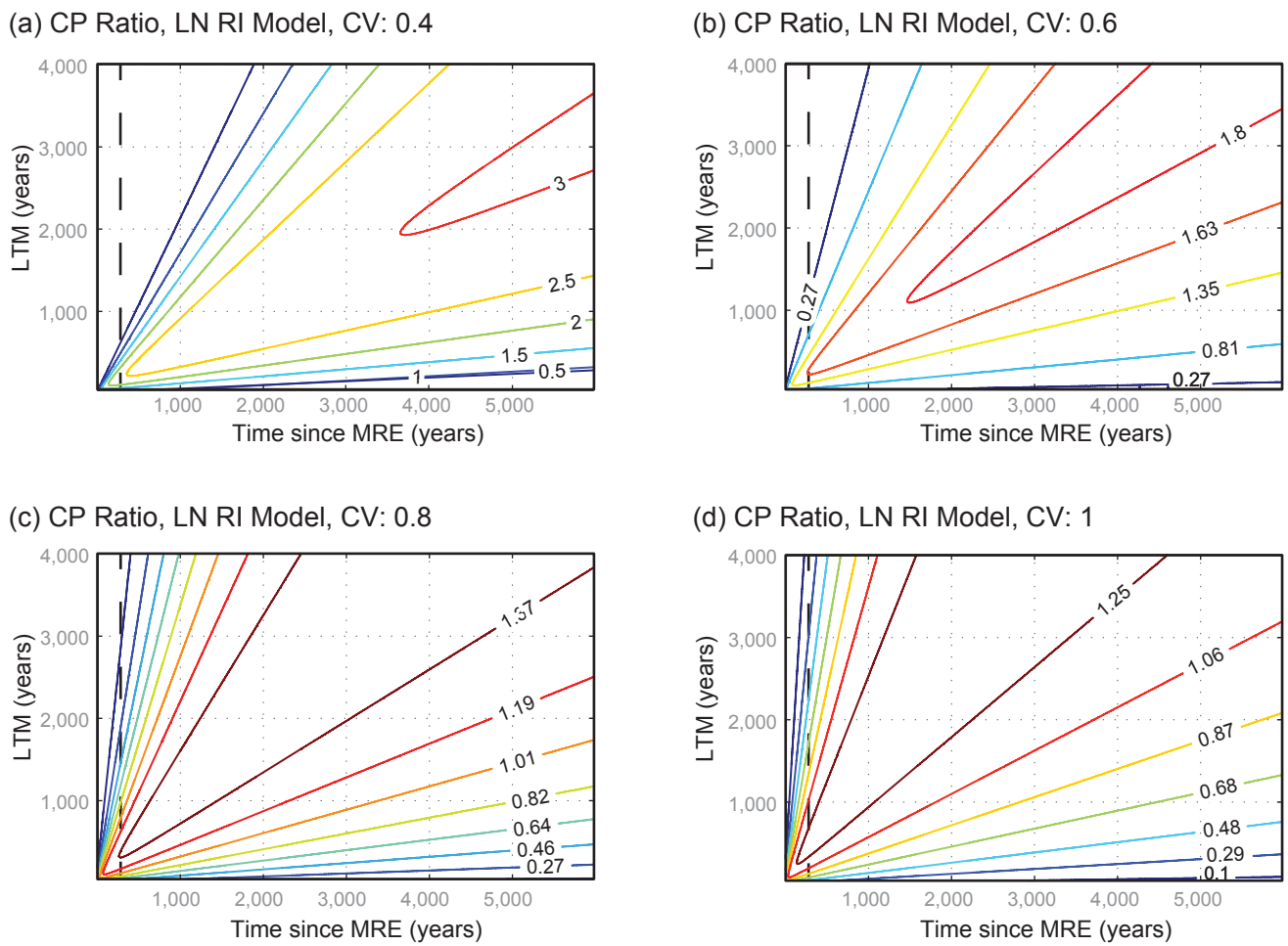

EXPLANATION

— — — tMRE = 242 years (founding of the Spanish mission at San Luis Obispo in 1772)

Note:
- Contours indicate conditional probability ratio for a given recurrence model PDF and coefficient of variation.
- The low conditional probability region to the left of the dashed line is excluded by the historical constraint T_{min} = 242 yr.

Conditional Probability Ratio of Lognormal to Exponential for Four Values of Coefficient of Variation

DCPP SSC REPORT

Pacific Gas and Electric Company

Figure **11-2**

File path: /s/1005/005/Final_Report_Figures/Figure_1100_02.ai; Date: 02/23/2015; User: Alex Remar, LCI; Rev. 1

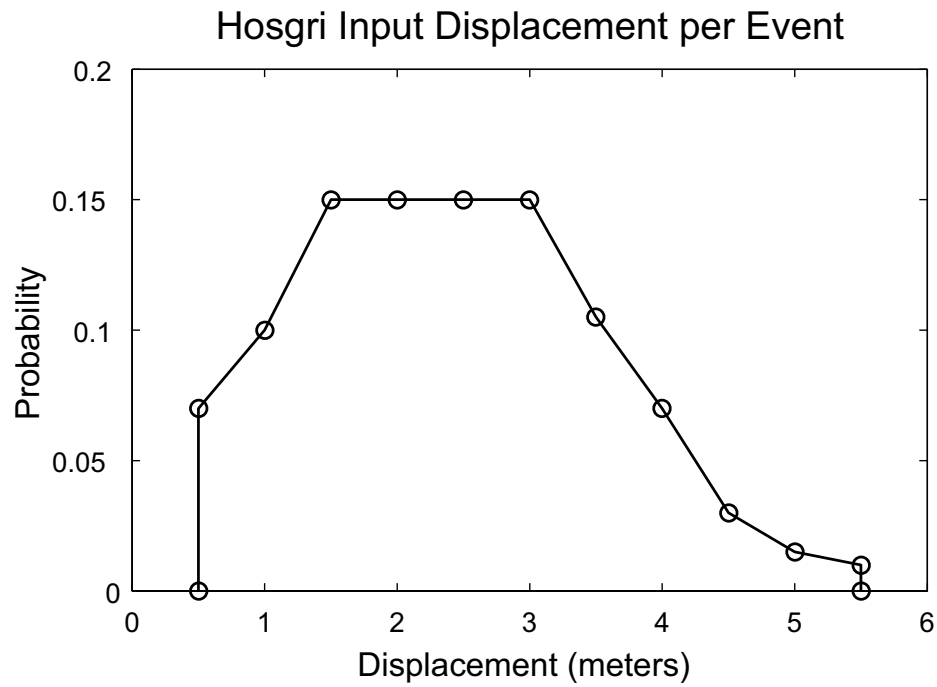

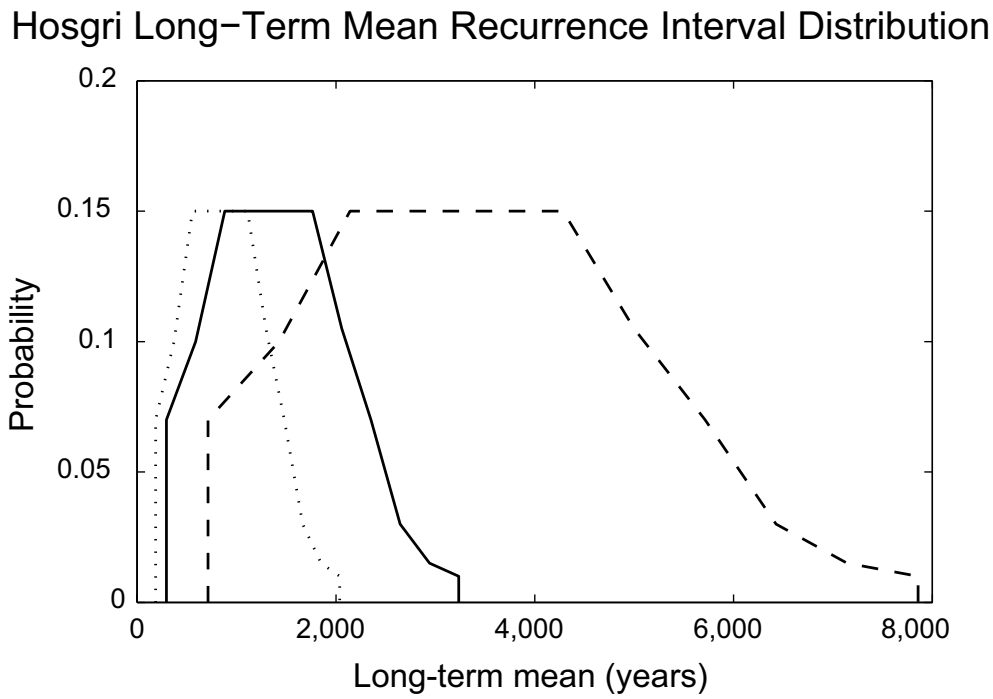

EXPLANATION

- 0.7 mm/yr
- 1.7 mm/yr
- 2.7 mm/yr

Displacement-per-Event Model Input for the Hosgri Fault and Calculated Long-Term Mean Rates for Three Slip Rates

DCPP SSC REPORT

Pacific Gas and Electric Company

Figure **11-3**

File path: /s/1005/005/Final_Report_Figures/Figure_1100_03.ai; Date: 03/11/2015; User: Brian Greer, LCI; Rev. 1

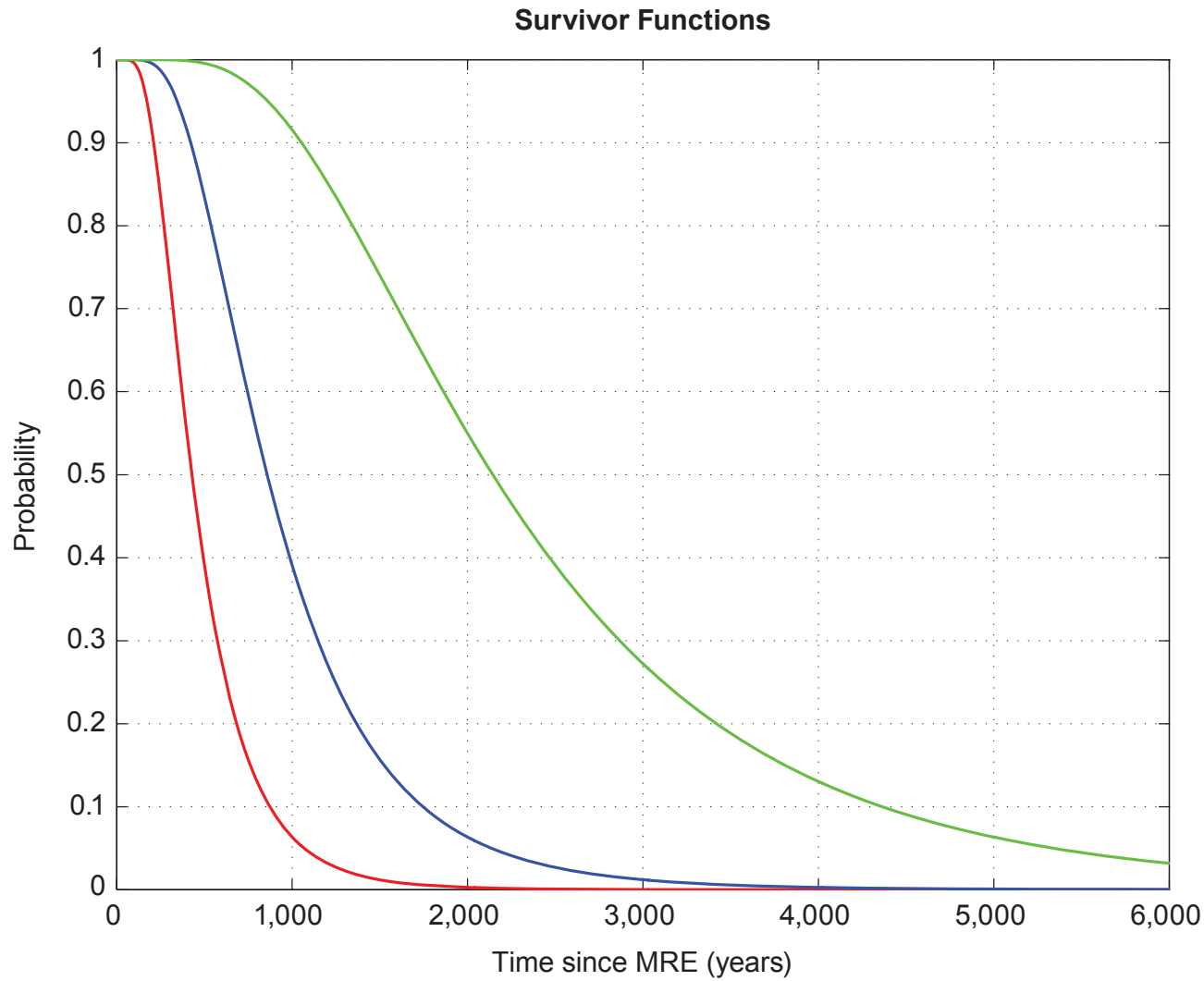

EXPLANATION

Long-Term Mean

- 500 yrs
- 1,000 yrs
- 2,500 yrs

Survivor Functions for a Lognormal CDF, CV = 0.6, and Three Values of Long-Term Mean

DCPP SSC REPORT

Pacific Gas and Electric Company

Figure **11-4**

File path: /s/1005/005/Final_Report_Figures/Figure_1100_04.ai; Date: 02/20/2015; User: Brian Greer, LCI; Rev. 1

(a) T_{min} = 0 yr

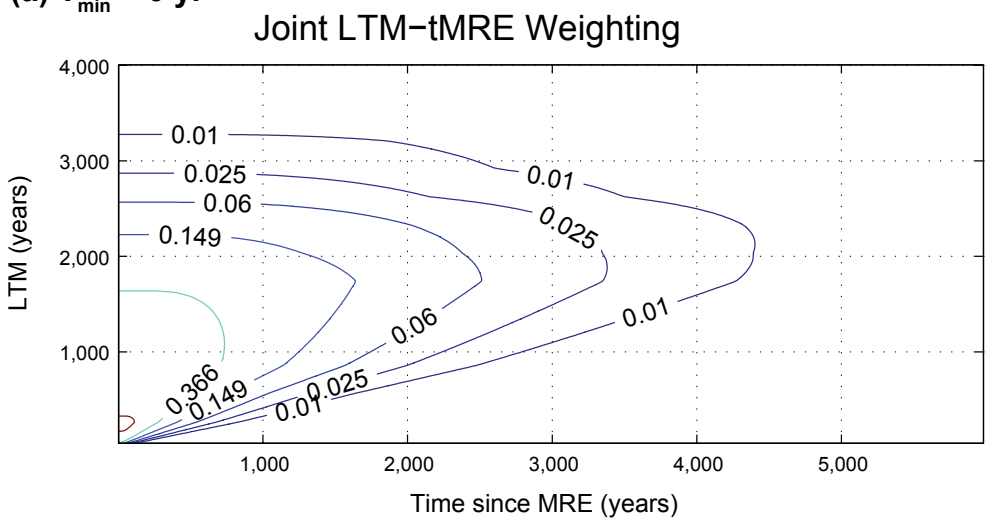

(b) T_{min} = 242 yr

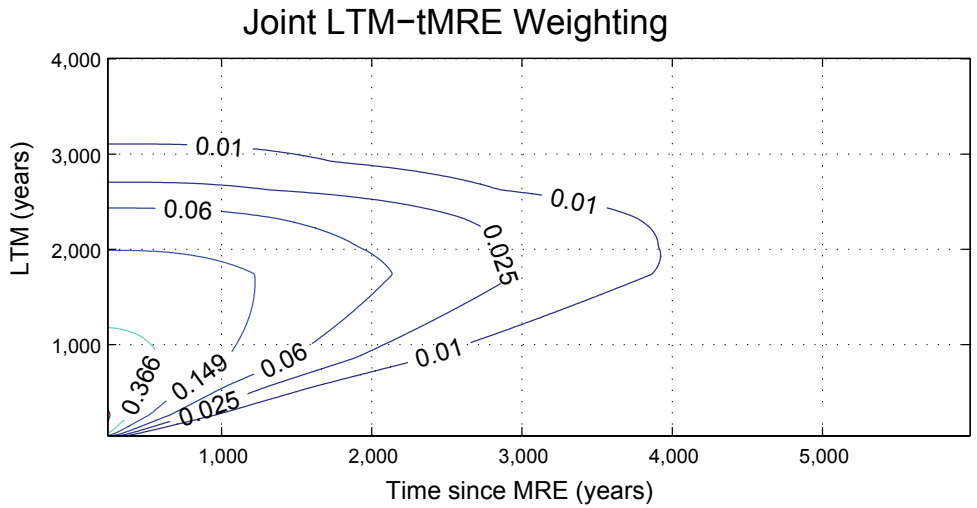

Notes:
- The probability of LTM is estimated from constraints of mean displacement per event and slip rate, as shown on Figure 11-3.
- Surface = Joint Probability of LTM and tMRE divided by its maximum value.

Relative Weighting of LTM and tMRE For Extracting Conditional Probability Ratios (Lognormal, CV = 0.6)

DCPP SSC REPORT

Pacific Gas and Electric Company

Figure **11-5**

File path: /s/1005/005/Final_Report_Figures/Figure_1100_05.ai; Date: 03/11/2015; User: Alex Remar, LCI; Rev. 1

(a) T_{min} = 0 yr

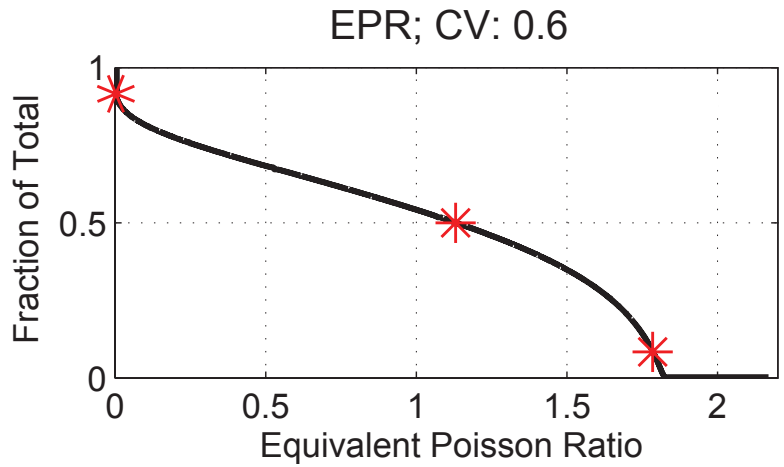

(b) T_{min} = 242 yr

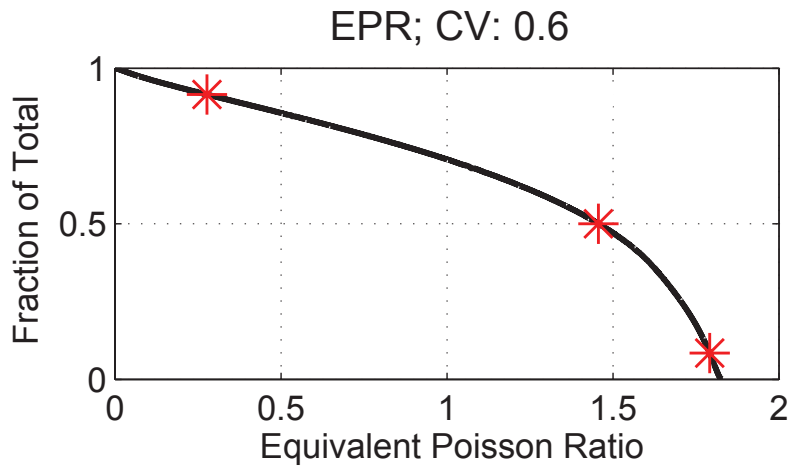

Note: Stars indicate 0.085, 0.50, and 0.915 distribution points for use with weights [0.25, 0.50, and 0.25], respectively.

Equivalent Poisson Ratio Complimentary Cumulative Distributions for Two Minimum Values of tMRE (Lognormal, CV=0.6)

DCPP SSC REPORT

Pacific Gas and Electric Company

Figure **11-6**

File path: /s/1005/005/Final_Report_Figures/Figure_1100_06.ai; Date: 02/23/2015; User: Alex Remar, LCI; Rev. 1

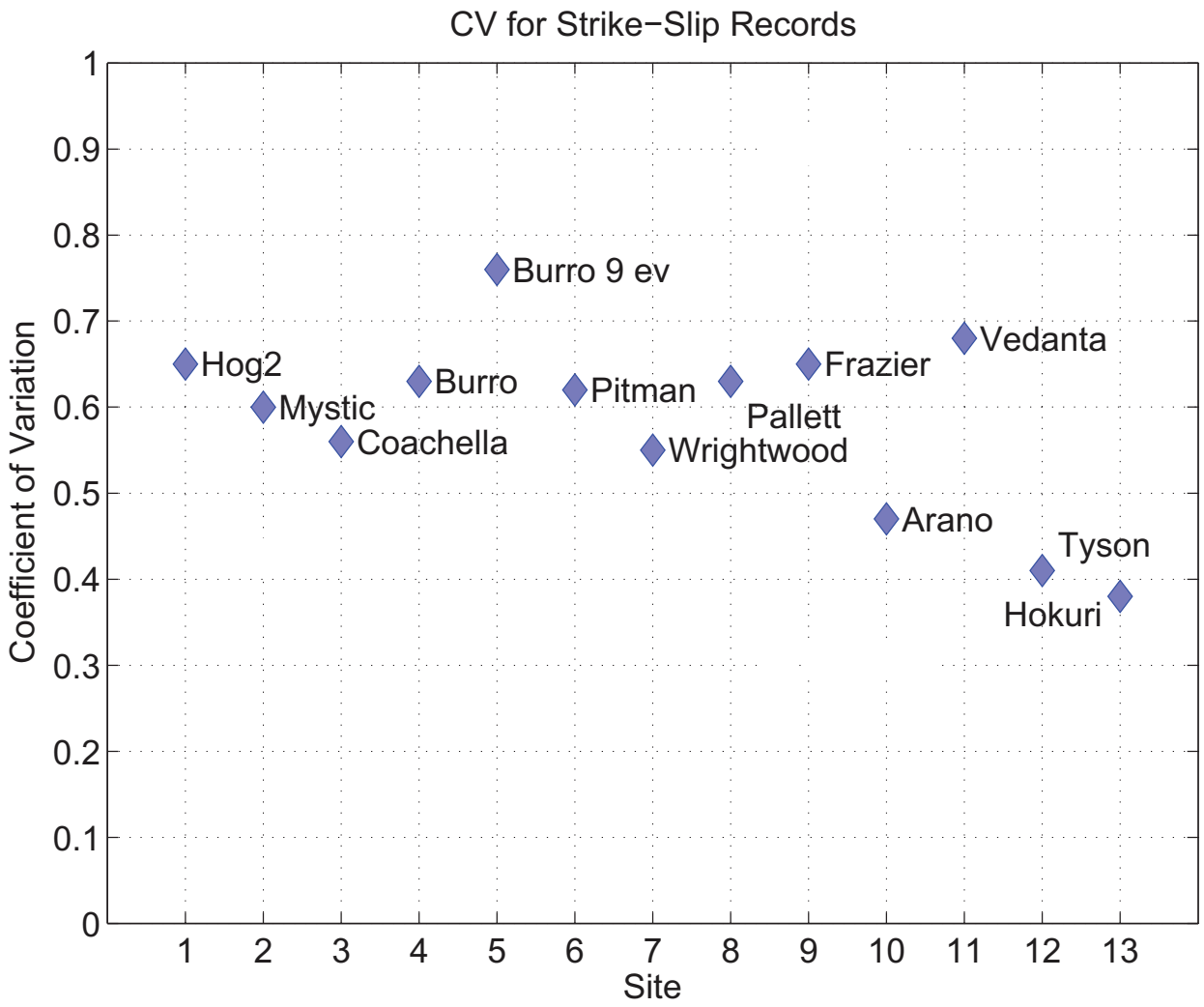

CV From Twelve Well-Studied Paleoseismic Sites on Strike-Slip Faults

DCPP SSC REPORT

Pacific Gas and Electric Company

Figure **11-7**

File path: /s/1005/005/Final_Report_Figures/Figure_1100_07.ai; Date: 02/23/2015; User: Alex Remar, LCI; Rev. 1

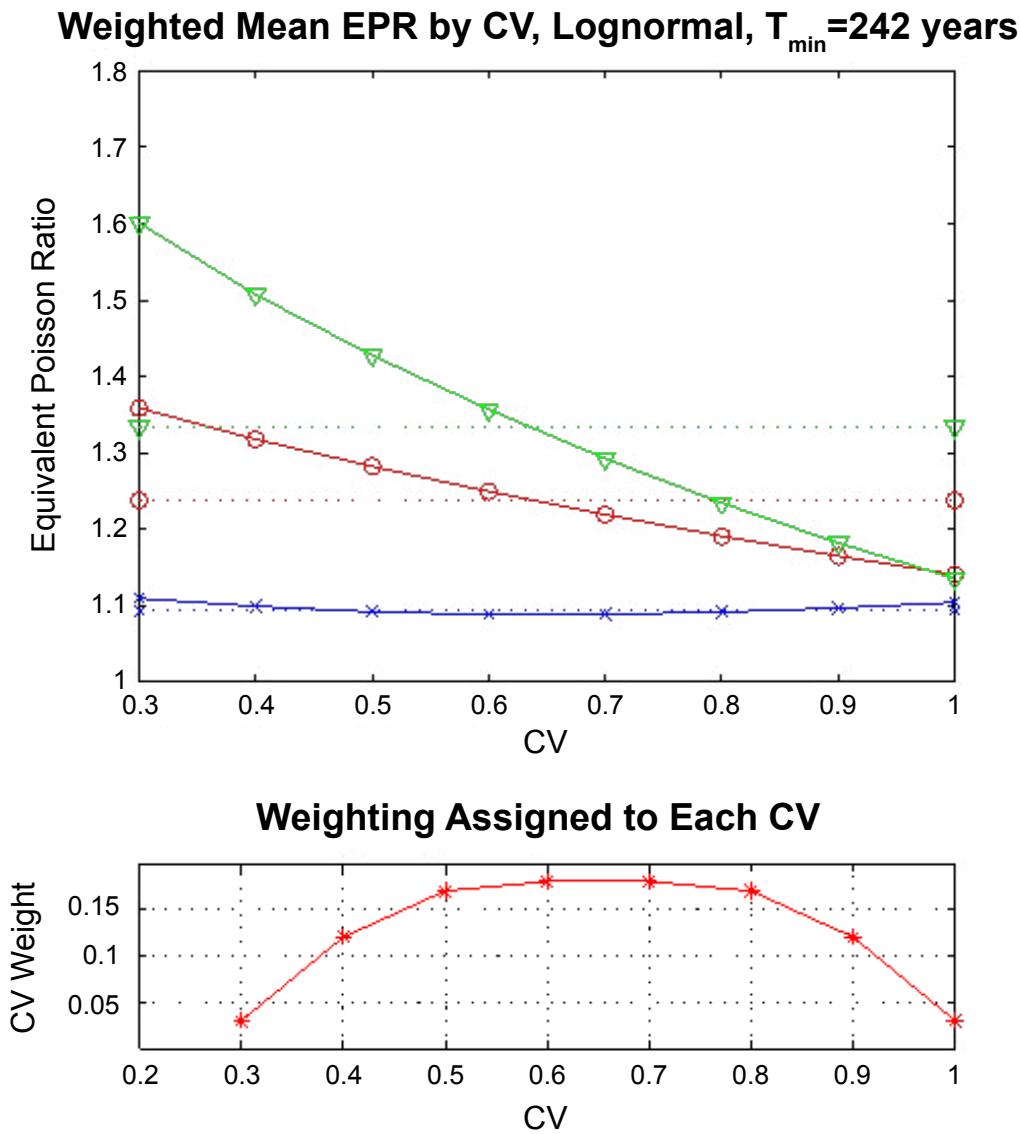

EXPLANATION

- 2.7 mm/yr
- 1.7 mm/yr
- 0.7 mm/yr

Mean EPR Estimates for a Range of CV Values (Solid Lines) and CV-Weighted Net EPR Estimates (Dotted) and the CV Weighting Function

DCPP SSC REPORT

Pacific Gas and Electric Company

Figure **11-8**

File path: /s/1005/005/Final_Report_Figures/Figure_1100_08.ai; Date: 02/23/2015; User: Alex Remar, LCI; Rev. 1

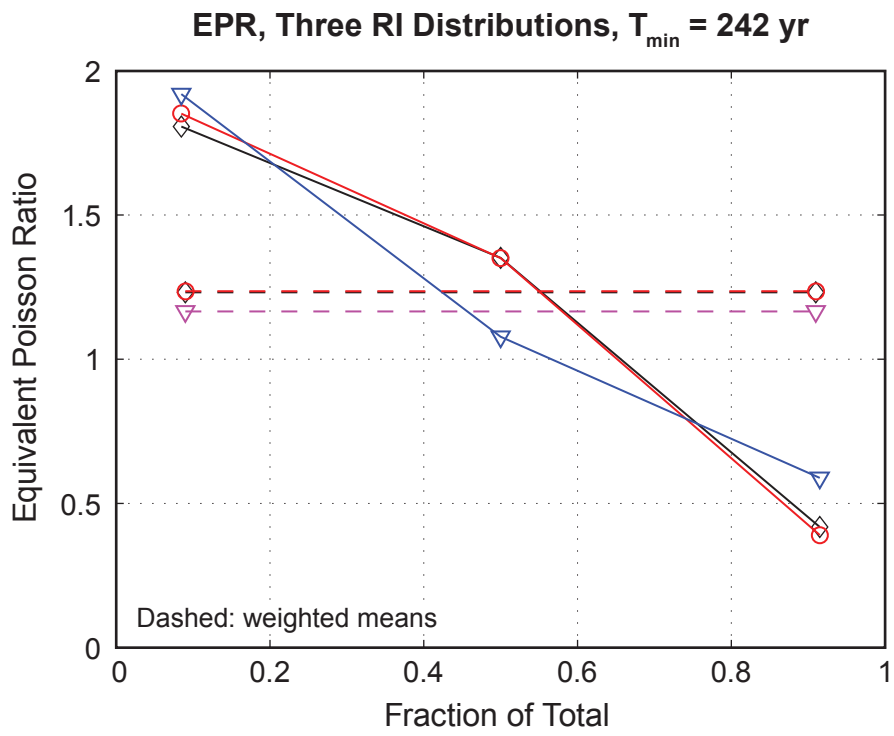

EXPLANATION

Recurrence Distribution

- Lognormal
- BPT
- Weibull

EPR Values for Three Recurrence Distribution Models, a Fault Slip Rate of 1.7 mm/yr, and T_{min} = 242 Yr

DCPP SSC REPORT

Pacific Gas and Electric Company

Figure **11-9**

File path: /s/1005/005/Final_Report_Figures/Figure_1100_09.ai; Date: 02/23/2015; User: Alex Remar, LCI; Rev. 1

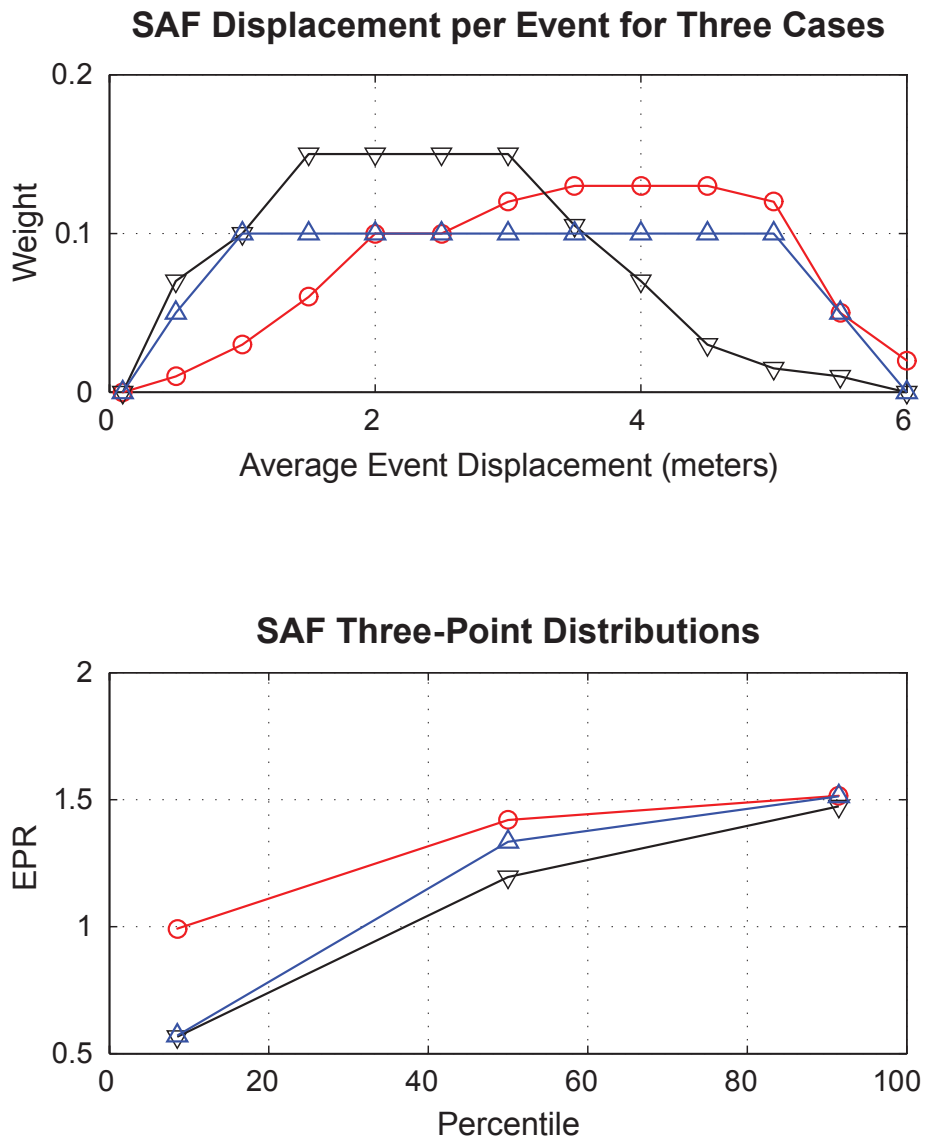

EXPLANATION

SAF1

SAF2

SAF3

San Andreas Fault EPR Values for Three Displacement-per-Event Cases and the Lognormal Recurrence Model

DCPP SSC REPORT

Pacific Gas and Electric Company

Figure **11-10**

File path: /s/1005/005/Final_Report_Figures/Figure_1100_10.ai; Date: 02/20/2015; User: Brian Greer, LCI; Rev. 1

12.0 REGIONAL FAULT SOURCES

Regional fault sources are model representations of active faults or fault systems in the 320 km (200 mi.) DCPP site region, exclusive of Primary and Connected fault sources that are considered capable of producing earthquakes and that are sufficiently active and well defined such that they may be characterized in the Diablo Canyon seismic source characterization (SSC) model. The DCPP site region includes many tens of active faults. This list includes approximately 610 km of the San Andreas fault, portions of the San Francisco Bay Area fault system, much of the Garlock fault bounding the northern Mojave region, and portions of Owens Valley fault east of the southern Sierra Nevada (Figure 12-1). Preliminary sensitivity studies showed that the contribution of Regional fault sources to hazard at the DCPP was less than a few percent (*Appendix D, Attachment D-1*). Results of sensitivity studies using the final Diablo Canyon SSC model confirmed these preliminary results (*Section 14.2.1*). Faults capable of producing moderate to large earthquakes that are not included as Regional fault sources are represented by the areal source zones (*Chapter 13*).

12.1 Definition and Applicability

Regional fault sources are distinguished from Primary and Connected fault sources in the SSC model in that the latter have been the objects of particular study in the SSC project because of their significant contribution to hazard.

Regional fault sources included in the Diablo Canyon SSC model are divided into three subsets:

1. The San Andreas fault source (SAF; Figure 12-2).
2. UCERF3 Regional fault sources (Figure 12-3).
3. Non-UCERF3 Regional fault sources (Figure 12-4).

The general approaches used to model activity on these subsets differ, as described in *Sections 12.2 and 12.3* below. More specific discussions of the SSC model for these sources are presented in *Sections 12.4, 12.5, and 12.6*, respectively.

12.2 Approach

The Uniform California Earthquake Rupture Forecast 3 (UCERF3) project (Field et al., 2013) developed a statewide earthquake rupture forecast for California. The UCERF3 approach uses an inversion-based methodology that incorporates fault slip rates regional geodetic and seismic data, and paleoseismic constraints. UCERF3 expanded on earlier rupture forecasts by relaxing *a priori* fault segmentation and including fault-to-fault ruptures. UCERF3 ruptures are formed by discretizing faults into subsections a few km in strike length, then combining subsections, subject to geometric compatibility rules, to approximate all possible ruptures on active California faults. UCERF3 fault definitions and rupture rates are considered by the U.S. Geological Survey (USGS) to be the best available for estimating regional fault hazard (Petersen et al., 2014). Because UCERF3 is

the best available regional fault hazard estimate and because regional sources do not control DCPP hazard, UCERF3 regional source rupture rates are adopted as Diablo Canyon SSC model Regional fault sources.

UCERF3 rupture rates and magnitudes are not adopted for Primary and Connected faults in the DCPP area, as discussed in *Section 6.3.3.2*. UCERF3 rupture rate estimates are fit to the statewide data and fault systems using global misfit criteria. The use of global misfit minimization means that the fit in some specific area, such as near the DCPP, could be compromised in order to achieve a lower overall misfit. Also, UCERF3 discretizes faults at a scale that is adequate for regional hazard, but is too large for detailed seismic source characterization. Subsections used to discretize faults extend to the base of the seismogenic zone, and half that in strike length, typically into planes of approximately 7 km by 14 km. The SSC model for the Primary and Connected faults must account for uncertainties in slip rate, dip and fault orientation not considered in UCERF3. UCERF3 rupture rates are used as an independent comparison to slip rate and magnitude-frequency distributions used for the rupture sources (*Chapters 8 and 10*).

The overall methodology used to implement the statewide UCERF3 model for characterization of the SAF and other Regional fault sources is outlined in *Section 12.3*. The TI Team judged the UCERF3 model to be incomplete for offshore fault sources in the DCPP site region west of the Hosgri fault, so additional fault sources were characterized using evaluations of available publications and information. The characterization of the non-UCERF3 Regional fault sources is described in *Section 12.6.2*.

The SAF and other UCERF3 Regional fault sources (discussed in *Sections 12.4 and 12.5*, respectively) are included separately to allow their effects to be tracked in the hazard calculations. Both source sets are direct subsets of the UCERF3 rupture rate solution.

UCERF3 rupture rates for each source set are considered by the TI Team to represent the time-independent hazard rates. Because the length of the open interval on the SAF closest to the DCPP is known from the 1857 Fort Tejon earthquake, the equivalent Poisson ratio (EPR) for the SAF source is adapted to use this information (see also *Appendix H* and *Chapter 11*).

12.3 Methodology to Implement the UCERF3 Statewide Model for the Diablo Canyon SSC Model

UCERF3 represents active faults in California with two fault models: FM3.1 and FM3.2. The fault models were given equal weight by the Working Group on California Earthquake Probabilities in the UCERF3 logic tree (Field et al., 2013, Figure 3). FM3.1 consists of 2,606 subsections and 253,706 ruptures, and FM3.2 consists of 2,664 subsections and 305,709 ruptures. FM3.2 has more ruptures primarily because it allows greater connectivity to the San Andreas fault in the southern Imperial Valley. Figure 12-5 shows ruptures from FM3.1 and ruptures unique to each fault model. Fault slip rates and net moment rate are the same for both models. Most of the fault representation is also identical for both the models. UCERF3 mean branch solutions are considered, accessible in zip files as follows:

- Fault Model 3.1: http://opensha.usc.edu/ftp/kmilner/ucerf3/2013_05_10-ucerf3p3-production-10runs/2013_05_10-ucerf3p3-production-10runs_COMPOUND_SOL_FM3_1_MEAN_BRANCH_AVG_SOL.zip.
- Fault Model 3.2: http://opensha.usc.edu/ftp/kmilner/ucerf3/2013_05_10-ucerf3p3-production-10runs/2013_05_10-ucerf3p3-production-10runs_COMPOUND_SOL_FM3_2_MEAN_BRANCH_AVG_SOL.zip.

FM3.1 and FM3.2 differ in the project area in how faults are represented south of the Irish Hills and beneath San Luis Obispo Bay (Figure 12-6; see also Field et al., 2013, and appendices). FM3.2 includes the San Luis Bay fault source with an extent comparable to the SSC model, while FM3.1 does not. In addition, FM3.2 includes three more subsections (and ~35 km) in its representation of the south margin of the San Luis Range fault, and a slightly higher fault slip rate on the East Huasna fault. FM3.1 uniquely includes a three-subsection fault called the San Luis Range–Oceano fault to represent reverse-mechanism structures on the southern San Luis Range and east of San Luis Obispo Bay. Because the differences in fault models are confined to the Diablo Canyon site vicinity where these fault sources are defined in the Fault Geometry Models (*Chapters 6 and 7*), the Regional fault sources in FM3.1 and FM3.2 are represented as indistinguishable in hazard. As a result FM3.1 has been used to develop the Regional fault source set.

The UCERF3 solution includes ruptures beyond the 320 km radius of interest for the DCPP. Before proceeding with the characterization of the San Andreas and Regional source subsets for this study, ruptures were removed from the UCERF3 solution if every part of the rupture was farther than 320 km from the DCPP. Distance is calculated from the DCPP to the nearest latitude-longitude point of any subsection included in the rupture.

The location and geometry for the San Andreas and UCERF3 Regional fault sources are taken to be the location and geometry of the nearest subsection in the UCERF3 rupture to the DCPP. Each subsection has an associated average dip, dip direction, and rake. These are converted to strike, dip, and rake in the input files provided as ASCII files for inclusion in the SSC logic tree (*Appendix C*).

12.4 San Andreas Fault Source

The SAF has the largest and highest slip rate of the faults in the DCPP site region. At its nearest point, the SAF is approximately 77 km to the northeast of the DCPP (Figure 12-3).

UCERF3 ruptures were considered part of the SAF rupture set if the rupture involves any part of the SAF within 320 km of the DCPP. Most of these ruptures are entirely on the SAF. However, in UCERF3, ruptures can jump from one fault to another if the faults are near each another and meet certain compatibility criteria. As a result, some sources that are counted as SAF ruptures have some component of slip on other faults, including some that extend south and west of the SAF. The ruptures closest to the DCPP in the SAF rupture set branch onto the San Juan fault and come as near as 65 km from the DCPP. The San Juan fault in UCERF3 is a vertical strike-slip fault with 0.48 mm/yr slip rate, a factor of 60 less than the SAF in the southern Coast Ranges. Thus the TI team concluded

that the inclusion of SAF ruptures branching onto other faults closer to the DCPP than the SAF itself will have a negligible effect on the resulting hazard.

Approximately 149,000 ruptures in the UCERF3 solution occupy some part on the San Andreas fault within the DCPP site region. Of this total, approximately 86,000 ruptures in FM3.1 have the same closest point on the San Andreas fault at Cholame subsection #8 (Figure 12-7). Most ruptures through this subsection are long, with very small annual rates of occurrence. Although their individual rates are small, the high number of ruptures means that the net rate of occurrence at any given magnitude is significant.

In order to simplify the SAF rupture set, the individual rates on Cholame subsection #8 are summed to a single net rate according to 0.1-magnitude increments (blue line, Figure 12-7). For example, all rupture rates for $7.5 \leq \mathbf{M} < 7.6$ are summed to a single annual rate of **M** 7.55. This method allows us to replace 85,974 FM3.1 ruptures with 22 magnitude-rate points, and it reduces the computational requirements for the SAF by 58%. The rupture set can be summarized because hazard is calculated using the nearest distance of a rupture to the DCPP, without reference to the rupture length or end points. Figure 12-7 includes two prominent linear trends at magnitudes $6.6<M<7.3$. These trends are a consequence of how ruptures are created in UCERF3 and of where subsection Cholame #8 is on the San Andreas fault. The linear trends themselves reflect a declining probability of individual ruptures as subsections are added to make new, unique, longer SAF ruptures. There are two parallel trends to distinguish ruptures added to the north versus ruptures of increasing length to the south. Ruptures that increase in length to the north must pass through the Parkfield and creeping sections of the fault (Figure 12-2). These sections have reduced slip rates available for earthquake generation because of creep and prescribed aseismicity factors. As a result, ruptures involving these subsections have about an order of magnitude lower probability than ruptures extending a similar length to the south. All SAF ruptures not summarized on Figure 12-7 are included in the Regional fault source model individually. No rupture in the UCERF3 solution is neglected or omitted in this approach.

SAF rates from UCERF3 are time-independent long-term rates. Following the approach outlined in *Section 11.2*, a time-dependent EPR is estimated for the SAF based on a most recent fault-resetting event in 1857. The SSC logic tree weighted mean and three-point distribution estimate of the EPR, presented in *Section 11.3*, are shown in Table 12-1.

Table 12-1. Equivalent Poisson Rate Estimated for the San Andreas Fault Source

Fault Source	EPR	Weight
San Andreas Fault (SAF)	1.5	0.25
	1.4	0.50
	1.1	0.25
Weighted Mean, SAF	1.35	--

12.5 UCERF3 Regional Fault Sources

Direct use the set of UCERF3 ruptures within the 320 km DCPP site region would double-count ruptures and slip rate from the Primary and Connected fault sources in the Fault Geometry, Fault Slip Rate, and Rupture Models presented in *Chapters 7, 8, and 9*. To adapt the UCERF3 solution, ruptures are removed if they involve any part of the south Hosgri Extension, Shoreline, Los Osos, and San Luis Range–Pecho FM3.1 fault sections (Table 12-2).

Table 12-2. UCERF3, FM 3.1 Fault Sections Whose Ruptures Were Completely Removed From the UCERF3 Solution and Equivalent Primary or Connected Fault Source Used Instead

Fault Section Name	Equivalent Primary or Connected Fault
Hosgri (Extension)	Hosgri
Shoreline	Shoreline
Los Osos 2011	Los Osos
San Luis Range—Oceano 2011 CFM	Oceano
San Luis Range—Pecho 2011 CFM	None

The method of removing whole fault sections could not be applied to the San Luis Range fault or northern portions of the Hosgri fault source (Table 12-3). In the UCERF3 model, the San Luis Range fault is a simplified source that represents multiple faults within the Southwestern Boundary zone as defined by PG&E (1988) and Lettis et al. (1994). Ruptures on the eastern portion of the San Luis Range fault that are southeast of the intersection with the Oceanic–West Huasna fault are part of the UCERF3 Regional fault source. Ruptures involving the western part of the San Luis Range—northwest of the intersection with the Oceanic–West Huasna fault—are covered in the SLBP Fault Geometry and Rupture Models; therefore, these ruptures are removed from the UCERF3 rupture set. The intersection of the San Luis Range and Oceanic–West Huasna faults is shown on Figure 12-6. The local source slip rate and magnitude-frequency distribution account for the full estimated slip rate of the fault, so full ruptures on the San Luis Range fault are included and accounted for at the intended source-to-site distance.

Table 12-3. UCERF3, FM 3.1 Fault Sections Whose Ruptures Were Partially Removed from the UCERF3 Solution and Equivalent Primary or Connected Fault Source Used Instead

Fault Section Name	Subsections Removed	Equivalent Primary or Connected Fault
Hosgri	South of 35.7° latitude	Hosgri and San Simeon fault south of the intersection with the Oceanic–West Huasna fault source
San Luis Range 2011 CFM	North of 34.92° latitude	Wilmar Ave, Nipomo, and Foxen Canyon faults north of the intersection with the Oceanic–West Huasna fault source

The Hosgri fault ruptures are also divided between the UCERF3 Regional fault source and Primary and Connected sources. UCERF3 ruptures on the Hosgri fault that end at or continue down the Oceanic–West Huasna fault are considered Regional fault sources. Ruptures that include any part of the Hosgri fault south of the Oceanic–West Huasna intersection, including ruptures that pass by the DCPP, are considered part of the Hosgri fault source and are removed from the UCERF3 rupture set, regardless of where they stop to the north. From a ground-motion hazard perspective, all ruptures, including the largest ruptures that continue north to the Mendocino Triple Junction, are included and accounted for at the appropriate source-to-site distance. Only when the full extent of the rupture is north of the Oceanic–West Huasna fault intersection (coinciding with the northern end of fault section SI; Figure 6-6 and Table 6-5) does a Hosgri–San Simeon–San Gregorio fault system rupture become part of the UCERF3 Regional fault source model.

The UCERF3 Regional fault source rupture set, including all San Andreas sources, contains 216,000 ruptures. The 320 km distance cutoff and exclusions for local faults around the DCPP remove only approximately 15% of ruptures from the UCERF3 model. After summarizing SAF ruptures as shown on Figure 12-7, the SAF and UCERF3 Regional fault sources total 63,504 and 67,354 ruptures, respectively. As mentioned in Section 12.3, the ruptures are provided as ASCII files for inclusion in the SSC logic tree (*Appendix C*).

12.6 Non-UCERF3 Regional Fault Sources

Five offshore Regional fault sources, which are not included in the UCERF3 model, are included in the Diablo Canyon SSC logic tree. These fault sources are shown on Figure 12-4 and listed in Table 12-4. Brief descriptions of these faults are provided in *Section 12.6.1*. A summary of the characterization parameters used in the Diablo Canyon SSC model is given in *Section 12.6.2*.

Table 12-4. Non-UCERF3 Regional Fault Sources in the Diablo Canyon SSC Logic Tree

Fault Source Name	Closest Distance to the DCPP	Primary Sources of Information
Lompoc Structure	36 km	Clark et al. (1991); Willingham et al. (2013)
Purisima Structure	32 km	Clark et al. (1991); Willingham et al. (2013)
Queenie Structure	35 km	Clark et al. (1991); Willingham et al. (2013)
Santa Lucia Bank	46 km	Miller and Meltzer (1999); Sorlien (2012)
West Basin—Southwest Channel	62 km	Sorlien, Nicholson, and Luyendyk (1999); Sorlien (2012)

12.6.1 Descriptions of Non-UCERF3 Regional Fault Sources

Geological and seismological information used to characterize the non-UCERF3 Regional fault sources listed in Table 12-4 are summarized here.

12.6.1.1 Lompoc and Purisima Structures

The Purisima and Lompoc structures form prominent antiformal uplifts in the southern part of the offshore Santa Maria Basin. These structures are inferred to fail in reverse-mechanism earthquakes. The antiformal uplifts in the southern part of the basin are bounded on one or both sides by Miocene normal faults that were reactivated in the Pliocene and Quaternary as moderately to steeply dipping thrust or reverse faults (PG&E 1990a; McIntosh et al., 1991; Meltzer and Levander, 1991). Seismic-reflection profiles across the Purisima and Lompoc structures show strong evidence of imbricated thrust faults, post–early Pliocene folding, and locally, evidence of warping or folding of the seafloor (Lettis and Hanson, 1991; Willingham et al., 2013). The deformation of the seafloor indicates that the Lompoc and Purisima structures are both active Quaternary features. Quantification of the rate of vertical deformation measured on the early–late Pliocene unconformity across both the Purisima structure and the Hosgri fault indicates a combined vertical slip rate of approximately 0.2 mm/yr (Hanson et al., 2004). The actual rate localized across only the Purisima fold is less, approximately 0.07 mm/yr, for example, as interpreted from the vertical separation of the early–late Pliocene unconformity in the vicinity of Point Sal (Hanson et al., 2004). The amplitude of the Lompoc structure is comparable to or less than the Purisima structure based on structure contour maps for the top of pre-Miocene basement, top of Miocene, and early-late Pliocene unconformities (Willingham et al., 2013).

12.6.1.2 Queenie Structure

The Queenie structure is the largest amplitude fold in the western offshore Santa Maria Basin. The structure, which plunges to the northwest, appears as a seafloor topographic

feature approximately 34 km west of Point Sal (Figure 12-4). On the basis of stratigraphic and structural relationships interpreted from seismic reflection profiles and oil industry well data, Clark et al. (1991) concluded that the principal growth of the Queenie structure occurred between 5.3 Ma and 3.4 Ma because the early–late Pliocene unconformity is not significantly deformed across the fold. Minor late Quaternary folds in the seafloor adjacent to the Queenie structure, visible on seismic-reflection profiles, are evidence of post–3.4 Ma shortening at a rate of 0.005 mm/yr. Clark et al. (1991) conclude that the reverse fault beneath the Queenie structure dips moderately (30°–50°) to the northeast and extends from the tip of the structure at a depth of approximately 1 km to the base of the seismogenic crust at a depth of about 12 km.

12.6.1.3 Santa Lucia Bank Fault

The Santa Lucia Bank fault (SLBF) is part of a 30 km wide anastomosing to *en echelon* pattern of faults along the west margin of the offshore Santa Maria Basin. The fault separates the offshore Santa Maria Basin from the Santa Lucia Bank high, a structurally uplifted block of Cretaceous rock (McCulloch et al., 1980; Richmond et al., 1981). The northern trace of the SLBF appears as an 85 km long linear seafloor escarpment that extends northwest from offshore Purisima Point to offshore Estero Bay. To the southeast, off Point Arguello, the fault zone consists of a number of splays having more westerly orientations. McCulloch et al. (1980) and McCulloch (1987) provide several lines of evidence to suggest that lateral displacement has occurred along the SLBF:

- The long linear trace typical of lateral-slip faults.
- Differences in the residual magnetic field across the fault, suggesting juxtaposition of different basement rocks.
- The presence of a linear magnetic anomaly that probably represents an ophiolitic body at depth that does not cross the SLBF.
- Considerable difference in thickness of the Miocene and Pliocene age sections across the SLBF.

These authors note that this evidence suggests that vertical separation on the SLBF was accompanied by considerable strike-slip displacement. McCulloch et al. (1980) concluded that the oblique trend of the basement structures between the SLBF and the Hosgri faults, and infilling during development of the structural lows accompanied by growth of normal faults and minor compression, suggest extension and sagging of the basement during transtensional wrenching throughout the Miocene. Sedlock and Hamilton (1991) proposed that the fault accommodated up to 280 km of late Miocene dextral slip. However, Sorlien, Nicholson, and Luyendyk (1999) note that the large amount of strike-slip inferred is based on a regional tectonic model, and they discount the large offset. They interpret the dip of the fault along the southern part to be gentle to moderate. Sorlien, Nicholson, and Luyendyk (1999) conclude that faults within this system retain inherited Miocene normal separations at deep levels and were reactivated by post–early Pliocene shortening discontinuously along strike. The primary topographic expression of the fault is down to the east, however, the east-facing scarp is interpreted to be largely a fault line erosional scarp rather than a fault scarp (McCulloch et al., 1980).

Local evidence for reactivation as a compressional system includes tight anticlinal folds immediately adjacent to the fault trace, broad seafloor uplifts on the east side, and truncation of the early–late Pliocene unconformity (McCulloch et al., 1980; McCulloch, 1987).

The fault is onlapped by Pliocene sediments west of Point Arguello, and Sorlien, Nicholson, and Luyendyk (1999) speculate that slip is transferred to parallel faults to the east and west. McCulloch (1987) noted that the southward continuations of the SLBF are visible on side-scan sonar records and that one of these lineaments crosses a submarine canyon at a right-deflection of the canyon. North of Estero Bay, the fault loses its seafloor expression and becomes buried beneath a thickening wedge of sediments. Buried, and possibly inactive, traces of the fault are noted as far north as offshore Cape San Martin.

12.6.1.4 West Basin–Southwest Channel Fault

Sorlien, Nicholson, and Luyendyk (1999) and Sorlien (2012) map the West Basin fault system as a family of faults that extend along the western part of the offshore Santa Maria Basin fault in the Point Sal to Point Arguello region. Previous studies (McCulloch, 1987, 1989; PG&E, 1990a) mapped part of the West Basin fault system as a southeastern branch of the SLBF but did not connect it north to join the faults beneath the Queenie structure.

Sorlien, Nicholson, and Luyendyk (1999) use single-channel seismic-reflection profiles to interpret the geometry of folding in the upper Pliocene-Quaternary sediments, and they use this geometry to infer an east dip of 35° on the West Basin fault system in the southern offshore Santa Maria Basin. Post-Miocene reactivation of this fault is represented by folding and basin inversion; the most important folding occurred toward the end of early Pliocene time. The fault system continues to the southeast into the Santa Barbara Channel region, where the main southeast-striking trace is referred to as the Southwest Channel fault.

Approximately 8 km north of latitude 34°30′, Sorlien, Nicholson, and Luyendyk (1999) measure approximately 240 m of vertical separation of the top of the early–late Pliocene unconformity across the West Basin fault. Corrected for erosion, the vertical separation is estimated to be 360 m, which correlates to 510 m of shortening and 630 m of dip-slip on a fault dipping 35° northeast. This yields a slip rate of 0.2 mm/yr since approximately 3.3 Ma. Sorlien, Nicholson, and Luyendyk (1999) note that the most important folding occurred toward the end of the early Pliocene.

The West Basin–Southwest Channel fault is a likely fault source for the 1927 M_S 7.0 Lompoc earthquake. Helmberger et al. (1992) and Satake and Somerville (1992) used teleseismic and regional seismogram analysis and tsunami modeling, respectively, to determine that the 1927 Lompoc earthquake occurred at the southern end the offshore Santa Maria Basin. The preferred mechanism for the 1927 Lompoc earthquake is slip on a N20°W, 66°NE dipping fault with a rake of 95° (Helmberger et al., 1992). McLaren and Savage (2001) noted that this earthquake, as well as the November 1969 Santa Lucia

Bank earthquakes, show reverse motion subparallel to nearby mapped fault planes, and the mechanisms for these larger earthquakes are evidence that the southern offshore region is dominated by reverse faulting along north-northwest-trending fault planes.

12.6.2 Characterization of Non-UCERF3 Regional Fault Sources

Sensitivity analyses presented at Workshop 1 by Wooddell (2011) show that the contribution to hazard at the DCPP from regional faults, excepting the contribution for long-period ground motion from the San Andreas fault, is negligible (0.0 to <0.1 percent at the 10^{-4} hazard level). The sensitivity analyses included faults such as the San Simeon fault with a slip rate of 1–3 mm/yr. Accordingly, the characterization of the Non-UCERF3 Regional fault sources, which are lower slip rate faults that lie at similar or greater distance from the DCPP, is simplified in the Diablo Canyon SSC model.

The fault source length, dip, dip direction, slip rate, style of faulting, and magnitude information for these fault sources are provided in Table 12-5. The SSC model has single values for dip, depth, slip rate, and M_{char}. In general, the approach used to assign the single values was to select conservative values based on review of available information and the results of the sensitivity analyses presented in Workshop 1. With regard to geometry, the total length of the fault chosen encompasses the full length of mapped folds or fault traces that are judged by the TI Team to represent a defensible fault source. The dip values used in this SSC model ranged between 40° and 45° and are consistent with the estimated dip of the Queenie structure as interpreted by Clark et al. (1991). The Queenie, Lompoc, and Purisima fault sources are each assigned a slip rate of 0.1 mm/yr. Stratigraphy to evaluate post-ELP and Quaternary deformation rates are most complete for the Queenie fault source, and as noted above Clark et al. (1991) conclude that that Quaternary shortening rate across the Queenie structure is low (0.005 mm/yr). This translates to net slip on a moderately (40°–65°) dipping plane of approximately 0.01 mm/yr. The best constraints on rates of post-ELP vertical slip for the Purisima structure is 0.07 mm/yr or less (Hanson et al., 2004).

Based on the evidence cited in Clark et al. (1991) and Sorlien, Nicholson, and Luyendyk (1999) for slowing of fold growth after the early Pliocene, the TI Team judged that 0.1 mm/yr is a conservative estimate of the present slip rate for these three fault sources. The higher rate assigned to the Santa Lucia Bank and West Channel faults of 1 mm/yr also is a conservative value in that the published post-3.3 Ma rate estimated for the West Channel fault is significantly less (~0.2 mm/yr). The higher value assigned to these two faults allows for a component of strike-slip. A rate of 1.0 mm/yr also is consistent with the absence of associated microseismicity and lack of reported evidence for significant Quaternary deformation. A single characteristic earthquake magnitude probability density function (Youngs and Coppersmith, 1985) is used for these fault sources, and earthquake recurrence is modeled as a time-independent Poisson process. The M_{char} values used are based on the bilinear area-magnitude relationship of Hanks and Bakun (2014) using the area of the fault source as estimated from the simplified geometry.

Table 12-5. Parameters for the Non-UCERF3 Regional Fault Sources

Fault Source Name	Length (km)	Dip	Dip Direction	Slip Rate (mm/yr)	Style of Faulting	M_{char}
Lompoc Structure	25.0	40°	NE	0.1	Reverse	6.7
Purisima Structure	20.6	40°	NE	0.1	Reverse	6.6
Queenie Structure	28.3	40°	NE	0.1	Reverse	6.7
Santa Lucia Bank	170	45°	NE	1	Strike-slip Reverse Oblique	7.6
West Basin–Southwest Channel	83.0	45°	NE	1	Strike-slip Reverse Oblique	7.2

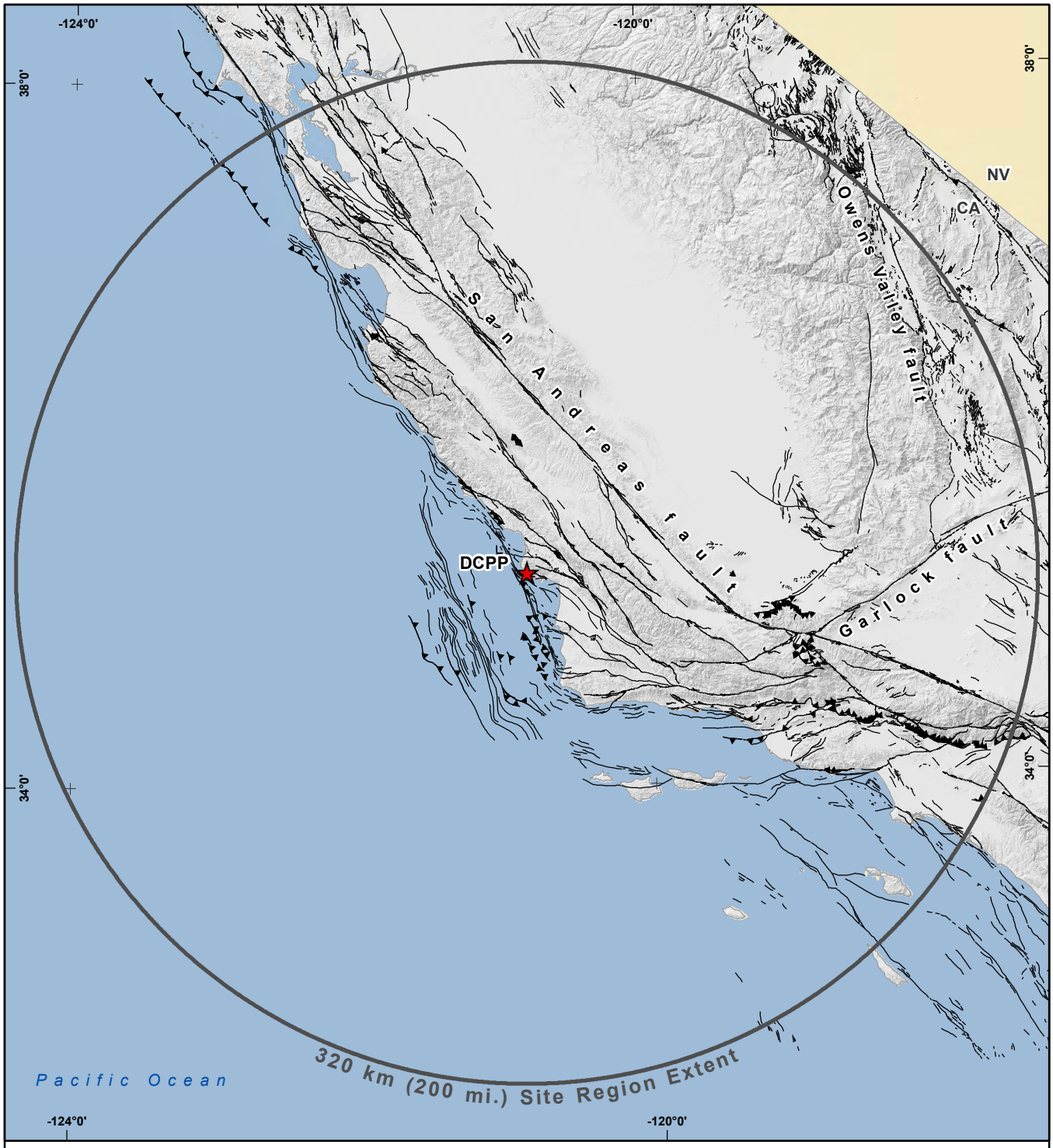

EXPLANATION

High-angle fault, mostly strike-slip

Reverse or thrust fault, teeth on hanging-wall block

N

0 50 100 mi.

0 100 200 km

Map projection and scale: WGS 1984 UTM Zone 10N, 1:3,700,000

Source: Regional faults from California Geologic Survey (2010).

Active Faults Within the 320 km (200 mi.) DCPP Site Region

DCPP SSC REPORT

Pacific Gas and Electric Company

Figure **12-1**

File path: S:\1005\005\Final_Report_Figures\Figure_1200-01.mxd; Date: 02/20/2015; User: Alex, LCI; Rev.1

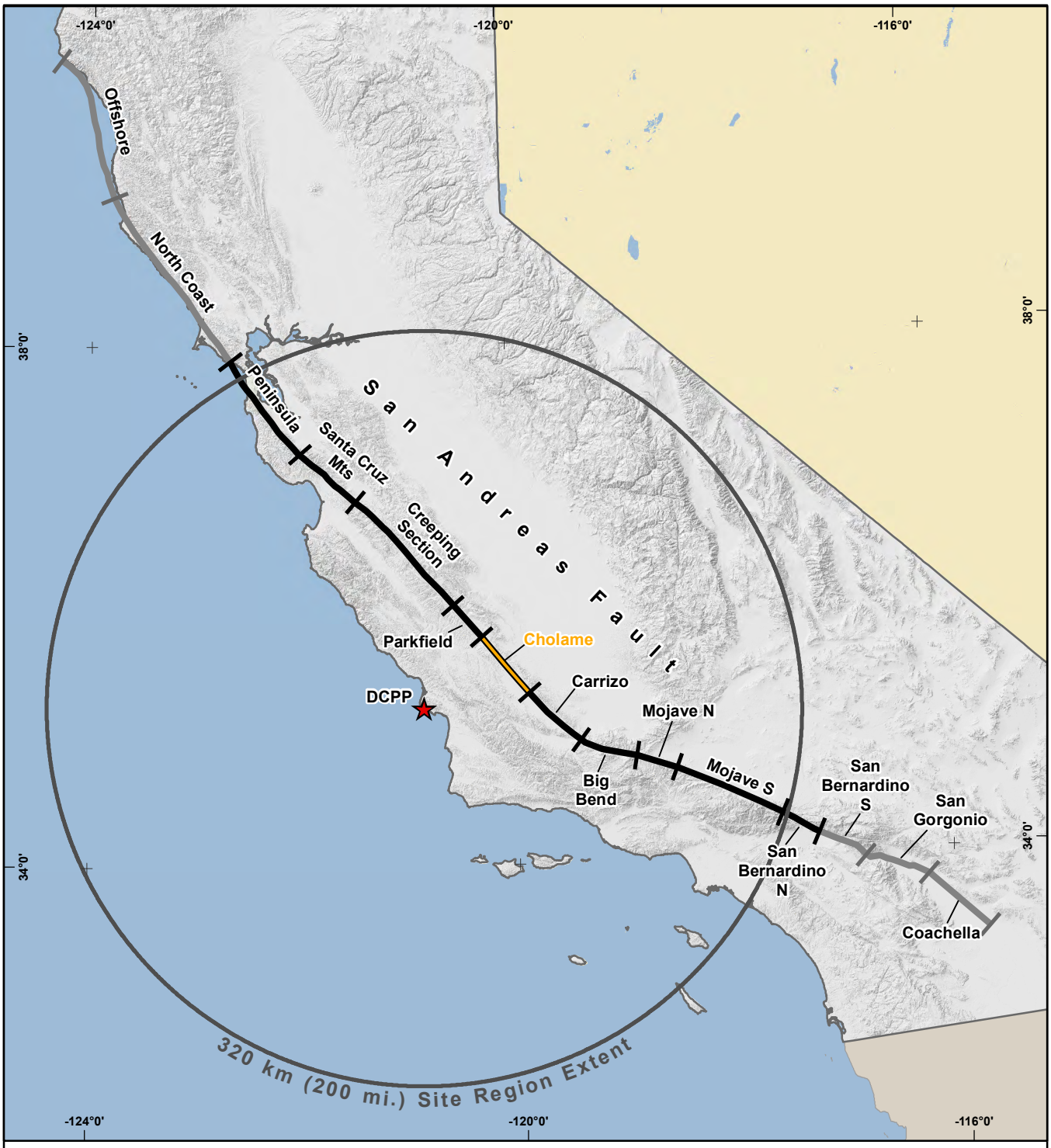

EXPLANATION

San Andreas Fault

- Cholame fault section
- Sections inside the site region
- Sections outside the site region

Note: San Andreas fault source and sections as defined by UCERF3 (Fault Model 3.1) are shown. The closest San Andreas fault section to the DCPP (Cholame) is highlighted in orange.

N

0 50 100 mi.

0 100 200 km

Map projection and scale: WGS 1984 UTM Zone 10N, 1:5,000,000

San Andreas Fault Source and Sections Defined by UCERF3

DCPP SSC REPORT

Pacific Gas and Electric Company

Figure **12-2**

File path: S:\1005\005\Final_Report_Figures\Figure_1200-02.mxd; Date: 02/20/2015; User: Alex, LCI; Rev.1

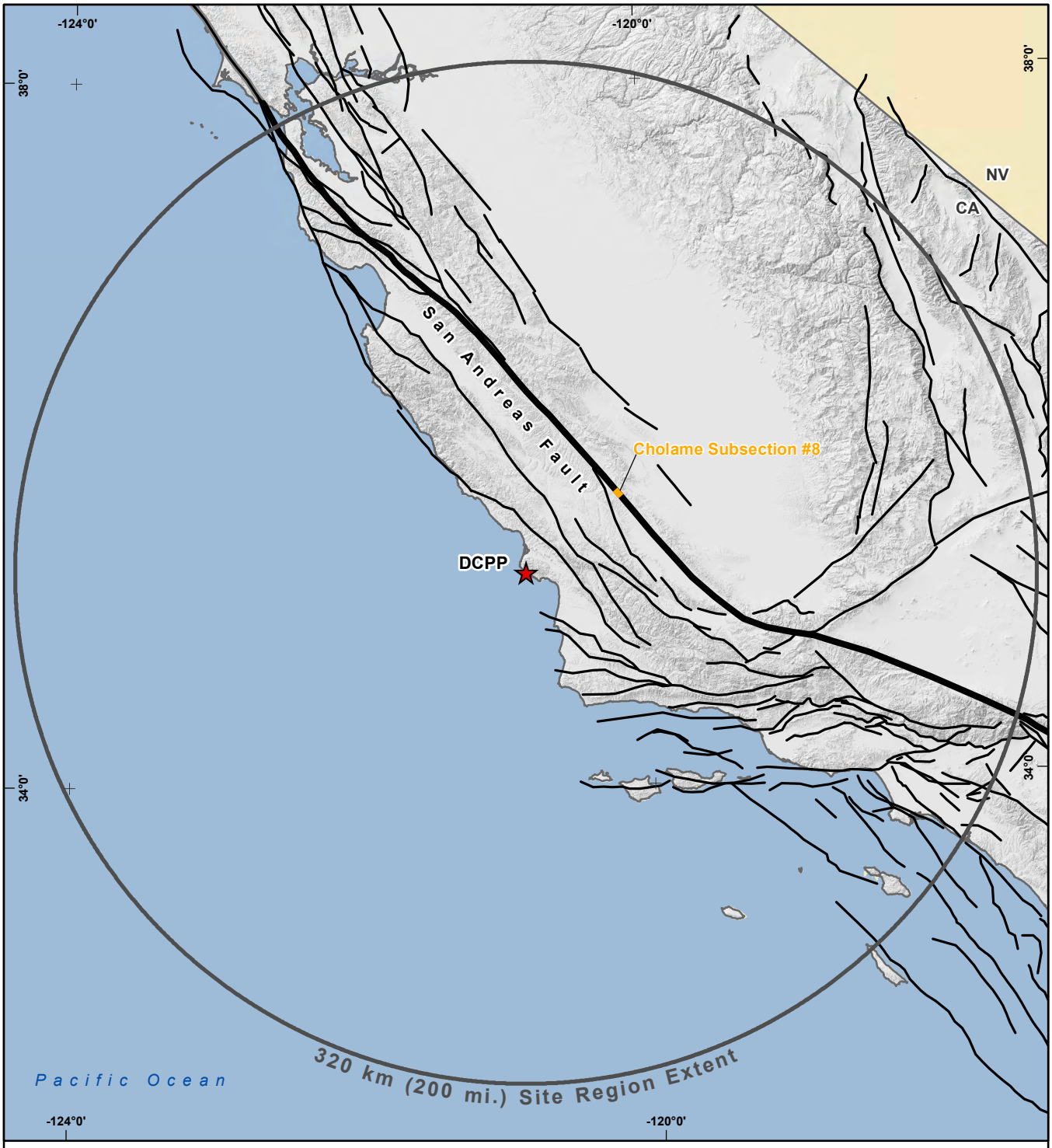

EXPLANATION

Faults from UCERF3 (Fault Model 3.1)

San Andreas Fault

Cholame Subsection #8

Sections inside the site region

Sections outside the site region

Note: Local faults around the DCPP are removed from the UCERF Regional fault source rupture set. Within the 320 km (200 mi.) site region, the UCERF3 Regional fault source rupture set contains 67,354 ruptures.

N

0 50 100 mi.

0 100 200 km

Map projection and scale: WGS 1984 UTM Zone 10N, 1:3,700,000

UCERF3 Regional Fault Sources

DCPP SSC REPORT

Pacific Gas and Electric Company

Figure **12-3**

File path: S:\1005\005\Final_Report_Figures\Figure_1200-03.mxd; Date: 02/20/2015; User: Alex, LCI; Rev.1

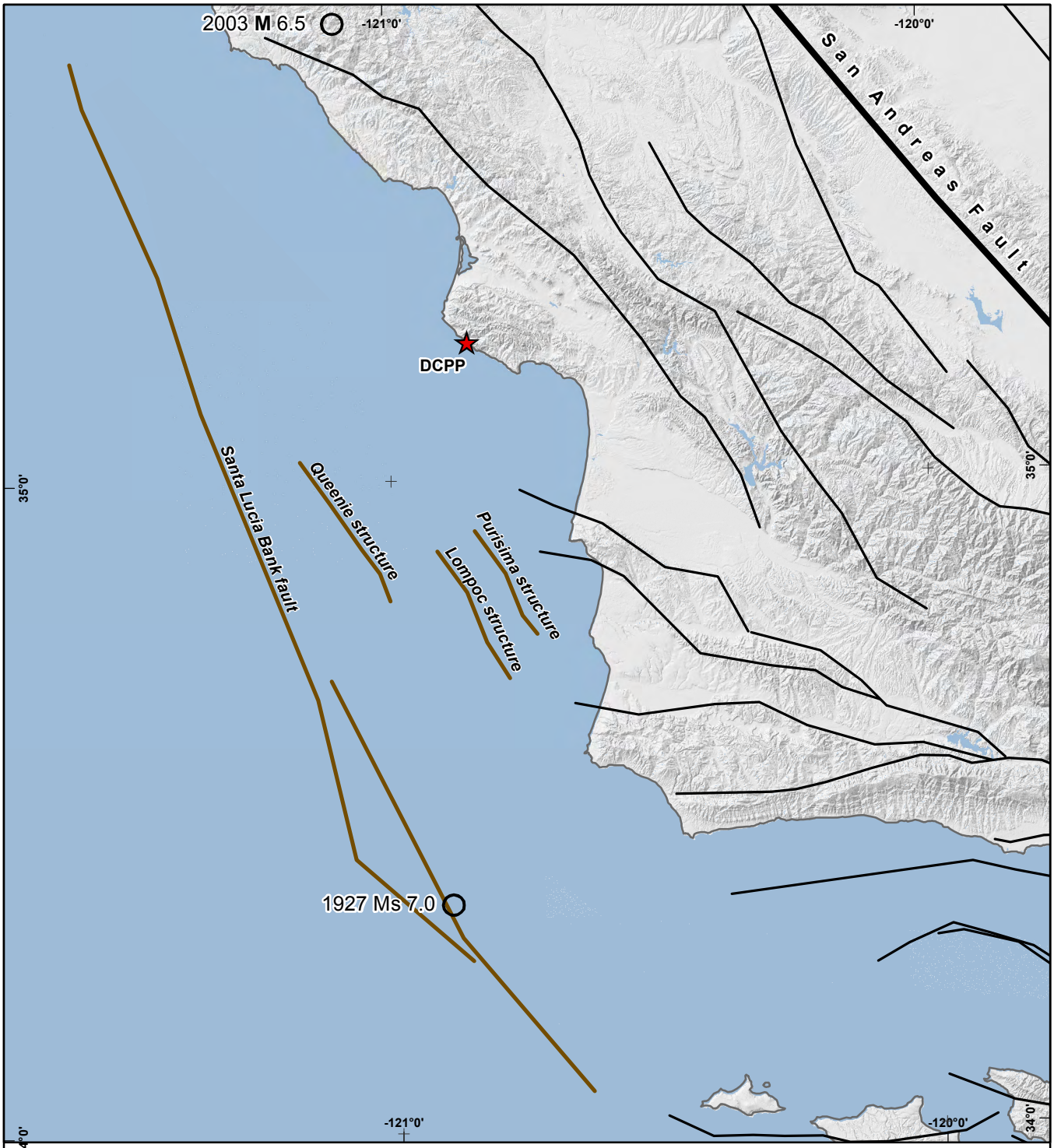

EXPLANATION

- Epicenters of key earthquakes
- Faults from UCERF3 (Fault Model 3.1)
- Non-UCERF3 offshore faults (modified from Lettis et al., 2004; Sorlien et al., 1999b; Sorlien, 2012)
- San Andreas fault

N

0 16 32 mi.

0 30 60 km

Map projection and scale: WGS 1984 UTM Zone 10N, 1:1,000,000

Non-UCERF3 Regional Fault Sources

DCPP SSC REPORT

Pacific Gas and Electric Company

Figure **12-4**

File path: S:\1005\005\Final_Report_Figures\Figure_1200-04.mxd; Date: 03/11/2015; User: alex, LCI; Rev.1

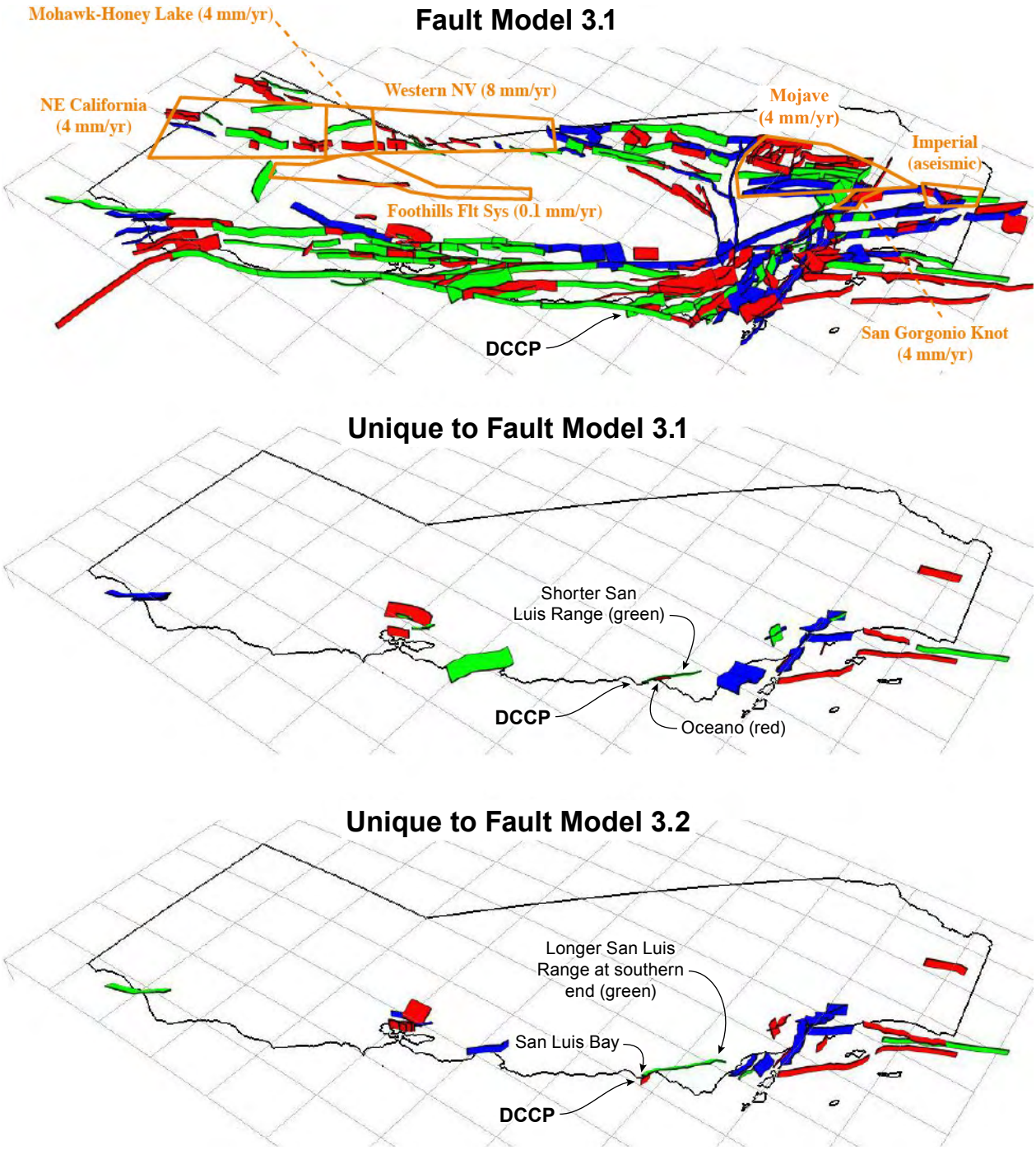

Note: Fault sections are colored to identify those that were added (red), modified (green), and unchanged (blue) since UCERF2. Orange polygons represent off-fault deformation characterized in UCERF2, with labels of modeled deformation rates.

Source: Modified from Field et al. (2013).

Comparison of UCERF3 Fault Models 3.1 and 3.2

DCPP SSC REPORT

Pacific Gas and Electric Company

Figure **12-5**

File path: /s/1005/005/Final_Report_Figures/Figure_1200-05.ai; Date: 02/19/2015; User: Brian Greer, LCI; Rev. 1

(a) UCERF3 Fault Model 3.1

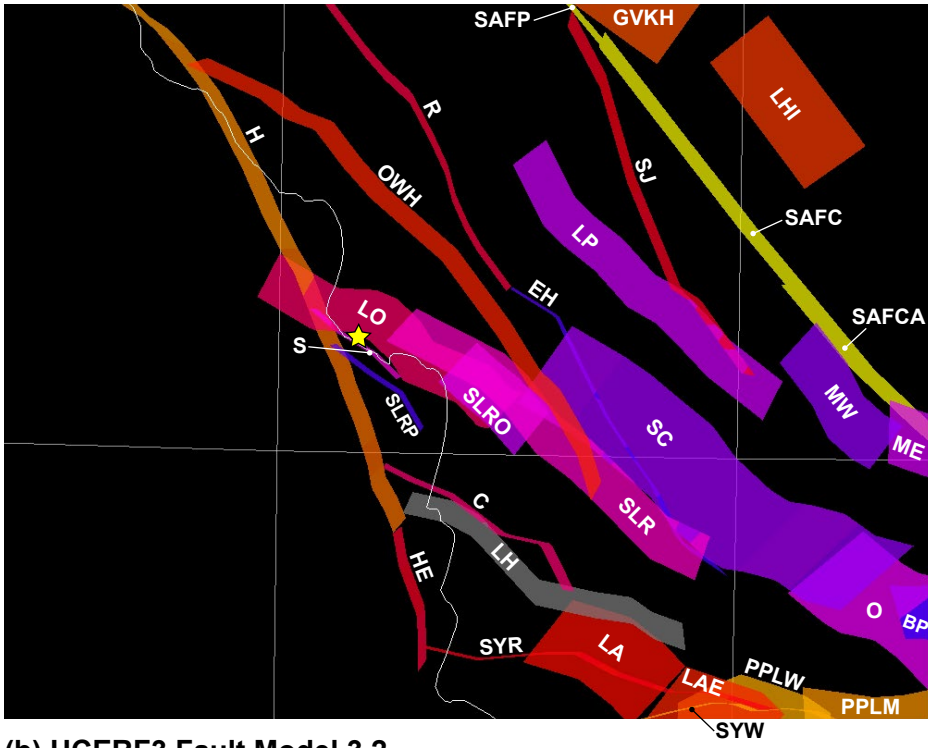

(b) UCERF3 Fault Model 3.2

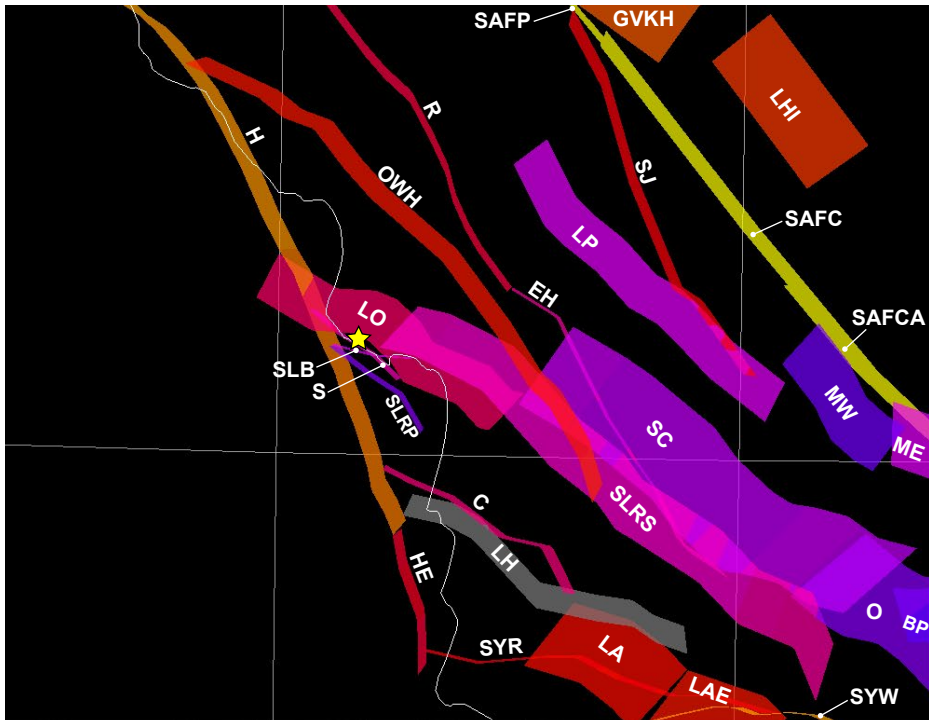

Fault Abbreviations

BP Big Pine
C Casmalia
EH East Huasna
GVKH Great Valley 14 (Kettleman Hills)
H Hosgri
HE Hosgri Extension
LA Los Alamos
LAE Los Alamos Extension
LH Lions Head
LHI Lost Hills
LO Los Osos
LP La Panza
ME Morales (East)
MW Morales (West)
O Ozena
OWH Oceanic-West Huasna
PPLM Pitas Point (Lower) Montalvo*
PPLW Pitas Point (Lower, West)*
R Rinconada
S Shoreline
SAFC San Andreas fault (Cholame)
SAFCA San Andreas fault (Carrizo)
SAFP San Andreas fault (Parkfield)
SC South Cuyama
SJ San Juan
SLB San Luis Bay†
SLR San Luis Range*
SLRO San Luis Range – Oceano*
SLRP San Luis Range – Pecho
SLRS San Luis Range – Southern Margin†
SYR Santa Ynez River
SYW Santa Ynez West

*Fault only appears in Fault Model 3.1
†Fault only appears in Fault Model 3.2

EXPLANATION

DCPP site

Slip Rate (mm/yr)

-1.5 -0.875 -0.25 0.375 1

Note: View is near vertical, so dipping subsections appear larger in plan area.

UCERF3 Fault Models 3.1 and 3.2 in the Greater DCPP Vicinity

DCPP SSC REPORT

Pacific Gas and Electric Company

Figure **12-6**

File path: /s/1005/005/Final_Report_Figures/Figure_1200-06.ai; Date: 02/20/2015; User: Brian Greer, LCI; Rev. 1

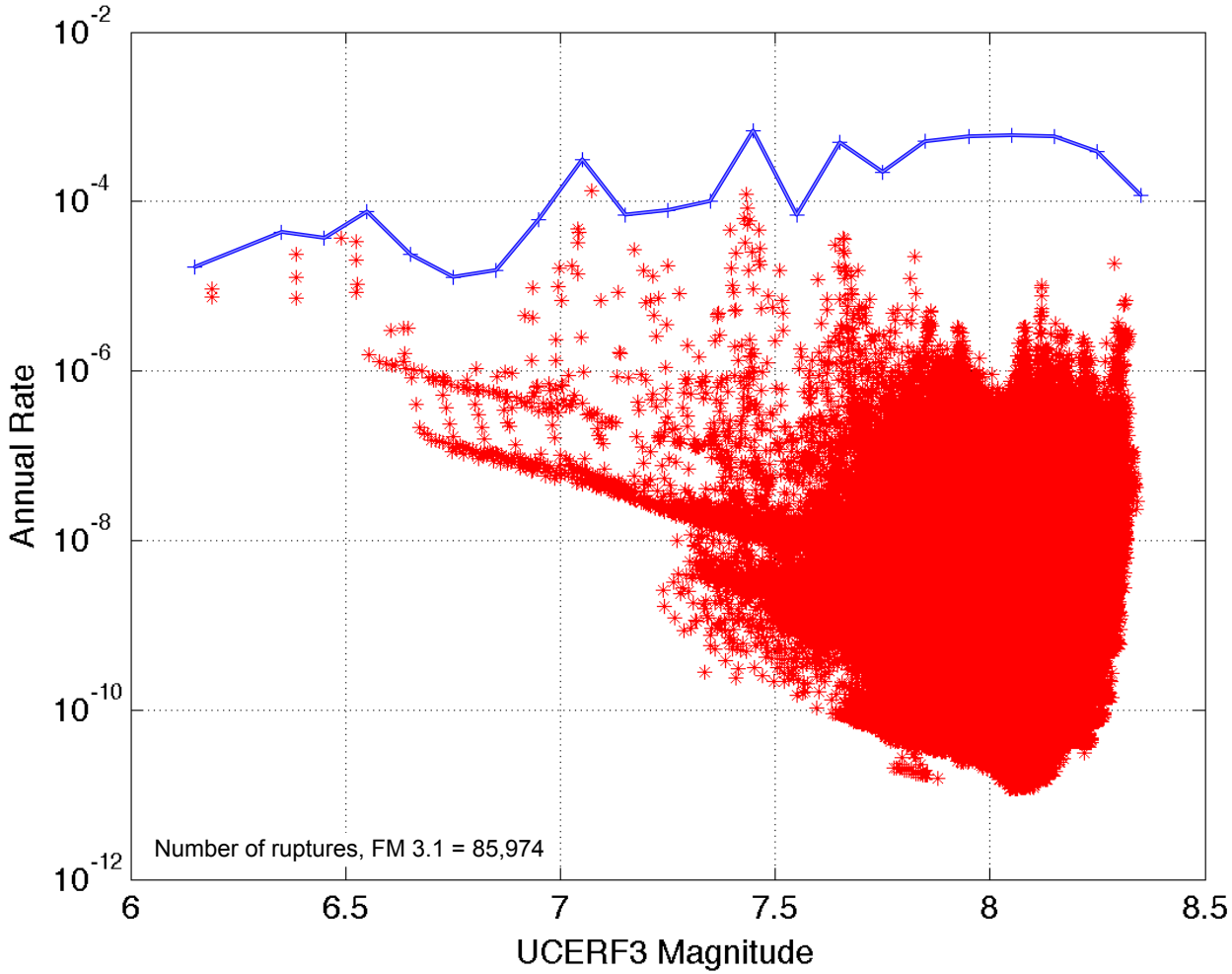

EXPLANATION

✳ Individual rupture frequency

\+ Summary rate for 0.1-magnitude unit bins

Note: Individual rupture frequencies shown for the nearest subsection on the San Andreas fault (Cholame Subsection #8). The total activity rate in red stars can be summarized by blue binned rate-magnitude values. See text for discussion of diagonal trends of red stars.

San Andreas (Cholame Subsection #8)
Rupture Rate Summary Plot

DCPP SSC REPORT

Pacific Gas and Electric Company

Figure **12-7**

File path: /s/1005/005/Final_Report_Figures/Figure_1200-07.ai; Date: 03/11/2015; User: Brian Greer, LCI; Rev. 1

13.0 AREAL SOURCE ZONES

Earthquakes occurring away from recognized fault sources within the DCPP site region are modeled to occur in areal source zones. This chapter defines the areal source zones used in the Diablo Canyon SSC model, describes the approach used by the TI Team to characterize their rates of activity, and presents the areal source zone logic tree parameters in the Diablo Canyon SSC model.

13.1 Definition and Applicability

The Diablo Canyon SSC model has three areal source zones: Regional, Vicinity, and Local, which are named in order of increasing proximity to the DCPP (Figure 13-1). The entire DCPP site region is within one of the three nested, non-overlapping source zones. As shown on Figure 13-1, the Regional and Vicinity areal source zones approximately correspond to the Site Region[3] and Site Vicinity[4] that are defined in NRC Regulatory Guide 1.208 (U.S. NRC, 2007). The areal source zones are volumes of crust containing faults whose general geometric and sense of slip characteristics are known, but whose activity, extent, and slip rate data are insufficient to model individual fault sources. In other words, earthquakes from the areal source zones may occur on faults that are known, proposed, or unknown, but the faults are not sufficiently active or well-constrained to be considered separate fault sources.

The Diablo Canyon SSC model uses two types of areal source zones: (1) source zones modeled as point sources from a grid and (2) source zones modeled with virtual faults. The Regional and Vicinity source zones model earthquakes from a set of point sources on a regularly spaced grid. Distance adjustments are applied to the site-to-grid-point distances when using the ground-motion-prediction equations to approximate the distance adjustments for extended planar faults that would be associated with moderate to larger magnitude earthquakes. The impact of these distance adjustments decreases as the site-to-grid-point distance increases and is also less significant for smaller magnitude earthquakes. Based on the relative distances from the DCPP to the gridded points in the Regional and Vicinity source zone, the use of these regularly spaced gridded source points with the distance adjustments is an accepted method of practice for seismic hazard analysis. The sizes and rates of earthquakes in the gridded source zones are determined based on spatially smoothed seismicity rates and estimates of maximum magnitude (M_{max}).

The Local areal source zone models earthquakes as occurring on a set of parallel virtual faults with defined aleatory and epistemic uncertainties in location, sense of slip, dip, and M_{max}. The Local areal source zone includes the DCPP and adjacent areas and represents an area where the general characteristics of faults are known (to varying degrees of uncertainty) or may be constrained by available information, but where resolution about

[3] The Site Region has a 320-kilometer (km), or 200-mile (mi.) radius from the DCPP.
[4] The Site Vicinity has a 40 km, or 25 mi. radius from the DCPP

specific fault subsurface geometry, continuity, fault activity, and fault slip rate is unresolved. The rates of earthquakes in the Local areal source zone are determined from observed seismicity rates, estimates of virtual fault area and M_{max}, and considerations of implied geologic rates of deformation. The magnitude PDF for all areal source zones is a truncated exponential distribution (*Section 10.2.1.1*), with Gutenberg-Richter *a*- and *b*-values determined based on seismicity rates from available earthquake catalogs (*Appendix F*).

13.2 Approach

The approach for developing the areal source zone models takes into account the results of past hazard sensitivity analyses that have shown that hazard at the DCPP at the spectral frequencies of interest is dominated by ground motions caused earthquakes at close distances occurring on the Primary fault sources (PG&E, 2011; Wooddell, 2011, presentation at Workshop 1). Given this understanding, the TI Team judged that simplified approaches for modeling off-fault seismicity in the study region are warranted, with an increase in the attention paid to capturing model uncertainty with increased proximity to the DCPP. The gridded seismicity file developed as part of UCERF2 (Petersen, Mueller, et al., 2008), and adopted for the 2008 National Seismic Hazard Mapping Project (NSHMP; Petersen, Frankel, et al., 2008), provides a simple baseline model for off-fault seismicity in the SSC model. The following subsections describe the baseline model and the approaches used to adjust the Gutenberg-Richter *a*- and *b*-values of the baseline gridded seismicity file for the Regional, Vicinity, and Local areal source zones. Complete descriptions of the boundaries and the SSC logic trees for the three areal source zones are provided in *Sections 13.3 through 13.5*.

13.2.1 Baseline Model: 2008 NSHMP Gridded Seismicity

The baseline model for the areal source zones is the gridded seismicity file used in the 2008 NSHMP (Petersen, Frankel, et al., 2008). The model accounts for the expectation that future earthquakes of engineering significance will occur near past small- and moderate-size events (Petersen, Mueller, et al., 2008). The 2008 NSHMP seismicity file is defined over a 0.1° by 0.1° grid, with the grid points representing the southwest corner of each grid cell. The seismicity rates are smoothed based on a two-dimensional (2D) spatial Gaussian smoothing function with a fixed uniform correlation distance of 50 km. The declustered catalog seismicity over the region is consistent with a uniform *b*-value of 0.8, where *a*- and *b*-values are based on the Gutenberg-Richter relationship:

$$Log_{10}(N) = a - bM \qquad (13\text{-}1)$$

and where N is the annualized rate of earthquakes having a magnitude $\geq M$, a is the log of the annualized rate of earthquakes having $M \geq 0$, and $-b$ is the slope of the relationship (Gutenberg and Richter, 1944).

The rate values in the gridded seismicity file are related to the *a*-values using the equation

$$rate = 0.184(10^{a}) \qquad (13\text{-}2)$$

where $0.184 = 10^{(0.05b)} - 10^{(-0.05b)}$ is a correction factor based on the discretized step size of 0.1 *M* units and the exponential density function.

13.2.2 Adjustments to the Baseline Model

As described above, three nested areal source zones are defined in the Diablo Canyon SSC model—Regional, Vicinity, and Local—in order of increasing proximity to the DCPP (Figure 13-1). No adjustments to the baseline model rates are made for the Regional areal source zone, which is located at distances greater than approximately 20 km from the DCPP. This simplified approach with no additional uncertainty in the Gutenberg-Richter *a*- and *b*-values is justified given the distance from the DCPP and results of past hazard sensitivity studies (PG&E, 2011; Wooddell, 2011).

For the Vicinity source zone, the gridded seismicity rates in the baseline model are adjusted based on comparison to observed seismicity rates in earthquake catalogs that are described briefly in this section and more completely in *Appendix F*. Epistemic uncertainty in the earthquake rates are incorporated in the model by a simple scaling of the rate up and down by a factor of 2; no adjustments to the 2008 NSHMP *b*-value of 0.8 are considered. The addition of epistemic uncertainty to the rates is justified based on the closer distance of the Vicinity source zone to the DCPP (4 km at closest distance) compared to the Regional source zone. The TI Team judged that the simple approach to adding epistemic uncertainty to the rate was appropriate given the findings of past hazard sensitivities that show a minimal contribution to hazard by off-fault seismicity (PG&E, 2011; Wooddell, 2011), and given that the DCPP is located within the adjacent areal source zone (the Local source zone). The analysis of earthquake rates and the parameters used for the Vicinity source zone are described in *Section 13.4*.

The DCPP is located within the Local areal source zone (Figure 13-1). Adjustments to both the *a*- and *b*-values provided in the 2008 NSHMP gridded seismicity file were considered for the Local source zone to better capture epistemic uncertainty. These adjustments are made based on consideration of observed seismicity rates provided by the available earthquake catalogs as described below and in *Appendix F*. The additional attention given to estimating epistemic uncertainty in Gutenberg-Richter *a*- and *b*-values for the Local source zone as compared to the Vicinity and Regional source zones is justified given the proximity of the source to the DCPP. The analysis of earthquake rates and the parameters used for the SSC logic tree for the Local source zone are described in *Section 13.5*.

Adjustments to the baseline-model gridded seismicity rates were considered for the Vicinity and Local source zones based on the rates of observed earthquakes of $M \geq 2.5$ and $M \geq 3$ from two earthquake catalogs compared to the predicted rate of earthquakes from the gridded seismicity file. The 26-year time period between the beginning of 1988 and the end of 2013 was selected to determine the rate of observed earthquakes $2.5 \leq M < 4.0$. This period was selected because the PG&E Central Coast Seismic Network had been installed and was fully operational by late 1987 (McLaren and Savage, 2001) and because the catalog of $M \geq 2.5$ earthquakes within the DCPP site vicinity is complete for

this period (*Section 13.5.3*). The rates of observed earthquakes of $M \geq 4$ are explored in *Section 13.5.3* for the Local source zone, but large rate uncertainties in this magnitude range do not provide useful constraints.

Four earthquake catalogs are used in the evaluation of earthquake rates. The first catalog is the relocated earthquake catalog of Hardebeck (2014a). This non-declustered catalog is shown over the Vicinity and Local source zone extent on Figure 13-2 and is provided as *Attachment F-1* in *Appendix F*. The Hardebeck (2014a) catalog is used to constrain earthquake rates in the Local source zone in three ways:

- The location information helps delineate the boundary between the Local and Vicinity source zones.
- The magnitude information helps evaluate the minimum magnitude of completeness over the time period from October 1987 through 2013.
- The magnitude information is used to estimate the *b*-value for the Local source zone.

Two declustered earthquake catalogs are considered for evaluating earthquake rates for the Vicinity and Local source zones. The PG&E Geosciences Department developed a catalog of $M \geq 3$ earthquakes for a sub-region surrounding the DCPP; herein we refer to this catalog as the PG&E catalog. The PG&E catalog includes earthquakes from the early nineteenth century through January 2009 for the entire sub-region and is complete through 2013 for the extent of the Vicinity and Local source zones (*Attachment F-4* in *Appendix F*). The development of the PG&E catalog involved conversion of magnitudes to a uniform moment magnitude (**M**) scale. Declustering of the $\mathbf{M} \geq 3$ catalog was performed using the CLUSTER2000 algorithm of Reasenberg (1985) to define a subset of independent earthquakes. Events from this catalog in the Vicinity and Local source zones from 1988 through 2013 are shown on Figure 13-3.

The second declustered catalog considered is an update to the statewide UCERF3 catalog of $M \geq 2.5$ earthquakes by Felzer (2013a); herein we refer to this catalog as the updated UCERF3 catalog. The updated UCERF3 catalog extended the Felzer (2013a) catalog of $M \geq 2.5$ earthquakes for the DCPP region from the end of 2011 through January 2014. PG&E's Geosciences Department compiled the earthquakes, and Karen Felzer of the USGS performed declustering using the Gardner and Knopoff (1974) algorithm to identify independent events from foreshocks and aftershocks. This catalog is provided in *Attachment F-3* in *Appendix F*. No magnitude conversion was performed for the updated UCERF3 catalog. Events from this catalog in the Vicinity and Local source zones from 1988 through 2013 are used for analysis and shown on Figure 13-4.

The fourth catalog considered for evaluating earthquake rates in the Local areal source zone is the compilation of historical $M \geq 5$ earthquakes by McLaren and Savage (2001). This compilation consists of events from the instrumental and pre-instrumental record for the Diablo Canyon subregion, and includes a brief description of the basis and uncertainty associated with each event. This information is considered in combination with the updated UCERF3 catalog for assessing rates of $M \geq 4$ earthquakes in the Local source zone. Events $M \geq 4$ from the updated UCERF3 catalog and $M \geq 5$ from the

McLaren and Savage (2001) compilation in the Vicinity and Local source zones are shown on Figure 13-5.

For the Diablo Canyon SSC model, no explicit adjustments are made to the areal source zones to account for the double counting of earthquakes modeled to occur both from gridded seismicity and from fault sources. Three types of adjustments to areal source zones are commonly performed in SSC models, as follows:

- Reduction of seismicity rate from the parts of the areal source zone that are spatially associated with fault sources, and modeling the resulting seismicity rate to be a part of the fault source magnitude-frequency distribution (e.g., Powers and Field, 2013).
- Lowering the M_{max} values for grid cells that are adjacent to fault sources so that larger-magnitude events occur on the fault sources (e.g., Petersen, Frankel, et al., 2008).
- Lowering the earthquake rates on grid cells at larger magnitudes to account for larger-magnitude earthquakes modeled to occur on the fault sources (e.g., Petersen, Frankel, et al., 2008).

The decision not to reduce the seismicity rate of the areal source zones to account for modeled rates of on-fault seismicity is made for the sake of simplicity and follows past practice for the DCPP (e.g., PG&E, 2011); this decision was supported by hazard results from previous studies and sensitivity analyses that showed that the “background” source zone contributed only a small amount to the total hazard (PG&E, 2011; Wooddell, 2011, presentation at Workshop 1).

13.3 Regional Areal Source Zone

The Regional areal source zone extends between 32°–39° north and 117°–125° west, beyond the 320 km DCPP Site Region (Figure 13-1). The inner boundary of the Regional areal source zone—and the boundary shared with the Vicinity areal source zone—is the 0.5° by 0.5° area approximately centered on the DCPP (35°–35.5° north and 120.6°–121.1° west).

The Regional areal source zone gridded seismicity rates are shown on Figure 13-6. As stated in *Section 13.2*, the grid coordinates and annualized grid cell rates (Equation 13-2) are adopted from the 2008 NSHMP model without modification. Other model parameters for the Regional source zone are provided in Table 13-1. Uncertainty in M_{max} for the Regional source zone is modeled with three branch options, with weights provided in square brackets, as follows: 7.9 [0.1], 7.6 [0.8], and 7.3 [0.1], following the UCERF3 model of maximum off-fault magnitude (Field et al., 2013). Earthquakes are modeled to nucleate from 0 to 12 km depth following a uniform depth distribution. The style of faulting is modeled with aleatory variability with 70% relative frequency for strike-slip earthquakes and 30% for reverse earthquakes based on consideration of the dominantly transpressional environment of the portion of the Regional source zone closest to the DCPP. No uncertainty in the relative frequency of styles of faulting is considered, for the sake of simplicity, and is justified based on past results and hazard sensitivities, as

described in *Section 13.2.2*. The Regional grid cell coordinates and rates for input in the PSHA are provided in *Appendix C*.

Table 13-1. Regional and Vicinity Areal Source Zone Parameters

Parameter	Regional	Vicinity
Grid cell size	0.1° × 0.1°	0.1° × 0.1° and 0.02° × 0.02°
b-value	0.8	0.8
M_{max} value [weight]	7.9 [0.1] 7.6 [0.8] 7.3 [0.1]	7.5 [0.1] 7.0 [0.5] 6.5 [0.4]
Depth distribution	Uniform: 0 to 12 km	Uniform: 0 to 12 km
Style of faulting	70% Strike-slip 30% Reverse	70% Strike-slip 30% Reverse
Activity rate baseline value	2008 NSHMP model (Petersen, Frankel, et al., 2008)	2008 NSHMP model (Petersen, Frankel, et al., 2008)
Activity rate uncertainty [weight]	Only baseline value used	2x baseline value [0.2] Baseline value [0.6] 0.5x baseline value [0.2]

13.4 Vicinity Areal Source Zone

The Vicinity source zone is located within a 0.5° by 0.5° area (35.0° to 35.5° latitude and –121.1° to –120.6° longitude) approximately centered on the DCPP (Figure 13-1). The Vicinity source zone includes an appreciable portion of the area within the 40 km (25 mi.) radius DCPP site vicinity (cf. U.S. NRC, 2007), but it does not encompass it (Figure 13-1).

13.4.1 Boundary Between the Vicinity and Local Source Zones

The Local areal source zone (*Section 13.5*) is entirely contained within the 0.5° by 0.5° area of the Vicinity source zone; therefore, the Vicinity source zone consists of the area within the 0.5° by 0.5° grid that is not within the Local source zone. The boundary between the Vicinity and Local source zones is drawn using 0.02° by 0.02° cell boundaries derived from the larger 0.1° cells. Baseline seismicity rates for each 0.02° cell were set equal to 1/25 the rate of the parent 0.1° cell from the 2008 NSHMP seismicity file (Petersen, Frankel, et al., 2008).

The delineation between the Vicinity and Local areal source zones was made based on inspection of microseismicity trends and density, as well as consideration of recent investigations evaluating potential faults near the DCPP east of the Hosgri fault zone. Figure 13-2 shows double-difference relocation seismicity data from Hardebeck (2014a) within the 0.5° Vicinity source zone boundary scaled by depth. These data, which consist of $M \geq 0$ events, represent the most precise earthquake locations available for the DCPP (*Chapter 4* and *Appendix F*). Seismicity trends along the Hosgri and Shoreline fault zones

are recognizable in the data and help define these steeply dipping to vertical strike-slip faults (Hardebeck, 2010, 2013; *Chapter 7*). East of the Hosgri and Shoreline fault zones, potential association of microseismicity with faults mapped independently based on geologic or geomorphic criteria is limited to Estero Bay. Within the Irish Hills, there is no clear association between microseismicity and mapped faults (see discussion of microseismicity in *Sections 13.5.2 and 13.5.3*). This is particularly true for the Los Osos and San Luis Bay fault zones, the two Primary reverse fault sources in the Diablo Canyon SSC model.

Beneath the Irish Hills and Estero Bay east of the Hosgri and Shoreline fault zones, there is a higher density of microearthquakes than in adjacent areas, except for the aftershocks of the 2003 San Simeon earthquake located along the Oceanic–West Huasna fault trend (which is mostly north of the 0.5° Vicinity source zone boundary; see Figure 13-2). The delineation between the Vicinity and Local areal source zones follows the difference in microseismicity density along its generally northwest-southeast trend, subparallel to the trend of many mapped Quaternary faults east of the Hosgri fault. For the sake of simplicity, the boundary is drawn so that the DCPP and Shoreline seismicity trends are within the Local source zone. Seismicity associated with the Hosgri fault zone is mostly, but not entirely, outside the Local source zone limits. Additional discussion of the Local source zone is provided in *Section 13.5*.

13.4.2 Vicinity Areal Source Zone Rate and Maximum Magnitude

The seismicity rate for the Vicinity source zone was evaluated by comparing the observed rate of $M \geq 3$ earthquakes in the 26-year period from 1988 through 2013 to the predicted number of $M \geq 3$ earthquakes from the 2008 NSHMP model (Petersen, Frankel, et al., 2008; *Section 13.2*). We define a scale factor as the ratio of the observed number of earthquakes to the predicted number in the 26-year period, and multiply the baseline (predicted) rate of earthquakes by the scale factor to define rates for use in the SSC model.

Figure 13-3 shows the $\mathbf{M} \geq 3$ earthquakes within the 0.5° Vicinity source zone boundary from the PG&E catalog from the beginning of 1988 through the end of 2013. Earthquakes classified as dependent events (foreshocks or aftershocks) using the CLUSTER2000 algorithm are shown as unfilled circles; independent events are blue circles. There are no $\mathbf{M} \geq 4$ earthquakes within the 0.5° area during this time period. Figure 13-4 shows the $M \geq 2.5$ earthquakes within the 0.5° Vicinity source zone boundary from the updated UCERF3 catalog from the beginning of 1988 through the end of 2013. Earthquakes are categorized by size for the bins $2.5 \leq M < 3.0$ and $M \geq 3.0$. Similar to the PG&E catalog, there are no $M \geq 4$ earthquakes within the 0.5° area during this time period. Earthquakes classified as dependent events (foreshocks or aftershocks) using the Gardner and Knopoff (1974) algorithm are shown as unfilled circles. Independent events $2.5 \leq M < 3.0$ are yellow circles, and $M \geq 3.0$ are green circles.

Table 13-2 summarizes the number of $M \geq 3.0$ earthquakes predicted by the baseline model gridded seismicity (Petersen, Frankel, et al., 2008) and the recorded (observed) number of earthquakes within the Vicinity source zone in the two catalogs for the 26-year

period. The locations of the $M \geq 3$ earthquakes in the double-difference relocated Hardebeck (2014a) catalog are very similar to those in the 2014 PG&E and updated UCERF3 catalogs, which suggests that the location uncertainty is not an important factor in assessing the number of earthquakes in the Local or Vicinity source zones.

Table 13-2. Number of Predicted vs. Observed Earthquakes *M* ≥ 3 in the Vicinity Source Zone

Catalog	Number of Earthquakes in the Vicinity Source Zone, *N*			
	Total	Independent Events*	90% Confidence Interval†	Scale Factor‡
Predicted *M* ≥ 3, 26-year period, 2008 NSHMP (Petersen, Frankel, et al., 2008)	N/A	5.07	N/A	N/A
Observed **M** ≥ 3, 1988–2013, PG&E catalog	6	5	10.5–2.0	1.0 (2.1–0.4)
Observed *M* ≥ 3, 1988–2013, updated UCERF3 catalog	6	5	10.5–2.0	1.0 (2.1–0.4)

N/A = not applicable
* Independent earthquakes are the total earthquakes minus foreshocks and aftershocks identified using declustering algorithms.
† Represents the 5% and 95% probability range of the "correct" average number of independent earthquakes to occur in the time interval given the observation *N*, with *N* representing a Poisson variable (Weichert, 1980, equation 11).
‡ Implied scale factor is defined as the number of independent *M* ≥ 3 earthquakes observed between 1988 and 2013 divided by the number predicted by the baseline model (Petersen, Frankel, et al., 2008). The range given in parentheses is the range of scale factors from the 90% confidence interval.

Table 13-2 shows that 6 earthquakes of $M \geq 3$ are recorded in the Vicinity source zone within the 26-year period in both catalogs, with 1 aftershock interpreted from each declustering algorithm. The predicted number of earthquakes in a 26-year period for the Vicinity source zone based on the 2008 NSHMP baseline model is 5.07, which is virtually identical to the number of earthquakes observed. The best estimate rate for the Vicinity source zone in the SSC model is set to be equal to the baseline rate (i.e., a scale factor of 1.0). The Vicinity source zone grid cells and baseline rates are shown on Figure 13-7, with separate rate scaling based on the cell size (0.1° versus 0.02° cells).

Uncertainty in the earthquake rate is estimated by considering the 90% confidence interval in the "correct" average number of earthquakes to occur in a 26-year period based on the method of Weichert (1980, his equation 11). This yields a range of approximately 2 to 10.5 earthquakes at the 5% and 95% probability levels for a 26-year period, respectively. The 90% confidence interval range is consistent with scale factors of approximately 0.4 to 2.1. For the sake of simplicity, the TI Team judged that scale factors of one half and twice the baseline rate were adequate for estimating uncertainty in the Vicinity source zone rate. The SSC logic tree for the Vicinity source zone adopts a three-

point distribution for the earthquake rate, with the central value equal to the baseline rate given a weight of 0.6, and high and low values that are twice and one half the baseline rate, respectively, each with a weight of 0.2 (Table 13-1).

Uncertainty in M_{max} for the Vicinity source zone is modeled with three branch options, with weights provided in square brackets, as follows: 7.5 [0.1], 7.0 [0.5], and 6.5 [0.4] (Table 13-1). The values and weights reflect the TI Team's judgment that earthquakes greater than the M_{max} values will occur on the defined fault sources within the Vicinity source zone. The rationale for an M_{max} distribution for the Vicinity source zone that has lower values than those used for the Regional source zone is that geologic and geophysical investigations have been conducted within the Vicinity source area to a greater extent than for parts of the Regional source zone, with a specific focus on fault source identification and characterization for seismic hazard analysis (e.g., PG&E, 1988; Alterman et al., 1994; PG&E, 2014, Chapters 3, 4, and 7; *Chapters 4 and 5*). The TI Team judges that these investigations have identified all faults that are capable of hosting earthquakes greater than the stated M_{max} values within the Vicinity source zone.

Earthquakes within the Vicinity source zone are modeled to nucleate from 0 to 12 km depth following a uniform depth distribution (Table 13-1). The style of faulting is modeled with aleatory variability with 70% relative frequency for strike-slip earthquakes and 30% for reverse earthquakes based on consideration of the dominantly transpressional environment of the Vicinity source zone. No uncertainty in the relative frequency of styles of faulting is considered for the sake of simplicity and is justified based on past seismic hazard analyses that show the "background" source zones contribute only a small amount to the total hazard at the DCPP for the spectral frequencies of interest (PG&E, 2011; Wooddell, 2011, presentation at Workshop 1). The Vicinity grid cell coordinates and rates for input in the PSHA are provided in *Appendix C*.

13.5 Local Areal Source Zone

The Local areal source zone covers the northwestern portion of the San Luis Range (i.e., the Irish Hills and adjacent area) and Estero Bay (*Section 13.4.1* and Figure 13-2). Because the DCPP is within the Local source zone, additional effort is taken to model the areal source zone and capture uncertainty in the earthquake rates and source geometries for the SSC model. Uncertainty in earthquake rates is captured by considering uncertainty in Gutenberg-Richter *a*- and *b*-values for the Local source zone, instead of the more simple examination of only *a*-value uncertainty for the Vicinity source zone (*Section 13.4.2*). The earthquake rate analysis is presented in *Section 13.5.1*. Uncertainty in source geometry is captured by modeling earthquakes in the Local source zone on a set of virtual faults instead of as point sources from a grid. The technical justification for this approach is presented in *Section 13.5.2*, and parameters developed to capture uncertainty in the sense of slip, geometry, and maximum magnitude for the virtual faults are described in *Section 13.5.3*.

13.5.1 Local Source Zone Rate

As shown on Figures 13-2, 13-3, and 13-4, the Local source zone is associated with a higher rate of seismicity in the past 26 years than the surrounding (and larger) Vicinity source zone. Whereas the earthquake rates from the 2008 NSHMP seismicity file (Petersen, Frankel, et al., 2008) predict approximately 2.3 earthquakes of $M \geq 3$ for a 26-year period within the Local source zone, approximately two to four times that number of independent earthquakes have occurred in the 26 years from 1988 through 2013, depending on the earthquake catalog and declustering algorithm used (Table 13-3).

The PG&E catalog, using the CLUSTER2000 algorithm (Reasenberg, 1985), estimates nine independent events of $\mathbf{M} \geq 3$ in the Local source zone (Table 13-3 and Figure 13-3). The updated UCERF3 catalog, using the Gardner and Knopoff (1974) algorithm, estimates five independent events of $M \geq 3$ (Table 13-3 and Figure 13-4). Both estimates exceed the baseline model prediction of approximately 2.3 earthquakes, suggesting scale factors in the range of 2 to 4. Within the 90% confidence intervals, the implied scale factors are less than 1 to almost 7 (Table 13-3).

Table 13-3. Number of Predicted vs. Observed Earthquakes *M* ≥ 3 in the Local Source Zone

Catalog	Number of Earthquakes in the Local Source Zone, *N*			
	Total	Independent Events*	90% Confidence Interval†	Scale Factor‡
Predicted $M \geq 3$, 26-year period, 2008 NSHMP (Petersen, Frankel, et al., 2008)	N/A	2.3	N/A	N/A
Observed $\mathbf{M} \geq 3$, 1988–2013, PG&E catalog	10	9	15.7–4.7	4.0 (2.1–6.9)
Observed $M \geq 3$, 1988–2013, updated UCERF3 catalog	9	5	10.5–2.0	2.2 (0.9–4.6)

N/A = not applicable
* Independent earthquakes are the total earthquakes minus foreshocks and aftershocks identified using declustering algorithms.
† Represents the 5% and 95% probability range of the "correct" average number of independent earthquakes to occur in the time interval given the observation *N*, with *N* representing a Poisson variable (Weichert, 1980, equation 11).
‡ Implied scale factor is defined as the number of independent $M \geq 3$ earthquakes observed between 1988 and 2013 divided by the number predicted by the baseline model (Petersen, Frankel, et al., 2008). The range given in parentheses is the range of scale factors from the 90% confidence interval.

Uncertainty in *b*-value for the Local source zone was evaluated by considering the statewide results of UCERF2 (Field et al., 2008) and UCERF3 (Field et al., 2013), the relocation catalog of Hardebeck (2014a; Figure 13-2), and the PG&E and updated UCERF declustered catalogs (Figures 13-3 and 13-4). As stated in *Section 13.2.2*, both declustered catalogs were updated through 2013 for the 0.5° by 0.5° area that

encompasses the Local and Vicinity source zones. The catalogs are described further and provided as attachments in *Appendix F*.

The California statewide *b*-value for magnitude 2.5 and greater earthquakes is indistinguishable from 1.0 based on analysis of the UCERF3 catalog without declustering (Felzer, 2013b). Previously, for UCERF2, Felzer (2008) estimated a statewide $b = 1.02 \pm 0.11$ for the entire catalog $M \geq 4.0$, and $b = 0.85 \pm 0.13$ for the declustered catalog using Gardner and Knopoff (1974). Felzer (2008) and Petersen, Frankel, et al. (2008) and Petersen, Mueller, et al. (2008) adopted a preferred *b*-value of 0.8 for the declustered catalog because the results of Felzer's statewide analysis were not significantly different from the $b = 0.8$ used for the prior 2002 National Seismic Hazard Maps (Frankel et al., 2002). Thus, an initial range of *b*-values to consider for the Local source zone is $b = 1.0$ to $b = 0.8$.

Based on the number of earthquakes, catalog precision, and magnitude range, the Hardebeck (2014a) catalog was analyzed to provide additional information on *b*-value for the Local source zone. Within the Local source zone boundary, the Hardebeck (2014a) catalog includes 627 events from late 1987 through 2013 in the range $0 \leq M \leq 3.5$ (Figure 13-2). No declustering was performed for the catalog, and there was no emphasis on magnitude conversion or magnitude adjustment as performed for the declustered catalogs. Because of this, and further reasons detailed below, the TI Team considers the information from the Hardebeck (2014a) catalog to be useful for general information on *b*-value to understand the extent to which earthquakes in the Local source zone have the same or different statistical properties compared to the state as a whole. However, the TI Team judged that a precise *b*-value determined from the Hardebeck (2014a) catalog should not be considered as an alternative for the SSC logic tree.

Figure 13-8a shows the distribution of earthquakes by magnitude with time from late 1987 through 2013. Inspection suggests there are gaps in the catalog at lower magnitudes (e.g., between approximately 1998 and 2002 for earthquakes $M \leq 2$) that may be related to incomplete records. Figure 13-8b shows the log of the cumulative number of earthquakes N of magnitude $m \geq m_0$ for the range 0 to 3.5. The increase in slope between magnitude 0 and approximately magnitude 1.1 clearly shows that magnitudes in this range are incomplete. Above $m_0 = 1.1$, casual inspection suggests the catalog may be complete.

The maximum likelihood method of Aki (1965) relates the *b*-value to the magnitude of completeness m_c based on the equation

$$b = \frac{1}{\ln(10)(\overline{m} - m_c)} \tag{13-3}$$

where $\overline{m}$ is the average magnitude of the catalog. A plot of *b*-values calculated using estimates of m_c from 1.0 to 2.0 is shown on Figure 13-9a. The upper part of the figure shows the number of earthquakes N that were included in the calculation of $\overline{m}$, and the lower part of the figure shows the value of b from equation (13-3). The results show a steady rise in *b*-value between magnitude 1.0 and approximately 1.5, a consistent *b*-value of approximately 1.0 between magnitude 1.5 and 1.9, then a larger *b*-value greater than

1.1 for mc = 2.0. Estimates of *b*-value for magnitudes 2 and greater are considered less reliable due to low *N* values and are not shown. The steady rise in *b*-value from magnitude 1 to 1.5 is consistent with the observation of the gaps in the catalog noted on Figure 13-8a, and suggests that the magnitude of completeness is equal to or greater than approximately 1.5.

A plot of annual rate of earthquakes $m \geq m_0$ versus magnitude for 0.5 magnitude increments is shown on Figure 13-9b. Error bars in the annual rate shown on the plot represent 5% and 95% uncertainties (based Weichert, 1980; his Equation 11). The data are shown with exponential distributions drawn through the observed rate of $M \geq 2.0$ earthquakes for b = 0.8, 0.9, 1.0, and 1.1. All *b*-value alternatives fit the data above *M* 2.5 within the 90% confidence interval, although *b*-values of 0.9 and 1.0 plot much closer to the observed rates. Based on these results, the TI Team judged that the *b*-value of the Local source zone does not appear to differ significantly from the statewide *b*-value reported by Felzer (2008; 2013b).

The range of Gutenberg-Richter *a*- and *b*-values for use in the SSC logic tree for the Local areal source zone was evaluated by considering the range of *b*-values estimated from the Hardebeck (2014a) data and rates of earthquakes from the two declustered catalogs. As declustering algorithms such as Gardner and Knopoff (1974) and Reasenberg (1985) can preferentially remove smaller earthquakes (Felzer, 2008), resulting in lower *b*-values as compared to non-declustered catalogs, the TI Team did not consider *b*-values greater than 1.0 for evaluating Gutenberg-Richter parameters for the Local source zone and focused on *b*-value alternatives of 1.0, 0.9, and 0.8. Rates of earthquakes from the 26-year period from 1988 through 2013 are shown for $\mathbf{M} \geq 3$ from the PG&E catalog (Figure 13-10a) and for $M \geq 2.5$ from the updated UCERF3 catalog (Figure 13-10b).

Table 13-4 shows the catalog of independent earthquakes $\mathbf{M} \geq 3$ within the Local source zone in the PG&E catalog for the 26-year time period 1988 through 2013. These 9 independent earthquakes and one dependent earthquake (aftershock or foreshock) are shown on Figure 13-3. The events are all less than **M** 3.5, and occurred within a 14-year period between January 1992 and January 2006.

Table 13-4. Independent Earthquakes M ≥ 3 in the PG&E Catalog, 1988 Through 2013

Year	Month	Day	Hour	Minute	Magnitude M	Independent	Latitude	Longitude
1992	01	17	08	27	3.02	Y	35.2622	–120.8487
1992	04	06	18	26	3.08	Y	35.4338	–120.9518
1994	09	28	01	11	3.41	Y	35.1502	–120.6202
1995	08	24	08	54	3.11	Y	35.1737	–120.6047
2000	08	10	14	15	3.40	Y	35.1325	–120.7518
2003	10	18	07	38	3.41	Y	35.2015	–120.8050
2005	06	27	00	30	3.46	Y	35.4252	–120.9992

Year	Month	Day	Hour	Minute	Magnitude M	Independent	Latitude	Longitude
2005	11	02	05	10	3.08	Y	35.4297	–120.9972
2006	01	04	23	56	3.14	Y	35.3132	–120.9453

Figure 13-10a shows the earthquake rates for the PG&E catalog for **M** ≥ 3.0 to **M** ≥ 3.4 along with uncertainty bars that encompass the 5% and 95% probability levels. Also shown is the 95% uncertainty rate of **M** ≥ 3.9 events for the 26-year time interval given no observations. Three exponential distributions are drawn with the data through the observed rate of **M** ≥ 3.0, with *b*-values of 1.0, 0.9, and 0.8. The three lines visually fit the data equally well.

The portion of the updated UCERF3 catalog used to estimate Gutenberg-Richter *a*- and *b*-values is shown in Table 13-5. The table shows the catalog of independent earthquakes $M \geq 2.5$ within the Local source zone for the 26-year time period from 1988 through 2013. The 16 independent earthquakes and 8 dependent earthquakes (aftershocks and foreshocks from the Gardner and Knopoff, 1974, algorithm) are shown on Figure 13-4. The independent earthquakes are all less than *M* 3.6, and occurred within an approximately 18-year period between September 1988 and November 2006 (Table 13-5).

Table 13-5. Independent Earthquakes *M* ≥ 2.5 in the Updated UCERF3 Catalog, 1988 Through 2013

Year	Month	Day	Hour	Minute	Magnitude *M*	Independent	Latitude	Longitude
1988	9	17	13	27	2.71	Y	35.2925	–120.790
1992	1	7	18	24	2.71	Y	35.2440	–120.740
1992	1	17	8	27	3.2	Y	35.2623	–120.849
1992	4	6	18	26	2.57	Y	35.4225	–120.929
1993	3	2	13	32	2.69	Y	35.1562	–120.657
1993	5	4	15	17	2.61	Y	35.3985	–120.913
1994	4	6	13	39	2.52	Y	35.2345	–120.781
1994	9	28	1	11	3.15	Y	35.1502	–120.620
1995	2	13	22	2	2.9	Y	35.2045	–120.856
1995	8	24	8	54	3.03	Y	35.1738	–120.605
1998	4	14	0	45	2.71	Y	35.4013	–120.913
2000	8	10	14	15	3.53	Y	35.1325	–120.752
2003	10	18	7	27	3.44	Y	35.2035	–120.805
2004	2	17	20	1	2.71	Y	35.1740	–120.606
2006	5	4	12	42	2.84	Y	35.2398	–120.912
2006	11	17	6	41	2.76	Y	35.2688	–120.775

Figure 13-10b shows the results for the updated UCERF3 catalog, with the rate of events $M \geq 2.5$ to $M \geq 3.5$ shown along with uncertainty bars that encompass the 5% and 95% probability levels. Similar to Figure 13-10a, the plot includes the 95% uncertainty rate of $M \geq 3.9$ events for the 26-year time interval given no observations. Three exponential distributions are drawn with the data through the observed rate of $M \geq 2.5$, with *b*-values of 1.0, 0.9, and 0.8. The three lines fit the data to within the uncertainty range, but the steeper *b*-value of 1.0 shows the best fit to the data and $b = 0.8$ fit the observed rates least well.

Earthquake rates for magnitudes 4 and greater do not provide meaningful constraints on the *a*- and *b*-values estimated from the lower magnitudes for the Local source zone. For the magnitude range $4.0 \leq M < 5.0$, the updated UCERF3 catalog is used. For rates of earthquakes of magnitude 5 and greater, the catalog of McLaren and Savage (2001) is used. These events $M \geq 4.0$ are shown on Figure 13-5.

Uncertainties in the rates of earthquakes $M \geq 4.0$ are evaluated based on the following completeness periods for different magnitude intervals:

- $2.5 \leq M < 4.0$; 1988 through 2013 (26 years).
- $4.0 \leq M < 5.0$; 1932 through 2013 (82 years).
- $5.0 \leq M < 6.5$; 1870 through 2013 (144 years).
- $M \geq 6.5$; 1772 through 2013 (242 years).

The 26-year period from 1988 through 2013 coincides with operation of the PG&E network and is the time period of the Hardebeck (2014a) catalog shown above to be complete to approximately $M = 1.5$ to 2 (Figures 13-8 and 13-9). For $4.0 \leq M < 5.0$, the completeness start date of 1932 is based on Felzer (2013b), who estimated a completeness start date of 1932 to *M* 4.1 for the central coastal region of California. For $5.0 \leq M < 6.5$, the completeness start date of 1870 coincides with the founding of the city of San Luis Obispo and the establishment of a newspaper there; this is also an alternative start date for $M \geq 6.5$ used for consideration of tMRE for the EPR calculations (*Chapter 11*). Felzer (2013b) estimates a completeness start date of 1905 for *M* 6.3 and 1870 for *M* 6.5 for the central coast region as a whole, but the TI Team judged that the record is probably more complete for the Local source zone based on its coastal location and proximity to San Luis Obispo. For $M \geq 6.5$, the completeness start date of 1772 coincides with the founding of the mission at San Luis Obispo (*Chapter 11*).

The record of events $M \geq 4$ are shown in Table 13-6 and are based on an evaluation of the updated UCERF3 catalog and from McLaren and Savage (2001). These and other historical earthquakes discussed below are plotted on Figure 13-5. Figure 13-11 show the earthquake rates and candidate Gutenberg-Richter fits to both the PG&E and updated UCERF3 catalogs (from Figure 13-10) along with rates and uncertainties for $M \geq 4$, 5, 6, and 7 earthquakes from evaluation of these larger historical events.

For $M \geq 4.0$, the updated UCERF3 catalog shows two earthquake epicenters within or bordering the Local source zone that are within (or close to) the estimated completeness period starting in 1932, as follows:

- 1931 M 4 earthquake, located in the southeastern portion of the source zone.
- 1980 M_L 4.19 earthquake, with an epicenter directly outside the southwestern boundary.

Table 13-6. Independent Earthquakes $M \geq 4$ Used and Considered to Estimate Earthquake Rates in the Local Source Zone Based on the Updated UCERF3 Catalog and McLaren and Savage (2001)

Year	Month	Day	Magnitude M	Source	Latitude	Longitude	Use
1830	unk	unk	6	McLaren and Savage (2001)	35.35	–120.65	Uncertainty in rate $M \geq 6$
1913	10	20	5	McLaren and Savage (2001)	35.1	–120.7	Uncertainty in rate $M \geq 5$
1916	12	1	5	McLaren and Savage (2001)	35.2	–120.7	Preferred rate, $M \geq 5$
1931	07	21	4.0	Felzer (2013a)	35.25	–120.67	Preferred rate, $M \geq 4$
1980	12	22	4.19	Felzer (2013a)	35.3565	–121.001	Uncertainty in rate $M \geq 4$

Note: unk = unknown

Of these two, only one—the 1931 earthquake—is included in Table 13-6 to estimate the preferred rate of $M \geq 4.0$. The 1931 and 1980 earthquakes both may, within location uncertainties, be inside or outside the Local source zone. The date and magnitude of the 1931 M 4 earthquake is very close to the 1932 completeness date for $M \geq 4.1$ for the coastal region by Felzer (2013b), which suggests its inclusion to determine rates is questionable. The 1980 M_L 4.19 earthquake epicenter is on the Hosgri fault zone (Figure 13-5); its inclusion for consideration of Local source zone earthquake rates is likewise questionable. To incorporate this uncertainty, the TI Team lists a single event in Table 13-6—in 1931—for use estimating the rate of $M \geq 4$ earthquakes. The 1980 earthquake is listed in Table 13-6 as contributing to the uncertainty in the rate of $M \geq 4$ earthquakes. Figure 13-11 shows uncertainty bars that encompass the 5% and 95% probability levels given alternative historically observed values of 0, 1, or 2 $M \geq 4$ earthquakes.

For $M \geq 5$ earthquakes, the TI Team adopts the results of McLaren and Savage (2001). Their thorough review of historical events suggested that as many as three historical earthquake could have, within uncertainties, occurred within the Local source zone within the estimated period of completeness that started in 1870. These earthquakes are shown on Figure 13-5 and listed as follows:

- 1906 M 5.7 earthquake, located approximately 13 km west of the northern boundary of the source zone.
- 1913 M 5 earthquake, located approximately 2 km south of the southern boundary.

- 1916 *M* 5 earthquake, located within the southeastern portion of the source zone.

The magnitude of the 1922 *M* 5.5 earthquake identified in the updated UCERF3 catalog is judged to be in error, as it is not discussed by McLaren and Savage (2001) who researched historical earthquakes in the DCPP vicinity thoroughly. Of the three candidate earthquakes listed above, only one—the 1916 earthquake—is included in Table 13-6 to estimate the preferred Local source zone rate of $M \geq 5.0$ shown on Figure 13-11. The 1906 earthquake could, within location uncertainties, have occurred within the Local source zone limits. However, the preferred location northwest of the zone and its spatial association with the Hosgri fault zone suggest it probably did not occur within the Local source zone. The 1913 and 1916 earthquakes both may, within an estimated 10 km location uncertainty (McLaren and Savage, 2001), be located within or outside the Local source zone. Also, uncertainties in magnitude described by McLaren and Savage (2001) suggest that one or both may be less than *M* 5. To incorporate the location and magnitude uncertainties, Table 13-6 lists a single event—1916—as contributing to the preferred rate of $M \geq 5$ earthquakes. Figure 13-11 shows uncertainty bars that encompass the 5% and 95% probability levels given alternative historically observed values of 0, 1, or 2 $M \geq 5$ earthquakes.

For $M \geq 6$ earthquakes, the only candidate event near the Local source zone is the 1830 *M* 6 earthquake. This event is noted in the annual report from the San Luis Obispo mission, which described buildings in “bad condition” (McLaren and Savage, 2001). The absence of reports of this earthquake from missions north and south suggest the event was not a large magnitude. Given the location and magnitude uncertainty for this historical earthquake, Table 13-6 lists the 1830 earthquake as contributing to uncertainty in the rate of $M \geq 6$ earthquakes, but zero events is the preferred number within the completeness period since 1772 for purposes of Figure 13-11. Table 13-6 likewise does not list any earthquakes for $M \geq 7$, and the 95% uncertainty bar is plotted on Figure 13-11 to reflect this robust observation.

The TI Team judged that the six exponential distributions shown on Figure 13-11 represent a reasonable range of for assessing earthquake rates for the Local source zone based on their fit to the available data and given the available information about the likely range of *b*-values for the region. The values and weights given to the Gutenberg-Richter *a*- and *b*-values for each exponential distribution are provided in Table 13-7. These six pairs of *a*- and *b*-values incorporate two sources of epistemic uncertainty. The first is the choice of declustering approach. The PG&E catalog used the Reasenberg (1985) method, which classified very few dependent events. Based on inspection and the absence of moderate to large earthquakes in the interval from 1988 through 2013, the TI Team judged this to be a reasonable result. The UCERF3 catalog used the Gardner and Knopoff (1974) method (Felzer, 2013b), which classified many more earthquakes as dependent events (Figure 13-4). The TI Team also considered this to be a plausible result, and judged that the removal of a significant fraction of the events by the declustering method could also be considered a proxy for removing some of the catalog events that could be considered to have occurred on one of the identified Primary fault sources. Given the evaluations, the TI Team gave equal weight to the PG&E and updated UCERF3 catalogs.

Table 13-7. Alternative Gutenberg-Richter *a*- and *b*-Value Pairs and Weights for the Local Source Zone

Catalog	Weight	*a*-Value	*b*-Value	Weight	Combined Weight
PG&E	[0.5]	2.54	1.0	[0.3]	[0.15]
		2.24	0.9	[0.4]	[0.20]
		1.94	0.8	[0.3]	[0.15]
Updated UCERF3	[0.5]	2.29	1.0	[0.3]	[0.15]
		2.04	0.9	[0.4]	[0.20]
		1.79	0.8	[0.3]	[0.15]
					Sum = [1.0]

Although the range of *b*-values evaluated all fit the data to within uncertainties, there is a clear preference in the analysis of the Hardebeck (2014a) and updated UCERF3 catalogs for *b*-values near 0.9 to 1.0 and a lesser fit to the *b*-value of 0.8 (Figures 13-9c and 13-10b). The PG&E catalog had less resolution for assessing a preferred *b*-value (Figure 13-10a). A preference for *b*-values close to 1.0 is consistent with the most recent statewide evaluation by Felzer (2013b), and *b*-values higher than 0.8 were also preferred from the declustered data evaluated previously (Felzer, 2008). Nonetheless, the TI Team judged that the *b*-values of 0.8 could not be precluded given the limited available data and the potential for non-stationarity in the catalog (Figure 13-8). Thus, given the limitations of the data at larger magnitudes and the consistent use of $b = 0.8$ for the national seismic hazard maps, and potential non-stationarity, the TI Team judged that the value should be included in the credible range. For both catalogs, the three *b*-values of 1.0, 0.9, and 0.8 were given symmetric weights, provided in square brackets, of [0.3], [0.4], and [0.3], respectively (Table 13-7). Given the broad range of predicted rates of $M \geq 6$ and $M \geq 7$ earthquakes represented by the range of *a*- and *b*-value pairs in Table 13-7 (Figure 13-11), the TI Team judged that incorporating additional uncertainty in *a*-value was unnecessary.

13.5.2 Justification for the Virtual Fault Approach

Many recent geologic and geophysical investigations have focused on shallow and deep mapping of geology and faults near the DCPP and within the limits of the Local areal source zone (*Chapter 4*). Shallow onshore geologic mapping was most recently reviewed and revised by PG&E (2014, Chapter 9). Deeper mapping and interpretation of faults based on geologic, well, and seismic-reflection and tomographic data is presented in Chapters 7, 8, and 12 of PG&E (2014). Recent shallow offshore geologic mapping, based on high-resolution seafloor bathymetric and seismic-reflection data, is provided by PG&E (2011, 2013a), Johnson and Watt (2012), and Chapters 2, 3, and 4 of PG&E (2014). In addition, deeper mapping of possible faults within the Local source zone based on the analysis of focal mechanisms (Figure 13-12) and microseismicity trends is provided by Hardebeck (2010, 2013, 2014b), McLaren (2012), and Hamilton (2012b). Many of these studies are discussed in earlier chapters of this report and were considered

by the TI Team for the constraints they placed on the characterization of the Primary and Connected fault sources in the Diablo Canyon SSC model.

Nearly all these studies interpreted faults within the Local source zone that are not included in the list of Primary and Connected faults. For example, Hardebeck (2010) recognizes linear alignments of epicenters in Estero Bay northwest of the Irish Hills that are consistent with strike-slip motion on steeply dipping, north-northwest-trending faults (Figure 13-13). For another example, the San Miguelito and Edna fault zones are long-recognized and well-mapped Quaternary or late Cenozoic fault zones that are located in the Irish Hills on the southern and northern margins of the Pismo syncline, respectively (Plate 7-1); many more such faults have been interpreted within the Irish Hills (e.g., PG&E, 2014, Chapters 7 and 8).

The TI Team judged that considering these faults as seismic sources in the aggregate within an areal source zone was preferable to evaluating and characterizing each interpreted fault within the Local source zone individually. This judgment is based on the following considerations with regard to the interpreted faults within the Local source zone other than the four Primary faults:

- None were observed to clearly offset late Quaternary geologic deposits or geomorphic surfaces, and none are required to explain the late Quaternary vertical deformation rates within the Local source zone. Thus there is a first-order conclusion that the slip rate on any individual fault is low relative to the slip rates of the Primary fault sources.
- The majority are oriented relative to the current stress/strain field such that slip is permissible.
- The majority lack clear and unambiguous direct evidence to show that they are inactive faults, or are incapable of producing moderate-sized earthquakes at depth (i.e., earthquakes that may not have ruptured the ground surface).
- Many are interpreted using data or methods that are judged to be of uncertain validity or applicability.
- The uncertainties are so profound—where some of the interpreted faults may or may not exist as proposed—that modeling such faults as fault sources would add no meaningful information and lead to unnecessary source characterization complexity, including logic tree branches for probability of existence and probability of activity.

The TI Team also considers that modeling the Local areal source zone with virtual faults has the following advantages:

- As microseismicity patterns are the basis for many of the interpreted faults, using the rates of microseismicity to constrain the overall rate of the source zone has a logical consistency.
- Microseismicity within the Local source zone is arguably not on the Los Osos or San Luis Bay faults (Figures 13-2 through 13-4; Hardebeck, 2014b). Therefore, the virtual faults represent alternative, plausible structures that may be hosting the microseismicity.

13.5.3 Virtual Fault Sense of Slip, Geometry, and Maximum Magnitude

The characterization of sense of slip and geometry assigned to the virtual faults in the Local source zone is based on the kinematics of the Local source zone, the orientation of faults interpreted within the source zone, and the characterization of the Primary fault sources in the Diablo Canyon SSC model. Sense of slip information was provided from single-event (Figure 13-12) and composite (Figure 13-13) focal mechanisms from Hardebeck (2010, 2011, 2014b), with additional data and analysis presented at Workshop 1 (McLaren, 2011), Workshop 2 (McLaren, 2012), and Workshop 3 (Lewandowski, 2014; PG&E, 2015b).

Interpreted fault orientations within the Local source zone considered by the TI Team included those based on microseismicity, mainly by Hardebeck (2010, 2014b). Uncertainties in location, strike, and dip included with these analyses bound alternative interpretations of microseismicity presented at Workshop 2 (McLaren, 2012; Hamilton, 2012b). The subvertical seismicity alignments interpreted in Estero Bay by Hardebeck (2010; Figure 13-13) appear to be based on visual inspection. At Workshop 3, Dr. Jeanne Hardebeck (2014b) evaluated her double-difference relocated seismicity (Hardebeck, 2014a) in Estero Bay and the Irish Hills for evidence of laterally continuous faults. Previously, Hardebeck (2013) used an algorithm called optimal anisotropic dynamic clustering (OADC; Ouillon et al., 2008) to evaluate the geometry of the Hosgri and Shoreline faults through the seismogenic crust, with the stated advantage that it provides an objective means of evaluating planar fits to data based on earthquake distances. The OADC analysis of the Shoreline and Hosgri fault zone seismicity was relatively straightforward, because of a clear spatial relationship between the relatively abundant seismicity along these steeply dipping faults and the relative absence of seismicity in areas adjacent to the faults. In contrast, this quantitative analysis of alignments of seismicity within the Local source zone, where seismicity is diffuse and there are a variety of slip types, is more problematic.

The Hardebeck (2014b) analysis used a modification of the OADC algorithm, called OADC-FM, which constrains planar fits to earthquakes based on focal mechanism information as well as distance. The OADC-FM algorithm fits planes to an earthquake data set using earthquake distance and misfit of *P*-wave first-motion polarities (Hardebeck, 2014b). Dr. Hardebeck identified several candidate planar alignments of seismicity beneath Estero Bay (Figure 13-14) and the Irish Hills (Figure 13-15) that were repeatable solutions in her OADC-FM inversion. The TI Team's review of these solutions after Workshop 3 found that the planar solutions from repeated OADC-FM runs had the following characteristics:

- In contrast to successes on the Shoreline and Hosgri faults, most OADC-FM planes did not convincingly represent a preferred alignment of hypocenters based on visual inspection.
- Solutions tended to vary significantly within the Irish Hills, and be less repeatable than for recognizable planes such as in Estero Bay.

- The locations and dip directions of the dipping planes, if allowed to slip, did not appear to be related to observed geomorphic patterns of uplift, such as the pattern of coastal marine terrace uplift (e.g., Figure 7-4).
- Adjacent planes commonly align poorly with their neighbors.

The TI Team had other more general concerns about the OADC-FM method. First, repeatability of plane identification across multiple Monte Carlo trials is not a true measure of reliability of the result in terms of geologic structure. Second, there is no way to tell which planes are properly individual surfaces versus being only locally planar and spatially extended by spurious correlation. False positive correlations can be expected since large portions of the stress field are aligned and thus will align focal mechanisms. Third, the approach does not appear to adequately evaluate the alternative hypothesis that a set of earthquake hypocenters may be semi-random and actually better characterized by volumetric compression and horizontal shortening.

The TI Team did not find the OADC-FM results to convincingly or conclusively reveal the locations of laterally continuous faults beneath the Irish Hills. At the same time, the TI Team found that the OADC-FM method and results offered plausible fault geometries and slip senses to consider that, by design, were compatible with the current style of deformation within the study area and thus could be used to model uncertain fault locations and geometries within the Local source zone. The TI Team noted that these orientations are consistent with fault orientations predicted from the results of analyses of regional patterns of stress and strain (Lewandowski, 2014, presentation at Workshop 3; PG&E, 2015b; Figure 5-12). Based on the lack of association between the fault locations and slip directions determined by the OADC-FM method and geomorphic expression of active tectonic deformation, the TI Team also concluded that such faults, if present, would likely have slip rates lower than the slip rates on the Primary and Connected fault sources.

Faults within the Local source zone were also interpreted from geologic maps, wells, potential-field geophysics, and seismic-reflection data recently collected as part of the Central Coastal California Seismic Imaging Project (CCCSIP; PG&E, 2014, Chapters 7, 8, 9, and 12). Figure 13-16 is a geologic map of the Irish Hills (PG&E, 2014, Chapter 9) that shows the locations of wells drilled for oil and gas exploration. In addition to the mostly northwest-trending faults mapped at the surface within the Irish Hills, Figure 13-16 shows the approximate location of buried high-angle faults interpreted from the geologic, well, and 2D land seismic-reflection data within the Tertiary units of the Pismo syncline (pink dots; locations taken from PG&E, 2014, Chapter 7). These buried faults were interpreted to strike northwest, subparallel to the trend of folds and faults mapped at the surface.

Figure 13-17 presents an interpretive cross section cut perpendicular to strike (line C-C′ on Figure 13-16) and shows the faults as high-angle Miocene normal faults that coalesce beneath the Irish Hills though the seismogenic crust. These faults were interpreted to have slipped more recently with a reverse component, suggesting that many of the anticlines mapped at the surface are in the hanging walls of the faults (PG&E, 2014,

Chapter 7). The TI Team notes that the traces of the buried faults on Figure 13-16 and their location and dip in cross section on Figure 13-17 are subject to considerable uncertainty. In addition, the seismic-reflection and well data used to develop the cross section on Figure 13-17 were resolved only to the upper few kilometers; the configuration of the faults through most of the seismogenic crust is a geologic model based on judgment and simple tests of permissibility (PG&E, 2014, Chapter 7). The TI Team judges that the definition of structures in the seismic reflection data was not sufficient for prescriptive use in seismic source characterization, echoing similar concerns expressed by the authors of Chapter 7 of PG&E (2014). At the same time, the TI Team judges that the general solution and geologic model basis for interpreting the Pismo syncline and the Irish Hills as a structure related to an inverted Miocene graben is permissible and consistent with surface geologic and well data. Thus the interpreted trend and steep dips of the faults were considered by the TI Team in developing the virtual fault geometries.

Table 13-8 shows the geometric and sense of slip parameters adopted for the virtual faults, based on the TI Team's review of interpreted faults within the Local source zone. The style of faulting for the Local source zone is modeled with aleatory variability. Strike-slip faulting occurs with 70% frequency and reverse faulting occurs with 30% frequency. The rationale behind the relative frequency values is based on the observation from focal mechanisms (Figure 13-8) that both strike-slip and reverse senses of slip are common in the Local source zone, but the Primary fault sources already account for the recognized vertical deformation within the source zone through the vertical component of slip rate on the Los Osos and San Luis Bay faults (*Sections 8.5 and 8.6*). Although slip rate constraints are available on the Shoreline fault source (*Section 8.4*), and a component of lateral slip rate is placed on the Los Osos fault source (*Section 8.5*), there are no fault sources in the SSC model that expressly accommodate the horizontal strike-slip deformation indicated by dextral focal mechanisms within the Irish Hills and Estero Bay. In recognition of this less well-constrained component of slip that is not accommodated by fault sources in the SSC model, the TI Team allocated a substantially higher (70%) rate of deformation for the Local areal source zone to the cases of strike-slip style of faulting, and a lesser (30%) rate to the cases of reverse style of faulting.

Table 13-8. Style of Faulting and Geometry Parameters for Virtual Faults

Parameter	Value	Weight	Value	Weight
Style of faulting (frequency)	Strike-slip (70%)		Reverse (30%)	
Fault length and spacing	50 km long, 1 km spacing		50 km long, 1 km spacing	
Fault strike	N50°W	1.0	N50°W	1.0
Dip	90°	0.4	70°	0.25
	75°	0.4	55°	0.5
	65°	0.2	35°	0.25
Dip direction (frequency)	NE (50%)		NE (50%)	
	SW (50%)		SW (50%)	

The virtual faults are modeled as 18 subparallel 50 km long faults striking N50°W, with a spacing of 1 km (Figure 13-18). Coordinates for the virtual faults are provided in *Appendix C*. The DCPP is located halfway between two virtual faults. A single fault strike was selected for the sake of simplicity and to maximize the length of the faults that would approximately fit within the Local source zone. The TI Team notes that this orientation is oblique to the faults mapped within the Irish Hills (Figure 13-16) and subparallel to faults interpreted in Estero Bay (Figures 13-13 and 13-14). Each style of faulting has an associated range of fault dips and dip directions that are summarized in Table 13-8. The values for fault dip for strike-slip faulting cases, with the weights provided in square brackets, are 90° [0.4], 75° [0.4], and 65° [0.2]. The greater weight given to the two steeper dips is based on the seismicity alignments in Estero Bay interpreted by Hardebeck (2010, 2014b), the steep dips on interpreted faults bounding and beneath the Pismo syncline as interpreted in Chapter 7 of PG&E (2014), and the steep dips measured for the Shoreline and Hosgri faults (Hardebeck, 2013; *Chapter 7*). The values, with weights provided in square brackets, for fault dip for reverse faulting cases are 70° [0.25], 55° [0.5], and 35° [0.25]. The values and range are consistent with the interpretations of Hardebeck (2014b) for the Irish Hills (Figure 13-15), and the steepest dip is consistent with the fault geometries interpreted beneath the Irish Hills in Chapter 7 of PG&E (2014). The dip direction of the virtual faults is modeled with aleatory variability, with equal 50/50 frequency for northeast- and southwest-dipping faults.

The M_{max} values for the Local source zone are shown in Table 13-9. Earthquakes larger than the M_{max} values in Table 13-9 within the Local areal source zone occur on the Primary fault sources in the SSC model (*Chapter 10*). The three branch values and weights developed for each style of faulting case were estimated based on consideration of the maximum dimensions of the virtual faults and the orientations and continuity of structures mapped and hypothesized within the Local source zone (e.g., Figures 13-13 through 13-16). The middle M_{max} values of 6.8 and 6.9 for the strike-slip and reverse-slip cases are based on rupture of the full 50 km virtual fault length, a rupture width based on a 12 km crustal thickness and a dip equal to the middle values in Table 13-8, and the empirical $\mathbf{M}$–$\log_{10}A$ scaling relation of HB14 (Equation 10-1). The middle branch values are given weights of 0.5 to reflect the TI Team's judgment that the 50 km length of the

virtual faults (with an average stress drop, represented by the median value of **M** from Equation 10-1) represents the most probable maximum earthquake within the Local source zone that could occur off of a recognized, Primary fault source (Table 13-9).

Table 13-9. Maximum Magnitude Logic Tree Parameters for the Local Source Zone

Parameter	Value	Weight	Value	Weight
Style of faulting (frequency)	Strike-slip (70%)		Reverse (30%)	
Maximum magnitude (M_{max})	7.0	0.25	7.1	0.3
	6.8	0.5	6.9	0.5
	6.6	0.25	6.7	0.2

The high M_{max} values of 7.0 and 7.1 for the strike-slip and reverse-slip cases, respectively, are based on Equation (10-1), with additional 0.2 magnitude units added to represent the epistemic uncertainty that the maximum earthquake consists of full rupture of the virtual faults with a higher than average stress drop. The value of 0.2 magnitude units above the median predicted value of **M** from *A* is the approximate standard deviation in **M**-log*A* scaling relations (Wells and Coppersmith, 1994). The low M_{max} branch values of 6.6 and 6.7 for the strike-slip and reverse-slip cases, respectively, are based on considering a 30 km maximum length for earthquakes in the Local source zone, a full rupture width of the virtual faults, and Equation (10-1). The maximum rupture length that is less than the full 50 km long virtual fault length is based on the TI Team's judgment that it is plausible that faults within the Local source zone other than the Primary fault sources are not sufficiently integrated and capable of producing ruptures that exceed an approximate length of 30 km—a length that coincides with the long dimension of the Irish Hills and parts of adjacent areas. Weights assigned to the high and low M_{max} branch values differ slightly for the two style of faulting categories (Table 13-9). Symmetric weights of 0.25 are assigned to the high and low branch values for the strike-slip style of faulting case because similar maximum rupture areas—and hence M_{max} estimates—result for all branch values of virtual fault dip. The asymmetric weights of 0.2 for the low branch and 0.3 for the high branch values for the reverse-slip style of faulting case are based on the asymmetrically larger M_{max} values that result from gentler fault dips and the resulting wider maximum rupture areas as compared to the lower M_{max} values from steeper fault dips. For the sake of simplicity, the TI Team decided not to correlate the logic trees on M_{max} values for the Local source zone with virtual fault dip.

13.5.4 Discussion of the Local Areal Source Zone

The complete logic tree for the Local areal source zone is presented on Figure 13-19. The logic tree highlights the aleatory uncertainty for style of faulting and dip direction, and the epistemic uncertainty for *a*- and *b*-values, M_{max}, and virtual fault dip. The location of the virtual faults shown on Figure 13-18 also represents aleatory uncertainty in the Local source zone model.

The equivalent slip rates for the virtual faults (i.e., the sum of slip rates calculated across all the virtual faults) can be estimated based on the information in Tables 13-7, 13-8, and 13-9. The slip rate is estimated based on the assumption that the moment rate from the modeled seismicity ($\dot{M}_{o,s}$, determined from the *a*, *b*, and M_{max} values) is equal to the moment rate on the virtual faults, $\dot{M}_{o,f}$, or

$$\dot{M}_{o,s} = \dot{M}_{o,f} \tag{13-4}$$

The moment rate from the modeled seismicity is calculated using the Gutenberg-Richter relationship (Equation 13-1) and calculating the incremental rate of earthquakes, *n*, from a defined minimum magnitude M_{min} to M_{max}. For this analysis, we use steps of 0.01 magnitude units to calculate *n*, with an M_{min} of 0 and an M_{max} from Table 13-9, and assume the magnitude scale is moment magnitude, **M**. The incremental rate of earthquakes *n* at a given magnitude **M** is given by the equation

$$n = 10^{(a-b(\boldsymbol{M}-0.005))} - 10^{(a-b(\boldsymbol{M}+0.005))} \tag{13-5}$$

For each magnitude step *i*, the moment rate is calculated by multiplying the incremental rate, *n*, by the seismic moment for the step, $M_{o,i}$, using the definition of moment magnitude (Hanks and Kanamori, 1979) rearranged to solve for seismic moment (in dyne centimeters):

$$M_o = 10^{3/2(10.7+\boldsymbol{M})} \tag{13-6}$$

The total moment rate for the source is then

$$\dot{M}_{o,s} = \sum_{i=M_{min}}^{i=M_{max}} n_i M_{o,i} \tag{13-7}$$

The total moment rate for the source based on parameters in Table 13-4 may then be modeled to occur on the virtual faults. To do this, we consider a single virtual fault with a moment rate equal to

$$\dot{M}_{o,f} = \mu A \dot{s} \tag{13-8}$$

where μ is the shear modulus and is assumed to equal 3×10^{11} dynes per square centimeter (cm^2), *A* is the fault area in cm^2, and $\dot{s}$ is the slip rate of the fault in centimeters per year (Brune, 1968).

Rearranging Equation (13-8) and substituting the fault moment rate for the seismic moment rate (Equation 13-4) yields the following equation for the fault slip rate:

$$\dot{s} = \frac{\dot{M}_{o,s}}{\mu A} \tag{13-9}$$

Equation (13-9) was implemented to calculate equivalent slip rates for the virtual faults using parameters in Tables 13-7, 13-8, and 13-9. Three equivalent slip rates are shown in Table 13-10 for three combinations of the *a*- and *b*-value pairs and M_{max} values, with separate results according to style of faulting. The three *a*- and *b*-value pairs from Table 13-7 used in the calculations are as follows:

- a = 1.94, b = 0.8, representing the parameters yielding the highest rate of **M** ≥ 5 earthquakes in the Local source zone, named "High rate" in Table 13-10.
- a = 2.29, b = 1.0, representing the parameters yielding the lowest rate of M ≥ 5 earthquakes in the Local source zone, named "Low rate" in Table 13-10.
- a = 2.24, b = 0.9, representing parameters that yield a middle rate of M ≥ 5 earthquakes in the Local source zone, which approximates a weighted average rate across the 6 alternative a- and b-value pairs, named "Middle rate" in Table 13-10.

Table 13-10 shows results with the high rate combined with the high M_{max} values from Table 13-9, the middle rate combined with the middle M_{max} values, and the low rate combined with the low M_{max} values. The tabulated results show the range and approximate weighted average equivalent slip rates for the virtual faults.

Table 13-10. Equivalent Slip Rates of the Virtual Faults in the Local Source Zone

	Strike-Slip Cases (70%)	Reverse Cases (30%)
Logic Tree Combination*	**Slip Rate† (mm/yr)**	**Slip Rate† (mm/yr)**
High rate, high M_{max}	0.34	0.14
Middle rate, middle M_{max}	0.13	0.05
Low rate, low M_{max}	0.03	0.01

* Weighted average of the dip combinations are tabulated; Logic tree values and weights are provided in Tables 13-7 to 13-9 and on Figure 13-19.
† Slip rates represent the sum of the slip rates across all virtual faults within the style of faulting category.

Fault area A was derived using the 50 km length of the virtual faults and the fault width W, based on $W = T\sin(\delta)$, where T = 12 km (seismogenic thickness) and δ = dip. In Table 13-10, for the sake of simplicity, we report the weighted average slip rate values across all dip values. The tabulated values give the equivalent slip rate for all virtual faults by sense of slip. The equivalent slip rate on any one realization of a virtual fault would be equal to the slip rates in one column of Table 13-10 divided by 36 (based on the 18 virtual fault locations and two alternative dip directions).

Table 13-10 shows that the average equivalent slip rate for the virtual faults is approximately 0.13 mm/yr for the strike-slip cases (representing 70% frequency for the virtual faults) and approximately 0.05 mm/yr for the reverse-slip cases (representing 30% frequency). The range in equivalent slip rates is on the order of a factor of 10 for each style of faulting. The approximate weighted average slip rate for strike-slip cases of 0.13 mm/yr is approximately two times the weighted average slip rate of 0.07 mm/yr for the Shoreline fault source (*Section 8.4*), which implies that the virtual faults host, on average the equivalent of two additional Shoreline fault sources spaced across the Local source zone. Within the range of 0.34 to 0.03 mm/yr, the virtual faults may host as many as approximately 5 additional Shoreline fault sources or as few as one-half. The TI Team

believes this provides a reasonable range of additional strike-slip motion that may be occurring across the Local source zone that would not be clearly expressed geomorphically or may be missed geologically.

The weighted average slip rate of 0.05 mm/yr for the reverse-slip cases represents approximately one third of the San Luis Bay fault slip rate of 0.16 mm/yr in the Outward-Vergent model (*Section 8.6*). The range of slip rates for the reverse-slip cases of 0.14 to 0.01 mm/yr implies that, at most, the equivalent of another San Luis Bay fault may be distributed across the areal source zone. Using the range of dips from Table 13-8 and the average 0.05 mm/yr reverse-slip rate for the virtual faults suggests that the Local source zone produces an additional 0.03 to 0.05 mm/yr of differential uplift rate across the source zone. This range represents approximately 15% to 25% of the approximately 0.2 mm/yr differential uplift rate measured from the coastal late Pleistocene marine terraces (Hanson et al., 1994; *Section 8.5*), and, in the TI Team's judgment, represents a reasonable upper limit of what may be undetected vertical deformation within the Local source zone.

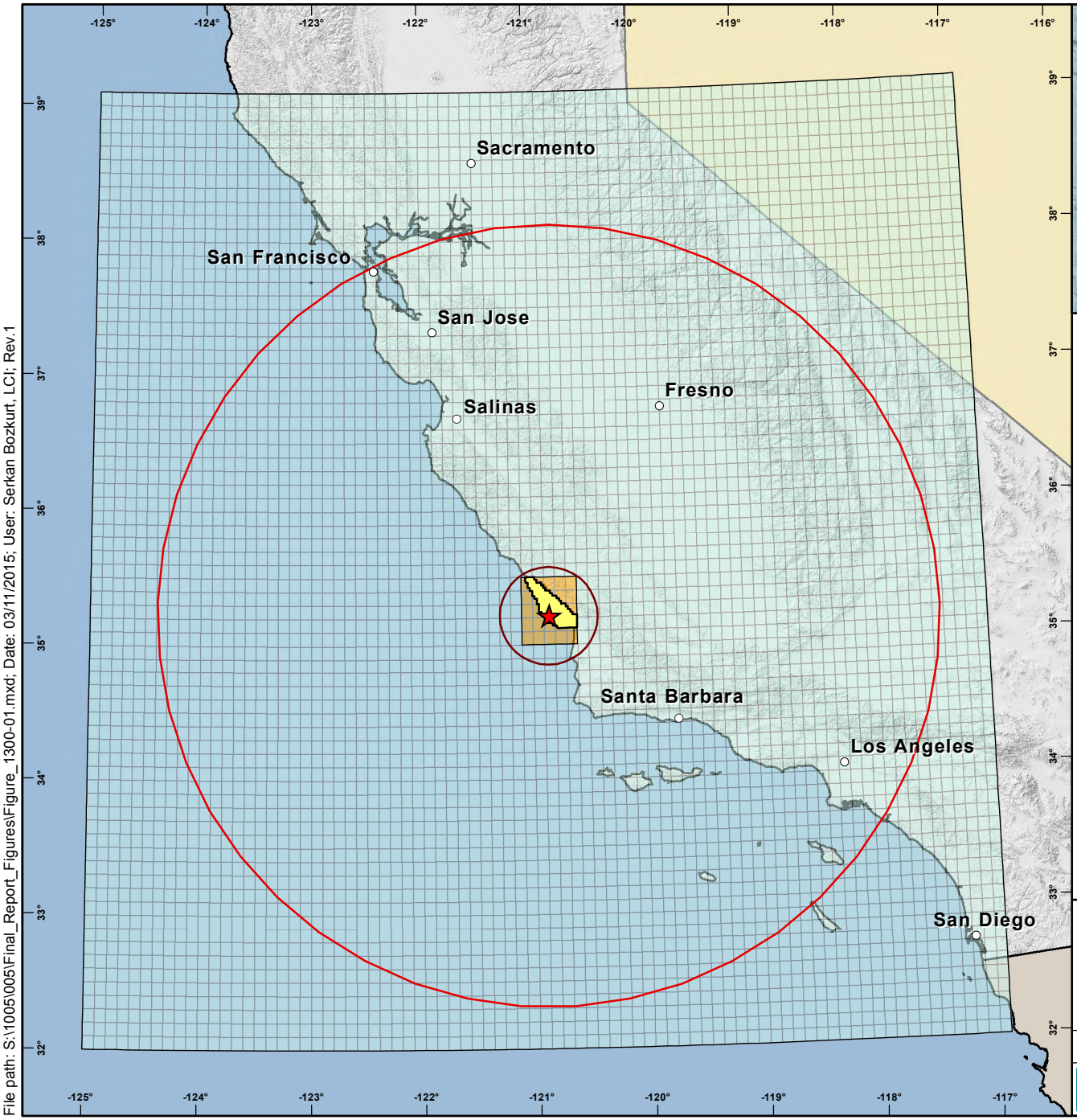

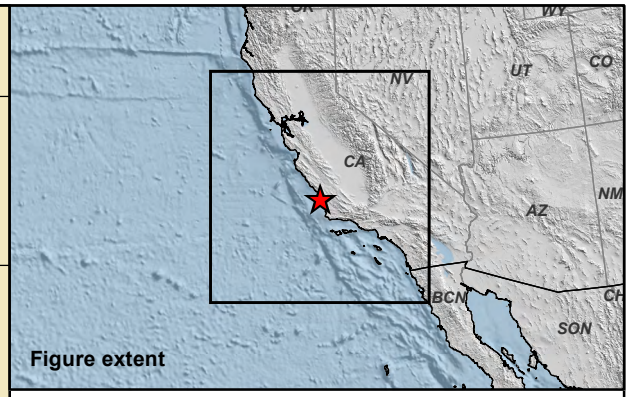

EXPLANATION

- DCPP
- 40 km (25 mi.) DCPP site vicinity boundary
- 320 km (200 mi.) DCPP site region boundary
- Local areal source zone
- Vicinity areal source zone
- Regional areal source zone

Note: 0.1° grid from the 2008 National Seismic Hazard Mapping Project (Petersen, Frankel, et al., 2008).

N

0 50 100 mi.

0 100 200 km

Map projection and scale: WGS 84 / UTM 10N, 1:5,000,000

Areal Source Zones Used in the Diablo Canyon SSC Model

DCPP SSC REPORT

Pacific Gas and Electric Company

Figure **13-1**

File path: S:\1005\005\Final_Report_Figures\Figure_1300-01.mxd; Date: 03/11/2015; User: Serkan Bozkurt, LCI; Rev.1

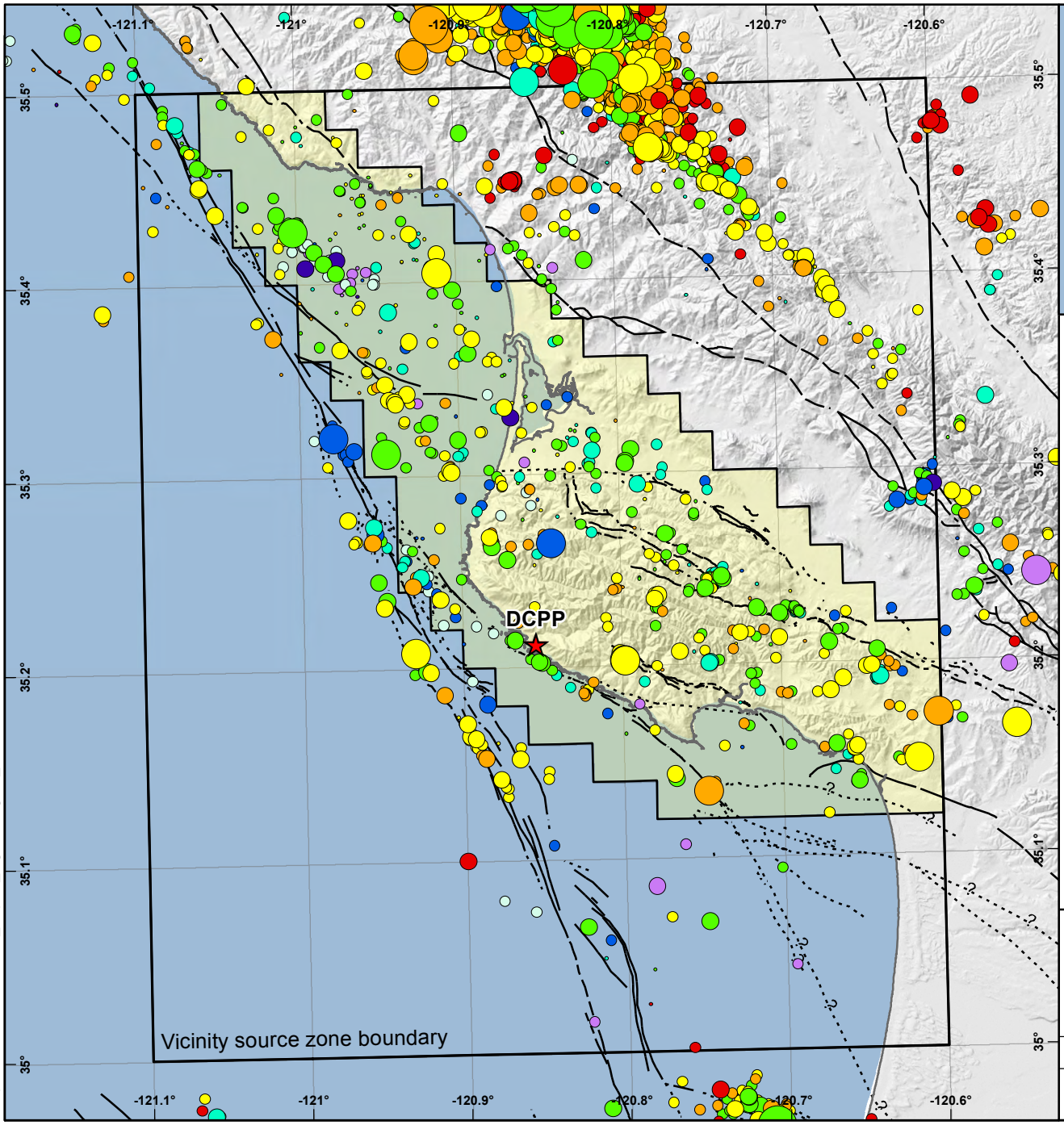

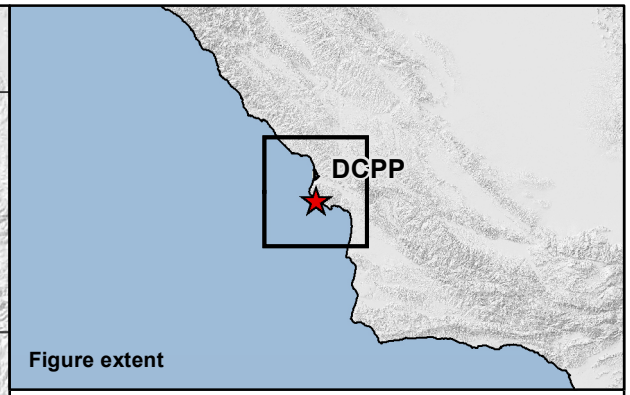

EXPLANATION

- DCPP
- Vicinity source zone
- Local source zone
- Quaternary fault trace; solid where well located, dashed where approximately located, dotted where buried, short dashed where inferred, queried where existence is uncertain.

Seismicity (Hardebeck, 2014a)

Depth (km)		Magnitude	
0.0–1.9	8.0–9.9	0.0–0.9	3.0–3.9
2.0–3.9	10.0–11.9	1.0–1.9	≥4.0
4.0–5.9	12.0–13.9	2.0–2.9	
6.0–7.9	14.0 +		

N

0 2 4 mi.

0 5 10 km

Map projection and scale: WGS 84 / UTM 10N, 1:350,000

Seismicity Oct. 1987 – Dec. 2013 from Hardebeck (2014a) Within the Vicinity and Local Areal Source Zones

DCPP SSC REPORT

Pacific Gas and Electric Company | Figure **13-2**

File path: S:\1005\005\Final_Report_Figures\Figure_1300-02.mxd; Date: 03/04/2015; User: Alex Remar, LCI; Rev.1

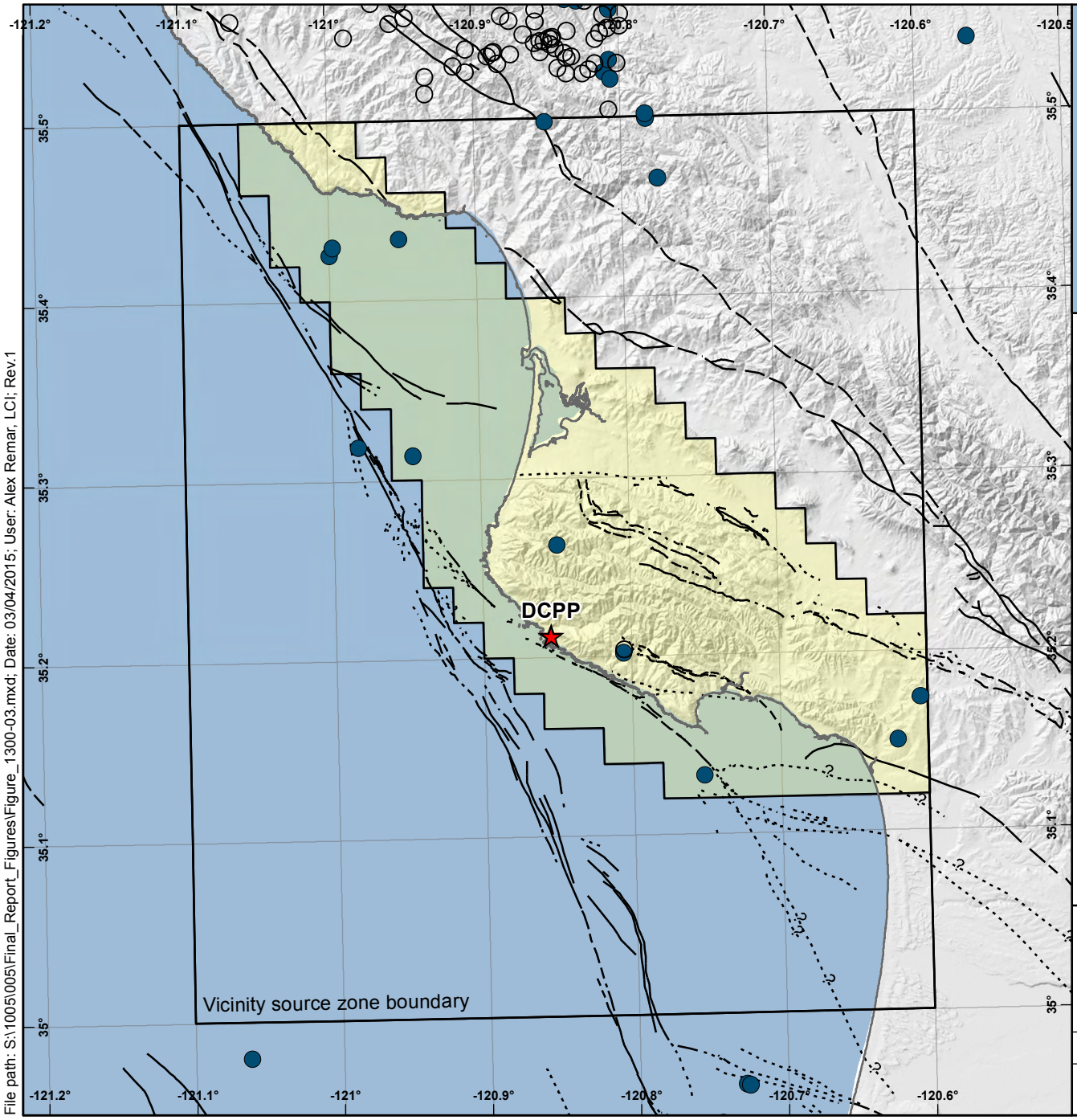

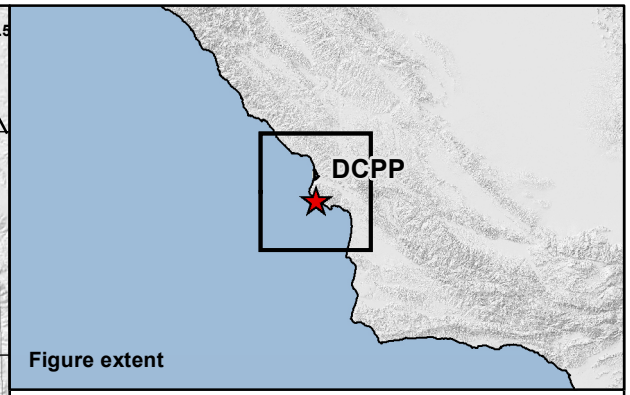

EXPLANATION

- DCPP
- Vicinity source zone
- Local source zone
- Quaternary fault trace; solid where well located, dashed where approximately located, dotted where buried, short dashed where inferred, queried where existence is uncertain.

Seismicity (from the PG&E catalog)
magnitude **M** ≥ 3.0

- Independent event
- Dependent event (foreshock or aftershock)

N

0 2 4 mi.
0 5 10 km

Map projection and scale: WGS 84 / UTM 10N, 1:375,000

Seismicity Jan. 1988 – Dec. 2013 from the PG&E Catalog Within the Vicinity and Local Areal Source Zones

DCPP SSC REPORT

Pacific Gas and Electric Company | Figure **13-3**

File path: S:\1005\005\Final_Report_Figures\Figure_1300-03.mxd; Date: 03/04/2015; User: Alex Remar, LCI; Rev.1

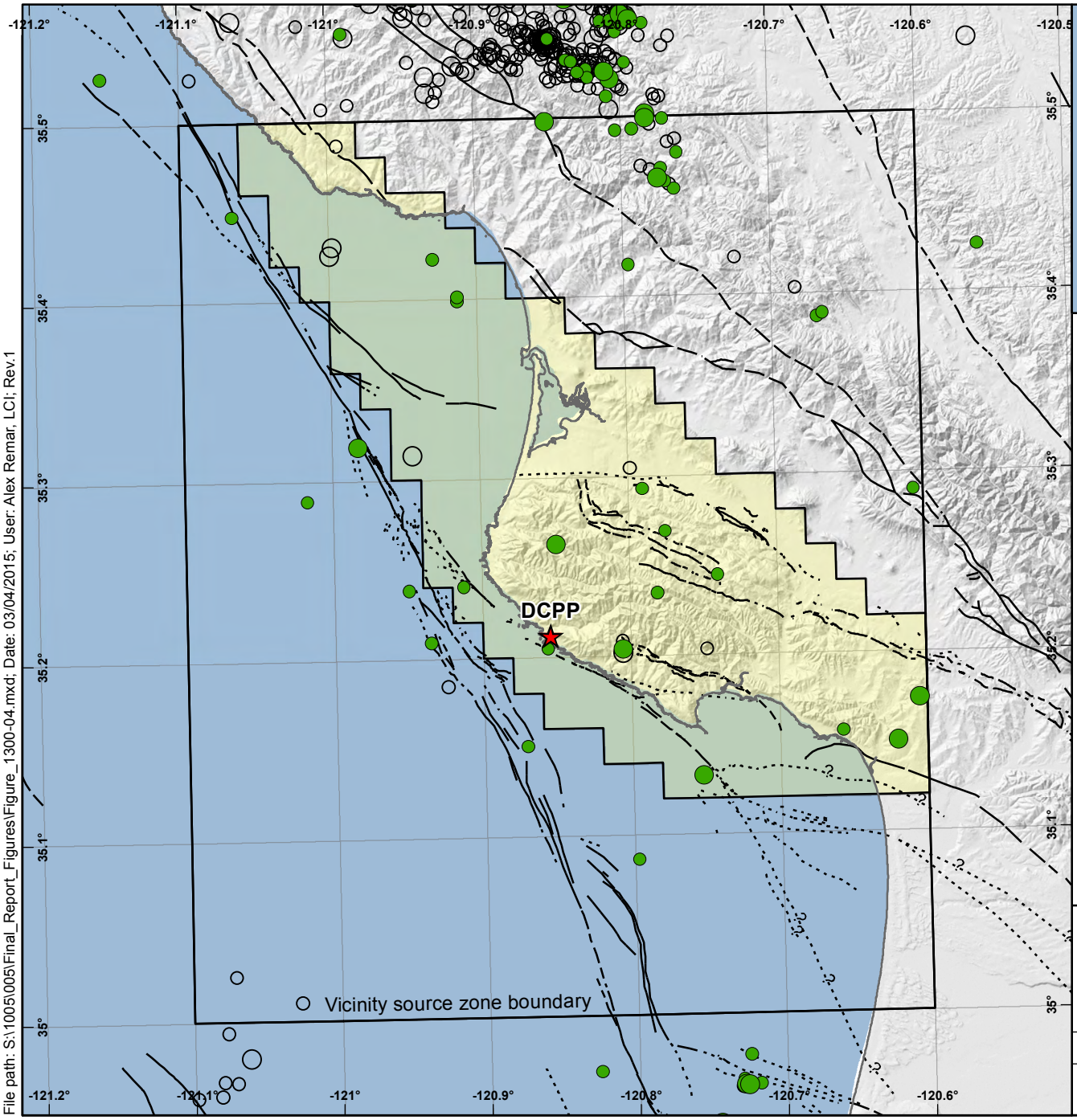

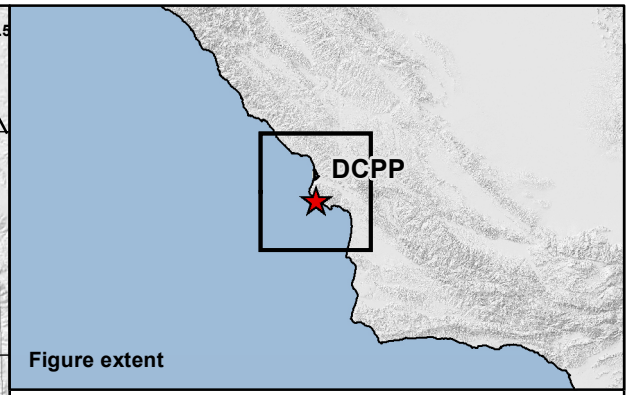

EXPLANATION

- DCPP
- Vicinity source zone
- Local source zone
- Quaternary fault trace; solid where well located, dashed where approximately located, dotted where buried, short dashed where inferred, queried where existence is uncertain.

Seismicity (from the updated UCERF 3 catalog)

$2.5 \le M \le 3.0$	$M \ge 3.0$
Independent event	Independent event
Dependent event (foreshock or aftershock)	Dependent event (foreshock or aftershock)

N

0 2 4 mi.

0 5 10 km

Map projection and scale: WGS 84 / UTM 10N, 1:375,000

Seismicity Jan. 1988 – Dec. 2013 from the Updated UCERF3 Catalog Within the Vicinity and Local Areal Source Zones

DCPP SSC REPORT

Pacific Gas and Electric Company

Figure **13-4**

File path: S:\1005\005\Final_Report_Figures\Figure_1300-04.mxd; Date: 03/04/2015; User: Alex Remar, LCI; Rev.1

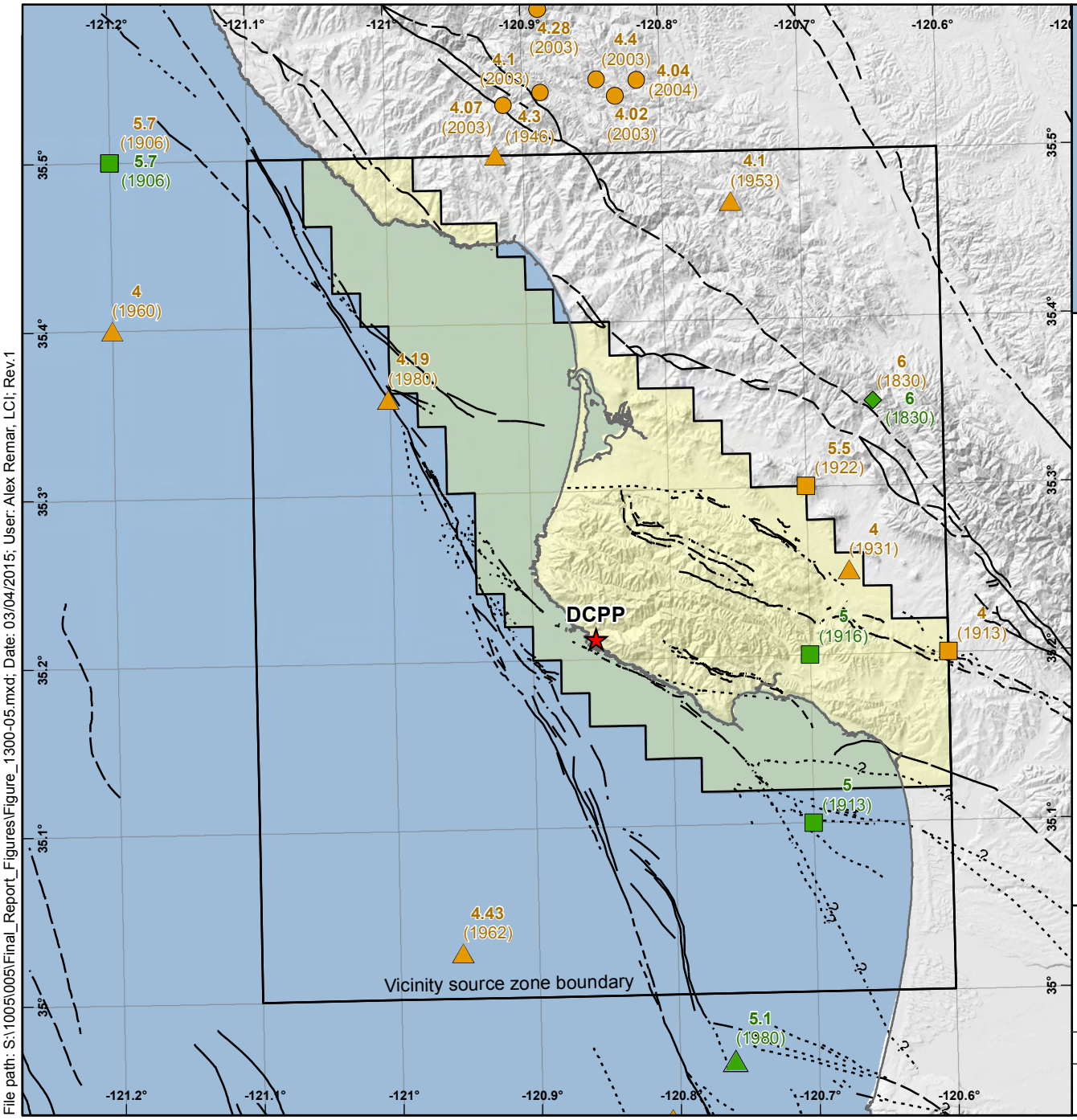

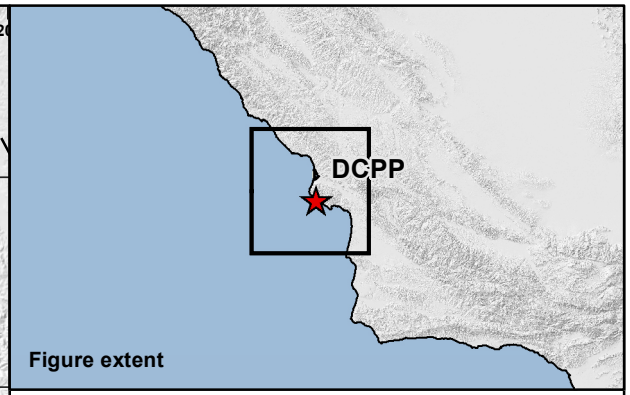

EXPLANATION

- DCPP
- Vicinity source zone
- Local source zone
- Quaternary fault trace; solid where well located, dashed where approximately located, dotted where buried, short dashed where inferred, queried where existence is uncertain.

Seismicity (M ≥ 4.0)

year

- 1988–2013
- 1932–1987
- 1870–1931
- 1772–1869

Note: Events in brown from McLaren & Savage (2001), green from updated UCERF3 catalog.

N

0 4 8 mi.

0 10 20 km

Map projection and scale: WGS 84 / UTM 10N, 1:400,000

Seismicity M ≥ 4 in the Vicinity and Local Areal Source Zones since 1830 from the Updated UCERF3 Catalog and McLaren and Savage (2001)

DCPP SSC REPORT

Pacific Gas and Electric Company

Figure **13-5**

File path: S:\1005\005\Final_Report_Figures\Figure_1300-05.mxd; Date: 03/04/2015; User: Alex Remar, LCI; Rev.1

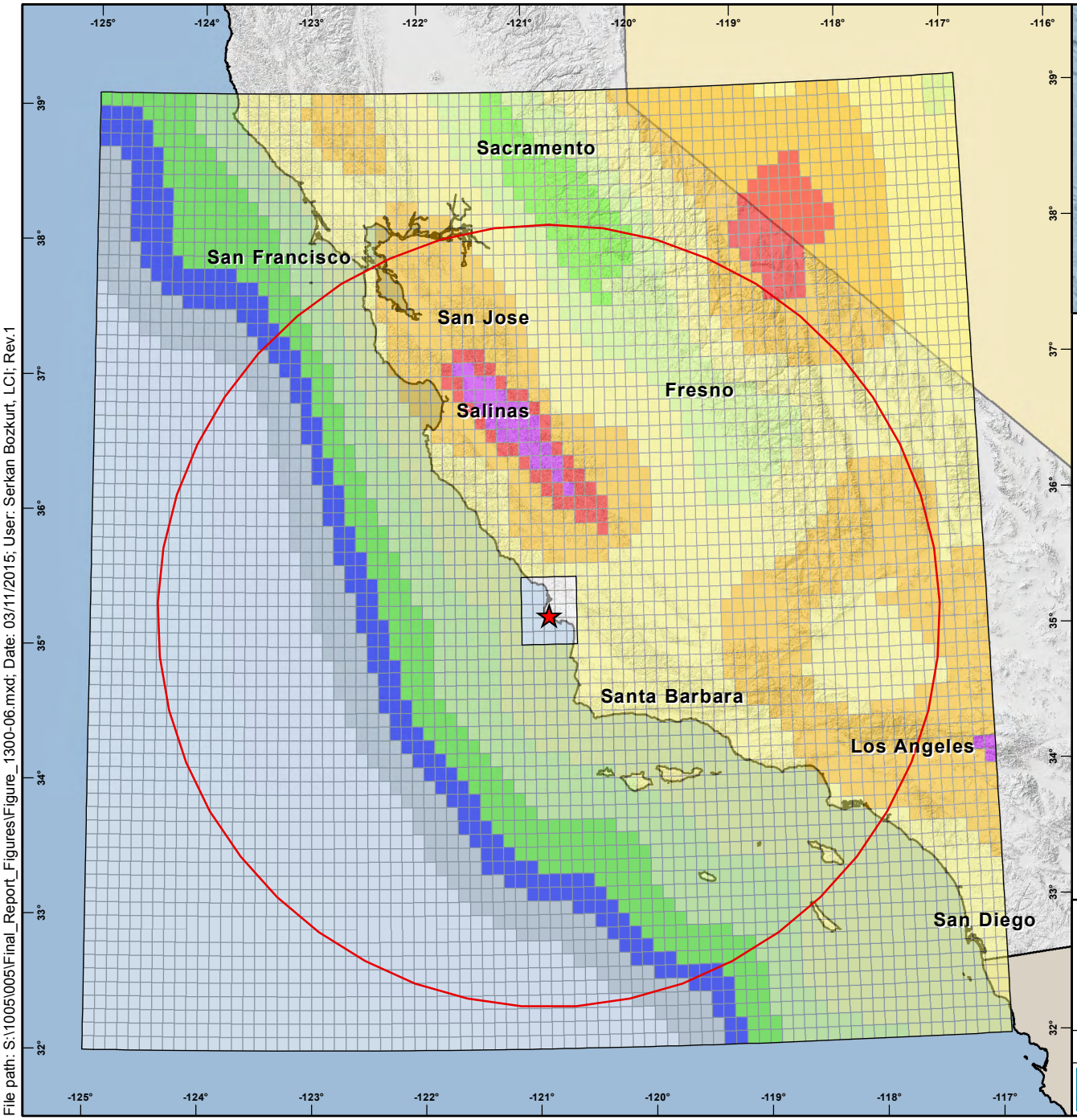

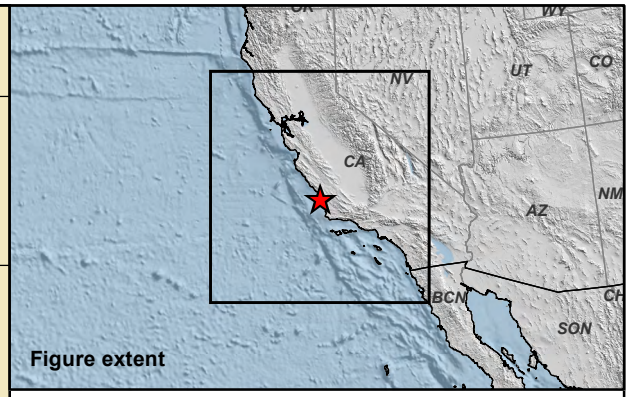

EXPLANATION

DCPP

320 km (200 mi.) DCPP site region boundary

Regional areal source rate (0.1° grid)

- 50
- 10
- 3
- 1
- 0.3
- 0.1
- 0.03
- 0.01
- 0.001
- 0.000

Note: Grid and rates from Petersen, Mueller, et al. (2008).

N

0 50 100 mi.

0 100 200 km

Map projection and scale: WGS 84 / UTM 10N, 1:5,000,000

Regional Areal Source Zone Showing 0.1° Gridded Seismicity Rates from the 2008 NSHMP

DCPP SSC REPORT

Pacific Gas and Electric Company

Figure **13-6**

File path: S:\1005\005\Final_Report_Figures\Figure_1300-06.mxd; Date: 03/11/2015; User: Serkan Bozkurt, LCI; Rev.1

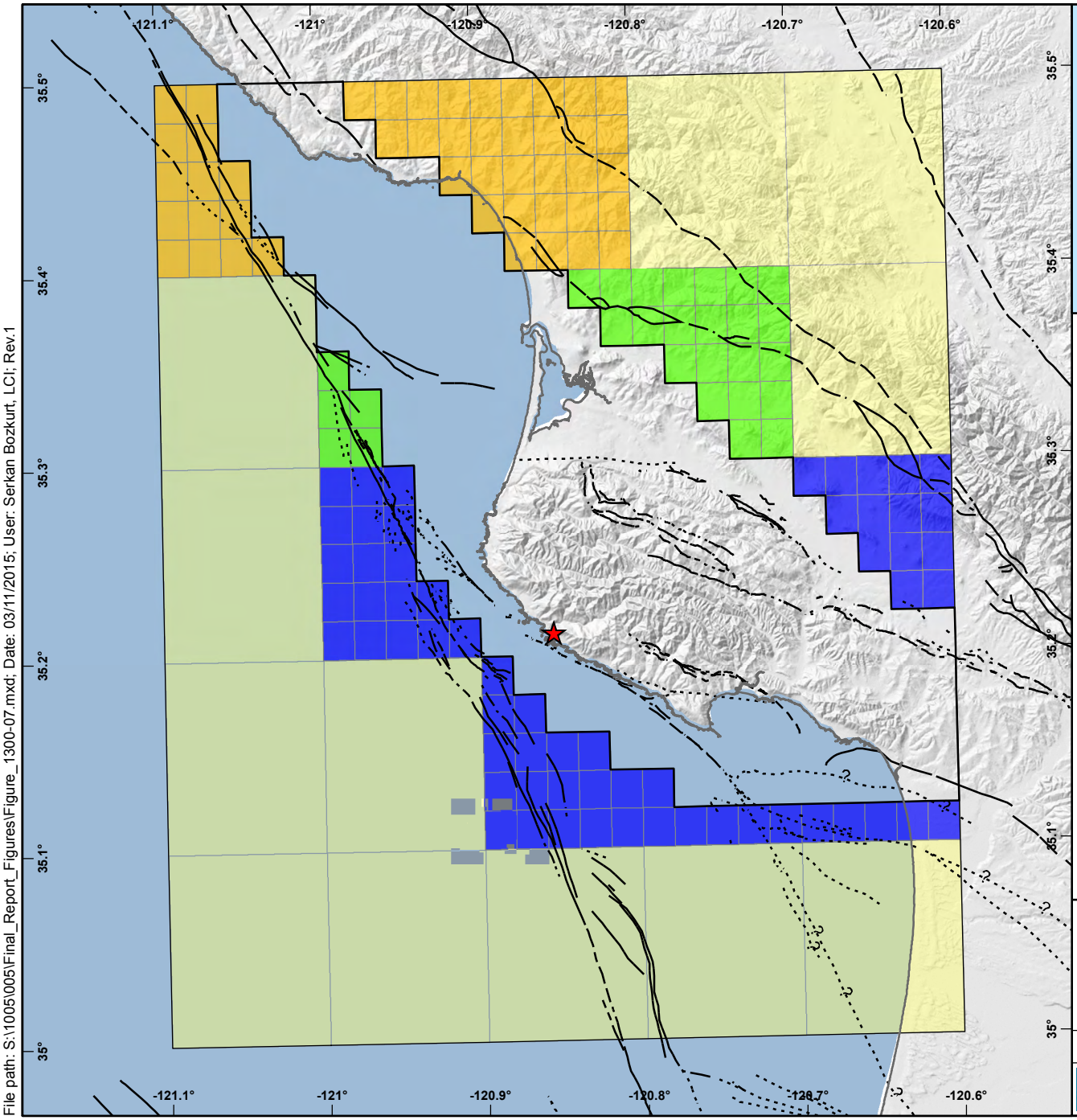

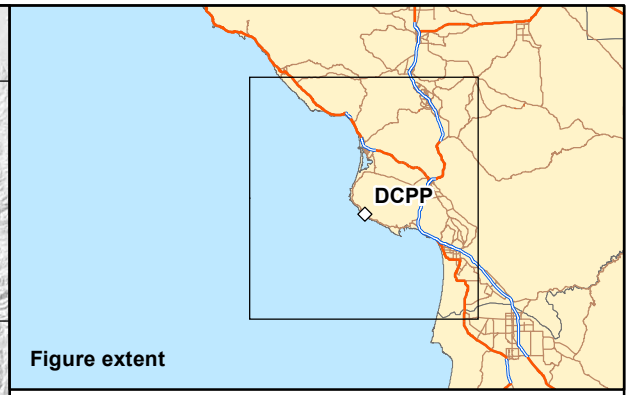

EXPLANATION

DCPP

Vicinity Areal Source Rate

0.1° Grid	0.02° Grid
1.000	0.035
0.300	0.025
	0.020
	0.015

Notes:
- 0.1° grid division values and color from Figure 13-6.
- 0.1° grid and rates, and scaled-down 0.02° grid and rates based on Petersen, Mueller, et al. (2008).

N

0 2 4 mi.

0 5 10 km

Map projection and scale: WGS 84 / UTM 10N, 1:350,000

Vicinity Areal Source Zone Showing 0.1° and Finer 0.02° Gridded Seismicity Rates Based on the 2008 NSHMP

DCPP SSC REPORT

Pacific Gas and Electric Company

Figure **13-7**

File path: S:\1005\005\Final_Report_Figures\Figure_1300-07.mxd; Date: 03/11/2015; User: Serkan Bozkurt, LCI; Rev.1

(a) Magnitude Versus Year, Late 1987 Through 2013

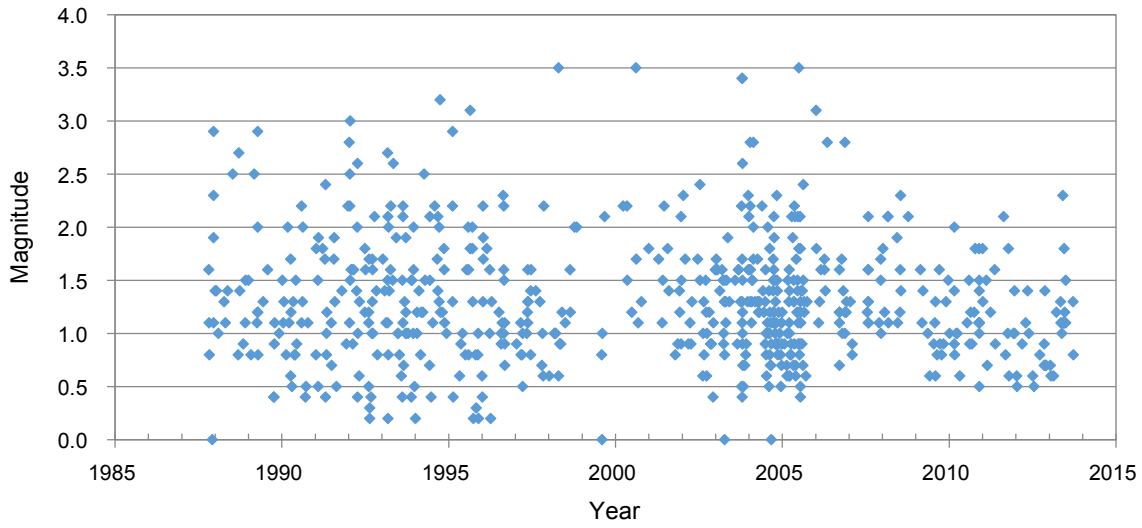

(b) Cumulative Number of Earthquakes Versus Magnitude

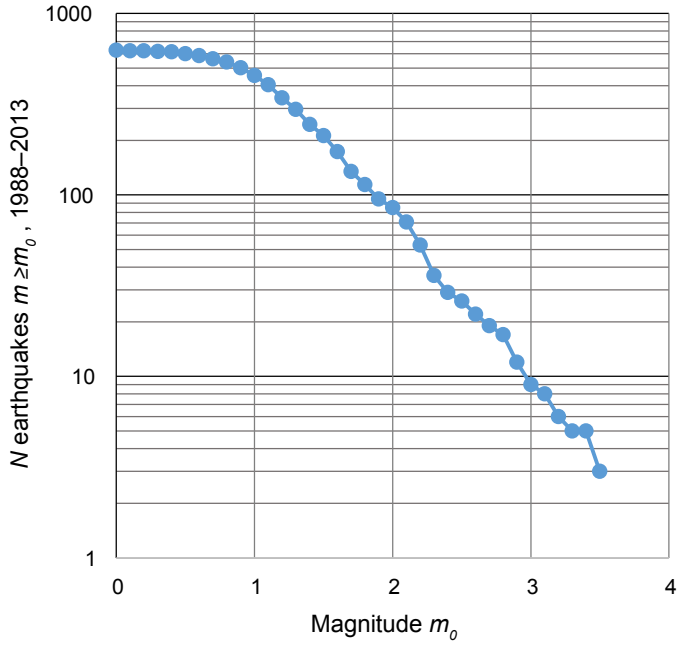

Evaluation of Hardebeck (2014a) Earthquake Catalog for Estimating the Magnitude of Completeness for the Local Source Zone

DCPP SSC REPORT

Pacific Gas and Electric Company

Figure **13-8**

File path: /s/1005/005/Final_Report_Figures/Figure_1300_08.ai; Date: 03/03/2015; User: Alex Remar, LCI; Rev. 1

(a) *b*-Value Calculated from Different Estimates of Completeness Magnitude m_c and Number of Earthquakes Used in the Calculations

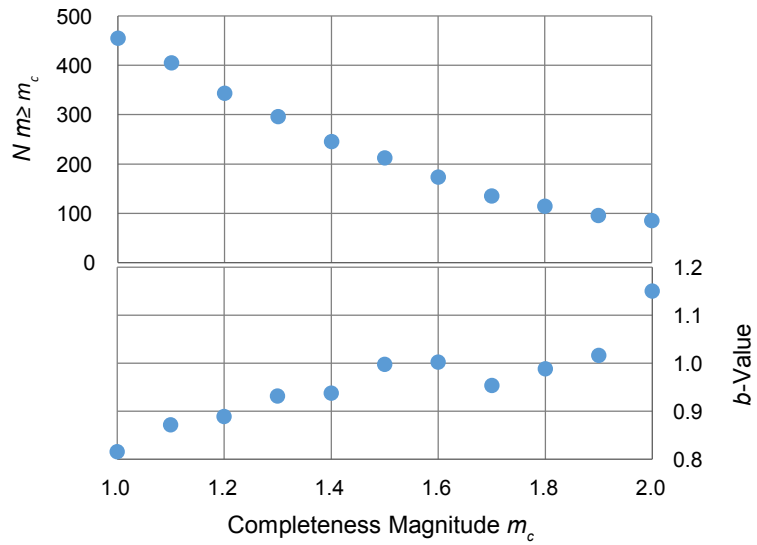

(b) Annual Rate of Earthquakes $m \geq m_0$ Versus Magnitude, 90% Confidence Interval Uncertainties, and Lines Showing b = 0.8 to 1.1 Drawn Through the Mean Rate of $M \geq 2$

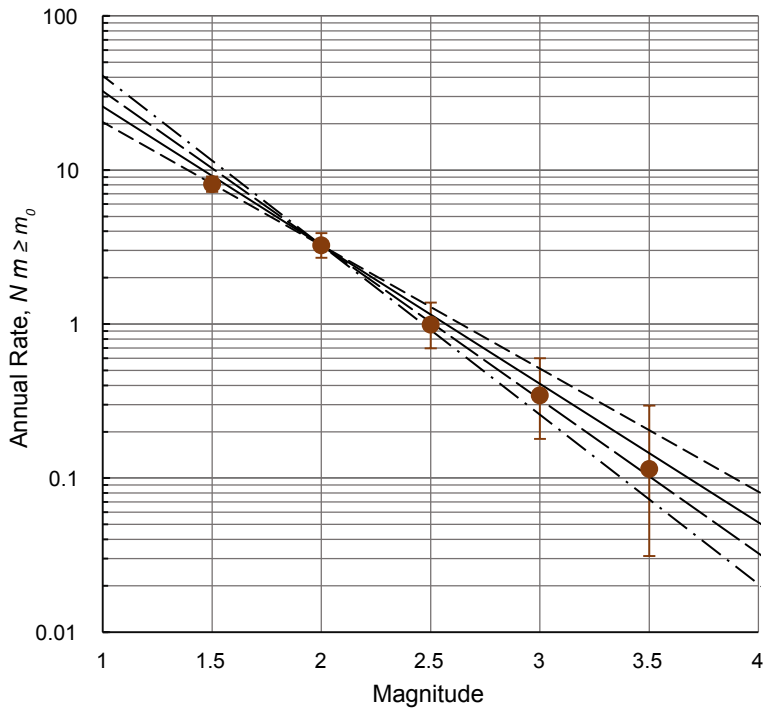

EXPLANATION

Observed rate and 90% confidence interval

Exponential Distribution Alternatives

- - - - b = 0.8
——— b = 0.9
— — — b = 1.0
—·—·— b = 1.1

Hardebeck (2014a) Earthquake Catalog *b*-Value Estimates for the Local Source Zone

DCPP SSC REPORT

Pacific Gas and Electric Company

Figure **13-9**

File path: /s/1005/005/Final_Report_Figures/Figure_1300-08.ai; Date: 03/04/2015; User: Alex Remar, LCi; Rev. 1

(a) PG&E Catalog, Annual Rate of Earthquakes $m \geq m_0$ Versus Magnitude, 90% Confidence Interval Uncertainties, and Lines Showing b = 0.8, 0.9, and 1.0 Drawn Through the Mean Rate of $M \geq 3$

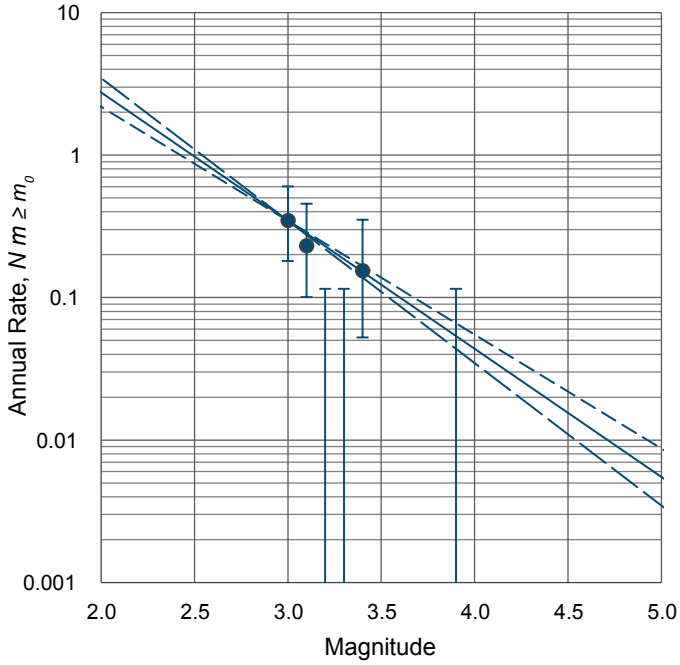

Numbers of Earthquakes M ≥ 3 in the Local Source Zone, PG&E Catalog

Magnitude Range	Time Period	No. of Events*
3.00-3.09	1988-2013	9
3.10-3.19	1988-2013	6
3.20-3.29	1988-2013	0
3.30-3.39	1988-2013	0
3.40-3.49	1988-2013	4
3.50-3.99	1988-2013	0

*Cumulative number of earthquakes ≥ the stated magnitude range over the stated time period.

(b) Updated UCERF3 Catalog, Annual Rate of Earthquakes $m \geq m_0$ Versus Magnitude, 90% Confidence Interval Uncertainties, and Lines Showing b = 0.8, 0.9, and 1.0 Drawn Through the Mean Rate of $M \geq 2.5$

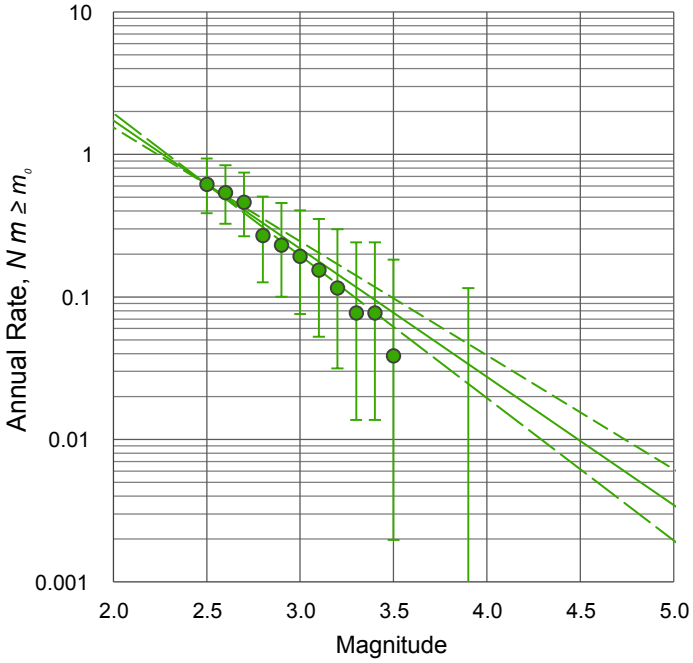

Numbers of Earthquakes M ≥ 2.5 in the Local Source Zone, Updated UCERF3 Catalog

Magnitude Range	Time Period	No. of Events*
2.50-2.59	1988-2013	16
2.60-2.69	1988-2013	14
2.70-2.79	1988-2013	12
2.80-2.89	1988-2013	7
2.90-2.99	1988-2013	6
3.00-3.09	1988-2013	5
3.10-3.19	1988-2013	4
3.20-3.29	1988-2013	3
3.30-3.39	1988-2013	2
3.40-3.49	1988-2013	2
3.50-3.59	1988-2013	1
3.60-3.99	1988-2013	0

*Cumulative number of earthquakes ≥ the stated magnitude range over the stated time period.

EXPLANATION

Observed rate and 90% confidence interval

Exponential Distribution Alternatives

- - - - b = 0.8
——— b = 0.9
— — — b = 1.0

Note: Explanation applies to both panels.

Annual Earthquake Rates from PG&E and Updated UCERF3 Catalogs and Alternative Exponential Distributions for the Local Source Zone

DCPP SSC REPORT

Pacific Gas and Electric Company

Figure **13-10**

File path: /s/1005/005/Final_Report_Figures/Figure_1100-10.ai; Date: 03/03/2015; User: Alex Remar, LCi; Rev. 1

(a) Annual Rate of Earthquakes m ≥ m_0 Versus Magnitude, 90% Confidence Interval Uncertainties, and Exponential Lines Considered for Gutenberg-Richter *a*- and *b*- Values for the Local Source Zone. Data from PG&E and Updated UCERF3 Catalogs and McLaren and Savage (2001).

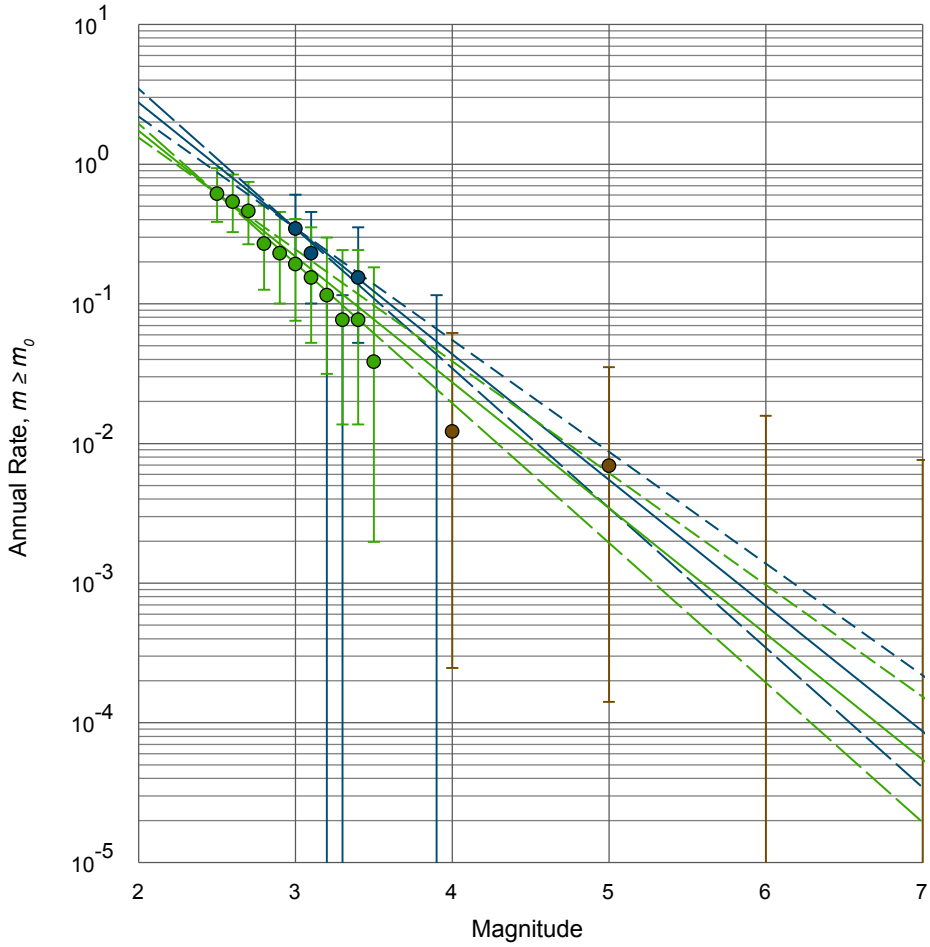

(b) Numbers of Earthquakes M ≥ 4 in the Local Source Zone, Updated UCERF3 Catalog and McLaren and Savage (2001)

Magnitude Range	Time Period	No. of Events*
4.0-4.9	1932-2013	1 ± 1
5.0-5.9	1870-2013	1 ± 1
6.0-6.9	1772-2013	0 or 1
7.0-7.9	1772-2013	0

*Cumulative number of earthquakes ≥ the stated magnitude range over the stated time period.

EXPLANATION

Observed rate and 90% confidence interval

- PG&E Catalog
- Updated UCERF3 Catalog
- McLaren and Savage (2001)

Exponential Distribution Alternatives

- PGE b=1.0
- UU3 b=1.0
- PGE b=0.9
- UU3 b=0.9
- PGE b=0.8
- UU3 b=0.8

Note: See Figure 13-10 for earthquake rate tabulated data for *M* < 4.

Earthquake Rates and Uncertainties for the Local Source Zone, Showing Constraints for *M* ≥ 4

DCPP SSC REPORT

Pacific Gas and Electric Company

Figure **13-11**

File path: /s/1005/005/Final_Report_Figures/Figure_1300_11.ai; Date: 03/04/2015; User: Alex Remar, LCI; Rev. 1

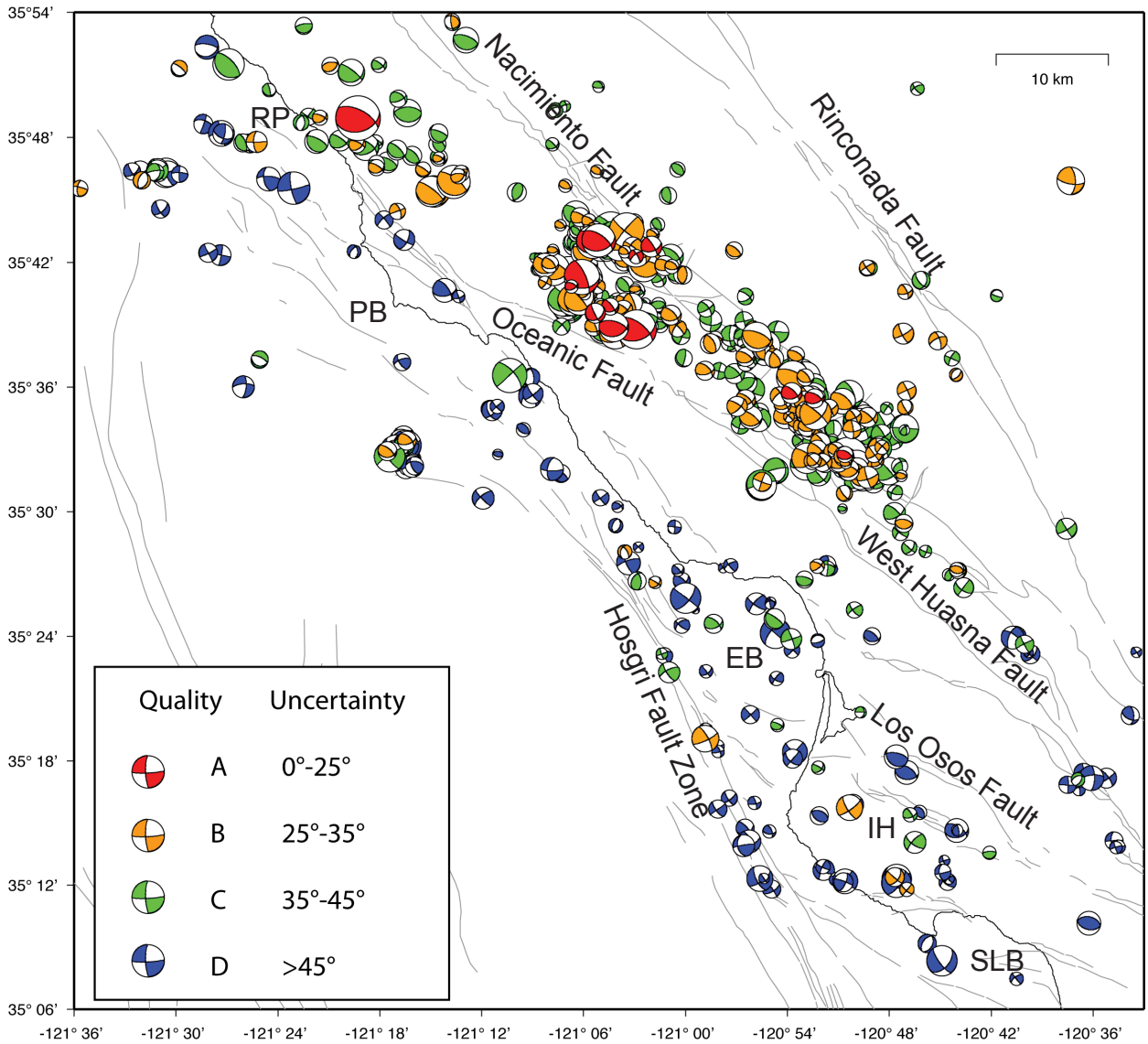

EXPLANATION

Magnitude

- <2.50
- 2.50–2.99
- 3.00–3.99
- 4.00–4.99
- 5.00–5.20

Abbreviations

EB	Estero Bay
IH	Irish Hills
PB	Point Piedras Blancas
RP	Ragged Point
SLB	San Luis Obispo Bay

Note: 2003 **M** 6.5 San Simeon focal mechanism is shown on Figure 13-13.

Source: Modified from Hardebeck (2011, 2014b).

Single-Event Focal Mechanisms of Central Coastal California, Oct. 1987 to Dec. 2008, Between San Luis Obispo Bay and Ragged Point

DCPP SSC REPORT

Pacific Gas and Electric Company

Figure **13-12**

File path: S:\1005\005\Final_Report_Figures\Figure_1300-12.ai; Date: 03/11/2015; User: Alex Remar, LCI; Rev.1

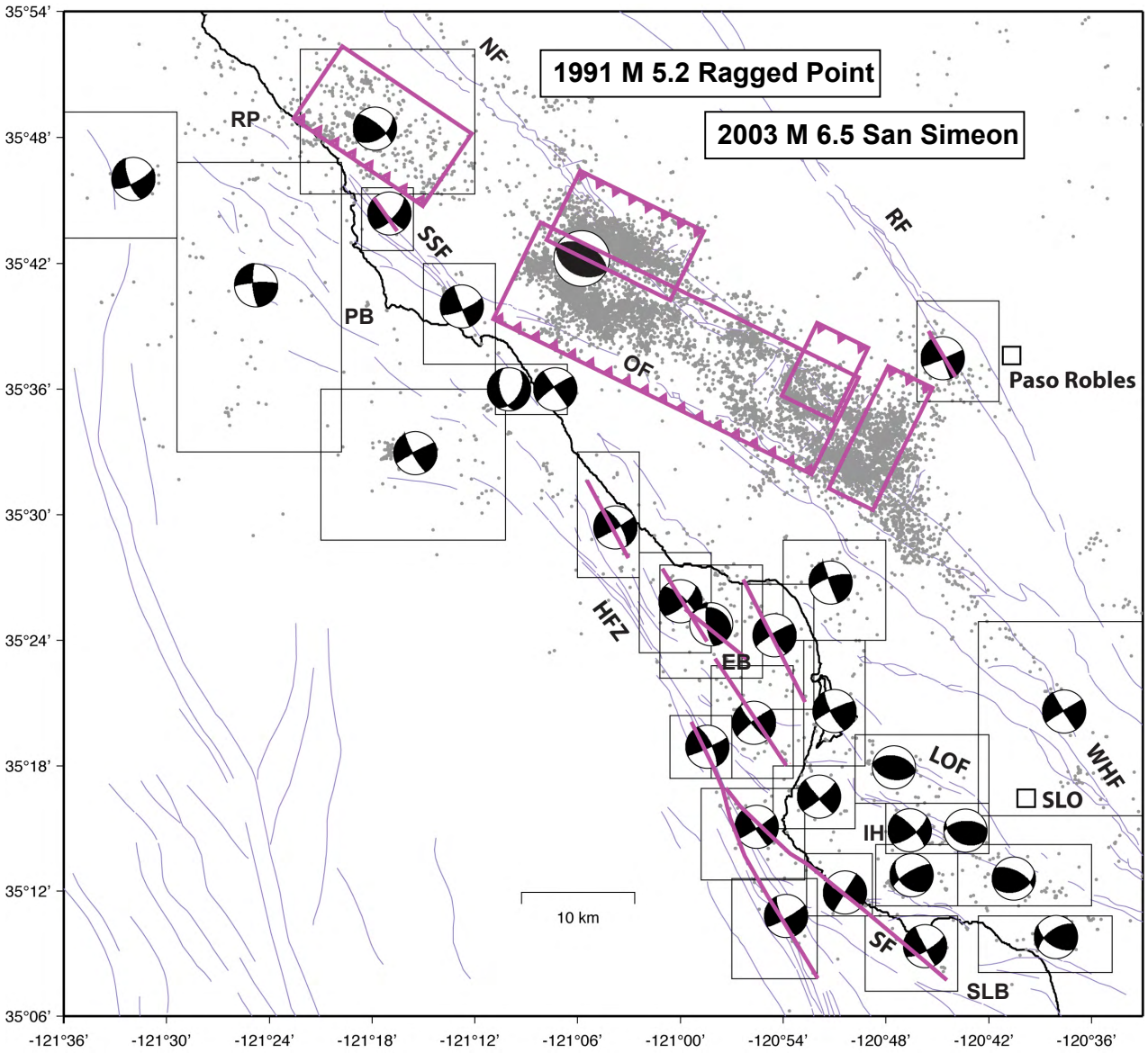

EXPLANATION

- Earthquake epicenter
- Composite focal mechanisms (box shows gather area)
- Subvertical structure inferred from seismicity locations
- Dipping structure inferred from seismicity locations; teeth point downdip

Abbreviations

EB	Estero Bay	RF	Rinconada fault
HFZ	Hosgri fault zone	RP	Ragged Point
LOF	Los Osos fault	SLB	San Luis Obispo Bay
IH	Irish Hills	SLO	San Luis Obispo
NF	Nacimiento Fault	SF	Shoreline fault
OF	Oceanic fault	SSF	San Simeon fault
PB	Point Piedras Blancas	WHF	West Huasna fault

Source: Modified from Hardebeck (2012c).

Composite Focal Mechanisms and Interpreted Seismicity Lineaments of Central Coastal California, Oct. 1987 to Dec. 2008, Between San Luis Obispo Bay and Ragged Point

DCPP SSC REPORT

Pacific Gas and Electric Company

Figure **13-13**

File path: S:\1005\005\Final_Report_Figures\Figure_1300-13.ai; Date: 03/11/2015; User: Alex Remar, LCI; Rev.1

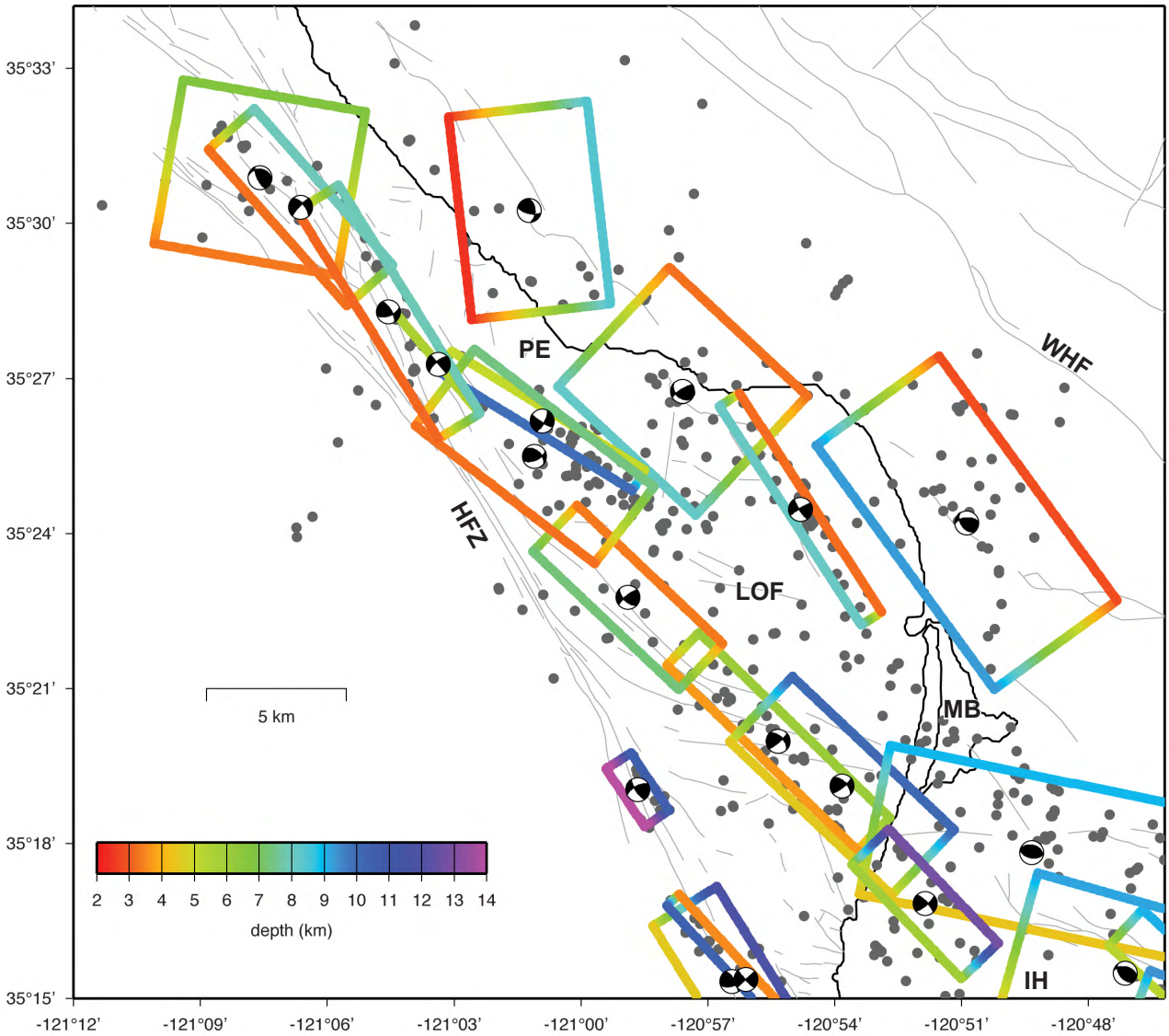

EXPLANATION

- Earthquake epicenter
- Planar fit to seismicity with compatible first motions (color ramp denotes depth and dip direction)
- Equivalent composite focal mechanism

Abbreviations

HFZ	Hosgri fault zone
IH	Irish Hills
LOF	Los Osos fault (offshore)
MB	Morro Bay
PE	Point Estero
WHF	West Huasna fault

Source: Modified from Hardebeck (2014b).

Best-Fit Planar Seismicity Alignments and Composite Focal Mechanisms from the OADC-FM Method, Estero Bay Area

DCPP SSC REPORT

Pacific Gas and Electric Company

Figure **13-14**

File path: S:\1005\005\Final_Report_Figures\Figure_1300-14.ai; Date: 03/04/2015; User: Alex Remar, LCI; Rev.1

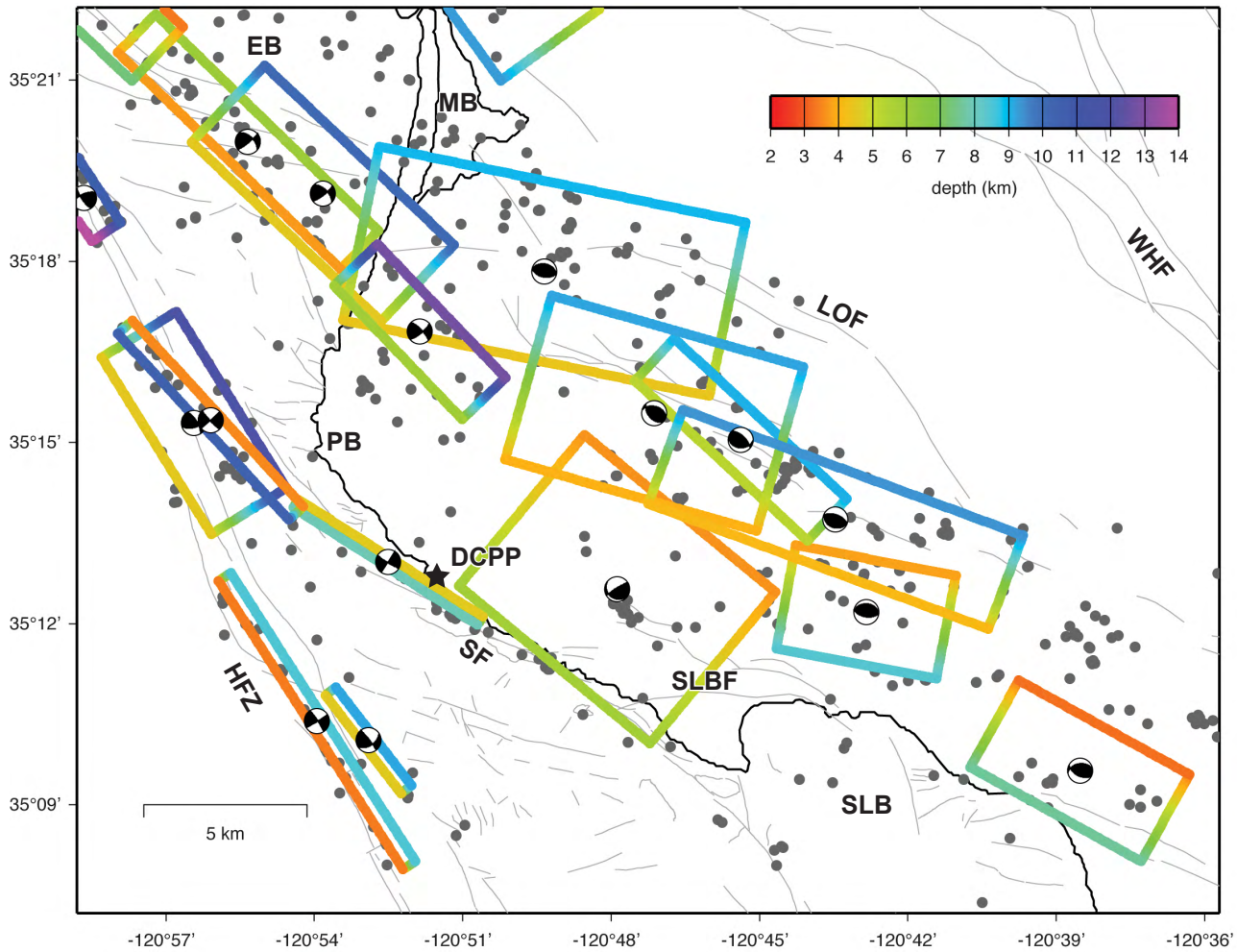

EXPLANATION

- ★ DCPP
- ● Earthquake epicenter
- Planar fit to seismicity with compatible first motions (color ramp denotes depth and dip direction)
- Equivalent composite focal mechanism

Abbreviations

EB	Estero Bay
HFZ	Hosgri fault zone
LOF	Los Osos fault (onshore)
MB	Morro Bay
PB	Point Buchon
SF	Shoreline fault
SLB	San Luis Obispo Bay
SLBF	San Luis Bay fault
WHF	West Huasna fault

Source: Modified from Hardebeck (2014b).

Best-Fit Planar Seismicity Alignments and Composite Focal Mechanisms from the OADC-FM Method, Irish Hills Area

DCPP SSC REPORT

Pacific Gas and Electric Company

Figure **13-15**

File path: S:\1005\005\Final_Report_Figures\Figure_1300-15.ai; Date: 03/11/2015; User: Alex Remar, LCI; Rev.1

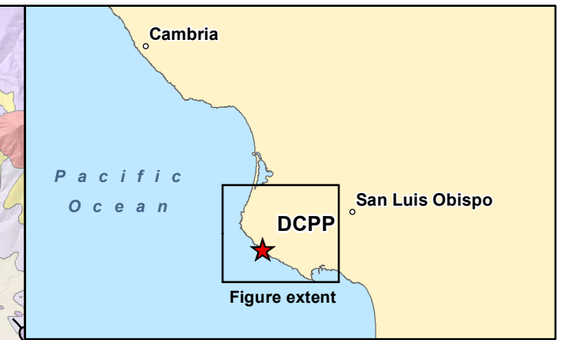

EXPLANATION

Wells

Abbreviated List of Geologic Units

Quaternary continental deposits

- Qe — Aeolian deposits
- Qal — Alluvial deposits
- Qm — Marine terrace deposits

Neogene marine deposits

- Tpps — Pismo Formation, Squire Member
- Tmpm — Pismo Formation, Miguelito Member
- Tmpe — Pismo Formation, Edna Member
- Tmm — Monterey Formation
- Tmod — Obispo Formation, diabase
- Tmo — Obispo Formation, undifferentiated

Continued

- Tmr — Rincon Formation
- Tov — Vaqueros Sandstone

Mesozoic basement

- Ks — Cretaceous sandstone
- KJf — Franciscan Complex, undifferentiated
- KJfm — Franciscan Complex, melange
- s — Franciscan Complex, serpentine
- KJg — Franciscan Complex, graywacke sandstone
- KJfmv — Franciscan Complex, metavolcanic rocks
- KJfo — Franciscan Complex, ophiolite

Geologic Structures

Solid where known; dashed where approximate; dotted where concealed; queried where uncertain. Ticks on lineaments indicate facing direction of topographic scarps.

Syncline — Fault

Anticline — Lineament

Buried fault interpreted by PG&E (2014, Chapter 7)

Notes:
- See PG&E (2014, Chapter 7) for full list of geologic units. Offshore geology from PG&E (2011).
- From PG&E (2014) Chapter 7.

N

0 1 2 mi.

0 1 2 km

Map projection and scale: WGS 84 / UTM Zone 10N, 1:70,000

Geologic Map of the Irish Hills Showing Faults Interpreted From Geologic, Well-Hole, and Seismic-Reflection Data

DCPP SSC REPORT

Pacific Gas and Electric Company

Figure **13-16**

File path: S:\1005\005\Final_Report_Figures\Figure_1300-16.mxd; Date: 03/11/2015; User: Alex Remar; LCI; Rev.1

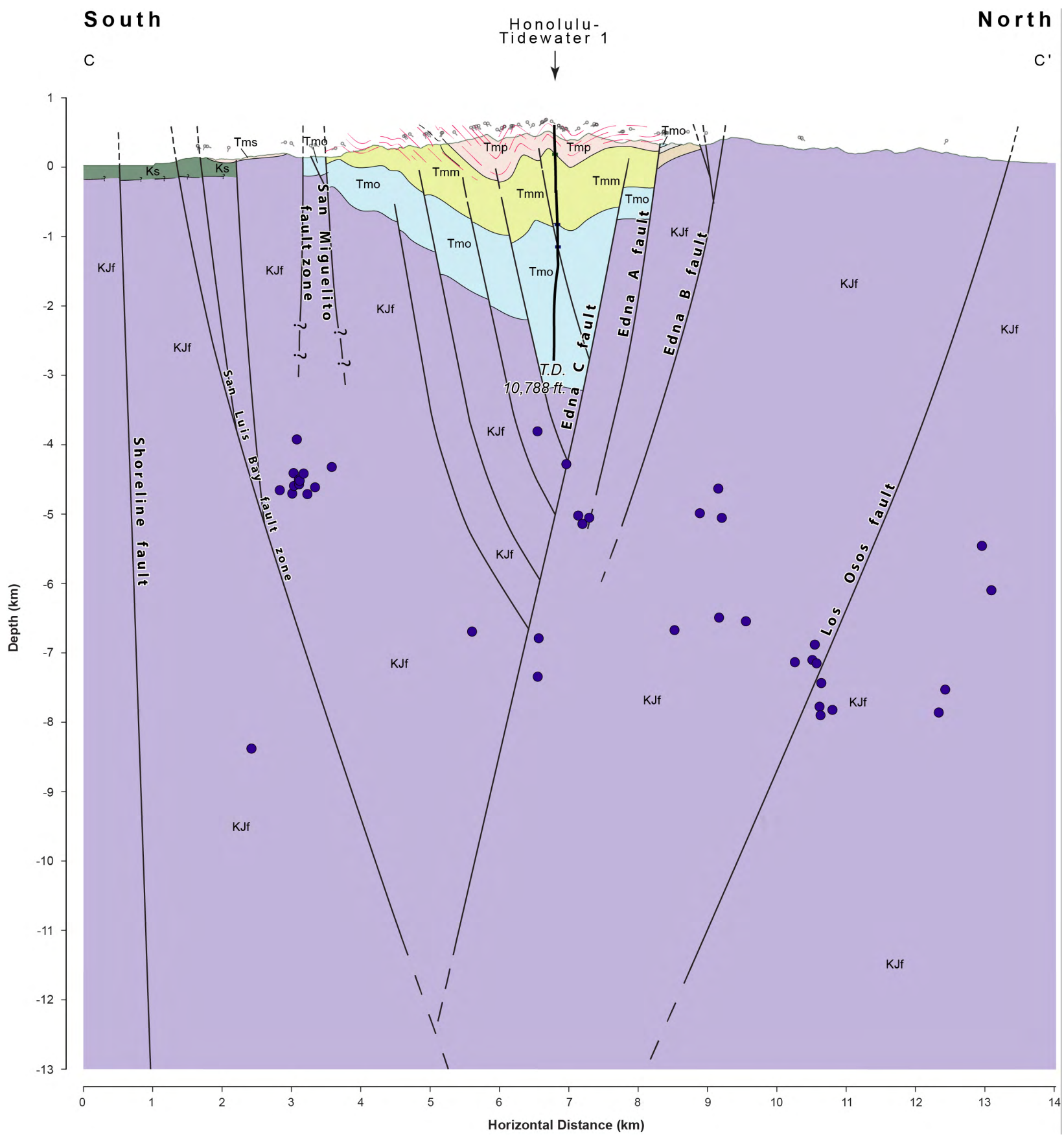

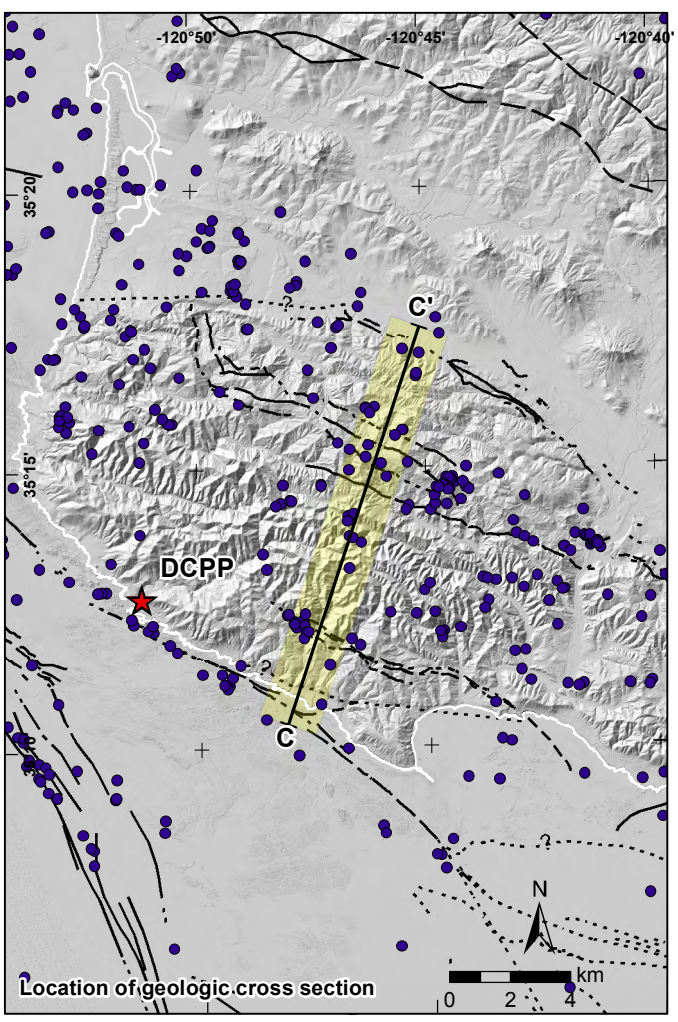

EXPLANATION

Earthquake from Hardebeck (2014a)

Geologic cross section

1 km seismicity box extent considered in geologic cross section

Geologic Units

- Tmp — Pismo Formation
- Tmm — Monterey Formation
- Tmo — Obispo Formation
- Ks — Cretaceous sandstone
- KJf — Franciscan Complex

Geologic Symbols

- Fault: dashed where inferred, queried where uncertain
- Form line
- Apparent dip

Note: See Figure 13-16 for geologic mapping.

Source: Modified from PG&E (2014, Chapter 7).

Geologic Cross Section of the Irish Hills Showing Faults Interpreted from Geologic, Well-Hole, and Seismic-Reflection Data

DCPP SSC REPORT

Pacific Gas and Electric Company

Figure 13-17

File path: S:\1005\005\Final_Report_Figures\Figure_1300-17.mxd; Date: 03/03/2015; User: Alex Remar, LCI; Rev.1

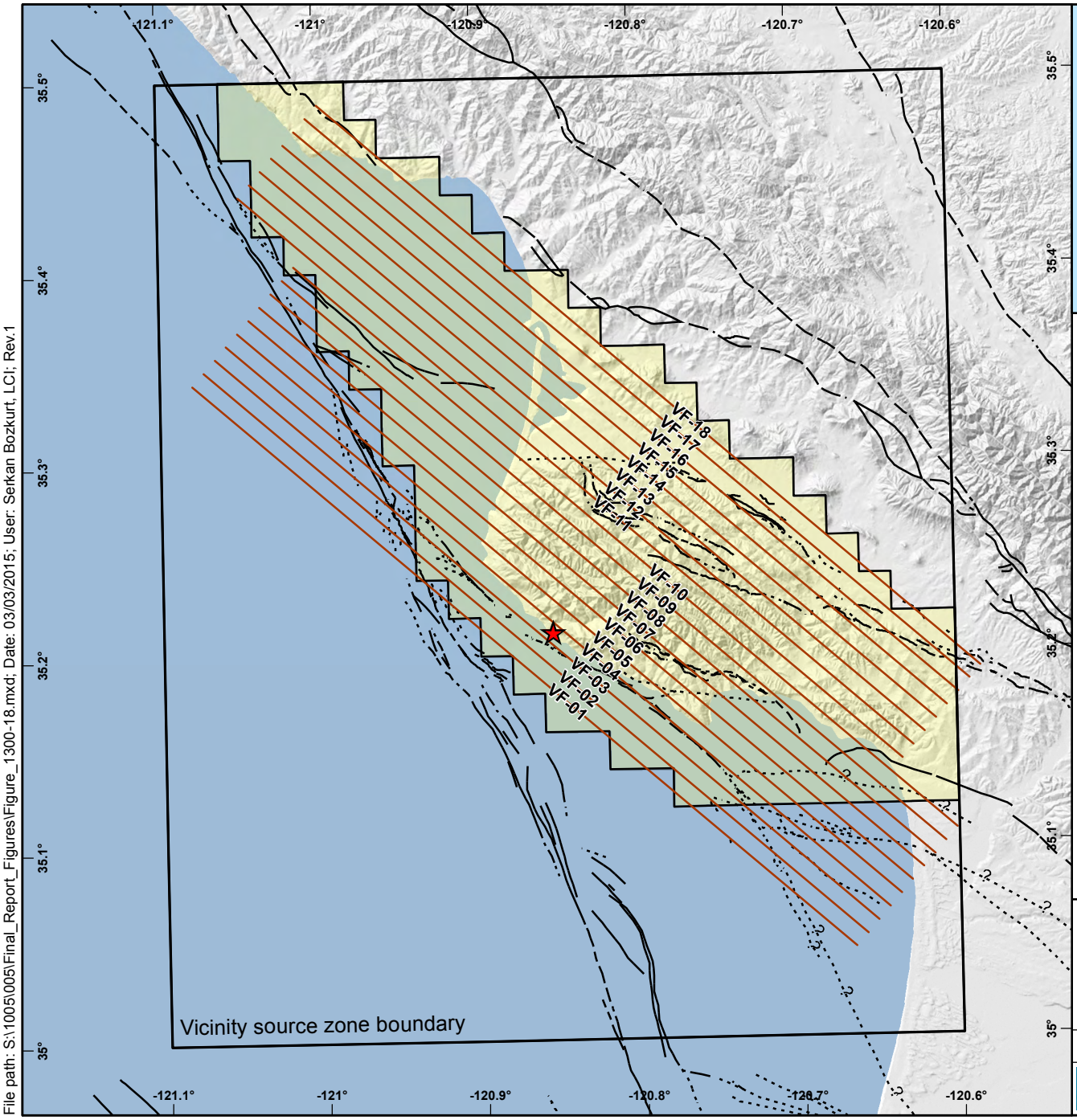

EXPLANATION

- DCPP
- Virtual faults
- Local areal source zone

N

0 2 4 mi.

0 5 10 km

Map projection and scale: WGS 84 / UTM 10N, 1:350,000

Local Areal Source Zone and Virtual Faults

DCPP SSC REPORT

Pacific Gas and Electric Company

Figure **13-18**

File path: S:\1005\005\Final_Report_Figures\Figure_1300-18.mxd; Date: 03/03/2015; User: Serkan Bozkurt, LCI; Rev.1

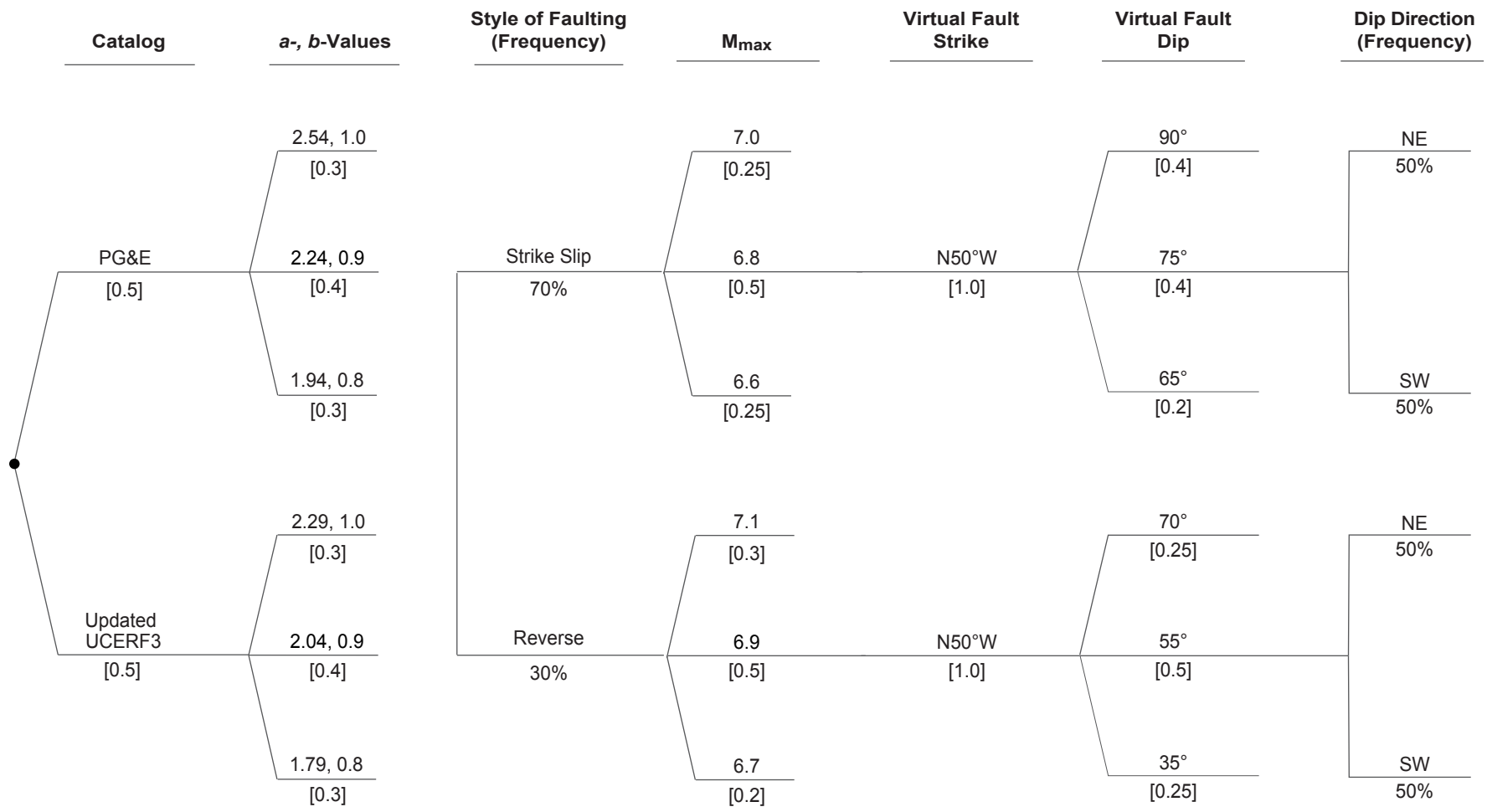

Note: Local areal source zone virtual faults are shown on Figure 13-18.

Logic Tree for the Local Areal Source Zone

DCPP SSC REPORT

Pacific Gas and Electric Company

Figure **13-19**

File path: S:\1005\005\Final_Report_Figures\Figure_1300-19.ai; Date: 03/04/2015; User: Alex Remar

14.0 HAZARD SENSITIVITY

In this chapter, hazard sensitivity is provided based on the Diablo Canyon SSC model described and presented in *Chapters 6 through 13* and in the Hazard Input Document (HID; *Appendix C*). Hazard sensitivity feedback was provided throughout the project to focus the SSC TI Team's evaluations on the uncertainties that are most important for the hazard at the DCPP site. Sensitivity results presented at the formal workshops are provided with the workshop summaries in *Appendix D*. The full GMC model applicable to the DCPP site was developed as part of the companion SWUS SSHAC Level 3 study (GeoPentech, 2015). A simplified version of the full SWUS GMC logic tree was used in the sensitivity analyses to focus on the sensitivity aspects of the SSC model, applying the following elements from the GMC model (GeoPentech, 2015):

- The "central model" GMPE of the "common form model" ("central common form model")—applied to sources closest to the DCPP site.
- The Campbell and Bozorgnia (2014; "CB14") Next Generation Attenuation (NGA) West 2 GMPE—applied to the more regional and distant sources relative to the DCPP.
- The central branch of the "total sigma model" and the "full mixture model"—applied to both GMPEs for all the sensitivity calculations.

Because the sensitivity analyses are not based on the full SWUS GMC model and do not include site response analysis, the hazard results (amplitudes of ground motions) presented in this chapter are for SSC model sensitivity only and do not represent final hazard results for the DCPP. All results are shown for a reference rock site condition for a 30 m average shear-wave velocity (V_{S30}) of 760 m per second (m/s).

14.1 Hazard Sensitivity Runs

The hazard sensitivity was conducted for two spectral frequencies: a high frequency of 5 hertz (Hz) and a low frequency of 0.5 Hz. These two spectral frequencies were selected to be representative of the expected range of importance for the DCPP. Hazard sensitivities at or near these frequencies have been evaluated periodically during the development of the SSC model (*Appendix D*).

Hazard sensitivity is provided in several ways. A comparison of mean hazard results using the Diablo Canyon SSC model developed in this study with the SSC model of the 2011 Shoreline fault zone study ("Shoreline Report"; PG&E, 2011) is provided as hazard curves (*Section 14.2*). The Diablo Canyon SSC model is explored further by evaluating fractional contribution to hazard by seismic source (*Section 14.2.1*), deaggregation plots (*Section 14.2.2*), and fractile hazard curves on the SSC model (*Section 14.2.3*).

The hazard sensitivity analyses are presented in *Sections 14.2.4 through 14.2.8*. The sensitivity analyses were conducted by isolating each node (in some cases, groups of nodes) of the SSC logic trees. For the node(s) of interest, one branch is given full weight and the mean hazard is computed by sampling all branches for the other nodes. The

results of the hazard sensitivity are presented in the form of tornado plots for a given hazard level (*y*-axis value). The tornado plots show the relative contribution to hazard uncertainty for each node of the logic tree, with the largest contributor to uncertainty placed at the top of the tornado diagram. The tornado plots show the ratio of the ground motion from the individual sensitivity case divided by the ground motion for the full logic tree (called the "base case"). These computed ratios for each branch of the logic tree are then normalized by the weighted mean of the ratio values to center the individual tornado results about the base case, which corresponds to a line of unity. Tornado plots are computed for the two spectral frequencies of 5 Hz and 0.5 Hz and for the mean annual exceedance probability (AEP) of 10^{-4} and 10^{-6} per year (yr^{-1}). Points on the sensitivity tornado plots representing the isolated branch values are plotted as center points of circles with radii that are proportional to the branch weights in the logic tree. The tornado plots also show the results of sensitivity analyses conducted for values that are not part of the final SSC model, and not in the logic tree. In these cases, such as the use of gridded seismicity for the Local areal source zone versus the use of virtual faults, the radii are proportional to a branch weight of 1.

14.2 Contribution by Source, Deaggregation, and Sensitivity Analyses

The SSC model developed for the 2011 Shoreline fault zone study (PG&E, 2011) represents the most recent site-specific SSC model for the DCPP prior to this study. Figure 14-1 plots the comparison between the mean hazard curves using the "2011 Shoreline Report SSC model" and the current "2015 Diablo Canyon SSC model." The mean hazard curves for the two SSC models are computed using the same GMPEs (i.e., the central common form and CB14 models; GeoPentech, 2015) for the reference rock site condition (V_{S30} = 760 m/s). Over the annual probability range of focus (i.e., 10^{-4} to 10^{-6}), the mean hazard curves from the two SSC models are similar for the spectral frequency case of 5 Hz (Figure 14-1a). For the lower spectral frequency case of 0.5 Hz, the two SSC model mean hazard curves are similar at 10^{-4} AEP, but the 2015 Diablo Canyon SSC model results in slightly higher ground motions at 10^{-5} and 10^{-6} AEP (Figure 14-1b).

14.2.1 Fractional Contribution by Source

The mean hazard curves shown on Figure 14-1 for the 2015 Diablo Canyon SSC model represent the total hazard at the DCPP from the contributing seismic sources as presented earlier in this report. Figure 14-2 shows the fractional contribution of the different seismic sources from the Diablo Canyon SSC model to the total mean hazard for spectral frequencies of 5 Hz and 0.5 Hz, respectively. The fractional contribution is plotted against spectral acceleration between 0.1 g and 10 g for the 5 Hz case (Figure 14-2a) and between 0.01 g and 1 g for the 0.5 Hz case (Figure 14-2b). The fractional contribution corresponding to a particular AEP of interest can be determined by comparing the ground motions with those on the mean hazard curves on Figure 14-1. For example, at an AEP of 10^{-4}, the mean spectral acceleration at 5 Hz is between 2 g and 3 g. Within this range of

spectral accelerations, the Hosgri fault contributes over 50% to the overall hazard, the San Luis Bay fault contributes slightly less than 20 %, and the Los Osos fault and Local areal zone each contribute slightly more than 10%. The remaining sources contribute less than 2%. As noted earlier, these results are based on using the two representative GMPEs with the central branch of the total sigma model (GeoPentech, 2015).

The Diablo Canyon SSC model models earthquake ruptures on the Primary and Connected fault sources by using numerous rupture sources, with several rupture sources located on each fault section closest to the DCPP (*Chapter 9*). To evaluate fractional contribution by fault source (and other hazard sensitivities), the rupture sources were grouped by fault source as shown in Table 14-1. The Hosgri fault source is represented by 21 rupture sources across all three Hosgri Fault Geometry Models (FGMs; H85, H75, and H90). The Shoreline, Los Osos, and San Luis Bay faults are represented by 11, 8, and 6 rupture sources, respectively, across all three FGMs developed for the San Luis–Pismo Block (SLPB) sources: Outward-Vergent (OV), Southwest-Vergent (SW), and Northeast-Vergent (NE). Nine other rupture sources tabulated under "Other Connected Faults" involve fault sections that are farther from the DCPP (including the Piedras Blancas and Wilmar Avenue faults, and the eastern portion of the Los Osos fault).

Table 14-1. Grouping of Rupture Sources by Fault Source for Hazard Sensitivity

Fault Source Group (Number of Rupture Sources in Group)				
Hosgri (21)	**Shoreline (11)**	**Los Osos (8)**	**San Luis Bay (6)**	**Other Connected Faults (9)**
H85-01 through H85-07 H75-01 through H75-07 H90-01 through H90-07	OV-01, OV-02, OV-03, OV-04 SW-01, SW-02, SW-03 NE-01, NE-02, NE-03, NE-04	OV-07, OV-08 SW-08 NE-05, NE-06, NE-07, NE-08, NE-11	OV-05, OV-06 SW-04, SW-05, SW-06, SW-07	H75-08, H85-08, H90-08 OV-09, OV-10 SW-09, SW-10 NE-09, NE-10

In this study, as in previous PSHA studies (PG&E, 1988, 2011), the Hosgri fault is the controlling seismic source for both the 5 Hz (Figure 14-2a) and 0.5 Hz (Figure 14-2b) cases. For the 5 Hz case and for ground motions greater than 2 g, the Hosgri fault contributes between 50% and 60% of the total hazard, with the remaining significant fractional contribution coming from the San Luis Bay fault, the Los Osos fault, the Local areal source zone and the Shoreline fault sources. The remaining seismic sources, in the aggregate, contribute less than 3% to the total hazard at ground motions greater than 2 g. For the lower spectral frequency case of 0.5 Hz, the Hosgri fault contributes between approximately 50% and 75% for ground motions greater than about 0.3 g (Figure 14-2b). For ground motions in the AEP range of interest (which corresponds to spectral accelerations of approximately 0.3 g to 1 g) other significant contributors to total hazard include the San Luis Bay fault, the Los Osos fault, the Local areal source zone, the other Connected faults, the San Andreas fault, and the Shoreline fault sources. The San

Andreas fault source also contributes significantly to total hazard at ground motions of less than about 0.3 g for the 0.5 Hz spectral frequency.

14.2.2 Deaggregation

Figure 14-3 shows deaggregation results by magnitude and distance for the hazard level of 10^{-4} for 5 Hz (Figure 14-3a) and 0.5 Hz (Figure 14-3b) spectral accelerations. These deaggregation plots show that the hazard at the DCPP for spectral acceleration at both 5 Hz and 0.5 Hz is controlled by the seismic sources located close to the site, with the highest peaks in the magnitude range of **M** 7.0–8.0.

14.2.3 Fractile Hazard Curves for the SSC Model

Figure 14-4 shows the Diablo Canyon SSC model fractile hazard curves for the 5 Hz (Figure 14-4a) and 0.5 Hz (Figure 14-4b) spectral accelerations. Note that these fractile hazard curves represent only that range in hazard curves based on the branches of the Diablo Canyon SSC logic tree. The fractile curves suggest that for the spectral frequency of 5 Hz and at the 10^{-4} AEP, there is an approximately 10% difference in ground motions between the 5% and 95% fractiles for the SSC logic tree. It can be expected that this observed range will be much larger when the corresponding SWUS GMC logic tree is included for the total fractile distribution, reflecting the general result observed in other site-specific PSHAs that uncertainty in hazard is typically controlled by uncertainty in the GMC model to a greater degree than uncertainty in the SSC model (PG&E, 2011; GeoPentech, 2015).

14.2.4 Slip Rate Sensitivity

Slip rates for the rupture sources in the Diablo Canyon SSC model are represented by three alternative branch values and weights (*Section 9.3*). The hazard sensitivity to this epistemic uncertainty in slip rate is investigated by grouping rupture sources by fault source according to Table 14-1, and by giving full weight to the highest weighted Fault Geometry Model (FGM) for the Hosgri fault source (the H85 FGM) and for the San Luis–Pismo Block sources (the OV FGM; to represent the Los Osos, San Luis Bay, and the Shoreline fault sources). Variations in the slip rates for other faults that are not significant contributors to the total hazard (Figure 14-2) can be expected to be negligible in terms of tornado plots (i.e., ground-motion ratio values of unity). Within each group, the sensitivity was based on systematically giving full weight to the low, middle, and high slip rate values for the rupture sources within each rupture source group. In addition to exploring slip rate sensitivity for the four main fault sources, Gutenberg-Richter activity rate sensitivity was explored for the virtual faults used to model the Local areal source zone (*Section 13.5*).

The ground-motion ratios at the 10^{-4} and 10^{-6} hazard levels are plotted for the 5 Hz spectral frequency on Figures 14-5a and 14-5b and for the 0.5 Hz spectral frequency on Figures 14-5c and 14-5d. Tornado ratio values are computed and plotted according to the approach described in *Section 14-1* for the range of slip rates for the Hosgri, San Luis

Bay, Shoreline, and Los Osos faults. The logic tree branch weights are identical across the sources with values of [0.185], [0.63], and [0.185] for the low, middle, and high slip rate values, respectively. The last row shows ground motion ratios for the range of Gutenberg-Richter *a*- and *b*-value pairs modeled for the virtual faults associated with the Local areal source zone (Table 13-7).

Based on the relative contribution of the Hosgri fault to the total hazard, the largest range in ground-motion ratio values is from the variation of the slip rate on the Hosgri fault (Figure 14-5). For the other sources, the range in variation is of a second order, as the three slip rate values produce tornado ratio values nearly equal to unity.

14.2.5 Fault Geometry Sensitivity

The next sensitivity analyses evaluate the contribution to ground-motion uncertainty based on fault source geometry as expressed by the different FGMs for the Primary and Connected fault sources and by the alternative geometries for the virtual faults in the Local areal source zone. These tornado results are plotted at the two hazard levels (i.e., 10^{-4} and 10^{-6}) for the 5 Hz and 0.5 Hz spectral frequencies on Figures 14-6a and 14-6b and Figures 14-6c and 14-6d, respectively.

The top rows of the geometry hazard sensitivity plots (Figure 14-6) are for the three FGMs (OV, SW, and NE models) developed for the Primary and Connected fault sources of the SLPB. These FGMs correspond to different geometries of the Los Osos, San Luis Bay, and other Connected fault sources, as described in *Chapter 7*. The weights assigned for these three models, the OV, SW, and NE models, are [0.4], [0.4], and [0.2], respectively. At the 5 Hz spectral frequency (Figures 14-6a and b), the different FGMs correspond to noticeable differences in hazard, with the OV Model resulting in ground-motion ratios slightly less than unity, the SW Model yielding ground-motion ratios near unity, and the NE Model yielding ground-motion ratios slightly greater than unity. There is less difference in ground-motion ratios for the SLPB geometry models at the 0.5 Hz spectral frequency (Figures 14-6c and 14-6d).

The second rows of the geometry hazard sensitivity plots (Figure 14-6) are for the three FGMs developed for the Hosgri fault sources; these FGMs are based on dip angles of 90° (H90), 85° east (H85), and 75° east (H75) for the fault section closest to the DCPP. The assigned weights for these three models are [0.2], [0.6], and [0.2], respectively. The tornado results from this sensitivity cluster near the unity line at both spectral frequencies, indicating that Hosgri dip uncertainty has a lesser impact on the total ground-motion uncertainty than the SLPB model uncertainty.

Two geometry sensitivities are shown for the Local areal source zone. The first of these is shown on the third row of each tornado plot, where a single point value is indicated with a default weight of 1.0. This sensitivity explores the hazard implication of modeling the Local areal source zone as a series of virtual faults (which was performed; see *Section 13.5.1*) versus modeling the areal source zone using gridded rates (which was not performed for the Local areal source, but was for the more distant and less hazard-significant Vicinity and Regional areal source zones; see *Sections 13.3 and 13.4*). The

sensitivity shows a ground-motion ratio of less than unity for the alternative approach of modeling the Local areal source zone from gridded rates, with the largest deviation from unity for the 5 Hz spectral frequency at the 10^{-4} AEP (Figure 14-7a), and the smallest deviation for the 0.5 Hz spectral frequency at the 10^{-6} hazard level (Figure 14-8b). This result shows that the contribution to ground-motion uncertainty for the DCPP does not depend significantly on the choice of method (virtual faults or gridded rates) for modeling the Local areal source zone, but that the Diablo Canyon SSC model choice of using virtual faults with full weight leads to slightly higher ground motions at 5 Hz and at the 10^{-4} hazard level than the alternative approach.

The bottom rows of the geometry hazard sensitivity plots (Figure 14-6) explore the contribution to ground-motion uncertainty based on the selection of virtual fault dip for the reverse fault cases (*Section 13.5.2*). From Table 13-3, the alternative dips are 70°, 55°, and 35°, with weights of [0.25], [0.5], and [0.25], respectively, and equal frequency of dip direction to the northeast or southwest. The range in tornado ratio values for the three alternative dips associated with the virtual faults shows a small difference from unity for both spectral frequencies (Figure 14-6), indicating that the choice of dip does not contribute significantly to ground-motion uncertainty.

14.2.6 Time Dependency Model and Complex/Splay Rupture Sensitivity

The Time Dependency Model in the Diablo Canyon SSC model uses equivalent Poisson ratios (EPRs) for the Hosgri and SLPB rupture sources to account for uncertainty in non-Poisson recurrence behavior, which may be related to a renewal process (*Chapter 11* and *Appendix H*). EPRs (multipliers on the Poisson rate) and weights are assigned for the Hosgri, SLPB, and San Andreas fault sources (Table 11-4). Because of the relative fractional contribution to hazard of these sources (Figure 14-2), the tornado plots for the Hosgri EPRs (top row on each plot, Figure 14-7) show the largest range in ground-motion ratio, followed by the EPRs applied to the SLPB sources (second row on each plot, Figure 14-7). Based on the low fractional contribution of the San Andreas fault source to the total hazard at the DCPP (Figure 14-2), the range of EPRs applied to the San Andreas fault source does not produce tornado ratio values visibly different from unity (Figure 14-7).

Added to the tornado plots for the Time Dependency Model hazard sensitivity is a sensitivity for the ground-motion modeling associated with complex and splay rupture sources (*Chapters 6, 9, and 10*), as shown in the bottom row of each plot on Figure 14-7. As directed in the SWUS GMC model for these cases (GeoPentech, 2015), the resulting ground motion from an earthquake on a complex or splay rupture source is a combination (i.e., square root of the sum of the squares) of the primary (or main) rupture event and the secondary (or splay) rupture event. For this last sensitivity case, the ground-motion ratio value shown on the plots is computed without the additional increase in ground motions from the second (i.e., secondary or splay) rupture event. As expected, these values have ground-motion ratios less than 1 because the secondary (or splay) rupture event was not included. The ground-motion ratios are between approximately 0.95 (for 5 Hz spectral frequency at the 10^{-4} hazard level; Figure 14-7a) and 0.98 (for 0.5 Hz spectral frequency

at the 10^{-6} hazard level; Figure 14-7d), and it can be concluded that the inclusion of these these complex and splay rupture sources and this method of modeling them does not have a significant impact on the resulting total hazard at the DCPP site.

14.2.7 Magnitude Distribution Model Sensitivity

Four functional forms of the magnitude probability density function (PDF) are defined in the Diablo Canyon SSC model (*Section 10.2*). For the sensitivity analyses based on the Magnitude Distribution Models, the base case used in computing the ground-motion ratios (i.e., the denominator) was simplified to be highest weighted logic tree branch: the H85 Model for the Hosgri fault and the OV Model for the SLPB faults. The Magnitude Distribution Model sensitivity plots are shown on Figure 14-8 for the 5 Hz and 0.5 Hz spectral frequencies.

The top row on each plot of Figure 14-8 is a sensitivity on the "Category B" rupture sources that are modeled using either a truncated exponential (weight of [0.2]) or a WAACY model (weight of [0.8]) magnitude PDF (Table 10-2). The Category B rupture sources are mostly Hosgri-group rupture sources located on the Hosgri–San Simeon–San Gregorio fault system (see *Chapter 9*) that are typified with maximum magnitude (M_{max}) values of approximately **M** 7.8–8.5 (e.g., Table 10-4). As expected given its high weight, the sensitivity for the WAACY case plots near unity for both frequencies and hazard levels (Figure 14-8). The smaller circles on the top row of each plot correspond to the hazard sensitivity for using the truncated exponential magnitude PDF. The plots show subtle deviations from unity for the exponential magnitude PDF, with a ratio that is slightly greater than unity for both spectral frequencies at the 10^{-4} hazard level (Figures 14-8a and 14-8c). The ratios are slightly lower than unity for both spectral frequencies at the 10^{-6} hazard level (Figures 14-8b and 14-8d).

The second row on each plot for the Magnitude Distribution Model sensitivities (Figure Figures 14-8) explores the model implication for omitting the largest-magnitude ruptures entirely. The second row shows the model implication of using the Youngs and Coppersmith (1983) characteristic magnitude (M_{char}) PDF model for all Category B rupture sources, with M_{char} values identical to those used in the WAACY model (e.g., Table 10-4). The tornado plots show ground-motion ratios slightly higher than unity for both spectral frequencies at the 10^{-4} AEP (Figures 14-8a and 14-8c), and slightly lower than unity for both spectral frequencies at the 10^{-6} hazard level (Figures 14-8b and 14-8d). Note that use of the characteristic earthquake magnitude PDF for Category B rupture sources is not an actual branch of the Diablo Canyon SSC logic tree, but it is included as an informative result on the impact that very large earthquakes and the magnitude PDF selection have on hazard and ground-motion uncertainty at the DCPP.

The third and fourth rows on each plot for the Magnitude Distribution Model sensitivities (Figure 14-8) explore the contribution to uncertainty of selection of M_{max} and M_{char}. These sensitivities were performed for the same Category B rupture sources that were used for the first two sensitivities, but the results should be representative of the total model uncertainty to M_{char} based on the high fractional contribution to hazard from the

Hosgri fault source (which is represented by nearly all the Category B rupture sources). The sensitivities were set up similar to those for the slip rate sensitivity, where the high, middle, and low branch values (mostly represented by the values for Hosgri sources H-01 to H-03 on Table 10-4) were selected as a group. M_{max} values [and weights] are 8.5 [0.1], 8.1 [0.5], and 7.8 [0.4], and M_{char} values [and weights] are 7.3 [0.2], 7.1 [0.5], and 6.8 [0.3]. The results show that the M_{max} selection has little impact on ground-motion uncertainty at the 10^{-4} hazard level for both spectral frequencies (Figures 14-8a and 14-8c). For the 10^{-6} hazard level at both spectral frequencies, the highest M_{max} value (**M** 8.5) results in a ground-motion ratio slightly greater than unity, and the lowest M_{max} value (**M** 7.8) results in a ratio slightly less than unity (Figures 14-8b and 14-8d). For M_{char}, ground-motion ratios for the 5 Hz spectral frequency at the 10^{-6} hazard level cluster around unity (Figure 14-8b). For the remaining three cases, the highest M_{char} value (**M** 7.3) results in a ground-motion ratio slightly less than unity, and the lowest M_{char} value (**M** 6.8) results in a ratio slightly greater than unity (Figures 14-8a, 14-8c, and 14-8d). In general, however, the ground-motion ratio values for these cases are tightly clustered around unity, indicating their relatively lower impact on the total ground-motion uncertainty at the DCPP.

14.2.8 Summary of Sensitivity Analyses

The above sensitivity analyses are summarized in tornado plots for the two spectral frequencies of 5 Hz (Figure 14-9) and 0.5 Hz (Figure 14-10) at the two hazard levels of 10^{-4} and 10^{-6}. In these compilation plots, the symbol size is constant and not scaled as a function of the individual weights for a specific branch of the logic tree. The order of the hazard sensitivities approximately follows the largest to smallest difference from unity in the ground-motion ratios (e.g., Figure 14-9), but the order of the hazard sensitivities is consistent from plot to plot.

The sensitivity analyses summarized on the plots indicate that the largest contribution from the Diablo Canyon SSC model to ground-motion uncertainty at the DCPP is uncertainty in the slip rate of the Hosgri fault source, followed by the EPR uncertainty for the Hosgri fault. This observation is not unexpected because both slip rate and EPR contribute directly to earthquake recurrence rate, and the Hosgri fault source is the largest contributor to total hazard at the DCPP site (*Section 14.2.1*; Figure 14-2).

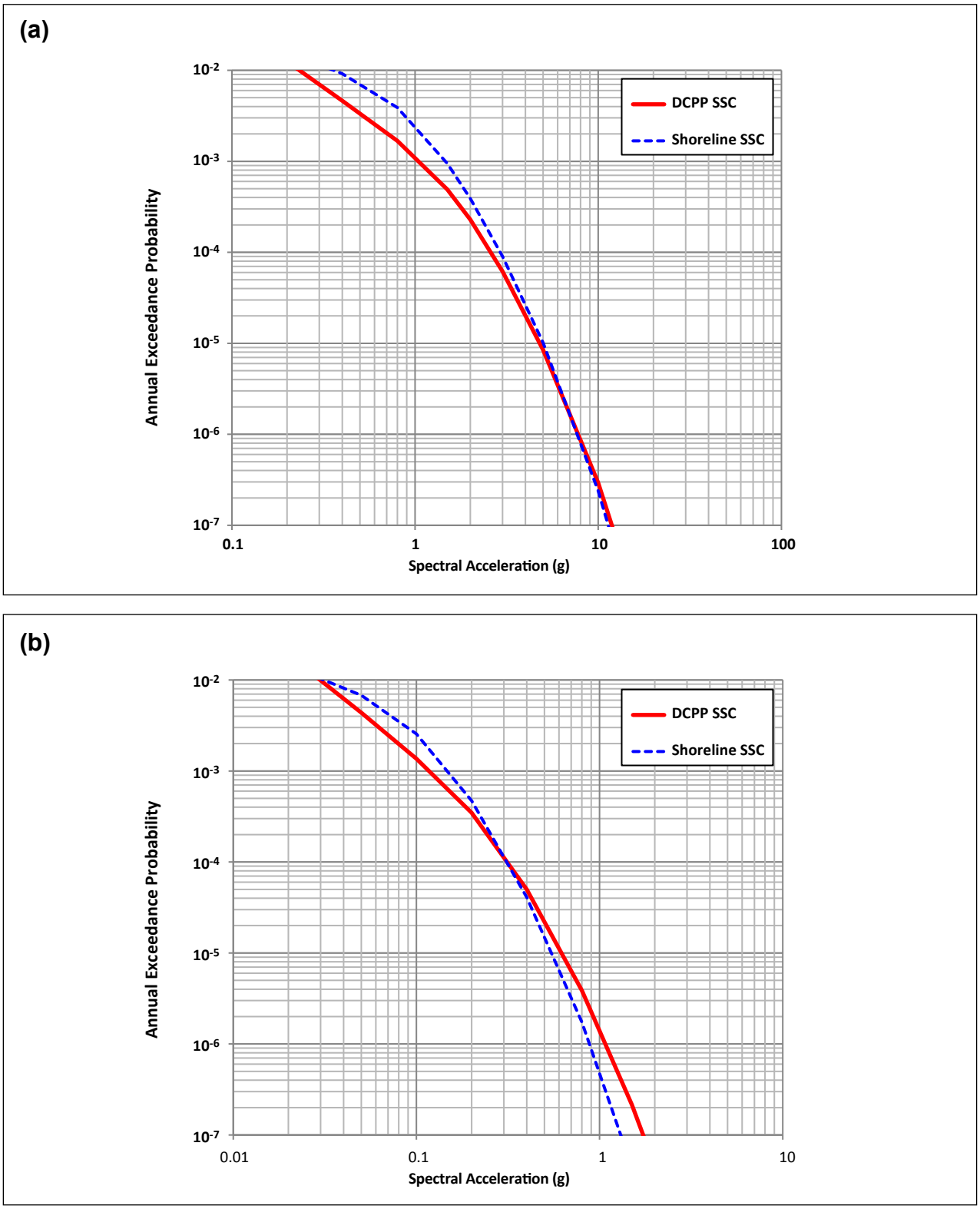

Note: Mean hazard curves were computed for both source models using a simplified version of the full SWUS GMC logic tree, as described in the text. For AEPs of 10^{-4} to 10^{-6}, the mean spectral accelerations computed from the 2015 Diablo Canyon SSC model at 5 Hz are between 2 g and 8 g (panel a), and the mean spectral accelerations at 0.5 Hz are between 0.3 g and 1.1 g (panel b).

Comparison of Mean Hazard Curves Using the Diablo Canyon SSC and 2011 Shoreline Report SSC Models: (a) for 5 Hz Spectral Frequency, and (b) for 0.5 Hz Spectral Frequency

DCPP SSC REPORT

Pacific Gas and Electric Company

Figure **14-1**

File path: S:\1005\005\Final_Report_Figures\Figure_1400-01.ai; Date: 03/10/2015; User: Serkan Bozkurt, LCI; Rev.1

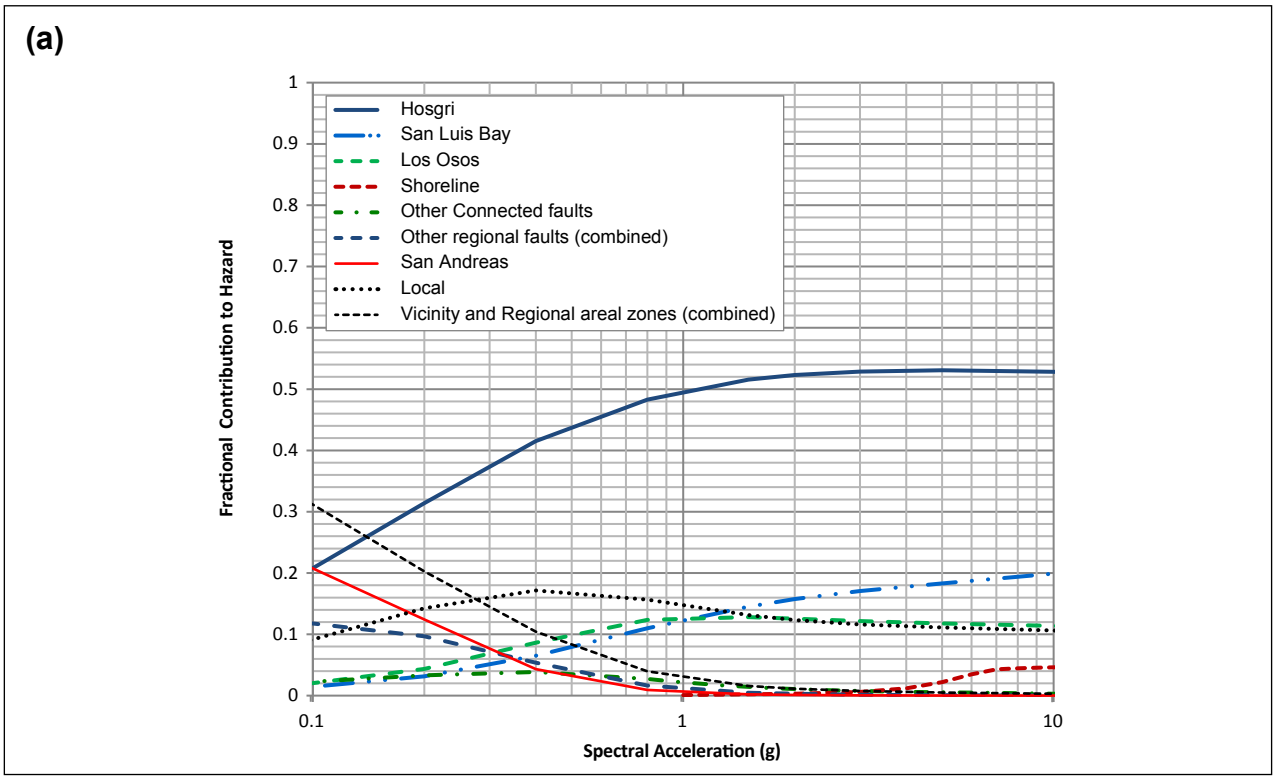

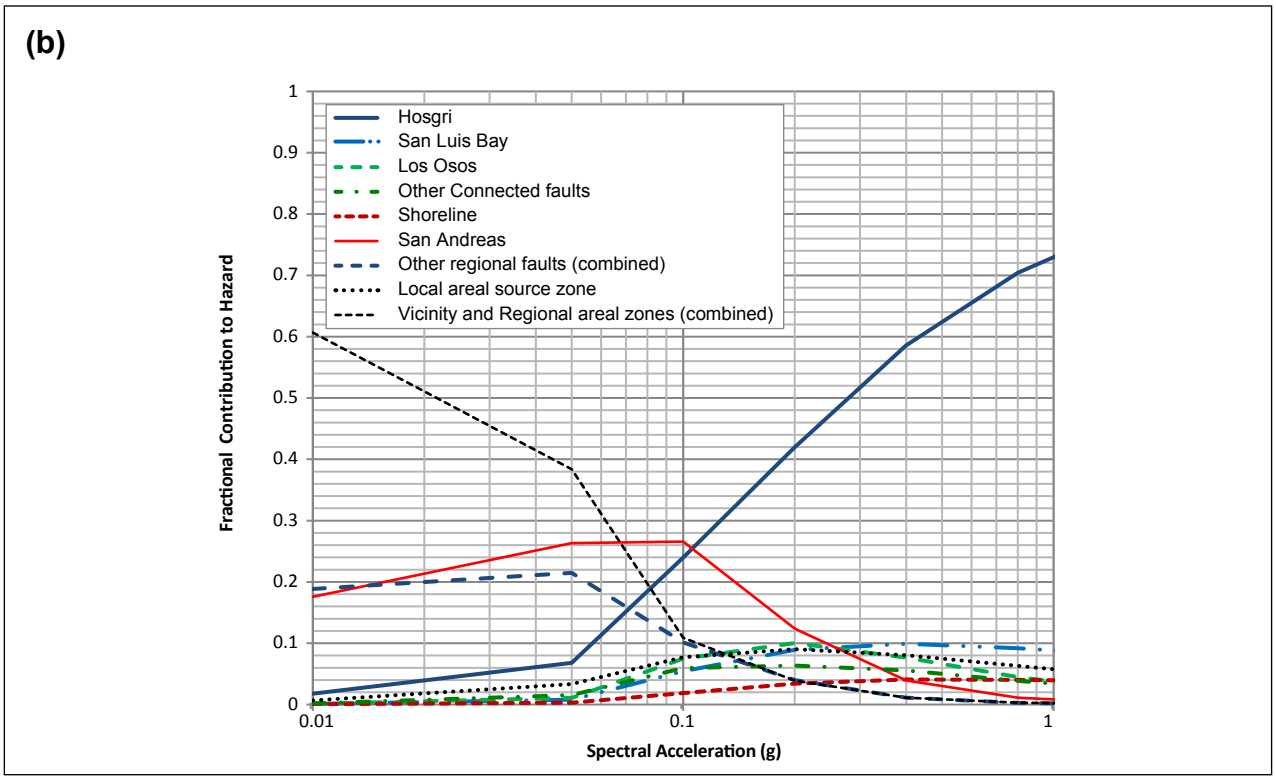

Note: The fractional contribution of individual seismic sources to total mean hazard at the DCPP is plotted against spectral acceleration for 5Hz (panel a) and 0.5 Hz (panel b) spectral frequencies. Within the AEPs of interest (between 2 g and 8 g at 5 Hz, and between 0.3 g and 1.1 g at 0.5 Hz; see Figure 14-1), the Hosgri fault is the dominant contributor. Contributions from sources that contribute less than 2% within the AEPs of interest were combined for this plot.

Fractional Contribution from Individual Seismic Sources to the Total Mean Hazard: (a) for 5 Hz Spectral Frequency, and (b) for 0.5 Hz Spectral Frequency

DCPP SSC REPORT

Pacific Gas and Electric Company

Figure **14-2**

File path: S:\1005\005\Final_Report_Figures\Figure_1400-02.ai; Date: 03/06/2015; User: Serkan Bozkurt, LCI; Rev.1

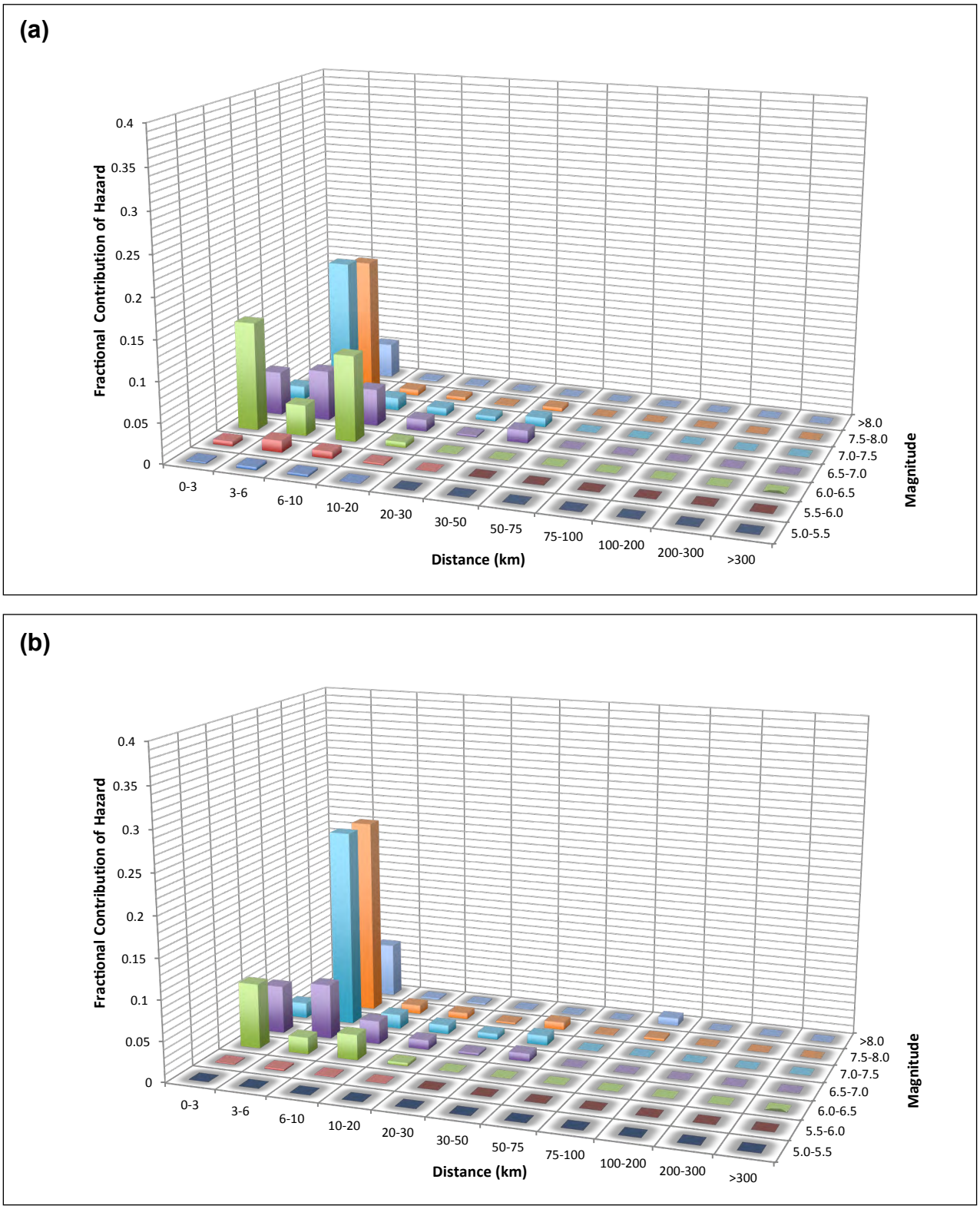

Note: Deaggregation plots show that the hazard at the DCPP is controlled by seismic sources close to the site. At high frequency (5 Hz on panel a), hazard is contributed over a variety of distances and magnitude ranges. At lower frequency (0.5 Hz on panel b), hazard is dominated by large-magnitude (**M** 7.0–8.0) events at 3–6 km distance.

Deaggregation of Rock Hazard for Hazard at 10^{-4} Annual Probability of Exceedance: (a) for 5 Hz Spectral Frequency, and (b) for 0.5 Hz Spectral Frequency

DCPP SSC REPORT

Pacific Gas and Electric Company

Figure **14-3**

File path: S:\1005\005\Final_Report_Figures\Figure_1400-03.ai; Date: 03/03/2015; User: Serkan Bozkurt, LCI; Rev.1

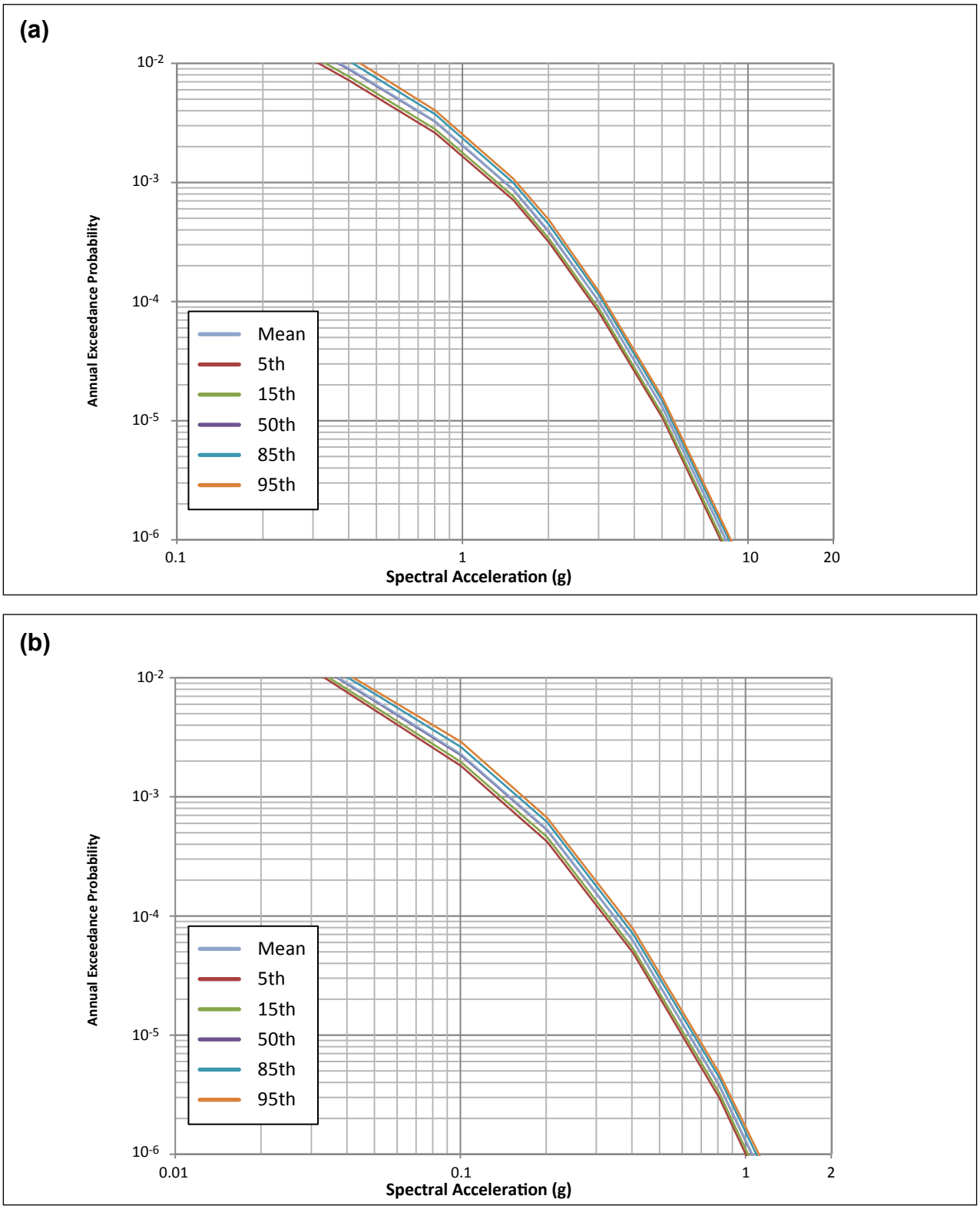

Note: Fractile hazard curves for the 5 Hz (panel a) and 0.5 Hz (panel b) spectral accelerations represent the range in hazard curves indicated by branches of the Diablo Canyon SSC logic tree.

Fractile Hazard Curves Based on the Diablo Canyon SSC Model and the Central Common Functional Form and CB14 GMPEs: (a) for 5 Hz Spectral Frequency, and (b) for 0.5 Hz Spectral Frequency

DCPP SSC REPORT

Pacific Gas and Electric Company

Figure **14-4**

File path: S:\1005\005\Final_Report_Figures\Figure_1400-04.ai; Date: 03/03/2015; User: Serkan Bozkurt, LCI; Rev.1

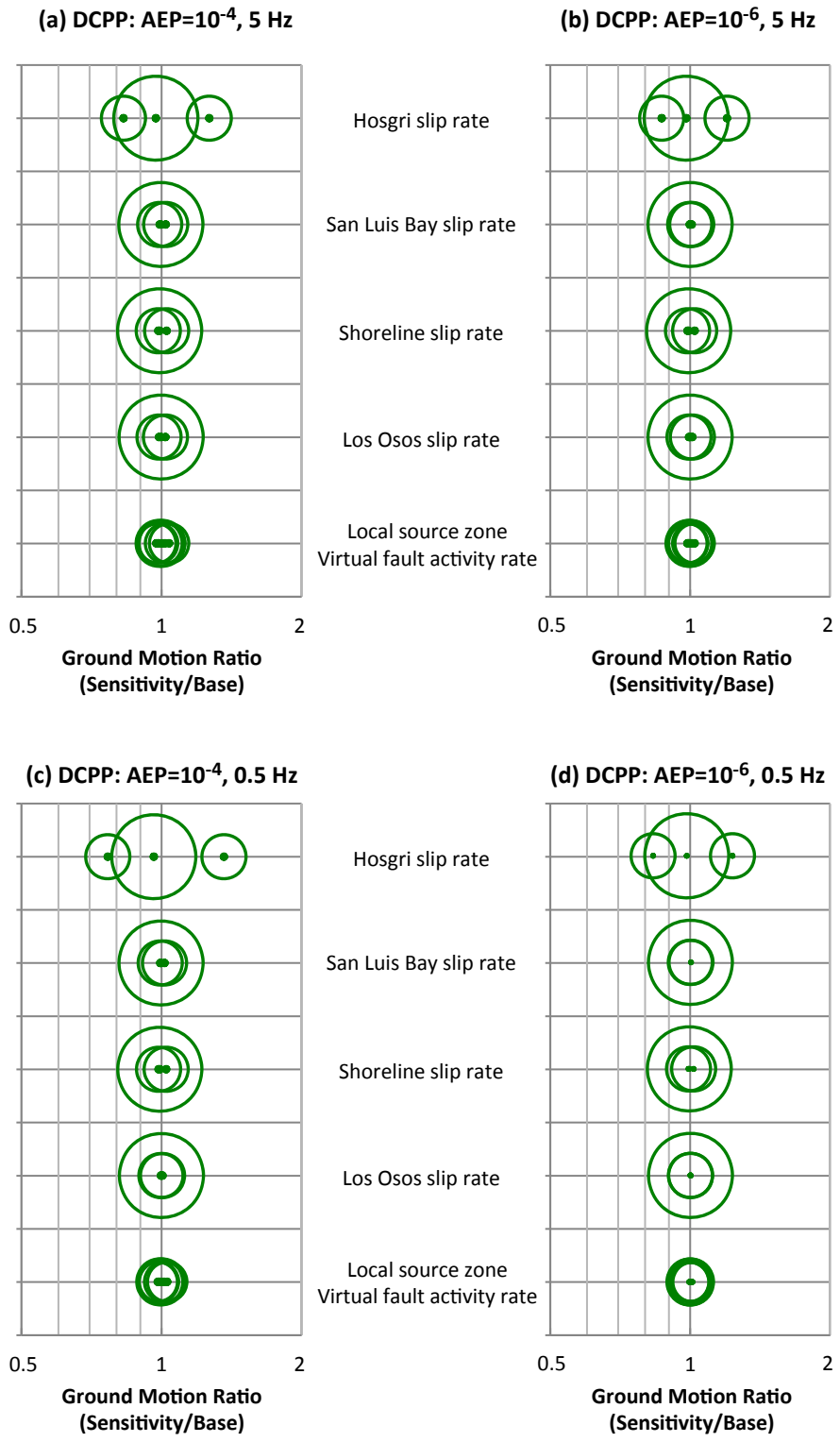

Note: Tornado plots show that at both spectral frequencies and both AEPs, hazard at the DCPP is more sensitive to uncertainty in the slip rate of the Hosgri fault than to slip rates of the other sources tested.

Tornado Plots for the Slip Rate Sensitivities

DCPP SSC REPORT

Pacific Gas and Electric Company

Figure **14-5**

File path: S:\1005\005\Final_Report_Figures\Figure_1400-05.ai; Date: 03/06/2015; User: Serkan Bozkurt, LCI; Rev.1

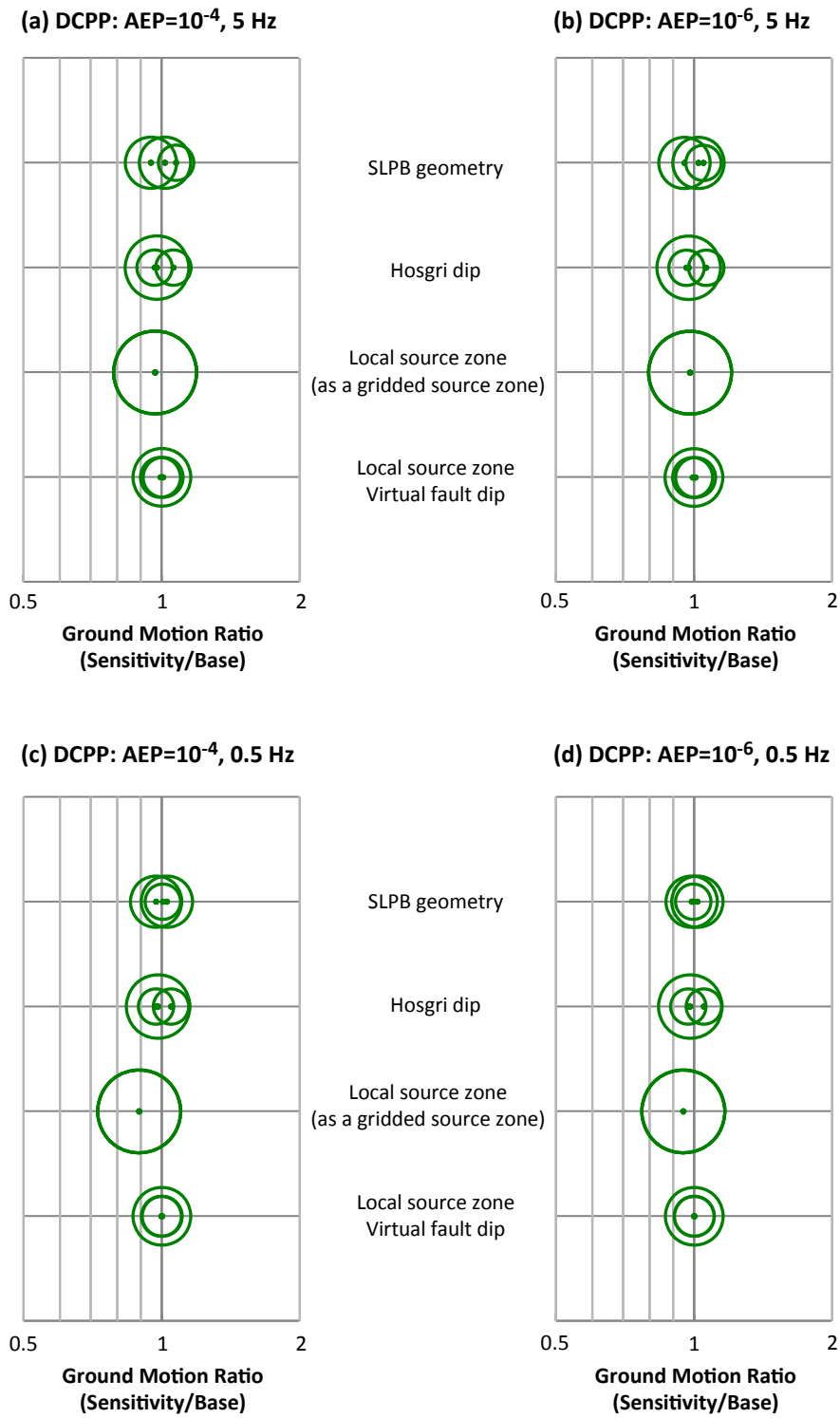

Note: Tornado plots show the relative effects of uncertainty in Fault Geometry Models to ground motions at the DCPP. The third line of each plot shows that modeling the Local areal source as gridded seismicity (which was not performed, and is shown by a single point less than unity) would result in lower hazard than modeling it with virtual faults (which was performed).

Tornado Plots for the Fault Geometry Sensitivities

DCPP SSC REPORT

Pacific Gas and Electric Company

Figure **14-6**

File path: S:\1005\005\Final_Report_Figures\Figure_1400-06.ai; Date: 03/03/2015; User: Serkan Bozkurt, LCI; Rev.1

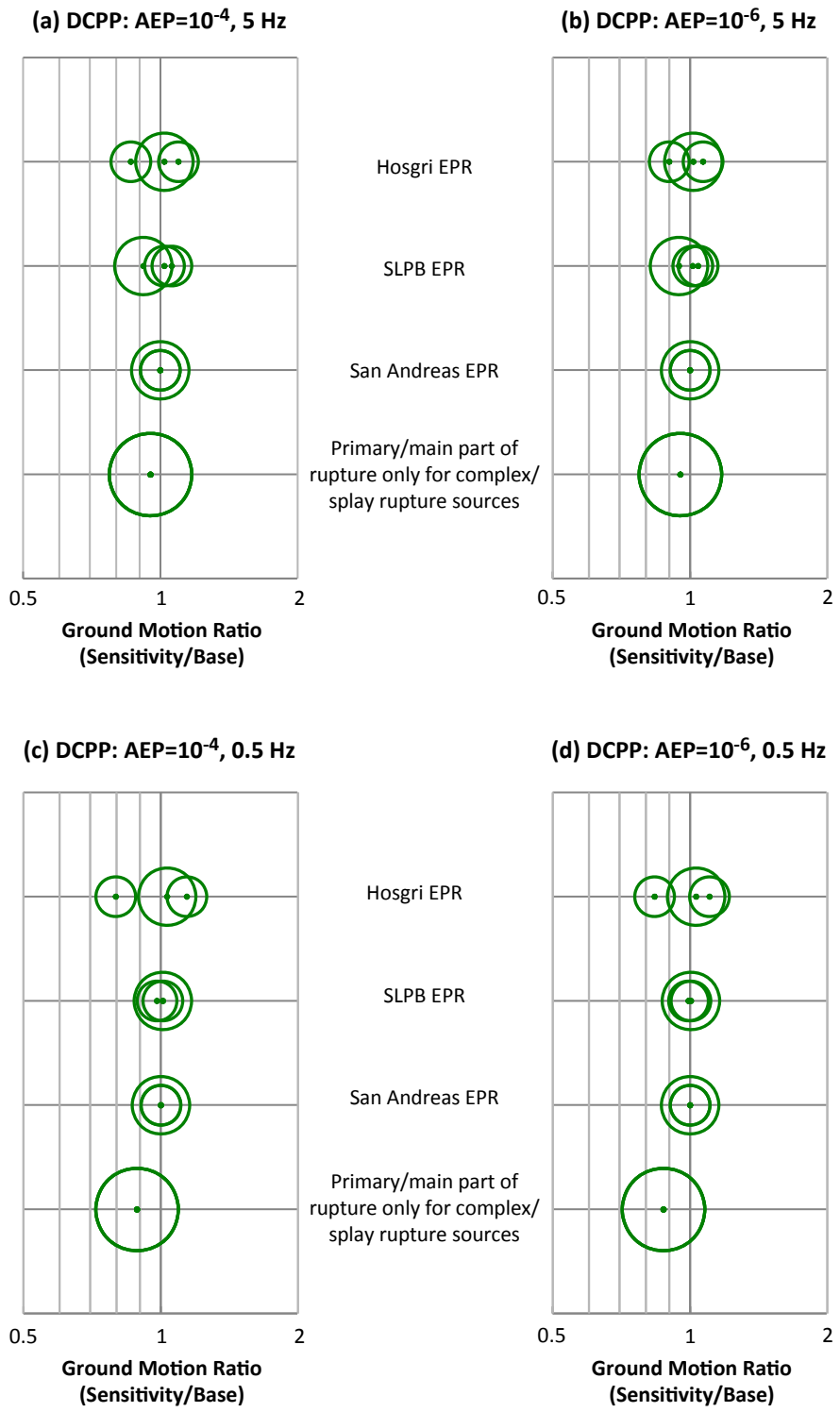

Note: Tornado plots show that the spectral accelerations at the DCPP are more sensitive to uncertainty in the EPR for the Hosgri fault than the other sources tested. The fourth line of each plot shows the relative hazard that would result from modeling splay and complex ruptures as single primary (or main) ruptures instead of modeling them as joint ruptures (which was performed).

Tornado Plots for the Time Dependency Model and Complex/Splay Rupture Sensitivities

DCPP SSC REPORT

Pacific Gas and Electric Company

Figure **14-7**

File path: S:\1005\005\Final_Report_Figures\Figure_1400-07.ai; Date: 03/03/2015; User: Serkan Bozkurt, LCI; Rev.1

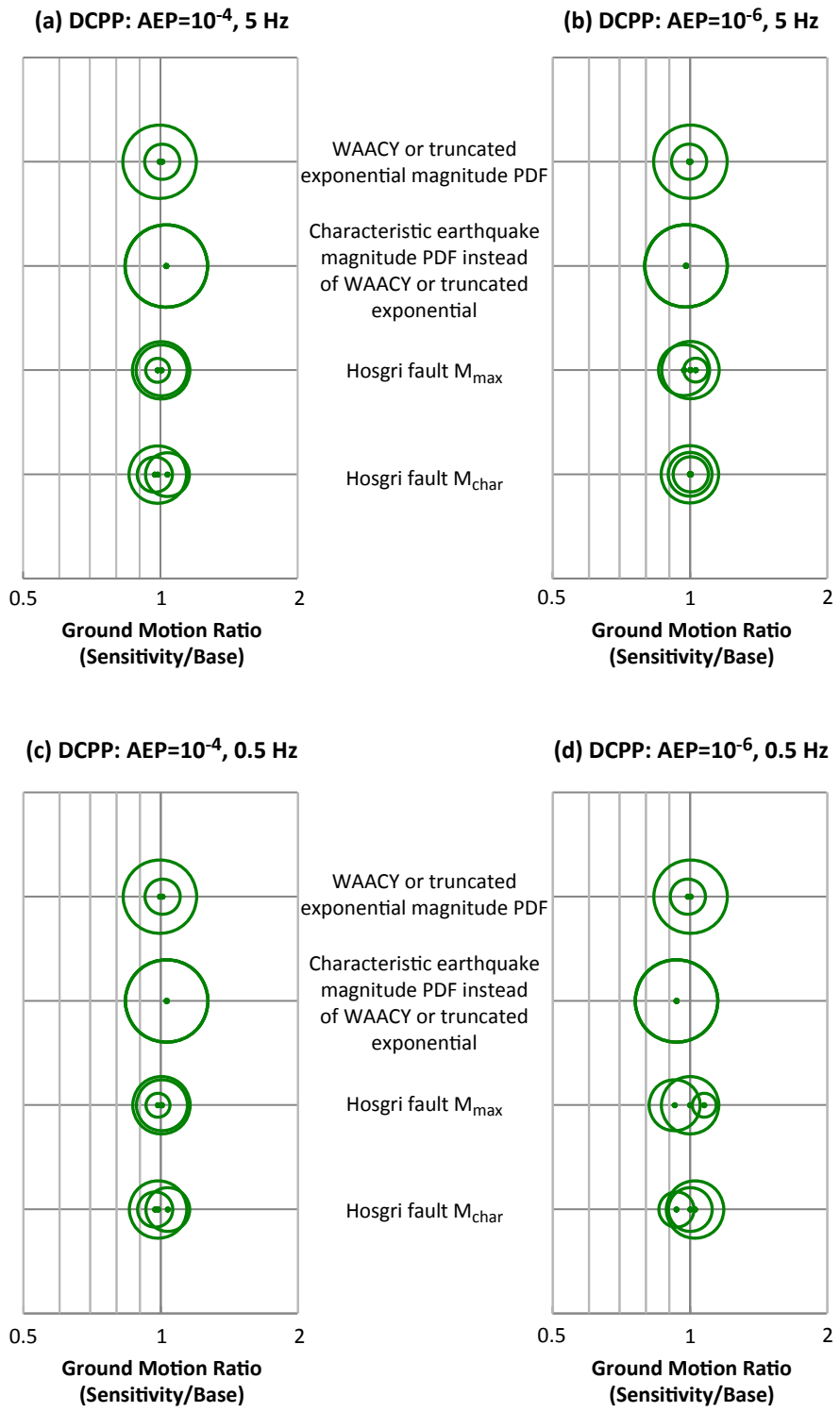

Note: The tornado plots above show the effects of various approaches to characterizing MFDs on Category B (very long) rupture sources. The second line of each panel shows the relative hazard that would result from omitting earthquakes larger than M_{char} on these sources. For three of the four combinations tested, omitting these larger-magnitude events would result in higher ground motions. At a 0.5 Hz spectral acceleration and AEP of 10^{-6}, omitting these larger events would decrease ground motions.

Tornado Plots for the Magnitude Distribution Model Sensitivities

DCPP SSC REPORT

Pacific Gas and Electric Company

Figure **14-8**

File path: S:\1005\005\Final_Report_Figures\Figure_1400-08.ai; Date: 03/03/2015; User: Serkan Bozkurt, LCI; Rev.1

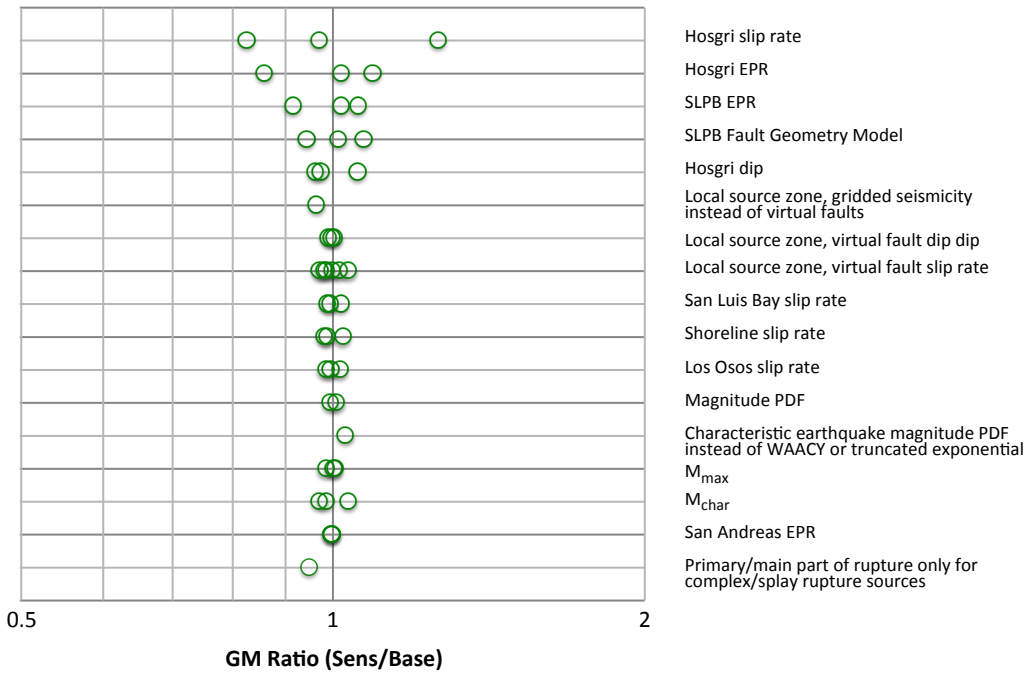

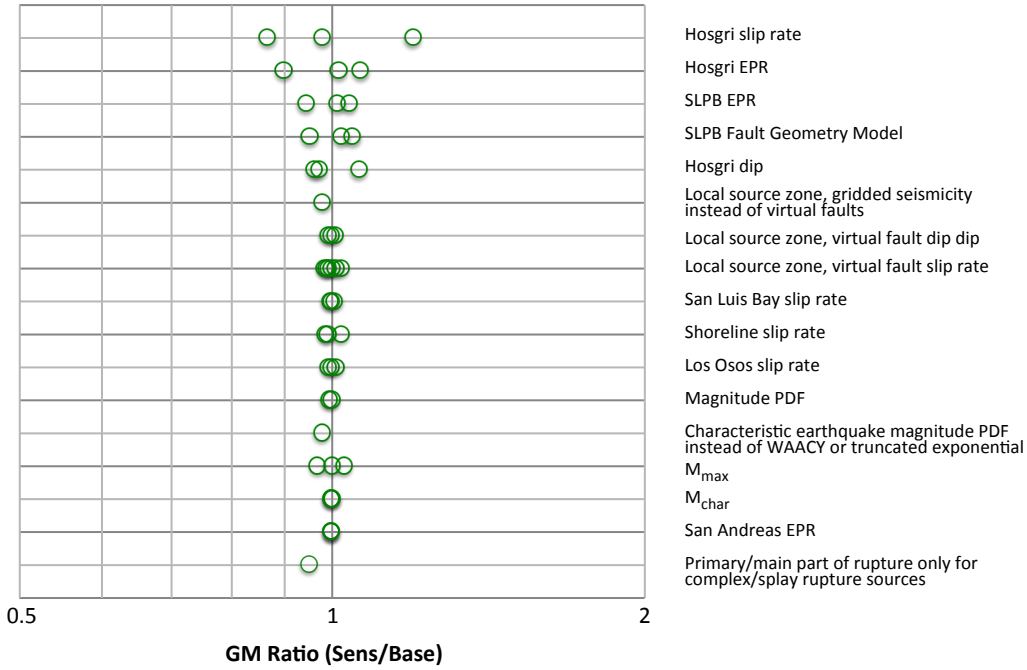

Note: Summary tornado plots showing the relative contribution to hazard uncertainty for each sensitivity case tested. The largest contributors to uncertainty are placed at the top of the tornado diagram.

Summary Tornado Plots for the SSC Model Sensitivity Analyses for 5 Hz Spectral Frequency: (a) at the 10^{-4} Hazard Level, and (b) at the 10^{-6} Hazard Level

DCPP SSC REPORT

Pacific Gas and Electric Company

Figure **14-9**

File path: S:\1005\005\Final_Report_Figures\Figure_1400-09.ai; Date: 03/03/2015; User: Serkan Bozkurt, LCI; Rev.1

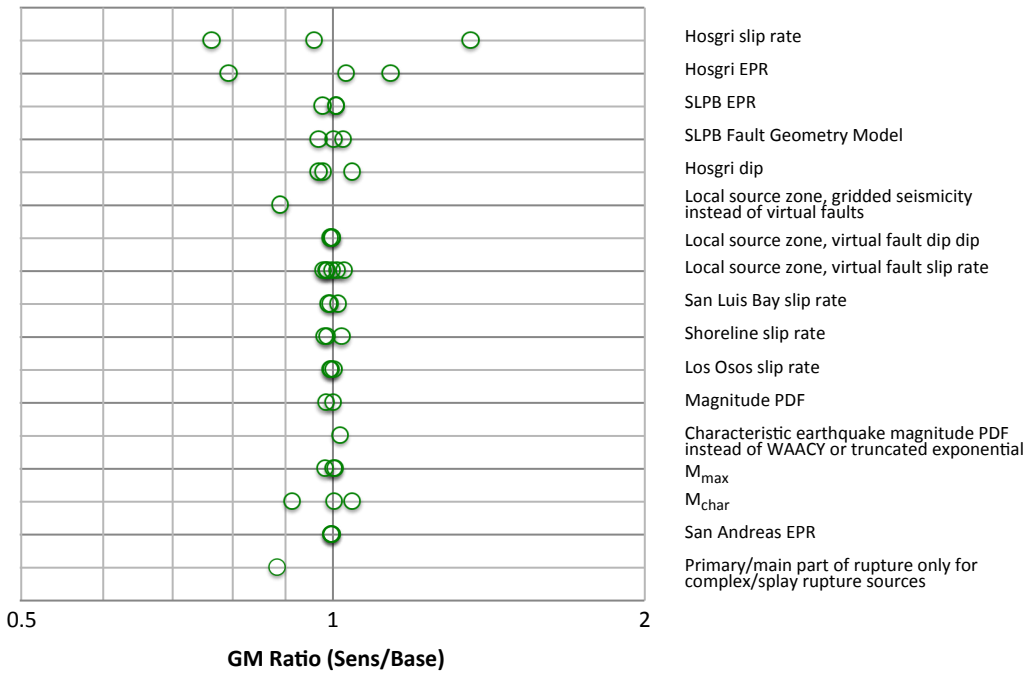

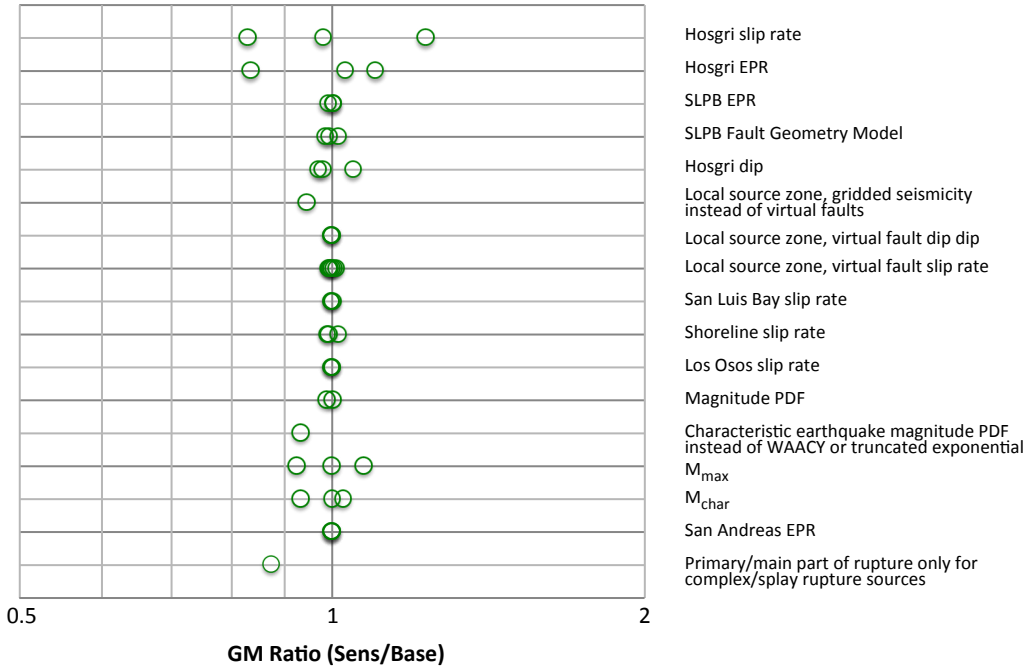

Note: Summary tornado plots showing the relative contribution to hazard uncertainty for each sensitivity case tested. The largest contributors to uncertainty are placed at the top of the tornado diagram.

Summary Tornado Plots for the SSC Model Sensitivity Analyses for 0.5 Hz Spectral Frequency: (a) at the 10^{-4} Hazard Level, and (b) at the 10^{-6} Hazard Level

DCPP SSC REPORT

Pacific Gas and Electric Company

Figure **14-10**

File path: S:\1005\005\Final_Report_Figures\Figure_1400-10.ai; Date: 03/03/2015; User: Serkan Bozkurt, LCI; Rev.1

15.0 REFERENCES

Abrahamson, N., 2014. WAACY Magnitude PDF Model (Wooddell, Abrahamson, Acevedo-Cabrera, and Youngs), presentation at DCPP SSC Workshop 3, March 25.

Akçiz, S.O., Ludwig, L.G., Arrowsmith, J.R., and Zielke, O., 2010. Century-long average time intervals between earthquake ruptures of the San Andreas fault in the Carrizo Plain, California, *Geology* **38** (9): 787–790.

Aki, K., 1965. Maximum likelihood estimate of b in the formula log $N = a - bM$ and its confidence limits, *Bulletin of the Earthquake Research Institute* [University of Tokyo] **43**: 237-239.

Aki, K., 1966. Generation and propagation of G waves from the Niigata earthquake of June 16, 1964, Part 2: Estimation of earthquake moment, released energy, and stress-strain drop from the G wave spectrum, *Bulletin of the Earthquake Research Institute* **44**: 73–88.

Aki, K., and Richards, P.G., 1980. *Quantitative Seismology: Theory and Methods, Vol. 1*, W.H. Freeman and Co., New York.

Alterman, I.B., McMullen, R.B., Cluff, L.S., and Slemmons, D.B. (editors), 1994. *Seismotectonics of the Central California Coast Ranges*, Geological Society of America Special Papers 292.

AMEC Geomatrix, Inc. (AMEC), 2011. Summary of Southwestern Boundary Zone Preliminary Geomorphic Studies and Subsurface Data Compilation, Diablo Canyon Power Plant, San Luis Obispo, California, draft report submitted to PG&E January 2011.

AMEC Environment & Infrastructure (AMEC), 2012a. Compilation of Geologic Maps and GIS Databases for the Irish Hills and Surrounding Areas, Diablo Canyon Power Plant, LTSP Update: Draft Consultants Report to PG&E, AMEC project 13838C01.CWA172, January 3.

AMEC Environment & Infrastructure, Inc. (AMEC), 2012b. Preliminary Reevaluation of Emergent Shoreline Angles, San Luis Range, Diablo Canyon Power Plant, San Luis Obispo, California, draft letter report submitted to PG&E, February.

AMEC Geomatrix, Inc. (AMEC), 2011. Summary of Southwestern Boundary Zone Preliminary Geomorphic Studies and Subsurface Data Compilation, Diablo Canyon Power Plant, San Luis Obispo, California, draft report submitted to PG&E, January.

Anastasakis, G., and Piper, D.J.W., 2013. The changing architecture of sea-level lowstand deposits across the Mid-Pleistocene transition: South Evoikos Gulf, Greece, *Quaternary Science Reviews* **73**: 103–114.

Ancheta, T.D., Darragh, R.B., Stewart, J.P., Seyhan, E., Silva, W.J., Chiou, B.S., Wooddell, K.E., Graves, R.W., Kottke, A.R., Boore, D.M., Kishida, T., and Donahue, J.L., 2013. *PEER NGA-West2 Database*, PEER Report 2013/03, Pacific Earthquake Engineering Research Center.

Archuleta, R.J., 1984. A faulting model for the 1979 Imperial Valley earthquake, *Journal of Geophysical Research* **89**: 4559–4585.

Atwater, T.M., 1970. Implications of plate tectonics for the Cenozoic tectonic evolution of western North America, *Geological Society of America Bulletin* **81**: 3513–3536.

Atwater T., and Stock, J., 1998. Pacific–North American plate tectonics of the Neogene southwestern United States: An update, *International Geology Review* **40** (5): 375–402, DOI: 10.1080/00206819809465216

Atwater, T.M., 2011. Downloads, *Educational Multimedia Visualization Center*; available at http://emvc.geol.ucsb.edu/1_DownloadPage/Download_Page.html, accessed February 12, 2015.

Baldwin, J., 2011. Los Osos Fault Data Compilation, presentation at DCPP SSHAC Workshop 1, December 1; available at http://www.pge.com/mybusiness/edusafety/systemworks/dcpp/SSHAC/workshops/index.shtml.

Bayasgalan, A., Jackson, J., Ritz, J.-F., and Carretier, S., 1999. Field examples of strike-slip fault terminations in Mongolia and their tectonic significance, *Tectonics* **18** (3): 394–411.

Bell, J.W., Caskey, S.J., Ramelli, A.R., and Guerrieri, L., 2004. Pattern and rates of faulting in the central Nevada seismic belt, and paleoseismic evidence for prior belt-like behavior, *Bulletin of the Seismological Society of America* **94** (4): 1229–1254.

Ben-Zion, Y. and Lyakhovsky, V., 2006, Analysis of aftershocks in a lithospheric model with seismogenic zone governed by damage rheology, *Geophys. J. Int.* **165**: 197–210, doi: 10.1111/j.1365-246X.2006.02878.x.

Bernreuter, D. L., Savy, J.B., Mensing, R.W., and Chen, J.C., 1989. Seismic Hazard Characterization of 69 Nuclear Plant Sites East of the Rocky Mountains. Report NUREG/CR-5250, vols. 1-8, prepared by Lawrence Livermore National Laboratory for the U.S. Nuclear Regulatory Commission.

Berryman, K.R., Cochran, U.A., Clark, K.J., Biasi, G.P., Langridge, R.M., and Villamor, P. 2012. Major earthquakes occur regularly on an isolated plate boundary fault, *Science*, **336** (6089): 1690 DOI: 10.1126/science.1218959.

Biasi, G.P., 2012. Fault-to-Fault Ruptures and Propagation through Geometric Complexities, presentation at DCPP SSHAC Workshop 2, November 7; available at

http://www.pge.com/mybusiness/edusafety/systemworks/dcpp/SSHAC/workshops/index.shtml.

Biasi, G.P., 2013. Appendix H—Maximum Likelihood Recurrence Intervals for California Paleoseismic Sites: in Field, E.H., Biasi, G.P., Bird, P., Dawson, T.E., Felzer, K.R., Jackson, D.D., Johnson, K.M., and 11 others [Working Group on California Earthquake Probabilities], 2013. *Uniform California Earthquake Rupture Forecast, Version 3 (UCERF3)—The Time-Independent Model*, U.S. Geological Survey Open-File Report 2013–1165, 25 pp.

Biasi, G.P., Parsons, T., Weldon, R.J., II, and Dawson, T.E., 2013. Appendix J—Fault-to-Fault Rupture Probabilities: in Field, E.H., Biasi, G.P., Bird, P., Dawson, T.E., Felzer, K.R., Jackson, D.D., Johnson, K.M., and 11 others [Working Group on California Earthquake Probabilities], 2013. *Uniform California Earthquake Rupture Forecast, Version 3 (UCERF3)—The Time-Independent Model*, U.S. Geological Survey Open-File Report 2013–1165/ California Geological Survey Special Report 228/ and Southern California Earthquake Center Publication 1792, 20 pp.

Biasi, G.P., and Weldon, R.J., II, 2009. San Andreas fault rupture scenarios from multiple paleoseismic records: Stringing pearls, *Bulletin of the Seismological Society of America* **99** (2A): 471–498.

Biasi, G.P., Weldon, R.J., II, and Dawson, T.E., 2013. Appendix F—Distribution of Slip in Ruptures: in Field, E.H., Biasi, G.P., Bird, P., Dawson, T.E., Felzer, K.R., Jackson, D.D., Johnson, K.M., and 11 others [Working Group on California Earthquake Probabilities], 2013. *Uniform California Earthquake Rupture Forecast, Version 3 (UCERF3)—The Time-Independent Model*, U.S. Geological Survey Open-File Report 2013-1165, 41 pp.

Biasi, G.P., Weldon, R.J., II, Fumal, T.E., and Seitz, G.G., 2002. Paleoseismic event dating and the conditional probability of large earthquakes on the southern San Andreas fault, California, *Bulletin of the Seismological Society of America* **92** (7): 2761–2781.

Bierman, P., 2013. *Terrace Dating and Basin Scale Erosion Rates—Proof of Concept, San Luis Obispo Area*, letter report to Pacific Gas and Electric Company, submitted May 16, 9 pp.

Bintanja, R., and van de Wal, R.S.W., 2008. North American ice-sheet dynamics and the onset of 100,000-year glacial cycles, *Nature* **454**: 869–872.

Bird, P., 2012. NeoKinema Fault-Based Deformation Model of the California Region for UCERF3, with Focus on the DCPP Region, presentation at DCPP SSHAC Workshop 2, November 7; available at http://www.pge.com/mybusiness/edusafety/systemworks/dcpp/SSHAC/workshops/index.shtml.

Bird, P., and Liu, Z., 2007. Seismic hazard inferred from tectonics: California, *Seismological Research Letters* **78** (1): 37–48.

Briggs, I.C., 1974. Machine contouring using minimum curvature, *Geophysics* **39**: 39–48.

Brune, J.N., 1968. Seismic moment, seismicity, and rate of slip along major fault zones, *Journal of Geophysical Research* **73** (2): 777-784.

Bruns, T.R., Cooper, A.K., Carlson, P.R., and McCulloch, D.S., 2002. Structure of the submerged San Andreas and San Gregorio fault zones in the Gulf of the Farallones off San Francisco, California, from high-resolution seismic-reflection data: in Parsons, T. (editor), *Crustal Structure of the Coastal and Marine San Francisco Bay Region, California*, U.S. Geological Survey Professional Paper 1658, pp. 77-117.

Budnitz R.J., Apostolakis, G., Boore, D.M., Cluff, L.S., Coppersmith, K.J., Cornell, C.A., and Morris, P.A., 1997. Recommendations for Probabilistic Seismic Hazard Analysis: Guidance on Uncertainty and Use of Experts—Main Report. NUREG/CR-6372, Vol. 1, U.S. Nuclear Regulatory Commission, Washington, D.C.

California Department of Water Resources (DWR), 2002. Water Resources of the Arroyo Grande—Nipomo Mesa Area, Southern District Report, 157 pp. and 6 appendices; available at www.dpla.water.ca.gov/sd/water_quality/arroyo_grande/arroyo_grande-nipomo_mesa.html.

California Energy Commission (CEC), 2008. *An Assessment of California's Nuclear Power Plants: AB 1632 Report*, Commission Report CEC-100-2008-009-CMF, 42 pp.

California State University, Monterey Bay, Sea Floor Mapping Lab (CSUMB), 2012. Multibeam echosounder (MBES) data for the California Central Coast. Available at http://seafloor.csumb.edu/SFMLwebDATA_c.htm (accessed December 2014).

Campbell, K.W., and Bozorgnia, Y., 2014. NGA-West2 ground motion model for the average horizontal components of PGA, PGV, and 5% damped linear acceleration response spectra, *Earthquake Spectra* **30** (3): 1087–1115.

Chiocci, F.L., Ercilla, G., and Torres, J., 1997. Stratal architecture of Western Mediterranean Margins as the result of the stacking of Quaternary lowstand deposits below "glacio-eustatic fluctuation base-level," *Sedimentary Geology* **112**: 195–217.

Clark, D.G., Slemmons, D.B., Caskey, S.J., DePolo, D.M., 1994, Seismotectonic framework of coastal central California: in Alterman, I.B., McMullen, R.B., Cluff, L.S., and Slemmons, D.B., eds., Seismotectonics of the Central California Coast Ranges: Boulder, Colorado, Geological Society of America Special Paper 292, pp. 9–30.

Clark, D.H., Hall, N.T., Hamilton, D.H., and Heck, R.G., 1991. Structural analysis of late Neogene deformation in the central offshore Santa Maria Basin, California, *Journal of Geophysical Research* **96** (B4): 6435–6457.

Clark, J.C., Brabb, E.E., Greene, H.G., and Ross, D.C., 1984. Geology of the Point Reyes Peninsula and implications for San Gregorio fault history: in Crouch, J.K., and Bachman, S.B. (editors), *Tectonics and Sedimentation Along the California Margin*, Pacific Sections, Society of Economic Paleontologists and Mineralogists, Vol. 38, pp. 67–85.

Cleath & Associates, 2003. Geologic Structure of the Los Osos Valley Ground Water Basin, unpublished consulting report: prepared for the Los Osos Community Services District, November.

Compton, J.S., 2011. Pleistocene sea-level fluctuations and human evolution on the southern coastal plain of South Africa, *Quaternary Science Reviews* **30**: 506–527.

Coppersmith, K.J., and Bommer, J.J., 2012. Use of the SSHAC methodology within regulated environments: Cost-effective application for seismic characterization at multiple sites, *Nuclear Engineering and Design* **245**: 233–240.

Coppersmith, K.J., Bommer, J.J., Kammerer, A.M., and Ake, J., 2010, Implementation guidance for SSHAC Level 3 and 4 processes, PSAM conference, Seattle, Washington.

Cornell, C.A., 1968. Engineering seismic risk analysis, *Bulletin of the Seismological Society of America* **58** (5): 1583–1606.

Cornell, C.A., and Vanmarcke, E.H., 1969. The major influences on seismic risk, *Proceedings of the Fourth World Conference on Earthquake Engineering, Santiago, Chile* **A-1**: 69-93.

Cornell, C.A., and Winterstein, S.R., 1988. Temporal and magnitude dependence in earthquake recurrence models, *Bulletin of the Seismological Society of America* **78** (4): 1522–1537.

Cox, A., and Engebretson, D., 1985. Change in motion of Pacific plate at 5 Myr BP, *Nature* **313**: 472–474.

Crone, A.J., Personius, S.F., Craw, P.A., Haeussler, P.J., and Staft, L.A., 2004. The Susitna Glacier thrust fault: Characteristics of surface ruptures on the fault that initiated the 2002 Denali fault earthquake, *Bulletin of the Seismological Society of America* **94** (6B): S5–S22.

Delattre, M.P., and Wiegers, M.O., 2014. Preliminary Geologic Map of the Nipomo 7.5′ Quadrangle, San Luis Obispo County, California: A Digital Database, Version 1.0, scale 1:24,000, California Geological Society.

DeMets, C., 2012a. Final report: Kinematics of coastal California inferred from GPS geodesy, Unpublished Technical Report Submitted to Pacific Gas and Electric Company, December: 21 pp.

DeMets, C., 2012b. Plate Margin Deformation and Kinematics from GPS Data, presentation at DCPP SSHAC Workshop 2, November 7; available at

http://www.pge.com/mybusiness/edusafety/systemworks/dcpp/SSHAC/workshops/index.shtml.

DeMets, C., Márquez-Azúa, B., Cabral-Cano, E., 2014. A new GPS velocity field for the Pacific Plate – Part 2: implications for fault slip rates in western California. *Geophysical Journal International* **199** (3): 1900-1909 doi:10.1093/gji/ggu347.

dePolo, C.M., 2012. Fault Segmentation and Earthquake Rupture Length, PowerPoint presentation at DCPP SSC Workshop 2, November 8.

Dibblee, T.W., 1976, The Rinconada and related faults in the southern Coast Ranges, California, and their tectonic significance, *USGS Professional Paper* **981**, 55p.

Dickinson, W.R., 1981. Plate tectonics and the continental margin of California. *The Geotectonic Development of California*: Englewood Cliffs, New Jersey, Prentice-Hall, 1–28.

Dickinson, W.R., Ducea, M., Rosenberg, L.I., Greene, H.G., Graham S.A., Clark, J.C., Weber, G.E., Kidder, S., Ernst, W.G., and Brabb, E.E., 2005. Net Dextral Slip, Neogene San Gregorio-Hosgri Fault Zone, Coastal California: Geologic Evidence and Tectonic Implications, *Geological Society of America Special Paper 391*, 43 pp.

Eberhart-Phillips, D., Haeussler, P.J., Freymuller, J.T., Frankel, A.D., Rubin, C.M., Craw, P., Ratchkovski, N.A., and 22 others, 2003. The 2002 Denali fault earthquake, Alaska: A large magnitude, slip-partitioned event, *Science* **300**: 1113–1118, doi:10.1126/science.1082703.

Electric Power Research Institute (EPRI), 1988. Seismic Hazard Methodology for Central and Eastern United States. EPRI NR-4726, vols. 1–10.

Electric Power Research Institute (EPRI), 2003. CEUS ground motion project, model development and results, Rept. 1008910, EPRI, Palo Alto, CA.

Electric Power Research Institute (EPRI), 2006. Truncation of the lognormal distribution for ground motion models, Unpublished Consulting Report NULL (1014101), 112 pp.

Electric Power Research Institute (EPRI), U.S. Department of Energy, and U.S. Nuclear Regulatory Commission, 2012. *Central and Eastern United States (CEUS) Seismic Source Characterization for Nuclear Facilities*, EPRI Report 1021097/ DOE/NE-0140/ NUREG-2115.

Ellsworth, W.L., Matthews, M.V., Nadeau, R.M., Nishenko, S.P., Reasenberg, P.A., and Simpson, R.W., 1999. *A Physically-Based Earthquake Recurrence Model for Estimation of Long-Term Probabilities*, U.S. Geological Survey Open-File Report 99-522, 22 pp.

Fagereng, Å., and Toy, V.G., 2011. Geology of the earthquake source: An introduction: in Fagereng, Å., Toy, V.G., and Rowland, J.V. (editors), *Geology of the Earthquake Source*, Geological Society, London, Special Publications 359, Chapter 1, pp. 1–16.

Felzer, K.R., 2008. Appendix I—Calculating California Seismicity Rates: in *The Uniform California Earthquake Rupture Forecast, Version 2 (UCERF2)*: U.S. Geological Survey Open-File Report 2007-1437I, 44 pp.

Felzer, K.R., 2013a. Appendix K—*The UCERF3 Earthquake Catalog*: in Field, E.H., Biasi, G.P., Bird, P., Dawson, T.E., Felzer, K.R., Jackson, D.D., Johnson, K.M., and 11 others [Working Group on California Earthquake Probabilities], 2013. *Uniform California Earthquake Rupture Forecast, Version 3 (UCERF3)—The Time-Independent Model*, U.S. Geological Survey Open-File Report 2013-1165; available at http://pubs.usgs.gov/of/2013/1165/.

Felzer, K.R., 2013b. Appendix L—Estimate of the Seismicity Rate and Magnitude-Frequency Distribution of Earthquakes in California from 1850 to 2011: in Field, E.H., Biasi, G.P., Bird, P., Dawson, T.E., Felzer, K.R., Jackson, D.D., Johnson, K.M., and 11 others [Working Group on California Earthquake Probabilities], 2013. *Uniform California Earthquake Rupture Forecast, Version 3 (UCERF3)—The Time-Independent Model*, U.S. Geological Survey Open-File Report 2013-1165, 13 pp.

Felzer, K.R., and Brodsky, E.E., 2005. Testing the stress shadow hypothesis, *Journal of Geophysical Research* **110** (B5), doi:10.1029/2004JB003277.

Field, E.H., Biasi, G.P., Bird, P., Dawson, T.E., Felzer, K.R., Jackson, D.D., Johnson, K.M., Jordan, T.H., Madden, C., Michael, A.J., Milner, K.R., Page, M.T., Parsons, T., Powers, P.M., Shaw, B.E., Thatcher, W.R., Weldon, R.J., II, and Zeng, Y. [Working Group on California Earthquake Probabilities], 2013. *Uniform California Earthquake Rupture Forecast, Version 3 (UCERF3)—The Time-Independent Model*, U.S. Geological Survey Open-File Report 2013–1165/ California Geological Survey Special Report 228/ and Southern California Earthquake Center Publication 1792, 115 pp.

Field, E.H., Biasi, G.P., Bird, P., Dawson, T.E., Felzer, K.R., Jackson, D.D., Johnson, K.M., and 11 others, 2014. Uniform California Earthquake Rupture Forecast, Version 3 (UCERF3)—The time-independent model, *Bulletin of the Seismological Society of America* **104** (3): 1122-1180.

Field, E.H., Dawson, T.E., Felzer, K.R., and 8 others [2007 Working Group on California Earthquake Probabilities], 2008. *The Uniform California Earthquake Rupture Forecast, Version 2 (UCERF 2)*, USGS Open File Report 2007-1437, CGS Special Report 203, and SCEC Contribution 1138, 104 pp.

Field, E.H., Dawson, T.E., Felzer, K.R., and 8 others, 2009. Uniform California Earthquake Rupture Forecast, Version 2 (UCERF2), *Bulletin of the Seismological Society of America* **99** (4): 2053–2107.

Fitzenz, D.D., Ferry, M.A., and Jalobeanu, A., 2010. Long-term slip history discriminates among occurrence models for seismic hazard assessment, *Geophysical Research Letters* **37** (2): L20307, doi:10.1029/2010GL044071.

Fletcher, J.M., Teran, O.J., Rockwell, T.J., Oskin, M.E., Hudnut, K.W., Mueller, K.J., Spelz, R.M., and 14 others, 2014. Assembly of a large earthquake from a complex fault system: Surface rupture kinematics of the 4 April 2010 El Mayor–Cucapah (Mexico) M_w 7.2 earthquake, *Geosphere* **10** (4): 797–827.

Florensov, N.A., and Solonenko, V.P. (editors), 1963. *The Gobi-Altay Earthquake* (in Russian), 391 pp., Akademii Nauk, Moscow; English translation in 1965, Israel Program for Scientific Translations, Jerusalem, 424 pp.

Ford, G.A., 1992. Geology and History of Faulting of the Santa Ynez Fault Near Juncal Dam, Santa Barbara County, California," Doctoral dissertation, Stanford University).

Frankel, A.D., Petersen, M.D., Mueller, C.S., Haller, K.M., Wheeler, R.L., Leyendecker, E.V., and 5 others, 2002. *Documentation for the 2002 Update of the National Seismic Hazard Maps*, U.S. Geological Survey Open-File Report 02-420.

Gardner, J.K., and Knopoff, L., 1974. Is the sequence of earthquakes in Southern California, with aftershocks removed, Poissonian? *Bulletin of the Seismological Society of America* **64**: 1363-1367.

GeoPentech, Inc., 2015. Southwestern United States Ground Motion Characterization SSHAC Level 3—Technical Report, Rev. 2, March, available at www.pge.com/dcpp-ltsp/.

Graveleau, F., Suppe, J., Chang, K-J., Dominguez, S., Ustazewski, M., and Huang, M-H., 2014. Incremental vs. geological growth of folds: Examples of Tungshih anticline and Neiwan syncline during Taiwan Mw7.6 1999 ChiChi earthquake, *Geophysical Research Abstracts* **15**, EGU2014-6910.

Gray, B., Lewandowski, N., AbramsonWard, H., Hanson, K.L., Arcos, M.E.M., Page, W.D., 2013, Regional stratigraphic framework along the central California shelf margin for assessment of Quaternary activity on the Hosgri fault zone (Abstract), poster presented at the *Pacific Section Meeting of the American Association of Petroleum Geologists (AAPG)*, Monterey, CA, April 19-25, 2013.

Graymer, R.W., 2012. Irish Hills Geologic Cross Section, presentation at DCPP SSHAC Workshop 2, November 7; available at http://www.pge.com/mybusiness/edusafety/systemworks/dcpp/SSHAC/workshops/index.shtml.

Greenhaus, M.R., and Cox, A., 1979. Paleomagnetism of the Morro Rock-Islay Hill complex as evidence for crustal block rotations in central coastal California, *Journal of Geophysical Research* **84**: 2393–2400.

Gregor, N., 2014. Hazard Sensitivity and Background Sources, PowerPoint presentations at DCPP SSC SSHAC Workshop 3, 25 and 27 March; available at http://www.pge.com/mybusiness/edusafety/systemworks/dcpp/SSHAC/workshops/index.shtml.

Guenther, L.D., 2004. "Tectonics of the northern California Coast Ranges, past and present, as inferred from analysis of kinematic data," M.S. thesis, University of California, Davis, 312 pp.

Gutenberg, B., and Richter, C.F., 1944. Frequency of earthquakes in California, *Bulletin of the Seismological Society of America* **34**: 185–188.

Haeussler, P.J., 2009. Surface rupture map of the 2002 M 7.9 Denali fault earthquake, Alaska: Digital data. USGS Data Series 422, 13 pp.

Haeussler, P.J., Schwartz, D.P., Dawson, T.E., Stenner, H.D., Lienkaemper, J.L., Sherrod, B., and 5 others, 2004. Surface rupture and slip distribution of the Denali and Totschunda faults in the 3 November 2002 **M** 7.9 earthquake, Alaska, *Bulletin of the Seismological Society of America* **94** (6B): S23–S52.

Hall, C.A., Jr., 1973. Geologic map of the Morro Bay South and Port San Luis quadrangles, San Luis Obispo County, California: U.S. Geological Survey Miscellaneous Field Studies Map MF-511, scale 1:24,000.

Hall, C.A., Jr.., 1978. Origin and development of the Lompoc-Santa Maria pull-apart basin and its relation to the San Simeon-Hosgri strike-slip fault, western California: in Silver, E.A., and Normark, W.R. (editors), *San Gregorio-Hosgri Fault Zone, California,* California Division of Mines and Geology Special Report 137, pp. 25–32.

Hall, C.A., Jr., 1981. San Luis transform fault and middle Miocene rotation of the western Transverse Ranges, California, *Journal of Geophysical Research* **80** (B2): 1015–1031.

Hall, C.A., Jr., 1982. Pre-Monterey subcrop and structure contour maps, western San Luis Obispo and Santa Barbara counties, south-central California, U.S. Geological Survey Miscellaneous Field Studies, Map MF-1384, 6 sheets, scale 1:62,500, plus text (28 pp.).

Hall, T., Hunt, T.D., and Vaughan, P.R., 1994. Holocene behavior of the San Simeon fault zone, south-central coastal California: in Alterman, I.B., McMullen, R.B., Cluff, L.S., and Slemmons, D.B. (editors*), Seismotectonics of the Central California Coast Ranges*, Geological Society of America Special Papers 292, pp. 167–189.

Hamilton, D.H., 2012a. Direct testimony of Douglas Hamilton, February 10, 2012, Before the Public Utilities Commission of the State of California, Application of Pacific Gas and Electric Company for Approval of Ratepayer Funding to perform Additional Seismic Studies Recommended by the California Energy Commission (U 39), Application No. 10-01-014.

Hamilton, D.H., 2012b. Irish Hills and San Luis Range Fault Model, presentation at DCPP SSHAC Workshop 2, November 6; available at http://www.pge.com/mybusiness /edusafety/systemworks/dcpp/SSHAC/workshops/index.shtml.

Hanks, T.C., 1979. The 1927 Lompoc, California, earthquake (November 4, 1927; *M* = 7.3) and it aftershocks, *Bulletin of the Seismological Society of America* **69** (2): 451–462.

Hanks, T.C., and Bakun, W.H., 2002. A bilinear source-scaling model for **M**–log *A* observations of continental earthquakes, *Bulletin of the Seismological Society of America* **92** (5): 1841–1846.

Hanks, T.C., and Bakun, W.H., 2008. **M**–log *A* observations for recent large earthquakes, *Bulletin of the Seismological Society of America* **98** (1): 490–494.

Hanks, T.C., and Bakun, W.H., 2014. **M**–log*A* models and other curiosities, *Bulletin of the Seismological Society of America* **104** (5): 2604–2610.

Hanks, T.C., and Kanamori, H., 1979. A moment magnitude scale, *Journal of Geophysical Research* **84** (B5): 2348–2350.

Hanks, T., C., Abrahamson, N., A., Boore, D., M., Coppersmith, K., J., Knepprath, N., E., 2009. Implementation of the SSHAC Guidelines for Level 3 and 4 PSHAs—Experience Gained from Actual Applications, U.S. Geological Survey Open-File Report 2009 (1093): 72 pp.

Hanson, K.L., and Lettis, W.R., 1994. Estimated Pleistocene slip rate for the San Simeon fault zone, south-central coastal California: in Alterman, I.B., McMullen, R.B., Cluff, L.S., and Slemmons, D.B. (editors), Seismotectonics of the Central California Coast Range, *Geological Society of America Special Paper* **292**, pp. 133–150.

Hanson, K.L., Wesling, J.R., Lettis, W.R., Kelson, K.I., and Mezger, L., 1994. Correlation, ages, and uplift rates of Quaternary marine terraces, south-central California: in Alterman, I.B., McMullen, R.B., Cluff, L.S., and Slemmons, D.B. (editors), Seismotectonics of the Central California Coast Ranges, *Geological Society of America Special Paper* **292**, pp. 45–72, incl. 2 plates

Hanson, K.L., Lettis, W.R., McLaren, M.K., Savage, W.U., and Hall, N.T., 2004. Style and rate of Quaternary deformation of the Hosgri fault zone, offshore south-central California: in Keller, M.A. (editor), Evolution of Sedimentary Basins/Onshore Oil and Gas Investigations—Santa Maria Province, *U.S. Geological Survey Bulletin* **1995-BB**, 33 pp.

Hardebeck, J.L., 2010. Seismotectonics and fault structure of the California central coast, *Bulletin of the Seismological Society of America* **100** (3): 1031–1050.

Hardebeck, J.L., 2011. Central Coast Focal Mechanisms, PowerPoint presentation at DCPP SSHAC Workshop 1, November 29; available at www.pge.com/mybusiness /edusafety/systemworks/dcpp/SSHAC/workshops/ws1.shtml.

Hardebeck, J.L., 2012a. Evidence against segmented earthquake rupture behavior, presentation at DCPP SSHAC Workshop 2, November 8; available at

http://www.pge.com/mybusiness/edusafety/systemworks/dcpp/SSHAC/workshops/index.shtml.

Hardebeck, J.L., 2012b. Report on Task 2 of Seismic Analyses of the South Central Coast Region, CA. Unpublished report provided to PG&E from U.S. Geological Survey, September 24, 2012, updated October 25, 2012. 5 pp.

Hardebeck, J.L., 2012c. Seismicity of the Shoreline and Hosgri Faults, Estero Bay and Irish Hills, presentation at DCPP SSHAC Workshop 2, November 6; available at http://www.pge.com/mybusiness/edusafety/systemworks/dcpp/SSHAC/workshops/index.shtml.

Hardebeck, J.L., 2013. Geometry and earthquake potential of the Shoreline Fault, Central California, *Bulletin of the Seismological Society of America* **103** (1): 447–462.

Hardebeck, J.L., 2014a. Earthquake epicenter locations in updated seismicity relocation catalog for the California central coast. Unpublished data file dated February 19, provided to PG&E, and provided in this study as *Attachment F-1*.

Hardebeck, J.L., 2014b. Seismicity and Fault Structure of Estero Bay and the Irish Hills, presentation at DCPP SSHAC Workshop 3, March 26; available at http://www.pge.com/mybusiness/edusafety/systemworks/dcpp/SSHAC/workshops/index.shtml.

Hardebeck, J.L., and Michael, A.J., 2006. Damped regional-scale stress inversions: Methodology and examples for southern California and the Coalinga aftershock sequence, *Journal of Geophysical Research* **111** (B11), doi:10.1029/2005JB004144.

Hardebeck, J.L., and Shearer, P.M., 2002. A new method for determining first-motion focal mechanisms, *Bulletin of the Seismological Society of America* **92(6)**: 2264–2276.

Harris, R.A., and Simpson, R.W., 1996. In the shadow of 1857—The effect of the great Ft. Tejon earthquake on subsequent earthquakes in southern California, *Geophysical Research* Letters **23** (3): 229–232.

Hartwell, S.R., Finlayson, D.P., Dartnell, P., and Johnson, S.Y., 2013. *Bathymetry and Acoustic Backscatter—Estero Bay, California*, U.S. Geological Survey Open-File Report 2013–1225.

Hartzell, S.H., and Heaton, T.H., 1983. Inversion of strong ground motion and teleseismic waveform data for the fault rupture history of the 1979 Imperial Valley, California, earthquake, *Seismological Society of America Bulletin* **73** (6): 1553–1583.

Hartzell, S.H., and Helmberger, D., 1982. Strong-motion modeling of the Imperial Valley earthquake of 1979, *Seismological Society of America Bulletin* **92** (2): 571–596.

Hauksson, E., Jones, L.M., and Hutton, K., 2002. The 1999 Mw 7.1 Hector Mine, California, earthquake sequence: complex conjugate strike-slip faulting, *Bulletin of the Seismological Society of America* **92**: 1154–1170.

Hecker, S., Abrahamson, N.A., and Wooddell, K.E., 2013. Variability of displacement at a point: Implications for earthquake-size distribution and rupture hazard on faults, *Bulletin of the Seismological Society of America* **103**: 651–674.

Helmberger, D.V., Somerville, P.G., and Garnero, E., 1992. The location and source parameters of the Lompoc, California, earthquake of 4 November 1927, *Bulletin of the Seismological Society of America* **82**: 1678–1709.

Hornafius, J.S., Luyendyk, B.P., Terres, R.R., and Kamerling, M.J., 1986. Timing and extent of Neogene rotation of western Transverse Ranges, California, *Geological Society of America Bulletin* **97**: 1476–1487.

Hoskins, E.G., and Griffiths, J.R., 1971. Hydrocarbon potential of northern and central California offshore: Region 2: in Cram, I.H. (editor), *Future Petroleum Provinces of the United States—Their Geology and Potential*, Vol. 1, American Association of Petroleum Geologists Memoir 15, pp. 212-228.

Howie, J., M., Miller, K., C., Savage, W., U., 1993. Integrated crustal structure across the south central California margin: Santa Lucia escarpment to the San Andreas Fault, *Journal of Geophysical Research* **98** (B5): 8173–8196.

Irwin, W.P., 1990. Geology and plate-tectonic development, in R.E. Wallace, ed., The San Andreas Fault System, California, *U.S. Geological Survey Professional Paper* 1515, pp. 61–82.

Ishibe, T., and Shimazaki, K., 2012. Characteristic earthquake model and seismicity around late Quaternary active faults in Japan, *Bulletin of the Seismological Society of America* **102** (3): 1041–1058.

Jackson, D.D., and Kagan, Y.Y., 2011. Characteristic earthquakes and seismic gaps: in Gupta, H.K. (editor), *Encyclopedia of Solid Earth Geophysics*, Vol. 1, Springer, pp. 37–40.

Jahns, R.H., 1966. *Geology of the Diablo Canyon Power Plant Site, San Luis Obispo County, California*, December 5.

Jahns, R.H., 1967a. *Geology of the Diablo Canyon Power Plant Site, San Luis Obispo County, California, Supplementary Report*, January 3.

Jahns, R.H., 1967b. *Geology of the Diablo Canyon Power Plant Site, San Luis Obispo County, California, Supplementary Report II*, July 8.

Jahns, R.H., 1968. *Geology of the Diablo Canyon Power Plant Site, San Luis Obispo County, California, Supplementary Report III*, June 19.

Jahns, R.H., Johnson, A.M., Blum, R.L., Korbay, S.R., Hamilton, D.H., and Harding, R.C., 1973. Geologic Map of Diablo Canyon Power Plant Site, unpublished(?) map based on mapping performed 1966-1973 for Pacific Gas and Electric Company, iterations of map used in PG&E (1974) FSAR for Units 1 and 2, approximate scale 1:500.

Jennings, C.W., Strand, R.G., and Rogers, T.H., 1977. Geologic Map of California, California Division of Mines and Geology Map 14, map scale 1:750,000.

Jennings, CW, and Bryant, W.A., compilers, 2010. Fault Activity Map of California, California Geological Survey Geologic Data Map 6, map scale 1:750,000.

Ji, C., Wald, D.J., and Helmberger, D.V., 2002. Source description of the 1999 Hector Mine, California earthquake, Part II: Complexity of slip history, *Bulletin of the Seismological Society of America* **92**: 1208–1226.

Ji, C., Larson, K.M., Tan, Y., Hudnut, K.W., and Choi, K., 2004. Slip history of the 2003 San Simeon earthquake constrained by combining 1-Hz GPS, strong motion, and teleseismic data, *Geophysical Research Letters* **31** (L17608), doi 10.1029/2004GL020448.

Johnson, S.Y., Hartwell, S.R., and Dartnell, P., 2014. Offset of latest Pleistocene shoreface reveal slip rate on the Hosgri strike-slip fault, offshore central California, *Bulletin of the Seismological Society of America* **104** (4): 1650–1662.

Johnson, S.Y., and Watt, J.T., 2012. Influence of fault trend, bends, and convergence on shallow structure and geomorphology of the Hosgri strike-slip fault, offshore central California, *Geosphere* **8** (6): 1632–1656.

Jónsson, S., Zebker, H., Segall, P., and Amelung, F., 2002, Fault slip distribution of the 1999 M_W 7.1 Hector Mine, California, earthquake, estimated from satellite radar and GPS measurements, *Bulletin of the Seismological Society of America* **92** (4): 1377–1389.

Kadinsky-Cade, K., and Reilinger, R., 1985. Surface deformation associated with the November 23, 1977, Caucete, Argentina, earthquake sequence, *Journal of Geophysical Research* **90** (B14): 12,691–12,700.

Kagan, Y.Y., 1993. Statistics of characteristic earthquakes, *Bulletin of the Seismological Society of America* **83** (1): 7–24.

Kame, N., Rice, J.R., and Dmowska, R., 2003. Effects of prestress state and rupture velocity on dynamic fault branching, *Journal of Geophysical Research* **108** (B5): ESE 13 ‑1–ESE 13-21.

Kaverina, A., Dreger, D., and Price, E., 2002. The combined inversion of seismic and geodetic data for the source process of the 16 October 1999 M_W 7.1 Hector Mine, California, earthquake, *Bulletin of the Seismological Society of America* **92** (4): 1266–1280.

Keefer, D.L., and Bodily, S.E., 1983. Three-point approximations for continuous random variables, *Management Science* **29** (5): 595–609.

Khan, S.O., Coe, R.S., Barron, J.A., 2001. Paleomagnetism of the middle-upper Miocene Monterey Formation, Shell Beach, Pismo Basin; implications for the age and origin of the Monterey and tectonic block rotation in central coastal California, *Society of Economic Paleontologists and Mineralogists, Pacific Section* **91**: 302–334.

Krijgsman, W., Hilgen, F.J., Raffi, I., Sierro, F.J., Wilson, D.S., 1999. Chronology, causes and progression of the Messinian salinity crisis, *Nature* **400** (2001): 652–655.

Kurushin, R.A., Bayasgalan, A., Ölziybat, M., Enkhtuvshin, B., Molnar, P., Bayarsaryhan, C., Hudnut, K.W., and Lin, J., 1997. The surface rupture of the 1957 Gobi-Altay, Mongolia, earthquake, *Geological Society of America Special Paper* 320, 143 pp.

Langenheim, V. E., 2012. Late Cenozoic Kinematic Model from Offset Geophysical Anomalies, presentation at DCPP SSHAC Workshop 2, November 7; available at http://www.pge.com/mybusiness/edusafety/systemworks/dcpp/SSHAC/workshops/index.shtml.

Langenheim, V.E., Jachens, R.C., Graymer, R.W., and Wentworth, C.M., 2008. Implications for fault and basin geometry in the central California Coast Ranges from preliminary gravity and magnetic data, *EOS (Abs. AGU), Fall Meeting 2008*, abstract #GP43B-0811.

Langenheim, V.E., Jachens, R.C., and Moussaoui, K., 2009, Aeromagnetic Survey Map of the Central California Coast Ranges: *U.S. Geological Survey Open-File Report 2009-1044*, http://pubs.usgs.gov/of/2009/1044/.

Langenheim, V.E., Jachens, R.C., Graymer, R.W., Colgan, J.P., Wentworth, C.M., and Stanley, R.G., 2012. Fault geometry and cumulative offsets in the central Coast Ranges, California: Evidence for northward increasing slip along the San Gregorio–San Simeon–Hosgri fault, *Lithosphere*, published online as doi: 10.1130/L233.1.

Langenheim, V.E., Watt, J.T., and Denton, K.M., 2012. Magnetic map of the Irish Hills and surrounding areas, San Luis Obispo County, central California: *U.S. Geological Survey Open-File Report 2012-1080*, scale 1:24,000; http://pubs.usgs.gov/of/2012/1080/.

Leonard, M., 2010. Earthquake fault scaling: Self-consistent relating of rupture length, width, average displacement, and moment release, *Bulletin of the Seismological Society of America* **100** (5A): 1971–1988.

Lettis, W.R., 2012. Geometric and Kinematic Models of the Irish Hills, presentation at DCPP SSHAC Workshop 2, November 6; available at

http://www.pge.com/mybusiness/edusafety/systemworks/dcpp/SSHAC/workshops/index.shtml.

Lettis, W.R., and Hall, N.T., 1994. Los Osos fault zone, San Luis Obispo County, California: in Alterman, I.B., McMullen, R.B., Cluff, L.S., and Slemmons, D.B. (editors), Seismotectonics of the Central California Coast Ranges, *Geological Society of America Special Paper* 292, pp. 73–102.

Lettis, W.R., and Hanson, K.L., 1991. Crustal strain partitioning—Implications for seismic hazard assessment in Western California, *Geology* **19**: 559–562.

Lettis, W.R., and Hanson, K.L., 1992. Quaternary tectonic influences on coastal morphology, south-central California, *Quaternary International* **15/16**: 135–148.

Lettis, W.R., Hanson, K.L., Unruh, J.R., McLaren, M.K., Savage, W.U., 2004. Quaternary Tectonic Setting of South-Central Coastal California, *U.S. Geological Survey Bulletin* **1995-AA**: 1–21.

Lettis, W.R., Kelson, K.I., Wesling, J.R., Angell, M., Hanson, K.L., and Hall, N.T., 1994. Quaternary deformation of the San Luis Range, San Luis Obispo County, California: in Alterman, I.B., McMullen, R.B., Cluff, L.S., and Slemmons, D.B. (editors), Seismotectonics of the Central California Coast Ranges, *Geological Society of America Special Paper* **292**, pp. 111–132.

Lettis, W.R., Unruh, J.R., and Hanson, K.L., 2009. Quaternary Tectonic Setting of South-Central Coastal California, *Seismological Research Letters* **80** (2): 323.

Lewandowski, N., 2014. Analysis of Stress and Strain in the Central Coast, California, presentation at DCPP SSHAC Workshop 3, March 25; available at http://www.pge.com/mybusiness/edusafety/systemworks/dcpp/SSHAC/workshops/index.shtml.

Lin, A., Ouchi, T., Chen, A., and Maruyama, T., 2001. Co-seismic displacements, folding and shortening structures along the Chelungpu surface rupture zone occurred during the 1999 Chi-Chi (Taiwan) earthquake, *Tectonophysics* **330**: 225–244.

Lisiecki, L.E., and Raymo, M.E., 2005. A Pliocene-Pleistocene stack of 57 globally distributed benthic $\delta^{18}O$ records, *Paleoceanography* **20** (1), doi:10.1029/2004PA001071.

Lobo, F.J., Maldonado, A., Hernández-Molina, F.J., Fernández-Salas, L.M., Ercilla, G., and Alonso, B., 2008. Growth patterns of a proximal terrigenous margin offshore the Guadalfeo River, northern Alboran Sea (SW Mediterranean Sea): Glacio-eustatic control and disturbing tectonic factors, *Marine Geophysical Researches* **29** (3): 195–216.

Lobo, F.J., and Ridente, D., 2014. Stratigraphic architecture and spatio-temporal variability of high-frequency (Milankovitch) depositional cycles on modern continental margins: An overview, *Marine Geology* **352**: 215-247.

Lozos, J., Oglesby, D., Duan, B., and Wesnousky, S., 2011. The effects of double fault bends on rupture propagation: a geometrical parameter study, *Bulletin of the Seismological Society of America* **101**: 385–398.

Luyendyk, B.P., 1991. A model for Neogene crustal rotations, transtension, and transpression in southern California, *Geological Society of America Bulletin* **103** (11): 1528–1536.

Luyendyk, B.P., Kamerling, M.J., Terres, R.R., Hornafius, J.S., 1985. Simple shear of southern California during Neogene time suggested by Paleomagnetic declinations, *Journal of Geophysical Research* **90** (B14): 12454–12466.

Madden, E.H., and Pollard, D.D., 2012. Integration of surface slip and aftershocks to constrain the 3D structure of faults involved in the *M* 7.3 Landers earthquake, Southern California, *Bulletin of the Seismological Society of America* **102** (1): 321–342.

Manighetti, I., Campillo, M., Bouley, S., and Cotton, F., 2007. Earthquake scaling, fault segmentation, and structural maturity, *Earth and Planetary Science Letters* **253** (3): 429–438.

Marshall, S.T., Funning, G.J., and Owen, S.E., 2013. Fault slip rates and interseismic deformation in the western Transverse Ranges, California, *Journal of Geophysical Research: Solid Earth* **118** (8): 4511–4534.

Maselli, V., Trincardi, F., Cattaneo, A., Ridente, D., and Asioli, A., 2010. Subsidence pattern in the central Adriatic and its influence on sediment architecture during the last 400 ka, *Journal of Geophysical Research* **115** (B12), doi:10.1029/2010JB007687.

Matsuda, T., Yamazaki, H., Nakata, T., and Imaizumi, T., 1980. The surface faults associated with the Rikuu Earthquake of 1896, *Bulletin of Earthquake Research Institute, University of Tokyo,* **55**, 795–855.

Matthews, M.V., Ellsworth, W.L. and Reasenberg, P.A., 2002. A Brownian model for recurrent earthquakes, *Bulletin of the Seismological Society of America* **92** (6): 2233–2250.

McCaffrey, R., 1997. Statistical significance of the seismic coupling coefficient, *Bulletin of the Seismological Society of America* **87** (4): 1069–1073.

McCaffrey, R., 2005. Block kinematics of the Pacific–North America plate boundary in the southwestern United States from inversion of GPS, seismological, and geologic data, *Journal of Geophysical Research* **110** (B7), doi:10.1029/2004JB003307.

McCulloch, D.S., 1987. Regional geology and hydrocarbon potential of offshore central California: in Scholl, D.W., Grantz, A., and Vedder, J.G. (editors), *Geology and Resource Potential of the Western North America and Adjacent Ocean Basins—Beaufort Sea to Baja California*, Earth Science Series Book 6, Chap. 16, pp. 353–361.

McCulloch, D.S., 1989. Evolution of the offshore central California margin: in Winterer, E.L., Hussong, D.M., and Decker, R.W. (editors), *The Eastern Pacific Ocean and Hawaii*, The Geology of North America, Vol. N, Geological Society of America, Boulder, Colo., pp. 439–469.

McCulloch, D.S., Greene, H.G., Heston, K.S., and Rubin, D.M., 1980. A Summary of the Geology and Geologic Hazards in Proposed Lease Sale 53, Central California Outer Continental Shelf, U.S. Geological Survey Open-File Report 80-1095, 76 pp, 12 plates.

McHugh, C.M., Hartin, C.A., Mountain, G.S., and Gould, H.M., 2010. The role of glacio-eustasy in sequence formation: Mid-Atlantic Continental Margin, USA, *Marine Geology* **277** (1-4): 31-47.

McIntosh, K.D., Reed, D.L., Silver, E.A., and Meltzer, A.S., 1991. Deep structure and structural inversion along the central California continental margin from EDGE seismic profile RU-3, *Journal of Geophysical Research* **96** (B4): 6459–6473.

McLaren, M.K., 2011. Central Coast Seismic Networks and Earthquake Catalogs, presentation at DCPP SSHAC Workshop 1, November 29; available at http://www.pge.com/mybusiness/edusafety/systemworks/dcpp/SSHAC/ workshops /index.shtml

McLaren, M.K., and Savage, W.U., 2001. Seismicity of south-central coastal California: October 1987 through January 1997, *Bulletin of the Seismological Society of America* **91**(6): 1629–1658.

McLaren, M.K., Hardebeck, J.L., van der Elst, N., Unruh, J.R., Bawden, G.W., Blair, J.L., 2008. Complex Faulting Associated with the 22 December 2003 Mw 6.5 San Simeon, California Earthquake, Aftershocks and Postseismic Surface Deformation, *Bulletin of the Seismological Society of America* **98** (4): 1659–1680.

Meigs, A.J., and Oskin, M.E., 2002, Convergence, block rotation, and structural interference across the Peninsular-Transverse Ranges boundary, eastern Santa Monica Mountains, California, in Barth, A., ed., Contributions to Crustal Evolution of the Southwestern United States: Boulder, Colorado, Geological Society of America Special Paper 365, p. 279–293.

Meltzer, A.S., Levander, A.R., 1991. Deep crustal reflection profiling offshore southern central California, *Journal of Geophysical Research* **96** (B4): 6475–6491.

Miller, A.C., and Rice, T.R., 1983. Discrete approximation of probability distributions, *Management Science* **29**: 352–362.

Miller, K.C., and Meltzer, A.S., 1999. Structure and Tectonics of the Central Offshore Santa Maria and Santa Lucia Basins, California: Results from the PG&E/EDGE Seismic Reflection Survey: in Keller, M.A. (editor), *Evolution of Sedimentary Basins/Offshore*

Oil and Gas Investigations—Santa Maria Province, U.S. Geological Survey Bulletin **1995-Z**, 12 pp.

Miller, K.C., Howie, J.M., and Ruppert, S.D., 1992. Shortening within underplated oceanic crust beneath the central California margin. *Journal of Geophysical Research: Solid Earth (1978–2012)*, **97** (B13), 19961–19980.

Miller, K.G., Wright, J.D., Browning, J.V., Kulpecz, A., Kominz, M., Naish, T.R., Cramer, B.S., Rosenthal, Y., Peltier, W.R., and Sosdian, S., 2012. High tide of the warm Pliocene: Implications of global sea level for Antarctic deglaciation, *Geology* **40**: 407–410.

Mooney, W.D., 2011. Deep, High-Energy Seismic Reflection and Refraction Data: Status and Gaps, presentation at DCPP SSHAC Workshop 1, November 29; available at http://www.pge.com/mybusiness/edusafety/systemworks/dcpp/SSHAC/workshops/index.shtml.

Muhs, D.R., Kennedy, G.L., and Rockwell, T.K., 1988. Uranium-series ages of corals from marine terraces, Pacific coast of North America: Implications for timing and magnitude of late Pleistocene sea-level changes, *American Quaternary Association Program and Abstracts, 10th Biennial Meeting*, p. 140.

Muhs, D.R., Rockwell, T.K., and Kennedy, G.L., 1992, Late Quaternary uplift rates of marine terraces on the Pacific Coast of North America, southern Oregon to Baja California Sur: Quaternary International **15/16**; 121–123.

Muhs, D.R., Simmons, K.R., Kennedy, G.L., and Rockwell, T.K., 2002. The last interglacial period on the Pacific Coast of North America: Timing and paleoclimate, *Geological Society of America Bulletin* **114** (5): 569–592.

Muhs, D.R., Simmons, K.R., Schumann, R.R., Groves, L.T., Laurel, D., and Mitrovica, J.X., 2012. Sea-level history during the Last Interglacial complex on San Nicolas Island, California: Implications for glacial isostatic adjustment processes, paleozoogeography and tectonics, *Quaternary Science Reviews* **37**: 1–25.

Muhs, D.R., Wehmiller, J.F., Simmons, K.R., and York, L.L., 2004. Quaternary sea-level history of the United States, *Developments in Quaternary Science* **1**: 147–183.

Murray, R.W., 2012. Regional Deformation and Kinematics from GPS Data, presentation at DCPP SSHAC Workshop 2, November 7; available at http://www.pge.com/mybusiness/edusafety/systemworks/dcpp/SSHAC/workshops/index.shtml.

Murray-Moraleda, J.R., Svarc, J., Onishi, T., and Thatcher, W., 2011. An Interseismic Velocity Field for the Central California Coast Region Derived from Global Positioning System Measurements, unpublished report provided to PG&E from U.S. Geological Survey, January 25, 90 pp.

Namson, J.S., and Davis, T.L., 1990. Late Cenozoic fold and thrust belt of the southern Coast Ranges and Santa Maria Basin, California, *AAPG Bulletin* **74** (4): 467–492.

New Sense Geophysics, 2010. *Point Buchon: Helicopter aeromagnetic geophysical survey for Pacific Gas and Electric Company, December 2nd– December 5th, 2009.* PG&E No. 2500257867, NSG No. HM191015, Toronto, Canada, 40 pp.

Nicholson, C., Sorlien, C.C., Atwater, T., Crowell, J.C., Luyendyk, B.P., 1994. Microplate capture, rotation of the Western Transverse Ranges, and initiation of the San Andreas transform as a low-angle fault system, *Geology* **22**: 491–495.

Nitchman, S.P., 1988. "Tectonic Geomorphology and Neotectonics of the San Luis Range, San Luis Obispo County, California," M.S. thesis, Reno University of Nevada, 120 pp.

Nitchman, S.P., and Slemmons, D.B., 1994. The Wilmar Avenue fault: A late Quaternary reverse fault near Pismo Beach, California: in Alterman, I.B., McMullen, R.B., Cluff, L.S., and Slemmons, D.B. (editors), *Seismotectonics of the Central California Coast Range*, Geological Society of America Special Paper 292, pp. 103–110.

Northern California Earthquake Data Center (NCEDC), 2010. Northern California Earthquake Catalog Search, http://www.ncedc.org/ncedc/catalog-search.html, accessed September 2010.

Northern California Earthquake Data Center (NCEDC), 2013. Northern California Earthquake Catalog Search, http://www.ncedc.org/ncedc/catalog-search.html, accessed December 2013.

Onderdonk, N.W., 2007. Vertical-axis rotation controlled by upper crustal stress based on force balance analysis: A case study of the western Transverse Ranges of California, *Tectonophysics* **436**: 1–8.

Ouillon, G., Ducorbier, C., and Sornette, D., 2008. Automatic reconstruction of fault networks from seismicity catalogs: Three-dimensional optimal anisotropic dynamic clustering, *Journal of Geophysical Research: Solid Earth* **113** (B1), doi:10.1029/2007JB005032.

Pacific Gas and Electric Company (PG&E), 1973. Section 2.5, Geology and Seismology, Final Safety Analysis Report, Units 1 and 2, Diablo Canyon Site: U.S. Atomic Energy Commission Docket nos. 50-275 and 50-323.

Pacific Gas and Electric Company (PG&E), 1974. Units 1 and 2 Diablo Canyon Power Plant, Final Safety Analysis Report, Update 20, U.S. Nuclear Regulatory Commission Docket Nos. 50-275 and 50-323, Also includes Earth Science Associates, 1974, Geologic Map of the Morro Bay South and Point San Luis Quadrangles, San Luis Obispo County, California, and Adjacent Offshore Area, Plate VIII, Appendix 2.5D, scale 1:24,000.

Pacific Gas and Electric Company (PG&E), 1975. Appendix 2.5E, Final Safety Analysis Report for Diablo Canyon Nuclear Power Plant: U.S. Atomic Energy Commission Docket Nos. 50-275 and 50-323.

Pacific Gas and Electric Company (PG&E), 1988. Final Report of the Diablo Canyon Long Term Seismic Program, Diablo Canyon Power Plant, U.S. Nuclear Regulatory Commission Docket Nos. 50-275 and 50-323.

Pacific Gas and Electric Company (PG&E), 1990a. Montage of geophysical data and interpretations, Hosgri fault zone, eastern offshore Santa Maria Basin data base, interpretational procedures, and key observations: Response to Nuclear Regulatory Commission question GSG-01A, Diablo Canyon Power Plant Long Term Seismic Program, Docket Nos. 50-275 and 50-323.

Pacific Gas and Electric Company (PG&E), 1990b. Response to Nuclear Regulatory Commission Questions GSG-13 on the Final Report of the Diablo Canyon Long Term Seismic Program, U.S. Nuclear Regulatory Commission Docket Nos. 50-275 and 50-323.

Pacific Gas and Electric Company (PG&E), 1990c. Response to Nuclear Regulatory Commission Question GSG-16 on the Final Report of the Diablo Canyon Long Term Seismic Program, U.S. Nuclear Regulatory Commission Docket Nos. 50-275 and 50-323.

Pacific Gas and Electric Company (PG&E), 1991. Addendum to the 1988 Final Report of the Diablo Canyon Long Term Seismic Program, report to the U.S. Nuclear Regulatory Commission, February.

Pacific Gas and Electric Company (PG&E), 2004. Final safety analysis report of the Diablo Canyon independent spent fuel storage installation, U.S. Nuclear Regulatory Commission Docket No. 72-26, Figures 2-6.6, 2.6-7, and 2.6-8.

Pacific Gas and Electric Company (PG&E), 2011. Report on the Analysis of the Shoreline Fault Zone, Central Coastal California, report to the U.S. Nuclear Regulatory Commission, January; www.pge.com/myhome/edusafety/systemworks/dcpp/shorelinereport/.

Pacific Gas and Electric Company (PG&E), 2011. Appendix B: Onshore-Offshore Geologic Map of the Shoreline Fault Zone Study Area, San Luis Obispo: in Report on the Analysis of the Shoreline Fault Zone, Central Coastal California, report to the U.S. Nuclear Regulatory Commission, January; available at http://www.pge.com/myhome/edusafety/systemworks/dcpp/shorelinereport/

Pacific Gas and Electric Company (PG&E), 2011. Appendix I: Identification, mapping, and analysis of offshore wave-cut platforms and strandlines (Paleoshorelines) in the Shoreline fault zone study area, San Luis Obispo County, California: in Report on the Analysis of the Shoreline Fault Zone, Central Coastal California, report to the U.S. Nuclear Regulatory Commission, January; available at http://www.pge.com/myhome/edusafety/systemworks/dcpp/shorelinereport/

Pacific Gas and Electric Company (PG&E), 2013a. *Stratigraphic Framework for Assessment of Fault Activity Offshore of the Central California Coast Between Point San Simeon and Point Sal*, PG&E Technical Report GEO.DCPP.TR.13.01, 76 pp.

Pacific Gas and Electric Company (PG&E), 2013b. *Quaternary Geomorphic Analysis of fluvial and Marine Terraces in the Los Osos and Edna Valley, San Luis Obispo County, California.* PG&E Technical Report GEO.DCPP.TR.13.02, 104 pp.

Pacific Gas and Electric Company (PG&E), 2014. Central Coastal California Seismic Imaging Project (CCCSIP), report to the California Public Utilities Commission; available at http://www.pge.com/en/safety/systemworks/dcpp/seismicsafety/report.page.

Pacific Gas and Electric Company (PG&E), 2014. Chapter 2: *DCPP 3D/2D Seismic-Reflection Investigation of Structures Associated with the Northern Shoreline Seismicity Sublineament of the Point Buchon Region*, PG&E Technical Report GEO.DCPP.TR.12.01, 53 pages, 3 plates, and 1 appendix: in *Central Coastal California Seismic Imaging Project*, report to the California Public Utilities Commission; available at www.pge.com/en/safety/systemworks/dcpp/seismicsafety/report.page.

Pacific Gas and Electric Company (PG&E), 2014. Chapter 3: *Offshore Low-Energy Seismic-Reflection Studies in Estero Bay, San Luis Obispo Bay, and Point Sal Areas*, PG&E Technical Report GEO.DCPP.TR.14.02, 178 pages, 8 plates, and 1 appendix: in *Central Coastal California Seismic Imaging Project*, report to the California Public Utilities Commission; available at www.pge.com/en/safety/systemworks/dcpp/seismicsafety/report.page.

Pacific Gas and Electric Company (PG&E), 2014. Chapter 4: Interpretation of Seismic-Reflection Data, Point Buchon to San Simeon Point, PG&E Technical Report GEO.DCPP.TR.14.05: in *Central Coastal California Seismic Imaging Project*, report to the California Public Utilities Commission; available at www.pge.com/en/safety/systemworks/dcpp/seismicsafety/report.page.

Pacific Gas and Electric Company (PG&E), 2014. Chapter 7: *ONSIP 2011 Data Report*, PG&E Technical Report GEO.DCPP.TR.14.03, 77 pages, 6 plates: in *Central Coastal California Seismic Imaging Project*, report to the California Public Utilities Commission; available at www.pge.com/en/safety/systemworks/dcpp/seismicsafety/report.page.

Pacific Gas and Electric Company (PG&E), 2014. Chapter 8: *2012 3D Onshore Seismic Survey Report*, Fugro PGEQ-PR-21 R0, 81 pages, 1 appendix: in *Central Coastal California Seismic Imaging Project*, report to the California Public Utilities Commission; available at www.pge.com/en/safety/systemworks/dcpp/seismicsafety/report.page.

Pacific Gas and Electric Company (PG&E), 2014. Chapter 9: *Geologic Mapping and Data Compilation for the Interpretation of Onshore Seismic-Reflection Data*, PG&E Technical Report GEO.DCPP.TR.14.01, 61 pages, 2 plates, 5 appendices: in *Central Coastal California Seismic Imaging Project*, report to the California Public Utilities

Commission; available at www.pge.com/en/safety/systemworks/dcpp/seismicsafety/report.page.

Pacific Gas and Electric Company (PG&E), 2014. Chapter 12: *Response to Administrative Law Judge's Decision Number 12-09-008 Regarding Dr. Douglas Hamilton's Concerns*, PG&E Technical Report GEO.DCPP.TR.14.07, 82 pages: in *Central Coastal California Seismic Imaging Project*, report to the California Public Utilities Commission; available at www.pge.com/en/safety/systemworks/dcpp/seismicsafety/report.page.

Pacific Gas and Electric Company (PG&E), 2015a. Seismic Hazard and Screening Report, Diablo Canyon Power Plant Units 1 and 2, Response to Request for Information Pursuant to Title 10 of the Code of Federal Regulations 50.54(f) Regarding Fukushima Near-Term Task Force Recommendation 2.1: Seismic, report to the U.S. Nuclear Regulatory Commission, March.

Pacific Gas and Electric Company (PG&E), 2015b. *Analysis of Stress and Strain in the Central Coast, California*, unpublished consulting report, 46 pp., January.

Pacific Northwest National Laboratory (PNNL), 2014. *Hanford Site-Wide Probabilistic Seismic Hazard Analysis*, Report No. PNNL-SA-2361, prepared for the U.S. Department of Energy under Contract DE-AC06076RL01830 and Energy Northwest, 10 volumes plus appendices.

Page, B.M., Thompson, G.A., Coleman, R.G., 1998. Late Cenozoic tectonics of the central and southern Coast Ranges of California, *Geological Society of America Bulletin* **110** (7): 846–890.

Page, B.M., Wagner, H.C., McCulloch, D.S., Silver, E. A., Spotts, J. H., 1979. Tectonic interpretation of a geologic section of the continental margin off San Luis Obispo, the southern Coast Ranges, and the San Joaquin Valley, California: Cross-section summary, *Geological Society of America Bulletin*, Part 1, v. 90, p. 808–812.

Page, M.T., Alderson, D., and Doyle, J., 2011. The magnitude distribution of earthquakes near Southern California faults, *Journal of Geophysical Research* **116** (B12), doi:10.1029/2010JB007933**.**

Page, M.T., Field, E.H., Milner, K.R., and Powers, P.M., 2013. Grand Inversion Implementation and Testing: in Field, E.H., Biasi, G.P., Bird, P., Dawson, T.E., Felzer, K.R., Jackson, D.D., Johnson, K.M., and 11 others, *Uniform California Earthquake Rupture Forecast, Version 3 (UCERF3)—The Time-Independent Model*, U.S. Geological Survey Open-File Report 2013-1165, Appendix N, 38 pp., California Geological Survey Special Report 228, and Southern California Earthquake Center Publication 1792; available at pubs.usgs.gov/of/2013/1165/pdf/ofr2013-1165_appendixN.pdf.

Page, M.T., Field, E.H., Milner, K.R., and Powers, P.M., 2014. The UCERF3 grand inversion: solving for the long-term rate of ruptures in a fault system, *Bulletin of the Seismological Society of America* **104** (3): 1181–1204.

Parsons, T., and Geist, E.L., 2009. Is there basis for preferring characteristic earthquakes over Gutenberg-Richter distributions on individual faults in probabilistic earthquake forecasting? *Bulletin of the Seismological Society of America* **99** (3): 2012–2019.

Petersen, M.D., Frankel, A.D., Harmsen, S.C., Mueller, C.S., Haller, K.M., Wheeler, R.L., Wesson, R.L., and 7 others, 2008. *Documentation for the 2008 Update of the United States National Seismic Hazard Maps*, U.S. Geological Survey Open-File Report 2008-1128, 61 pp.

Petersen, M.D., Mueller, C.S., Frankel, A.D., and Zeng, Y., 2008b. Appendix J—Spatial Seismicity Rates and Maximum Magnitudes for Background Earthquakes: in Field, E.H., Dawson, T.E., Felzer, K.R., and 8 others [2007 Working Group on California Earthquake Probabilities], 2008. *The Uniform California Earthquake Rupture Forecast, Version 2 (UCERF 2)*, USGS Open File Report 2007-1437, CGS Special Report 203, and SCEC Contribution 1138, 8 pp.

Petersen, M.D., Moschetti, M.P., Powers, P.M., Mueller, C.S., Haller, K.M., Frankel, A.D., Zeng, Y., and 10 others, 2014. *Documentation for the 2014 Update of the United States National Seismic Hazard Maps*, U.S. Geological Survey Open-File Report 2014-1091, 243 pp.; *pubs.usgs.gov/of/2014/1091/pdf/ofr2014-1091.pdf.*

Pollitz, F.F., and Sacks, I.S., 2002. Stress triggering of the 1999 Hector Mine earthquake by transient deformation following the 1992 Landers earthquake, *Bulletin of the Seismological Society of America* **92** (4): 1487–1496.

Powers, P.M., and Field, E.H., 2013. Appendix O—Gridded Seismicity Sources: in Field, E.H., Biasi, G.P., Bird, P., Dawson, T.E., Felzer, K.R., Jackson, D.D., Johnson, K.M., and 11 others [Working Group on California Earthquake Probabilities], 2013. *Uniform California Earthquake Rupture Forecast, Version 3 (UCERF3)—The Time-Independent Model*, U.S. Geological Survey Open-File Report 2013-1165; available at http://pubs.usgs.gov/of/2013/1165/.

Putzig, N.E., 1988. Modeling wide-angle seismic data from the central California margin, Rice University: 214 pp.

Rabineau, M., Berné, S., Aslanian, D., Olivet, J.-L., Joseph, P., Guillocheau, F., Bourillet, J.F., Le Drezen, E., and Granjeon, D., 2005. Sedimentary sequences in the Gulf of Lion: A record of 100,000 years climatic cycles, *Marine and Petroleum Geology* **22**: 775-804.

Rabineau, M., Berné, S., Olivet, J., Aslanian, D., Guillocheau, F., and Joseph, P., 2006. Paleo sea levels recognized from direct observation of paleoshoreline during Glacial Maxima (for the last 500,000 yr), *Earth and Planetary Science Letters* **252** (1-2): 119-137.

Reasenberg, P.A., 1985. Second-order moment of central California seismicity, 1969-1982, *Journal of Geophysical Research* **90** (B7): 5479-5495.

Reasenberg, P.A. and Oppenheimer, D., 1985. FPFIT, FPPLOT, FPPAGE: Fortran computer programs for calculating and displaying earthquake fault-plane solutions, Open-File Report 85-739, U.S. Geological Survey.

Regnier, M., Chatelain, J.L., Smalley, R., Jr., Chiu, J.-M, Isacks, B.L., and Araujo, M., 1992. Seismotectonics of Sierra Pie de Palo, a basement block uplift in the Andean foreland of Argentina, *Bulletin of the Seismological Society of America* **82** (6): 2549–2571.

Reis, A.T., Maia, R.M.C., Silva, C.G., Rabineau, M., Guerra, J.V., Gorini, C., Arantes-Oliveira, M., Benabdellouahed, M., Simões, I., and Tardin, R., 2013. Origin of step-like and lobate seafloor features along the continental shelf off Rio de Janeiro State, Santos basin-Brazil, *Geomorphology* **203**: 25–45.

Richmond, W.C., Burdick, D.J., Phillips, D., and Norris, P.J., 1981. *Regional Geology, Seismicity, and Potential Geologic Hazards and Constraints, OCS Oil and Gas Lease Sale 53, Northern and Central California*, USGS Open File Report 81-318, 39 pp.

Ridente, D., Petrungaro, R., Falese, F., and Chiocci, F.L., 2012. Middle–Upper Pleistocene record of 100-ka depositional cycles on the Southern Tuscany continental margin (Tyrrhenian Sea, Italy): Sequence architecture and margin growth pattern, Marine Geology 326-328: 1–13.

Ridente, D., Trincardi, F., Piva, A., Asioli, A., and Cattaneo, A., 2008. Sedimentary response to climate and sea level change during the past ~400 ka from borehole PRAD1-2 (Adriatic margin), *Geochemistry, Geophysics, Geosystems* **9** (9), doi:10.1029/2007GC001783.

Ritz, J.-F., Vassallo, R., Braucher, R., Brown, E.T., Carretier, S., and Bourlès, D.L., 2006. Using in situ-produced ^{10}Be to quantify active tectonics in the Gurvan Bogd mountain range (Gobi-Altay, Mongolia): in Alonso-Zarza, A.M., and Tanner, L.H. (editors), *In Situ–Produced Cosmogenic Nuclides and Quantification of Geological Processes*, Geological Society of America Special Papers 415, pp. 87–110.

Roberts, D.L., Karkanas, P., Jacobs, Z., Marean, C.W., and Roberts, R.G., 2012. Melting ice sheets 400,000 years ago raised sea level by 13 m: Past analogue for future trends, *Earth and Planetary Science Letters* **357/358**: 226-237.

Rockwell, T., Vaughn, P.R., Bickner, F., and Hanson, K.L., 1994. Correlation and age estimates of soils developed in marine terraces across the San Simeon fault zone, central California: in Alterman, I.B., McMullen, R.B., Cluff, L.S., and Slemmons, D.B. (editors), *Seismotectonics of the Central California Coast Ranges*, Geological Society of America Special Papers 292, pp. 151–166.

Rockwell, T.K., Dawson, T.E., Young, J., and Seitz, G., 2014. A 21-event, 4,000-year history of surface ruptures in the Anza seismic gap, San Jacinto fault and implications for long-term earthquake production on a major plate boundary fault, *Pure and Applied Geophysics*, doi:10.1007/s00024-014-0955-z.

Rockwell, T.K., and Klinger, Y., 2013. Surface rupture and slip distribution of the 1940 Imperial Valley earthquake, Imperial fault, southern California: Implications for rupture segmentation and dynamics, *Bulletin of the Seismological Society of America* **103** (2A), 629–640.

Rockwell, T.K., Lindvall, S., Herzberg, M., Murbach, D., Dawson, T., and Berger, G., 2000. Paleoseismology of the Johnson Valley, Kickapoo, and Homestead Valley faults: Clustering of earthquakes in the eastern California shear zone, *Bulletin of the Seismological Society of America* **90** (5): 1200–1236.

Rockwell, T.K., Nolan, J.M., Johnson, D.L., and Patterson, R.H., 1992. Ages and deformation of marine terraces between Point Conception and Gaviota, western Transverse Ranges, California: in Fletcher, C.H., III, and Wehmiller, J.F. (editors), *Quaternary Coasts of the United States: Marine and Lacustrine Systems*, SEPM (Society for Sedimentary Geology) Special Publication 48, pp. 333-341.

Rolandone, F., Bürgmann, R., and Nadeau, R.M., 2004. The evolution of the seismic-aseismic transition during the earthquake cycle: Constraints from the time-dependent depth distribution of aftershocks, *Geophysical Research Letters* **31** (23), doi:10.10292004GL021379.

Rolandone, F., Dreger, D., Murray, M., and Bürgmann, R., 2006. Coseismic slip distribution of the 2003 M_w 6.6 San Simeon earthquake, California, determined from GPS measurements and seismic waveform data, *Geophysical Research Letters* **33** (16), doi:10.10292006GL027079.

Ryan, H.F., Parsons, T., and Sliter, R.W., 2008. Vertical tectonic deformation associated with the San Andreas fault zone offshore of San Francisco, California, *Tectonophysics* **457** (3): 209–223.

Salisbury, J.B., Rockwell, T.K., Middleton, T.J., and Hudnut, K.W., 2012. LiDAR and field observations of slip distribution for the most recent surface ruptures along the central San Jacinto fault, *Bulletin of the Seismological Society of America* **102** (2): 598–619.

Satake, K., and Somerville, P., 1992. Location and size of the 1927 Lompoc, California earthquake from tsunami data, *Bulletin of the Seismological Society of America* **82**: 1710–1725.

Scharer, K.M., 2013. New paleoseismic data from SoSAFE: time dependency and rupture patterns on the San Andreas and San Jacinto Faults, *Southern California Earthquake Center Annual Meeting, 2013, Proceedings Volume XXIII,* p. 76.

Scharer, K.M., Biasi, G.P., Weldon, R.J., II, and Fumal, T.E., 2010. Quasi-periodic recurrence of large earthquakes on the southern San Andreas fault, *Geology* **38** (6): 555–558.

Scharer, K., Weldon, R., II, Streig, A., and Fumal, T., 2014. Paleoearthquakes at Frazier Mountain, California delimit extent and frequency of past San Andreas fault ruptures along 1857 trace, *Geophysical Research Letters* **41** (13): 4527–4534.

Scholz C.H., 1998. Earthquakes and friction laws, *Nature* **391**: 37–42.

Schwartz, D.P., 2012. Fault Segmentation and Its Application to Predicting Fault Rupture, presentation at DCPP SSHAC Workshop 2, November 8; available at http://www.pge.com/mybusiness/edusafety/systemworks/dcpp/SSHAC/workshops/index.shtml.

Schwartz, D.P., and Coppersmith, K.J., 1984. Fault behavior and characteristic earthquakes: Examples from the Wasatch and San Andreas fault zones, *Journal of Geophysical Research* **89** (B7): 5681–5698.

Schwartz, D.P., and Coppersmith, K.J., 1986. Seismic hazards: New trends in analysis using geologic data: in The Geophysics Study Committee (editor), *Studies in Geophysics, Active Tectonics*, National Academy Press, Washington, D.C., pp. 215–230.

Schwartz, D.P., Haeussler, P.J., Seitz, G.G., and Dawson, T.E., 2012. Why the 2002 Denali fault rupture propagated onto the Totschunda fault: Implications for fault branching and seismic hazards, *Journal of Geophysical Research* **117 (**B11), doi:10.1029/2011JB008918, 25 pp.

Sedlock, R.L., and Hamilton, D.H., 1991. Late Cenozoic tectonic evolution of southwestern California, *Journal of Geophysical Research* **96**: 2325–2351.

Sharp, R.V., Lienkaemper, J.J., Bonilla, M.G., Burke, D.B., Fox, B.F., Herd, D.G., Miller, D.M., Morton, D.M., Ponti, D.J., Rymer, M.J., Tinsley, J.C., Yount, J.C., Kahle, J.E., Hart, E.W., and Sieh, K.E., 1982. Surface faulting in the central Imperial Valley: in *The Imperial Valley Earthquake of October 15, 1979*, U.S. Geological Survey Professional Paper 1254, pp. 119–143.

Shaw, B.E., 2009. Constant stress drop from small to great earthquakes in magnitude-area scaling, *Bulletin of the Seismological Society of America* **99** (2A): 871–875.

Shaw, B.E., 2013. Appendix E—Evaluation of Magnitude-Scaling Relationships and Depth of Rupture: in Field, E.H., Biasi, G.P., Bird, P., Dawson, T.E., Felzer, K.R., Jackson, D.D., Johnson, K.M., and 11 others [Working Group on California Earthquake Probabilities], 2013. *Uniform California Earthquake Rupture Forecast, Version 3 (UCERF3)—The Time-Independent Model*, U.S. Geological Survey Open-File Report 2013-1165, 23 pp.

Sibson, R.H., 1982. Fault zone models, heat flow, and the depth distribution of earthquakes in the continental crust of the United States, *Bulletin of the Seismological Society of America* **72** (1): 151–163.

Sibson, R.H., 1986. Earthquakes and rock deformation in crustal fault zone, *Annual Review of Earth and Planetary Sciences* **14**: 149–175.

Sieh, K., 1996. The repetition of large-earthquake ruptures, *Proc. Natl. Acad. Sci. USA* **93**: 3764–3771.

Sieh, K., Jones, L., Hauksson, E., Hudnut, K., Eberhart-Phillips, D., Heaton, T., Hough, S., and 13 others, 1993. Near-field investigations of the Landers earthquake sequence, April to July 1992, *Science* **260**: 171–176.

Simons, M., Fialko, Y., and Rivera, L., 2002, Coseismic deformation from the 1999 M_W 7.1 Hector Mine, California, earthquake as inferred from InSAR and GPS observations, *Bulletin of the Seismological Society of America* **92** (4): 1390–1402.

Sliter, R.W., Triezenberg, P.J., Hart, P.E., Watt, J.T., Johnson, S.Y., and Scheirer, D.S., 2010. *High-Resolution Seismic Reflection and Marine Magnetic Data Along the Hosgri Fault Zone, Central California*, U.S. Geological Survey Open-File Report 2009-1100, version 1.1; available at pubs.usgs.gov/of/2009/1100.

Somerville, P., 2011. Analysis of inhibition of faulting at fault branches: in Pacific Gas and Electric Company, *Report on the Analysis of the Shoreline Fault Zone, Central Coastal California*: *Report to the U.S. Nuclear Regulatory Commission*, Appendix J, 22 pp., January; available at www.pge.com/myhome/edusafety/systemworks/dcpp/shorelinereport/.

Sorlien, C., 2012. Late Cenozoic kinematic model for transfer of strain along the California margin, presentation at DCPP SSHAC Workshop 2, November 7; available at http://www.pge.com/mybusiness/edusafety/systemworks/dcpp/SSHAC/workshops/index.shtml.

Sorlien, C.C., Kamerling, M.J., and Mayerson, D., 1999. Block rotation and termination of the Hosgri strike-slip fault, California, from three-dimensional map restoration, *Geology* **27** (11): 1039–1042.

Sorlien, C.C., Nicholson, C., and Luyendyk, B.P., 1999. *Miocene Extension and Post-Miocene Transpression Offshore of South-Central California* (including Plate 1 [Seismic Reflection Profiles]), U.S. Geological Survey Bulletin 1995-Y: 1–38.

Sowers, J.M., Unruh, J.R., Lettis, W.R., and Rubin, T.D., 1994. Relationship of the Kickapoo fault to the Johnson Valley and Homestead Valley faults, San Bernardino County, California, *Bulletin of the Seismological Society of America* **84**: 528–536.

Stanford, J.D., Hemingway, R., Rohling, E.J., Challenor, P.G., Medina-Elizalde, M., and Lester, A.J., 2011. Sea-level probability for the last deglaciation: A statistical analysis of far-field records, *Global and Planetary Change* **79** (3-4): 193–203.

Stanley, K. O., and Surdam, R. C., 1984. The role of wrench fault tectonics and relative changes of sea level on deposition of upper Mio-Pliocene Pismo Formation, Pismo Syncline, California, in, Surdam, R. C., ed., Stratigraphic, Tectonic, Thermal, and Digenetic Histories of the Monterey Formation, Pismo and Huasna Basin, California, *Society of Economic Paleontologists and Mineralogists Guidebook, No. 2*, San Jose, California, pp. 21–37.

Stein, M., Wasserburg, G.J., Lajoie, K.R., and Chen, J.H., 1991. U-series ages of solitary corals from the California coast by mass spectrometry, *Geochimica et Cosmochimica Acta* **55**: 3709–3722.

Steritz, J.W., Luyendyk, B.P., 1994. Hosgri Fault Zone, Offshore Santa Maria Basin, California, *Geological Society of America Special Paper* (292): 191–209.

Stirling, M.W., Gerstenberger, M.C., Litchfield, N.J., McVerry, G.H., Smith, W.D., Pettinga, J., and Barnes, P., 2008. Seismic hazard of the Canterbury region, New Zealand: New earthquake source model and methodology, *Bulletin of the New Zealand National Society for Earthquake Engineering* **41** (2): 51–67.

Stirling, M.W., Wesnousky, S.G., and Shimizaki, K., 1996. Fault trace complexity, cumulative slip, and the shape of the magnitude-frequency distribution for strike-slip faults: A global survey, *Geophysical Journal International* **124** (3): 833–868.

Sylvester, A.G., and Darrow, A.C., 1979. Structure and neotectonics of the western Santa Ynez fault system in southern California. *Tectonophysics*, **52** (1), 389–405.

Tanaka, A., 2004. Geothermal gradient and heat flow data in and around Japan (II): Crustal thermal structure and its relationship to seismogenic layer, *Earth, Planets, and Space* **56**: 1195–1199.

Tanaka, A., and Ito, H., 2002. Temperature at the base of the seismogenic zone and its relationship to the focal depth of the western Nagano Prefecture area, *Journal of the Seismological Society of Japan* **55**: 1–10 (in Japanese with English abstract).

Titus, S.J., Crump, S., McGuire, Z., Horsman, E., Housen, B., 2011. Using vertical axis rotations to characterize off-fault deformation across the San Andreas fault system, central California, *Geology* **39** (8): 711–714.

Toppozada, T.R., Branum, D.M., Reichle, M.S., and Hallstrom, C.L., 2002. San Andreas fault zone, California: M ≥ 5.5 earthquake history, *Bulletin of the Seismological Society of America* **92** (7): 2555–2601.

Toppozada, T.R., Real, C.R., and Parke, D.L., 1981. *Preparation of Isoseismal Maps and Summaries of Reported Effects for Pre-1900 California Earthquakes*, California Division of Mines and Geology Open-File Report 81-11, 182 pp.

Trehu, A.M., 1991. Tracing the subducted oceanic crust beneath the central California continental margin: Results from ocean bottom seismometers deployed during the 1986 Pacific Gas and Electric EDGE experiment, *Journal of Geophysical Research* **96** (B4): 6493–6506.

Trehu, A.M., and Wheeler, W.H., 1987. Seismic reflection profile across the Coast Ranges of central California, Morro Bay to the San Andreas fault, *U.S. Geological Survey Miscellaneous Field Studies Map*.

Treiman, J.A., Kendrick, K.J., Bryant, W.A. Bryant, Rockwell, T.K., and McGill, S.F., 2002. Primary surface rupture associated with the Mw 7.1 16 October 1999 Hector Mine earthquake, San Bernadino County, California, *Bulletin of the Seismological Society of America* **92**: 1171–1191.

Trifunac, M.D., and Brune, J.N., 1970. Complexity of energy release during the Imperial Valley, California, earthquake of 1940, *Bulletin of the Seismological Society of America* **60** (1): 137–160.

Twiss, R.J., Souter, B.J., and Unruh, J.R., 1993. The effect of block rotations on the global seismic moment tensor and patterns of seismic P and T axes, *Journal of Geophysical Research* **98**: 645–674.

Twiss, R.J., and Unruh, J.R., 1998. Analysis of fault-slip inversions: do they constrain stress or strain rate? *Journal of Geophysical Research* **103**: 12,205–12,222.

U.S. Nuclear Regulatory Commission (NRC), 1991. Diablo Canyon SSER 34 (Safety Evaluation Report Related to the Operation of Diablo Canyon Nuclear Power Plant, Units 1 and 2, Docket Nos. 50-275 and 50-323, NUREG-0675, Supplement No. 34), USNRC NULL (NULL): 353 pp.

U.S. Nuclear Regulatory Commission (NRC), 2007. Regulatory Guide 1.208: A Performance-Based Approach to Define the Site-Specific Earthquake Ground Motion, Regulatory Guide Published by the U.S. Nuclear Regulatory Commission. 53 p. Available for download at http://www.nrc.gov/reading-rm/doc-collections/reg-guides/power-reactors/rg/01-208/01-208.pdf

U.S. Nuclear Regulatory Commission (NRC), 2012a. Request for Information Pursuant to Title 10 of the Code of Federal Regulations 50.54 (f) Regarding Recommendations 2.1, 2.3, and 9.3 of the Near-Term Task Force Review of Insights from the Fukushima Dai-ichi Accident, ADAMS Accession No. ML12056A046, Washington, D.C.

U.S. Nuclear Regulatory Commission (NRC). 2012b. Practical Implementation Guidelines for SSHAC Level 3 and 4 Hazard Studies. NUREG-2117, Rev 1, U.S. Nuclear Regulatory Commission, Washington, D.C.

U.S. Nuclear Regulatory Commission (NRC), 2012c. Research Information Letter 12 001, Confirmatory Analysis of Seismic Hazard at the Diablo Canyon Power Plant from the Shoreline Fault Zone, ADAMS Accession No. ML121230035, Washington, D.C.

Unruh, J.R., 2014. PG&E 2011 Onshore Seismic Interpretation Program (ONSIP), presentation at DCPP SSHAC Workshop 3, March 26; available at http://www.pge.com/mybusiness/edusafety/systemworks/dcpp/SSHAC/workshops/index.shtml.

Ustaszewski, K., Schumacher, M.E., Schmid, S.M., and Nieuwland, D., 2005. Fault reactivation in brittle-viscous wrench systems—Dynamically scaled analogue models and application to the Rhine-Bresse transfer zone, *Quaternary Science Reviews* **24**: 365–382.

Vassallo, R., Ritz, J.-F., Braucher, R., and Carretier, S., 2005. Dating faulted alluvial fans with cosmogenic ^{10}Be in the Gurvan Bogd mountain (Gobi-Altay, Mongolia): Climatic and tectonic implications, *Terra Nova* **17** (3): 278–285.

Waelbroeck, C., Labeyrie, L., Michel, E., Duplessy, J.C., McManus, J.F., Lambeck, K., Balbon, E., and Labracherie, M., 2002. Sea-level and deep water temperature changes derived from benthic foraminifera isotopic records, *Quaternary Science Reviews* **21**: 295–305.

Waldhauser, F. and Ellsworth, W.L., 2000. A double-difference earthquake location algorithm: Method and application to the northern Hayward fault, California, *Bulletin of the Seismological Society of America* **90** (6): 1353–1368.

Watt, J.T., 2012. Gravity and magnetic constraints for the Hosgri and Shoreline faults, presentation at DCPP SSHAC Workshop 2, November 6; available at http://www.pge.com/mybusiness/edusafety/systemworks/dcpp/SSHAC/workshops/index.shtml.

Watt, J.T., Johnson, S.Y., Hartwell, S.R., and Roberts, M., in prep. Offshore geology and geomorphology maps from Piedras Blancas to Pismo Beach, San Luis Obispo and Santa Barbara counties, California: U.S. Geological Survey Scientific Investigations Map XXXX, pamphlet XX p., 6 sheets, 1:35,000 scale, and database, available at http://pubs.usgs.gov/sim/XXXX/

Webb, T.H., Somerville, P.G., Doser, D.I., Rhoades, A., and Pancha, A., 1999. Moment-Area Scaling of Crustal Earthquakes in New Zealand, prepared for the Electricity Corporation of New Zealand Ltd. and Institute of Geological & Nuclear Sciences Ltd. Client Report No. 1999/119.

Weber, G.E., 1983. *Geologic Investigation of the Marine Terraces of the San Simeon Region and Pleistocene Activity on the San Simeon Fault Zone, San Luis Obispo County, California*, U.S. Geological Survey Technical Report, 66 pp.

Weichert, D.H., 1980. Estimation of the earthquake recurrence parameters for unequal observation periods for different magnitudes, *Bulletin of the Seismological Society of America* **70** (4): 1337-1346.

Weldon, R.J., Dawson, T.E., Biasi, G., Madden, C., and Streig, A.R., 2013. Appendix G—Paleoseismic Sites Recurrence Database: in Field, E.H., Biasi, G.P., Bird, P., Dawson, T.E., Felzer, K.R., Jackson, D.D., Johnson, K.M., and 11 others [Working Group on California Earthquake Probabilities], 2013. *Uniform California Earthquake Rupture Forecast, Version 3 (UCERF3)—The Time-Independent Model*, U.S. Geological Survey Open-File Report 2013-1165, 73 pp.

Wells, D.L, and Coppersmith, K.J., 1994. New empirical relationships among magnitude, rupture length, rupture width, rupture area, and surface displacement, *Bulletin of the Seismological Society of America* **84** (4): 974–1002.

Wesnousky, S.G., 2006. Predicting the endpoints of earthquake ruptures, *Nature* **444**: 358–360.

Wesnousky, S.G., 2008. Displacement and geometrical characteristics of earthquake surface ruptures: Issues and implications for seismic-hazard analysis and the process of earthquake rupture, *Bulletin of the Seismological Society of America* **98**: 1609–1632.

Wesnousky, S.G., and Biasi, G.P., 2011. The length to which an earthquake will go to rupture, *Bulletin of the Seismological Society of America* **101** (4): 1948–1950.

Wesnousky, S.G., Scholz, C.H., Shimazaki, K., and Matsuda, T., 1983. Earthquake frequency distribution and the mechanics of faulting, *Journal of Geophysical Research* **88**: 9331–9340.

Wiegers, M.O., 2009. Geologic Map of the Morro Bay South 7.5′ Quadrangle, San Luis Obispo County, California: A Digital Database, Version 1.0, scale 1:24,000, California Geological Survey.

Wiegers, M.O., 2010. Geologic Map of the San Luis Obispo 7.5′ Quadrangle, San Luis Obispo County, California: A Digital Database, Version 1.0, scale 1:24,000, California Geological Survey.

Wiegers, M.O., 2011. Preliminary Geologic Map of the Pismo Beach 7.5′ Quadrangle, San Luis Obispo County, California: A Digital Database, Version 1.0, scale 1:24,000, California Geological Survey.

Wiegers, M.O., 2013. Preliminary Geologic Map of the Arroyo Grande NE 7.5′ Quadrangle, San Luis Obispo County, California: A Digital Database, Version 1.0, scale 1:24,000, California Geological Survey.

Willingham, C.R., Rietman, J.D., Heck, R.G., and Lettis, W.R., 2013. Characterization of the Hosgri Fault Zone and adjacent structures in the offshore Santa Maria Basin, south-central California: in Keller, M.A. (editor), *Evolution of Sedimentary Basins/Onshore Oil and Gas Investigations—Santa Maria Province*, U.S. Geological Survey Bulletin 1995-CC, 105 pp.

Wilson, D.S., 1993. Confirmation of the Astronomical Calibration of the Magnetic Polarity Timescale from Sea-Floor Spreading Rates, *Nature* **364**: 788–790.

Wilson, D.S., McCrory, P.A., Stanley, R.G., 2005. Implications of volcanism in coastal California for the Neogene deformation history of western North America, *Tectonics* **24** (3): 1–22.

Wolf, S.C., and Wagner, H.C., 1970. Preliminary Reconnaissance Marine Geology of Area Between Santa Lucia Escarpment and Point Buchon, California, unpublished U.S. Geological Survey administrative report, 5 pp.

Wooddell, K., 2011. Sensitivity Studies, presentation at DCPP SSHAC Workshop 1, November 29; available at http://www.pge.com/mybusiness/edusafety/systemworks/dcpp/SSHAC/workshops/index.shtml.

Wooddell, K., and Abrahamson, N., 2013. Constraints on magnitude-frequency distributions for evaluating the hazard of multi-segment ruptures, abstract, Annual Meeting of the Seismological Society of America, April 19.

Working Group on California Earthquake Probabilities (WGCEP), 2003. *Earthquake Probabilities in the San Francisco Bay Region: 2002–2031*, U.S. Geological Survey Open-File Report 03-214, 253 pp.

Yeats, R.S., Sieh, K., and Allen, C.R., 1997. *The Geology of Earthquakes*, Oxford University Press, New York, 568 pp.

Yen, Y.T., and Ma, K.F., 2011. Source-scaling relationship for M 4.6–8.9 earthquakes, specifically for earthquakes in the collision zone of Taiwan, *Bulletin of the Seismological Society of America* **101** (2): 464–481.

Youngs, R.R., and Coppersmith, K.J., 1985. Implications of fault slip rates and earthquake recurrence models to probabilistic hazard estimates, *Bulletin of the Seismological Society of America* **75**: 939–964.

Youngs, R.R., Coppersmith, K.J., Taylor, C.J., Power, M.S., DiSilvestro, L.A., Angell, M.I., Hall, N.T., Wesling, J.R., and Mualchin, L., 1992. A comprehensive seismic hazard model for the San Francisco Bay region: in Borchardt, G., Hirschfeld, S.E., Lienkaemper, J.J., McClellan, P., Williams, P.L., and Wong, I.G. (editors), *Proceedings of the Second Conference on Earthquake Hazards in the Eastern San Francisco Bay Area*, Special

Publication 113, pp. 431-441, California Division of Conservation, Division of Mines and Geology, Sacramento, Calif.

Zechar, J.D., and Frankel, K.L., 2009. Incorporating and reporting uncertainties in fault slip rates, *Journal of Geophysical Research* **114** (B12), doi:10.1029/2009JB006325.

Zeng, Y., and Shen, Z.K., 2014. Fault network modeling of crustal deformation in California constrained using GPS and geologic observations, *Tectonophysics* **612-613**: 1–17.

Zhang, H., and Thurber, C.H., 2003. Double-difference tomography: The method and its application to the Hayward Fault, California, *Bulletin of the Seismological Society of America* **93** (5): 1875–1889.